NASA/CR—2012-217415

Flow Control Under Low-Pressure Turbine Conditions Using Pulsed Jets

Final Report

Ralph J. Volino
United States Naval Academy, Annapolis, Maryland

Mounir B. Ibrahim
Cleveland State University, Cleveland, Ohio

September 2012

NASA STI Program . . . in Profile

Since its founding, NASA has been dedicated to the advancement of aeronautics and space science. The NASA Scientific and Technical Information (STI) program plays a key part in helping NASA maintain this important role.

The NASA STI Program operates under the auspices of the Agency Chief Information Officer. It collects, organizes, provides for archiving, and disseminates NASA's STI. The NASA STI program provides access to the NASA Aeronautics and Space Database and its public interface, the NASA Technical Reports Server, thus providing one of the largest collections of aeronautical and space science STI in the world. Results are published in both non-NASA channels and by NASA in the NASA STI Report Series, which includes the following report types:

- TECHNICAL PUBLICATION. Reports of completed research or a major significant phase of research that present the results of NASA programs and include extensive data or theoretical analysis. Includes compilations of significant scientific and technical data and information deemed to be of continuing reference value. NASA counterpart of peer-reviewed formal professional papers but has less stringent limitations on manuscript length and extent of graphic presentations.

- TECHNICAL MEMORANDUM. Scientific and technical findings that are preliminary or of specialized interest, e.g., quick release reports, working papers, and bibliographies that contain minimal annotation. Does not contain extensive analysis.

- CONTRACTOR REPORT. Scientific and technical findings by NASA-sponsored contractors and grantees.

- CONFERENCE PUBLICATION. Collected papers from scientific and technical conferences, symposia, seminars, or other meetings sponsored or cosponsored by NASA.

- SPECIAL PUBLICATION. Scientific, technical, or historical information from NASA programs, projects, and missions, often concerned with subjects having substantial public interest.

- TECHNICAL TRANSLATION. English-language translations of foreign scientific and technical material pertinent to NASA's mission.

Specialized services also include creating custom thesauri, building customized databases, organizing and publishing research results.

For more information about the NASA STI program, see the following:

- Access the NASA STI program home page at *http://www.sti.nasa.gov*

- E-mail your question to *help@sti.nasa.gov*

- Fax your question to the NASA STI Information Desk at 443–757–5803

- Telephone the NASA STI Information Desk at 443–757–5802

- Write to:
  STI Information Desk
  NASA Center for AeroSpace Information (CASI)
  7115 Standard Drive
  Hanover, MD 21076–1320

NASA/CR—2012-217415

Flow Control Under Low-Pressure Turbine Conditions Using Pulsed Jets

Final Report

Ralph J. Volino
United States Naval Academy, Annapolis, Maryland

Mounir B. Ibrahim
Cleveland State University, Cleveland, Ohio

Prepared under NASA Interagency Agreement No. NNC07IA10I
(through U.S. Navy Agreement No. N00189–07–P–A253)

National Aeronautics and
Space Administration

Glenn Research Center
Cleveland, Ohio 44135

September 2012

Acknowledgments

This research was made possible by a NASA Interagency Agreement No. NNC07IA10I (through U.S. Navy Agreement No. N00189–07–P–A253), awarded in response to NASA Research Announcement (NRA) solicitation (2006). The research was in support of the Subsonic Fixed-Wing Project of NASA's Fundamental Aeronautics Program. The period of performance was January 2007 to September 2010. The following served as the Technical Officers (Technical Monitors or COTR's): Anthony J. Strazisar, James D. Heidmann, and David E. Ashpis, NASA Glenn Research Center. The authors appreciated their support, as well as useful discussions and comments. American Society of Mechanical Engineers (ASME) permission to reproduce copyrighted material is greatly appreciated.

This work was sponsored by the Fundamental Aeronautics Program at the NASA Glenn Research Center.

Level of Review: This material has been technically reviewed by NASA technical management.

Available from

NASA Center for Aerospace Information
7115 Standard Drive
Hanover, MD 21076–1320

National Technical Information Service
5301 Shawnee Road
Alexandria, VA 22312

Available electronically at http://www.sti.nasa.gov

Flow Control Under Low-Pressure Turbine Conditions Using Pulsed Jets

Ralph J. Volino
United States Naval Academy
Annapolis, Maryland 21402

Mounir B. Ibrahim
Cleveland State University
Cleveland, Ohio 44115

Summary

In this study the effects of unsteady wakes and flow control using vortex generator jets (VGJs) were studied experimentally and computationally on the flow over a low pressure turbine airfoil. High loading is desirable for turbomachinery airfoils to reduce the number of airfoils and stages required to produce a given amount of power. Reducing the number of airfoils can reduce cost and weight and lead to increased efficiency. Increased loading, however, can lead to boundary layer separation as the magnitude of the adverse pressure gradients on the suction side of the airfoils is increased. Separation leads to loss of lift and increased aerodynamic losses, which reduce power and efficiency. The focus of the present study is on the low pressure turbine (LPT). The LPT is the heaviest component in an engine and produces the net output power. Any improvements to LPT weight and efficiency therefore have a large impact on overall engine performance. Boundary layer separation is a particular problem in the LPT because Reynolds numbers are typically low, particularly in aircraft engines at altitude, where the low density of the air can result in very low Reynolds numbers. The focus of the present work is avoiding or controlling separation while maintaining high loading. Work was done under simulated LPT conditions using a modern, very highly loaded airfoil.

The airfoil selected for the study is the L1A, which was designed at the Air Force Research Laboratory. It is an aft loaded design with very high lift (Zweifel=1.35). Aft loading is desirable in that it reduces the strength of secondary flows, but it also requires a strong adverse pressure gradient on the downstream section of the airfoil, which makes the boundary layer more likely to separate. The L1A was designed specifically to provide a challenging case for separation control. In steady flow without flow control, the flow over the L1A is well behaved at high Reynolds numbers, but at low Reynolds numbers the boundary layer separates from the suction side of the airfoil and does not reattach. This results in a partial loss of lift and very high aerodynamic losses.

An experimental facility consisting of a six passage linear cascade in a low speed wind tunnel was constructed and used in the experimental study at the U.S. Naval Academy. In the first phase of the work, the flow through the cascade was documented under steady inflow conditions without flow control. Reynolds numbers (based on suction surface length and nominal exit velocity from the cascade) ranged from 25,000 to 300,000. Inlet freestream turbulence levels of 0.6% and 4% were used. For $Re \geq 200{,}000$ the separation bubble was small. For $Re \leq 50{,}000$ the boundary layer separated and did not reattach. The boundary layer was laminar at separation and transition to turbulence occurred in the separated shear layer in all cases. Transition did not cause reattachment at the low Reynolds numbers. This result contrasted with previous work on less aggressive airfoils, in which transition in the shear layer forced reattachment. With the L1A, the adverse pressure gradient is so strong that turbulence in the shear layer is not always able to force reattachment. At intermediate Reynolds numbers reattachment depended on the freestream turbulence. With high freestream turbulence the shear layer was more likely to reattach after a large separation bubble, while with low freestream turbulence it was more likely to remain separated. Large separation bubbles resulted in a large increase in profile loss by a factor of up to 5, a reduction in flow turning of as much as 16 degrees, and a reduction in lift of up to 20%.

In parallel with the experimental work, computational work was done at Cleveland State University. Reynolds Averaged Navier Stokes (RANS) calculations were done using a variety of turbulence models. With most models, transition was predicted too early, and separation was not predicted, even at low Reynolds numbers. Two models, the Standard k-ω model with shear stress transport (SKW-SST) and the four equation Transition shear stress transport model (Transition-SST) did better. Of these two, the Transition-SST model generally gave results in better agreement with the experiments. Over the full range of Reynolds numbers, with only a few exceptions, the separation bubble locations were predicted correctly as were the total pressure loss profiles, the pressure distributions on the airfoil, the transition locations, and the mean velocity profiles in the boundary layer. The Transition-SST model was developed using data from flows over less aggressive airfoils, so it was encouraging that it performed well predicting the flow over the L1A without any modification to the model.

In the next phase of the work, flow control was added using vortex generator jets. Each blade in the cascade had a central cavity to which compressed air was supplied through high speed solenoid valves. A spanwise row of small holes was drilled into the suction side of each blade at the streamwise location corresponding to the inviscid pressure minimum. The holes had a compound angle of 90 degrees to the main flow and 30 degrees to the surface, and extended into the central cavity. When air was supplied to the cavity, vortex generator jets were produced from the small holes. By pulsing the supply air, the VGJs could be pulsed. Cases were documented with different combinations of VGJ amplitudes, pulsing frequencies, and duty cycles. Reynolds numbers from 25,000 to 100,000 were considered under both high and low free-stream turbulence conditions. Measurements were the same as in the baseline cases, and the velocity measurements were also ensemble averaged at different phases within the jet pulsing cycle. The VGJs successfully suppressed separation and reduced aerodynamic losses. General observations were that the vortex generator jets control separation if they are of high enough amplitude and pulsing frequency. Steady jets tend to delay separation, but the boundary layer does still separate at low Reynolds numbers. Blowing ratios (jet velocity/local freestream velocity) of 2 to 3 were needed to achieve any separation control at the lowest Reynolds number. Pulsed jets are more effective than steady jets, allowing control with lower velocity jets. The jet mass flow requirements are very low, and the required jet velocities are low enough to be practically feasible in most cases. With a dimensionless frequency ($F=fL_{j\text{-}te}/U_{ave}$ where f is the pulsing frequency, $L_{j\text{-}te}$ is the distance from the jets to the trailing edge, and U_{ave} is the average freestream velocity) of 0.5 or higher with Re=25,000, separation could be controlled with a blowing ratio of 1. When Re=50,000, a dimensionless pulsing frequency of 0.3 was adequate with a blowing ratio of 1. At lower frequencies it was sometimes possible to achieve partial control, particularly if higher blowing ratios were used. Once separation was fully controlled, increasing the pulsing frequency or blowing ratio further had no additional benefit. Freestream turbulence had some effect in reducing separation, but the effect was small in comparison to the VGJ effect.

Numerical simulations of cases with VGJs showed that unsteady RANS (URANS) calculations with the Transition-SST model failed to predict reattachment for cases in which the VGJs caused reattachment in the experiments. Although the Transition-SST model worked well without the VGJs, it failed to capture the effect of the jets. Large Eddy Simulations (LES) were then tried, and the results were generally better. Although the match to the experiments was not perfect, the LES generally predicted separation and reattachment in the correct cases to match the experiments.

Cases with VGJs were followed by cases with unsteady wakes. A wake generator was constructed and installed in the wind tunnel. The wake generator had two chains which formed loops around the cascade near the top and bottom endwalls. Each chain traversed around a drive gear and six idler sprockets. The drive gears were on a common axle, so both chains moved together. The top and bottom chains were connected by carbon fiber rods which were spaced between 1 and 2 blade spacings apart. The rods moved across the inlet of the cascade, 0.54 axial chord upstream of the leading edges, and then returned to complete the loop downstream of the cascade. The rod shed wakes which simulated the wakes from an upstream blade row. Rod speed was set to produce flow coefficients ranging from 0.35 to 1.4. Cases were documented with various flow coefficients and rod spacings at Re=25,000 and 50,000 under both high and low background freestream turbulence conditions. A photo detector was used to

sense the passing of each wake, and the voltage signal from the photo detector was digitized along with hot wire data so that velocity results could be ensemble averaged at different phases within the wake passing events. The wakes caused the boundary layer to reattach, but if the time between wakes was sufficiently long, the boundary layer would separate. In agreement with the VGJ results, a dimensionless rod passing frequency, F (defined as described above for the pulsed VGJs), of about 0.5 was sufficient to keep the boundary layer attached over most of the airfoil surface when Re=25,000. For Re=50,000, a dimensionless wake passing frequency of 0.3 was sufficient. Whether the frequency was achieved by increasing the rod speed or by decreasing the rod spacing did not appear to matter. As with the VGJs, high background freestream turbulence had some effect in reducing separation, but the effect was small in comparison to the wake effect. The turbulence level in the rod wakes was about 14% at the leading edge of the cascade regardless of whether the turbulence level between wakes was low (0.6%) or high (4%).

Cases with wakes were simulated using URANS and LES. Both were able to capture the wake effect and generally predicted separation and reattachment to occur in the right cases to match those experiments simulated. Quantitatively the results were mixed. In some cases the match between the calculations and experiments were good for pressure and velocity results, but in other cases there were significant differences.

In the final phase of the study, wakes and VGJs were combined. The valves controlling the VGJs were triggered and timed using the signal from the photo detector used to sense the wake passing. Various timings were used for the VGJs with respect to the wakes, including cases in which the jet pulses coincided with the wakes and cases with the jets occurring between wakes. Cases with multiple jet pulses for each wake were also considered. Cases were acquired for Re=25,000 and 50,000 with both low and high background freestream turbulence. The timing of the jets with respect to the wakes had some effect, but in general once the disturbance frequency was high enough to control separation, the timing was not very important. Results were nearly identical for otherwise similar low and high freestream turbulence cases, indicating that the wake and VGJ effects overwhelmed the effect of the background turbulence.

Contents of the Report

Most of the results of the present study, including description of the experiments and computations, have been provided in a series of technical papers that were published during the course of the study. These papers were peer reviewed for various conferences and several have also become journal publications. These papers are included in this report as the primary documentation of the work. The final report is divided into three separate NASA Contractor Reports prepared under NASA Interagency Agreement No. NNC07IA10I (NASA/CR—2012-217415, NASA/CR—2012-217416, and NASA/CR—2012-217417). The following sections comprise Part I (NASA/CR—2012-217415) of this report:

1. Brief description of experimental facility with pictures that did not appear in other publications.
2. List of experimental cases.
3. Lists of conference and journal papers.
4. Appendix A—Reprints of Papers and Publications.
    a. Copies of conference papers.
    b. Copies of journal papers.
5. Appendix B—Additional Information.
    a. Measurements of transient velocity during VGJ pulses measured with the main flow in the wind tunnel turned off.
    b. Discussion and figures for cases with VGJs and cases with wakes including data that did not all appear in other papers. Included are figures showing the effect of changing VGJ spanwise spacing.
    c. Phase averaged boundary layer velocity and turbulence profiles for cases with VGJs and wakes combined that did not all appear in other papers.
    d. Phase averaged velocity and turbulence contours from downstream of the cascade for cases with VGJs and wakes combined that did not all appear in other papers.

In addition to this written report, a supplementary CD–ROM is available containing data files with processed experimental data from the study and text files with explanations of the file formats for the data. The CD–ROM can be obtained from the Center for AeroSpace Information (CASI) Web site at http://www.sti.nasa.gov.

Parts II and III of the reports, contained in separate volumes (NASA/CR—2012-217416 and NASA/CR—2012-217417), are the following Ph.D. dissertation and M.S. thesis, respectively. These reports are also on the CD–ROM mentioned above.

> Kartuzova, Olga V. "A Computational Study for the Utilization of Jet Pulsations in Gas Turbine Film Cooling and Flow Control," Ph.D. Dissertation, Cleveland State University, May 2010 (NASA/CR—2012-217416).
>
> Vinci, Samuel J. "CFD Simulations for the Effect of Unsteady Wakes on the Boundary Layer of a Highly Loaded Low Pressure Turbine Airfoil (L1A)," M.S. thesis, Cleveland State University, May 2011 (NASA/CR—2012-217417).

1. Experimental Facility and Measurements

Experiments were conducted in the low speed, recirculating wind tunnel shown in Fig. 1.1. An axial fan sends air through a turn, where it passes through a heat exchanger. The heat exchanger maintains steady uniform temperature throughout the flow. The flow then moves through a second turn, where it passes through a honeycomb and screens before entering a three dimensional contraction. It then enters an 18- by 18-ft test section. This test section is not used in the present study. The flow then passes through a shallow angle diffuser which expands the flow area to 29- by 29-ft as it enters the wind tunnel's third turn. The third turn contains the cascade test section as shown in Fig. 1.2. A fine screen or course grid is placed in the plane between the diffuser and corner test section to break up the thick boundary layers which grow in the diffuser. This provides a uniform flow with low (0.6%) freestream turbulence in the case of the screen, or high (4%) freestream turbulence in the case of the grid. More about the screen, grid, freestream turbulence, and cascade is provided in the papers below. The flow exits the corner test section and passes through turning vanes in the wind tunnel's fourth turn before returning to the fan.

Fig. 1.1: Recirculating wind tunnel.

Fig. 1.2: Corner cascade test section, a) test section with fine screen visible at exit of diffuser and hardware below test section for producing pulsed VGJs, b) top view of cascade blades, c) view of cascade from upstream, d) view of cascade from downstream with traverse for probe movement to the right.

Figure 1.3 shows the pressure regulator, manifolds and solenoid valves used to produce the VGJs. Compressed air is supplied through a pressure regulator to one of the manifolds (black rectangular bars) shown in the figure. Two valves operating in parallel connect the two manifolds. The second manifold supplies air through separate tubes to each of the cascade blades. Each of the blades has a central cavity which receives the air, as described in the papers below. The frequency and timing of the jet pulsing is set with a controller that drives the solenoid valves. Frequencies ranging from 3 to 48 Hz were used in the study. The velocity of the jets is controlled with the pressure regulator. The cavity in the center blade of the cascade has a tap which was used to measure cavity pressure. Air was supplied to the cavity in calibration tests with the main flow in the wind tunnel off. The instantaneous velocity of the VGJ jets was measured with a hot film probe with short sensor length. Examples of these velocity traces are provided in the last section of this report. Cavity pressure and jet velocity were both measured for all combinations of jet velocity, pulsing frequency and duty cycle used in subsequent experiments. In the experiments with the wind tunnel running, the difference between the cavity pressure and the local static pressure of the blade surface at the VGJ exit was measured and set to produce the desired jet velocity based on the earlier calibration.

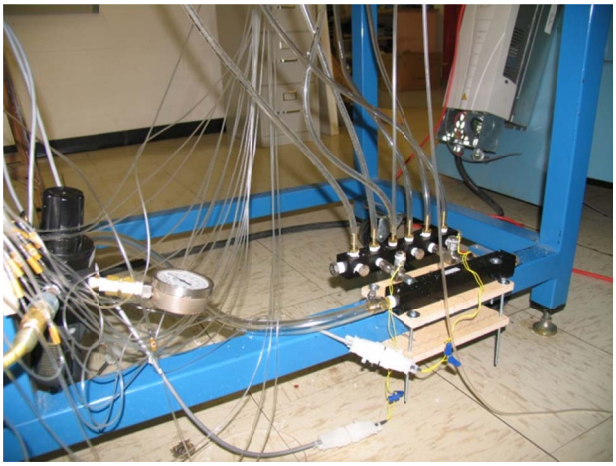

Fig. 1.3: Pressure regulator, manifolds and solenoid valves for VGJ control.
Tubes lead upward from one manifold to the cascade blades.

a) 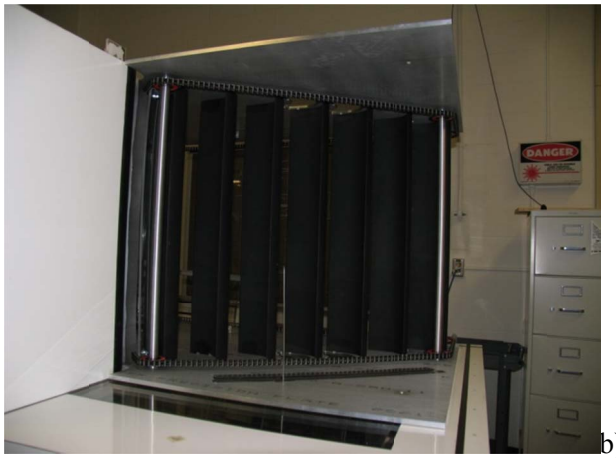

b) 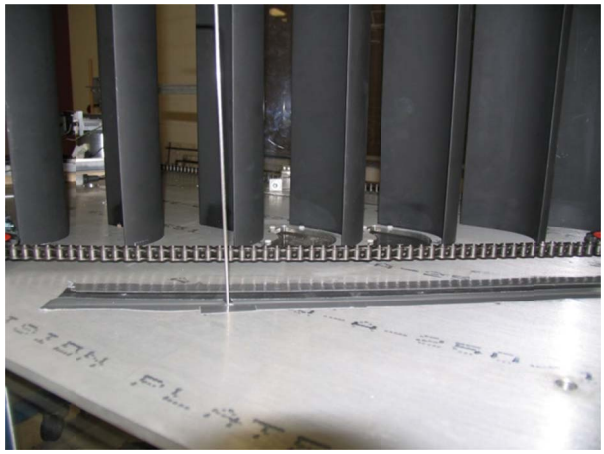

c) 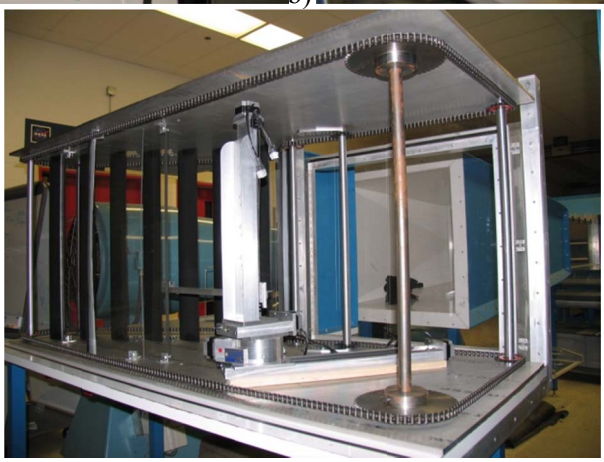

Fig. 1.4: Wake generator during assembly, a) upstream view of cascade with idler sprockets and chains to hold wake generating rods visible at endwalls, b) upstream close-up of chain which will hold wake generating rods, c) downstream view of cascade in wake generator with drive gear visible in foreground and traverse mechanism visible within chain path.

Wakes were generated with the mechanism described briefly above and in more detail in the papers below. Figure 1.4 shows views of the wake generator during assembly. The rods which produce the wakes are not present in the figure, but would extend vertically between the upper and lower chain. In Fig. 1.4c the traverse for probe motion is visible. It is located downstream of the cascade within the wake generator circuit. The traverse has three linear stages and a rotating stage. Details of the wakes produced by the rods, including the velocity deficit, turbulence level and spectra are provided in the papers below.

Measurements were made near the midspan of the airfoils, where the flow was free of endwall effects. The center airfoil included static pressure taps which were used to document the pressure distribution on the blade. An upstream Pitot tube and a Kiel probe traversed downstream of the cascade were used to document the total pressure loss through the cascade. A hot wire probe was used to measure the velocity and turbulence at the cascade inlet, and was also traversed downstream of the cascade in the wakes of the airfoils and at six streamwise stations in the suction surface boundary layer. From the hot wire data, mean and fluctuating velocity and spectra were computed.

2. Experimental Cases

The following tables show the experimental cases documented and the types of data acquired for the cases. Baseline experiments were run with steady inflow to the cascade and without wakes or VGJs. For the cases with VGJs, B is the blowing ratio (jet velocity/local freestream velocity), f is the pulsing frequency, and D is the duty cycle. Those cases with y in the Cp column are cases where pressure distributions were acquired on the airfoil. The Loss column indicates cases in which the total pressure loss between the upstream Pitot tube and the traversing Kiel probe 0.6 axial chord downstream of the cascade was documented. The Downstream U, u′ column indicates that the hot wire probe was traversed across the cascade in the same position as the Kiel probe traverse. The B.L. Profiles column indicates that velocity profiles were acquired at six streamwise stations in the suction surface boundary layer. The stations extended from near the beginning of the adverse pressure gradient region to near the trailing edge.

The cases with VGJs were done with a spanwise jet spacing of 10 hole diameters, which corresponds to 0.063 axial chord. A few cases were also considered with some of the holes covered, increasing the spacing to 20, 40 and 80 diameters. These cases were with Re=50,000 and low freestream turbulence. Steady blowing was done with a blowing ratio of 2, and pulsed blowing with a frequency of 24 Hz, duty cycle of 10% and blowing ratio of 1. For these cases, the Station 6 column indicates that velocity profiles were acquired at streamwise Station 6, near the trailing edge. Velocity profiles were not acquired at the other streamwise stations. Both the Station 6 velocity profiles and total pressure loss profiles were acquired at 5 different spanwise positions between two VGJ holes. The spanwise locations were labeled a-e, with location b being ¼ hole pitch from location a, location c being ¼ pitch from location b (and ½ pitch from location a), location d being ¼ pitch from location b and ¾ pitch from location a, and location e being ¼ pitch from d and one full pitch from location a. In general, there was not much variation across the span at the measurement locations considered. There was little difference between the results with 10D and 20D spacing. With 40D spacing, a slightly higher blowing ratio was needed with the pulsed jets (1.5 vs. 1) to achieve the same separation control observed with the closer spacing. With 80D spacing, the jets still had some effect, but separation control was largely lost. These results indicate that the 10D spacing used in most of the experiments was more conservative than necessary. Unlike the rest of the results, which appear in the attached conference and journal papers, the results with different VGJ spacing do not appear in any papers. Some discussion and figures from these cases are in the last section below, and the data files from these cases are included with the other data files from the study.

For the cases with wakes and without VGJs, the Spacing column indicates the spacing between the wake generator rods divided by the blade spacing in the cascade. The column marked Upstream indicates that velocity data were acquired at the inlet plane of the cascade at a fixed point between two blades. The velocity data were then ensemble averaged at different phases during the wake passing cycle.

Cases with Wakes and VGJs combine were considered last. Reynolds numbers of 25,000 and 50,000 were considered. For these cases a rod spacing of two blade spacings was used. The rod velocity was 0.73 times the cascade inlet velocity for a flow coefficient of 1.13. This gave a dimensionless wake passing frequency of 0.14. Without VGJs, this wake passing frequency was too low for full separation control at Re=25,000 and 50,000. Nine different VGJ timings relative to the wakes were considered, as shown below. Timings were chosen to place the jet pulses at different times within or between wakes. Case (a) is the baseline case with only wakes. Cases (b-d) have a single pulse for each wake passing. Timings (e-g) have two pulses per wake period. To maintain the same overall blowing period, the pulses in cases (e-g) are half as long as those in (b-d). Timings (h-i) have three pulses per wake.

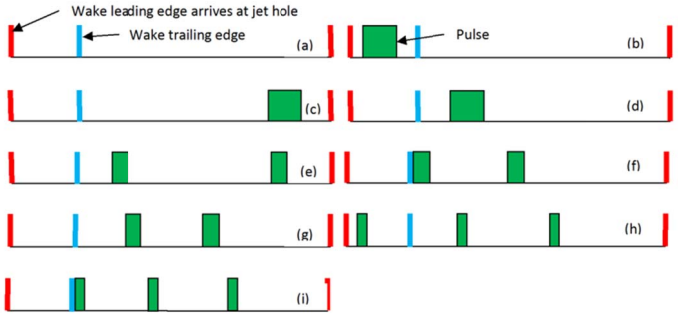

The labels a-i were used to name the cases in the papers submitted for publication and included below. A different ordering of the names was used when the data were originally acquired, and these original names are on the data files included with this report. The corresponding names are as follows.

Name on data files and in tables below	a	b	c	d	e	f	g	i	j
Name as shown above and used in papers	a	c	d	e	f	i	b	g	h

Low Freestream Turbulence Baseline and VGJ cases (no wakes)

Case	Re	B	f [Hz]	D [%]	Cp	Loss	Downstream U, u'	B.L. Profiles, 6 stations
Baseline	25000				y	y	y	y
	50000				y	y	y	y
	100000				y	y	y	y
	125000				y	y	y	y
	200000				y	y	y	y
	300000				y	y	y	y
	333000				y	y	y	y
Steady Jets	25000	1			y	y		
	25000	2			y	y		
	25000	2.5			y			
	25000	3			y	y		y

Case	Re	B	f [Hz]	D [%]	Cp	Loss	Downstream U, u'	B.L. Profiles, 6 stations
Steady Jets	50000	0.25			y			
	50000	0.5			y			
	50000	0.75			y	y		
	50000	1			y	y		
	50000	1.5			y	y		
	50000	2			y	y		y
Steady Jets	100000	0.25			y	y		
	100000	0.5			y	y		y
	100000	0.75			y	y	y	
	100000	1			y	y		
Pulsed Jets	25000	1	3	10	y			
	25000	2	3	10	y			
	25000	3	3	10	y	y		
Pulsed Jets	25000	0.5	3	50	y			
	25000	0.75	3	50	y			
	25000	1	3	50	y	y		
	25000	1.5	3	50	y			
	25000	2	3	50	y	y		
	25000	2.5	3	50	y			
	25000	3	3	50	y	y		
Pulsed Jets	50000	1	3	50				y
Pulsed Jets	25000	0.5	6	10	y			
	25000	0.75	6	10	y			
	25000	1	6	10	y	y		y
	25000	1.5	6	10	y	y		
	25000	2	6	10	y	y		
	25000	2.5	6	10	y			
	25000	3	6	10	y	y		
Pulsed Jets	25000	0.5	6	50	y			
	25000	0.75	6	50	y			
	25000	1	6	50	y			y
	25000	1.5	6	50	y	y		
	25000	2	6	50	y			
	25000	2.5	6	50	y			
	25000	3	6	50	y			
Pulsed Jets	50000	0.25	6	10	y			
	50000	0.5	6	10	y			
	50000	0.75	6	10	y			

Case	Re	B	f [Hz]	D [%]	Cp	Loss	Downstream U, u'	B.L. Profiles, 6 stations
	50000	1	6	10	y	y	y	y
	50000	1.5	6	10		y		
	50000	2	6	10	y	y		
Pulsed Jets	50000	0.25	6	50	y			
	50000	0.5	6	50	y	y		
	50000	0.75	6	50	y	y		
	50000	1	6	50	y	y	y	y
	50000	1.5	6	50		y		
	50000	2	6	50	y			
Pulsed Jets	25000	0.25	12	10	y			
	25000	0.5	12	10	y	y		
	25000	0.75	12	10	y	y		
	25000	1	12	10	y	y		y
	25000	1.5	12	10	y	y		
	25000	2	12	10	y	y		
	25000	2.5	12	10	y			
	25000	3	12	10	y	y		
Pulsed Jets	25000	0.25	12	50	y			
	25000	0.5	12	50	y			
	25000	0.75	12	50	y			
	25000	1	12	50	y			
	25000	1.5	12	50	y	y		
	25000	2	12	50	y			
	25000	2.5	12	50	y			
	25000	3	12	50	y			
Pulsed Jets	50000	0.25	12	10	y	y		
	50000	0.5	12	10	y	y	y	
	50000	0.75	12	10	y	y		
	50000	1	12	10	y	y		y
	50000	1.5	12	10		y		
	50000	2	12	10	y	y		
Pulsed Jets	50000	0.25	12	50	y	y		
	50000	0.5	12	50	y	y	y	
	50000	0.75	12	50	y	y		
	50000	1	12	50	y	y		
	50000	1.5	12	50		y		
	50000	2	12	50	y	y		
	50000	3	12	50		y		

Case	Re	B	f [Hz]	D [%]	Cp	Loss	Downstream U, u'	B.L. Profiles, 6 stations
Pulsed Jets	100000	0.25	12	10	y			
	100000	0.5	12	10	y			
	100000	0.75	12	10	y			
	100000	1	12	10	y			
Pulsed Jets	100000	0.25	12	50	y			
	100000	0.5	12	50	y			
	100000	0.75	12	50	y			
	100000	1	12	50	y			
Pulsed Jets	25000	0.25	24	10	y	y		
	25000	0.5	24	10	y	y		
	25000	0.75	24	10	y			
	25000	1	24	10	y	y		y
	25000	1.5	24	10	y			
	25000	2	24	10	y	y		
	25000	2.5	24	10	y			
	25000	3	24	10	y	y		
Pulsed Jets	25000	0.25	24	50	y			
	25000	0.5	24	50	y			
	25000	0.75	24	50	y			
	25000	1	24	50	y			
	25000	1.5	24	50	y			
	25000	2	24	50	y			
	25000	2.5	24	50	y			
	25000	3	24	50	y			
Pulsed Jets	50000	0.25	24	10	y	y		
	50000	0.5	24	10	y	y	y	y
	50000	0.75	24	10	y			
	50000	1	24	10	y	y	y	y
	50000	1.5	24	10	y			
	50000	2	24	10	y			
Pulsed Jets	50000	0.25	24	50	y	y		
	50000	0.5	24	50	y			
	50000	0.75	24	50	y			
	50000	1	24	50	y	y		y
	50000	2	24	50	y			
Pulsed Jets	100000	0.25	24	10	y			
	100000	0.5	24	10	y			y
	100000	0.75	24	10	y			
	100000	1	24	10	y			

Case	Re	B	f [Hz]	D [%]	Cp	Loss	Downstream U, u'	B.L. Profiles, 6 stations
Pulsed Jets	100000	0.25	24	50	y			
	100000	0.5	24	50	y			
	100000	0.75	24	50	y			
	100000	1	24	50	y			
Pulsed Jets	50000	1	48	10				y
Pulsed Jets	100000	0.25	48	10	y			
	100000	0.5	48	10	y			
	100000	0.75	48	10	y			
Pulsed Jets	100000	0.25	48	50	y			
	100000	0.5	48	50	y			
	100000	0.75	48	50	y			
	100000	1	48	50	y			

High Freestream Turbulence Baseline and VGJ cases (no wakes)

Case	Re	B	f [Hz]	D [%]	Cp	Loss	Downstream U, u'	B.L. Profiles, 6 stations
Baseline	25000				y	y	y	y
	50000				y	y	y	y
	100000				y	y	y	y
	150000				y	y	y	y
	200000				y	y	y	y
	300000				y	y	y	y
Steady Jets	25000	1			y			
	25000	2			y			
	25000	2.5			y			
	25000	3			y	y		
Steady Jets	50000	0.5			y			
	50000	0.75			y			
	50000	1			y	y		
	50000	1.5			y	y		
	50000	2			y	y		
Pulsed Jets	25000	2	3	10	y	y		
	25000	2.5	3	10		y		
	25000	3	3	10	y	y		

Case	Re	B	f [Hz]	D [%]	Cp	Loss	Downstream U, u'	B.L. Profiles, 6 stations
Pulsed Jets	25000	1	3	50	y			
	25000	2	3	50	y	y		
	25000	3	3	50	y	y		
Pulsed Jets	25000	1	6	10	y			
	25000	1.5	6	10	y	y		
	25000	2	6	10	y	y		y
	25000	3	6	10	y	y		y
Pulsed Jets	25000	1	6	50	y			
	25000	2	6	50	y	y		
	25000	2.5	6	50	y			
	25000	3	6	50	y	y		
Pulsed Jets	50000	0.25	6	10	y			
	50000	0.5	6	10	y			
	50000	0.75	6	10	y			
	50000	1	6	10	y	y		
	50000	1.5	6	10	y	y		
	50000	2	6	10	y	y		
Pulsed Jets	50000	0.25	6	50	y			
	50000	0.5	6	50	y			
	50000	0.75	6	50	y			
	50000	1	6	50	y	y		
	50000	1.5	6	50	y	y		
	50000	2	6	50	y			
Pulsed Jets	25000	0.5	12	10	y			
	25000	0.75	12	10	y	y		
	25000	1	12	10	y	y		y
	25000	1.5	12	10	y			
	25000	2	12	10	y	y		y
	25000	2.5	12	10	y			
	25000	3	12	10	y			
Pulsed Jets	25000	0.5	12	50	y			
	25000	0.75	12	50		y		
	25000	1	12	50	y	y		
	25000	2	12	50	y	y		
Pulsed Jets	50000	0.13	12	10	y			
	50000	0.25	12	10	y			
	50000	0.5	12	10	y			
	50000	0.75	12	10	y	y		

Case	Re	B	f [Hz]	D [%]	Cp	Loss	Downstream U, u'	B.L. Profiles, 6 stations
	50000	1	12	10	y	y		y
	50000	1.5	12	10	y			
Pulsed Jets	50000	0.25	12	50	y			
	50000	0.5	12	50	y	y		
	50000	0.75	12	50	y	y		
	50000	1	12	50	y	y		
Pulsed Jets	25000	0.5	24	10	y			
	25000	0.75	24	10	y			
	25000	1	24	10	y	y		
	25000	1.5	24	10	y			
	25000	2	24	10	y	y		
Pulsed Jets	50000	0.25	24	10	y			
		0.5	24	10	y	y		
		0.75	24	10	y	y		y
		1	24	10	y	y		
Pulsed Jets	50000	0.25	24	50	y			
		0.5	24	50	y	y		
		0.75	24	50	y	y		

Low Freestream Turbulence cases with different VGJ spacings (no wakes)

Case	VGJ spacing	Re	B	f [Hz]	D [%]	Cp	Loss	Station 6
Pulsed Jet	1	50000	1	24	10	y	y	y
Steady Jet	1	50000	2			y	y	y
Pulsed Jet	2	50000	1	24	10	y	y	y
Steady Jet	2	50000	2			y	y	y
Pulsed Jet	4	50000	1	24	10	y	y	y
Steady Jet	4	50000	2			y	y	y
Pulsed Jet	4	50000	1.5	24	10	y	y*	y*
Pulsed Jet	8	50000	2.3	24	10	y	y*	y
*only one spanwise location								

Cases with Wakes (no VGJs)

Case	Re	Spacing/Pitch	f [Hz]	Upstream U, u'	Cp	Loss	Downstream U, u'	B.L. Profiles, 6 stations
Low TI	25000	1.6	6	y	y	y	y	y
	37500	1.6	9	y	y	y	y	y
	50000	1.6	12	y	y	y	y	y
	100000	1.6	12	y	y	y		
	200000	1.6	12	y	y	y		
	25000	1.6	12		y	y		
	50000	1.6	6		y	y		y
	200000	1.6	6		y	y		
Low TI	25000	1	6	y	y	y	y	
	37500	1	9	y	y	y		
	50000	1	12	y	y	y	y	
Low TI	25000	2	6	y	y	y	y	y
	37500	2	9	y	y	y	y	y
	50000	2	12	y	y	y	y	y
High TI	25000	1.6	6	y	y	y	y	
	37500	1.6	9	y	y	y		
	50000	1.6	12	y	y	y	y	
	50000	1.6	6		y	y		
High TI	25000	1	6	y	y	y	y	
	37500	1	9	y	y	y		
	50000	1	12	y	y	y	y	

Cases with Wakes and VGJs

Case	Re	Timing	f [Hz]	Cp	Loss	Downstream U, u'	B.L. Profiles, 6 stations
Low TI	Re=25000	a	3	y	y	y	y
		b	3	y	y	y	y
		c	3	y	y	y	y
		d	3	y	y	y	y
		e	3	y	y	y	y
		f	3	y	y	y	y
		i	3	y	y	y	y
		j	3	y	y	y	y
	50000	a	6	y	y	y	y
		b	6	y	y	y	y
		c	6	y	y	y	y
		d	6	y	y	y	y
		e	6	y	y	y	y

		g	6	y	y	y	y
High TI	Re=25000	a	3	y	y	y	y
		b	3	y	y	y	y
		c	3	y	y	y	y
		d	3	y	y	y	y
		e	3	y	y	y	y
		f	3	y	y	y	y
	50000	a	6	y	y	y	y
		b	6	y	y	y	y
		c	6	y	y	y	y
		d	6	y	y	y	y
		e	6	y	y	y	y
		g	6	y	y		

3. Lists of publications

Dissertations and Theses

1. Kartuzova, Olga V. "A Computational Study for the Utilization of Jet Pulsations in Gas Turbine Film Cooling and Flow Control," PhD Dissertation, Cleveland State University, May 2010.

2. Vinci, Samuel J. "CFD Simulations for the Effect of Unsteady Wakes on the Boundary Layer of a Highly Loaded Low Pressure Turbine Airfoil (L1A)," MS thesis, Cleveland State University, May 2011.

Conference papers

3. Volino, R.J. "Separated Flow Measurements on a Highly Loaded Low-Pressure Turbine Airfoil," ASME paper GT2008-51445. Presented at the 2008 ASME International Gas Turbine Conference, Berlin, Germany.

4. Ibrahim, M., Kartuzova, O., and Volino, R.J., "Experimental and Computational Investigations of Separation and Transition on a Highly Loaded Low-Pressure Turbine Airfoil: Part 1 – Low Freestream Turbulence Intensity," ASME paper IMECE2008-68879. Presented at the ASME IMECE, Boston, MA, November 2008.

5. Volino, R.J., Kartuzova, O., and Ibrahim, M., "Experimental and Computational Investigations of Separation and Transition on a Highly Loaded Low-Pressure Turbine Airfoil: Part 2 – High Freestream Turbulence Intensity," ASME paper IMECE2008-68776. Presented at the ASME IMECE, Boston, MA, November 2008.

6. Volino, R.J., Kartuzova, O., and Ibrahim, M.B., "Experimental and Computational Investigations of Low-Pressure Turbine Separation Control Using Vortex Generator Jets," ASME paper GT2009-59983. Presented at the 2009 ASME International Gas Turbine Conference, Orlando, FL.

7. Ibrahim, M.B., Kartuzova, O., and Volino, R.J., "LES and URANS Computational Investigations of LPT Blade (L1A) Separation Control using Vortex Generator Jets," Proceedings of Turbulence, Heat and Mass Transfer 6, 2009. Presented at Turbulence, Heat and Mass Transfer 6, Rome, Italy.

8. Volino, R.J. and Ibrahim, M.B., "Separation Control on High Lift Low Pressure Turbine Airfoils Using Pulsed Jet Vortex Generator Jets," Proceedings of the ASME-ATI-UIT 2010 Conference on Thermal and Environmental Issues in Energy Systems, 2010. Presented at ASME-ATI-UIT 2010, Sorrento, Italy.

9. Volino, R.J., Kartuzova, O., and Ibrahim, M.B., "Separation Control on a Very High Lift Low Pressure Turbine Airfoil Using Pulsed Vortex Generator Jets," ASME paper GT2010-23567. Presented at the 2010 ASME International Gas Turbine Conference, Glasgow, UK.

10. Volino, R.J., "Effect of Unsteady Wakes on Boundary Layer Separation on a Very High Lift Low Pressure Turbine Airfoil," ASME paper GT2010-23573. Presented at the 2010 ASME International Gas Turbine Conference, Glasgow, UK.

11. Ibrahim, M., Kartuzova, O., Doucet, D., and Volino, R.J., "LES Flow Control Simulations for Highly Loaded Low Pressure Turbine Airfoil (L1A) Using Pulsed Vortex Generator Jets," ASME paper GT2010-23015. Presented at the 2010 ASME International Gas Turbine Conference, Glasgow, UK.

12. Volino, R.J., "Combined Effects of Wakes and Pulsed Vortex Generator Jet Flow Control on Boundary Layer Separation on a Very High Lift Low Pressure Turbine Airfoil," ASME paper GT2011-46106. Presented at the 2011 ASME International Gas Turbine Conference, Vancouver, BC, Canada.

13. Ibrahim, M., Vinci, S., Kartuzova, O., and Volino, R.J., "CFD Simulations of Unsteady Wakes on a Highly Loaded Low Pressure Turbine Airfoil (L1A)," ASME Paper GT2012-69770. Presented at the 2012 ASME International Gas Turbine Conference, Copenhagen.

Other Conference Presentations

14. Volino, R.J., Ibrahim, M.B. and Kartuzova, O. "Flow Control on Low-Pressure Turbine Airfoils Using Vortex Generator Jets," In: 2009 Minnowbrook VI Workshop on Flow Physics and Control for Internal and External Aerodynamics, Blue Mountain Lake, NY, August 2009, NASA/CP-2010-216112 (Editors: Lagraff, J.A., Povinelli, L.A., Gostelow, J.P., and Glauser, M.).

15. Volino, R.J. "Separation Control on a Cascade of Airfoils using Pulsed Vortex Generator Jets," 62nd Annual meeting of the Division of Fluid Dynamics of the American Physical Society, Minneapolis, MN, November 2009.

Journal Papers

16. Volino, R.J., "Separated Flow Measurements on a Highly Loaded Low-Pressure Turbine Airfoil," *ASME Journal of Turbomachinery*, Vol. 132, paper 011007, 2010.

17. Volino, R.J., Kartuzova, O., and Ibrahim, M.B., "Separation Control on a Very High Lift Low Pressure Turbine Airfoil Using Pulsed Vortex Generator Jets," *ASME Journal of Turbomachinery*, Vol. 133, paper 041021-1, 2011.

18. Volino, R.J., "Effect of Unsteady Wakes on Boundary Layer Separation on a Very High Lift Low Pressure Turbine Airfoil," *ASME Journal of Turbomachinery*, Vol. 134, paper 011011-1, 2012.

Appendix A

Reprints of Papers and Publications

Copyrighted papers are reprinted with permission of the publisher.

Proceedings of ASME Turbo Expo 2008: Power for Land, Sea and Air
GT2008
June 9-13, 2008, Berlin, Germany

GT2008-51445

SEPARATED FLOW MEASUREMENTS ON A HIGHLY LOADED LOW-PRESSURE TURBINE AIRFOIL

Ralph J. Volino
Mechanical Engineering Department
United States Naval Academy
Annapolis, Maryland 21402
volino@usna.edu

ABSTRACT

Boundary layer separation, transition and reattachment have been studied on a new, very high lift, low-pressure turbine airfoil. Experiments were done under low freestream turbulence conditions on a linear cascade in a low speed wind tunnel. Pressure surveys on the airfoil surface and downstream total pressure loss surveys were documented. Velocity profiles were acquired in the suction side boundary layer at several streamwise locations using hot-wire anemometry. Cases were considered at Reynolds numbers (based on the suction surface length and the nominal exit velocity from the cascade) ranging from 25,000 to 330,000. In all cases the boundary layer separated, but at high Reynolds number the separation bubble remained very thin and quickly reattached after transition to turbulence. In the low Reynolds number cases, the boundary layer separated and did not reattach, even when transition occurred. This behavior contrasts with previous research on other airfoils, in which transition, if it occurred, always induced reattachment, regardless of Reynolds number.

NOMENCLATURE

C_f	skin friction coefficient
Cp	$2(P_T - P)/\rho U_e^2$, pressure coefficient
C_x	axial chord length
f	frequency
H	δ^*/θ, shape factor
K	$(\nu/U_\infty^2)(dU_\infty/ds)$, acceleration parameter
L_s	suction surface length
L_ϕ	blade spacing (pitch)
P	pressure
P_S	upstream static pressure
P_T	upstream stagnation pressure
P_{Te}	downstream stagnation pressure
PSD	power spectral density
Re	$U_e L_S/\nu$, exit Reynolds number
$Re_{\delta*}$	displacement thickness Reynolds number
Re_θ	momentum thickness Reynolds number
s	streamwise coordinate, distance from leading edge
TI	freestream turbulence intensity
U	mean streamwise velocity
U_∞	local freestream velocity
U_e	nominal exit freestream velocity, based on inviscid solution
u'	time averaged rms streamwise fluctuating velocity
x	axial distance from leading edge
y	distance from wall
Zw	Zweifel coefficient
α_1	inlet flow angle
α_2	exit flow angle
δ^*	displacement thickness
ϕ	coordinate along blade spacing, normal to axial chord
γ	intermittency, fraction of time flow is turbulent
ν	kinematic viscosity
ρ	density
θ	momentum thickness
ψ	$(P_T-P_{Te})/(P_T-P_S)$, total pressure loss coefficient
ψ_{int}	total pressure loss integrated over blade spacing

Subscripts

p	pressure minimum (suction peak) location
pt	distance from suction peak to transition start
s	separation location
st	distance from separation location to transition start
∞	free-stream

INTRODUCTION

Boundary layer separation can lead to partial loss of lift and higher aerodynamic losses on low-pressure turbine (LPT) airfoils (e.g. Hourmouziadis [1], Mayle [2], and Sharma et al. [3]). As designers impose higher loading to improve efficiency and lower cost, the associated strong adverse pressure gradients on the suction side of the airfoil can exacerbate separation problems. The problem is particularly relevant in aircraft engines. Airfoils optimized for maximum power under takeoff conditions may still experience separation at cruise conditions, due to the lower density and therefore lower Reynolds numbers at altitude. A component efficiency drop of

2% may occur between takeoff and cruise in large commercial transport engines, and the difference could be as large as 7% in smaller engines operating at higher altitudes [4, 5]. Prediction and control of suction side separation, without sacrifice of the benefits of higher loading, is therefore, crucial for improved engine design.

Separation and separated flow transition, which can lead to boundary layer reattachment, have received considerable attention. Studies have included flows over flat plates subject to pressure gradients similar to those on the suction side of LPT airfoils, and flows over airfoils either in single passage facilities or multi-blade cascades. Some have considered steady inflow conditions, while others have included the effect of unsteady wakes. Recent examples include [6, 7, 8, 9, 10, 11, 12]. Volino [13] provides a review of some earlier studies. In general, previous work shows that the strong acceleration on the leading section of the airfoil keeps the boundary layer thin and laminar, even in the presence of elevated freestream turbulence. When separation does occur, it is usually just downstream of the suction peak. If transition then occurs in the shear layer over the separation bubble, it is typically rapid and causes the boundary layer to reattach [13, 14]. Transition is dependent on Reynolds number, freestream turbulence level, and the surface roughness conditions upstream of the separation point. Several correlations for separated flow transition have been developed based on experimental data, including those of Mayle [2], Hatman and Wang [15], Davis et al. [16], Yaras [17], Volino and Bohl [18], and Praisner and Clark [19].

The advances in separation understanding and prediction have led to attempts at separation control. Zhang et al. [20], Bohl and Volino [21], Volino [22], and others provide examples using passive devices such as boundary layer trips. Others have used active devices such as vortex generator jets (e.g. Bons et al. [4], and Volino [23]) or plasma devices (e.g. Huang et al. [24]).

Another way to improve performance is to design airfoils with pressure gradients more resistant to separation, as described by Praisner and Clark [19]. Forward loading, for example, makes airfoils more separation resistant by extending the adverse pressure gradient on the aft portion of the suction side over a longer distance. This reduces the local pressure gradient at all locations, making separation less likely. If separation does occur, forward loading provides a longer distance along the airfoil surface for reattachment. Forward loading has some disadvantages, however. As noted by Zhang et al. [20], the longer region of turbulent flow on a forward loaded airfoil can lead to increased profile losses. Forward loading also creates longer regions of strong pressure gradient on the endwalls, which can produce stronger secondary flows and losses. If flow control were incorporated in the design of an advanced airfoil, as discussed by Bons et al. [25], it might be possible to produce an aft loaded airfoil that was resistant to separation and had low profile and secondary loss characteristics over a range of Reynolds numbers.

The objective of the present study is to document the flow over a very highly loaded LPT airfoil. The airfoil chosen was designed at the Air Force Research Laboratory (AFRL), and is designated the L1A. It is available on a limited basis to U.S. researchers from Clark [26]. Dimensions of the L1A as used in the present experiments are given in Table 1. Based on the design calculations of Clark [26], the L1A has 10% higher loading than the "ultra-high lift" airfoils described by Zhang and Hodson [27], and 17% higher loading than the Pak B airfoil considered in several studies such as Volino [13, 14] and Bons et al. [4]. The design calculations indicate that the Zweifel coefficient increases from about 1.15 on the Pak B to about 1.35 on the L1A. If the definition for the Zweifel coefficient is taken as

$$Zw=2\cos^2\alpha_2(L_\phi/C_x)(\tan\alpha_1+\tan\alpha_2) \quad (1)$$

Table 1: Cascade parameters

Axial Chord, C_x [mm]	True Chord [mm]	Pitch, L_ϕ [mm]	Span [mm]	Suction side, L_s [mm]	Inlet flow angle	Exit flow angle
134	146	136	724	203	35°	60°

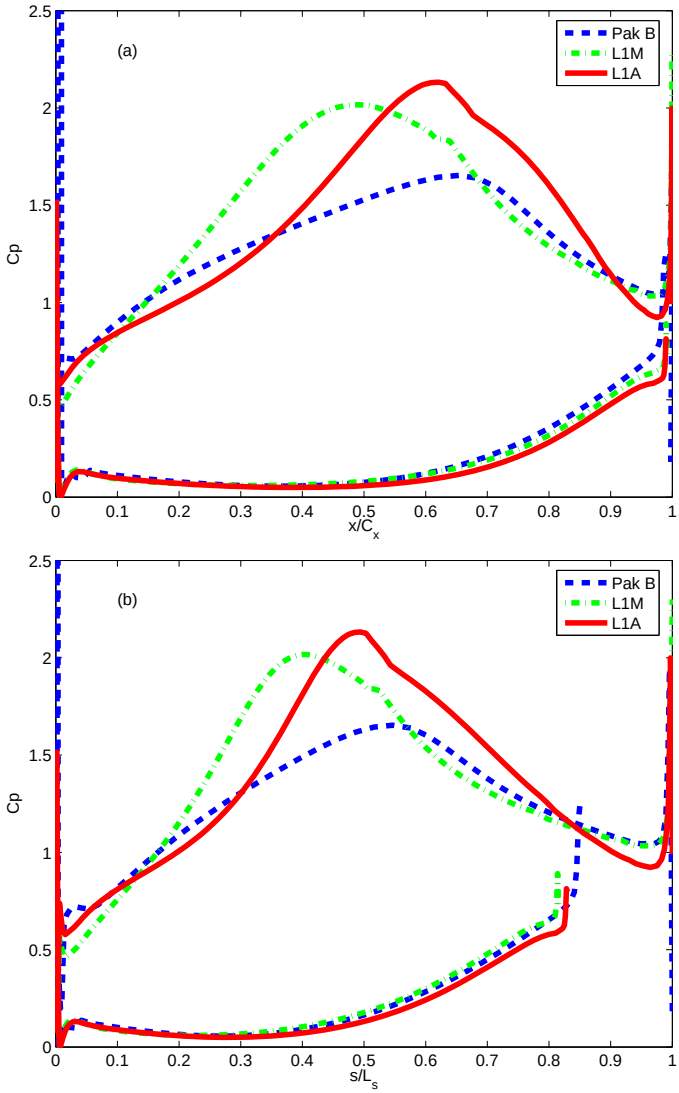

Fig. 1 Comparison of inviscid pressure profiles for the Pak B, L1M and L1A airfoils, a) *Cp* vs axial position, b) *Cp* vs streamwise location

as given by Lakshminarayana [28], Zw=1.08 for the Pak B (in agreement with the value given by McAuliffe and Sjolander [29]) and Zw=1.23 for the L1A. The L1A has the same inlet and exit flow angles and loading as the L1M airfoil used by Bons et al. [25]. The L1M is a mid-chord loaded design, and is resistant to separation even at very low Reynolds numbers. While the L1M and L1A were designed with the same methodology, the L1A is aft loaded, and is therefore expected to be more prone to separation. It is expected to be a good test airfoil for future flow control work, in which separation may be suppressed while maintaining the benefits of both very high loading and aft loading. Figure 1 shows the inviscid flow pressure profiles for the L1A, L1M and Pak B airfoils. The inviscid code used

for the computations was adapted from Lewis [30]. Figure 1a shows the pressure coefficient *Cp* as a function of dimensionless axial position, x/C_x. These coordinates are useful for comparing the lift generated by the airfoils. Figure 1b shows *Cp* as a function of the streamwise distance along the airfoil surface, s/L_s, where L_s is the wetted surface length along the suction side. These coordinates are most useful for explaining the boundary layer development and are used to present the results below. The higher lift of the L1A and L1M compared to the Pak B is clear in Fig. 1. Also clear is the stronger adverse pressure gradient of the L1A on the downstream region of the suction side. The pressure gradient is shown again in Fig. 2 as the product of the local acceleration parameter *K* and the Reynolds number. The Reynolds number, *Re*, is based on L_s and the nominal exit velocity from the cascade U_e (computed using the inlet velocity and the design inlet and exit flow angles). The parameter *K* is inversely proportional to *Re*, so *KRe* is independent of Reynolds number. The negative *K* values downstream of s/L_s=0.7 are about twice as strong for the L1A than for the other two airfoils. This suggests more of a tendency for boundary layer separation and possibly less of a tendency for the flow to reattach.

EXPERIMENTAL FACILITY AND MEASUREMENTS

Experiments were conducted in a closed loop wind tunnel with a linear cascade in one corner of the loop. An axial fan sends air through turning vanes in the first corner of the tunnel and then through a heat exchanger. Following the heat exchanger is the second turn and a 6.25:1 area ratio contraction. Following the contraction is a 0.46 m square by 1.1 m long test section, which was not used in the present study. Following this test section is a 2.4 m long diffuser which expands the flow area to 0.75 m × 0.75 m. A fine screen with 0.12 mm mesh thickness, 0.42 mm mesh spacing and 49% blockage is located in the exit plane of the diffuser. The screen breaks up the boundary layers which form on the diffuser walls and provides a uniform flow into the cascade test section. A seven blade cascade is located in the wind tunnel's third turn, as shown in Fig. 3. A generic airfoil shape is shown in the figure. The flow continues from the cascade into the tunnel's fourth turn, then through a second diffuser before returning to the fan.

The freestream turbulence entering the cascade was measured with a cross-wire probe positioned just upstream of the center blade. The streamwise velocity component had a turbulence intensity, *TI*, of 0.8%, while the component intensity in the direction across the cascade was 0.5%. The spanwise component intensity was assumed to also be 0.5% based on the symmetry of the wind tunnel. The combined freestream turbulence intensity based on all three components was 0.6%. Spectral measurements showed that 80% of the energy in the streamwise fluctuations was due to unsteadiness at dimensionless frequencies $fL_s/U_e<2$, where *f* is the frequency in Hz. Approximately 70% of the energy in the cross stream components was also below this frequency. If the turbulence is high pass filtered to remove this unsteadiness, the streamwise and cross stream component intensities are 0.36% and 0.27% respectively, for an overall freestream turbulence intensity of 0.3%. The integral length scale of the freestream turbulence is 6.3 cm in the streamwise direction and 6.7 cm in the other directions. While such low freestream turbulence and large length scales are not representative of engine conditions, they are still of interest. In zero or favorable pressure gradient boundary layers, high *TI* can cause bypass transition, but under adverse pressure gradients, natural transition appears to play a role at all *TI* levels. Hughes and Walker [31], for example observed evidence of Tollmien-Schlichting (TS) waves in cases with *TI* as high as 8%. Volino [14] also saw evidence of TS waves in both high and low *TI* cases. Low *TI*

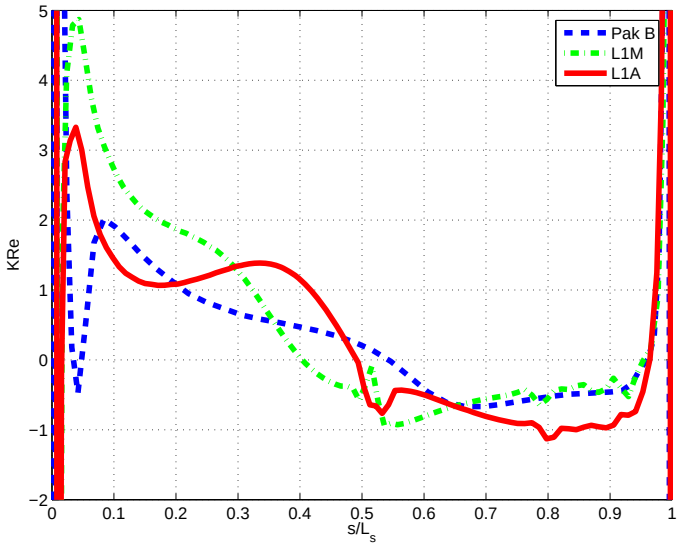

Fig. 2 Acceleration, *KRe*, vs streamwise location for Pak B, L1M and L1A airfoils based on inviscid solution

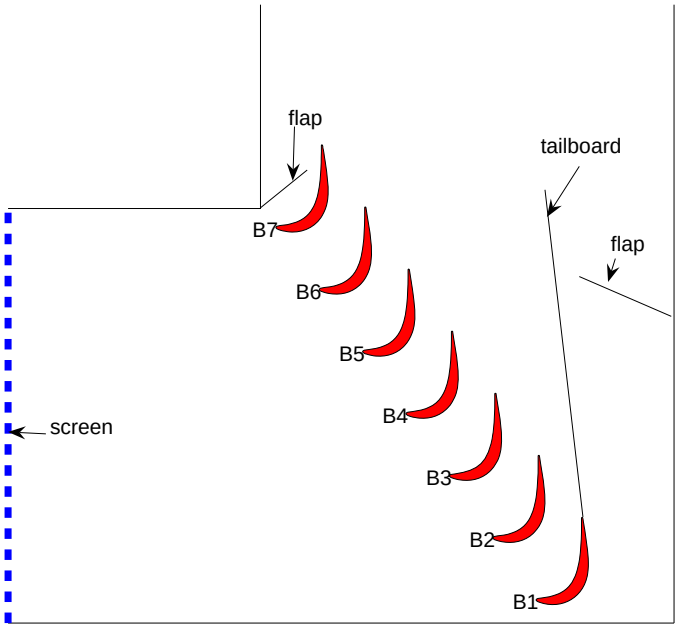

Fig. 3 Schematic of linear cascade

cases provide a somewhat simpler environment for explaining the already complex phenomenon of separated flow transition. The present low *TI* cases will also serve as comparison cases for future work with elevated *TI*. Higher *TI* and length scales closer to the boundary layer thickness are expected to hasten the transition process.

The blades in the cascade were machined from high density foam, which has a consistency much like hard wood. The center blade, designated B4 in Fig. 3, contains pressure taps near the spanwise centerline. A tailboard, shown in Fig. 3, was needed to produce the correct exit flow angle from the cascade. Its position was set to produce periodicity at high Reynolds numbers. A tailboard on the opposite side of the cascade, and inlet guide vanes were found to be unnecessary. To produce the correct approach flow to the end blades

(B1 and B7), the amount of flow escaping around the two ends of the cascade was controlled with the flaps shown in Fig. 3. The flap positions were set using a wool tuft upstream of each blade to check that the incoming flow approached the stagnation points with the correct angle. The inlet flow angle at the center of the cascade was also checked with a three-hole pressure probe and found to be within 2° of the design angle. At high Reynolds numbers, the approach velocity to the middle four passages was measured to be uniform to within 6%, and the difference between any two adjacent passages was within 3%. At low Reynolds numbers, slightly more variation was observed, but the approach velocity to the middle two passages still agreed to within 5%. Good periodicity at high Reynolds numbers was also observed in the exit flow from the cascade, as evidenced by suction side velocity profiles acquired near the trailing edge of blades B2-B6, and by total pressure loss surveys, which are shown below. At low Reynolds numbers, when significant separation bubbles were present, the periodicity was not as good due to suppression of the separation bubble thickness on the blades closest to the tailboard. This is an unavoidable result when using a finite linear cascade to study separated flow. It is considered acceptable for the present facility, since its intended purpose is for the study of flow control, which if successful should suppress separation on all blades, thereby restoring periodicity even at low Reynolds numbers.

Measurements

Pressure surveys were made using a pressure transducer (0-870 Pa range Validyne transducer). Stagnation pressure was measured with a pitot tube upstream of the cascade. Static pressure taps were located in the center blade as noted above. The uncertainty in the suction side pressure coefficients was 0.07. Most of this uncertainty was due to bias error. Stochastic error was minimized by averaging pressure transducer readings over a 10 second period.

A four component traverse with three linear stages and one rotating stage was located in the wind tunnel downstream of the cascade. The traverse produced an acceptably low blockage when it was located at least two axial chord lengths downstream of the cascade. Variations in the wind tunnel velocity were less than 2% as the traverse was moved to various positions. The traverse was used to hold and move probes for velocity and downstream pressure measurements.

Total pressure losses were documented using a Kiel probe traversed across three blade spacings, 0.63 C_x downstream of the cascade. To compute the mass flow averaged pressure loss, a velocity profile was also acquired along the same line as the total pressure surveys using a single sensor hot-film probe.

Velocity profiles on the suction surface were measured at the six streamwise stations listed in Table 2. All stations are downstream of the inviscid pressure minimum at s/L_s=0.49. Profiles were measured near the spanwise centerline of the airfoil. Profiles were acquired with a hot-wire anemometer (AA Lab Systems model AN-1003) and a single sensor hot-film probe (TSI model 1201-20). The sensor diameter is 51 μm, and the active length is 1.02 mm. At each measurement location, data were acquired for 26 seconds at a 20 kHz sampling rate (2^{19} samples). All raw data were saved. The high sampling rate provides an essentially continuous signal, and the long sampling time results in low uncertainty in both statistical and spectral quantities. Data were acquired at 40 wall normal locations in each profile, extending from the wall to the free-stream, with most points concentrated in the near wall region. The probe was positioned as close to tangent to the airfoil surface as possible at each station, such that the probe body extended downstream of the sensor and the direction of the traverse was within 5° of normal to the surface. In most cases the closest point to the wall in each profile was within about 0.2 mm of the wall, which compares to boundary layer thicknesses ranging from 1.1 mm to over 40 mm.

Table 2: Velocity profile measurement stations

Station	1	2	3	4	5	6
s/L_s	0.53	0.59	0.69	0.78	0.88	0.97
x/C_x	0.65	0.72	0.80	0.86	0.92	0.97

Flow direction in a separation bubble cannot be determined with a single-sensor hot-wire, but velocity magnitude can be measured and was found to be near zero within the bubbles of the present cases when the flow was laminar. In cases where the flow became turbulent but remained separated, fluctuating velocities caused false high mean velocity readings in the separation bubble. With the exception of these turbulent separated cases, the uncertainty in the mean velocity is 3-5% except in the very near wall region, where near-wall corrections (Wills [32]) were applied to the mean velocity. Uncertainties in the momentum and displacement thicknesses computed from the mean profiles are 10%. Uncertainty in the shape factor, *H*, is 8%. Local skin friction coefficients were computed from the near wall mean velocity profiles using the technique of Volino and Simon [33]. This technique accounts for streamwise pressure gradient effects on the mean profile. The uncertainty in C_f is 8%. The uncertainty in the fluctuating streamwise velocity is below 10%.

Pressure surveys and velocity profiles were acquired at nominal *Re*=25,000, 50,000, 100,000, 200,000, 300,000, and 330,000. An additional pressure survey was acquired at *Re*=125,000. The Reynolds number, as defined above, is based on the suction surface length and the nominal cascade exit velocity. The corresponding Reynolds numbers based on the cascade inlet velocity and the axial chord length ranged from 10,000 to 133,000.

RESULTS

Pressure Profiles

Pressure profiles for all cases are shown in Fig. 4. The inviscid profile for the L1A airfoil is shown for comparison. At the three highest *Re*, with the exception of a slightly higher suction side peak, the data generally agree with the inviscid profile. This indicates that the boundary layer is attached over most of the airfoil in these cases. Some deviation between the three highest *Re* cases is visible at s/L_s=0.6 with the *Cp* value rising slightly at the lower *Re*. This may indicate a small separation bubble at this location. At the three lowest Reynolds numbers, the suction peak is suppressed and the *Cp* values have a constant value on the downstream part of the suction side. This plateau indicates that the boundary layer has separated. The *Cp* values never return to the inviscid line, indicating that the boundary layer never reattaches (i.e. the separation bubble bursts). At Reynolds numbers of 100,000 and below, the separation bubble always appeared to burst. At *Re* above 150,000 the boundary layer was attached over most of the airfoil. Between *Re*=100,000 and 150,000 the behavior was less predictable, with some dependence on whether the desired wind tunnel velocity was approached from above or below. The *Re*=124,500 case in Fig. 4 shows the suppressed suction peak and burst bubble of the lower Re cases, but in some trials (not shown) the *Cp* values dropped somewhat from their plateau near the trailing edge.

The pressure side *Cp* values also show some change with Reynolds number. Near the leading edge, *Cp* is higher for the lower *Re* cases, suggesting more of a leading edge separation bubble. Near the trailing edge the *Cp* values are again higher at the lower *Re*. This is believed to result when the suction side separation bubble forces fluid toward the pressure side, thereby increasing the pressure side velocity.

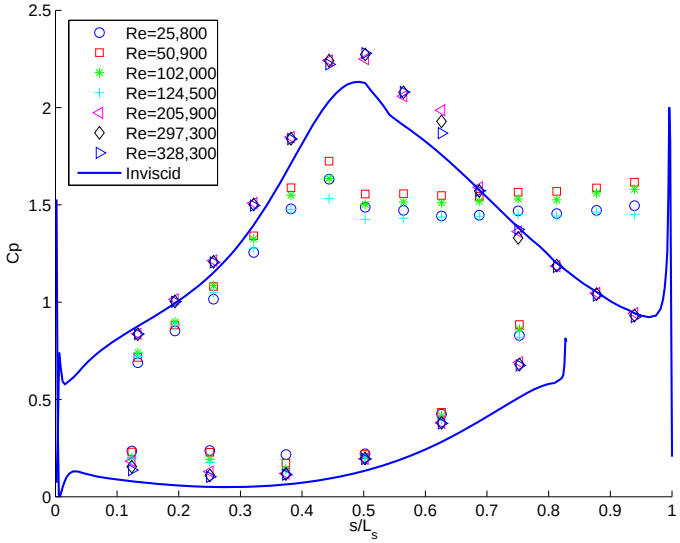

Fig. 4 *Cp* profiles

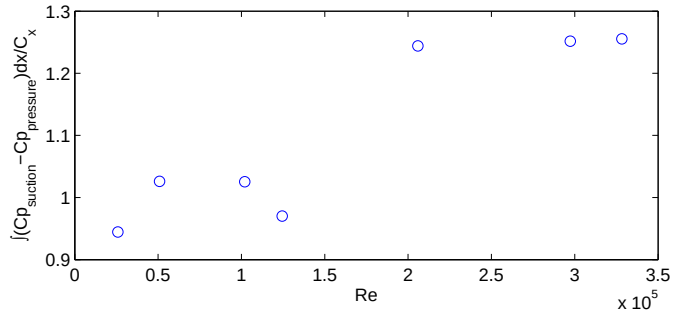

Fig. 5 Lift based on integrated *Cp* profile

The lift on the airfoil can be determined by integrating the difference between the suction and pressure side *Cp* values along the axial direction. The result is shown as a function of Reynolds number in Fig. 5. The lift is about 20% lower for the separated flow cases.

The results in Fig. 4 contrast with results for the Pak B airfoil presented by Volino [13], Bons et al. [4], Simon et al. [34] and others. With low freestream turbulence, at $Re \leq 50{,}000$ the boundary layer on the Pak B airfoil separated and did not reattach, much like the L1A behavior of the present study. At $Re \geq 300{,}000$, the boundary layer remained attached over most of the surface, again similar to the L1A behavior shown above. At intermediate Reynolds numbers, however, the Pak B results showed separation with reattachment after a large separation bubble. At Re=100,000, for example, the boundary layer on the Pak B airfoil separated just after the suction peak and did not reattach until near the trailing edge. As Reynolds number increased, the reattachment location gradually moved upstream. The L1A does not show this large separation bubble behavior, instead appearing to switch more abruptly between a nearly fully attached boundary layer and a burst bubble. This will be explored in more detail with the velocity profiles below.

Total Pressure Losses

The loss coefficient, ψ, is shown for all cases in Fig. 6. The coordinate ϕ indicates the distance in the direction perpendicular to the axial chord. The normalizing quantity L_ϕ is the blade spacing. The origin, ϕ=0, corresponds to the location directly downstream of the trailing edge of the center blade in the direction of the exit design flow

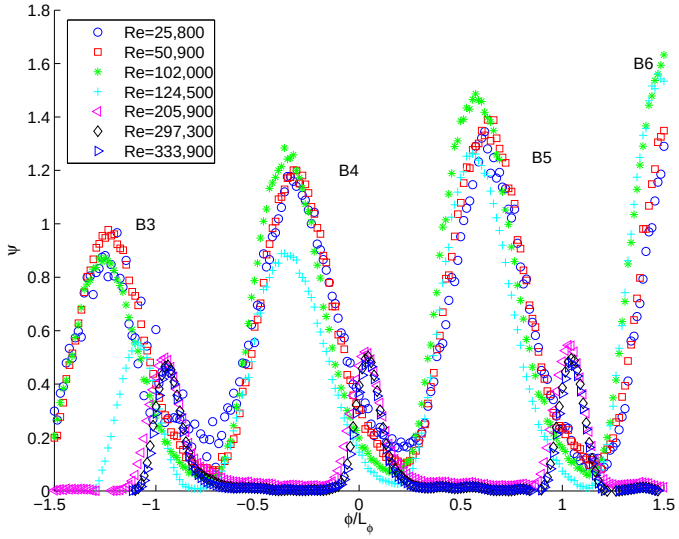

Fig. 6 Total pressure loss coefficient at 0.63 C_x downstream of cascade

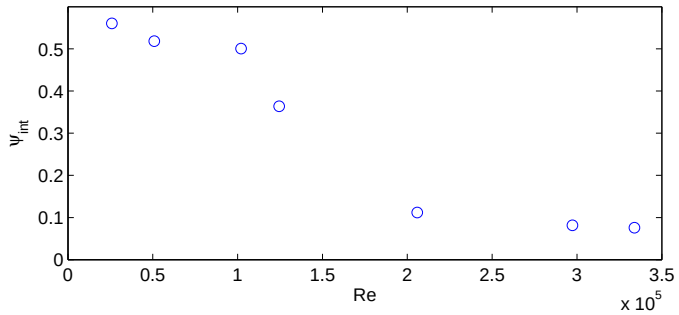

Fig. 7 Integrated total pressure loss coefficient for center blade as function of *Re*

angle. At the two highest Reynolds numbers the losses are low, and the location of the loss peaks are in the expected positions downstream of the airfoils. This indicates that the actual flow angle is essentially equal to the design angle. The peaks downstream of blades B3-B5 are similar to each other, indicating periodicity in the cascade. The loss coefficient is near zero between the peaks. At Re=205,900, the loss coefficients are slightly larger than at the higher Re. Although the difference is within the uncertainty, the trend is consistent with the appearance of a small separation bubble at this Reynolds number, seen in Fig. 4 at s/L_s=0.6. At the lower Reynolds numbers, the burst separation bubble results in much higher losses, and forces the peaks about $0.35L_\phi$ toward the pressure side of each passage. This shift corresponds to a 30° change in the exit flow angle. The reduction in flow turning is consistent with the lower lift shown in Fig. 5. The peaks become noticeably smaller moving from B6 to B3, indicating the effect of the tailboard in reducing the separation bubble thickness.

The integrated loss around the center blade is computed as

$$\psi_{int} = \int_{-L_\phi/2}^{L_\phi/2} \psi U d\phi \Big/ \int_{-L_\phi/2}^{L_\phi/2} U d\phi \qquad (2)$$

and is shown in Fig. 7 as a function of Reynolds number. Losses increase with decreasing Re. Between Re=300,000 and 200,000, ψ_{int}

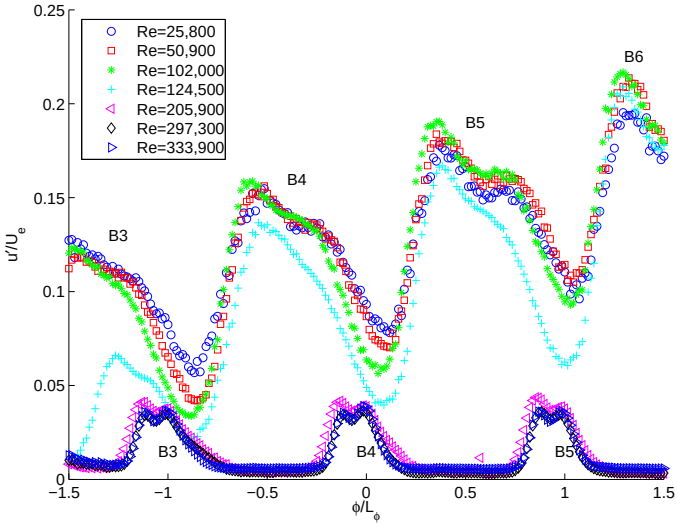

Fig. 8 Rms fluctuating streamwise velocity at 0.63 C_x downstream of cascade

increases by 37%, due to the thicker boundary layer at lower Reynolds numbers. The most dramatic increase, however, occurs between the attached and separated flow cases. The integrated loss increases by a factor of 7 between the highest and lowest Reynolds numbers.

The turbulence associated with the airfoil wakes is shown in Fig. 8. The rms fluctuating streamwise velocity at 0.63 C_x downstream of the trailing edge is normalized on the nominal exit velocity for each case. At the higher Reynolds numbers the boundary layer turbulence has decayed to about 4% of U_e. A double peak is apparent, with the slightly higher peak resulting from the suction side boundary layer and the smaller peak from the pressure side. Between blades the turbulence intensity is at the background level of the wind tunnel. At the lower Reynolds numbers, the turbulence level is much higher and in agreement with the loss coefficients, the peaks are shifted toward the pressure side of the passages.

Velocity Profiles

Velocity profiles for the six suction surface measurement stations are shown in Fig. 9 for the nominal *Re*=25,000 case. The top row in the figure shows the distance from the wall normalized on the suction surface length plotted against the local mean velocity normalized on the nominal exit velocity, U_e. The boundary layer has just separated at the first measurement station and the separation bubble grows larger at the downstream stations. The boundary layer does not reattach. The second row in Fig. 9 shows the rms streamwise fluctuating velocity, u', normalized with U_e. There is a very large peak located in the shear layer over the separation bubble which reaches a dimensionless magnitude of about 0.2. The third row in Fig. 9 shows the intermittency, γ. The intermittency is the fraction of time the flow is turbulent. It was determined at each measurement location based on the instantaneous streamwise velocity signal, using the technique described in Volino et al. [35]. Turbulent flow is defined here to include a range of large and small scale eddies. A boundary layer or shear layer may have significant u' fluctuations but still be considered non-turbulent if these fluctuations are induced by an external source such as freestream turbulence or are associated with instability in a narrow frequency band. Transition to turbulence is characterized by the appearance of broadband fluctuations. In the intermittency processing routine, the velocity signal is high pass filtered, and the appearance of high frequency fluctuations is used to distinguish

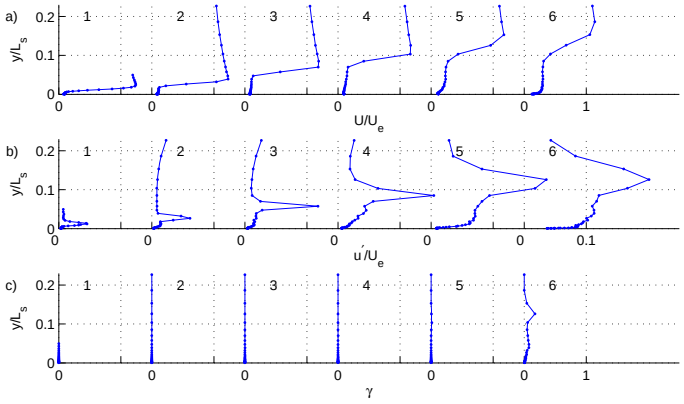

Fig. 9 Profiles for *Re*=25,000 case: (a) mean velocity, (b) u′/Ue, (c) intermittency

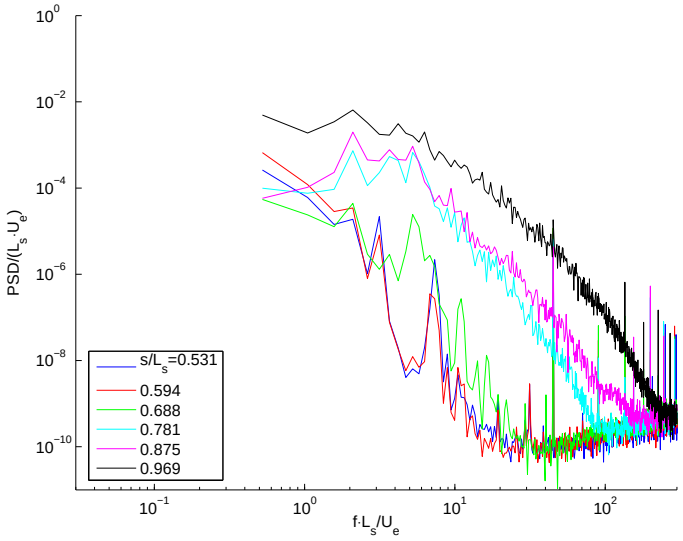

Fig. 10 Turbulence spectra for *Re*=25,000 case

between turbulent and non-turbulent flow. The results in Fig. 9 indicate that the shear layer remains non-turbulent until the last measurement station, where a small peak indicates the possible beginning of transition.

Figure 10 presents another view of the transition process using turbulence spectra. The spectra are computed from the fluctuating velocity signal acquired at the location of peak u' at each measurement station shown in Fig. 9. Frequencies are resolved from 4.88 Hz to 10 kHz in 4.88 Hz increments using 4096 point Fast Fourier Transforms to compute the spectra. The frequencies and power spectral density (PSD) are normalized using L_s and U_e. There is a clear broad band rise in the spectra between the third and fourth measurement stations, and the magnitude continues to rise downstream. The rise indicates that transition may be beginning by the fourth station. The rise in the spectra is not as abrupt as at higher Reynolds numbers (shown below), however, which may indicate that transition is only in its earliest stages. This may explain the intermittency values near zero in Fig. 9.

The velocity profiles for the *Re*=50,000 case are shown in Fig. 11. The mean and fluctuating velocity show essentially the same behavior observed in the *Re*=25,000 case of Fig. 9. The boundary layer does not reattach, in agreement with the pressure profile of Fig. 4. The intermittency values rise slightly above zero at the third station and indicate that transition is clearly underway by the fourth station. The

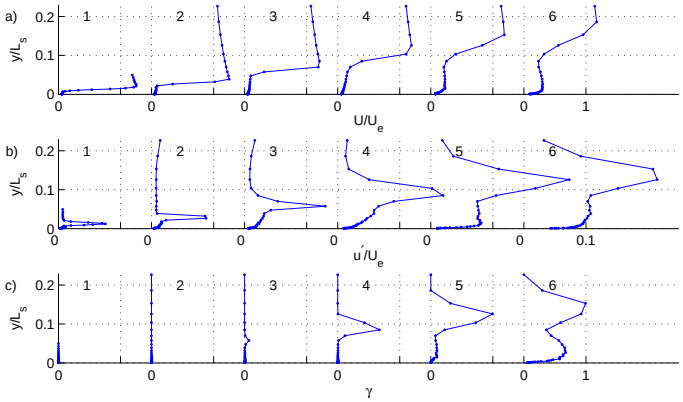

Fig. 11 Profiles for *Re*=50,000 case: (a) mean velocity, (b) u′/Ue, (c) intermittency

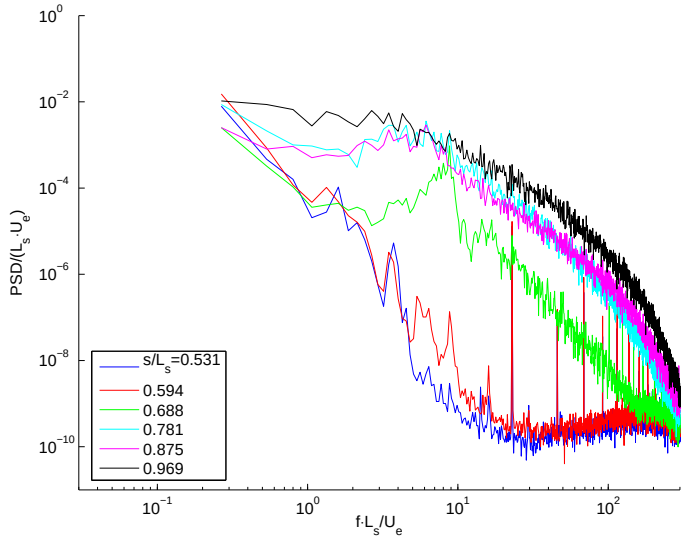

Fig. 12 Turbulence spectra for *Re*=50,000 case

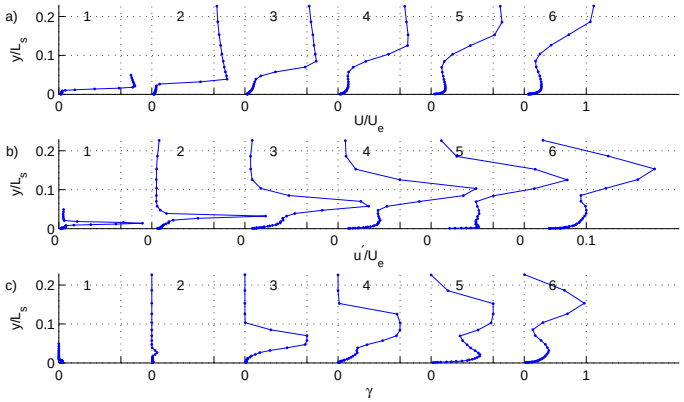

Fig. 13 Profiles for *Re*=100,000 case: (a) mean velocity, (b) u′/Ue, (c) intermittency

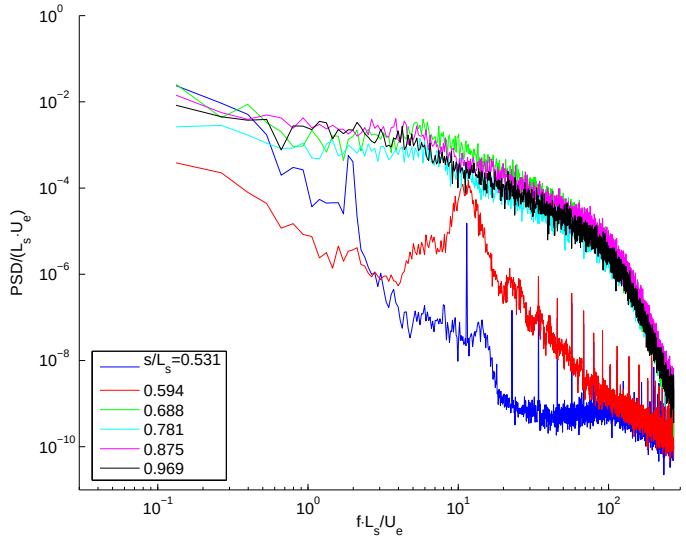

Fig. 14 Turbulence spectra for *Re*=100,000 case

corresponding turbulence spectra of Fig. 12 agree, showing a clear rise in the power spectrum between the second and third stations and a further rise to a more turbulent state by the fourth station.

The initiation of transition without boundary layer reattachment shown in Figs. 11 and 12 is markedly different than the behavior observed in previous studies with other LPT airfoils. Volino [13] noted that on the Pak B airfoil, when transition began in the separated shear layer, the associated mixing almost immediately induced boundary layer reattachment. This behavior was utilized by Volino [22] and by Zhang et al. [20], who used small passive devices on their airfoils to control separation. These devices were too small to trip the boundary layer to turbulent, but introduced small disturbances which accelerated the transition process in the shear layer, thereby moving reattachment upstream. Both Volino [22] and Zhang and Hodson [27] found that these small devices resulted in lower losses than large devices which immediately tripped the boundary layer to turbulent. The present results suggest that such devices may not work with the L1A airfoil, because transition is not sufficient to force reattachment. The strong negative acceleration parameter, shown in Fig. 2, particularly at low *Re* is apparently strong enough to prevent reattachment of the turbulent shear layer.

Figure 13 shows the velocity profiles for the *Re*=100,000 case. Similar to the previous cases, the separation bubble grows in the streamwise direction, the boundary layer does not reattach, and there is a very high peak in the fluctuating velocity in the shear layer over the separation bubble. The intermittency rises slightly above zero at the second station and indicates fully turbulent flow by the third station, where γ=1 in the shear layer. As in the previous case, the transition is not sufficient to induce boundary layer reattachment. Fig. 14 shows the spectra for the *Re*=100,000 case. There is a clear narrowband rise in the spectrum between the first and second stations, centered about a dimensionless frequency of 12. A further broadband rise occurs by the third station, indicating a turbulent shear layer, in agreement with the intermittency profiles of Fig. 13. The peak at the second station in Fig. 14 indicates a shear layer instability which likely initiates transition. Similar peaks are visible in the other Reynolds number cases, and will be discussed further below.

Velocity profiles for the *Re*=200,000 case are shown in Fig. 15. The boundary layer was laminar and on the verge of separation at the first two measurement stations. The small peak in intermittency at the first measurement station is believed to be erroneous, based on the spectra and the zero intermittency measurement at the second station. The skin friction, as determined from the near wall velocity profile, was near zero at the first two stations, but any separation bubble was very thin. Between the second and third stations the boundary layer underwent transition. The boundary layer was clearly attached and

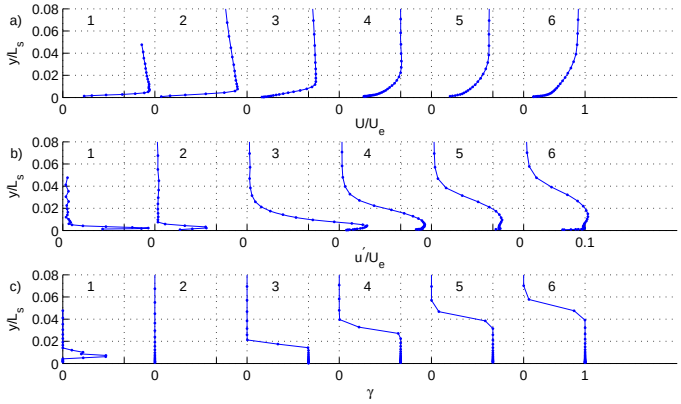

Fig. 15 Profiles for *Re*=200,000 case: (a) mean velocity, (b) u′/Ue, (c) intermittency

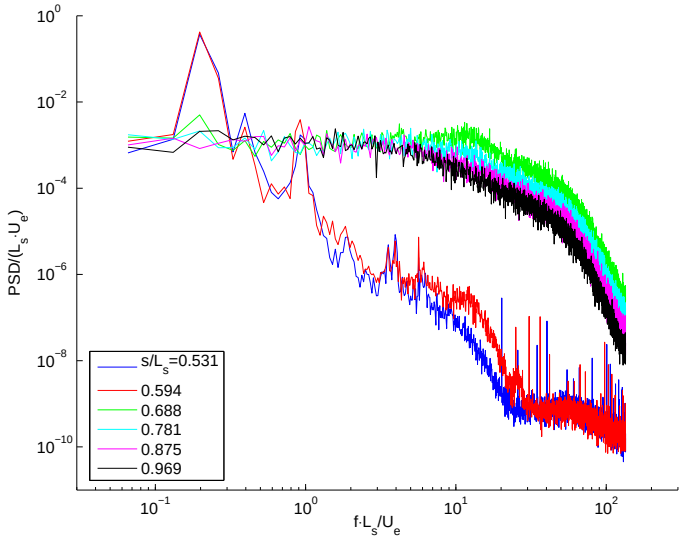

Fig. 16 Turbulence spectra for *Re*=200,000 case

fully turbulent at the third station and remained attached at all downstream stations, in agreement with the pressure profiles of Fig. 4. The spectra for this case are shown in Fig. 16. The clear jump from laminar to turbulent flow is clear between the second and third stations.

The velocity profiles and spectra for the *Re*=300,000 case are shown in Figs. 17 and 18. The results are very similar to those of the *Re*=200,000 case, with transition occurring between the second and third stations, and the boundary layer remaining attached and turbulent downstream.

The shape factor, *H*, and skin friction coefficient C_f are good indicators of the state of the boundary layer with respect to separation and transition. The shape factor is shown for the high *Re* cases in Fig. 19. It is between 2.5 and 3.5 at the first two measurement stations, where the boundary layer is laminar and on the verge of separation. It then drops rapidly with the onset of transition, reaching a minimum of about 1.57 at the fourth measurement station. While this value clearly indicates that the boundary layer is attached and turbulent, it is still above the zero pressure gradient turbulent value of about 1.4. At the downstream stations, *H* begins to rise, and it exceeds 1.7 by the last station. The skin friction coefficient is shown as a function of momentum thickness Reynolds number in Fig. 20. It rises from near zero after transition and decreases in the streamwise direction. Also

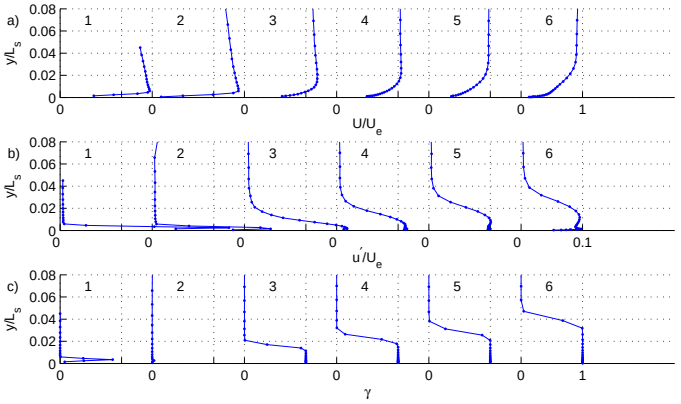

Fig. 17 Profiles for *Re*=300,000 case: (a) mean velocity, (b) u′/Ue, (c) intermittency

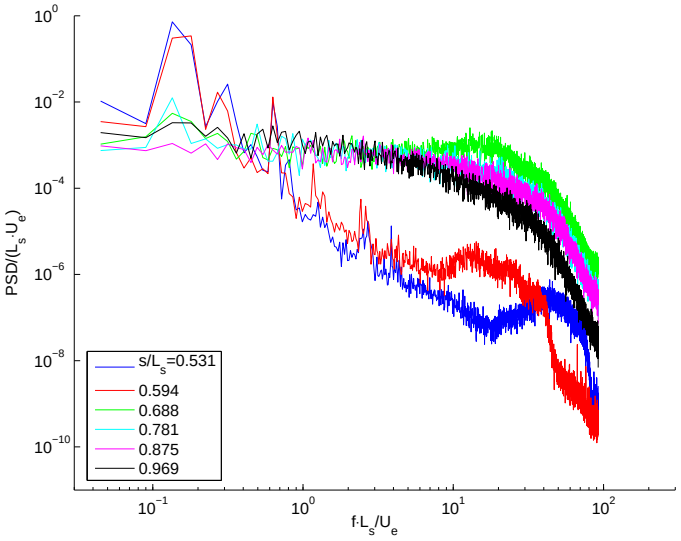

Fig. 18 Turbulence spectra for *Re*=300,000 case

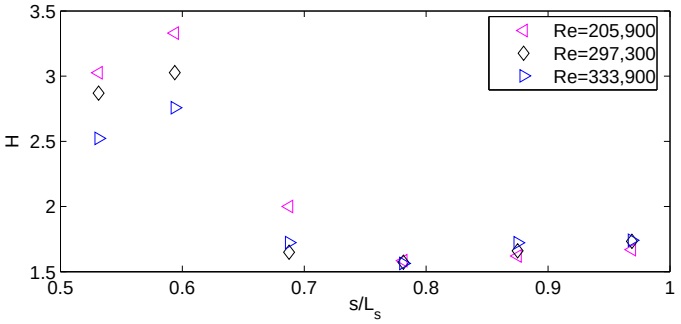

Fig. 19 Shape factor for high *Re* cases

shown is a standard flat-plate correlation for turbulent boundary layers from Schlichting [36] and the Ludwieg-Tillmann correlation. The present C_f values are as much as 40% lower than the flat-plate correlation and agree well with the Ludwieg-Tillmann correlation. The rising *H* and low C_f values are indicative of the strong adverse pressure gradient. The corresponding values on the Pak B airfoil [13] were closer to typical zero pressure gradient values, which is consistent with the weaker pressure gradient on the Pak B and the stronger tendency for reattachment at low *Re* on the Pak B.

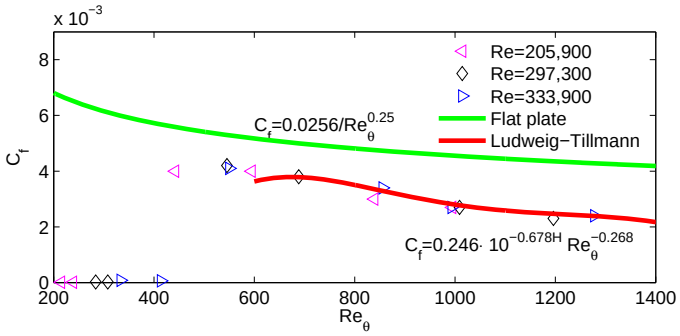

Fig. 20 Skin friction coefficient for high *Re* cases

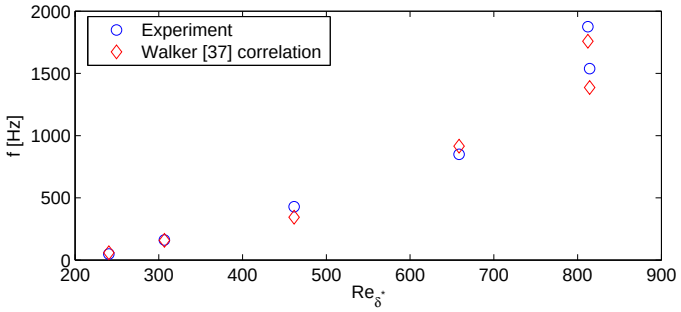

Fig. 21 Frequencies of spectral peaks along with predicted most unstable TS frequencies at separation location

Instability Prediction

The spectral peak noted above at the second station in Fig. 14 suggests an instability in the shear layer that likely initiates transition. Although less distinct, similar peaks are visible just before or just after transition inception at all Reynolds numbers. Volino [14] observed similar peaks in the boundary layer on the Pak B airfoil and associated them with TS waves, using an analysis from Walker [37]. The TS waves are believed to form in the attached boundary layer between the beginning of the adverse pressure gradient region and the separation location. The TS waves then continued to grow in the separated shear layer until they became large enough to induce transition, as discussed in Volino and Bohl [18]. Walker [37] gave the most unstable frequency for TS waves as

$$2\pi\nu f / U_\infty^2 = 3.2\,\mathrm{Re}_{\delta^*}^{-3/2} \qquad (3)$$

Hughes and Walker [31] note that the frequency predicted by Eq. (3) is a function of streamwise position, since the freestream velocity, U_∞, varies in non-zero pressure gradient cases, and the displacement thickness, δ^*, changes as the boundary layer grows. Hence, a single frequency cannot be expected for all TS waves in a boundary layer. For the present study, U_∞ and Re_{δ^*} were taken at the separation location. The Re_{δ^*} value was estimated with the boundary layer code TEXSTAN [38]. The code was used to a compute the laminar suction side boundary layer from the leading edge to the separation point using the pressure gradient from Fig. 4 as input for each case. The code stops when the flow separates, and the separation points computed were in good agreement with the pressure and velocity profiles presented above. Figure 21 shows the peak frequencies extracted from Figs. 10, 12, 14, 16 and 18 along with frequencies predicted by Eq. (3). The good agreement between the experimental and predicted values indicates that TS waves may play a role in the transition. It is also possible that other instability mechanisms are present. Stieger and Hodson [39], and Roberts and Yaras [40], for example, observed Kelvin-Helmholtz rollup of the shear layer.

Transition Correlations

Several correlations for predicting the starting location for separated flow transition are available in the literature, and some of these are tested below against the present data.

Mayle [2] presents the following correlations for short and long separation bubbles.

$$Re_{st} = 300\,Re_{\theta s}^{0.7} \quad \text{short bubble} \qquad (4)$$

$$Re_{st} = 1000\,Re_{\theta s}^{0.7} \quad \text{long bubble} \qquad (5)$$

where Re_{st} is the Reynolds number based on the freestream velocity at separation and the distance from separation to transition start.

The correlation of Davis et al. [16] is

$$Re_{st} = 25000\,\log_{10}[\coth(0.1732\,TI)] \qquad (6)$$

For the present experiments, *TI* could reasonably be set between 0.3% and 0.8%, as discussed above. Varying *TI* within this range does not significantly affect the correlation predictions. For Eq. (6) and all the correlations below, *TI* was set to 0.5%.

Hatman and Wang [15] identify several transition modes and present correlations for each of them. Their laminar separation mode transition correlation can be cast in terms of Re_{st} as

$$Re_{st} = 0.0816\,Re_s + 26805 \qquad (7)$$

Yaras [17] proposes

$$Re_{st} = 0.04\,Re_s + 6.3 \times 10^4 [1 - \tanh^3(TF')] \qquad (8)$$

where $TF' = max(TF, 1\%)$, and $TF = TI(s_s/\lambda)^{0.2}$, where s_s is the distance from the leading edge to the separation point and λ is the integral length scale of the freestream turbulence.

Praisner and Clark [19] present the correlation

$$Re_{st} = 173.0\,Re_s\,Re_{\theta s}^{-1.227} \qquad (9)$$

The above correlations are based on the conditions at the separation location and in some cases the freestream turbulence intensity. Volino and Bohl [18] reasoned that instabilities begin to grow when the boundary layer becomes unstable at the start of the adverse pressure gradient region, and present the following correlation

$$Re_{pt} = 8.80\,[6.37 - \log_{10}(TI^2)]\,Re_{\theta p}^{4/3} \qquad (10)$$

where Re_{pt} is based on the freestream velocity at the suction peak and the distance from the suction peak to the transition start.

The location of the suction peak for each case was taken from the experimental data of Fig. 4. The separation location and the momentum thickness Reynolds numbers at separation, $Re_{\theta s}$, and at the suction peak, $Re_{\theta p}$, were taken from the TEXSTAN calculations described above. Equations (4) – (10) were then used to compute s_t, which is defined as the distance from the leading edge to the start of transition. The Reynolds numbers used with the correlations are listed in Table 3. The s_t results are shown as a function of *Re* in Fig. 22. The experimental transition locations, as determined from Figs. 9-18

Table 3: Conditions at suction peak and separation location based on laminar boundary layer calculation

Re	s_p/L_s	s_s/L_s	$Re_{\theta p}$	$Re_{\theta s}$
25,800	0.438	0.496	48	61
50,900	0.438	0.494	68	85
102,000	0.438	0.496	96	122
205,900	0.493	0.538	151	182
297,300	0.493	0.538	182	220
333,900	0.493	0.537	193	231

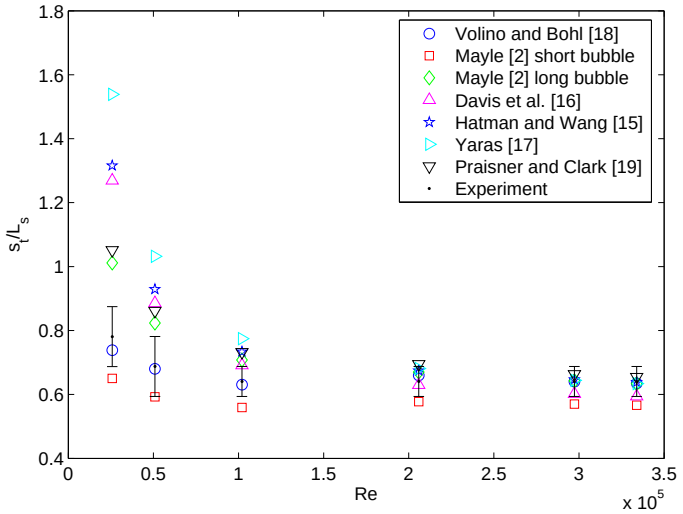

Fig. 22 Predicted and experimental transition start location, error bars indicate uncertainty due to finite spacing of measurement stations

are also shown. The uncertainties in the experimental locations, which result from the finite spacing between the measurement stations, are indicated by the error bars in Fig. 22. Values of $s_t/L_s>1$ in the figure indicate that transition is predicted downstream of the trailing edge of the airfoil.

The Mayle [2] short bubble correlation, which is only intended for separation bubbles that reattach, predicts transition somewhat too far upstream at all Reynolds numbers. For the $Re\geq$200,000 cases, all of the other correlations agree with the experimental results. For the lower *Re* cases, the Volino and Bohl [18] correlation continues to agree with the experiment, while the other correlations predict transition too far downstream.

CONCLUSIONS

The flow over the very high lift L1A airfoil was studied experimentally using a linear cascade. Reynolds numbers based on suction surface length and nominal exit velocity ranging from 25,000 to 330,000 were considered. In all cases the laminar suction surface boundary layer separated, but at Reynolds numbers greater than 150,000 the separation bubble was very thin and short, and the boundary layer was attached over most of the surface. At lower Reynolds numbers the boundary layer separated and never reattached. Separation without reattachment caused the lift on the airfoil to decrease by 20% and the total pressure losses increased by a factor of 7 above the highest Reynolds number case. Transition to turbulence occurred in all cases in the shear layer after separation, and appeared to be caused by the growth of Tollmien-Schlichting waves which originated in the boundary layer upstream of separation. The transition location was well predicted by the correlation of Volino and Bohl [18]. Transition caused immediate reattachment in the high Reynolds number cases, but the turbulent shear layer remained separated in the low *Re* cases. This behavior contrasts with previous studies on other LPT airfoils. In those studies, transition immediately triggered reattachment, even at low Reynolds numbers. On the present airfoil, the strong adverse pressure gradient prevents reattachment at low *Re*, even after transition occurs.

ACKNOWLEDGMENTS

This work was sponsored by the National Aeronautics and Space Administration. The grant monitor is Dr. Anthony Strasizar of the NASA Glenn Research Center. The support of the United States Naval Academy Technical Support Department Shop and Fluids Laboratory is greatly appreciated.

REFERENCES

[1] Hourmouziadis, J., 1989, "Aerodynamic Design of Low Pressure Turbines," AGARD Lecture Series 167.

[2] Mayle, R.E., 1991, "The Role of Laminar-Turbulent Transition in Gas Turbine Engines," ASME *Journal of Turbomachinery*, **113**, pp. 509-537.

[3] Sharma, O.P., Ni, R.H., and Tanrikut, S., 1994, "Unsteady Flow in Turbines," AGARD Lecture Series 195, Paper No. 5.

[4] Bons, J.P., Sondergaard, R., and Rivir, R.B., 2001, "Turbine Separation Control Using Pulsed Vortex Generator Jets," ASME *Journal of Turbomachinery*, **123**, pp. 198-206.

[5] Volino, R.J., and Hultgren, L.S., 2001, "Measurements in Separated and Transitional Boundary Layers Under Low-Pressure Turbine Airfoil Conditions," ASME *Journal of Turbomachinery*, **123**, pp. 189-197.

[6] McAuliffe, B.R., and Yaras, M.I., 2007, "Transition Mechanisms in Separation Bubbles Under Low and Elevated Freestream Turbulence," ASME Paper GT2007-27605.

[7] Mahallati, A., Sjolander, S.A., McAuliffe, B.R., and Praisner, T.J., 2007, "Aerodynamics of a Low-Pressure Turbine Airfoil at Low-Reynolds Numbers Part 1 -- Steady Flow Measurements," ASME Paper GT2007-27347.

[8] Mahallati, A., and Sjolander, S.A., 2007, "Aerodynamics of a Low-Pressure Turbine Airfoil at Low Reynolds Numbers Part 2 -- Blade-Wake Interaction," ASME Paper GT2007-27348.

[9] Zhang, X.F., and Howard Hodson, H., 2007, "Effects of Reynolds Number and Freestream Turbulence Intensity on the Unsteady Boundary Layer Development on an Ultra-High-Lift LPT Airfoil," ASME Paper GT2007-27274.

[10] Uzol, O., Zhang, X.F., Cranstone, A., and Hodson, H., 2007, "Investigation of Unsteady Wake-Separated Boundary Layer Interaction Using Particle-Image-Velocimetry," ASME Paper GT2007-28099.

[11] Opoka, M.M. and Hodson, H.P., 2007, "Transition on the T106 LP Turbine Blade in the Presence of Moving Upstream Wakes and Downstream Potential Fields," ASME Paper GT2007-28077.

[12] Zoric, T., Popovic, I., Sjolander, S.A., Praisner, T., and Grover, E., 2007, "Comparative Investigation of Three Highly Loaded LP Turbine Airfoils: Part I -- Measured Profile and Secondary Losses at Design Incidence," ASME Paper GT2007-27537.

[13] Volino, R.J., 2002, "Separated Flow Transition Under Simulated Low-Pressure Turbine Airfoil Conditions: Part 1 – Mean Flow and Turbulence Statistics," ASME *Journal of Turbomachinery*, **124**, pp. 645-655.

[14] Volino, R.J., 2002, "Separated Flow Transition Under Simulated Low-Pressure Turbine Airfoil Conditions: Part 2 –Turbulence Spectra," ASME *Journal of Turbomachinery*, **124**, pp. 656-664.
[15] Hatman, A., and Wang, T., 1999, "A Prediction Model for Separated Flow Transition," ASME *Journal of Turbomachinery*, **121**, pp. 594-602.
[16] Davis, R.L., Carter, J.E., and Reshotko, E., 1985, "Analysis of Transitional Separation Bubbles on Infinite Swept Wings," AIAA Paper 85-1685.
[17] Yaras, M. I., 2002, "Measurements of the Effects of Freestream Turbulence on Separation-Bubble Transition," ASME Paper GT-2002-30232.
[18] Volino, R.J., and Bohl, D.G., 2004, "Separated Flow Transition Mechanisms and Prediction With High and Low Freestream Turbulence Under Low Pressure Turbine Conditions," ASME Paper GT2004-63360.
[19] Praisner, T.J., and Clark, J.P., 2007, "Predicting Transition in Turbomachinery – Part 1: A Review and New Model Development," ASME *Journal of Turbomachinery*, **129**, pp. 1-13.
[20] Zhang, X.F., Vera, M., Hodson, H., and Harvey, N., 2007, "Separation and Transition Control on an Aft-Loaded Ultra-High-Lift LP Turbine Blade at Low Reynolds Numbers: Low-Speed Investigation," ASME *Journal of Turbomachinery*, **128**, pp. 517-527.
[21] Bohl, D.G. and Volino, R.J., 2006, "Experiments with Three-Dimensional Passive Flow Control Devices on Low-Pressure Turbine Airfoils," ASME *Journal of Turbomachinery*, **128**, pp. 251-260.
[22] Volino, R.J., 2003, "Passive Flow Control on Low-Pressure Turbine Airfoils," ASME *Journal of Turbomachinery*, **125**, pp. 754-764.
[23] Volino, R.J., 2003, "Separation Control on Low-Pressure Turbine Airfoils Using Synthetic Vortex Generator Jets," ASME *Journal of Turbomachinery*, **125**, pp. 765-777.
[24] Huang, J., Corke, T., and Thomas, F., 2003, "Plasma Actuators for Separation Control on Low Pressure Turbine Blades," AIAA Paper 2003-1027.
[25] Bons, J.P., Hansen, L.C., Clark, J.P., Koch, P.J., and Sondergaard, R., 2005, "Designing Low-Pressure Turbine Blades With Integrated Flow Control," ASME Paper GT2005-68962
[26] Clark J.P., 2007, Private Communication, Air Force Research Laboratory.
[27] Zhang, X.F., and Hodson, H., 2005, "Combined Effects of Surface Trips and Unsteady Wakes on the Boundary Layer Development of an Ultra-High-Lift LP Turbine Blade," ASME *Journal of Turbomachinery*, **127**, pp. 479-488.
[28] Lakshminarayana, B., 1996, *Fluid Dynamics and Heat Transfer of Turbomachinery*, Wiley, New York.
[29] McAuliffe, B.R. and Sjolander, S.A., "Active Flow Control Using Steady Blowing for a Low-Pressure Turbine Cascade," ASME *Journal of Turbomachinery*, **126**, pp. 560-569.
[30] Lewis, R.I., 1991, *Vortex Element Methods for Fluid Dynamic Analysis of Engineering Systems*, Cambridge University Press, Cambridge.
[31] Hughes, J.D. and Walker, G.J., 2001, "Natural Transition Phenomena on an Axial Compressor Blade," ASME *Journal of Turbomachinery*, **123**, pp. 392-401.
[32] Wills, J.A.B., 1962, "The Correction of Hot-Wire Readings for Proximity to a Solid Boundary," *Journal of Fluid Mechanics*, **12**, pp. 65-92.
[33] Volino, R.J., and Simon, T.W., 1997, "Velocity and Temperature Profiles in Turbulent Boundary Layers Experiencing Streamwise Pressure Gradients," ASME *Journal of Heat Transfer*, **119**, pp. 433-439.
[34] Simon, T.W., Qiu, S., and Yuan, K., 2000, "Measurements in a Transitional Boundary Layer Under Low-Pressure Turbine Conditions," NASA/CR-2000-209957.
[35] Volino, R.J., Schultz, M.P., and Pratt, C.M., 2001, "Conditional Sampling in a Transitional Boundary Layer Under High Free-Stream Turbulence Conditions," ASME *Journal of Fluids Engineering*, **125**, pp. 28-37.
[36] Schlichting, H., 1979, *Boundary Layer Theory*, 7th ed., McGraw-Hill, New York.
[37] Walker, G.J., 1989, "Transitional Flow on Axial Turbomachine Blading," *AIAA Journal*, **27**, pp. 595-602.
[38] Crawford, M.E., and Kays, W.M., 1976, "STAN5 – A Program for Numerical Computation of Two-Dimensional Internal and External Boundary Layer Flows," NASA CR-2742.
[39] Stieger, R.D., and Hodson, H.P., 2004, "The Transition Mechanism of Highly Loaded Low-Pressure Turbine Blades," ASME *Journal of Turbomachinery*, **126**, pp. 536-543.
[40] Roberts, S.K, and Yaras, M.I., 2006, "Effects of Surface-Roughness Geometry on Separation-Bubble Transition," ASME *Journal of Turbomachinery*, **128**, pp. 349-356.

Proceedings of IMECE2008
2008 ASME International Mechanical Engineering Congress and Exhibition
November 2-6, 2008, Boston, Massachusetts, USA

IMECE2008-68879

EXPERIMENTAL AND COMPUTATIONAL INVESTIGATIONS OF SEPARATION AND TRANSITION ON A HIGHLY LOADED LOW-PRESSURE TURBINE AIRFOIL: PART 1 – LOW FREESTREAM TURBULENCE INTENSITY

Mounir Ibrahim and Olga Kartuzova
Mechanical Engineering Department
Cleveland State University
Cleveland, Ohio 44115-2425
(216) 687-2580, m.ibrahim@csuohio.edu

Ralph J. Volino
Mechanical Engineering Department
United States Naval Academy
Annapolis, Maryland 21402-5042
(410) 293-6520, volino@usna.edu

ABSTRACT

Boundary layer separation, transition and reattachment have been studied on a new, very high lift, low-pressure turbine airfoil. Experiments were done under low freestream turbulence conditions on a linear cascade in a low speed wind tunnel. Pressure surveys on the airfoil surface and downstream total pressure loss surveys were documented. Velocity profiles were acquired in the suction side boundary layer at several streamwise locations using hot-wire anemometry. Cases were considered at Reynolds numbers (based on the suction surface length and the nominal exit velocity from the cascade) ranging from 25,000 to 330,000. In all cases the boundary layer separated, but at high Reynolds number the separation bubble remained very thin and quickly reattached after transition to turbulence. In the low Reynolds number cases, the boundary layer separated and did not reattach, even when transition occurred.

Three different CFD URANS (unsteady Reynolds averaged Navier-Stokes) models were utilized in this study (using Fluent CFD Code), the k-ω shear stress transport model, the v^2-f k-ε model, and the 4 equation Transition model of Menter. At Re=25,000, the Transition model seems to perform the best. At Re=100,000 the Transition model seems to perform the best also, although it under-predicts the pressure coefficient downstream of the suction peak. At Re= 300,000 all models perform very similar with each other. The Transition model showed a small bump in the pressure coefficient downstream from the suction peak indicating the presence of a small bubble at that location.

NOMENCLATURE

Cp	$2(P_T - P)/\rho U_e^2$, pressure coefficient
C_x	axial chord length
L_s	suction surface length
L_ϕ	blade spacing (pitch)
P	pressure
P_S	upstream static pressure
P_T	upstream stagnation pressure
P_{Te}	downstream stagnation pressure
Re	$U_e L_S / \nu$, exit Reynolds number
Re_θ	$U_\infty \theta / \nu$, momentum thickness Reynolds number
s	streamwise coordinate, distance from leading edge
TI	freestream turbulence intensity
U	mean streamwise velocity
U_e	nominal exit freestream velocity, based on inviscid solution
U_∞	freestream velocity
u'	time averaged rms streamwise fluctuating velocity
x	axial distance from leading edge
y	distance from wall
y^+	distance from wall in viscous units
α_1	inlet flow angle
α_2	exit flow angle
ϕ	coordinate along blade spacing, normal to axial chord
ν	kinematic viscosity
ρ	density
θ	momentum thickness
ψ	$(P_T-P_{Te})/(P_T-P_S)$, total pressure loss coefficient

Subscripts

p	pressure minimum (suction peak) location
pt	distance from suction peak to transition start
s	separation location
t	transition start

INTRODUCTION

Flow separation on the suction surface of low-pressure turbine (LPT) airfoils often occurs when turbine engines operate at low Reynolds numbers, as in the case of aircraft engines at high altitude cruise conditions. Low Reynolds numbers can cause the boundary layer to remain laminar and easily separate. This laminar separation results in an engine efficiency drop and an increase in fuel consumption (Mayle [1], Howell [2], and Singh [3]).

Simulation and prediction of transitional flow over LPT airfoils under a wide variety of Reynolds numbers, freestream turbulence parameters and with flow separation is essential for improvement in aircraft engine design. A great number of experimental and numerical investigations had been carried out in order to better understand the

mechanisms of flow separation and transition on LPT airfoils. Volino [4] provides a review of some earlier studies. In general, previous work shows that the strong acceleration on the leading section of the airfoil keeps the boundary layer thin and laminar, even in the presence of elevated freestream turbulence. Some recent examples of those experimental studies are: Volino, [4,5], Mahallati et al.[6,7], Zoric et al. [8], and Zhang and Hodson [9]. Downstream of the suction peak the adverse pressure gradient can cause boundary layer separation, which may be followed by transition to turbulence and flow reattachment (Volino, [4,5]).

The advances in separation understanding and prediction have led to attempts at separation control. Zhang et al. [10], Bohl and Volino [11], Volino [12], and others provide examples using passive devices such as boundary layer trips. Others have used active devices such as vortex generator jets (e.g. Bons et al. [13], and Volino [14]) or plasma devices (e.g. Huang et al. [15]).

Another way to improve performance is to design airfoils with pressure gradients more resistant to separation, as described by Praisner and Clark [16]. Forward loading, for example, makes airfoils more separation resistant by extending the adverse pressure gradient on the aft portion of the suction side over a longer distance. This reduces the local pressure gradient at all locations, making separation less likely. If separation does occur, forward loading provides a longer distance along the airfoil surface for reattachment. Forward loading has some disadvantages, however. As noted by Zhang et al. [10], the longer region of turbulent flow on a forward loaded airfoil can lead to increased profile losses. Forward loading also creates longer regions of strong pressure gradient on the endwalls, which can produce stronger secondary flows and losses. If flow control were incorporated in the design of an advanced airfoil, as discussed by Bons et al. [17], it might be possible to produce an aft loaded airfoil that was resistant to separation and had low profile and secondary loss characteristics over a range of Reynolds numbers.

A reduction in the production costs as well as the weight of an engine can be achieved by increasing the loading on LPT airfoils, thereby allowing a reduction in the number of LPT blades. Therefore, very highly loaded airfoils are of great interest. Volino [18] experimentally studied the flow over a very highly loaded LPT airfoil, designed at the Air Force Research Laboratory (AFRL) and designated L1A. The L1A is available on a limited basis to US researchers from Clark [private communication]. Dimensions of the L1A as used in the present experiments are given in Table 1.

Table 1: Cascade parameters for L1A airfoil

Axial Chord, C_x [mm]	True Chord [mm]	Pitch, L_ϕ [mm]	Span [mm]	Suction side, L_s [mm]	Inlet flow angle	Exit flow angle
134	146	136	724	203	35°	60°

Volino [18] reported that for the low Reynolds numbers considered (Re = 25,000 – 125000, based on exit velocity and suction side length) the flow separated and never reattached, even after transition to turbulence. For the higher Re (Re = 200,000 - 300,000) a very thin separation bubble was observed and the flow quickly reattached after transition occurred. Volino, [18] concluded that L1A differs from many previously studied LPT airfoils, where transition forced separated flow to reattach even at low Re. The L1A is considered to be a good airfoil for future flow control work, combining very high loading with a need for separation control.

Along with experimental work significant computational effort has been devoted to better understanding of separation and transition mechanisms in the LPT. McAuliffe and Yaras [19] conducted a Direct Numerical Simulation (DNS) study of laminar boundary layer separation on a flat surface in the presence of an adverse pressure gradient. Separation and transition mechanisms were examined under low and high disturbance environments. Singh [3] studied the flow physics in a LPT cascade under low Re number conditions using Large Eddy Simulation (LES). Calculations were carried out for Re = 10,000 and 25,000 (based on inlet velocity and axial chord). The flow for both Reynolds numbers separated and never reattached.

DNS and LES calculation require high resolution grids, which results in high computational time, therefore these methods are very computationally expensive. This makes modification of Reynolds Averaged Navier-Stokes (RANS) methods to better predict separation and transition processes very attractive. Many studies have been done in the area of developing and testing transition models capable of accurate prediction of flow physics in turbomachinery. Some of the latest examples include Suzen et al. [20], who applied a transition model based on an intermittency transport equation to predictions of LPT experiments on the Pack B airfoil. Howell [2] used the Prescribed Unsteady Intermittency Model (PUIM) to study wake - surface flow interactions on a high lift LPT airfoil. This approach employs a set of correlations for transition onset and for spot production rate. A different approach was proposed by Menter et al. [21], based on two transport equations. The intermittency transport equation is used to trigger the transition onset. The transport equation for the transition momentum thickness Reynolds number ($Re_{\theta t}$) is used to capture non-local effect of freestream turbulence intensity and pressure gradient at the boundary layer edge. These two equations were coupled with a shear stress transport turbulence model (SST). This model was validated against experimental data for various turbomachinery and aerodynamic applications (Langtry et al. [22] and Menter et al. [21]).

The objective of the present work is to conduct a computational study of a very highly loaded low pressure turbine airfoil, designated the L1A under low freestream turbulence conditions. The experimental data have been presented previously (Volino [18]) and a summary is provided in this paper. On the computational side the problem has been extensively investigated utilizing different: 1) grid structures, 2) inlet velocity conditions, 3) turbulence models, and 4) Reynolds numbers. The present results will serve as baseline results for future work, in which attempts will be made to suppress separation through flow control at low Reynolds numbers.

EXPERIMENTAL FACILITY AND MEASUREMENTS

Experiments (described in details in Volino [18]) were conducted in a closed loop wind tunnel with a linear cascade in one corner of the loop. A seven blade cascade is located in the wind tunnel's third turn, as shown in Fig. 1. A generic airfoil shape is shown in the figure.

The freestream turbulence entering the cascade was measured with a cross-wire probe positioned just upstream of the center blade. The streamwise velocity component had a turbulence intensity, TI, of 0.8% and integral length scale of 6.3 cm. These values were used in all the calculations described below. Further details of the freestream turbulence are in Volino [18]. While such low freestream turbulence and large length scales are not representative of engine conditions, they are still of interest as a limiting case. Also, in zero or favorable pressure gradient boundary layers, high TI can cause bypass transition, but under adverse pressure gradients, natural transition appears to play a role at all TI levels.

A tailboard, shown in Fig. 1, was needed to produce the correct exit flow angle from the cascade. Its position was set to produce periodicity at high Reynolds numbers. A tailboard on the opposite side of the cascade, and inlet guide vanes were found to be

unnecessary. To produce the correct approach flow to the end blades (B1 and B7), the amount of flow escaping around the two ends of the cascade was controlled with the flaps shown in Fig. 1. The flap positions were set using a wool tuft upstream of each blade to check that the incoming flow approached the stagnation points with the correct angle. The inlet flow angle at the center of the cascade was also checked with a three-hole pressure probe and found to agree with the design angle to within about 2° of uncertainty. At high Reynolds numbers, the approach velocity to the middle four passages was measured to be uniform to within 6%, and the difference between any two adjacent passages was within 3%. At low Reynolds numbers, slightly more variation was observed, but the approach velocity to the middle two passages still agreed to within 5%. Good periodicity at high Reynolds numbers was also observed in the exit flow from the cascade, as evidenced by suction side velocity profiles acquired near the trailing edge of blades B2-B6, and by total pressure loss surveys, which are shown below. At low Reynolds numbers, when significant separation bubbles were present, the periodicity was not as good due to suppression of the separation bubble thickness on the blades closest to the tailboard. This deviation from periodicity is considered acceptable for the present facility, since its intended purpose is for the study of flow control, which if successful should suppress separation on all blades, thereby restoring periodicity even at low Reynolds numbers.

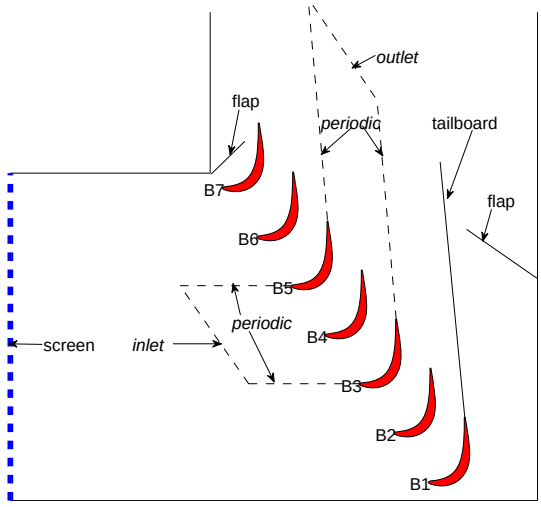

Fig. 1 Schematic of a linear cascade of 7 airfoils (Volino [18]) with boundary conditions and computational domain used in present study, shown in dashed lines

COMPUTATIONAL METHOD

The CFD predictions were performed with the numerical software tool FLUENT [23]. Predictions with three turbulence models were compared with the experimental results of Volino [18]. These models are described below. The computational domain consisted of two channels and the airfoil in the middle. It is shown on Fig. 1 in dashed lines. The boundary conditions applied along the sides of the domain are periodic, except along the airfoil surfaces, which are walls. No-slip boundary conditions were applied for all walls.

The inlet boundary condition was a prescribed uniform velocity, and is described in more detail below. The inlet into the two channels is located at 1.9 C_x upstream of the airfoil leading edge in the flow direction. At the outlet zero gage pressure was applied. The exit was located at 3.8 C_x downstream of the airfoil trailing edge in the flow direction. Different exit locations were tested to insure that 3.8 C_x was far enough downstream to achieve independent results (as indicated by pressure coefficients, pressure losses downstream of the cascade and velocity profiles on the airfoil) through the passages.

Unsteady calculations were performed for all cases. Convergence was established when: 1) residuals reduced to a value of 10^{-4}, 2) velocity at the outlet and pressure on the airfoil suction side settled (fluctuations around certain mean values were observed, however there were no equal cycles), and 3) the mass imbalance was less than 0.01 %. After convergence was achieved within each time step (Δt = 0.0005 s) with the conditions listed above, time averaged results were obtained for 2000 time steps.

Grid independence study

A grid independence study for 2D grids was conducted for *Re* = 102,000. The V2F turbulence model (described below) was applied. Differences in grids are summarized in Table 2. Grids 2 and 3 showed maximum difference in C_p on the suction side of an airfoil less than 2%, therefore grid 2 was used in this study.

Table 2 Grid characteristics for grid independence study

Grid number	Size	y^+ on the airfoil walls	Number of points on airfoil ss	Number of points on airfoil ps
1	91516	2.95 (range 0.1-8)	290	240
2	62469	0.20 (range 0.01-0.6)	290	240
3	312393	0.20 (range 0.01-0.6)	1369	933

Boundary conditions influence study

After grid independence was established several inlet velocity boundary conditions were tested. First, a uniform inlet velocity was applied in the direction of the design inlet flow angle (35°). This condition resulted in a slightly higher pressure on the leading section of the suction side of the airfoil compared to the experiment, indicating that the actual inlet angle could be different from the design angle. To investigate this possibility, a 2D inviscid calculation was done for the full cascade shown in Fig. 1, including the tailboard and flaps. The inlet velocity magnitude and direction were taken from the inviscid calculation along a line parallel to the blade row and 1.9 C_x upstream of the blades in the flow direction, and used to set the inlet boundary conditions to the 2 channel domain described above. The inlet boundary conditions tested are summarized in Table 3, all were tested at *Re*=102,000. Four different inlet conditions are presented in Table 3. The first condition assumed a uniform inlet velocity at the design flow angle of 35°. The second condition used the velocity profile entering the two channel domain as obtained from the invisicid calculation. This condition shows a slight variation in the velocity profile at the inlet both in x and ϕ directions with spatial averaged velocities V_x= 3.78 and V_ϕ = 2.32 m/s. Accordingly, the spatial averaged inlet flow angle is 31.5°. The third condition used a uniform inlet velocity and flow angle (V_x= 3.78 and V_ϕ = 2.32 m/s and inlet flow angle = 31.5°) based on the average values across the inlet of the two channel domain from the inviscid calculation. Thus the difference between conditions (2) and (3) are in the spatial variation in the inlet velocity while the averaged values are the same. The fourth condition

used a uniform inlet velocity and angle based on the spatial averaged values across the full cascade (instead of averaging over two channels only as in condition (3)) from the inviscid calculation. Therefore the inlet velocity variations chosen in this exercise involve different inlet flow velocity magnitude and angle based on the design or the inviscid CFD results for the 7 blades (see Fig. 1).

Boundary condition 4 produced results in better agreement with the experimental data and was chosen for the rest of this investigation. The deviation of the inlet angle from the design angle is about 2°, which is within the uncertainty of the experimental measurement and therefore plausible.

Table 3 Inlet boundary conditions for 2 channels tested, Re=102,000

#	Description	V_x, m/s	V_ϕ, m/s	V_{mag}, m/s	α_1, deg
1	Design condition	3.65	2.56	4.46	35
2	Velocity profile from cascade simulation taken at inlet into 2 channels	3.78 (avg)	2.32 (avg)	4.43 (avg)	31.5 (avg)
3	Velocity from cascade simulation averaged across inlet into 2 channels	3.78	2.32	4.43	31.5
4	Velocity from cascade simulation averaged across full cascade at streamwise location of inlet into 2 channels.	3.71	2.36	4.4	32.5

Turbulence Modeling

In this study, the $k-\omega$ - *sst* model of Menter [24], the $\overline{v^2}-f$ model of Durbin [25], and new Transition-sst (4 eq.) model of Menter [21], were compared for separated flow predictions on the highly loaded LPT airfoil. The unsteady Reynolds-averaged Navier-Stokes (URANS) equations were used as the transport equations for the mean flow. The governing equations and the detailed description of each model have been published elsewhere and therefore are not shown in this paper.

Shear-stress transport $k-\omega$ model (SKW-sst): This model, developed by Menter [24] is similar to the standard $k-\omega$ of Wilcox [26], but has an ability to account for the transport of the principal shear stress in adverse pressure gradient boundary layers. The model is based on Bradshaw's [27] assumption that the principal shear stress is proportional to the turbulent kinetic energy, which is introduced into the definition of the eddy-viscosity. These features make the SST $k-\omega$ model more accurate and reliable for a wider class of flows (e.g., adverse pressure gradient flows, airfoils, transonic shock waves) than the standard $k-\omega$ model [23].

$\overline{v^2}-f$ model (V2F): According to Launder [28], the normal stress $\overline{v^2}$, perpendicular to the local streamline plays the most important role to the eddy viscosity. Motivated by this idea, Durbin [25] devised a "four-equation" model, known as the $k-\varepsilon-v^2$ model, or $\overline{v^2}-f$ model. It eliminates the need to patch models in order to predict wall phenomena like heat transfer or flow separation. It makes use of the standard $k-\varepsilon$ model, but extends it by incorporating the anisotropy of near-wall turbulence and non-local pressure strain effects, while retaining a linear eddy viscosity assumption.

Transition-sst (4 eq.) model: A new correlation-based transition model was proposed by Menter et al. [21]. This model is based on two transport equations. The intermittency transport equation is used to trigger the transition onset. The transport equation for the transition momentum thickness Reynolds number ($Re_{\theta t}$) is used to capture non-local effects of freestream turbulence intensity and pressure gradient at the boundary layer edge. Outside the boundary layer the transport variable was forced to follow the value of $Re_{\theta t}$ given by correlations. Those two equations were coupled with the shear stress transport turbulence model (SST). This model has recently become available in Fluent code.

RESULTS

Re =25,000

Figure 2 shows the pressure coefficient plotted versus s/L_s along the suction and pressure surfaces for the turbulence models tested and Re = 25,000. Notice the abscissa is the distance along the blade surface normalized with respect to the suction surface length. The experimental data shows that the *Cp* values have a constant value on the downstream part of the suction side. This plateau indicates that the boundary layer has separated and that the boundary layer never reattaches (i.e. the separation bubble bursts); this of course refers to the time-averaged bubble as the bubble will probably burst sporadically. All turbulence models predict the pressure coefficient reasonably well with some deviation near the leading edge. The deviation could be partially attributed to uncertainty in the measurements and the inlet velocity profile as discussed above. All the models do well in predicting the separation location and the failure of the flow to reattach, as seen in the experiment.

Figure 3 shows the total pressure loss coefficient, ψ, plotted versus dimensionless distance (ϕ/L_ϕ) at a location 0.63 C_x downstream of the cascade. The definition of ψ used in this study is the same as the one used in earlier work by Volino [18] and Bons et al. [29]. The coordinate ϕ indicates the distance in the direction perpendicular to the axial chord. The normalizing quantity L_ϕ is the blade spacing. The origin, ϕ=0, corresponds to the location directly downstream of the trailing edge of the center blade in the direction of the exit design flow angle. At low Reynolds numbers the burst separation bubble results in high losses and forces the peaks about $0.35L_\phi$ toward the pressure side of each passage. The peaks become noticeably smaller moving from B5 to B3, indicating the effect of the tailboard in reducing the separation bubble thickness. Due to the lack of periodicity in the experiment, the predicted loss coefficient is not expected to agree precisely with the experiment. The prediction is based on periodic boundary conditions and is not influenced by tailboard effects, so it should show higher losses and possibly lower flow turning (peaks shifted more to the left in the figure). This is indeed the case, as shown in Fig. 3.

Velocity profiles for the six suction surface measurement stations on blade B4 documented in the experiment are shown in Fig. 4 for the nominal Re=25,000 case. The figure shows the distance from the wall normalized on the suction surface length plotted against the local mean velocity normalized on the nominal exit velocity, U_e. The boundary layer has just separated at the first measurement station and the separation bubble grows larger at the downstream stations.

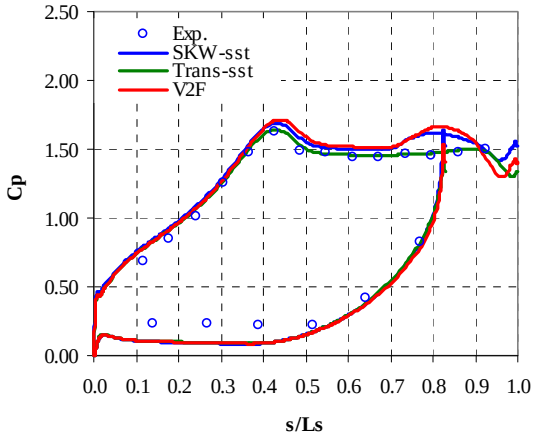

Fig. 2 C_p profiles, Re=25,000

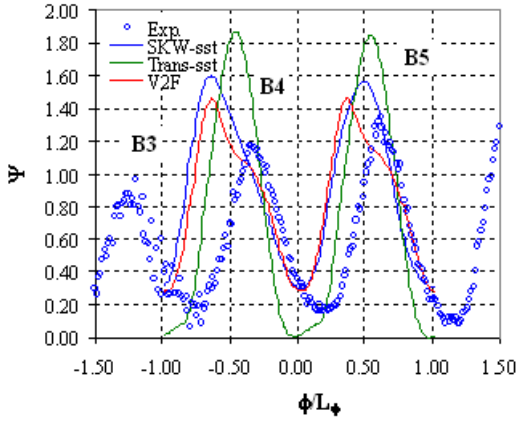

Fig. 3 Pressure loss coefficients at 0.63 C_x downstream of cascade, Re=25,000

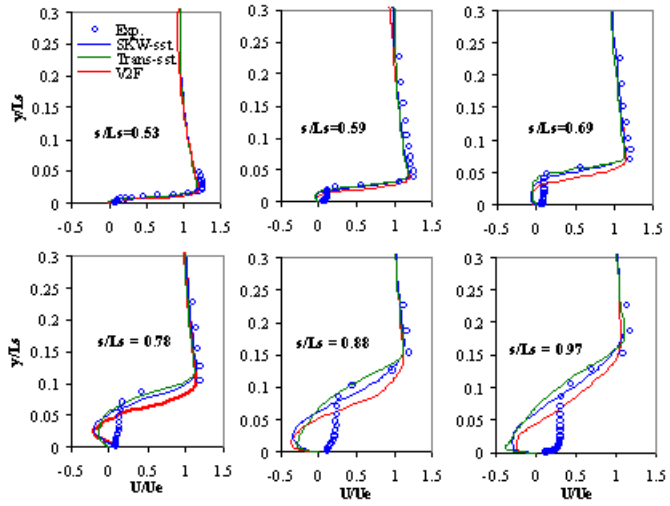

Fig. 4 Mean velocity profiles, Re = 25,000

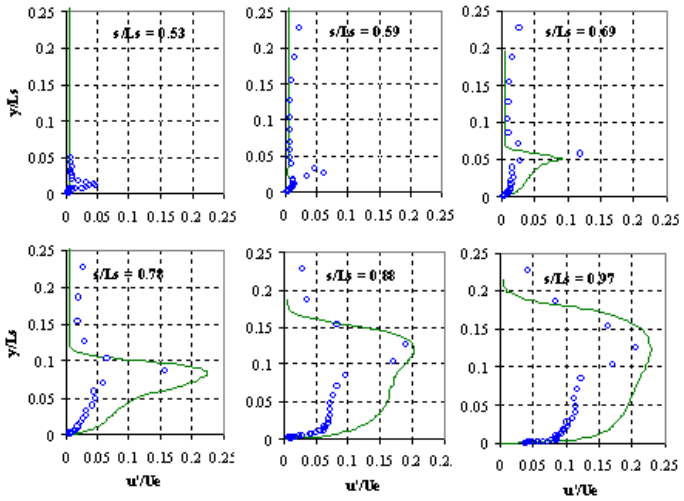

Fig. 5 Comparison of Transition-sst and experimental u'/U_e profiles, Re= 25,000

The boundary layer does not reattach. The velocity profiles at the six stations along the suction surface are predicted reasonably well by all models with the Transition model doing better overall. The prediction in the near wall region is different than the data since the measurements were done using hot-wire anemometry and therefore can not register negative velocities when separation occurs.

Figure 5 shows u'/U_e profile versus y/L_s at the six different stations along the suction side. u' was obtained from CFD (using the Transition model only because of its best overall prediction) from the kinetic energy of turbulence and assuming an isotropic flow field (i.e. $u' = v' = w'$). Despite this assumption the CFD shows reasonable agreement with the data. The CFD shows a peak in the u' profile that moves away from the wall as one travels from station (1) to (6). This peak value will be utilized (as will be shown later) to predict the start of transition. It is interesting that the experimental data show a very large peak located in the shear layer over the separation bubble which reaches a dimensionless magnitude of about 0.2.

At this Re (=25,000) the Transition model seems to perform the best (compared to SKW and V2F).

Re =100,000

Figure 6 shows the pressure coefficient plotted versus s/L_s along the suction and pressure surfaces for the turbulence models tested and Re = 100,000. All turbulence models predict the pressure coefficient very well except the Transition model, which shows under-prediction downstream from the suction peak. One possible explanation for this is that at s/L_s = 0.6 transition starts (as discussed below). The mixing associated with transition will tend to promote reattachment, which would result in a drop in the pressure coefficient. The simulation may be over predicting this tendency toward reattachment in this case, although the velocity profiles shown below do not indicate reattachment.

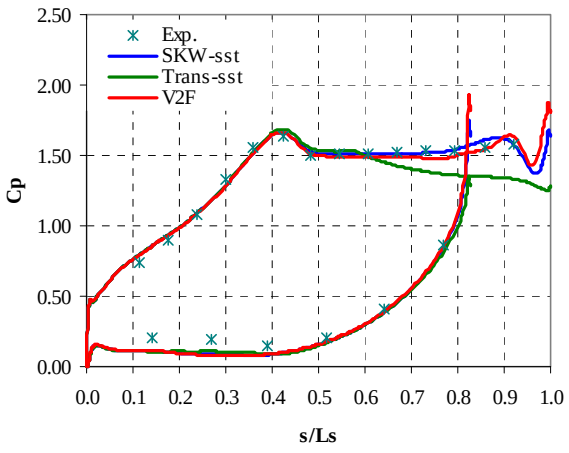

Fig. 6 C_p profiles, *Re*=100,000

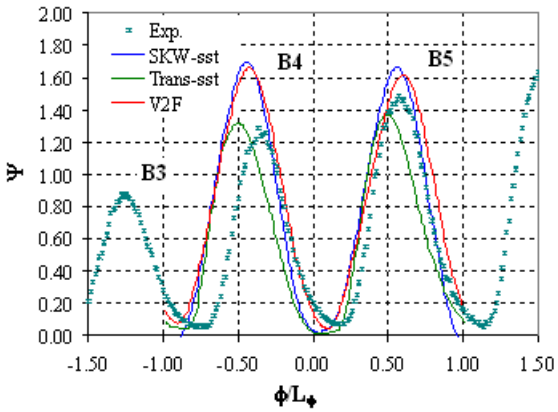

Fig. 7 Pressure loss coefficients at 0.63 C_x downstream of cascade, *Re*=100,000

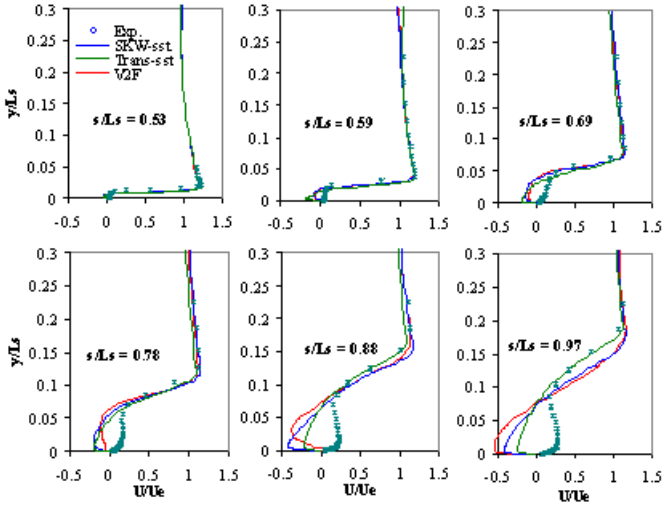

Fig. 8 Mean velocity profiles, *Re* = 100,000

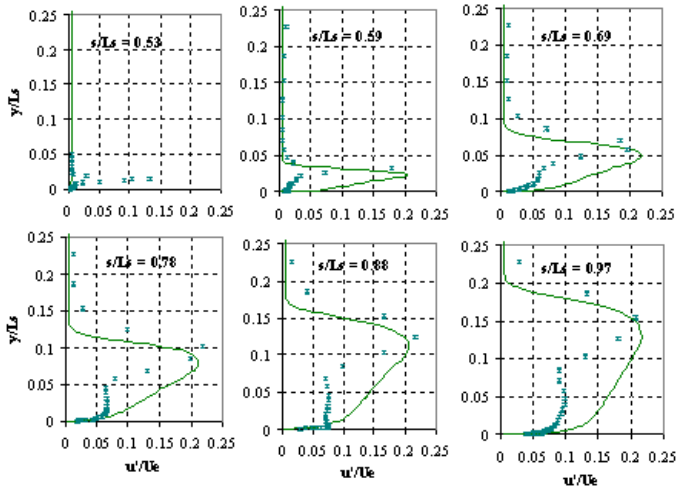

Fig. 9 Comparison of Transition-sst and experimental u'/U_e profiles, Re= 100,000

Figure 7 shows the total pressure loss coefficient plotted versus dimensionless distance at 0.63 C_x downstream of the cascade. The loss coefficient was predicted reasonably well by all models with the Transition model showing the best agreement. As in the *Re* = 25,000 case, the experimental results were not periodic, so precise agreement is not expected between the prediction and the data.

Figure 8 shows the velocity profiles (normalized with respect to the exit free stream velocity) versus y/L_s at the 6 stations along the suction side. The velocity profiles are predicted reasonably well by all models with the Transition model doing better overall. Again the near wall region is different than the data since the measurements were done using hot-wire anemometry and therefore can not register negative velocities when separation occurs.

Figure 9 shows u'/U_e profiles versus y/L_s at 6 stations along the suction side. As explained above, u' was obtained from the CFD (using the Transition model) using the kinetic energy of turbulence and assuming an isotropic flow field. Again the CFD results show a peak in the u' profile that moves away from the wall as one travels from station (1) to (6). Similarly, from the experimental data, the separation bubble grows in the streamwise direction, the boundary layer does not reattach, and there is a very high peak in the fluctuating velocity in the shear layer over the separation bubble.

At this *Re* (=100,000) the Transition model seems to perform the best (compared to SKW and V2F). Its one discrepancy is under-prediction in the pressure coefficient downstream of the suction peak.

Re =300,000

The experimental data for this case indicate that the boundary layer is attached over most of the airfoil. Figure 10 shows the pressure coefficient plotted versus s/L_s along the suction and pressure surfaces for the turbulence models tested and *Re* = 300,000. All turbulence models predict the pressure coefficient reasonably well including the area near the leading edge. The Transition model shows a bump at s/L_s = 0.6 indicating a small bubble that appears and then closes quickly. Although not as clear in the data, the predicted bubble may be correct. The predicted location is between two pressure measurement locations in the experiment, so the bubble presence would not necessarily be visible in the data. Also, a small bubble at this location was clearly noticed in the experimental data at a lower *Re* (=200,000).

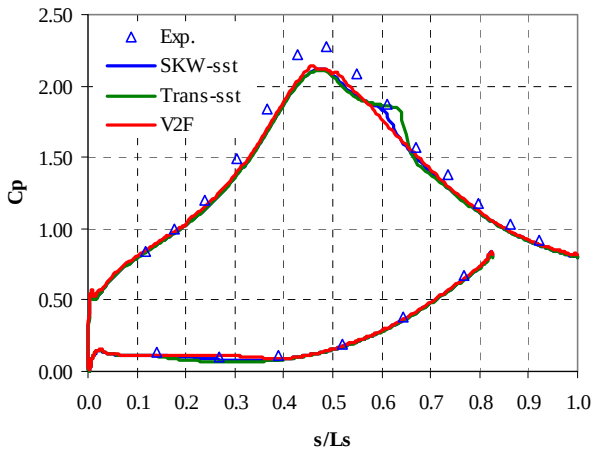

Fig. 10 C_p profiles, *Re*=300,000

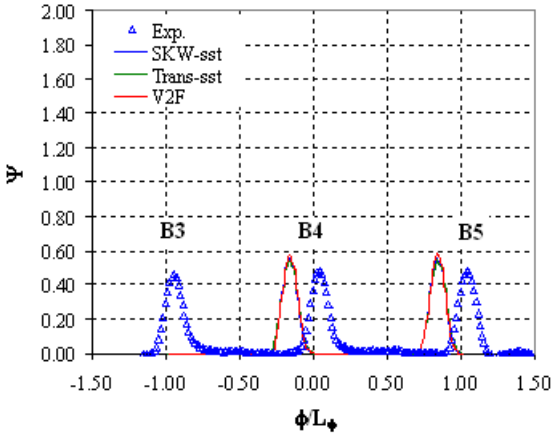

Fig. 11 Pressure loss coefficients at 0.63 C_x downstream of cascade, *Re*=300,000

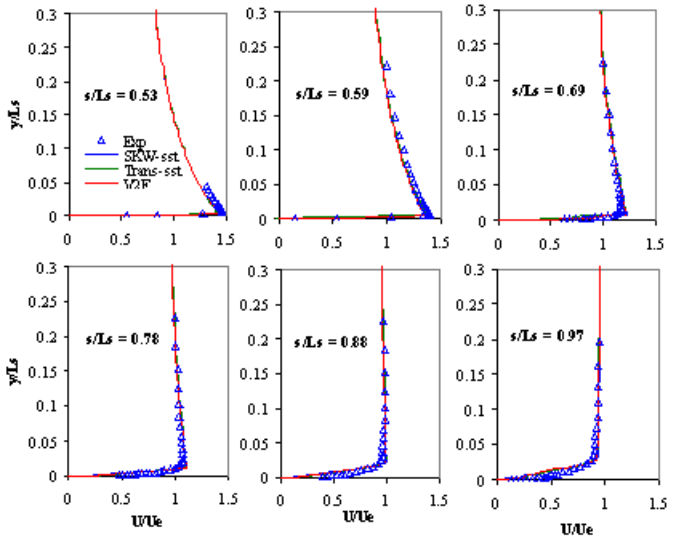

Fig. 12 Mean velocity profiles, *Re* =300,000

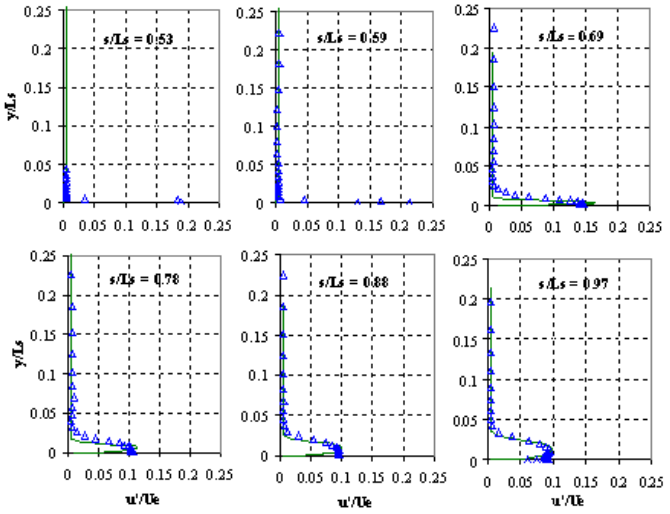

Fig. 13 Comparison of Transition-sst and experimental u'/U_e profiles, Re= 300,000

Figure 11 shows the total pressure loss coefficient plotted versus dimensionless distance at 0.63 C_x downstream of the cascade. The loss coefficient was predicted reasonably well by all models. The experimental data showed periodic results at this higher *Re*. Therefore the periodic boundary condition applied in the CFD is consistent with the experiment. Nevertheless, the magnitude of the pressure loss coefficient is over predicted by about 15%. The location of the peaks is also shifted to the left of the experimental peaks in Fig. 11. The amount of the shift corresponds to about a 4° difference in flow angle.

Figure 12 shows the velocity profile (normalized with respect to the exit free stream velocity) versus y/L_s at 6 stations along the suction side. The velocity profiles are predicted very well by all models. Figure 13 shows u'/U_e profiles versus y/L_s at the 6 stations along the suction side. The CFD shows good agreement with the data.

At this *Re* (300,000) all models perform very similar with each other. The Transition model shows a small bump in the pressure coefficient downstream from the suction peak indicating the presence of a small bubble at that location.

Prediction of Transition

From the above investigation one can conclude that the Transition model shows overall better agreement with the experimental data. Therefore in this section this model will be utilized to show how its predictions compare with data for the locations of separation and the start of transition.

Figure 14 shows contours of u'/U_e over the suction side of the airfoil overlapped with velocity vectors at 14a) *Re*=25,000, 14b) *Re* =100,000 and 14c) *Re* = 300,000. On each plot the location of the 1) suction peak, 2) six stations used earlier in the velocity comparison with the data, 3) separation point and 4) transition start are shown. The CFD results of Fig. 14a show that the flow separates (at station (1)) with no reattachment, as observed experimentally. The location of transition was taken as the location where u'/U_e peaks in the shear layer over the separation bubble (between station (3) and (4) and close to (4)). In Fig. 14b the CFD data show that the flow separates (at station (1)) with no reattachment as observed experimentally. Again the location of transition was obtained where u'/U_e peaks in the shear layer (between station (1) and (2)). Notice that the suction peak is at about the same location as in the case with *Re* = 25,000. In Fig. 14c the CFD data show that with the possible exception of a small bubble appearing

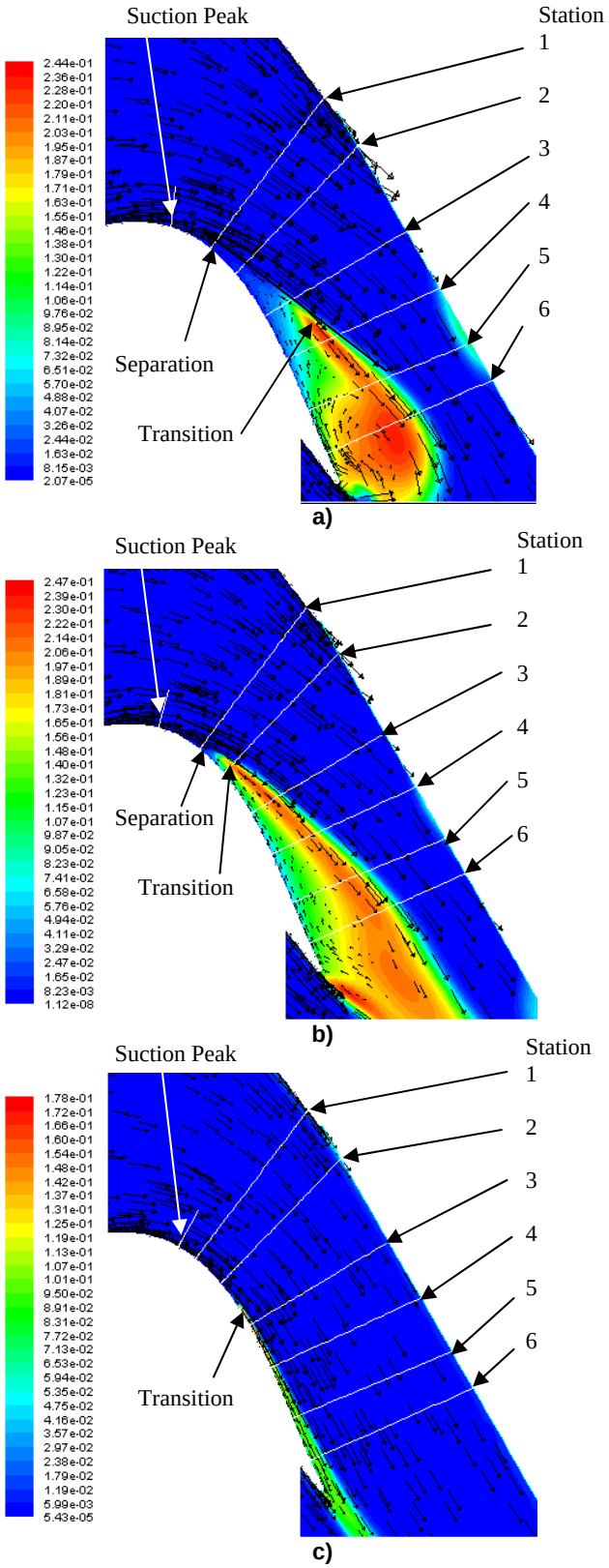

Fig. 14 Contours of u'/U_e, and velocity vectors (for Transition model) showing the location of: 1) suction peak, 2) separation and 3) transition for a) *Re* = 25,000, b) Re = 100,000, and c) Re = 300,000

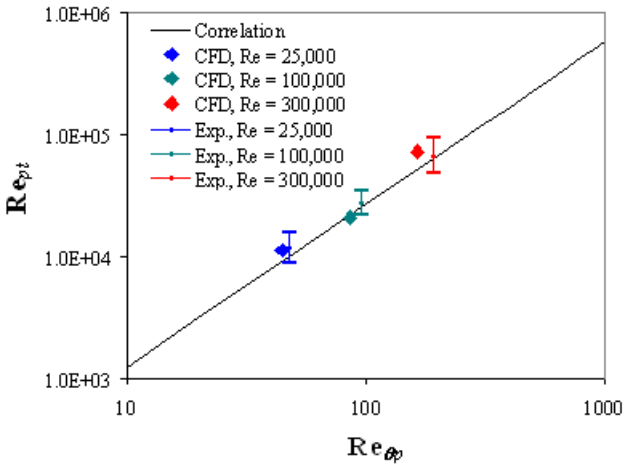

Fig. 15 Comparison between CFD data (Transition Model) and correlation for the start of transition

at s/L_s = 0.6, the boundary layer is attached, which is consistent with the experimental data. Again the location of transition was obtained where the u'/U_e peaks (between station (2) and (3)).

To quantify the results in Fig. 14, Table 4 shows the numerical values of the predicted momentum thickness Reynolds number at the suction peak ($Re_{\theta p}$), the Reynolds number based on the freestream velocity at the suction peak and the streamwise distance from the suction peak to transition (Re_{pt}), and the streamwise locations of the suction peak, transition and separation. Table 5 shows corresponding measured quantities from the experiment. Note that $Re_{\theta p}$ and s_s in Table 5 were approximated using a laminar boundary layer calculation as explained in Volino [18]. The ranges given for Re_{pt} and s_t/L_s result from the finite spacing between measurement stations. The transition location is shown again in Fig. 15 along with a correlation from Volino and Bohl [30]:

$$Re_{pt}=8.80\,[6.37-\log_{10}(TI^2)]\,Re_{\theta p}^{4/3}$$

The agreement between the CFD and experiment shown in Tables 4 and 5 and Fig. 15 is reasonably good.

Table 4 CFD results for separation and transition locations (Transition Model)

Re	25,000	100,000	300,000
$Re_{\theta p}$	45	87	165
Re_{pt}	11274	20816	73145
s_p/L_s	0.43	0.42	0.47
s_t/L_s	0.74	0.59	0.64
s_s/L_s	0.53	0.53	0.6

CONCLUSIONS

The flow over the very high lift L1A airfoil was studied experimentally using a linear cascade and reported by Volino [18]. Reynolds numbers based on suction surface length and nominal exit velocity ranging from 25,000 to 330,000 were considered. The experimental data showed that in all cases the laminar suction surface boundary layer separated, but at Reynolds numbers greater than 150,000 the separation bubble was very thin and short, and the boundary layer was attached over most of the surface. At lower

Reynolds numbers the boundary layer separated and never reattached. Transition to turbulence occurred in all cases in the shear layer after separation. Transition caused immediate reattachment in the high Reynolds number cases, but the turbulent shear layer remained separated in the low *Re* cases.

Three different CFD URANS models were utilized in this study, the SKW-sst, V2F and Transition models. At *Re*=25,000, the Transition model seems to perform the best. At *Re*=100,000 the Transition model again seems to perform the best, although it under-predicts in the pressure coefficient downstream of the suction peak. At *Re*= 300,000 all models perform very similar with each other. The Transition model shows a small bump in the pressure coefficient downstream from the suction peak indicating the presence of a small bubble at that location.

Upon comparing the pressure loss coefficient at 0.63 C_x downstream of the cascade, the CFD shows a shift toward the pressure side of the passage compared to the data. Further investigation of the cause of this shift is needed.

Reasonably good agreement was obtained upon comparing the start of transition as obtained from CFD (using the Transition model), a published correlation and the experimental data.

Table 5 Experimental Results for separation and transition locations

Re	25,000	100,000	300,000
$Re_{\theta p}$	48	96	193
Re_{pt}	12140 +/-3300	28340 +/-6500	71170 +/-22600
s_p/L_s	0.44	0.44	0.49
s_t/L_s	0.78 +/-0.094	0.64 +/-0.047	0.64 +/-0.047
s_s/L_s	0.50	0.50	0.54

ACKNOWLEDGMENTS

This work was sponsored by the National Aeronautics and Space Administration. The grant monitor is Dr. Anthony Strasizar of the NASA Glenn Research Center.

REFERENCES

[1] Mayle, R.E., 1991, "The Role of Laminar-Turbulent Transition in Gas Turbine Engines," ASME *Journal of Turbomachinery*, **113**, pp. 509-537

[2] Howell, R. J., (1999) "Wake - Separation Bubble Interactions in Low Reynolds Number Turbomachinery," Ph.D. dissertation, Cambridge University, Cambridge, UK.

[3] Singh, N., (2005) "A Study of Separated Flow through a Low-Pressure Turbine Cascade," MS thesis, University of Cincinnati, Cincinnati, OH.

[4] Volino, R.J., 2002, "Separated Flow Transition Under Simulated Low-Pressure Turbine Airfoil Conditions: Part 1 –Mean Flow and Turbulence Statistics," ASME *Journal of Turbomachinery*, **124**, pp. 645-655.

[5] Volino, R.J., 2002, "Separated Flow Transition Under Simulated Low-Pressure Turbine Airfoil Conditions: Part 2 – Turbulence Spectra," ASME *Journal of Turbomachinery*, **124**, pp. 656-664.

[6] Mahallati, A., Sjolander, S.A., McAuliffe, B.R., and Praisner, T.J., 2007, "Aerodynamics of a Low-Pressure Turbine Airfoil at Low-Reynolds Numbers Part 1 -- Steady Flow Measurements, ASME Paper GT2007-27347.

[7] Mahallati, A., and Sjolander, S.A., 2007, "Aerodynamics of a Low-Pressure Turbine Airfoil at Low Reynolds Numbers Part 2 -- Blade-Wake Interaction," ASME Paper GT2007-27348.

[8] Zoric, T., Popovic, I., Sjolander, S.A., Praisner, T., and Grover, E., 2007, "Comparative Investigation of Three Highly Loaded LP Turbine Airfoils: Part I -- Measured Profile and Secondary Losses at Design Incidence," ASME Paper GT2007-27537.

[9] Zhang, X.F., and Howard Hodson, H., 2007, "Effects of Reynolds umber and Freestream Turbulence Intensity on the Unsteady boundary Layer Development on an Ultra-High-Lift LPT airfoil," ASME Paper GT2007-27274

[10] Zhang, X.F., Vera, M., Hodson, H., and Harvey, N., 2007, "Separation and Transition Control on an Aft-Loaded Ultra-High-Lift LP Turbine Blade at Low Reynolds Numbers: Low-Speed Investigation," ASME *Journal of Turbomachinery*, **128**, pp. 517-527.

[11] Bohl, D.G. and Volino, R.J., 2006, "Experiments with Three-Dimensional Passive Flow Control Devices on Low-Pressure Turbine Airfoils," ASME *Journal of Turbomachinery*, **128**, pp. 251-260.

[12] Volino, R.J., 2003, "Passive Flow Control on Low-Pressure Turbine Airfoils," ASME *Journal of Turbomachinery*, **125**, pp. 754-764.

[13] Bons, J.P., Sondergaard, R., and Rivir, R.B., 2001, "Turbine Separation Control Using Pulsed Vortex Generator Jets," ASME *Journal of Turbomachinery*, **123**, pp. 198-206.

[14] Volino, R.J., 2003, "Separation Control on Low-Pressure Turbine Airfoils Using Synthetic Vortex Generator Jets," ASME *Journal of Turbomachinery*, **125**, pp. 765-777.

[15] Huang, J., Corke, T., and Thomas, F., 2003, "Plasma Actuators for Separation Control on Low Pressure Turbine Blades," AIAA Paper 2003-1027.

[16] Praisner, T.J., and Clark, J.P., 2007, "Predicting Transition in Turbomachinery – Part 1: A Review and New Model Development," ASME *Journal of Turbomachinery*, **129**, pp. 1-13.

[17] Bons, J.P., Hansen, L.C., Clark, J.P., Koch, P.J., and Sondergaard, R., 2005, "Designing Low-Pressure Turbine Blades With Integrated Flow Control," ASME Paper GT2005-68962.

[18] Volino, R.J. "Separated Flow Measurements on a Highly Loaded Low-Pressure Turbine Airfoil", ASME Paper GT2008-51445.

[19] McAuliffe, B.R., and Yaras, M.I., 2007, "Transition Mechanisms in Separation Bubbles Under Low and Elevated Freestream Turbulence," ASME Paper GT2007-27605.

[20] Suzen, Y. B., Huang, P. G., Volino, R.J., Corke, T.C., Thomas, F. O., Huang, J, Lake, J. P., King, P.I., 2003, "A Comprehensive CFD Study of Transitional Flows in Low-Pressure Turbines Under a Wide Range of Operating Conditions," AIAA Paper AIAA2003-3591.

[21] Menter, F.R., Langtry, R.B., Likki, S.R., Suzen, Y.B., Huang, P.G., and Völker, S., 2006, "A Correlation based Transition Model using Local Variables Part 1- Model Formulation", ASME *Journal of Turbomachinery*, **128**, pp. 413-422.

[22] Langtry, R.B., Menter, F.R., Likki, S.R., Suzen, Y.B., Huang, P.G., and Völker, S., 2006, "A Correlation based Transition Model using Local Variables Part II: Test Cases and Industrial Applications," ASME *Journal of Turbomachinery*, **128**, pp. 423-444.

[23] Fluent 6, 2001, Users manual, Fluent Inc., Lebanon NH, USA.

[24] Menter, F. R., 1994, "Two-Equation Eddy-Viscosity Turbulence Models for Engineering Applications," *AIAA Journal*, **32**(8), pp. 1598-1605.

[25] Durbin, P.A., 1995, "Separated Flow Computations with the k-ε-v^2 Model," *AIAA Journal*, **33**(4), pp. 659-664.
[26] Wilcox, D.C., 1998, Turbulent Modeling for CFD, DCW Industries, Inc., La Canada, California.
[27] Bradshaw, P., Ferriss, D.H., and Atwell, N.P., 1967, "Calculation of Boundary-Layer Development Using the Turbulent Energy Equation," *Journal of Fluid Mechanics*, **28**(3), pp. 593-616.
[28] Launder, B.E., and Spalding, D.B., 1974, "The Numerical Computation of Turbulent Flows," *Computer Methods in Applied Mechanics and Engineering*, **3**, pp. 269-289.
[29] Bons, J.P., Pluim, J., Gompertz, K., Bloxham, M., and Clark, J.P., 2008, "The Application of Flow Control to an Aft-Loaded Low Pressure Turbine Cascade with Unsteady Wakes," ASME Paper GT2008-50864.
[30] Volino, R.J., and Bohl, D.G., 2004, "Separated Flow Transition Mechanisms and Prediction With High and Low Freestream Turbulence Under Low Pressure Turbine Conditions," ASME Paper GT2004-63360.

Proceedings of IMECE2008
2008 ASME International Mechanical Engineering Congress and Exhibition
November 2-6, 2008, Boston, Massachusetts, USA

IMECE2008-68879

EXPERIMENTAL AND COMPUTATIONAL INVESTIGATIONS OF SEPARATION AND TRANSITION ON A HIGHLY LOADED LOW-PRESSURE TURBINE AIRFOIL: PART 1 – LOW FREESTREAM TURBULENCE INTENSITY

Mounir Ibrahim and Olga Kartuzova
Mechanical Engineering Department
Cleveland State University
Cleveland, Ohio 44115-2425
(216) 687-2580, m.ibrahim@csuohio.edu

Ralph J. Volino
Mechanical Engineering Department
United States Naval Academy
Annapolis, Maryland 21402-5042
(410) 293-6520, volino@usna.edu

ABSTRACT

Boundary layer separation, transition and reattachment have been studied on a new, very high lift, low-pressure turbine airfoil. Experiments were done under low freestream turbulence conditions on a linear cascade in a low speed wind tunnel. Pressure surveys on the airfoil surface and downstream total pressure loss surveys were documented. Velocity profiles were acquired in the suction side boundary layer at several streamwise locations using hot-wire anemometry. Cases were considered at Reynolds numbers (based on the suction surface length and the nominal exit velocity from the cascade) ranging from 25,000 to 330,000. In all cases the boundary layer separated, but at high Reynolds number the separation bubble remained very thin and quickly reattached after transition to turbulence. In the low Reynolds number cases, the boundary layer separated and did not reattach, even when transition occurred.

Three different CFD URANS (unsteady Reynolds averaged Navier-Stokes) models were utilized in this study (using Fluent CFD Code), the k-ω shear stress transport model, the v^2-f k-ε model, and the 4 equation Transition model of Menter. At Re=25,000, the Transition model seems to perform the best. At Re=100,000 the Transition model seems to perform the best also, although it under-predicts the pressure coefficient downstream of the suction peak. At Re= 300,000 all models perform very similar with each other. The Transition model showed a small bump in the pressure coefficient downstream from the suction peak indicating the presence of a small bubble at that location.

NOMENCLATURE

Cp	$2(P_T - P)/\rho U_e^2$, pressure coefficient
C_x	axial chord length
L_s	suction surface length
L_ϕ	blade spacing (pitch)
P	pressure
P_S	upstream static pressure
P_T	upstream stagnation pressure
P_{Te}	downstream stagnation pressure
Re	$U_e L_S / \nu$, exit Reynolds number
Re_θ	$U_\infty \theta / \nu$, momentum thickness Reynolds number
s	streamwise coordinate, distance from leading edge
TI	freestream turbulence intensity
U	mean streamwise velocity
U_e	nominal exit freestream velocity, based on inviscid solution
U_∞	freestream velocity
u'	time averaged rms streamwise fluctuating velocity
x	axial distance from leading edge
y	distance from wall
y^+	distance from wall in viscous units
α_1	inlet flow angle
α_2	exit flow angle
ϕ	coordinate along blade spacing, normal to axial chord
ν	kinematic viscosity
ρ	density
θ	momentum thickness
ψ	$(P_T-P_{Te})/(P_T-P_S)$, total pressure loss coefficient

Subscripts

p	pressure minimum (suction peak) location
pt	distance from suction peak to transition start
s	separation location
t	transition start

INTRODUCTION

Flow separation on the suction surface of low-pressure turbine (LPT) airfoils often occurs when turbine engines operate at low Reynolds numbers, as in the case of aircraft engines at high altitude cruise conditions. Low Reynolds numbers can cause the boundary layer to remain laminar and easily separate. This laminar separation results in an engine efficiency drop and an increase in fuel consumption (Mayle [1], Howell [2], and Singh [3]).

Simulation and prediction of transitional flow over LPT airfoils under a wide variety of Reynolds numbers, freestream turbulence parameters and with flow separation is essential for improvement in aircraft engine design. A great number of experimental and numerical investigations had been carried out in order to better understand the

mechanisms of flow separation and transition on LPT airfoils. Volino [4] provides a review of some earlier studies. In general, previous work shows that the strong acceleration on the leading section of the airfoil keeps the boundary layer thin and laminar, even in the presence of elevated freestream turbulence. Some recent examples of those experimental studies are: Volino, [4,5], Mahallati et al.[6,7], Zoric et al. [8], and Zhang and Hodson [9]. Downstream of the suction peak the adverse pressure gradient can cause boundary layer separation, which may be followed by transition to turbulence and flow reattachment (Volino, [4,5]).

The advances in separation understanding and prediction have led to attempts at separation control. Zhang et al. [10], Bohl and Volino [11], Volino [12], and others provide examples using passive devices such as boundary layer trips. Others have used active devices such as vortex generator jets (e.g. Bons et al. [13], and Volino [14]) or plasma devices (e.g. Huang et al. [15]).

Another way to improve performance is to design airfoils with pressure gradients more resistant to separation, as described by Praisner and Clark [16]. Forward loading, for example, makes airfoils more separation resistant by extending the adverse pressure gradient on the aft portion of the suction side over a longer distance. This reduces the local pressure gradient at all locations, making separation less likely. If separation does occur, forward loading provides a longer distance along the airfoil surface for reattachment. Forward loading has some disadvantages, however. As noted by Zhang et al. [10], the longer region of turbulent flow on a forward loaded airfoil can lead to increased profile losses. Forward loading also creates longer regions of strong pressure gradient on the endwalls, which can produce stronger secondary flows and losses. If flow control were incorporated in the design of an advanced airfoil, as discussed by Bons et al. [17], it might be possible to produce an aft loaded airfoil that was resistant to separation and had low profile and secondary loss characteristics over a range of Reynolds numbers.

A reduction in the production costs as well as the weight of an engine can be achieved by increasing the loading on LPT airfoils, thereby allowing a reduction in the number of LPT blades. Therefore, very highly loaded airfoils are of great interest. Volino [18] experimentally studied the flow over a very highly loaded LPT airfoil, designed at the Air Force Research Laboratory (AFRL) and designated L1A. The L1A is available on a limited basis to US researchers from Clark [private communication]. Dimensions of the L1A as used in the present experiments are given in Table 1.

Table 1: Cascade parameters for L1A airfoil

Axial Chord, C_x [mm]	True Chord [mm]	Pitch, L_ϕ [mm]	Span [mm]	Suction side, L_s [mm]	Inlet flow angle	Exit flow angle
134	146	136	724	203	35°	60°

Volino [18] reported that for the low Reynolds numbers considered (Re = 25,000 – 125000, based on exit velocity and suction side length) the flow separated and never reattached, even after transition to turbulence. For the higher Re (Re = 200,000 - 300,000) a very thin separation bubble was observed and the flow quickly reattached after transition occurred. Volino, [18] concluded that L1A differs from many previously studied LPT airfoils, where transition forced separated flow to reattach even at low Re. The L1A is considered to be a good airfoil for future flow control work, combining very high loading with a need for separation control.

Along with experimental work significant computational effort has been devoted to better understanding of separation and transition mechanisms in the LPT. McAuliffe and Yaras [19] conducted a Direct Numerical Simulation (DNS) study of laminar boundary layer separation on a flat surface in the presence of an adverse pressure gradient. Separation and transition mechanisms were examined under low and high disturbance environments. Singh [3] studied the flow physics in a LPT cascade under low Re number conditions using Large Eddy Simulation (LES). Calculations were carried out for Re = 10,000 and 25,000 (based on inlet velocity and axial chord). The flow for both Reynolds numbers separated and never reattached.

DNS and LES calculation require high resolution grids, which results in high computational time, therefore these methods are very computationally expensive. This makes modification of Reynolds Averaged Navier-Stokes (RANS) methods to better predict separation and transition processes very attractive. Many studies have been done in the area of developing and testing transition models capable of accurate prediction of flow physics in turbomachinery. Some of the latest examples include Suzen et al. [20], who applied a transition model based on an intermittency transport equation to predictions of LPT experiments on the Pack B airfoil. Howell [2] used the Prescribed Unsteady Intermittency Model (PUIM) to study wake - surface flow interactions on a high lift LPT airfoil. This approach employs a set of correlations for transition onset and for spot production rate. A different approach was proposed by Menter et al. [21], based on two transport equations. The intermittency transport equation is used to trigger the transition onset. The transport equation for the transition momentum thickness Reynolds number ($Re_{\theta t}$) is used to capture non-local effect of freestream turbulence intensity and pressure gradient at the boundary layer edge. These two equations were coupled with a shear stress transport turbulence model (SST). This model was validated against experimental data for various turbomachinery and aerodynamic applications (Langtry et al. [22] and Menter et al. [21]).

The objective of the present work is to conduct a computational study of a very highly loaded low pressure turbine airfoil, designated the L1A under low freestream turbulence conditions. The experimental data have been presented previously (Volino [18]) and a summary is provided in this paper. On the computational side the problem has been extensively investigated utilizing different: 1) grid structures, 2) inlet velocity conditions, 3) turbulence models, and 4) Reynolds numbers. The present results will serve as baseline results for future work, in which attempts will be made to suppress separation through flow control at low Reynolds numbers.

EXPERIMENTAL FACILITY AND MEASUREMENTS

Experiments (described in details in Volino [18]) were conducted in a closed loop wind tunnel with a linear cascade in one corner of the loop. A seven blade cascade is located in the wind tunnel's third turn, as shown in Fig. 1. A generic airfoil shape is shown in the figure.

The freestream turbulence entering the cascade was measured with a cross-wire probe positioned just upstream of the center blade. The streamwise velocity component had a turbulence intensity, TI, of 0.8% and integral length scale of 6.3 cm. These values were used in all the calculations described below. Further details of the freestream turbulence are in Volino [18]. While such low freestream turbulence and large length scales are not representative of engine conditions, they are still of interest as a limiting case. Also, in zero or favorable pressure gradient boundary layers, high TI can cause bypass transition, but under adverse pressure gradients, natural transition appears to play a role at all TI levels.

A tailboard, shown in Fig. 1, was needed to produce the correct exit flow angle from the cascade. Its position was set to produce periodicity at high Reynolds numbers. A tailboard on the opposite side of the cascade, and inlet guide vanes were found to be

unnecessary. To produce the correct approach flow to the end blades (B1 and B7), the amount of flow escaping around the two ends of the cascade was controlled with the flaps shown in Fig. 1. The flap positions were set using a wool tuft upstream of each blade to check that the incoming flow approached the stagnation points with the correct angle. The inlet flow angle at the center of the cascade was also checked with a three-hole pressure probe and found to agree with the design angle to within about 2° of uncertainty. At high Reynolds numbers, the approach velocity to the middle four passages was measured to be uniform to within 6%, and the difference between any two adjacent passages was within 3%. At low Reynolds numbers, slightly more variation was observed, but the approach velocity to the middle two passages still agreed to within 5%. Good periodicity at high Reynolds numbers was also observed in the exit flow from the cascade, as evidenced by suction side velocity profiles acquired near the trailing edge of blades B2-B6, and by total pressure loss surveys, which are shown below. At low Reynolds numbers, when significant separation bubbles were present, the periodicity was not as good due to suppression of the separation bubble thickness on the blades closest to the tailboard. This deviation from periodicity is considered acceptable for the present facility, since its intended purpose is for the study of flow control, which if successful should suppress separation on all blades, thereby restoring periodicity even at low Reynolds numbers.

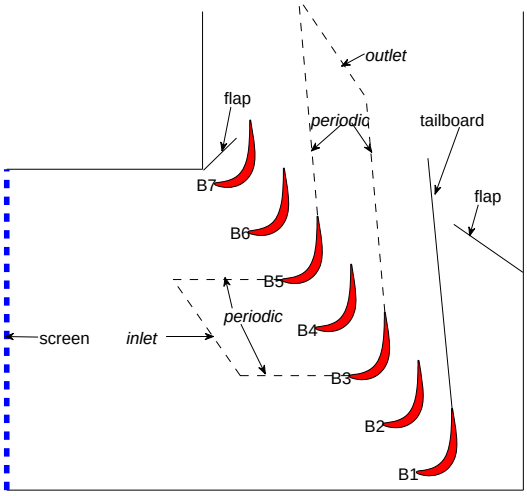

Fig. 1 Schematic of a linear cascade of 7 airfoils (Volino [18]) with boundary conditions and computational domain used in present study, shown in dashed lines

COMPUTATIONAL METHOD

The CFD predictions were performed with the numerical software tool FLUENT [23]. Predictions with three turbulence models were compared with the experimental results of Volino [18]. These models are described below. The computational domain consisted of two channels and the airfoil in the middle. It is shown on Fig. 1 in dashed lines. The boundary conditions applied along the sides of the domain are periodic, except along the airfoil surfaces, which are walls. No-slip boundary conditions were applied for all walls.

The inlet boundary condition was a prescribed uniform velocity, and is described in more detail below. The inlet into the two channels is located at 1.9 C_x upstream of the airfoil leading edge in the flow direction. At the outlet zero gage pressure was applied. The exit was located at 3.8 C_x downstream of the airfoil trailing edge in the flow direction. Different exit locations were tested to insure that 3.8 C_x was far enough downstream to achieve independent results (as indicated by pressure coefficients, pressure losses downstream of the cascade and velocity profiles on the airfoil) through the passages.

Unsteady calculations were performed for all cases. Convergence was established when: 1) residuals reduced to a value of 10^{-4}, 2) velocity at the outlet and pressure on the airfoil suction side settled (fluctuations around certain mean values were observed, however there were no equal cycles), and 3) the mass imbalance was less than 0.01 %. After convergence was achieved within each time step (Δt = 0.0005 s) with the conditions listed above, time averaged results were obtained for 2000 time steps.

Grid independence study

A grid independence study for 2D grids was conducted for *Re* = 102,000. The V2F turbulence model (described below) was applied. Differences in grids are summarized in Table 2. Grids 2 and 3 showed maximum difference in C_p on the suction side of an airfoil less than 2%, therefore grid 2 was used in this study.

Table 2 Grid characteristics for grid independence study

Grid number	Size	y^+ on the airfoil walls	Number of points on airfoil ss	Number of points on airfoil ps
1	91516	2.95 (range 0.1-8)	290	240
2	62469	0.20 (range 0.01-0.6)	290	240
3	312393	0.20 (range 0.01-0.6)	1369	933

Boundary conditions influence study

After grid independence was established several inlet velocity boundary conditions were tested. First, a uniform inlet velocity was applied in the direction of the design inlet flow angle (35°). This condition resulted in a slightly higher pressure on the leading section of the suction side of the airfoil compared to the experiment, indicating that the actual inlet angle could be different from the design angle. To investigate this possibility, a 2D inviscid calculation was done for the full cascade shown in Fig. 1, including the tailboard and flaps. The inlet velocity magnitude and direction were taken from the inviscid calculation along a line parallel to the blade row and 1.9 C_x upstream of the blades in the flow direction, and used to set the inlet boundary conditions to the 2 channel domain described above. The inlet boundary conditions tested are summarized in Table 3, all were tested at *Re*=102,000. Four different inlet conditions are presented in Table 3. The first condition assumed a uniform inlet velocity at the design flow angle of 35°. The second condition used the velocity profile entering the two channel domain as obtained from the invisicid calculation. This condition shows a slight variation in the velocity profile at the inlet both in x and ϕ directions with spatial averaged velocities V_x= 3.78 and V_ϕ = 2.32 m/s. Accordingly, the spatial averaged inlet flow angle is 31.5°. The third condition used a uniform inlet velocity and flow angle (V_x= 3.78 and V_ϕ = 2.32 m/s and inlet flow angle = 31.5°) based on the average values across the inlet of the two channel domain from the inviscid calculation. Thus the difference between conditions (2) and (3) are in the spatial variation in the inlet velocity while the averaged values are the same. The fourth condition

used a uniform inlet velocity and angle based on the spatial averaged values across the full cascade (instead of averaging over two channels only as in condition (3)) from the inviscid calculation. Therefore the inlet velocity variations chosen in this exercise involve different inlet flow velocity magnitude and angle based on the design or the inviscid CFD results for the 7 blades (see Fig. 1).

Boundary condition 4 produced results in better agreement with the experimental data and was chosen for the rest of this investigation. The deviation of the inlet angle from the design angle is about 2°, which is within the uncertainty of the experimental measurement and therefore plausible.

Table 3 Inlet boundary conditions for 2 channels tested, Re=102,000

#	Description	V_x, m/s	V_ϕ, m/s	V_{mag}, m/s	α_1, deg
1	Design condition	3.65	2.56	4.46	35
2	Velocity profile from cascade simulation taken at inlet into 2 channels	3.78 (avg)	2.32 (avg)	4.43 (avg)	31.5 (avg)
3	Velocity from cascade simulation averaged across inlet into 2 channels	3.78	2.32	4.43	31.5
4	Velocity from cascade simulation averaged across full cascade at streamwise location of inlet into 2 channels.	3.71	2.36	4.4	32.5

Turbulence Modeling

In this study, the $k-\omega$ - *sst* model of Menter [24], the $\overline{v^2}-f$ model of Durbin [25], and new Transition-sst (4 eq.) model of Menter [21], were compared for separated flow predictions on the highly loaded LPT airfoil. The unsteady Reynolds-averaged Navier-Stokes (URANS) equations were used as the transport equations for the mean flow. The governing equations and the detailed description of each model have been published elsewhere and therefore are not shown in this paper.

Shear-stress transport $k-\omega$ model (SKW-sst): This model, developed by Menter [24] is similar to the standard $k-\omega$ of Wilcox [26], but has an ability to account for the transport of the principal shear stress in adverse pressure gradient boundary layers. The model is based on Bradshaw's [27] assumption that the principal shear stress is proportional to the turbulent kinetic energy, which is introduced into the definition of the eddy-viscosity. These features make the SST $k-\omega$ model more accurate and reliable for a wider class of flows (e.g., adverse pressure gradient flows, airfoils, transonic shock waves) than the standard $k-\omega$ model [23].

$\overline{v^2}-f$ model (V2F): According to Launder [28], the normal stress $\overline{v^2}$, perpendicular to the local streamline plays the most important role to the eddy viscosity. Motivated by this idea, Durbin [25] devised a "four-equation" model, known as the $k-\varepsilon-v^2$ model, or $\overline{v^2}-f$ model. It eliminates the need to patch models in order to predict wall phenomena like heat transfer or flow separation. It makes use of the standard $k-\varepsilon$ model, but extends it by incorporating the anisotropy of near-wall turbulence and non-local pressure strain effects, while retaining a linear eddy viscosity assumption.

Transition-sst (4 eq.) model: A new correlation-based transition model was proposed by Menter et al. [21]. This model is based on two transport equations. The intermittency transport equation is used to trigger the transition onset. The transport equation for the transition momentum thickness Reynolds number ($Re_{\theta t}$) is used to capture non-local effects of freestream turbulence intensity and pressure gradient at the boundary layer edge. Outside the boundary layer the transport variable was forced to follow the value of $Re_{\theta t}$ given by correlations. Those two equations were coupled with the shear stress transport turbulence model (SST). This model has recently become available in Fluent code.

RESULTS

Re =25,000

Figure 2 shows the pressure coefficient plotted versus s/L_s along the suction and pressure surfaces for the turbulence models tested and Re = 25,000. Notice the abscissa is the distance along the blade surface normalized with respect to the suction surface length. The experimental data shows that the *Cp* values have a constant value on the downstream part of the suction side. This plateau indicates that the boundary layer has separated and that the boundary layer never reattaches (i.e. the separation bubble bursts); this of course refers to the time-averaged bubble as the bubble will probably burst sporadically. All turbulence models predict the pressure coefficient reasonably well with some deviation near the leading edge. The deviation could be partially attributed to uncertainty in the measurements and the inlet velocity profile as discussed above. All the models do well in predicting the separation location and the failure of the flow to reattach, as seen in the experiment.

Figure 3 shows the total pressure loss coefficient, ψ, plotted versus dimensionless distance (ϕ/L_ϕ) at a location 0.63 C_x downstream of the cascade. The definition of ψ used in this study is the same as the one used in earlier work by Volino [18] and Bons et al. [29]. The coordinate ϕ indicates the distance in the direction perpendicular to the axial chord. The normalizing quantity L_ϕ is the blade spacing. The origin, ϕ=0, corresponds to the location directly downstream of the trailing edge of the center blade in the direction of the exit design flow angle. At low Reynolds numbers the burst separation bubble results in high losses and forces the peaks about $0.35L_\phi$ toward the pressure side of each passage. The peaks become noticeably smaller moving from B5 to B3, indicating the effect of the tailboard in reducing the separation bubble thickness. Due to the lack of periodicity in the experiment, the predicted loss coefficient is not expected to agree precisely with the experiment. The prediction is based on periodic boundary conditions and is not influenced by tailboard effects, so it should show higher losses and possibly lower flow turning (peaks shifted more to the left in the figure). This is indeed the case, as shown in Fig. 3.

Velocity profiles for the six suction surface measurement stations on blade B4 documented in the experiment are shown in Fig. 4 for the nominal Re=25,000 case. The figure shows the distance from the wall normalized on the suction surface length plotted against the local mean velocity normalized on the nominal exit velocity, U_e. The boundary layer has just separated at the first measurement station and the separation bubble grows larger at the downstream stations.

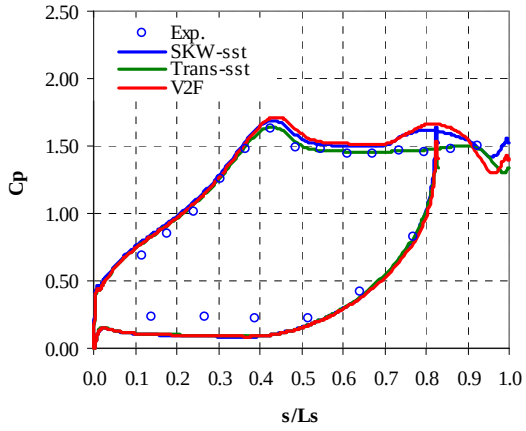

Fig. 2 C_p profiles, Re=25,000

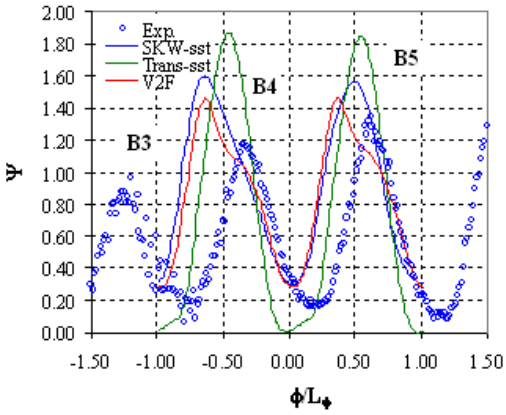

Fig. 3 Pressure loss coefficients at 0.63 C_x downstream of cascade, Re=25,000

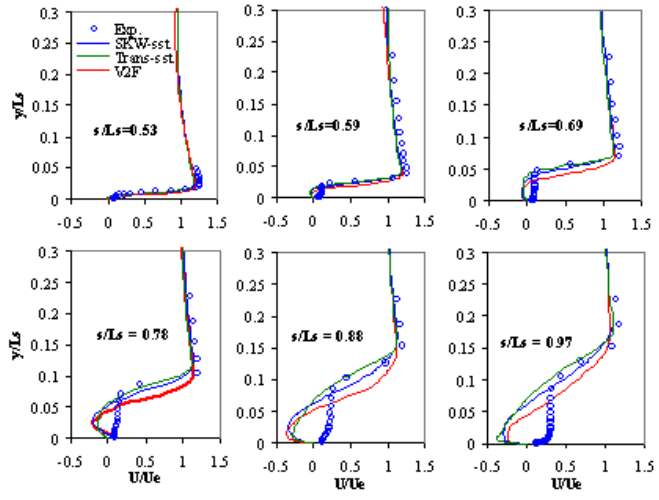

Fig. 4 Mean velocity profiles, Re = 25,000

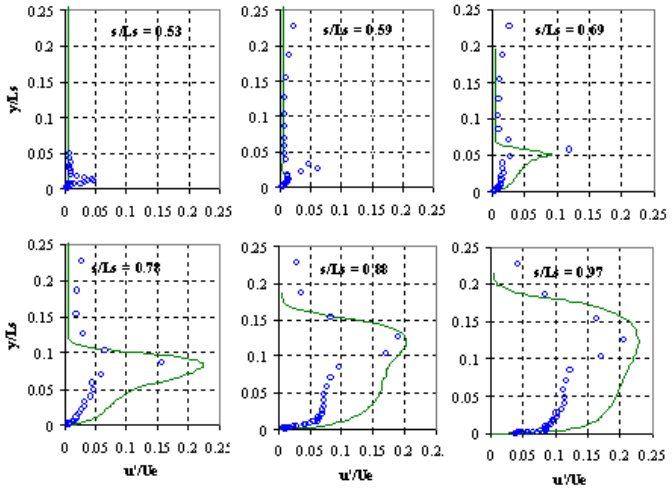

Fig. 5 Comparison of Transition-sst and experimental u'/U_e profiles, Re= 25,000

The boundary layer does not reattach. The velocity profiles at the six stations along the suction surface are predicted reasonably well by all models with the Transition model doing better overall. The prediction in the near wall region is different than the data since the measurements were done using hot-wire anemometry and therefore can not register negative velocities when separation occurs.

Figure 5 shows u'/U_e profile versus y/L_s at the six different stations along the suction side. u' was obtained from CFD (using the Transition model only because of its best overall prediction) from the kinetic energy of turbulence and assuming an isotropic flow field (i.e. $u' = v' = w'$). Despite this assumption the CFD shows reasonable agreement with the data. The CFD shows a peak in the u' profile that moves away from the wall as one travels from station (1) to (6). This peak value will be utilized (as will be shown later) to predict the start of transition. It is interesting that the experimental data show a very large peak located in the shear layer over the separation bubble which reaches a dimensionless magnitude of about 0.2.

At this Re (=25,000) the Transition model seems to perform the best (compared to SKW and V2F).

Re =100,000

Figure 6 shows the pressure coefficient plotted versus s/L_s along the suction and pressure surfaces for the turbulence models tested and Re = 100,000. All turbulence models predict the pressure coefficient very well except the Transition model, which shows under-prediction downstream from the suction peak. One possible explanation for this is that at s/L_s = 0.6 transition starts (as discussed below). The mixing associated with transition will tend to promote reattachment, which would result in a drop in the pressure coefficient. The simulation may be over predicting this tendency toward reattachment in this case, although the velocity profiles shown below do not indicate reattachment.

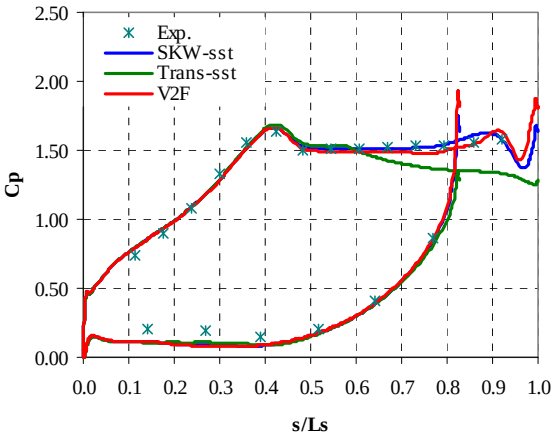

Fig. 6 C_p profiles, *Re*=100,000

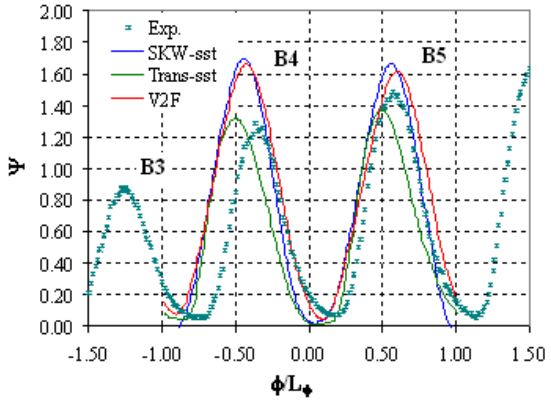

Fig. 7 Pressure loss coefficients at 0.63 C_x downstream of cascade, *Re*=100,000

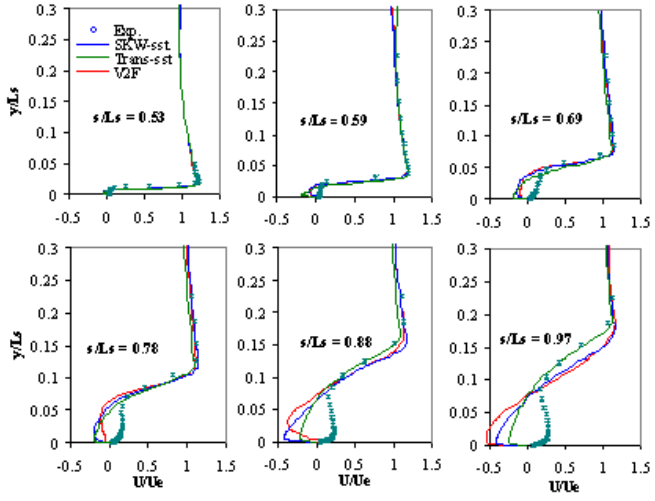

Fig. 8 Mean velocity profiles, *Re* = 100,000

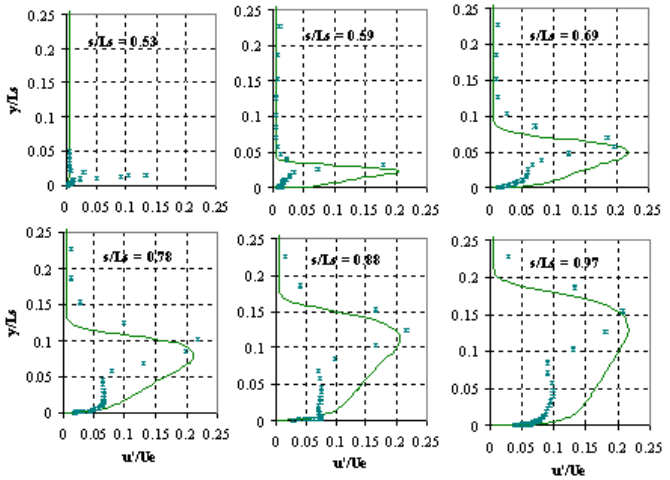

Fig. 9 Comparison of Transition-sst and experimental u'/U_e profiles, Re= 100,000

Figure 7 shows the total pressure loss coefficient plotted versus dimensionless distance at 0.63 C_x downstream of the cascade. The loss coefficient was predicted reasonably well by all models with the Transition model showing the best agreement. As in the *Re* = 25,000 case, the experimental results were not periodic, so precise agreement is not expected between the prediction and the data.

Figure 8 shows the velocity profiles (normalized with respect to the exit free stream velocity) versus y/L_s at the 6 stations along the suction side. The velocity profiles are predicted reasonably well by all models with the Transition model doing better overall. Again the near wall region is different than the data since the measurements were done using hot-wire anemometry and therefore can not register negative velocities when separation occurs.

Figure 9 shows u'/U_e profiles versus y/L_s at 6 stations along the suction side. As explained above, u' was obtained from the CFD (using the Transition model) using the kinetic energy of turbulence and assuming an isotropic flow field. Again the CFD results show a peak in the u' profile that moves away from the wall as one travels from station (1) to (6). Similarly, from the experimental data, the separation bubble grows in the streamwise direction, the boundary layer does not reattach, and there is a very high peak in the fluctuating velocity in the shear layer over the separation bubble.

At this *Re* (=100,000) the Transition model seems to perform the best (compared to SKW and V2F). Its one discrepancy is under-prediction in the pressure coefficient downstream of the suction peak.

Re =300,000

The experimental data for this case indicate that the boundary layer is attached over most of the airfoil. Figure 10 shows the pressure coefficient plotted versus s/L_s along the suction and pressure surfaces for the turbulence models tested and *Re* = 300,000. All turbulence models predict the pressure coefficient reasonably well including the area near the leading edge. The Transition model shows a bump at s/L_s = 0.6 indicating a small bubble that appears and then closes quickly. Although not as clear in the data, the predicted bubble may be correct. The predicted location is between two pressure measurement locations in the experiment, so the bubble presence would not necessarily be visible in the data. Also, a small bubble at this location was clearly noticed in the experimental data at a lower *Re* (=200,000).

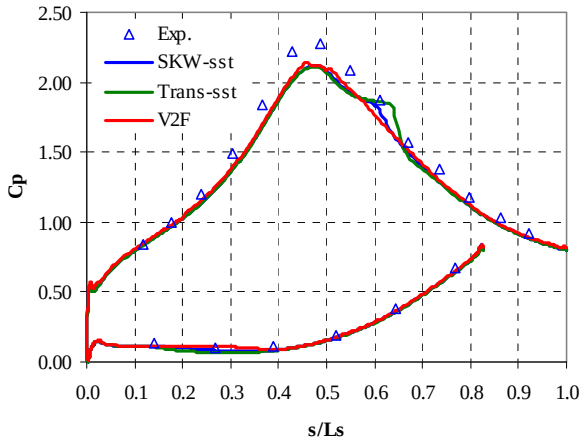

Fig. 10 C_p profiles, *Re*=300,000

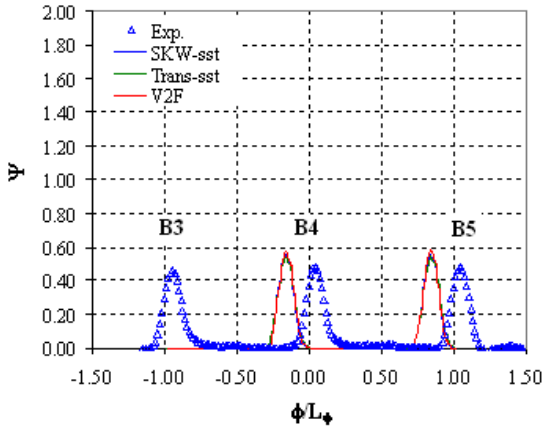

Fig. 11 Pressure loss coefficients at 0.63 C_x downstream of cascade, *Re*=300,000

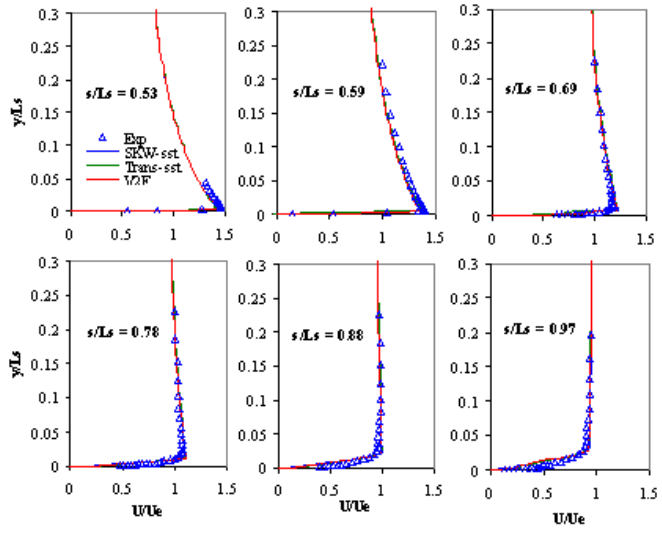

Fig. 12 Mean velocity profiles, *Re* =300,000

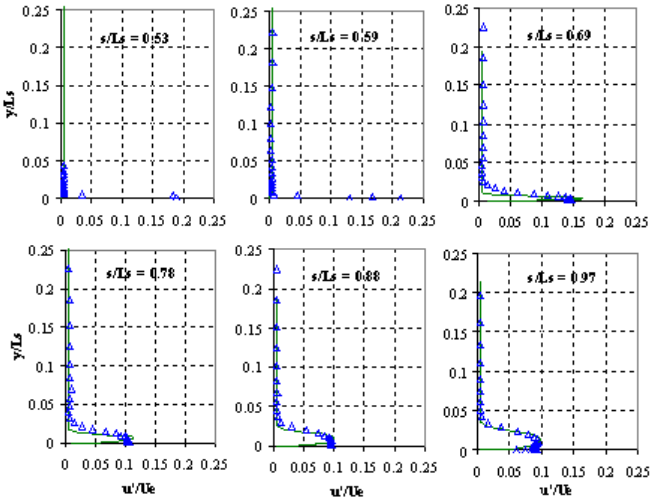

Fig. 13 Comparison of Transition-sst and experimental u'/U_e profiles, Re= 300,000

Figure 11 shows the total pressure loss coefficient plotted versus dimensionless distance at 0.63 C_x downstream of the cascade. The loss coefficient was predicted reasonably well by all models. The experimental data showed periodic results at this higher *Re*. Therefore the periodic boundary condition applied in the CFD is consistent with the experiment. Nevertheless, the magnitude of the pressure loss coefficient is over predicted by about 15%. The location of the peaks is also shifted to the left of the experimental peaks in Fig. 11. The amount of the shift corresponds to about a 4° difference in flow angle.

Figure 12 shows the velocity profile (normalized with respect to the exit free stream velocity) versus y/L_s at 6 stations along the suction side. The velocity profiles are predicted very well by all models. Figure 13 shows u'/U_e profiles versus y/L_s at the 6 stations along the suction side. The CFD shows good agreement with the data.

At this *Re* (300,000) all models perform very similar with each other. The Transition model shows a small bump in the pressure coefficient downstream from the suction peak indicating the presence of a small bubble at that location.

Prediction of Transition

From the above investigation one can conclude that the Transition model shows overall better agreement with the experimental data. Therefore in this section this model will be utilized to show how its predictions compare with data for the locations of separation and the start of transition.

Figure 14 shows contours of u'/U_e over the suction side of the airfoil overlapped with velocity vectors at 14a) *Re*=25,000, 14b) *Re* =100,000 and 14c) *Re* = 300,000. On each plot the location of the 1) suction peak, 2) six stations used earlier in the velocity comparison with the data, 3) separation point and 4) transition start are shown. The CFD results of Fig. 14a show that the flow separates (at station (1)) with no reattachment, as observed experimentally. The location of transition was taken as the location where u'/U_e peaks in the shear layer over the separation bubble (between station (3) and (4) and close to (4)). In Fig. 14b the CFD data show that the flow separates (at station (1)) with no reattachment as observed experimentally. Again the location of transition was obtained where u'/U_e peaks in the shear layer (between station (1) and (2)). Notice that the suction peak is at about the same location as in the case with *Re* = 25,000. In Fig. 14c the CFD data show that with the possible exception of a small bubble appearing

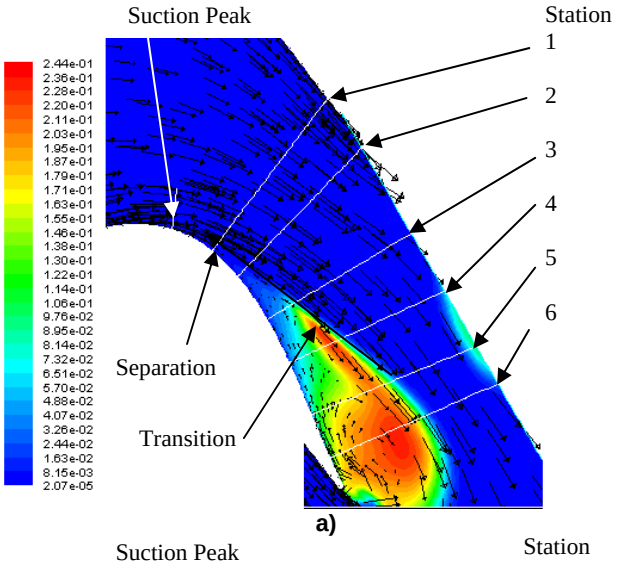

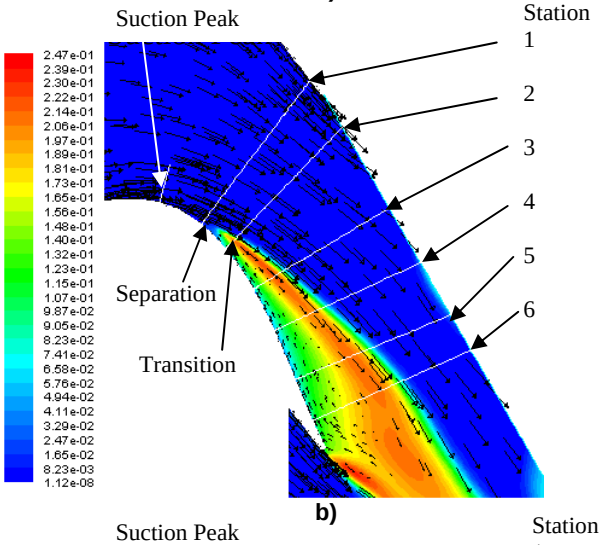

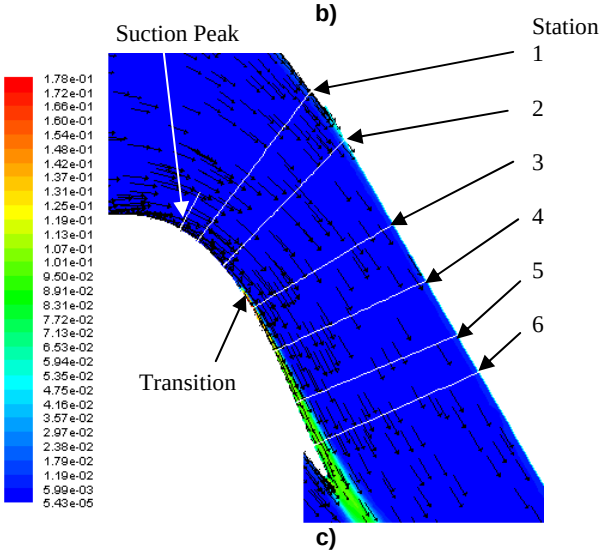

Fig. 14 Contours of u'/U_e, and velocity vectors (for Transition model) showing the location of: 1) suction peak, 2) separation and 3) transition for a) Re = 25,000, b) Re = 100,000, and c) Re = 300,000

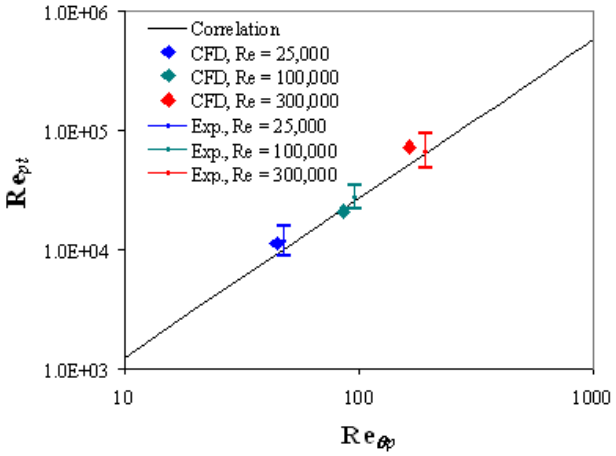

Fig. 15 Comparison between CFD data (Transition Model) and correlation for the start of transition

at s/L_s = 0.6, the boundary layer is attached, which is consistent with the experimental data. Again the location of transition was obtained where the u'/U_e peaks (between station (2) and (3)).

To quantify the results in Fig. 14, Table 4 shows the numerical values of the predicted momentum thickness Reynolds number at the suction peak ($Re_{\theta p}$), the Reynolds number based on the freestream velocity at the suction peak and the streamwise distance from the suction peak to transition (Re_{pt}), and the streamwise locations of the suction peak, transition and separation. Table 5 shows corresponding measured quantities from the experiment. Note that $Re_{\theta p}$ and s_s in Table 5 were approximated using a laminar boundary layer calculation as explained in Volino [18]. The ranges given for Re_{pt} and s_t/L_s result from the finite spacing between measurement stations. The transition location is shown again in Fig. 15 along with a correlation from Volino and Bohl [30]:

$$Re_{pt}=8.80\,[6.37 - log_{10}(TI^2)]\,Re_{\theta p}^{4/3}$$

The agreement between the CFD and experiment shown in Tables 4 and 5 and Fig. 15 is reasonably good.

Table 4 CFD results for separation and transition locations (Transition Model)

Re	25,000	100,000	300,000
$Re_{\theta p}$	45	87	165
Re_{pt}	11274	20816	73145
s_p/L_s	0.43	0.42	0.47
s_t/L_s	0.74	0.59	0.64
s_s/L_s	0.53	0.53	0.6

CONCLUSIONS

The flow over the very high lift L1A airfoil was studied experimentally using a linear cascade and reported by Volino [18]. Reynolds numbers based on suction surface length and nominal exit velocity ranging from 25,000 to 330,000 were considered. The experimental data showed that in all cases the laminar suction surface boundary layer separated, but at Reynolds numbers greater than 150,000 the separation bubble was very thin and short, and the boundary layer was attached over most of the surface. At lower

Reynolds numbers the boundary layer separated and never reattached. Transition to turbulence occurred in all cases in the shear layer after separation. Transition caused immediate reattachment in the high Reynolds number cases, but the turbulent shear layer remained separated in the low *Re* cases.

Three different CFD URANS models were utilized in this study, the SKW-sst, V2F and Transition models. At *Re*=25,000, the Transition model seems to perform the best. At *Re*=100,000 the Transition model again seems to perform the best, although it under-predicts in the pressure coefficient downstream of the suction peak. At *Re*= 300,000 all models perform very similar with each other. The Transition model shows a small bump in the pressure coefficient downstream from the suction peak indicating the presence of a small bubble at that location.

Upon comparing the pressure loss coefficient at 0.63 C_x downstream of the cascade, the CFD shows a shift toward the pressure side of the passage compared to the data. Further investigation of the cause of this shift is needed.

Reasonably good agreement was obtained upon comparing the start of transition as obtained from CFD (using the Transition model), a published correlation and the experimental data.

Table 5 Experimental Results for separation and transition locations

Re	25,000	100,000	300,000
$Re_{\theta p}$	48	96	193
Re_{pt}	12140 +/-3300	28340 +/-6500	71170 +/-22600
s_p/L_s	0.44	0.44	0.49
s_t/L_s	0.78 +/-0.094	0.64 +/-0.047	0.64 +/-0.047
s_s/L_s	0.50	0.50	0.54

ACKNOWLEDGMENTS

This work was sponsored by the National Aeronautics and Space Administration. The grant monitor is Dr. Anthony Strasizar of the NASA Glenn Research Center.

REFERENCES

[1] Mayle, R.E., 1991, "The Role of Laminar-Turbulent Transition in Gas Turbine Engines," ASME *Journal of Turbomachinery*, **113**, pp. 509-537

[2] Howell, R. J., (1999) "Wake - Separation Bubble Interactions in Low Reynolds Number Turbomachinery," Ph.D. dissertation, Cambridge University, Cambridge, UK.

[3] Singh, N., (2005) "A Study of Separated Flow through a Low-Pressure Turbine Cascade," MS thesis, University of Cincinnati, Cincinnati, OH.

[4] Volino, R.J., 2002, "Separated Flow Transition Under Simulated Low-Pressure Turbine Airfoil Conditions: Part 1 –Mean Flow and Turbulence Statistics," ASME *Journal of Turbomachinery*, **124**, pp. 645-655.

[5] Volino, R.J., 2002, "Separated Flow Transition Under Simulated Low-Pressure Turbine Airfoil Conditions: Part 2 – Turbulence Spectra," ASME *Journal of Turbomachinery*, **124**, pp. 656-664.

[6] Mahallati, A., Sjolander, S.A., McAuliffe, B.R., and Praisner, T.J., 2007, "Aerodynamics of a Low-Pressure Turbine Airfoil at Low-Reynolds Numbers Part 1 -- Steady Flow Measurements, ASME Paper GT2007-27347.

[7] Mahallati, A., and Sjolander, S.A., 2007, "Aerodynamics of a Low-Pressure Turbine Airfoil at Low Reynolds Numbers Part 2 -- Blade-Wake Interaction," ASME Paper GT2007-27348.

[8] Zoric, T., Popovic, I., Sjolander, S.A., Praisner, T., and Grover, E., 2007, "Comparative Investigation of Three Highly Loaded LP Turbine Airfoils: Part I -- Measured Profile and Secondary Losses at Design Incidence," ASME Paper GT2007-27537.

[9] Zhang, X.F., and Howard Hodson, H., 2007, "Effects of Reynolds umber and Freestream Turbulence Intensity on the Unsteady boundary Layer Development on an Ultra-High-Lift LPT airfoil," ASME Paper GT2007-27274

[10] Zhang, X.F., Vera, M., Hodson, H., and Harvey, N., 2007, "Separation and Transition Control on an Aft-Loaded Ultra-High-Lift LP Turbine Blade at Low Reynolds Numbers: Low-Speed Investigation," ASME *Journal of Turbomachinery*, **128**, pp. 517-527.

[11] Bohl, D.G. and Volino, R.J., 2006, "Experiments with Three-Dimensional Passive Flow Control Devices on Low-Pressure Turbine Airfoils," ASME *Journal of Turbomachinery*, **128**, pp. 251-260.

[12] Volino, R.J., 2003, "Passive Flow Control on Low-Pressure Turbine Airfoils," ASME *Journal of Turbomachinery*, **125**, pp. 754-764.

[13] Bons, J.P., Sondergaard, R., and Rivir, R.B., 2001, "Turbine Separation Control Using Pulsed Vortex Generator Jets," ASME *Journal of Turbomachinery*, **123**, pp. 198-206.

[14] Volino, R.J., 2003, "Separation Control on Low-Pressure Turbine Airfoils Using Synthetic Vortex Generator Jets," ASME *Journal of Turbomachinery*, **125**, pp. 765-777.

[15] Huang, J., Corke, T., and Thomas, F., 2003, "Plasma Actuators for Separation Control on Low Pressure Turbine Blades," AIAA Paper 2003-1027.

[16] Praisner, T.J., and Clark, J.P., 2007, "Predicting Transition in Turbomachinery – Part 1: A Review and New Model Development," ASME *Journal of Turbomachinery*, **129**, pp. 1-13.

[17] Bons, J.P., Hansen, L.C., Clark, J.P., Koch, P.J., and Sondergaard, R., 2005, "Designing Low-Pressure Turbine Blades With Integrated Flow Control," ASME Paper GT2005-68962.

[18] Volino, R.J. "Separated Flow Measurements on a Highly Loaded Low-Pressure Turbine Airfoil", ASME Paper GT2008-51445.

[19] McAuliffe, B.R., and Yaras, M.I., 2007, "Transition Mechanisms in Separation Bubbles Under Low and Elevated Freestream Turbulence," ASME Paper GT2007-27605.

[20] Suzen, Y. B., Huang, P. G., Volino, R.J., Corke, T.C., Thomas, F. O., Huang, J, Lake, J. P., King, P.I., 2003, "A Comprehensive CFD Study of Transitional Flows in Low-Pressure Turbines Under a Wide Range of Operating Conditions," AIAA Paper AIAA2003-3591.

[21] Menter, F.R., Langtry, R.B., Likki, S.R., Suzen, Y.B., Huang, P.G., and Völker, S., 2006, "A Correlation based Transition Model using Local Variables Part 1- Model Formulation", ASME *Journal of Turbomachinery*, **128**, pp. 413-422.

[22] Langtry, R.B., Menter, F.R., Likki, S.R., Suzen, Y.B., Huang, P.G., and Völker, S., 2006, "A Correlation based Transition Model using Local Variables Part II: Test Cases and Industrial Applications," ASME *Journal of Turbomachinery*, **128**, pp. 423-444.

[23] Fluent 6, 2001, Users manual, Fluent Inc., Lebanon NH, USA.

[24] Menter, F. R., 1994, "Two-Equation Eddy-Viscosity Turbulence Models for Engineering Applications," *AIAA Journal*, **32**(8), pp. 1598-1605.

[25] Durbin, P.A., 1995, "Separated Flow Computations with the k-ε-v^2 Model," *AIAA Journal*, **33**(4), pp. 659-664.
[26] Wilcox, D.C., 1998, Turbulent Modeling for CFD, DCW Industries, Inc., La Canada, California.
[27] Bradshaw, P., Ferriss, D.H., and Atwell, N.P., 1967, "Calculation of Boundary-Layer Development Using the Turbulent Energy Equation," *Journal of Fluid Mechanics*, **28**(3), pp. 593-616.
[28] Launder, B.E., and Spalding, D.B., 1974, "The Numerical Computation of Turbulent Flows," *Computer Methods in Applied Mechanics and Engineering*, **3**, pp. 269-289.
[29] Bons, J.P., Pluim, J., Gompertz, K., Bloxham, M., and Clark, J.P., 2008, "The Application of Flow Control to an Aft-Loaded Low Pressure Turbine Cascade with Unsteady Wakes," ASME Paper GT2008-50864.
[30] Volino, R.J., and Bohl, D.G., 2004, "Separated Flow Transition Mechanisms and Prediction With High and Low Freestream Turbulence Under Low Pressure Turbine Conditions," ASME Paper GT2004-63360.

Proceedings of IMECE2008
2008 ASME International Mechanical Engineering Congress and Exposition
October 31-November 6, 2008, Boston, Massachusetts, USA

IMECE2008-68776

EXPERIMENTAL AND COMPUTATIONAL INVESTIGATIONS OF SEPARATION AND TRANSITION ON A HIGHLY LOADED LOW-PRESSURE TURBINE AIRFOIL: PART 2 – HIGH FREESTREAM TURBULENCE INTENSITY

Ralph J. Volino
Mechanical Engineering Department
United States Naval Academy
Annapolis, Maryland 21402-5042
volino@usna.edu

Olga Kartuzova and Mounir B. Ibrahim
Mechanical Engineering Department
Cleveland State University
Cleveland, Ohio 44115-2425
m.ibrahim@csuohio.edu

ABSTRACT

Boundary layer separation, transition and reattachment have been studied on a very high lift, low-pressure turbine airfoil. Experiments were done under high (4%) freestream turbulence conditions on a linear cascade in a low speed wind tunnel. Pressure surveys on the airfoil surface and downstream total pressure loss surveys were documented. Velocity profiles were acquired in the suction side boundary layer at several streamwise locations using hot-wire anemometry. Cases were considered at Reynolds numbers (based on the suction surface length and the nominal exit velocity from the cascade) ranging from 25,000 to 300,000. At the lowest Reynolds number the boundary layer separated and did not reattach, in spite of transition in the separated shear layer. At higher Reynolds numbers the boundary layer did reattach, and the separation bubble became smaller as Re increased. High freestream turbulence increased the thickness of the separated shear layer, resulting in a thinner separation bubble. This effect resulted in reattachment at intermediate Reynolds numbers, which was not observed at the same *Re* under low freestream turbulence conditions. Numerical simulations were performed using an unsteady Reynolds averaged Navier-Stokes (URANS) code with both a shear stress transport *k-ω* model and a 4 equation shear stress transport Transition model. Both models correctly predicted separation and reattachment (if it occurred) at all Reynolds numbers. The Transition model generally provided better quantitative results, correctly predicting velocities, pressure, and separation and transition locations. The model also correctly predicted the difference between high and low freestream turbulence cases.

NOMENCLATURE

C_f	skin friction coefficient
Cp	$2(P_T - P)/\rho U_e^2$, pressure coefficient
C_x	axial chord length
f	frequency
H	δ^*/θ, shape factor
L_s	suction surface length
L_ϕ	blade spacing (pitch)
P	pressure
P_S	upstream static pressure
P_T	upstream stagnation pressure
P_{Te}	downstream stagnation pressure
PSD	power spectral density
Re	$U_e L_S / \nu$, exit Reynolds number
Re_θ	momentum thickness Reynolds number, $U_\infty\theta/\nu$
s	streamwise distance from leading edge along surface
TI	freestream turbulence intensity
U	mean streamwise velocity
U_e	nominal exit freestream velocity, based on inviscid solution
U_∞	local freestream velocity
u'	time averaged rms streamwise fluctuating velocity
x	axial distance from leading edge
y	distance from wall
y^+	distance from wall in viscous lengths
Zw	Zweifel coefficient
α_1	inlet flow angle
α_2	exit flow angle
δ^*	displacement thickness
ϕ	coordinate along blade spacing, normal to axial chord
γ	intermittency, fraction of time flow is turbulent
ν	kinematic viscosity
ρ	density
θ	momentum thickness
ψ	$(P_T-P_{Te})/(P_T-P_S)$, total pressure loss coefficient
ψ_{int}	total pressure loss integrated over blade spacing

Subscripts

p	pressure minimum (suction peak) location
s	separation location
t	transition start

INTRODUCTION

Boundary layer separation can lead to partial loss of lift and higher aerodynamic losses on low-pressure turbine (LPT) airfoils (e.g. Hourmouziadis [1], Mayle [2], and Sharma et al. [3]). As designers impose higher loading to improve efficiency and lower cost, the

associated strong adverse pressure gradients on the suction side of the airfoil can exacerbate separation problems, particularly at low Reynolds numbers. Prediction and control of suction side separation, without sacrifice of the benefits of higher loading, is therefore, crucial for improved engine design.

Separation and separated flow transition, which can lead to boundary layer reattachment, have received considerable attention. Studies have included flows over flat plates and airfoils in cascades. Some have considered steady inflow conditions, while others have included the effect of unsteady wakes. Volino [4] lists some recent examples. In general, the strong acceleration on the leading section of the airfoil keeps the suction side boundary layer thin and laminar, even in the presence of elevated freestream turbulence. When separation does occur, it is usually just downstream of the suction peak. If transition then occurs in the shear layer over the separation bubble, it is typically rapid and causes the boundary layer to reattach [5, 6]. Transition is dependent on Reynolds number, freestream turbulence level, and the surface roughness conditions upstream of the separation point.

Building on the understanding developed in earlier studies, higher lift airfoils with pressure gradients more resistant to separation have been designed, as described by Praisner and Clark [7]. Forward loading, for example, makes airfoils more separation resistant by extending the adverse pressure gradient on the aft portion of the suction side over a longer distance. This reduces the local pressure gradient at all locations, making separation less likely. If separation does occur, forward loading provides a longer distance along the airfoil surface for reattachment. An example is the L1M airfoil used by Bons et al. [8]. The L1M is a mid-chord loaded design, and is resistant to separation even at very low Reynolds numbers. The L1M has 10% higher loading than the "ultra-high lift" airfoils described by Zhang and Hodson [9], and 17% higher loading than the Pack B airfoil considered in several studies such as Volino [5, 6] and Bons et al. [10]. The design calculations indicate that the Zweifel coefficient increases from about 1.15 on the Pack B to about 1.35 on the L1M. If the definition for the Zweifel coefficient is taken as

$$Zw=2\cos^2\alpha_2(L_\phi/C_x)(\tan\alpha_1+\tan\alpha_2) \quad (1)$$

as given by Lakshminarayana [11], Zw=1.08 for the Pack B (in agreement with the value given by McAuliffe and Sjolander [12]) and Zw=1.23 for the L1M. The L1M has the same inlet and exit flow angles as the Pack B.

Although higher lift without separation is possible, forward loading has some disadvantages. As noted by Zhang et al. [13], the longer region of turbulent flow on a forward loaded airfoil can lead to increased profile losses. Forward loading also creates longer regions of strong pressure gradient on the endwalls, which can produce stronger secondary flows and losses. It might be possible to produce an aft loaded airfoil that was resistant to separation and had low profile and secondary loss characteristics over a range of Reynolds numbers if flow control were incorporated to suppress separation, as discussed by Bons et al. [8].

Bons et al. [14], Volino [15], and Ibrahim et al. [16] studied the flow over the L1A airfoil. The L1A was designed at the Air Force Research Laboratory (AFRL) and is available on a limited basis to U.S. researchers from Clark [17]. It is an aft loaded blade with the same flow angles and loading as the L1M. Dimensions of the L1A as used in the present study are given in Table 1.

Volino [15] showed that with low (0.6%) freestream turbulence and steady inflow conditions, the boundary layer separates on the L1A at Re≤120,000 and the time averaged separation bubble does not show reattachment (i.e. the time averaged separation bubble bursts). The Reynolds number, Re, is based on L_s and the nominal exit velocity from the cascade U_e (computed using the inlet velocity and the design inlet and exit flow angles). At Re≥200,000 a very small separation bubble may be present, but the boundary layer is largely attached and very high lift is achieved. Transition occurred in all cases, even at Re as low as 25,000. The L1A results contrast with those of earlier studies on airfoils such as the Pack B. At intermediate Re on the Pack B, transition in the shear layer over the separation bubble induced almost immediate reattachment. With increasing Re, or with elevated freestream turbulence, transition moved upstream and the separation bubble became progressively smaller. Only at the very lowest Re, where the shear layer remained laminar, did the separation bubble burst. As shown in Volino [15], the adverse pressure gradient is stronger on the L1A than on the Pack B, and this prevented reattachment, even with the mixing caused by a turbulent shear layer. Separation without reattachment on the L1A resulted in a 20% reduction in lift and a factor of 7 increase in total pressure loss. Bons et al. [14] reported similar results, although some differences were present at intermediate Re, possibly due to the higher (3%) freestream turbulence intensity in their study. The Bons et al. [14] work also included the effect of upstream wakes and flow control.

Table 1: Cascade parameters

Axial Chord, C_x [mm]	True Chord [mm]	Pitch, L_ϕ [mm]	Span [mm]	Suction side, L_s [mm]	Inlet flow angle	Exit flow angle
134	146	136	724	203	35°	60°

Ibrahim et al. [16] computed the flow over the L1A airfoil, matching the conditions of Volino [15]. They used the commercial code Fluent [18] with three of its turbulence and transition models. These were the shear-stress transport k-ω model of Menter [19] (SKW-sst), the v^2-f model of Durbin [20], and the transition model of Menter et al. [21] (Transition-sst) which includes a shear-stress transport model. All three models correctly predicted separation without reattachment at Re=25,000 and 100,000 and attached flow at Re=300,000. At the highest Re all three models did well and predicted about the same pressure profile on the airfoil, total pressure loss profiles, and velocity profiles at several streamwise locations in the suction side boundary layer. At the lower Re, all models did reasonably well predicting the pressure profiles, but the Menter et al. [21] transition model was generally better at predicting the velocity profiles, particularly when the boundary layer was separated.

The present study extends the results of Volino [15] and Ibrahim et al. [16] to cases with higher inlet freestream turbulence. Elevated freestream turbulence is intended to more closely match engine conditions. The results of the present study and those of Volino [15] will serve as baseline cases for future work in which unsteady wakes and separation control will be added.

EXPERIMENTAL FACILITY AND MEASUREMENTS

Experiments were conducted in a closed loop wind tunnel with a seven blade linear cascade in one corner of the loop, as shown in Fig. 1. Details are available in Volino [15]. A fine screen located 5.3 C_x upstream of the center airfoil and positioned perpendicular to the flow was used by Volino [15] to produce uniform inlet flow with low freestream turbulence. In the present study, this screen was replaced by a coarse grid, consisting of a 1.5 mm thick sheet metal plate with 19 mm square holes spaced 25.4 mm apart, center to center, in both directions. In a plane perpendicular to the inlet flow and 1.7 C_x upstream of the center blade, the grid produced uniform flow with a turbulence intensity, TI, of 6.0% in the streamwise component and

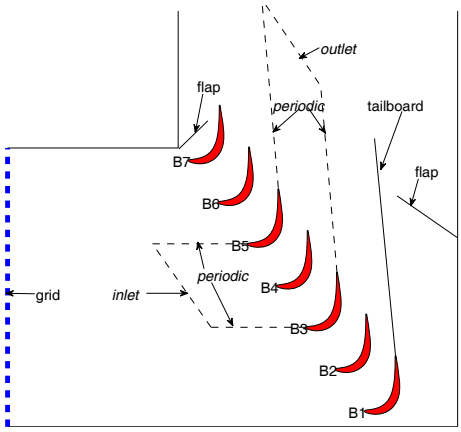

Fig. 1 Schematic of linear cascade and computational domain (dashed line)

4.2% in the cross stream components, for an overall intensity of 4.9%. The streamwise component was also measured at the inlet plane of the cascade, near the center blade, where it had decayed to 4%. The integral length scale of the freestream turbulence is 0.12 C_x in the streamwise direction and 0.04 C_x in the other directions.

The center blade, designated B4 in Fig. 1, contains pressure taps near the spanwise centerline. As described in Volino [15], a tailboard, was needed to produce the correct exit flow angle from the cascade. Its position was set to produce periodicity at high Reynolds numbers. The flaps shown in Fig. 1 were used to control the amount of flow escaping around the two ends of the cascade and produce the correct approach flow. Figure 1 also shows the computation domain (dashed line) with boundary conditions used in the CFD analysis.

Measurements

Pressure surveys were made using a pressure transducer (0-870 Pa range Validyne transducer). Stagnation pressure was measured with a pitot tube upstream of the cascade. Static pressure taps were located in the center blade as noted above. The uncertainty in the suction side pressure coefficients was 0.07. Most of this uncertainty was due to bias error. Stochastic error was minimized by averaging pressure transducer readings over a 10 second period.

A four component traverse with three linear stages and one rotating stage was located in the wind tunnel downstream of the cascade. The traverse produced an acceptably low blockage when it was located at least two axial chord lengths downstream of the cascade. Variations in the wind tunnel velocity were less than 2% as the traverse was moved to various positions. The traverse was used to hold and move probes for velocity and downstream pressure measurements.

Total pressure losses were documented using a Kiel probe traversed across three blade spacings, 0.63 C_x downstream of the cascade. To compute the mass flow averaged pressure loss, a velocity profile was also acquired along the same line as the total pressure surveys using a single sensor hot-film probe.

Velocity profiles on the suction surface were measured at the six streamwise stations listed in Table 2. All stations are downstream of the inviscid pressure minimum at s/L_s=0.49. Profiles were measured near the spanwise centerline of airfoil B4 with a hot-wire anemometer (AA Lab Systems model AN-1003) and a single sensor hot-film probe (TSI model 1201-20). The sensor diameter is 51 μm, and the active length is 1.02 mm. At each measurement location, data were acquired for 26 seconds at a 20 kHz sampling rate (2^{19} samples). All raw data were saved. The high sampling rate provides an essentially continuous signal, and the long sampling time results in low uncertainty in both

Table 2: Velocity profile measurement stations

Station	1	2	3	4	5	6
s/L_s	0.53	0.59	0.69	0.78	0.88	0.97
x/C_x	0.65	0.72	0.80	0.86	0.92	0.97

statistical and spectral quantities. Data were acquired at 40 wall normal locations in each profile, extending from the wall to the free-stream, with most points concentrated in the near wall region. The probe was positioned as close to tangent to the airfoil surface as possible at each station, such that the probe body extended downstream of the sensor and the direction of the traverse was within 5° of normal to the surface. In most cases the closest point in each profile was within about 0.2 mm of the wall, which compares to boundary layer thicknesses ranging from 1.3 mm to 37 mm.

Flow direction in a separation bubble cannot be determined with a single-sensor hot-wire, so measurements within the bubble provide only a rough estimate of the mean and fluctuating velocity magnitude. With the exception of the separation bubbles, the uncertainty in the mean velocity is 3-5% except in the very near wall region, where near-wall corrections (Wills [22]) were applied to the mean velocity. Uncertainties in the momentum and displacement thicknesses computed from the mean profiles are 10%. Uncertainty in the shape factor, H, is 8%. Local skin friction coefficients were computed from the near wall mean velocity profiles using the technique of Volino and Simon [23]. This technique accounts for streamwise pressure gradient effects on the mean profile. The uncertainty in C_f is 8%. The uncertainty in the fluctuating streamwise velocity is below 10%.

Pressure surveys and velocity profiles were acquired at nominal Re=25,000, 50,000, 100,000, 150,000, 200,000, and 300,000. The Reynolds number, as defined above, is based on the suction surface length and the nominal cascade exit velocity. The corresponding Reynolds numbers based on the cascade inlet velocity and the axial chord length ranged from 10,000 to 120,000.

NUMERICAL SIMULATIONS

The turbulence models and computational method used in the present study are described briefly here and more completely in Ibrahim et al. [16]. An unsteady Reynolds averaged Navier-Stokes (URANS) code was used. Sufficient time steps were computed so that the flow converged to a steady mean. Results were then time averaged based on 2000 time steps computed after convergence. Ibrahim et al. [16] considered several turbulence models and selected the three most promising noted above (SKW-sst, v^2-f and Transition-sst) for extended study. Of these, the SKW-sst and Transition-sst performed best and are used in the present study. The Transition-sst model is a 4 equation model and includes an intermittency transport equation. It has been validated against experimental data for turbomachinery applications (Langtry et al. [24]).

The computational domain consisted of the two passages between blades B3 and B5 in Fig. 1, with blade B4 in the middle. The boundary conditions on the sides of the passages were periodic with the exception of the pressure side of blade B3 and the suction side of blade B5, which were solid walls. The exit boundary was located 3.8 C_x downstream of the trailing edges in the flow direction. Zero gage pressure was specified at the exit. As described in Ibrahim et al. [16], exit locations extending farther downstream were tested to insure the results were independent of the location chosen. A uniform velocity inflow condition was specified 1.9 C_x upstream of the blade leading edges in the flow direction. The inlet flow angle was set to 33° based on an inviscid calculation of the full cascade shown in Fig. 1. This angle agreed with the experimentally measured inlet angle to within the experimental uncertainty. The experimental value matched the 35°

design inlet angle. Ibrahim et al. [16], in the low *TI* cases, showed that calculated *Cp* results with the 33° angle matched the experimental results slightly better than calculations with a 35° angle specified, but the differences were small and within the experimental uncertainty.

The computational grid was two-dimensional, consisting of 62469 nodes with the closest points to the airfoil walls between y^+=0.01 and 0.6, with an average of y^+=0.2. Ibrahim et al. [16] also considered a finer grid to establish grid independence. Simulations were done for Reynolds numbers of 25,000, 100,000 and 300,000. The freestream turbulence intensity was set to 5% at the inlet to the computational domain to match the experiments.

RESULTS

Pressure Profiles

Pressure profiles for all cases are shown in Fig. 2. The inviscid profile for the L1A airfoil, computed using a panel code, is shown for comparison. For *Re*≥50,000, the data generally agree with the inviscid profile, indicating that the boundary layer is attached over most of the airfoil. The data lie somewhat above the inviscid line on the suction side at s/L_s between 0.6 and 0.8, indicating a separation bubble followed by reattachment. The size of the bubble appears to decrease as *Re* increases. At *Re*=25,000 the suction peak is suppressed and the *Cp* values have a constant value on the downstream part of the suction side, indicating a separated boundary layer that does not reattach. The pressure side *Cp* values show less variation with Reynolds number, but in the *Re*=25,000 case *Cp* is slightly higher than in the other cases at s/L_s=0.25 and near the trailing edge. This suggests more of a leading edge separation bubble on the pressure side and higher velocity near the trailing edge when the burst suction side separation bubble forces fluid toward the pressure side.

The present *Cp* results agree with the low *TI* cases of Volino [15] for *Re*≥200,000. At *Re* between 50,000 and 150,000, the high *TI* causes reattachment, whereas the flow remained separated with low *TI*. The high and low *TI* results bracket the results of Bons et al. [14], who had an intermediate *TI* level.

The lift on the airfoil can be determined by integrating the difference between the suction and pressure side *Cp* values along the axial direction. The result is shown as a function of Reynolds number in Fig. 3. Also shown are the low *TI* cases of Volino [15] for comparison. In the high *TI* cases, the lift drops about 10% between the high *Re* cases and the *Re*=25,000 case due to the burst separation bubble. In agreement with the difference in reattachment, the lift is higher for the high *TI* cases than the low *TI* at *Re* below 200,000.

Total Pressure Losses

The loss coefficient, ψ, is shown for all cases in Fig. 4. The coordinate ϕ indicates the distance in the direction perpendicular to the axial chord. The normalizing quantity L_ϕ is the blade spacing. The origin, ϕ=0, corresponds to the location directly downstream of the trailing edge of the center blade in the direction of the exit design flow angle. At the two highest Reynolds numbers the losses are low, and the location of the loss peaks are in the expected positions downstream of the airfoils. This indicates that the actual flow angle is essentially equal to the design angle. The peaks downstream of blades B3-B5 are similar to each other, indicating periodicity in the cascade. These results agree with those of Volino [15] for the corresponding low *TI* cases. The loss coefficient is low between the peaks, although not as close to zero as in the low *TI* cases. This suggests some loss associated with the decay of the freestream turbulence. At *Re*=100,000 and 150,000 the loss peaks increase slightly, particularly on the left side of each peak. At *Re*=50,000 the loss peak has increased further, and is about 40% higher than in the highest *Re*

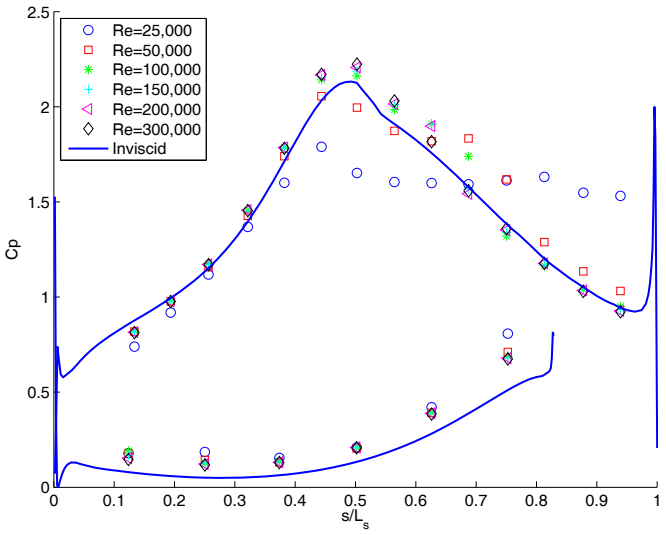

Fig. 2 *Cp* profiles

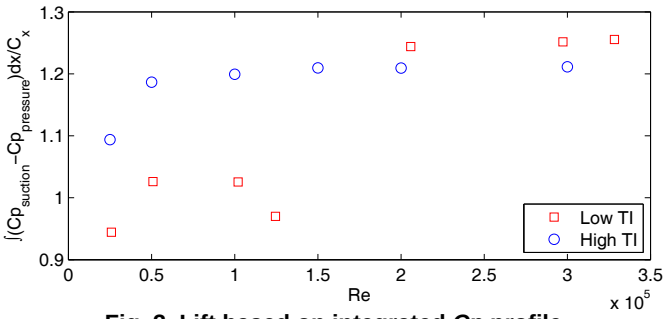

Fig. 3 Lift based on integrated *Cp* profile

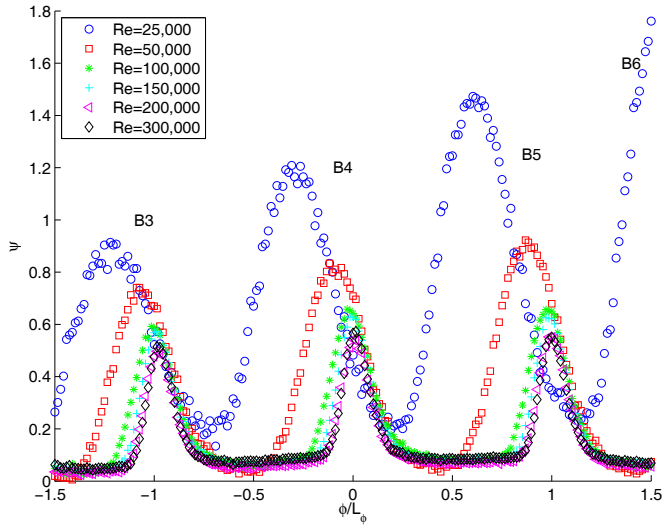

Fig. 4 Total pressure loss coefficient at 0.63 C_x downstream of cascade

cases. The increasing loss at lower *Re* is consistent with the increasing size of the separation bubble at lower *Re*, shown in Fig. 2. The separation bubble would tend to increase the suction side boundary layer thickness after reattachment, which would increase losses and

reduce the flow turning, moving the wake to the left in Fig. 4. At *Re*=25,000, the burst separation bubble results in much higher losses, and forces the peaks about $0.35L_\phi$ toward the pressure side of each passage. This shift corresponds to a 30° change in the exit flow angle. The reduction in flow turning is consistent with the lower lift shown in Fig. 3. The *Re*=25,000 results match those of the corresponding low *TI* case in Volino [15]. The peaks in the *Re*=25,000 case become noticeably smaller moving from B6 to B3, which results from the tailboard reducing the separation bubble thickness on the closer blades. As discussed in Volino [15], the tailboard was set for periodicity in the high *Re* cases. In cases with burst separation bubbles, the periodicity is lost. This is considered acceptable for the experiment, since the eventual goal is separation control, and if the separation can be suppressed, periodicity will be restored.

The integrated loss around the center blade is computed as

$$\psi_{int} = \int_{-L_\phi/2}^{L_\phi/2} \psi U d\phi \Big/ \int_{-L_\phi/2}^{L_\phi/2} U d\phi \qquad (2)$$

and is shown in Fig. 5 as a function of Reynolds number. Losses increase with decreasing *Re*, rising by about a factor of 2 between the highest and lowest Reynolds numbers. This difference is smaller than that observed in the low *TI* cases.

The turbulence associated with the airfoil wakes is shown in Fig. 6. The rms fluctuating streamwise velocity at 0.63 C_x downstream of the trailing edge is normalized on the nominal exit velocity for each case. At the higher Reynolds numbers the boundary layer turbulence has decayed to about 4% of U_e., matching the low *TI* results of Volino [15]. A double peak is apparent, with the left and right peaks corresponding the suction and pressure side boundary layers respectively. Between blades the turbulence intensity is at the background level of the wind tunnel. As *Re* drops to 100,000, there is a 20% rise in the wake turbulence, corresponding to the rise in the pressure loss in Fig. 4. Dropping to *Re*=50,000 the wake becomes much wider, and there is a large rise in the turbulence, particularly on the suction side of the wake, where the peak is about double the high *Re* value. There is some loss of periodicity at *Re*=50,000, with the turbulence rising from B3 to B6. The same rise is observed in the pressure loss peaks of Fig. 4, suggesting that the separation bubble is large enough that the tailboard is affecting it at *Re*=50,000. The turbulence level is still only about 40% of the value in the low *TI* *Re*=50,000 case, where the separation bubble burst. At *Re*=25,000 the turbulence level is much higher, and in agreement with the loss coefficients, the peaks are shifted toward the pressure side of the passages. The peak values at *Re*=25,000 were about 50% higher in the corresponding low *TI* case.

Velocity Profiles

Velocity profiles for the six suction surface measurement stations are shown in Fig. 7 for the *Re*=25,000 case. The low *TI* profiles of Volino [15] are shown for comparison. The top row in the figure shows the distance from the wall normalized on the suction surface length plotted against the local mean velocity normalized on the nominal exit velocity, U_e. The boundary layer has just separated at the first measurement station and the separation bubble grows larger at the downstream stations. The boundary layer does not reattach. The second row in Fig. 7 shows the rms streamwise fluctuating velocity, u', normalized with U_e. There is a very large peak located in the shear layer over the separation bubble which reaches a dimensionless magnitude of about 0.22. The high and low *TI* cases are similar, with

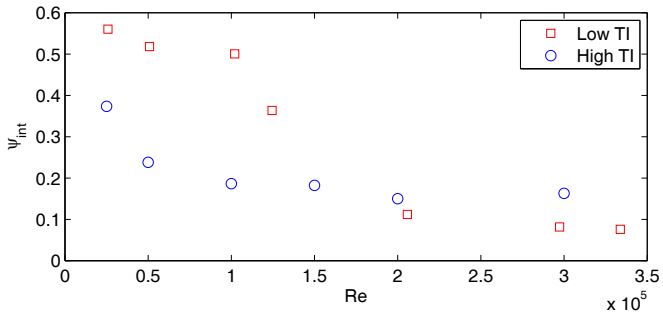

Fig. 5 Integrated total pressure loss coefficient for center blade as function of *Re*

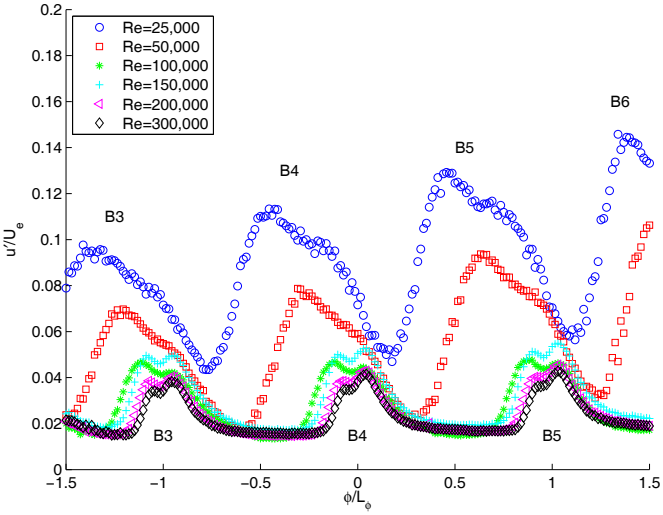

Fig. 6 Rms fluctuating streamwise velocity at 0.63 C_x downstream of cascade

a thick separation bubble in both cases and strong fluctuations in the shear layer over the bubble. The boundary layer thickness is nearly equal in the two cases. The shear layer, however, is noticeably thicker in the high *TI* case, extending closer to the wall. The thicker shear layer suggests stronger mixing closer to the wall, which would tend to promote reattachment. Although reattachment did not occur at *Re*=25,000, a thicker shear layer may help explain differences between the high and low *TI* cases at slightly higher Re. The third row in Fig. 7 shows the intermittency, γ. The intermittency is the fraction of time the flow is turbulent. It was determined at each measurement location based on the instantaneous streamwise velocity signal, using the technique described in Volino et al. [25]. Turbulent flow is defined here to include a range of large and small scale eddies. A boundary layer or shear layer may have significant u' fluctuations but still be considered non-turbulent if these fluctuations are induced by an external source such as freestream turbulence or are associated with instability in a narrow frequency band. Transition to turbulence is characterized by the appearance of broadband fluctuations. In the intermittency processing routine, the velocity signal is high pass filtered, and the appearance of high frequency fluctuations is used to distinguish between turbulent and non-turbulent flow. The results in Fig. 7 indicate that the shear layer begins transition between stations 3 and 4.

Figure 8 presents another view of the transition process using turbulence spectra. The spectra are computed from the fluctuating

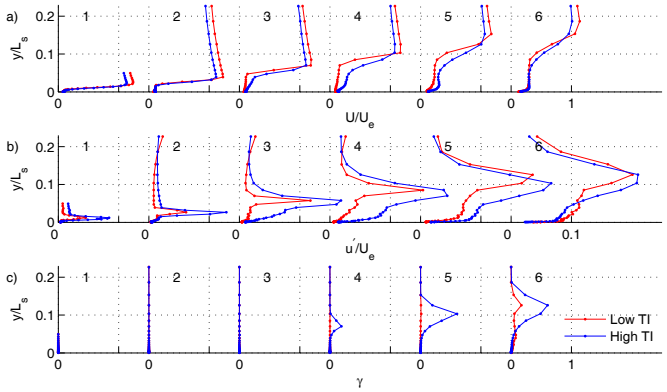

Fig. 7 Profiles for *Re*=25,000 case: (a) mean velocity, (b) u′/Ue, (c) intermittency

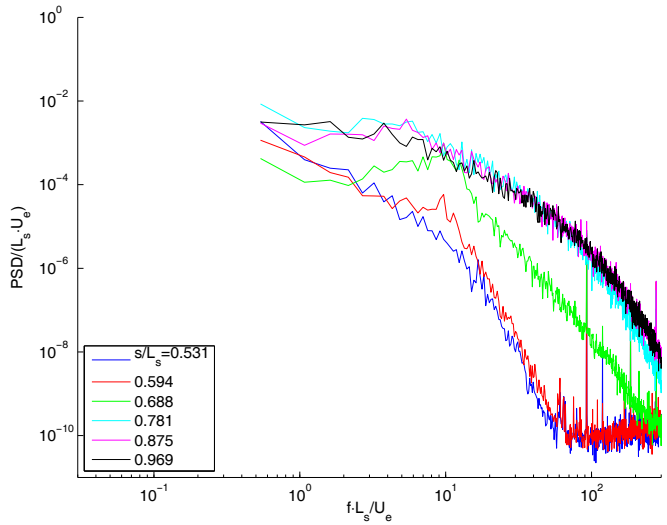

Fig. 8 Turbulence spectra for *Re*=25,000 case

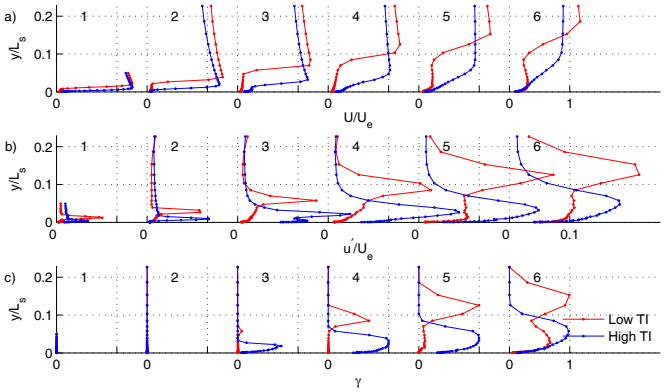

Fig. 9 Profiles for *Re*=50,000 case: (a) mean velocity, (b) u′/Ue, (c) intermittency

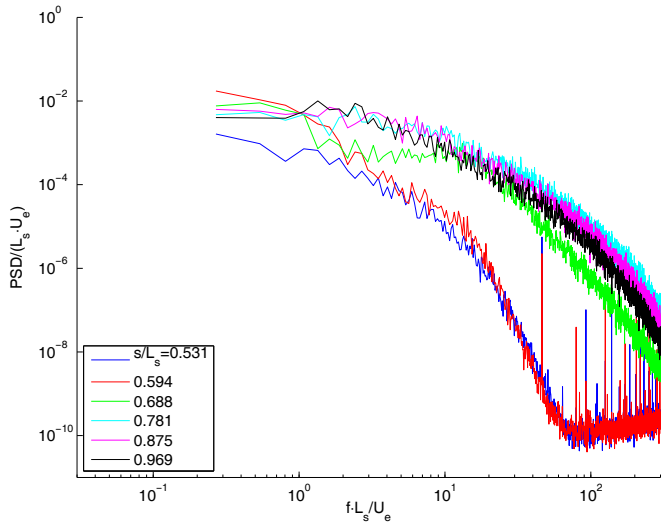

Fig. 10 Turbulence spectra for *Re*=50,000 case

velocity signal acquired at the location of peak u' at each measurement station shown in Fig. 7. Frequencies are resolved from 4.88 Hz to 10 kHz in 4.88 Hz increments using 4096 point Fast Fourier Transforms to compute the spectra. The frequencies and power spectral density (PSD) are normalized using L_s and U_e. There is a clear rise in the spectra between the second and third measurement stations, reaching a final high value by station 4. The spectra indicate that transition is in its early stages at station 3 and well underway or possibly complete by station 4. This agrees with the rise in intermittency between stations 3 and 4 in Fig. 7, although the spectra suggest the intermittency should reach a fully turbulent value of 1. The narrow range of scales resulting from the low velocity of the *Re*=25,000 case is believed to result in artificially low γ values from the intermittency processing routine. At higher *Re*, the range of scales is broader, and γ is believed to be correctly computed.

The spectra of Fig. 8 show a peak at stations 2 and 3 at a dimensionless frequency of 10. This peak suggests a shear layer instability which likely initiates transition. Although less distinct, spectral peaks are visible just before or just after transition at higher Reynolds numbers in the figures below. Volino [6, 15] observed similar peaks in the low *TI* cases and in the boundary layer on the Pack B airfoil and associated them with Tollmien-Schlicthing (TS) waves. The TS waves were believed to form in the attached boundary layer and grow in the separated shear layer until they became large enough to induce transition. The frequencies of the peaks in the present high *TI* cases can similarly be associated with TS frequencies. Kelvin-Helmholtz rollup of the shear layer, as observed by Stieger and Hodson [26], and Roberts and Yaras [27], is another possible explanation for the peaks. Hughes and Walker [28], Volino [6], and others have noted that in adverse pressure gradient cases, transition does not occur through a pure bypass mode, even in the presence of elevated freestream turbulence.

The velocity profiles for the *Re*=50,000 case are shown in Fig. 9. The boundary layer appears to have just separated at station 2, is separated at station 3, and is reattaching by station 4. There is a clear difference from the low *TI* case, which shows a burst separation bubble. Transition is underway in the shear layer at station 3 and complete by station 4, which likely promotes the reattachment. The spectra in Fig. 10 agree with the intermittency, showing a rise between stations 2 and 3, and fully turbulent values by station 4. The delay in separation relative to the low *TI* case results in a thinner separation bubble, which makes reattachment possible when transition begins.

Figure 11 shows the velocity profiles for the *Re*=100,000 case. Separation appears to be delayed relative to the Re=50,000 case to about station 3. Transition moves upstream and is complete by station 3. The result is a near elimination of the separation bubble and a

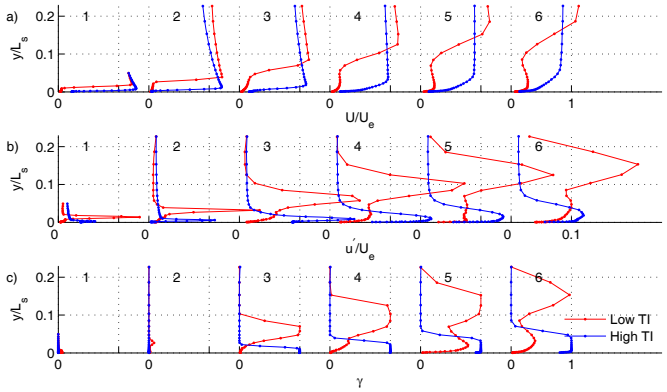

Fig. 11 Profiles for *Re*=100,000 case: (a) mean velocity, (b) u′/Ue, (c) intermittency

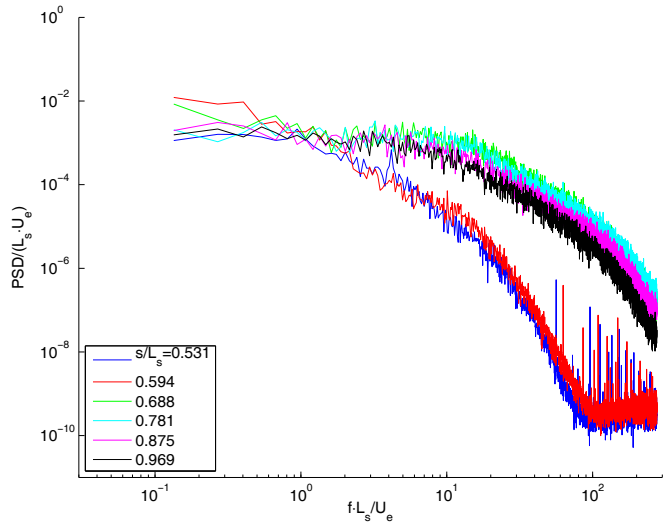

Fig. 12 Turbulence spectra for *Re*=100,000 case

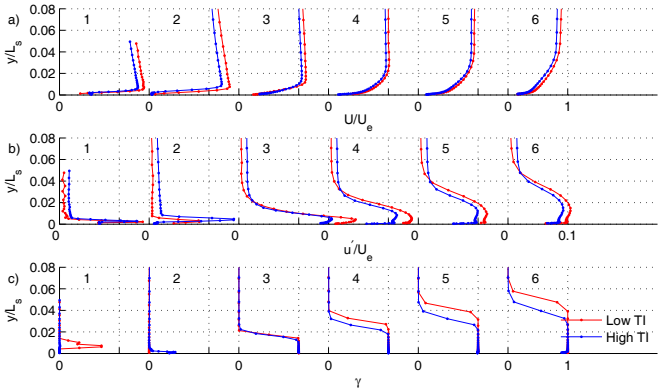

Fig. 13 Profiles for *Re*=200,000 case: (a) mean velocity, (b) u′/Ue, (c) intermittency

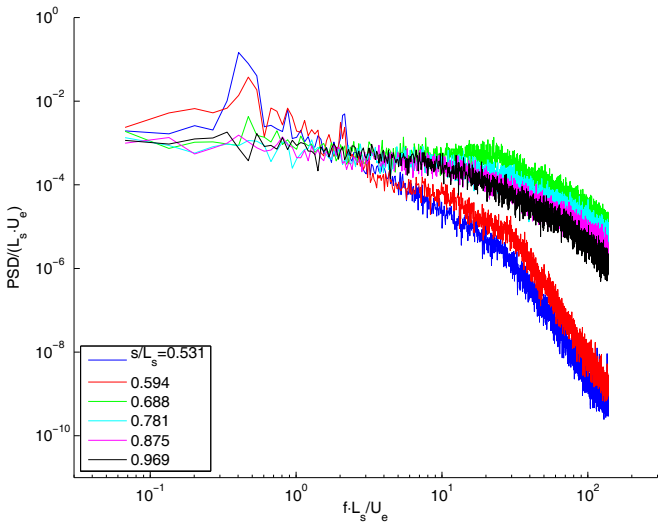

Fig. 14 Turbulence spectra for *Re*=200,000 case

significantly thinner boundary layer downstream. The maximum u'/U_e at the last measurement station is 65% of its level in the *Re*=50,000 case. The thinner boundary layer and lower turbulence correspond to the drop in total pressure loss and wake turbulence between the *Re*=50,000 and 100,000 cases in Figs. 4-6. Figure 12 shows the spectra for the *Re*=100,000 case. The rise between stations 2 and 3 indicates transition in agreement with the γ profiles of Fig. 11.

Velocity profiles and spectra for the *Re*=200,000 case are shown in Figs. 13 and 14. The separation bubble has been effectively eliminated. This reduces the boundary layer thickness and fluctuating velocity levels relative to the *Re*=100,000 case. The boundary layer also remained attached in the low *TI* *Re*=200,000 case, and the profiles in Fig. 13 are in close agreement for the high and low *TI* cases. Profiles and spectra for the *Re*=300,000 case are not shown, but with the exception of a slightly thinner boundary layer, appear the same as those for the *Re*=200,000 case.

The shape factor, *H*, and skin friction coefficient C_f are good indicators of the state of the boundary layer with respect to separation and transition. The shape factor is shown Fig. 15. At the first measurement stations, *H*=1.8 at *Re*=300,000, indicating an attached boundary layer. At Re=25,000, *H*=3.6, indicating the boundary layer is separated or on the verge of separation. With low *TI*, *H* at station 1 was above 2.5 at all *Re*. Particularly in the high *Re* cases, high *TI*

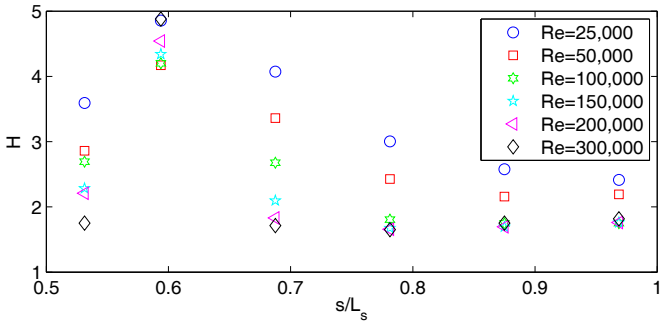

Fig. 15 Shape factor

reduces the shape factor, indicating that separation is delayed. At the second station in Fig. 15, *H* is between 4 and 5 in all cases, indicating that the boundary layer is separated. Note that these high *H* values are not quantitatively accurate since the hot-wire is unable to accurately measure velocity within the separation bubble. The high *H* values, do, however, provide a good qualitative indicator that the flow is locally separated. By the third station, *H* has dropped to an attached turbulent boundary layer level for *Re*≥200,000 and by station 4 all but the two lowest *Re* cases are fully reattached. In the *Re*=25,000 case *H* remains

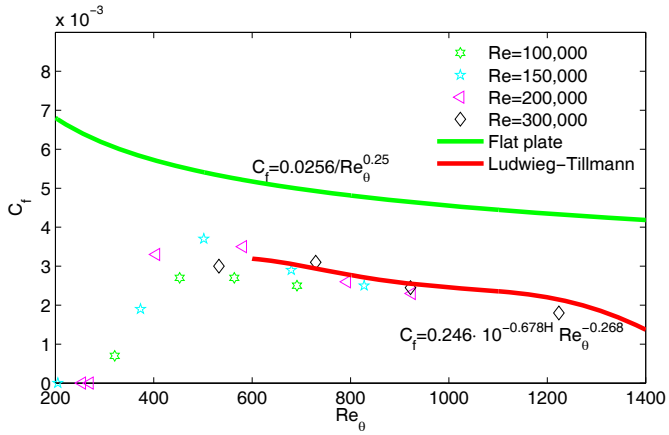

Fig. 16 Skin friction coefficient for high *Re* cases

high, since the boundary layer never reattaches. At *Re*=50,000, *H* at the downstream stations lies between the attached values at high *Re* and the separated values at *Re*=25,000, indicating that the boundary layer has reattached but has not fully recovered from the separation. The skin friction coefficient is shown as a function of momentum thickness Reynolds number in Fig. 16 for the high *Re* cases. It rises from zero after separation and then decreases in the streamwise direction. Also shown is a standard flat-plate correlation for turbulent boundary layers from Schlichting [29] and the Ludwieg-Tillmann correlation which accounts for pressure gradient effects. The present C_f values are as much as 50% lower than the flat-plate correlation and agree well with the Ludwieg-Tillmann correlation.

Transition Correlations

Several correlations for predicting the starting location for separated flow transition are available in the literature, and some of these are tested below against the present data. The correlation equations are available in Volino [15]. Most of the correlations predict the distance from the separation point to the start of transition. Mayle [2] presents correlations for short and long separation bubbles which depend on Re_θ at separation. Davis et al. [30] uses only the freestream turbulence intensity. Due to the acceleration through the passage, the local *TI* dropped from the inlet value to about 1.3% at separation, and was set to this value for use with all correlations. Hatman and Wang [31] identify several transition modes and present correlations for each of them. Their laminar separation mode transition correlation depends on Re_s (based on local freestream velocity and distance from the leading edge to the separation point). Yaras [32] uses Re_s and a turbulence factor based on the freestream turbulence intensity and its integral length scale. Praisner and Clark [7] use Re_s and Re_θ at separation. An additional correlation proposed by Roberts and Yaras [27] is

$$Re_{st} = (785\text{-}30\ TF)\ Re_{\theta s}^{0.7} \qquad (3)$$

where $TF=TI(s_s/\lambda)^{0.2}$, s_s is the distance from the leading edge to the separation point and λ is the integral length scale of the freestream turbulence.

While the above correlations are based on the conditions at the separation location, Volino and Bohl [33] reasoned that instabilities begin to grow when the boundary layer becomes unstable at the start of the adverse pressure gradient region. They compute the distance from the suction peak to the start of transition based on *TI* and Re_θ at the suction peak.

Table 3: Conditions at suction peak and separation location based on laminar boundary layer calculation

Re	s_p/L_s	s_s/L_s	$Re_{\theta p}$	$Re_{\theta s}$
25,000	0.438	0.496	47	60
50,000	0.438	0.536	64	89
100,000	0.493	0.538	106	127
150,000	0.493	0.539	130	157
200,000	0.493	0.538	150	181
300,000	0.493	0.538	183	221

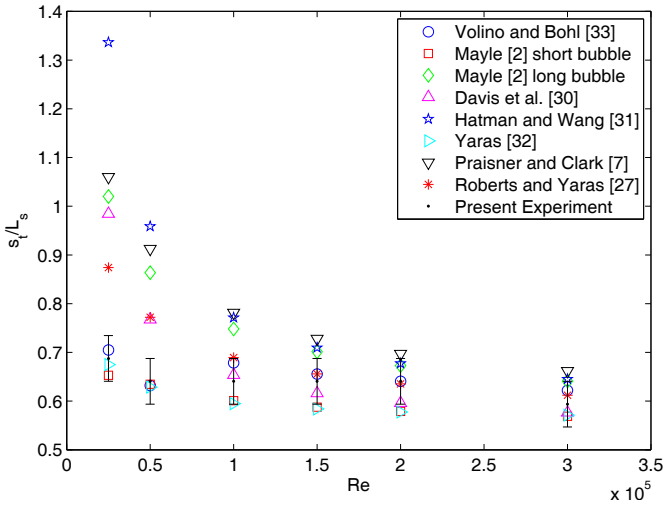

Fig. 17 Predicted and experimental transition start location, error bars indicate uncertainty due to finite spacing of measurement stations

The location of the suction peak for each case was taken from the experimental data of Fig. 2. The separation location and the momentum thickness Reynolds numbers at separation, $Re_{\theta s}$, and at the suction peak, $Re_{\theta p}$, were estimated using a laminar calculation with the measured pressure gradient using the TEXSTAN [34] boundary layer code, as described in Volino [15]. The Reynolds numbers used with the correlations are listed in Table 3. The various correlations were then used to compute s_t, shown in Fig. 17, which is defined as the distance from the leading edge to the start of transition. The experimental transition locations, as determined from Figs. 7-14 are also shown. The uncertainties in the experimental locations, which result from the finite spacing between the measurement stations, are indicated by the error bars. Values of $s_t/L_s>1$ in the figure indicate that transition is predicted downstream of the trailing edge of the airfoil.

The Mayle [2] short bubble correlation, which is only intended for separation bubbles that reattach, predicts transition well in most cases, as does the Yaras [32] correlation. The Volino and Bohl [33] correlation agrees with the experiment at all *Re*. The Davis et al. [30] and Roberts and Yaras [27] correlations predict transition well for $Re\geq100{,}000$, but too far downstream at lower *Re*. The other correlations predict transition too far downstream, but approach the experimental results at high *Re*. With low *TI*, all the correlations predicted the data well at high Re. At low Re, the Mayle [2] short bubble correlation predicted transition too far upstream, the Roberts and Yaras [27] and Volino and Bohl [33] correlations agreed with the data, and the other correlations predicted transition too far downstream.

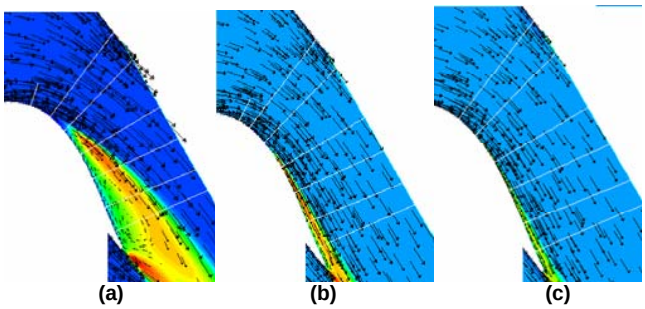

Fig. 18 Flow field on suction side of airfoil showing u'/U_e (contours) and mean velocity (vectors): a) *Re*=25,000, b) 100,000, c) 300,000

Numerical Results

Velocity vector fields and contours of u'/U_e are shown in Fig. 18 for the simulation results using the Transition-sst model. As will be shown below, the Transition-sst model generally performed better than the SKW-sst model. The flow along the suction side of the airfoil is shown in the figure. For reference, the white lines in the figure correspond to the experimental measurement stations listed in Table 2. The short white line upstream of the others indicates the location of the suction peak. In agreement with the experimental results, the simulation predicts a burst separation bubble at *Re*=25,000. The turbulence level is high in the shear layer above the separation bubble, but the boundary layer does not reattach. The velocity vectors show a significant reduction in flow turning. At *Re*=100,000 and 300,000, again in agreement with the experiment, the boundary layer is attached. The turbulence contours indicate a thicker boundary layer at *Re*=100,000 than at 300,000. The location of the suction peaks and separation locations in Fig. 18 agree with those in Table 3 to within 0.013 and 0.034 in s_p/L_s and s_s/L_s respectively. This lends support to the simple laminar boundary layer calculations used to produce the estimates in Table 3. The $Re_{\theta p}$ values which can be extracted from the simulation are about 11% lower than the values in Table 3. This difference is not large enough to significantly change the correlation predictions in Fig. 17.

To quantify the simulation results, pressure profiles for the numerical simulations are compared to the experimental results in Fig. 19. At all Reynolds numbers, both the SKW-sst and Transition-sst models agree reasonably well with the experimental data. At *Re*=25,000, the Transition-sst model agrees with the data to within the experimental uncertainty from s/L_s=0.1 to 0.6. The SKW-sst *Cp* prediction is slightly lower, but both models correctly predict that the boundary layer does not reattach. The Transition-sst model predicts a drop in *Cp* downstream of s/L_s=0.6 which is not seen in the data. The drop corresponds to the start of transition, as will be discussed below. At *Re*=100,000 (Fig. 18b), both models correctly predict an attached boundary layer. In the low *TI* case at this Re, both models correctly predicted a burst separation bubble, so they appear to handle the freestream turbulence effect correctly. The Transition-sst model provides a better prediction than the SKW-sst model at *Re*=100,000, particularly between s/L_s=0.5 and 0.7 where the data and the Transition-sst models show a slight plateau in *Cp*. The plateau indicates a boundary layer on the verge of separation or possibly a small separation bubble. For the *Re*=300,000 case (Fig. 18c), neither model or the experiment show any indication of separation. Both models agree well with the experiment, with the Transition-sst model providing a slightly better prediction downstream of the suction peak. The simulations under predict the peak *Cp* in the *Re*=100,000 and 300,000 cases, and although the difference is not large, it is consistent

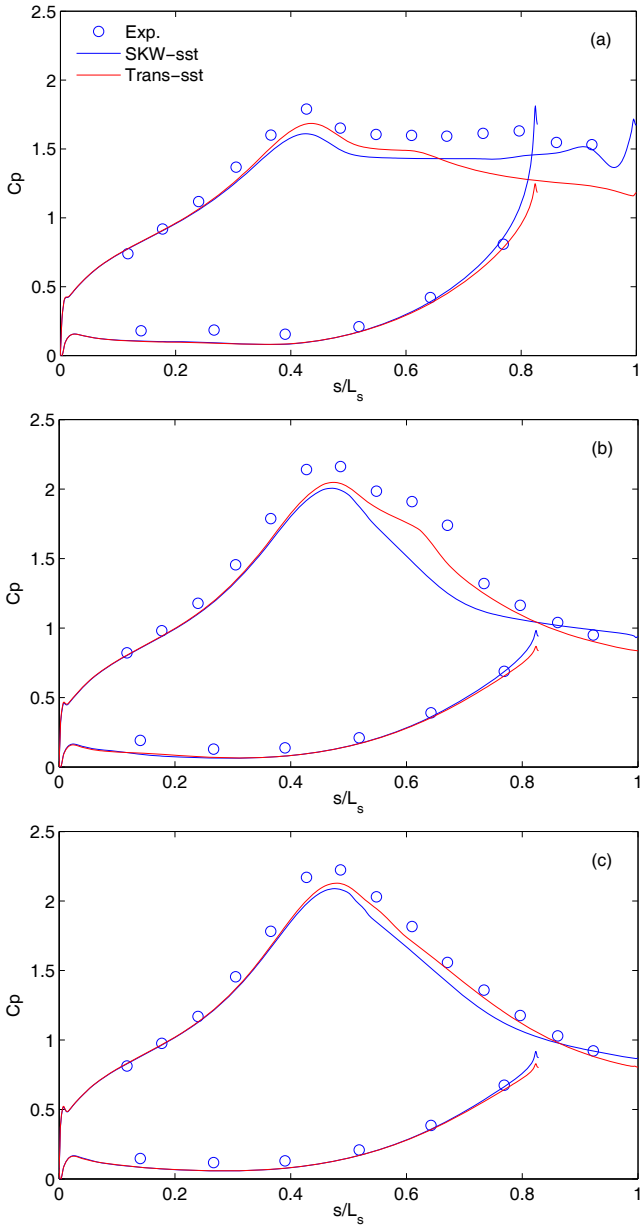

Fig. 19 *Cp* profiles comparing simulations to experiment: a) *Re*=25,000, b) 100,000, c) 300,000

with the difference between the data and the inviscid solution in Fig. 2. Bons et al. [14] saw a similar difference between their experimental data and simulations for similar conditions.

Mean velocity profiles for the *Re*=25,000 case are compared to the experiment in Fig. 20. Up to s/L_s=0.59, the turbulence model predictions agree well with each other and the experiment. Differences from the experiment inside the separation bubble are not meaningful, since the hot-wire cannot distinguish the direction of reverse flow. Downstream of s/L_s=0.59, the models correctly predict the growth of the separation bubble. The Transition-sst model generally provides a better match to the data, although the SKW-sst model is closer at s/L_s=0.88. A thicker separation bubble in the simulation than the experiment, as shown at s/L_s=0.97, is expected in cases with burst separation bubbles, particularly at downstream

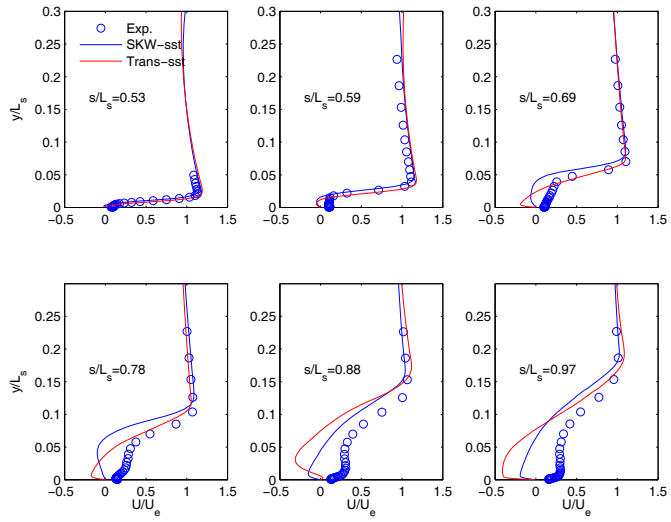

Fig. 20: Comparison of simulation and experimental mean velocity profiles, *Re*=25,000

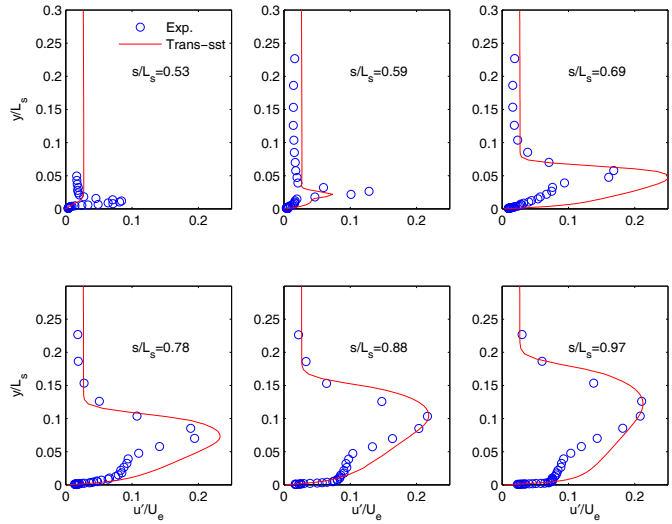

Fig. 21: Comparison of Transition-sst and experimental u'/U_e profiles, *Re*=25,000

stations. As noted above, the tailboard in the experiment suppresses the separation bubble somewhat in cases without reattachment, particularly on the airfoils closest to the tailboard. The simulation, with its periodic boundary conditions, corresponds to an infinite cascade with no tailboard effects.

The turbulence kinetic energy provides some information about how the simulation computes transition. The rms fluctuating streamwise velocity, u', is estimated from the simulations using the computed turbulence kinetic energy and an assumption of isotropic turbulence. This assumption is clearly not strictly correct, but allows an estimate of u' to compare to the experimental data. This comparison is shown in Fig. 21 for the Transition-sst model in the *Re*=25,000 case. At s/L_s=0.53, there is a near wall peak in the experimental data which is not captured by the calculation. This is upstream of transition, so the peak is likely caused by the freestream turbulence buffeting the boundary layer. At all the other stations the peak is predicted at the correct distance from the wall. The simulation peak is still too low at s/L_s=0.59 and about 40% too high at s/L_s=0.69, but at all the other stations the simulation and experiment peak magnitudes match closely. An exact match should not be expected given the approximation in estimating u' from the turbulence kinetic energy. Above the peak the match is also good, but closer to the wall the simulation shows higher fluctuating velocity than the experiment. Some of the difference may be attributable to the inability of the hot-wire to measure velocity accurately inside the separation bubble, but it appears that the simulation predicts a thicker shear layer than the experiment. Ibrahim et al. [16] also saw a thicker shear layer than the experiment in the low *TI* cases.

The rise in turbulence in the simulation can be used to predict the start of transition. The transition start location is designated as the location of the local maximum in turbulence kinetic energy following the suction peak, determined using the contours of Fig. 18. This particular location is a somewhat arbitrary choice, as one could also reasonably designate a location slightly upstream of the peak as the transition start. The local peak is, however, an unambiguous location and is useful for comparing transition among different cases. In the *Re*=25,000 case, the simulation predicts transition start at s/L_s=0.64, which agrees with the experimental location indicated in Figs. 8 and 17. The start of transition corresponds to the start of the slow drop in *Cp* shown in Fig. 19a. The mixing associated with transition makes a shear layer more likely to reattach. Perhaps the transition and turbulence predicted by the Transition-sst model is pushing the shear layer closer to reattachment than observed in the experiment, which could cause the lower *Cp*. The thicker shear layer in the simulation may cause this effect. The effect is not large enough to cause a full reattachment in the simulation, so the simulation and experiment remain in overall good agreement. Ibrahim et al. [16] did not see the same drop *Cp* in their low *TI* *Re*=25,000 case, possibly because transition did not occur until s/L_s=0.74, and the separation bubble had become too thick for any hint of reattachment. In their *Re*=100,000 case, Ibrahim et al. [16] saw transition start at s/L_s=0.59, and it induced the same slow drop in *Cp* shown in Fig. 19a.

Figures 22 and 23 show the mean velocity and u' profiles for the *Re*=100,000 case. The Transition-sst model predicts the data well at most locations. Some difference in the shape of the mean profile is visible at the two most downstream stations, and the magnitude of the u' peak is under predicted at the upstream stations. The freestream turbulence level in the experiment has also decayed more than in the simulation. The SKW-sst model does not do as well at the downstream stations, predicting a thicker boundary layer and a small separation bubble which were not observed in the experiment. Velocity and turbulence profiles for the *Re*=300,000 case are shown in Figs. 24 and 25. The Transition-sst model provides good agreement with the experimental mean profiles at all locations. With the same exceptions noted in Fig. 23, agreement is also good for the u' profiles. The SKW-sst model again predicts a thicker boundary layer than the experiment at the downstream stations. The Transition-sst model predicts transition start at s/L_s=0.66 and 0.64 in the *Re*=100,000 and 300,000 cases respectively. To within the experimental uncertainty, these locations agree with the experimental locations shown in Fig. 17.

Total pressure loss coefficients are shown in Fig. 26. The magnitude and width of the loss peaks in the experiments and simulations generally agree, showing the correct trend with Reynolds number. In the *Re*=25,000 case (Fig. 26a), the simulations predict higher loss peaks and less flow turning than the experiment. This is expected since the tailboard suppresses the separation bubble somewhat in the experiment, as noted above. A thicker bubble in the simulation will result in higher losses and divert the flow toward the pressure side of the passage, moving the loss peak to lower ϕ/L_ϕ.

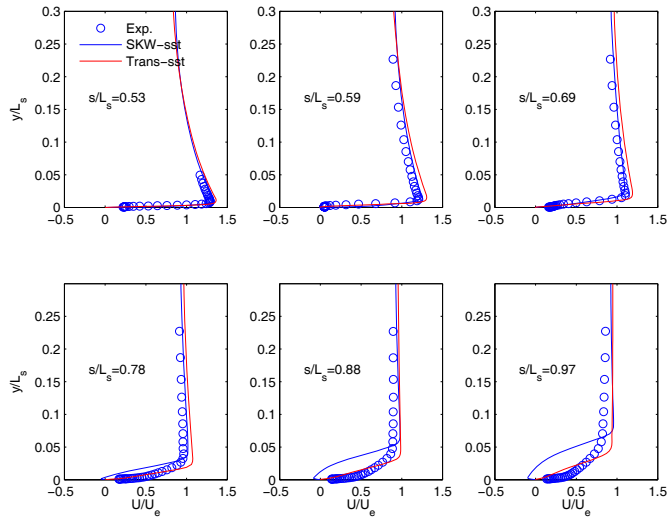

Fig. 22: Comparison of simulation and experimental mean velocity profiles, *Re*=100,000

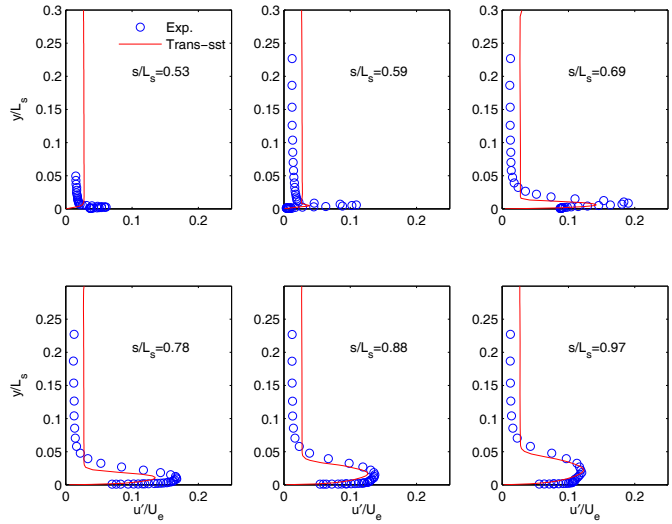

Fig. 23: Comparison of Transition-sst and experimental u'/U_e profiles, *Re*=100,000

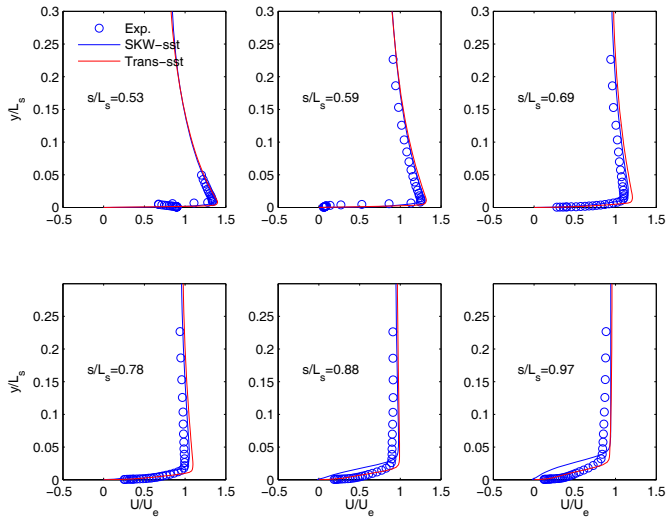

Fig. 24: Comparison of simulation and experimental mean velocity profiles, *Re*=300,000

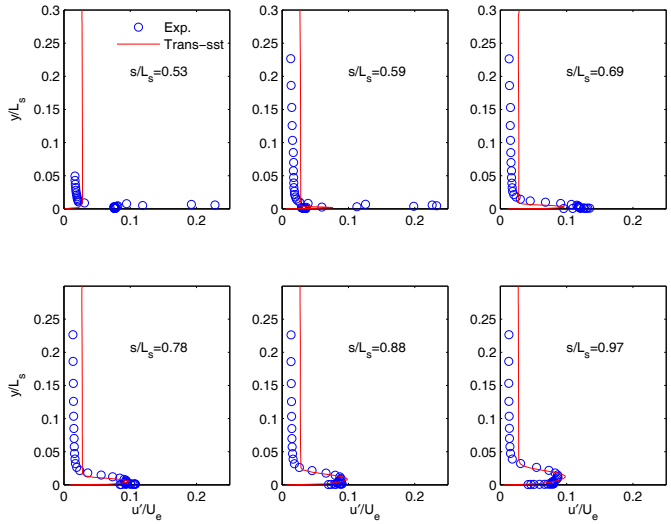

Fig. 25: Comparison of Transition-sst and experimental u'/U_e profiles, *Re*=300,000

Between wakes the Transition-sst model indicates lower loss than the experiment. This difference may be related to the under prediction of the freestream turbulence decay noted in Figs. 23 and 25. The *Re*=100,000 and 300,000 cases (Figs. 26b and 26c) do not suffer from tailboard effects in the experiment since the boundary layer reattaches. In both cases the Transition-sst model predicts the peak magnitudes to within about 5%, but the peak location is shifted slightly toward the pressure side of the passage in the simulation. The SKW-sst model does not do as well, predicting a higher peak and more of a shift toward the pressure side. As in the lower *Re* case, both models under predict the loss between wakes.

CONCLUSIONS

The flow over the very high lift L1A airfoil was studied under high freestream turbulence conditions. Reynolds numbers based on suction surface length and nominal exit velocity ranged from 25,000 to 300,000. At the lowest Reynolds number, the laminar suction surface boundary layer separated and did not reattach. At the higher Reynolds numbers, a separation bubble was followed by transition and reattachment. Spectral peaks suggest that transition is caused by the growth of an instability, as opposed to a pure bypass, in spite of the high freestream turbulence. The transition locations in both high and low *TI* cases were well predicted by the correlation of Volino and Bohl [33]. The separation bubble became smaller as Reynolds number increased, and was effectively eliminated at the highest Reynolds numbers. The tendency toward separation at intermediate Reynolds numbers was still large enough to increase the boundary layer thickness and significantly increase pressure losses above the high *Re* cases. The present results contrast with low freestream turbulence results acquired in the same facility. With low *TI*, the boundary layer did not reattach at intermediate Reynolds numbers, in spite of transition taking place in the separated shear layer. High freestream turbulence appears to increase the thickness of the shear layer over the separation bubble, thereby decreasing the bubble thickness. The

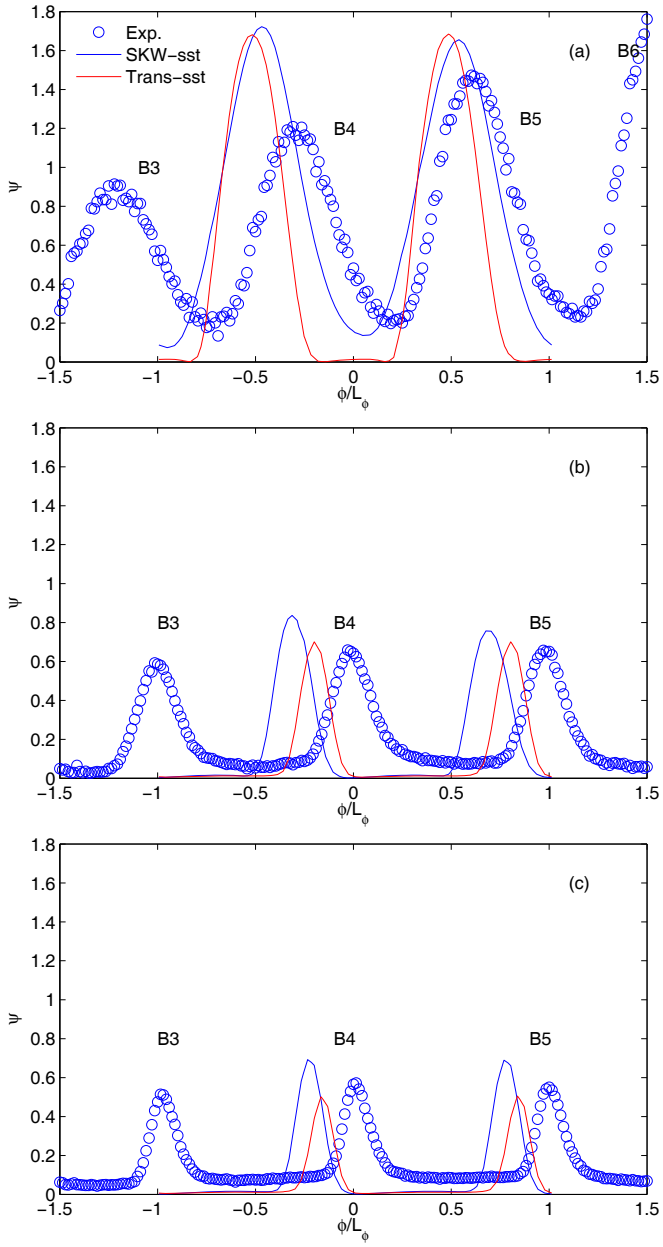

Fig. 26 Total pressure loss coefficient at 0.63 C_x downstream of cascade comparing simulations to experiment: a) *Re*=25,000, b) 100,000, c) 300,000

thinner bubble results in turbulence closer to the wall when transition begins, which promotes reattachment. Reattachment changes the pressure distribution on the airfoil, causing the suction peak to rise and move downstream and delaying separation. The result is higher lift and an even smaller separation bubble.

Numerical simulations with the 4 equation Transition-sst model of Menter et al. [21] correctly predicted separation, transition and reattachment at all Reynolds numbers. Some discrepancies between the model prediction and the experimental data were noted, but in general the model predicted well the pressure distribution on the airfoil, the total pressure losses, and mean and fluctuating velocity profiles along the suction surface of the airfoil. The k-ω-sst (SKW-sst) model of Menter [19] did not do quite as well. Comparing to the results of Ibrahim et al. [16], the simulations correctly predicted the major differences between the high and low freestream turbulence cases.

ACKNOWLEDGMENTS

This work was sponsored by the National Aeronautics and Space Administration. The grant monitor is Dr. Anthony Strasizar of the NASA Glenn Research Center. The support of the United States Naval Academy Technical Support Department Shop and Fluids Laboratory is greatly appreciated.

REFERENCES

[1] Hourmouziadis, J., 1989, "Aerodynamic Design of Low Pressure Turbines," AGARD Lecture Series 167.

[2] Mayle, R.E., 1991, "The Role of Laminar-Turbulent Transition in Gas Turbine Engines," ASME *Journal of Turbomachinery*, **113**, pp. 509-537.

[3] Sharma, O.P., Ni, R.H., and Tanrikut, S., 1994, "Unsteady Flow in Turbines," AGARD Lecture Series 195, Paper No. 5.

[4] Volino, R.J., 2008, "Separated Flow Measurements on a Highly Loaded Low-Pressure Turbine Airfoil," ASME Paper GT2008-51445.

[5] Volino, R.J., 2002, "Separated Flow Transition Under Simulated Low-Pressure Turbine Airfoil Conditions: Part 1 –Mean Flow and Turbulence Statistics," ASME *Journal of Turbomachinery*, **124**, pp. 645-655.

[6] Volino, R.J., 2002, "Separated Flow Transition Under Simulated Low-Pressure Turbine Airfoil Conditions: Part 2 –Turbulence Spectra," ASME *Journal of Turbomachinery*, **124**, pp. 656-664.

[7] Praisner, T.J., and Clark, J.P., 2007, "Predicting Transition in Turbomachinery – Part 1: A Review and New Model Development," ASME *Journal of Turbomachinery*, **129**, pp. 1-13.

[8] Bons, J.P., Hansen, L.C., Clark, J.P., Koch, P.J., and Sondergaard, R., 2005, "Designing Low-Pressure Turbine Blades With Integrated Flow Control," ASME Paper GT2005-68962.

[9] Zhang, X.F., and Hodson, H., 2005, "Combined Effects of Surface Trips and Unsteady Wakes on the Boundary Layer Development of an Ultra-High-Lift LP Turbine Blade," ASME *Journal of Turbomachinery*, **127**, pp. 479-488.

[10] Bons, J.P., Sondergaard, R., and Rivir, R.B., 2001, "Turbine Separation Control Using Pulsed Vortex Generator Jets," ASME *Journal of Turbomachinery*, **123**, pp. 198-206.

[11] Lakshminarayana, B., 1996, *Fluid Dynamics and Heat Transfer of Turbomachinery*, Wiley, New York.

[12] McAuliffe, B.R. and Sjolander, S.A., "Active Flow Control Using Steady Blowing for a Low-Pressure Turbine Cascade," ASME *Journal of Turbomachinery*, **126**, pp. 560-569.

[13] Zhang, X.F., Vera, M., Hodson, H., and Harvey, N., 2007, "Separation and Transition Control on an Aft-Loaded Ultra-High-Lift LP Turbine Blade at Low Reynolds Numbers: Low-Speed Investigation," ASME *Journal of Turbomachinery*, **128**, pp. 517-527.

[14] Bons, J.P., Pluim, J., Gompertz, K., Bloxham, M., and Clark, J.P., 2008, "The Application of Flow Control to an Aft-Loaded Low Pressure Turbine Cascade with Unsteady Wakes," ASME Paper GT2008-50864.

[15] Volino, R.J., 2008, "Separated Flow Measurements on a Highly Loaded Low-Pressure Turbine Airfoil," ASME Paper GT2008-51445.

[16] Ibrahim, M., Kartuzova, O., and Volino, R.J., 2008, "Experimental and Computational Investigations of Separation and Transition on a Highly Loaded Low Pressure Turbine Airfoil: Part 1 – Low Freestream Turbulence Intensity," ASME Paper IMECE2008-68879.
[17] Clark J.P., 2007, Private Communication, Air Force Research Laboratory.
[18] Fluent Inc., 2001, *Fluent 6 Users Manual*, Lebanon NH, USA.
[19] Menter, F.R. 1994, "Two-Equation Eddy-Viscosity Turbulence Models for Engineering Applications," *AIAA Journal*, **32**, pp. 1598-1605.
[20] Durbin, P.A., 1995, "Separated Flow Computations with the k-ε-v^2 Model," *AIAA Journal*, **33**, pp. 659-664.
[21] Menter, F.R., Langtry, R.B., Likki, S.R., Suzen, Y.B., Huang, P.G., and Völker, S., 2006, "A Correlation Based Transition Model Using Local Variables – Part I: Model Formulation", ASME *Journal of Turbomachinery*, **128**, pp. 413-422.
[22] Wills, J.A.B., 1962, "The Correction of Hot-Wire Readings for Proximity to a Solid Boundary," *Journal of Fluid Mechanics*, **12**, pp. 65-92.
[23] Volino, R.J., and Simon, T.W., 1997, "Velocity and Temperature Profiles in Turbulent Boundary Layers Experiencing Streamwise Pressure Gradients," ASME *Journal of Heat Transfer*, **119**, pp. 433-439.
[24] Langtry, R.B., Menter, F.R., Likki, S.R., Suzen, Y.B., Huang, P.G., and Völker, S., 2006, "A Correlation Based Transition Model Using Local Variables – Part II: Test Cases and Industrial Applications", ASME *Journal of Turbomachinery*, **128**, pp. 423-434.
[25] Volino, R.J., Schultz, M.P., and Pratt, C.M., 2001, "Conditional Sampling in a Transitional Boundary Layer Under High Free-Stream Turbulence Conditions," ASME *Journal of Fluids Engineering*, **125**, pp. 28-37.
[26] Stieger, R.D., and Hodson, H.P., 2004, "The Transition Mechanism of Highly Loaded Low-Pressure Turbine Blades," ASME *Journal of Turbomachinery*, **126**, pp. 536-543.
[27] Roberts, S.K, and Yaras, M.I., 2006, "Effects of Surface-Roughness Geometry on Separation-Bubble Transition," ASME *Journal of Turbomachinery*, **128**, pp. 349-356.
[28] Hughes, J.D. and Walker, G.J., 2001, "Natural Transition Phenomena on an Axial Compressor Blade," ASME *Journal of Turbomachinery*, **123**, pp. 392-401.
[29] Schlichting, H., 1979, *Boundary Layer Theory*, 7th ed., McGraw-Hill, New York.
[30] Davis, R.L., Carter, J.E., and Reshotko, E., 1985, "Analysis of Transitional Separation Bubbles on Infinite Swept Wings," AIAA Paper 85-1685.
[31] Hatman, A., and Wang, T., 1999, "A Prediction Model for Separated Flow Transition," ASME *Journal of Turbomachinery*, **121**, pp. 594-602.
[32] Yaras, M.I., 2002, "Measurements of the Effects of Freestream Turbulence on Separation-Bubble Transition," ASME Paper GT-2002-30232.
[33] Volino, R.J., and Bohl, D.G., 2004, "Separated Flow Transition Mechanisms and Prediction With High and Low Freestream Turbulence Under Low Pressure Turbine Conditions," ASME Paper GT2004-53360.
[34] Crawford, M.E., and Kays, W.M., 1976, "STAN5 – A Program for Numerical Computation of Two-Dimensional Internal and External Boundary Layer Flows," NASA CR-2742.

Proceedings of ASME Turbo Expo 2009: Power for Land, Sea and Air
GT2009
June 8-12, 2009, Orlando, Florida, USA

GT2009-59983

EXPERIMENTAL AND COMPUTATIONAL INVESTIGATIONS OF LOW-PRESSURE TURBINE SEPARATION CONTROL USING VORTEX GENERATOR JETS

Ralph J. Volino
Mechanical Engineering Department
United States Naval Academy
Annapolis, Maryland 21402-5042
volino@usna.edu

Olga Kartuzova and Mounir B. Ibrahim
Mechanical Engineering Department
Cleveland State University
Cleveland, Ohio 44115-2425
m.ibrahim@csuohio.edu

ABSTRACT

Boundary layer separation control has been studied using vortex generator jets (VGJs) on a very high lift, low-pressure turbine airfoil. Experiments were done under low freestream turbulence conditions on a linear cascade in a low speed wind tunnel. Pressure surveys on the airfoil surface and downstream total pressure loss surveys were documented. Cases were considered at Reynolds numbers (based on the suction surface length and the nominal exit velocity from the cascade) of 25,000, 50,000 and 100,000. Jet pulsing frequency, duty cycle, and blowing ratio were all varied. In all cases without flow control, the boundary layer separated and did not reattach. With the VGJs, separation control was possible even at the lowest Reynolds number. Pulsed VGJs were more effective than steady jets. At sufficiently high pulsing frequencies, separation control was possible even with low jet velocities and low duty cycles. At lower frequencies, higher jet velocity was required, particularly at low Reynolds numbers. Effective separation control resulted in an increase in lift of up to 20% and a reduction in total pressure losses of up to 70%. Simulations of the flow using an unsteady RANS code with the four equation Transition-sst model produced good agreement with experiments in cases without flow control, correctly predicting separation, transition and reattachment. In cases with VGJs, however, the CFD did not predict the reattachment observed in the experiments.

NOMENCLATURE

B	blowing ratio, maximum jet velocity/local freestream velocity
Cp	$2(P_T - P)/\rho U_e^2$, pressure coefficient
Cp_{int}	pressure coefficient integrated in axial direction
Cp_{inv}	Cp_{int} for invisid flow through cascade
C_x	axial chord length
D	duty cycle, fraction of time valve is open
F	$fL_{j\text{-}te}/U_{ave}$, dimensionless frequency
f	frequency
$L_{j\text{-}te}$	distance from VGJs to trailing edge
L_s	suction surface length
L_ϕ	blade spacing (pitch)
P	pressure
P_S	upstream static pressure
P_T	upstream stagnation pressure
P_{Te}	downstream stagnation pressure
Re	$U_e L_s/\nu$, exit Reynolds number
s	streamwise coordinate, distance from leading edge
T	period of jet pulsing cycle
t	time
U_{ave}	average freestream velocity between VGJs and trailing edge
U_e	nominal exit freestream velocity, based on inviscid solution
x	axial distance from leading edge
ϕ	coordinate along blade spacing, normal to axial chord
ν	kinematic viscosity
ρ	density
ψ	$(P_T\text{-}P_{Te})/(P_T\text{-}P_S)$, total pressure loss coefficient
ψ_{int}	total pressure loss integrated over blade spacing

INTRODUCTION

Boundary layer separation can lead to partial loss of lift and higher aerodynamic losses on low-pressure turbine (LPT) airfoils (e.g. Hourmouziadis [1], Mayle [2], and Sharma et al. [3]). As designers impose higher loading to improve efficiency and lower cost, the associated strong adverse pressure gradients on the suction side of the airfoil can exacerbate separation problems. The problem is particularly relevant in aircraft engines at cruise conditions, due to the lower density and therefore lower Reynolds numbers at altitude. A component efficiency drop of 2% may occur between takeoff and cruise in large commercial transport engines, and the difference could be as large as 7% in smaller engines operating at higher altitudes [4, 5]. Prediction and control of suction side separation, without sacrifice of the benefits of higher loading, is therefore, crucial for improved engine design.

Separation and separated flow transition, which can lead to boundary layer reattachment, have received considerable attention. Lists of various studies are provided by Volino [6, 7]. In general, previous work shows that the strong acceleration on the leading section of the airfoil keeps the boundary layer thin and laminar, even in the presence of elevated freestream turbulence. When separation does occur, it is usually just downstream of the suction peak. If transition then occurs in the shear layer over the separation bubble, it

is typically rapid and often causes the boundary layer to reattach [6, 8]. Bons et al. [9] and Volino [6], found that with very high loading, however, the separation bubble can become so thick that transition alone is not sufficient to cause reattachment.

One way to improve performance is to design airfoils with pressure gradients more resistant to separation, as described by Praisner and Clark [10]. Forward loading, for example, makes airfoils more separation resistant by extending the adverse pressure gradient on the aft portion of the suction side over a longer distance. This reduces the local pressure gradient at all locations, making separation less likely. If separation does occur, forward loading provides a longer distance along the airfoil surface for reattachment. Forward loading has some disadvantages, however. As noted by Zhang et al. [11], the longer region of turbulent flow on a forward loaded airfoil can lead to increased profile losses. Forward loading also creates longer regions of strong pressure gradient on the endwalls, which can produce stronger secondary flows and losses. If flow control were incorporated in the design of an advanced airfoil, as discussed by Bons et al. [12], it might be possible to produce an aft loaded airfoil that was resistant to separation and had low profile and secondary loss characteristics over a range of Reynolds numbers.

Separation control with passive devices such as boundary layer trips has been shown effective by Zhang et al. [11], Bohl and Volino [13], Volino [14], and others. Passive devices have the distinct advantage of simplicity, but they also introduce parasitic losses. Devices which are large enough to control separation at the lowest Reynolds numbers in an engine's operating range would tend to produce higher than necessary losses at higher Reynolds numbers. Active devices could potentially provide better control over the entire operating range of interest and be reduced in strength or turned off to avoid unnecessary losses when they are not needed.

The literature contains many examples of active separation control. A few which could be applied in turbomachinery are discussed in Volino [15]. Plasma devices, as used by Huang et al. [16], could be viable, and are under active study. Vortex generator jets (VGJs), as introduced by Johnston and Nishi [17], are another alternative, and are the subject of the present study. Blowing from small, compound angled holes is used to create streamwise vortices. The vortices bring high momentum fluid into the near wall region, which can help to control separation. The most effective VGJs enter the boundary layer at a relatively shallow pitch angle (typically 30 to 45 degrees) relative to the wall and a high skew angle (45 to 90 degrees) relative to the main flow. Additionally, the jets promote transition, and turbulent mixing also helps to mitigate separation. Bons et al. [12] noted that in the case of pulsed VGJs, the turbulence effect was more significant than the action of the vortices. Bons et al. [4, 18], Volino [19], Volino and Bohl [20], McQuilling and Jacob [21], and Eldredge and Bons [22] all used VGJs on the highly loaded Pack B LPT airfoil. Separation was essentially eliminated, even at the lowest Reynolds number considered, (Re=25,000 based on suction surface length and nominal exit velocity). Pulsed jets were more effective than steady jets. The initial disturbance created by each pulse caused the boundary layer to attach. The turbulence was followed by a calmed period (Gostelow et al. [23] and Schulte and Hodson [24]) during which the boundary layer was very resistant to separation, much like a turbulent boundary layer, but very laminar-like in terms of its fluctuation levels and low losses. When the time between pulses was long enough, the boundary layer did eventually relax to a separated state, but due to the control which persisted during the calmed period, the VGJs were effective even with low jet pulsing frequencies, duty cycles and mass flow rates. Since the boundary layer was attached and undisturbed for much of the jet pulsing cycle, profile losses were low.

Similar results with pulsed VGJs were found on the L1M airfoil by Bons et al. [25]. The L1M is more highly loaded than the Pack B, but more resistant to separation because of forward loading. A large separation bubble followed by boundary layer reattachment was observed at low Reynolds numbers, and pulsed VGJs reduced the size of the bubble.

In the present study, the very highly loaded L1A airfoil is used. The L1A was designed at the Air Force Research Laboratory (AFRL) and is available on a limited basis from Clark [26]. It is an aft loaded blade with the same flow angles and loading as the L1M. Dimensions of the L1A as used in the present study are given in Table 1. Based on the design calculations of Clark [26], the L1A has a Zweifel coefficient of 1.35, which corresponds to 10% higher loading than the "ultra-high lift" airfoils described by Zhang and Hodson [27], and 17% higher loading than the Pack B. Because the L1A is aft loaded, it is more prone to separation than the L1M, as documented in Bons et al. [9], Volino [6], Ibrahim et al. [28], and Volino et al. [29]. In cases without flow control and with low freestream turbulence, the boundary layer separates when Re<150,000 and does not reattach, in spite of transition to turbulence in the shear layer over the separation bubble in all cases. This result contrasts with the results of earlier studies on less aggressive airfoils, which all showed reattachment after transition. The separation bubble on the L1A is about four times thicker than that on the Pack B. The larger distance from the shear layer to the wall on the L1A apparently prevents the turbulent mixing in the shear layer from reaching the wall and causing reattachment. The failure of the boundary layer to reattach results in a 20% loss in lift and increases profile losses by a factor of 7. At higher Reynolds numbers the separation bubble is small and the boundary layer is attached over most of the airfoil. In cases with high freestream turbulence, results are similar, but the shear layer is somewhat thicker and the separation bubble thinner due to increased mixing induced in the shear layer. This results in reattachment after transition at Re=50,000 and 100,000. At the lowest Re considered (25,000) the boundary layer still does not reattach.

Attempts to simulate LPT flows computationally have met with varying degrees of success. A few are discussed in Ibrahim et al. [28]. Most turbulence models, such as the standard k-ε model, fail to predict separation, typically because transition is predicted too far upstream. A few have more success in cases without flow control. Suzen et al. [30], for example, successfully predicted the flow over the Pack B airfoil for a wide range of conditions using an intermittency transport model. Menter et al. [31] and Langtry et al. [32] used an intermittency transport equation to trigger transition onset along with a transport equation for the transition momentum thickness Reynolds number. These two equations were coupled with a shear stress transport turbulence model (SST). The combined model, referred to here as the Transition-sst model, successfully predicted separation, transition, and reattachment on the Pack B airfoil. Gross and Fasel [33] used course grid direct numerical simulations (DNS), implicit large eddy simulations (ILES) and unsteady Reynolds averaged Navier-Stokes (URANS) models to predict Pack B flows. The DNS and ILES results agreed when the computational grid was sufficiently fine, and some of the URANS models agreed as well. Agreement with experimental data was good in some instances, but significant differences were observed in others. This was attributed to possible differences between the inlet flow conditions in the experiment and computations. Rizzetta and Visbal [34] used DNS and found reasonable agreement with Pack B experiments, although differences in velocity profiles were observed at some locations.

The flow over the L1A airfoil was computed by Ibrahim et al. [28] and Volino et al. [29] using the Transition-sst model. As with the

Table 1: Cascade parameters

Axial Chord, C_x [mm]	True Chord [mm]	Pitch, L_ϕ [mm]	Span [mm]	Suction side, L_s [mm]	Inlet flow angle	Exit flow angle
134	146	136	724	203	35°	60°

Pack B airfoil, this model correctly predicted separation, transition and reattachment for both high and low freestream turbulence and at high and low Reynolds numbers. Agreement with experimental total pressure loss surveys and velocity profiles in the suction side boundary layer were also good.

A few attempts have been made to simulate LPT flows with vortex generator jets. Garg [35] used a RANS calculation utilizing the *k-ω*-sst model of Menter [36]. Although some trends were correct, the flow control seen in the experiments was not well predicted. Rizzetta and Visbal [34] had more success with their DNS, but differences from experimental results were still observed.

In the present study, flow control with vortex generator jets is investigated experimentally and computationally on the L1A airfoil. As noted above, the L1A provides a good test case for flow control since it is a modern aggressive airfoil with severe separation problems at low Reynolds numbers. Bons et al. [9] have shown that VGJs can be effective with the L1A for some cases. The present study considers a wide range of cases with different jet pulsing frequencies, amplitudes and duty cycles. Low (0.6%) freestream turbulence cases are considered with Reynolds numbers ranging from 25,000 to 100,000, as these were the cases with significant separation bubbles in the baseline experiments. For the computations URANS is used since it could provide a less computationally expensive design tool than LES or DNS. The Transition-sst model is used, as it was the most successful of the models used in the baseline cases.

EXPERIMENTAL FACILITY AND MEASUREMENTS

Experiments were conducted in a closed loop wind tunnel with a seven blade linear cascade located in the wind tunnel's third turn, as shown in Fig. 1a. A fine screen located upstream of the cascade is used to break up the boundary layers which form upstream of the test section and to provide uniform inlet conditions to the cascade. The freestream turbulence entering the cascade was measured with a cross-wire probe positioned just upstream of the center blade. The turbulence intensity is 0.8% in the streamwise component and 0.5% in the cross stream components. The integral length scale of the streamwise component is 6.3 cm. Further details of the facility and inlet flow are in Volino [6]. The freestream turbulence intensity in an engine is expected to be of the order 4%, which is significantly higher than in the present experiments. The freestream length scales are expected to be smaller in the engine. Higher intensity and smaller length scales promote more rapid transition of the boundary layer and more resistance to separation, as shown in Volino et al. [29]. The effect of wakes from upstream airfoils would be similar. The present experiments provide a lower bound for the expected freestream conditions in an engine and a more challenging case for flow control. The present results will serve as a baseline for future work with higher freestream turbulence and wakes, allowing separation of the effects of flow control, freestream turbulence and wakes. Better understanding of the separate effects may lead to better prediction of the combined effects under engine conditions.

A tailboard, shown in Fig. 1a, is needed to produce the correct exit flow angle from the cascade. Its position was set to produce periodicity at high Reynolds numbers. A tailboard on the opposite side of the cascade, and inlet guide vanes were found to be unnecessary. To produce the correct approach flow to the end blades

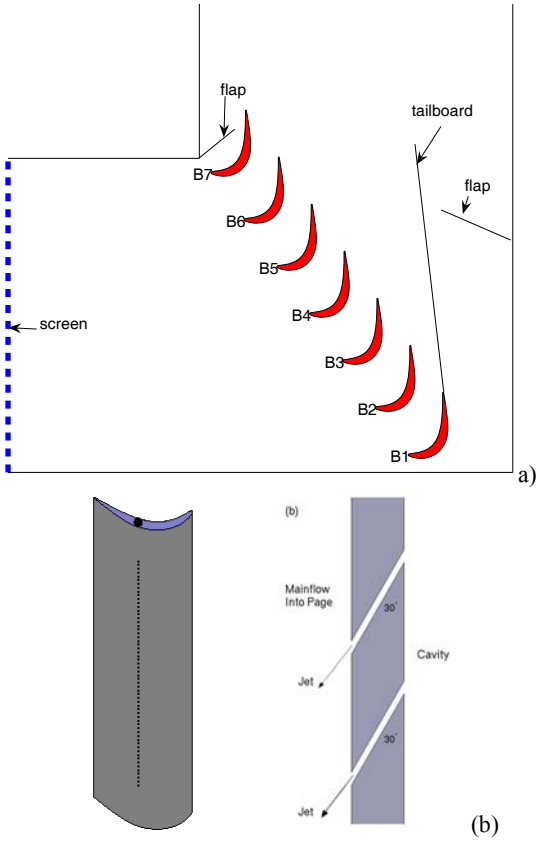

Fig. 1 Drawings of test section: a) linear cascade, b) airfoil with VGJ holes and cross section of hole geometry

(B1 and B7), the amount of flow escaping around the two ends of the cascade is controlled with the flaps shown in Fig. 1a. The inlet flow angle was checked with a three-hole pressure probe and found to agree with the design angle to within 2° of uncertainty. Good periodicity at high Reynolds numbers was obtained in the exit flow. At low Reynolds numbers, when significant separation bubbles are present, the periodicity is not as good due to suppression of the separation bubble thickness on the blades closest to the tailboard. In cases with effective flow control, periodicity is reestablished. The lack of periodicity in cases with large separation bubbles is considered acceptable since the focus of the study is separation control, and not documentation of cases with large separation that would be unacceptable in practice. This compromise facilitates the study of a larger number of cases with flow control by obviating the need to adjust the tailboard by trial and error for each case. It also provides for better repeatability in the experiments, since the position of the tailboard is fixed for all cases. Any improvements made with flow control will be larger in practice than documented in the experiment, due to the effect of the tailboard in suppressing the bubble size in the uncontrolled cases.

Each blade in the cascade has a central cavity which extends along the entire span. The cavity is closed at one end and has a fitting at the opposite end connected to a compressed air line. Air is supplied to the cavities from a common manifold. Manual ball valves are placed in the tubing between the manifold and blades to insure that each blade receives the same air flow. The valves also help to damp high frequency oscillations in the jet velocity when the VGJs are pulsed. The manifold is supplied through two fast response solenoid valves (Parker Hannifin 009-0339-900 with General Valve Iota One pulse

driver) operating in parallel. The valves are supplied through a pressure regulator by the building air supply. A single spanwise row of holes was drilled into the suction surface of each blade at the inviscid pressure minimum location, s/L_s=0.5 (x/C_x=0.62), where s is the distance from the leading edge and L_s is the suction surface length. The pressure minimum has been shown in the studies listed above to be about the optimal location for flow control devices. The effects of devices located farther upstream are damped by the favorable pressure gradient, and devices located downstream of the separation point can also lose effectiveness. The holes are 0.8 mm in diameter and drilled at 30° to the surface and 90° to the main flow direction, as shown in Fig. 1b. This is the same orientation used in all the VGJ studies listed above. The hole spacing is 10.6 diameters, and the length to diameter ratio is 12.

The solenoid valves pulse the VGJs, and the pulsing frequency is presented below in dimensionless form as $F=fL_{j\text{-}te}/U_{ave}$, where $L_{j\text{-}te}$ is the streamwise distance from the VGJ holes to the trailing edge, and U_{ave} is the average freestream velocity over this distance. For flow over single airfoils, $F\geq1$ is typically needed to maintain separation control, but for cascades, Bons et al. [18] showed that control is possible in some cases with F=0.1. As shown in Volino [15] and Bons et al. [18], this is due to the extended calmed region which follows the jet disturbance. In practice, VGJs could be timed to wake passing in an LPT, which has a typical frequency of about F=0.3.

The center blade, designated B4 in Fig. 1, contains pressure taps near the spanwise centerline. Pressure surveys are made using a pressure transducer (0-870 Pa range Validyne transducer). Stagnation pressure is measured with a pitot tube upstream of the cascade. The uncertainty in the suction side pressure coefficients is 0.07. Most of this uncertainty is due to bias error. Stochastic error is minimized by averaging pressure transducer readings over a 10 second period.

Total pressure losses are documented using a Kiel probe traversed across three blade spacings, 0.63 C_x downstream of the cascade. A traverse is located in the wind tunnel downstream of the cascade to move the probe. The traverse causes an acceptably low blockage when it is located at least two C_x downstream of the cascade.

Pressure and loss surveys were acquired at nominal Re=25,000, 50,000, 100,000. The Reynolds number, as defined above, is based on the suction surface length and the nominal cascade exit velocity. The corresponding Reynolds numbers based on the cascade inlet velocity and the axial chord length are 10,000, 20,000 and 40,000.

NUMERICAL SIMULATIONS

Calculations were done using the commercial code Fluent with a URANS solver and the Transition-sst model of Menter et al. [31]. The three dimensional computational domain includes a single passage. The boundary conditions on the sides of the passage are periodic. The exit boundary is located 3.8 C_x downstream of the trailing edges in the flow direction. Zero gage pressure is specified at the exit. As described in Ibrahim et al. [28], exit locations extending farther downstream were tested to insure the results were independent of the location chosen. A uniform velocity inflow condition is specified 1.9 C_x upstream of the blade leading edges in the flow direction. The inlet flow angle is set to 33° based on an inviscid calculation of the full cascade shown in Fig. 1. This angle agrees with the experimentally measured inlet angle to within the experimental uncertainty. In the spanwise direction, the domain includes one VGJ, and periodic boundary conditions are used. The full length of the hole is included in the simulations, allowing the jet velocity profile to develop before entering the main flow. A uniform velocity boundary condition is specified at the hole inlet. For the pulsed jet cases, the inlet velocity is set as a square wave. The upstream plenum is not included in the calculations. Grid independent results were obtained using 1.5 million cells with 593 nodes on the airfoil (362 nodes on the suction surface and 230 nodes on the pressure surface). The closest grid points to the wall were within one viscous unit (y^+<1) on all surfaces. A structured grid is clustered around the VGJ exit, and an unstructured grid is used for the rest of the computational domain. Boundary layer grid resolution is used inside of the jet tube. The three dimensional grid was checked by comparing results for a baseline case to previous results with a two dimensional grid. The periodic boundary conditions were checked by performing calculations for a two channel domain and a domain with three VGJs in the spanwise direction.

RESULTS

Jet Velocity

The center blade in the cascade includes a pressure tap in the central cavity to measure the supply pressure to the VGJs. The jet velocity is calibrated against the cavity pressure using a hot-film probe with a 0.25 mm active sensor length located at the center of the exit plane of a VGJ hole. Calibration is done with the main flow in the wind tunnel turned off. In subsequent experiments, the desired jet velocity is produced by setting the difference between the cavity pressure and the static pressure in the freestream. During calibration, for each case of interest, the time averaged pressure in the cavity is measured along with the instantaneous jet velocity. For pulsed jet cases, the velocity is then phase averaged over the jet pulsing cycle. A typical result is shown in Fig. 2. The blowing ratio, B, is defined as the ratio of the measured jet velocity to the expected freestream velocity at the jet exit, based on an inviscid flow solution for the cascade. In the figure, the time during the cycle, t, is normalized on the pulsing period, T. The examples shown in Fig. 2 correspond to a pulsing frequency of 3 Hz, with duty cycles, D, of 2%, 10%, and 50%. The duty cycle is the fraction of time the solenoid valve is open during each pulsing cycle. The nominal blowing ratio is set as the maximum value measured during the cycle. The maximum typically occurs shortly after the solenoid valve is opened, and is followed by a decay toward a steady value. The maximum is used because the initial pulse from the jet is believed to be most influential for flow control. Since the calibration is done with the main flow off, the freestream velocity used to define the blowing ratio (B=1) for Fig. 2 is arbitrary, and was chosen to corresponds to the lowest Reynolds number case (Re=25,000) considered in the study. For a Re=50,000 case, the results in Fig. 2 would correspond to B=0.5. As shown in Fig. 2, the velocity from the jets does not form a perfect square wave when the jets are pulsed. The decay after the initial peak and other oscillations are believed to result from viscous losses and pressure waves reflecting in the manifold, tubing and cavity upstream of the VGJ holes. Similar behavior was observed by Bons et al. [9]. The oscillations shown in Fig. 2 are repeatable, as shown by the agreement between the three cases shown during the valve-open part of the cycle. The exact pattern of the oscillations is expected to be facility dependent. The success of the VGJs at low duty cycle, as shown below, suggests that it is the initial velocity peak, and not the oscillations which follow, which are most important for flow control. Further testing in a different facility or through CFD would be useful to confirm this.

It should be noted that the jet velocity used to define the blowing ratio is the measured value from the hot film probe. The jets are expected to be laminar with nearly parabolic velocity profiles, at least under steady conditions, since the length to diameter ratio of the holes is large. This is confirmed by the CFD predictions shown in Fig. 3. The maximum velocity in each profile is about 1.8 times the mean, which is near the fully developed value of 2 for a parabolic profile.

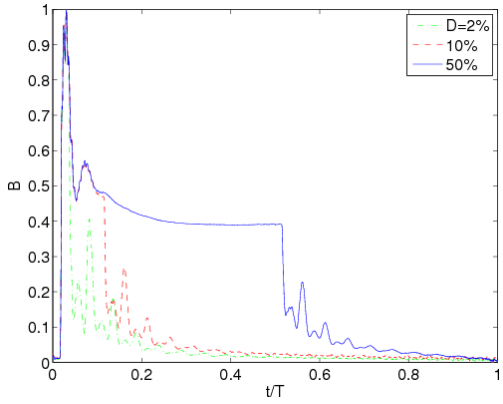

Fig. 2 Ensemble averaged jet velocity at f=3 Hz, with D=2%, 10% and 50%

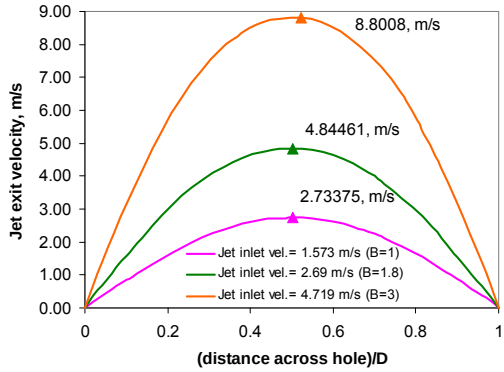

Fig. 3 CFD prediction of VGJ velocity profile at hole exit

Given a parabolic profile and the length of the hot film sensor, the average velocity over the sensor is 0.97 times the maximum velocity at the jet center. The measured velocity, therefore, essentially matches the maximum jet velocity.

Examples of CFD results for pulsed film cooling cases are shown in Fig. 4 for cases with 12 Hz pulsing. With D=10%, the CFD provides a good approximation to the experiment. The ratio of the maximum jet exit velocity to inlet velocity is about 1.7. Computed results with longer duration pulses did not show the expected decay after the initial maximum, indicating a difference in the imposed velocity at the hole inlet between CFD and experiment. Computational results presented below are limited to cases with f=12 Hz and D=10%.

Re=25,000

Pressure profiles for all cases with Re=25,000 are shown in Fig. 5. The inviscid profile for the L1A airfoil is shown for comparison. Figure 5a shows that with B=0.25, there is little change from the baseline case. The VGJs are ineffective. With B=0.5 in Fig. 5b, there is no evidence of control at the two lowest frequencies, but at F=0.56 (12 Hz) and 1.12, there is a drop in Cp near the trailing edge, indicating at least partial reattachment. This drop occurs even with a duty cycle of 10%. A lower duty cycle at high frequency could not be achieved in the experiments due to limitations in the solenoid valve response time. Increasing to B=0.75, Fig. 5c shows a small effect of pulsing at F=0.28, particularly with D=50%, and a stronger effect at the higher frequencies independent of duty cycle. Although the boundary layer appears to reattach near the trailing edge at the higher frequencies, a plateau in Cp up to s/L_s=0.7 indicates a large separation bubble is still present. As the blowing rate is increased to B=1.0, 1.5,

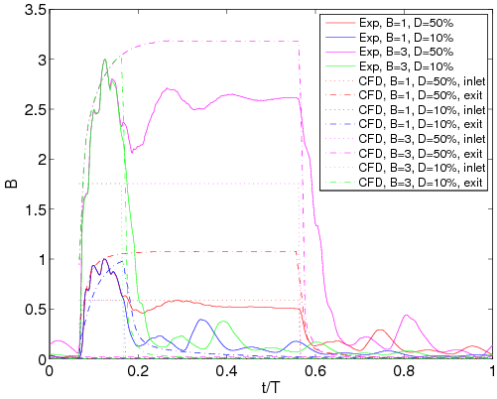

Fig. 4 Comparison of measured and computed VGJ exit velocity with inlet velocity also shown for CFD results

2.0, 2.5 and 3.0 in Figs. 5d-5h, there is little or no control at F=0.14 unless B is larger than 2.0 and D=50%. At F=0.28, the control gets progressively better as B increases and tends to be better at the higher duty cycles. For the higher frequencies, B=0.75 appears to be sufficient, and raising B further does not appear to improve the results. A high blowing ratio of 3.0 might be impractical for application if the jets choke before reaching this velocity. If achievable, however, the VGJ mass flow rate with steady blowing at B=3.0 would be only about 0.2% of the main flow. The mass flow rate with lower B or pulsing would be even lower.

The loss coefficient, ψ, is shown in Fig. 6. The coordinate ϕ indicates the distance in the direction perpendicular to the axial chord. The normalizing quantity L_ϕ is the blade spacing. The origin, ϕ=0, corresponds to the location directly downstream of the trailing edge of the center blade in the direction of the exit design flow angle. Low blowing ratio cases are shown in Fig. 6a. Only the higher frequencies were considered at low B since the Cp results indicate that lower frequency pulsing is ineffective. The pulsed VGJs help to reduce the magnitude of the loss peaks by about 20%. The peaks are still much higher and wider (by about a factor of 2) than those observed in the high Re≥200,000 baseline cases [6]. The peaks are also shifted to the left of the design positions of ϕ/L_ϕ =-1, 0 and 1, indicating that compared to the high Re cases there is a 6 degree reduction in flow turning caused by the separation bubble. This is still better than the 13 degree reduction in turning in the uncontrolled case. Results with B=1.0 (Fig 6b) again show little effect at the low frequencies and a significant reduction in losses and greater turning at the two higher frequencies. Increasing B further to 1.5 in Fig. 6c shows a further reduction in the loss peak magnitudes, and the effect is now visible even at F=0.28, particular with D=50%. With B increased to 2.0 and 3.0 in Figs. 6d and 6e, there is not much change in the loss magnitude, but the flow turning increases by about 2 degrees in the best cases.

To summarize the results, the lift on the airfoil can be determined by integrating the difference between the suction and pressure side Cp values along the axial direction.

$$Cp_{int} = \frac{\int_0^{C_x} (Cp_{suction} - Cp_{pressure})dx}{C_x} \qquad (1)$$

This result is normalized with the result from the inviscid solution and shown as a function of B Fig. 7 for all the Re=25,000 cases. The VGJs are able to increase the lift by up to 20%, and as noted above, the effect increases with pulsing frequency and blowing ratio. If F=0.56 or higher, B=0.75 is sufficient to reach the maximum lift attained.

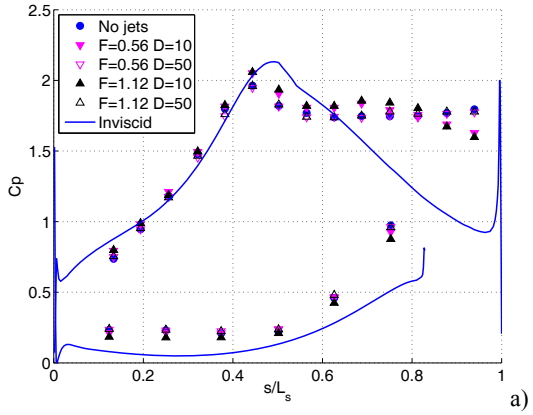

a)

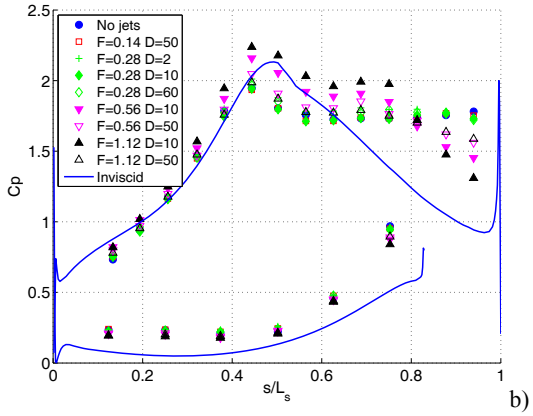

b)

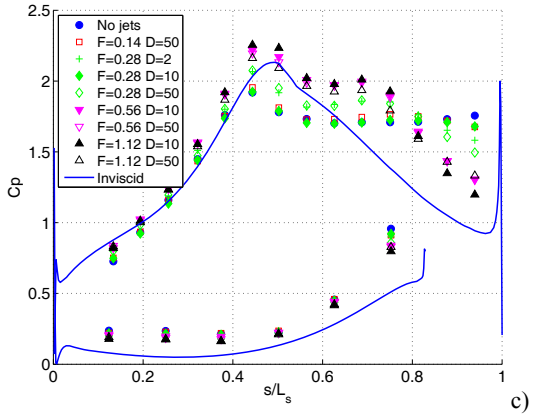

c)

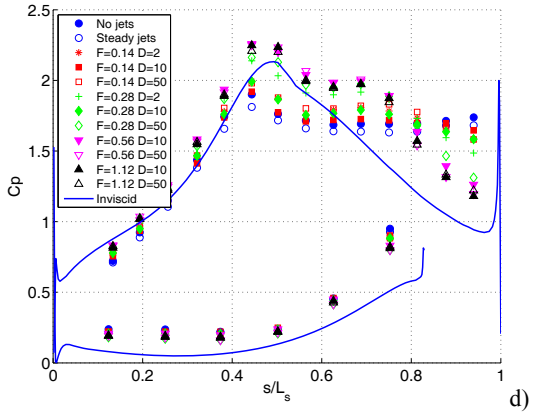

d)

Fig. 5 Cp profiles for Re=25,000 cases, B: a) 0.25, b) 0.5, c) 0.75, d) 1.0, e) 1.5, f) 2.0, g) 2.5, h) 3.0

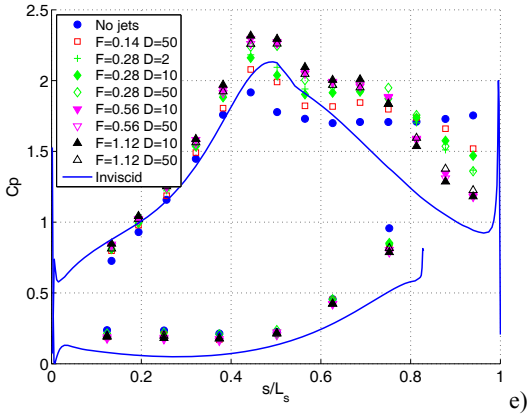

e)

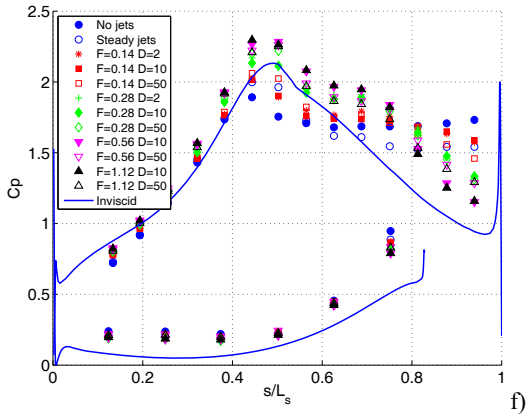

f)

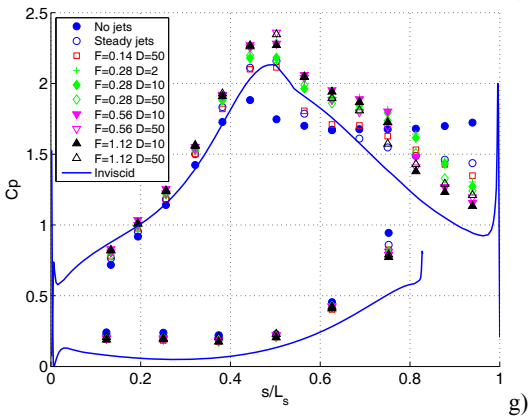

g)

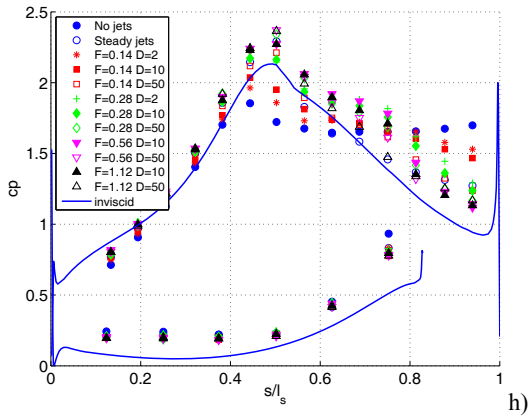

h)

Fig. 5 Cp profiles for Re=25,000 cases, B: a) 0.25, b) 0.5, c) 0.75, d) 1.0, e) 1.5, f) 2.0, g) 2.5, h) 3.0

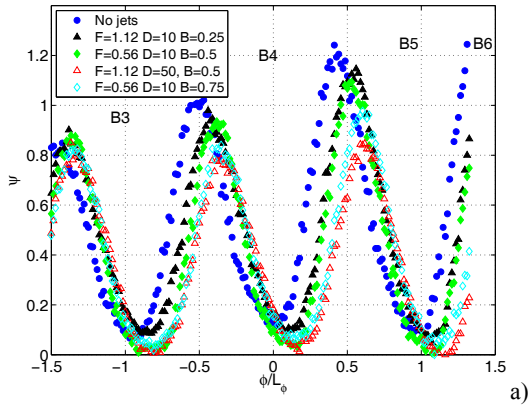

a)

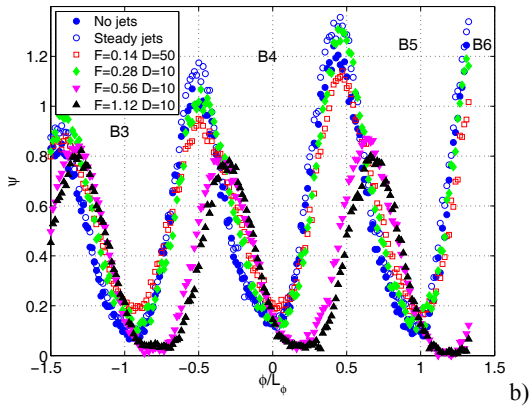

b)

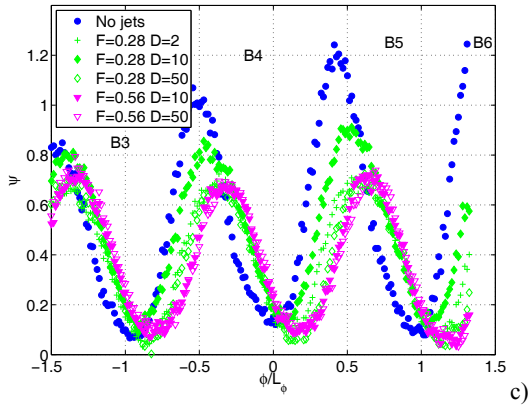

c)

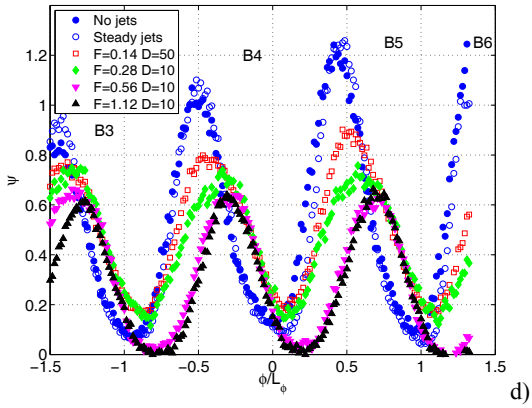

d)

Fig. 6 Total pressure loss profiles for Re=25,000 cases, B: a) 0.25-0.75, b) 1.0, c) 1.5, d) 2.0, e) 3.0

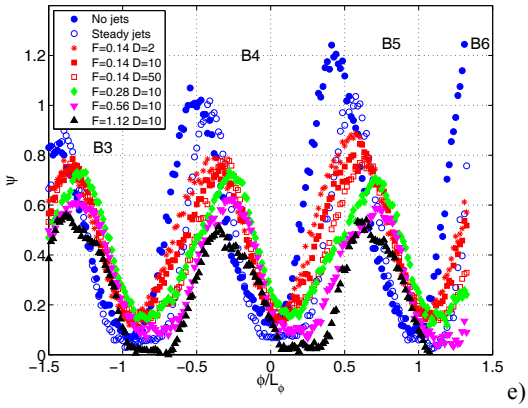

e)

Fig. 6 Total pressure loss profiles for Re=25,000 cases, B: a) 0.25-0.75, b) 1.0, c) 1.5, d) 2.0, e) 3.0

To summarize the losses, the integrated loss around the center blade is computed as

$$\psi_{int} = \int_{-L_\phi/2}^{L_\phi/2} \frac{\psi d\phi}{L_\phi} + \frac{\dot{m}_j}{\dot{m}_1}\frac{\left(P_j - P_{Te}\right)}{\left(P_T - P_S\right)}. \qquad (2)$$

The first term on the right in Eq. (2) is an area averaged value as used in Bons et al. [25], as opposed to a mass average value as presented in Volino [6]. The mass and area average values are nearly equal for the present cases since the velocity deficit in the wake at $0.63C_x$ downstream of the trailing edge is low. The second term on the right in Eq. (2) accounts for the pressure loss associated with the jet flow, as explained by Cully et al. [37]. The terms $\dot{m}_1$, $\dot{m}_j$ and P_j are the main and jet mass flow rates and the cavity pressure. With steady jets, this jet associated loss term has a value of 0.21 when B=3, drops to about 0.05 when B=2, and is below 0.01 for B=1 or lower. For pulsed jet cases, the jet loss term should be integrated over the pulsing cycle, but since the instantaneous cavity pressure is not measured, the term is estimated by multiplying the steady flow value by the duty cycle. This approximation overestimates the loss, since the jet velocity and mass flow rate drop after the initial peak, as shown in Figs. 2 and 4. Given the low jet mass flow rate, particularly at low B and D, the absolute value of the term is small and the approximation has a negligible effect on the overall ψ_{int}. The integrated loss is shown in Fig. 8. The VGJs clearly have a favorable effect, particularly at the higher frequencies. In the best case, ψ_{int} is reduced to about 40% of the baseline case level. With B at an achievable level of 1.0, ψ_{int} is reduced to about 60% of the baseline level.

Re=50,000

Figure 9a shows Cp profiles for cases with Re=50,000 and B=0.25. The jets have no effect at F=0.14 (6 Hz), and some effect at F=0.28, which increases with duty cycle. With F=0.56 and D=50%, the separation bubble appears to close, although the plateau between s/L_s=0.55 and 0.8 indicates a large bubble is still present. When B is raised to 0.5, Fig. 9b again shows little effect with F=0.14, and a significant but closed bubble at the higher frequencies. As B is increased from 0.75 to 2.0 (Figs. 9c-9e), pulsing at F=0.14 begins to have an effect in reducing separation. With B=2.0, F=0.56, and D=50%, the separation bubble appears to be nearly eliminated, as in the B=2.0 steady blowing case.

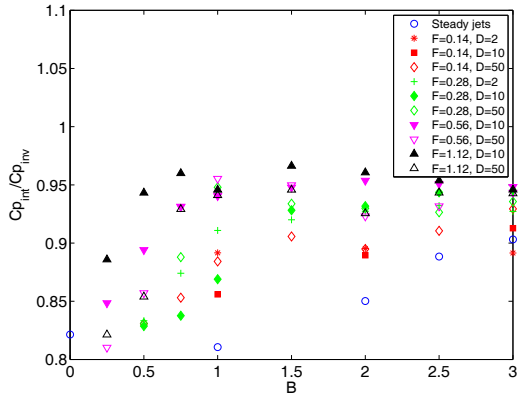

Fig. 7 Ratio of lift to lift in inviscid case, as indicated by integrated Cp result for Re=25,000 cases

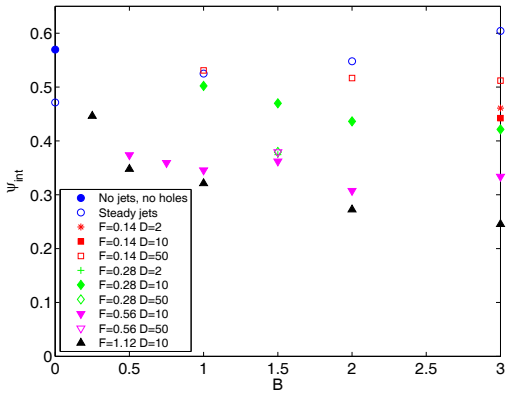

Fig. 8 Integrated total pressure loss for Re=25,000 cases

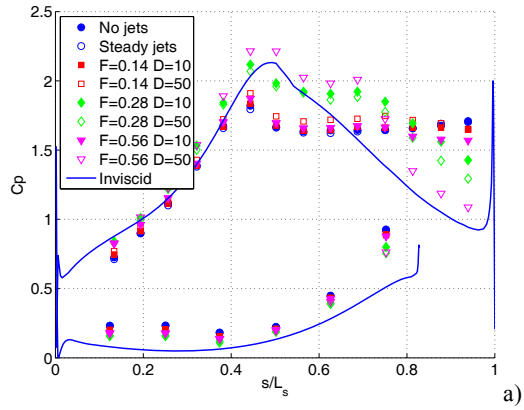

a)

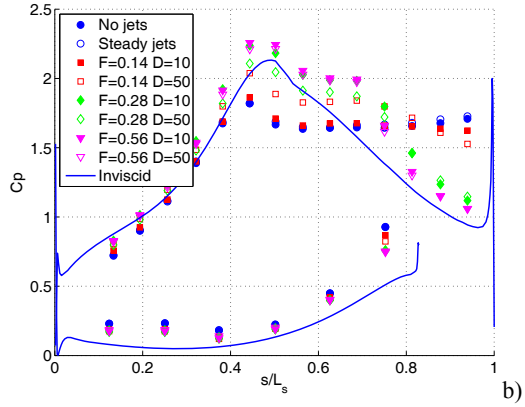

b)

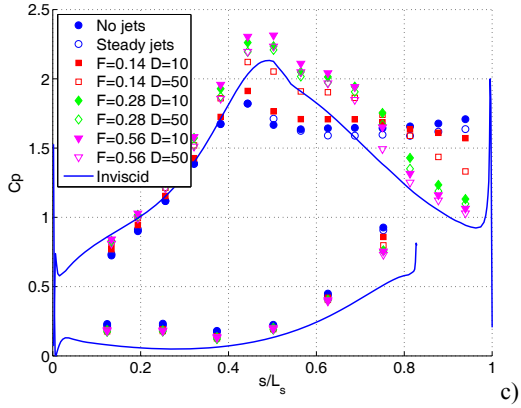

c)

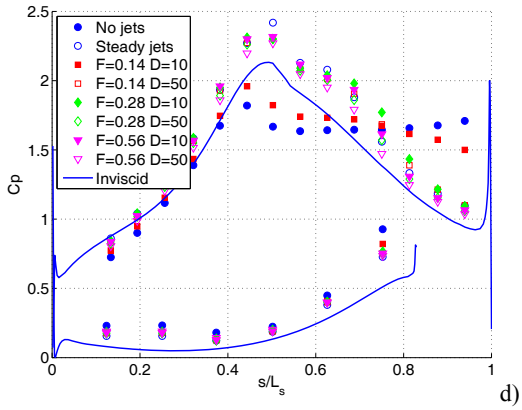

d)

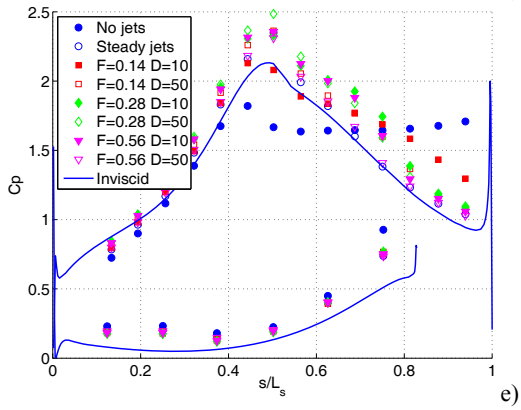

e)

Fig. 9 Cp profiles for Re=50,000 cases, B: a) 0.25, b) 0.5, c) 0.75, d) 1.0, e) 2.0

The corresponding loss coefficients are shown in Fig. 10. With *B*=0.25 in Fig. 10a, *F*=0.28 pulsing reduces losses below the steady case and pulsing with *F*=0.56 reduces losses further. The magnitude of the loss peaks at *F*=0.56 are about 80% of those in the best cases with steady blowing in Fig. 10e-f, and with much lower *B*. No affect of duty cycle is apparent in Fig. 10a. As *B* is increased from 0.5 to 2.0 (Figs. 10b-10f), the loss results are consistent with the pressure profiles of Fig. 9. With *F*=0.56, the losses are already low with *B*=0.25, so increasing *B* further has a relatively small effect. With *F*=0.14 and 0.28, the losses drop as *B* and *D* are increased, eventually approaching the *F*=0.56 results. In all cases pulsed blowing reduces losses compared to steady blowing. Even in the best case, however, the loss peaks are still about 30% higher than in the high *Re*≥200,000 baseline cases [6].

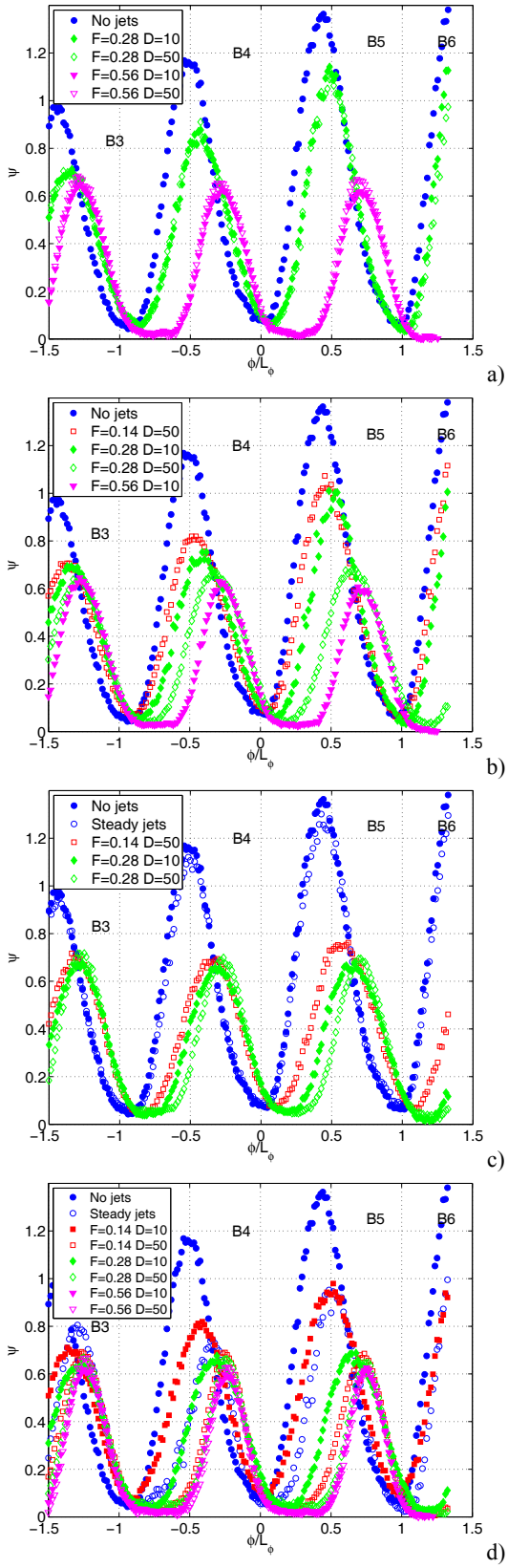

Fig. 10 Total pressure loss profiles for Re=50,000 cases, B: a) 0.25, b) 0.5, c) 0.75, d) 1.0, e) 1.5, f) 2.0

The *Cp* results for the *Re*=50,000 cases are summarized in Fig. 11. As at *Re*=25,000, the VGJs are able to increase the lift by about 20% over the baseline case, and are more effective at higher *B* and *F*. The jets are most effective for $F \geq 0.28$, even with *B*=0.25 and *D*=10%. The integrated total pressure loss in Fig. 12 shows that losses can be reduced by about 55% below baseline levels. With *F*=0.28, *B*=1 to 1.5 is needed to achieve this reduction, but with *F*=0.56, the same reduction is possible with *B*=0.25.

Re=100,000

In the baseline case at *Re*=100,000, the boundary layer separated and did not reattach. With the VGJ holes present, even without blowing, the shear layer was on the verge of reattachment. Pressure coefficients are shown in Fig. 13. All cases show boundary layer reattachment, even with *B*=0.25, *F*=0.14 and *D*=10%. At this Reynolds number, almost any small disturbance is sufficient to cause the boundary layer to reattach. Once it is attached, it tends to stay attached even if the flow control is turned off, and will only occasionally separate again. Raising *B* and the pulsing frequency does help to reduce the size of the separation bubble slightly, as indicated by the pressure coefficients.

Loss profiles for some of the *Re*=100,000 cases are shown in Fig. 14. It appears that with *B*=0.5 or greater for steady blowing or *B*=025 or greater with pulsed jets, the total pressure loss is driven to its lowest possible value at this Reynolds number. This is well below the uncontrolled value at this *Re*, but the peaks are about 30% higher than in baseline cases with $Re \geq 200{,}000$ [6]. Even with the best VGJ flow control at *Re*=100,000, it appears a small separation bubble is still present, which increases the boundary layer thickness and losses compared to higher Reynolds number cases.

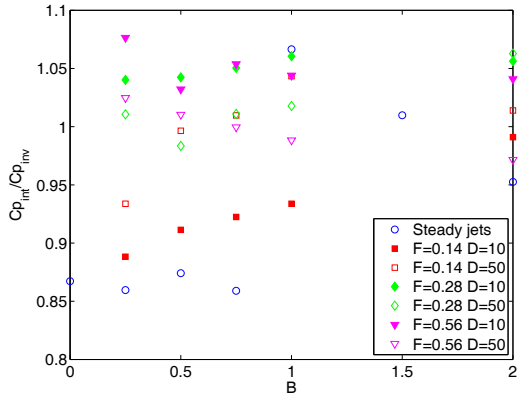

Fig. 11 Ratio of lift to lift in inviscid case, as indicated by integrated Cp result for Re=50,000 cases

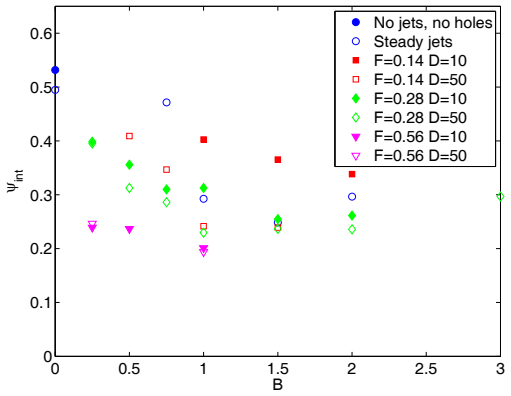

Fig. 12 Integrated total pressure loss for Re=50,000 cases

The integrated *Cp* and loss are shown in Figs. 15 and 16. As in the lower *Re* cases, the lift rises about 20% above the baseline value in all cases with flow control. The total pressure loss drops by about 70%.

NUMERICAL RESULTS

Although the Transition-sst model predicted the baseline cases well, its performance is not good in cases with VGJ flow control. The model fails to predict reattachment, so the predictions of the pressure coefficients are still generally satisfactory when the experiments do not show reattachment. Some examples of *Cp* results are shown in Fig. 17 for cases at *Re*=50,000. In the baseline case and with steady jets at *B*=0.5, both the experiments and the CFD show separation without reattachment, with little change due to the VGJs. Raising *B* to 2.0 with steady blowing, the experiment shows clear reattachment. In fact, steady blowing with *B*=1.0 was shown to be sufficient for reattachment in Fig. 9. The CFD correctly shows a rise in the *Cp* peak and some drop toward the trailing edge, but the effect of the VGJs is much weaker than in the experiment, and reattachment is not predicted. With pulsed jets at *B*=0.5, *F*=0.28 and *D*=10%, the experiment shows reattachment after a large separation bubble. The CFD shows no difference from the steady blowing case at *B*=0.5 and does not predict reattachment. Results are similar at the other Reynolds numbers. At *Re*=25,000 with *B*=1, *F*=0.56 and *D*=10%, the experiment shows reattachment after a large separation bubble, but the CFD indicates no reattachment and essentially no change in *Cp* from the baseline case. At *Re*=100,000, cases were tried with steady blowing at *B*=0.25 and 1.0 and with pulsed jets at *B*=0.25, *F*=0.14 and *D*=10%. All of these cases show a slight rise in the *Cp* maximum. The CFD cases all agree with each other, showing no additional effect

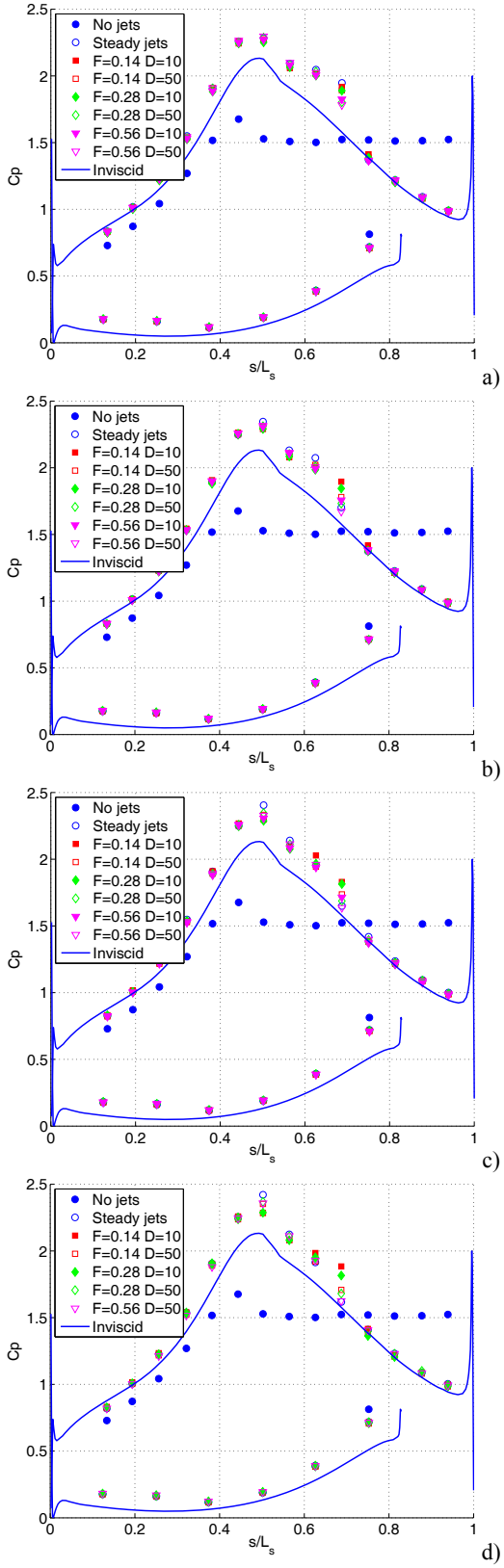

Fig. 13 Cp profiles for Re=100,000 cases, B: a) 0.25, b) 0.5, c) 0.75, d) 1.0

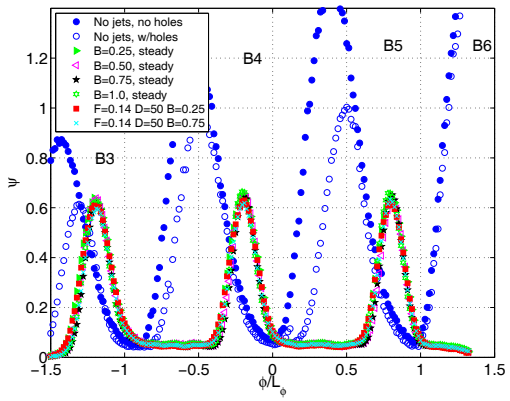

Fig. 14 Total pressure loss profiles for Re=100,000 cases

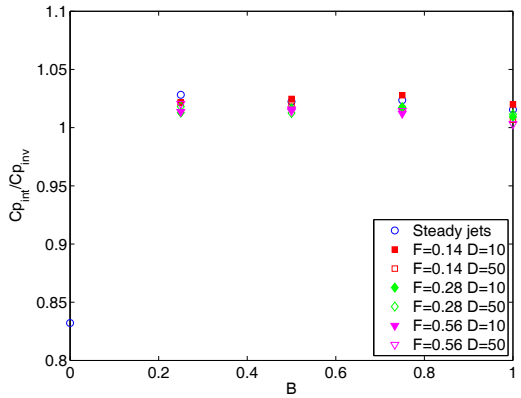

Fig. 15 Ratio of lift to lift in inviscid case, as indicated by integrated Cp result for Re=100,000 cases

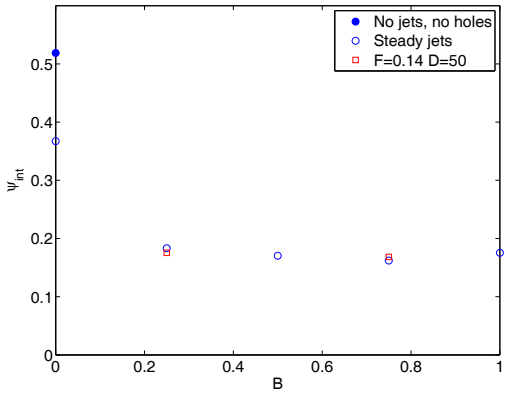

Fig. 16 Integrated total pressure loss for Re=100,000 cases

of the pulsing or increased *B*. As in the *Re*=50,000 cases, the effect of the VGJs is much smaller than in the experiments, and the reattachment is missed.

Although the Transition-sst model produced good results in the baseline cases, it was clearly unable to capture the effect of the VGJs. The VGJs must produce flows with are locally three dimensional and the resulting local turbulence may be highly anisotropic. Perhaps a higher order model may be able to capture these effects. The moderate success that others such as Rizzeta and Visbal [34] had with LES suggest that additional grid refinement away from the wall, where the jets are interacting with the main flow may also help.

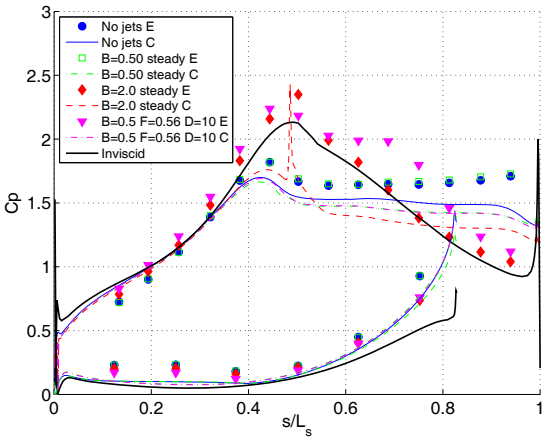

Fig. 17 Comparison of experimental (E) and CFD (C) Cp profiles for Re=50,000 cases

DISCUSSION

When *Re*=100,000, the boundary layer is on the verge of reattachment even without the jets, so any jet blowing causes reattachment, an increase in lift and a large reduction in losses, independent of blowing ratio, frequency or duty cycle. At the lower Reynolds numbers, the effect of varying the VGJ parameters is more significant. It appears that pulsing with *F*=0.14 is not effective unless the blowing ratio is so strong and the duty cycle so long that the results begin to approach the steady blowing case. Pulsing with *F*=0.28 is more effective and is duty cycle dependent. It appears that intermittent control may be achieved at this frequency with periods of no control between pulses. Increasing the duty cycle may help to lengthen the period of separation control, as does increasing the blowing rate. Pulsing with *F*=0.56 or higher results in flow control even with a low duty cycle and moderate blowing ratio of *B*=0.75 in the *Re*=25,000 case, and with *B*=0.25 in the *Re*=50,000 case. The favorable results at low duty cycle indicate that the initial pulse is able to induce boundary layer reattachment, and the effect is sustained long enough when the jets are off to maintain some control until the next pulse.

Volino [15] found that the trailing edge of the calmed region following a VGJ disturbance travels at about 0.3 times the freestream velocity. This suggests that if the VGJs are pulsed at *F*=0.3 or higher, a disturbance or its calmed region would always be present in the boundary layer. At lower frequencies there would be periods between pulses when the boundary layer could relax to its uncontrolled state and separate. The present results agree with this, showing more effective control when *F* is above 0.28 than when it is below. If the boundary layer does begin to relax between pulses, the amount of relaxation necessary before separation occurs would likely depend on the pressure gradient and Reynolds number. This may explain why pulsing at $F \leq 0.28$ is more effective as *Re* is increased from 25,000 to 100,000, and why Bons et al. [18] were able to able to suppress separation with *F*=0.1 and very low duty cycle on the less aggressive Pack B airfoil.

CONCLUSIONS

The effect of vortex generator jets on the flow over the very high lift L1A airfoil was studied experimentally and computationally under low freestream turbulence conditions. Reynolds numbers based on suction surface length and nominal exit velocity of 25,000, 50,000 and 100,000 were considered. Without flow control, the boundary layer separated in all cases and did not reattach. Flow control with VGJs

was possible even at the lowest Reynolds numbers. In agreement with previous studies, pulsed jets were found more effective than steady jets. A pulsing frequency of F=0.28 was marginal for good control at moderate blowing ratios. Pulsing with F=0.56 or higher allowed for separation control even with blowing ratios as low as 0.25 and duty cycles of 10%. Effective separation control resulted in a 20% increase in lift and up to a 70% reduction in total pressure loss compared to baseline cases at the same Reynolds number.

The Transition-sst model, which showed promising results in the cases without flow control, did not predict reattachment in the URANS calculations in any cases with VGJs. A finer grid away from the wall or a higher order model which could better capture the three dimensionality and anisotropy of the jets might give better results.

The present experimental results show the parameter ranges where VGJs can be effective with the L1A airfoil. Further measurements of instantaneous velocity, both in the boundary layer and wake may be helpful for clarifying the physics of how the VGJs work. Such knowledge may be useful for developing improved computational models.

ACKNOWLEDGMENTS

This work was sponsored by the National Aeronautics and Space Administration. The grant monitor is Dr. Anthony Strazisar of the NASA Glenn Research Center. The support of the United States Naval Academy Technical Support Department Shop and Fluids Laboratory is greatly appreciated.

REFERENCES

[1] Hourmouziadis, J., 1989, "Aerodynamic Design of Low Pressure Turbines," AGARD Lecture Series 167.

[2] Mayle, R.E., 1991, "The Role of Laminar-Turbulent Transition in Gas Turbine Engines," ASME *Journal of Turbomachinery*, **113**, pp. 509-537.

[3] Sharma, O.P., Ni, R.H., and Tanrikut, S., 1994, "Unsteady Flow in Turbines," AGARD Lecture Series 195, Paper No. 5.

[4] Bons, J.P., Sondergaard, R., and Rivir, R.B., 2001, "Turbine Separation Control Using Pulsed Vortex Generator Jets," ASME *Journal of Turbomachinery*, **123**, pp. 198-206.

[5] Volino, R.J., and Hultgren, L.S., 2001, "Measurements in Separated and Transitional Boundary Layers Under Low-Pressure Turbine Airfoil Conditions," ASME *Journal of Turbomachinery*, **123**, pp. 189-197.

[6] Volino, R.J., 2008, "Separated Flow Measurements on a Highly Loaded Low-Pressure Turbine Airfoil," ASME Paper GT2008-51445.

[7] Volino, R.J., 2002, "Separated Flow Transition Under Simulated Low-Pressure Turbine Airfoil Conditions: Part 1 – Mean Flow and Turbulence Statistics," ASME *Journal of Turbomachinery*, **124**, pp. 645-655.

[8] Volino, R.J., 2002, "Separated Flow Transition Under Simulated Low-Pressure Turbine Airfoil Conditions: Part 2 –Turbulence Spectra," ASME *Journal of Turbomachinery*, **124**, pp. 656-664.

[9] Bons, J.P., Pluim, J., Gompertz, K., Bloxham, M., and Clark, J.P., 2008, "The Application of Flow Control to an Aft-Loaded Low Pressure Turbine Cascade with Unsteady Wakes," ASME Paper GT2008-50864.

[10] Praisner, T.J., and Clark, J.P., 2007, "Predicting Transition in Turbomachinery – Part 1: A Review and New Model Development," ASME *Journal of Turbomachinery*, **129**, pp. 1-13.

[11] Zhang, X.F., Vera, M., Hodson, H., and Harvey, N., 2007, "Separation and Transition Control on an Aft-Loaded Ultra-High-Lift LP Turbine Blade at Low Reynolds Numbers: Low-Speed Investigation," ASME *Journal of Turbomachinery*, **128**, pp. 517-527.

[12] Bons, J.P., Hansen, L.C., Clark, J.P., Koch, P.J., and Sondergaard, R., 2005, "Designing Low-Pressure Turbine Blades With Integrated Flow Control," ASME Paper GT2005-68962

[13] Bohl, D.G., and Volino, R.J., 2006, "Experiments with Three-Dimensional Passive Flow Control Devices on Low-Pressure Turbine Airfoils," ASME *Journal of Turbomachinery*, **128**, pp. 251-260.

[14] Volino, R.J., 2003, "Passive Flow Control on Low-Pressure Turbine Airfoils," ASME *Journal of Turbomachinery*, **125**, pp. 754-764.

[15] Volino, R.J., 2003, "Separation Control on Low-Pressure Turbine Airfoils Using Synthetic Vortex Generator Jets," ASME *Journal of Turbomachinery*, **125**, pp. 765-777.

[16] Huang, J., Corke, T., and Thomas, F., 2003, "Plasma Actuators for Separation Control on Low Pressure Turbine Blades," AIAA Paper 2003-1027.

[17] Johnston, J.P., and Nishi, M., 1990, "Vortex Generator Jets. Means for Flow Separation Control," *AIAA Journal*, **28**, pp. 989-994.

[18] Bons, J.P., Sondergaard, R., and Rivir, R.B., 2002, "The Fluid Dynamics of LPT Blade Separation Control Using Pulsed Jets," ASME *Journal of Turbomachinery*, **124**, pp. 77-85.

[19] Volino, R.J., 2003, "Separation Control on Low-Pressure Turbine Airfoils Using Synthetic Vortex Generator Jets," ASME *Journal of Turbomachinery*, **125**, pp. 765-777.

[20] Volino, R.J., and Bohl, D.G., 2005, "Structure of Oscillating Vortex Generator Jets," Proceedings of the Fourth International Symposium on Turbulence and Shear Flow Phenomena, **2**, pp. 589-594.

[21] McQuilling, M., and Jacob, J., 2004, "Effect of Chord Location on Separation Control With Vortex Generator Jets on Low Pressure Turbine Blades," AIAA Paper 2004-2205.

[22] Eldredge, R. G., and Bons, J. P., 2004, "Active Control of a Separating Boundary Layer With Steady Vortex Generating Jets—Detailed Flow Measurements," AIAA Paper 2004-751.

[23] Gostelow, J.P., Walker, G.J., Solomon, W.J., Hong, G., and Melwani, N., 1997, "Investigation of the Calmed Region Behind a Turbulent Spot," ASME *Journal of Turbomachinery*, **119**, pp. 802-809.

[24] Schulte, V., and Hodson, H.P., 1998, "Prediction of the Becalmed Region for LP Turbine Profile Design," ASME *Journal of Turbomachinery*, **120**, pp. 839-846.

[25] Bons, J.P., Reimann, D., and Bloxham, M., 2008, "Separated Flow Transition on an LP Turbine Blade With Pulsed Flow Control," ASME *Journal of Turbomachinery*, **130**, 021014.

[26] Clark J.P., 2007, Private Communication, Air Force Research Laboratory.

[27] Zhang, X.F., and Hodson, H., 2005, "Combined Effects of Surface Trips and Unsteady Wakes on the Boundary Layer Development of an Ultra-High-Lift LP Turbine Blade," ASME *Journal of Turbomachinery*, **127**, pp. 479-488.

[28] Ibrahim, M., Kartuzova, O., and Volino, R.J., 2008, "Experimental and Computational Investigations of Separation and Transition on a Highly Loaded Low Pressure Turbine Airfoil: Part 1 – Low Freestream Turbulence Intensity," ASME Paper IMECE2008-68879.

[29] Volino, R.J, Kartuzova, O., and Ibrahim, M., 2008, "Experimental and Computational Investigations of Separation and Transition on a Highly Loaded Low Pressure Turbine Airfoil: Part 2 – High Freestream Turbulence Intensity," ASME Paper IMECE2008-68776.

[30] Suzen, Y.B., Huang, P.G., Ashpis, D.E., Volino, R.J., Corke, T.C., Thomas, F.O., Huang, J., Lake, J.P. and King, P.I., 2007, "A Computational Fluid Dynamics Study of Transitional Flows in Low-Pressure Turbines Under a Wide Range of Operating Conditions," ASME *Journal of Turbomachinery*, **129**, pp. 527-541.

[31] Menter, F.R., Langtry, R.B., Likki, S.R., Suzen, Y.B., Huang, P.G., and Völker, S., 2006, "A Correlation Based Transition Model Using Local Variables – Part I: Model Formulation", ASME *Journal of Turbomachinery*, **128**, pp. 413-422.

[32] Langtry, R.B., Menter, F.R., Likki, S.R., Suzen, Y.B., Huang, P.G., and Völker, S., 2006, "A Correlation based Transition Model using Local Variables Part II: Test Cases and Industrial Applications," ASME *Journal of Turbomachinery*, **128**, pp. 423-444.

[33] Gross, A., Fasel, H.F., 2008 "Strategies for Simulating Flow Through Low-Pressure Turbine Cascade," ASME *Journal of Fluids Engineering*, **130,** 111105.

[34] Rizzetta, D.P., and Visbal, M.R., 2005, "Numerical Simulation of Separation Control for Transitional Highly Loaded Low-Pressure Turbines," *AIAA Journal*, **43**, pp.1958-1967.

[35] Garg V.K., 2002 "Low-Pressure Turbine Separation Control - Comparison with Experimental Data," ASME Paper GT-2002-30229.

[36] Menter, F.R., 1994, "Two-Equation Eddy-Viscosity Turbulence Models for Engineering Applications," *AIAA Journal*, **32**, pp. 1598-1605.

[37] Culley, D.E., Bright, M.M., Prahst, P.S., and Stazisar, A.J., 2004, "Active Flow Separation Control of a Stator Vane Using Embedded Injection in a Multistage Compressor Experiment," ASME *Journal of Turbomachinery*, **126**, pp. 24-34.

Final draft.
Submitted for publication in: K. Hanjalić, Y. Nagano and S. Jakirlić (Editors), "Turbulence, Heat and Mass Transfer 6," Begell House, Inc., 2009.

LES and URANS Computational Investigations of LPT Blade (L1A) Separation Control using Vortex Generator Jets

M. B. Ibrahim[1], O. Kartuzova[2] and R. J. Volino[3]

[1]Department of Mechanical Engineering, Cleveland State University,
2121 Euclid Ave., SH232, Cleveland, OH 44115, m.ibrahim@csuohio.edu

[2]Department of Mechanical Engineering, Cleveland State University,
2121 Euclid Ave., SH232, Cleveland, OH 44115, kartuzova_olga@hotmail.com

[3]Mechanical Engineering Department, United States Naval Academy,
Annapolis, Maryland 21402-5042, volino@usna.edu

Abstract - This paper describes active flow control utilizing steady VGJs both experimentally and computationally for the L1A airfoil. URANS approach is compared with LES to test the ability to accurately predict effect of VGJs on the boundary layer separation. Cases were considered at Reynolds numbers (based on the suction surface length and the nominal exit velocity from the cascade) of 25,000, 50,000 and 100,000. In all cases without flow control, the boundary layer separated and did not reattach. The VGJs were successful in reducing the bubble size or removing it completely depending on the Re number and blowing ratio (B). Transition-sst RANS model was successful in predicting the flow separation and attachments with no jet flow. LES showed superior performance for the VGJs cases and much better agreement with the experimental data for the flow field at different values of Re and B.

1. Nomenclature

B	blowing ratio, maximum jet velocity/local freestream velocity
Cp	$2(P_T - P)/\rho U_e^2$, pressure coefficient
C_x	axial chord length
D	jet diameter (=0.8 mm)
L_s	suction surface length
L_ϕ	blade spacing (pitch)
P	pressure
P_T	upstream stagnation pressure
Re	$U_e L_s/\nu$, exit Reynolds number
$Re_{\theta t}$	transition momentum thickness Reynolds number
s	streamwise coordinate, distance from leading edge
u'	RMS of the fluctuating component of the streamwise velocity
U	streamwise velocity
U_e	nominal exit freestream velocity, based on inviscid solution

V_x velocity in the axial direction
x axial distance from leading edge
y distance from the wall
z distance in the spanwise direction
ν kinematic viscosity
ρ density

2. Introduction

Boundary layer separation on the suction side of low-pressure turbine (LPT) airfoils can occur due to strong adverse pressure gradients. The problem is becoming more severe as airfoil loading is increased. If the boundary layer separates, the lift from the airfoil decreases and the aerodynamic loss increases, resulting in a drop in overall engine efficiency. A significant increase in efficiency could be achieved if separation could be prevented, or minimized. Active flow control could provide a means for minimizing separation under conditions where it is most severe (low Re), without causing additional losses under other conditions (high Re). Minimizing separation will allow improved designs with fewer stages and fewer airfoils per stage to generate the same power. The active flow control technique called Vortex Generator Jets (VGJs), introduced by Johnston and Nishi [1], is the subject of this paper. In this technique blowing from small, compound angled holes is used to create streamwise vortices. The vortices bring high momentum fluid into the near wall region as well as promote transition and turbulent mixing. This helps to control separation. A review of experimental work on this topic was given in Volino et al. [2].

Along with the experimental investigations, numerical simulations of the flow over LPT blades, utilizing steady and pulsed vortex generator jets (VGJs) were performed by different researchers. This type of flow is challenging for CFD because of its transitional nature in combination with highly 3D jet flow.

Rizzetta and Visbal [3] used ILES (Implicit Large Eddy Simulation) to investigate the effect of flow control by pulsed VGJs on the flow separation in a Pack B cascade. The Pack B is a widely studied LPT airfoil. They reported that for inlet Re = 25,000 and B=2 flow control helped to keep the flow attached for an additional 15% of the chord. Despite some differences with experiment, numerical and experimental time-mean velocity profiles were in reasonable agreement.

Postl et al. [4] studied the effect of active flow control utilizing steady and pulsed VGJs on preventing laminar separation on the Pack B airfoil. In their study they used two computational approaches. The first was direct numerical simulation (DNS) of the flow over a flat plate with imposed streamwise pressure gradient as measured on the suction side of the Pack B airfoil. In the second approach a linear LPT cascade was simulated with the flow control cases performed in 2D using slots. They observed two different physical mechanisms to affect the control for the steady versus pulsed VGJs. The steady jets developed streamwise structures which enhanced momentum exchange between the near wall region and free stream. For the pulsed VGJs accelerated boundary layer transition helped to achieve flow reattachment. Their results are in reasonably good agreement with experimental data except in the separated region, where the size of the separation bubble was under predicted.

Garg [5] used the NASA Glenn-HT code with the k-ω SST model of Menter [6] to compute the flow over the Pack B blade with and without use of VGJs. This work resulted in correct predictions of the separation location in the baseline case (without VGJs) as well as showing that separation vanishes in the flow control case as in experiment. However, the separated region and the wake were not well predicted, which is common for RANS.

In the present study the very highly loaded L1A airfoil was considered. The L1A was designed at the Air Force Research Laboratory (AFRL) and is available on a limited basis

from Clark [7]. It is an aft loaded blade with the same flow angles and loading as the mid chord loaded L1M. Based on the design calculations of Clark, [7], the L1A has 10% higher loading than the "ultra-high lift" airfoils described by Zhang and Hodson [8], and 17% higher loading than the Pack B. Because the L1A is aft loaded, it is more prone to separation than the L1M, as documented in Bons et al. [9], Ibrahim et al. [10], and Volino et al. [11]. In cases without flow control and with low freestream turbulence, the boundary layer separates when Re<150,000 and does not reattach, in spite of transition to turbulence in the shear layer over the separation bubble in all cases. This result contrasts with the results of earlier studies on less aggressive airfoils, which all showed reattachment after transition. The separation bubble on the L1A is about four times thicker than that on the Pack B. The larger distance from the shear layer to the wall on the L1A apparently prevents the turbulent mixing in the shear layer from reaching the wall and causing reattachment. The failure of the boundary layer to reattach results in a 20% loss in lift and increases profile losses by a factor of 7 [2]. At higher Reynolds numbers the separation bubble is small and the boundary layer is attached over most of the airfoil. In cases with high freestream turbulence, results are similar, but the shear layer is somewhat thicker and the separation bubble thinner due to increased mixing induced in the shear layer. This results in reattachment after transition at Re=50,000 and 100,000. At the lowest Re considered (25,000) the boundary layer still does not reattach.

Boundary layer separation control has been studied using Vortex Generator Jets (VGJs) on the L1A airfoil. Experiments were done under low freestream turbulence conditions on a linear cascade in a low speed wind tunnel (see Volino et al., [2]). In that paper the pressure surveys on the airfoil surface and downstream total pressure loss surveys were documented. Cases were considered at Reynolds numbers (based on the suction surface length and the nominal exit velocity from the cascade) of 25,000, 50,000 and 100,000. In all cases without flow control, the boundary layer separated and did not reattach. These cases (without jets) were documented experimentally and computationally for low freestream turbulence intensity (see Ibrahim et al. [10]) and high freestream turbulence intensity (see Volino et al. [11]).

This paper describes active flow control utilizing steady VGJs both experimentally and computationally for the L1A airfoil. A previously developed computational model for the baseline cases (without VGJs), by the authors, [10,11] is enhanced by additional grid independence study for the necessary grid resolution around the jets and in the spanwise direction. Unsteady RANS approach is compared with LES to test the ability to accurately predict the effect of VGJs on the boundary layer separation.

3. Numerical Simulation

The numerical simulations were conducted for the L1A airfoil utilizing version 6.3.26 of the finite-volume code Fluent^{TM}[12]. Cases (with jet) were considered, in this paper, at different Reynolds numbers and blowing ratios. Table 1. shows a summary of all the cases presented in this paper both experimentally and computationally. Comparison for the results of these cases are shown in Section 5. Due to high flow unsteadiness even for steady blowing, unsteady calculations were done for all cases. The three dimensional computational domain includes a single passage (see Table 2. for cascade parameters). A uniform velocity inflow condition is specified 1.9 Cx upstream of the blade leading edge in the flow direction. The inlet flow angle is set to 33^{o} based on an inviscid calculation of the full cascade used in the experiment [10]. This angle agrees with the experimentally measured inlet angle to within the experiment uncertainty. The exit boundary is located 3.8 Cx downstream of the trailing edges in the flow direction. In the spanwise direction, the domain includes one VGJ. The boundary conditions on the sides of the passage are periodic. The full length of the hole is included in the simulations, allowing the jet velocity profile to develop before entering the main domain [2]. A uniform velocity boundary condition is specified at the hole inlet.

Convergence was established when: 1) residuals reduced to a value 10^{-5}, 2) no change was observed in any field results, and 3) the mass imbalance was less than 0.01 %.

Table 1. Test matrix used in experiments and CFD (NA = not available).

Reynolds number, Re		25,000		50,000		100,000		
Blowing ratio, B		1	3	0.5	2	0.25	0.75	1
Cp	Experiment	✓	✓	✓	✓	✓	NA	✓
	LES	✓	✓	✓	✓	✓	NA	✓
	Transition-sst	NA	✓	NA	✓	NA	NA	✓
U/Ue	Experiment	NA	✓	NA	✓	NA	✓	NA
	LES	✓	✓	✓	✓	✓	NA	✓
	Transition-sst	NA	✓	NA	✓	NA	NA	✓
u'/Ue	Experiment	NA	✓	NA	✓	NA	✓	NA
	LES	NA	✓	NA	✓	NA	NA	✓
	Transition-sst	NA						

Table 2. Cascade parameters.

Axial Chord, C_x [mm]	True Chord [mm]	Pitch, L_ϕ [mm]	Span [mm]	Suction side, L_s [mm]	Inlet flow angle	Exit flow angle
134	146	136	724	203	35°	60°

4. Turbulence Models Description

4.1. Transition-sst (4 eq.) model

A new correlation-based transition model was proposed by Menter et al. [13]. This model is based on two transport equations. The intermittency transport equation is used to trigger the transition onset. The transport equation for the transition momentum thickness Reynolds number ($Re_{\theta t}$) is used to capture non-local effects of freestream turbulence intensity and pressure gradient at the boundary layer edge. Outside the boundary layer the transport variable was forced to follow the value of $Re_{\theta t}$ given by correlations. Those two equations were coupled with the shear stress transport turbulence model (SST). This model has recently become available in Fluent code [12].

4.2. Large Eddy Simulation with Dynamic Kinetic Energy Subgrid-Scale model

In LES, large eddies are resolved directly, while small eddies are modeled. The rationale behind LES are: a) Momentum, mass, energy, and other passive scalars are transported mostly by large eddies, b) Large eddies are more problem-dependent; they are dictated by the geometries and boundary conditions of the flow involved, c) Small eddies are less dependent on the geometry, tend to be more isotropic, and are consequently more

universal, and d) The chance of finding a universal turbulence model is much higher for small eddies.

The governing equations employed for LES are obtained by filtering the time-dependent Navier-Stokes equations in either Fourier (wave-number) space or configuration (physical) space. The filtering process effectively filters out the eddies whose scales are smaller than the filter width or grid spacing used in the computations. The resulting equations thus govern the dynamics of large eddies. The subgrid-scale stresses resulting from the filtering operation are unknown, and require modeling. The subgrid-scale turbulence models in Fluent employ the Boussinesq hypothesis as in the RANS models.

The dynamic subgrid-scale kinetic energy model in Fluent is based on the model proposed by Kim and Menon [14]. In this model a separate transport equation is solved for subgrid-scale kinetic energy. The model constants are determined dynamically. The details of the implementation of this model in Fluent and it's validation are given by Kim [15].

5. Results and Discussion

5.1. Code Validation

Three different grids were designed for this study as shown in Table 3. Figure 1shows the grid structure in the vicinity of the jet for Grid#37.

Table 3. Grid#3, 35 and 37 used in this investigation.

Grid #	Size (Cells)	Number of grids in z direction	y+	Δz+	Δx+
3	1,500,000	15	0.5	12.6	1 – 100
35 (airf-mid)	5,900,000	30	0.5	6.3	0.4 – 52
37 (airf-mid)	11,900,000	54	0.5	0.4 - 3.5	0.4 – 52

To accurately represent structures in the near-wall region (for LES) recommended values are: y+~ 2; Δx+ ~ 50-150; Δz+ ~ 15-40 (see Piomelli and Chasnov [16]). Based on results (not shown for space limitation) for the pressure coefficient versus the dimensionless location on the suction side s/Ls, Grid#37 showed closet agreement to the data and therefore was chosen for further computation. This Grid#37 was then run for different time steps (0.0005, 0.0001 and 0.00005 s) and time step =0.0001 s was selected since no much improvement were achieved using the smaller one (0.00005 s). It should be noted that grid independence tests were conducted for the Transition-sst model without jet flow (see Ibrahim et al. [10]). In this study further grid refinement was conducted for two reasons: a) to handle highly 3D jet flow and b) to utilize LES computation.

Velocity measurements were conducted at 6 different stations downstream of the suction peak (see Table 4.). Comparison will be made between the velocity profiles at these stations from CFD and experiments.

Table 4. Velocity profile measurement stations.

Station	1	2	3	4	5	6
s/Ls	0.53	0.59	0.69	0.78	0.88	0.97
x/Cx	0.65	0.72	0.80	0.86	0.92	0.97

5.2. Re - 25,000 steady VGJs cases

Pressure coefficient plotted versus dimensionless distance along the suction side of an airfoil is presented in Fig. 2. The experiment for B=1 shows separation at s/Ls between 0.53 and 0.59, with no reattachment. At B=2 there is no clear indication if the flow is attached along the airfoil since there seems to be a bubble present. Computational (LES) results for two blowing ratios (B = 1 and 3) are compared to the experiment with the same blowing conditions. For B = 1 both LES and experiment show flow separation starting after the suction peak with no reattachment, which is indicated by the large plateau in C_p after the suction peak. C_p at the suction peak is lower in CFD compared to experiment, but it is within the range of experimental uncertainty (0.07). The CFD results from the Transition-sst model (B=3) are shown in Fig. 2 also for comparison between RANS and LES. The Transition-sst model predicts C_p similar to LES, except for downstream locations (s/Ls = 0.8 - 1.0), where it predicts lower C_p values, than LES. This indicates a smaller separation bubble modeled by RANS than by LES for Re = 25,000 and B = 3. The reason for not showing results from Transition-sst model and B = 1 is that at lower blowing ratio jets have no effect on separation and conditions are close to the "no-jets" cases. We know from our previous work [10,11] that the Transition-sst model predicts C_p reasonably well compared to experiment for "no-jets" cases.

Velocity profiles normalized by the nominal exit velocity are plotted versus dimensionless distance from the wall in the direction normal to the wall in Fig. 3. The results for the 6 measurement stations (see Table 4.) located downstream of the suction peak of the airfoil are shown. Computational velocity profiles from LES for B = 1 and B = 3 are shown. Experimental data and Transition-sst results are only available for B = 3. For B = 1, LES shows separation starting at station 2 and large separation bubble is present at all stations from 2 to 6, based on negative velocities near the wall at those locations. For B = 3 both Transition-sst and LES show separation started at station 4 and continuing at stations 5 and 6. Separation bubble is smaller than that for B = 1. LES is in reasonably good agreement with experiment. It should be noted the larger disagreement near the wall is due to the fact that hot wire anemometry was used in the experiment, which is not capable of measuring negative velocities. The Transition-sst model underpredicts velocities near the wall and the size of the bubble, compared to LES and experiment.

Profiles of the streamwise component of the RMS fluctuating velocity, u', normalized by the nominal exit velocity are plotted versus dimensionless distance from the wall in Fig. 4. The results for 6 measurement stations located downstream of the suction peak of the airfoil are shown. Computational and experimental profiles are for B = 3. The experiment shows the location of the peak is away from the wall indicating the presence of a bubble. LES compares reasonably well with data including magnitude and location of u'.

For the purpose of visualization of the separated region as well as the influence of the jet's blowing ratio, iso-surfaces of instantaneous axial velocity Vx = 0.01 m/s are shown in Fig. 5 for B = 1 and B = 3. These CFD results are from the LES model. The reason for choosing Vx = 0.01 m/s is that this small (but not negative) value represents velocity in the shear layer of the separation bubble and helps to visualize the size of the bubble and shapes of the vortices created by the jets. The airfoil with 3 jets on the suction side near the suction peak is shown. In the case with B = 1 the low velocities in the shear layer of the separation bubble are at a distance from the wall, thus the separation bubble is large. It looks like not enough mixing is happening at this iso-surface and the fluid issuing from the jet is moving aligned with the cross flow direction at this low blowing ratio. The separation bubble is smaller in the B = 3 case, low velocities in the shear layer are closer to the wall than in the B = 1 case. The visualization shows more mixing happening near the wall (the iso-surface is

less smooth than in B = 1 case). The fluid coming from the jet is moving at an angle with the flow direction downstream of the suction peak of the airfoil due to the high momentum jets at B = 3.

Instantaneous axial vorticity contours are presented in Fig. 6 for the B = 1 and B = 3 cases for the LES model. For B = 1 maximum vorticity is in the shear layer of the separation bubble away from the wall between stations 3 and 4. In the B = 3 case, the region with high vorticity (more mixing) is in the shear layer, but closer to the wall than in the B = 1 case. Its location is moved upstream and is between stations 2 and 3. More mixing in the high blowing ratio case (indicated by the streamwise vorticity contours) helps to reduce the size of the separation bubble (indicated also by the velocity plots - Fig. 3).

Fig. 7 presents a plane view of the 6 measurement stations (see Table 4.) along the airfoil suction side downstream of the jets locations. Subgrid turbulent kinetic energy (TKE) contours are displayed for B = 1 (7a) and B = 3 (7b).

In summary, for B = 1: a) separation starts between stations 1 and 2, b) transition to turbulence starts between stations 3 and 4 (max subgird TKE and X-vorticity locations). For B = 3: a) separation starts near station 3 (see Figs. 2, 3 and 4), b) transition to turbulence starts earlier at station 1 (max subgrid TKE), and c) the location of the peak of u' is away from the wall indicating the presence of a bubble.

5.3. Re - 50,000 steady VGJs cases

In the case of Re=50,000, and B =0.5, the flow was still separated and not attached. A value of B=2 was needed to get the flow attached with very small separation near the trailing edge. Below are more detailed results for the Re=50,000 case.

Pressure coefficient plotted versus dimensionless distance along the suction side of an airfoil is presented in Fig. 8. Computational LES results for two blowing ratios (B = 0.5 and B = 2) are compared to the experiment with the same blowing conditions. For B = 0.5 large separation is shown by both LES and experiment, which is indicated by the large plateau in C_p downstream of the suction peak (starting at s/Ls = 0.5 - upstream of station 1). For B = 2 separation is reduced in size and delayed to a further downstream location, compared to the B = 0.5 case. The location of the start of the plateau in C_p has moved downstream to s/Ls = 0.8 (between stations 4 and 5). The LES is well below the experiment and the experiment does not show any plateau. The Transition-sst model over predicts C_p downstream of the s/Ls = 0.6 (starting at station 2), compared to LES and experiment for the B = 2 case. This indicates a larger separation bubble predicted by the Transition-sst model with the location of the separation moved upstream.

Fig. 9 shows velocity profiles normalized by the nominal exit velocity, plotted versus dimensionless distance from the wall in the direction normal to the wall. Computational velocity profiles from LES for B = 0.5 and B = 2 are presented. Experimental and Transition-sst model results are only available for B = 2. The results for 6 measurement stations from LES for B = 0.5, show separation present already at station 1 and continuous through station 6, which is consistent with the location of the plateau in C_p, observed from Fig. 8. For B = 2 LES shows separation started between stations 4 and 5 with no reattachment. Separation bubble is smaller than for B = 0.5. Results are in a reasonably good agreement with experiment with some underprediction of the velocities at stations 3-6. The experiment shows low velocities near the wall, indicating that it may be approaching separation near the trailing edge, but the boundary layer does not appear to separate. The Transition-sst model underpredicts velocities near the wall and shows larger size of the bubble, compared to LES and experiment. This model predicts starting separation earlier i.e. at station 2.

RMS u' profiles normalized by the nominal exit velocity are plotted versus dimensionless distance from the wall in Fig. 10. Computational (LES) and experimental profiles are for B = 2. CFD overpredicts u' at stations 3-6. The location and the magnitude of the maximum u' are in a reasonable agreement with experiment.

In summary, for B = 0.5: a) separation starts already at station 1, and b) transition to turbulence starts between stations 3 and 4 (max subgird TKE, u' and X-vorticity locations). For B = 2: a) separation starts near station 3 (Figs. 8, and 9), and b) transition to turbulence starts before or at station 1 (max subgrid TKE), and c) The location of the peak of u' is away from the wall indicating the presence of a small bubble.

5.4. Re - 100,000 steady VGJs cases

In the case of Re=100,000 and B=0.25 the flow separates with reattachment downstream the suction peak. At higher blowing ratios (B=1) the flow becomes attached along the whole airfoil length. Below are more detailed results for the Re=100,000 case.

On the pressure coefficient plot (Fig. 11) computational (LES) results for B = 0.25 and 1 are compared to experimental data for the same blowing ratios. Blowing with B = 0.25 causes the flow to reattach after a small separation region starting near s/Ls = 0.6 in both CFD and experiment. In the higher blowing ratio case (B=1) experimental and computational Cp profiles show attached flow at all locations on the suction side of the airfoil. The computational Cp profile from the Transition-sst model is shown only for B=1. The Transition-sst model predicts separated flow on the suction side of the airfoil, starting at s/Ls = 0.5 with no reattachment downstream. Overall LES is in a good agreement with experiment, while RANS is not able to predict the flow correctly.

Fig.12 shows velocity profiles from LES for B = 0.25 and B = 1 and experimental velocity profiles for B = 0.75. The Transition-sst model results are shown for B = 1. The results for 6 measurement stations from LES for B = 0.25 show separation starting at station 2 and reattached flow at station 4, which is consistent with the location of the plateau in C_p, observed from Fig. 11. LES with B = 1 shows attached flow at all six measurement stations. Experimental results for B = 0.75 indicate attached flow as well. For stations 1-4 LES velocity profiles for B=1 match the experimental profiles for B=0.75 very well. At stations 5 and 6 the CFD results are in reasonable agreement with the experimental data for B=0.75. The Transition-sst model predicts separation starting at station 2 and continuing through station 6. Velocity profiles from this model are significantly underpredicted compared to LES and experiment.

RMS of the fluctuating component of streamwise velocity normalized by the nominal exit velocity is plotted versus dimensionless distance from the wall in the direction normal to the wall in Fig.13. The results for 6 measurement stations located downstream of the suction peak of the airfoil are shown for B = 1 (CFD) and B = 0.75 (experiment). The agreement between CFD and the experiment is good, including the location of the maximum u'.

In summary for B = 0.25, separation starts at station 2, flow reattachment is observed at station 4. For B = 1: a) attached flow is observed on the whole length of the airfoil's suction side (see Figs. 11 and 12), b) transition to turbulence starts at station 3 and c) the location of the peak of u' is close to the wall indicating attached flow.

6. Summary and Conclusions

This paper describes active flow control utilizing steady VGJs both experimentally and computationally for the L1A airfoil. This study is based on previous work by the authors, both experimentally (on a linear cascade in a low speed wind tunnel) and computationally (URANS) for the baseline cases (without VGJs). This study is enhanced by additional grid

independence study for the necessary grid resolution around the jets and in the spanwise direction. URANS approach is compared with LES to test the ability to accurately predict effect of VGJs on the boundary layer separation.

Cases were considered at Reynolds numbers (based on the suction surface length and the nominal exit velocity from the cascade) of 25,000, 50,000 and 100,000. In all cases without flow control, the boundary layer separated and did not reattach.

6.1. Re=25,000

Experimental data for Cp show that for B=1, the flow separates at s/Ls between 0.53 and 0.59, with no reattachment; while at B=3, it is not clear if the flow is attached along the airfoil. The velocity profiles data, however, show that the flow separates between s/Ls =0.59 and 0.69. Furthermore the location of the peak of u' is away from the wall indicating the presence of a bubble.

The LES results are in good agreement with the data for B=1; for B=3 both LES and Transition-sst model (for both Cp and U/Ue) are in good agreement with data up to s/Ls = 0.8. The LES data for u' compare well with the experiment. Overall the LES predictions are in much better agreement with the data.

6.2. Re=50,000

Experimental data for both Cp and velocity profiles show that for B=0.5, the flow separates at s/Ls = 0.53 with no reattachment; while at B=2, flow is attached along the airfoil.

The LES results are in excellent agreement with the data for B=0.5 and showing the same trend for B=2. Also, for B=2, LES compares reasonably well with data including magnitude and location of u'. As for the Transition-sst model for B=2 it overpredicts C_p downstream of the s/Ls = 0.6, and underpredicts velocities near the wall. This indicates a larger separation bubble predicted by the Transition-sst model with the location of the separation moved upstream. Overall the LES predictions are far superior to the Transition-sst model and in much better agreement with the data.

6.3. Re=100,000

Experimental data for Cp show that for B=0.25, the flow separates at s/Ls = 0.53 with reattachment at s/Ls = 0.7; while at B=1, the flow is fully attached along the airfoil. Also, the velocity profiles data for B=0.75 show that the flow does not separate. Furthermore the location of the peak of u' is close to the wall indicating attached flow.

The LES results are in excellent agreement with the data. On the other hand the Transition-sst model, with B=1, shows separation at s/Ls = 0.59 and no reattachment; it significantly underpredicts velocity profiles compared to LES or experiment. Again, overall the LES predictions are far superior to the Transition-sst model and in much better agreement with the data.

7. Acknowledgements

This work was sponsored by the National Aeronautics and Space Administration. The grant monitor is Dr. Anthony Strazisar of the NASA Glenn Research Center. The support of the United States Naval Academy Technical Support Department Shop and Fluids Laboratory is greatly appreciated. We greatly appreciate the computer time provided for us by the Ohio Super Computer (OSC). The OSC Computer Cluster has been made available as part of the Center's mission to support Ohio Universities.

8. References

1. J.P. Johnston and M. Nishi. Vortex Generator Jets. Means for Flow Separation Control. *AIAA Journal*, **28**, pp. 989-994, 1990.
2. R.J. Volino, O. Kartuzova, and M.B. Ibrahim. Experimental and Computational Investigations of Low-Pressure Turbine Separation Control using Vortex Generator Jets. *GT2009-59983, Proceedings of ASME Turbo Expo 2009: Power for Land, Sea and Air GT2009*, June 8-12, 2009, Orlando, Florida, USA.
3. D.P. Rizzetta and M.R. Visbal. Numerical Simulation of Separation Control for Transitional Highly Loaded Low-Pressure Turbines. *AIAA Journal*, **43**, pp.1958-1967, 2005.
4. D. Postl, A. Gross, H.F. Fasel. Numerical Investigation of Active Control for Low-Pressure Turbine Blade Separation. *AIAA2004-750, Proceedings of 42nd AIAA Aerospace Science Meeting and Exhibit*, January 5-8, 2004, Reno, Nevada, USA, 2004.
5. V.K. Garg. Low-Pressure Turbine Separation Control - Comparison with Experimental Data. *ASME Paper GT-2002-30229*, 2002.
6. F.R. Menter. Two-Equation Eddy-Viscosity Turbulence Models for Engineering Applications. *AIAA Journal*, **32**, pp. 1598-1605, 1994.
7. J.P. Clark. *Private Communication*, Air Force Research Laboratory, 2007.
8. X.F. Zhang and H. Hodson. Combined Effects of Surface Trips and Unsteady Wakes on the Boundary Layer Development of an Ultra-High-Lift LP Turbine Blade. *ASME Journal of Turbomachinery*, **127**, pp. 479-488, 2005.
9. J.P. Bons, J. Pluim, K. Gompertz and M. Bloxham. The Application of Flow Control to an Aft-Loaded Low Pressure Turbine Cascade with Unsteady Wakes. *ASME Paper GT2008-50864*, 2008.
10. M.B. Ibrahim, O. Kartuzova, and R.J. Volino. Experimental and Computational Investigations of Separation and Transition on a Highly Loaded Low Pressure Turbine Airfoil: Part 1 – Low Freestream Turbulence Intensity. *ASME Paper IMECE2008-68879*, 2008.
11. R.J. Volino, O. Kartuzova, and M.B. Ibrahim. Experimental and Computational Investigations of Separation and Transition on a Highly Loaded Low Pressure Turbine Airfoil: Part 2 – High Freestream Turbulence Intensity. *ASME Paper IMECE2008-68776*, 2008.
12. Fluent, Inc., 2005. Fluent 6.3 - User Guide.
13. F.R. Menter, R.B. Langtry, S.R. Likki, Y.B. Suzen, P.G. Huang and S. Völker. A Correlation Based Transition Model Using Local Variables – Part I: Model Formulation. *ASME Journal of Turbomachinery*, **128**, pp. 413-422, 2006.
14. W.W. Kim and S. Menon. Application of the localized dynamic subgrid-scale model to turbulent wall-bounded flows. *Technical Report AIAA-97-0210, American Institute of Aeronautics and Astronautics*, 35th Aerospace Sciences Meeting, Reno, NV, 1997.
15. S.E. Kim. Large eddy simulation using unstructured meshes and dynamic subgridscale turbulence models. *Technical Report AIAA-2004-2548, American Institute of Aeronautics and Astronautics*, 34th Fluid Dynamics Conference and Exhibit, 2004.
16. U. Piomelli and J.R. Chasnov. Large-Eddy Simulations: Theory and Applications. *Turbulence and Transition Modeling, lecture notes from the ERCOFTAC/IUTAM* summer school held in Stockholm, 12-20 June, 1995.

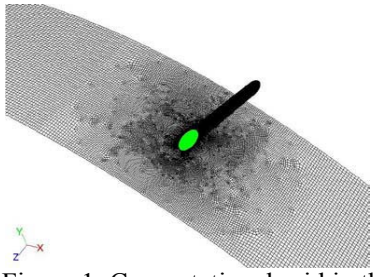

Figure 1: Computational grid in the jet vicinity

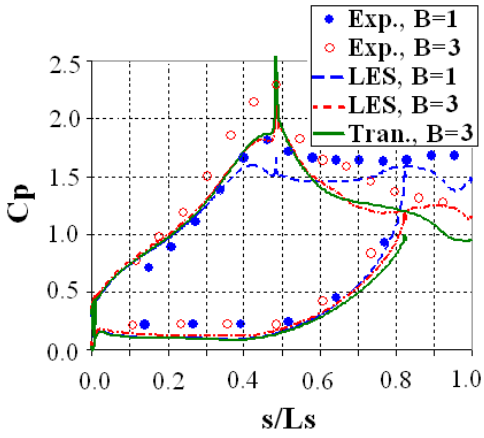

Figure 2: Pressure coefficient, Re = 25,000

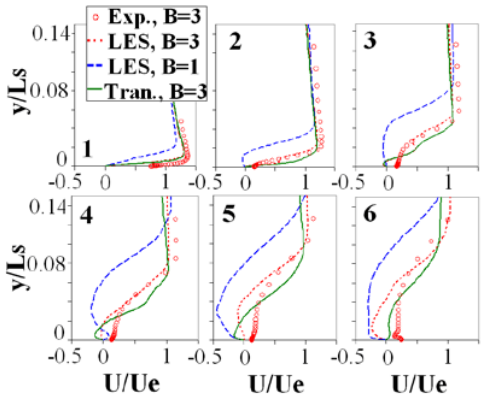

Figure 3: Velocity profiles, Re = 25,000

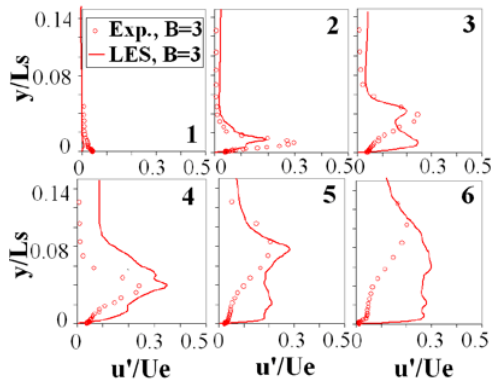

Figure 4: RMS of the fluctuating component of the streamwise velocity, Re = 25,000

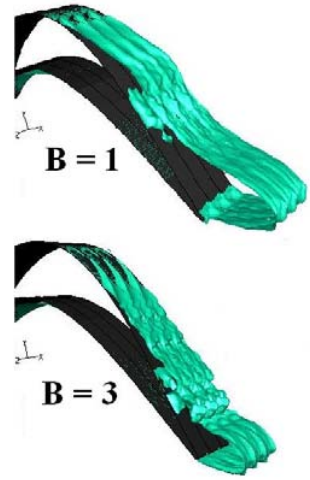

Figure 5: Instantaneous isosurfaces of Vx=0.01 m/s, Re = 25,000

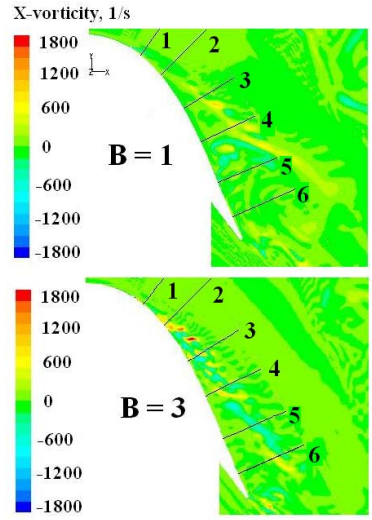

Figure 6: Instantaneous X-vorticity, Re = 25,000

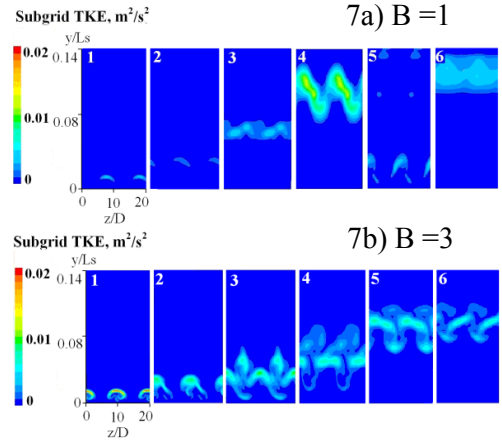

Figure 7: Subgrid turbulence kintic energy (TKE) at the spanwise oriented planes of 6 measurement stations , Re = 25,000

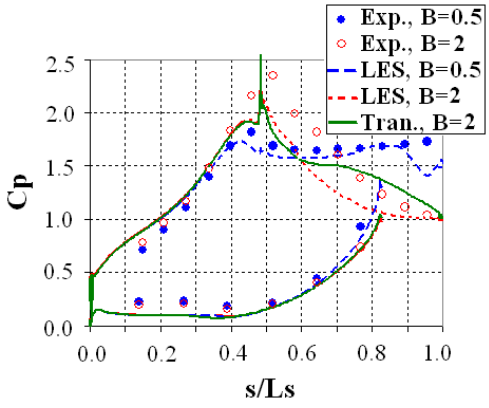

Figure 8: Pressure coefficient, Re = 50,000

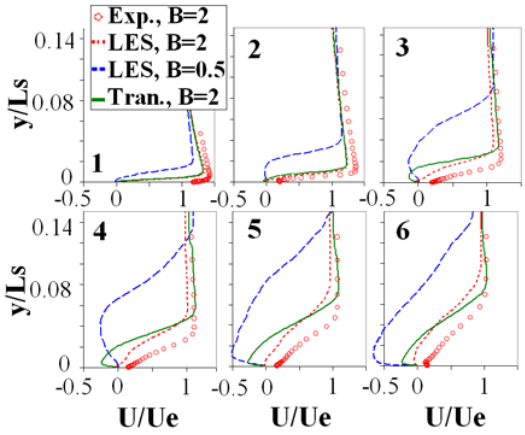

Figure 9: Velocity profiles, Re = 50,000

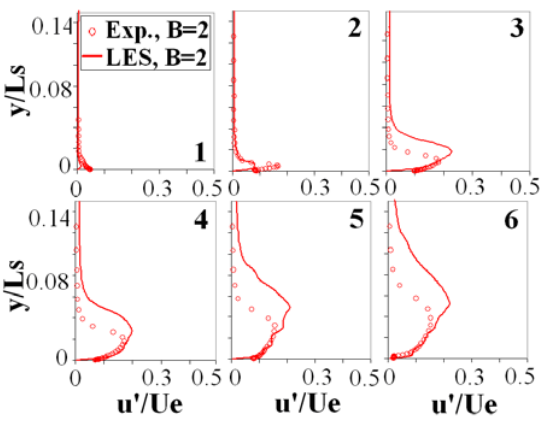

Figure 10: RMS of the fluctuating component of the streamwise velocity, Re = 50,000

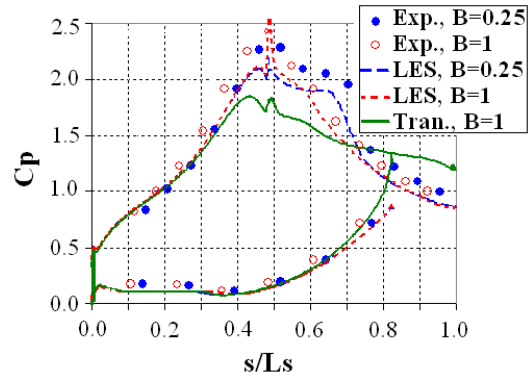

Figure 11: Pressure coefficient, Re = 100,000

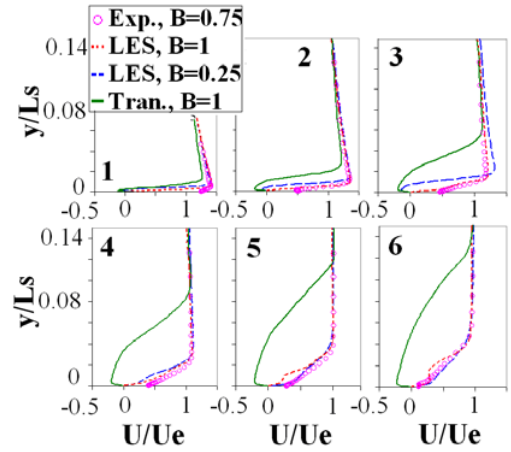

Figure 12: Velocity profiles, Re = 100,000

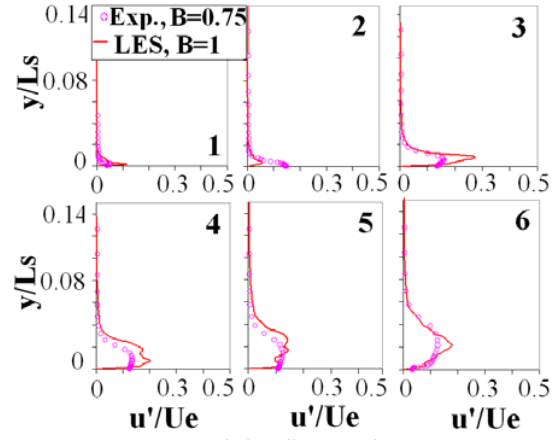

Figure 13: RMS of the fluctuating component of the streamwise velocity, Re = 100,000

ASME-ATI-UIT 2010 Conference on Thermal and Environmental Issues in Energy Systems
16 – 19 May, 2010, Sorrento, Italy

SEPARATION CONTROL ON HIGH LIFT LOW PRESSURE TURBINE AIRFOILS USING PULSED JET VORTEX GENERATOR JETS

Ralph J. Volino*, Mounir B. Ibrahim°

*United States Naval Academy, Annapolis, MD 21402 USA
°Cleveland State University, Cleveland, OH 44115 USA

ABSTRACT

Boundary layer separation control has been studied using vortex generator jets (VGJs) on a very high lift, low-pressure turbine airfoil. Experiments were done under low (0.6%) freestream turbulence conditions on a linear cascade in a low speed wind tunnel. Pressure surveys on the airfoil surface and downstream total pressure loss surveys were documented. Instantaneous velocity profile measurements were acquired in the suction surface boundary layer. Cases were considered at Reynolds numbers (based on the suction surface length and the nominal exit velocity from the cascade) of 25000 and 50000. Jet pulsing frequency and duty cycle were varied. In cases without flow control, the boundary layer separated and did not reattach. With the VGJs, separation control was achieved. At sufficiently high pulsing frequencies, separation control was possible with low jet velocities and 10% duty cycle. At lower frequencies, a 50% duty cycle helped by separating the disturbances associated with the jets turning on and turning off, thereby doubling the frequency of separation control events above the pulsing frequency. Phase averaged velocity profiles and wavelet spectra of the velocity show the VGJ disturbance causes the boundary layer to reattach, but that it can re-separate between disturbances. When the disturbances occur at high enough frequency, the time available for separation is reduced, and the separation bubble remains closed at all times.

INTRODUCTION

Gas turbine engines power nearly all commercial and military aircraft and are used extensively for ship propulsion and land based power generation. Given the hundreds of billions of liters of fuel used in gas turbines each year, any improvement in their efficiency, even an improvement of only 1%, would result in a huge savings in fuel and reduction in emissions. The low-pressure turbine (LPT) is the heaviest component in a gas turbine engine and produces the net power from the engine. Increases in LPT component efficiency result in almost equal increase in overall engine efficiency [1]. One way to potentially improve the LPT is to reduce part count, weight and cost through the use of very highly loaded blading. The limitation on loading is boundary layer separation, which leads to partial loss of lift and higher aerodynamic losses (e.g. Mayle [2]).

Separation and separated flow transition, which can lead to boundary layer reattachment, have received considerable attention, as noted by Volino [3,4]. In general, previous work shows that the strong acceleration on the leading section of the airfoil keeps the boundary layer thin and laminar. When separation does occur, it is usually just downstream of the suction peak. If transition then occurs in the shear layer over the separation bubble, it is typically rapid and often causes the boundary layer to reattach [4,5].

Airfoils can be designed with high resistance to separation, as described by Praisner and Clark [6], but a loading limit will always exist, above which separation will still occur. If flow control were incorporated in the design of an advanced airfoil, it might be possible to increase the loading limit. Passive devices such as boundary layer trips (eg. Zhang et al. [7] and Bohl and Volino [8]) have been shown effective for separation control and have the distinct advantage of simplicity, but they also introduce parasitic losses and cannot be adjusted to account for changes in flow conditions. Active devices would be more costly and potentially risky in terms of reliability, but could potentially provide better control over the entire operating range of interest.

The literature contains many examples of active separation control. In turbomachinery, plasma devices, as used by Huang et al. [9], could be viable. Vortex generator jets (VGJs), as introduced by Johnston and Nishi [10], are another alternative and the subject of the present study. Blowing from small, compound angled holes is used to create streamwise vortices. The vortices bring high momentum fluid into the near wall region, which can help to control separation. The most effective VGJs enter the boundary layer at a relatively shallow pitch angle (typically 30 to 45 degrees) relative to the wall and a high skew angle (45 to 90 degrees) relative to the main flow. The jets also promote transition, and turbulent mixing helps to mitigate separation. Several studies (e.g. [11,12]) used VGJs on the highly loaded Pack B LPT airfoil. Separation was essentially eliminated, even at the lowest Reynolds number considered, (Re=25000 based on suction surface length and nominal exit velocity). Pulsed jets were more effective than steady jets. The initial disturbance created by each pulse caused the boundary layer to attach. The turbulence was followed by a calmed period (Gostelow et al. [13] and Schulte and Hodson [14]) during which the boundary layer was very resistant to separation but very laminar-like in terms of its fluctuation levels and low losses. When the time between pulses was long enough, the boundary layer did eventually relax to a separated state, but due to the control which persisted during the calmed period, the VGJs were effective even with low jet pulsing frequencies, duty cycles and mass flow rates. Since the boundary layer was attached and undisturbed for much of the jet pulsing cycle, profile losses were low.

In the present study, the very highly loaded L1A airfoil is used. The L1A is an aft loaded blade designed at the Air Force Research Laboratory (AFRL) and available on a limited basis from Clark [15]. Dimensions as used in the present study are given in Table 1. The L1A has a Zweifel coefficient of 1.35, which corresponds to 10% higher loading than the "ultra-high lift" airfoils described by Zhang and Hodson [7], and 17% higher loading than the Pack B. Because the L1A is highly loaded and aft loaded, it is prone to separation, as documented in Bons et al. [16] and Volino [3]. In cases without flow control and low Reynolds numbers, the boundary layer separates and does not reattach, in spite of transition to turbulence in the shear layer over the separation bubble. This result contrasts with the results of studies on less aggressive airfoils, which all showed reattachment after transition. The failure to reattach results in a 20% loss in lift and increases profile losses by up to a factor of 7 compared to high Reynolds number cases.

Separation control with VGJs has been demonstrated on the L1A airfoil by Bons et al. [16], who considered a case with *Re*=50000, background freestream turbulence *TI*=3%, and periodic wakes, and by Volino et al. [17], who considered cases with *TI*=0.6% and documented pressure distributions on the airfoils and total pressure losses. Cases were considered at Reynolds numbers from 25000 to 100000 (10000 to 40000 based on inlet velocity and axial chord). Jet pulsing frequency was varied from *F*=0.14 to 1.12 with duty cycles of 10% and 50% and blowing ratios ranging from 0.25 to 3.0. In agreement with previous studies, pulsed jets were more effective than steady jets. Separation control was achieved at *Re*=25000 with *B*=0.75, *F*=0.56 and *D*=10%, and at *Re*=50000 with *F*=0.56, *B*=0.25 and *D*=10%. Partial control was possible at lower frequencies, particularly with higher blowing ratios or duty cycles. Lower frequencies were more effective at *Re*=50000 than at *Re*=25000. Effective separation control resulted in a 20% increase in lift, and up to a 60% reduction in total pressure loss, dropping from about 5 times the high *Re* value to about twice the high *Re* value.

In the present study, the cases of Volino et al. [17] are examined in more detail. In addition to the measurements presented previously, velocity in the suction surface boundary layer is used to document and explain the flow separation and reattachment, and the effect of the VGJs.

EXPERIMENTAL FACILITY AND MEASUREMENTS

Experiments were conducted in a closed loop wind tunnel with a seven blade linear cascade located in the wind tunnel's third turn, as shown in Fig. 1a. A fine screen located upstream of the cascade is used to provide uniform inlet conditions and 0.6% freestream turbulence intensity as noted in Volino [3]. The freestream turbulence intensity in an engine is expected to be of the order 4%, which would result in more rapid transition of the boundary layer and resistance to separation, as shown in Volino et al. [18]. The effect of wakes from upstream airfoils would be similar. The present experiments provide a more challenging case for flow control and a baseline for cases with higher freestream turbulence and wakes, some of which are documented in Volino et al. [19].

A tailboard and flaps, shown in Fig. 1a, are used to produce periodicity at high Reynolds numbers. At low Reynolds numbers, when significant separation bubbles are present, the periodicity is not as good due to suppression of the separation bubble thickness on the blades closest to the tailboard as discussed in Volino [3]. In cases with effective flow control, periodicity is reestablished.

Each blade in the cascade has a central cavity which extends along the entire span. As explained in Volino et al. [17], compressed air is supplied to the cavities through fast response solenoid valves. A single spanwise row of holes was drilled into the suction surface of each blade at the inviscid pressure minimum location, s/L_s=0.5 (x/C_x=0.62), which is about the optimal location for flow control devices. The holes are 0.8 mm in diameter and drilled at 30° to the surface and 90° to the main flow direction, as shown in Fig. 1b. The hole spacing is 10.6 diameters, and the length to diameter ratio is 12. With steady blowing and *B*=1, the mass flow rate of the jets is 0.04% of the main flow. With pulsed jets the mass flow is proportionally lower. The solenoid valves pulse the VGJs, and the pulsing frequency in dimensionless form is $F=fL_{j\text{-}te}/U_{ave}$. Blowing ratio for pulsed jets is the ratio of maximum velocity in the pulse to local freestream velocity, as explained in Volino et al. [17].

The center blade, designated B4 in Fig. 1, contains pressure taps near the spanwise centerline. Stagnation pressure is measured with a pitot tube upstream of the cascade. The uncertainty in the suction side pressure coefficients, *Cp*, is 0.07. Total pressure losses are documented using a Kiel probe traversed across three blade spacings, 0.63 C_x downstream of the cascade.

Velocity profiles on the suction surface were measured near the midspan at the six streamwise stations listed in Table 2 with a hot-wire probe. At each measurement location, data were acquired for 26 seconds at a 20 kHz sampling rate (2^{19} samples). Data were acquired at 40 wall normal locations in each profile. The data were both time averaged and ensemble averaged based on the phase within the jet pulsing cycle at 24 dimensionless times, *t/T*, within the pulsing cycle.

Table 1: Cascade parameters

Axial Chord, C_x [mm]	True Chord [mm]	Pitch, L_ϕ [mm]	Span [mm]	Suction side, L_s [mm]	Inlet flow angle	Exit flow angle
134	146	136	724	203	35°	60°

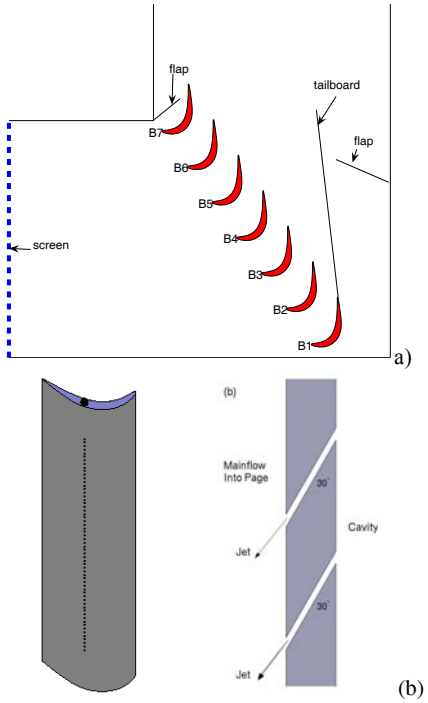

Fig. 1 Drawings of test section: a) linear cascade, b) airfoil with VGJ holes and cross section of hole geometry

Table 2: Velocity profile measurement stations

Station	1	2	3	4	5	6
s/L_s	0.53	0.59	0.69	0.78	0.88	0.97
x/C_x	0.65	0.72	0.80	0.86	0.92	0.97

Wavelet spectra of the fluctuating velocity were computed using the method described in Volino [20]. In contrast to Fourier spectra, in which a signal is transformed from the time domain to the frequency domain, wavelet spectra provide the frequency content of a signal on a time resolved basis. The Mexican Hat wavelet was used for the analysis. The wavelet spectra were ensemble averaged to show frequency as a function of phase within the pulsing cycle.

RESULTS

Re=25000

Pressure profiles for cases with *Re*=25000 are shown in Fig. 2. The inviscid profile for the L1A airfoil is shown as a reference. The low peak followed by a plateau in the case without jets indicates separation without reattachment. As shown in Volino et al. [17], steady blowing with *B*=2.0 or lower has no effect on separation, but with *B*=3.0, there are some signs of reattachment, although the *Cp* profile remains significantly different from the inviscid profile. With *B*=1.0, pulsed jets with *F*=0.28 and *D*=10% have little effect, but with *F*=0.28 and *D*=50% the *Cp* values drop near the trailing edge, indicating some reattachment after a large separation bubble. The *F*=0.56 and *F*=1.12 profiles with *D*=10% are very similar to the *F*=0.28, *D*=50% case. Total pressure loss profiles are shown in Fig. 2b and agree with the *Cp* profiles. A high Reynolds number (300000) case from Volino [3] is shown for comparison. The loss, ψ, is shown as a function of distance across the cascade, ϕ, normalized on the blade spacing L_ϕ. The origin, ϕ=0, corresponds to the location downstream of the trailing edge of the center blade (B4 in Fig. 1a) in the flow direction. Steady blowing with *B*=3.0 reduces

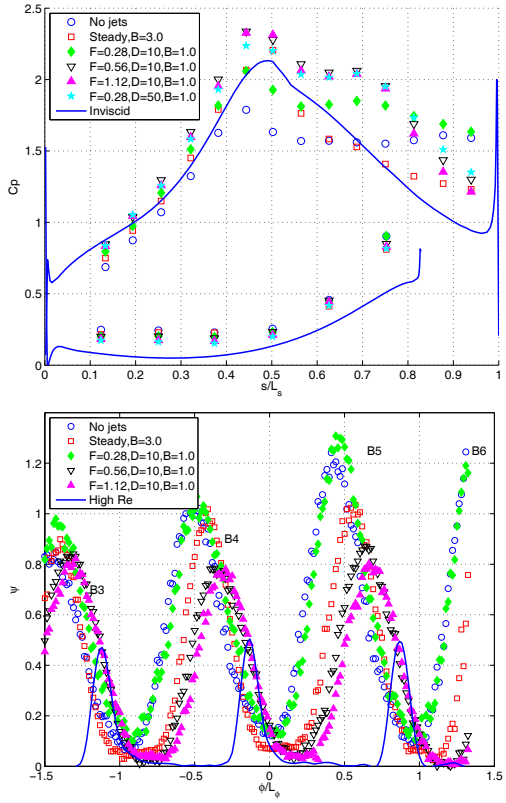

Fig. 2 Pressure results for Re=25000 cases: a) Cp, b) total pressure loss

the loss peaks somewhat, reestablishes periodicity, and causes the loss peaks to shift to the right. The shift indicates an increase in flow turning of about 6°. The integrated total pressure loss for the passage, however, actually increases by 28% over the no-jet case due to the losses in the jets between the plenum and hole exit, as documented in Volino et al. [17]. Pulsed jets at F=0.28, D=10% and B=1.0 have no effect in reducing losses. The F=0.56 and 1.12 cases with D=10% are very similar to each other and have about 29% lower losses than the no-jet case. The flow turning is increased by about 9° compared to case without jets. In these higher F cases the integrated loss is still almost 4 times higher and the flow turning is 4° lower than the high Re case. The exit flow angle for the high Re case is within 1° of the design exit flow angle.

Figure 3 shows time averaged velocity profiles. The top row shows the mean velocity at the six streamwise stations of Table 2, and the lower row shows the rms fluctuating streamwise velocity, u'. Without flow control, the boundary layer has separated by Station 1 and the separation bubble grows at the downstream stations. The peak in u' is in the shear layer far from the wall. With steady B=3.0, u' is higher at the upstream stations, and separation appears to be delayed until Station 2. The boundary layer still separates, however, and does not reattach. The separation bubble is about ¾ the thickness of the no-jet case. The reduction in bubble thickness agrees with the slightly lower loss peaks and somewhat greater flow turning in Fig. 2 compared to the no-jet case. With F=0.28 and D=10%, u' is higher and the shear layer slightly thicker than in the no-jet case, but there is no significant change in the separation bubble thickness, in agreement with the Fig. 2 results. With F=0.28 and D=50% and with F=0.56 or 1.12 and D=10%, a separation bubble is still visible between Stations 2 and 5, but it is much thinner than in the other cases, and the boundary layer is reattached by the trailing edge. The peak in u' is close to the wall.

Phase averaged mean velocity profiles for the F=0.28 cases are shown in Fig. 4. The columns correspond to the six streamwise stations, and rows are for different phases in the pulsing cycle. With D=10%, the boundary layer separates and does not reattach at most phases. The low, nearly constant velocity near the wall indicates the bubble. The measured velocity is not zero in the bubble because the hot-wire cannot distinguish direction, so reversed flow and

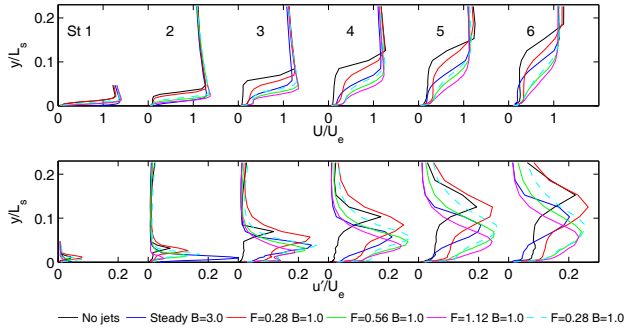

Fig. 3 Time averaged velocity profiles for Re=25000 cases with steady jets or D=10% (solid lines), and D=50% (dashed lines): top – mean velocity, bottom – rms velocity

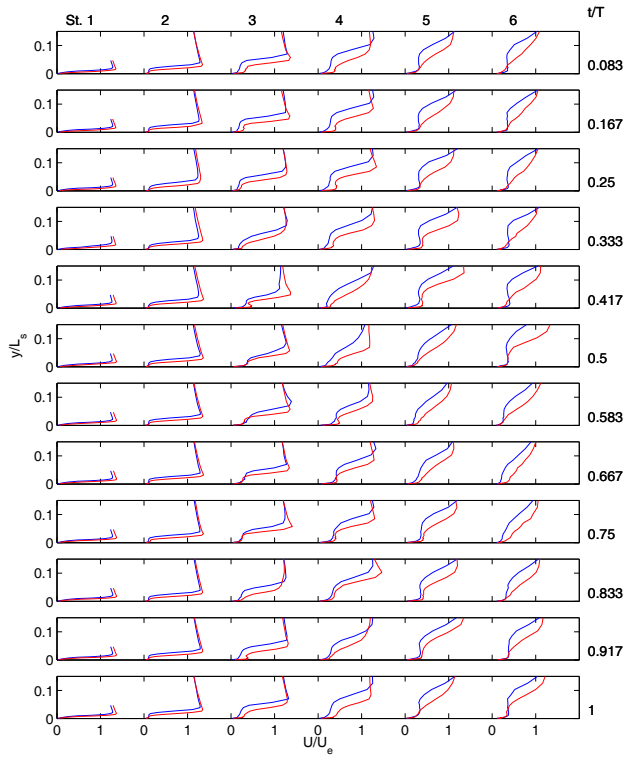

Fig. 4 Phase averaged mean velocity profiles for Re=25000, F=0.28, B=1.0 cases, columns for six streamwise stations, rows for phases in pulsing cycle: blue – D=10%, red – D=50%

turbulence cause a false positive mean velocity in the bubble. At t/T=0.333, 0.5, 0.583, and 0.667 to 0.75 at Stations 3-6 respectively, the near wall region of low velocity is less apparent and the velocity goes more continuously toward zero at the wall. This indicates reattachment at these phases. Figure 5a shows wavelet spectra for the F=0.28, D=10% case. The six plots in the figure correspond to the six streamwise stations. In each plot, the horizontal axis shows dimensionless frequency, fL_s/U_e on a log scale, and the vertical axis shows dimensionless time, t/T, for one pulsing cycle. Power spectral density is computed from instantaneous velocity data at all y locations and is shown for the y location corresponding to maximum time averaged u' at each station. The contours show the power spectral density premultiplied by frequency and normalized by U_e^2. The color scale is the same for all plots. The VGJs creates a disturbance at the beginning of a pulse, and the leading edge of this disturbance is visible as high contours centered at t/T=0.11, 0.24, 0.26, 0.36, 0.43 and 0.49 at Stations 1-6 respectively. The arrival times at each station indicate that the leading edge of the disturbance convects along the surface at about 0.5 times the local freestream velocity (marked by solid white line). A second peak appears centered at t/T=0.19, 0.39, 0.46, 0.60, 0.75 and 0.91 at Stations 1-6

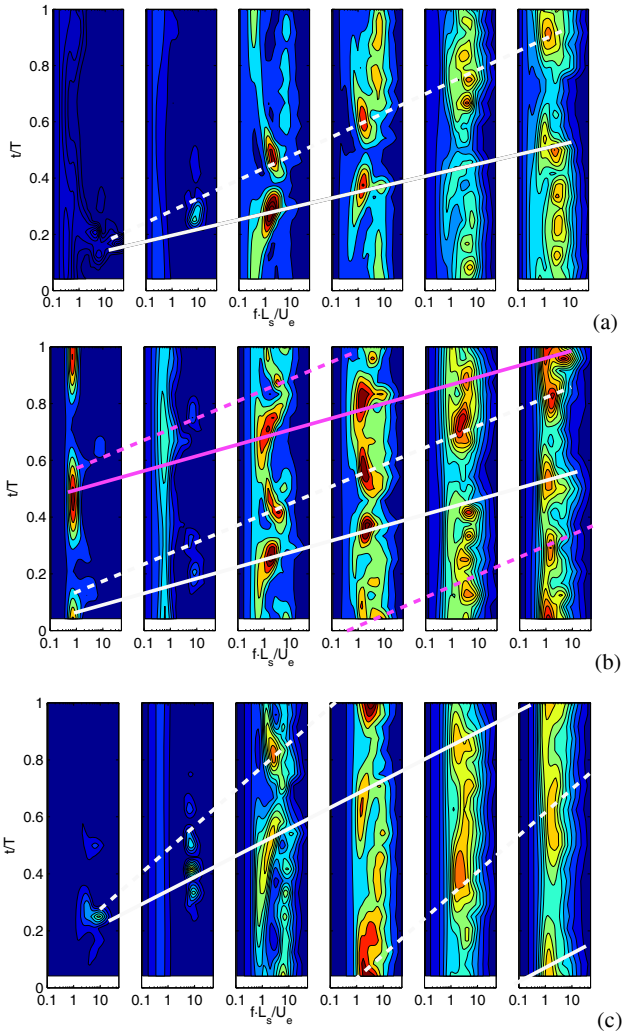

Fig. 5 Wavelet spectra for Re=25000, B=1.0 computed at y locations of maximum u′ in time averaged profiles and shown as function of time and frequency at six streamwise stations: a) F=0.28, D=10%, b) F=0.28, D=50%, c) F=0.56, D=10%

respectively. These peaks are believed to result when the trailing edge of the VGJ disturbance passes, and the times indicate a convection speed of about 0.3 times the freestream velocity (marked by dashed white line). The arrival times of the disturbance in Fig. 5 are just prior to the reattachment times in Fig. 4. With the strong adverse pressure gradient, the boundary layer separates again even before the trailing edge of the disturbance passes. Peaks appear in Fig. 5 at the dimensionless frequency, fL_s/U_e=1.4, and tails of these peaks extend to the pulsing frequency, which is 0.7 for this case. A higher frequency peak at fL_s/U_e≈7 is also visible, particularly at Stations 1 and 2. The higher frequency is likely related to shear layer transition, and matches the frequency peak observed in transition without flow control in Volino et al. [3]. At the downstream stations there is a broader range of frequencies for the full cycle, since the shear layer has transitioned to turbulent.

When the duty cycle is increased to 50% with F=0.28, the separation bubble is thinner. Figure 4 shows boundary layer reattachment at about the same phases as in the *D*=10% case. It then starts to re-separates, but at Stations 5 and 6 it reattaches again about half a cycle later. This second reattachment means less time for the separation bubble to grow, resulting in a thinner separation at all times. The wavelet spectra of Fig. 5b show the disturbance responsible for the second reattachment. When the VGJ turns on, it creates a disturbance much like that in the *D*=10% case. When the jet turns off half a cycle later, it creates a second disturbance which moves down the surface at about the same velocity as the first disturbance (marked by magenta lines). This second disturbance also causes reattachment. In the *D*=10% case, the jets turn off only 0.1 cycle after they turn on, so the on and off disturbances act essentially as a single event. With *D*=50% there is more time between the on and off disturbances, so they act as two separate events. The result is two effective disturbances per cycle, thereby doubling the disturbance frequency above the pulsing frequency and providing better separation control.

Figures 5c shows wavelet spectra for the *F*=0.56, *D*=10% case. The convection velocity of the disturbances is about the same as with *F*=0.28, but the period, *T*, is shorter, so the disturbances occupy a larger fraction of the cycle, and there is less time between disturbances for the separation bubble to grow. The time averaged profiles for the *F*=0.28, *D*=50% and *F*=0.56, *D*=10% cases in Fig. 3 are very similar, since these two cases have the same effective disturbance frequency (due to the doubling of the pulsing frequency with *D*=50% discussed above). The frequencies of the largest peaks in Fig. 5c are about fL_s/U_e=2.6, which is which is roughly double that in the *F*=0.28 cases, probably due to the higher pulsing frequency. As in the *F*=0.28 case, peaks associated with shear layer transition at fL_s/U_e≈7 are visible at Stations 1 and 2. The wavelet spectra for the *F*=1.12, *D*=10% case (not shown) are very similar to those with *F*=0.56, although the peak frequency is increased to about fL_s/U_e=3.7 since the pulsing frequency is higher. Upstream peaks at fL_s/U_e≈7 are still visible. Since the disturbance occupy nearly the entire cycle by the downstream stations with *F*=0.56, increasing to *F*=1.12 has little additional effect, as shown by the mean profiles in Fig. 3.

Re=50000

Pressure profiles for the cases with *Re*=50000 are shown in Fig. 6. Without flow control the boundary layer does not reattach. As shown in Volino et al. [17], steady jets become effective when $B \geq 1.5$, and by *B*=2 the separation is nearly eliminated and the loss peak magnitude and width are greatly reduced. The integrated loss is about the same as in the no-jet case due to the loss associated with the pressure drop from the plenum to the jet exit. Flow turning is increased 12° compared to the no-jet case. With pulsed jets and *B*=1.0, pulsing with *F*=0.14 has only a limited affect with *D*=10%, but with *F*=0.14 and *D*=50% the boundary layer reattaches after a large separation bubble. Losses drop to about half the value in the no-jet case and flow turning increases 12° from the no-jet case. With *F*=0.28 and *D*=10%, the *Cp* profile is about the same as in the *F*=0.14, *D*=50% case, but the loss peak is somewhat wider and the shift in the peak indicates about 3° less flow turning. With *F*=0.56, Cp shows a slightly smaller separation bubble than at the lower frequencies, the losses are reduced to 40% of the no-jet case, and flow turning is 13° higher than the no-jet case. Increasing the duty cycle from 10% to 50% has little effect when *F*=0.56. The losses with *F*=0.56 are about 2.4 times those in the high *Re* reference case and there is about 3° less flow turning due to the presence of the separation bubble and thicker boundary layer at *Re*=50000.

Figure 7 shows time averaged velocity profiles for the steady and *D*=10%, *Re*=50000 cases. A large separation bubble without reattachment is present without flow control. Steady jets with *B*=2.0 eliminate the separation, in agreement with the *Cp* profiles of Fig. 6. With *F*=0.14 the separation is nearly as large as in the no-jet case, but the shear layer is somewhat thicker and u′ levels are higher. With *F*=0.28 there is small separation bubble at Stations 3 and 4, but the boundary layer reattaches downstream. With *F*=0.56 the boundary layer appears attached at all stations. Figure 8 shows the effect of duty cycle. With *F*=0.14, increasing the duty cycle from 10% to 50% greatly reduces the separation bubble thickness, although a small bubble is still present when *D*=50%. When *F*=0.56, duty cycle appears to have no effect, in agreement with the pressure results of Fig. 6. The boundary layer is attached with both *D*=10% and 50%.

Phase averaged mean velocity is shown for the *F*=0.14 cases in Fig. 9. With *D*=10%, the boundary layer appears to be close to reattaching at *t/T*=0.25, 0.333, 0.417 and 0.5 at Stations 3 through 6 respectively. With *D*=50%, reattachment occurs at about the same phases as in the *D*=10% case. The boundary layer then starts to re-separate, but at Stations 5 and 6 it reattaches again about half a cycle

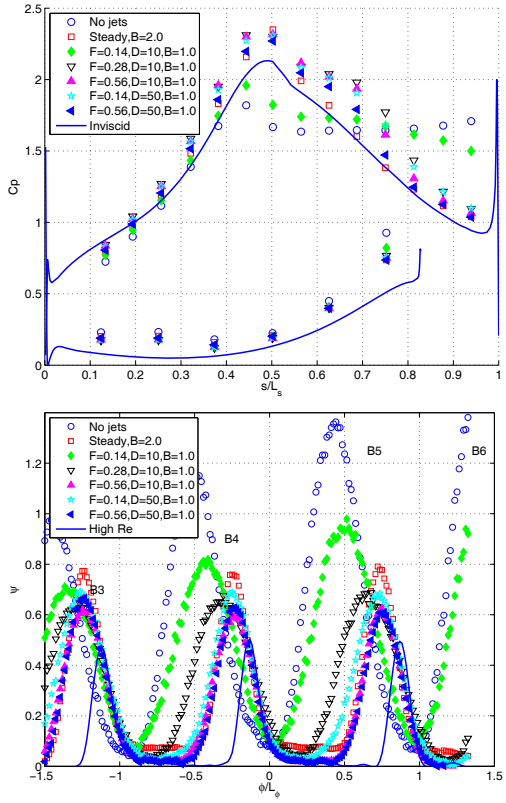

Fig. 6 Pressure results for Re=50000 cases: a) Cp, b) total pressure loss

later. This second reattachment means less time for the separation bubble to grow, resulting in a thinner separation at all times. The first reattachment corresponds to the arrival of the disturbance created when the VGJs are turned on. The second reattachment corresponds to the disturbance created when the VGJs turn off. As in the Re=25000 case, increasing the duty cycle to 50% separates in time the disturbances created when the VGJs turn on and off, thereby doubling the frequency of separation control events above the pulsing frequency. The result, as shown in Fig. 9, is a reattached boundary layer for most of the cycle by the downstream stations. The same effect can be achieved by doubling the pulsing frequency to F=0.28 with D=10%.

CONCLUSIONS

The effect of vortex generator jets on the flow over the very high lift L1A airfoil was studied under low freestream turbulence conditions. Reynolds numbers based on suction surface length and nominal exit velocity of 25000 and 50000 were considered. Without flow control, the boundary layer separated and did not reattach. Flow control with VGJs was possible even at Re=25000. In agreement with previous studies, pulsed jets were more effective than steady jets. Effective separation control resulted in a 20% increase in lift and up to a 60% reduction in total pressure loss compared to baseline cases at the same Reynolds number. Loss values still remain higher than in high Reynolds number cases. Phase averaged velocity profiles and wavelet spectra show the boundary layer intermittently reattaching as disturbances pass and then separating between disturbances. Increasing the pulsing frequency reduces the time available for separation. When the time available is sufficiently small, the boundary layer remains attached at all times. At Re=25000, separation was nearly fully controlled for the full pulsing cycle when F=0.5 and D=10%. Higher frequency pulsing provided little additional benefit. At Re=50000 the separation bubble grows more slowly, so F=0.3 is sufficient. At lower pulsing frequencies, increasing the duty cycle to 50% is helpful. The most effective disturbances for controlling separation are created when the VGJs turn on and off, and increasing the duty

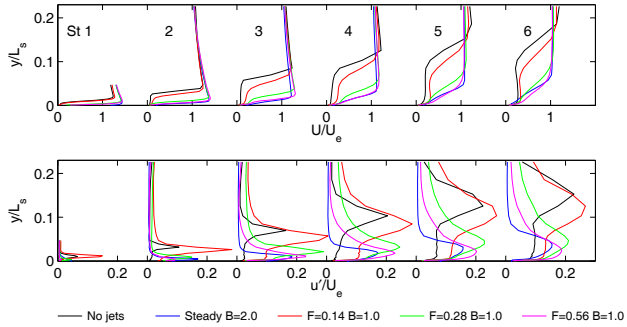

Fig. 7 Time averaged velocity profiles at six streamwise stations for Re=50000 cases with steady jets or D=10%: top – mean velocity, bottom – rms velocity

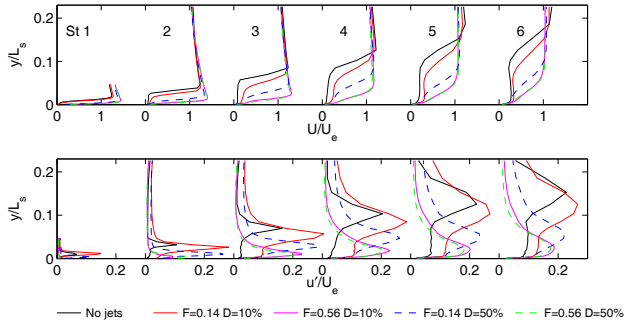

Fig. 8 Time averaged velocity profiles at six streamwise stations for Re=50000 cases with D=10% (solid lines), and D=50% (dashed lines): top – mean velocity, bottom – rms velocity

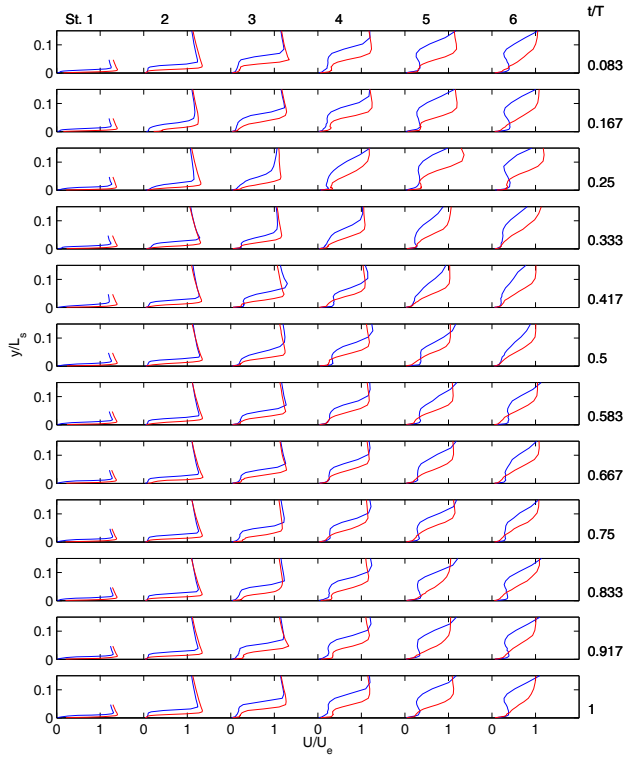

Fig. 9 Phase averaged mean velocity profiles for Re=50000, F=0.14, B=1.0 cases, columns for six streamwise stations, rows for phases in pulsing cycle: blue – D=10%, red – D=50%

cycle to 50% separates in time the on and off events, thereby doubling the frequency of flow control events above the pulsing frequency.

ACKNOWLEDGMENT

This work was sponsored by the National Aeronautics and Space Administration under grant NNC07IA10I. The grant monitors were Drs. Anthony Strazisar and James Heidmann of the NASA Glenn Research Center. The support of the United States Naval Academy Technical Support Department Shop and Fluids Laboratory is greatly appreciated.

NOMENCLATURE

Symbol	Quantity	SI Unit
B	blowing ratio	
Cp	$2(P_T - P)/\rho U_e^2$, pressure coefficient	
C_x	axial chord	m
D	duty cycle	%
F	$fL_{j\text{-}te}/U_{ave}$	
f	frequency	Hz
$L_{j\text{-}te}$	distance from VGJs to trailing edge	m
L_s	suction surface length	m
L_ϕ	blade spacing (pitch)	m
P	pressure	kPa
P_S	upstream static pressure	kPa
P_T	upstream stagnation pressure	kPa
P_{Te}	downstream stagnation pressure	kPa
Re	$U_e L_s/\nu$, exit Reynolds number	
s	streamwise coordinate	m
T	period of jet pulsing cycle	s
t	time	s
U_{ave}	average freestream velocity between VGJ holes and trailing edge	m/s
U_e	nominal exit freestream velocity	m/s
u'	rms fluctuating streamwise velocity	m/s
x	axial distance from leading edge	m
ϕ	coordinate along blade spacing	m
ν	kinematic viscosity	m^2/s
ρ	density	kg/m^3
ψ	$(P_T\text{-}P_{Te})/(P_T\text{-}P_S)$, total pressure loss	

REFERENCES

[1] Wisler, D.C., 1998, "The Technical and Economic Relevance of Understanding Boundary Layer Transition in Gas Turbine Engines," *Minnowbrook II, 1997 Workshop on Boundary Layer Transition in Turbomachines*, LaGraff, J.E., and Ashpis, D.E., eds., NASA/CP-1998-206958, pp. 53-64.

[2] Mayle, R.E., 1991, "The Role of Laminar-Turbulent Transition in Gas Turbine Engines," ASME *Journal of Turbomachinery*, **113**, pp. 509-537.

[3] Volino, R.J., 2010, "Separated Flow Measurements on a Highly Loaded Low-Pressure Turbine Airfoil," ASME *Journal of Turbomachinery*, **132**, 011007.

[4] Volino, R.J., 2002, "Separated Flow Transition Under Simulated Low-Pressure Turbine Airfoil Conditions: Part 1 – Mean Flow and Turbulence Statistics," ASME *Journal of Turbomachinery*, **124**, pp. 645-655.

[5] Volino, R.J., 2002, "Separated Flow Transition Under Simulated Low-Pressure Turbine Airfoil Conditions: Part 2 – Turbulence Spectra," ASME *Journal of Turbomachinery*, **124**, pp. 656-664.

[6] Praisner, T.J., and Clark, J.P., 2007, "Predicting Transition in Turbomachinery – Part 1: A Review and New Model Development," ASME *Journal of Turbomachinery*, **129**, pp. 1-13.

[7] Zhang, X.F., Vera, M., Hodson, H., and Harvey, N., 2007, Separation and Transition Control on an Aft-Loaded Ultra-High-Lift LP Turbine Blade at Low Reynolds Numbers: Low-Speed Investigation," ASME *Journal of Turbomachinery*, **128**, pp. 517-527.

[8] Bohl, D.G., and Volino, R.J., 2006, "Experiments with Three-Dimensional Passive Flow Control Devices on Low-Pressure Turbine Airfoils," ASME *Journal of Turbomachinery*, **128**, pp. 251-260.

[9] Huang, J., Corke, T., and Thomas, F., 2003, "Plasma Actuators for Separation Control on Low Pressure Turbine Blades," AIAA Paper 2003-1027.

[10] Johnston, J.P., and Nishi, M., 1990, "Vortex Generator Jets. Means for Flow Separation Control," *AIAA Journal*, **28**, pp. 989-994.

[11] Bons, J.P., Sondergaard, R., and Rivir, R.B., 2002, "The Fluid Dynamics of LPT Blade Separation Control Using Pulsed Jets," ASME *Journal of Turbomachinery*, **124**, pp. 77-85.

[12] Volino, R.J., 2003, "Separation Control on Low-Pressure Turbine Airfoils Using Synthetic Vortex Generator Jets," ASME *Journal of Turbomachinery*, **125**, pp. 765-777.

[13] Gostelow, J.P., Walker, G.J., Solomon, W.J., Hong, G., and Melwani, N., 1997, "Investigation of the Calmed Region Behind a Turbulent Spot," ASME *Journal of Turbomachinery*, **119**, pp. 802-809.

[14] Schulte, V., and Hodson, H.P., 1998, "Prediction of the Becalmed Region for LP Turbine Profile Design," ASME *Journal of Turbomachinery*, **120**, pp. 839-846.

[15] Clark J.P., 2007, Private Communication, Air Force Research Laboratory.

[16] Bons, J.P., Pluim, J., Gompertz, K., Bloxham, M., and Clark, J.P., 2008, "The Application of Flow Control to an Aft-Loaded Low Pressure Turbine Cascade with Unsteady Wakes," ASME Paper GT2008-50864.

[17] Volino, R.J., Kartuzova, O., and Ibrahim, M.B., 2009, "Experimental and Computational Investigations of Low-Pressure Turbine Separation Control Using Vortex Generator Jets," ASME Paper GT2009-59983.

[18] Volino, R.J, Kartuzova, O., and Ibrahim, M., 2008, "Experimental and Computational Investigations of Separation and Transition on a Highly Loaded Low Pressure Turbine Airfoil: Part 2 – High Freestream Turbulence Intensity," ASME Paper IMECE2008-68776.

[19] Volino, R.J., Kartuzova, O., and Ibrahim, M.B., 2010, "Separation Control on a Very High Lift Low Pressure Turbine Airfoil Using Pulsed Vortex Generator Jets," ASME Paper GT2010-23567.

[20] Volino, R.J., 2005, "An Investigation of the Scales in Transitional Boundary Layers under High Freestream Turbulence Conditions," *Experiments in Fluids*, **38**, pp. 516-633.

Proceedings of ASME Turbo Expo 2010: Power for Land, Sea and Air
GT2010
June 14-18, 2010, Glasgow, UK

GT2010-23567

SEPARATION CONTROL ON A VERY HIGH LIFT LOW PRESSURE TURBINE AIRFOIL USING PULSED VORTEX GENERATOR JETS

Ralph J. Volino
Mechanical Engineering Department
United States Naval Academy
Annapolis, Maryland 21402-5042
volino@usna.edu

Olga Kartuzova and Mounir B. Ibrahim
Mechanical Engineering Department
Cleveland State University
Cleveland, Ohio 44115-2425
m.ibrahim@csuohio.edu

ABSTRACT

Boundary layer separation control has been studied using vortex generator jets (VGJs) on a very high lift, low-pressure turbine airfoil. Experiments were done under high (4%) freestream turbulence conditions on a linear cascade in a low speed wind tunnel. Pressure surveys on the airfoil surface and downstream total pressure loss surveys were documented. Instantaneous velocity profile measurements were acquired in the suction surface boundary layer. Cases were considered at Reynolds numbers (based on the suction surface length and the nominal exit velocity from the cascade) of 25,000 and 50,000. Jet pulsing frequency, duty cycle, and blowing ratio were all varied. Computational results from a large eddy simulation of one case showed reattachment in agreement with the experiment. In cases without flow control, the boundary layer separated and did not reattach. With the VGJs, separation control was possible even at the lowest Reynolds number. Pulsed VGJs were more effective than steady jets. At sufficiently high pulsing frequencies, separation control was possible even with low jet velocities and low duty cycles. At lower frequencies, higher jet velocity was required, particularly at low Reynolds numbers. Effective separation control resulted in an increase in lift and a reduction in total pressure losses. Phase averaged velocity profiles and wavelet spectra of the velocity show the VGJ disturbance causes the boundary layer to reattach, but that it can re-separate between disturbances. When the disturbances occur at high enough frequency, the time available for separation is reduced, and the separation bubble remains closed at all times.

NOMENCLATURE

B	blowing ratio, maximum jet velocity/local freestream velocity
Cp	$2(P_T - P)/\rho U_e^2$, pressure coefficient
Cp_{int}	pressure coefficient integrated in axial direction
Cp_{inv}	Cp_{int} for invisid flow through cascade
C_x	axial chord length
D	duty cycle, fraction of time valve is open
F	$fL_{j\text{-}te}/U_{ave}$, dimensionless frequency
f	frequency
$L_{j\text{-}te}$	distance from VGJs to trailing edge
L_s	suction surface length
L_ϕ	blade spacing (pitch)
$\dot{m}_j$	jet mass flow rate
$\dot{m}_1$	main flow mass flow rate
P	pressure
P_j	jet plenum pressure
P_S	upstream static pressure
P_T	upstream stagnation pressure
P_{Te}	downstream stagnation pressure
Re	$U_e L_s/\nu$, exit Reynolds number
s	streamwise coordinate, distance from leading edge
T	period of jet pulsing cycle
t	time
U_{ave}	average freestream velocity between VGJs and trailing edge
U_e	nominal exit freestream velocity, based on inviscid solution
u'	rms fluctuating streamwise velocity
x	axial distance from leading edge
Δx^+	grid spacing in axial direction in viscous units
y^+	location of closest grid point to wall in viscous units
Δz^+	grid spacing in spanwise direction in viscous units
ϕ	coordinate along blade spacing, normal to axial chord
ν	kinematic viscosity
ρ	density
ψ	$(P_T\text{-}P_{Te})/(P_T\text{-}P_S)$, total pressure loss coefficient
ψ_{int}	total pressure loss integrated over blade spacing

INTRODUCTION

Boundary layer separation can lead to partial loss of lift and higher aerodynamic losses on low-pressure turbine (LPT) airfoils (e.g. Hourmouziadis [1], Mayle [2], and Sharma et al. [3]). As designers impose higher loading to improve efficiency and lower cost, the associated strong adverse pressure gradients on the suction side of the airfoil can exacerbate separation problems. In aircraft engines, the lower density and therefore lower Reynolds numbers at altitude can lead to a component efficiency drop of 2% between takeoff and cruise in large commercial transport engines, and possibly as much as 7% in smaller engines operating at higher altitudes [4, 5]. Prediction and control of suction side separation, without sacrifice of the benefits of higher loading is, therefore, crucial for improved engine design.

Separation and separated flow transition, which can lead to boundary layer reattachment, have received considerable attention. Lists of various studies are provided by Volino [6, 7]. In general, previous work shows that the strong acceleration on the leading section of the airfoil keeps the boundary layer thin and laminar, even in the presence of elevated freestream turbulence. When separation does occur, it is usually just downstream of the suction peak. If transition then occurs in the shear layer over the separation bubble, it is typically rapid and often causes the boundary layer to reattach [7, 8].

Airfoils can be designed with high resistance to separation, as described by Praisner and Clark [9], but a loading limit will always exist, above which separation will still occur. If flow control were incorporated in the design of an advanced airfoil, as discussed by Bons et al. [10], it might be possible to increase the loading limit. Separation control with passive devices such as boundary layer trips has been shown effective by Zhang et al. [11], Bohl and Volino [12], Volino [13], and others. Passive devices have the distinct advantage of simplicity, but they also introduce parasitic losses and cannot be adjusted to account for changes in flow conditions. Active devices could potentially provide better control over the entire operating range of interest and be reduced in strength or turned off to avoid unnecessary losses when they are not needed. Potential disadvantages of active devices are the cost of implementation and the possibility of control failure, particularly in aircraft engines.

The literature contains many examples of active separation control. A few which could be applied in turbomachinery are discussed in Volino [14]. Plasma devices, as used by Huang et al. [15], could be viable, and are under active study. Vortex generator jets (VGJs), as introduced by Johnston and Nishi [16], are another alternative and the subject of the present study. Blowing from small, compound angled holes is used to create streamwise vortices. The vortices bring high momentum fluid into the near wall region, which can help to control separation. The most effective VGJs enter the boundary layer at a relatively shallow pitch angle (typically 30 to 45 degrees) relative to the wall and a high skew angle (45 to 90 degrees) relative to the main flow. Additionally, the jets promote transition, and turbulent mixing also helps to mitigate separation. Bons et al. [10] noted that in the case of pulsed VGJs, the turbulence effect is more significant than the action of the vortices. Bons et al. [4, 17], Volino [14], Volino and Bohl [18], McQuilling and Jacob [19], and Eldredge and Bons [20] all used VGJs on the highly loaded Pack B LPT airfoil. Separation was essentially eliminated, even at the lowest Reynolds number considered, (Re=25,000 based on suction surface length and nominal exit velocity). Pulsed jets were more effective than steady jets. The initial disturbance created by each pulse caused the boundary layer to attach. The turbulence was followed by a calmed period (Gostelow et al. [21] and Schulte and Hodson [22]) during which the boundary layer was very resistant to separation, much like a turbulent boundary layer, but very laminar-like in terms of its fluctuation levels and low losses. When the time between pulses was long enough, the boundary layer did eventually relax to a separated state, but due to the control which persisted during the calmed period, the VGJs were effective even with low jet pulsing frequencies, duty cycles and mass flow rates. Since the boundary layer was attached and undisturbed for much of the jet pulsing cycle, profile losses were low.

Similar results with pulsed VGJs were found on the L1M airfoil by Bons et al. [23]. The L1M is more highly loaded than the Pack B, but more resistant to separation because of forward loading. A large separation bubble followed by boundary layer reattachment was observed at low Reynolds numbers, and pulsed VGJs reduced the size of the bubble.

In the present study, the very highly loaded L1A airfoil is used. The L1A was designed at the Air Force Research Laboratory (AFRL) and is available on a limited basis from Clark [24]. It is an aft loaded blade with the same flow angles and loading as the L1M. Dimensions of the L1A as used in the present study are given in Table 1. Based on the design calculations of Clark [24], the L1A has a Zweifel coefficient of 1.35, which corresponds to 10% higher loading than the "ultra-high lift" airfoils described by Zhang and Hodson [25], and 17% higher loading than the Pack B. Because the L1A is aft loaded, it is more prone to separation than the L1M, as documented in Bons et al. [26], Volino [6], Ibrahim et al. [27], and Volino et al. [28]. In cases without flow control and low Reynolds numbers, the boundary layer separates and does not reattach, in spite of transition to turbulence in the shear layer over the separation bubble. This result contrasts with the results of studies on less aggressive airfoils, which all showed reattachment after transition. The separation bubble on the L1A is about four times thicker than that on the Pack B. The larger distance from the shear layer to the wall on the L1A apparently prevents the turbulent mixing in the shear layer from reaching the wall and causing reattachment. The failure of the boundary layer to reattach results in a 20% loss in lift and increases profile losses by up to a factor of 7. At higher Reynolds numbers the separation bubble is small and the boundary layer is attached over most of the airfoil.

Separation control with VGJs has been demonstrated on the L1A airfoil. Bons et al. [26] considered a case with Re=50,000, background freestream turbulence TI=3%, and periodic wakes produced with moving rods upstream of the airfoils. The VGJs had a duty cycle (fraction of time the jets are on during a pulsing cycle) D=30% and a blowing ratio B=2.3 (based on the maximum jet velocity in the pulsing cycle and the local freestream velocity). The dimensionless frequency of the wake passing and VGJ pulsing were both $F=fL_{j\text{-}te}/U_{ave}$=0.34, where $L_{j\text{-}te}$ is the streamwise distance from the VGJ holes to the trailing edge, and U_{ave} is the average freestream velocity over this distance. Two different streamwise locations for the VGJs were considered. The VGJs reduced the separation bubble size and reduced total pressure losses. Volino et al. [29] considered cases with TI=0.6%. Pressure distributions on the airfoils and total pressure losses were documented. Cases were considered at Reynolds numbers from 25,000 to 100,000. Jet pulsing frequency was varied from F=0.14 to 1.12 with duty cycles of 10% and 50% and blowing ratios ranging from 0.25 to 3.0. In agreement with previous studies, pulsed jets were more effective than steady jets. At Re=25,000, separation control was achieved with B=0.75, F=0.56 and D=10%. Without flow control the lift at Re=25,000 was about 80% of the high Re lift, and with flow control it was 94% of the high Re lift. Flow control caused the total pressure loss to drop from about five times the high Re value to about 3 times the high Re value. Once good control was achieved, further increasing the frequency, blowing ratio or duty cycle provided little additional benefit. Partial control was possible at lower frequencies, particularly with higher blowing ratios or duty cycles. At Re=50,000 with F=0.56, B=0.25 was sufficient with D=10%. Lower frequencies were more effective at Re=50,000 than at Re=25,000. Effective separation control resulted in a 20% increase in lift, and up to a 60% reduction in total pressure loss, dropping from about 5 times the high Re value to about twice the high Re value.

In the present study, flow control with vortex generator jets is investigated under high (4%) freestream turbulence conditions, which is more representative of engine conditions than the low TI considered in Volino et al. [29]. Cases with a range of pulsing frequencies and blowing ratios are considered. In addition to pressure distributions, instantaneous boundary layer velocity measurements are used to explain the mechanism by which the VGJs control separation.

Table 1: Cascade parameters

Axial Chord, C_x [mm]	True Chord [mm]	Pitch, L_ϕ [mm]	Span [mm]	Suction side, L_s [mm]	Inlet flow angle	Exit flow angle
134	146	136	724	203	35°	60°

EXPERIMENTAL FACILITY AND MEASUREMENTS

Experiments were conducted in a closed loop wind tunnel with a seven blade linear cascade located in the wind tunnel's third turn, as shown in Fig. 1a. A coarse grid, consisting of a 1.5 mm thick sheet metal plate with 19 mm square holes spaced 25.4 mm apart, center to center, in both directions is located upstream of the cascade. In a plane perpendicular to the inlet flow and $1.7C_x$ upstream of the center blade, the grid produced uniform flow with TI=6.0% in the streamwise component and 4.2% in the cross stream components, for an overall intensity of 4.9%. The integral length scale of the freestream turbulence is $0.12C_x$ in the streamwise component and $0.04C_x$ in the other components. The streamwise component was also measured at the inlet plane of the cascade in the four center passages, where it had decayed to between 4 and 4.2% between blades B2 and B5 and 4.6% between blades B5 and B6. Downstream of the cascade, the local TI is 1.8% across all passages, as documented in Volino et al. [28]. The local freestream turbulence intensity in the passage at the beginning of the adverse pressure gradient region is 1.4%. The change in TI through the passage is due mainly to the change in the local freestream velocity along with some decay of the turbulence.

A tailboard, shown in Fig. 1a, is needed to produce the correct exit flow angle from the cascade. Its position was set to produce periodicity at high Reynolds numbers. A tailboard on the opposite side of the cascade, and inlet guide vanes were found to be unnecessary. To produce the correct approach flow to the end blades (B1 and B7), the amount of flow escaping around the two ends of the cascade is controlled with the flaps shown in Fig. 1a. The inlet flow angle was checked with a three-hole pressure probe and found to agree with the design angle to within 2° of uncertainty. Good periodicity at high Reynolds numbers was obtained in the exit flow. At low Reynolds numbers, when significant separation bubbles are present, the periodicity is not as good due to suppression of the separation bubble thickness on the blades closest to the tailboard. In cases with effective flow control, periodicity is reestablished. The lack of periodicity in cases with large separation bubbles is considered acceptable since the focus of the study is separation control, and not documentation of cases with large separation that would be unacceptable in practice. This compromise facilitates the study of a larger number of cases with flow control by obviating the need to adjust the tailboard by trial and error for each case. It also provides for better repeatability in the experiments, since the position of the tailboard is fixed for all cases. Any improvements made with flow control will be larger in practice than documented in the experiment, due to the effect of the tailboard in suppressing the bubble size in the uncontrolled cases.

Each blade in the cascade has a central cavity which extends along the entire span. As explained in Volino et al. [29], compressed air is supplied to the cavities from a common manifold. The manifold is supplied through two fast response solenoid valves (Parker Hannifin 009-0339-900 with General Valve Iota One pulse driver) operating in parallel. A single spanwise row of holes was drilled into the suction surface of each blade at the inviscid pressure minimum location, s/L_s=0.5 (x/C_x=0.62), where s is the distance from the leading edge and L_s is the suction surface length. The pressure minimum has been shown in the studies listed above to be about the optimal location for flow control devices. The holes are 0.8 mm ($0.006C_x$) in diameter and

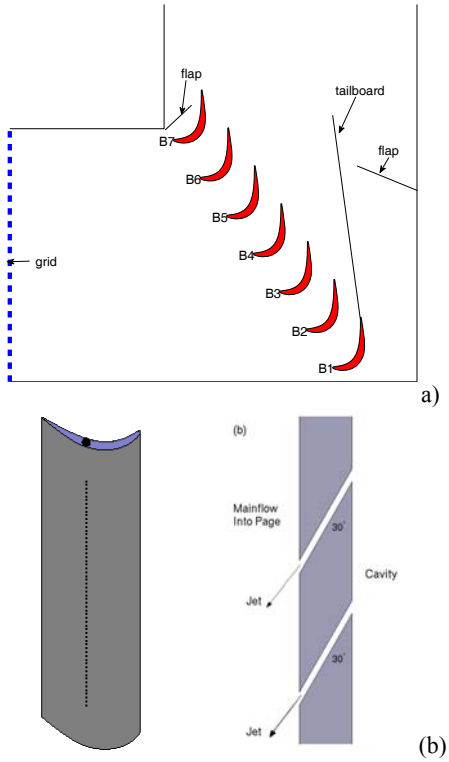

Fig. 1 Drawings of test section: a) linear cascade, b) airfoil with VGJ holes and cross section of hole geometry

drilled at 30° to the surface and 90° to the main flow direction, as shown in Fig. 1b. This is the same orientation used in all the VGJ studies listed above. The hole spacing is 10.6 diameters, and the length to diameter ratio is 12. With steady blowing and B=1, the mass flow rate of the jets is 0.04% of the main flow mass flow rate. With pulsed jets the mass flow is lower, particularly in low duty cycle cases.

The solenoid valves pulse the VGJs, and the pulsing frequency is presented below in dimensionless form as $F=fL_{j\text{-}te}/U_{ave}$. For flow over single airfoils, $F\geq1$ is typically needed to maintain separation control, but for cascades, Bons et al. [17] showed that control is possible in some cases with F=0.1. As shown in Volino [14] and Bons et al. [17], this is due to the extended calmed region which follows the jet disturbance. In practice, VGJs could be timed to wake passing in an LPT, which has a typical frequency of about F=0.3.

The center blade, designated B4 in Fig. 1, contains pressure taps near the spanwise centerline. Pressure surveys are made using a pressure transducer (0-870 Pa range Validyne transducer). Stagnation pressure is measured with a pitot tube upstream of the cascade. The uncertainty in the suction side pressure coefficients, Cp, is 0.07. Most of this uncertainty is due to bias error. Stochastic error is minimized by averaging pressure transducer readings over a 10 second period.

Total pressure losses are documented using a Kiel probe traversed across three blade spacings, 0.63 C_x downstream of the cascade. A traverse is located in the wind tunnel downstream of the cascade to move the probe. The traverse causes an acceptably low blockage when it is located at least two C_x downstream of the cascade.

Pressure and loss surveys were acquired at nominal Re=25,000 and 50,000. The Reynolds number, as defined above, is based on the suction surface length and the nominal cascade exit velocity. The corresponding Reynolds numbers based on the cascade inlet velocity and the axial chord length are 10,000 and 20,000.

The jet velocity was measured at the exit plane of the VGJ holes and was documented in Volino et al. [29]. There is about a 5 ms delay between the opening of the solenoid valve and the beginning of the rise of the jet velocity above zero at the exit plane. The delay corresponds to the time required for a pressure wave to travel from the valve to the jet hole. The jet velocity rises rapidly and nearly continuously for another 6 ms to a maximum and then drops for about 6 ms toward a steady value which is maintained for the rest of the time the valve is open. When the valve closes, the jet velocity drops to zero. In cases with high pulsing frequency or low duty cycle, the jet turns off before a steady velocity is reached. As will be shown below, the transient that occurs when the VGJ turns on is more effective for separation control than the steady blowing which may follow. The initial velocity maximum is therefore used to define the blowing ratio rather than the average velocity for the pulse.

Velocity profiles on the suction surface were measured at the six streamwise stations listed in Table 2. All stations are downstream of the inviscid pressure minimum at s/L_s=0.49. Profiles were acquired near the spanwise centerline of the airfoil with a hot-wire anemometer (AA Lab Systems model AN-1003) and a single sensor hot-film probe (TSI model 1201-20). The sensor diameter is 51 μm, and the active length is 1.02 mm. At each measurement location, data were acquired for 26 seconds at a 20 kHz sampling rate (2^{19} samples). All raw data were saved. The high sampling rate provides an essentially continuous signal, and the long sampling time results in low uncertainty in both statistical and spectral quantities. Data were acquired at 40 wall normal locations in each profile, extending from the wall to the free-stream, with most points concentrated in the near wall region. The probe was positioned as close to tangent to the airfoil surface as possible at each station, such that the probe body extended downstream of the sensor and the direction of the traverse was within 5° of normal to the surface. In most cases the closest point to the wall in each profile was within about 0.2 mm of the wall, which compares to boundary layer thicknesses ranging from 1.1 mm to over 40 mm.

Flow direction in a separation bubble cannot be determined with a single-sensor hot-wire, but velocity magnitude can be measured and was found to be near zero within the bubbles of the present cases when the flow was laminar. In cases where the flow became turbulent but remained separated, fluctuating velocities caused false high mean velocity readings in the separation bubble. With the exception of these turbulent separated cases, the uncertainty in the mean velocity is 3-5% except in the very near wall region, where near-wall corrections (Wills [30]) were applied to the mean velocity.

Velocity data were both time averaged and ensemble averaged based on the phase within the jet pulsing cycle. Phase averages of mean and fluctuating velocity are shown below at 24 dimensionless times, t/T, within the pulsing cycle, where t is time and T is the period of the cycle. The time t/T=0 corresponds to the opening of the solenoid valve.

Wavelet spectra of the fluctuating velocity were computed using the method described in Volino [31]. In contrast to Fourier spectra, in which a signal is transformed from the time domain to the frequency domain, wavelet spectra provide the frequency content of a signal on a time resolved basis. The Mexican Hat wavelet was used for the analysis. The wavelet spectra were phase averaged to show the variation of frequency content in the velocity as a function of time within the jet pulsing cycle.

NUMERICAL SIMULATIONS

Numerical simulations were conducted utilizing version 6.3.26 of the finite-volume code Fluent™[32]. The three dimensional computational domain includes a single passage. A uniform velocity inflow condition is specified $1.9C_x$ upstream of the blade leading edge in the flow direction. The inlet flow angle is set to 33° based on an inviscid calculation of the full cascade used in the experiment [27]. This angle agrees with the experimentally measured inlet angle to within the experiment uncertainty. The exit boundary is located $3.8C_x$ downstream of the trailing edges in the flow direction. In the spanwise direction, the domain includes one VGJ. The boundary conditions on the sides of the passage are periodic. The full length of the hole is included in the simulations, allowing the jet velocity profile to develop before entering the main domain [29]. A uniform velocity boundary condition is specified at the hole inlet during jet blowing. Computation was continued until no variation cycle-to-cycle was reached.

Table 2: Velocity profile measurement stations

Station	1	2	3	4	5	6
s/L_s	0.53	0.59	0.69	0.78	0.88	0.97
x/C_x	0.65	0.72	0.80	0.86	0.92	0.97

Convergence was established when: 1) residuals reduced to a value 10^{-5}, 2) no change was observed in any field results, and 3) the mass imbalance was less than 0.01 %.

Large eddy simulations (LES) were done using the dynamic subgrid-scale kinetic energy model in Fluent, which is based on the model proposed by Kim and Menon [33]. In this model a separate transport equation is solved for subgrid-scale kinetic energy. The model constants are determined dynamically. The details of the implementation of this model in Fluent and its validation are given by Kim [34].

Code Validation

Three different grids were tested as shown in Table 3. Grid#37 was selected. Details of the grid structure are in Ibrahim et al. [35]. To accurately represent structures in the near-wall region (for LES) recommended values are: y^+~2; Δx^+~50-150; Δz^+~15-40 (see Piomelli and Chasnov [36]). Grid#37 produced Cp versus s/L_s results in closest agreement to the experimental data and therefore was chosen for further computation. Computations with Grid#37 were then run for different time steps (0.0005, 0.0001 and 0.00005s) and time step=0.0001s was selected since not much improvement was achieved using the smaller step (0.00005s).

RESULTS

Re=25,000

Pressure profiles for cases with Re=25,000 and steady VGJ blowing are shown in Fig. 2. The inviscid profile for the L1A airfoil is shown as a common reference for comparing results between figures. At high Reynolds numbers (e.g. Re=300,000), experimental results agree with the inviscid line, as shown in Volino et al. [28]. The low peak followed by a plateau in the case without jets in Fig. 2 indicates separation without reattachment. As in the low freestream turbulence cases of Volino et al. [29] at this Reynolds number, blowing with B=2.0 or lower has no effect on separation. When B is increased to 2.5 or 3.0, there are some signs of reattachment, but the Cp profile remains significantly different from the inviscid profile.

Figures 3 shows results for cases with pulsed jets and F=0.14. As in the low freestream turbulence cases, this frequency is too low to be very effective. The jets have some effect on Cp when B=3.0 and this effect increases at higher duty cycle. The total pressure losses for these cases are shown in Fig. 3b. A high Reynolds number (Re=300,000) baseline case from Volino et al. [28] is shown for comparison. The loss, ψ, is shown as a function of distance across the

Table 3: Grid#3, 35 and 37 used in this investigation

Grid #	Size (Cells)	Number of grids in z direction	y^+	Δz^+	Δx^+
3	1,500,000	15	0.5	12.6	1–100
35	5,900,000	30	0.5	6.3	0.4-52
37	11,900,000	54	0.5	0.4-3.5	0.4-52

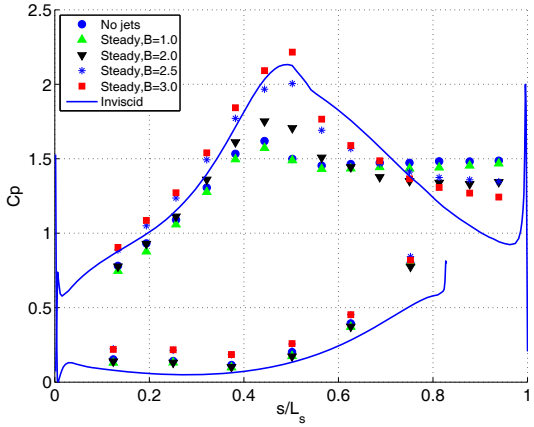

Fig. 2 Cp profiles for steady blowing, Re=25,000 cases

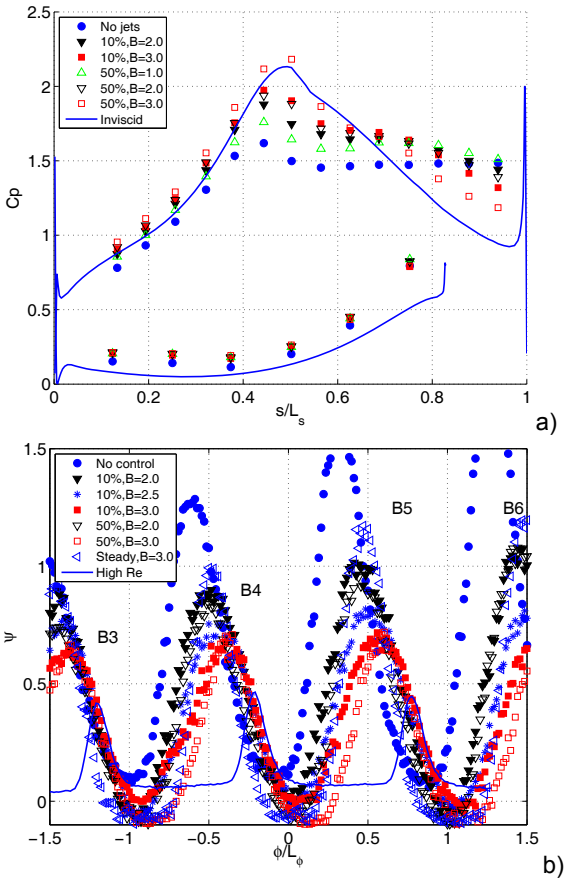

Fig. 3 Pressure results for F=0.14, Re=25,000 cases: a) Cp, b) total pressure loss

cascade, ϕ, normalized on the blade spacing L_ϕ. The origin, ϕ=0, corresponds to the location downstream of the trailing edge of the center blade in the cascade (B4 in Fig. 1a) in the design flow direction.

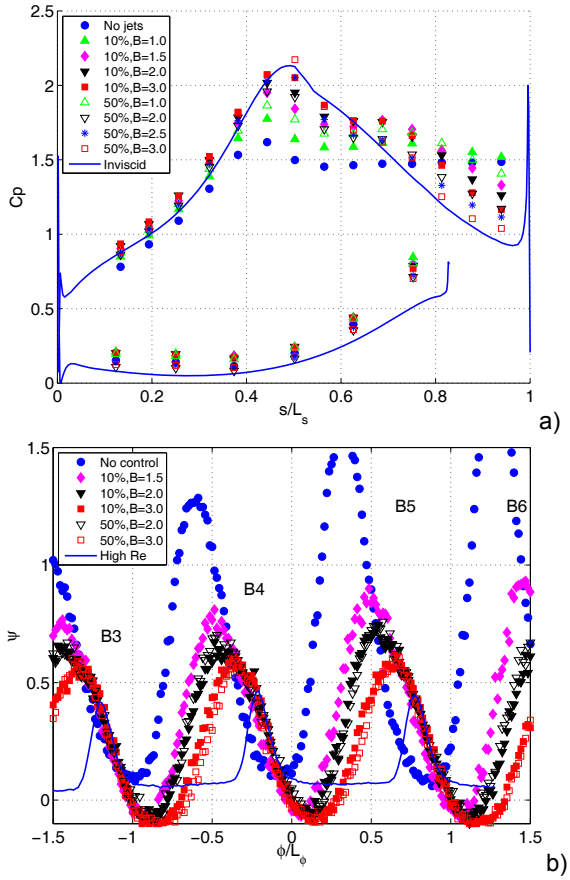

Fig. 4 Pressure results for F=0.28, Re=25,000 cases: a) Cp, b) total pressure loss

The pulsed jets reduce the loss significantly and shift the loss peaks to the right. This indicates that the separation bubble must be thinner, particularly when B=3.0, and that flow turning is increased. The loss peak at B=3.0 is narrower for the D=50% case than for the lower duty cycle, in agreement with the larger drop in Cp near the trailing edge for this case. Even in this best case, the loss peaks are significantly higher and to the left of the high Re case.

Results with F=0.28 are shown in Fig. 4. The jets begin to have an effect when B=1.5, and significant separation control is apparent when B=2.0 or higher, particularly with D=50%. The jets are not as effective when D=10%. The loss results show the VGJs at F=0.28 have a strong effect. The duty cycle effect is less apparent than in the Cp results.

Figure 5 shows Cp results with F=0.56. The VGJs have some effect even at low blowing ratios, and when B=1.0 the boundary layer appears to reattach. The results do not appear to depend significantly on the duty cycle. This is consistent with the low freestream turbulence results, which showed that when F=0.56 the pulses occur frequently enough to control separation even at low duty cycles. Figure 6 shows results with F=1.12. Results are similar to those with F=0.56. Separation is controlled when B=0.75, and increasing B further does not appear to have much effect. Losses for the F=0.56 and 1.12 cases are shown in Fig. 7. The losses are greatly reduced when separation is controlled, and with a few exceptions the loss results are consistent with the Cp results.

Integrated Cp and loss results are shown in Fig. 8. The Cp difference between the pressure and suction sides of the passage is

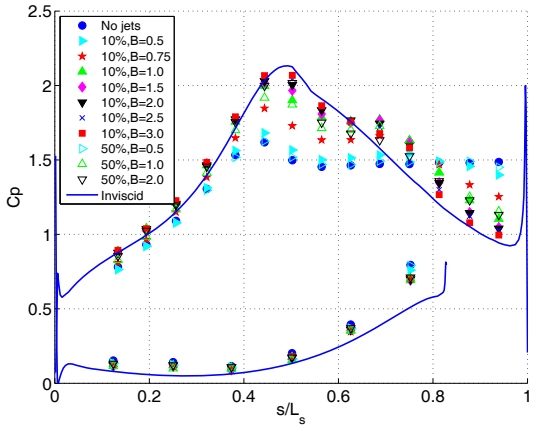

Fig. 5 Cp profiles for F=0.56, Re=25,000 cases

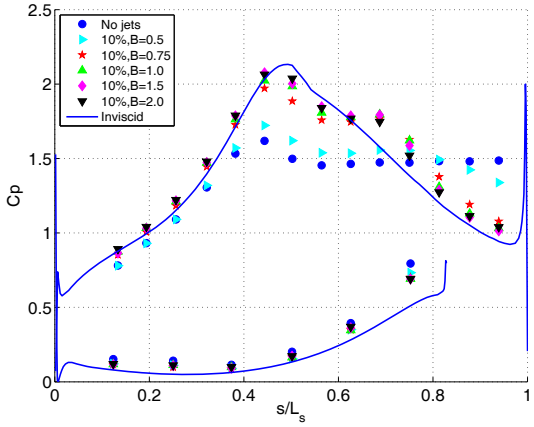

Fig. 6 Cp profiles for F=1.12, Re=25,000 cases

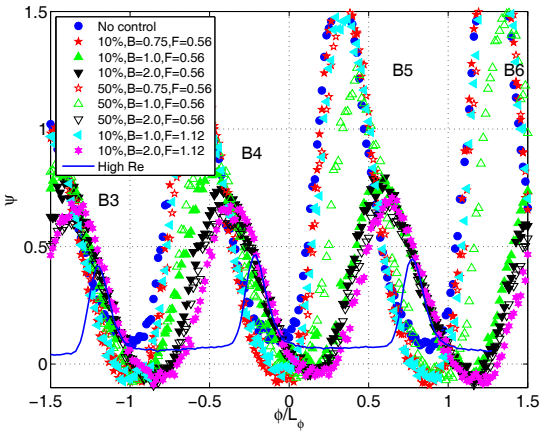

Fig. 7 Total pressure loss profiles for F=0.56 and F=1.12, Re=25,000 cases

integrated in the axial direction to produce a quantity proportional to the lift on the airfoil,

$$Cp_{int} = \int_0^{C_x} \frac{(Cp_{suction} - Cp_{pressure})dx}{C_x} \qquad (1)$$

and this quantity is normalized using the same integrated quantity for the inviscid profile. The integrated total pressure loss,

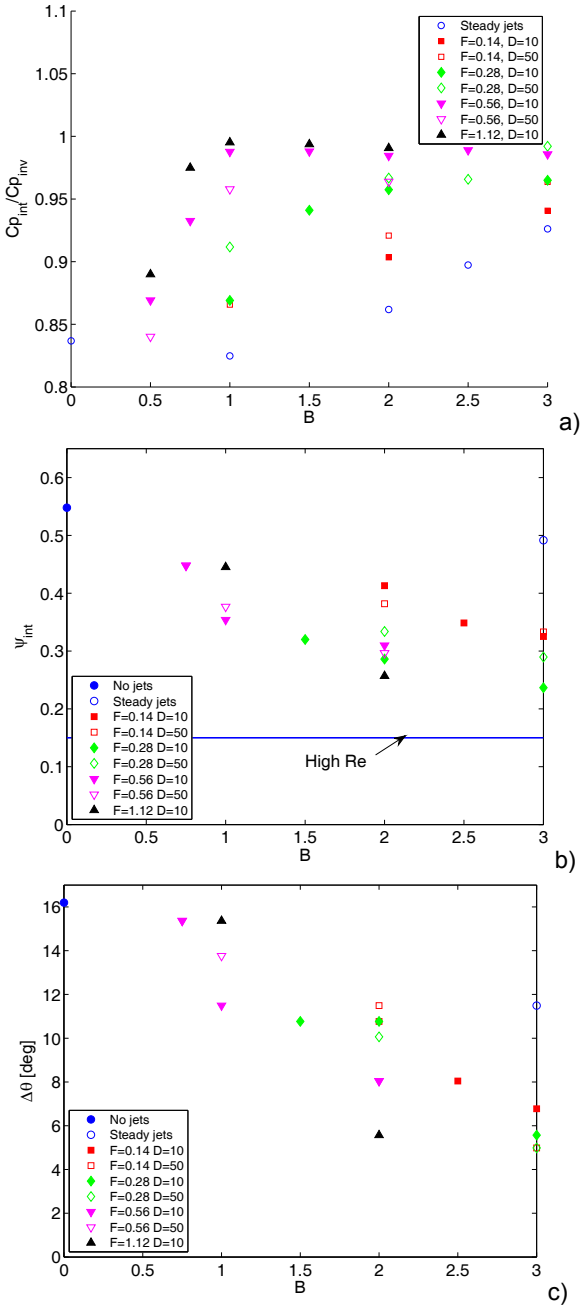

Fig. 8 Integrated pressure results for Re=25,000 cases: a) ratio of lift to lift in inviscid case, b) total pressure loss, c) change in exit flow angle from high Re case

$$\psi_{int} = \int_{-L_\phi/2}^{L_\phi/2} \frac{\psi d\phi}{L_\phi} + \frac{\dot{m}_j}{\dot{m}_1}\frac{(P_j - P_{Te})}{(P_T - P_S)}. \qquad (2)$$

is an average of the loss profile result across one blade spacing centered on the peak corresponding to blade B4. As explained in Volino et al. [29], the loss associated with the jets themselves is included in the integrated loss. With steady jets the lift increases slowly as blowing ratio is increased, but never achieves the inviscid

case value. The lift increases at each blowing ratio as F is increased, and is higher at the higher duty cycle. With F=0.56 and 1.12, the lift increases rapidly with B, reaching the invisid value when B=1, and then remains constant as B is increased further. In agreement with the lift, the integrated loss decreases with B from a high value of 0.55 without flow control to about 0.22, with the best results at the higher pulsing frequencies. These values compare to a high Re value of about 0.15. The losses with F=0.28 are somewhat lower than in the corresponding low TI cases of Volino et al. [29], but otherwise the high and low TI results are very similar. The change in exit flow angle is inferred from the shift in the location of the loss peaks from ϕ/L_ϕ=0 in Figs. 3b, 4b and 7, and is shown as the difference from the high Re case angle in Fig. 8c. The location of the peak in the high Re case corresponds to an exit flow angle of 54°, which agrees within the experimental uncertainty with the design exit flow angle of 57° corresponding to the design Zweifel=1.35. The design exit flow angle is lower than the 60° design metal angle of Table 1. Without flow control, turning is reduced by 16° compared to the high Re case. In the best controlled case, about 11° of turning is recovered, but there is still a 5.5° difference from the high Re case due to the much thicker boundary layer at low Re even with reattachment.

Time averaged velocity profiles for the baseline case and four cases with pulsed jets are shown in Fig. 9. The top row shows the mean velocity at the six streamwise stations noted in Table 2, and the lower row shows the rms fluctuating streamwise velocity, u'. Without flow control, the boundary layer has separated by Station 1 and the separation bubble grows at the downstream stations. The peak in u' is in the shear layer far from the wall. With flow control it appears there may be a small separation bubble at the third and fourth stations, in agreement with the short plateau in Cp at this location in Figs. 4a and 5, but it is much smaller than in the baseline case, and the boundary layer appears attached at the downstream stations. With F=0.28, increasing the blowing ratio from B=2 to 3 moves the u' peak toward the wall, indicating a thinner bubble. The same trend is observed as B in increased from 1 to 2 with F=0.56. Increasing F from 0.28 to 0.56 results in significantly lower u' in the outer part of the boundary layer, which is explained below.

Figure 10 shows phase averaged mean velocity profiles for the cases with F=0.28, D=10% and B=2.0, and with F=0.56, D=10% and B=2.0. The columns correspond to the six streamwise stations, and rows are for different phases in the pulsing cycle. A small separation bubble appears to form at Station 3 in the F=0.28 case, but is suppressed for several phases starting at t/T=0.417. The same is true at Station 4, with the suppression of the separation beginning at about t/T=0.5. At Station 5 the boundary layer appears to reattach at t/T=0.583, and remain attached until t/T=0.917. At station 6, reattachment occurs at about t/T=0.667, and the boundary layer remains attached until t/T=0.167 in the next cycle.

In the F=0.56 case there is less variation in the mean profile during the cycle. Variation in the velocity as the boundary layer separates and reattaches results in significant u', and as the variation is reduced at higher F, u' decreases. This is particularly apparent at y/L_s>0.1. As the separation bubble grows, fluid is forced away from the wall and the velocity at y/L_s>0.1 increases. When the boundary layer reattaches the velocity at y/L_s>0.1 drops. The result is high u' in this region for the F=0.28 case in Fig. 9. The boundary layer appears to approach separation in the F=0.56 case for much of the cycle at Station 4, particularly between t/T=0.5 and 0.708, and at t/T=0.75 to 0.917 at Station 5 and t/T=0.083 at Station 6. At other times separation appears controlled.

Wavelet spectra help to explain the velocity profile results. Figure 11 shows wavelet spectra for the F=0.28, D=10%, B=2.0 case. The

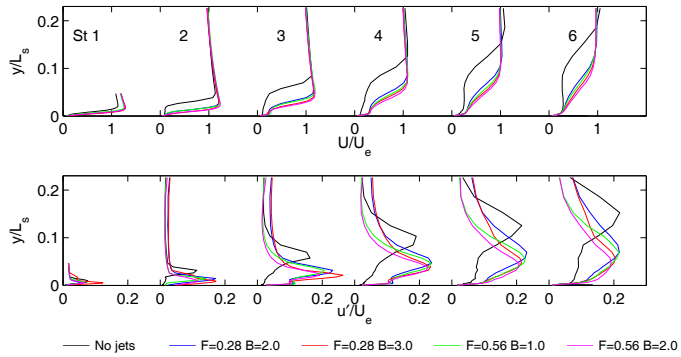

Fig. 9 Time averaged velocity profiles at six streamwise stations for Re=25,000 cases with no jets and jets with D=10%: top – mean velocity, bottom – rms velocity

six plots in the figure correspond to the six streamwise stations. In each plot, the horizontal axis shows dimensionless frequency, fL_s/U_e on a log scale, and the vertical axis shows dimensionless time, t/T, for one pulsing cycle. Power spectral density is computed from instantaneous velocity data at all y locations and is shown in Fig. 11 for the y locations corresponding to maximum time averaged u' at each station. The contours show the power spectral density premultiplied by frequency and normalized by U_e^2. The color scale is the same for all plots. The VGJ creates a disturbance at the beginning of a pulse, and the leading edge of this disturbance is visible as high contours centered at t/T=0.16, 0.25, 0.31, 0.38, 0.46 and 0.54 at Stations 1-6 respectively. The arrival times at each station indicate that the leading edge of the disturbance convects along the surface at about 0.6 times the local freestream velocity. A second peak appears centered at t/T=0.24, 0.42, 0.54, 0.71, 0.93 and 0.06 at Stations 1-6 respectively. These peaks are believed to result when the trailing edge of the VGJ disturbance passes, and the times indicate a convection speed of about 0.3 times the freestream velocity. Comparison of Figs. 10 and 11 shows that at each station, the separation bubble is thickest at about the time the disturbance first arrives. Shortly after this, the velocity profile appears reattached. The profile remains attached at each station until about the time when the second peak appears in Fig. 11, indicating that the disturbance has past. The separation bubble then begins to grow almost immediately. Since the leading and trailing edges of the disturbance move at different velocities, the duration of the disturbance increases at the downstream stations. Hence, the duration of the separation bubble decreases at the downstream stations. If the pulsing frequency were increased, disturbances would follow each other more closely in time, and if the frequency were sufficiently high, the leading edge of each disturbance would overtake the trailing edge of the preceding disturbance, thereby eliminating the period of separated flow. Based on the convection speeds observed in Fig. 11, F=0.5 would be sufficient to eliminate separation at the trailing edge.

Low frequency peaks appear in Fig. 11 at the pulsing frequency, fL_s/U_e=0.7, at all stations. A higher frequency peak at fL_s/U_e=10 is also visible, particularly at Stations 1 and 2. The higher frequency is likely related to shear layer transition, and matches the frequency peak observed in transition without flow control in Volino et al. [28]. Figure 12 shows contours of the dimensionless, premultiplied wavelet spectra as a function of distance from the wall on the vertical axis and dimensionless frequency on the horizontal axis. The columns correspond to Stations 2 through 6, and the rows to different times during the cycle. The peak at fL_s/U_e=0.7 appears at all times. Higher frequencies extending beyond fL_s/U_e=10 are also present. The high frequency fluctuations have their highest magnitude in the shear layer

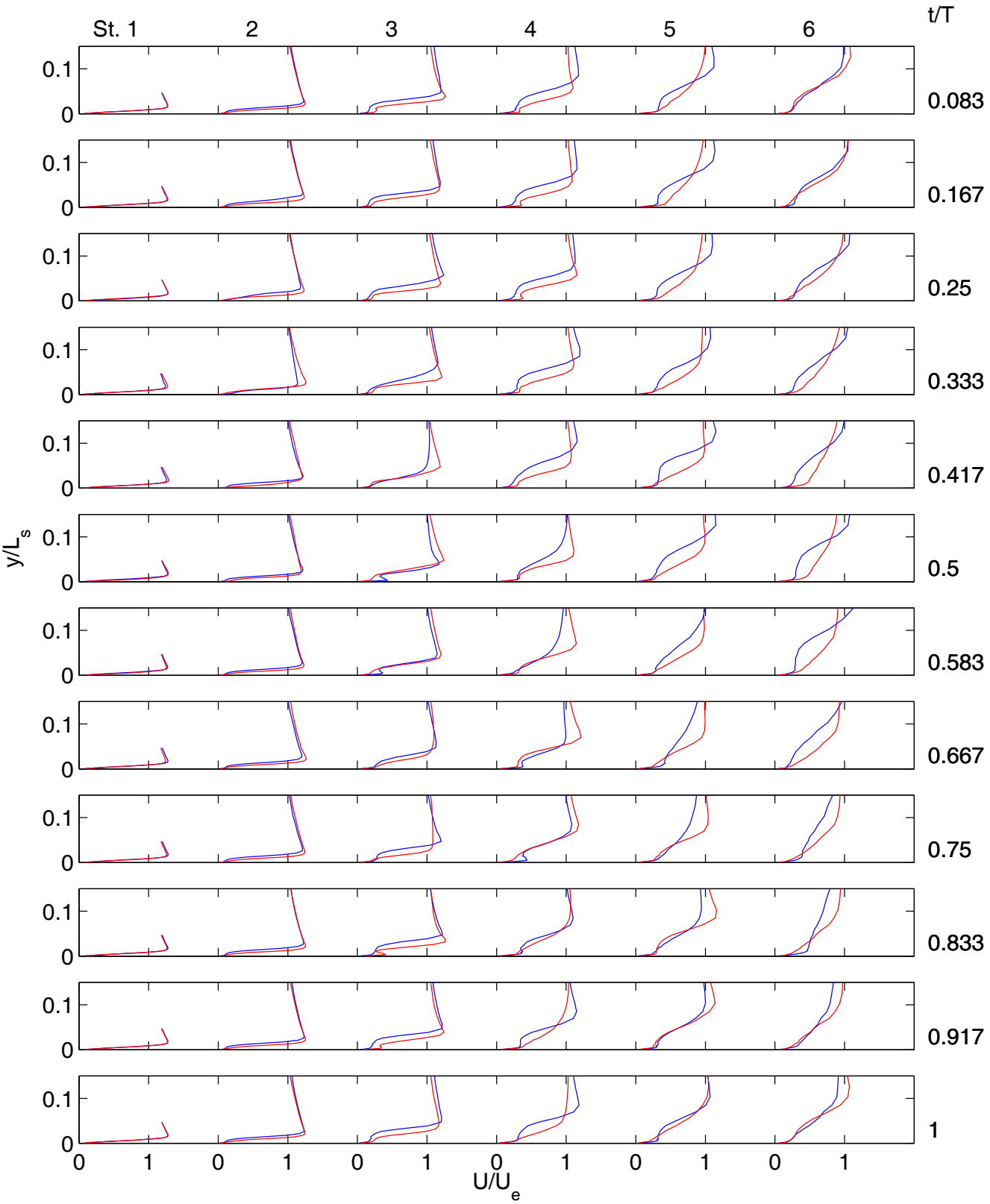

Fig. 10 Phase averaged mean velocity profiles for Re=25,000 cases, columns for six streamwise stations, rows for phases in pulsing cycle: blue – F=0.28, D=10%, B=2.0, red – F=0.56, D=10%, B=2.0

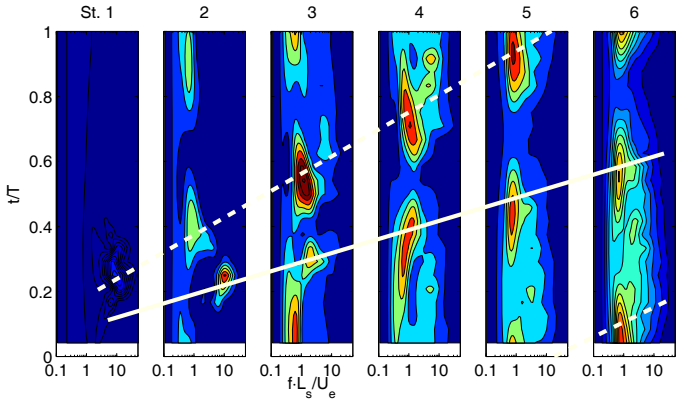

Fig. 11 Wavelet spectra computed at y locations of maximum u′ in time averaged profiles and shown as function of time and frequency at six streamwise stations, F=0.28, D=10%, B=2.0, Re=25,000, solid white line is leading edge of disturbance, dashed white line is trailing edge

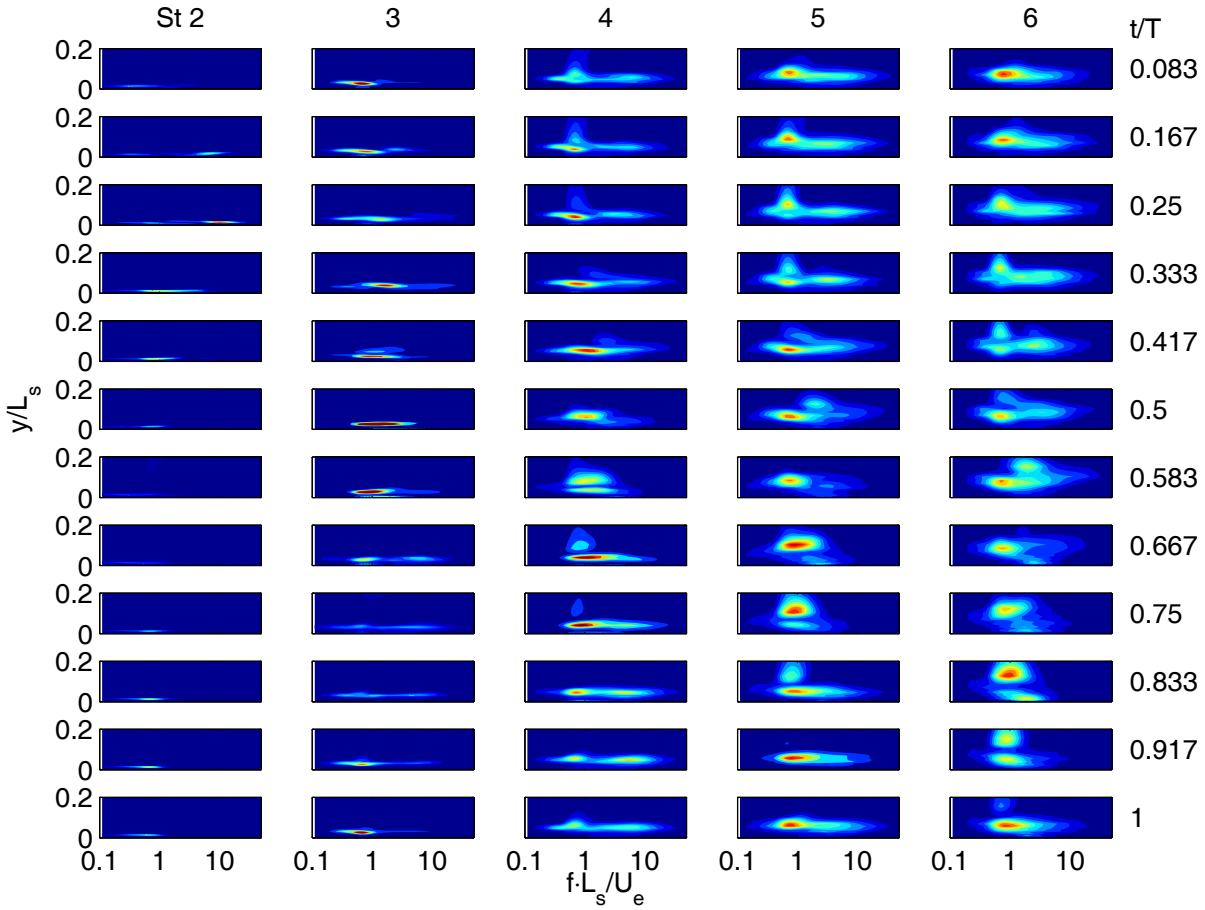

Fig. 12 Wavelet spectra as function of distance from wall and frequency at Stations 2-6 (columns) and various phases (rows), F=0.28, D=10%, B=2.0, Re=25,000

when the boundary layer is most separated and are suppressed when the VGJs cause reattachment. Another peak at fL_s/U_e=2 and y/L_s between 0.11 and 0.16 appears in the shear layer at t/T=0.417, 0.5 and 0.583 at Stations 4 through 6 respectively. These are the arrival times of the VGJ disturbance at these stations.

Increasing the blowing ratio from 2 to 3 with F=0.28 increases the magnitude of the disturbances, but otherwise does not change the behavior observed in Figs. 9-12. The effect of pulsing frequency is shown in Figure 13 for the F=0.56, D=10%, B=2.0 case in the same format as Fig. 11. A peak frequency of about fL_s/U_e=10 is still present at Stations 1 and 2, as in Fig. 11. High magnitudes are also visible at all stations at the pulsing frequency, which is now doubled to about fL_s/U_e=1.4. In the format of Fig. 12 for this case (not shown), the arrival of the VGJ disturbance is again marked by a spectral peak in

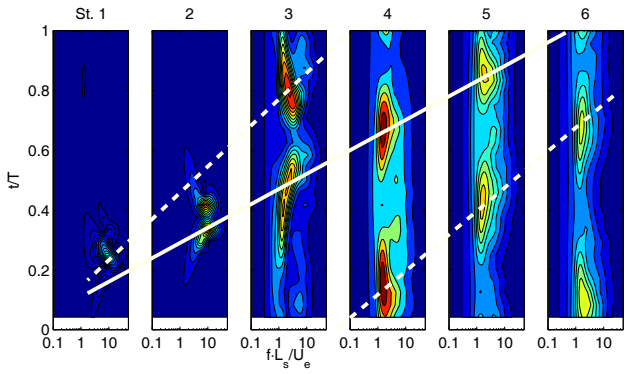

Fig. 13 Wavelet spectra computed at y locations of maximum u′ in time averaged profiles and shown as function of time and frequency at six streamwise stations, F=0.56, D=10%, B=2.0, Re=25,000, solid white line is leading edge of disturbance, dashed white line is trailing edge

the shear layer at a frequency of about fL_s/U_e=2. In Fig. 13, the center of the spectral peaks which presumably correspond to the first arrival of the VGJ disturbance appear at Stations 1-6 at t/T=0.17, 0.34, 0.5, 0.67, 0.94 and 0.1 respectively. These dimensionless times are greater than those in Fig. 11 since the convection velocities are about the same in both cases but the pulsing period is halved. Comparing Figs. 13 and 10, the separation bubble begins to grow at each station after the passing of the trailing edge of the disturbance, and the bubble is suppressed about 0.1T after the arrival of the next disturbance. This is the same behavior observed at F=0.28, but there is less time available for the bubble to grow at the higher frequency, so there is less variation of the velocity profile shape with time at F=0.56. The reduced separation at higher frequency is reflected in the lower losses and the Cp profiles, which are closer to the inviscid solution.

Re=50,000

Pressure profiles for the cases with steady VGJs and Re=50,000 are shown in Fig. 14. The jets become effective when $B\geq$1.5. Results for pulsed jets with F=0.14 are shown in Fig. 15. In terms of Cp, the jets begin to have an effect when B=0.75, but do not appear to fully control separation until B=1.5. Between B=0.75 and 1.5, a higher duty cycle appears to help, but at B=1.5 and above the results are about the same with D=10% or 50%. The total pressure loss profiles agree with the Cp results. In the best controlled case the loss peaks are still significantly higher and to the left of the high Re comparison case, but the difference is not as great as in the Re=25,000 cases above. Figure 16 shows results with F=0.28. The jets have some effect with B=0.5 and 0.75, and the effect increases at higher duty cycle. With B=1.0 and higher, separation is controlled at both duty cycles. The loss peak is slightly narrower with D=50%. The Cp profiles show a small separation bubble still appears to remain at s/L_s=0.7. With F=0.56, as shown in Fig. 17, blowing with B=0.5 has some effect, particularly with D=50%, and with B=0.75 and D=10% the separation is controlled. Increasing B or D further has no additional effect. As in the lower frequency cases, a small separation bubble remains at s/L_s=0.7. The integrated Cp and loss results are shown in Fig. 18. The trends are the same as in the Re=25,000 cases of Fig. 8 and the low TI cases of Volino et al. [29], but effective separation control and loss reduction is possible with somewhat lower B and F as Re or TI is increased. The reduction in flow turning compared to the high Re case is shown in Fig. 18c. Separation control increases the flow turning by about 12°, reducing the difference from the high Re case to 2°.

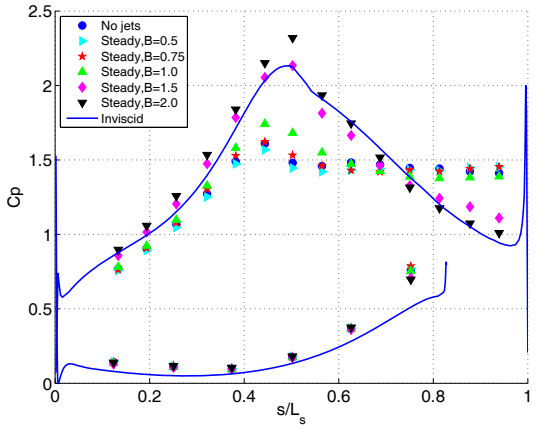

Fig. 14 Cp profiles for steady blowing, Re=50,000 cases

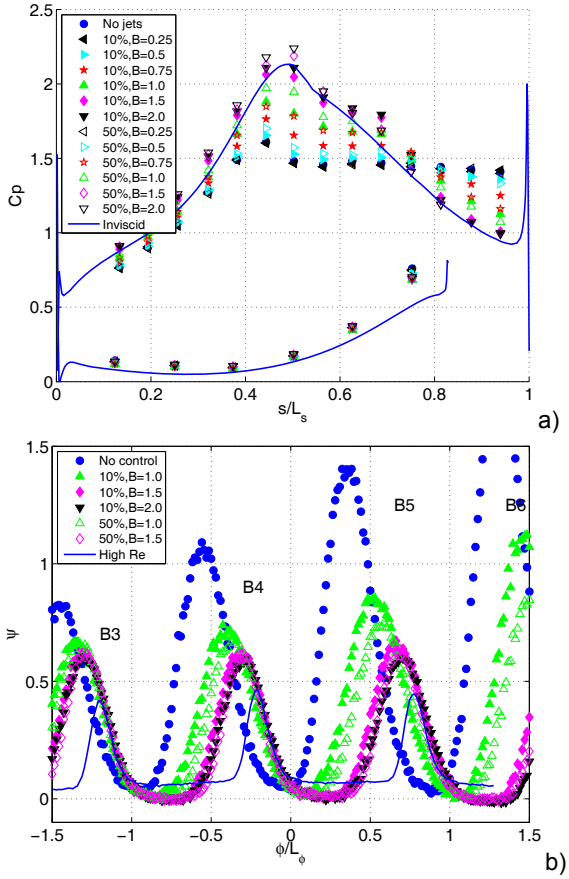

Fig. 15 Pressure results for F=0.14, Re=50,000 cases: a) Cp, b) total pressure loss

Time averaged velocity profiles for some of the Re=50,000 cases are shown in Fig. 19. A large separation bubble without reattachment is present without flow control. Pulsed VGJs largely eliminate the bubble, although a small separation is still present at Station 3, in agreement with the small plateau in the Cp profiles of Figs. 16 and 17 at s/L_s=0.7. Figure 20 shows phase averaged velocity profiles. With F=0.28, there is a small separation at t/T=0.417 at Station 4, at t/T=0.5 at Station 5 and at t/T=0.583 at Station 6. Figure 21 shows the wavelet spectra for this case in the format of Fig. 11. The frequencies and times of the peaks in Figs. 21 and 11 are similar since the pulsing

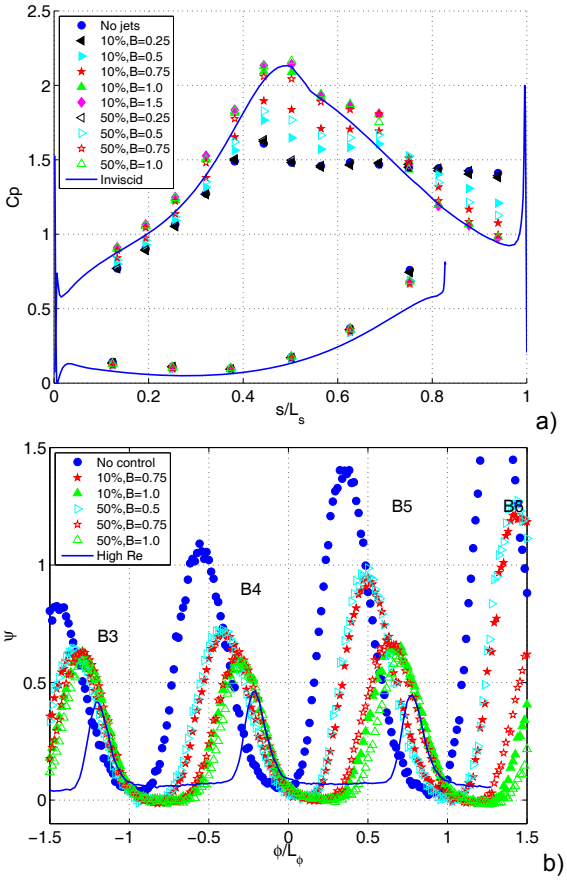

Fig. 16 Pressure results for F=0.28, Re=50,000 cases: a) Cp, b) total pressure loss

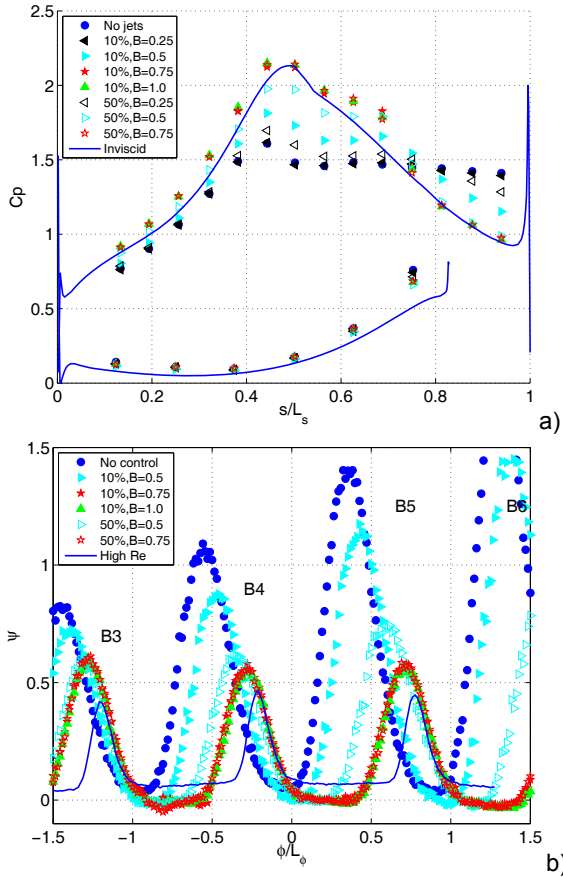

Fig. 17 Pressure results for F=0.56, Re=50,000 cases: a) Cp, b) total pressure loss

frequency, F=0.28, is the same for both cases. As in the lower Re case, the boundary layer reattaches shortly after the appearance of the VGJ disturbance at each station. In contrast to the lower Re case, the boundary layer remains attached for about 0.2T after the disturbance has passed, resulting in attached flow for most of the pulsing cycle. The F=0.56, D=10%, B=0.75 case in Fig. 20 shows little variation of the velocity profiles during the pulsing cycle. The spectra for this case, shown in Fig. 22 show nearly a continuous disturbance through the cycle. There may be some signs of separation with a thin bubble at Station 3, but at the downstream stations the near overlap of the disturbance period between consecutive pulses combined with the lesser tendency toward separation at Re=50,000 than at 25,000, results in an attached boundary layer for the full cycle.

Computational Results

Figure 23 shows Cp for the Re=50,000, B=1, D=10%, F=0.28 case. The spike at the suction peak is at the jet location. In agreement with the experimental data, the CFD shows a small separation bubble occurs but the flow remains reattached over most of the airfoil. Figure 24 show time averaged mean velocity at six streamwise stations comparing the CFD results with the experimental data. The agreement is good upstream, but differences are apparent at the downstream stations, particularly near the wall. The CFD predicts an exit flow angle of 57° both in the present case and in a high Re case. The exit angle difference between the high Re and controlled Re=50,000 case was also small in the experimental result in Fig. 18c. The 57° agrees with the design exit flow angle, but is a few degrees higher than the experimental value. Figure 25 shows the Q-Criterion, which is used to illustrate vortices [32], colored by axial velocity, V_x, at different times in the cycle. At the beginning of the blowing there is no separation bubble present near the trailing edge of the airfoil. This is in contrast with the corresponding low TI case (see Ibrahim et al. [35]). However there is a small bubble located midway between the jet and the trailing edge. During blowing that separated region travels downstream while the flow is attached along most of the airfoil. Right after shutdown of the jet the separation region is smaller. Also at that time the shear layer is highly energized. Near the end of the cycle the flow is attached at the trailing edge, but a small separated region begins to appear again upstream. These results are consistent with the experimental velocity profiles of Fig. 20, which show a small separation bubble moving down the airfoil between wakes, but attached flow at all locations for most of the cycle.

DISCUSSION

The VGJ disturbances convect downstream in the shear layer over the separation bubble, and if they are of sufficient amplitude, cause the boundary layer to attach at a given streamwise location shortly after the arrival of the disturbance. The boundary layer tends to remain attached until after the passage of the trailing edge of the disturbance, although at the lowest Reynolds numbers there may be some tendency, as shown in Fig. 10, to separate earlier. After the disturbance passes, the separation bubble begins to re-grow. This happens almost immediately at very low Reynolds number and more slowly at higher Re. The trailing edge of each disturbance travels slower than the

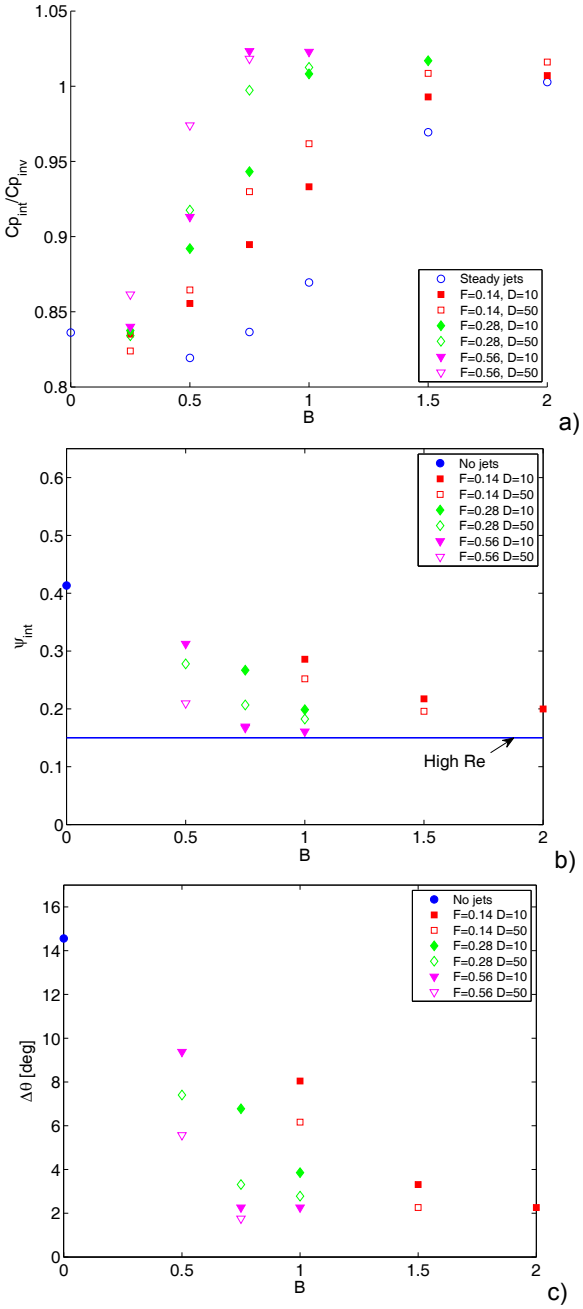

Fig. 18 Integrated pressure results for Re=50,000 cases: a) ratio of lift to lift in inviscid case, b) total pressure loss, c) change in exit flow angle from high Re case

leading edge, resulting in a stretching of the disturbance in the streamwise direction as it moves downstream and a longer duration of the disturbance at downstream locations. The result is a shorter period between disturbances at downstream stations and less separated flow. Increasing the pulsing frequency reduces the period between disturbances at all locations and results in better separation control.

The present results, in agreement with all the previous VGJ studies referenced above, show that pulsed jets are more effective than steady jets. The disturbance created when a jet is first turned on is more effective than any steady blowing which may follow. Velocity results from cases with low freestream turbulence (not shown in the present

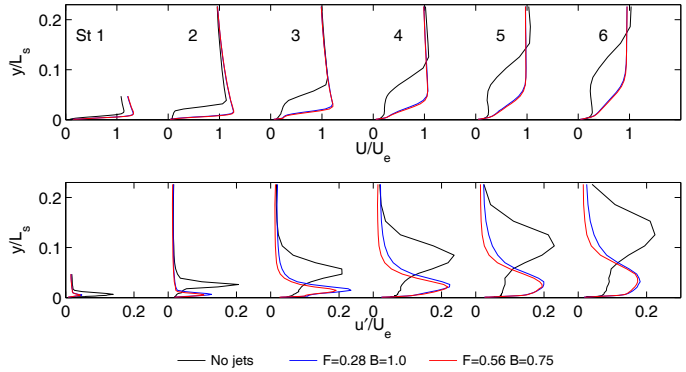

Fig. 19 Time averaged velocity profiles at six streamwise stations for Re=50,000 cases with no jets and jets with D=10%: top – mean velocity, bottom – rms velocity

paper) show that when pulsing with *D*=50%, the boundary layer may re-separate during the period of steady blowing. Increasing the duty cycle from 10 to 50% can, however, provide better separation control, particularly at low pulsing frequencies, as shown above and in Volino et al. [29]. Velocity profiles and spectra from the low *TI*, D=50% cases show a second effective disturbance occurs each cycle when the VGJs turns off, thereby doubling the disturbance frequency above the pulsing frequency. In the *D*=10% cases, the disturbances created when the jets turn on and off occur so close together in time that they effectively constitute a single disturbance.

The present results are very similar to the low *TI* results of Volino et al. [29]. High *TI* does help to control separation, allowing VGJ flow control with slightly lower amplitude and frequency jets in some cases, but the physics of the separation and flow control appears to be the same at high and low *TI*. Increasing the VGJ velocity and frequency help to reduce the separation bubble extent both temporally and spatially, and this increases lift and reduces total pressure losses. Once the separation is largely eliminated, increasing the blowing ratio or pulsing frequency further provides no additional benefit.

CONCLUSIONS

The effect of vortex generator jets on the flow over the very high lift L1A airfoil was studied under high freestream turbulence conditions. Reynolds numbers based on suction surface length and nominal exit velocity of 25,000 and 50,000 were considered. Without flow control, the boundary layer separated and did not reattach. Flow control with VGJs was possible even at *Re*=25,000. In agreement with previous studies, pulsed jets were more effective than steady jets. Pulsing with a dimensionless frequency of *F*=0.56 or higher allowed for separation control with blowing ratio of at most 1.0 and 10% duty cycle. Effective separation control resulted in a 20% increase in lift and up to a 60% reduction in total pressure loss compared to baseline cases at the same Reynolds number. Loss values still remain higher than in high Reynolds number cases. Pulsed jets at lower frequencies provided partial separation control and some loss reduction and could be improved somewhat by increasing the blowing ratio or duty cycle.

Phase averaged velocity profiles and wavelet spectra show the boundary layer intermittently reattaching as disturbances pass and then separating between disturbances. Increasing the pulsing frequency reduces the time available for separation. When the time available is sufficiently small, the boundary layer remains attached at all times. At Re=25,000, separation was nearly fully controlled for the full pulsing cycle when *F*=0.5. Higher frequency pulsing provided little additional benefit. At higher Reynolds numbers the separation bubble grows more slowly, so lower pulsing frequencies can be tolerated.

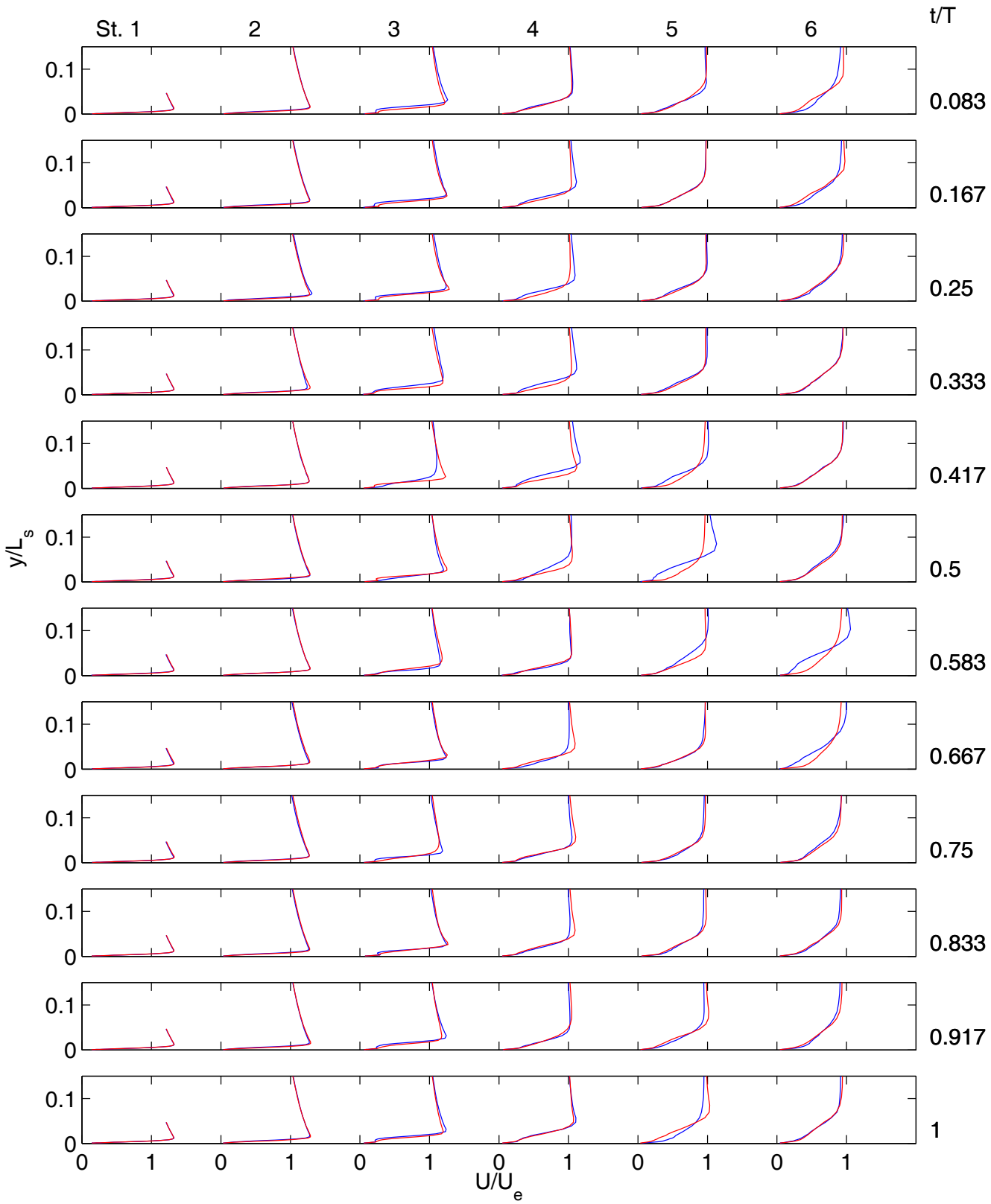

Fig. 20 Phase averaged mean velocity profiles for Re=50,000 cases, columns for six streamwise stations, rows for phases in pulsing cycle: blue – F=0.28, D=10%, B=1.0, red – F=0.56, D=10%, B=0.75

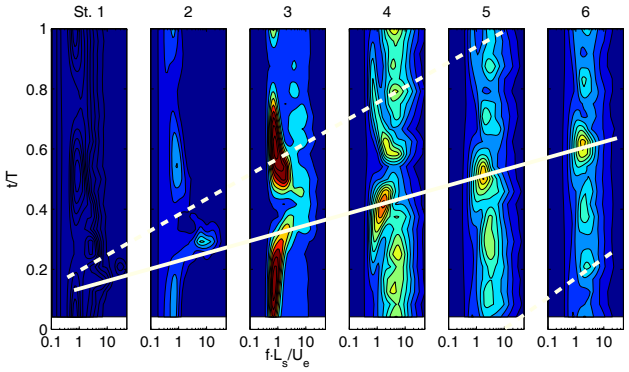

Fig. 21 Wavelet spectra computed at y locations of maximum u′ in time averaged profiles and shown as function of time and frequency at six streamwise stations, F=0.28, D=10%, B=1.0, Re=50,000, solid white line is leading edge of disturbance, dashed white line is trailing edge

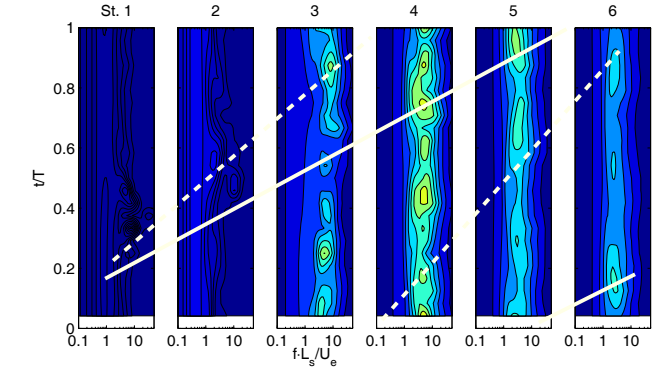

Fig. 22 Wavelet spectra computed at y locations of maximum u′ in time averaged profiles and shown as function of time and frequency at six streamwise stations, F=0.56, D=10%, B=0.75, Re=50,000, solid white line is leading edge of disturbance, dashed line is trailing edge

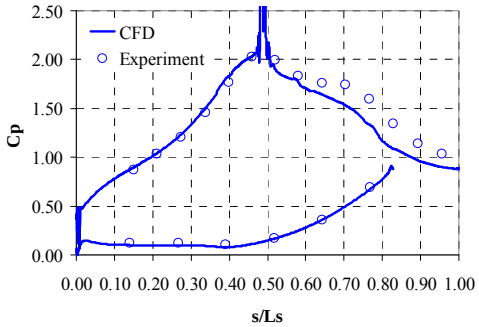

Fig. 23 Cp profile for B=1, F=0.28, D=10%, Re=50,000

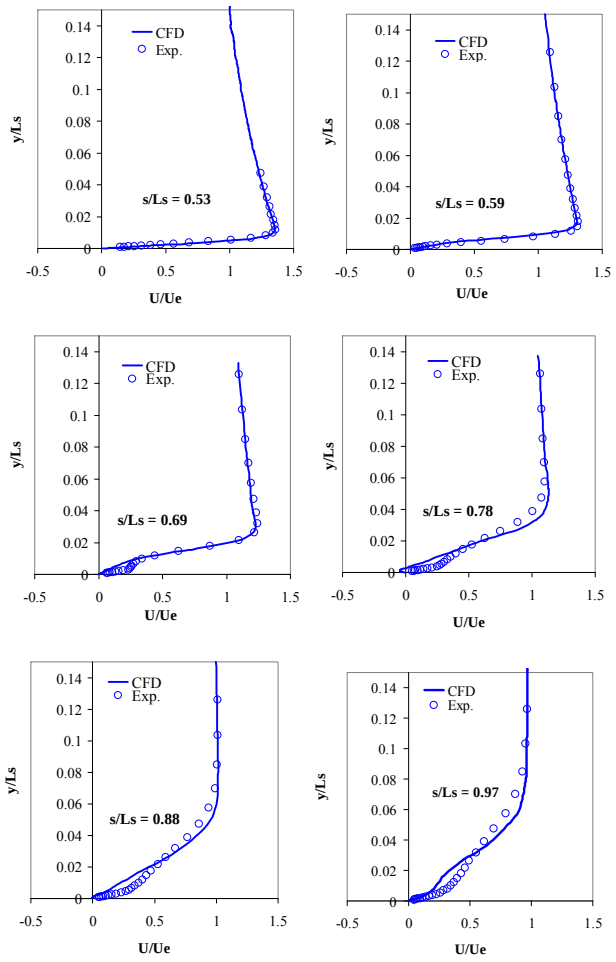

Fig 24 U/U_e at for B=1, F=0.28, D=10%, Re=50,000

Computational results from a large eddy simulation show reattachment in agreement with the experiments for a case with effective VGJ flow control. The LES results allow visualization of structures such as vortices, providing insight into the flow behavior.

High freestream turbulence makes the boundary layer less likely to separate and allows for separation control with slightly lower blowing ratios and pulsing frequencies than in low *TI* cases. The differences observed between high and low *TI* were small, however, and the physics of the separation and flow control appear to be the same in both cases.

ACKNOWLEDGMENTS

This work was sponsored by the National Aeronautics and Space Administration under grant NNC07IA10I. The grant monitors were Drs. Anthony Strazisar and James Heidmann of the NASA Glenn Research Center. The support of the United States Naval Academy Technical Support Department Shop and Fluids Laboratory is greatly appreciated. We greatly appreciate the computer time provided for us by the Ohio Super Computer (OSC). The OSC Computer Cluster has been made available as part of the Center's mission to support Ohio Universities.

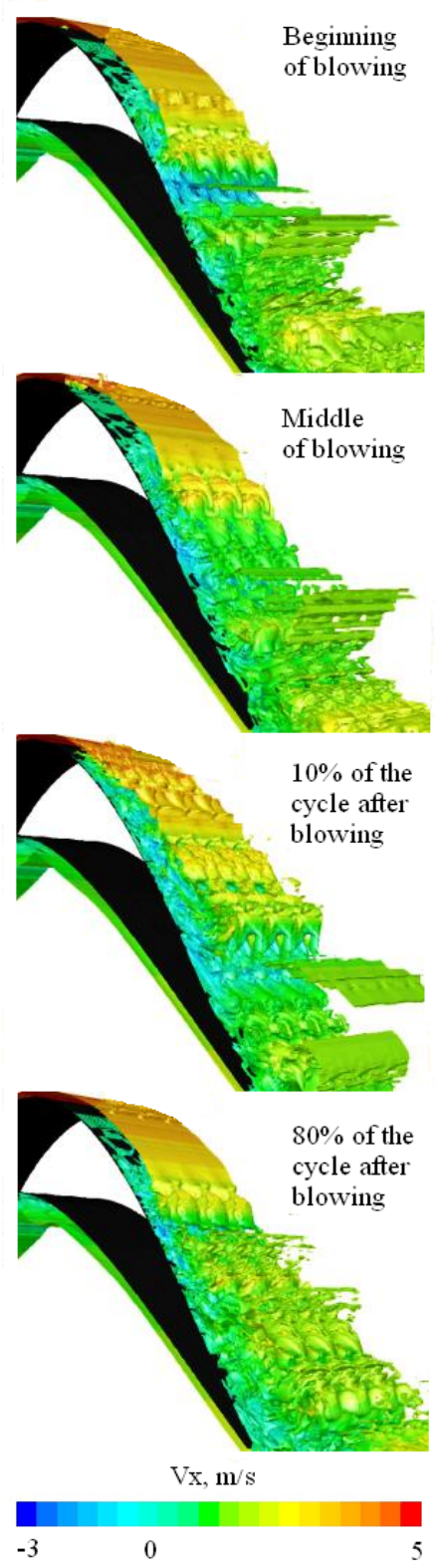

Fig 25 Q-Criterion contours colored by axial velocity, B=1, F=0.28, D=10%, Re=50,000, at different times in the cycle

REFERENCES

[1] Hourmouziadis, J., 1989, "Aerodynamic Design of Low Pressure Turbines," AGARD Lecture Series 167.

[2] Mayle, R.E., 1991, "The Role of Laminar-Turbulent Transition in Gas Turbine Engines," ASME *Journal of Turbomachinery*, **113**, pp. 509-537.

[3] Sharma, O.P., Ni, R.H., and Tanrikut, S., 1994, "Unsteady Flow in Turbines," AGARD Lecture Series 195, Paper No. 5.

[4] Bons, J.P., Sondergaard, R., and Rivir, R.B., 2001, "Turbine Separation Control Using Pulsed Vortex Generator Jets," ASME *Journal of Turbomachinery*, **123**, pp. 198-206.

[5] Volino, R.J., and Hultgren, L.S., 2001, "Measurements in Separated and Transitional Boundary Layers Under Low-Pressure Turbine Airfoil Conditions," ASME *Journal of Turbomachinery*, **123**, pp. 189-197.

[6] Volino, R.J., 2010, "Separated Flow Measurements on a Highly Loaded Low-Pressure Turbine Airfoil," ASME *Journal of Turbomachinery*, **132**, 011007.

[7] Volino, R.J., 2002, "Separated Flow Transition Under Simulated Low-Pressure Turbine Airfoil Conditions: Part 1 – Mean Flow and Turbulence Statistics," ASME *Journal of Turbomachinery*, **124**, pp. 645-655.

[8] Volino, R.J., 2002, "Separated Flow Transition Under Simulated Low-Pressure Turbine Airfoil Conditions: Part 2 –Turbulence Spectra," ASME *Journal of Turbomachinery*, **124**, pp. 656-664.

[9] Praisner, T.J., and Clark, J.P., 2007, "Predicting Transition in Turbomachinery – Part 1: A Review and New Model Development," ASME *Journal of Turbomachinery*, **129**, pp. 1-13.

[10] Bons, J.P., Hansen, L.C., Clark, J.P., Koch, P.J., and Sondergaard, R., 2005, "Designing Low-Pressure Turbine Blades With Integrated Flow Control," ASME Paper GT2005-68962

[11] Zhang, X.F., Vera, M., Hodson, H., and Harvey, N., 2007, Separation and Transition Control on an Aft-Loaded Ultra-High-Lift LP Turbine Blade at Low Reynolds Numbers: Low-Speed Investigation," ASME *Journal of Turbomachinery*, **128**, pp. 517-527.

[12] Bohl, D.G., and Volino, R.J., 2006, "Experiments with Three-Dimensional Passive Flow Control Devices on Low-Pressure Turbine Airfoils," ASME *Journal of Turbomachinery*, **128**, pp. 251-260.

[13] Volino, R.J., 2003, "Passive Flow Control on Low-Pressure Turbine Airfoils," ASME *Journal of Turbomachinery*, **125**, pp. 754-764.

[14] Volino, R.J., 2003, "Separation Control on Low-Pressure Turbine Airfoils Using Synthetic Vortex Generator Jets," ASME *Journal of Turbomachinery*, **125**, pp. 765-777.

[15] Huang, J., Corke, T., and Thomas, F., 2003, "Plasma Actuators for Separation Control on Low Pressure Turbine Blades," AIAA Paper 2003-1027.

[16] Johnston, J.P., and Nishi, M., 1990, "Vortex Generator Jets. Means for Flow Separation Control," *AIAA Journal*, **28**, pp. 989-994.

[17] Bons, J.P., Sondergaard, R., and Rivir, R.B., 2002, "The Fluid Dynamics of LPT Blade Separation Control Using Pulsed Jets," ASME *Journal of Turbomachinery*, **124**, pp. 77-85.

[18] Volino, R.J., and Bohl, D.G., 2005, "Structure of Oscillating Vortex Generator Jets," Proceedings of the Fourth International Symposium on Turbulence and Shear Flow Phenomena, **2**, pp. 589-594.

[19] McQuilling, M., and Jacob, J., 2004, "Effect of Chord Location on Separation Control With Vortex Generator Jets on Low Pressure Turbine Blades," AIAA Paper 2004-2205.
[20] Eldredge, R. G., and Bons, J. P., 2004, "Active Control of a Separating Boundary Layer With Steady Vortex Generating Jets—Detailed Flow Measurements," AIAA Paper 2004-751.
[21] Gostelow, J.P., Walker, G.J., Solomon, W.J., Hong, G., and Melwani, N., 1997, "Investigation of the Calmed Region Behind a Turbulent Spot," ASME *Journal of Turbomachinery*, **119**, pp. 802-809.
[22] Schulte, V., and Hodson, H.P., 1998, "Prediction of the Becalmed Region for LP Turbine Profile Design," ASME *Journal of Turbomachinery*, **120**, pp. 839-846.
[23] Bons, J.P., Reimann, D., and Bloxham, M., 2008, "Separated Flow Transition on an LP Turbine Blade With Pulsed Flow Control," ASME *Journal of Turbomachinery*, **130**, 021014.
[24] Clark J.P., 2007, Private Communication, Air Force Research Laboratory.
[25] Zhang, X.F., and Hodson, H., 2005, "Combined Effects of Surface Trips and Unsteady Wakes on the Boundary Layer Development of an Ultra-High-Lift LP Turbine Blade," ASME *Journal of Turbomachinery*, **127**, pp. 479-488.
[26] Bons, J.P., Pluim, J., Gompertz, K., Bloxham, M., and Clark, J.P., 2008, "The Application of Flow Control to an Aft-Loaded Low Pressure Turbine Cascade with Unsteady Wakes," ASME Paper GT2008-50864.
[27] Ibrahim, M., Kartuzova, O., and Volino, R.J., 2008, "Experimental and Computational Investigations of Separation and Transition on a Highly Loaded Low Pressure Turbine Airfoil: Part 1 – Low Freestream Turbulence Intensity," ASME Paper IMECE2008-68879.
[28] Volino, R.J, Kartuzova, O., and Ibrahim, M., 2008, "Experimental and Computational Investigations of Separation and Transition on a Highly Loaded Low Pressure Turbine Airfoil: Part 2 – High Freestream Turbulence Intensity," ASME Paper IMECE2008-68776.
[29] Volino, R.J., Kartuzova, O., and Ibrahim, M.B., 2009, "Experimental and Computational Investigations of Low-Pressure Turbine Separation Control Using Vortex Generator Jets," ASME Paper GT2009-59983.
[30] Wills, J.A.B., 1962, "The Correction of Hot-Wire Readings for Proximity to a Solid Boundary," *Journal of Fluid Mechanics*, **12**, pp. 65-92.
[31] Volino, R.J., 2005, "An Investigation of the Scales in Transitional Boundary Layers under High Freestream Turbulence Conditions," *Experiments in Fluids*, **38**, pp. 516-633.
[32] Fluent, Inc., 2005, *Fluent 6.3 - User Guide*.
[33] Kim, W.W., and Menon, S., 1997, "Application of the localized dynamic subgrid-scale model to turbulent wall-bounded flows," AIAA Paper AIAA-97-0210.
[34] Kim, S.E., 2004, "Large eddy simulation using unstructured meshes and dynamic subgridscale turbulence models," AIAA Paper AIAA-2004-2548.
[35] Ibrahim, M.B., Kartuzova, O., Doucet, D., and Volino, R.J., 2010, "LES Flow Control Simulations for Highly Loaded Low Pressure Turbine Airfoil (L1A) Using Pulsed Vortex Generator Jets," ASME Paper GT2010-23015.
[36] Piomelli, U., and Chasnov, J.R., 1995, "Large-Eddy Simulations: Theory and Applications," *Turbulence and Transition Modeling, lecture notes from the ERCOFTAC/IUTAM* summer school, Stockholm, 12-20 June, 1995.

Proceedings of ASME Turbo Expo 2010: Power for Land, Sea and Air
GT2010
June 14-18, 2010, Glasgow, UK

GT2010-23573

EFFECT OF UNSTEADY WAKES ON BOUNDARY LAYER SEPARATION ON A VERY HIGH LIFT LOW PRESSURE TURBINE AIRFOIL

Ralph J. Volino
Mechanical Engineering Department
United States Naval Academy
Annapolis, Maryland 21402-5042
volino@usna.edu

ABSTRACT

Boundary layer separation has been studied on a very high lift, low-pressure turbine airfoil in the presence of unsteady wakes. Experiments were done under low (0.6%) and high (4%) freestream turbulence conditions on a linear cascade in a low speed wind tunnel. Wakes were produced from moving rods upstream of the cascade. Flow coefficients were varied from 0.35 to 1.4 and wake spacing was varied from 1 to 2 blade spacings, resulting in dimensionless wake passing frequencies $F=fL_{j\text{-}te}/U_{ave}$ (f is the frequency, $L_{j\text{-}te}$ is the length of the adverse pressure gradient region on the suction surface of the airfoils, and U_{ave} is the average freestream velocity) ranging from 0.14 to 0.56. Pressure surveys on the airfoil surface and downstream total pressure loss surveys were documented. Instantaneous velocity profile measurements were acquired in the suction surface boundary layer and downstream of the cascade. Cases were considered at Reynolds numbers (based on the suction surface length and the nominal exit velocity from the cascade) of 25,000 and 50,000. In cases without wakes, the boundary layer separated and did not reattach. With wakes, separation was largely suppressed, particularly if the wake passing frequency was sufficiently high. At lower frequencies the boundary layer separated between wakes. Background freestream turbulence had some effect on separation, but its role was secondary to the wake effect.

NOMENCLATURE

Cp	$2(P_T - P)/\rho U_e^2$, pressure coefficient
C_x	axial chord length
F	$fL_{j\text{-}te}/U_{ave}$, dimensionless frequency
f	frequency
$L_{j\text{-}te}$	length of adverse pressure gradient region on suction surface
L_s	suction surface length
L_ϕ	blade spacing (pitch)
P	pressure
P_S	upstream static pressure
P_T	upstream stagnation pressure
P_{Te}	downstream stagnation pressure
Re	U_eL_s/ν, exit Reynolds number
s	streamwise coordinate, distance from leading edge
T	period of jet pulsing cycle
t	time
TI	background freestream turbulence intensity
U	local mean velocity
U_{ave}	average freestream velocity in adverse pressure gradient region
U_i	inlet freestream velocity
U_e	nominal exit freestream velocity, based on inviscid solution
u'	rms fluctuating streamwise velocity
x	axial distance from leading edge
ϕ	coordinate along blade spacing, normal to axial chord
ν	kinematic viscosity
ρ	density
ψ	$(P_T\text{-}P_{Te})/(P_T\text{-}P_S)$, total pressure loss coefficient
ζ	$U_i\cos(\alpha_i)/U_{rod} = U_{axial}/U_{rod}$, flow coefficient

INTRODUCTION

Partial loss of lift and higher aerodynamic losses can be caused by boundary layer separation on low-pressure turbine (LPT) airfoils (e.g. Hourmouziadis [1], Mayle [2], and Sharma et al. [3]). In aircraft engines the lower density and therefore lower Reynolds numbers at altitude can lead to a component efficiency drop of 2% between takeoff and cruise in large commercial transport engines, and possibly as much as 7% in smaller engines operating at higher altitudes [4, 5]. Separation can occur when airfoil loading is too high because of the strong adverse pressure gradients on the suction surface. High loading is, however, desirable since it can be used to reduce airfoil count, weight and cost. The challenge is to design high lift airfoils which do not have separation problems. This requires accurate prediction of suction side separation under relevant conditions.

Separation can be strongly affected by wakes shed from the airfoils in upstream stages in an engine. The velocity deficit and elevated turbulence in periodic wakes help to suppress separation and can cause a separated boundary layer to reattach. Hodson and Howell [6] describe the mechanisms by which wakes promote reattachment, including the "negative jet" which results when the velocity deficit in the wake causes the flow outside the wake to accelerate and impinge on the surface, and the unsteadiness which promotes transition in the boundary layer. Following the wake itself is a calmed period (Gostelow et al. [7] and Schulte and Hodson [8]) in which the

boundary layer has low turbulence but is resistant to separation. Numerous studies have considered the wake effect in the LPT, including those listed in Hodson and Howell [6], and more recent references in Bons et al. [9] and Pluim et al. [10]. Examples include Schobeiri et al. [11], Öztürk and Schobeiri [12], Jiang and Simon [13], and Mahallati and Sjolander [14] who all used the Pack B airfoil. Zhang and Hodson [15] and Funazaki et al. [16] used more highly loaded airfoils. Many additional studies are available from these research groups and others.

Airfoils can be designed with high resistance to separation, as described by Praisner and Clark [17], and knowledge of wake effects allows for designs with higher loading than would be possible under steady inflow conditions. Even with wakes, however, a loading limit will always exist, above which separation will still occur.

In the present study, a very highly loaded airfoil that exhibits separation even in the presence of wakes is used. The airfoil, known as the L1A, was designed at the Air Force Research Laboratory (AFRL) and is available on a limited basis from Clark [18]. Dimensions of the L1A as used in the present study are given in Table 1. Based on the design calculations of Clark [18], the L1A has a Zweifel coefficient of 1.35, which corresponds to 10% higher loading than the "ultra-high lift" airfoils described by Zhang and Hodson [19], and 17% higher loading than the Pack B airfoil. The L1A is aft loaded, which is advantageous for reducing secondary flow losses at the endwalls, but makes the boundary layer more prone to separation than a forward loaded blade, as documented in Bons et al. [9], Volino [20], Ibrahim et al. [21], and Volino et al. [22]. In cases without wakes and low Reynolds numbers, the boundary layer separates and does not reattach, in spite of transition to turbulence in the shear layer over the separation bubble. This result contrasts with the results of studies on less aggressive airfoils (e.g. Volino [23]), which all showed reattachment after transition. The separation bubble on the L1A is about four times thicker than that on the Pack B. The larger distance from the shear layer to the wall on the L1A apparently prevents the turbulent mixing in the shear layer from reaching the wall and causing reattachment. The failure of the boundary layer to reattach results in a 20% loss in lift and increases profile losses by up to a factor of 7. At higher Reynolds numbers the separation bubble closes, and for Re>200,000 the separation bubble is small and the boundary layer is attached over most of the airfoil.

The effect of wakes on the L1A boundary layer was studied by Bons et al. [9], who considered a case with Re=50,000 (based on the suction surface length and the nominal exit velocity from the cascade), background freestream turbulence TI=3%, and periodic wakes produced with moving rods upstream of the airfoils. The dimensionless frequency of the wake passing was $F=fL_{j\text{-}te}/U_{ave}$=0.34, where $L_{j\text{-}te}$ is the length of the adverse pressure gradient region on the suction surface, and U_{ave} is the average freestream velocity over this distance. The length $L_{j\text{-}te}$ is also the distance from a row of vortex generator jet (VGJ) holes to the trailing edge. Pulsed vortex generator jets were used by Bons et al. [9] and Volino et al. [24] to control separation on the L1A. Although these jets are not considered in the present work, the same dimensionless frequency, F, is used to describe the wake passing in the present study and the jet pulsing in [9] and [24]. Bons et al. [9] found that wakes reduced the separation bubble thickness significantly and reduced total pressure losses by more than 50%, but did not cause boundary layer reattachment. This result contrasts with earlier work on less aggressive airfoils (e.g. Reimann et al. [25] on the Pack B) which showed reattachment for at least part of the wake passing period, or a reduction in bubble size in cases with already reattached boundary layers (e.g. Schobeiri et al. [11]). The much thicker separation bubble on the L1A prevents the mixing associated with the wake from penetrating all the way to the airfoil surface and causing full reattachment.

Table 1: Cascade parameters

Axial Chord, C_x [mm]	True Chord [mm]	Pitch, L_ϕ [mm]	Span [mm]	Suction side, L_s [mm]	Inlet flow angle	Exit flow angle
134	146	136	724	203	35°	60°

In the present study, the effect of wakes is considered with Re=25,000 and 50,000 under low (0.6%) and high (4%) freestream turbulence conditions. Cases with various wake passing frequencies and flow coefficients are documented. Surface pressure distributions, total pressure loss profiles, and instantaneous boundary layer velocity measurements are used to explain the mechanism by which the wakes affect separation.

EXPERIMENTAL FACILITY AND MEASUREMENTS

Experiments were conducted in a closed loop wind tunnel with a seven blade linear cascade as shown in Fig. 1. A fine screen located upstream of the cascade is used to break up the boundary layers which form upstream of the test section and to provide uniform inlet conditions to the cascade. The freestream turbulence entering the cascade was measured with a cross-wire probe positioned just upstream of the center blade. The turbulence intensity is 0.8% in the streamwise component and 0.5% in the cross stream components. The integral length scale of the streamwise component is 6.3 cm. To produce high freestream turbulence, the screen is replaced with a coarse grid, consisting of a 1.5 mm thick sheet metal plate with 19 mm square holes spaced 25.4 mm apart, center to center, in both directions. In a plane perpendicular to the inlet flow and $1.7C_x$ upstream of the center blade, the grid produced uniform flow with TI=6.0% in the streamwise component and 4.2% in the cross stream components, for an overall intensity of 4.9%. The streamwise component was also measured at the inlet plane of the cascade in the four center passages, where it had decayed to between 4 and 4.2% between blades B2 and B5 and 4.6% between blades B5 and B6. Downstream of the cascade, the local TI is 1.8% across all passages, as documented in Volino et al. [22]. The local freestream turbulence intensity in the passage at the beginning of the adverse pressure gradient region is 1.4%. The change in TI through the passage is due mainly to the change in the local freestream velocity along with some decay of the turbulence. The upstream integral length scale of the freestream turbulence is $0.12C_x$ in the streamwise component and $0.04C_x$ in the other components. Further details of the facility and inlet flow are in Volino et al. [22].

A tailboard, shown in Fig. 1, is needed to produce the correct exit flow angle from the cascade. Its position was set to produce periodicity at high Reynolds numbers. A tailboard on the opposite side of the cascade and inlet guide vanes were found to be unnecessary. To produce the correct approach flow to the end blades (B1 and B7), the amount of flow escaping around the two ends of the cascade is controlled with the flaps shown in Fig. 1. The inlet flow angle was checked with a three-hole pressure probe and found to agree with the design angle to within 2° of uncertainty. Good periodicity at high Reynolds numbers was obtained in the exit flow. At low Reynolds numbers, when significant separation bubbles are present, the periodicity is not as good due to suppression of the separation bubble thickness on the blades closest to the tailboard. In cases where wakes or other flow control suppress separation, periodicity is reestablished. The lack of periodicity in cases with large separation bubbles is considered acceptable since the focus of the research is separation control, and not documentation of cases with large separation that would be unacceptable in practice. This compromise

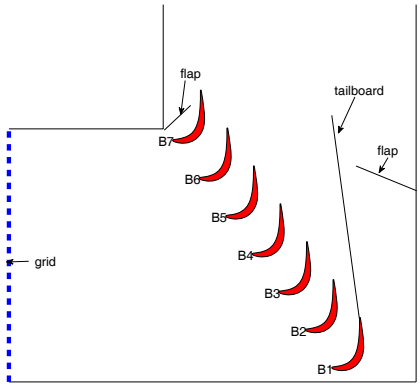

Fig. 1 Schematic of linear cascade

facilitates the study of a larger number of cases by obviating the need to adjust the tailboard by trial and error for each case. It also provides for better repeatability in the experiments, since the position of the tailboard is fixed for all cases. Any changes in separation with wakes will be larger in practice than documented in the experiment, due to the effect of the tailboard in suppressing the bubble size in the no-wake cases.

The wake generator includes a chain near each endwall of the cascade that passes $0.54C_x$ upstream of the leading edges of the cascade blades. The chains then pass downstream around blade B7 on the inside turn of the cascade and pass well downstream of the cascade before returning upstream around blade B1 on the outside turn of the cascade. This completes the chain circuit. A traverse for probe movement is located within the chain circuit downstream of the blade row. Each chain is driven by a drive gear and also passes around six idler sprockets. One of the idler sprockets is adjustable to maintain tension in the chain. The drive gears for the upper and lower chains are on a common axle and driven by a single electric motor so both chains move in unison. The motor speed is set with a variable frequency inverter. The chain links have hollow pins, through which the wake generator rods are attached. Each rod consists of a 4 mm diameter carbon fiber tube with a steel pin attached at each end. The steel pins are inserted through the holes in the upper and lower chain, and then secured with small clips. Tests were run with average distances between rods of 136 mm, 221 mm, and 272 mm, which correspond to $1L_\phi$, $1.6L_\phi$ and $2L_\phi$, where L_ϕ is the blade spacing in the cascade. These ratios of rod to blade spacing are in the range expected for vane to rotor blade spacing in an engine.

The ratio of the rod diameter to the axial chord is 0.03, which is consistent with the wake generators of Bons et al. [9] and Funazaki et al. [16]. The rods are smaller than those of Kaszeta et al. [26] who had a diameter to chord ratio of 0.06. The present rods are larger than those of Schobeiri et al. [11] and Zhang and Hodson [15] who had rod diameter to chord ratios of about 0.01. In the present study, as in Bons et al. [9] and Kaszeta et al. [26], the rod wakes are intended to simulate the wakes of very highly loaded airfoils under low Reynolds number conditions with thick boundary layers and in some cases large separation bubbles. A large diameter rod is therefore needed to simulate an airfoil wake with a large velocity deficit. The studies using smaller diameter rods were done at higher Reynolds numbers, so separation bubbles were smaller and rods producing lower velocity deficits were more appropriate.

For most tests, the rods were driven at a velocity of 1.18 times the cascade inlet velocity, U_i. This gives a flow coefficient, $\zeta = U_i \cos(\alpha_i)/U_{rod} = 0.7$, where α_i is the inlet flow angle. This is in the expected range for an engine. The timing of the wake generator is recorded with an infrared photo detector, which senses the passage of each rod and emits a voltage that is recorded simultaneously as other data are acquired, allowing phase averaging of the results.

Measurements

The center blade, designated B4 in Fig. 1, contains pressure taps near the spanwise centerline. Pressure surveys are made using a pressure transducer (0-870 Pa range Validyne transducer). Stagnation pressure is measured with a pitot tube upstream of the cascade and wake generator. The uncertainty in the suction side pressure coefficients, Cp, is 0.07. Most of this uncertainty is due to bias error. Stochastic error is minimized by averaging pressure transducer readings over a 10 second period.

Total pressure losses are documented using a Kiel probe traversed across three blade spacings, $0.63C_x$ downstream of the cascade. A traverse is located in the wind tunnel downstream of the cascade to move the probe. The traverse causes an acceptably low blockage when it is located at least two C_x downstream of the cascade.

Pressure and loss surveys were acquired at nominal Re=25,000 and 50,000. The Reynolds number, as defined above, is based on the suction surface length and the nominal cascade exit velocity. The corresponding Reynolds numbers based on the cascade inlet velocity and the axial chord length are 10,000 and 20,000.

Velocity profiles on the suction surface were measured at the six streamwise stations listed in Table 2. All stations are downstream of the inviscid pressure minimum at s/L_s=0.49. Profiles were acquired near the spanwise centerline of the airfoil with a hot-wire anemometer (AA Lab Systems model AN-1003) and a single sensor hot-film probe (TSI model 1201-20). The sensor diameter is 51 μm, and the active length is 1.02 mm. At each measurement location, data were acquired for 26 seconds at a 20 kHz sampling rate (2^{19} samples). All raw data were saved. The high sampling rate provides an essentially continuous signal, and the long sampling time results in low uncertainty in both statistical and spectral quantities. Data were acquired at 40 wall normal locations in each profile, extending from the wall to the free-stream, with most points concentrated in the near wall region. The probe was positioned as close to tangent to the airfoil surface as possible at each station, such that the probe body extended downstream of the sensor and the direction of the traverse was within 5° of normal to the surface. In most cases the closest point to the wall in each profile was within about 0.2 mm of the wall, which compares to boundary layer thicknesses ranging from 1.1 mm to over 40 mm.

Flow direction in a separation bubble cannot be determined with a single-sensor hot-wire, but velocity magnitude can be measured and was found to be near zero within the bubbles of the present cases when the flow was laminar. In cases where the flow became turbulent but remained separated, fluctuating velocities caused false high mean velocity readings in the separation bubble. With the exception of these turbulent separated cases, the uncertainty in the mean velocity is 3-5% except in the very near wall region, where near-wall corrections (Wills [27]) were applied to the mean velocity.

Velocity was also measured downstream of the cascade along the same line used for the total pressure loss measurements. Downstream and boundary layer velocity data were both time averaged and ensemble averaged based on the phase within the wake passing period. Phase averages of mean and fluctuating velocity are shown below at 24 dimensionless times, t/T, within the wake passing period, where t is time and T is the period between wakes.

Table 2: Velocity profile measurement stations

Station	1	2	3	4	5	6
s/L_s	0.53	0.59	0.69	0.78	0.88	0.97
x/C_x	0.65	0.72	0.80	0.86	0.92	0.97

RESULTS

Wake Characteristics

Several studies have compared rod wakes to airfoil wakes. Schobeiri et al. [28] discussed the theory for describing wake flows. Pfeil and Herbst [29] showed that the far wake of an airfoil has almost the same wake as a cylinder having the same drag, although the rods have no means of matching the correct potential field of adjacent blade rows [30, 31]. Pluim et al. [10] tested rods of various shapes and provide references to earlier studies. They found that the wakes from wedge shaped rods agreed best with L1A airfoil wakes, but cylindrical rods also provided a reasonable approximation. Figure 2 shows the mean and rms fluctuating streamwise velocity in the wakes of the moving rods and the cascade blades of the present study. The cascade wakes were measured by traversing a hot-wire probe in lines $0.3C_x$ and $0.63C_x$ downstream of the trailing edges of the blades, perpendicular to the axial direction. The variable ϕ denotes the distance across the cascade. The origin, ϕ=0, is directly downstream of the center blade (B4) in the design flow direction, while ϕ/L_ϕ = -1 and 1 are downstream of blades B3 and B5 respectively. The spacing between airfoil rows in an engine is expected to be about $0.3C_x$ according to Pluim et al. [10], so this location would be where the wake from an upstream airfoil would reach the leading edge of the next row. The moving rod wakes were measured by placing a stationary hot-wire midway between blades B4 and B5 in the plane of the leading edges. The moving rods traversed $0.54C_x$ upstream of the hot-wire. The data from the probe were phase averaged on the rod passing cycle to determine the mean and fluctuating velocity as functions of time. For comparison in the figures, the rod velocity was then used to convert time to distance traversed. Curves in the figures were shifted along the horizontal axis to align the peaks for comparison. All curves were normalized using the average local mean velocity.

The wakes from the upstream rods, when shown in dimensionless form as in Fig. 2, did not depend on Reynolds number. For all of the flow and rod velocities considered, the Reynolds number based on rod diameter is between about 400 and 2000, which should result in laminar separation for the boundary layer on the rod and similar wakes for all cases. The wake for low *TI*, *Re*=50,000, ζ=0.7, $1.6L_\phi$ rod spacing, and dimensionless wake passing frequency of *F*=0.28 is shown. In contrast to the rod wakes, the wakes of the cascade airfoils depend strongly on Reynolds number, as shown in Volino [20]. Due to a large separation bubble, the airfoil wake at *Re*=50,000 has a large mean velocity deficit at $0.3C_x$ which decreases 80% in peak magnitude by $0.63C_x$. The peak turbulence intensity drops by 40% over this distance. At *Re*=200,000 the boundary layer remains attached, so the airfoil wake is about half as wide as at the lower *Re*, and the peak velocity deficit is about 25% as large. The peak turbulence intensity is 7%, which is about a third that at the lower *Re*. The change in the wake between $0.3C_x$ and $0.63C_x$ is much smaller than at the lower *Re*. The rod wake lies between the high and low *Re* airfoil wakes. Its peak turbulence intensity is 14%. The velocity deficit and turbulence level in the rod wakes in Fig. 2 appear to be reasonable approximations for an airfoil wake, although they do not fully match either the high or low *Re* case. One could conceivably use a rod of either larger or smaller diameter to match the low or high *Re* airfoil cases better. In cases with high freestream turbulence, the rod wakes are nearly the same as those in Fig. 2, with 14% peak turbulence intensity. The only difference is between the wakes, where the background turbulence rises to 4% with high *TI*.

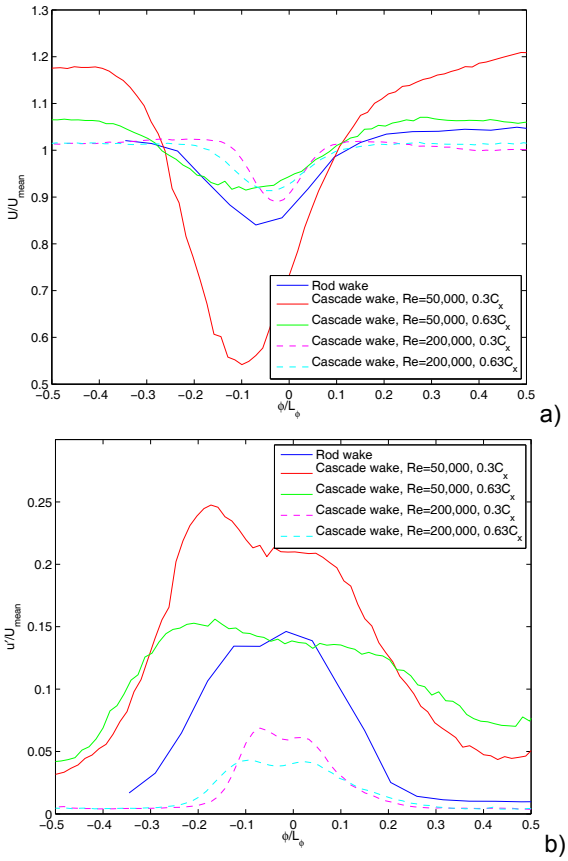

Fig. 2 Velocity in wakes of wake generator rods and cascade wakes with low TI: a) mean, b) rms

The cases of the present study will be used for comparison to future cases with wakes and vortex generator jet flow control. Figure 3 compares the upstream rod wake to the airfoil wake in a case with *Re*=50,000, and pulsed VGJ blowing with *F*=0.56, 10% duty cycle and blowing ratio (jet velocity/freestream velocity) equal 1. The VGJs provided good flow control in this case. The boundary layer separates very briefly but reattaches. Further details are available in Volino et al. [24]. For the airfoil wake in Fig. 3, the phase averaged results at 24 phases through the VGJ pulsing cycle are shown. Since the boundary layer approaches separation during part of the cycle, the wake velocity profile magnitude and position changes somewhat during the cycle. The mean velocity deficit and wake width of the upstream rod and airfoil are about the same. The peak turbulence intensity in the rod wake is about 40% higher than the highest value in the airfoil wake.

Turbulence spectra provide additional information about the wakes. Spectra of the fluctuating streamwise velocity were computed for the cascade airfoil wakes and the rod wakes. Without flow control, the airfoil wakes at *Re*=50,000 exhibit sharp, high amplitude, low frequency (*F*=0.7) peaks associated with the shedding frequency of the separation bubble. With *Re*=200,000, the amplitude of the peaks is about two orders of magnitude lower than at the lower *Re*, and the peaks are broad banded and centered at *F*=2.5. These peaks are likely associated with the turbulence in the airfoil boundary layers. The spectra of the upstream rod wakes have amplitude and frequency between the high and low *Re* cases, agreeing most closely with the *Re*=50,000 VGJ controlled case mentioned above. Figure 4 shows

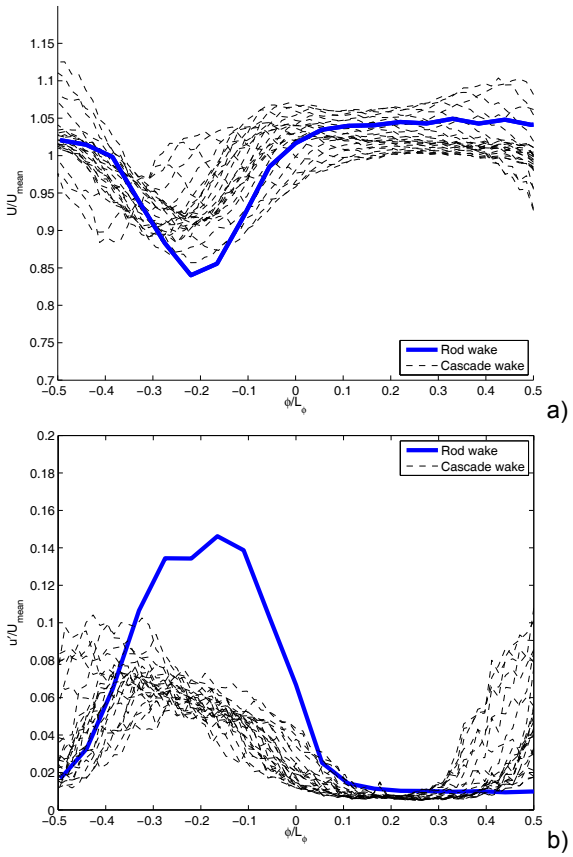

Fig. 3 Velocity in wakes of wake generator rods and phase averaged velocity in wakes of cascade blades for low TI, Re=50,000 case with VGJ flow control [24]: a) mean, b) rms

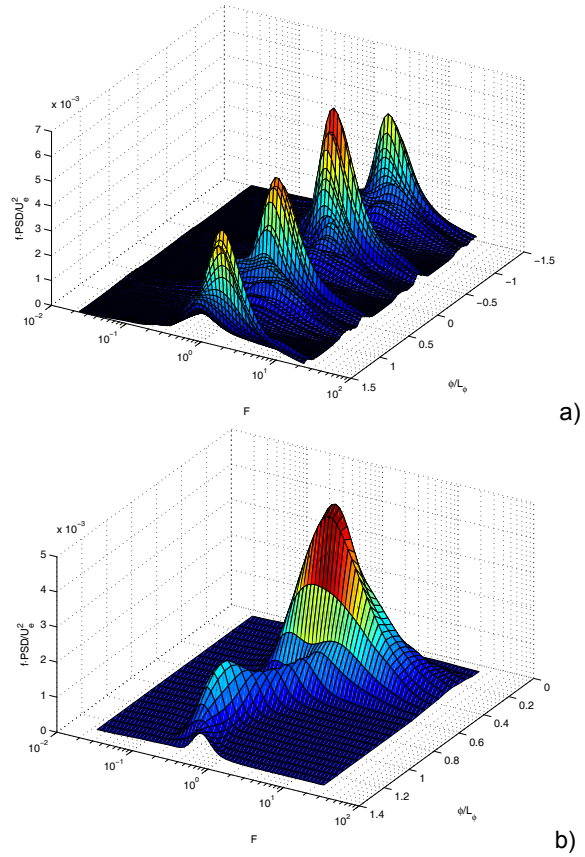

Fig. 4: Wavelet spectra of wake velocity: a) cascade blades for low TI, Re=50,000 case with VGJ flow control [24], b) wake generator rods

wavelet spectra (computed as described in Volino [32] using the Mexican Hat wavelet) for the airfoil and rod wakes. Power spectral density premultiplied by frequency is shown as a function of dimensionless frequency and distance across the cascade. One representative phase within the VGJ pulsing cycle is shown for the airfoil wake. As in Figs. 2 and 3, time is converted to position for the rod wake. For the airfoil wake there is a large peak at F=1.8 with magnitude 0.0052 and a smaller peak at F=0.6 with magnitude 0.0029 that is hidden behind the larger peak in Fig. 4a. The magnitude of the two peaks varies during the VGJ cycle. The rod wake has a large peak at F=0.8 with magnitude 0.0047 and a smaller peak at F=0.2 with magnitude 0.0016. Figs. 2-4 show that the velocity deficit, turbulence intensity and spectral content are of the same order for the airfoil and rod wakes, although the agreement with any one case is not perfect. Since the wake of an upstream airfoil will not necessarily match exactly the wake of the airfoil on which it impinges, the present rod wakes are considered to provide a reasonable approximation to the wakes that might be shed from an upstream blade row at low Reynolds numbers.

Low TI

***Re*=25,000.** The *Cp* and total pressure loss profiles for cases with *Re*=25,000 and low *TI* are shown in Fig. 5. The inviscid *Cp* profile for the L1A airfoil is shown for comparison. The low peak followed by a plateau in the case without wakes indicates separation without reattachment. For the cases with ζ=0.7, decreasing the rod spacing from $2L_\phi$ to $1L_\phi$ (which corresponds to increasing the wake passing frequency, F from 0.22 to 0.45) causes *Cp* to approach the inviscid line and reduces the loss by over 40% compared to the no wake case. The wakes also cause the loss peaks to shift to the right in Fig. 4b, indicating greater flow turning resulting from a thinner separation bubble. The greater turning agrees with a 20% increase in lift indicated by the *Cp* profiles. Also shown in Fig. 5 is a case with $1.6L_\phi$ rod spacing and the rod speed and F doubled so ζ=0.35. The higher wake passing frequency helps to reduce the separation.

Figures 6-9 show time-space plots of the phase averaged mean and fluctuating velocity $0.63C_x$ downstream of the blade row for the cases of Fig. 5. The contours are normalized by the exit velocity U_e. In Fig. 6, the rod spacing is $2L_\phi$, so the flow in alternating passages is in phase, with the passages between a half cycle out of phase. The turbulence (Fig. 6b) shows vertical strips of moderately high fluctuations at ϕ/L_ϕ = -1.5, -0.5, 0.5 and 1.5 associated with the airfoil wakes. These positions correspond to the loss peaks in Fig. 5b. Between these peaks the fluctuation levels range from very low (corresponding to the low background *TI*) to high when the rod wakes pass. The rod wakes proceed at an angle in the figure, rising from left to right, as they move forward in time and transit across the cascade. The highest turbulence peaks occur where the rod wakes interact with the separation bubble and airfoil wakes. At the position and time of each rod wake peak in the turbulence is a corresponding velocity deficit in the mean velocity (Fig. 6a). Following the velocity deficit is a mean velocity maximum as the flow accelerates after the wake passes. In Fig. 7, the rod spacing is reduced to $1.6L_\phi$. All passages are out of phase with each other, and the peaks are stretched along the

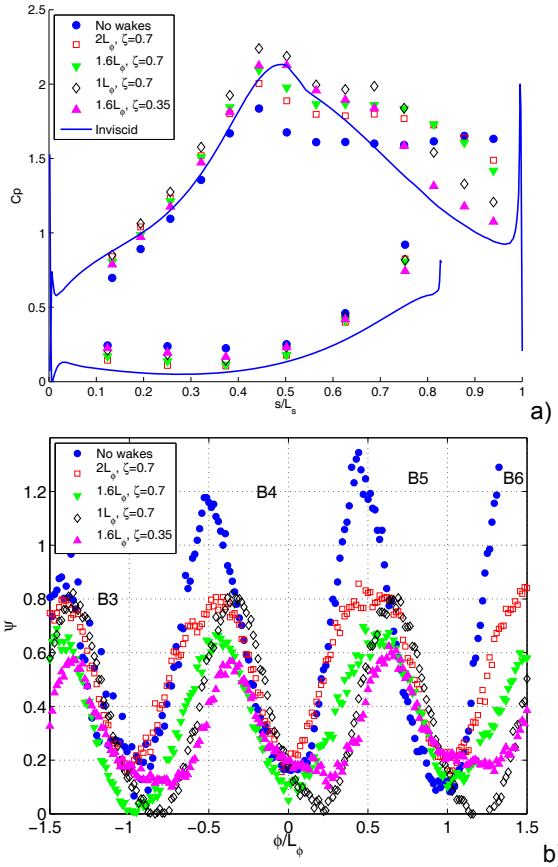

Fig. 5 Pressure profiles for low TI, Re=25,000 cases: a) Cp, b) Total pressure loss

time axis compared to Fig. 6 since the rod speed is the same but the wake passing period is shorter. In Fig. 8, the rod and blade spacing are equal, so all passages are in phase with each other. The wake passing frequency is high enough that there is little time for the boundary layer to separate between wakes. This reduces the peak turbulence level. There is still a mean velocity deficit associated with each rod wake followed by a velocity rise, but the difference between the minima and maxima is reduced since suppression of the separation bubble reduces the flow unsteadiness. Figure 9 shows the effect of increasing the rod speed. Again, the increased wake passing frequency helps to suppress the separation and reduce unsteadiness.

Figure 10 shows time averaged mean and fluctuation velocity profiles at the six streamwise stations of Table 2. Without wakes the separation bubble is very thick, and the peak fluctuating velocity is in the shear layer over the bubble. As shown in Volino [20], the shear layer does transition to turbulent between Stations 3 and 4, but this does not cause reattachment. Wakes with rod spacing of $2L_\phi$ and $1.6L_\phi$ reduce the separation bubble thickness by about half, but do not eliminate it. Figure 11 shows phase averaged mean velocity for the $2L_\phi$ spacing case. The six columns correspond to the six streamwise stations, and the rows correspond to different phases in the wake passing cycle. The boundary layer separates with a very thin bubble at Station 2 that becomes thicker at the downstream stations at most phases. The bubble appears as a region of nearly constant, but non-zero velocity near the wall. The non-zero velocity is an artifact of the hot-wire sensor's inability to distinguish flow direction and the turbulent fluctuations within the bubble. There is also a period of

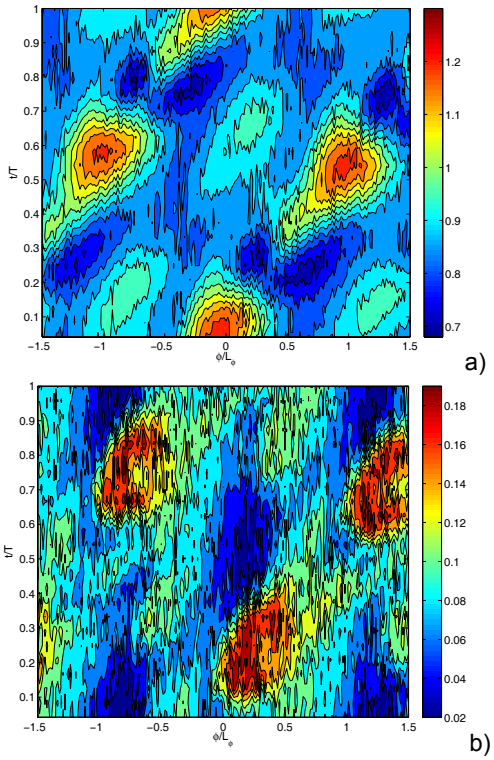

Fig. 6 Time space plot of phase averaged velocity 0.63C_x downstream of cascade for low TI, Re=25,000, ζ=0.7, 2L_ϕ rod spacing: a) U/U_e, b) u′/U_e

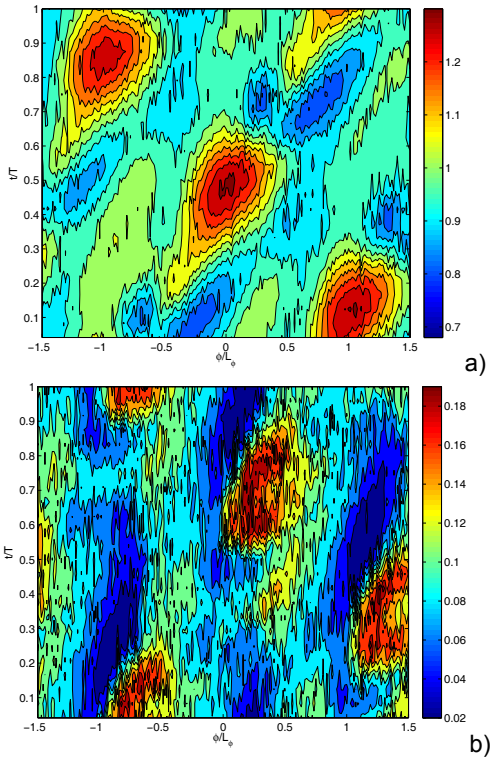

Fig. 7 Time space plot of phase averaged velocity 0.63C_x downstream of cascade for low TI, Re=25,000, ζ=0.7, 1.6L_ϕ rod spacing: a) U/U_e, b) u′/U_e

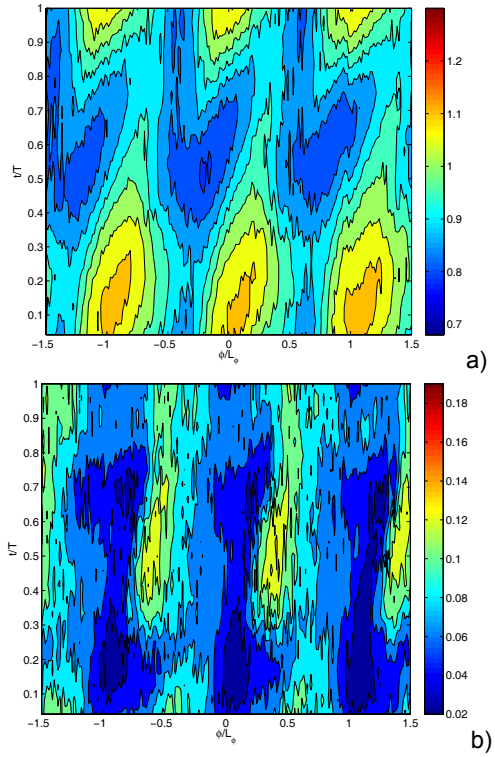

Fig. 8 Time space plot of phase averaged velocity $0.63C_x$ downstream of cascade for low TI, Re=25,000, ζ=0.7, $1L_\phi$ rod spacing: a) U/U_e, b) u'/U_e

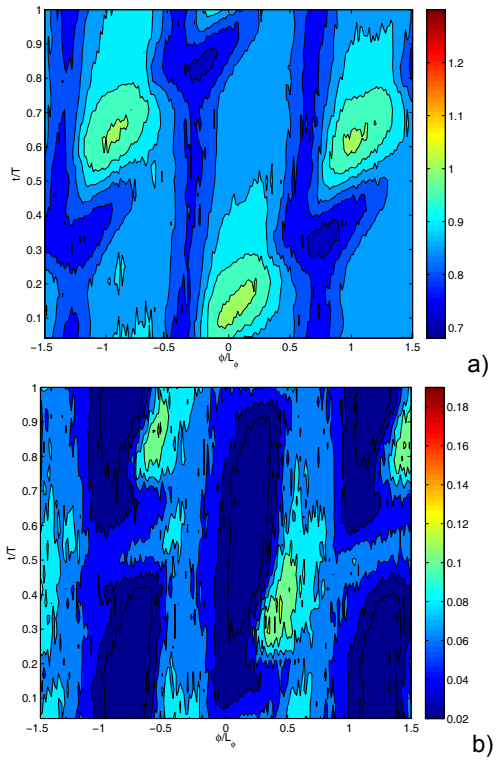

Fig. 9 Time space plot of phase averaged velocity $0.63C_x$ downstream of cascade for low TI, Re=25,000, ζ=0.35, $1.6L_\phi$ rod spacing: a) U/U_e, b) u'/U_e

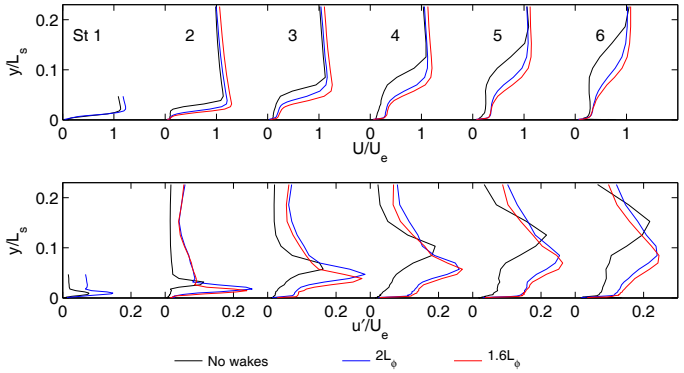

Fig. 10 Time averaged velocity profiles at six streamwise stations for low TI, Re=25,000, ζ=0.7 cases: top – mean, bottom – rms

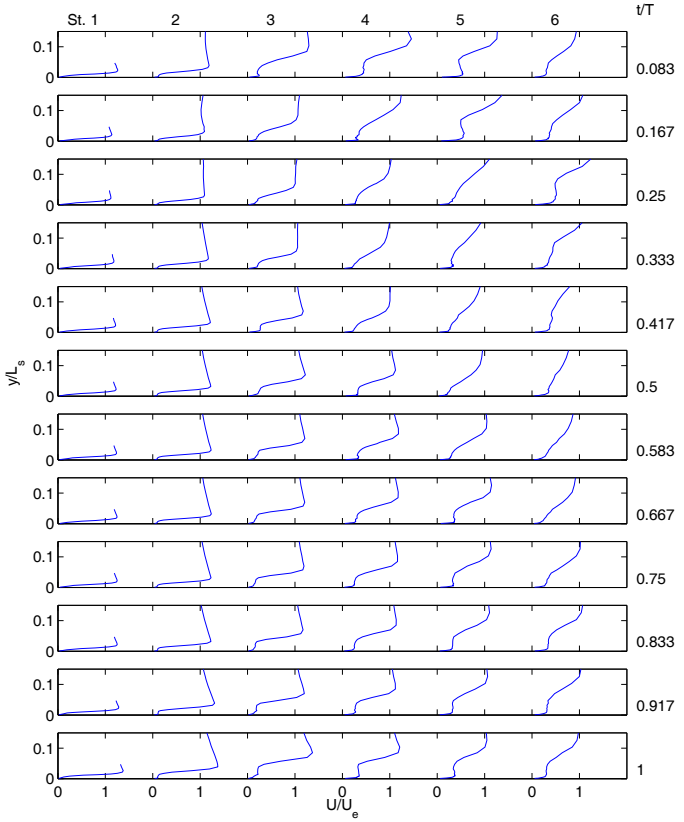

Fig. 11 Phase averaged mean velocity profiles for low TI, Re=25,000, ζ=0.7, $2L_\phi$ rod spacing; columns for six streamwise stations, rows for phases in wake cycle

attached flow at each station where the velocity far from the wall is somewhat lower than at other phases and the near wall velocity more smoothly approaches zero, as fluid from the outer flow fills in the region near the wall when the separation bubble collapses. The reattachment occurs at t/T=0.125-0.25, t/T=0.167-0.333, t/T=0.25-0.458, t/T=0.375-0.583, and t/T=0.458-0.708 at Stations 2-6 respectively.

More results for the low *TI*, *Re*=25,000 cases are shown in Fig. 12 as contour plots of the phase averaged velocity at different phases within the wake passing cycle. The vertical axis shows distance from

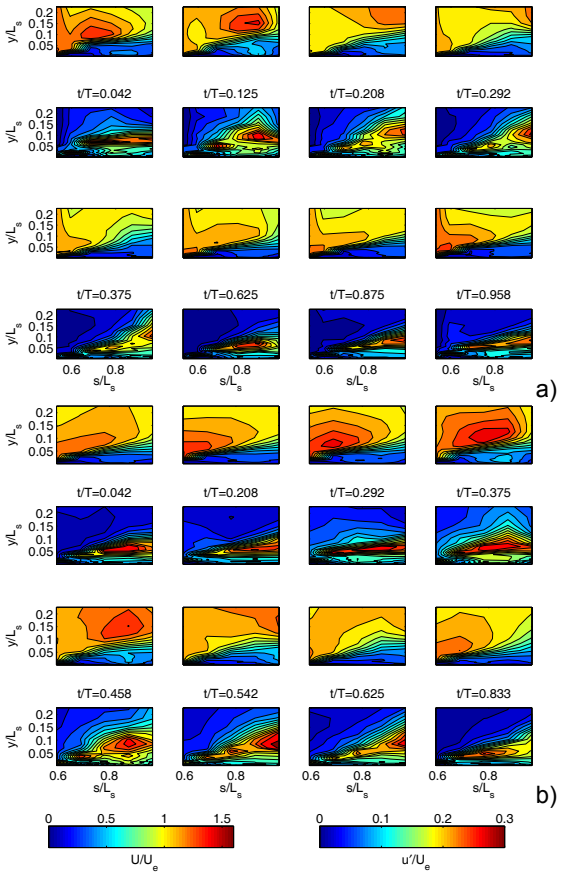

Fig. 12 Phase averaged mean (rows 1 and 3) and rms streamwise fluctuating (rows 2 and 4) velocity for low TI, Re=25,000, ζ=0.7: a) 2L$_\phi$ rod spacing, b) 1.6L$_\phi$ rod spacing

the wall and the horizontal axis shows distance along the suction surface. The first and third row in each case show mean velocity, and the second and fourth row show the corresponding fluctuating velocity. Figure 12a shows the same case as Fig. 11. The effect of the rod wake appears in the mean velocity as elevated freestream velocity at t/T=0.958. The location of high freestream velocity is farther downstream at t/T=0.042, and reaches the trailing edge at about t/T=0.292. During this time the boundary layer remains thick, as shown by the blue color in the figure, but the near wall velocity is slightly elevated (lighter blue). The higher near wall velocity corresponds to the attached profiles at these phases in Fig. 11. As the wake passes, the fluctuating velocity rises in the freestream and near the wall. Between t/T=0.375 and 0.625 the boundary layer relaxes to an undisturbed, separated state, and then continues in this state until the next wake arrives. Figure 12b shows results with the wake spacing reduced to 1.6L_ϕ. The wake passing is similar to that in Fig. 12a, but the dimensionless duration of the wake passing is longer since the wake travels at the same velocity but the period is shorter. This results in less time for recovery between wakes.

Figure 13 presents another view of the wake passing effect as time-space plots of momentum thickness. The horizontal axis shows distance along the suction surface and the vertical axis shows dimensionless time. The data are repeated for two cycles to show the periodicity in time. The white lines in the figure show the approximate location of the wake and the calmed region following the wake. The leading edge of the wake affected region in the boundary

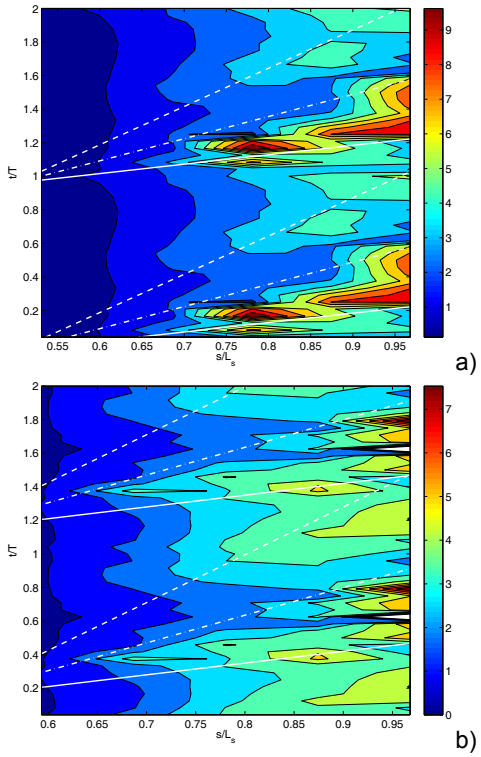

Fig. 13 Phase averaged momentum thickness for low TI, Re=25,000, ζ=0.7: a) 2L$_\phi$ rod spacing, b) 1.6L$_\phi$ rod spacing; lines show leading edge (solid) and trailing edge (dash-dot) of wake, and trailing edge of calm region (dashed)

layer travels at about the freestream velocity, while the trailing edges of the wake and calmed region move at about 50% and 30% of the freestream velocity respectively. These convection velocities agree with values in the literature, such as those reported by Stieger and Hodson [33] and Zhang and Hodson [15]. Momentum thickness is shown since it is proportional to losses in the boundary layer. Plots of other quantities such as the shape factor also show the wake and calmed regions, as shown in Stieger and Hodson [33]. In Fig. 13a, the wake causes a strip of elevated momentum thickness corresponding to the reattachment and elevated near wall turbulence in Figs. 11 and 12a. The periods of high momentum thickness and turbulence produce the high turbulence peaks observed in the airfoil wake in Fig. 6. In Fig. 13, during the early part of the calmed period the momentum thickness is slightly suppressed compared to the value between wake events. During the calmed period the disturbance has already passed, as shown in Fig. 12a, but the boundary layer remains attached, as shown in Fig. 11. Figure 13b shows results with 1.6L_ϕ wake spacing. As in Fig. 13a, the momentum thickness increases as the wake passes and is reduced in the calm region. With less time for recovery between wakes, the variation in momentum thickness is lower in Fig. 13b.

The present results are similar to those in other studies with wakes, such as Schobeiri et al. [11] and Zhang and Hodson [15]. In those studies the boundary layer reattached even without wakes, and the passing wake caused a reduction in the separation bubble size. In the present study, because the Reynolds numbers are lower and the pressure gradients stronger, the boundary layer only intermittently reattaches as the wake passes. There are several mechanism by which wakes could induce reattachment. The elevated freestream turbulence in the wake will cause transition to move upstream in the shear layer, and if transition occurs before the separation bubble becomes too

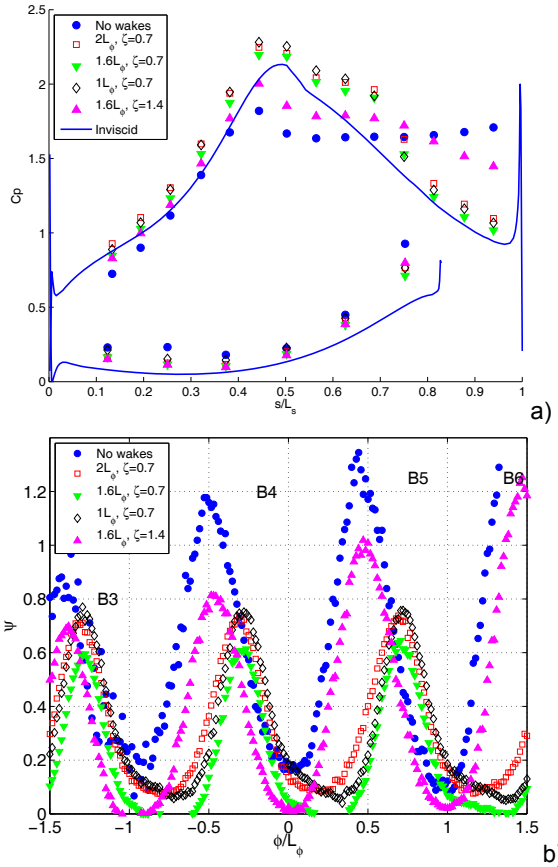

Fig. 14 Pressure profiles for low TI, Re=50,000 cases: a) Cp, b) Total pressure loss

thick, the turbulent mixing could extend close enough to the wall to cause reattachment. Volino et al. [22] showed, however, that elevated background turbulence alone did not cause reattachment on the L1A at *Re*=25,000. The upstream turbulence intensity in the wake is 14%, as documented above, but as the flow is accelerated through the passage, this local intensity drops to about 3% at the beginning of the adverse pressure gradient region. Separated flow transition correlations, such as those of Roberts and Yaras [34] and Volino and Bohl [35], indicate that a rise to 3% *TI* would cause transition to shift upstream by about $0.06L_s$, which may not be enough to explain the full wake effect on reattachment. Other effects of wakes are explained in detail by Stieger and Hodson [33] and Zhang and Hodson [15], who used instantaneous velocity field measurements to document negative jets resulting from temporal freestream acceleration and rollup vortices in the shear layer which caused reattachment. These are likely the same mechanisms responsible for reattachment in the present study.

***Re*=50,000.** Pressure results for low *TI* cases with *Re*=50,000 are shown in Fig. 14. Without wakes the shear layer does not reattach, as in the *Re*=25,000 case. With wakes and ζ=0.7, reattachment is clear for all rod spacings and losses are reduced by over 40%. With the rod speed reduced so ζ=1.4 (*F* reduced to 0.14), only partial reattachment is observed. Wake velocity is shown in Figs. 15-17 for the ζ=0.7 cases with rod spacings of $2L_\phi$, $1.6L_\phi$ and $1L_\phi$ respectively. The airfoil wakes, appearing as vertical strips of low mean velocity and about 7% turbulence, are in the expected positions based on the loss peaks of Fig. 14b. There is some rise in the magnitude of the turbulence to

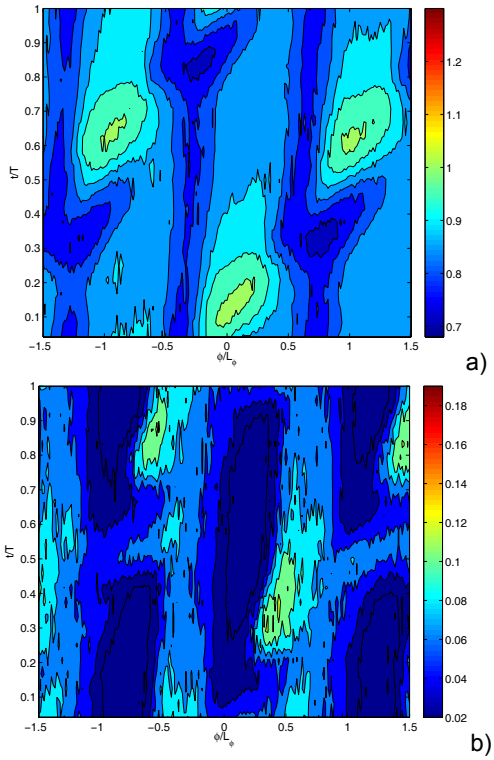

Fig. 15 Time space plot of phase averaged velocity $0.63C_x$ downstream of cascade for low TI, Re=50,000, ζ=0.7, $2L_\phi$ rod spacing: a) U/U_e, b) u'/U_e

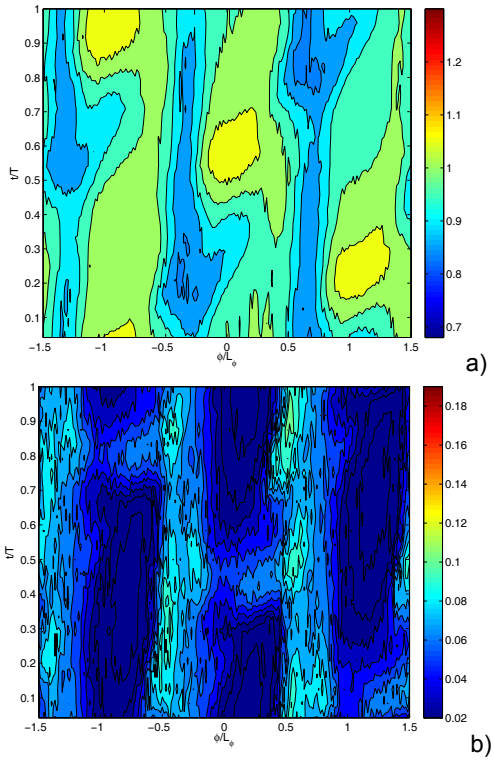

Fig. 16 Time space plot of phase averaged velocity $0.63C_x$ downstream of cascade for low TI, Re=50,000, ζ=0.7, $1.6L_\phi$ rod spacing: a) U/U_e, b) u'/U_e

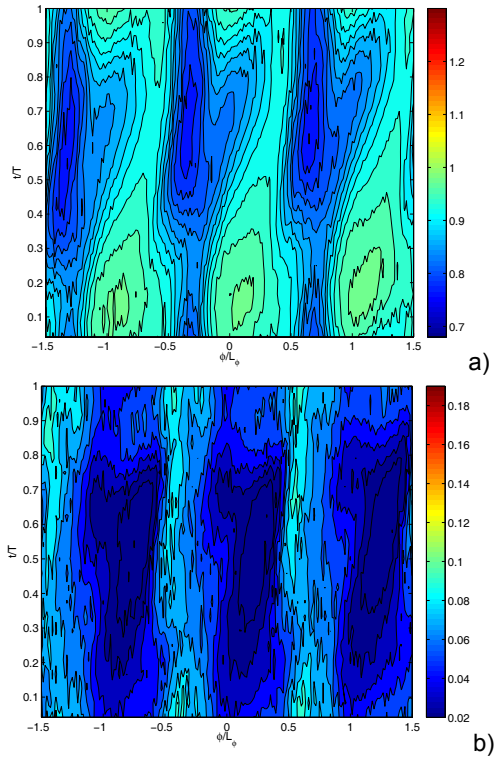

Fig. 17 Time space plot of phase averaged velocity 0.63C_x downstream of cascade for low TI, Re=50,000, ζ=0.7, 1L_ϕ rod spacing: a) U/U_e, b) u′/U_e

about 10% when the airfoil and rod wakes combine in each cycle, particularly in the cases with farther rod spacing. Between the airfoil wakes, the rod wakes appear in the freestream once per cycle with about 5% turbulence. The mean velocity drops during the rod wakes and then rises after the wake passes. The variability in the velocity and turbulence are much lower than in the *Re*=25,000 cases because the wakes suppress the separation bubble more at the higher *Re*. This is shown in the time averaged velocity profiles in Fig. 18. Without wakes there is a large separation bubble. With wakes the boundary layer is attached. The phase averaged mean velocity profiles are shown in Fig. 19 for the ζ=0.7, $2L_\phi$ (*F*=0.22) case. The wakes affect the freestream velocity, particularly at the upstream stations, and a thin separation bubble is visible at Stations 3 and 4 between wakes. At the downstream stations the boundary layer appears attached at all times. Figure 20a shows contours of the phase averaged mean and fluctuating velocity for the ζ=0.7, $2L_\phi$ case. The velocity variation in the freestream is visible between *t/T*=0.042 and 0.375 as the wake passes, and the freestream turbulence is slightly elevated during this period as well. The boundary layer turbulence also rises as the wake passes. The variation during the cycle is not as great as in the *Re*=25,000 cases of Fig. 12. The boundary layer remains relatively thin and attached at all phases. The time-space plot of the momentum thickness is shown for this case in Fig. 21a. As in the lower *Re* cases, the wake causes an increase in momentum thickness as it passes. Any delay in momentum thickness growth in the calmed region is slight. The overall value of the momentum thickness is less than half the value in the *Re*=25,000 cases, which corresponds to the lower losses in Fig. 14 compared to Fig. 5 for the ζ=0.7, $2L_\phi$ cases and the lower wake turbulence in Fig. 15 compared to Fig. 6. A case was also documented with ζ=0.7 and $1.6L_\phi$. It showed little difference from the ζ=0.7, $2L_\phi$ case. A reduction of the wake rod velocity to ζ=1.4, $1.6L_\phi$ (*F*=0.14) produces the results in Figs. 20b and 21b. With the reduced wake frequency the boundary layer is separated for much of the cycle and the momentum thickness is over double its value in the ζ=0.7 case. These results agree with the high loss and separated flow *Cp* profile with ζ=1.4 in Fig. 14.

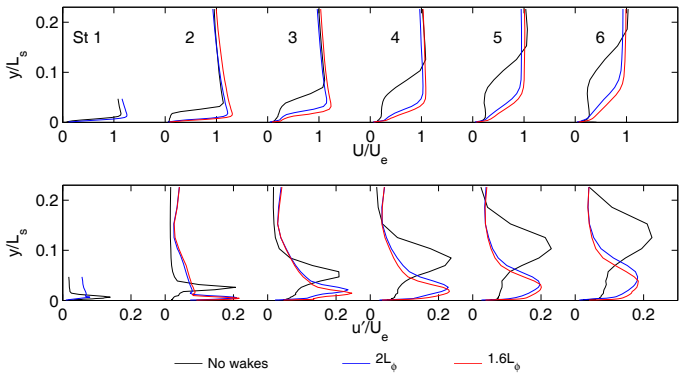

Fig. 18 Time averaged velocity profiles at six streamwise stations for low TI, Re=50,000, ζ=0.7 cases: top – mean, bottom – rms

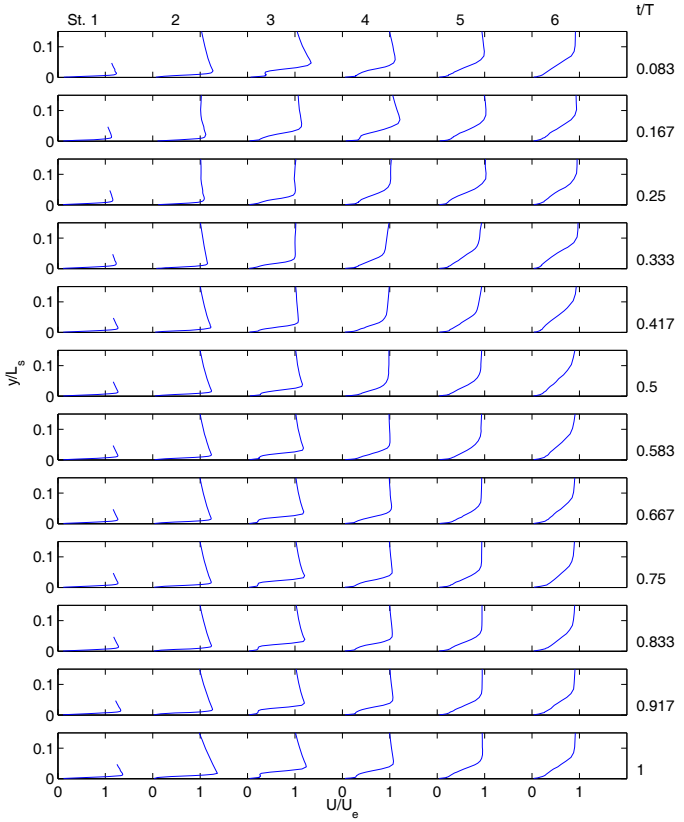

Fig. 19 Phase averaged mean velocity profiles for low TI, Re=50,000, ζ=0.7 cases, 2L_ϕ rod spacing; columns for six streamwise stations, rows for phases in wake cycle

High TI

The pressure results for the high freestream turbulence cases with *Re*=25,000 are shown in Fig. 22. Wake velocity contours are shown in

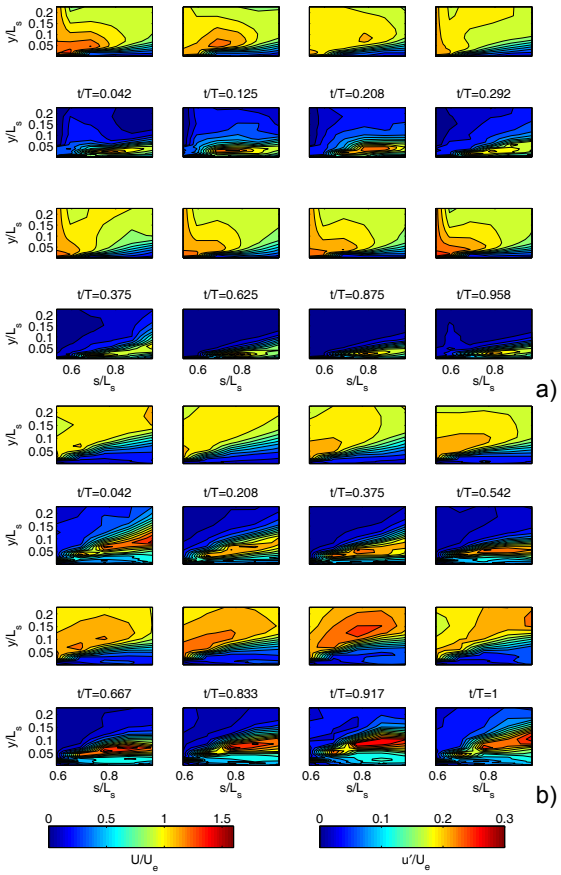

Fig. 20 Phase averaged mean (rows 1 and 3) and rms streamwise fluctuating (rows 2 and 4) velocity for low TI, Re=50,000: a) ζ=0.7, 2L_ϕ, b) ζ=1.4,1.6L_ϕ

Figs. 23 and 24. The results are similar to the corresponding low *TI* results of Figs. 5, 7 and 8. The *Cp* distributions indicate slightly less separation with high *TI*, and in agreement the mean velocities show less variation and the turbulence values are slightly lower with high *TI*.

Results for the Re=50,000 cases are shown in Figs. 25-27. For the ζ=0.7 cases, the results are nearly the same as in the corresponding low *TI* cases of Figs. 14, 16 and 17. In the 1.6L_ϕ, ζ=1.4 cases separation and losses are higher than with lower ζ, but are clearly reduced by the high *TI*. The effect of the rod wakes appears to dominate over the background freestream turbulence effect, and if the wake passing frequency is high enough to suppress separation, the *TI* level between wakes is largely irrelevant. If there is sufficient time between wakes for the boundary layer to separate, high background *TI* helps to limit the separation.

In agreement with results from the literature for other airfoils, wakes help to suppress boundary layer separation. For the L1A airfoil with *Re*=25,000, a dimensionless wake passing frequency of about *F*=0.5 appears sufficient to effectively eliminate separation. At lower frequencies the boundary layer separates between wakes. For *Re*=50,000, *F*=0.3 is sufficient to eliminate separation. It does not appear to matter if a particular frequency is achieved by reducing the spacing between wakes or by increasing the wake generator velocity, so long as *F* is sufficiently high. The required wake frequencies are about equal to the vortex generator jet pulsing frequencies required for separation control with steady inflow observed by Volino et al. [24, 36].

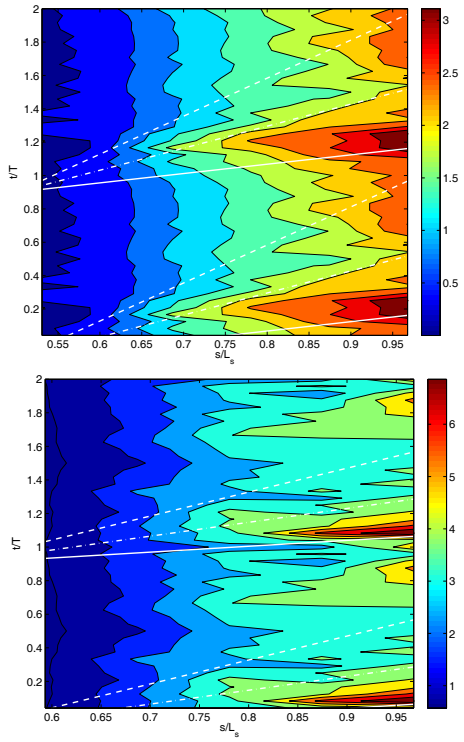

Fig. 21 Phase averaged momentum thickness for low TI, Re=50,000: a) ζ=0.7, 2L_ϕ, b) ζ=1.4,1.6L_ϕ

CONCLUSIONS

The effect of unsteady wakes on the flow over the very high lift L1A airfoil was studied experimentally under low and high freestream turbulence conditions. Reynolds numbers based on suction surface length and nominal exit velocity of 25,000 and 50,000 were considered. Without wakes, the boundary layer separated and did not reattach. Wakes shed by upstream rods caused the boundary layer to reattach. When the wake passing frequency was low, either due to large spacing between wake generator rods or low rod velocity, the boundary layer separated between wakes. With a dimensionless wake passing frequency of *F*=0.5 or higher at *Re*=25,000 or with *F*=0.3 or higher at *Re*=50,000, separation was largely suppressed. Background freestream turbulence also helps to reduce separation, but the effect is secondary to the wake effect.

The expected wake passing frequency in an engine is near the frequency at which separation begins to be a problem on the L1A. The present cases will serve as baseline results for future cases in which wakes and flow control with vortex generator jets are combined.

ACKNOWLEDGMENTS

This work was sponsored by the National Aeronautics and Space Administration under grant NNC07IA10I. The grant monitor were Drs. Anthony Strazisar and James Heidmann of the NASA Glenn Research Center. The support of the United States Naval Academy Technical Support Department Shop and Fluids Laboratory is greatly appreciated.

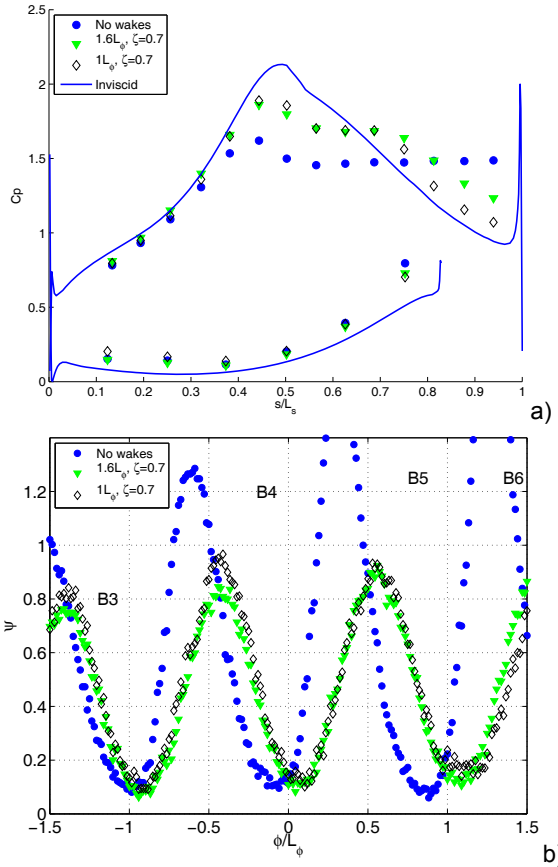

Fig. 22 Pressure profiles for high TI, Re=25,000 cases: a) Cp, b) Total pressure loss

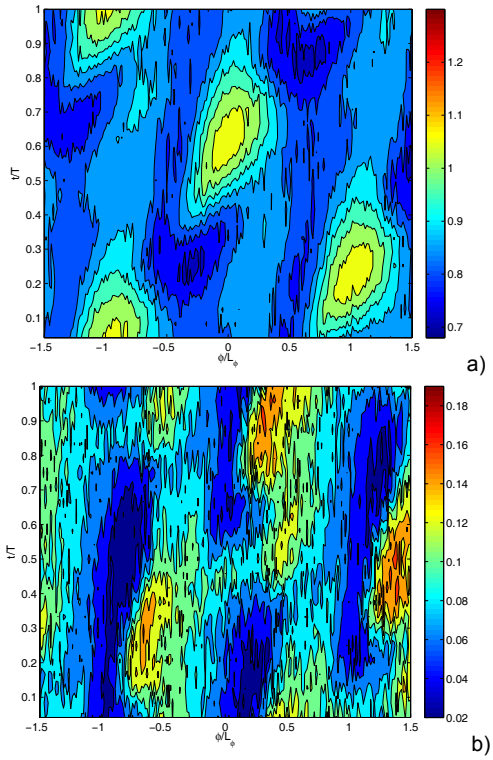

Fig. 23 Time space plot of phase averaged velocity 0.63C_x downstream of cascade for high TI, Re=25,000, ζ=0.7, 1.6L_ϕ rod spacing: a) U/U_e, b) u'/U_e

REFERENCES

[1] Hourmouziadis, J., 1989, "Aerodynamic Design of Low Pressure Turbines," AGARD Lecture Series 167.

[2] Mayle, R.E., 1991, "The Role of Laminar-Turbulent Transition in Gas Turbine Engines," ASME *Journal of Turbomachinery*, **113**, pp. 509-537.

[3] Sharma, O.P., Ni, R.H., and Tanrikut, S., 1994, "Unsteady Flow in Turbines," AGARD Lecture Series 195, Paper No. 5.

[4] Bons, J.P., Sondergaard, R., and Rivir, R.B., 2001, "Turbine Separation Control Using Pulsed Vortex Generator Jets," ASME *Journal of Turbomachinery*, **123**, pp. 198-206.

[5] Volino, R.J., and Hultgren, L.S., 2001, "Measurements in Separated and Transitional Boundary Layers Under Low-Pressure Turbine Airfoil Conditions," ASME *Journal of Turbomachinery*, **123**, pp. 189-197.

[6] Hodson, H.P., and Howell, R.J., 2005, "Bladerow Interactions, Transition, and High-Lift Aerofoils in Low-Pressure Turbine," Annual Review of Fluid Mechanics, **37**, pp. 71-98.

[7] Gostelow, J.P., Walker, G.J., Solomon, W.J., Hong, G., and Melwani, N., 1997, "Investigation of the Calmed Region Behind a Turbulent Spot," ASME *Journal of Turbomachinery*, **119**, pp. 802-809.

[8] Schulte, V., and Hodson, H.P., 1998, "Prediction of the Becalmed Region for LP Turbine Profile Design," ASME *Journal of Turbomachinery*, **120**, pp. 839-846.

[9] Bons, J.P., Pluim, J., Gompertz, K., Bloxham, M., and Clark, J.P., 2008, "The Application of Flow Control to an Aft-Loaded Low Pressure Turbine Cascade with Unsteady Wakes," ASME Paper GT2008-50864.

[10] Pluim, J., Memory, C., Bons, J., and Chen, J.P., 2009, "Designing a High Fidelity Wake Simulator for Research Using Linear Cascades," ASME Paper GT2009-52276.

[11] Schobeiri, M.T., Öztürk, B., and Ashpis, D.E., 2007, "Effects of Reynolds Number and Periodic Unsteady Wake Flow Condition on Boundary Layer Development, Separation, and Intermittency Behavior Along the Suction Surface of a Low Pressure Turbine Blade," ASME *Journal of Turbomachinery*, **129**, pp. 92-107.

[12] Öztürk, B., and Schobeiri, M.T., 2007, "Effects of Turbulence Intensity and Periodic Unsteady Wake Flow Condition on Boundary Layer Development, Separation, and Reattachment Along the Suction Surface of a Low-Pressure Turbine Blade," ASME *Journal of Fluid Engineering*, **129**, pp. 747-763.

[13] Jiang, N., and Simon, T.W., 2005, "Transition in Low-Pressure Turbines: Effects of Unsteady Acceleration and Turbulence Intensity," AIAA *Journal of Thermophysics and Heat Transfer*, **19**, 148-155.

[14] Mahallati, A., and Sjolander, S.A., 2007, "Aerodyanmics of a Low-Pressure Turbine Airfoil at Low-Reynolds Numbers Part 2: Blade-Wake Interaction," ASME Paper GT2007-27348.

[15] Zhang, X.F., and Hodson, H.P., 2010, "Effects of Reynolds Number and Freestream Turbulence Intensity on the Unsteady Boundary Layer Development on an Ultra-High-Lift Low Pressure Turbine Airfoil," ASME *Journal of Turbomachinery*, **132**, 011016.

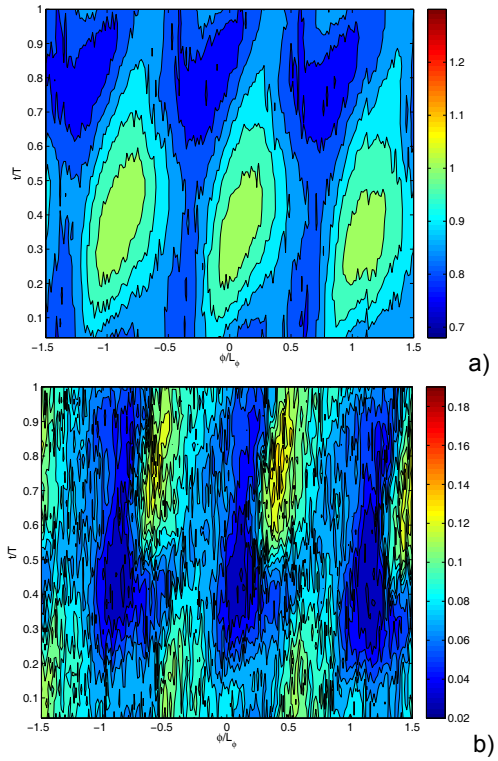

Fig. 24 Time space plot of phase averaged velocity 0.63C_x downstream of cascade for high TI, Re=25,000, ζ=0.7, 1L_ϕ rod spacing: a) U/U_e, b) u′/U_e

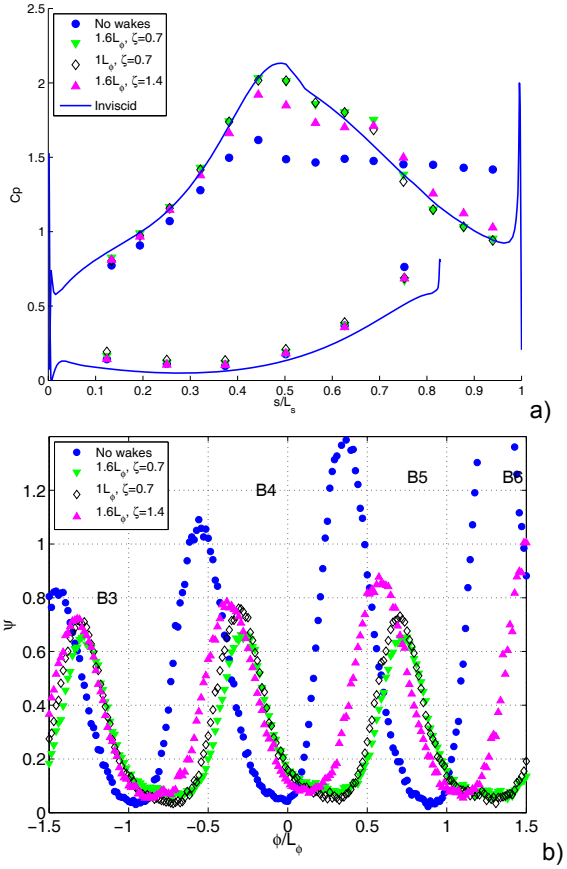

Fig. 25 Pressure profiles for high TI, Re=50,000 cases: a) Cp, b) Total pressure loss

[16] Funazaki, K., Yamada, K., Ono, T., Segawa, K., Hamazaki, H., Takahashi, A., and Tanimitsu, H., 2006, "Experimental and Numerical Investigations of Wake Passing Effects upon Aerodynamic Performance of a LP Turbine Linear Cascade With Variable Solidity," ASME Paper GT2006-90507.

[17] Praisner, T.J., and Clark, J.P., 2007, "Predicting Transition in Turbomachinery – Part 1: A Review and New Model Development," ASME *Journal of Turbomachinery*, **129**, pp. 1-13.

[18] Clark J.P., 2007, Private Communication, Air Force Research Laboratory.

[19] Zhang, X.F., and Hodson, H., 2005, "Combined Effects of Surface Trips and Unsteady Wakes on the Boundary Layer Development of an Ultra-High-Lift LP Turbine Blade," ASME *Journal of Turbomachinery*, **127**, pp. 479-488.

[20] Volino, R.J., 2010, "Separated Flow Measurements on a Highly Loaded Low-Pressure Turbine Airfoil," ASME *Journal of Turbomachinery*, **132**, 011007.

[21] Ibrahim, M., Kartuzova, O., and Volino, R.J., 2008, "Experimental and Computational Investigations of Separation and Transition on a Highly Loaded Low Pressure Turbine Airfoil: Part 1 – Low Freestream Turbulence Intensity," ASME Paper IMECE2008-68879.

[22] Volino, R.J, Kartuzova, O., and Ibrahim, M., 2008, "Experimental and Computational Investigations of Separation and Transition on a Highly Loaded Low Pressure Turbine Airfoil: Part 2 – High Freestream Turbulence Intensity," ASME Paper IMECE2008-68776.

[23] Volino, R.J., 2002, "Separated Flow Transition Under Simulated Low-Pressure Turbine Airfoil Conditions: Part 1 – Mean Flow and Turbulence Statistics," ASME *Journal of Turbomachinery*, **124**, pp. 645-655.

[24] Volino, R.J., Kartuzova, O., and Ibrahim, M.B., 2009, "Experimental and Computational Investigations of Low-Pressure Turbine Separation Control Using Vortex Generator Jets," ASME Paper GT2009-59983.

[25] Reimann, D., Bloxham, M., Pluim, J., and Bons, J.P., 2007, "Comparison of Spanwise Wake and Discrete Jet Disturbances on a Separating Low-Pressure Turbine Blade," AIAA Paper 2007-0525.

[26] Kaszeta, R.W., Simon, T.W., Jiang, N., and Ottaviani, F., 2005, "Influence of Wake Passing Frequency and Elevated Turbulence Intensity on Transition," AIAA *Journal of Thermophysics and Heat Transfer*, **19**, 137-147.

[27] Wills, J.A.B., 1962, "The Correction of Hot-Wire Readings for Proximity to a Solid Boundary," *Journal of Fluid Mechanics*, **12**, pp. 65-92.

[28] Schobeiri, M.T., John, J., and Pappu, K., 1996, "Development of Two-Dimensional Wakes Within Curved Channels: Theoretical Framework and Experimental Investigation," ASME *Journal of Turbomachinery*, **118**, pp. 506-518.

[29] Pfeil, H. and Herbst, R., 1979, "Transition Procedure of Instationary Boundary Layers", ASME Paper 79-GT-128.

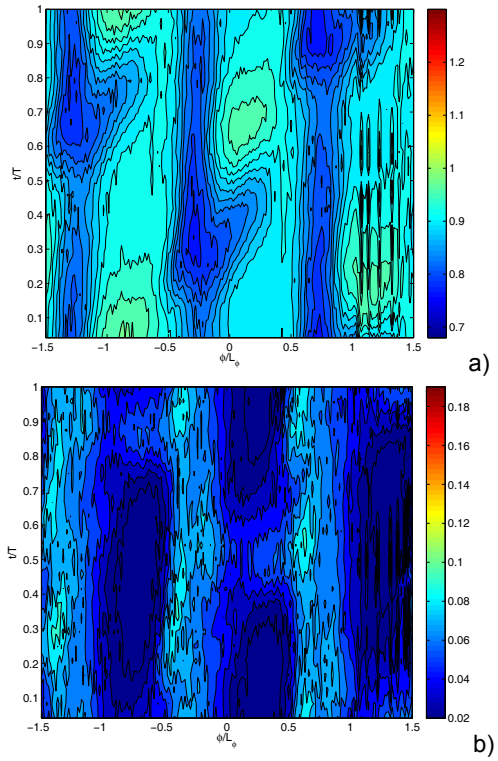

Fig. 26 Time space plot of phase averaged velocity $0.63C_x$ downstream of cascade for high TI, Re=50,000, ζ=0.7, $1.6L_\phi$ rod spacing: a) U/U_e, b) u'/U_e

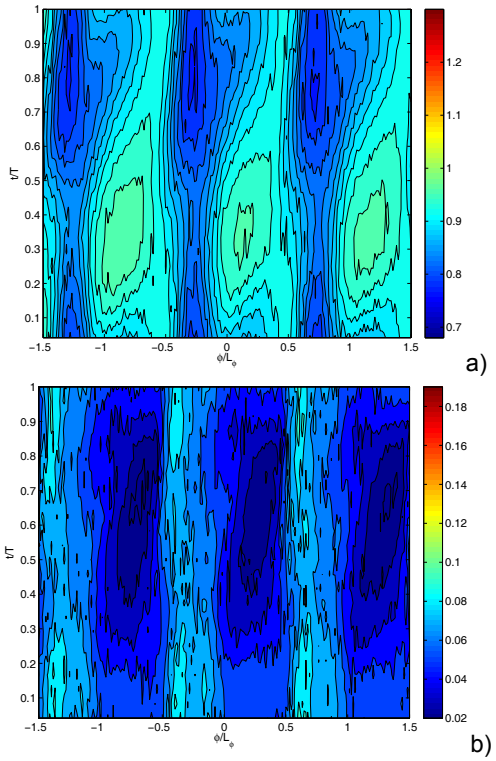

Fig. 27 Time space plot of phase averaged velocity $0.63C_x$ downstream of cascade for high TI, Re=50,000, ζ=0.7, $1L_\phi$ rod spacing: a) U/U_e, b) u'/U_e

[30] Stieger, R. D., 2002, ‘‘The Effects of Wakes on Separating Boundary Layers in Low Pressure Turbines,’’ Ph.D. thesis, University of Cambridge, Cambridge, UK.

[31] Stieger, R.D., and Hodson, H.P., 2005, “The Unsteady Development of a Turbulent Wake Through a Downstream Low-Pressure Turbine Blade Passage,” ASME *Journal of Turbomachinery*, **127**, pp. 388-394.

[32] Volino, R.J., 2005, “An Investigation of the Scales in Transitional Boundary Layers under High Freestream Turbulence Conditions,” *Experiments in Fluids*, **38**, pp. 516-633.

[33] Stieger, R.D., and Hodson, H.P., 2004, “The Transition Mechanism of Highly Loaded Low-Pressure Turbine Blades,” ASME *Journal of Turbomachinery*, **126**, pp. 536-543.

[34] Roberts, S.K., and Yaras, M.I., 2006, “Effects of Surface-Roughness Geometry on Separation-Bubble Transition,” ASME *Journal of Turbomachinery*, **128**, pp. 349-356.

[35] Volino, R.J., and Bohl, D.G., 2004, “Separated Flow Transition Mechanisms and Prediction with High and Low Freestream Turbulence Under Low Pressure Turbine Conditions,” ASME Paper GT2004-53360.

[36] Volino, R.J., Kartuzova, O., and Ibrahim, M.B., 2010, “Separation Control on a Very High Lift Low Pressure Turbine Airfoil Using Pulsed Vortex Generator Jets,” ASME Paper GT2010-23567.

Proceedings of ASME Turbo Expo 2010: Power for Land, Sea and Air

GT2010

June 14-18, 2010, Glasgow, UK

GT2010-23015

LES FLOW CONTROL SIMULATIONS FOR HIGHLY LOADED LOW PRESSURE TURBINE AIRFOIL (L1A) USING PULSED VORTEX GENERATOR JETS

Mounir B. Ibrahim, Olga Kartuzova and Daniel J. Doucet
Mechanical Engineering Department
Cleveland State University
Cleveland, Ohio 44115-2425
m.ibrahim@csuohio.edu

Ralph J. Volino
Mechanical Engineering Department
United States Naval Academy
Annapolis, Maryland 21402-5042
volino@usna.edu

ABSTRACT

Seven different cases were examined experimentally and computationally to study LPT flow control using pulsed VGJs for the L1A airfoil. These cases represent a combination of variation in Reynolds number, Re (25,000, 50,000 and 100,000), based on the suction surface length and the nominal exit velocity from the cascade, blowing ratio, B (from 0.25 to 1), dimensionless frequency, F (from 0.035 to 0.56) and duty cycle, DC (10% and 50%). The data was obtained for the pressure distribution along the airfoil and downstream in the wake as well as for velocity profiles at six different stations downstream of the suction peak. The CFD was done with LES utilizing version 6.3.26 of the finite-volume code ANSYS Fluent. The CFD did provide further insight to better understand the physics of flow control. The comparison between CFD and experimental results for Cp, velocity profiles and ψ_{int} is reasonable for all cases examined.

Two of the cases examined did indicate that the higher DC could compensate for the lower F value. However, the effect of increasing the frequency appears to be stronger than increasing the DC value. The results from CFD using the Q-Criterion clearly illustrate how a separation bubble will persist at the lower frequency case (Case (2)) and the disturbances created from the jet flow do not have enough energy or time to travel further downstream to cause reattachment. On the other hand, the higher frequency case (Case (6)) did exhibit a penetration of the disturbance created by the jet into the separated region and caused reattachment, especially at the trailing edge. It appears that the jet was capable of breaking the large bubble into smaller ones with reattachment in between.

NOMENCLATURE

B	blowing ratio, maximum jet velocity/local freestream velocity
Cp	$2(P_T - P)/\rho U_e^2$, pressure coefficient
C_x	axial chord length
DC	duty cycle, fraction of time valve is open
F	$fL_{j\text{-}te}/U_{ave}$, dimensionless frequency
f	frequency
$L_{j\text{-}te}$	distance from VGJs to trailing edge
L_s	suction surface length
L_ϕ	blade spacing (pitch)
P	pressure
P_S	upstream static pressure
P_T	upstream stagnation pressure
P_{Te}	downstream stagnation pressure

Re	$U_e L_s/\nu$, exit Reynolds number
s	streamwise coordinate, distance from leading edge
T	period of jet pulsing cycle
t	time
u'	RMS of the fluctuating component of the streamwise velocity
TKE	turbulent kinetic energy
U_{ave}	average freestream velocity between VGJs and trailing edge
U_e	nominal exit freestream velocity, based on inviscid solution
V_x	axial velocity
x	axial distance from leading edge
ν	kinematic viscosity
ρ	density
ψ	$(P_T-P_{Te})/(P_T-P_S)$, total pressure loss coefficient
ψ_{int}	total pressure loss integrated over blade spacing

INTRODUCTION

Boundary layer separation on the suction side of low-pressure turbine (LPT) airfoils can occur due to strong adverse pressure gradients. The problem is becoming more severe as airfoil loading is increased. If the boundary layer separates, the lift from the airfoil decreases and the aerodynamic loss increases, resulting in a drop in overall engine efficiency. A significant increase in efficiency could be achieved if separation could be prevented or minimized. Active flow control could provide a means for minimizing separation under conditions where it is most severe (low Re), without causing additional losses under other conditions (high Re). Minimizing separation will allow for improved designs with fewer stages and fewer airfoils per stage to generate the same power. The active flow control technique called Vortex Generator Jets (VGJs), introduced by Johnston and Nishi [1], is the subject of this paper. In this technique, blowing from small, compound angled holes is used to create streamwise vortices. The vortices bring high momentum fluid into the near wall region as well as promote transition and turbulent mixing. This helps to control separation. A review of experimental work on this topic was given in Volino et al. [2].

Along with the experimental investigations, numerical simulations of the flow over LPT blades, utilizing steady and pulsed vortex generator jets (VGJs), were performed by different researchers. This type of flow is challenging for CFD because of its transitional nature in combination with highly three-dimensional jet flow.

Rizzetta and Visbal [3] used ILES (Implicit Large Eddy Simulation) to investigate the effect of flow control by pulsed VGJs on the flow separation in a Pack B cascade. The Pack B is a widely studied LPT airfoil. They reported that for inlet Re=25,000 and B=2, flow control helped to keep flow attached for an additional 15% of the chord. Despite some differences with experimental data, numerical and experimental time-mean velocity profiles were in reasonable agreement.

Postl et al. [4] studied the effect of active flow control utilizing steady and pulsed VGJs on preventing laminar separation on the Pack B airfoil. In their study they used two computational approaches. The first was direct numerical simulation (DNS) of the flow over a flat plate with imposed streamwise pressure gradient as measured on the suction side of the Pack B airfoil. In the second approach, a linear LPT cascade was simulated with the flow control cases performed in 2D using slots. They observed two different physical mechanisms to affect the control for the steady versus pulsed VGJs. The steady jets developed streamwise structures which enhanced momentum exchange between the near wall region and free stream. For the pulsed VGJs, an accelerated boundary layer transition helped to achieve flow reattachment. Their results are in reasonably good agreement with experimental data except in the separated region, where the size of the separation bubble was under predicted.

Garg [5] used the NASA Glenn-HT code with the k-ω SST model of Menter [6] to compute the flow over the Pack B blade with and without the use of VGJs. This work resulted in correct predictions of the separation location in the baseline case (without VGJs) as well as showing that separation vanishes in the flow control case as in the experiment. However, the separated region and the wake were not well predicted, which is common for RANS.

In the present study the very highly loaded L1A airfoil was considered [7]. The L1A was designed at the Air Force Research Laboratory (AFRL) and is available on a limited basis from Clark [8]. It is an aft-loaded blade with the same flow angles and loading as the mid-chord loaded L1M. Based on the design calculations of Clark [8], the L1A has 10% higher loading than the "ultra-high lift" airfoils described by Zhang and Hodson [9], and 17% higher loading than the Pack B. Because the L1A is aft-loaded, it is more prone to separation than the L1M, as documented in Bons et al. [10], Ibrahim et al. [11], and Volino et al. [12]. In cases without flow control and with low freestream turbulence, the boundary layer separates when Re<150,000 and does not reattach, in spite of transition to turbulence in the shear layer over the separation bubble in all cases. This result contrasts with the results of earlier studies on less aggressive airfoils, which all showed reattachment after transition. The separation bubble on the L1A is about four times thicker than that on the Pack B. The larger distance from the shear layer to the wall on the L1A apparently prevents the turbulent mixing in the shear layer from reaching the wall and causing reattachment. The failure of the boundary layer to reattach results in a 20% loss in lift and increases profile losses by a factor of 7 [2]. At higher Reynolds numbers, the separation bubble is small and the boundary layer is attached over most of the airfoil. In cases with high freestream turbulence, results are similar, but the shear layer is somewhat thicker and the separation bubble thinner due to increased mixing induced in the shear layer. This results in reattachment after transition at Re=50,000 and 100,000. At the lowest Re considered (25,000) the boundary layer still does not reattach.

Boundary layer separation control has been studied using VGJs on the L1A airfoil. Experiments were done under low freestream turbulence conditions on a linear cascade in a low-speed wind tunnel (see Volino et al., [2]). In that paper, the pressure surveys on the airfoil surface and downstream total pressure loss surveys were documented. Cases were considered at Reynolds numbers (based on the suction surface length and the nominal exit velocity from the cascade) of 25,000, 50,000 and 100,000. In all cases without flow control, the boundary layer separated and did not reattach. These cases (without jets) were documented experimentally and computationally for low freestream turbulence intensity (see Ibrahim et al. [12]) and high freestream turbulence intensity (see Volino et al. [13]). Cases with steady jets were documented for low freestream turbulence intensity (see Volino et al. [2] and Ibrahim et al. [7]). Bons et al. [14] considered a case with Re=50,000, background freestream turbulence intensity of 3%, and periodic wakes produced with moving rods upstream of the airfoils. The VGJs had a duty cycle (fraction of time the jets are on during a pulsing cycle) of 30% and a blowing ratio of 2.3 (based on the maximum jet velocity in the pulsing cycle and the local freestream velocity). The dimensionless frequency of the wake passing and VGJ pulsing were both F= $fL_{j\text{-}te}/U_{ave}$,=0.34, where $L_{j\text{-}te}$ is the streamwise distance from the VGJ holes to the trailing edge, and U_{ave}, is the average freestream velocity over this distance. Two different streamwise locations for the VGJs were considered. The VGJs reduced the separation bubble size and reduced total pressure losses.

This paper describes in detail the effects of using pulsed VGJs to control the flow over highly loaded LPT airfoil L1A discussed earlier. Experimental and computational methods are used to show how changes in pulsing frequency, blowing ratio, and duty cycle can achieve boundary layer separation control and even reattachment.

EXPERIMENTAL FACILITY AND MEASUREMENTS

Experiments were conducted in a closed loop wind tunnel with a seven blade linear cascade located in the wind tunnel's third turn, as shown in Fig. 1a. Cascade parameters are shown in Table 1. A fine screen located upstream of the cascade is used to break up the boundary layers which form on the diffuser walls upstream of the test section and to provide uniform inlet conditions to the cascade. The freestream turbulence entering the cascade was measured with a cross-wire probe positioned just upstream of the center blade. The turbulence intensity is 0.8% in the streamwise component and 0.5% in the cross stream components. The integral length scale of the streamwise component is 6.3 cm. Further details of the facility and inlet flow are in Volino [13].

A tailboard, shown in Fig. 1a, is needed to produce the correct exit flow angle from the cascade. Its position was set to produce periodicity at high Reynolds numbers. A tailboard on the opposite side of the cascade and inlet guide vanes were found to be unnecessary. To produce the correct approach flow to the end blades (B1 and B7), the amount of flow escaping around the two ends of the cascade is controlled with the flaps shown in Fig. 1a. The inlet flow angle at the center of the cascade was checked with a three-hole pressure probe and found to agree with the design angle to within 2° of uncertainty. Good periodicity at high Reynolds numbers was obtained in the exit flow. At low Reynolds numbers, when significant separation bubbles are present, the periodicity is not as good due to suppression of the separation bubble thickness on the blades closest to the tailboard.

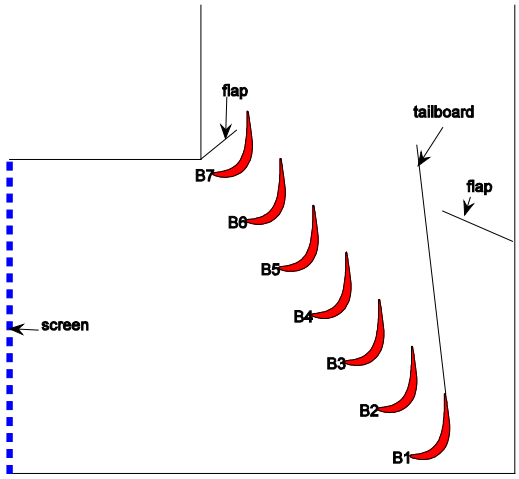

Figure 1a. Schematic of linear cascade

Table 1: Cascade parameters

Axial Chord, C_x [mm]	True Chord [mm]	Pitch, L_ϕ [mm]	Span [mm]	Suction side, L_s [mm]	Inlet flow angle	Exit flow angle
134	146	136	724	203	35°	60°

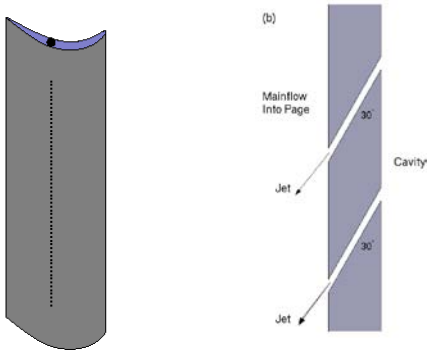

Figure 1b. Airfoil with VGJ holes and cross section of hole geometry.

In cases with effective flow control, periodicity is reestablished. The lack of periodicity in cases with large separation bubbles is considered acceptable since the focus of the study is separation control, and not documentation of cases

with large separation that would be unacceptable in practice. This compromise facilitates the study of a larger number of cases with flow control by obviating the need to adjust the tailboard by trial and error for each case. It also provides for better repeatability in the experiments, since the position of the tailboard is fixed for all cases. Any improvements made with flow control will be larger in practice than documented in the experiment, due to the effect of the tailboard in suppressing the bubble size in the uncontrolled cases.

Each blade in the cascade has a central cavity which extends along the entire span. The cavity is closed at one end and has a fitting at the opposite end connected to a compressed air line. Air is supplied to the cavities from a common manifold. Manual ball valves are placed in the tubing between the manifold and blades to insure that each blade receives the same air flow. The valves also help to damp high frequency oscillations in the jet velocity when the VGJs are pulsed. The manifold is supplied through two fast response solenoid valves (Parker Hannifin 009-0339-900 with General Valve Iota One pulse driver) operating in parallel. The valves are supplied through a pressure regulator by the building air supply. A single spanwise row of holes was drilled into the suction surface of each blade at the inviscid pressure minimum location, s/L_s=0.5 (x/C_x=0.62), where s is the distance from the leading edge and L_s is the suction surface length. The pressure minimum has been shown in the studies listed above to be about the optimal location for flow control devices. The effects of devices located farther upstream are damped by the favorable pressure gradient, and devices located downstream of the separation point can also lose effectiveness. The holes are 0.8 mm in diameter and drilled at 30° to the surface and 90° to the main flow direction (see Figure 1b). This is the same orientation used in all the VGJ studies listed above. The hole spacing is 10.6 diameters, and the length to diameter ratio is 12.

The solenoid valves pulse the VGJs, and the pulsing frequency is presented below in dimensionless form as $F= fL_{j\text{-}te}/U_{ave}$,, where $L_{j\text{-}te}$ is the streamwise distance from the VGJ holes to the trailing edge, and U_{ave}, is the average freestream velocity over this distance. For flow over single airfoils, F≥1 is typically needed to maintain separation control, but for cascades, Bons et al. [14] showed that control is possible in some cases with F=0.1. As shown in Volino [15] and Bons et al. [14], this is due to the extended calmed region which follows the jet disturbance. In practice, VGJs could be timed to wake passing in an LPT, which has a typical frequency of about F=0.3.

The center blade, designated B4 in Fig. 1a, contains pressure taps near the spanwise centerline. Pressure surveys are made using a pressure transducer (0-870 Pa range Validyne transducer). Stagnation pressure is measured with a pitot tube upstream of the cascade. The uncertainty in the suction side pressure coefficients is 0.07. Most of this uncertainty is due to bias error. Stochastic error is minimized by averaging pressure transducer readings over a 10 second period.

Total pressure losses are documented using a Kiel probe traversed across three blade spacings, 0.63 C_x downstream of the cascade. A traverse is located in the wind tunnel downstream of the cascade to move the probe. The traverse causes an acceptably low blockage when it is located at least two C_x downstream of the cascade.

Pressure and loss surveys were acquired at nominal Re=25,000, 50,000 and 100,000. The Reynolds number, as defined above, is based on the suction surface length and the nominal cascade exit velocity. The corresponding Reynolds numbers based on the cascade inlet velocity and the axial chord length are 10,000, 20,000 and 40,000, respectively.

NUMERICAL SIMULATION

The numerical simulations were conducted for the L1A airfoil utilizing version 6.3.26 of the finite-volume code ANSYS Fluent [16]. In this paper, cases were considered at different Reynolds numbers, blowing ratios, frequencies and duty cycles of blowing. Table 2 shows a summary of all the CFD cases presented in this paper. The three dimensional computational domain includes a single passage (see Table 1 for cascade parameters). A uniform velocity inflow condition is specified 1.9 C_x upstream of the blade leading edge in the flow direction. The inlet flow angle is set to 33^o based on an inviscid calculation of the full cascade used in the experiment [11]. This angle agrees with the experimentally measured inlet angle to within the experimental uncertainty. The exit boundary is located 3.8 C_x downstream of the trailing edges in the flow direction. In the spanwise direction, the domain includes one VGJ. The boundary conditions on the sides of the passage are periodic. The full length of the feeding tube is included in the simulations, allowing the jet velocity profile to develop before entering the main domain [2]. A uniform velocity boundary condition during jet blowing is specified at the hole inlet, otherwise there would be no jet flow. For a duty cycle of 10%, this means the jet is on only for 10% of the cycle. Computation was continued until no variation (cycle-to-cycle) was reached.

Convergence was established when residuals were reduced to a value 10^{-5} and the mass imbalance was less than 0.01 %.

Table 2. CFD Test matrix (NA = not available).

f, Hz	DC %	Re/B		
		25,000/ 1.0	50,000/ 0.5	100,000/ 0.25
3	10	Case (1)	Case (2)	Case (3)
12	10	Case (4)	Case (5)	NA
24	10	NA	Case (6)	NA
12	50	NA	Case (7)	NA

TURBULENCE MODEL DESCRIPTION

Large Eddy Simulation with Dynamic Kinetic Energy Subgrid-Scale model

In LES, large eddies are resolved directly, while small eddies are modeled. The rationale behind LES is as follows: a) Momentum, mass, energy, and other passive scalars are transported mostly by large eddies, b) Large eddies are more problem-dependent and are dictated by the geometries and boundary conditions of the flow involved, c) Small eddies are less dependent on the geometry, tend to be more isotropic, and are consequently more universal, and d) The chance of finding a universal turbulence model is much higher for small eddies.

The governing equations employed for LES are obtained by filtering the time-dependent Navier-Stokes equations in either Fourier (wave-number) space or configuration (physical) space. The filtering process effectively filters out the eddies whose scales are smaller than the filter width or grid spacing used in the computations. The resulting equations thus govern the dynamics of large eddies. The subgrid-scale stresses resulting from the filtering operation are unknown and require modeling. The subgrid-scale turbulence models in ANSYS Fluent employ the Boussinesq hypothesis as in the RANS models [16].

The dynamic subgrid-scale kinetic energy model used in present study is based on the model proposed by Kim and Menon [17]. In this model a separate transport equation is solved for subgrid-scale kinetic energy. The model constants are determined dynamically. The details of the implementation of this model in ANSYS Fluent and its validation are given by Kim [18].

RESULTS AND DISCUSSION

Code Validation

Three different grids were attempted for this study as shown in Table 3. Grid#3 was selected (as will be shown later) and Figure 2 shows this grid structure at: a) leading edge, b) trailing edge and c) jet exit, while Table 4 shows more specifications of the grid.

Table 3. Grids#1, 2 and 3 used in this investigation.

Grid #	Size (Cells)	Number of grids in z direction	y+	Δz+	Δx+
1	1,500,000	15	0.5	12.6	1 – 100
2	5,900,000	30	0.5	6.3	0.4 – 52
3	11,900,000	54	0.5	0.4 - 3.5	0.4 – 52

Table 4. Specification of computational Grid#3

Number of cells	11.9 millions
Number of nodes on the suction surface	768
Number of nodes on the pressure surface	392
Number of nodes in span direction	54
y+	<1
Δz+	0.4 - 3.5
Δx+	0.4 - 52
Distance from inlet boundary to the leading edge	3.8 C_x
Distance from the trailing edge to the outlet boundary	1.9 C_x

To accurately represent structures in the near-wall region (for LES), recommended values are: y+~ 2;Δx+ ~ 50 - 150; Δz+ ~ 15-40 (see Piomelli and Chasnov, [19]). Based on results (not shown for space limitation) for the pressure coefficient versus the dimensionless location on the suction side s/L_s , Grid#3 showed the closest agreement with the data and therefore was chosen for further computation. This grid was then run for different time steps (0.0005, 0.0001 and 0.00005 s) and a time step of 0.0001 s was selected since not much improvement was achieved using the smaller one (0.00005 s).

Velocity measurements were conducted at six different stations downstream of the suction peak (see Table 5). Comparison will be made between the velocity profiles at these stations from CFD and experiments.

Table 5. Velocity profile measurement stations.

Station	1	2	3	4	5	6
s/L_s	0.53	0.59	0.69	0.78	0.88	0.97
x/C_x	0.65	0.72	0.80	0.86	0.92	0.97

Pressure Distribution over Airfoil

Statistical averages of the pressure coefficient plotted versus dimensionless distance along the suction side of an airfoil are presented on Figures 3 through 9 for all (7) cases shown in Table 2. These cases represent a combination of variation in Re (25,000, 50,000 and 100,000), F (0.035 to 0.56) and duty cycle (10% and 50%).

Figures 3, 4 and 5 show *Cp* for Cases (1) (F=0.14), (2) (F=0.07), and (3) (F=0.035), respectively with the same frequency (3 Hz) and duty cycle (10%). The Reynolds number varied from 25,000 to 100,000. The figures show flow separation starting after the suction peak with no reattachment, which is indicated by the large plateau in *Cp* after the suction peak. The experimental data are shown with error bar (0.07). *Cp* at the suction peak is lower in CFD compared to experiment. The LES predictions are shown together with experimental data for the same case as well as no jet flow (due to the absence of experimental data for Cases (2) and (3)). It is clear that all cases exhibit separation with no reattachment similar to no jet blowing. The main reason for that is the low frequency at which

blowing occurred together with a low duty cycle that resulted in minimizing the effect of the jet in removing the bubble.

Figures 6 and 7 show *Cp* for Cases (4) (F=0.56) and (5) (F=0.28) respectively, with the same frequency (12 Hz) and duty cycle (10%). The Reynolds number varied from 25,000 to 50,000. The figures show flow separation starting after the suction peak with reattachment. The LES predictions are shown together with experimental data for the same case. The agreement between the CFD and experimental results is reasonable for most of the flow field. The main reason for the reattachment to occur is the higher frequency at which blowing occurred (compare Cases (1) and (4) and Cases (2) and (5)).

Figure 8 shows *Cp* for Case (6) with Re=50,000, F=0.56 (f=24 Hz) and DC=10%. The figure shows flow separation starting after the suction peak with reattachment downstream as a result of the higher blowing frequency. The LES predictions are in reasonable agreement with experimental data for the same case. More details are given for Case (6) below.

Figure 9 shows *Cp* for Case (7) with Re=50,000, F=0.28 (f=12 Hz) and DC=50%. The figure shows flow separation starting after the suction peak with reattachment. This case yielded similar results to Case (6) above. It is believed that increasing the duty cycle (from 10% to 50%) could result in the same effect as increasing the frequency from 12 to 24 Hz. More discussion will be presented later on those effects.

Predictions for Case (6)

From the cases studied above, Case (6) was selected for more detailed examination. This case has experimental data for *Cp* and velocity profiles for comparison.

Figure 10 shows the U velocity contours and velocity vectors for Case (6). The flow shows a small separation bubble with reattachment. Velocity profiles normalized by the nominal exit velocity are plotted versus dimensionless distance from the wall in the direction normal to the wall on Fig. 11. The results for the six measurement stations (see Table 5) located downstream of the suction peak of the airfoil are shown. The agreement between the LES and experimental results is reasonable. Both CFD and experiment show separation starting at station 2 and a large separation bubble present at all stations from 2 to 5, based on negative velocities near the wall at those locations. However, the bubble size is larger in the experiment than in the CFD. It should be noted that the larger disagreement near the wall is due to the fact that hot wire anemometry was used in the experiment, which is not capable of measuring negative velocities.

Profiles of the streamwise component of the RMS fluctuating velocity, u' (for both experiment and the resolved u' from LES), normalized by the nominal exit velocity are plotted versus dimensionless distance from the wall in Fig. 12. The results for the six measurement stations located downstream of the suction peak of the airfoil are shown. LES results compare reasonably well with experiment in the magnitude of u'. Separation starts at station 2 and transition to turbulence starts between stations 3 and 4 (maximum subgrid TKE, u'). The location of the peak of u' is away from the wall (between station 2 and 5) indicating the presence of a small bubble. The peak of u' from the experiment is further away from the wall, indicating a larger bubble than predicted by CFD.

For the purpose of visualization of the separated region as well as the influence of the jet's blowing ratio, iso-surfaces of the mean axial velocity V_x =0.01 m/s are shown in Fig. 13 for Case (6). The reason for choosing V_x =0.01 m/s is that this small (but not negative) value represents velocity in the shear layer of the separation bubble and helps to visualize the size of the bubble and shapes of the vortices created by the jets. The airfoil with three jets on the suction side near the suction peak is shown. The visualization shows that mixing is happening near the wall which causes the flow to reattach near the trailing edge.

Velocity Contours at Jet Exit

CFD analysis provides further insight into the physics of the problem compared to the experiments. The velocity contours were examined at the jet exit for Cases (2), (5), and (6). Those cases have the same Re (50,000), B (0.5) and DC (10%) values but vary in F (0.07, 0.28 and 0.56 for the three cases respectively). Figures 14, 15 and 16 show the contours of the velocity magnitude at the jet exit for the three cases respectively. The traveling time in the feeding tube for all cases is about 6.1 ms. The blowing times, however, vary for the three cases (33.3 ms for Case (2); 8.33 ms for Case (5); and 4.17 ms for Case (6)). A lower frequency results in a higher blowing time. Thus more time is given for the flow to reach the jet exit and exhibit a parabolic profile (compare Figures 14 and 16). On the other hand, lower frequencies (with the same DC) result in the higher quiet time (no blowing) and thus the case gets closer to uncontrolled one. This explains the poor flow control results (flow separation) in Case (2) as shown earlier in Figure 4.

Figure 17 shows the velocity contours at the jet exit for Case (7). This case has Re=50,000, B=0.5, DC=50% and F=0.28. One additional feature that exists in this case (that differs from the above Cases (2), (5) and (6)) is the fact that the blowing during the 50% DC was split into two parts. The first 10% was at the nominal blowing value while that velocity was reduced to lower values at the second part of the blowing. This was done to match the jet velocity profile seen in the experiment with no cross flow present (see Figure 2 of Volino et al. [2]).

Effect of Re, F and DC

Table 6 shows the main characteristics for all the cases examined. The seven cases represent a combination of the variation in Re, F and DC. The total pressure loss integrated over blade spacing, ψ_{int}, is also shown in the table for both CFD and experimental results.

Table 6. Main Parameters of all Cases Examined.
(NA = not available)

Case	1	2	3	4	5	6	7
Re/1000	25	50	100	25	50	50	50
B	1.0	0.5	0.25	1.0	0.5	0.5	0.5
DC %	10	10	10	10	10	10	50
f, Hz	3	3	3	12	12	24	12
U_{ave},, m/s	2.17	4.35	8.7	2.17	4.35	4.35	4.35
F	0.14	0.07	0.035	0.56	0.28	0.56	0.28
$\psi_{int,}$ *CFD*	0.923	1.026	0.825	0.515	0.372	0.246	0.384
ψ_{int} *Exp*	NA	NA	NA	0.346	0.356	0.237	0.313

As the Reynolds number increases the losses decrease. Cases (4) and (6) show that despite having the same F value, more losses are encountered at lower Re.

As the value of F increases the losses decrease, see Cases (2), (5) and (6). It appears that a value of F of 0.28 or above is sufficient enough to cause reattachment and possible removal of the bubble, depending on the Reynolds number.

Cases (6) and (7) show that the higher DC (Case (6)) could compensate for the lower F (Case (7)). However, the effect of increasing the frequency appears to be stronger than increasing the DC value.

The comparison between CFD and experimental results for ψ_{int} is good for Cases (5), (6) and (7). As for Case (4) the larger differences is due to the fact that it is not a fully attached case and therefore there is no complete periodicity across the cascade in the experiment. Therefore, the experimental value is expected to be lower than the CFD equivalent.

Q-Criterion Applied for Cases (2) and (6)

In order to show the effect of frequency, the Q-Criterion was used for two cases: Case (2)-low frequency, and Case (6)-high frequency. The Q-Criterion is defined as $Q=½(\Omega_{ij}\Omega_{ij}-S_{ij}S_{ij})$, which is the second invariant of the velocity gradient tensor. The components Ω_{ij} and S_{ij} are the symmetric and antisymmetric parts of the velocity gradient tensor.

For the case of Re=50,000 and B=0.5 under steady blowing a separation bubble will exist on the airfoil [7]. Furthermore, at the lower frequency (Case (2)), the time-averaged flow field shows separation without reattachment (see Figure 4). At the higher frequency (Case (6)), the time-averaged flow field shows separation and reattachment (see Figure 8).

Figure 18 shows the iso-surfaces of Q-Criterion colored by V_x (m/s) for Case (2) at different times in the cycle. At the beginning of blowing, a large separation bubble is present and the shear layer above the jet is undisturbed. In the middle of blowing, the large separated region remains above the airfoil surface but the boundary layer downstream of the jet is energized. Shortly after shut down (t/T=10% of the cycle), the boundary layer in the vicinity of the jet starts to relax with the energized region moving downstream. This energized region causes shrinkage of the separation bubble downstream of the jet, but it does not have enough energy or time to travel further downstream to cause reattachment. At t/T=80% of the cycle after the jet's shutdown, the flow looks very similar to steady blowing where a large separation bubble does exist as indicated above.

Figure 19 shows the iso-surfaces of Q-Criterion colored by V_x (m/s) for Case (6) at different times in the cycle. At the beginning of blowing there is a large separation bubble present near the trailing edge of the airfoil. During blowing the separated region is traveling downstream and the flow becomes attached in that region. Right after shutdown of the jet (t/T=10% of the cycle time) an overall smaller separation region is present and the flow starts to reattach at the trailing edge. At t/T=80% of the cycle after the jet's shutdown, the flow is attached at the trailing edge, but the separated region starts to appear upstream.

SUMMARY AND CONCLUSIONS

Seven different cases were examined experimentally and computationally to study LPT flow control using pulsed VGJs for the L1A airfoil. These cases represent a combination of variation in Re (25,000, 50,000 and 100,000), based on the suction surface length and the nominal exit velocity from the cascade, B (from 0.25 to 1.0), F (from 0.035 to 0.56) and DC (10% and 50%). The data was obtained for the pressure distribution along the airfoil and downstream in the wake as well as velocity profiles at six different stations downstream of the suction peak. The CFD was done with LES utilizing version 6.3.26 of the finite-volume code ANSYS Fluent. The CFD provided further insight to better understand the physics of the flow control.

All cases examined did show flow separation with no jet blowing. At lower Re, a larger separation bubble existed and accordingly it was more difficult to remove. As the Re increased, the separation bubble size was reduced and the losses decreased. As the value of F increased, the losses decreased and it appears that a value of F>0.28 is sufficient for achieving reattachment and possible removal of the bubble, depending on the Re. Two of the cases examined did indicate that a higher DC could compensate for the lower F value. However, the effect of increasing the frequency appeared to be stronger than increasing the duty cycle value. The comparison between CFD and experimental results for *Cp*, velocity profiles and ψ_{int} are reasonably good for all cases examined. The LES predictions show smaller separation bubbles than those measured in the experiment. This could be attributed to : 1) the mesh coarsening in the normal to wall direction was not fine enough and/or 2) the inadequate turbulence model used in the subgrid to resolve the turbulence near the wall.

The Q-Criterion was used for two cases: Case (2)-low frequency, and Case (6)-high frequency. The results of CFD clearly illustrate how a separation bubble will persist in the

lower frequency case and the disturbances created from the jet flow do not have enough energy or time to travel further downstream to cause reattachment. On the other hand, the higher frequency case did exhibit a penetration of the disturbance created by the jet into the separated region and cause reattachment, especially at the trailing edge. It appears that the jet was capable of breaking the large bubble into smaller ones, with reattachment in between.

ACKNOWLEDGMENTS

This work was sponsored by the National Aeronautics and Space Administration. The grant monitor is Dr. Anthony Strazisar of the NASA Glenn Research Center. The support of the United States Naval Academy Technical Support Department Shop and Fluids Laboratory is greatly appreciated. We also greatly appreciate the computer time provided for us by the Ohio Super Computer (OSC). The OSC Computer Cluster has been made available as part of the center's mission to support Ohio universities.

REFERENCES

1. Johnston, J.P. and Nishi, M. "Vortex Generator Jets. Means for Flow Separation Control", *AIAA Journal*, **28**, pp. 989-994, 1990.
2. Volino, R.J., Kartuzova, O. and Ibrahim, M.B. "Experimental and Computational Investigations of Low-Pressure Turbine Separation Control using Vortex Generator Jets", *GT2009-59983, Proceedings of ASME Turbo Expo 2009: Power for Land, Sea and Air GT2009*, June 8-12, 2009, Orlando, Florida, USA.
3. Rizzetta, D.P. and Visbal, M.R., "Numerical Simulation of Separation Control for Transitional Highly Loaded Low-Pressure Turbines", *AIAA Journal*, **43**, pp.1958-1967, 2005.
4. Postl, D., Gross, A., Fasel, H.F. "Numerical Investigation of Active Control for Low-Pressure Turbine Blade Separation", *AIAA2004-750, Proceedings of 42nd AIAA Aerospace Science Meeting and Exhibit*, January 5-8, 2004, Reno, Nevada, USA, 2004.
5. Garg, V.K., "Low-Pressure Turbine Separation Control - Comparison with Experimental Data", *ASME Paper GT-2002-30229*, 2002.
6. Menter, F.R. "Two-Equation Eddy-Viscosity Turbulence Models for Engineering Applications", *AIAA Journal*, **32**, pp. 1598-1605, 1994.
7. Ibrahim, M.B., Kartuzova, O., and Volino, R.J., "LES and URANS Computational Investigations of LPT Blade (L1A) Separation Control using Vortex Generator Jets", *Proceedings of Turbulence, Heat and Mass Transfer 6*, 2009, Rome, Italy.
8. Clark, J.P. *Private Communication*, Air Force Research Laboratory, 2007.
9. Zhang, X.F. and Hodson, H. "Combined Effects of Surface Trips and Unsteady Wakes on the Boundary Layer Development of an Ultra-High-Lift LP Turbine Blade", *ASME Journal of Turbomachinery*, **127**, pp. 479-488, 2005.
10. Bons, J.P., Pluim, J., Gompertz, K. and Bloxham, M. "The Application of Flow Control to an Aft-Loaded Low Pressure Turbine Cascade with Unsteady Wakes", *ASME Paper GT2008-50864*, 2008.
11. Ibrahim, M.B., Kartuzova, O. and Volino, R.J., "Experimental and Computational Investigations of Separation and Transition on a Highly Loaded Low Pressure Turbine Airfoil: Part 1 – Low Freestream Turbulence Intensity", *ASME Paper IMECE2008-68879*, 2008.
12. Volino, R.J., Kartuzova, O. and Ibrahim, M.B., "Experimental and Computational Investigations of Separation and Transition on a Highly Loaded Low Pressure Turbine Airfoil: Part 2 – High Freestream Turbulence Intensity", ASME Paper IMECE2008-68776, 2008.
13. Volino, R.J., 2008, "Separated Flow Measurements on a Highly Loaded Low-Pressure Turbine Airfoil," ASME Paper GT2008-51445.
14. Bons, J.P., Sondergaard, R., and Rivir, R.B., 2002, "The Fluid Dynamics of LPT Blade Separation Control Using Pulsed Jets," ASME *Journal of Turbomachinery*, **124**, pp. 77-85.
15. Volino, R.J., 2003, "Separation Control on Low-Pressure Turbine Airfoils Using Synthetic Vortex Generator Jets," ASME *Journal of Turbomachinery*, **125**, pp. 765-777.
16. ANSYS Fluent, Inc., 2005. Fluent 6.3 - User Guide.
17. Kim, W.W. and Menon, S. "Application of the localized dynamic subgrid-scale model to turbulent wall-bounded flows", *Technical Report AIAA-97-0210, American Institute of Aeronautics and Astronautics*, 35th Aerospace Sciences Meeting, Reno, NV, 1997.
18. Kim, S.E. "Large eddy simulation using unstructured meshes and dynamic subgridscale turbulence models", *Technical Report AIAA-2004-2548, American Institute of Aeronautics and Astronautics*, 34th Fluid Dynamics Conference and Exhibit, 2004.
19. Piomelli, U. and Chasnov, J.R., "Large-Eddy Simulations: Theory and Applications", *Turbulence and Transition Modeling, lecture notes from the ERCOFTAC/IUTAM* summer school held in Stockholm, 12-20 June, 1995.

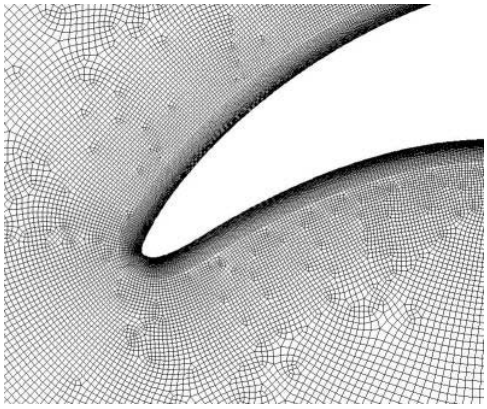

a) Leading Edge

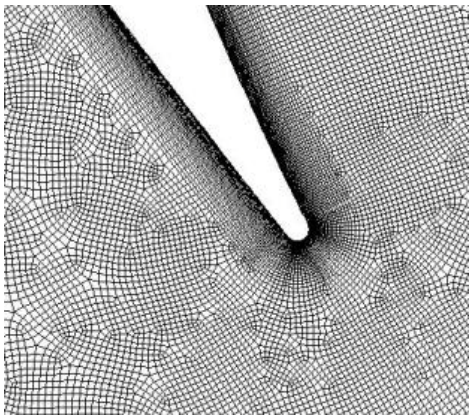

b) Trailing Edge

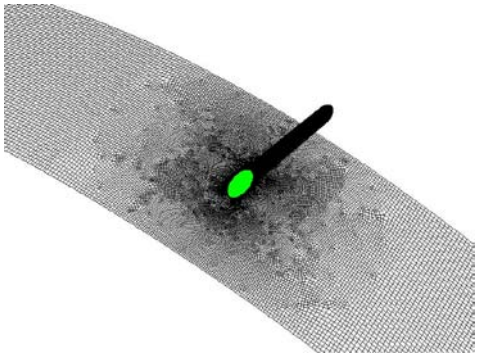

c) Jet Exit

Figure 2. Grid#3 used in pulsed jets flow control cases: a) Leading Edge, b) Trailing Edge and c) Jet Exit.

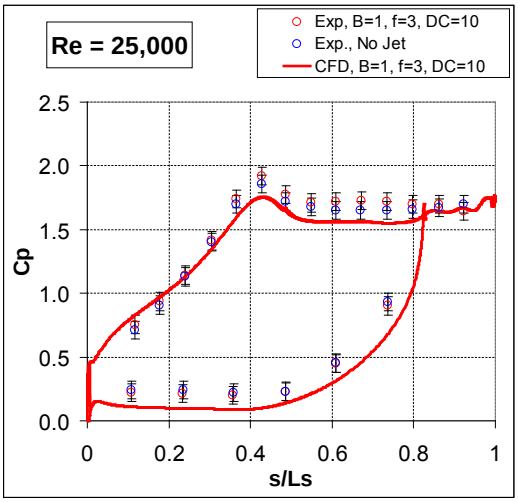

Figure 3. *Cp* for Case (1), Re=25,000, B=1.0, F=0.14, DC=10%.

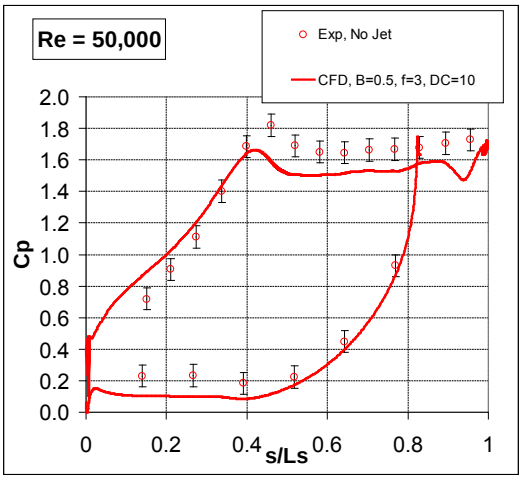

Figure 4. *Cp* for Case (2), Re= 50,000-B=0.5-F=0.07, DC=10%.

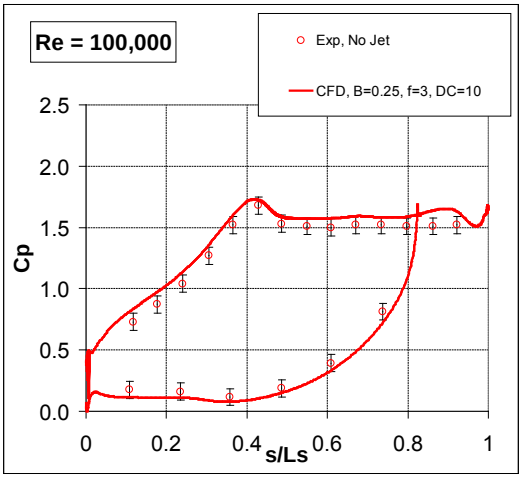

Figure 5. *Cp* for Case (3), Re= 100,000, B=0.25, F=0.035, DC=10%.

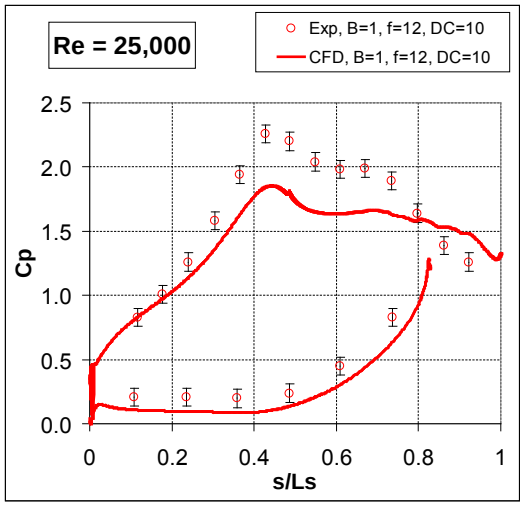

Figure 6. *Cp* for Case (4), Re=25,000, B=1, F=0.56, DC=10%.

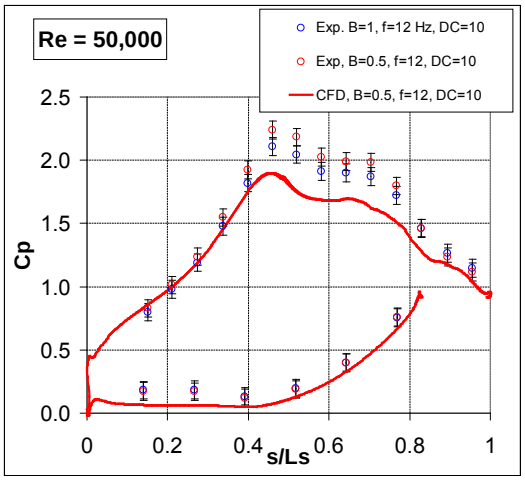

Figure 7. *Cp* for Case (5), Re= 50,000, B=0.5, F=0.28, DC=10%.

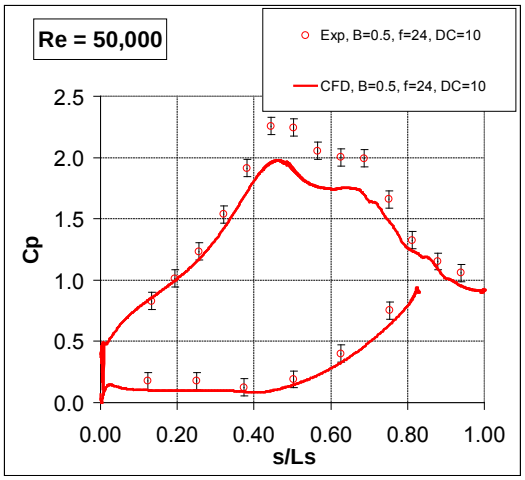

Figure 8. *Cp* for Case (6), Re=50,000, B=0.5, F=0.56, DC=10%.

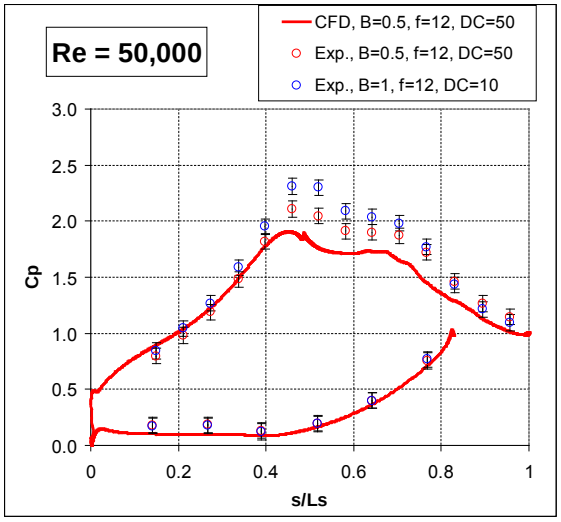

Figure 9. *Cp* for Case (7), Re=2, 50,000, B=0.5, F=0.28, DC=50%.

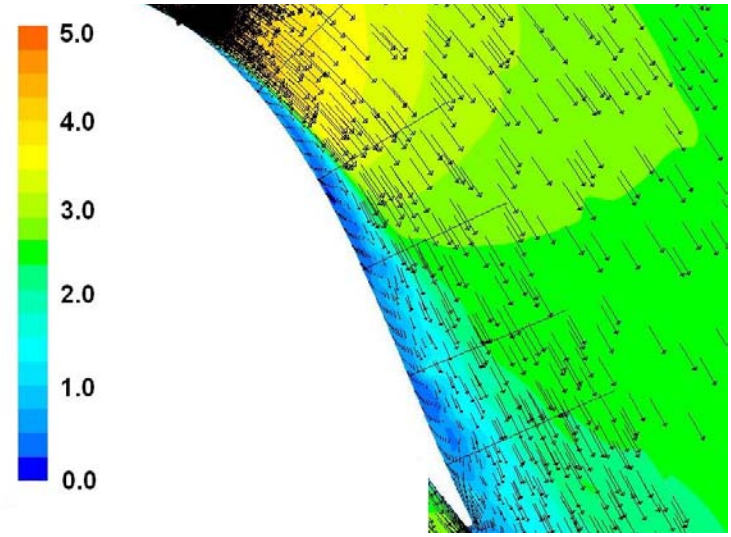

Figure 10. Contours of U, m/s, and velocity vectors for Case (6), Re=50,000, B=0.5, F=0.56, DC=10%.

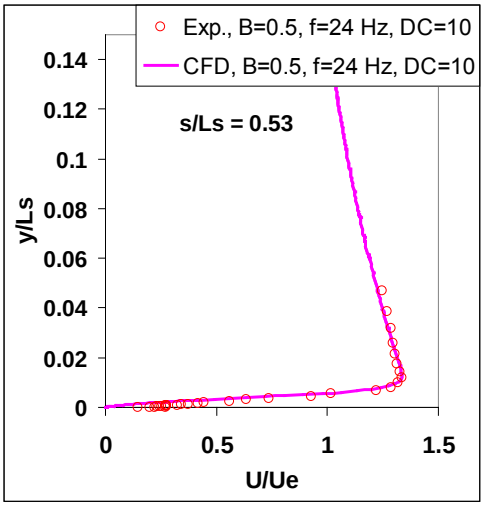

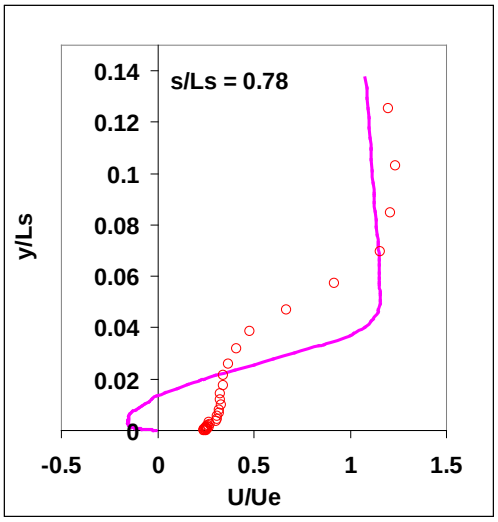

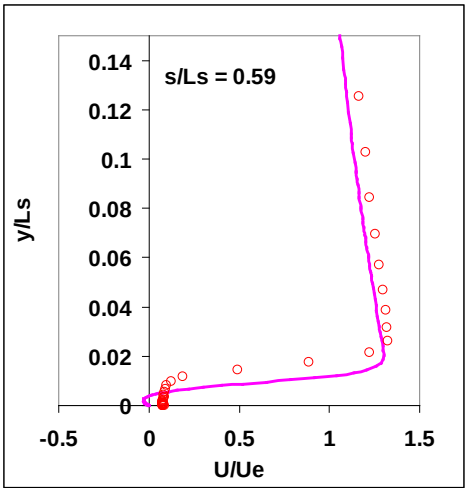

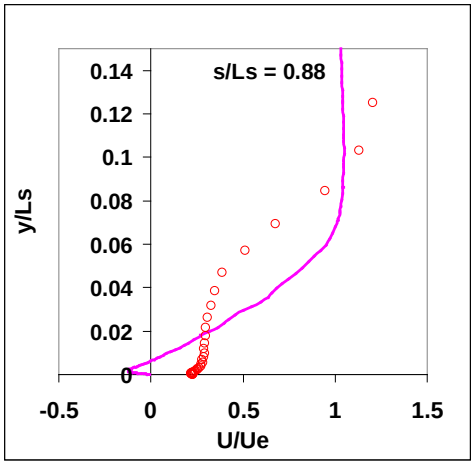

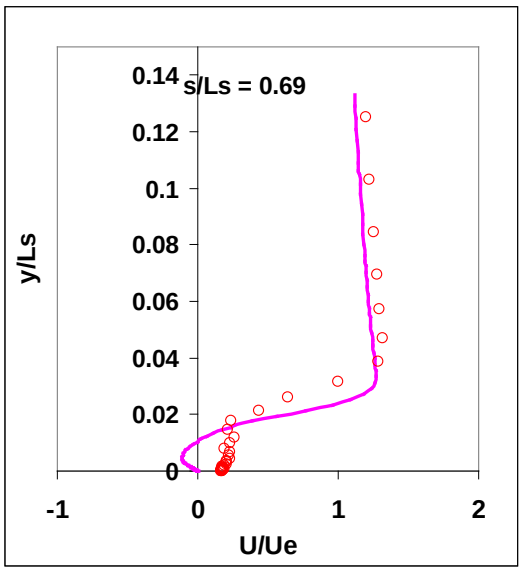

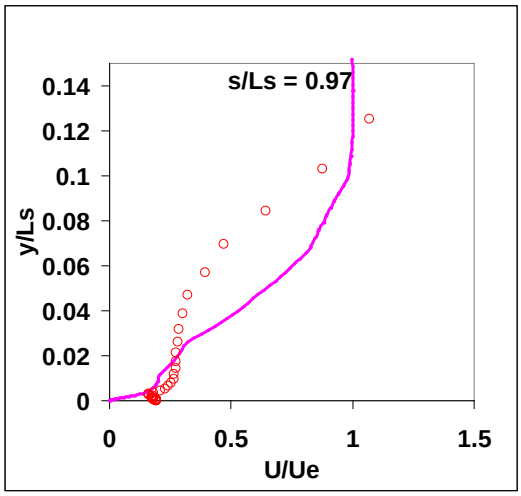

Figure 11. U/Ue at the different 6 stations for Case (6), Re=50,000, B=0.5, F=0.56, DC=10%.

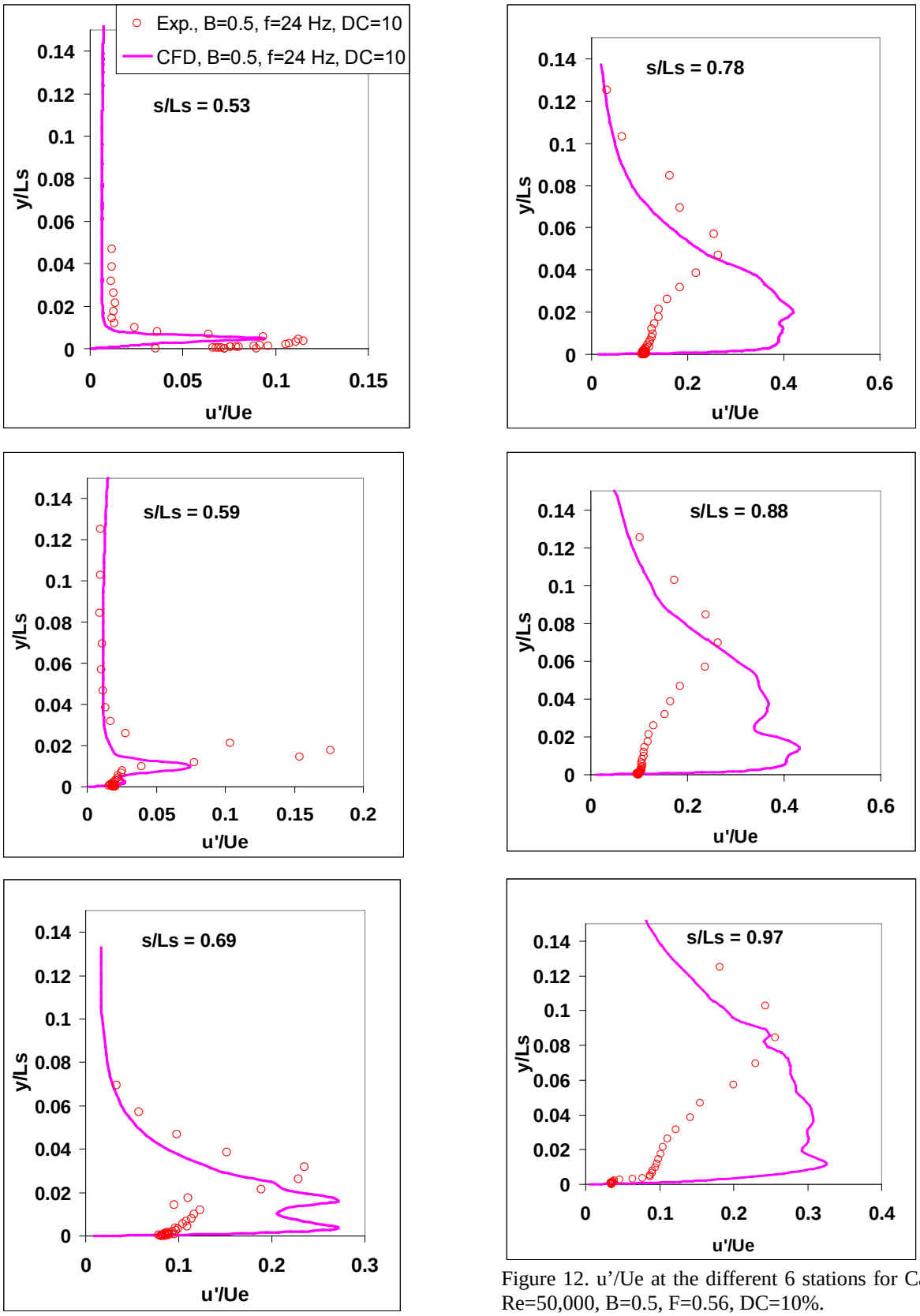

Figure 12. u'/Ue at the different 6 stations for Case (6), Re=50,000, B=0.5, F=0.56, DC=10%.

Figure 13. Isosurface of mean V_x = 0.01 m/s
for Case (6), Re=50,000, B=0.5, F=0.56, DC=10%.

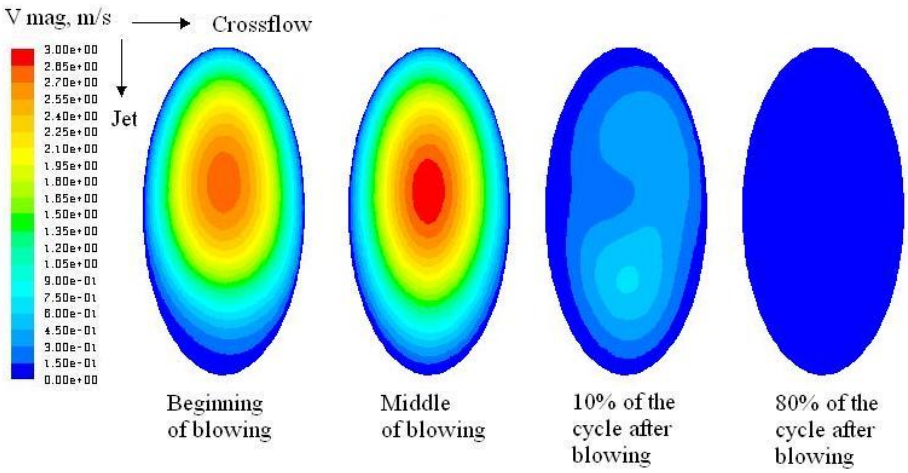

Figure 14. Velocity contour (m/s) at the jet exit for Case (2) Re=50,000, B=0.5, F=0.07, DC=10%.

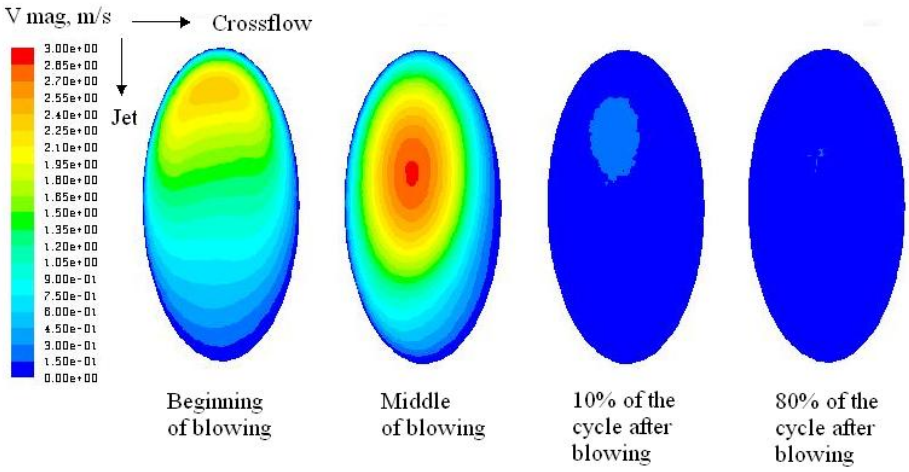

Figure 15. Velocity contour (m/s) at the jet exit for Case (5) Re=50,000, B=0.5, F=0.28, DC=10%.

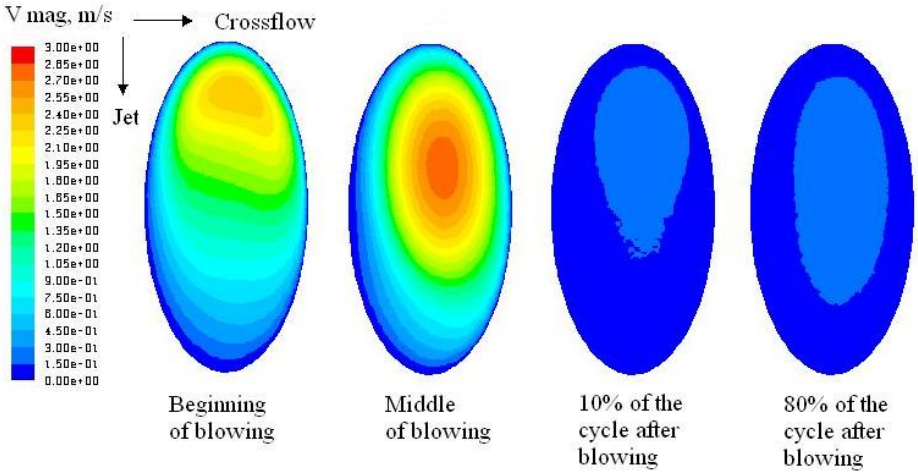

Figure 16. Velocity contour (m/s) at the jet exit for Case (6) Re=50,000, B=0.5, F=0.56, DC=10%.

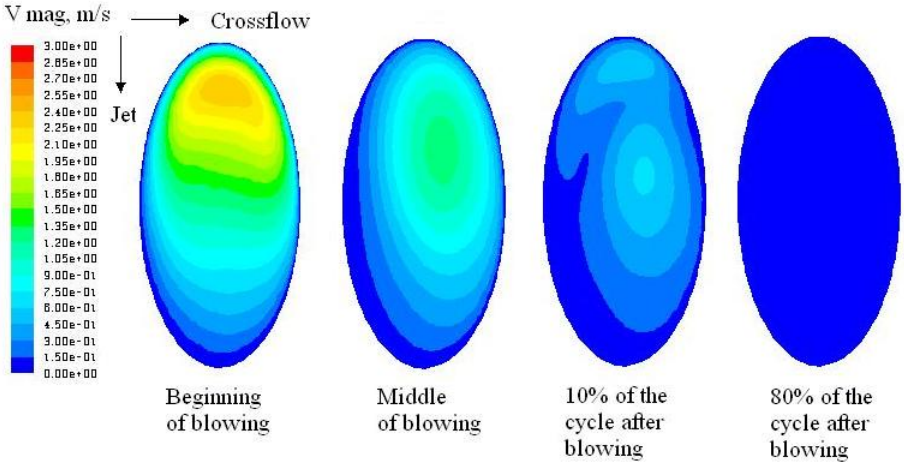

Figure 17. Velocity contour (m/s) at the jet exit for Case (7) Re=50,000, B=0.5, F=0.28, DC=50%.

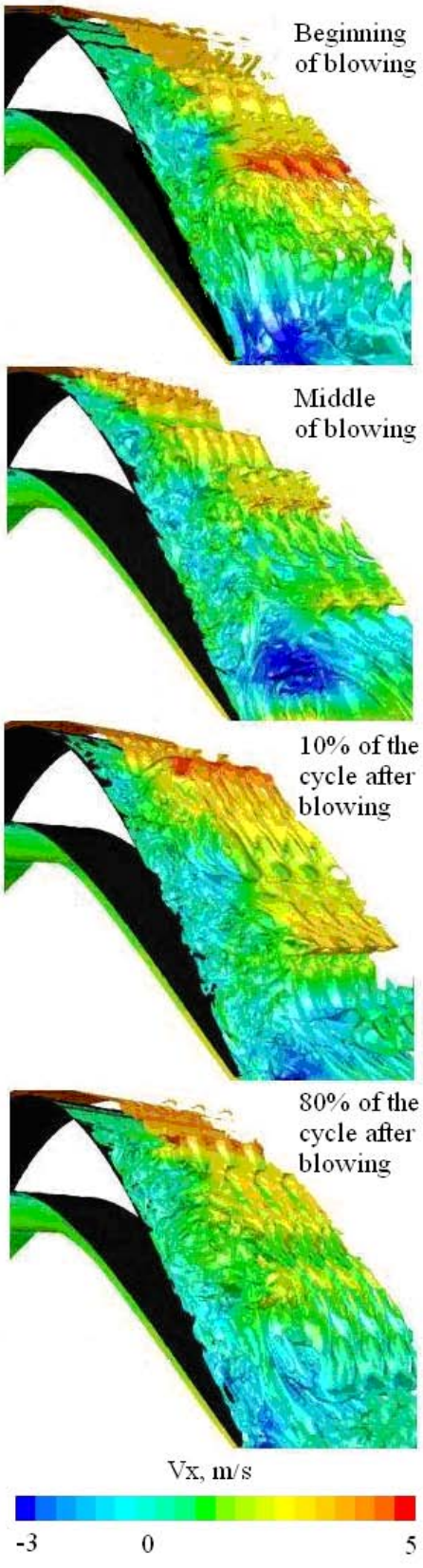

Figure 18. Q-criterion contours colored by V_x (m/s), Cases (2), Re= 50,000, B=0.5, F=0.07, DC=50%, at different times in the cycle.

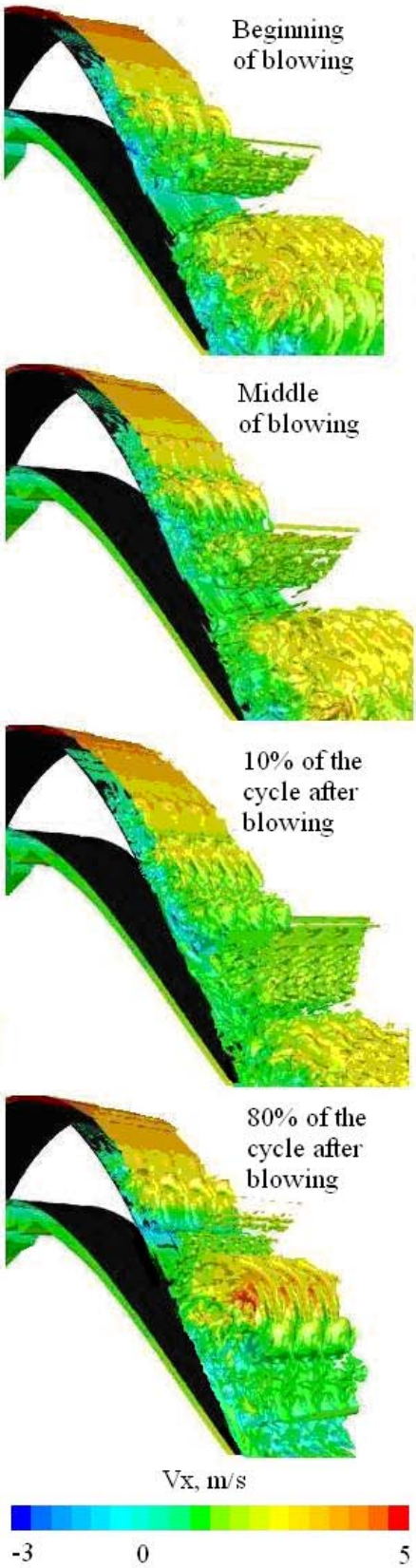

Figure 19. Q-criterion contours colored by V_x (m/s), Cases (6), Re= 50,000, B=0.5, F=0.56, DC=10%, at different times in the cycle.

Proceedings of ASME Turbo Expo 2011
GT2011
June 6-10, 2011, Vancouver, British Columbia, Canada

GT2011-46106

COMBINED EFFECTS OF WAKES AND PULSED VORTEX GENERATOR JET FLOW CONTROL ON BOUNDARY LAYER SEPARATION ON A VERY HIGH LIFT LOW PRESSURE TURBINE AIRFOIL

Ralph J. Volino
Mechanical Engineering Department
United States Naval Academy
Annapolis, Maryland 21402-5042
volino@usna.edu

ABSTRACT

Boundary layer separation control with pulsed vortex generator jets (VGJs) has been studied on a very high lift, low-pressure turbine airfoil in the presence of unsteady wakes. Experiments were done under low (0.6%) and high (4%) freestream turbulence conditions on a linear cascade in a low speed wind tunnel. Cases were considered at Reynolds numbers (based on the suction surface length and the nominal exit velocity from the cascade) of 25,000 and 50,000. Wakes were produced from moving rods upstream of the cascade with flow coefficient 1.13 and rod spacing equal 2 blade pitches, resulting in a dimensionless wake passing frequency $F=fL_{j\text{-}te}/U_{ave}$=0.14, where f is the frequency, $L_{j\text{-}te}$ is the length of the adverse pressure gradient region on the suction surface, and U_{ave} is the average freestream velocity. The VGJs were injected at the beginning of the adverse pressure gradient region on the suction surface with maximum jet velocity in each pulse equal to the local freestream velocity and a jet duty cycle of 10%. Several different timings of the VGJs with respect to the wakes were considered. Pressure surveys on the airfoil surface and downstream total pressure loss surveys were documented. Instantaneous velocity profile measurements were acquired in the suction surface boundary layer and downstream of the cascade. In cases without VGJs, the boundary layer momentarily reattached in response to the wake passing, but separated between wakes. The VGJs also caused reattachment, and if the VGJ pulsing frequency was sufficiently high, separation was largely suppressed for the full wake passing cycle. The timing of the VGJs with respect to the wakes was not very important. The jet pulsing frequency needed for separation control was about the same as found previously in cases without wakes. The background freestream turbulence effect was negligible in the presence of the larger wake and VGJ disturbances.

NOMENCLATURE

Cp	$2(P_T\text{-}P)/(\rho U_e^2)$, pressure coefficient
C_x	axial chord length
F	$fL_{j\text{-}te}/U_{ave}$, dimensionless frequency
f	wake passing frequency
$L_{j\text{-}te}$	length of adverse pressure gradient region on suction surface
L_s	suction surface length
L_ϕ	blade spacing (pitch)
P	pressure
P_S	upstream static pressure
P_T	upstream stagnation pressure
P_{Te}	downstream stagnation pressure
Re	U_eL_s/ν, exit Reynolds number
s	streamwise coordinate, distance from leading edge
T	period of jet pulsing cycle
t	time
TI	background freestream turbulence intensity
U	local mean velocity
U_{ave}	average freestream velocity in adverse pressure gradient region
U_i	inlet freestream velocity
U_e	nominal exit freestream velocity, based on inviscid solution
U_{rod}	wake generator velocity
u'	rms fluctuating streamwise velocity
x	axial distance from leading edge
α_i	inlet flow angle
ϕ	coordinate along blade spacing, normal to axial chord
ν	kinematic viscosity
ρ	density
ψ	$(P_T\text{-}P_{Te})/(P_T\text{-}P_S)$, total pressure loss coefficient
ζ	$U_i\cos(\alpha_i)/U_{rod} = U_{axial}/U_{rod}$, flow coefficient

INTRODUCTION

Boundary layer separation on the suction side of low-pressure turbine (LPT) airfoils can cause partial loss of lift and high aerodynamic losses (Hourmouziadis [1], Mayle [2], Sharma et al. [3]). In aircraft engines the lower Reynolds numbers at altitude can lead to a component efficiency drop of 2% between takeoff and cruise in large commercial transport engines, and possibly as much as 7% in smaller engines operating at higher altitudes [4, 5]. Separation becomes more likely when airfoil loading is high because of the strong adverse pressure gradients on the suction surface, but high loading is desirable since it can be used to reduce airfoil count, weight and cost. Accurate prediction of separation under relevant conditions, including the effects of boundary layer transition and periodic unsteadiness, is needed to design high lift airfoils without separation problems.

Separation can be mitigated in a few ways. One is by wakes shed from the airfoils in upstream stages in an engine. The velocity deficit and elevated turbulence in periodic wakes help to suppress separation and can cause a separated boundary layer to reattach. Hodson and Howell [6] describe the mechanisms by which wakes promote reattachment, including the "negative jet" which results when the velocity deficit in the wake causes the flow outside the wake to accelerate and impinge on the surface, and the unsteadiness which promotes transition in the boundary layer. Following the wake itself is a calmed period (Gostelow et al. [7] and Schulte and Hodson [8]) in which the boundary layer has low turbulence and greater resistance to separation. Numerous studies have considered the wake effect in the LPT, including those listed in Hodson and Howell [6], and more recent references in Bons et al. [9] and Pluim et al. [10]. Examples include Schobeiri et al. [11], Öztürk and Schobeiri [12], Jiang and Simon [13], and Mahallati and Sjolander [14] who all used the Pack B airfoil. Zhang and Hodson [15] and Funazaki et al. [16] used more highly loaded airfoils. Many additional studies are available from these research groups and others.

Separation problems can also be limited through good airfoil design, as described by Praisner and Clark [17]. In recent years, knowledge of wake effects has allowed for designs with higher loading than would be possible under steady inflow conditions. Even with the best design methods, however, a loading limit will always exist, above which separation will still occur. Flow control, either active or passive, might allow an extension of this limit.

Separation control with passive devices such as boundary layer trips has been shown effective by Zhang et al. [18], Bohl and Volino [19], Volino [20], and others. Passive devices have the distinct advantage of simplicity, but they also introduce parasitic losses and cannot be adjusted to account for changes in flow conditions. Active devices are also possible, and although their complexity and reliability would create challenges, they could be made adjustable and provide potentially better control. In turbomachinery, plasma devices as used by Huang et al. [21] could be viable, and are under active study. Vortex generator jets (VGJs), as introduced by Johnston and Nishi [22], have also been considered. Blowing from small, compound angled holes is used to create streamwise vortices which promote transition and bring high momentum fluid into the near wall region to help control separation. The most effective VGJs enter the boundary layer at a relatively shallow pitch angle (typically 30 to 45 degrees) relative to the wall and a high skew angle (45 to 90 degrees) relative to the main flow. Bons et al. [4, 23], Volino [24], Volino and Bohl [25], McQuilling and Jacob [26], and Eldredge and Bons [27] all used VGJs on the highly loaded Pack B LPT airfoil. Separation was essentially eliminated, even at the lowest Reynolds number considered. Similar results with were found on the very highly loaded L1M airfoil by Bons et al. [28], who saw the size of a large separation bubble reduced by VGJs. Pulsed jets were more effective than steady jets in all studies. The initial disturbance created by each pulse caused the boundary layer to attach. The boundary then remained resistant to separation during the calmed period which followed the VGJ disturbance. When the time between pulses was long enough, the boundary layer did eventually relax to a separated state, but due to the control which persisted during the calmed period, the VGJs were effective even with low jet pulsing frequencies, duty cycles and mass flow rates. Since the boundary layer was attached and undisturbed for much of the jet pulsing cycle, profile losses were low.

The present study uses the L1A airfoil, which was designed at the Air Force Research Laboratory (AFRL) and is available on a limited basis from Clark [29]. Dimensions of the L1A as used in the present study are given in Table 1. It was deliberately designed to provide a challenging case for flow control. The L1A has a Zweifel coefficient of 1.35, which corresponds to 10% higher loading than the "ultra-high lift" airfoils described by Zhang and Hodson [30], and 17% higher loading than the Pack B airfoil. The L1A is also aft loaded, which is advantageous for reducing secondary flow losses at the endwalls, but makes the boundary layer more prone to separation than a forward loaded blade, as documented in Bons et al. [9], Volino [31], Ibrahim et al. [32], and Volino et al. [33]. In cases without wakes and low Reynolds numbers, the boundary layer separates and does not reattach, in spite of transition to turbulence in the shear layer over the separation bubble. This result contrasts with the results of studies on less aggressive airfoils (e.g. Volino [34]), which all showed reattachment after transition. The failure to reattach can occur even when transition starts farther upstream on the L1A than on other airfoils (e.g. with low freestream turbulence and Re=100,000, transition starts at s/L_s=0.8 on the Pack B and causes reattachment, and at s/L_s=0.6 on the L1A without reattachment). The adverse pressure gradient on the L1A is roughly twice as strong as on the Pack B, and is apparently strong enough to prevent reattachment at low Reynolds numbers in spite of transition and turbulent mixing in the shear layer over the separation bubble. The failure of the boundary layer to reattach results in a 20% loss in lift and increases profile losses by up to a factor of 7. At higher Reynolds numbers the separation bubble closes, and for Re≥200,000 the separation bubble on the L1A is small and the boundary layer is attached over most of the airfoil.

Two studies have considered the effect of wakes on the L1A boundary layer. Bons et al. [9] considered a case with Re=50,000 (based on the suction surface length and the nominal exit velocity from the cascade), background freestream turbulence TI=3%, and periodic wakes produced with moving rods upstream of the airfoils. The dimensionless frequency of the wake passing was $F=fL_{j\text{-}te}/U_{ave}$=0.34, where $L_{j\text{-}te}$ is the length of the adverse pressure gradient region on the suction surface, and U_{ave} is the average freestream velocity over this distance. The length $L_{j\text{-}te}$ is also the distance from a row of vortex generator jet (VGJ) holes to the trailing edge. Volino [35] considered cases at high (4%) and low (0.6%) freestream turbulence with Re=25,000 and 50,000. The spacing and speed of moving rods were varied to produce wake passing frequencies between F=0.14 and 0.56. Wakes largely suppressed separation at Re=25,000 when F was above 0.5. At lower frequencies the disturbances caused by the wakes caused momentary reattachment, but the boundary layer re-separated between wake passing events. For Re=50,000, F=0.3 was sufficient to largely suppress separation. The effect was the same whether a particular frequency was achieved by changing rod spacing or rod velocity. Higher freestream turbulence helped to promote transition and reattachment, but the effect was small compared to the wake passing effect.

Flow control with vortex generator jets on the L1A has been considered in Bons et al. [9], Volino et al. [36, 37, 38], and Ibrahim et al. [39, 40]. The same Reynolds numbers and freestream turbulence levels were considered as with the wakes. With a VGJ blowing ratio of 1 (i.e. maximum jet velocity equal to the freestream velocity) and 10% duty cycle, a dimensionless jet pulsing frequency of F=0.5 was sufficient to control separation with Re=25,000, and F=0.3 was sufficient for Re=50,000. These frequencies match the wake passing frequencies required for separation control at each Reynolds number, suggesting that the type of disturbance is not as important as the frequency of the disturbance for controlling the boundary layer. At lower frequencies the flow control was not as good, and the boundary layer separated between pulses.

The combined effect of wakes and vortex generator jets on separation control has been studied on the Pack B airfoil by Bloxham

et al. [41] and on the L1A by Bons et al. [9]. On the L1A, a case was considered with Re=50,000, 3% freestream turbulence, and dimensionless wake passing frequency F=0.34. The VGJ pulsing frequency was equal to the wake passing frequency, and the timing of the jets was varied relative to the wakes. Without VGJs the wakes caused only partial separation control. With the VGJs injected near the pressure minimum on the suction side, good separation control was achieved even without wakes. The timing of the jets to the wakes was, therefore, unimportant. When the VGJs were injected farther downstream, they were only effective when combined with wakes and the effectiveness depended on the timing.

In the present study, the combined effect of wakes and VGJs is considered with Re=25,000 and 50,000 under low (0.6%) and high (4%) freestream turbulence conditions. These Reynolds numbers are very low, but could still be of interest in small engines operating at high altitudes (e.g. in future unmanned vehicles). They are also of interest for the present study because they result in a very large separation bubble, providing a challenging case for flow control and a good case for exploring the response of the boundary layer to VGJs and wakes. The wake passing frequency is set to a low value so that without flow control the boundary layer only intermittently reattaches during wake passing events. Cases with various VGJ frequencies and timings relative to the wake passing are documented. Surface pressure distributions, total pressure loss profiles, and instantaneous boundary layer velocity measurements are used to show how wakes and VGJs combine to affect separation.

Table 1: Cascade parameters

Axial Chord, C_x [mm]	True Chord [mm]	Pitch, L_ϕ [mm]	Span [mm]	Suction side, L_s [mm]	Inlet flow angle	Exit flow angle
134	146	136	724	203	35°	60°

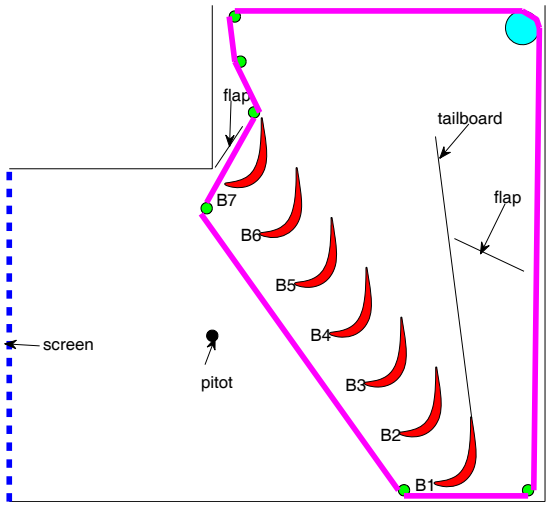

Fig. 1 Schematic of linear cascade with wake generator

EXPERIMENTAL FACILITY AND MEASUREMENTS

Experiments were conducted in a closed loop wind tunnel with a seven blade linear cascade as shown in Fig. 1. A fine screen located upstream of the cascade is used to break up the boundary layers which form upstream of the test section and to provide uniform inlet conditions to the cascade. The freestream turbulence entering the cascade was measured with a cross-wire probe positioned just upstream of the center blade. The turbulence intensity is 0.8% in the streamwise component and 0.5% in the cross stream components. The integral length scale of the streamwise component is $0.47C_x$. To produce high freestream turbulence, the screen is replaced with a coarse grid, consisting of a 1.5 mm thick sheet metal plate with 19 mm square holes spaced 25.4 mm apart, center to center, in both directions. In a plane perpendicular to the inlet flow and $1.7C_x$ upstream of the center blade, the grid produced uniform flow with TI=6.0% in the streamwise component and 4.2% in the cross stream components, for an overall intensity of 4.9%. The streamwise component was also measured at the inlet plane of the cascade in the four center passages, where it had decayed to about 4.2%. Downstream of the cascade, the local TI is 1.8% across all passages. The local freestream turbulence intensity in the passage at the beginning of the adverse pressure gradient region is 1.4%. The change in TI through the passage is due mainly to the change in the local freestream velocity along with some decay of the turbulence. The upstream integral length scale of the freestream turbulence is $0.12C_x$ in the streamwise component and $0.04C_x$ in the other components. Further details of the facility and inlet flow are in Volino et al. [33].

A tailboard and two flaps, shown in Fig. 1, are needed to produce the correct inlet and exit flow angle from the cascade. Their position was set to produce periodicity at high Reynolds numbers as discussed in Volino [35]. At low Reynolds numbers, when significant separation bubbles are present, the periodicity is not as good due to suppression of the separation bubble thickness on the blades closest to the tailboard. In cases where wakes or other flow control suppress separation, periodicity is reestablished. The lack of periodicity in cases with large separation bubbles is considered acceptable since the focus of the research is separation control, and not documentation of cases with large separation that would be unacceptable in practice. This compromise facilitates the study of a larger number of cases by obviating the need to adjust the tailboard by trial and error for each case. It also provides for better repeatability in the experiments, since the position of the tailboard is fixed for all cases. Any changes in separation with wakes or VGJs will be larger in practice than documented in the experiment, due to the effect of the tailboard in suppressing the bubble size in the uncontrolled cases.

The wake generator includes a chain near each endwall of the cascade that passes $0.54C_x$ upstream of the leading edges of the cascade blades. The chains then pass downstream around blade B7 on the inside turn of the cascade and pass well downstream of the cascade before returning upstream around blade B1 on the outside turn of the cascade. This completes the chain circuit. The magenta line surrounding the cascade in Fig. 1 shows the location of the chain. A traverse for probe movement is located within the chain circuit downstream of the blade row. Each chain is driven by a drive gear (large circle in Fig. 1) and also passes around six idler sprockets (small circles). One of the idler sprockets is adjustable to maintain tension in the chain. The drive gears for the upper and lower chains are on a common axle and driven by a single electric motor so both chains move in unison. The motor speed is set with a variable frequency inverter. The chain links have hollow pins, through which the wake generator rods are attached. Each rod consists of a 4 mm diameter carbon fiber tube with a steel pin attached at each end. The steel pins are inserted through the holes in the upper and lower chain, and then secured with small clips. The distance between rods was 272 mm, which correspond to $2L_\phi$, where L_ϕ is the blade spacing in the cascade. The ratio of rod to blade spacing is at the very high end of what might be found for vane to rotor blade spacing in an engine. The ratio of vane to rotor blade spacing is typically about 1.6 as indicated by Bloxham et al. [41], so the high ratio in the present case provides a more challenging case for flow control, as shown in Volino [35].

The ratio of the rod diameter to the axial chord is 0.03, which is consistent with the wake generators of Bons et al. [9] and Funazaki et al. [16]. The rods are smaller than those of Kaszeta et al. [42] who had a diameter to chord ratio of 0.06. The present rods are larger than those of Schobeiri et al. [11] and Zhang and Hodson [15] who had rod diameter to chord ratios of about 0.01. In the present study, as in Bons et al. [9] and Kaszeta et al. [42], the rod wakes are intended to simulate the wakes of very highly loaded airfoils under low Reynolds number conditions with thick boundary layers and in some cases large separation bubbles. A large diameter rod is therefore needed to simulate an airfoil wake with a large velocity deficit. The velocity deficit and turbulence level in the rod wakes are documented in Volino [35], and compared to the wakes of the cascade airfoil. The rod wakes were found to be reasonable approximations of airfoil wakes. At the cascade inlet, the peak turbulence level in the rod wakes was 14%, and the level between wakes was at the background *TI* in the wind tunnel.

The rods were driven at a velocity of 0.73 times the cascade inlet velocity, U_i. This gives a flow coefficient, $\zeta = U_i \cos(\alpha_i)/U_{rod} = 1.13$, where α_i is the inlet flow angle. This is at the high end of the expected range for an engine. The flow coefficient and rod spacing were chosen to be large to provide cases in which the wakes alone would not completely eliminate separation. This allows for investigation of the interaction of the wakes and VGJs in controlling separation. The dimensionless wake passing frequency is $F=0.14$. The timing of the wake generator is recorded with an infrared photo detector, which senses the passage of each rod and emits a voltage that is used to trigger a function generator which drives the solenoid valves used to produce the pulsed VGJs. The signal to the valves is recorded with other data, allowing phase averaging of the results.

To produce the VGJs, each blade in the cascade has a central cavity which extends along the entire span. As explained in Volino et al. [36], compressed air is supplied to the cavities from a common manifold. The manifold is supplied through two fast response solenoid valves (Parker Hannifin 009-0339-900 with General Valve Iota One pulse driver) operating in parallel. A single spanwise row of holes was drilled into the suction surface of each blade at the inviscid pressure minimum location, $s/L_s=0.5$ ($x/C_x=0.62$), where s is the distance from the leading edge and L_s is the suction surface length. The pressure minimum has been shown in the studies listed above to be about the optimal location for flow control devices. The holes are 0.8 mm ($0.006C_x$) in diameter and drilled at 30° to the surface and 90° to the main flow direction. This is the same orientation used in all the VGJ studies listed above. The hole spacing is 10.6 diameters, and the length to diameter ratio is 12. When the solenoid valves are opened, the jet velocity rises quickly for about 0.01 s to a maximum and then immediately begins to drop. If the period of the pulse is long enough the velocity reaches a steady value, but for the short duration pulses of the present study, the 0.01 s rise time compares to valve-open times between about 0.01 s and 0.03 s, so there is insufficient time for the jet velocity to reach a steady value. When the valves close, the jet velocity quickly drops to zero. The maximum jet velocity in each pulse is used to define the blowing ratio and is set equal to the nominal local freestream velocity at the VGJ holes, for a blowing ratio of 1. The jet duty cycle is 10%. The mass flow rate of the jets is approximately 0.004% of the main flow mass flow rate. More on the characteristics of the pulses is available in Volino et al. [36].

Nine different VGJ timings relative to the wakes were considered, as shown in Fig. 2. Timings were chosen to place the jet pulses at different times within or between wakes. Case (a) is the baseline case with only wakes. Cases (b-d) have a single pulse for each wake passing. Timings (e-g) have two pulsed per wake period. To maintain the same overall blowing period, the pulses in cases (e-g) are half as long as those in (b-d). Timings (h-i) have three pulses per wake.

Table 2: Velocity profile measurement stations

Station	1	2	3	4	5	6
s/L_s	0.53	0.59	0.69	0.78	0.88	0.97
x/C_x	0.65	0.72	0.80	0.86	0.92	0.97

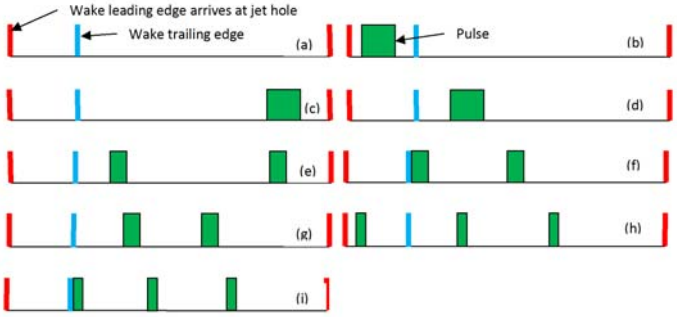

Fig. 2 VGJ timings (a) through (i)

Measurements

The center blade, designated B4 in Fig. 1, contains pressure taps near the spanwise centerline. Pressure surveys are made using a pressure transducer (0-870 Pa range Validyne transducer). Stagnation pressure is measured with a pitot tube upstream of the cascade and wake generator. The uncertainty in the suction side pressure coefficients, *Cp*, is 0.07. Most of this uncertainty is due to bias error. Stochastic error is minimized by averaging pressure transducer readings acquired at a 10 kHz sampling rate over a 10 second period.

Total pressure losses are documented using a Kiel probe traversed across three blade spacings, $0.63C_x$ downstream of the cascade. A traverse is located in the wind tunnel downstream of the cascade to move the probe. The traverse causes an acceptably low blockage when it is located at least two C_x downstream of the cascade.

Velocity profiles on the suction surface were measured at the six streamwise stations listed in Table 2. All stations are downstream of the inviscid pressure minimum at $s/L_s=0.49$. Profiles were acquired near the spanwise centerline of the airfoil with a hot-wire anemometer (AA Lab Systems model AN-1003) and a single sensor hot-film probe (TSI model 1201-20). The sensor diameter is 51 μm, and the active length is 1.02 mm. At each measurement location, data were acquired for 26 seconds at a 20 kHz sampling rate (2^{19} samples). All raw data were saved. The high sampling rate provides an essentially continuous signal, and the long sampling time results in low uncertainty in both statistical and spectral quantities. Data were acquired at 40 wall normal locations in each profile, extending from the wall to the free-stream, with most points concentrated in the near wall region. The probe was positioned as close to tangent to the airfoil surface as possible at each station, such that the probe body extended downstream of the sensor and the direction of the traverse was within 5° of normal to the surface. In most cases the closest point to the wall in each profile was within about 0.2 mm of the wall, which compares to boundary layer thicknesses ranging from 1.1 mm to over 40 mm.

Flow direction in a separation bubble cannot be determined with a single-sensor hot-wire, but velocity magnitude can be measured and was found to be near zero within the bubbles of the present cases when the flow was laminar. In cases where the flow became turbulent but remained separated, fluctuating velocities caused false high mean velocity readings in the separation bubble. With the exception of these turbulent separated cases, the uncertainty in the mean velocity is 3-5%

except in the very near wall region, where near-wall corrections (Wills [43]) were applied to the mean velocity.

Velocity was also measured downstream of the cascade along the same line used for the total pressure loss measurements. Downstream and boundary layer velocity data were both time averaged and ensemble averaged based on the phase within the wake passing period. Phase averages of mean and fluctuating velocity are shown below at 24 dimensionless times, t/T, within the wake passing period, where t is time and T is the period between wakes. With the wake passing frequency of F=0.14 (corresponding to 3 Hz at Re=25,000 and 6 Hz at Re=50,000) and a 26 s data acquisition length at each measurement location, 78 and 157 wake passing periods are averaged for each ensemble for the Re=25,000 and 50,000 cases respectively.

Data were acquired at nominal Re=25,000 and 50,000. The Reynolds number, as defined above, is based on the suction surface length and the nominal cascade exit velocity. The corresponding Reynolds numbers based on the cascade inlet velocity and the axial chord length are 10,000 and 20,000. For Re=25,000, data were acquired for timings (a) and (c-i). For Re=50,000, timings (a-f) were used. Data were acquired for cases with both high and low freestream turbulence.

RESULTS

Re=25,000

The Cp and total pressure loss profiles for cases with Re=25,000 and low TI are shown in Fig. 3. The integrated total pressure losses for all cases are shown in Fig. 4. As explained in Volino [31], the integrated loss is an average of the loss coefficient across one blade spacing centered on the blade B4 wake. The inviscid Cp profile for the L1A airfoil is shown in Fig. 3a for comparison. The low peak in Cp followed by a plateau in the case without wakes indicates separation without reattachment. Wakes alone (case (a)) do not cause much change, although there is a slight drop in Cp near the trailing edge, indicating possible reattachment for part of the wake passing cycle. Little change is observed for cases (c-f). The corresponding loss profiles in Fig. 3b show no significant change from the no-wake case for cases (a-f) indicating that neither the wakes nor VGJs are effective in controlling separation. Case (g), which has two pulses evenly spaced between wakes, has slightly more of a drop in Cp near the trailing edge, which would suggest more reattachment, but no change is observed in the loss profile. Cases (h-i) show better Cp results with three pulses. In case (h) one of the VGJ disturbances coincides with the wake disturbance, while for case (i) all three pulses lie between wakes. The loss profiles for cases (h-i) agree with the Cp results, with a noticeable drop in the loss peaks, better periodicity across the cascade, and a shift in the peaks to the right. The shift corresponds to an increase in flow turning of about 3°. For the low TI, Re=25,000 cases, the variation in the integrated loss, ψ_{int}, among cases (a)-(i) is about 0.1, which is of the order of the measurement uncertainty. Although cases (h) and (i) show some improvement over the other cases, the Cp profiles are still far from reattached flow behavior, the loss profiles are still very high, and the flow turning is still well below the design point. The results suggest only partial or intermittent reattachment in cases (h) and (i), in agreement with the velocity results shown below. The timing of the VGJ pulses does not appear to matter. Cases (g) and (h) both have two pulses between wakes, but case (h) shows better results due to an extra pulse, even though this pulse occurs during a wake. Cases (h) and (i) both have three pulses, and they have similar results, even though one of the pulses in case (h) occurs during the wake. Comparison of the present results to a high Reynolds number (Re=200,000) case from Volino

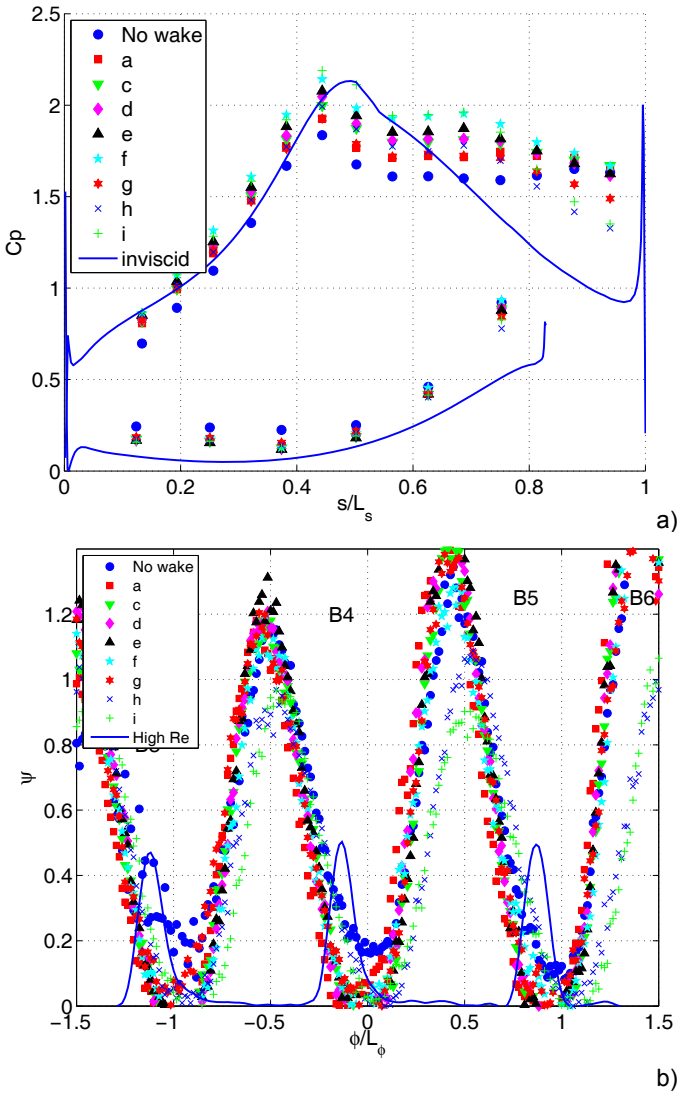

Fig. 3 Pressure profiles for low TI, Re=25,000 cases: a) Cp, b) Total pressure loss

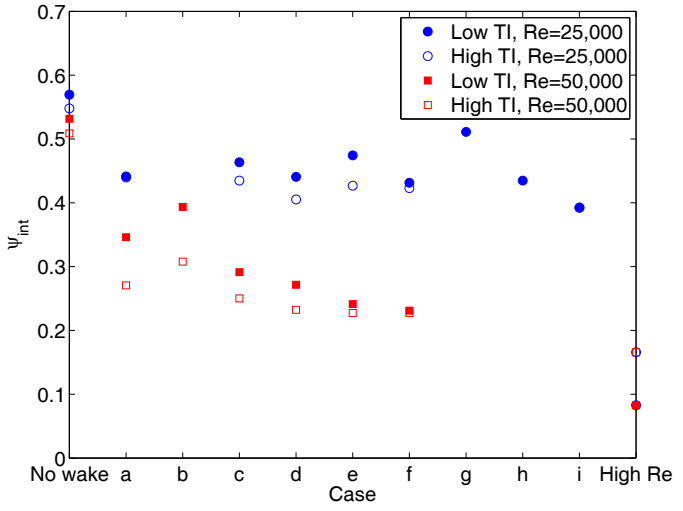

Fig. 4 Integrated total pressure loss

[31] shows that even in the best of the present cases, the loss peaks are over twice as high and there is 13° less flow turning than at high *Re*. Comparison to cases with VGJs but without wakes in Volino et al. [36] shows that loss peaks at *Re*=25,000 can be lowered another 10% and the flow turning increased another 6° if the pulsing frequency is increased to *F*=0.56. In cases (h-i) the average VGJ frequency is 0.42. The average disturbance frequency (wakes plus VGJs) in case (i) is 0.56. Comparison to cases with wakes but without VGJs in Volino [35] show similar improvements over the present results if the wake passing frequency is increased. These results suggest that the combination of wakes and VGJs is not particularly beneficial. Either can result in some separation control if the frequency is sufficiently high, but the presence of the other does not necessarily improve the results even if their combined frequency is relatively high.

Figure 5 shows the *Cp* and loss results for the high freestream turbulence *Re*=25,000 cases. Comparison of Figs. 4 and 5 shows virtually no differences. The integrated loss of Fig. 4 shows the same agreement. Boundary layer velocity results show the same similarity between the corresponding high and low *TI* cases. The same similarity between high and low *TI* is observed for all of the *Re*=50,000 cases. Previous results with wakes alone [35] or VGJs alone [36] showed that freestream turbulence effects were small compared to wake or VGJ effects on boundary layer behavior. The present results show that this small effect is reduced to near zero when both wakes and VGJs are present. Because the results for both background *TI* levels are the same, only the low *TI* results will be presented for the remainder of this paper. One result that is unexpected in Fig. 5 is the near zero loss value between wakes, as some loss should be caused by the decay of the high freestream turbulence, as seen in the high *Re* case. The near zero values may be due to bias error within the experimental uncertainty of 0.07.

Time averaged mean and fluctuating boundary layer velocity profiles are shown in Fig. 6 for the six streamwise measurements stations of Table 2. Results agree with the pressure data of Fig. 3. The separation bubble is thick for the case without wakes or VGJs. The addition of wakes (case (a)) reduces the bubble thickness only slightly. Cases (c-g) are essentially identical to each other and have a slightly thinner separation bubble than case (a). Cases (h-i), with three pulses per wake, are nearly identical to each other and show a noticeably thinner separation bubble than the other cases. It should be noted, however, that the bubble thickness is still quite thick even in cases (h-i). This agrees with the high loss and reduced flow turning compared to high *Re* results shown in Fig. 3. Comparison to cases in Volino and Ibrahim [38] shows that a reduced bubble thickness is possible if the VGJ pulsing frequency is increased to 0.56.

Figure 7 shows phase averaged mean velocity for cases (a), (c), and (d). The six columns correspond to the six streamwise stations, and the rows correspond to a few representative phases in the wake passing cycle. When the separation bubble is most distinct, the measured near wall velocity is low and nearly constant, but non-zero due to the inability of a single sensor hot-wire probe to distinguish direction in a reversing flow. When the boundary layer begins to reattach, the velocity profile goes more continuously toward zero at the wall. Cases (c) and (d) have a single VGJ pulse, and separation control is limited. Differences between the three cases in Fig. 7 are slight, but discernable. The boundary layer separates at Station 2 in all three cases, and the separation bubble grows at Station 3. The profiles for the three cases are nearly identical at Station 2. At Stations 4-6, the wake is causing some reattachment at *t/T*=0-0.333, and the profiles for the three cases are in close agreement with each other. At *t/T*=0.5-0.583, case (d) shows slight signs of reattachment at the downstream stations due to a VGJ pulse, while the other cases are more separated.

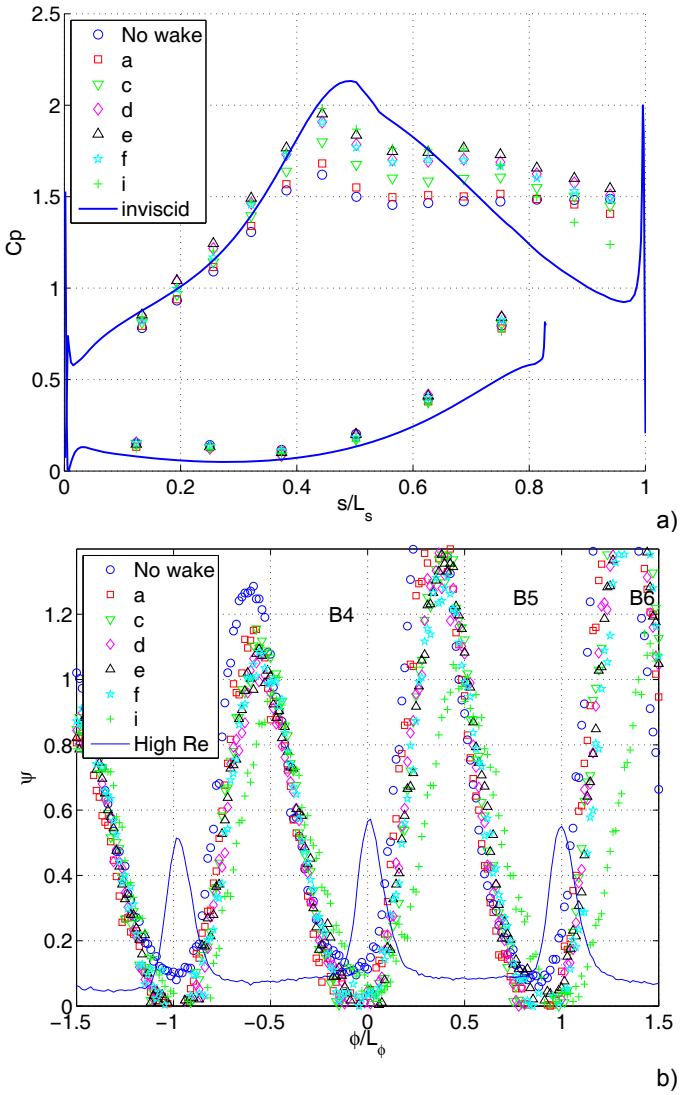

Fig. 5 Pressure profiles for high TI, Re=25,000 cases: a) Cp, b) Total pressure loss

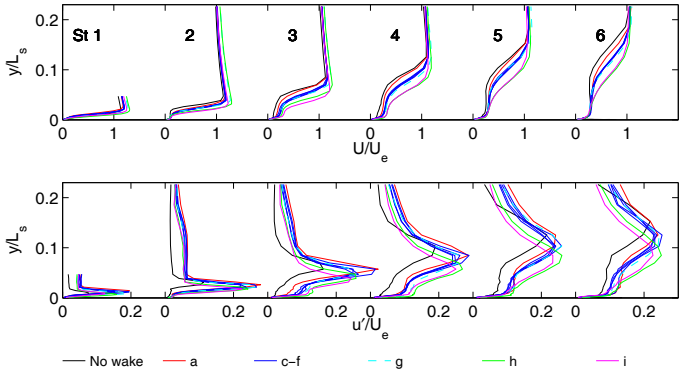

Fig. 6 Time averaged velocity profiles at six streamwise stations for low TI, Re=25,000: top – mean, bottom – rms

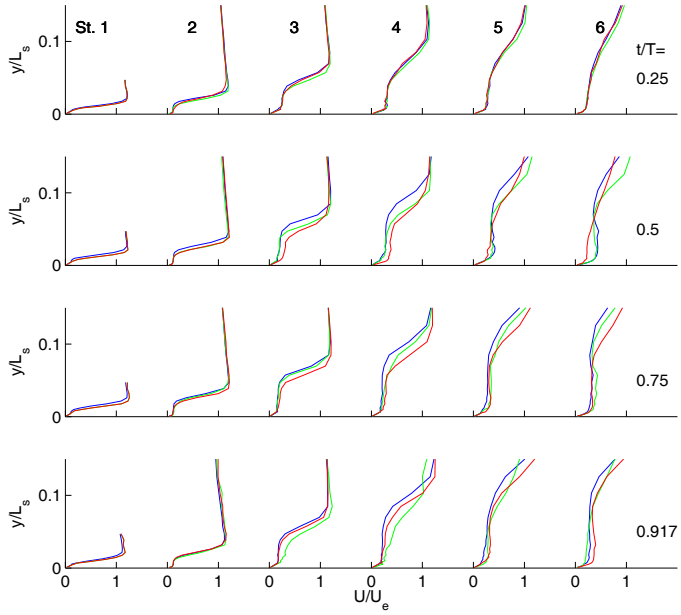

Fig. 7 Phase averaged mean velocity profiles for Re=25,000 cases, columns for six streamwise stations, rows for phases in pulsing cycle: blue – case (a), green – case (c), red – case (d)

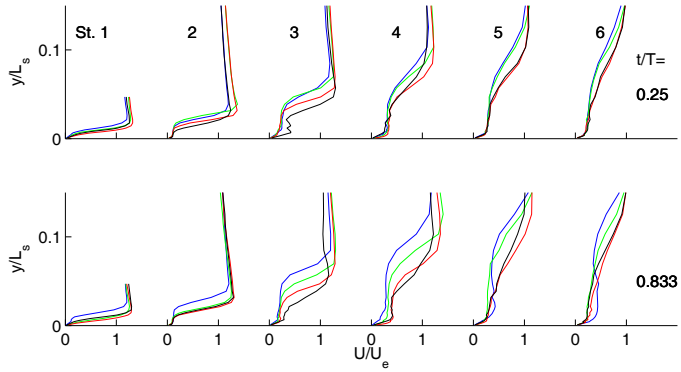

Fig. 8 Phase averaged mean velocity profiles for Re=25,000 cases: blue – case (a), green – case (g), red – case (h), black – case (i)

At t/T=0.667-0.75 all cases show a thick separation bubble. At t/T=0.833, case (c) shows reattachment at Station 3 due to a VGJ pulse, and this continues to Station 4 at t/T=0.917 and Station 5 at t/T=1. The profiles of Fig. 7 show that the VGJ pulses clearly do have some effect, albeit small at this *Re*, and the appearance of the effect depends on the jet timing, although overall separation control is very limited, as shown by the time averaged profiles of Fig. 6.

Figure 8 shows the effect of multiple VGJ pulses on the phase averaged velocity. Case (a), shown for reference, has only wakes. Case (g) has two pulses between the wakes. Case (h) has three pulses, with two occurring at about the same timings as in case (g) and the third coinciding with the wake. Case (i) has three pulses between wakes. Comparison to Fig. 7 shows that separation control is better with multiple jet pulses, in agreement with the time averaged profiles of Fig. 6. Cases (a) and (g) are in close agreement for t/T=0-0.333, which corresponds to the wake passing. At later times, case (g) shows a somewhat thinner separation bubble than case (a) as the VGJs help to control separation. With some minor exceptions, cases (h) and (i) are in good agreement with each other for the full cycle. The addition of a third VGJ pulse reduces separation from case (g) at all phases, both during and between wakes. Whether the third pulse occurs during or between wakes does not seem to matter. With three pulses the separation bubble is present at Stations 2-4, but by the downstream stations the VGJ pulses occur frequently enough to prevent a distinct bubble from forming. The strong adverse pressure gradient still results in a thick boundary layer in cases (h-i), and at some phases the boundary layer is on the verge of separating.

The time averaged boundary layer thickness, $\delta_{99.5}$, is shown in Fig. 9 for the *Re*=25,000 cases, and these values are used in Fig. 10, which shows the phase averaged separation bubble thickness as a fraction of the local, time averaged $\delta_{99.5}$. The bubble thickness is estimated as the distance from the wall to the farthest point in the shear layer with $\partial u / \partial y < 0$. The bubble thickness as a fraction of the boundary layer thickness is used to show the local extent of separation. One could also use the shape factor, but the uncertainty in the displacement and momentum thicknesses resulting from the inability of the hot wire to accurately measure velocity within the separation bubble makes the shape factor a somewhat less reliable quantity than the bubble thickness used here. The dimensional bubble thickness at any given time and location can be determined using the data in Figs. 9 and 10 together. In each time-space plot of Fig. 10, the data are repeated for two cycles to show the periodicity. The solid and dashed white lines indicate the leading and trailing edges of the wake affected regions. The magenta lines bound the VGJ affected regions. In all cases, the suppression of the bubble by both the wake and VGJs is clear. As shown in previous studies ([4], [38], [37]), the initial transient at the start of a VGJ pulse is most effective for flow control. For the wakes, it appears that the separation control is effective for the full duration of the wake. Hence, the separation bubble is suppressed for about three times as long by each wake than by each VGJ pulse. Cases (g) and (h) appear very similar in Fig. 10, which would suggest that the extra pulse within the wake of case (h) is ineffective. The normalizing quantity, $\delta_{99.5}$ is lower for case (h), however, so the extra pulse does help, as shown in Figs. 3, 6 and 8.

The effects of the boundary layer behavior on the downstream flow are shown in Figs. 11 and 12, which show the phase averaged mean and fluctuating velocity $0.63C_x$ downstream of the blade row. The phase averaged mean velocity is the average of all the velocity data at a particular location and phase. The fluctuating velocity is the rms of the difference between the instantaneous velocity and the local phase averaged mean at each location and phase. Cases (a) and (i) are shown as examples. The contours are normalized by the exit velocity U_e. Since the rod spacing is $2L_\phi$ the flow in alternating passages is in phase, with the passages between a half cycle out of phase. In Figs. 11a and 12a, there are vertical strips of low mean velocity at ϕ/L_ϕ = -1.5, -0.5, 0.5 and 1.5 which result from the velocity deficit in the airfoil wakes. Strips of high fluctuating velocity are present at these same locations in Figs. 11b and 12b. These positions correspond to the loss peaks in Fig. 3b. The dimensionless mean velocity between the airfoil wakes cycles between a low of about 0.85 and a high of about 1.1 showing the velocity deficit in the rod wakes and the acceleration between wakes. The rod wakes proceed at an angle in the figure, rising from left to right, as they move forward in time and transit across the cascade. The highest turbulence peaks occur where the rod wakes interact with the separation bubble and airfoil wakes. Comparing Figs. 11 and 12, the amount of mean velocity variation and turbulence in case (i) is less than in case (a) as the VGJs reduce the amount of separation and reattachment in the boundary layer. The separation control, as shown above, is not complete, however, so the

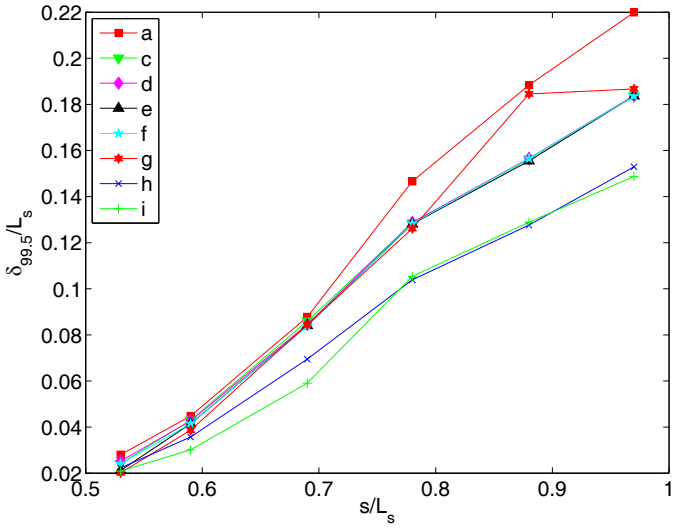

Fig. 9 Time averaged boundary layer thickness, $\delta_{99.5}$, for Re=25,000 cases

results for case (a) with wakes only and case (i) with the best control of the cases considered at *Re*=25,000, are not drastically different. Larger differences were observed in Volino [35] in cases where higher wake passing frequencies resulted in better separation control.

Re=50,000

When the Reynolds number is increased to 50,000, the boundary layer is less prone to separation and more easily controlled. As noted above, full data sets were acquired at *Re*=50,000 for both high and low background freestream turbulence, but since the high and low *TI* results are nearly indistinguishable, only the low *TI* results are presented below. The *Cp* and total pressure loss profiles are shown in Fig. 13. Without wakes or VGJs, the boundary layer separates and does not reattach. With wakes alone (case (a)) the *Cp* profile shows a large drop near the trailing edge, indicating reattachment, but the peak *Cp* value is below the value in the better controlled cases, indicating that reattachment is likely not complete for the full cycle. Cases (b), which has a single VGJ pulse occurring coincident with the wake, matches case (a), indicating that the single pulse provides no benefit when it overlaps the wake. In cases (c) and (d), which both have a single VGJ pulse between wakes, the separation control is better. The *Cp* profiles suggest a bubble is present between s/L_s=0.6 and 0.8, but the boundary layer is attached farther downstream. With two pulses per wake in cases (e) and (f), results are similar, but reattachment appears to move slightly upstream. The loss profiles of Fig. 12b are consistent with the *Cp* results, particularly for the center blade, B4. Cases (a) and (b) are similar to each other and have loss peaks about 30% lower than in the case without wakes. This is consistent with the integrated results shown in Fig. 4. The peaks are also shifted to the right of the no-wake case, indicating an increase in flow turning of about 3°. For cases (c-f) there is an additional drop in the loss peak and a further shift to the right, indicating about 8° more flow turning than the no-wake case. Even in the best case the loss peak is much larger and indicates about 5° less flow turning than in the high Reynolds number comparison case. For cases (e) and (f), which have the best separation control, the wakes of blades B4 and B5 appear similar. For the other cases, the control is partial and as noted above the tailboard has an effect of further suppressing separation on the closer blades, resulting in poorer periodicity. This effect may be more apparent at *Re*=50,000 than in the *Re*=25,000 case of Figs. 3 and 5

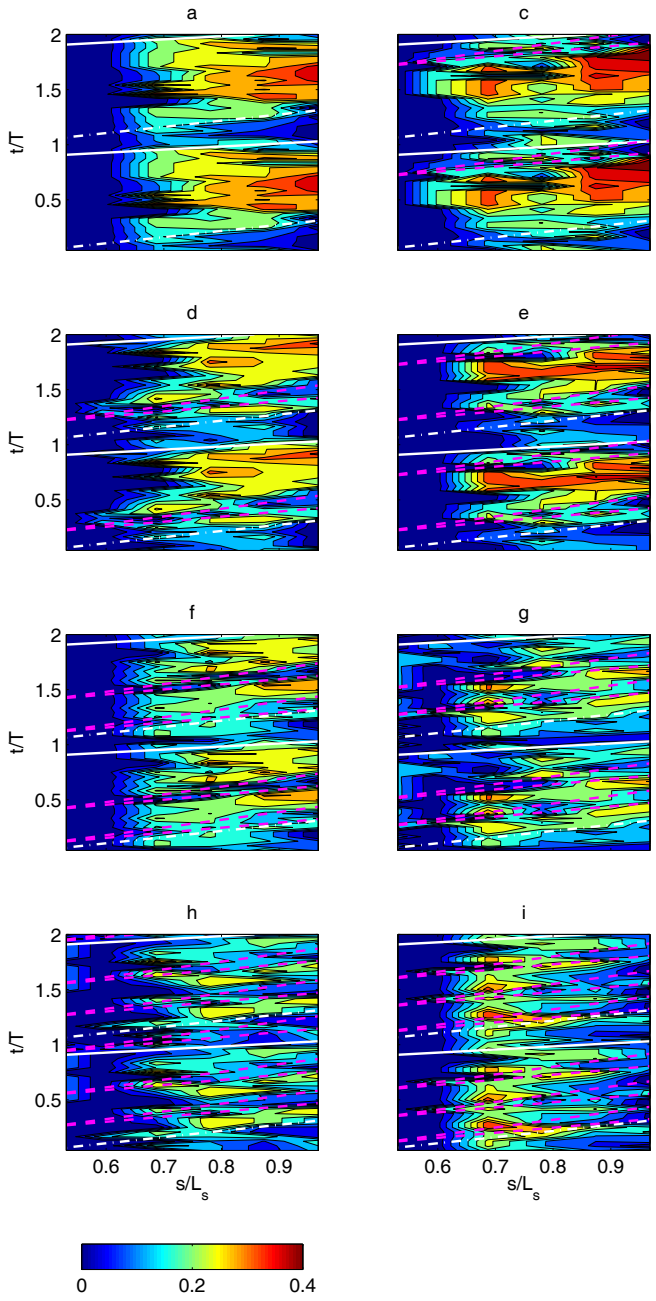

Fig. 10 Time space plots of phase averaged separation bubble thickness normalized on local time averaged $\delta_{99.5}$ for Re=25,000 cases: solid white line – leading edge of wake, dashed white line – trailing edge of wake, magenta lines – extent of VGJ affected region

since *Re*=50,000 is a borderline case with respect to separation, and the boundary layer can go from fully separated to nearly fully attached with relatively small changes in conditions. This appears to make the boundary layer more sensitive to the influence of the tailboard and leads to differences between passages. At Re=25,000, separation control was only partial even in the best cases. The tailboard may act to reduce the bubble thickness more in some passages than others, but it is less likely to produce reattachment. Hence there tends to be more variability between passages at Re=50,000 than 25,000.

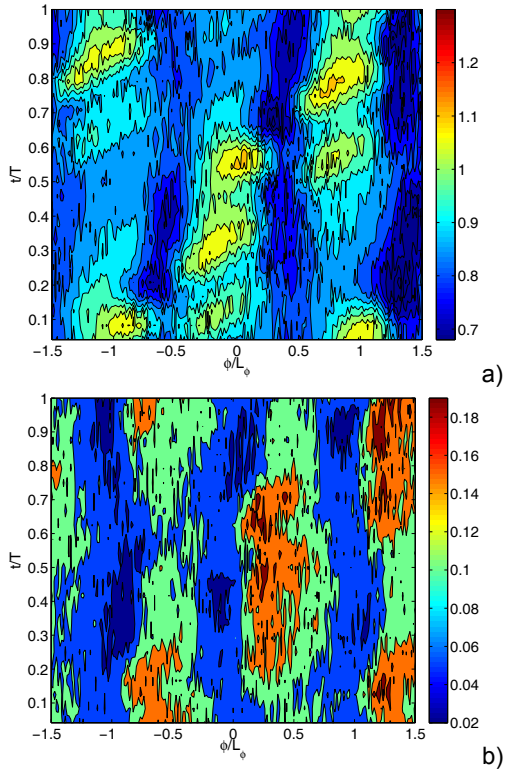

Fig. 11 Time space plot of phase averaged velocity 0.63C_x downstream of cascade for Re=25,000 case (a): a) U/U_e, b) u'/U_e

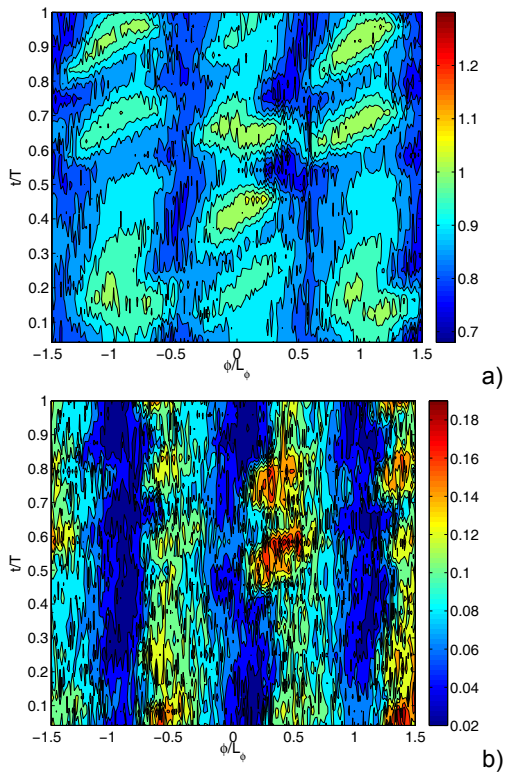

Fig. 12 Time space plot of phase averaged velocity 0.63C_x downstream of cascade for Re=25,000 case (i): a) U/U_e, b) u'/U_e

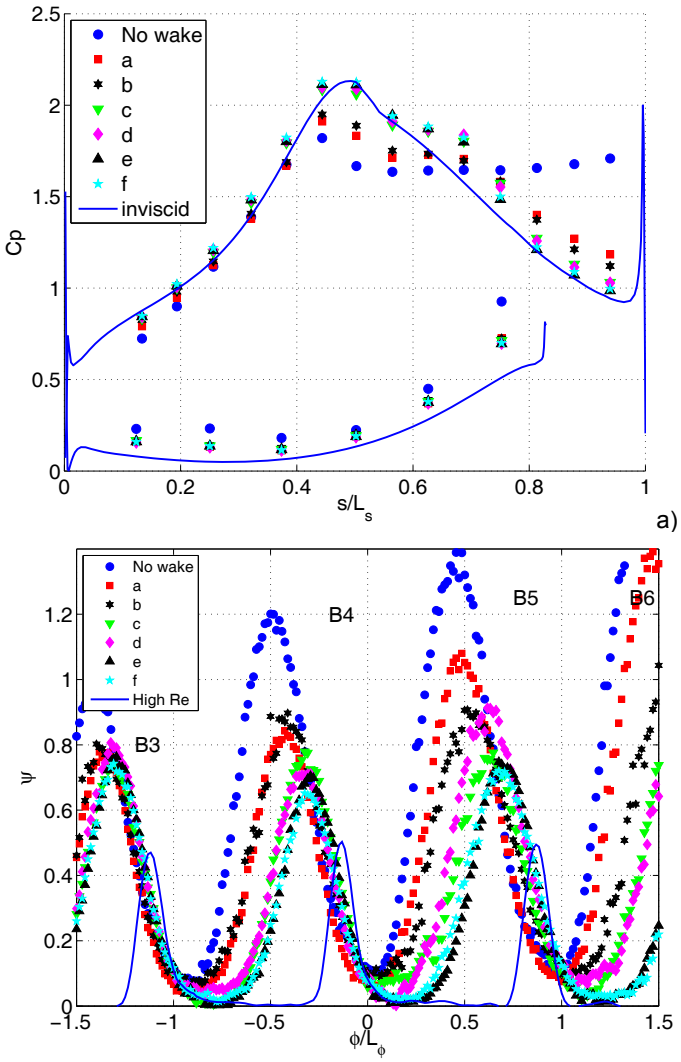

Fig. 13 Pressure profiles for low TI, Re=50,000 cases: a) Cp, b) Total pressure loss

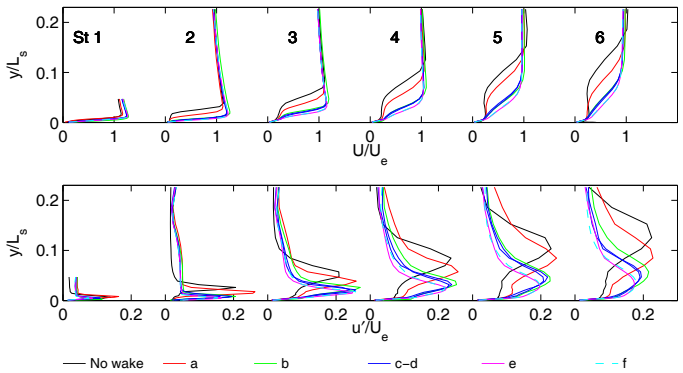

Fig. 14 Time averaged velocity profiles at six streamwise stations for low TI, Re=50,000: top – mean, bottom – rms

Time averaged velocity profiles for the *Re*=50,000 cases are shown in Fig. 14. Without wakes there is a large separation bubble, in agreement with the pressure results of Fig. 13. With wakes alone in case (a), the separation bubble is slightly thinner. In cases (b-d), which all have one VGJ pulse per wake, the separation bubble is much thinner. At Station 6, there is no clear separation bubble, although the boundary layer appears to be on the verge of separating. In the mean profiles, cases (b-d) are virtually indistinguishable from each other. In the fluctuating profiles, the peak in case (b) is slightly farther from the wall than in cases (c-d). This result agrees with the trend in Fig. 13, which shows that separation control is slightly less effective when the pulse coincides with the wake, but the differences associated with the timing are small and are not apparent in all measured quantities. In cases (e-f), which have two pulses per wake, the separation bubble is slightly thinner than in cases (b-d), and the peak in the fluctuating velocity is smaller and closer to the wall.

The boundary layer thicknesses, determined from the profiles of Fig. 14, are shown in Fig. 15. Figure 16 shows the phase averaged separation bubble thickness as a fraction of $\delta_{99.5}$. The wake and VGJ pulses both suppress separation at all locations. Between wakes and pulses the boundary layer separates at $s/L_s \approx 0.7$ in all cases. Without VGJs (case (a)) this separation persists to the trailing edge. With VGJs, regardless of timing, the boundary layer reattaches at all phases.

Figures 17 and 18 show the phase averaged mean and fluctuating velocity in the airfoil wakes for cases (a) and (e). As in Figs. 11 and 12, the velocity deficits and turbulence in the airfoil wakes are clear at ϕ/L_ϕ = -1.5, -0.5, 0.5 and 1.5. The rod wakes appear between the airfoil wakes as areas of slightly elevated fluctuating velocity in Figs. 16b and 17b at ϕ/L_ϕ = -1, and 1 when t/T=0.15; and at ϕ/L_ϕ = 0 when t/T=0.65. As in Figs. 11 and 12, the fluctuating velocity is highest when the rod wakes interact with the airfoil wakes. The variation in the mean velocity and the turbulence are lower for case (e) than case (a) because the VGJs reduce the growth of the separation bubble. The reduction in wake strength and turbulence is in agreement with the thinner boundary layer and separation bubble shown in Figs. 14-16, and the reduced losses of Fig. 13b. Wake measurements for the other *Re*=50,000 cases show the same trend.

The results at both *Re*=25,000 and 50,000 show that when acting together, wakes and VGJs suppress separation. This result is expected since wakes and VGJs were both previously shown to suppress separation when acting alone. Somewhat surprisingly, the boundary layer was not very sensitive to the timing of the VGJs with respect to the wakes. It had been expected that VGJs timed to pulse between wakes would help suppress the growth of the separation bubble between the wakes, while VGJs timed to coincide with the wakes might be wasted since the wake would already be acting to suppress separation at the instant when the jets were pulsed. Cases (b-d) at *Re*=50,000 indicate that timing the VGJs to avoid the wakes may have some benefit, but the influence of timing is small. A pulse lying completely within a wake (case (b)) still helps suppress separation and reduce losses, and is nearly as effective as a pulse between wakes (cases (c) and (d)). For the *Re*=25,000 cases, two pulses between wakes (case (g)) were not enough to significantly reduce separation and losses, but when a third pulse was added within the wake (case (h)), separation was reduced. In fact, case (h) was just as effective as case (i), which had all three pulses between wakes.

CONCLUSIONS

The combined effects of unsteady wakes and vortex generator jets on the flow over the very high lift L1A airfoil were studied experimentally under low and high freestream turbulence conditions.

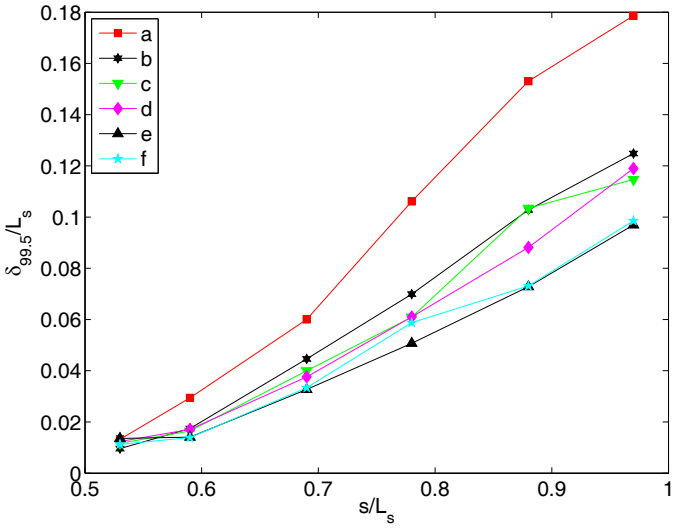

Fig. 15 Time averaged boundary layer thickness, $\delta_{99.5}$, for Re=50,000 cases

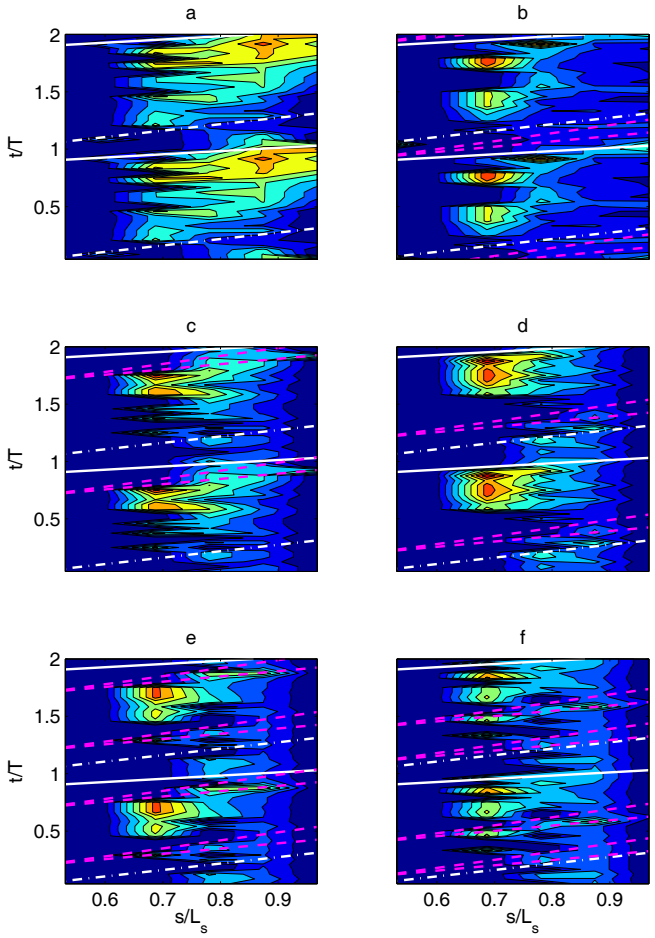

Fig. 16 Time space plots of phase averaged separation bubble thickness normalized on local time averaged $\delta_{99.5}$ for Re=50,000 cases: solid white line – leading edge of wake, dashed white line – trailing edge of wake, magenta lines – extent of VGJ affected region (same color scale as Fig. 9)

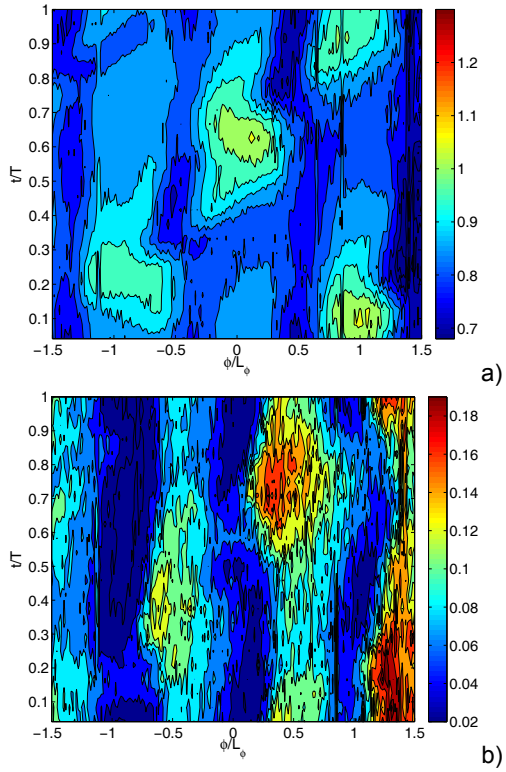

Fig. 17 Time space plot of phase averaged velocity $0.63C_x$ downstream of cascade for Re=50,000 case (a): a) U/U_e, b) u'/U_e

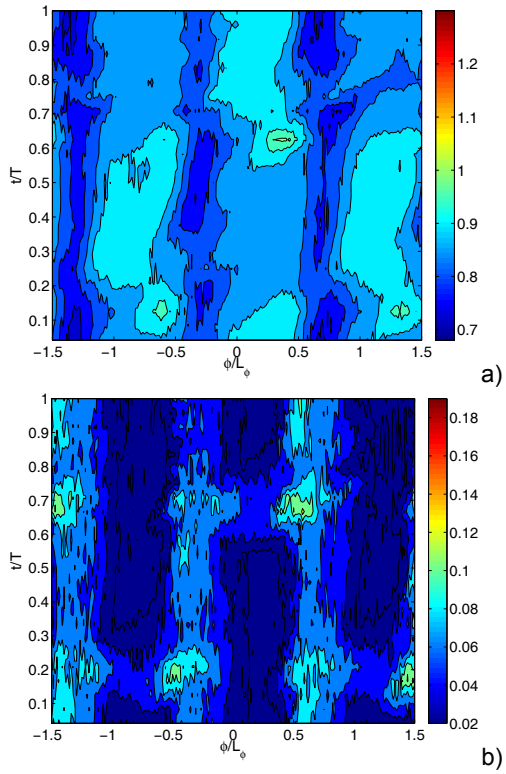

Fig. 18 Time space plot of phase averaged velocity $0.63C_x$ downstream of cascade for Re=50,000 case (e): a) U/U_e, b) u'/U_e

Reynolds numbers based on suction surface length and nominal exit velocity of 25,000 and 50,000 were considered. The effect of the background freestream turbulence between wakes was negligible in the presence of larger wake and VGJ disturbances. Results for cases with *TI*=0.6% and 4% were nearly identical. The wake passing frequency considered in the present study was sufficiently low that the wakes caused only intermittent reattachment with a large, unclosed separation bubble appearing between wakes. Vortex generator jets were able to help reduce this separation if their pulsing frequency was sufficiently high. The timing of the jets with respect to the wakes was not particularly important. For the cases considered, the beneficial effects of the wakes and VGJs did not appear to be additive. The jet pulsing frequency required to fully control separation was about the same as needed in cases without wakes.

ACKNOWLEDGMENTS

This work was sponsored by the National Aeronautics and Space Administration under grant NNC07IA10I. The grant monitors were Drs. Anthony Strazisar and James Heidmann of the NASA Glenn Research Center. The support of the United States Naval Academy Technical Support Department Shop and Fluids Laboratory is greatly appreciated.

REFERENCES

[1] Hourmouziadis, J., 1989, "Aerodynamic Design of Low Pressure Turbines," AGARD Lecture Series 167.

[2] Mayle, R.E., 1991, "The Role of Laminar-Turbulent Transition in Gas Turbine Engines," ASME *Journal of Turbomachinery*, **113**, pp. 509-537.

[3] Sharma, O.P., Ni, R.H., and Tanrikut, S., 1994, "Unsteady Flow in Turbines," AGARD Lecture Series 195, Paper No. 5.

[4] Bons, J.P., Sondergaard, R., and Rivir, R.B., 2001, "Turbine Separation Control Using Pulsed Vortex Generator Jets," ASME *Journal of Turbomachinery*, **123**, pp. 198-206.

[5] Volino, R.J., and Hultgren, L.S., 2001, "Measurements in Separated and Transitional Boundary Layers Under Low-Pressure Turbine Airfoil Conditions," ASME *Journal of Turbomachinery*, **123**, pp. 189-197.

[6] Hodson, H.P., and Howell, R.J., 2005, "Bladerow Interactions, Transition, and High-Lift Aerofoils in Low-Pressure Turbine," *Annual Review of Fluid Mechanics*, **37**, pp. 71-98.

[7] Gostelow, J.P., Walker, G.J., Solomon, W.J., Hong, G., and Melwani, N., 1997, "Investigation of the Calmed Region Behind a Turbulent Spot," ASME *Journal of Turbomachinery*, **119**, pp. 802-809.

[8] Schulte, V., and Hodson, H.P., 1998, "Prediction of the Becalmed Region for LP Turbine Profile Design," ASME *Journal of Turbomachinery*, **120**, pp. 839-846.

[9] Bons, J.P., Pluim, J., Gompertz, K., Bloxham, M., and Clark, J.P., 2008, "The Application of Flow Control to an Aft-Loaded Low Pressure Turbine Cascade with Unsteady Wakes," ASME Paper GT2008-50864.

[10] Pluim, J., Memory, C., Bons, J., and Chen, J.P., 2009, "Designing a High Fidelity Wake Simulator for Research Using Linear Cascades," ASME Paper GT2009-52276.

[11] Schobeiri, M.T., Öztürk, B., and Ashpis, D.E., 2007, "Effects of Reynolds Number and Periodic Unsteady Wake Flow Condition on Boundary Layer Development, Separation, and Intermittency Behavior Along the Suction Surface of a Low Pressure Turbine Blade," ASME *Journal of Turbomachinery*, **129**, pp. 92-107.

[12] Öztürk, B., and Schobeiri, M.T., 2007, "Effects of Turbulence Intensity and Periodic Unsteady Wake Flow Condition on Boundary Layer Development, Separation, and Reattachment Along the Suction Surface of a Low-Pressure Turbine Blade," ASME *Journal of Fluid Engineering*, **129**, pp. 747-763.

[13] Jiang, N., and Simon, T.W., 2005, "Transition in Low-Pressure Turbines: Effects of Unsteady Acceleration and Turbulence Intensity," AIAA *Journal of Thermophysics and Heat Transfer*, **19**, 148-155.

[14] Mahallati, A., and Sjolander, S.A., 2007, "Aerodyanmics of a Low-Pressure Turbine Airfoil at Low-Reynolds Numbers Part 2: Blade-Wake Interaction," ASME Paper GT2007-27348.

[15] Zhang, X.F., and Hodson, H.P., 2010, "Effects of Reynolds Number and Freestream Turbulence Intensity on the Unsteady Boundary Layer Development on an Ultra-High-Lift Low Pressure Turbine Airfoil," ASME *Journal of Turbomachinery*, **132**, 011016.

[16] Funazaki, K., Yamada, K., Ono, T., Segawa, K., Hamazaki, H., Takahashi, A., and Tanimitsu, H., 2006, "Experimental and Numerical Investigations of Wake Passing Effects upon Aerodynamic Performance of a LP Turbine Linear Cascade With Variable Solidity," ASME Paper GT2006-90507.

[17] Praisner, T.J., and Clark, J.P., 2007, "Predicting Transition in Turbomachinery – Part 1: A Review and New Model Development," ASME *Journal of Turbomachinery*, **129**, pp. 1-13.

[18] Zhang, X.F., Vera, M., Hodson, H., and Harvey, N., 2007, "Separation and Transition Control on an Aft-Loaded Ultra-High-Lift LP Turbine Blade at Low Reynolds Numbers: Low-Speed Investigation," ASME *Journal of Turbomachinery*, **128**, pp. 517-527.

[19] Bohl, D.G., and Volino, R.J., 2006, "Experiments with Three-Dimensional Passive Flow Control Devices on Low-Pressure Turbine Airfoils," ASME *Journal of Turbomachinery*, **128**, pp. 251-260.

[20] Volino, R.J., 2003, "Passive Flow Control on Low-Pressure Turbine Airfoils," ASME *Journal of Turbomachinery*, **125**, pp. 754-764.

[21] Huang, J., Corke, T., and Thomas, F., 2003, "Plasma Actuators for Separation Control on Low Pressure Turbine Blades," AIAA Paper 2003-1027.

[22] Johnston, J.P., and Nishi, M., 1990, "Vortex Generator Jets. Means for Flow Separation Control," *AIAA Journal*, **28**, pp. 989-994.

[23] Bons, J.P., Sondergaard, R., and Rivir, R.B., 2002, "The Fluid Dynamics of LPT Blade Separation Control Using Pulsed Jets," ASME *Journal of Turbomachinery*, **124**, pp. 77-85.

[24] Volino, R.J., 2003, "Separation Control on Low-Pressure Turbine Airfoils Using Synthetic Vortex Generator Jets," ASME *Journal of Turbomachinery*, **125**, pp. 765-777.

[25] Volino, R.J., and Bohl, D.G., 2005, "Structure of Oscillating Vortex Generator Jets," Proceedings of the Fourth International Symposium on Turbulence and Shear Flow Phenomena, **2**, pp. 589-594.

[26] McQuilling, M., and Jacob, J., 2004, "Effect of Chord Location on Separation Control With Vortex Generator Jets on Low Pressure Turbine Blades," AIAA Paper 2004-2205.

[27] Eldredge, R. G., and Bons, J. P., 2004, "Active Control of a Separating Boundary Layer With Steady Vortex Generating Jets—Detailed Flow Measurements," AIAA Paper 2004-751.

[28] Bons, J.P., Reimann, D., and Bloxham, M., 2008, "Separated Flow Transition on an LP Turbine Blade With Pulsed Flow Control," ASME *Journal of Turbomachinery*, **130**, 021014.

[29] Clark J.P., 2007, Private Communication, Air Force Research Laboratory.

[30] Zhang, X.F., and Hodson, H., 2005, "Combined Effects of Surface Trips and Unsteady Wakes on the Boundary Layer Development of an Ultra-High-Lift LP Turbine Blade," ASME *Journal of Turbomachinery*, **127**, pp. 479-488.

[31] Volino, R.J., 2010, "Separated Flow Measurements on a Highly Loaded Low-Pressure Turbine Airfoil," ASME *Journal of Turbomachinery*, **132**, 011007.

[32] Ibrahim, M., Kartuzova, O., and Volino, R.J., 2008, "Experimental and Computational Investigations of Separation and Transition on a Highly Loaded Low Pressure Turbine Airfoil: Part 1 – Low Freestream Turbulence Intensity," ASME Paper IMECE2008-68879.

[33] Volino, R.J, Kartuzova, O., and Ibrahim, M., 2008, "Experimental and Computational Investigations of Separation and Transition on a Highly Loaded Low Pressure Turbine Airfoil: Part 2 – High Freestream Turbulence Intensity," ASME Paper IMECE2008-68776.

[34] Volino, R.J., 2002, "Separated Flow Transition Under Simulated Low-Pressure Turbine Airfoil Conditions: Part 1 – Mean Flow and Turbulence Statistics," ASME *Journal of Turbomachinery*, **124**, pp. 645-655.

[35] Volino, R.J., 2010, "Effect of Unsteady Wakes on Boundary Layer Separation on a Very High Lift Low Pressure Turbine Airfoil," ASME Paper GT2010-23573.

[36] Volino, R.J., Kartuzova, O., and Ibrahim, M.B., 2009, "Experimental and Computational Investigations of Low-Pressure Turbine Separation Control Using Vortex Generator Jets," ASME Paper GT2009-59983.

[37] Volino, R.J., Kartuzova, O., and Ibrahim, M.B., 2010, "Separation Control on a Very High Lift Low Pressure Turbine Airfoil Using Pulsed Vortex Generator Jets," ASME Paper GT2010-23567.

[38] Volino, R.J., and Ibrahim, M.B., 2010, "Separation Control on High Lift Low Pressure Turbine Airfoils Using Pulsed Jet Vortex Generator Jets," Proceedings of the ASME-ATI-UIT 2010 Conference on Thermal and Environmental Issues in Energy Systems, 2010.

[39] Ibrahim, M., Kartuzova, O., Doucet, D., and Volino, R.J., 2010, "LES Flow Control Simulations for Highly Loaded Low Pressure Turbine Airfoil (L1A) Using Pulsed Vortex Generator Jets," ASME paper GT2010-23015.

[40] Ibrahim, M.B., Kartuzova, O., and Volino, R.J., 2009, "LES and URANS Computational Investigations of LPT Blade (L1A) Separation Control using Vortex Generator Jets," Proceedings of Turbulence, Heat and Mass Transfer 6, 2009.

[41] Bloxham, M., Reimann, D., Crapo, K., Pluim, J., and Bons, J.P., 2007, "Synchronizing Separation Flow Control with Unsteady Wakes in a Low-Pressure Turbine Cascade," ASME Paper GT2007-27529.

[42] Kaszeta, R.W., Simon, T.W., Jiang, N., and Ottaviani, F., 2005, "Influence of Wake Passing Frequency and Elevated Turbulence Intensity on Transition," AIAA *Journal of Thermophysics and Heat Transfer*, **19**, 137-147.

[43] Wills, J.A.B., 1962, "The Correction of Hot-Wire Readings for Proximity to a Solid Boundary," *Journal of Fluid Mechanics*, **12**, pp. 65-92.

Proceedings of ASME Turbo Expo 2012
GT2012
June 11-15, 2012, Copenhagen, Denmark

GT2012-69770

CFD SIMULATIONS OF UNSTEADY WAKES ON A HIGHLY LOADED LOW PRESSURE TURBINE AIRFOIL (L1A)

Mounir B. Ibrahim and Samuel Vinci

Mechanical Engineering Department
Cleveland State University
Cleveland, Ohio 44115-2425
m.ibrahim@csuohio.edu

Olga Kartuzova

National Center for Space
Exploration Research
NASA Glenn Research Center
Cleveland, Ohio 44135
olga.kartuzova@nasa.gov

Ralph J. Volino

Mechanical Engineering Department
United States Naval Academy
Annapolis, Maryland 21402-5042
volino@usna.edu

ABSTRACT

A study of a very high lift, low-pressure turbine airfoil in the presence of unsteady wakes was performed computationally and compared against experimental results. The experiments were conducted in a low speed wind tunnel under high (4.9%) and then low (0.6%) freestream turbulence intensity conditions with a flow coefficient (ζ) of 0.7. The experiments were done on a linear cascade with wakes that were produced from moving rods upstream of the cascade with the rod to blade spacing varied from 1 to 1.6 to 2. In the present study two different Reynolds numbers (25,000 and 50,000, based on the suction surface length and the nominal exit velocity from the cascade) were considered.

The experimental and computational data have shown that in cases without wakes, the boundary layer separated and did not reattach. The CFD was performed with Large Eddy Simulation (LES) and Unsteady Reynolds-Averaged Navier-Stokes (URANS), Transition-SST, utilizing the finite-volume code ANSYS FLUENT under the same freestream turbulence and Reynolds number conditions as the experiment but only at a rod to blade spacing of 1.

With wakes, separation was largely suppressed, particularly if the wake passing frequency was sufficiently high. Similar effect was predicted by 3D CFD simulations. Computational results for the pressure coefficients and velocity profiles were in a reasonable agreement with experimental ones for all cases examined. The 2D CFD efforts failed to capture the three dimensionality effects of the wake and thus were less consistent with the experimental data.

As a further computational study, cases were run to simulate higher wake passing frequencies which were not run experimentally. The results of these computational cases showed that an initial 25% increase from the experimental dimensionless wake passing frequency of F=0.45 greatly reduced the size of the separation bubble, nearly completely suppressing it, however an additional 33% increase on top of this did not prove to have much of an effect.

NOMENCLATURE

C_p	$2(P_T - P)/\rho U_e^2$, pressure coefficient
C_x	axial chord length
C_f	$\tau_w/(1/2\rho U_\infty)$, skin friction coefficient
F	$fL_{j\text{-}te}/U_{ave}$, dimensionless wake passing frequency
f	frequency
HFSTI	High Freestream Turbulence Intensity (4.9%)
$L_{j\text{-}te}$	length of an adverse pressure gradient region on the suction surface
LFSTI	Low Freestream Turbulence Intensity (0.6%)
L_s	suction surface length
L_ϕ	blade spacing (pitch)
P	pressure
P_S	upstream static pressure
P_T	upstream stagnation pressure
P_{Te}	downstream stagnation pressure
Re	$U_e L_s/\nu$, exit Reynolds number
s	streamwise coordinate, distance from leading edge
T	period of wake passing cycle
t	time
τ_w	$\mu(dU/dy)_{y=0}$, wall shear stress

U	local mean velocity
U_{ave}	average freestream velocity in adverse pressure gradient region, based on inviscid solution
U_i	inlet freestream velocity
U_e	nominal exit freestream velocity, based on inviscid solution
u'	rms fluctuating streamwise velocity
x	axial distance from leading edge
y	wall normal distance from suction surface
ϕ	coordinate along blade spacing, normal to axial chord
ν	kinematic viscosity
ρ	density
ψ	$(P_T-P_{Te})/(P_T-P_S)$, total pressure loss coefficient
ζ	$U_i\cos(\alpha_i)/U_{rod} = U_{axial}/U_{rod}$, flow coefficient

INTRODUCTION

The desire to reduce fuel costs and improve engine performance in the gas turbine industry has led many to conduct experimental and computational fluid dynamics (CFD) research on the effects of flow over the low-pressure turbine (LPT) blades. This research has shown that separation of the flow can occur on the suction surface of these blades due to the presence of adverse pressure gradients. Separation results in partial loss of lift and higher aerodynamic losses at high altitude cruise conditions and becomes increasingly more severe as the aft loading of the airfoils increases.

Early experimental and computational studies of the flow over these high lift airfoils were performed by examining the airfoils by themselves in a wind tunnel with varying levels of freestream turbulence intensities. However, it has become evident that the presence of the forward stages of stator vanes in front of the rotor airfoil blades creates wake shedding vortices, which have significant effect on the boundary layer of these rotor blades. The velocity deficit in these wakes causes flow outside of the wake to accelerate and impinge on the suction surface of blades creating a so called "negative jet" Hodson and Howell [1]. The study of this wake and the wake induced transition associated with it has started to become the topic of study in a number of experiments; however this type of flow has yet to be extensively modeled computationally due to the difficulties associated with creating these models.

The creation of the impinging wake on a blade has been studied by Pluim et al. [2] and it was shown that a circular rod provides a sufficient representation of the form of the true wake that comes off the upstream vane. Thus experimental data are collected by passing a line of circular rods upstream of a cascade of airfoils with data collected by hot wire anemometers over the suction side of these airfoils. Many experiments have been run analyzing the wake/blade interaction effects; see Bons et al. [3] and Pluim et al. [2]. Present computational study is based on the experiment of Volino [4]. Numerical studies of the wake and its subsequent interaction with an airfoil was studied by Sarkar [5]. Sakar in his study applied a wake that was generated by a circular rod. The results of the wake were then interpolated into a domain containing the airfoil. The analysis of a circular wake generating rod and its effect on a downstream airfoil was examined for a Reynolds number of 78,000 (based on the axial chord and the inlet velocity). In this study airfoil T106 (see Stieger et al. [6]) was considered with flow coefficient (ζ) of 0.83 and reduced blade passing frequency of 0.68. The wake was originally generated in both 2D and 3D simulations using URANS and LES turbulence models respectively. These results were then interpolated into a 3D airfoil geometry and the effects of the wake/airfoil interaction were studied with LES. It was shown that the wakes produced with LES and interpolated into the airfoil domain produced smaller scale eddies and thus produced more accurate predictions of separated flow than the 2D wakes.

Suzen and Huang [7] numerically studied unsteady wake/blade interactions in LPT Pack-B flows using an intermittency transport equation. They followed experiments of Kaszeta et al. [8, 9] and Stieger [10]. In that study, predictions of the flow with the intermittency transport model were in a good agreement with experimental data for the pressure coefficient. Differences in velocity predictions in the separated region were attributed to the inability of hot wire anemometry, used in the experiment, to measure negative velocities. The observation was made that high wake passing frequency resulted in suppression of the separation zone due to higher turbulence levels generated in the wake.

Rodi [11] conducted DNS and LES studies of the flow past turbine blades with incoming wakes. Reynolds number based on axial chord and inlet velocity was 51,800 in the low Re case and 148,000 in the high Re case. In both cases DNS and LES showed similar results for the pressure coefficient, which were in reasonable agreement with experimental data. Some disagreement in pressure coefficient near the leading edge on the suction side was attributed to the difference in the inlet flow angle and compressibility effects of the flow, which was modeled as incompressible. In the high Re case, where the flow was attached, LES predicted transition a little later compared to DNS and therefore it was concluded that LES is not a good tool for predicting this type of flow. However, it is necessary to mention that DNS required 10 times longer to compute, compared to LES and it cost the author several months of calculations on a supercomputer.

Lardeau [12] applied the URANS approach to simulate a moving wake generating rod and airfoil blade geometry. He showed that the URANS models were very sensitive to the grid size and the time step size of the calculation. The results

showed that too coarse of a grid or time step size would result in the vortex shedding not developing due to the small length scale of the circular wake generating rod as compared to the blade.

In this paper a computational model was developed and applied to simulate effect of the moving upstream rod on the flow transition and separation over highly loaded LPT airfoil L1A. URANS and LES approaches to turbulence modeling were compared. The results were compared with experimental data of Volino [4]. CFD provided further insight to the effect of the upstream wake on the flow over the airfoil. Additional cases were run to analyze effects of rod speed on the boundary layer of the airfoil suction surface.

EXPERIMENTAL FACILITY AND MEASUREMENTS

Details of experimental setup are presented in Volino [4] and summarized below.

Experiments were conducted in a closed loop wind tunnel with a seven blade linear cascade as shown in Fig. 1 with the cascade parameters shown in Table 1. The streamwise component of the turbulence intensity was 0.6% with the integral length scale of 6.3 cm. A tailboard, shown on Fig. 1, was used to ensure the correct flow angle from the cascade with periodicity at high Reynolds numbers. At low Reynolds numbers the periodicity was not as good because large separation was present and due to suppression of the separation on the blades closest to the tailboard.

The wake generator includes a chain near each endwall of the cascade that passes $0.54C_x$ upstream of the leading edges of the cascade blades. The chain links have hollow pins, through which the wake generator rods are attached with a diameter of 4 mm. Tests were run with average distances between rods of 136 mm, 221 mm, and 272 mm, which correspond to $1L_\varphi$, $1.6L_\varphi$ and $2L_\varphi$, where L_φ is the blade spacing in the cascade. These ratios of rod to blade spacing are in the range expected for vane to rotor blade spacing in an engine.

For most tests, the rods were driven at a velocity of 1.18 times the cascade inlet velocity, U_i. This gives a flow coefficient, $\zeta = U_i \cos(\alpha_i)/U_{rod} = 0.7$, where α_i is the inlet flow angle. This is also in the expected range for an engine.

Table 1: Cascade parameters

Axial Chord, C_x [mm]	True Chord [mm]	Pitch, L_ϕ [mm]	Span [mm]	Suction side, L_s [mm]	Inlet flow angle	Exit flow angle
134	146	136	724	203	35°	60°

NUMERICAL METHODS

The numerical simulations were conducted utilizing the finite-volume code ANSYS FLUENT [13]. Cases were run at different Reynolds numbers, wake passing frequencies, and free stream turbulence intensity levels. Table 2 shows a summary of all CFD cases conducted in this study.

The computational domain was based on earlier work (see Ibrahim et al. [14]). However the grid was sub-divided into three cell-zone domains, a stationary inlet zone, a moving (sliding, periodically repeating) translational zone containing the circular wake generating rod in it, and a stationary zone with the airfoil and rest of the downstream domain in it. The mesh generated around the rod was refined until it showed a wake that was produced and did not dissipate as it propagated downstream to the cascade.

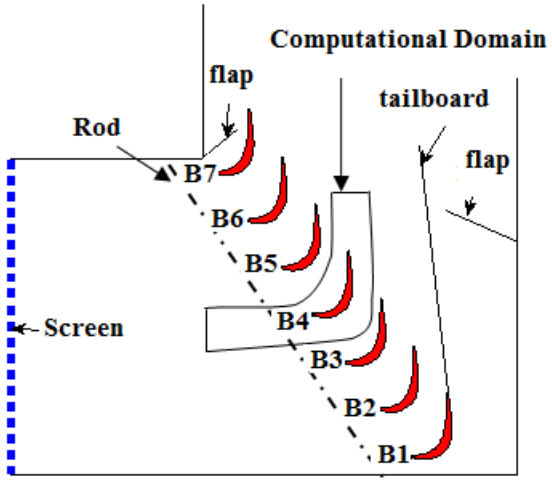

Figure 1. Cascade Passage

The interaction between the interface zones was set up so the conditions periodically repeated themselves allowing for the wake to carry between zones even as the interfaces became unaligned. The inlet and outlet conditions varied based on Reynolds number and the freestream turbulence intensity of the flow and the boundaries on each face of the grid were set up as periodic in order to simulate a full blade and a full cascade. For the two dimensional cases this assumed no variation in the z direction, which proved to cause some modeling issues.

For the two dimensional cases, a URANS calculation utilizing the Transition-SST turbulence model of Menter et al. [15] was used. The three dimensional computational domain was used for both the URANS calculations and LES calculations. The number of passages used was varied for the

Table 2: CFD cases investigated

Case	Re	Free Stream Turbulence Intensity	F	Turbulence Model
1	25,000	LFSTI*	0.45	Trans-SST (2D)
2	50,000		0.45	
3	25,000	LFSTI*	0.45	LES
4		HFSTI*		
5	50,000	LFSTI*	0.45	
6		HFSTI*		
7		HFSTI	0.56	
8			0.75	

Experimental Data available from Volino [4].

two dimensional and three dimensional domains and will be explained further below (see Table 1. for cascade parameters). A uniform velocity inflow condition is specified 1.9 C_x upstream of the blade leading edge in the flow direction. The inlet flow angle is set to 33^o based on an inviscid calculation of the full cascade used in the experiment (see Ibrahim et al. [16]). This angle agrees with the experimentally measured inlet angle to within the experiment uncertainty. The exit boundary is located 3.8 C_x downstream of the trailing edges in the flow direction. The boundary conditions on the sides of the passage are periodic.

Convergence was established when: 1) residuals reduced to a value 10^{-5}, 2) no change was observed in any field results, and 3) the mass imbalance was less than 0.01 %.

For the 2D cases, a two-channel domain was designed, having an entire airfoil in the middle, with two rods spaced equally one blade spacing apart. The details of this grid are given in Table 3. In the 3D simulations, with rod to blade spacing of 1, a single airfoil with half channel spacing above and below was used. Periodic boundary conditions were applied to simulate the entire cascade and in order to save on computational memory and time. Adding multiple rods to a single domain (in the 2D cases) did not increase the mesh size significantly nor computational time, therefore two blade passages with two rods were used, however for the 3D domain one full blade passage (half a blade passage above and below an airfoil) was simulated to keep the mesh size at a minimum.

Table 2 summarizes cases examined in this paper, with the same cases also studied experimentally by Volino [4] indicated. A combination of variation in Re (25,000 and 50,000), free stream turbulence intensities (LFSTI and HFSTI) and turbulence modeling approach (URANS with Transition-SST model and LES) were considered to match the experimental data. Additional cases with increased rod speeds, and thus increased dimensionless wake passing frequency values (F) were studied.

TURBULENCE MODELING

LES with Dynamic Kinetic Energy Subgrid-Scale model

The governing equations employed for LES are obtained by filtering the time-dependent Navier-Stokes equations. The filtering process effectively filters out eddies whose scales are smaller than the grid spacing used in the computations. The resulting equations thus govern the dynamics of large eddies. The subgrid-scale stresses resulting from the filtering operation are unknown, and require modeling. The subgrid-scale turbulence models in Fluent employ the Boussinesq hypothesis as in the RANS models.

The dynamic subgrid-scale kinetic energy model, used in the present study, is based on the model proposed by Kim and Menon [17]. In this model a separate transport equation is solved for subgrid-scale kinetic energy. The model constants are determined dynamically. The details of the implementation of this model in ANSYS FLUENT and its validation are given by Kim [18].

Transition-SST (4 equation) model of Menter et al. [15]

A correlation-based transition model was proposed by Menter et al. [15]. This model is based on two transport equations. The intermittency transport equation is used to trigger the transition onset. The transport equation for the transition momentum thickness Reynolds number ($Re_{\theta t}$) is used to capture non-local effects of freestream turbulence intensity and pressure gradient at the boundary layer edge. Outside the boundary layer the transport variable was forced to follow the value of $Re_{\theta t}$ given by correlations. Those two equations were coupled with the shear stress transport turbulence (SST) model. This model is available in ANSYS FLUENT Version-12 [13] as Transition-SST (4 equation) turbulence model.

RESULTS AND DISCUSSION

Code Validation

Four different grids were compared in this study as shown in Table 3. Velocity magnitude contours were analyzed for the 2D, Re = 50,000 case comparing Grids#1 and #2. The CFD data from Grid#2 & #3 did not vary much and Grid#3 only increased computation time. Based on the above Grid#2 was selected for 2D simulations of the present study. Grid#4 was generated for 3D simulations of the present study. This grid is similar to the Grid#2 and expanded in the spanwise direction. Grid#4 is suitable for LES since grid resolution is within recommended values for this type of simulation (in the near-wall region recommended values are: y+~ 2; Δx+ ~ 50-150;

$\Delta z+ \sim 15\text{-}40$ (Piomelli and Chasnov [19]). Table 4 shows more specifics of Grid#4. Time step size of 0.001 s was used for 2D URANS simulations and 0.0001 s for LES.

Statistical averages of the pressure coefficient plotted versus dimensionless distance along both the suction and pressure side of an airfoil are presented on Figure 2 for Re=50,000, LFSTI. On the figure, the peak of C_p on the suction side of the airfoil is located between s/Ls 0.4 and 0.5 in both CFD and experiment. A plateau in C_p downstream of the C_p peak indicates flow separation.

Table 3 Grids used in this investigation

Grid #	Size (Cells)	Number of grids in z direction	y+	$\Delta z+$	$\Delta x+$
1 (2-D)	60,600	NA	0.132	NA	< 28
2* (2-D)	122,000	NA	0.115	NA	< 10
3 (2-D)	200,000	NA	0.113	NA	< 4
4* (3-D)	1.7 million	32	0.117	<1	< 18

Table 4: Specification of computational Grid#4

Number of cells (million)	1.7
Number of nodes on the suction surface	292
Number of nodes on the pressure surface	240
Number of nodes in span direction	32
y+	0.117
$\Delta z+$	< 1
$\Delta x+$	< 18
Distance from inlet boundary to the leading edge	3.8 C_x
Distance from the trailing edge to the outlet boundary	1.9 C_x

In cases without wakes (Ibrahim et al. [14]), this plateau is large and C_p remains almost constant downstream of the peak in both CFD and experiment. This corresponds to a large separation without reattachment. In cases with an upstream rod the plateau in C_p on the suction side is much shorter compared with the cases without a rod and the value of C_p decreases downstream of the plateau. This indicates a smaller separation with reattachment at the end of the plateau in C_p. For cases with an upstream rod the comparison between the 2D and the 3D C_p profiles shows a similar trend of separation and reattachment. However, in 2D simulation values of the C_p peak are under-predicted, compared with experiment. Results of the 3D LES simulation show excellent agreement with experiment in values and the slope of the C_p profile at all airfoil locations. Computational velocity profiles at the inlet into the cascade are compared with experimental ones in Fig. 3. The wake from a rod predicted in 3D LES simulation is in a reasonable agreement with experimental data for the same freestream turbulence conditions. Velocities in the wake are over-predicted in the 2D simulation between ϕ/L -0.1 and 0.1.

Wake Characteristics

Several studies have compared rod wakes to airfoil wakes. Pluim et al. [2] tested rods of various shapes and provided references to earlier studies. They found that the wakes from wedge shaped rods agreed best with L1A airfoil wakes, but cylindrical rods also provided a reasonable approximation.

In the experiment, the moving rod wakes were measured by placing a stationary hot-wire midway between blades B4 and B5 (see Fig. 1) in the plane of the leading edges. The moving rods traversed $0.54C_x$ upstream of the hot-wire. The data from the probe were phase-averaged on the rod passing cycle to determine the mean and fluctuating velocity as functions of time. For comparison, the time averaged velocity profile was taken $0.54C_x$ downstream of the rod, as shown in Fig. 3. All curves were normalized using the average local mean velocity. The agreement between CFD and the experiment is reasonable.

Figure 4 shows instantaneous vorticity contours for the flow behind the rod in the simulations, for Re 50,000. The Reynolds number based on the rod diameter for these cases is about 594 and the Strouhal number is 0.117 (based on the cylinder shedding frequency) which matched the empirical correlation obtained by Norberg [20]. The 2D simulation (not shown here) showed large organized coherent structures (Karman vortex shedding) consistent with a laminar-like flow. The 3D, LES simulation (Fig. 4a), on the other hand, shows the wake structures with small-scale eddies as expected in reality. Fig. 4b shows the initial attempt to run a URANS, 3D model at the same time step size as 2D (t = 0.001 s). The figure shows that this time step was not sufficiently fine enough to capture the vortex shedding Lardeau [12]. Thus the same size time step used for the LES calculations was necessary to get satisfactory results, losing the computational advantage of using a URANS model with a larger time step. Thus for the rest of the paper, all 3D cases were run using LES.

Re=25,000, F=0.45

Figures 5 and 6 show the time averaged C_p profiles and total pressure loss coefficient (ψ) profiles for the 2D and 3D cases, compared against the experimental data. Here it can be seen that in the 2D case, the lack of ability to accurately predict the magnitude of the C_p peak, along with an over-prediction in the separation bubble size (shown by a large plateau in the C_p values), result in greater prediction in the peak of the Total Pressure Loss Coefficient (ψ) and a sharper drop in the profile.

For the 3D cases, both the LFSTI and HFSTI cases match reasonably good to the experimental data, however the lack of ability to locate the separation and reattachment points lead to a larger predicted separation bubble in the LFSTI case and a smaller predicted one in the HFSTI case. This affects ψ, showing a peak loss greater than the experimental data for the LFSTI case and a peak loss less than the experimental data for the HFSTI case. There is also a much sharper drop in the profile due to a sharp drop in the C_p profile after reattachment.

Reynolds 25,000 cases are difficult to document due to the small change in pressure associated with the C_p and total pressure loss coefficients, thus leading to significant uncertainty in both the experimental and computational cases. Higher accuracy is expected as the Reynolds number is increased.

Re=50,000, F=0.45

Figures 7 and 8 show the results of the time averaged C_p profiles and Total Pressure Loss Coefficient (ψ) profiles for the 2D URANS and 3D LES cases compared against the experimental data. Once again, in the 2D URANS simulation the magnitude of the C_p peak is under predicted, however the size of the bubble is much more accurate compared to the Re=25,000 case, and is consistent with both the 3D LES case and the experimental data. This results in a ψ peak value that is consistent with the experimental data, however values of ψ between -0.2 and 0.5 φ/L_φ are over-predicted compared with experiment. The poorer agreement between the experiment and predicted ψ profiles (compared to C_p profiles) could be attributed to: 1) the mesh structure used in this wake region and 2) the turbulence model applied.

Results of the 3D LES LFSTI and HFSTI cases match the experimental data reasonably well in both the magnitude of the C_p profile as well as in predicting the locations of separation and reattachment. In these cases the magnitude of the ψ peak as well as an overall shape of the ψ profile for φ/L_φ between -0.5 and 0.2 agree with experimental data.

To provide further insight into the wake influence on the suction surface boundary layer separation and reattachment data from the 3D LES simulations under LFSTI and HFSTI conditions are analyzed below.

Velocity measurements were conducted at 5 different stations downstream of the location of the C_p peak (see Table 5).

Table 5: Velocity profile measurement stations

Station	1	2	3	4	5
s/Ls	0.59	0.69	0.78	0.88	0.97
x/Cx	0.72	0.80	0.86	0.92	0.97

Figure 9 shows the velocity profiles at the 5 streamwise locations described in Table 5 for the CFD Re=50,000, HFSTI case with a rod to blade spacing of 1. Experimental velocity profiles from the case with the rod to blade spacing of 1.6 are shown for comparison. This comparison is justified, since pressure coefficients obtained from experiment with rod to blade spacings of 1.6 and 1 are similar and also similar to the C_p profile predicted in CFD (spacing 1). Predicted mean velocity profiles, shown on Fig. 10a, agree with experimental ones well. A small separation bubble is predicted in CFD at stations 1 and 2 which is indicated by the negative velocities near the wall. Reattachment is predicted at stations 3-5. This is consistent with separation and reattachment locations derived from the C_p profile shown on Fig. 7. It is more difficult to determine separation and reattachment locations from experimental velocity profiles, since the hot wire anemometry method, used in the experiment to measure velocities, does not allow identifying flow direction. Figure 9b shows the RMS velocity profiles for the same cases. Here, the CFD shows the same general profile, matching well with the data; however it is consistently greater in $ú/U_e$, even in the freestream. This may be the result of the fact that the wake profile seen in Fig. 3 shows a wake with a greater deficit and larger width than the experiment, thus resulting in the increase in turbulence levels in the passage. This large width in the wake indicates that Direct Numerical Simulation (DNS) might be needed to resolve turbulence in the wake of the rod and in the cascade, however due to large computational times associated with DNS this would be prohibitive.

Figures 10 and 11 show the same mean C_p profiles for the LFSTI and HFSTI cases shown earlier in Fig. 8, however this time they are plotted along with the mean coefficient of friction (C_f) profiles. Marked on these profiles are dotted lines showing the indications of separation, transition, and reattachment. It can be seen that in the C_f profile, where the plateau in the C_p profile begins, thus indicating separation, an inflection in the C_f curve is also seen. This inflection reduces the slope of the curve slightly, allowing for C_f to more slowly approach a point where it hits zero and then equally slowly starts to increase again. At a point just before reattachment, indicated by the C_p profile, there is another inflection in the C_f curve resulting in a more increased slope and a more rapid

increase in C_f. This is the indication of transition beginning to occur. Finally, at the point of reattachment, the C_f curve indicates another inflection right before it reaches its peak.

In Figures 12-1 through 12-4, instantaneous results for the Re=50,000, HFSTI case are shown for one full wake passing cycle. The C_f and C_p profiles are visualized by plotting their values on separate y-axis while the Q-Criterion contours colored by C_p values are shown beneath to give a visualization of the location of the wake in the passage and its effect on the pressure profile.

Figure 12-1 shows that as the wake has collapsed over the C_p peak and suppression of the separation bubble begins, the bubble is rolled downstream with the C_p peak, with the associated peak C_f being compressed and increasing in magnitude. Trailing behind this spike in turbulence is a calmed region which has near zero C_f, but is resistant to separation. These peaks as well as the trailing calmed region were predicted in Hodson and Howell [1]. The contour plot shows the elongated wake structures forcing the separation bubble downstream.

Figure 12-2 shows 30% through a cycle, the separation bubble has been rolled nearly all the way out of the cascade passage and has been removed from the surface. The curves show a large amount of turbulence still present on the aft portion of the suction surface; however the once calmed region is starting to show localized points of separation. The C_p peak is nearly fully reestablished as another wake approaches upstream.

Figure 12-3 shows 60% of a cycle at which point the C_p peak has a very dominant profile. The separation bubble is nearly fully re-grown, with the presence of the wake in the forward part of the passage showing no effect on the boundary layer of the suction surface.

Figure 12-4 shows that at 90% through the cycle, the wake is beginning to collapse over the C_p peak and affect the separation bubble. The bubble is being rolled up, with the new peak in C_p and a peak in C_f developed.

Re=50,000, F=0.56, F=0.75

For a further analysis of the effect of the wake, the dimensionless wake passing frequency, F, was increased by increasing the speed of the rod. Figure 13 shows that the initial 25% increase in F (to the value of F=0.56) resulted in a significant reduction in the size of the separation bubble as compared to the original F=0.45 case, nearly suppressing separation completely. The result in the Total Pressure Loss Coefficient (ψ) seen in Fig. 14 shows a peak loss also greatly reduced. However, when trying to further increase the rod speed an additional 33% (to the value of F=0.75), the resulting profiles are nearly identical to the F=0.56 case. The size of the separation bubble and thus the resulting ψ profile are nearly identical. This illustrates that a wake can suppress separation given a high enough passing frequency, however any further increase in the wake frequency will have little effect on the flow separation on the suction surface.

Summary and Conclusions

In the present study 2D URANS and 3D LES simulations were performed in order to investigate the effect of the wake from an upstream moving rod on the flow separation and reattachment on the highly loaded airfoil L1A. Computational results were compared with experimental data [4]. Results of 2D URANS simulations matched the experimental trend of interaction between the wake and the boundary layer on the suction surface of the airfoil with the mean pressure coefficient profiles (C_p) indicating separation followed by reattachment. These trends were only marginally accurate in comparison to the experimental data for both Re=25,000 and Re=50,000 cases, since the predicted magnitude of the C_p profile and the location of reattachment were not very consistent with the experimental data. This was mainly attributed to the lack of ability to take into account the three dimensional structure of a wake and its subsequent interaction with the boundary layer. Thus the CFD mesh was then projected into a 3D domain and the same URANS (Trans-SST) model was run at the same time step as in the 2D cases. These 3D URANS cases were unable to capture any wake vortex shedding of the rod, which had been seen in cases run by Ladreau [12]. It was determined that in order to capture the wake, the time step size would have to be reduced to levels associated with LES turbulence, thus the remainder of the cases were run using LES since the computational cost savings of using a URANS model with a larger time step were diminished.

For Re=50,000 3D LES predictions were in a reasonably good agreement with experimental data in both pressure and velocity profiles on the airfoil. For Re=25,000 the predictions were not as good. Instantaneous profiles of C_p and C_f were analyzed, in order to explain the effect of the wake, as it passes through the cascade passage, on the suction surface boundary layer. These instantaneous results showed that as a wake reaches the location of the C_p peak, it collapses down, compressing the peak C_p value and eventually rolling it up into three defined peaks. These peaks first experience a shear, stretching effect and eventually begin to roll down the aft side of the suction surface, remaining attached to the surface and being further compressed and increasing in C_p magnitude. The corresponding effect on the C_f values over these events show that as the suction bubble is broken down and compressed, the three defined C_p peaks are associated with defined peaks in the C_f values, thus showing a high amount of turbulence in this region. Trailing behind this turbulent peak is the predicted calmed region described by Hodson and Howell [1]. This calmed region remains near zero in C_f value,

but shows resistance to separation as long as the separation bubble remains attached to the surface. As this bubble is eventually rolled off the surface, the calmed regions show an immediate location of separation with a zero C_f value. This separation grows and eventually spans across the width of the suction surface as the C_p values start to show a defined separation bubble, indicated by a "plateau" in the C_p profile. Also shown by the C_f profile is where separation is indicated to start by an inflection in the decreasing C_f values. The leveling out of this curve as it approaches, hits, and recovers from a zero C_f value indicates where the separation bubble exists, as seen by the plateau in the C_p profile. As it starts to increase out of this zero value, another inflection occurs in the curve slightly before reattachment as indicated on the C_p values. This inflection shows a start of a sharp increase in C_f and indicates the start of transition in the boundary layer. Reattachment occurs just before another peak in the C_f values, which then shows turbulence in the flow as it stays attached to the trailing edge.

For Re=50,000 the effect of the wake passing frequency on the flow separation and reattachment on the airfoils suction surface was investigated. Initial increase in dimensionless wake frequency, from F = 0.45 to F= 0.56, helped to reduce the size of the separation bubble to near nonexistent; however a slight indication of one still was present. Additional increase in dimensionless wake frequency, from F = 0.56 to F = 0.75, showed little effect on the airfoil flow.

Acknowledgements

This work was sponsored by the National Aeronautics and Space Administration. The grant monitor is Dr. James Heidmann of the NASA Glenn Research Center. The support of the United States Naval Academy Technical Support Department Shop and Fluids Laboratory is greatly appreciated. We greatly appreciate the computer time provided for us by the Ohio Super Computer (OSC). The OSC Computer Cluster has been made available as part of the Center's mission to support Ohio Universities.

References

[1] Hodson, H.P., and Howell, R.J., 2005, "Blade Row Interactions, Transition, and High-Lift Airfoils in Low-Pressure Turbine," Annual Review of Fluid Mechanics, **37**, 71-98.

[2] Pluim, J., Memory, C., Bons, J., and Chen, J.P., 2009, "Designing a High Fidelity Wake Simulator for Research Using Linear Cascades," *ASME Paper GT2009-52276*.

[3] Bons, J.P., Pluim, J., Gompertz, K. and Bloxham, M., 2008, "The Application of Flow Control to an Aft-Loaded Low Pressure Turbine Cascade with Unsteady Wakes", *ASME Paper GT2008-50864*.

[4] Volino, R.J., 2012, "Effect of Unsteady Wakes on Boundary Layer Separation on a Very High Lift Low Pressure Turbine Airfoil," *ASME J. Turbomachinery*, **134**, paper 011011.

[5] Sarkar, S., 2009, "Influent of Wake Structure on Unsteady Flow in a Low Pressure Turbine Blade Passage," *ASME J. Turbomachinery*, **131,** paper 041016.

[6] Stieger, R., Hollis, D. and Hodson, H., 2003, "Unsteady Surface Pressures Due to Wake Induced Transition in Laminar Separation bubble on a LP Turbine Cascade", *ASME Paper GT2003-38303.*

[7] Suzen, Y.B. and Huang, P.G., 2005, "Numerical Simulation of Unsteady Wake/Blade Interactions in Low-Pressure Turbine Flows Using and Intermittency Transport Equation", *ASME J. Turbomachinery*, **127**, 431-444.

[8] Kaszeta, R. W., Simon, T. W., and Ashpis, D. E., 2001, "Experimental Investigation of Transition to Turbulence as Affected by Passing Wakes," *ASME Paper 2001-GT-0195*.

[9] Kaszeta, R. W., and Simon, T. W., 2002, "Experimental Investigation of Transition to Turbulence as Affected by Passing Wakes," NASA Contractor Report, NASA-CR-2002-212104, Cleveland.

[10] Stieger, R. D., 2002, "The Effects of Wakes on Separating Boundary Layers in Low-Pressure Turbines," Ph.D. Dissertation, Cambridge University, Eng. Dept., Cambridge, UK

[11] Rodi, W., 2006, "DNS and LES of some Engineering Flows", *Fluid Dynamics Research*, **38**, 145-173.

[12] Lardeau, S., 2005, "Unsteady RANS modeling of wake-blade interaction: computational requirements and limitations," *Computers and Fluids*, **34**, 3-21.

[13] ANSYS FLUENT Documentation, 2009.

[14] Ibrahim, M.B., Kartuzova, O., Doucet, D.J. and Volino, R.J., 2010, "LES Flow Control Simulations For Highly Loaded Low Pressure Turbine Airfoil (L1A) Using Pulsed Vortex Generator Jets"**,** *ASME Paper GT2010-23015*.

[15] Menter, F.R., Langtry, R.B., Likki, S.R., Suzen, Y.B., Huang, P.G., and Völker, S., 2006, "A Correlation based Transition Model using Local Variables Part 1-Model Formulation", *ASME J. Turbomachinery*, **128**, 413-422.

[16] Ibrahim, M.B., Kartuzova, O. and Volino, R.J., 2008, "Experimental and Computational Investigations of Separation and Transition on a Highly Loaded Low Pressure Turbine Airfoil: Part 1 – Low Freestream Turbulence Intensity", *ASME Paper IMECE2008-68879*.

[17] Kim, W.W. and Menon, S., 1997, "Application of the localized dynamic subgrid-scale model to turbulent wall-bounded flows," *AIAA Paper AIAA-97-0210*.
[18] Kim S.E., 2004, "Large eddy simulation using unstructured meshes and dynamic subgridscale turbulence models," *AIAA Paper AIAA-2004-2548*.
[19] Piomelli, U. and Chasnov, J.R., 1995, "Large-Eddy Simulations: Theory and Applications", *Turbulence and Transition Modeling, lecture notes from the ERCOFTAC/IUTAM* summer school held in Stockholm, 12-20 June, 1995.
[20] Norberg, C., 2003, "Fluctuating Lift on a Circular Cylinder: Review and New Measurements", *J. Fluid Struct.*, **17**, 57-96.

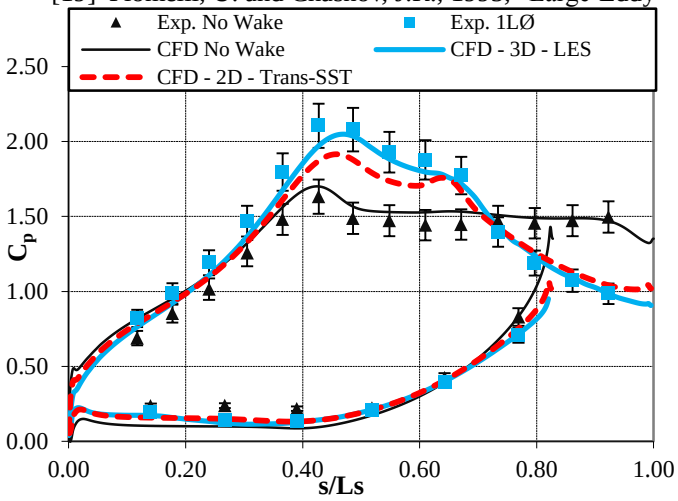

Figure 2. C_p profiles for Re=50,000, LFSTI: Comparison between Grid and Turbulence Model against Experimental data.

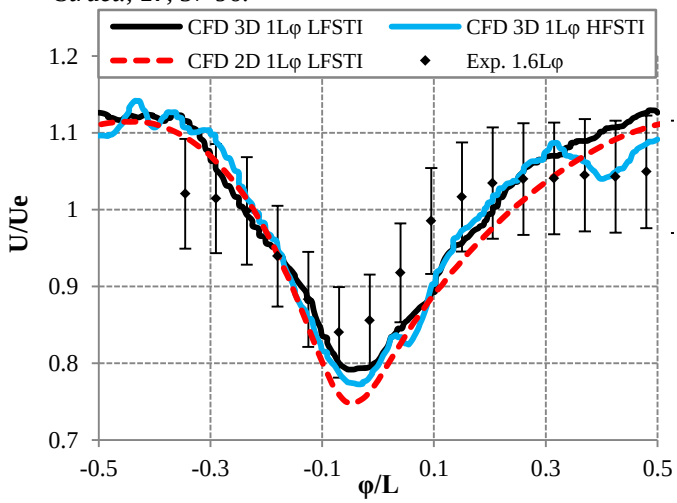

Figure 3. Rod Wake Velocity Profile at Inlet Cascade Plane, Re=50,000: Comparison between 3D (LES) LFSTI, 3D (LES) HFSTI, and Experimental Data.

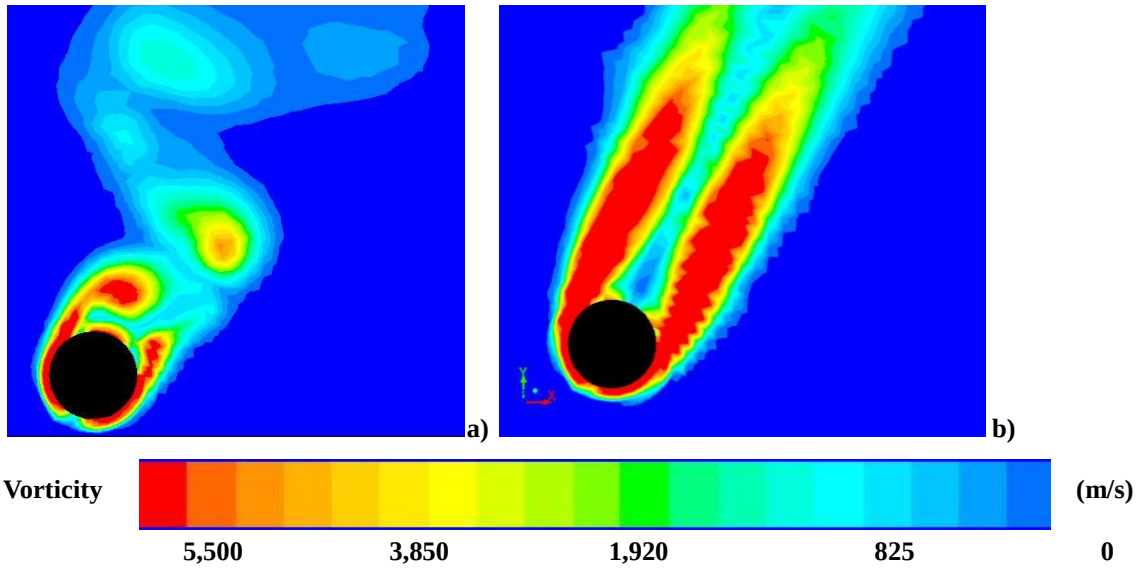

Figure 4. Vorticity Contours for Re = 50,0000: Comparison between a) 3D (LES) b) 3D (Trans-SST).

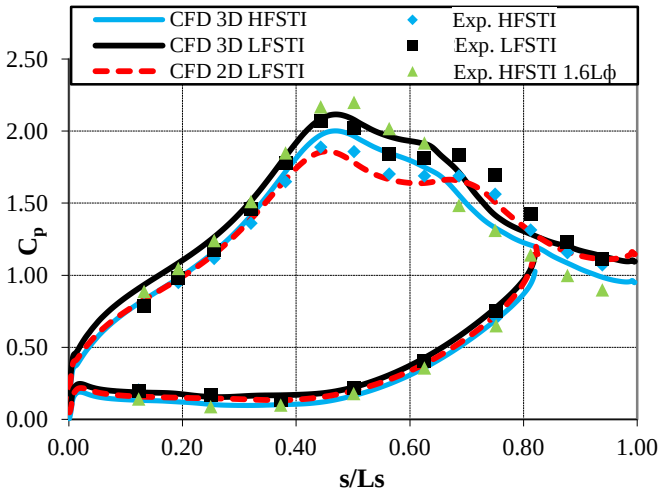

Figure 5. C_p profiles for Re=25,000, F=0.45: Comparison between LFSTI, HFSTI, 3D (LES), 2D (URANS) and Experimental data.

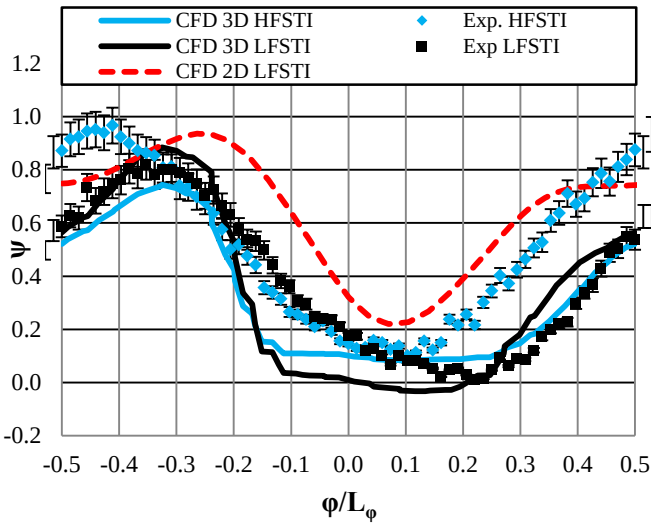

Figure 6. Total Pressure Loss Coefficient for Re=25,000, F=0.45, 0.68C_x Downstream: Comparison between LFSTI, HFSTI, 3D (LES), 2D (URANS) and Experimental data.

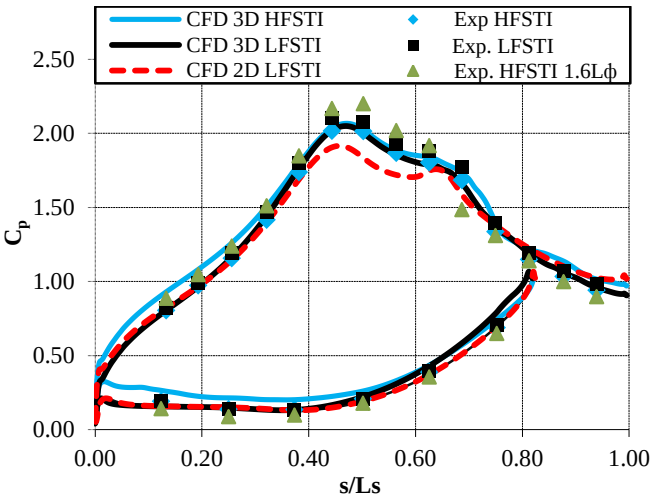

Figure 7. C_p profiles for Re=50,000, F=0.45: Comparison between LFSTI, HFSTI, 3D (LES), 2D (URANS) and Experimental data.

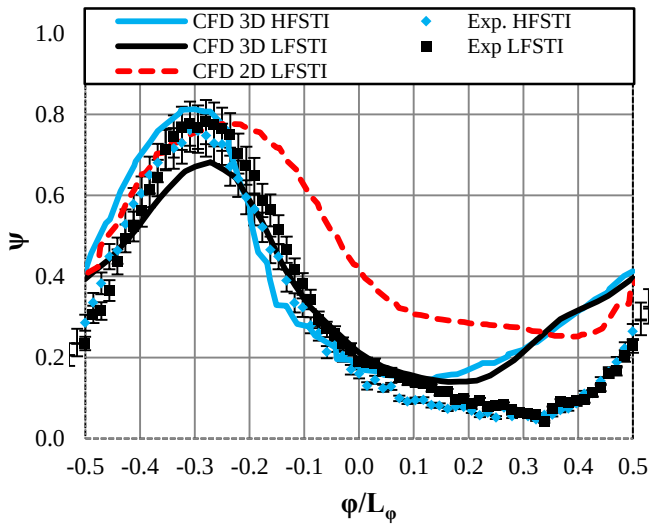

Figure 8. Total Pressure Loss Coefficient for Re=50,000, F=0.45, 0.68C_x Downstream: Comparison between LFSTI, HFSTI, 3D (LES), 2D (URANS) and Experimental data.

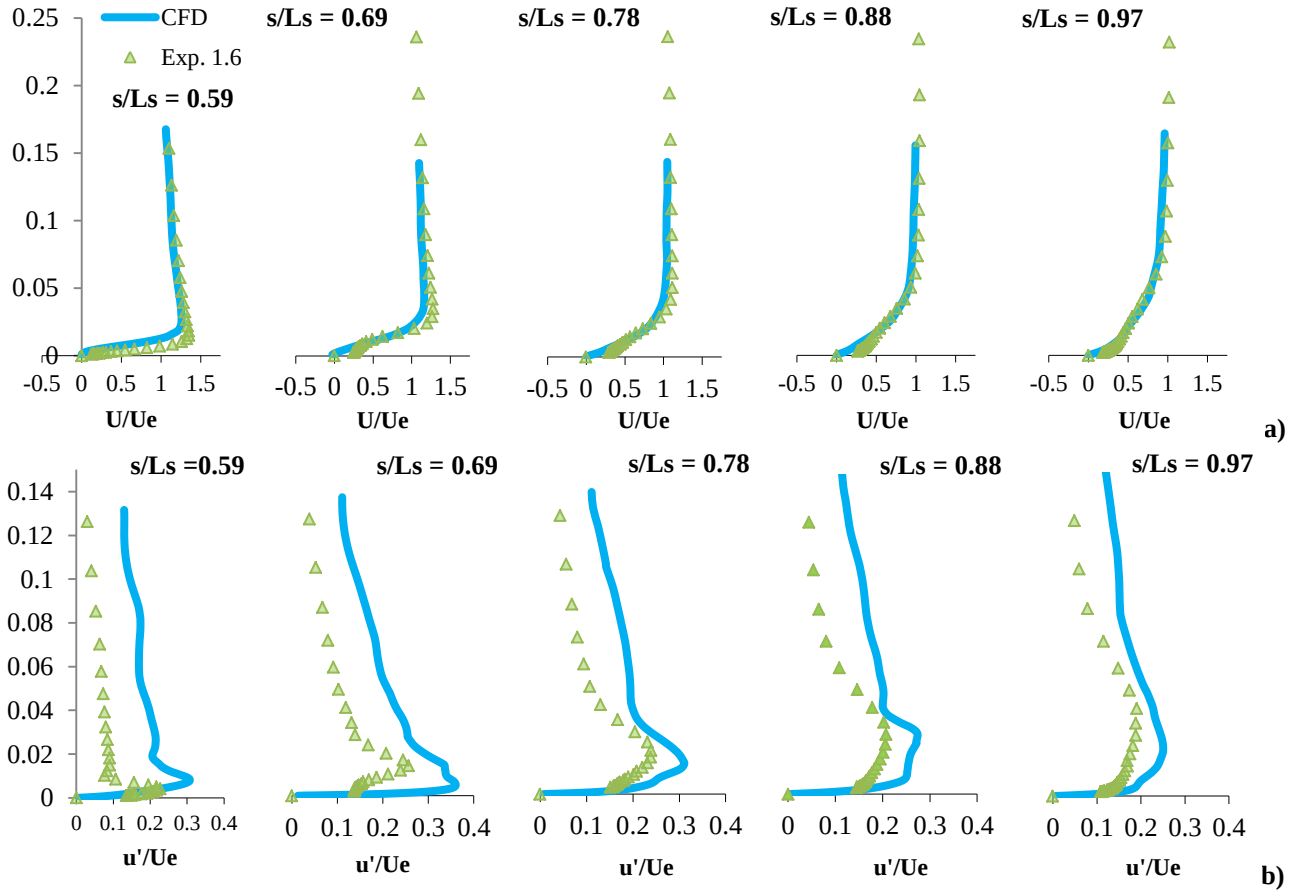

Figure 9. Time averaged velocity profiles at five streamwise stations for Re=50,000, HFSTI: Comparison between CFD (LES) and Experimental data: a - Mean, b – RMS.

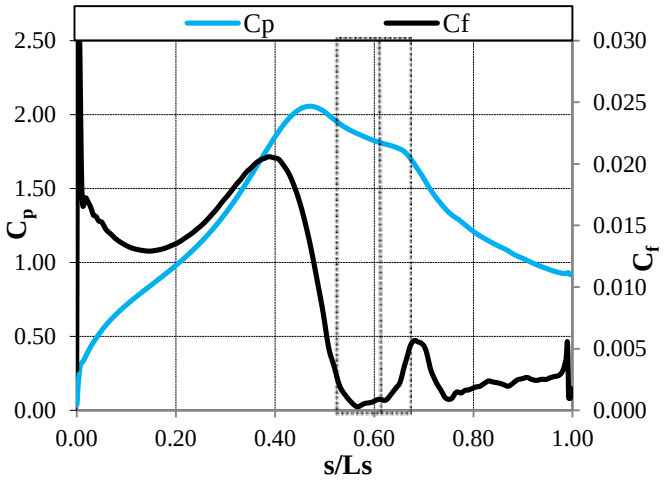

Figure 10. Comparison of Mean C_p and C_f on suction surface for Re=50,000, LFSTI, F=0.45.

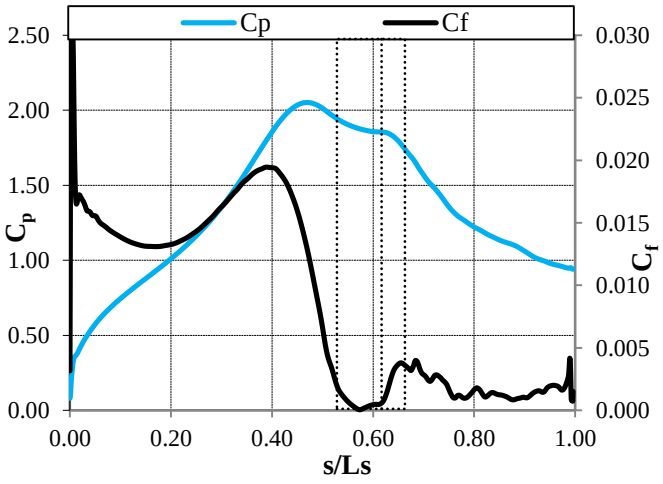

Figure 11. Comparison of Mean C_p and C_f on suction surface for Re=50,000, HFSTI, F=0.45.

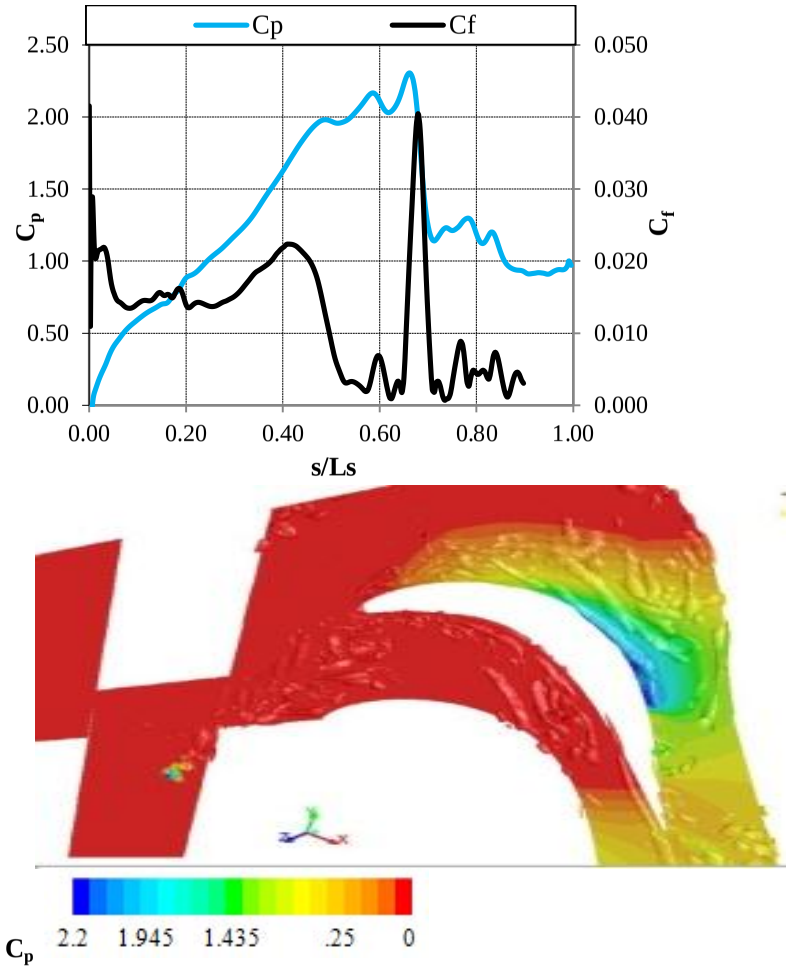

Figure 12-1. Comparison of Re=50,000, LFSTI, F=0.45: Instantaneous C_p and C_f on suction surface and Q-criterion contours colored by C_p values at time t/T = 0.

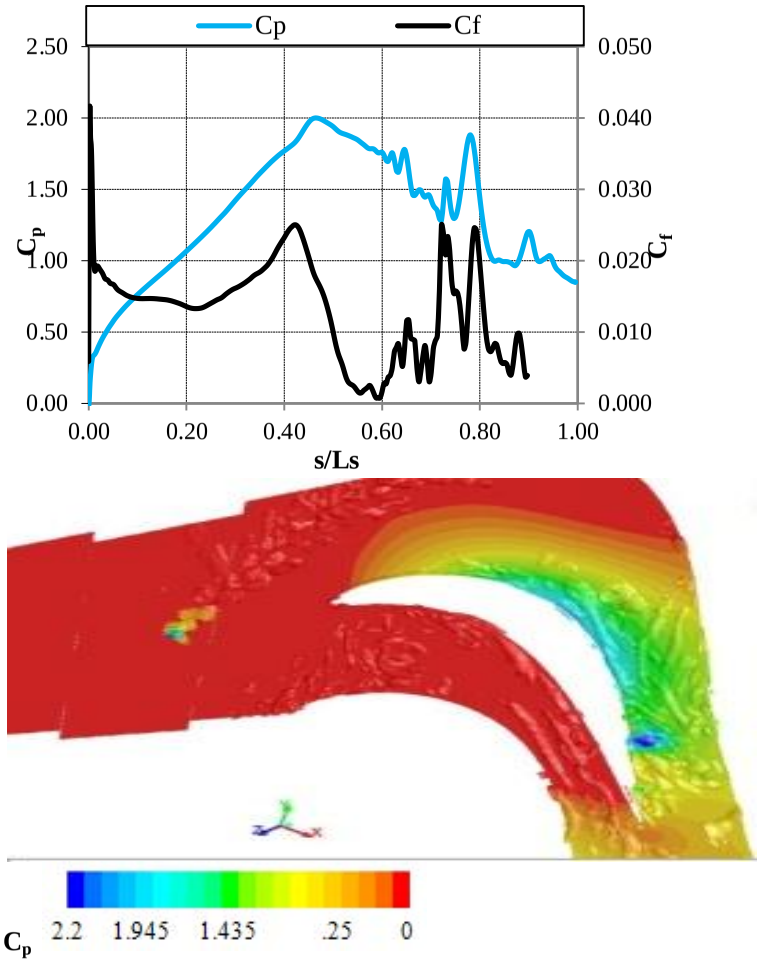

Figure 12-2. Comparison of Re=50,000, LFSTI, F=0.45: Instantaneous C_p and C_f on suction surface and Q-criterion contours colored by C_p values at time t/T = 0.30.

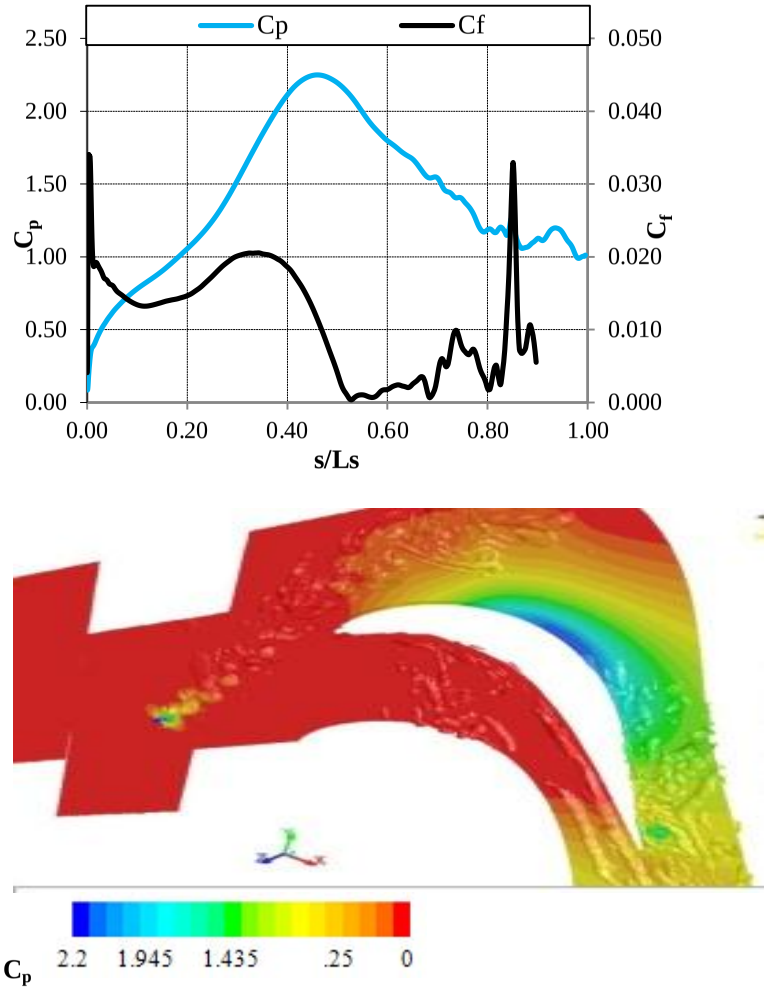

Figure 12-3. Comparison of Re=50,000, LFSTI, F=0.45: Instantaneous C_p and C_f on suction surface and Q-criterion contours colored by C_p values at time t/T = 0.60.

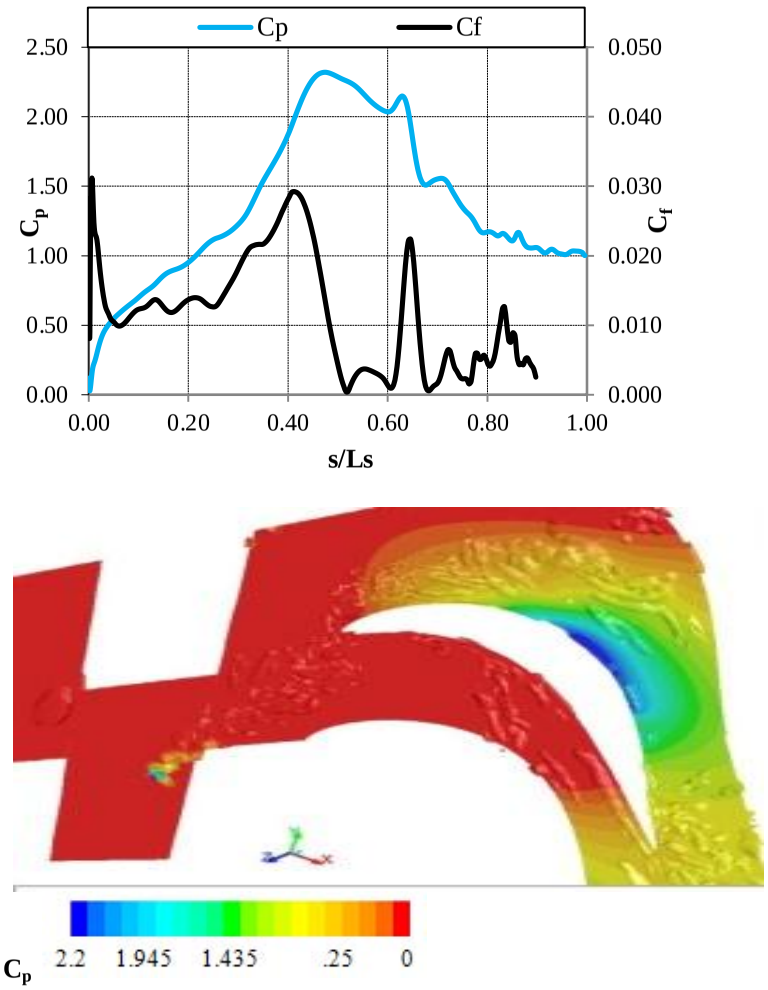

Figure 12-4. Comparison of Re=50,000, LFSTI, F=0.45: Instantaneous C_p and C_f on suction surface and Q-criterion contours colored by C_p values at time t/T = 0.90.

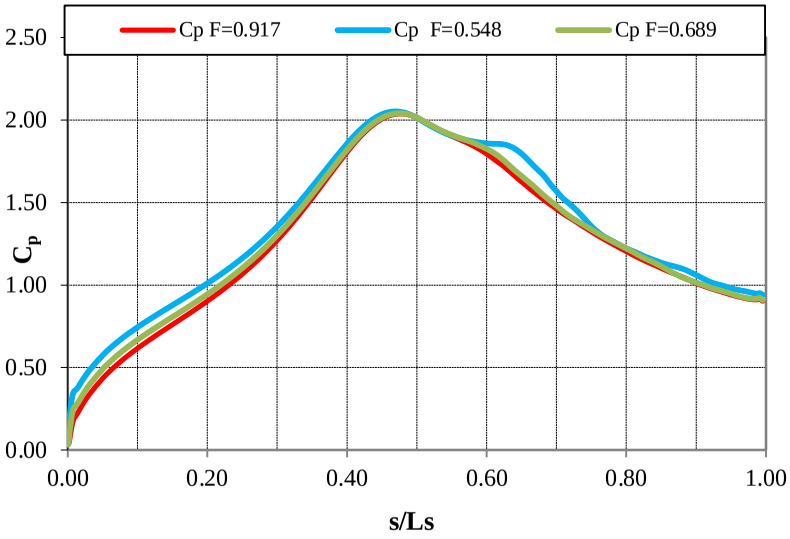

Figure 13. Mean C_p on suction surface for Re=50,000, HFSTI: Comparison between CFD F=0.45, F=0.56, and F=0.75.

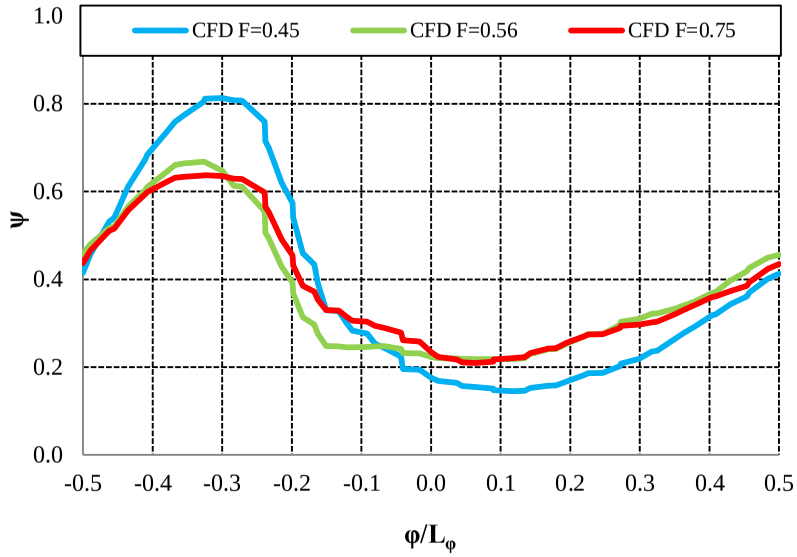

Figure 14. Total Pressure Loss Coefficient for Re=50,000, HFSTI: Comparison between CFD F=0.45, F=0.56, and F=0.75.

Separated Flow Measurements on a Highly Loaded Low-Pressure Turbine Airfoil

Ralph J. Volino
Department of Mechanical Engineering,
United States Naval Academy,
Annapolis, MD 21402
e-mail: volino@usna.edu

Boundary layer separation, transition, and reattachment have been studied on a new, very high lift, low-pressure turbine airfoil. Experiments were done under low freestream turbulence conditions on a linear cascade in a low speed wind tunnel. Pressure surveys on the airfoil surface and downstream total pressure loss surveys were documented. Velocity profiles were acquired in the suction side boundary layer at several streamwise locations using hot-wire anemometry. Cases were considered at Reynolds numbers (based on the suction surface length and the nominal exit velocity from the cascade) ranging from 25,000 to 330,000. In all cases, the boundary layer separated, but at high Reynolds number the separation bubble remained very thin and quickly reattached after transition to turbulence. In the low Reynolds number cases, the boundary layer separated and did not reattach, even when transition occurred. This behavior contrasts with previous research on other airfoils, in which transition, if it occurred, always induced reattachment, regardless of Reynolds number. [DOI: 10.1115/1.3104608]

1 Introduction

Boundary layer separation can lead to partial loss of lift and higher aerodynamic losses on low-pressure turbine (LPT) airfoils (e.g., Refs. [1–3]). As designers impose higher loading to improve efficiency and lower cost, the associated strong adverse pressure gradients on the suction side of the airfoil can exacerbate separation problems. The problem is particularly relevant in aircraft engines due to the lower density and therefore lower Reynolds numbers at altitude. A component efficiency drop of 2% may occur between takeoff and cruise in large commercial transport engines, and the difference could be as large as 7% in smaller engines operating at higher altitudes [4,5]. Prediction and control of suction side separation, without sacrifice of the benefits of higher loading, are therefore crucial for improved engine design.

Separation and separated flow transition, which can lead to boundary layer reattachment, have received considerable attention. Studies have included flows over flat plates subject to pressure gradients similar to those on the suction side of LPT airfoils, and flows over airfoils either in single passage facilities or multiblade cascades. Some have considered steady inflow conditions, while others have included the effect of unsteady wakes. Recent examples include Refs. [6–12]. Volino [13] provided a review of some earlier studies. In general, previous work shows that the strong acceleration on the leading section of the airfoil keeps the boundary layer thin and laminar, even in the presence of elevated freestream turbulence. When separation does occur, it is usually just downstream of the suction peak. If transition then occurs in the shear layer over the separation bubble, it is typically rapid and causes the boundary layer to reattach [13,14]. Transition is dependent on Reynolds number, freestream turbulence level, and the surface roughness conditions upstream of the separation point. Several correlations for separated flow transition have been developed based on experimental data, including those of Mayle [2], Hatman and Wang [15], Davis et al. [16], Yaras [17], Volino and Bohl [18], and Praisner and Clark [19].

The advances in separation understanding and prediction have led to attempts at separation control. Zhang et al. [20], Bohl and Volino [21], Volino [22], and others provided examples using passive devices such as boundary layer trips. Others have used active devices such as vortex generator jets (e.g., Refs. [4,23]) or plasma devices (e.g., Ref. [24]).

Another way to improve performance is to design airfoils with pressure gradients more resistant to separation, as described by Praisner and Clark [19]. Forward loading, for example, makes airfoils more separation resistant by extending the adverse pressure gradient on the aft portion of the suction side over a longer distance. This reduces the local pressure gradient at all locations, making separation less likely. If separation does occur, forward loading provides a longer distance along the airfoil surface for reattachment. Forward loading has some disadvantages, however. As noted by Zhang et al. [20], the longer region of turbulent flow on a forward loaded airfoil can lead to increased profile losses. Forward loading also creates longer regions of strong pressure gradient on the endwalls, which can produce stronger secondary flows and losses. If flow control were incorporated in the design of an advanced airfoil, as discussed by Bons et al. [25], it might be possible to produce an aft loaded airfoil that was resistant to separation and had low profile and secondary loss characteristics over a range of Reynolds numbers.

The objective of the present study is to document the flow over a very highly loaded LPT airfoil. The airfoil chosen was designed at the Air Force Research Laboratory (AFRL), and is designated the L1A. It is available on a limited basis to U.S. researchers from Ref. [26]. Dimensions of the L1A as used in the present experiments are given in Table 1. Based on the design calculations of Clark [26], the L1A has 10% higher loading than the "ultrahigh lift" airfoils described by Zhang and Hodson [27], and 17% higher loading than the Pack B airfoil considered in several studies such as Refs. [13,14,4]. The design calculations indicate that the Zweifel coefficient increases from about 1.15 on the Pack B to about 1.35 on the L1A. If the definition for the Zweifel coefficient is taken as

$$\mathrm{Zw} = 2\cos^2\alpha_2(L_\phi/C_x)(\tan\alpha_1 + \tan\alpha_2) \quad (1)$$

as given by Lakshminarayana [28], Zw=1.08 for the Pack B (in agreement with the value given by McAuliffe and Sjolander [29]) and Zw=1.23 for the L1A. The L1A has the same inlet and exit flow angles and loading as the L1M airfoil used by Bons et al. [25]. The L1M is a midchord loaded design and is resistant to

Contributed by the International Gas Turbine Institute of ASME for publication in the JOURNAL OF TURBOMACHINERY. Manuscript received July 7, 2008, final manuscript received: February 2, 2009; published online September 16, 2009. Review conducted by David Wisler. Paper presented at the ASME Turbo Expo 2008: Land, Sea and Air (GT2008), Berlin, Germany, June 9–13, 2008.

Table 1 Cascade parameters

Axial chord, C_x (mm)	True chord (mm)	Pitch, L_ϕ (mm)	Span (mm)	Suction side, L_s (mm)	Inlet flow angle (deg)	Exit flow angle (deg)
134	146	136	724	203	35	60

separation even at very low Reynolds numbers. While the L1M and L1A were designed with the same methodology, the L1A is aft loaded, and is therefore expected to be more prone to separation. It is expected to be a good test airfoil for future flow control work, in which separation may be suppressed while maintaining the benefits of both very high loading and aft loading. Figure 1 shows the inviscid flow pressure profiles for the L1A, L1M, and Pack B airfoils. The inviscid code used for the computations was adapted from Ref. [30]. Figure 1(*a*) shows the pressure coefficient *Cp* as a function of dimensionless axial position, x/C_x. These coordinates are useful for comparing the lift generated by the airfoils. Figure 1(*b*) shows *Cp* as a function of the streamwise distance along the airfoil surface, s/L_s, where L_s is the wetted surface length along the suction side. These coordinates are most useful for explaining the boundary layer development and are used to present the results below. The higher lift of the L1A and L1M compared with the Pack B is clear in Fig. 1. Also clear is the stronger adverse pressure gradient of the L1A on the downstream region of the suction side. The pressure gradient is shown again in Fig. 2 as the product of the local acceleration parameter *K* and the Reynolds number. The Reynolds number, Re, is based on L_s and the nominal exit velocity from the cascade U_e (computed using the inlet velocity and the design inlet and exit flow angles). The parameter *K* is inversely proportional to Re, so *K* Re is independent of Reynolds number. The negative *K* values downstream of $s/L_s=0.7$ are about twice as strong for the L1A than for the other two airfoils. This suggests more of a tendency for boundary layer separation and possibly less of a tendency for the flow to reattach.

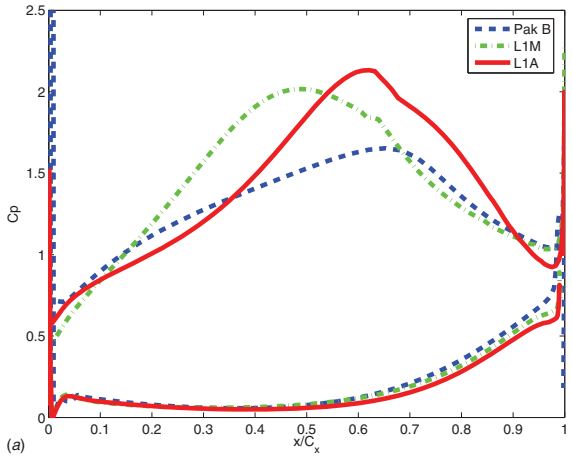

Fig. 1 Comparison of inviscid pressure profiles for the Pack B, L1M, and L1A airfoils: (*a*) *Cp* versus axial position; (*b*) *Cp* versus streamwise location

2 Experimental Facility and Measurements

Experiments were conducted in a closed loop wind tunnel with a linear cascade in one corner of the loop. An axial fan sends air through turning vanes in the first corner of the tunnel and then through a heat exchanger. Following the heat exchanger is the second turn and a 6.25:1 area ratio contraction. Following the contraction is a 0.46 m square by 1.1 m long test section, which was not used in the present study. Following this test section is a 2.4 m long diffuser, which expands the flow area to 0.75 $\times$0.75 m^2. A fine screen with 0.12 mm mesh thickness, 0.42 mm mesh spacing and 49% blockage is located in the exit plane of the diffuser. The screen breaks up the boundary layers, which form on the diffuser walls and provides a uniform flow into the cascade test section. A seven blade cascade is located in the wind tunnel's third turn, as shown in Fig. 3. A generic airfoil shape is shown in the figure. The flow continues from the cascade into the tunnel's fourth turn, then through a second diffuser before returning to the fan.

The freestream turbulence entering the cascade was measured with a cross-wire probe positioned just upstream of the center blade. The streamwise velocity component had a turbulence intensity, TI, of 0.8%, while the component intensity in the direction across the cascade was 0.5%. The spanwise component intensity was assumed to also be 0.5% based on the symmetry of the wind tunnel. The combined freestream turbulence intensity based on all

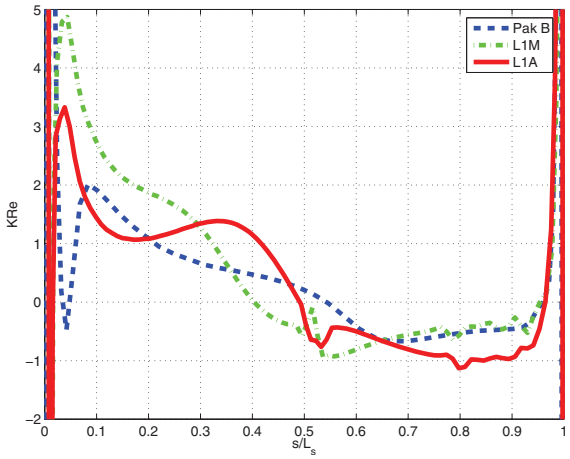

Fig. 2 Acceleration, *K* Re, versus streamwise location for Pack B, L1M, and L1A airfoils based on inviscid solution

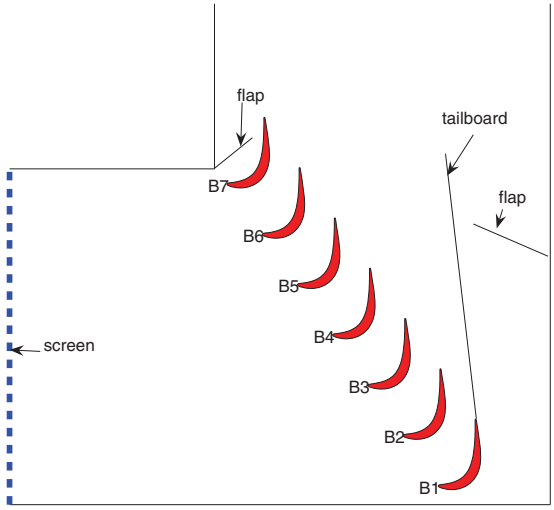

Fig. 3 Schematic of linear cascade

three components was 0.6%. Spectral measurements showed that 80% of the energy in the streamwise fluctuations was due to the unsteadiness at dimensionless frequencies $fL_s/U_e < 2$, where f is the frequency in hertz. Approximately 70% of the energy in the cross stream components was also below this frequency. If the turbulence is high pass filtered to remove this unsteadiness, the streamwise and cross stream component intensities are 0.36% and 0.27%, respectively, for an overall freestream turbulence intensity of 0.3%. The integral length scale of the freestream turbulence is 6.3 cm in the streamwise direction and 6.7 cm in the other directions. While such low freestream turbulence and large length scales are not representative of engine conditions, they are still of interest. In zero or favorable pressure gradient boundary layers, high TI can cause bypass transition, but under adverse pressure gradients, natural transition appears to play a role at all TI levels. Hughes and Walker [31], for example, observed evidence of Tollmien–Schlichting (TS) waves in cases with TI as high as 8%. Volino [14] also saw evidence of TS waves in both high and low TI cases. Low TI cases provide a somewhat simpler environment for explaining the already complex phenomenon of separated flow transition. The present low TI cases will also serve as comparison cases for future work with elevated TI. Higher TI and length scales closer to the boundary layer thickness are expected to hasten the transition process.

The blades in the cascade were machined from high density foam, which has a consistency much like hard wood. The center blade, designated B4 in Fig. 3, contains pressure taps near the spanwise centerline. A tailboard, shown in Fig. 3, was needed to produce the correct exit flow angle from the cascade. Its position was set to produce periodicity at high Reynolds numbers. A tailboard on the opposite side of the cascade and inlet guide vanes were found to be unnecessary. To produce the correct approach flow to the end blades (B1 and B7), the amount of flow escaping around the two ends of the cascade was controlled with the flaps shown in Fig. 3. The flap positions were set using a wool tuft upstream of each blade to check that the incoming flow approached the stagnation points with the correct angle. The inlet flow angle at the center of the cascade was also checked with a three-hole pressure probe and found to be within 2 deg of the design angle. At high Reynolds numbers, the approach velocity to the middle four passages was measured to be uniform to within 6%, and the difference between any two adjacent passages was within 3%. At low Reynolds numbers, slightly more variation was observed, but the approach velocity to the middle two passages still agreed to within 5%. Good periodicity at high Reynolds numbers was also observed in the exit flow from the cascade, as evidenced by suction side velocity profiles acquired near the trailing edge of blades B2–B6 and by total pressure loss surveys, which are shown below. At low Reynolds numbers, when significant separation bubbles were present, the periodicity was not as good due to the suppression of the separation bubble thickness on the blades closest to the tailboard. This is an unavoidable result when using a finite linear cascade to study separated flow. It is considered acceptable for the present facility, since its intended purpose is for the study of flow control, which if successful should suppress separation on all blades, thereby restoring periodicity even at low Reynolds numbers.

2.1 Measurements. Pressure surveys were made using a pressure transducer (0–870 Pa range Validyne transducer). Stagnation pressure was measured with a pitot tube upstream of the cascade. Static pressure taps were located in the center blade as noted above. The uncertainty in the suction side pressure coefficients was 0.07. Most of this uncertainty was due to the bias error. Stochastic error was minimized by averaging pressure transducer readings over a 10 s period.

A four component traverse with three linear stages and one rotating stage was located in the wind tunnel downstream of the cascade. The traverse produced an acceptably low blockage when it was located at least two axial chord lengths downstream of the cascade. Variations in the wind tunnel velocity were less than 2% as the traverse was moved to various positions. The traverse was used to hold and move probes for velocity and downstream pressure measurements.

Total pressure losses were documented using a Kiel probe traversed across three blade spacings, $0.63C_x$ downstream of the cascade. To compute the mass flow averaged pressure loss, a velocity profile was also acquired along the same line as the total pressure surveys using a single-sensor hot-film probe.

Velocity profiles on the suction surface were measured at the six streamwise stations listed in Table 2. All stations are downstream of the inviscid pressure minimum at $s/L_s = 0.49$. Profiles were measured near the spanwise centerline of the airfoil. Profiles were acquired with a hot-wire anemometer (AA Lab Systems model AN-1003) and a single-sensor hot-film probe (TSI model 1201-20). The sensor diameter is 51 μm, and the active length is 1.02 mm. At each measurement location, data were acquired for 26 s at a 20 kHz sampling rate (2^{19} samples). All raw data were saved. The high sampling rate provides an essentially continuous signal, and the long sampling time results in low uncertainty in both statistical and spectral quantities. Data were acquired at 40 wall normal locations in each profile, extending from the wall to the freestream, with most points concentrated in the near-wall region. The probe was positioned as close to tangent to the airfoil surface as possible at each station, such that the probe body extended downstream of the sensor and the direction of the traverse was within 5 deg of normal to the surface. In most cases the closest point to the wall in each profile was within about 0.2 mm of the wall, which compares to boundary layer thicknesses rang-

Table 2 Velocity profile measurement stations

Station	1	2	3	4	5	6
s/L_s	0.53	0.59	0.69	0.78	0.88	0.97
x/C_x	0.65	0.72	0.80	0.86	0.92	0.97

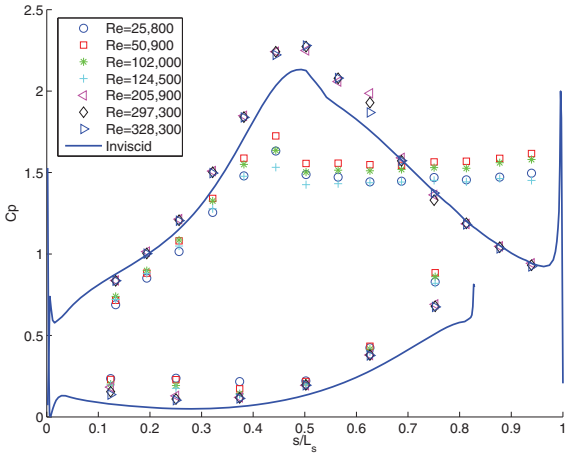

Fig. 4 *Cp* profiles

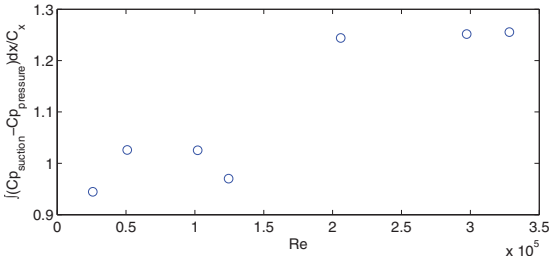

Fig. 5 Lift based on integrated *Cp* profile

ing from 1.1 mm to over 40 mm.

Flow direction in a separation bubble cannot be determined with a single-sensor hot-wire, but velocity magnitude can be measured and was found to be near zero within the bubbles of the present cases when the flow was laminar. In cases where the flow became turbulent but remained separated, fluctuating velocities caused false high mean velocity readings in the separation bubble. With the exception of these turbulent separated cases, the uncertainty in the mean velocity is 3–5% except in the very near-wall region, where near-wall corrections [32] were applied to the mean velocity. Uncertainties in the momentum and displacement thicknesses computed from the mean profiles are 10%. The uncertainty in the shape factor, H, is 8%. Local skin friction coefficients were computed from the near-wall mean velocity profiles using the technique of Volino and Simon [33]. This technique accounts for streamwise pressure gradient effects on the mean profile. The uncertainty in C_f is 8%. The uncertainty in the fluctuating streamwise velocity is below 10%.

Pressure surveys and velocity profiles were acquired at nominal Re=25,000, 50,000, 100,000, 200,000, 300,000, and 330,000. An additional pressure survey was acquired at Re=125,000. The Reynolds number, as defined above, is based on the suction surface length and the nominal cascade exit velocity. The corresponding Reynolds numbers based on the cascade inlet velocity and the axial chord length ranged from 10,000 to 133,000.

3 Results

3.1 Pressure Profiles. Pressure profiles for all cases are shown in Fig. 4. The inviscid profile for the L1A airfoil is shown for comparison. At the three highest Re, with the exception of a slightly higher suction side peak, the data generally agree with the inviscid profile. This indicates that the boundary layer is attached over most of the airfoil in these cases. Some deviation between the three highest Re cases is visible at $s/L_s=0.6$ with the Cp value rising slightly at the lower Re. This may indicate a small separation bubble at this location. At the three lowest Reynolds numbers, the suction peak is suppressed and the Cp values have a constant value on the downstream part of the suction side. This plateau indicates that the boundary layer has separated. The Cp values never return to the inviscid line, indicating that the boundary layer never reattaches (i.e., the separation bubble bursts). At Reynolds numbers of 100,000 and below, the separation bubble always appeared to burst. At Re above 150,000 the boundary layer was attached over most of the airfoil. Between Re=100,000 and 150,000 the behavior was less predictable, with some dependence on whether the desired wind tunnel velocity was approached from above or below. The Re=124,500 case in Fig. 4 shows the suppressed suction peak and burst bubble of the lower Re cases, but in some trials (not shown) the Cp values dropped somewhat from their plateau near the trailing edge.

The pressure side Cp values also show some change with Reynolds number. Near the leading edge, Cp is higher for the lower Re cases, suggesting more of a leading edge separation bubble. Near the trailing edge the Cp values are again higher at the lower Re. This is believed to result when the suction side separation bubble forces fluid toward the pressure side, thereby increasing the pressure side velocity.

The lift on the airfoil can be determined by integrating the difference between the suction and pressure side Cp values along the axial direction. The result is shown as a function of Reynolds number in Fig. 5. The lift is about 20% lower for the separated flow cases.

The results in Fig. 4 contrast with the results for the Pack B airfoil presented by Volino [13], Bons et al. [4], Simon et al. [34], and others. With low freestream turbulence, at Re≤50,000 the boundary layer on the Pack B airfoil separated and did not reattach, much like the L1A behavior of the present study. At Re≥300,000, the boundary layer remained attached over most of the surface, again similar to the L1A behavior shown above. At intermediate Reynolds numbers, however, the Pack B results showed separation with reattachment after a large separation bubble. At Re=100,000, for example, the boundary layer on the Pack B airfoil separated just after the suction peak and did not reattach until near the trailing edge. As Reynolds number increased, the reattachment location gradually moved upstream. The L1A does not show this large separation bubble behavior, instead appearing to switch more abruptly between a nearly fully attached boundary layer and a burst bubble. This will be explored in more detail with the velocity profiles below.

3.2 Total Pressure Losses. The loss coefficient, ψ, is shown for all cases in Fig. 6. The coordinate ϕ indicates the distance in the direction perpendicular to the axial chord. The normalizing quantity L_ϕ is the blade spacing. The origin, $\phi=0$, corresponds to the location directly downstream of the trailing edge of the center blade in the direction of the exit design flow angle. At the two highest Reynolds numbers, the losses are low, and the locations of the loss peaks are in the expected positions downstream of the airfoils. This indicates that the actual flow angle is about equal to the design angle. The peaks downstream of blades B3–B5 are similar to each other, indicating periodicity in the cascade. The loss coefficient is near zero between the peaks. At Re=205,900, the loss coefficients are slightly larger than at the higher Re. Although the difference is within the uncertainty, the trend is consistent with the appearance of a small separation bubble at this Reynolds number, seen in Fig. 4 at $s/L_s=0.6$. At the lower Reynolds numbers, the burst separation bubble results in much higher losses, and forces the peaks about $0.35L_\phi$ toward the pressure side of each passage. This shift corresponds to a 14 deg change in the exit flow angle. The reduction in flow turning is consistent with

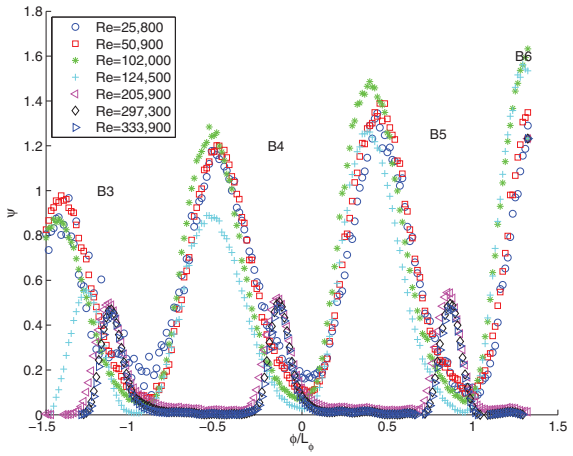

Fig. 6 Total pressure loss coefficient at $0.63C_x$ downstream of cascade

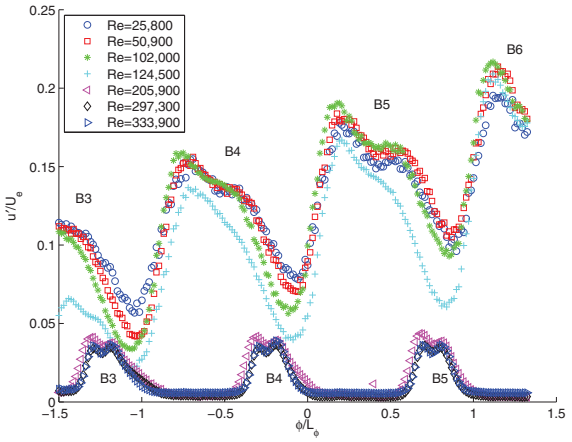

Fig. 8 rms fluctuating streamwise velocity at $0.63C_x$ downstream of cascade

the lower lift shown in Fig. 5. The peaks become noticeably smaller moving from B6 to B3, indicating the effect of the tailboard in reducing the separation bubble thickness.

The integrated loss around the center blade is computed as

$$\psi_{\text{int}} = \int_{-L_\phi/2}^{L_\phi/2} \psi U d\phi \Big/ \int_{-L_\phi/2}^{L_\phi/2} U d\phi \tag{2}$$

and is shown in Fig. 7 as a function of Reynolds number. Losses increase with decreasing Re. Between Re=300,000 and 200,000, ψ_{int} increases by 37%, due to the thicker boundary layer at lower Reynolds numbers. The most dramatic increase, however, occurs between the attached and separated flow cases. The integrated loss increases by a factor of 7 between the highest and lowest Reynolds numbers.

The turbulence associated with the airfoil wakes is shown in Fig. 8. The rms fluctuating streamwise velocity at $0.63C_x$ downstream of the trailing edge is normalized on the nominal exit velocity for each case. At the higher Reynolds numbers, the boundary layer turbulence has decayed to about 4% of U_e. A double peak is apparent, with the slightly higher peak resulting from the suction side boundary layer and the smaller peak from the pressure side. Between blades the turbulence intensity is at the background level of the wind tunnel. At the lower Reynolds numbers, the turbulence level is much higher and in agreement with the loss coefficients, the peaks are shifted toward the pressure side of the passages.

3.3 Velocity Profiles. Velocity profiles for the six suction surface measurement stations are shown in Fig. 9 for the nominal Re=25,000 case. The top row in the figure shows the distance from the wall normalized on the suction surface length plotted against the local mean velocity normalized on the nominal exit velocity, U_e. The boundary layer has just separated at the first measurement station and the separation bubble grows larger at the downstream stations. The boundary layer does not reattach. The second row in Fig. 9 shows the rms streamwise fluctuating velocity, u', normalized with U_e. There is a very large peak located in the shear layer over the separation bubble, which reaches a dimensionless magnitude of about 0.2. The third row in Fig. 9 shows the intermittency, γ. The intermittency is the fraction of time the flow is turbulent. It was determined at each measurement location based on the instantaneous streamwise velocity signal, using the technique described in Ref. [35]. Turbulent flow is defined here to include a range of large and small scale eddies. A boundary layer or shear layer may have significant u' fluctuations but still be considered nonturbulent if these fluctuations are induced by an external source such as freestream turbulence or are associated with instability in a narrow frequency band. Transition to turbulence is characterized by the appearance of broadband fluctuations. In the intermittency processing routine, the velocity signal is high pass filtered, and the appearance of high frequency fluctuations is used to distinguish between turbulent and nonturbulent flows. The results in Fig. 9 indicate that the shear layer remains nonturbulent until the last measurement station, where a small peak indicates the possible beginning of transition.

Figure 10 presents another view of the transition process using the turbulence spectra. The spectra are computed from the fluctuating velocity signal acquired at the location of peak u' at each

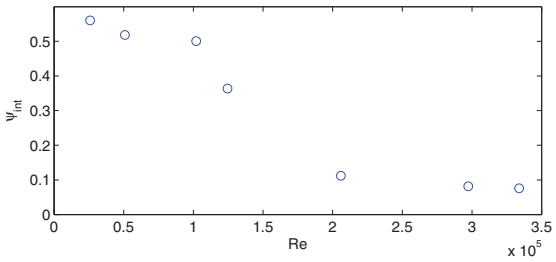

Fig. 7 Integrated total pressure loss coefficient for center blade as function of Re

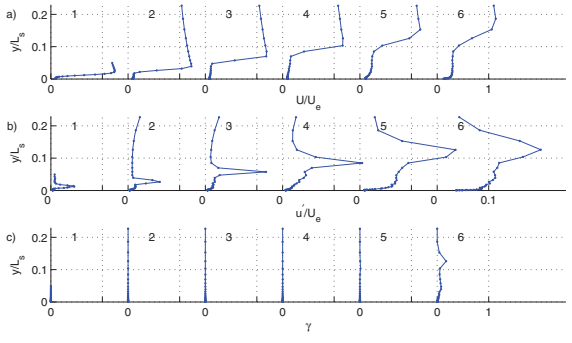

Fig. 9 Profiles for Re=25,000 case: (*a*) mean velocity, (*b*) u'/U_e, and (*c*) intermittency

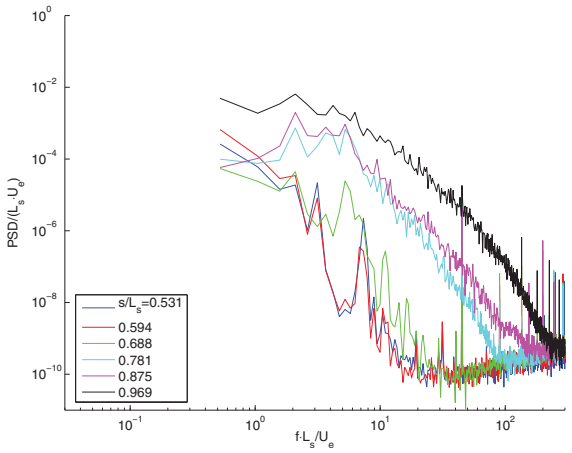

Fig. 10 Turbulence spectra for Re=25,000 case

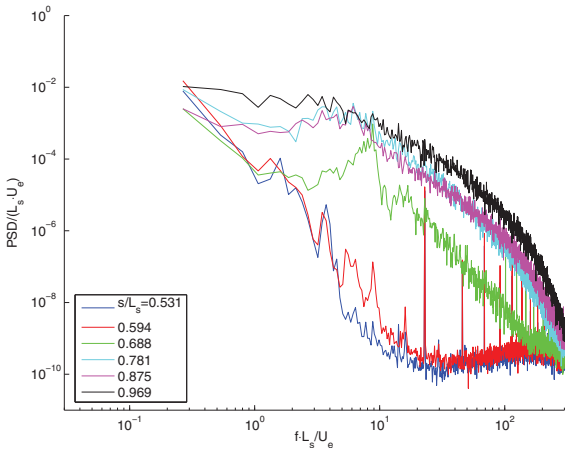

Fig. 12 Turbulence spectra for Re=50,000 case

measurement station shown in Fig. 9. Frequencies are resolved from 4.88 Hz to 10 kHz in 4.88 Hz increments using 4096 point fast Fourier transforms to compute the spectra. The frequencies and power spectral density (PSD) are normalized using L_s and U_e. There is a clear broadband rise in the spectra between the third and fourth measurement stations, and the magnitude continues to rise downstream. The rise indicates that transition may be beginning by the fourth station. The rise in the spectra is not as abrupt as at higher Reynolds numbers (shown below), however, which may indicate that transition is only in its earliest stages. This may explain the intermittency values near zero in Fig. 9.

The velocity profiles for the Re=50,000 case are shown in Fig. 11. The mean and fluctuating velocity show essentially the same behavior observed in the Re=25,000 case of Fig. 9. The boundary layer does not reattach, in agreement with the pressure profile of Fig. 4. The intermittency values rise slightly above zero at the third station and indicate that transition is clearly underway by the fourth station. The corresponding turbulence spectra of Fig. 12 agree, showing a clear rise in the power spectrum between the second and third stations and a further rise to a more turbulent state by the fourth station.

The initiation of transition without boundary layer reattachment shown in Figs. 11 and 12 is markedly different than the behavior observed in previous studies with other LPT airfoils. Volino [13] noted that on the Pack B airfoil, when transition began in the separated shear layer, the associated mixing almost immediately induced boundary layer reattachment. This behavior was utilized by Volino [22] and by Zhang et al. [20], who used small passive devices on their airfoils to control separation. These devices were too small to trip the boundary layer to turbulent but introduced small disturbances, which accelerated the transition process in the shear layer, thereby moving reattachment upstream. Both Volino [22] and Zhang and Hodson [27] found that these small devices resulted in lower losses than large devices, which immediately tripped the boundary layer to turbulent. The present results suggest that such devices may not work with the L1A airfoil because transition is not sufficient to force reattachment. The strong negative acceleration parameter, shown in Fig. 2, particularly at low Re is apparently strong enough to prevent reattachment of the turbulent shear layer. A comparison of the present results to those of Volino [13] shows that the stronger pressure gradient results in a separation bubble on the L1A that is about four times thicker than that on the Pack B airfoil in terms of y/L_s at a given Reynolds number. When transition occurs, the turbulence in the shear layer is apparently too far from the airfoil to induce enough near-wall mixing to force reattachment. This suggests that transition, whether naturally occurring or induced through flow control, must occur far enough upstream to cause reattachment before the separation bubble becomes too thick.

Figure 13 shows the velocity profiles for the Re=100,000 case. Similar to the previous cases, the separation bubble grows in the streamwise direction, the boundary layer does not reattach, and there is a very high peak in the fluctuating velocity in the shear layer over the separation bubble. The intermittency rises slightly above zero at the second station and indicates fully turbulent flow by the third station, where $\gamma=1$ in the shear layer. As in the

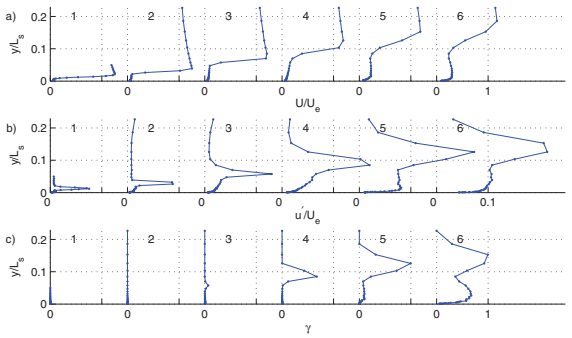

Fig. 11 Profiles for Re=50,000 case: (*a*) mean velocity, (*b*) u'/U_e, and (*c*) intermittency

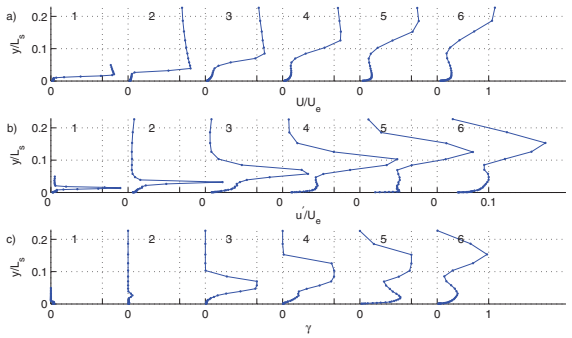

Fig. 13 Profiles for Re=100,000 case: (*a*) mean velocity, (*b*) u'/U_e, and (*c*) intermittency

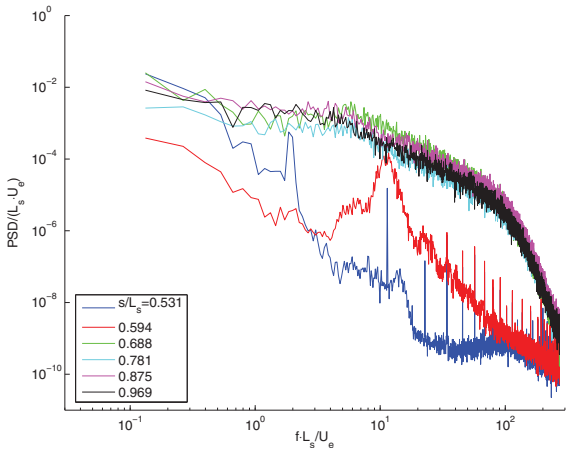

Fig. 14 Turbulence spectra for Re=100,000 case

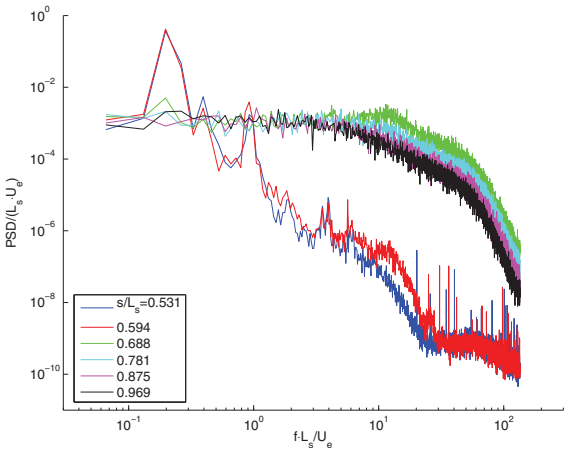

Fig. 16 Turbulence spectra for Re=200,000 case

previous case, the transition is not sufficient to induce boundary layer reattachment. Figure 14 shows the spectra for the Re =100,000 case. There is a clear narrowband rise in the spectrum between the first and second stations, centered about a dimensionless frequency of 12. A further broadband rise occurs by the third station, indicating a turbulent shear layer, in agreement with the intermittency profiles of Fig. 13. The peak at the second station in Fig. 14 indicates a shear layer instability, which likely initiates transition. Similar peaks are visible in the other Reynolds number cases, and will be discussed further below.

Velocity profiles for the Re=200,000 case are shown in Fig. 15. The boundary layer was laminar and on the verge of separation at the first two measurement stations. The small peak in intermittency at the first measurement station is believed to be erroneous, based on the spectra and the zero intermittency measurement at the second station. The skin friction, as determined from the near-wall velocity profile, was near zero at the first two stations, but any separation bubble was very thin. Between the second and third stations, the boundary layer underwent transition. The boundary layer was clearly attached and fully turbulent at the third station and remained attached at all downstream stations, in agreement with the pressure profiles of Fig. 4. The spectra for this case are shown in Fig. 16. The clear jump from laminar to turbulent flow is clear between the second and third stations.

The velocity profiles and spectra for the Re=300,000 case are shown in Figs. 17 and 18. The results are very similar to those of the Re=200,000 case, with transition occurring between the second and third stations, and the boundary layer remaining attached and turbulent downstream.

The shape factor, H, and skin friction coefficient C_f are good indicators of the state of the boundary layer with respect to separation and transition. The shape factor is shown for the high Re cases in Fig. 19. It is between 2.5 and 3.5 at the first two measurement stations, where the boundary layer is laminar and on the verge of separation. It then drops rapidly with the onset of transi-

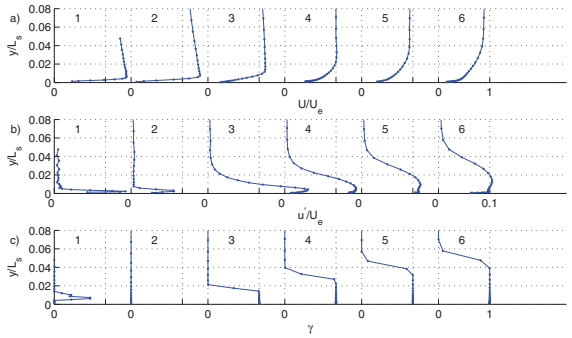

Fig. 15 Profiles for Re=200,000 case: (*a*) mean velocity, (*b*) u'/U_e, and (*c*) intermittency

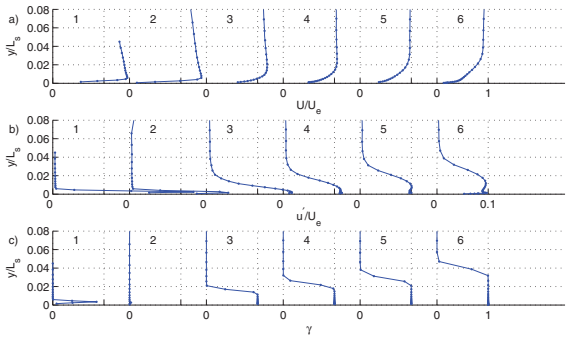

Fig. 17 Profiles for Re=300,000 case: (*a*) mean velocity, (*b*) u'/U_e, and (*c*) intermittency

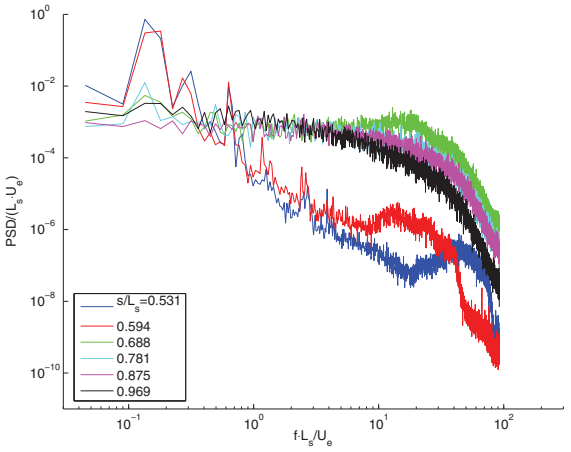

Fig. 18 Turbulence spectra for Re=300,000 case

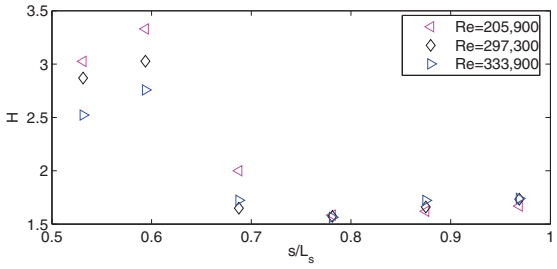

Fig. 19 Shape factor for high Re cases

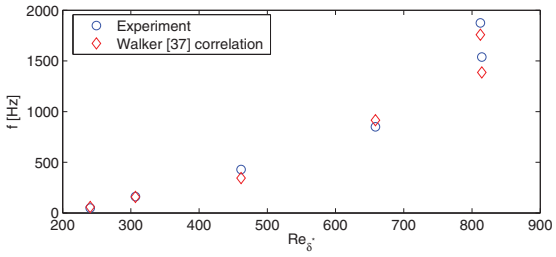

Fig. 21 Frequencies of spectral peaks along with predicted most unstable TS frequencies at separation location

tion, reaching a minimum of about 1.57 at the fourth measurement station. While this value clearly indicates that the boundary layer is attached and turbulent, it is still above the zero pressure gradient turbulent value of about 1.4. At the downstream stations, H begins to rise, and it exceeds 1.7 by the last station. The skin friction coefficient is shown as a function of momentum thickness Reynolds number in Fig. 20. It rises from near zero after transition and decreases in the streamwise direction. Also shown is a standard flat-plate correlation for turbulent boundary layers from Schlichting [36] and the Ludwieg–Tillmann correlation. The present C_f values are as much as 40% lower than the flat-plate correlation and agree well with the Ludwieg–Tillmann correlation. The rising H and low C_f values are indicative of the strong adverse pressure gradient. The corresponding values on the Pack B airfoil [13] were closer to typical zero pressure gradient values, which is consistent with the weaker pressure gradient on the Pack B and the stronger tendency for reattachment at low Re on the Pack B.

3.4 Instability Prediction. The spectral peak noted above at the second station in Fig. 14 suggests an instability in the shear layer that likely initiates transition. Although less distinct, similar peaks are visible just before or just after transition inception at all Reynolds numbers. Volino [14] observed similar peaks in the boundary layer on the Pack B airfoil and associated them with TS waves, using an analysis from Ref. [37]. The TS waves are believed to form in the attached boundary layer between the beginning of the adverse pressure gradient region and the separation location. The TS waves then continued to grow in the separated shear layer until they became large enough to induce transition, as discussed in Ref. [18]. Walker [37] gave the most unstable frequency for TS waves as

$$2\pi\nu f/U_\infty^2 = 3.2\ \mathrm{Re}_{\delta^*}^{-3/2} \tag{3}$$

Hughes and Walker [31] noted that the frequency predicted by Eq. (3) is a function of streamwise position, since the freestream velocity, U_∞, varies in nonzero pressure gradient cases, and the displacement thickness, δ^*, changes as the boundary layer grows. Hence, a single frequency cannot be expected for all TS waves in a boundary layer. For the present study, U_∞ and Re_{δ^*} were taken at the separation location. The Re_{δ^*} value was estimated with the boundary layer code TEXSTAN [38]. The code was used to compute the laminar suction side boundary layer from the leading edge to the separation point using the pressure gradient from Fig. 4 as input for each case. The code stops when the flow separates, and the separation points computed were in good agreement with the pressure and velocity profiles presented above. Figure 21 shows the peak frequencies extracted from Figs. 10, 12, 14, 16, and 18 along with frequencies predicted by Eq. (3). The good agreement between the experimental and predicted values indicates that TS waves may play a role in the transition. It is also possible that other instability mechanisms are present. Stieger and Hodson [39], and Roberts and Yaras [40], for example, observed Kelvin–Helmholtz rollup of the shear layer.

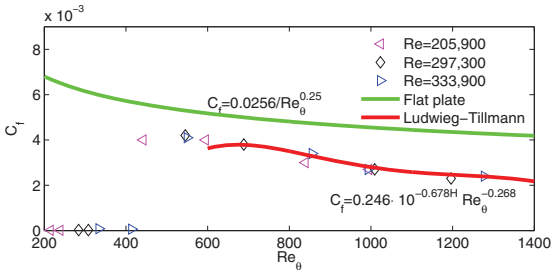

Fig. 20 Skin friction coefficient for high Re cases

3.5 Transition Correlations. Several correlations for predicting the starting location for separated flow transition are available in the literature, and some of these are tested below against the present data.

Mayle [2] presented the following correlations for short and long separation bubbles.

$$\mathrm{Re}_{st} = 300\ \mathrm{Re}_{\theta s}^{0.7}\ \ \text{short bubble} \tag{4}$$

$$\mathrm{Re}_{st} = 1000\ \mathrm{Re}_{\theta s}^{0.7}\ \ \text{long bubble} \tag{5}$$

where Re_{st} is the Reynolds number based on the freestream velocity at separation and the distance from separation to transition start.

The correlation of Davis et al. [16] is

$$\mathrm{Re}_{st} = 25000\ \log_{10}[\coth(0.1732\mathrm{TI})] \tag{6}$$

For the present experiments, TI could reasonably be set between 0.3% and 0.8%, as discussed above. Varying TI within this range does not significantly affect the correlation predictions. For Eq. (6) and all the correlations below, TI was set to 0.5%.

Hatman and Wang [15] identified several transition modes and present correlations for each of them. Their laminar separation mode transition correlation can be cast in terms of Re_{st} as

$$\mathrm{Re}_{st} = 0.0816\ \mathrm{Re}_s + 26805 \tag{7}$$

Yaras [17] proposed

$$\mathrm{Re}_{st} = 0.04\ \mathrm{Re}_s + 6.3 \times 10^4[1 - \tanh^3(TF')] \tag{8}$$

where $TF' = \max(TF, 1\%)$, and $TF = \mathrm{TI}(s_s/\lambda)^{0.2}$, where s_s is the distance from the leading edge to the separation point and λ is the integral length scale of the freestream turbulence.

Roberts and Yaras [40] presented

$$\mathrm{Re}_{st} = (785 - 30TF)\mathrm{Re}_{\theta s}^{0.7} \tag{9}$$

Praisner and Clark [19] presented the correlation

$$\mathrm{Re}_{st} = 173.0\ \mathrm{Re}_s\ \mathrm{Re}_{\theta s}^{-1.227} \tag{10}$$

The above correlations are based on the conditions at the separation location and in some cases the freestream turbulence inten-

Table 3 Conditions at suction peak and separation location based on laminar boundary layer calculation

Re	s_p/L_s	s_s/L_s	$\mathrm{Re}_{\theta p}$	$\mathrm{Re}_{\theta s}$
25,800	0.438	0.496	48	61
50,900	0.438	0.494	68	85
102,000	0.438	0.496	96	122
205,900	0.493	0.538	151	182
297,300	0.493	0.538	182	220
333,900	0.493	0.537	193	231

sity. Volino and Bohl [18] reasoned that instabilities begin to grow when the boundary layer becomes unstable at the start of the adverse pressure gradient region, and presented the following correlation:

$$\mathrm{Re}_{pt} = 8.80[6.37 - \log_{10}(\mathrm{TI}^2)]\mathrm{Re}_{\theta p}^{4/3} \tag{11}$$

where Re_{pt} is based on the freestream velocity at the suction peak and the distance from the suction peak to the transition start.

The location of the suction peak for each case was taken from the experimental data of Fig. 4. The separation location and the momentum thickness Reynolds numbers at separation, $\mathrm{Re}_{\theta s}$, and at the suction peak, $\mathrm{Re}_{\theta p}$, were taken from the TEXSTAN calculations described above. Equations (4)–(11) were then used to compute s_t, which is defined as the distance from the leading edge to the start of transition. The Reynolds numbers used with the correlations are listed in Table 3. The s_t results are shown as a function of Re in Fig. 22. The experimental transition locations, as determined from Figs. 9–18, are also shown. The uncertainties in the experimental locations, which result from the finite spacing between the measurement stations, are indicated by the error bars in Fig. 22. Values of $s_t/L_s > 1$ in the figure indicate that transition is predicted downstream of the trailing edge of the airfoil.

The Mayle [2] short bubble correlation, which is only intended for separation bubbles that reattach, predicts transition somewhat too far upstream at all Reynolds numbers. For the $\mathrm{Re} \geq 200{,}000$ cases, all of the other correlations agree with the experimental results. For the lower Re cases, the Roberts and Yaras [40] and Volino and Bohl [18] correlations continue to agree with the experiment, while the other correlations predict transition too far downstream.

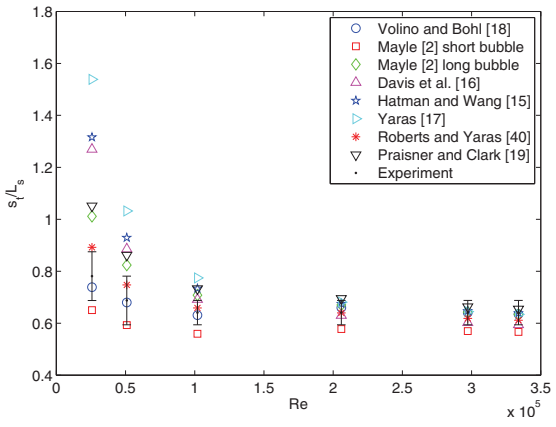

Fig. 22 Predicted and experimental transition start location: error bars indicate uncertainty due to finite spacing of measurement stations

4 Conclusions

The flow over the very high lift L1A airfoil was studied experimentally using a linear cascade. Reynolds numbers based on the suction surface length and nominal exit velocity ranging from 25,000 to 330,000 were considered. In all cases the laminar suction surface boundary layer separated, but at Reynolds numbers greater than 150,000, the separation bubble was very thin and short, and the boundary layer was attached over most of the surface. At lower Reynolds numbers, the boundary layer separated and never reattached. Separation without reattachment caused the lift on the airfoil to decrease by 20% and the total pressure losses increased by a factor of 7 above the highest Reynolds number case. Transition to turbulence occurred in all cases in the shear layer after separation, and appeared to be caused by the growth of Tollmien–Schlichting waves, which originated in the boundary layer upstream of separation. The transition location was well predicted by the correlations of Roberts and Yaras [40] and Volino and Bohl [18]. Transition caused immediate reattachment in the high Reynolds number cases, but the turbulent shear layer remained separated in the low Re cases. This behavior contrasts with previous studies on other LPT airfoils. In those studies, transition immediately triggered reattachment, even at low Reynolds numbers. On the present airfoil, the strong adverse pressure gradient prevents reattachment at low Re, even after transition occurs.

Acknowledgment

This work was sponsored by the National Aeronautics and Space Administration (Award No. NNC07IA10I. The grant monitor is Dr. Anthony Strazisar of the NASA Glenn Research Center. The support of the United States Naval Academy Technical Support Department Shop and Fluids Laboratory is greatly appreciated.

Nomenclature

C_f = skin friction coefficient
Cp = $2(P_T - P)/\rho U_e^2$, pressure coefficient
C_x = axial chord length
f = frequency
H = δ^*/θ, shape factor
K = $(\nu/U_\infty^2)(dU_\infty/ds)$, acceleration parameter
L_s = suction surface length
L_ϕ = blade spacing (pitch)
P = pressure
P_S = upstream static pressure
P_T = upstream stagnation pressure
P_{Te} = downstream stagnation pressure
Re = $U_e L_s/\nu$, exit Reynolds number
Re_{δ^*} = displacement thickness Reynolds number
Re_θ = momentum thickness Reynolds number
s = streamwise coordinate, distance from leading edge
TI = freestream turbulence intensity
U = mean streamwise velocity
U_∞ = local freestream velocity
U_e = nominal exit freestream velocity, based on inviscid solution
u' = time averaged rms streamwise fluctuating velocity
x = axial distance from leading edge
y = distance from wall
Zw = Zweifel coefficient
α_1 = inlet flow angle
α_2 = exit flow angle
δ^* = displacement thickness
ϕ = coordinate along blade spacing, normal to axial chord

γ = intermittency, fraction of time flow is turbulent
ν = kinematic viscosity
ρ = density
θ = momentum thickness
ψ = $(P_T - P_{Te})/(P_T - P_S)$, total pressure loss coefficient
ψ_{int} = total pressure loss integrated over blade spacing

Subscripts

p = pressure minimum (suction peak) location
pt = distance from suction peak to transition start
s = separation location
st = distance from separation location to transition start
∞ = freestream

References

[1] Hourmouziadis, J., 1989, "Aerodynamic Design of Low Pressure Turbines," *AGARD Lecture Series*, Vol. 167, Advisory Group for Aeronautical Research and Development, Paris.
[2] Mayle, R. E., 1991, "The Role of Laminar-Turbulent Transition in Gas Turbine Engines," ASME J. Turbomach., **113**, pp. 509–537.
[3] Sharma, O.P., Ni, R.H., and Tanrikut, S., 1994, "Unsteady Flow in Turbines," *AGARD Lecture Series*, Vol. 195, Advisory Group for Aeronautical Research and Development, Paris, Paper No. 5.
[4] Bons, J. P., Sondergaard, R., and Rivir, R. B., 2001, "Turbine Separation Control Using Pulsed Vortex Generator Jets," ASME J. Turbomach., **123**, pp. 198–206.
[5] Volino, R. J., and Hultgren, L. S., 2001, "Measurements in Separated and Transitional Boundary Layers Under Low-Pressure Turbine Airfoil Conditions," ASME J. Turbomach., **123**, pp. 189–197.
[6] McAuliffe, B.R., and Yaras, M.I., 2007, "Transition Mechanisms in Separation Bubbles Under Low and Elevated Freestream Turbulence," ASME Paper GT2007-27605.
[7] Mahallati, A., McAuliffe, B.R., Sjolander, S.A., and Praisner, T.J., 2007, "Aerodynamics of a Low-Pressure Turbine Airfoil at Low-Reynolds Numbers—Part 1: Steady Flow Measurements," ASME Paper GT2007-27347.
[8] Mahallati, A., and Sjolander, S.A., 2007, "Aerodynamics of a Low-Pressure Turbine Airfoil at Low Reynolds Numbers—Part 2: Blade-Wake Interaction," ASME Paper GT2007-27348.
[9] Zhang, X.F., and Howard Hodson, H., 2007, "Effects of Reynolds Number and Freestream Turbulence Intensity on the Unsteady Boundary Layer Development on an Ultra-High-Lift LPT Airfoil," ASME Paper GT2007-27274.
[10] Uzol, O., Zhang, X.F., Cranstone, A., and Hodson, H., 2007, "Investigation of Unsteady Wake-Separated Boundary Layer Interaction Using Particle-Image-Velocimetry," ASME Paper GT2007-28099.
[11] Opoka, M. M., and Hodson, H. P., 2008, "Transition on the T106 LP Turbine Blade in the Presence of Moving Upstream Wakes and Downstream Potential Fields," ASME J. Turbomach., **130**, p. 041017.
[12] Zoric, T., Popovic, I., Sjolander, S.A., Praisner, T., and Grover, E., 2007, "Comparative Investigation of Three Highly Loaded LP Turbine Airfoils—Part I: Measured Profile and Secondary Losses at Design Incidence," ASME Paper GT2007–27537.
[13] Volino, R. J., 2002, "Separated Flow Transition Under Simulated Low-Pressure Turbine Airfoil Conditions—Part 1: Mean Flow and Turbulence Statistics," ASME J. Turbomach., **124**, pp. 645–655.
[14] Volino, R. J., 2002, "Separated Flow Transition Under Simulated Low-Pressure Turbine Airfoil Conditions—Part 2: Turbulence Spectra," ASME J. Turbomach., **124**, pp. 656–664.
[15] Hatman, A., and Wang, T., 1999, "A Prediction Model for Separated Flow Transition," ASME J. Turbomach., **121**, pp. 594–602.
[16] Davis, R. L., Carter, J. E., and Reshotko, E., 1985, "Analysis of Transitional Separation Bubbles on Infinite Swept Wings," AIAA Paper No. 85-1685.
[17] Yaras, M. I., 2002, "Measurements of the Effects of Freestream Turbulence on Separation-Bubble Transition," ASME Paper GT-2002-30232.
[18] Volino, R.J., and Bohl, D.G., 2004, "Separated Flow Transition Mechanisms and Prediction With High and Low Freestream Turbulence Under Low Pressure Turbine Conditions," ASME Paper GT2004-53360.
[19] Praisner, T. J., and Clark, J. P., 2007, "Predicting Transition in Turbomachinery—Part 1: A Review and New Model Development," ASME J. Turbomach., **129**, pp. 1–13.
[20] Zhang, X. F., Vera, M., Hodson, H., and Harvey, N., 2006, "Separation and Transition Control on an Aft-Loaded Ultra-High-Lift LP Turbine Blade at Low Reynolds Numbers: Low-Speed Investigation," ASME J. Turbomach., **128**, pp. 517–527.
[21] Bohl, D. G., and Volino, R. J., 2006, "Experiments With Three-Dimensional Passive Flow Control Devices on Low-Pressure Turbine Airfoils," ASME J. Turbomach., **128**, pp. 251–260.
[22] Volino, R. J., 2003, "Passive Flow Control on Low-Pressure Turbine Airfoils," ASME J. Turbomach., **125**, pp. 754–764.
[23] Volino, R. J., 2003, "Separation Control on Low-Pressure Turbine Airfoils Using Synthetic Vortex Generator Jets," ASME J. Turbomach., **125**, pp. 765–777.
[24] Huang, J., Corke, T., and Thomas, F., 2003, "Plasma Actuators for Separation Control on Low Pressure Turbine Blades," AIAA Paper No. 2003-1027.
[25] Bons, J.P., Hansen, L.C., Clark, J.P., Koch, P.J., and Sondergaard, R., 2005, "Designing Low-Pressure Turbine Blades With Integrated Flow Control," ASME Paper GT2005-68962.
[26] Clark, J. P., 2007, private communication.
[27] Zhang, X. F., and Hodson, H., 2005, "Combined Effects of Surface Trips and Unsteady Wakes on the Boundary Layer Development of an Ultra-High-Lift LP Turbine Blade," ASME J. Turbomach., **127**, pp. 479–488.
[28] Lakshminarayana, B., 1996, *Fluid Dynamics and Heat Transfer of Turbomachinery*, Wiley, New York.
[29] McAuliffe, B. R., and Sjolander, S. A., 2004, "Active Flow Control Using Steady Blowing for a Low-Pressure Turbine Cascade," ASME J. Turbomach., **126**, pp. 560–569.
[30] Lewis, R. I., 1991, *Vortex Element Methods for Fluid Dynamic Analysis of Engineering Systems*, Cambridge University Press, Cambridge.
[31] Hughes, J. D., and Walker, G. J., 2001, "Natural Transition Phenomena on an Axial Compressor Blade," ASME J. Turbomach., **123**, pp. 392–401.
[32] Wills, J. A. B., 1962, "The Correction of Hot-Wire Readings for Proximity to a Solid Boundary," J. Fluid Mech., **12**, pp. 388–396.
[33] Volino, R. J., and Simon, T. W., 1997, "Velocity and Temperature Profiles in Turbulent Boundary Layers Experiencing Streamwise Pressure Gradients," ASME J. Heat Transfer, **119**, pp. 433–439.
[34] Simon, T. W., Qiu, S., and Yuan, K., 2000, "Measurements in a Transitional Boundary Layer Under Low-Pressure Turbine Conditions," NASA Report No. CR-2000-209957.
[35] Volino, R. J., Schultz, M. P., and Pratt, C. M., 2003, "Conditional Sampling in a Transitional Boundary Layer Under High Free-Stream Turbulence Conditions," ASME J. Fluids Eng., **125**, pp. 28–37.
[36] Schlichting, H., 1979, *Boundary Layer Theory*, 7th ed., McGraw-Hill, New York.
[37] Walker, G. J., 1989, "Transitional Flow on Axial Turbomachine Blading," AIAA J., **27**, pp. 595–602.
[38] Crawford, M.E., and Kays, W.M., 1976, "STAN5—A Program for Numerical Computation of Two-Dimensional Internal and External Boundary Layer Flows," NASA Report No. CR-2742.
[39] Stieger, R. D., and Hodson, H. P., 2004, "The Transition Mechanism of Highly Loaded Low-Pressure Turbine Blades," ASME J. Turbomach., **126**, pp. 536–543.
[40] Roberts, S. K., and Yaras, M. I., 2006, "Effects of Surface-Roughness Geometry on Separation-Bubble Transition," ASME J. Turbomach., **128**, pp. 349–356.

Separation Control on a Very High Lift Low Pressure Turbine Airfoil Using Pulsed Vortex Generator Jets

Ralph J. Volino
Department of Mechanical Engineering,
United States Naval Academy,
Annapolis, MD 21402-5042
e-mail: volino@usna.edu

Olga Kartuzova
e-mail: kartuzova_olga@hotmail.com

Mounir B. Ibrahim
e-mail: m.ibrahim@csuohio.edu

Department of Mechanical Engineering,
Cleveland State University,
Cleveland, OH 44115-2425

Boundary layer separation control has been studied using vortex generator jets (VGJs) on a very high lift, low-pressure turbine airfoil. Experiments were done under high (4%) freestream turbulence conditions on a linear cascade in a low speed wind tunnel. Pressure surveys on the airfoil surface and downstream total pressure loss surveys were documented. Instantaneous velocity profile measurements were acquired in the suction surface boundary layer. Cases were considered at Reynolds numbers (based on the suction surface length and the nominal exit velocity from the cascade) of 25,000 and 50,000. Jet pulsing frequency, duty cycle, and blowing ratio were all varied. Computational results from a large eddy simulation of one case showed reattachment in agreement with the experiment. In cases without flow control, the boundary layer separated and did not reattach. With the VGJs, separation control was possible even at the lowest Reynolds number. Pulsed VGJs were more effective than steady jets. At sufficiently high pulsing frequencies, separation control was possible even with low jet velocities and low duty cycles. At lower frequencies, higher jet velocity was required, particularly at low Reynolds numbers. Effective separation control resulted in an increase in lift and a reduction in total pressure losses. Phase averaged velocity profiles and wavelet spectra of the velocity show the VGJ disturbance causes the boundary layer to reattach, but that it can reseparate between disturbances. When the disturbances occur at high enough frequency, the time available for separation is reduced, and the separation bubble remains closed at all times. [DOI: 10.1115/1.4003024]

1 Introduction

Boundary layer separation can lead to partial loss of lift and higher aerodynamic losses on low-pressure turbine (LPT) airfoils (e.g., Refs. [1–3]). As designers impose higher loading to improve efficiency and lower cost, the associated strong adverse pressure gradients on the suction side of the airfoil can exacerbate separation problems. In aircraft engines, the lower density and therefore lower Reynolds numbers at altitude can lead to a component efficiency drop of 2% between takeoff and cruise in large commercial transport engines, and possibly as much as 7% in smaller engines operating at higher altitudes [4,5]. Prediction and control of suction side separation, without sacrifice of the benefits of higher loading, are, therefore, crucial for improved engine design.

Separation and separated flow transition, which can lead to boundary layer reattachment, have received considerable attention. Lists of various studies are provided by Volino [6,7]. In general, previous work shows that the strong acceleration on the leading section of the airfoil keeps the boundary layer thin and laminar, even in the presence of elevated freestream turbulence. When separation does occur, it is usually just downstream of the suction peak. If transition then occurs in the shear layer over the separation bubble, it is typically rapid and often causes the boundary layer to reattach [7,8].

Airfoils can be designed with high resistance to separation, as described by Praisner and Clark [9], but a loading limit will always exist, above which separation will still occur. If flow control were incorporated in the design of an advanced airfoil, as discussed by Bons et al. [10], it might be possible to increase the loading limit. Separation control with passive devices such as boundary layer trips has been shown effective by Zhang et al. [11], Bohl and Volino [12], Volino [13], and others. Passive devices have the distinct advantage of simplicity, but they also introduce parasitic losses and cannot be adjusted to account for changes in flow conditions. Active devices could potentially provide better control over the entire operating range of interest and be reduced in strength or turned off to avoid unnecessary losses when they are not needed. Potential disadvantages of active devices are the cost of implementation and the possibility of control failure, particularly in aircraft engines.

The literature contains many examples of active separation control. A few which could be applied in turbomachinery are discussed in Ref. [14]. Plasma devices, as used by Huang et al. [15], could be viable, and are under active study. Vortex generator jets (VGJs), as introduced by Johnston and Nishi [16], are another alternative and the subject of the present study. Blowing from small, compound angled holes is used to create streamwise vortices. The vortices bring high momentum fluid into the near wall region, which can help to control separation. The most effective VGJs enter the boundary layer at a relatively shallow pitch angle (typically 30–45 deg) relative to the wall and a high skew angle (45–90 deg) relative to the main flow. Additionally, the jets promote transition, and turbulent mixing also helps to mitigate separation. Bons et al. [10] noted that in the case of pulsed VGJs, the turbulence effect is more significant than the action of the vortices. Bons et al. [4,17], Volino [14], Volino and Bohl [18], McQuilling and Jacob [19], and Eldredge and Bons [20] all used VGJs on the highly loaded Pack B LPT airfoil. Separation was essentially eliminated, even at the lowest Reynolds number considered (Re=25,000 based on suction surface length and nominal exit velocity). Pulsed jets were more effective than steady jets. The initial disturbance created by each pulse caused the boundary

Contributed by the International Gas Turbine Institute (IGTI) of ASME for publication in the JOURNAL OF TURBOMACHINERY. Manuscript received June 29, 2010; final manuscript July 11, 2010; published online April 25, 2011. Editor: David Wisler.

Table 1 Cascade parameters

Axial chord, C_x (mm)	True chord (mm)	Pitch, L_ϕ (mm)	Span (mm)	Suction side, L_s (mm)	Inlet flow angle (deg)	Exit flow angle (deg)
134	146	136	724	203	35	60

layer to attach. The turbulence was followed by a calmed period [21,22] during which the boundary layer was very resistant to separation, much like a turbulent boundary layer, but very laminarlike in terms of its fluctuation levels and low losses. When the time between pulses was long enough, the boundary layer did eventually relax to a separated state, but due to the control which persisted during the calmed period, the VGJs were effective even with low jet pulsing frequencies, duty cycles, and mass flow rates. Since the boundary layer was attached and undisturbed for much of the jet pulsing cycle, profile losses were low.

Similar results with pulsed VGJs were found on the L1M airfoil by Bons et al. [23]. The L1M is more highly loaded than the Pack B, but more resistant to separation because of forward loading. A large separation bubble followed by boundary layer reattachment was observed at low Reynolds numbers, and pulsed VGJs reduced the size of the bubble.

In the present study, the very highly loaded L1A airfoil is used. The L1A was designed at the Air Force Research Laboratory (AFRL) and is available on a limited basis from Ref. [24]. It is an aft loaded blade with the same flow angles and loading as the L1M. Dimensions of the L1A as used in the present study are given in Table 1. Based on the design calculations of Clark [24], the L1A has a Zweifel coefficient of 1.35, which corresponds to 10% higher loading than the "ultrahigh lift" airfoils described by Zhang and Hodson [25], and 17% higher loading than the Pack B. Because the L1A is aft loaded, it is more prone to separation than the L1M, as documented in Refs. [26,6,27,28]. In cases without flow control and low Reynolds numbers, the boundary layer separates and does not reattach, in spite of transition to turbulence in the shear layer over the separation bubble. This result contrasts with the results of studies on less aggressive airfoils, which all showed reattachment after transition. The separation bubble on the L1A is about four times thicker than that on the Pack B. The larger distance from the shear layer to the wall on the L1A apparently prevents the turbulent mixing in the shear layer from reaching the wall and causing reattachment. The failure of the boundary layer to reattach results in a 20% loss in lift and increases profile losses by up to a factor of 7. At higher Reynolds numbers, the separation bubble is small and the boundary layer is attached over most of the airfoil.

Separation control with VGJs has been demonstrated on the L1A airfoil. Bons et al. [26] considered a case with Re=50,000, background freestream turbulence $TI=3\%$, and periodic wakes produced with moving rods upstream of the airfoils. The VGJs had a duty cycle (fraction of time the jets are on during a pulsing cycle) $D=30\%$ and a blowing ratio $B=2.3$ (based on the maximum jet velocity in the pulsing cycle and the local freestream velocity). The dimensionless frequency of the wake passing and VGJ pulsing were both $F=fL_{j-te}/U_{\text{ave}}=0.34$, where L_{j-te} is the streamwise distance from the VGJ holes to the trailing edge, and U_{ave} is the average freestream velocity over this distance. Two different streamwise locations for the VGJs were considered. The VGJs reduced the separation bubble size and reduced total pressure losses. Volino et al. [29] considered cases with $TI=0.6\%$. Pressure distributions on the airfoils and total pressure losses were documented. Cases were considered at Reynolds numbers from 25,000 to 100,000. Jet pulsing frequency was varied from $F=0.14$ to 1.12 with duty cycles of 10% and 50% and blowing ratios ranging from 0.25 to 3.0. In agreement with previous studies, pulsed jets were more effective than steady jets. At Re =25,000, separation control was achieved with $B=0.75$, $F=0.56$, and $D=10\%$. Without flow control the lift at Re=25,000 was about 80% of the high Re lift, and with flow control it was 94% of the high Re lift. Flow control caused the total pressure loss to drop from about five times the high Re value to about three times the high Re value. Once good control was achieved, further increasing the frequency, blowing ratio, or duty cycle provided little additional benefit. Partial control was possible at lower frequencies, particularly with higher blowing ratios or duty cycles. At Re =50,000 with $F=0.56$, $B=0.25$ was sufficient with $D=10\%$. Lower frequencies were more effective at Re=50,000 than at Re=25,000. Effective separation control resulted in a 20% increase in lift, and up to a 60% reduction in total pressure loss, dropping from about five times the high Re value to about twice the high Re value.

In the present study, flow control with vortex generator jets is investigated under high (4%) freestream turbulence conditions, which is more representative of engine conditions than the low *TI* considered in Ref. [29]. Cases with a range of pulsing frequencies and blowing ratios are considered. In addition to pressure distributions, instantaneous boundary layer velocity measurements are used to explain the mechanism by which the VGJs control separation.

2 Experimental Facility and Measurements

Experiments were conducted in a closed loop wind tunnel with a seven blade linear cascade located in the wind tunnel's third turn, as shown in Fig. 1(*a*). A coarse grid, consisting of a 1.5 mm thick sheet metal plate with 19 mm square holes spaced 25.4 mm apart, center to center, in both directions is located upstream of the cascade. In a plane perpendicular to the inlet flow and $1.7C_x$ upstream of the center blade, the grid produced uniform flow with $TI=6.0\%$ in the streamwise component and 4.2% in the cross stream components, for an overall intensity of 4.9%. The integral length scale of the freestream turbulence is $0.12C_x$ in the streamwise component and $0.04C_x$ in the other components. The streamwise component was also measured at the inlet plane of the cascade in the four center passages, where it had decayed to between 4% and 4.2% between blades B2 and B5 and 4.6% between blades B5 and B6. Downstream of the cascade, the local *TI* is 1.8% across all passages, as documented in Ref. [28]. The local freestream turbulence intensity in the passage at the beginning of the adverse pressure gradient region is 1.4%. The change in *TI* through the passage is due mainly to the change in the local freestream velocity along with some decay of the turbulence.

A tailboard, shown in Fig. 1(*a*), is needed to produce the correct exit flow angle from the cascade. Its position was set to produce periodicity at high Reynolds numbers. A tailboard on the opposite side of the cascade, and inlet guide vanes were found to be unnecessary. To produce the correct approach flow to the end blades (B1 and B7), the amount of flow escaping around the two ends of the cascade is controlled with the flaps shown in Fig. 1(*a*). The inlet flow angle was checked with a three-hole pressure probe and found to agree with the design angle to within 2 deg of uncertainty. Good periodicity at high Reynolds numbers was obtained in the exit flow. At low Reynolds numbers, when significant separation bubbles are present, the periodicity is not as good due to suppression of the separation bubble thickness on the blades closest to the tailboard. In cases with effective flow control, periodicity is reestablished. The lack of periodicity in cases with large separation bubbles is considered acceptable since the focus of the

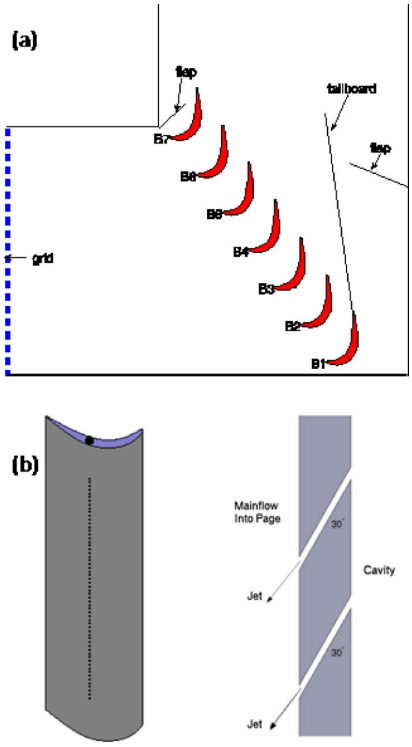

Fig. 1 Drawings of test section: (*a*) linear cascade and (*b*) airfoil with VGJ holes and cross section of hole geometry

study is separation control and not documentation of cases with large separation that would be unacceptable in practice. This compromise facilitates the study of a larger number of cases with flow control by obviating the need to adjust the tailboard by trial and error for each case. It also provides for better repeatability in the experiments, since the position of the tailboard is fixed for all cases. Any improvements made with flow control will be larger in practice than documented in the experiment, due to the effect of the tailboard in suppressing the bubble size in the uncontrolled cases.

Each blade in the cascade has a central cavity, which extends along the entire span. As explained in Ref. [29], compressed air is supplied to the cavities from a common manifold. The manifold is supplied through two fast response solenoid valves (Parker Hannifin 009-0339-900 with General Valve Iota One pulse driver) operating in parallel. A single spanwise row of holes was drilled into the suction surface of each blade at the inviscid pressure minimum location, $s/L_s=0.5$ ($x/C_x=0.62$), where s is the distance from the leading edge and L_s is the suction surface length. The pressure minimum has been shown in the studies listed above to be about the optimal location for flow control devices. The holes are 0.8 mm ($0.006C_x$) in diameter and drilled at 30 deg to the surface and 90 deg to the main flow direction, as shown in Fig. 1(*b*). This is the same orientation used in all the VGJ studies listed above. The hole spacing is 10.6 diameters, and the length to diameter ratio is 12. With steady blowing and $B=1$, the mass flow rate of the jets is 0.04% of the main flow mass flow rate. With pulsed jets the mass flow is lower, particularly in low duty cycle cases. The solenoid valves pulse the VGJs, and the pulsing frequency is presented below in dimensionless form as $F=fL_{j-te}/U_{\text{ave}}$. For flow over single airfoils, $F\geq 1$ is typically needed to maintain separation control, but for cascades, Bons et al. [17] showed that control is possible in some cases with $F=0.1$. As shown in Refs. [14,17], this is due to the extended calmed region which follows the jet disturbance. In practice, VGJs could be timed to wake passing in an LPT, which has a typical frequency of about $F=0.3$.

Table 2 Velocity profile measurement stations

	Station					
	1	2	3	4	5	6
s/L_s	0.53	0.59	0.69	0.78	0.88	0.97
x/C_x	0.65	0.72	0.80	0.86	0.92	0.97

The center blade, designated B4 in Fig. 1, contains pressure taps near the spanwise centerline. Pressure surveys are made using a pressure transducer (0–870 Pa range Validyne transducer). Stagnation pressure is measured with a pitot tube upstream of the cascade. The uncertainty in the suction side pressure coefficients, Cp, is 0.07. Most of this uncertainty is due to bias error. Stochastic error is minimized by averaging pressure transducer readings over a 10 s period.

Total pressure losses are documented using a Kiel probe traversed across three blade spacings, $0.63C_x$ downstream of the cascade. A traverse is located in the wind tunnel downstream of the cascade to move the probe. The traverse causes an acceptably low blockage when it is located at least two C_x downstream of the cascade.

Pressure and loss surveys were acquired at nominal Re =25,000 and 50,000. The Reynolds number, as defined above, is based on the suction surface length and the nominal cascade exit velocity. The corresponding Reynolds numbers based on the cascade inlet velocity and the axial chord length are 10,000 and 20,000.

The jet velocity was measured at the exit plane of the VGJ holes and was documented in Ref. [29]. There is about a 5 ms delay between the opening of the solenoid valve and the beginning of the rise of the jet velocity above zero at the exit plane. The delay corresponds to the time required for a pressure wave to travel from the valve to the jet hole. The jet velocity rises rapidly and nearly continuously for another 6 ms to a maximum and then drops for about 6 ms toward a steady value which is maintained for the rest of the time the valve is open. When the valve closes, the jet velocity drops to zero. In cases with high pulsing frequency or low duty cycle, the jet turns off before a steady velocity is reached. As will be shown below, the transient that occurs when the VGJ turns on is more effective for separation control than the steady blowing which may follow. The initial velocity maximum is therefore used to define the blowing ratio rather than the average velocity for the pulse.

Velocity profiles on the suction surface were measured at the six streamwise stations listed in Table 2. All stations are downstream of the inviscid pressure minimum at $s/L_s=0.49$. Profiles were acquired near the spanwise centerline of the airfoil with a hot-wire anemometer (AA Lab Systems model AN-1003) and a single-sensor hot-film probe (TSI model 1201-20). The sensor diameter is 51 μm, and the active length is 1.02 mm. At each measurement location, data were acquired for 26 s at a 20 kHz sampling rate (2^{19} samples). All raw data were saved. The high sampling rate provides an essentially continuous signal, and the long sampling time results in low uncertainty in both statistical and spectral quantities. Data were acquired at 40 wall normal locations in each profile, extending from the wall to the freestream, with most points concentrated in the near wall region. The probe was positioned as close to tangent to the airfoil surface as possible at each station, such that the probe body extended downstream of the sensor and the direction of the traverse was within 5 deg of normal to the surface. In most cases the closest

Table 3 Grids 3, 35, and 37 used in this investigation

Grid nos.	Size (cells)	Number of grids in z direction	y^+	Δz^+	Δx^+
3	1,500,000	15	0.5	12.6	1–100
35	5,900,000	30	0.5	6.3	0.4–52
37	11,900,000	54	0.5	0.4–3.5	0.4–52

point to the wall in each profile was within about 0.2 mm of the wall, which compares to boundary layer thicknesses ranging from 1.1 mm to over 40 mm.

Flow direction in a separation bubble cannot be determined with a single-sensor hot-wire, but velocity magnitude can be measured and was found to be near zero within the bubbles of the present cases when the flow was laminar. In cases where the flow became turbulent but remained separated, fluctuating velocities caused false high mean velocity readings in the separation bubble. With the exception of these turbulent separated cases, the uncertainty in the mean velocity is 3–5% except in the very near wall region, where near wall corrections [30] were applied to the mean velocity.

Velocity data were both time averaged and ensemble averaged based on the phase within the jet pulsing cycle. Phase averages of mean and fluctuating velocity are shown below at 24 dimensionless times, t/T, within the pulsing cycle, where t is time and T is the period of the cycle. The time $t/T=0$ corresponds to the opening of the solenoid valve.

Wavelet spectra of the fluctuating velocity were computed using the method described in Ref. [31]. In contrast to Fourier spectra, in which a signal is transformed from the time domain to the frequency domain, wavelet spectra provide the frequency content of a signal on a time resolved basis. The Mexican Hat wavelet was used for the analysis. The wavelet spectra were phase averaged to show the variation of frequency content in the velocity as a function of time within the jet pulsing cycle.

3 Numerical Simulations

Numerical simulations were conducted utilizing version 6.3.26 of the finite-volume code FLUENT™ [32]. The three dimensional computational domain includes a single passage. A uniform velocity inflow condition is specified $1.9C_x$ upstream of the blade leading edge in the flow direction. The inlet flow angle is set to 33 deg based on an inviscid calculation of the full cascade used in the experiment [27]. This angle agrees with the experimentally measured inlet angle to within the experiment uncertainty. The exit boundary is located $3.8C_x$ downstream of the trailing edges in the flow direction. In the spanwise direction, the domain includes one VGJ. The boundary conditions on the sides of the passage are periodic. The full length of the hole is included in the simulations, allowing the jet velocity profile to develop before entering the main domain [29]. A uniform velocity boundary condition is specified at the hole inlet during jet blowing. Computation was continued until no variation cycle-to-cycle was reached.

Convergence was established when (1) residuals reduced to a value 10^{-5}, (2) no change was observed in any field results, and (3) the mass imbalance was less than 0.01%.

Large eddy simulations (LESs) were done using the dynamic subgrid-scale kinetic energy model in FLUENT, which is based on the model proposed by Kim and Menon [33]. In this model, a separate transport equation is solved for subgrid-scale kinetic energy. The model constants are determined dynamically. The details of the implementation of this model in FLUENT and its validation are given by Kim [34].

3.1 Code Validation. Three different grids were tested as shown in Table 3. Grid 37 was selected. Details of the grid structure are in Ref. [35]. To accurately represent structures in the near wall region (for LES), the recommended values are $y^+\sim 2$, $\Delta x^+ \sim 50-150$, and $\Delta z^+\sim 15-40$ (see Ref. [36]). Grid 37 produced Cp versus s/L_s results in closest agreement to the experimental data and therefore was chosen for further computation. Computations with grid 37 were then run for different time steps (0.0005, 0.0001, and 0.00005s) and time step=0.0001 s was selected since not much improvement was achieved using the smaller step (0.00005 s).

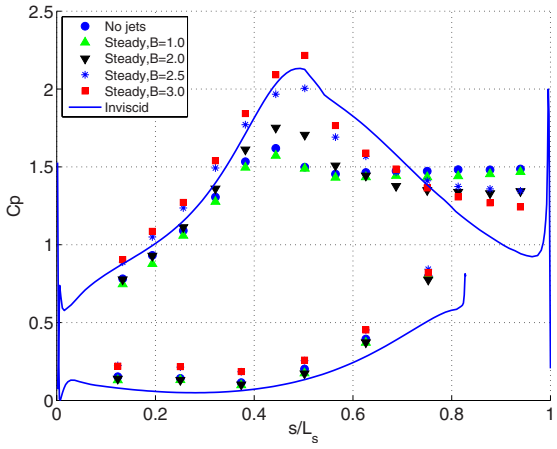

Fig. 2 *Cp* profiles for steady blowing, Re=25,000 cases

4 Results

4.1 Re=25,000. Pressure profiles for cases with Re=25,000 and steady VGJ blowing are shown in Fig. 2. The inviscid profile for the L1A airfoil is shown as a common reference for comparing results between figures. At high Reynolds numbers (e.g., Re =300,000), experimental results agree with the inviscid line, as shown in Ref. [28]. The low peak followed by a plateau in the case without jets in Fig. 2 indicates separation without reattachment. As in the low freestream turbulence cases of Ref. [29] at this Reynolds number, blowing with $B=2.0$ or lower has no effect on separation. When B is increased to 2.5 or 3.0, there are some signs of reattachment, but the Cp profile remains significantly different from the inviscid profile.

Figures 3 shows results for cases with pulsed jets and $F=0.14$. As in the low freestream turbulence cases, this frequency is too low to be very effective. The jets have some effect on Cp when $B=3.0$ and this effect increases at higher duty cycle. The total pressure losses for these cases are shown in Fig. 3(b). A high Reynolds number (Re=300,000) baseline case from Ref. [28] is shown for comparison. The loss, ψ, is shown as a function of distance across the cascade, ϕ, normalized on the blade spacing L_ϕ. The origin, $\phi=0$, corresponds to the location downstream of the trailing edge of the center blade in the cascade (B4 in Fig. 1(a)) in the design flow direction. The pulsed jets reduce the loss significantly and shift the loss peaks to the right. This indicates that the separation bubble must be thinner, particularly when $B=3.0$, and that flow turning is increased. The loss peak at $B=3.0$ is narrower for the $D=50\%$ case than for the lower duty cycle, in agreement with the larger drop in Cp near the trailing edge for this case. Even in this best case, the loss peaks are significantly higher and to the left of the high Re case.

Results with $F=0.28$ are shown in Fig. 4. The jets begin to have an effect when $B=1.5$, and significant separation control is apparent when $B=2.0$ or higher, particularly with $D=50\%$. The jets are not as effective when $D=10\%$. The loss results show the VGJs at

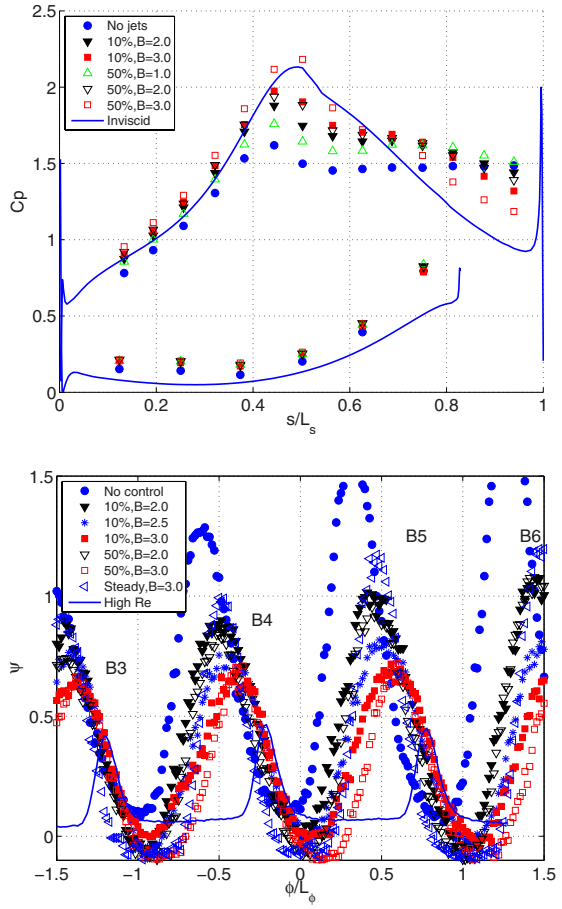

Fig. 3 Pressure results for F=0.14, Re=25,000 cases: (a) *Cp* and (*b*) total pressure loss

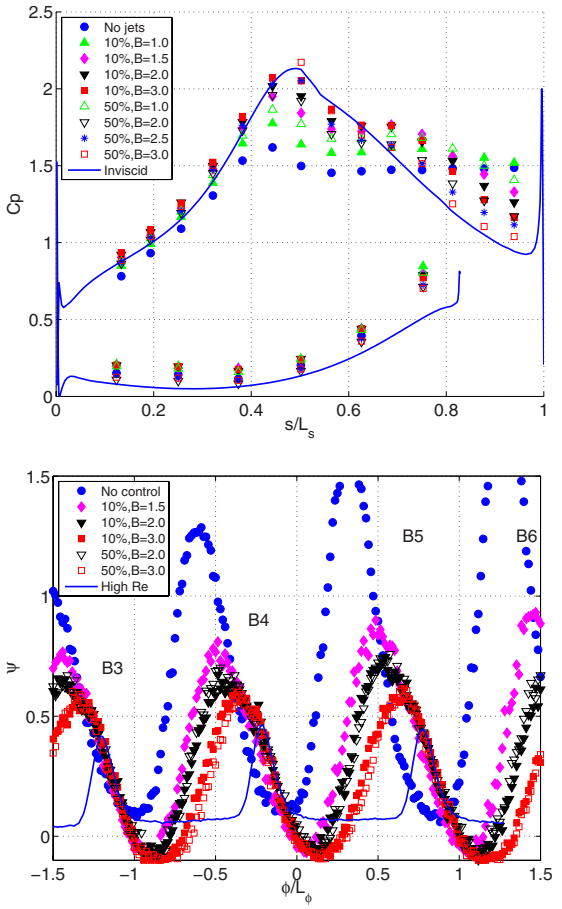

Fig. 4 Pressure results for F=0.28, Re=25,000 cases: (a) *Cp* and (*b*) total pressure loss

F=0.28 have a strong effect. The duty cycle effect is less apparent than in the *Cp* results.

Figure 5 shows *Cp* results with F=0.56. The VGJs have some effect even at low blowing ratios, and when B=1.0 the boundary layer appears to reattach. The results do not appear to depend significantly on the duty cycle. This is consistent with the low freestream turbulence results, which showed that when F=0.56 the pulses occur frequently enough to control separation even at low duty cycles. Figure 6 shows results with F=1.12. Results are similar to those with F=0.56. Separation is controlled when B=0.75, and increasing B further does not appear to have much effect. Losses for the F=0.56 and 1.12 cases are shown in Fig. 7. The losses are greatly reduced when separation is controlled, and with a few exceptions the loss results are consistent with the *Cp* results.

Integrated *Cp* and loss results are shown in Fig. 8. The *Cp* difference between the pressure and suction sides of the passage is integrated in the axial direction to produce a quantity proportional to the lift on the airfoil,

$$Cp_{\text{int}} = \int_0^{C_x} \frac{(Cp_{\text{suction}} - Cp_{\text{pressure}})dx}{C_x} \tag{1}$$

and this quantity is normalized using the same integrated quantity for the inviscid profile. The integrated total pressure loss,

$$\psi_{\text{int}} = \int_{-L_\phi/2}^{L_\phi/2} \frac{\psi d\phi}{L_\phi} + \frac{\dot{m}_j}{\dot{m}_1}\frac{(P_j - P_{Te})}{(P_T - P_S)} \tag{2}$$

is an average of the loss profile result across one blade spacing centered on the peak corresponding to blade B4. As explained in

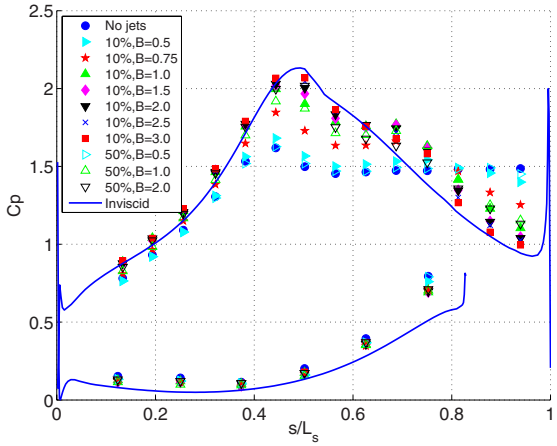

Fig. 5 *Cp* profiles for F=0.56, Re=25,000 cases

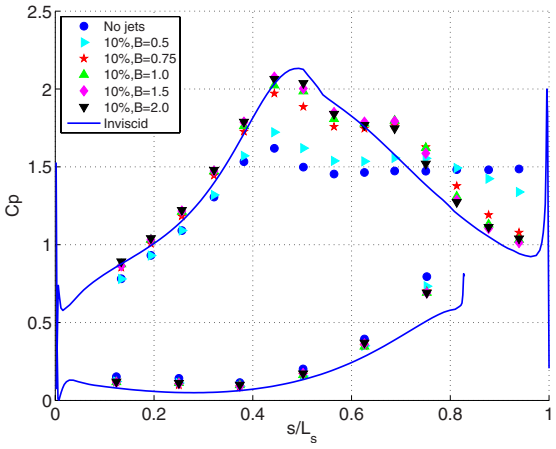

Fig. 6 *Cp* profiles for *F*=1.12, Re=25,000 cases

Ref. [29], the loss associated with the jets themselves is included in the integrated loss. With steady jets the lift increases slowly as blowing ratio is increased but never achieves the inviscid case value. The lift increases at each blowing ratio as F is increased and is higher at the higher duty cycle. With $F=0.56$ and 1.12, the lift increases rapidly with B, reaching the inviscid value when $B=1$, and then remains constant as B is increased further. In agreement with the lift, the integrated loss decreases with B from a high value of 0.55 without flow control to about 0.22, with the best results at the higher pulsing frequencies. These values compare with a high Re value of about 0.15. The losses with $F=0.28$ are somewhat lower than in the corresponding low *TI* cases of Volino et al. [29], but otherwise the high and low *TI* results are very similar. The change in exit flow angle is inferred from the shift in the location of the loss peaks from $\phi/L_\phi=0$ in Figs. 3(*b*), 4(*b*), and 7, and is shown as the difference from the high Re case angle in Fig. 8(*c*). The location of the peak in the high Re case corresponds to an exit flow angle of 54 deg, which agrees within the experimental uncertainty with the design exit flow angle of 57 deg corresponding to the design Zweifel=1.35. The design exit flow angle is lower than the 60 deg design metal angle of Table 1. Without flow control, turning is reduced by 16 deg compared with the high Re case. In the best controlled case, about 11 deg of turning is recovered, but there is still a 5.5 deg difference from the

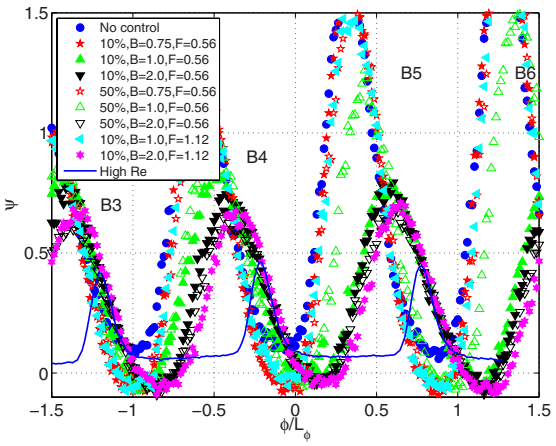

Fig. 7 Total pressure loss profiles for *F*=0.56 and *F*=1.12, Re =25,000 cases

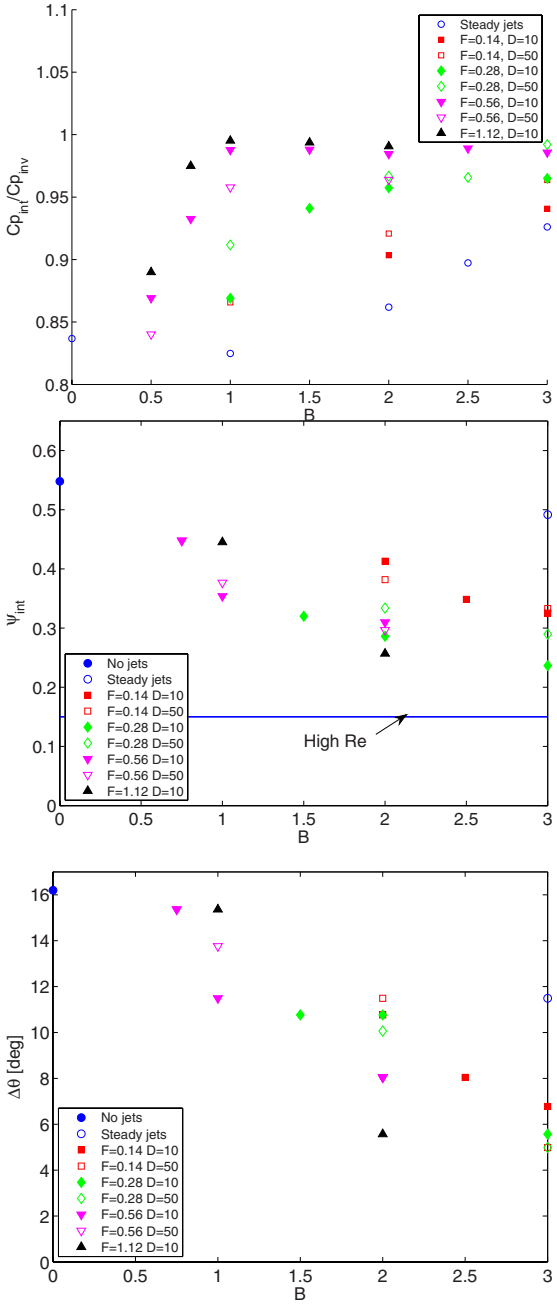

Fig. 8 Integrated pressure results for Re=25,000 cases: (*a*) ratio of lift to lift in inviscid case, (*b*) total pressure loss, and (*c*) change in exit flow angle from high Re case

high Re case due to the much thicker boundary layer at low Re even with reattachment.

Time averaged velocity profiles for the baseline case and four cases with pulsed jets are shown in Fig. 9. The top row shows the mean velocity at the six streamwise stations noted in Table 2, and the lower row shows the rms fluctuating streamwise velocity, u'. Without flow control, the boundary layer has separated by Station 1 and the separation bubble grows at the downstream stations. The peak in u' is in the shear layer far from the wall. With flow control, it appears there may be a small separation bubble at the

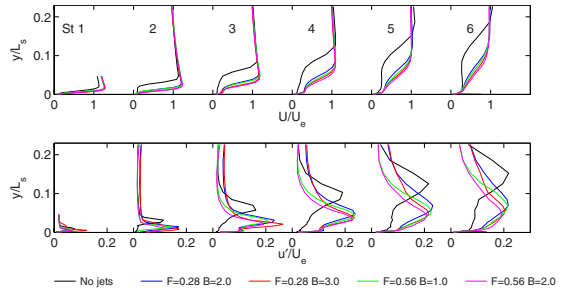

Fig. 9 Time averaged velocity profiles at six streamwise stations for Re=25,000 cases with no jets and jets with *D*=10%: (top) mean velocity and (bottom) rms velocity

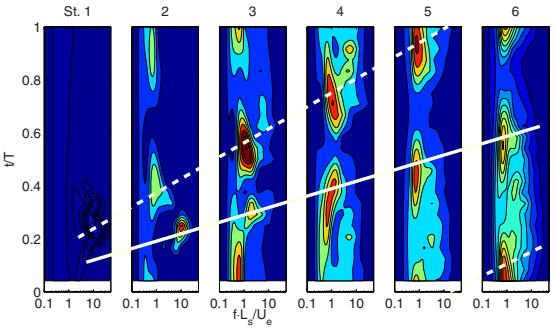

Fig. 11 Wavelet spectra computed at *y* locations of maximum *u′* in time averaged profiles and shown as function of time and frequency at six streamwise stations, *F*=0.28, *D*=10%, *B*=2.0, Re=25,000, solid white line is leading edge of disturbance, dashed white line is trailing edge

third and fourth stations, in agreement with the short plateau in Cp at this location in Figs. 4(a) and 5, but it is much smaller than in the baseline case, and the boundary layer appears attached at the downstream stations. With $F=0.28$, increasing the blowing ratio from $B=2$ to 3 moves the u' peak toward the wall, indicating a thinner bubble. The same trend is observed as B in increased from 1 to 2 with $F=0.56$. Increasing F from 0.28 to 0.56 results in significantly lower u' in the outer part of the boundary layer, which is explained below.

Figure 10 shows the phase averaged mean velocity profiles for the cases with $F=0.28$, $D=10\%$, and $B=2.0$, and with $F=0.56$, $D=10\%$, and $B=2.0$. The columns correspond to the six streamwise stations, and rows are for different phases in the pulsing cycle. A small separation bubble appears to form at station 3 in the $F=0.28$ case, but is suppressed for several phases starting at $t/T=0.417$. The same is true at station 4, with the suppression of the separation beginning at about $t/T=0.5$. At station 5, the boundary

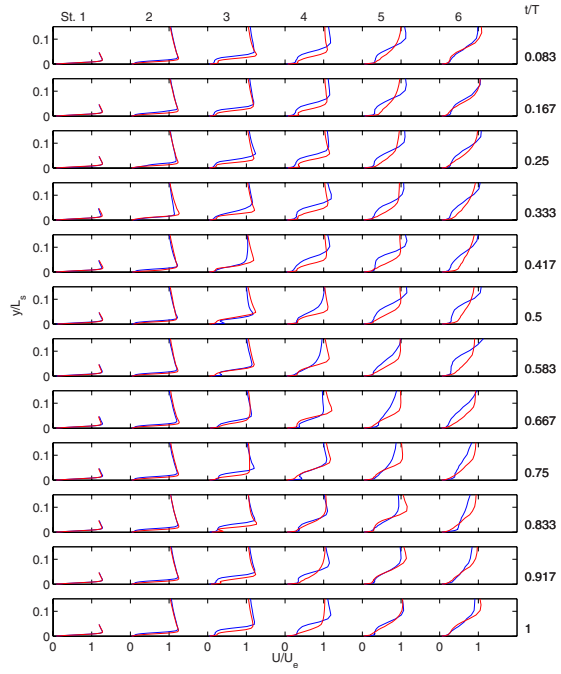

Fig. 10 Phase averaged mean velocity profiles for Re=25,000 cases, columns for six streamwise stations, rows for phases in pulsing cycle: black (blue)—*F*=0.28, *D*=10%, *B*=2.0; gray (red)—*F*=0.56, *D*=10%, *B*=2.0

layer appears to reattach at $t/T=0.583$ and remain attached until $t/T=0.917$. At station 6, reattachment occurs at about $t/T=0.667$, and the boundary layer remains attached until $t/T=0.167$ in the next cycle.

In the $F=0.56$ case, there is less variation in the mean profile during the cycle. Variation in the velocity as the boundary layer separates and reattaches results in significant u', and as the variation is reduced at higher F, u' decreases. This is particularly apparent at $y/L_s>0.1$. As the separation bubble grows, fluid is forced away from the wall and the velocity at $y/L_s>0.1$ increases. When the boundary layer reattaches, the velocity at $y/L_s>0.1$ drops. The result is high u' in this region for the $F=0.28$ case in Fig. 9. The boundary layer appears to approach separation in the $F=0.56$ case for much of the cycle at station 4, particularly between $t/T=0.5$ and 0.708, and at $t/T=0.75$ to 0.917 at station 5 and $t/T=0.083$ at station 6. At other times, separation appears controlled.

Wavelet spectra help to explain the velocity profile results. Figure 11 shows wavelet spectra for the $F=0.28$, $D=10\%$, and $B=2.0$ case. The six plots in the figure correspond to the six streamwise stations. In each plot, the horizontal axis shows dimensionless frequency, fL_s/U_e on a log scale, and the vertical axis shows dimensionless time, t/T, for one pulsing cycle. Power spectral density is computed from instantaneous velocity data at all y locations and is shown in Fig. 11 for the y locations corresponding to maximum time averaged u' at each station. The contours show the power spectral density premultiplied by frequency and normalized by U_e^2. The color scale is the same for all plots. The VGJ creates a disturbance at the beginning of a pulse, and the leading edge of this disturbance is visible as high contours centered at $t/T=0.16$, 0.25, 0.31, 0.38, 0.46, and 0.54 at stations 1–6, respectively. The arrival times at each station indicate that the leading edge of the disturbance convects along the surface at about 0.6 times the local freestream velocity. A second peak appears centered at $t/T=0.24$, 0.42, 0.54, 0.71, 0.93, and 0.06 at stations 1–6, respectively. These peaks are believed to result when the trailing edge of the VGJ disturbance passes, and the times indicate a convection speed of about 0.3 times the freestream velocity. Comparison of Figs. 10 and 11 shows that at each station, the separation bubble is thickest at about the time the disturbance first arrives. Shortly after this, the velocity profile appears reattached. The profile remains attached at each station until about the time when the second peak appears in Fig. 11, indicating that the disturbance has past. The separation bubble then begins to grow almost immediately. Since the leading and trailing edges of the disturbance move at different velocities, the duration of the disturbance increases at the downstream stations. Hence, the duration of the separation bubble decreases at the downstream stations. If the pulsing fre-

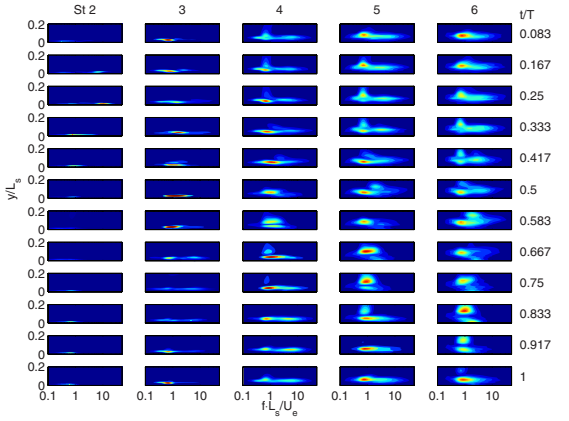

Fig. 12 Wavelet spectra as function of distance from wall and frequency at stations 2–6 (columns) and various phases (rows), $F=0.28$, $D=10\%$, $B=2.0$, Re=25,000

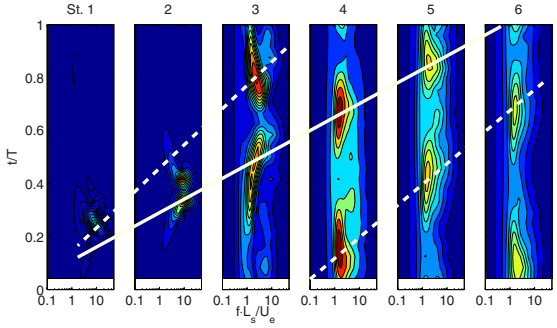

Fig. 13 Wavelet spectra computed at y locations of maximum u' in time averaged profiles and shown as function of time and frequency at six streamwise stations, $F=0.56$, $D=10\%$, $B=2.0$, Re=25,000, solid white line is leading edge of disturbance, dashed white line is trailing edge

quency were increased, disturbances would follow each other more closely in time, and if the frequency were sufficiently high, the leading edge of each disturbance would overtake the trailing edge of the preceding disturbance, thereby eliminating the period of separated flow. Based on the convection speeds observed in Fig. 11, $F=0.5$ would be sufficient to eliminate separation at the trailing edge.

Low frequency peaks appear in Fig. 11 at the pulsing frequency, $fL_s/U_e=0.7$, at all stations. A higher frequency peak at $fL_s/U_e=10$ is also visible, particularly at stations 1 and 2. The higher frequency is likely related to shear layer transition and matches the frequency peak observed in transition without flow control in Ref. [28]. Figure 12 shows the contours of the dimensionless, premultiplied wavelet spectra as a function of distance from the wall on the vertical axis and dimensionless frequency on the horizontal axis. The columns correspond to stations 2–6, and the rows to different times during the cycle. The peak at $fL_s/U_e=0.7$ appears at all times. Higher frequencies extending beyond $fL_s/U_e=10$ are also present. The high frequency fluctuations have their highest magnitude in the shear layer when the boundary layer is most separated and are suppressed when the VGJs cause reattachment. Another peak at $fL_s/U_e=2$ and y/L_s between 0.11 and 0.16 appears in the shear layer at $t/T=0.417$, 0.5, and 0.583 at stations 4–6, respectively. These are the arrival times of the VGJ disturbance at these stations.

Increasing the blowing ratio from 2 to 3 with $F=0.28$ increases the magnitude of the disturbances, but otherwise does not change the behavior observed in Figs. 9–12. The effect of pulsing frequency is shown in Fig. 13 for the $F=0.56$, $D=10\%$, and $B=2.0$ case in the same format as Fig. 11. A peak frequency of about $fL_s/U_e=10$ is still present at stations 1 and 2, as in Fig. 11. High magnitudes are also visible at all stations at the pulsing frequency, which is now doubled to about $fL_s/U_e=1.4$. In the format of Fig. 12 for this case (not shown), the arrival of the VGJ disturbance is again marked by a spectral peak in the shear layer at a frequency of about $fL_s/U_e=2$. In Fig. 13, the center of the spectral peaks which presumably correspond to the first arrival of the VGJ disturbance appear at stations 1–6 at $t/T=0.17$, 0.34, 0.5, 0.67, 0.94, and 0.1 respectively. These dimensionless times are greater than those in Fig. 11 since the convection velocities are about the same in both cases but the pulsing period is halved. Comparing Figs. 13 and 10, the separation bubble begins to grow at each station after the passing of the trailing edge of the disturbance, and the bubble is suppressed about $0.1T$ after the arrival of the next disturbance. This is the same behavior observed at $F=0.28$, but there is less time available for the bubble to grow at the higher frequency, so there is less variation of the velocity profile shape with time at $F=0.56$. The reduced separation at higher frequency is reflected in the lower losses and the Cp profiles, which are closer to the inviscid solution.

4.2 Re=50,000. Pressure profiles for the cases with steady VGJs and Re=50,000 are shown in Fig. 14. The jets become effective when $B\geq 1.5$. Results for pulsed jets with $F=0.14$ are shown in Fig. 15. In terms of Cp, the jets begin to have an effect when $B=0.75$ but do not appear to fully control separation until $B=1.5$. Between $B=0.75$ and 1.5, a higher duty cycle appears to help, but at $B=1.5$ and above, the results are about the same with $D=10\%$ or 50%. The total pressure loss profiles agree with the Cp results. In the best controlled case, the loss peaks are still significantly higher and to the left of the high Re comparison case, but the difference is not as great as in the Re=25,000 cases above. Figure 16 shows results with $F=0.28$. The jets have some effect with $B=0.5$ and 0.75, and the effect increases at higher duty cycle. With $B=1.0$ and higher, separation is controlled at both duty cycles. The loss peak is slightly narrower with $D=50\%$. The Cp profiles show a small separation bubble still appears to remain at $s/L_s=0.7$. With $F=0.56$, as shown in Fig. 17, blowing with $B=0.5$ has some effect, particularly with $D=50\%$, and with $B=0.75$ and $D=10\%$ the separation is controlled. Increasing B or D further has no additional effect. As in the lower frequency cases, a small separation bubble remains at $s/L_s=0.7$. The integrated Cp

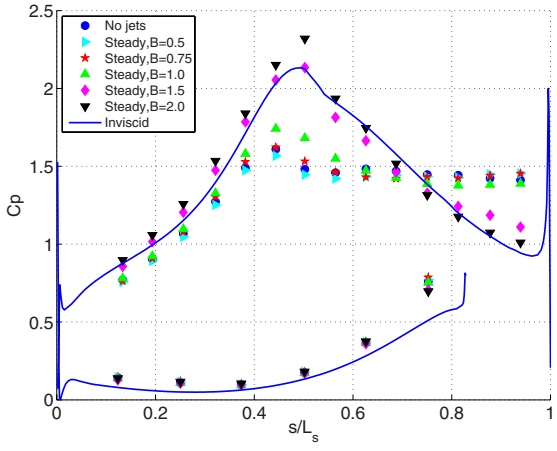

Fig. 14 Cp profiles for steady blowing, Re=50,000 cases

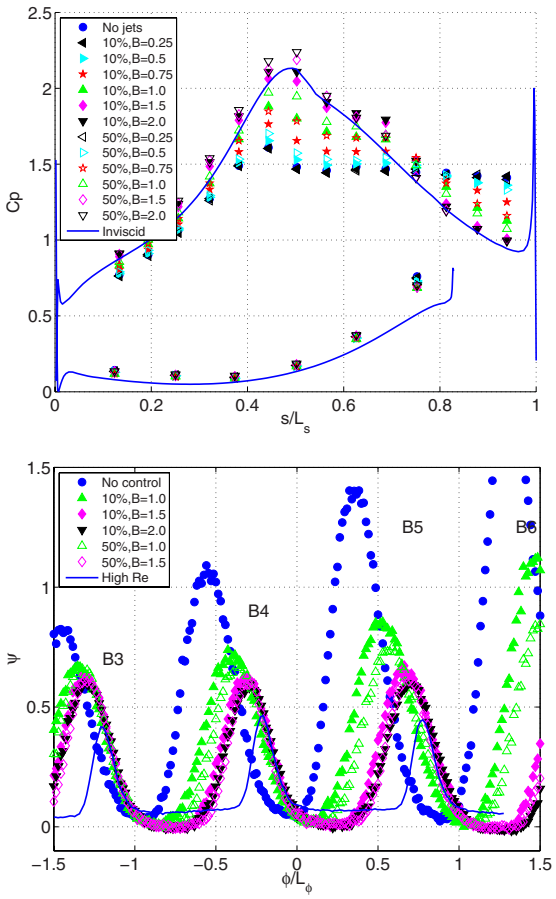

Fig. 15 Pressure results for F=0.14, Re=50,000 cases: (*a*) *Cp* and (*b*) total pressure loss

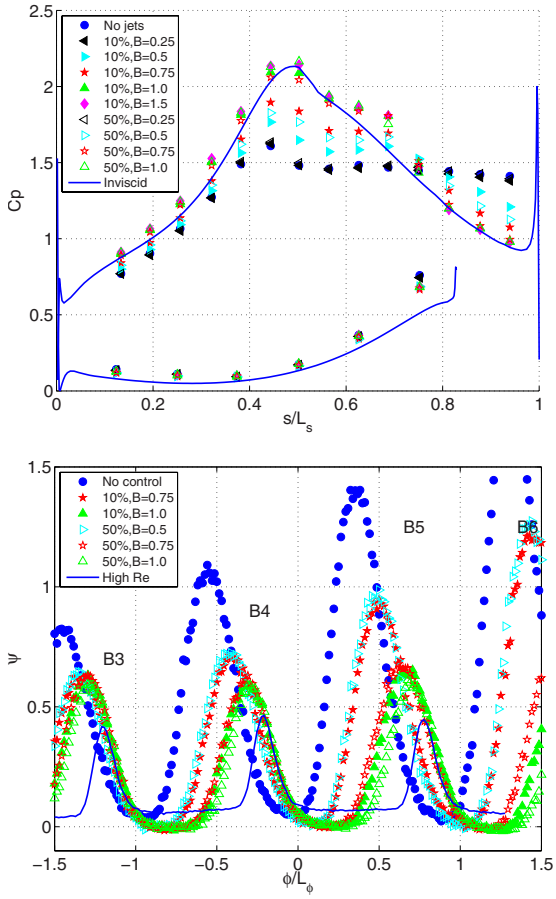

Fig. 16 Pressure results for F=0.28, Re=50,000 cases: (*a*) *Cp* and (*b*) total pressure loss

and loss results are shown in Fig. 18. The trends are the same as in the Re=25,000 cases of Fig. 8 and the low *TI* cases of Volino et al. [29], but effective separation control and loss reduction is possible with somewhat lower B and F as Re or *TI* is increased. The reduction in flow turning compared with the high Re case is shown in Fig. 18(*c*). Separation control increases the flow turning by about 12 deg, reducing the difference from the high Re case to 2 deg.

Time averaged velocity profiles for some of the Re=50,000 cases are shown in Fig. 19. A large separation bubble without reattachment is present without flow control. Pulsed VGJs largely eliminate the bubble, although a small separation is still present at station 3, in agreement with the small plateau in the *Cp* profiles of Figs. 16 and 17 at s/L_s=0.7. Figure 20 shows phase averaged velocity profiles. With F=0.28, there is a small separation at t/T=0.417 at station 4, at t/T=0.5 at station 5, and at t/T=0.583 at station 6. Figure 21 shows the wavelet spectra for this case in the format of Fig. 11. The frequencies and times of the peaks in Figs. 21 and 11 are similar since the pulsing frequency, F=0.28, is the same for both cases. As in the lower Re case, the boundary layer reattaches shortly after the appearance of the VGJ disturbance at each station. In contrast to the lower Re case, the boundary layer remains attached for about 0.2T after the disturbance has passed, resulting in attached flow for most of the pulsing cycle. The F=0.56, D=10%, B=0.75 case in Fig. 20 shows little variation of the velocity profiles during the pulsing cycle. The spectra for this case, shown in Fig. 22, show nearly a continuous disturbance through the cycle. There may be some signs of separation with a thin bubble at station 3, but at the downstream stations the near overlap of the disturbance period between consecutive pulses combined with the lesser tendency toward separation at Re=50,000 than at 25,000, results in an attached boundary layer for the full cycle.

4.3 Computational Results. Figure 23 shows *Cp* for the Re=50,000, B=1, D=10%, F=0.28 case. The spike at the suction peak is at the jet location. In agreement with the experimental data, the CFD shows a small separation bubble occurs but the flow remains reattached over most of the airfoil. Figure 24 shows time averaged mean velocity at six streamwise stations comparing the CFD results with the experimental data. The agreement is good upstream, but differences are apparent at the downstream stations, particularly near the wall. The CFD predicts an exit flow angle of 57 deg both in the present case and in a high Re case. The exit angle difference between the high Re and controlled Re=50,000 case was also small in the experimental result in Fig. 18(*c*). 57 deg agrees with the design exit flow angle but is a few degrees higher than the experimental value. Figure 25 shows the Q-criterion, which is used to illustrate vortices [32], colored by axial velocity, V_x, at different times in the cycle. At the beginning of the blowing, there is no separation bubble present near the trailing edge of the airfoil. This is in contrast with the corresponding low *TI* case (see Ref. [35]). However, there is a small bubble located midway between the jet and the trailing edge. During blowing that separated region travels downstream while the flow is attached along most

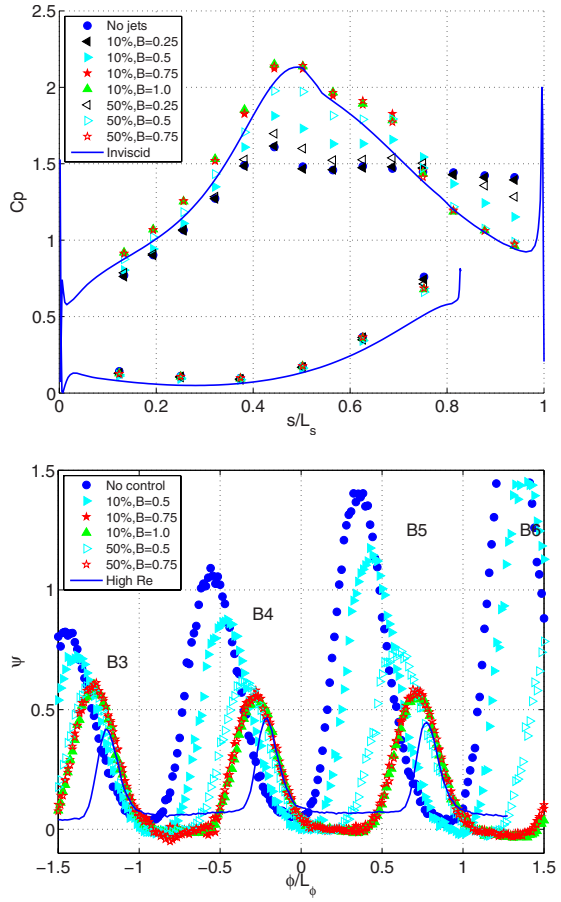

Fig. 17 Pressure results for *F*=0.56, Re=50,000 cases: (*a*) *Cp* and (*b*) total pressure loss

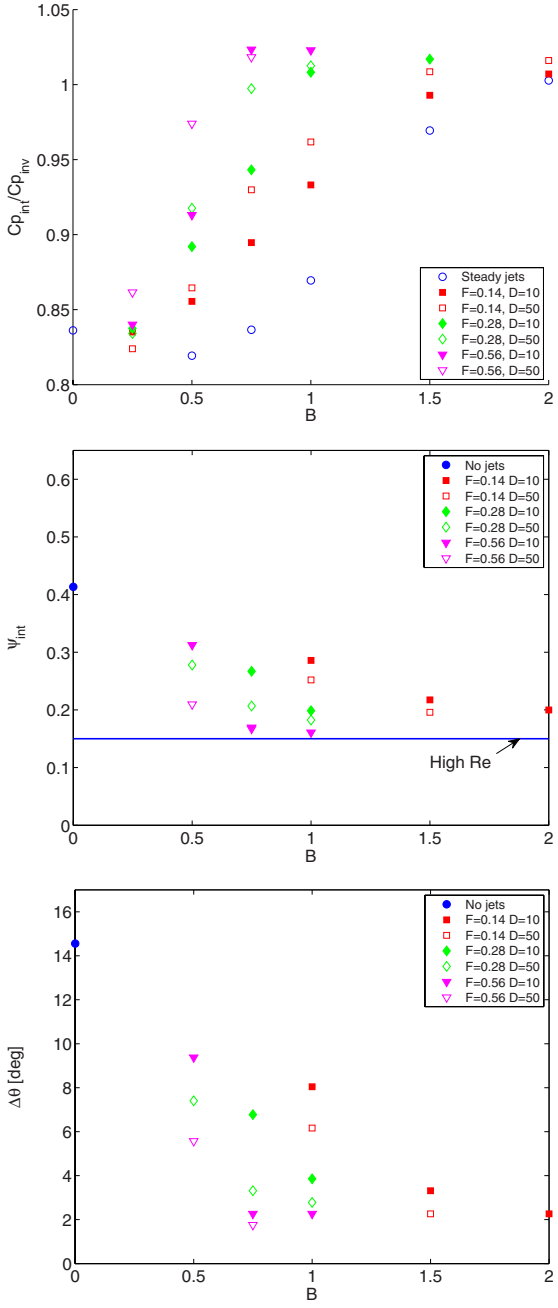

Fig. 18 Integrated pressure results for Re=50,000 cases: (*a*) ratio of lift to lift in inviscid case, (*b*) total pressure loss, and (*c*) change in exit flow angle from high Re case

of the airfoil. Right after shutdown of the jet, the separation region is smaller. Also at that time the shear layer is highly energized. Near the end of the cycle the flow is attached at the trailing edge, but a small separated region begins to appear again upstream. These results are consistent with the experimental velocity profiles of Fig. 20, which show a small separation bubble moving down the airfoil between wakes, but attached flow at all locations for most of the cycle.

5 Discussion

The VGJ disturbances convect downstream in the shear layer over the separation bubble, and if they are of sufficient amplitude, cause the boundary layer to attach at a given streamwise location shortly after the arrival of the disturbance. The boundary layer tends to remain attached until after the passage of the trailing edge of the disturbance, although at the lowest Reynolds numbers there may be some tendency, as shown in Fig. 10, to separate earlier. After the disturbance passes, the separation bubble begins to regrow. This happens almost immediately at very low Reynolds number and more slowly at higher Re. The trailing edge of each disturbance travels slower than the leading edge, resulting in a stretching of the disturbance in the streamwise direction as it moves downstream and a longer duration of the disturbance at downstream locations. The result is a shorter period between disturbances at downstream stations and less separated flow. Increasing the pulsing frequency reduces the period between disturbances at all locations and results in better separation control.

The present results, in agreement with all the previous VGJ studies referenced above, show that pulsed jets are more effective than steady jets. The disturbance created when a jet is first turned on is more effective than any steady blowing that may follow. Velocity results from cases with low freestream turbulence [37] show that when pulsing with $D=50\%$, the boundary layer may reseparate during the period of steady blowing. Increasing the duty cycle from 10% to 50% can, however, provide better separation control, particularly at low pulsing frequencies, as shown above and in Ref. [29]. Velocity profiles and spectra from the low

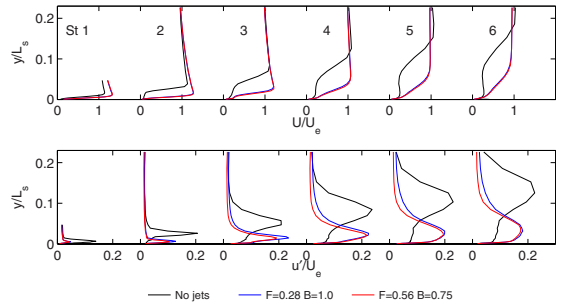

Fig. 19 Time averaged velocity profiles at six streamwise stations for Re=50,000 cases with no jets and jets with *D*=10%: (top) mean velocity and (bottom) rms velocity

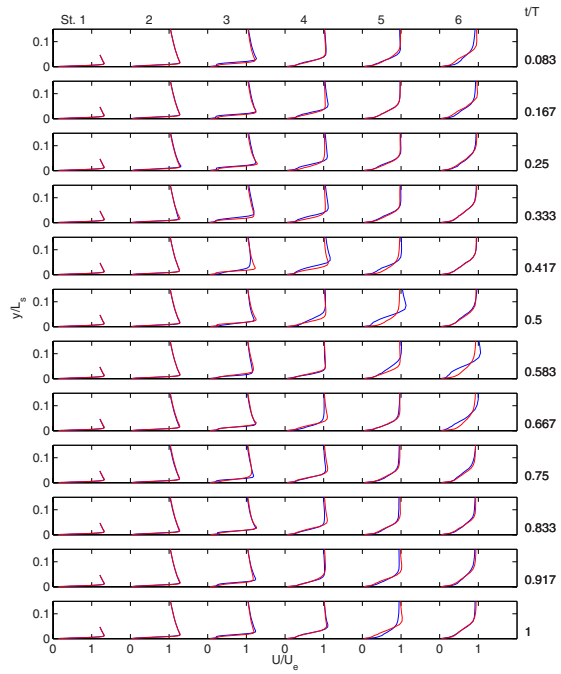

Fig. 20 Phase averaged mean velocity profiles for Re=50,000 cases, columns for six streamwise stations, rows for phases in pulsing cycle: black (blue)—*F*=0.28, *D*=10%, *B*=1.0; gray (red)—*F*=0.56, *D*=10%, *B*=0.75

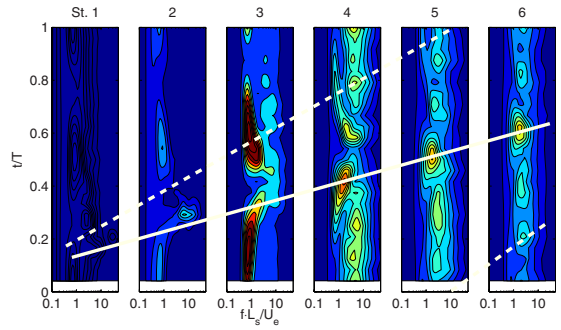

Fig. 21 Wavelet spectra computed at y locations of maximum *u′* in time averaged profiles and shown as function of time and frequency at six streamwise stations, *F*=0.28, *D*=10%, *B*=1.0, Re=50,000; the solid white line is the leading edge of disturbance, and the dashed white line is the trailing edge

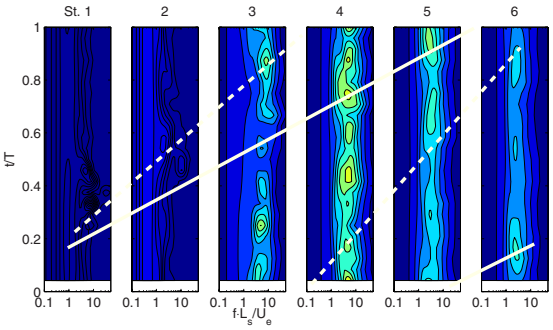

Fig. 22 Wavelet spectra computed at y locations of maximum *u′* in time averaged profiles and shown as function of time and frequency at six streamwise stations, *F*=0.56, *D*=10%, *B*=0.75, Re=50,000; the solid white line is leading edge of disturbance, and the dashed line is trailing edge

TI, *D*=50% cases show a second effective disturbance occurs each cycle when the VGJs turns off, thereby doubling the disturbance frequency above the pulsing frequency. In the *D*=10% cases, the disturbances created when the jets turn on and off occur so close together in time that they effectively constitute a single disturbance.

The present results are very similar to the low *TI* results of Volino et al. [29]. High *TI* does help to control separation, allowing VGJ flow control with slightly lower amplitude and frequency jets in some cases, but the physics of the separation and flow control appears to be the same at high and low *TI*. Increasing the VGJ velocity and frequency help to reduce the separation bubble extent both temporally and spatially, and this increases lift and reduces total pressure losses. Once the separation is largely eliminated, increasing the blowing ratio or pulsing frequency further provides no additional benefit.

6 Conclusions

The effect of vortex generator jets on the flow over the very high lift L1A airfoil was studied under high freestream turbulence conditions. Reynolds numbers based on suction surface length and nominal exit velocity of 25,000 and 50,000 were considered. Without flow control, the boundary layer separated and did not reattach. Flow control with VGJs was possible even at Re =25,000. In agreement with previous studies, pulsed jets were more effective than steady jets. Pulsing with a dimensionless frequency of *F*=0.56 or higher allowed for separation control with a blowing ratio of at most 1.0 and 10% duty cycle. Effective separation control resulted in a 20% increase in lift and up to a 60% reduction in total pressure loss compared with baseline cases at the same Reynolds number. Loss values still remain higher than in high Reynolds number cases. Pulsed jets at lower frequencies pro-

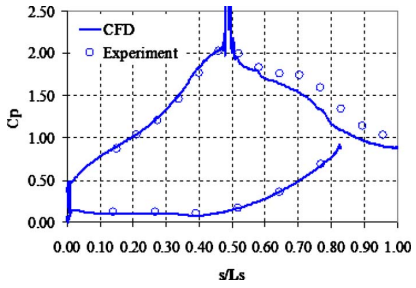

Fig. 23 *Cp* profile for *B*=1, *F*=0.28, *D*=10%, Re=50,000

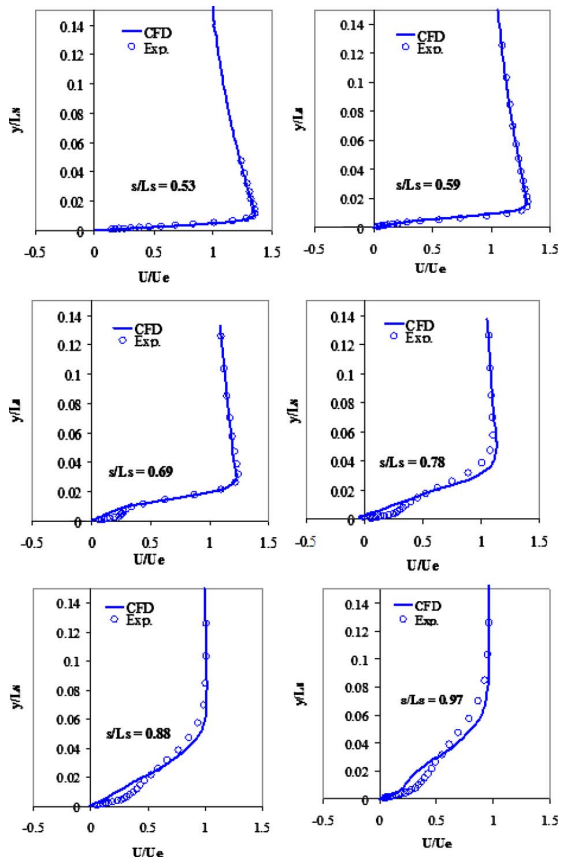

Fig. 24 U/U_e **for** $B=1$, $F=0.28$, $D=10\%$, Re=50,000

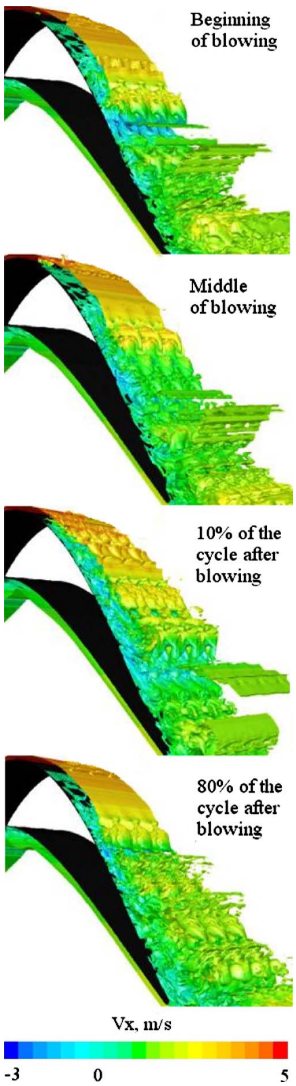

Fig. 25 Q-criterion contours colored by axial velocity, $B=1$, $F=0.28$, $D=10\%$, Re=50,000, **at different times in the cycle**

vided partial separation control and some loss reduction and could be improved somewhat by increasing the blowing ratio or duty cycle.

Phase averaged velocity profiles and wavelet spectra show the boundary layer intermittently reattaching as disturbances pass and then separating between disturbances. Increasing the pulsing frequency reduces the time available for separation. When the time available is sufficiently small, the boundary layer remains attached at all times. At Re=25,000, separation was nearly fully controlled for the full pulsing cycle when $F=0.5$. Higher frequency pulsing provided little additional benefit. At higher Reynolds numbers, the separation bubble grows more slowly, so lower pulsing frequencies can be tolerated.

Computational results from a large eddy simulation show reattachment in agreement with the experiments for a case with effective VGJ flow control. The LES results allow visualization of structures such as vortices, providing insight into the flow behavior.

High freestream turbulence makes the boundary layer less likely to separate and allows for separation control with slightly lower blowing ratios and pulsing frequencies than in low *TI* cases. The differences observed between high and low *TI* were small, however, and the physics of the separation and flow control appear to be the same in both cases.

Acknowledgment

This work was sponsored by the National Aeronautics and Space Administration under Grant No. NNC07IA10I. The grant monitors were Dr. Anthony Strazisar and Dr. James Heidmann of the NASA Glenn Research Center. The support of the United States Naval Academy Technical Support Department Shop and Fluids Laboratory is greatly appreciated. We greatly appreciate the computer time provided for us by the Ohio Super Computer (OSC). The OSC Computer Cluster has been made available as part of the Center's mission to support Ohio Universities.

Nomenclature

B = blowing ratio, maximum jet velocity/local freestream velocity
Cp = $2(P_T-P)/\rho U_e^2$, pressure coefficient
Cp_{int} = pressure coefficient integrated in axial direction
Cp_{inv} = Cp_{int} for inviscid flow through cascade
C_x = axial chord length
D = duty cycle, fraction of time valve is open
F = fL_{j-te}/U_{ave}, dimensionless frequency
f = frequency
L_{j-te} = distance from VGJs to trailing edge
L_s = suction surface length

L_ϕ = blade spacing (pitch)
$\dot{m}_j$ = jet mass flow rate
$\dot{m}_1$ = main flow mass flow rate
P = pressure
P_j = jet plenum pressure
P_S = upstream static pressure
P_T = upstream stagnation pressure
P_{Te} = downstream stagnation pressure
Re = $U_e L_s/\nu$, exit Reynolds number
s = streamwise coordinate, distance from leading edge
T = period of jet pulsing cycle
t = time
U_{ave} = average freestream velocity between VGJs and trailing edge
U_e = nominal exit freestream velocity, based on inviscid solution
u' = rms fluctuating streamwise velocity
x = axial distance from leading edge
Δx^+ = grid spacing in axial direction in viscous units
y^+ = location of closest grid point to wall in viscous units
Δz^+ = grid spacing in spanwise direction in viscous units
ϕ = coordinate along blade spacing, normal to axial chord
ν = kinematic viscosity
ρ = density
ψ = $(P_T - P_{Te})/(P_T - P_S)$, total pressure loss coefficient
ψ_{int} = total pressure loss integrated over blade spacing

References

[1] Hourmouziadis, J., 1989, "Aerodynamic Design of Low Pressure Turbines," AGARD Lecture Series 167.
[2] Mayle, R. E., 1991, "The Role of Laminar-Turbulent Transition in Gas Turbine Engines," ASME J. Turbomach., **113**, pp. 509–537.
[3] Sharma, O.P., Ni, R.H., and Tanrikut, S., 1994, "Unsteady Flow in Turbines," AGARD Lecture Series 195, Paper No. 5.
[4] Bons, J. P., Sondergaard, R., and Rivir, R. B., 2001, "Turbine Separation Control Using Pulsed Vortex Generator Jets," ASME J. Turbomach., **123**, pp. 198–206.
[5] Volino, R. J., and Hultgren, L. S., 2001, "Measurements in Separated and Transitional Boundary Layers Under Low-Pressure Turbine Airfoil Conditions," ASME J. Turbomach., **123**, pp. 189–197.
[6] Volino, R. J., 2010, "Separated Flow Measurements on a Highly Loaded Low-Pressure Turbine Airfoil," ASME J. Turbomach., **132**, p. 011007.
[7] Volino, R. J., 2002, "Separated Flow Transition Under Simulated Low-Pressure Turbine Airfoil Conditions: Part 1—Mean Flow and Turbulence Statistics," ASME J. Turbomach., **124**, pp. 645–655.
[8] Volino, R. J., 2002, "Separated Flow Transition Under Simulated Low-Pressure Turbine Airfoil Conditions: Part 2—Turbulence Spectra," ASME J. Turbomach., **124**, pp. 656–664.
[9] Praisner, T. J., and Clark, J. P., 2007, "Predicting Transition in Turbomachinery—Part 1: A Review and New Model Development," ASME J. Turbomach., **129**, pp. 1–13.
[10] Bons, J.P., Hansen, L.C., Clark, J.P., Koch, P.J., and Sondergaard, R., 2005, "Designing Low-Pressure Turbine Blades With Integrated Flow Control," ASME Paper No. GT2005-68962.
[11] Zhang, X. F., Vera, M., Hodson, H., and Harvey, N., 2006, "Separation and Transition Control on an Aft-Loaded Ultra-High-Lift LP Turbine Blade at Low Reynolds Numbers: Low-Speed Investigation," ASME J. Turbomach., **128**, pp. 517–527.
[12] Bohl, D. G., and Volino, R. J., 2006, "Experiments With Three-Dimensional Passive Flow Control Devices on Low-Pressure Turbine Airfoils," ASME J. Turbomach., **128**, pp. 251–260.
[13] Volino, R. J., 2003, "Passive Flow Control on Low-Pressure Turbine Airfoils," ASME J. Turbomach., **125**, pp. 754–764.
[14] Volino, R. J., 2003, "Separation Control on Low-Pressure Turbine Airfoils Using Synthetic Vortex Generator Jets," ASME J. Turbomach., **125**, pp. 765–777.
[15] Huang, J., Corke, T., and Thomas, F., 2003, "Plasma Actuators for Separation Control on Low Pressure Turbine Blades," AIAA Paper No. 2003-1027.
[16] Johnston, J. P., and Nishi, M., 1990, "Vortex Generator Jets—Means for Flow Separation Control," AIAA J., **28**, pp. 989–994.
[17] Bons, J. P., Sondergaard, R., and Rivir, R. B., 2002, "The Fluid Dynamics of LPT Blade Separation Control Using Pulsed Jets," ASME J. Turbomach., **124**, pp. 77–85.
[18] Volino, R. J., and Bohl, D. G., 2005, "Structure of Oscillating Vortex Generator Jets," *Proceedings of the Fourth International Symposium on Turbulence and Shear Flow Phenomena*, Vol. 2, pp. 589–594.
[19] McQuilling, M., and Jacob, J., 2004, "Effect of Chord Location on Separation Control With Vortex Generator Jets on Low Pressure Turbine Blades," AIAA Paper No. 2004-2205.
[20] Eldredge, R. G., and Bons, J. P., 2004, "Active Control of a Separating Boundary Layer With Steady Vortex Generating Jets—Detailed Flow Measurements," AIAA Paper No. 2004-751.
[21] Gostelow, J. P., Walker, G. J., Solomon, W. J., Hong, G., and Melwani, N., 1997, "Investigation of the Calmed Region Behind a Turbulent Spot," ASME J. Turbomach., **119**, pp. 802–809.
[22] Schulte, V., and Hodson, H. P., 1998, "Prediction of the Becalmed Region for LP Turbine Profile Design," ASME J. Turbomach., **120**, pp. 839–846.
[23] Bons, J. P., Reimann, D., and Bloxham, M., 2008, "Separated Flow Transition on an LP Turbine Blade With Pulsed Flow Control," ASME J. Turbomach., **130**, p. 021014.
[24] Clark, J. P., 2007, Private Communication, Air Force Research Laboratory.
[25] Zhang, X. F., and Hodson, H., 2005, "Combined Effects of Surface Trips and Unsteady Wakes on the Boundary Layer Development of an Ultra-High-Lift LP Turbine Blade," ASME J. Turbomach., **127**, pp. 479–488.
[26] Bons, J. P., Pluim, J., Gompertz, K., Bloxham, M., and Clark, J. P., 2008, "The Application of Flow Control to an Aft-Loaded Low Pressure Turbine Cascade With Unsteady Wakes," ASME Paper No. GT2008-50864.
[27] Ibrahim, M., Kartuzova, O., and Volino, R. J., 2008, "Experimental and Computational Investigations of Separation and Transition on a Highly Loaded Low Pressure Turbine Airfoil: Part 1—Low Freestream Turbulence Intensity," ASME Paper No. IMECE2008-68879.
[28] Volino, R. J., Kartuzova, O., and Ibrahim, M., 2008, "Experimental and Computational Investigations of Separation and Transition on a Highly Loaded Low Pressure Turbine Airfoil: Part 2—High Freestream Turbulence Intensity," ASME Paper No. IMECE2008-68776.
[29] Volino, R. J., Kartuzova, O., and Ibrahim, M. B., 2009, "Experimental and Computational Investigations of Low-Pressure Turbine Separation Control Using Vortex Generator Jets," ASME Paper No. GT2009-59983.
[30] Wills, J. A. B., 1962, "The Correction of Hot-Wire Readings for Proximity to a Solid Boundary," J. Fluid Mech., **12**, pp. 388–396.
[31] Volino, R. J., 2005, "An Investigation of the Scales in Transitional Boundary Layers Under High Freestream Turbulence Conditions," Exp. Fluids, **38**, pp. 516–533.
[32] Fluent, Inc., 2005, FLUENT 6.3 User Guide.
[33] Kim, W. W., and Menon, S., 1997, "Application of the Localized Dynamic Subgrid-Scale Model to Turbulent Wall-Bounded Flows," AIAA Paper No. AIAA-97-0210.
[34] Kim, S.E., 2004, "Large Eddy Simulation Using Unstructured Meshes and Dynamic Subgridscale Turbulence Models," AIAA Paper No. AIAA-2004-2548.
[35] Ibrahim, M. B., Kartuzova, O., Doucet, D., and Volino, R. J., 2010, "LES Flow Control Simulations for Highly Loaded Low Pressure Turbine Airfoil (L1A) Using Pulsed Vortex Generator Jets," ASME Paper No. GT2010-23015.
[36] Piomelli, U., and Chasnov, J. R., 1995, "Large-Eddy Simulations: Theory and Applications," Turbulence and Transition Modeling, Lecture Notes From the ERCOFTAC/IUTAM Summer School, Stockholm, Jun. 12–20.
[37] Volino, R. J., and Ibrahim, M. B., 2010, "Separation Control on High Lift Low Pressure Turbine Airfoils Using Pulsed Jet Vortex Generator Jets," *Proceedings of ASME-ATI UIT Thermal and Environmental Issues in Energy Systems*, Vol. 1, pp. 273–278.

Effect of Unsteady Wakes on Boundary Layer Separation on a Very High Lift Low Pressure Turbine Airfoil

Ralph J. Volino
Department of Mechanical Engineering,
United States Naval Academy,
Annapolis, MD 21402-5042
e-mail: volino@usna.edu

Boundary layer separation has been studied on a very high lift, low pressure turbine airfoil in the presence of unsteady wakes. Experiments were done under low (0.6%) and high (4%) freestream turbulence conditions on a linear cascade in a low speed wind tunnel. Wakes were produced from moving rods upstream of the cascade. Flow coefficients were varied from 0.35 to 1.4 and wake spacing was varied from one to two blade spacings, resulting in dimensionless wake passing frequencies $F = fL_{j\text{-}te}/U_{ave}$ *(f is the frequency,* $L_{j\text{-}te}$ *is the length of the adverse pressure gradient region on the suction surface of the airfoils, and* U_{ave} *is the average freestream velocity) ranging from 0.14 to 0.56. Pressure surveys on the airfoil surface and downstream total pressure loss surveys were documented. Instantaneous velocity profile measurements were acquired in the suction surface boundary layer and downstream of the cascade. Cases were considered at Reynolds numbers (based on the suction surface length and the nominal exit velocity from the cascade) of 25,000 and 50,000. In cases without wakes, the boundary layer separated and did not reattach. With wakes, separation was largely suppressed, particularly if the wake passing frequency was sufficiently high. At lower frequencies the boundary layer separated between wakes. Background freestream turbulence had some effect on separation, but its role was secondary to the wake effect.* [DOI: 10.1115/1.4003232]

1 Introduction

Partial loss of lift and higher aerodynamic losses can be caused by boundary layer separation on low pressure turbine (LPT) airfoils (e.g., Hourmouziadis [1], Mayle [2], and Sharma et al. [3]). In aircraft engines the lower density and therefore lower Reynolds numbers at altitude can lead to a component efficiency drop of 2% between takeoff and cruise in large commercial transport engines and possibly as much as 7% in smaller engines operating at higher altitudes [4,5]. Separation can occur when airfoil loading is too high because of the strong adverse pressure gradients on the suction surface. High loading is, however, desirable since it can be used to reduce airfoil count, weight, and cost. The challenge is to design high lift airfoils, which do not have separation problems. This requires accurate prediction of suction side separation under relevant conditions.

Separation can be strongly affected by wakes shed from the airfoils in upstream stages in an engine. The velocity deficit and elevated turbulence in periodic wakes help to suppress separation and can cause a separated boundary layer to reattach. Hodson and Howell [6] described the mechanisms by which wakes promote reattachment, including the "negative jet," which results when the velocity deficit in the wake causes the flow outside the wake to accelerate and impinge on the surface, and the unsteadiness, which promotes transition in the boundary layer. Following the wake itself is a calmed period (Gostelow et al. [7] and Schulte and Hodson [8]) in which the boundary layer has low turbulence but is resistant to separation. Numerous studies have considered the wake effect in the LPT, including those listed in Hodson and Howell [6], and more recent references in Bons et al. [9] and Pluim et al. [10]. Examples include Schobeiri et al. [11], Öztürk and Schobeiri [12], Jiang and Simon [13], and Mahallati and Sjolander [14] who all used the Pack B airfoil. Zhang and Hodson [15] and Funazaki et al. [16] used more highly loaded airfoils. Many additional studies are available from these research groups and others.

Airfoils can be designed with high resistance to separation, as described by Praisner and Clark [17], and knowledge of wake effects allows for designs with higher loading than would be possible under steady inflow conditions. Even with wakes, however, a loading limit will always exist, above which separation will still occur.

In the present study, a very highly loaded airfoil that exhibits separation even in the presence of wakes is used. The airfoil, known as the L1A, was designed at the Air Force Research Laboratory (AFRL) and is available on a limited basis from Clark [18]. Dimensions of the L1A as used in the present study are given in Table 1. Based on the design calculations of Clark [18], the L1A has a Zweifel coefficient of 1.35, which corresponds to 10% higher loading than the "ultrahigh lift" airfoils described by Zhang and Hodson [19] and 17% higher loading than the Pack B airfoil. The L1A is aft loaded, which is advantageous for reducing secondary flow losses at the endwalls, but makes the boundary layer more prone to separation than a forward loaded blade, as documented in Bons et al. [9], Volino [20], Ibrahim et al. [21], and Volino et al. [22]. In cases without wakes and low Reynolds numbers, the boundary layer separates and does not reattach, in spite of transition to turbulence in the shear layer over the separation bubble. This result contrasts with the results of studies on less aggressive airfoils (e.g., Volino [23]), which all showed reattachment after transition. The separation bubble on the L1A is about four times thicker than that on the Pack B. The larger distance from the shear layer to the wall on the L1A apparently prevents the turbulent mixing in the shear layer from reaching the wall and causing reattachment. The failure of the boundary layer to reattach

Contributed by the International Gas Turbine Institute (IGTI) of ASME for publication in the JOURNAL OF TURBOMACHINERY. Manuscript received September 3, 2010; final manuscript received October 23, 2010; published online May 26, 2011. Editor: David Wisler.

Table 1 Cascade parameters

Axial chord, C_x (mm)	True chord (mm)	Pitch, L_ϕ (mm)	Span (mm)	Suction side, L_s (mm)	Inlet flow angle (deg)	Exit flow angle (deg)
134	146	136	724	203	35	60

results in a 20% loss in lift and increases profile losses by up to a factor of 7. At higher Reynolds numbers the separation bubble closes, and for Re > 200,000 the separation bubble is small and the boundary layer is attached over most of the airfoil.

The effect of wakes on the L1A boundary layer was studied by Bons et al. [9], who considered a case with Re=50,000 (based on the suction surface length and the nominal exit velocity from the cascade), background freestream turbulence TI=3%, and periodic wakes produced with moving rods upstream of the airfoils. The dimensionless frequency of the wake passing was $F=fL_{j\text{-}te}/U_{\text{ave}}=0.34$, where $L_{j\text{-}te}$ is the length of the adverse pressure gradient region on the suction surface and U_{ave} is the average freestream velocity over this distance. The length $L_{j\text{-}te}$ is also the distance from a row of vortex generator jet (VGJ) holes to the trailing edge. Pulsed vortex generator jets were used by Bons et al. [9] and Volino et al. [24] to control separation on the L1A. Although these jets are not considered in the present work, the same dimensionless frequency, F, is used to describe the wake passing in the present study and the jet pulsing in Refs. [9,24]. Bons et al. [9] found that wakes reduced the separation bubble thickness significantly and reduced total pressure losses by more than 50%, but did not cause boundary layer reattachment. This result contrasts with earlier work on less aggressive airfoils (e.g., Reimann et al. [25] on the Pack B), which showed reattachment for at least part of the wake passing period or a reduction in bubble size in cases with already reattached boundary layers (e.g., Schobeiri et al. [11]). The much thicker separation bubble on the L1A prevents the mixing associated with the wake from penetrating all the way to the airfoil surface and causing full reattachment.

In the present study, the effect of wakes is considered with Re=25,000 and 50,000 under low (0.6%) and high (4%) freestream turbulence conditions. Cases with various wake passing frequencies and flow coefficients are documented. Surface pressure distributions, total pressure loss profiles, and instantaneous boundary layer velocity measurements are used to explain the mechanism by which the wakes affect separation.

2 Experimental Facility and Measurements

Experiments were conducted in a closed loop wind tunnel with a seven blade linear cascade, as shown in Fig. 1. A fine screen located upstream of the cascade is used to break up the boundary layers that form upstream of the test section and to provide uniform inlet conditions to the cascade. The freestream turbulence entering the cascade was measured with a cross-wire probe positioned just upstream of the center blade. The turbulence intensities are 0.8% in the streamwise component and 0.5% in the cross stream components. The integral length scale of the streamwise component is 6.3 cm. To produce high freestream turbulence, the screen is replaced with a coarse grid, consisting of a 1.5 mm thick sheet metal plate with 19 mm square holes spaced 25.4 mm apart, center to center, in both directions. In a plane perpendicular to the inlet flow and $1.7C_x$ upstream of the center blade, the grid produced uniform flow with TI=6.0% in the streamwise component and 4.2% in the cross stream components for an overall intensity of 4.9%. The streamwise component was also measured at the inlet plane of the cascade in the four center passages, where it had decayed to between 4% and 4.2% between blades B2 and B5 and 4.6% between blades B5 and B6. Downstream of the cascade, the

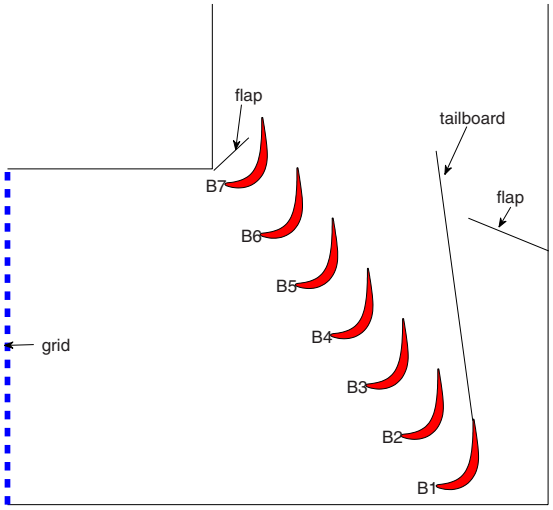

Fig. 1 Schematic of linear cascade

local TI is 1.8% across all passages, as documented in Volino et al. [22]. The local freestream turbulence intensity in the passage at the beginning of the adverse pressure gradient region is 1.4%. The change in TI through the passage is due mainly to the change in the local freestream velocity along with some decay of the turbulence. The upstream integral length scales of the freestream turbulence are $0.12C_x$ in the streamwise component and $0.04C_x$ in the other components. Further details of the facility and inlet flow are in Volino et al. [22].

A tailboard, shown in Fig. 1, is needed to produce the correct exit flow angle from the cascade. Its position was set to produce periodicity at high Reynolds numbers. A tailboard on the opposite side of the cascade and inlet guide vanes were found to be unnecessary. To produce the correct approach flow to the end blades (B1 and B7), the amount of flow escaping around the two ends of the cascade is controlled with the flaps shown in Fig. 1. The inlet flow angle was checked with a three-hole pressure probe and found to agree with the design angle to within 2 deg of uncertainty. Good periodicity at high Reynolds numbers was obtained in the exit flow. At low Reynolds numbers, when significant separation bubbles are present, the periodicity is not as good due to suppression of the separation bubble thickness on the blades closest to the tailboard. In cases where wakes or other flow control suppress separation, periodicity is reestablished. The lack of periodicity in cases with large separation bubbles is considered acceptable since the focus of the research is separation control, and not documentation of cases with large separation that would be unacceptable in practice. This compromise facilitates the study of a larger number of cases by obviating the need to adjust the tailboard by trial and error for each case. It also provides for better repeatability in the experiments since the position of the tailboard is fixed for all cases. Any changes in separation with wakes will be larger in practice than documented in the experiment due to the effect of the tailboard in suppressing the bubble size in the no-wake cases.

The wake generator includes a chain near each endwall of the cascade that passes $0.54C_x$ upstream of the leading edges of the cascade blades. The chains then pass downstream around blade B7 on the inside turn of the cascade and pass well downstream of the cascade before returning upstream around blade B1 on the outside turn of the cascade. This completes the chain circuit. A traverse for probe movement is located within the chain circuit downstream of the blade row. Each chain is driven by a drive gear and also passes around six idler sprockets. One of the idler sprockets is adjustable to maintain tension in the chain. The drive

Table 2 Velocity profile measurement stations

Station	1	2	3	4	5	6
s/L_s	0.53	0.59	0.69	0.78	0.88	0.97
x/C_x	0.65	0.72	0.80	0.86	0.92	0.97

gears for the upper and lower chains are on a common axle and driven by a single electric motor so both chains move in unison. The motor speed is set with a variable frequency inverter. The chain links have hollow pins, through which the wake generator rods are attached. Each rod consists of a 4 mm diameter carbon fiber tube with a steel pin attached at each end. The steel pins are inserted through the holes in the upper and lower chains, and then secured with small clips. Tests were run with average distances between rods of 136 mm, 221 mm, and 272 mm, which correspond to $1L_\phi$, $1.6L_\phi$, and $2L_\phi$, where L_ϕ is the blade spacing in the cascade. These ratios of rod to blade spacing are in the range expected for vane to rotor blade spacing in an engine.

The ratio of the rod diameter to the axial chord is 0.03, which is consistent with the wake generators of Bons et al. [9] and Funazaki et al. [16]. The rods are smaller than those of Kaszeta et al. [26] who had a diameter to chord ratio of 0.06. The present rods are larger than those of Schobeiri et al. [11] and Zhang and Hodson [15] who had rod diameter to chord ratios of about 0.01. In the present study, as in Bons et al. [9] and Kaszeta et al. [26], the rod wakes are intended to simulate the wakes of very highly loaded airfoils under low Reynolds number conditions with thick boundary layers and in some cases large separation bubbles. A large diameter rod is therefore needed to simulate an airfoil wake with a large velocity deficit. The studies using smaller diameter rods were done at higher Reynolds numbers, so separation bubbles were smaller and rods producing lower velocity deficits were more appropriate.

For most tests, the rods were driven at a velocity of 1.18 times the cascade inlet velocity, U_i. This gives a flow coefficient $\zeta = U_i \cos(\alpha_i)/U_{\text{rod}} = 0.7$, where α_i is the inlet flow angle. This is in the expected range for an engine. The timing of the wake generator is recorded with an infrared photodetector, which senses the passage of each rod and emits a voltage that is recorded simultaneously as other data are acquired, allowing phase averaging of the results.

2.1 Measurements. The center blade, designated B4 in Fig. 1, contains pressure taps near the spanwise centerline. Pressure surveys are made using a pressure transducer (0–870 Pa range Validyne transducer). Stagnation pressure is measured with a pitot tube upstream of the cascade and wake generator. The uncertainty in the suction side pressure coefficients, C_p, is 0.07. Most of this uncertainty is due to bias error. Stochastic error is minimized by averaging pressure transducer readings over a 10 s period.

Total pressure losses are documented using a Kiel probe traversed across three blade spacings, $0.63C_x$ downstream of the cascade. A traverse is located in the wind tunnel downstream of the cascade to move the probe. The traverse causes an acceptably low blockage when it is located at least two C_x downstream of the cascade.

Pressure and loss surveys were acquired at nominal Re = 25,000 and 50,000. The Reynolds number, as defined above, is based on the suction surface length and the nominal cascade exit velocity. The corresponding Reynolds numbers based on the cascade inlet velocity and the axial chord length are 10,000 and 20,000.

Velocity profiles on the suction surface were measured at the six streamwise stations listed in Table 2. All stations are downstream of the inviscid pressure minimum at $s/L_s = 0.49$. Profiles were acquired near the spanwise centerline of the airfoil with a hot-wire anemometer (AA Lab Systems model AN-1003) and a

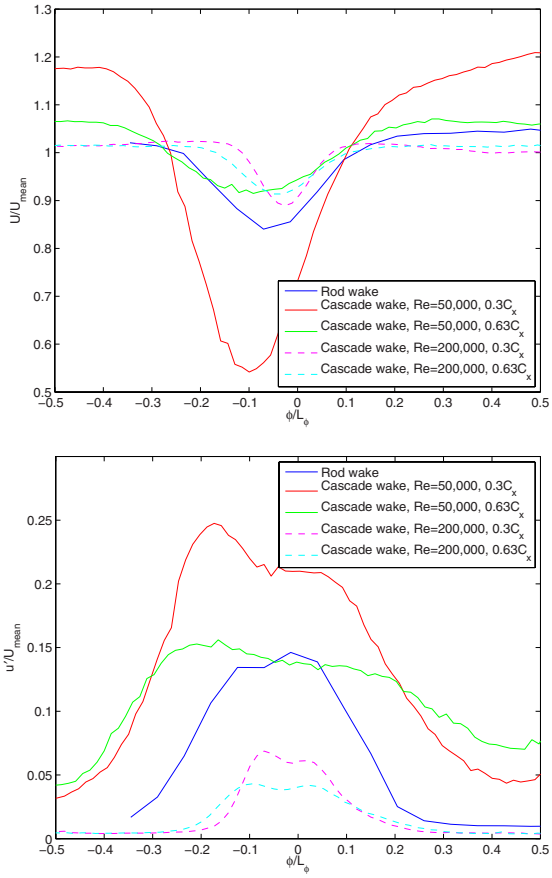

Fig. 2 Velocity in wakes of wake generator rods and cascade wakes with low TI: (*a*) mean and (*b*) rms

single-sensor hot-film probe (TSI model 1201-20). The sensor diameter is 51 μm, and the active length is 1.02 mm. At each measurement location, data were acquired for 26 s at a 20 kHz sampling rate (2^{19} samples). All raw data were saved. The high sampling rate provides an essentially continuous signal, and the long sampling time results in low uncertainty in both statistical and spectral quantities. Data were acquired at 40 wall normal locations in each profile, extending from the wall to the freestream, with most points concentrated in the near-wall region. The probe was positioned as close to tangent to the airfoil surface as possible at each station, such that the probe body extended downstream of the sensor and the direction of the traverse was within 5 deg of normal to the surface. In most cases the closest point to the wall in each profile was within about 0.2 mm of the wall, which compares to boundary layer thicknesses ranging from 1.1 mm to over 40 mm.

Flow direction in a separation bubble cannot be determined with a single-sensor hot-wire, but velocity magnitude can be measured and was found to be near zero within the bubbles of the present cases when the flow was laminar. In cases where the flow became turbulent but remained separated, fluctuating velocities caused false high mean velocity readings in the separation bubble. With the exception of these turbulent separated cases, the uncertainty in the mean velocity is 3–5% except in the very near-wall region, where near-wall corrections (Wills [27]) were applied to the mean velocity.

Velocity was also measured downstream of the cascade along the same line used for the total pressure loss measurements.

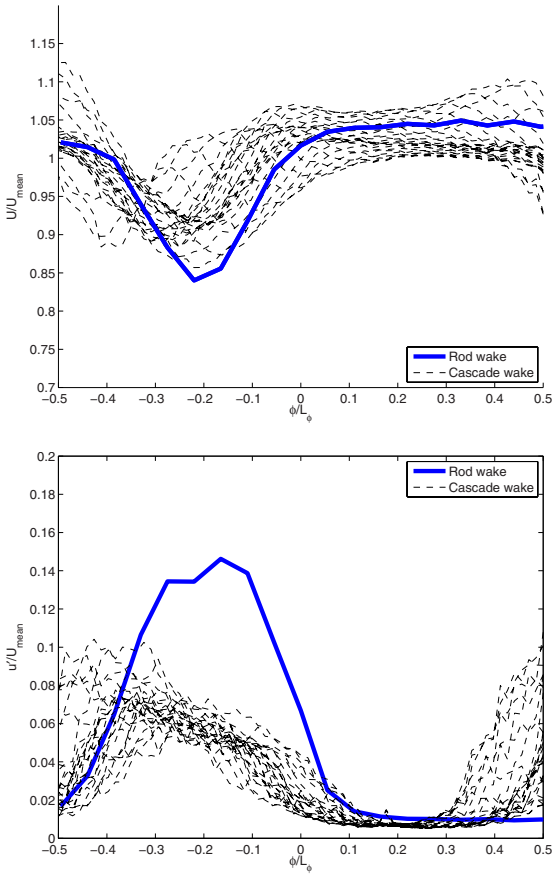

Fig. 3 Velocity in wakes of wake generator rods and phase averaged velocity in wakes of cascade blades for low TI, Re =50,000 case with VGJ flow control [24]: (*a*) mean and (*b*) rms

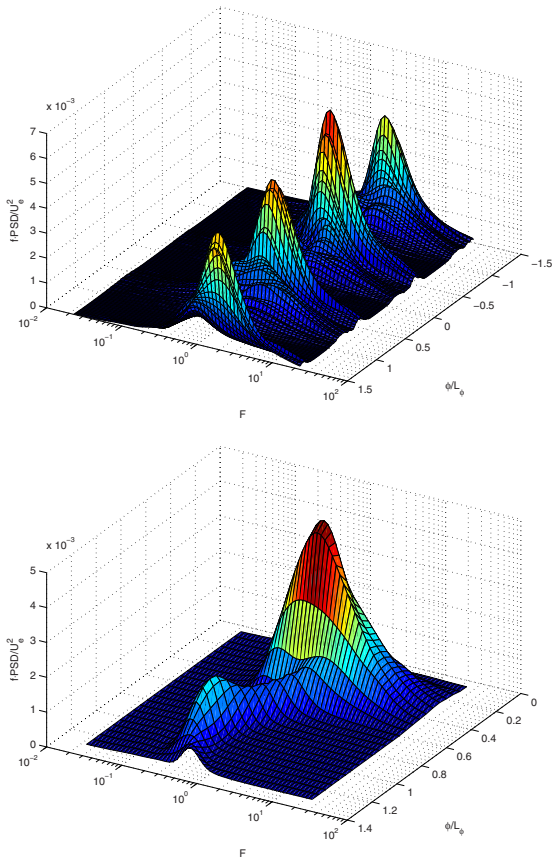

Fig. 4 Wavelet spectra of wake velocity: (*a*) cascade blades for low TI, Re=50,000 case with VGJ flow control [24] and (*b*) wake generator rods

Downstream and boundary layer velocity data were both time averaged and ensemble averaged based on the phase within the wake passing period. Phase averages of mean and fluctuating velocity are shown below at 24 dimensionless times, t/T, within the wake passing period, where t is time and T is the period between wakes.

3 Results

3.1 Wake Characteristics. Several studies have compared rod wakes to airfoil wakes. Schobeiri et al. [28] discussed the theory for describing wake flows. Pfeil and Herbst [29] showed that the far wake of an airfoil has almost the same wake as a cylinder having the same drag, although the rods have no means of matching the correct potential field of adjacent blade rows [30,31]. Pluim et al. [10] tested rods of various shapes and provided references to earlier studies. They found that the wakes from wedge shaped rods agreed best with L1A airfoil wakes, but cylindrical rods also provided a reasonable approximation. Figure 2 shows the mean and rms fluctuating streamwise velocity in the wakes of the moving rods and the cascade blades of the present study. The cascade wakes were measured by traversing a hot-wire probe in lines $0.3C_x$ and $0.63C_x$ downstream of the trailing edges of the blades perpendicular to the axial direction. The variable ϕ denotes the distance across the cascade. The origin, $\phi=0$, is directly downstream of the center blade (B4) in the design flow direction, while $\phi/L_\phi=-1$ and 1 are downstream of blades B3 and B5, respectively. The spacing between airfoil rows in an engine is expected to be about $0.3C_x$ according to Pluim et al. [10], so this location would be where the wake from an upstream airfoil would reach the leading edge of the next row. The moving rod wakes were measured by placing a stationary hot-wire midway between blades B4 and B5 in the plane of the leading edges. The moving rods traversed $0.54C_x$ upstream of the hot-wire. The data from the probe were phase averaged on the rod passing cycle to determine the mean and fluctuating velocity as functions of time. For comparison in the figures, the rod velocity was then used to convert time to distance traversed. Curves in the figures were shifted along the horizontal axis to align the peaks for comparison. All curves were normalized using the average local mean velocity.

The wakes from the upstream rods, when shown in dimensionless form as in Fig. 2, did not depend on Reynolds number. For all of the flow and rod velocities considered, the Reynolds number based on rod diameter is between about 400 and 2000, which should result in laminar separation for the boundary layer on the rod and similar wakes for all cases. The wake for low TI, Re =50,000, $\zeta=0.7$, $1.6L_\phi$ rod spacing, and dimensionless wake passing frequency of $F=0.28$ is shown. In contrast to the rod wakes, the wakes of the cascade airfoils depend strongly on Reynolds number, as shown in Volino [20]. Due to a large separation bubble, the airfoil wake at Re=50,000 has a large mean velocity deficit at $0.3C_x$, which decreases 80% in peak magnitude by $0.63C_x$. The peak turbulence intensity drops by 40% over this

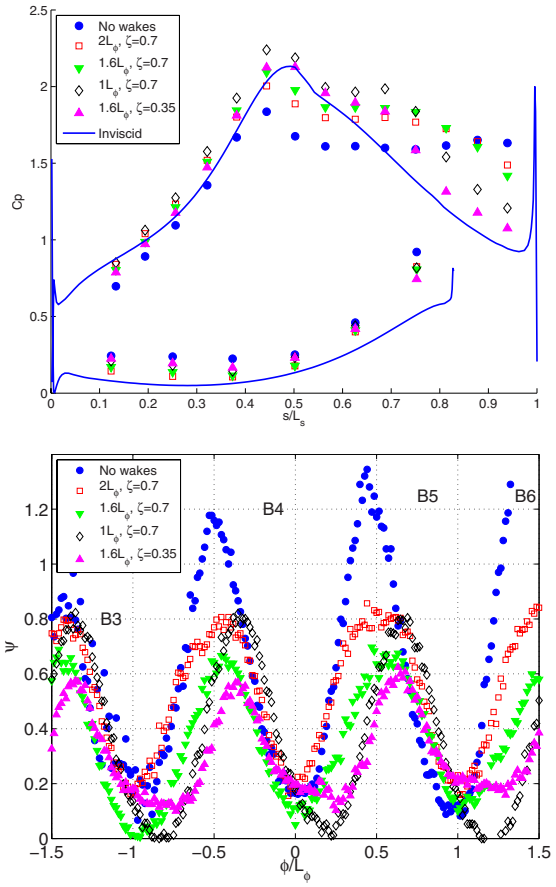

Fig. 5 Pressure profiles for low TI, Re=25,000 cases: (*a*) C_p and (*b*) total pressure loss

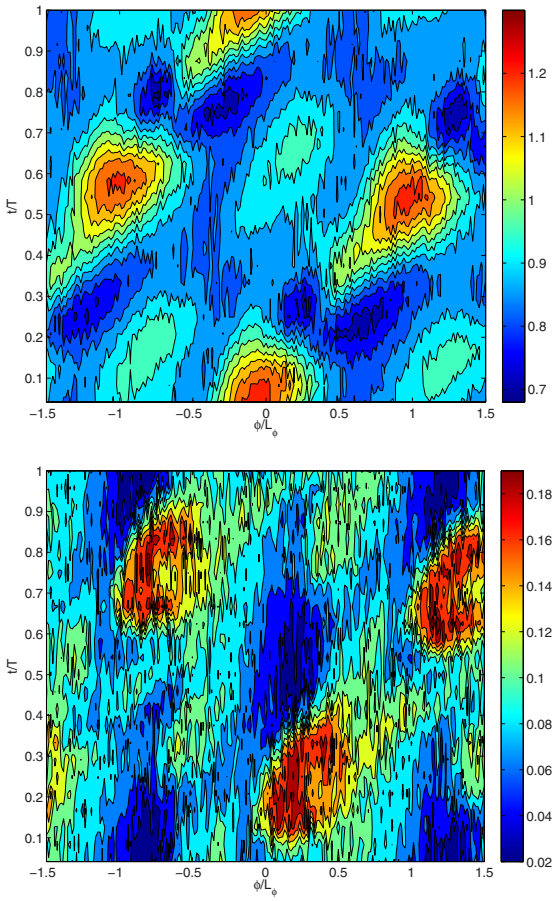

Fig. 6 Time-space plot of phase averaged velocity $0.63C_x$ downstream of cascade for low TI, Re=25,000, ζ=0.7, and $2L_\phi$ rod spacing: (*a*) U/U_e and (*b*) u'/U_e

distance. At Re=200,000 the boundary layer remains attached, so the airfoil wake is about half as wide as at the lower Re, and the peak velocity deficit is about 25% as large. The peak turbulence intensity is 7%, which is about a third that at the lower Re. The change in the wake between $0.3C_x$ and $0.63C_x$ is much smaller than at the lower Re. The rod wake lies between the high and low Re airfoil wakes. Its peak turbulence intensity is 14%. The velocity deficit and turbulence level in the rod wakes in Fig. 2 appear to be reasonable approximations for an airfoil wake, although they do not fully match either the high or low Re case. One could conceivably use a rod of either larger or smaller diameter to match the low or high Re airfoil cases better. In cases with high freestream turbulence, the rod wakes are nearly the same as those in Fig. 2, with 14% peak turbulence intensity. The only difference is between the wakes, where the background turbulence rises to 4% with high TI.

The cases of the present study will be used for comparison to future cases with wakes and vortex generator jet flow control. Figure 3 compares the upstream rod wake to the airfoil wake in a case with Re=50,000 and pulsed VGJ blowing with $F=0.56, 10\%$ duty cycle and blowing ratio (jet velocity/freestream velocity) equal to 1. The VGJs provided good flow control in this case. The boundary layer separates very briefly but reattaches. Further details are available in Volino et al. [24]. For the airfoil wake in Fig. 3, the phase averaged results at 24 phases through the VGJ pulsing cycle are shown. Since the boundary layer approaches separation during part of the cycle, the wake velocity profile magnitude and position change somewhat during the cycle. The mean velocity deficit and wake width of the upstream rod and airfoil are about the same. The peak turbulence intensity in the rod wake is about 40% higher than the highest value in the airfoil wake.

Turbulence spectra provide additional information about the wakes. Spectra of the fluctuating streamwise velocity were computed for the cascade airfoil wakes and the rod wakes. Without flow control, the airfoil wakes at Re=50,000 exhibit sharp, high amplitude, low frequency ($F=0.7$) peaks associated with the shedding frequency of the separation bubble. With Re=200,000, the amplitude of the peaks is about two orders of magnitude lower than at the lower Re, and the peaks are broad banded and centered at $F=2.5$. These peaks are likely associated with the turbulence in the airfoil boundary layers. The spectra of the upstream rod wakes have amplitude and frequency between the high and low Re cases, agreeing most closely with the Re=50,000 VGJ controlled case mentioned above. Figure 4 shows wavelet spectra (computed as described in Volino [32] using the Mexican Hat wavelet) for the airfoil and rod wakes. Power spectral density premultiplied by frequency is shown as a function of dimensionless frequency and distance across the cascade. One representative phase within the VGJ pulsing cycle is shown for the airfoil wake. As in Figs. 2 and 3, time is converted to position for the rod wake. For the airfoil wake there is a large peak at $F=1.8$ with a magnitude of 0.0052 and a smaller peak at $F=0.6$ with a magnitude of 0.0029 that is hidden behind the larger peak in Fig. 4(*a*). The magnitude of the

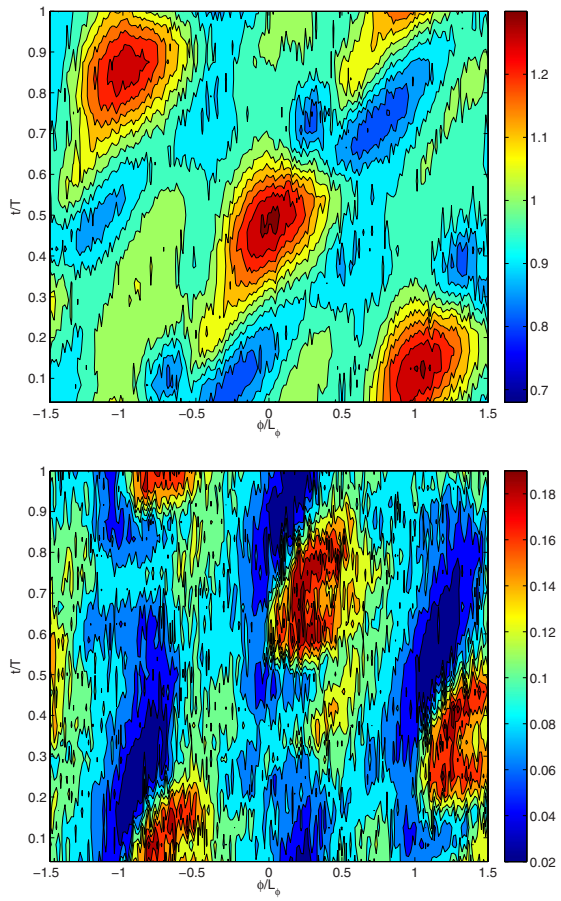

Fig. 7 Time-space plot of phase averaged velocity $0.63C_x$ downstream of cascade for low TI, Re=25,000, ζ=0.7, and $1.6L_\phi$ rod spacing: (*a*) U/U_e and (*b*) u'/U_e

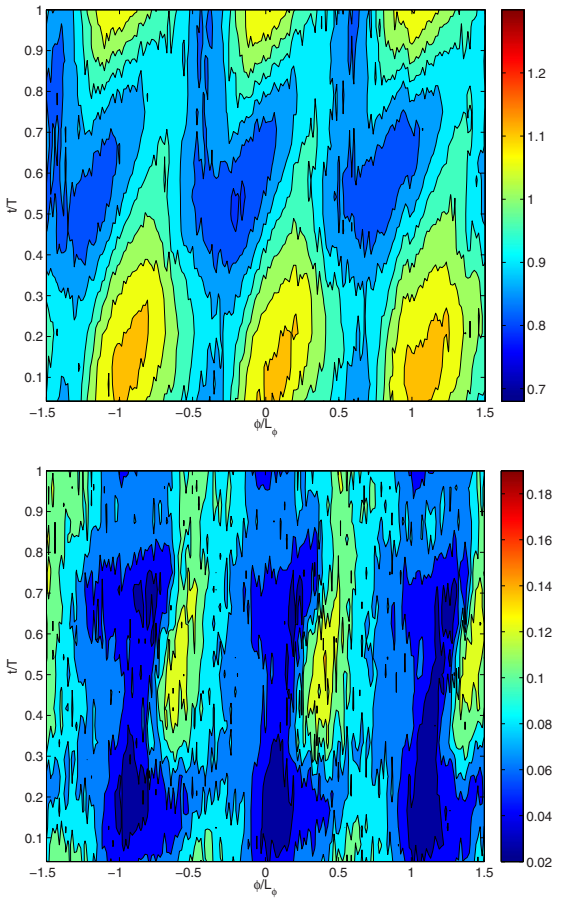

Fig. 8 Time-space plot of phase averaged velocity $0.63C_x$ downstream of cascade for low TI, Re=25,000, ζ=0.7, and $1L_\phi$ rod spacing: (*a*) U/U_e and (*b*) u'/U_e

two peaks varies during the VGJ cycle. The rod wake has a large peak at F=0.8 with a magnitude of 0.0047 and a smaller peak at F=0.2 with a magnitude of 0.0016. Figures 2–4 show that the velocity deficit, turbulence intensity, and spectral content are of the same order for the airfoil and rod wakes, although the agreement with any one case is not perfect. Since the wake of an upstream airfoil will not necessarily match exactly the wake of the airfoil on which it impinges, the present rod wakes are considered to provide a reasonable approximation to the wakes that might be shed from an upstream blade row at low Reynolds numbers.

3.2 Low TI

3.2.1 Re=25,000. The C_p and total pressure loss profiles for cases with Re=25,000 and low TI are shown in Fig. 5. The inviscid C_p profile for the L1A airfoil is shown for comparison. The low peak followed by a plateau in the case without wakes indicates separation without reattachment. For the cases with ζ=0.7, decreasing the rod spacing from $2L_\phi$ to $1L_\phi$ (which corresponds to increasing the wake passing frequency F from 0.22 to 0.45) causes C_p to approach the inviscid line and reduces the loss by over 40% compared with the no-wake case. The wakes also cause the loss peaks to shift to the right in Fig. 4(*b*), indicating greater flow turning resulting from a thinner separation bubble. The greater turning agrees with a 20% increase in lift indicated by the C_p profiles. Also shown in Fig. 5 is a case with $1.6L_\phi$ rod spacing and the rod speed and F doubled so ζ=0.35. The higher wake passing frequency helps to reduce the separation.

Figures 6–9 show time-space plots of the phase averaged mean and fluctuating velocity $0.63C_x$ downstream of the blade row for the cases of Fig. 5. The contours are normalized by the exit velocity U_e. In Fig. 6, the rod spacing is $2L_\phi$, so the flow in alternating passages is in phase, with the passages between a half cycle out of phase. The turbulence (Fig. 6(*b*)) shows vertical strips of moderately high fluctuations at ϕ/L_ϕ=−1.5, −0.5, 0.5, and 1.5 associated with the airfoil wakes. These positions correspond to the loss peaks in Fig. 5(*b*). Between these peaks the fluctuation levels range from very low (corresponding to the low background TI) to high when the rod wakes pass. The rod wakes proceed at an angle in the figure, rising from left to right, as they move forward in time and transit across the cascade. The highest turbulence peaks occur where the rod wakes interact with the separation bubble and airfoil wakes. At the position and time of each rod wake peak in the turbulence is a corresponding velocity deficit in the mean velocity (Fig. 6(*a*)). Following the velocity deficit is a mean velocity maximum as the flow accelerates after the wake passes. In Fig. 7, the rod spacing is reduced to $1.6L_\phi$. All passages are out of phase with each other, and the peaks are stretched along the time axis compared with Fig. 6 since the rod speed is the same but the wake passing period is shorter. In Fig. 8, the rod and blade spacing are equal, so all passages are in phase with each other. The wake passing frequency is high enough that there is little time for the boundary layer to separate between wakes. This reduces

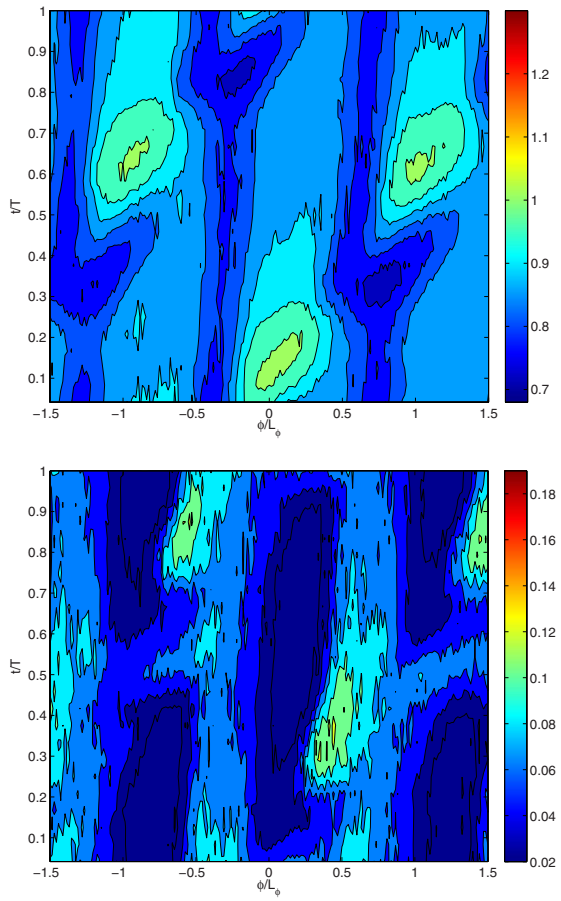

Fig. 9 Time-space plot of phase averaged velocity $0.63C_x$ downstream of cascade for low TI, Re=25,000, ζ=0.35, and $1.6L_\phi$ rod spacing: (*a*) U/U_e and (*b*) u'/U_e

the peak turbulence level. There is still a mean velocity deficit associated with each rod wake followed by a velocity rise, but the difference between the minima and maxima is reduced since suppression of the separation bubble reduces the flow unsteadiness. Figure 9 shows the effect of increasing the rod speed. Again, the increased wake passing frequency helps to suppress the separation and reduce unsteadiness.

Figure 10 shows time averaged mean and fluctuation velocity

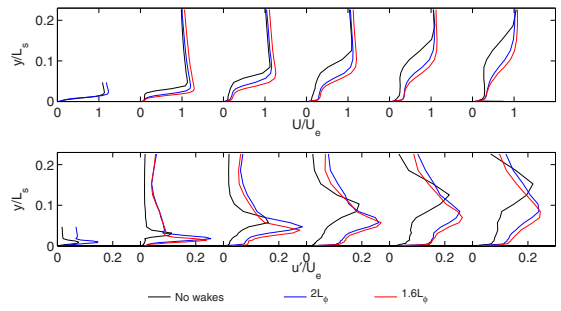

Fig. 10 Time averaged velocity profiles at six streamwise stations for low TI, Re=25,000, and ζ=0.7 cases: top—mean and bottom—rms

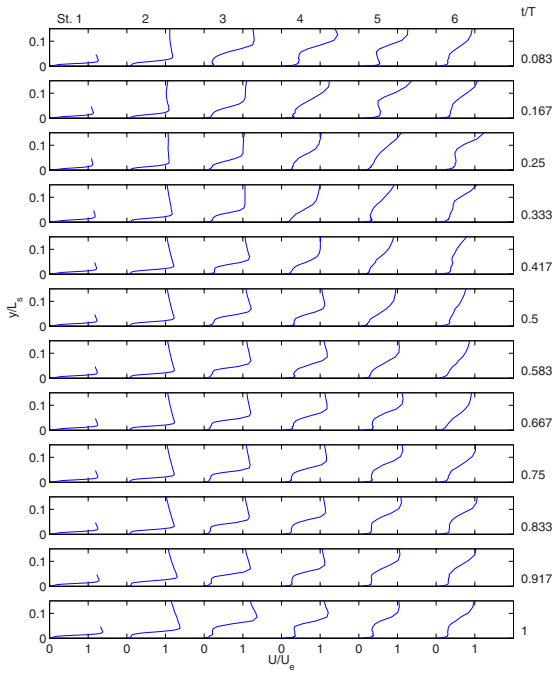

Fig. 11 Phase averaged mean velocity profiles for low TI, Re =25,000, ζ=0.7, and $2L_\phi$ rod spacing; columns for six streamwise stations; rows for phases in wake cycle

profiles at the six streamwise stations of Table 2. Without wakes the separation bubble is very thick, and the peak fluctuating velocity is in the shear layer over the bubble. As shown in Volino [20], the shear layer does transition to turbulent between stations 3 and 4, but this does not cause reattachment. Wakes with rod spacing of $2L_\phi$ and $1.6L_\phi$ reduce the separation bubble thickness by about half, but do not eliminate it. Figure 11 shows phase averaged mean velocity for the $2L_\phi$ spacing case. The six columns correspond to the six streamwise stations, and the rows correspond to different phases in the wake passing cycle. The boundary layer separates with a very thin bubble at station 2 that becomes thicker at the downstream stations at most phases. The bubble appears as a region of nearly constant, but nonzero velocity near the wall. The nonzero velocity is an artifact of the hot-wire sensor's inability to distinguish flow direction and the turbulent fluctuations within the bubble. There is also a period of attached flow at each station where the velocity far from the wall is somewhat lower than at other phases and the near-wall velocity more smoothly approaches zero, as fluid from the outer flow fills in the region near the wall when the separation bubble collapses. The reattachment occurs at t/T=0.125–0.25, t/T=0.167–0.333, t/T =0.25–0.458, t/T=0.375–0.583, and t/T=0.458–0.708 at stations 2–6, respectively.

More results for the low TI, Re=25,000 cases are shown in Fig. 12 as contour plots of the phase averaged velocity at different phases within the wake passing cycle. The vertical axis shows distance from the wall and the horizontal axis shows distance along the suction surface. The first and third rows in each case show mean velocity, and the second and fourth rows show the corresponding fluctuating velocity. Figure 12(*a*) shows the same case as Fig. 11. The effect of the rod wake appears in the mean velocity as elevated freestream velocity at t/T=0.958. The location of high freestream velocity is farther downstream at t/T =0.042 and reaches the trailing edge at about t/T=0.292. During

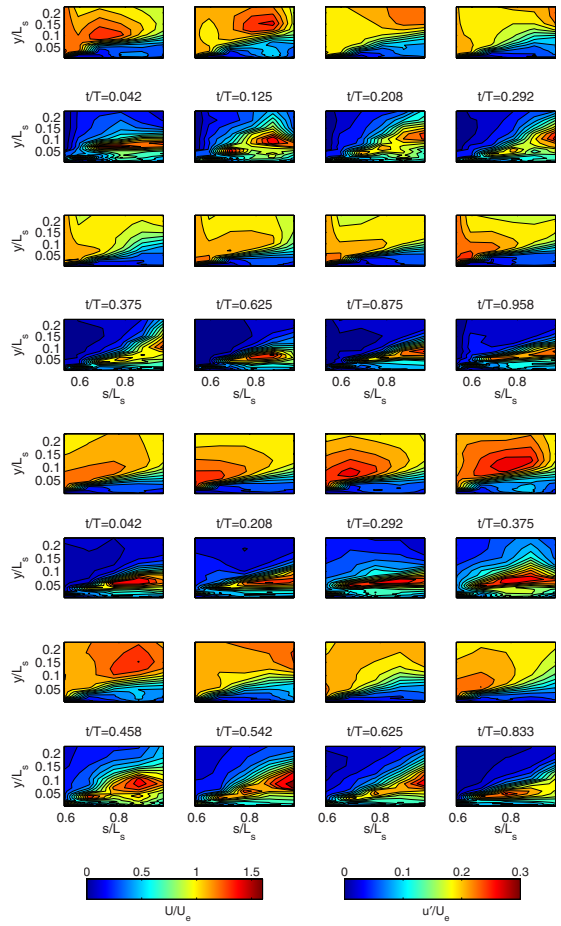

Fig. 12 Phase averaged mean (rows 1 and 3) and rms streamwise fluctuating (rows 2 and 4) velocity for low TI, Re=25,000, and ζ=0.7: (*a*) $2L_\phi$ rod spacing and (*b*) $1.6L_\phi$ rod spacing

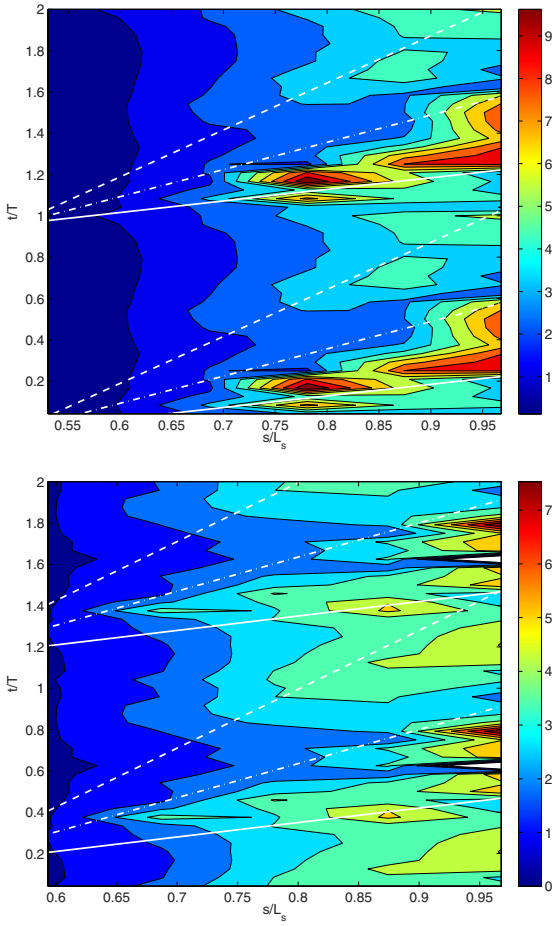

Fig. 13 Phase averaged momentum thickness for low TI, Re =25,000, and ζ=0.7: (*a*) $2L_\phi$ rod spacing and (*b*) $1.6L_\phi$ rod spacing; lines show leading edge (solid) and trailing edge (dashed-dotted) of wake, and trailing edge of the calm region (dashed)

this time the boundary layer remains thick, as shown by the dark (blue) color in the figure, but the near-wall velocity is slightly elevated (lighter shade). The higher near-wall velocity corresponds to the attached profiles at these phases in Fig. 11. As the wake passes, the fluctuating velocity rises in the freestream and near the wall. Between t/T=0.375 and 0.625 the boundary layer relaxes to an undisturbed, separated state, and then continues in this state until the next wake arrives. Figure 12(*b*) shows results with the wake spacing reduced to $1.6L_\phi$. The wake passing is similar to that in Fig. 12(*a*), but the dimensionless duration of the wake passing is longer since the wake travels at the same velocity but the period is shorter. This results in less time for recovery between wakes.

Figure 13 presents another view of the wake passing effect as time-space plots of momentum thickness. The horizontal axis shows distance along the suction surface and the vertical axis shows dimensionless time. The data are repeated for two cycles to show the periodicity in time. The white lines in the figure show the approximate location of the wake and the calmed region following the wake. The leading edge of the wake affected region in the boundary layer travels at about the freestream velocity, while the trailing edges of the wake and calmed regions move at about 50% and 30% of the freestream velocity, respectively. These convection velocities agree with values in the literature, such as those reported by Stieger and Hodson [33] and Zhang and Hodson [15].

Momentum thickness is shown since it is proportional to losses in the boundary layer. Plots of other quantities such as the shape factor also show the wake and calmed regions, as shown in Stieger and Hodson [33]. In Fig. 13(*a*), the wake causes a strip of elevated momentum thickness corresponding to the reattachment and elevated near-wall turbulence in Figs. 11 and 12(*a*). The periods of high momentum thickness and turbulence produce the high turbulence peaks observed in the airfoil wake in Fig. 6. In Fig. 13, during the early part of the calmed period the momentum thickness is slightly suppressed compared with the value between wake events. During the calmed period the disturbance has already passed, as shown in Fig. 12(*a*), but the boundary layer remains attached, as shown in Fig. 11. Figure 13(*b*) shows results with $1.6L_\phi$ wake spacing. As in Fig. 13(*a*), the momentum thickness increases as the wake passes and is reduced in the calm region. With less time for recovery between wakes, the variation in momentum thickness is lower in Fig. 13(*b*).

The present results are similar to those in other studies with wakes, such as Schobeiri et al. [11] and Zhang and Hodson [15]. In those studies the boundary layer reattached even without wakes, and the passing wake caused a reduction in the separation bubble size. In the present study, because the Reynolds numbers are lower and the pressure gradients are stronger, the boundary layer only intermittently reattaches as the wake passes. There are

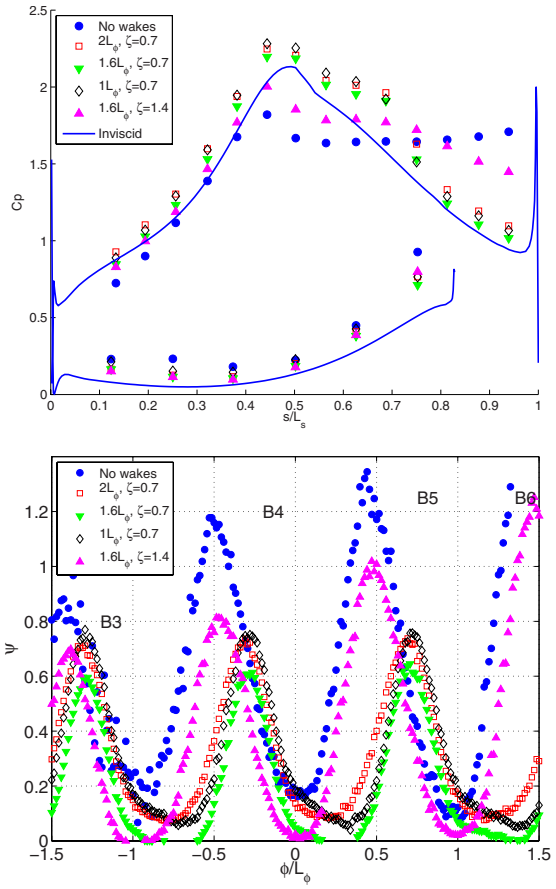

Fig. 14 Pressure profiles for low TI and Re=50,000 cases: (*a*) C_p and (*b*) total pressure loss

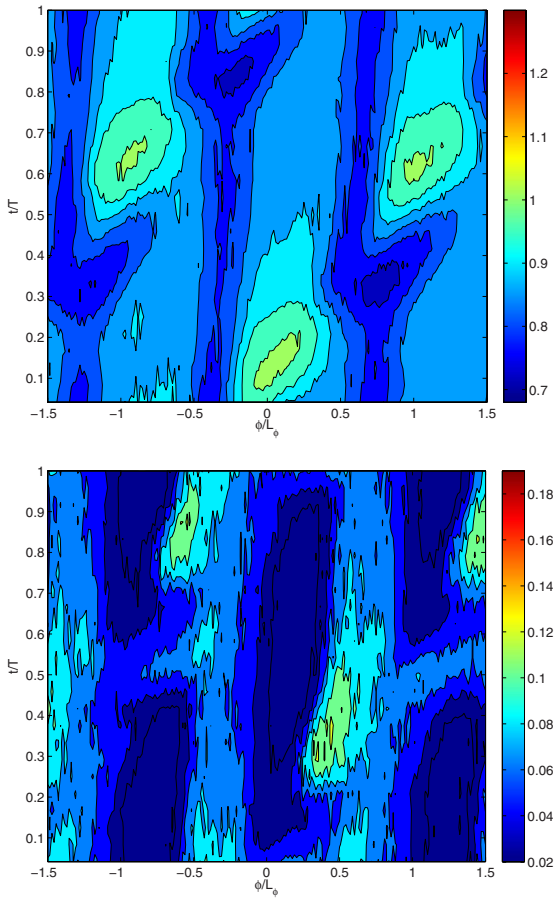

Fig. 15 Time-space plot of phase averaged velocity $0.63C_x$ downstream of cascade for low TI, Re=50,000, ζ=0.7, and $2L_\phi$ rod spacing: (*a*) U/U_e and (*b*) u'/U_e

several mechanisms by which wakes could induce reattachment. The elevated freestream turbulence in the wake will cause transition to move upstream in the shear layer, and if transition occurs before the separation bubble becomes too thick, the turbulent mixing could extend close enough to the wall to cause reattachment. Volino et al. [22] showed, however, that elevated background turbulence alone did not cause reattachment on the L1A at Re =25,000. The upstream turbulence intensity in the wake is 14%, as documented above, but as the flow is accelerated through the passage, this local intensity drops to about 3% at the beginning of the adverse pressure gradient region. Separated flow transition correlations, such as those of Roberts and Yaras [34] and Volino and Bohl [35], indicate that a rise to 3% TI would cause transition to shift upstream by about $0.06L_s$, which may not be enough to explain the full wake effect on reattachment. Other effects of wakes are explained in detail by Stieger and Hodson [33] and Zhang and Hodson [15], who used instantaneous velocity field measurements to document negative jets resulting from temporal freestream acceleration and rollup vortices in the shear layer that caused reattachment. These are likely the same mechanisms responsible for reattachment in the present study.

3.2.2 Re=50,000. Pressure results for low TI cases with Re =50,000 are shown in Fig. 14. Without wakes the shear layer does not reattach, as in the Re=25,000 case. With wakes and ζ=0.7, reattachment is clear for all rod spacings and losses are reduced by over 40%. With the rod speed reduced to ζ=1.4 (F reduced to 0.14), only partial reattachment is observed. Wake velocity is shown in Figs. 15–17 for the ζ=0.7 cases with rod spacings of $2L_\phi$, $1.6L_\phi$, and $1L_\phi$, respectively. The airfoil wakes, appearing as vertical strips of low mean velocity and about 7% turbulence, are in the expected positions based on the loss peaks of Fig. 14(*b*). There is some rise in the magnitude of the turbulence to about 10% when the airfoil and rod wakes combine in each cycle, particularly in the cases with farther rod spacing. Between the airfoil wakes, the rod wakes appear in the freestream once per cycle with about 5% turbulence. The mean velocity drops during the rod wakes and then rises after the wake passes. The variability in the velocity and turbulence is much lower than in the Re=25,000 cases because the wakes suppress the separation bubble more at the higher Re. This is shown in the time averaged velocity profiles in Fig. 18. Without wakes there is a large separation bubble. With wakes the boundary layer is attached. The phase averaged mean velocity profiles are shown in Fig. 19 for the ζ=0.7, $2L_\phi$ (F =0.22) case. The wakes affect the freestream velocity, particularly at the upstream stations, and a thin separation bubble is visible at stations 3 and 4 between wakes. At the downstream stations the boundary layer appears attached at all times. Figure 20(*a*) shows contours of the phase averaged mean and fluctuating velocity for the ζ=0.7, $2L_\phi$ case. The velocity variation in the freestream is visible between t/T=0.042 and 0.375 as the wake passes, and the freestream turbulence is slightly elevated during this period as well. The boundary layer turbulence also rises as the wake passes. The variation during the cycle is not as great as in the Re

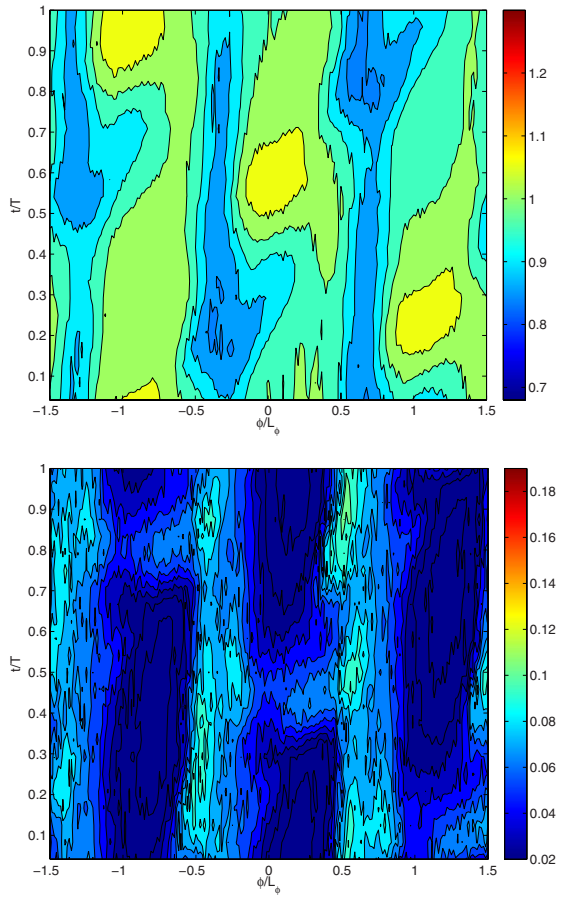

Fig. 16 Time-space plot of phase averaged velocity $0.63C_x$ downstream of cascade for low TI, Re=50,000, ζ=0.7, and $1.6L_\phi$ rod spacing: (*a*) U/U_e and (*b*) u'/U_e

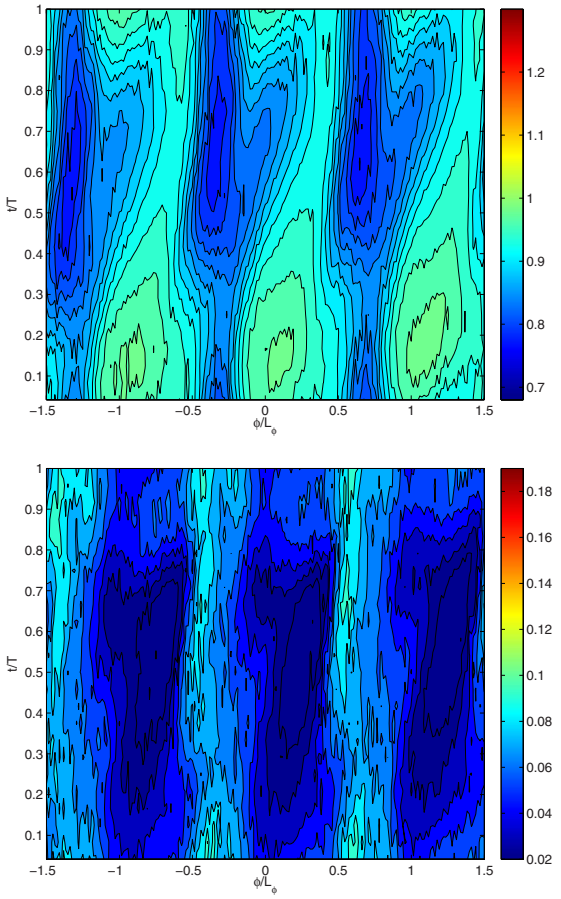

Fig. 17 Time-space plot of phase averaged velocity $0.63C_x$ downstream of cascade for low TI, Re=50,000, ζ=0.7, and $1L_\phi$ rod spacing: (*a*) U/U_e and (*b*) u'/U_e

=25,000 cases of Fig. 12. The boundary layer remains relatively thin and attached at all phases. The time-space plot of the momentum thickness is shown for this case in Fig. 21(*a*). As in the lower Re cases, the wake causes an increase in momentum thickness as it passes. Any delay in momentum thickness growth in the calmed region is slight. The overall value of the momentum thickness is less than half the value in the Re=25,000 cases, which corresponds to the lower losses in Fig. 14 compared with Fig. 5 for the ζ=0.7, $2L_\phi$ cases and the lower wake turbulence in Fig. 15 compared with Fig. 6. A case was also documented with ζ=0.7 and $1.6L_\phi$. It showed little difference from the ζ=0.7, $2L_\phi$ case. A reduction of the wake rod velocity to ζ=1.4, $1.6L_\phi$ (F=0.14) produces the results in Figs. 20(*b*) and 21(*b*). With the reduced wake frequency the boundary layer is separated for much of the cycle and the momentum thickness is over double its value in the ζ=0.7 case. These results agree with the high loss and separated flow C_p profile with ζ=1.4 in Fig. 14.

3.3 High TI. The pressure results for the high freestream turbulence cases with Re=25,000 are shown in Fig. 22. Wake velocity contours are shown in Figs. 23 and 24. The results are similar to the corresponding low TI results of Figs. 5, 7, and 8. The C_p distributions indicate slightly less separation with high TI, and in agreement the mean velocities show less variation and the turbulence values are slightly lower with high TI.

Results for the Re=50,000 cases are shown in Figs. 25–27. For the ζ=0.7 cases, the results are nearly the same as in the corresponding low TI cases of Figs. 14, 16, and 17. In the $1.6L_\phi$, ζ=1.4 cases separation and losses are higher than with lower ζ, but are clearly reduced by the high TI. The effect of the rod wakes

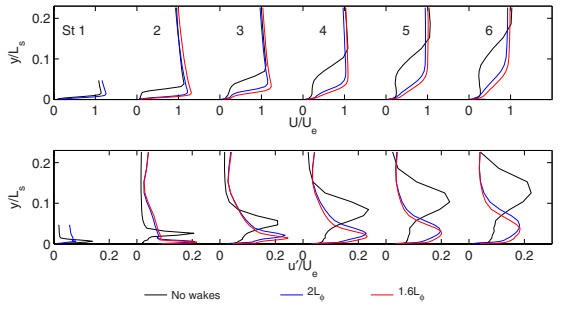

Fig. 18 Time averaged velocity profiles at six streamwise stations for low TI, Re=50,000, and ζ=0.7 cases: top—mean and bottom—rms

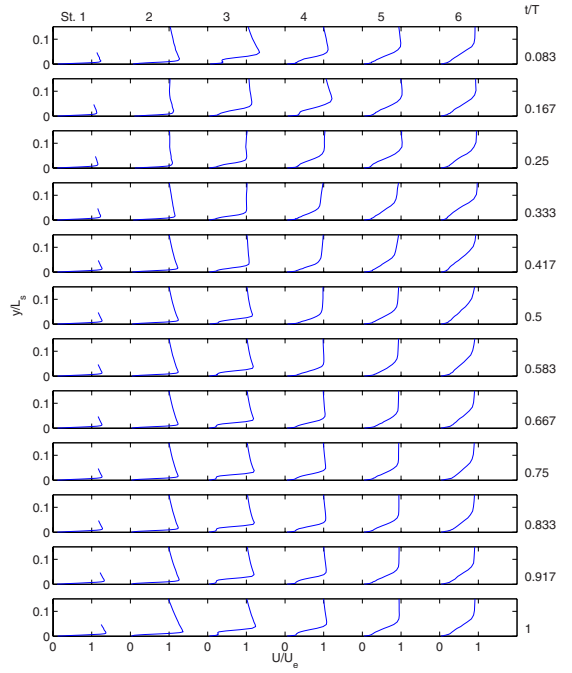

Fig. 19 Phase averaged mean velocity profiles for low TI, Re =50,000, ζ=0.7 cases, and $2L_\phi$ rod spacing; columns for six streamwise stations; rows for phases in wake cycle

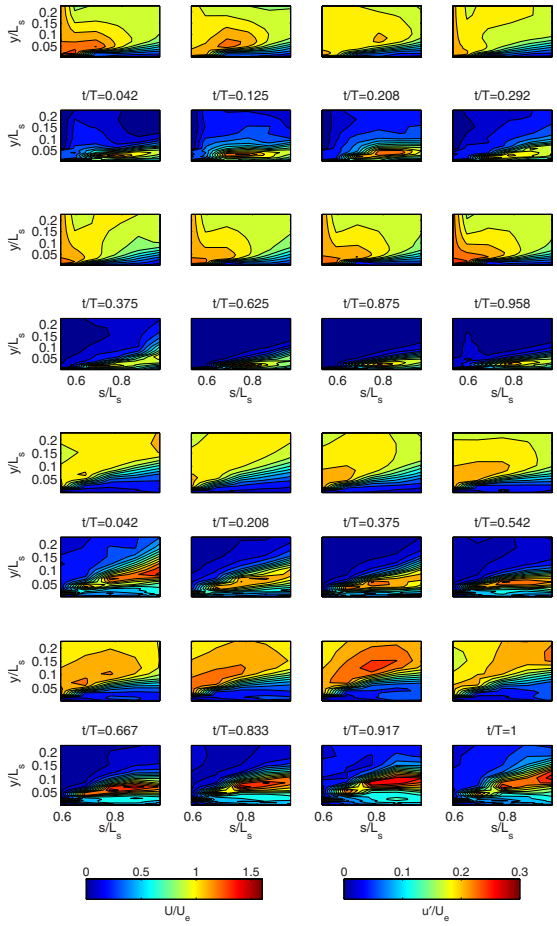

Fig. 20 Phase averaged mean (rows 1 and 3) and rms streamwise fluctuating (rows 2 and 4) velocity for low TI and Re =50,000: (*a*) ζ=0.7,2L_ϕ and (*b*) ζ=1.4,1.6L_ϕ

appears to dominate over the background freestream turbulence effect, and if the wake passing frequency is high enough to suppress separation, the TI level between wakes is largely irrelevant. If there is sufficient time between wakes for the boundary layer to separate, high background TI helps to limit the separation.

In agreement with results from the literature for other airfoils, wakes help to suppress boundary layer separation. For the L1A airfoil with Re=25,000, a dimensionless wake passing frequency of about F=0.5 appears sufficient to effectively eliminate separation. At lower frequencies the boundary layer separates between wakes. For Re=50,000, F=0.3 is sufficient to eliminate separation. It does not appear to matter if a particular frequency is achieved by reducing the spacing between wakes or by increasing the wake generator velocity, so long as F is sufficiently high. The required wake frequencies are about equal to the vortex generator jet pulsing frequencies required for separation control with steady inflow observed by Volino et al. [24,36].

4 Conclusions

The effect of unsteady wakes on the flow over the very high lift L1A airfoil was studied experimentally under low and high freestream turbulence conditions. Reynolds numbers based on suction surface length and nominal exit velocity of 25,000 and 50,000 were considered. Without wakes, the boundary layer separated and did not reattach. Wakes shed by upstream rods caused the boundary layer to reattach. When the wake passing frequency was low, either due to large spacing between wake generator rods or low rod velocity, the boundary layer separated between wakes. With a dimensionless wake passing frequency of F=0.5 or higher at Re=25,000 or with F=0.3 or higher at Re=50,000, separation was largely suppressed. Background freestream turbulence also helps to reduce separation, but the effect is secondary to the wake effect.

The expected wake passing frequency in an engine is near the frequency at which separation begins to be a problem on the L1A. The present cases will serve as baseline results for future cases in which wakes and flow control with vortex generator jets are combined.

Acknowledgment

This work was sponsored by the National Aeronautics and Space Administration under Grant No. NNC07IA10I. The grant monitors were Dr. Anthony Strazisar and Dr. James Heidmann of the NASA Glenn Research Center. The support of the United States Naval Academy Technical Support Department Shop and Fluids Laboratory is greatly appreciated.

Nomenclature

C_p = $2(P_T-P)/\rho U_e^2$, pressure coefficient
C_x = axial chord length
F = $fL_{j\text{-}te}/U_{\text{ave}}$, dimensionless frequency
f = frequency
$L_{j\text{-}te}$ = length of adverse pressure gradient region on the suction surface
L_s = suction surface length
L_ϕ = blade spacing (pitch)
P = pressure
P_S = upstream static pressure
P_T = upstream stagnation pressure

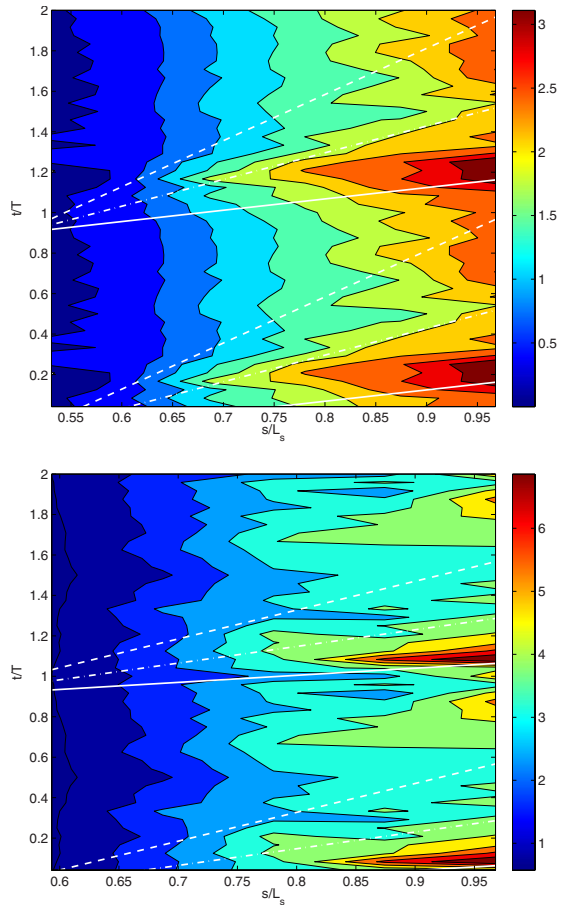

Fig. 21 Phase averaged momentum thickness for low TI and Re=50,000: (*a*) $\zeta=0.7,2L_\phi$ and (*b*) $\zeta=1.4,1.6L_\phi$

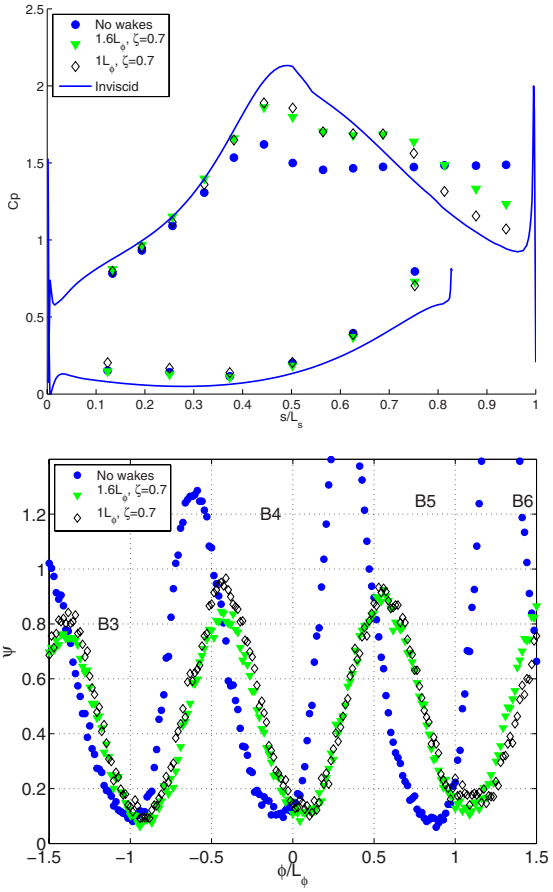

Fig. 22 Pressure profiles for high TI and Re=25,000 cases: (*a*) C_p and (*b*) total pressure loss

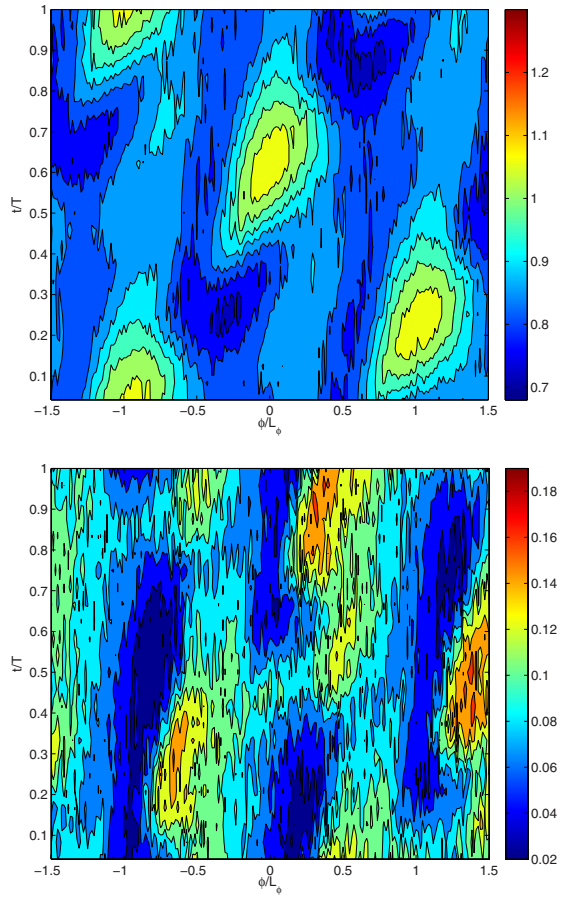

Fig. 23 Time-space plot of phase averaged velocity $0.63C_x$ downstream of cascade for high TI, Re=25,000, ζ=0.7, and $1.6L_\phi$ rod spacing: (*a*) U/U_e and (*b*) u'/U_e

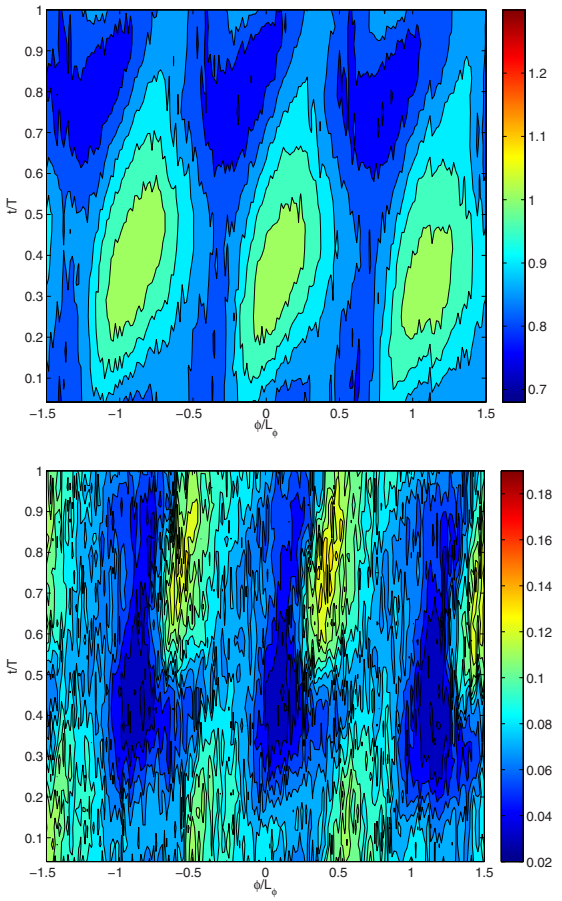

Fig. 24 Time-space plot of phase averaged velocity $0.63C_x$ downstream of cascade for high TI, Re=25,000, ζ=0.7, and $1L_\phi$ rod spacing: (*a*) U/U_e and (*b*) u'/U_e

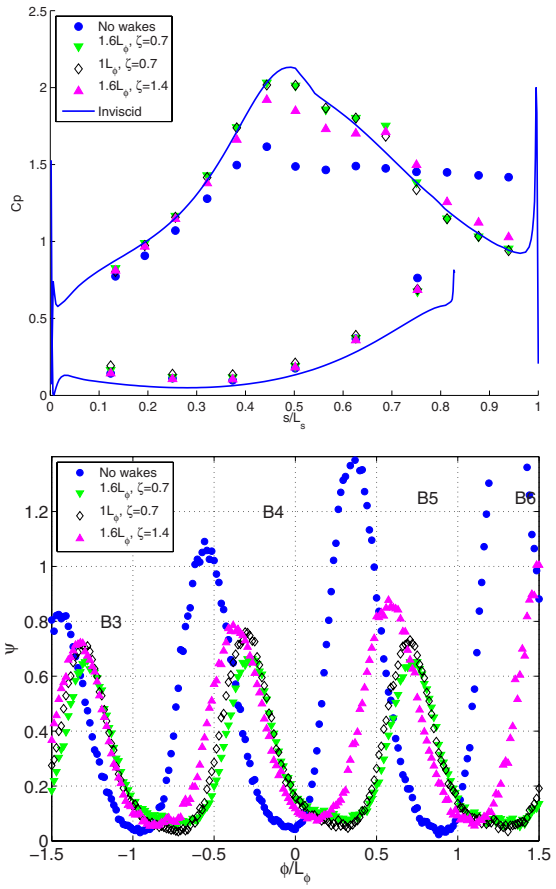

Fig. 25 Pressure profiles for high TI and Re=50,000 cases: (*a*) C_p and (*b*) total pressure loss spacing: (*a*) U/U_e and (*b*) u'/U_e

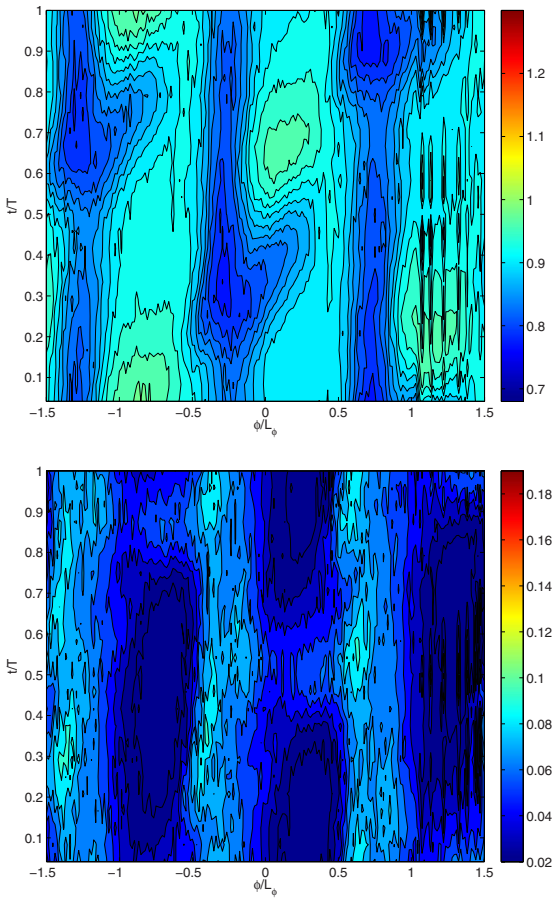

Fig. 26 Time-space plot of phase averaged velocity $0.63C_x$ downstream of cascade for high TI, Re=50,000, ζ=0.7, and $1.6L_\phi$ rod spacing: (*a*) U/U_e and (*b*) u'/U_e

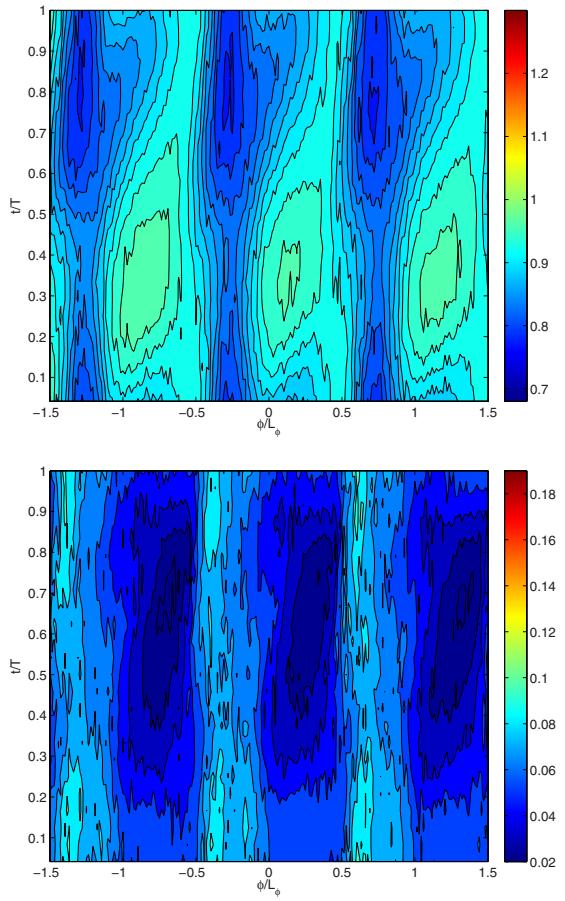

Fig. 27 Time-space plot of phase averaged velocity $0.63C_x$ downstream of cascade for high TI, Re=50,000, ζ=0.7, and $1L_\phi$ rod spacing: (*a*) U/U_e and (*b*) u'/U_e

P_{Te} = downstream stagnation pressure
Re = $U_e L_s/\nu$, exit Reynolds number
s = streamwise coordinate, distance from the leading edge
T = period of jet pulsing cycle
t = time
TI = background freestream turbulence intensity
U = local mean velocity
U_{ave} = average freestream velocity in the adverse pressure gradient region
U_i = inlet freestream velocity
U_e = nominal exit freestream velocity based on inviscid solution
u' = rms fluctuating streamwise velocity
x = axial distance from the leading edge
ϕ = coordinate along the blade spacing, normal to the axial chord
ν = kinematic viscosity
ρ = density
ψ = $(P_T - P_{Te})/(P_T - P_S)$, total pressure loss coefficient
ζ = $U_i \cos(\alpha_i)/U_{\text{rod}} = U_{\text{axial}}/U_{\text{rod}}$, flow coefficient

References

[1] Hourmouziadis, J., 1989, "Aerodynamic Design of Low Pressure Turbines," AGARD Lecture Series 167.
[2] Mayle, R. E., 1991, "The Role of Laminar-Turbulent Transition in Gas Turbine Engines," ASME J. Turbomach., **113**, pp. 509–537.
[3] Sharma, O. P., Ni, R. H., and Tanrikut, S., 1994, "Unsteady Flow in Turbines," AGARD Lecture Series 195, Paper No. 5.
[4] Bons, J. P., Sondergaard, R., and Rivir, R. B., 2001, "Turbine Separation Control Using Pulsed Vortex Generator Jets," ASME J. Turbomach., **123**, pp. 198–206.
[5] Volino, R. J., and Hultgren, L. S., 2001, "Measurements in Separated and Transitional Boundary Layers Under Low-Pressure Turbine Airfoil Conditions," ASME J. Turbomach., **123**, pp. 189–197.
[6] Hodson, H. P., and Howell, R. J., 2005, "Bladerow Interactions, Transition, and High-Lift Aerofoils in Low-Pressure Turbine," Annu. Rev. Fluid Mech., **37**, pp. 71–98.
[7] Gostelow, J. P., Walker, G. J., Solomon, W. J., Hong, G., and Melwani, N., 1997, "Investigation of the Calmed Region Behind a Turbulent Spot," ASME J. Turbomach., **119**, pp. 802–809.
[8] Schulte, V., and Hodson, H. P., 1998, "Prediction of the Becalmed Region for LP Turbine Profile Design," ASME J. Turbomach., **120**, pp. 839–846.
[9] Bons, J. P., Pluim, J., Gompertz, K., Bloxham, M., and Clark, J. P., 2008, "The Application of Flow Control to an Aft-Loaded Low Pressure Turbine Cascade With Unsteady Wakes," ASME Paper No. GT2008-50864.
[10] Pluim, J., Memory, C., Bons, J., and Chen, J. P., 2009, "Designing a High Fidelity Wake Simulator for Research Using Linear Cascades," ASME Paper No. GT2009-52276.
[11] Schobeiri, M. T., Öztürk, B., and Ashpis, D. E., 2007, "Effects of Reynolds Number and Periodic Unsteady Wake Flow Condition on Boundary Layer Development, Separation, and Intermittency Behavior Along the Suction Surface of a Low Pressure Turbine Blade," ASME J. Turbomach., **129**, pp. 92–107.
[12] Öztürk, B., and Schobeiri, M. T., 2007, "Effects of Turbulence Intensity and Periodic Unsteady Wake Flow Condition on Boundary Layer Development, Separation, and Reattachment Along the Suction Surface of a Low-Pressure Turbine Blade," ASME J. Fluids Eng., **129**, pp. 747–763.
[13] Jiang, N., and Simon, T. W., 2005, "Transition in Low-Pressure Turbines: Effects of Unsteady Acceleration and Turbulence Intensity," J. Thermophys. Heat Transfer, **19**, pp. 148–155.
[14] Mahallati, A., and Sjolander, S. A., 2007, "Aerodynamics of a Low-Pressure Turbine Airfoil at Low-Reynolds Numbers Part 2: Blade-Wake Interaction," ASME Paper No. GT2007-27348.
[15] Zhang, X. F., and Hodson, H. P., 2010, "Effects of Reynolds Number and Freestream Turbulence Intensity on the Unsteady Boundary Layer Development on an Ultra-High-Lift Low Pressure Turbine Airfoil," ASME J. Turbomach., **132**, p. 011016.
[16] Funazaki, K., Yamada, K., Ono, T., Segawa, K., Hamazaki, H., Takahashi, A., and Tanimitsu, H., 2006, "Experimental and Numerical Investigations of Wake Passing Effects Upon Aerodynamic Performance of a LP Turbine Linear Cascade With Variable Solidity," ASME Paper No. GT2006-90507.
[17] Praisner, T. J., and Clark, J. P., 2007, "Predicting Transition in Turbomachinery—Part 1: A Review and New Model Development," ASME J. Turbomach., **129**, pp. 1–13.
[18] Clark, J. P., 2007, private communication.
[19] Zhang, X. F., and Hodson, H., 2005, "Combined Effects of Surface Trips and Unsteady Wakes on the Boundary Layer Development of an Ultra-High-Lift LP Turbine Blade," ASME J. Turbomach., **127**, pp. 479–488.
[20] Volino, R. J., 2010, "Separated Flow Measurements on a Highly Loaded Low-Pressure Turbine Airfoil," ASME J. Turbomach., **132**, p. 011007.
[21] Ibrahim, M., Kartuzova, O., and Volino, R. J., 2008, "Experimental and Computational Investigations of Separation and Transition on a Highly Loaded Low Pressure Turbine Airfoil: Part 1—Low Freestream Turbulence Intensity," ASME Paper No. IMECE2008-68879.
[22] Volino, R. J., Kartuzova, O., and Ibrahim, M., 2008, "Experimental and Computational Investigations of Separation and Transition on a Highly Loaded Low Pressure Turbine Airfoil: Part 2—High Freestream Turbulence Intensity," ASME Paper No. IMECE2008-68776.
[23] Volino, R. J., 2002, "Separated Flow Transition Under Simulated Low-Pressure Turbine Airfoil Conditions: Part 1—Mean Flow and Turbulence Statistics," ASME J. Turbomach., **124**, pp. 645–655.
[24] Volino, R. J., Kartuzova, O., and Ibrahim, M. B., 2009, "Experimental and Computational Investigations of Low-Pressure Turbine Separation Control Using Vortex Generator Jets," ASME Paper No. GT2009-59983.
[25] Reimann, D., Bloxham, M., Pluim, J., and Bons, J. P., 2007, "Comparison of Spanwise Wake and Discrete Jet Disturbances on a Separating Low-Pressure Turbine Blade," AIAA Paper No. 2007-0525.
[26] Kaszeta, R. W., Simon, T. W., Jiang, N., and Ottaviani, F., 2005, "Influence of Wake Passing Frequency and Elevated Turbulence Intensity on Transition," J. Thermophys. Heat Transfer, **19**, pp. 137–147.
[27] Wills, J. A. B., 1962, "The Correction of Hot-Wire Readings for Proximity to a Solid Boundary," J. Fluid Mech., **12**, pp. 388–396.
[28] Schobeiri, M. T., John, J., and Pappu, K., 1996, "Development of Two-Dimensional Wakes Within Curved Channels: Theoretical Framework and Experimental Investigation," ASME J. Turbomach., **118**, pp. 506–518.
[29] Pfeil, H., and Herbst, R., 1979, "Transition Procedure of Instationary Boundary Layers," ASME Paper No. 79-GT-128.
[30] Stieger, R. D., 2002, "The Effects of Wakes on Separating Boundary Layers in Low Pressure Turbines," Ph.D. thesis, University of Cambridge, Cambridge, UK.
[31] Stieger, R. D., and Hodson, H. P., 2005, "The Unsteady Development of a

Turbulent Wake Through a Downstream Low-Pressure Turbine Blade Passage," ASME J. Turbomach., **127**, pp. 388–394.
[32] Volino, R. J., 2005, "An Investigation of the Scales in Transitional Boundary Layers Under High Freestream Turbulence Conditions," Exp. Fluids, **38**, pp. 516–533.
[33] Stieger, R. D., and Hodson, H. P., 2004, "The Transition Mechanism of Highly Loaded Low-Pressure Turbine Blades," ASME J. Turbomach., **126**, pp. 536–543.
[34] Roberts, S. K., and Yaras, M. I., 2006, "Effects of Surface-Roughness Geometry on Separation-Bubble Transition," ASME J. Turbomach., **128**, pp. 349–356.
[35] Volino, R. J., and Bohl, D. G., 2004, "Separated Flow Transition Mechanisms and Prediction With High and Low Freestream Turbulence Under Low Pressure Turbine Conditions," ASME Paper No. GT2004-53360.
[36] Volino, R. J., Kartuzova, O., and Ibrahim, M. B., 2011, "Separation Control on a Very High Lift Low Pressure Turbine Airfoil Using Pulsed Vortex Generator Jets," ASME J. Turbomach., **133**(4), p. 041021.

Appendix B

Additional results

6. Additional Results

The following figures show the ensemble averaged jet velocity measured at the exit of a VGJ hole with the main flow in the wind tunnel off.

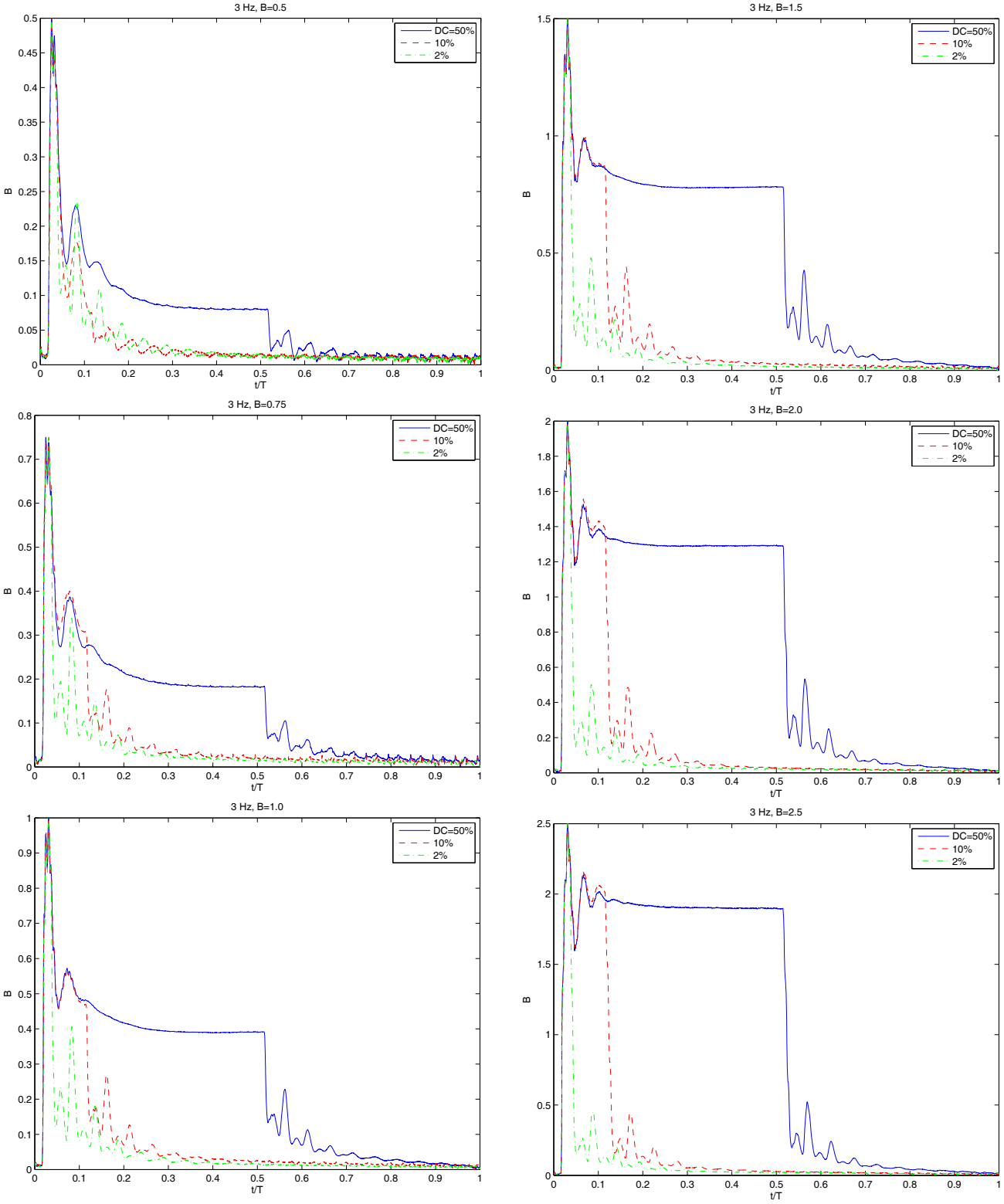

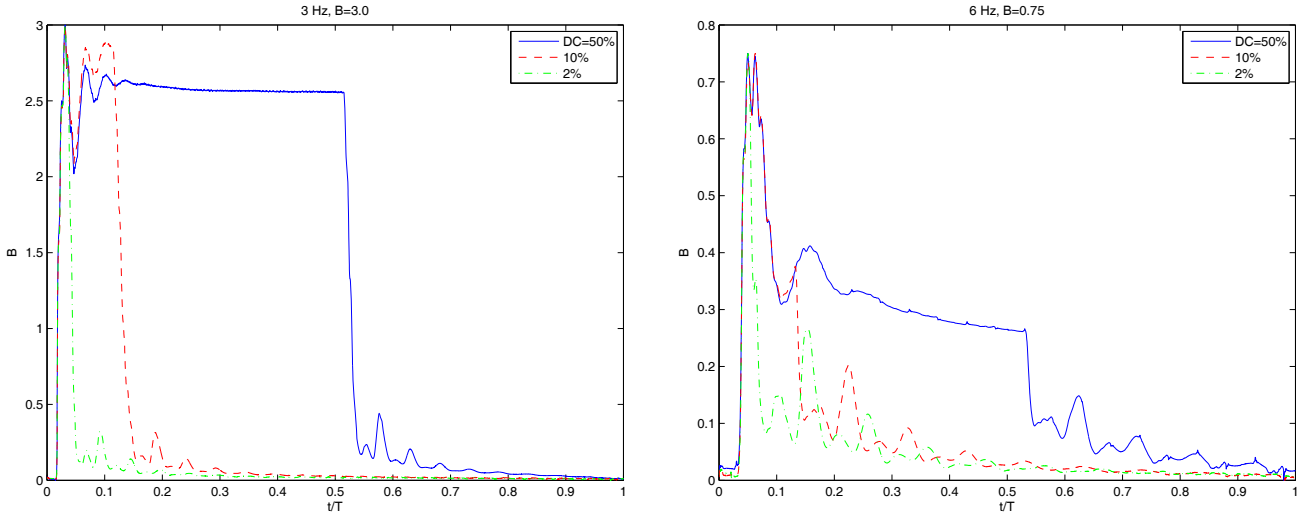
3 Hz, B=3.0
DC=50%
10%
2%
B
t/T

6 Hz, B=0.75
DC=50%
10%
2%
B
t/T

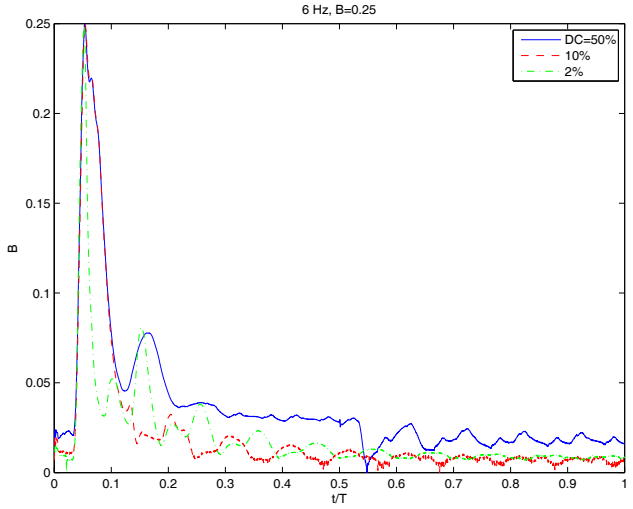
6 Hz, B=0.25
DC=50%
10%
2%
B
t/T

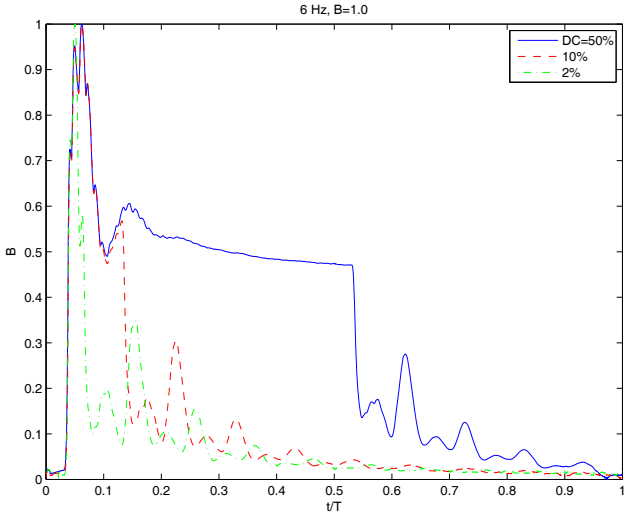
6 Hz, B=1.0
DC=50%
10%
2%
B
t/T

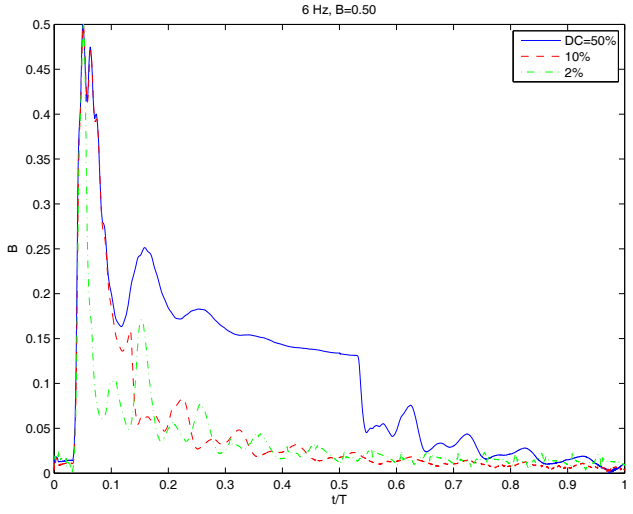
6 Hz, B=0.50
DC=50%
10%
2%
B
t/T

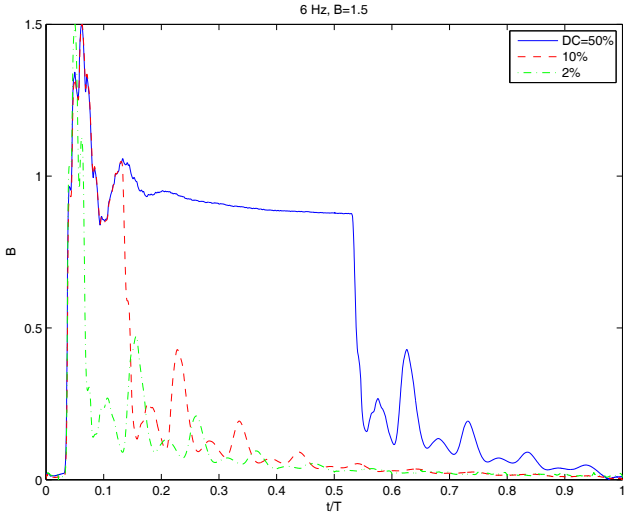
6 Hz, B=1.5
DC=50%
10%
2%
B
t/T

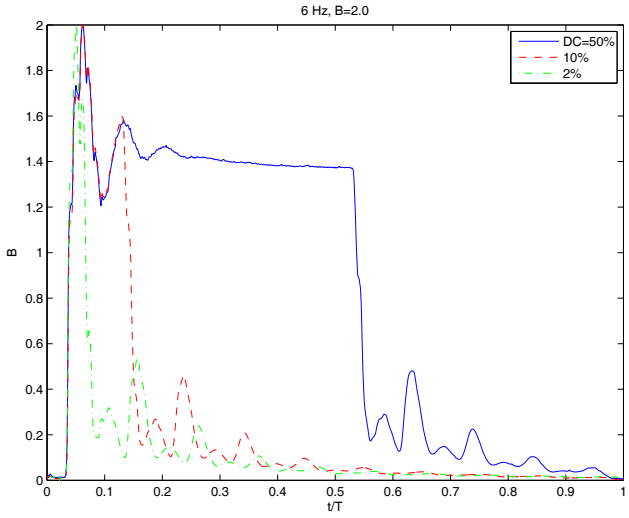
6 Hz, B=2.0
DC=50%
10%
2%
B
t/T

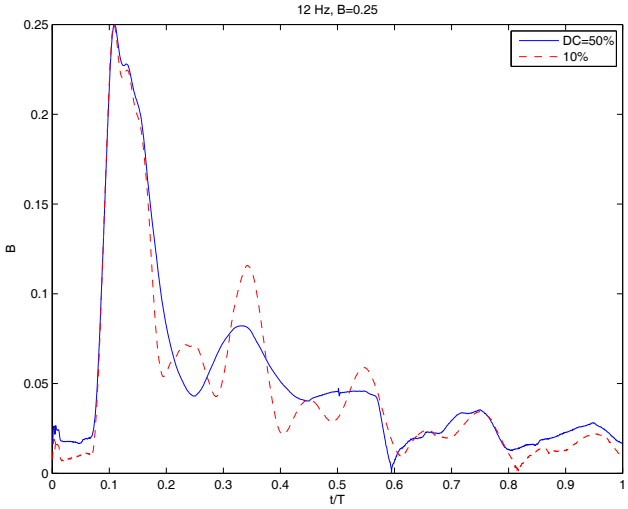
12 Hz, B=0.25
DC=50%
10%
B
t/T

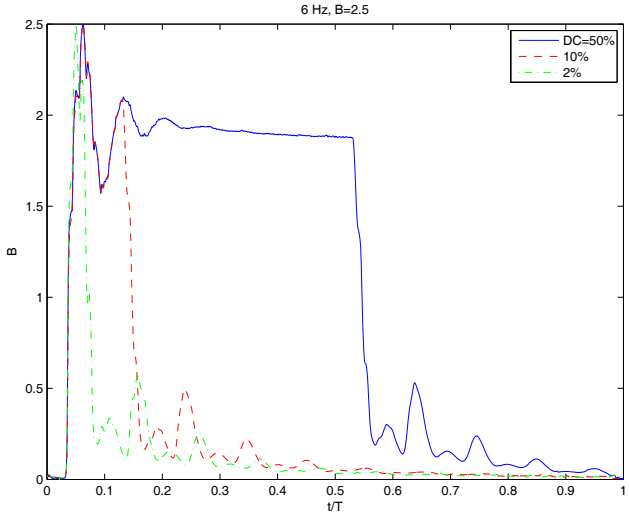
6 Hz, B=2.5
DC=50%
10%
2%
B
t/T

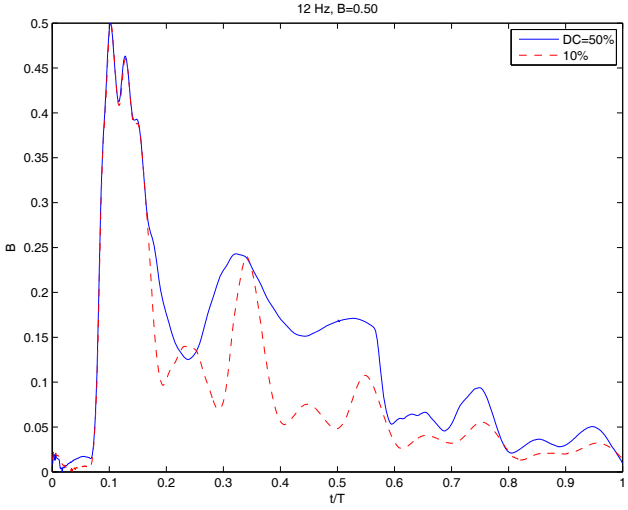
12 Hz, B=0.50
DC=50%
10%
B
t/T

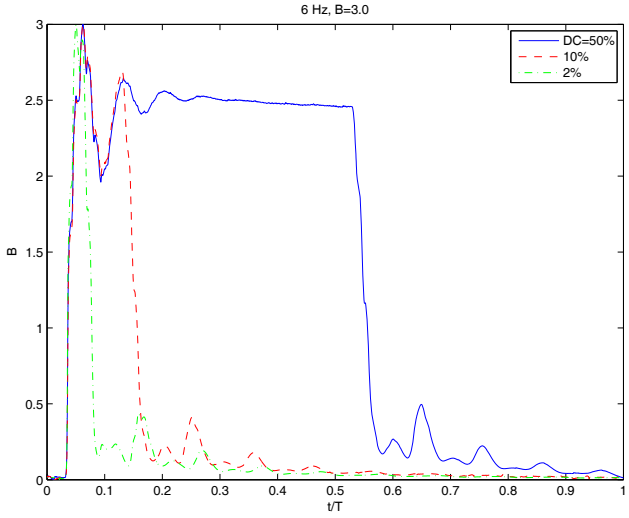
6 Hz, B=3.0
DC=50%
10%
2%
B
t/T

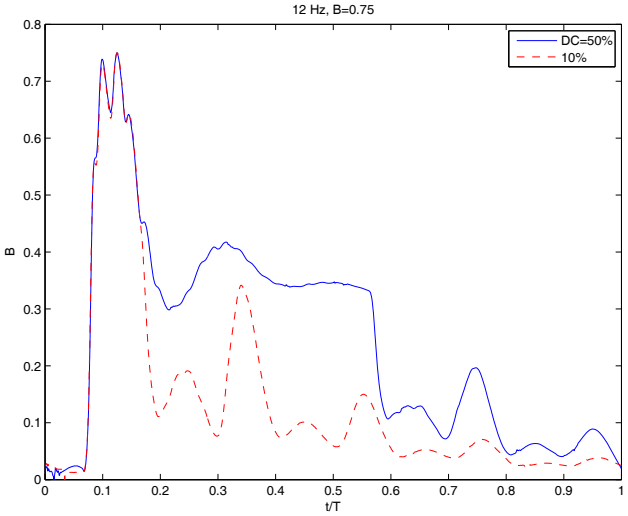
12 Hz, B=0.75
DC=50%
10%
B
t/T

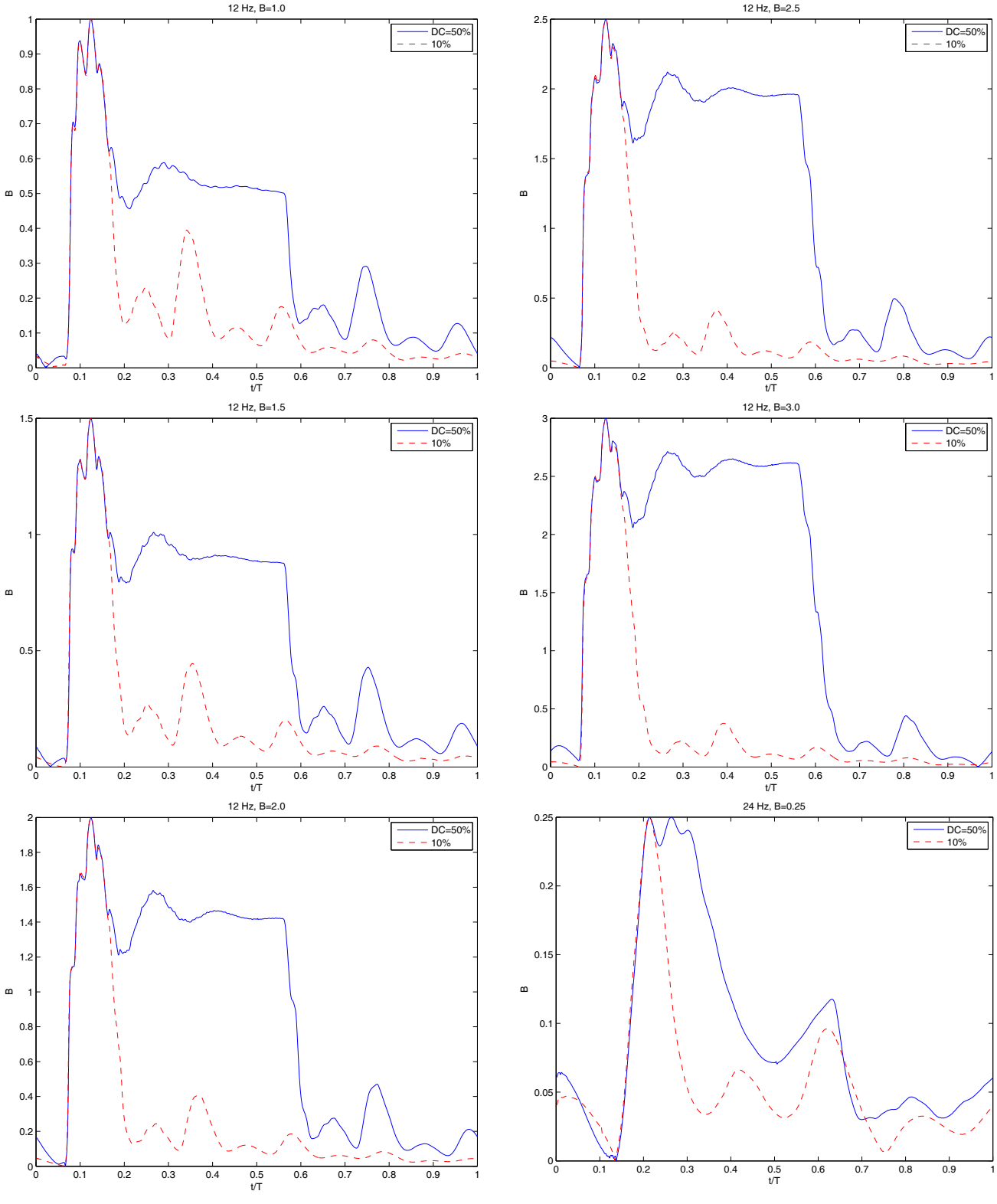
12 Hz, B=1.0
12 Hz, B=2.5
12 Hz, B=1.5
12 Hz, B=3.0
12 Hz, B=2.0
24 Hz, B=0.25
DC=50%
10%
B
t/T

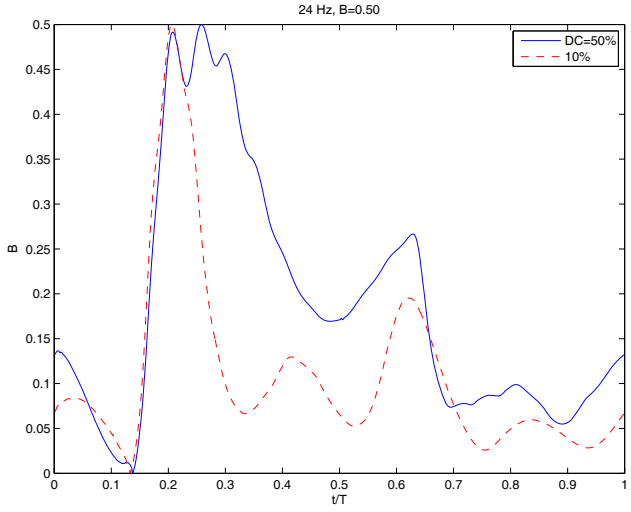
24 Hz, B=0.50
DC=50%
10%
B
t/T

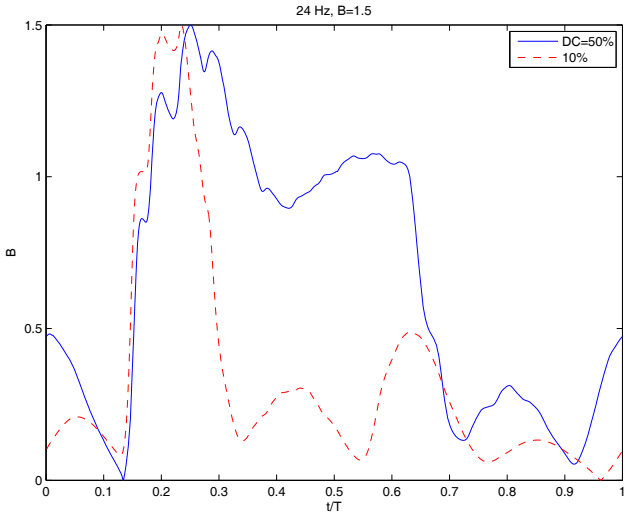
24 Hz, B=1.5
DC=50%
10%
B
t/T

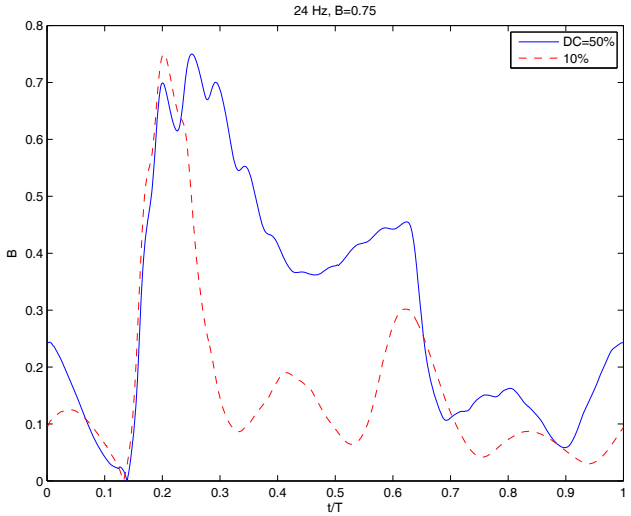
24 Hz, B=0.75
DC=50%
10%
B
t/T

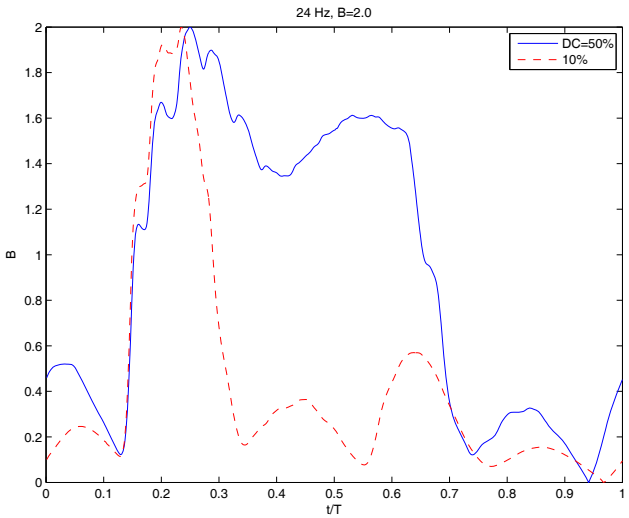
24 Hz, B=2.0
DC=50%
10%
B
t/T

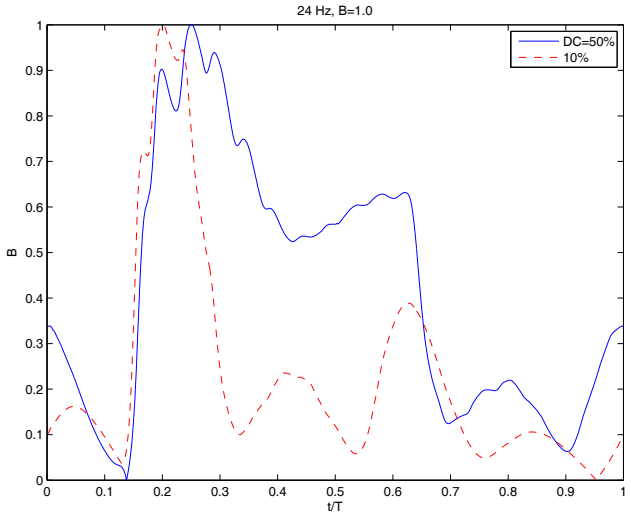
24 Hz, B=1.0
DC=50%
10%
B
t/T

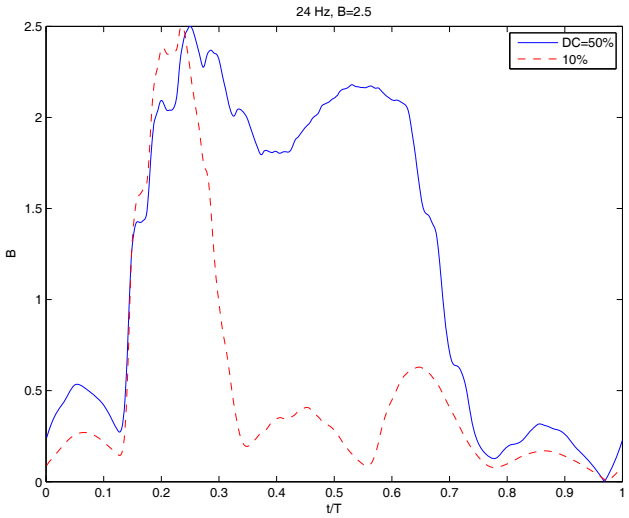
24 Hz, B=2.5
DC=50%
10%
B
t/T

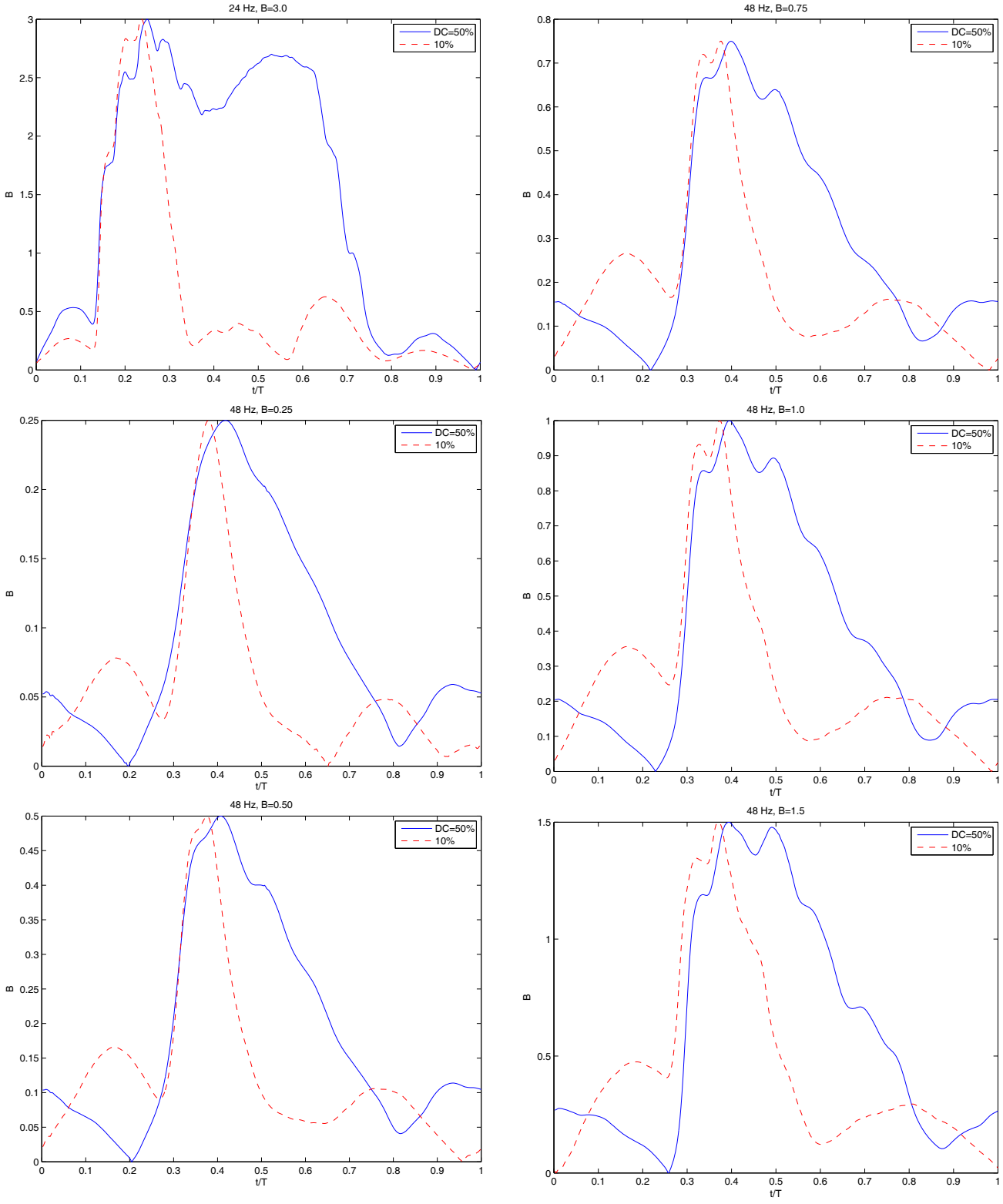
24 Hz, B=3.0
48 Hz, B=0.75
48 Hz, B=0.25
48 Hz, B=1.0
48 Hz, B=0.50
48 Hz, B=1.5
DC=50%
10%
B
t/T

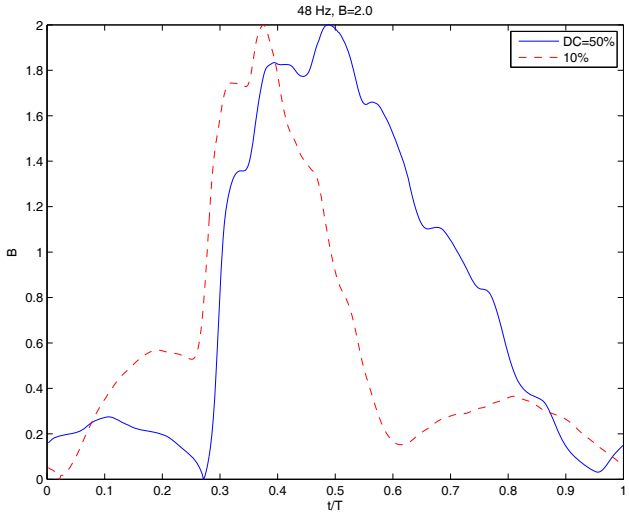
48 Hz, B=2.0
DC=50%
10%
B
t/T

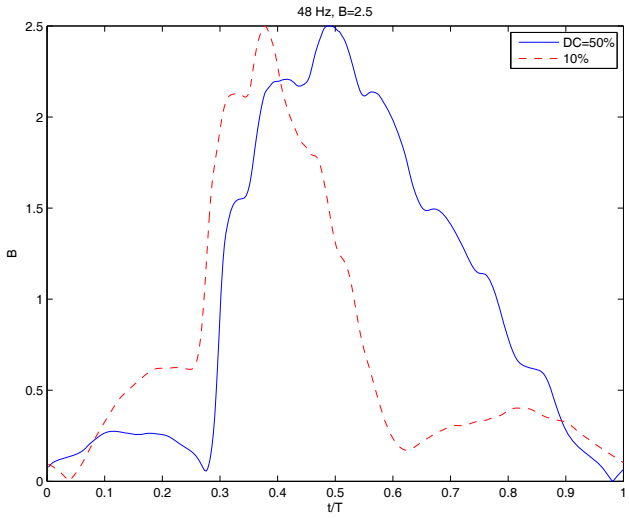
48 Hz, B=2.5
DC=50%
10%
B
t/T

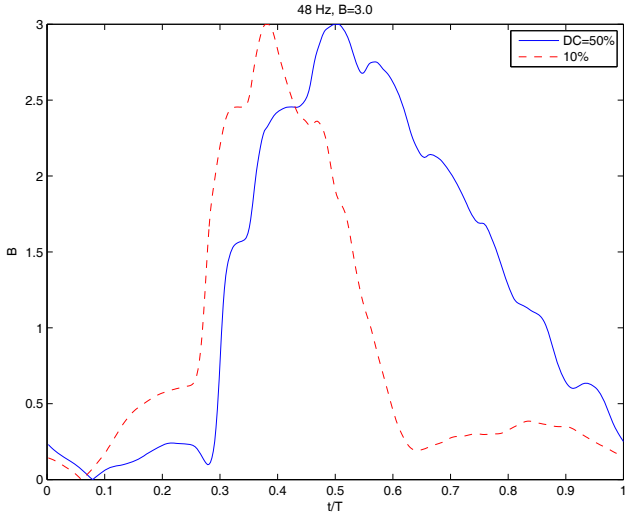
48 Hz, B=3.0
DC=50%
10%
B
t/T

The following section is a taken from the progress report for January – June 2009. It provides additional results and figures in addition to those published in the papers included above.

Summary

During this period, data were acquired for experimental cases with flow control using Vortex Generator Jets (VGJs) under low and high freestream turbulence conditions. Various jet amplitude, pulsing frequency and duty cycle combinations were considered. A paper was presented at Turbo Expo in Orlando (Volino et al., 2009) showing the pressure profile and total pressure loss results for the low freestream turbulence cases. The effect of jet spacing was considered by blocking some of the jets. Additionally, the wake generator was completed, and experimental cases were documented with unsteady wakes under low freestream turbulence conditions. Phase averaging of the velocity data has been done to show the behavior of the boundary layer and wake velocity as a function of time during the jet pulsing cycle or the wake passing period. Spectral processing using Fourier and wavelet analysis has been done on all the velocity data to determine the important frequencies in the fluctuating velocity, again as a function of time during the pulsing or wake cycle.

Computationally, unsteady RANS simulations were completed using the Transition-sst model for cases with steady and pulsed VGJs. They did not predict the flow control with VGJs observed in the experiments. Large eddy simulations (LES) were more successful, correctly predicting which cases had flow reattachment. A conference paper (Ibrahim et al., 2009) has been accepted for presentation showing results for cases with steady VGJs.

The next experiments will be with combined wakes and VGJs. The valves for the pulsing will be driven using a signal from the wake generator. A delay can be programmed into the circuit to set any delay desired to time the VGJs to the wakes.

The CFD work continues, looking at unsteady wakes next. In addition, more work will be done with unsteady RANS calculations to try and better predict the flow with a finer grid than used previously, but still courser than required for LES.

Facility

The wind tunnel, cascade and pulsing hardware were described in previous progress reports and in Volino (2008), Volino et al. (2008), Ibrahim et al. (2008), and Volino et al. (2009). Since then, the wake generator has been completed and used. It includes a chain near each endwall of the cascade which passes 0.54 C_x (C_x=axial chord) upstream of the leading edges of the cascade blades. The chain then passes downstream around the end blade on the inside turn of the cascade and passes well downstream of the cascade before returning upstream around the opposite end blade on the outside turn of the cascade. This completes the chain circuit. Each chain is driven by a drive gear and also passes around six idler sprockets. One of the idler sprockets is adjustable to maintain tension in the chain. The drive gears for the upper and lower chains are on a common axle and driven by a single electric motor so both chains move in unison. The motor speed is set with a variable frequency inverter. The chain links have hollow pins, through which the wake generator rods are attached. Each rod consists of a 4 mm diameter carbon fiber tube with a steel pin attached at each end. The steel pins are inserted through the holes in the upper and lower chain, and then secured with small clips. The rods were spaced 17 or 18 chain links apart, for an average distance between rods of 221 mm. This compares to the blade spacing in the cascade of 136 mm. The ratio of rod to blade spacing (1.6) is at the upper end of what is

expected for vane to rotor spacing in an engine. This spacing was chosen instead of a closer spacing because it is more challenging for flow control.

The rods were driven at a velocity of 1.18 times the cascade inlet velocity, U_i. This gives a flow coefficient, $U_i\cos(\alpha_i)/U_{rod} = 0.7$, where α_i is the inlet flow angle. This is in the expected range for an engine. For the pulsed VGJ cases, a dimensionless frequency was defined as $F=fL_{j\text{-}te}/U_{ave}$, where f is the pulsing frequency in Hz, $L_{j\text{-}te}$ is the distance from the VGJ holes to the trailing edge, and U_{ave} is the average freestream velocity between the VGJ holes and the trailing edge. Using this same definition for the wake passing, the wake passing frequency for the present experiments is F=0.28. This corresponds to one of the VGJ frequencies studied previously. For a blade Reynolds number of 50,000 (based on exit velocity and suction surface length), the rod velocity is 2.2 m/s. The wake generator was run for an extended period at this speed. It was also operated at double this speed, but in these cases a rod broke loose after a short time. It is possible that adjustments could be made to allow sustained higher speed operation, but this is likely not necessary since the cases of most interest for flow control are at Re=50,000 and below. In addition to the cases with F=0.28, the wake generator speed was adjusted for a few cases with F above or below 0.28 to investigate the effect of wake frequency.

The timing of the wake generator is recorded with an infrared photo detector located near the lower endwall between the cascade leading edge and the wake generator. The detector emits light, and when a wake rod passes, it reflects the light back into the detector. The voltage signal from the detector is recorded simultaneously as other data are acquired, allowing phase averaging locked to the wake passing. The detector signal is also sent to a function generator, which produces a square wave for driving the solenoid valves for the VGJs. The duration of the high voltage in the square wave and the delay between the detector signal and the function generator output can be set to produce any duty cycle desired for the VGJs and any delay desired between the wake passing and the VGJ pulse.

Results

VGJ Cases, Low Freestream Turbulence

Pressure (Cp) profiles from the test airfoil and total pressure loss profiles measured downstream of the cascade were presented for multiple cases in the previous progress report and in Volino et al. (2009). This paper is attached at the end of this report. The VGJs are located at the pressure minimum on the suction surface, $s/L_s=0.5$, where s is the distance from the leading edge along the surface and L_s is the suction surface length. The holes are inclined at 30 degrees to the surface and 90 degrees to the main flow direction. The hole spacing is 10.7 diameters or $0.041C_x$. As explained in Volino et al. (2009), the blowing ratio, B, of the VGJs is defined as the ratio of the maximum velocity in the jet pulse, measured at the jet centerline, divided by the local freestream velocity. The duty cycle, D, is the fraction of time the jets are turned on during each pulsing cycle.

Velocity profiles were acquired for several cases at six streamwise positions along the suction side of the test blade. Velocity was also measured $0.63C_x$ downstream of the cascade in the same location used for the total pressure loss measurements. Velocity data were acquired using a traversing hot-film probe and digitized at a 20 kHz sampling rate. All raw data were saved for subsequent phase averaging and spectral analysis. The velocity data help to explain how the VGJs control separation and why certain pulsing frequencies and duty cycles work

better than others. The data are also used for CFD validation. Velocity results are presented next.

Re=25,000. Figure 1 shows the pressure coefficients for cases with Re=25,000 and steady VGJs. The pressure coefficient $Cp=2(P_T-P)/\rho U_e^2$, where P_T is the upstream total pressure, P is the static pressure on the airfoil surface, and U_e is the nominal exit velocity from the cascade based on the inlet velocity and the design flow angles. The Cp values are shown verses s/L_s, where is the distance along the surface from the leading edge, and L_s is the suction surface length. In Volino et al. (2009) it was shown that with steady blowing, a jet to freestream velocity ratio of B=2.0 is needed for any effect of the VGJs on Cp, and the effect increases at larger B. With pulsed jets, some effect on Cp is observed with B=0.5 if F=0.56 or greater. At higher B, pulsing with F=0.28 has some effect. Figure 1 shows cases for which velocity profile data are also available. If the difference between the suction and pressure side Cp values is integrated in the axial direction, the result is proportional to the lift on the airfoil. Figure 1b shows integrated results for the cases in Fig. 1a normalized on the integrated Cp for the inviscid solution for the passage. Steady blowing with B=3.0 lowers Cp near the trailing edge on the suction surface and increases the overall lift by about 10% over the case with no blowing. Pulsed jets with B=1.0 and F=0.28 are more effective, particularly when the duty cycle is increased from D=10% to 50%. At higher frequencies the jets are effective even with D=10%. The Cp profiles are significantly different than the inviscid solution in all cases, suggesting that separation is not completely controlled, even in the best case.

Figure 2 shows total pressure loss profiles for the cases in Fig. 1. The total pressure loss is measured with a Kiel probe traversed along a line 0.63 C_x downstream of the cascade. The loss coefficient is defined as $\Psi=(P_T-P_{Te})/(P_T-P_s)$, where P_{Te} is the total pressure downstream of the cascade, P_T is the upstream total pressure, and P_s is the upstream static pressure. The coordinate ϕ is the spanwise position measured perpendicular to the axial direction with $\phi=0$ corresponding to the location directly downstream of the center blade in the direction of the design exit flow angle. The coordinate ϕ is normalized by the blade spacing, L_ϕ. The labels B3, B4, etc., refer to the blades in the cascade. The loss peak labeled B4 corresponds to the wake of the center blade. Integrated loss results across one L_ϕ centered on the B4 peak are shown in Fig. 2b. The integrated results also include the loss associated with the jets themselves, as explained in Volino et al. (2009). Without flow control there is a large separation bubble which does not reattach. As explained in Volino et al. (2008), the tailboard on one side of the cascade reduces the bubble size on the nearer blade, so the flow is not periodic across the cascade. Steady blowing with B=3.0 lowers the loss peaks and reestablishes periodicity, but the integrated loss still rises compared to the uncontrolled case due to the loss associated with the jets themselves at this high blowing ratio. In agreement with the Cp profiles, pulsing with B=1.0, F=0.28 and D=10% is not very effective, but with increased duty cycle or higher frequency the losses are reduced to about 70% of the baseline value.

The velocity profile measurements help explain the Cp and pressure loss results. Figure 3 shows velocity profiles from the boundary layer at six streamwise locations along the suction surface for the baseline case without flow control. The stations are spaced along the surface at s/L_s= 0.53, 0.59, 0.69, 0.78, 0.88, and 0.97. The VGJ holes are located at the suction peak at s/L_s=0.5. The top row in Fig. 3 shows the local mean velocity and the second row show the rms fluctuating streamwise velocity u′. The boundary layer has already separated at the first station,

and the separation bubble grows larger at the downstream stations. The fluctuating velocity has its maximum in the shear layer over the separation bubble.

Figure 4 shows the velocity results with steady blowing and B=3.0. Separation is delayed until Station 2, and the separation bubble is clearly thinner than in the baseline case, but the separation bubble is still clearly large and reattachment does not occur. The velocity results agree with the Cp and pressure loss results of Figs. 1 and 2, which showed that steady VGJs at B=3.0 have some effect, but do not appear to fully control the separation.

Figure 5 shows time averaged results for pulsed VGJs with F=0.28, D=10% and B=1.0. There is clearly a large separation, although the thickness of the separation bubble is smaller than in the baseline case. Phase averaged results are shown in Fig. 6 for the same case. Figure 6a shows the mean velocity. The format is the same as in Fig. 5, but each row shows a different phase in the pulsing cycle. The phase t/T=0, where T is the pulsing period, corresponds to the opening of the solenoid valves, which provide air to the cavity in the airfoil that supplies the VGJs. At Station 3, the profile appears nearly attached at t/T=0.375. As the flow convects downstream, the phase of near attachment at Station 4 is centered at t/T=0.5, continuing to t/T=0.625 at Station 5 and t/T=0.708 at Station 6. Figure 6b shows u′ results for this case. At the times and locations corresponding to near reattachment in Fig. 6a, the fluctuating velocity is somewhat lower than at other phases.

Pulsing with F=0.28 and D=10% appears to induce boundary layer reattachment, but only for a short period of time. The duration of the pulse effect is too short and the pulses occur too infrequently to cause reattachment for most of the cycle. When the duty cycle is increased to D=50%, as shown in Fig. 7, the time averaged flow appears more attached, although the boundary layer is still very thick, the mean velocity profile has an inflection point, and the peaks in u′ are far from the wall, as in a separated flow case. The phase averaged results in Fig. 8 show that the boundary layer alternates between separated and attached states during the pulsing cycle. Separation is delayed until Station 2, and at Station 3 there is a thin but clear separation bubble at most phases. At t/T=0.333 and at t/T=0.833, however, the boundary layer appears close to reattachment. The t/T=0.333 reattachment occurs at about the same time as observed in the D=10% case in Fig. 6. The t/T=0.833 reattachment occurs half a cycle later. It appears that turning on the VGJ induces reattachment, and turning off the VGJ at the end of the 50% duty cycle also induces reattachment. During the blowing between t/T=0.333 and 0.833, the boundary layer separates. As the flow convects downstream, the reattachment phases are centered at t/T=0.417 and 0.875 at Station 4, 0.583 and 0.042 at Station 5, and 0.708 and 0.208 at Station 6. The duration of the reattached flow increases at the downstream stations. By Station 6, the boundary layer appears to be attached about 70% of the time, and the separation bubble is much thinner during the remaining phases than in the cases considered above. It appears that turning the VGJ off is also effective for flow control. Increasing the duty cycle to 50% separates the turning on and off of the VGJs compared to the D=10% case, resulting in two distinct flow control events for each pulsing cycle. Because the boundary layer has less time to separate between events, the boundary layer remains attached more of the time and the separation bubble thickness is reduced. Increasing the duty cycle from 10 to 50% effectively doubles the flow control frequency and results in significantly better separation control. The fluctuating velocities shown in Figs. 8b are lower when the flow is attached than when separated. The same observation was made in Fig. 6 for the D=10% case.

Time averaged results for the F=0.56, D=10%, B=1.0 case are shown in Fig. 9. The boundary layer is slightly thinner than in the F=0.28, D=50%, B=1.0 case of Fig. 7, but

otherwise the two cases appear very similar. Phase averaged results are shown in Fig. 10. Separation occurs between Stations 2 and 3 at all phases. By Station 4, reattachment has occurred between about t/T=0.792 and 0.917. These dimensionless times are roughly double those observed at Station 4 in Figs. 6 and 8, where F=0.28. Hence, the dimensional time between the opening of the solenoid valve and reattachment at Station 4 is about the same in all three cases. This is consistent with the convection time between the VGJ hole and Station 4 being the same in all three cases, which are at the same Re=25,000. As in the previous cases, u′ is lower when the flow is attached. The duration of the attached flow increases between Stations 4 and 5, and by Station 6 the flow is attached for about 90% of the cycle.

The pulsing frequency is increased to F=1.12, D=10%, B=1.0 in Fig. 11, which shows time averaged results. The boundary layer is slightly thinner, but otherwise similar to the previous case with F=0.56. The phase averaged results in Fig. 12 show that separation occurs at most phases at Station 3, but that at about 25% of the phases the boundary layer remains attached. By Station 4 the boundary layer has reattached by t/T=0.45, and remains attached until about t/T=0.75. The dimensional times corresponding to this period match those observed when F=0.28 and F=0.56 in Figs. 6, 8 and 10. As in the previous cases, the fluctuating velocity is lower during the attached flow period. The separation bubble remains thin at the other phases. By Station 5 the boundary layer is attached 70% of the time. By Station 6 it appears attached for the entire cycle, although some profiles have inflection points and the boundary layer is still relatively thick compared to cases at higher Reynolds numbers.

In summary, with low freestream turbulence and Re=25,000 on the present L1A airfoil, a disturbance frequency of about 0.56 is needed to provide effective separation control. This can be achieved by pulsing with F=0.56 or by pulsing with F=0.28 and a 50% duty cycle so that the switching on and off of the jets provide two effective disturbances spaced half a cycle apart for every pulse. A moderate blowing ratio of 1.0 is sufficient. When the separation is controlled, the lift as indicated by the Cp profiles rises by about 28% compared to the baseline case, and the total pressure loss pressure loss drops by about 28%. The switching on and off of the VGJs provides a more effective disturbance for flow control than steady blowing. Although blowing with steady jets and B=3.0 reduced the thickness of the separation bubble slightly compared to the baseline case, the boundary layer did not reattach and losses remained high in this case. The adverse pressure gradient is sufficiently strong at this Reynolds number that the boundary layer remains close to separation even when the flow control is effective. Hence the boundary layer is significantly thicker than observed at higher Reynolds numbers, the Cp profile does not match the inviscid solution, and the total pressure losses remain over double those observed at high Re.

Re=50,000. The Cp profiles for several cases with Re=50,000 and the integrated Cp results are shown in Figs. 13. Without flow control, the boundary layer separates and does not reattach, as in the Re=25,000 case. Steady jets at B=2.0 control separation and increase the lift by 20%. Pulsed jets at F=0.14 with D=10% and B=1.0 have a small effect, but the lift is only increased about 8% over the baseline case. Increasing the duty cycle to 50% with F=0.14 and B=1.0 appears to eliminate the separation and increases the lift to its maximum value. With higher frequencies a 10% duty cycle is sufficient for the same flow control, and with F=0.56 and D=10%, a blowing ratio of B=0.5 is sufficient. Flow control appears to be more complete and is possible at lower dimensionless frequencies than in the Re=25,000 cases.

Total pressure loss results are shown in Figs. 14. Without flow control the losses are high and equal to those in the Re=25,000 case. With steady VGJs and B=2.0, the separation is

controlled, as shown in Fig. 13, and the loss is reduced by about 40%. It is still higher, however, than in some of the pulsed jet cases. With F=0.14 and B=1.0, pulsing with D=10% was shown in Fig. 13 to have only a limited effect controlling separation, and although the integrated total pressure loss is about 20% lower than in the baseline case, it is still much higher than in the other pulsed jet cases. The loss peaks in this case are also shifted to the left of the other VGJ cases in Fig. 14, indicating a reduction in flow turning. Increasing the duty cycle to 50% greatly reduces the losses to about 50% of the baseline case level and increases flow turning. With F=0.28, D=10% and B=1.0, the magnitude of the loss peaks are reduced about 40% below the baseline level, but the peaks are wider than in some of the other cases. Increasing F to 0.56 with B=1.0, the losses are reduced by 60% below the baseline level and the VGJs are equally effective with D=10% or 50%. The jets are slightly less effective at this frequency when B is reduced to 0.5.

Velocity profiles for the baseline case are shown in Fig. 15. There is a large separation, and the dimensionless profiles are nearly identical to those in the uncontrolled case at Re=25,000. With steady jets at B=2.0, the profiles in Fig. 16 show that the separation bubble is eliminated and the boundary layer is fully turbulent at all stations.

Time averaged velocity profiles for the case with pulsed jets at F=0.07, D=50% and B=1.0 are shown in Fig. 17. The boundary layer remains separated, but the separation bubble is thinner than in the baseline case. Phase averaged results for this case are shown in Fig. 18. The boundary layer has separated by Station 2 and the separation bubble becomes thicker at the downstream stations. By Station 4 at t/T=0.167 it appears the boundary layer is close to reattaching. The same is true at Stations 5 at t/T=0.208 and t/T=0.667. By Station 6 the boundary layer appears close to reattachment at t/T=0.25 and t/T=0.708. At all other phases the boundary layer is clearly separated. The appearance of two times for reattachment spaced about a half cycle apart agrees with the results of the Re=25,000 case with D=50%, indicating that turning off the VGJs causes a disturbance which helps to control the boundary layer. Since no sign of reattachment occurs until Station 4 and the reattachment at a second phase only appears at Station 5, the disturbance caused by the VGJs must be too small to have an immediate effect. Perhaps it must grow in the separated shear layer or spread in the spanwise direction before its effect is visible. Although the boundary layer separates and remains separated at most phases, by causing the boundary layer to approach reattachment at least intermittently, the VGJs significantly reduce the thickness of the separation bubble and the total pressure losses.

Velocity results with F=0.14, D=10% and B=1.0 are shown in Figs. 19 and 20. The time averaged results in Fig. 19 are very similar to the previous case with F=0.07, showing that the boundary layer separates and does not reattach. As indicated by the Cp and loss profiles of Figs. 13 and 14, the VGJs have a relatively small effect in this case. The phase averaged results in Fig. 20 show that the boundary layer is near reattachment at t/T=0.25, 0.333, 0.417, and 0.5 at Stations 3-6 respectively. At other phases it is clearly separated. As in the previous case, the VGJs cause the boundary layer to approach reattachment with sufficient frequency to reduce the overall thickness of the separation bubble and reduce losses somewhat, but the boundary layer still remains separated between jet pulses.

When the duty cycle is increased to D=50% with F=0.14 and B=1.0, the boundary layer reattaches, as shown in the Cp profiles and loss profiles and the time averaged velocity in Fig. 21. The phase averaged velocity profiles in Fig. 22 show that separation is delayed until Station 3. At phases near t/T=0.25 and 0.75 the boundary layer appears to remain attached. At other phases the separation bubble is thinner than in the D=10% case. The boundary layer appears

attached for about 25% of the cycle at Station 4 and about half the cycle at Station 5. By Station 6 it is attached for about 75% of the cycle, only clearly separating near t/T=0.25.

In Figs. 23 and 24, the pulsing frequency is increased to F=0.28 with D=10% and B=1.0. The boundary layer is somewhat thinner than in the previous case of Figs. 21 and 22, corresponding to the narrower loss peaks and lower total pressure losses in Fig. 14. As in the previous case, the boundary layer is attached for most of the cycle by the downstream stations.

With the frequency increased to F=0.56 with D=10% and B=1.0, the separation bubble is nearly eliminated, as seen in Figs. 25 and 26. A very thin bubble appears briefly at Station 3 at t/T=0.5 and at Station 4 at t/T=0.708, but everywhere else the boundary layer appears attached. It appears close to separation at a few phases at the downstream stations, but at most phases the boundary layer is significantly thinner than in any of the previous cases. The fluctuating velocity peaks are all very close to the wall. These results are consistent with the low losses for this case. When the duty cycle is increased to 50% with F and B remaining at 0.56 and 1.0, Figs. 27 and 28 show there is little change from the D=10% case. The boundary layer becomes slightly thinner, but the losses, as shown in Fig. 14 are about the same for the D=10% and 50% cases. Once F=0.56, the separation is nearly fully controlled, so increasing the duty cycle does not provide further benefit. Similarly, increasing the frequency to F=1.12 with D=10% and B=1.0, as shown in Figs. 29 and 30 causes little change.

Figures 31 and 32 show the effect of lowering the blowing ratio to B=0.5 with F=0.56 and D=10%. The boundary layer separates and does not reattach. Although the separation bubble is much thinner and the pressure loss is much lower than in the baseline case, stronger blowing helps to further reduce the separation.

Re=100,000. The Cp results for cases with Re=100,000 are shown in Figs. 33. Without flow control, the boundary layer separates and does not reattach, as at the lower Reynolds numbers. At Re=100,000, however, the boundary layer is close to a Reynolds number where it would reattach even without flow control. With any blowing from the VGJs, whether steady or pulsed, separation is controlled. Fig. 33 shows two examples, with steady blowing and B=0.75, and pulsed blowing with F=0.28, D=10% and B=0.5. Lift increases about 30% when the boundary layer reattaches. Total pressure losses are reduced by over 50% with the VGJs, as shown in Figs. 34.

Velocity profiles for the case without VGJs are shown in Fig. 35. The profiles match those without flow control at the lower Reynolds numbers. With flow control the boundary layer is fully attached, as shown in Fig. 36 for the case with steady jets and B=0.75 and in Figs. 37 and 38 for F=0.28, D=10% and B=0.5. The phase averaged results show the boundary layer is attached at all times during the pulsing cycle.

Effect of VGJ Spacing

The pitch to diameter ratio of the VGJ holes was 10.7. To investigate the effect of hole spacing, some holes were covered with thin tape. First, before any holes were covered, velocity profiles were acquired at five spanwise locations at the most downstream station on the suction surface, s/L_s=0.97, with Re=50,000, and steady VGJs with B=2.0. These are shown in Fig. 39, where z is the spanwise position, and L_p is the hole pitch. The spanwise positions z/L_p=0 and 1 correspond to the same streamwise location with respect to adjacent holes. The mean velocity profiles in Fig. 39a show an attached boundary layer with no variability across the span, and the fluctuating velocity in Fig. 39b also shows little change across the span. Hence the holes are

close enough together to provide spanwise uniform flow control. Figure 40 shows pulsed jet results with F=0.56, D=10% and B=1.0. Again separation is controlled and there is no variation across the span. The phase averaged velocity profiles (not shown) are the same as shown in Fig. 26 for this case. A small separation does form for about 10% of the pulsing cycle, and it is uniform at all spanwise locations.

Three additional hole pitches were considered. Every other hole was covered to increase the pitch, L_p, to $L_p/d=21.3$, where d is the 0.8 mm VGJ hole diameter. Every other remaining hole was then covered to increase the pitch to $L_p/d=42.7$. Finally, every other remaining hole was again covered to increase the pitch to $L_p/d=85.3$. Figure 41 shows the Cp results for these cases. With $L_p/d=10.7$ and 21.3, steady blowing with B=2.0 or pulsed blowing with F=0.56, D=10% and B=1.0 both cause the boundary layer to reattach. The plateau at $s/L_s=0.65$ indicates a larger separation bubble in the $L_p/d=21.3$ cases, but the boundary layer still reattaches well before the trailing edge. With the pitch increased to $L_p/d=42.7$, steady blowing with B=2.0 or pulsed jets with F=0.56, D=10% and B=1.0 are insufficient. The Cp profiles in these two cases show some improvement over the baseline case, but the boundary layer does not appear to reattach. With F=0.56, D=10% and B increased to 1.5, however, the boundary layer does reattach. With $L_p/d=85.3$, it was not possible to force reattachment. With F=0.56 and D=10%, B must be increased to about 2.3 to have any effect, and as shown in Fig. 41, it does not provide complete separation control. Raising B even more did not appear to provide further benefit.

The total pressure loss results support the Cp measurements. Figure 42 shows results with $L_p/d=21.3$, steady jets and B=2.0. Profiles at five spanwise positions are shown. There is no variability across the span, and the profiles essentially match those with $L_p/d=10.7$ documented previously. The same is true for the F=0.56, D=10%, B=1.0 case shown in Fig. 43. With L_p/d increased to 42.7, as shown in Fig. 44 for the steady B=2.0 case and Fig. 45 for the F=0.56, D=10%, B=1.0 case, there is still good uniformity across the span, but the losses are much higher than in the cases with closer hole spacing, and the peaks are shifted to the left due to the large separation bubble. Figure 46 compares loss profiles acquired at $z/L_p=0$ with F=0.56, D=10%, $L_p/d=42.7$ and 85.3, and various blowing ratios. In agreement with the Cp results of Fig. 41, when Lp/d=42.7, B=1.0 is insufficient to control separation and losses are high. Increasing B to 1.5 lowers the losses to match those in the cases with closer VGJ holes shown in Figs. 42 and 43. Losses are high in the case with $L_p/d=85.3$ even with B=2.3.

Velocity profile measurements at $s/L_s=0.97$ are consistent with the pressure measurements. Figure 47 shows velocity profiles with $L_p/d=21.3$, steady jets and B=2.0. Some variation across the span is visible, with the profiles at $z/L_p=0.25$ and 0.5 having a larger velocity deficit than at the other locations. The variation is small, however, and separation is controlled across the span. The velocity deficits in Fig. 47 are lower than those in Fig. 39, indicating that increasing the hole spacing resulted in a thinner boundary layer. With the same hole pitch and pulsed jets with F=0.56, D=10% and B=1.0, Fig. 48 again shows good uniformity and separation control across the span. Opposite to the steady blowing case, the velocity deficit with pulsed jets is slightly larger than in the corresponding case with closer holes in Fig. 40. Phase averaged results show that a thin separation bubble forms for about 10% of the pulsing cycle, and that it is uniform across the span.

With the VGJ spacing increased to $L_p/d=42.7$, the velocity profiles for the steady jet, B=2.0 case are shown in Fig. 49. In agreement with the pressure results for this case, the boundary layer is separated. There is more variation across the span than in the cases with closer VGJs, but the variation is not great. The separation bubble appears thickest at $z/L_p=0.25$ and 0.5, and

thinnest at z/L_p=0.75. With pulsed jets at F=0.56, D=10% and B=1.0 with Lp/d=42.7, Fig. 50 shows the boundary layer is clearly separated, again in agreement with the pressure results. In this case very good spanwise uniformity is maintained in spite of the VGJ spacing. Phase averaged results (not presented) show only a small variation in the separation bubble thickness during the pulsing cycle with the boundary layer remaining separated at all phases. Spanwise uniformity is maintained throughout the cycle. Also shown in Fig. 50 is the velocity profile from z/L_p=0 for the case with F=0.56, D=10%, and B=1.5. As indicated by the pressure results, increasing B to 1.5 causes the boundary layer to reattach. Phase averaged results show a small separation bubble forms for about 10% of the pulsing cycle.

As shown above in the pressure results, with the VGJ spacing increased to L_p/d=85.3, it was not possible to control separation. Figure 51 shows velocity profiles from the case with F=0.56, D=10% and B=2.3. The boundary layer is clearly separated and there is some variation across the span. Phase averaged results show there is little variation with time during the pulsing cycle.

In summary, it appears the original VGJ spacing of L_p/d=10.7 was conservative, at least for the Re=50,000, low freestream turbulence cases investigated on the present airfoil. The spacing can be doubled with little change in the flow control. If the spacing is increased to four times the original spacing, separation control is still possible with an increase in blowing ratio from 1.0 to 1.5 in the pulsed jet case. There is an upper limit to the jet spacing, however, and if L_p/d is increased to 85.3, separation control becomes impossible. In all cases, whether separation control was achieved or not, good spanwise uniformity was observed near the trailing edge even with large VGJ spacing. This may indicate that it is necessary for the VGJs to be close enough together to maintain an attached boundary layer across the entire span. If the VGJs are spaced too far apart, strips of attached flow between regions of separation will not occur. Instead the boundary layer will separate across the entire span.

VGJ Cases, High Freestream Turbulence

Re=25,000. As documented in Volino et al. (2008), a passive grid is used to produce elevated freestream turbulence. At the inlet plane of the cascade, the intensity of the streamwise component freestream turbulence is about 4%. High freestream turbulence makes the boundary layer more resistant to separation, but for the present airfoil without flow control, separation without reattachment still occurs at Re=50,000 and below. Figure 52 shows Cp results for cases with Re=25,000 and steady VGJs. As in the low freestream turbulence cases at this Reynolds number, blowing with B=2.0 or lower has no effect on separation. When B is increased to 2.5 or 3.0, there are some signs of reattachment, but the Cp profile remains significantly different from the inviscid profile and the lift remains low.

Figures 53 shows Cp results for cases with pulsed jets and F=0.14. As in the low freestream turbulence cases, this frequency is too low to be effective. The jets have some effect when B=3.0 and the duty cycle is high, but even then the lift remains low. Figure 54 shows corresponding total pressure loss results. The jets do have an effect, reducing the loss significantly with pulsed VGJs and shifting the loss peaks to the right. This indicates that the separation bubble must be thinner, particularly when B=3.0, and flow turning is increased.

The Cp results with F=0.28 are shown in Fig. 55. The jets begin to have an effect when B=1.5, and significant separation control is apparent when B=2.0 or higher and D=50%. The lift increases about 20% over the baseline case. The jets are not as effective when D=10%. The loss results in Fig. 56 show the VGJs at F=0.28 have a strong effect. Losses are reduced by as much

as 50%, and flow turning is increased as B increases. In contrast to the Cp results, there is little variation with duty cycle. Velocity profiles for the baseline case are shown in Fig. 57. The boundary layer has separated by Station 1 and the separation bubble grows at the downstream stations. Figure 58 shows time averaged profiles for the F=0.28, D=10%, B=2.0 case, and Fig. 59 shows the corresponding phase averaged results. Boundary layer separation is delayed until about Station 3. At Station 3 separation is suppressed for about 25% of the cycle centered on t/T=0.375. This attached flow period is centered at t/T=0.583, 0.792 and 0.958 at Stations 4-6 respectively. As noted in the low freestream turbulence cases, the fluctuating velocity peaks are lower during the attached flow periods. Between these periods the boundary layer separates, but the separation bubble is much thinner than in the baseline case. The results are essentially the same when B=3.0, as shown in Figs. 60 and 61.

Figure 62 shows Cp results with F=0.56. The VGJs have some effect even at low blowing ratios, and when B=1.0 the boundary layer appears to reattach. The results do not appear to depend significantly on the duty cycle. This is consistent with the low freestream turbulence results, which showed that when F=0.56 the pulses occur frequently enough to control separation even at low duty cycles. Figure 63 shows Cp results with F=1.12. Results are similar to those with F=0.56. Separation is controlled when B=0.75, and increasing B further does not appear to have much effect. Loss results are shown in Figs. 64. Losses are greatly reduced in some of the cases with flow control, consistent with all the results above. There are some anomalies, however, comparing the loss results to the Cp profiles. A few of the cases showing reattached boundary layers in Figs. 62 and 64 have losses equal to the uncontrolled case in Fig. 64.

Velocity profiles for the F=0.56, D=10%, B=1.0 case are shown in Figs. 65 and 66. The boundary layer separates by Station 3, except for a period near t/T=0.708. The period of attached flow is centered at t/T=0.958 and 0.208 at Stations 4 and 5. By Station 6 the boundary layer appears to be attached for most of the cycle, although the mean profile is inflectional and may be close to separation. The boundary layer is more attached than in the F=0.28 cases. Increasing B to 2.0, as shown in Figs. 67 and 68 does not significantly change the velocity profiles.

Re=50,000. The Cp results with steady VGJs and Re=50,000 are shown in Fig. 69. With B=1.0 the VGJs appear ineffective, but with B=1.5 and 2.0 the boundary layer reattaches and the separation bubble appears to be eliminated. The lift increases about 16% with flow control. Loss results are shown in Fig. 70. In agreement with Cp, the loss peaks with B=1.0 are not much different than in the baseline case, but they are much lower with B=1.5 and about 40% lower than the baseline case with B=2.0. As the losses decrease the peaks shift to the right in Fig. 70, indicating more flow turning. This is consistent with the higher lift in Fig. 69b.

Figure 71 shows Cp results for pulsed VGJs with F=0.14. As in the steady jet cases, separation control is best when B=1.5 or higher, and the jets are ineffective when B=0.5 or lower. When B=1.0, there appears to be partial separation control which is better than in the steady jet cases. In general the duty cycle does not affect the results, except at B=0.75 where the lift is higher with D=50% than with D=10%. The loss results in Fig. 72 again show some effectiveness with B=1.0, but the separation is not fully controlled on all blades. Results are better with B=1.5, with losses about half those in the baseline case at both high and low duty cycles.

The Cp results with F=0.28 are shown in Fig. 73. The VGJs have some positive effect when B=0.5 and become more effective as B increases to 1.0. Increasing B further has little effect.

With B=0.5 and 0.75, results are better with D=50% than 10%, but at higher B the jets are equally effective at both duty cycles. The loss results in Fig. 74 are consistent with Cp. Velocity profiles for the baseline case are shown in Fig. 75 and for the F=0.28, D=10%, B=1.0 case in Figs. 76 and 77. The baseline results at Re=50,000 agree closely with those at Re=25,000. The boundary layer separates and does not reattach. With the VGJs a small separation bubble may form between Station 3 and 4, and the boundary layer appears to be approaching separation at the downstream stations at some phases (e.g. t/T=0.583 at Station 6), but for the most part the boundary layer remains attached.

With F=0.56, Fig. 78 shows the Cp results. Separation is controlled with B=0.75 or higher, independent of duty cycle. Higher duty cycle results in higher lift when B=0.5. Loss results in Fig. 79 are consistent with the Cp results. Velocity profiles in Figs. 80 and 81 for the F=0.56, D=10%, B=0.75 case show that the boundary layer remains attached for the full pulsing cycle.

Summary of VGJ Cases

Boundary layer separation was controlled using VGJs at all Reynolds numbers considered. The disturbance caused when the jets are turned on or off is more effective for flow control than steady blowing. With a low duty cycle of 10%, the switching on and off of the jets occur close enough together in time that they provided essentially a single disturbance each pulsing cycle. Hence the disturbance frequency is the same as the pulsing frequency. When the duty cycle is increased to 50%, the switching on and off are separated by half a cycle and provide two disturbances per cycle. This effectively doubles the disturbance frequency over the pulsing frequency. A strong enough disturbance from the VGJs causes the boundary layer to either remain attached or reattach farther downstream. After the disturbance passes, the boundary layer can relax and eventually re-separate. As the disturbance frequency is increased, the time available for separation between disturbances shrinks, allowing the separation bubble less time to grow. This reduces the average size of the bubble, resulting in greater flow turning, higher lift, and lower losses. If the disturbance frequency is sufficiently high, the separation bubble can be eliminated in some cases. The acceleration parameter, $K=(\nu/U_\infty^2)(dU_\infty/ds)$, is an indicator of the tendency of the boundary layer to separate, and is inversely proportional to the Reynolds number. At lower Reynolds numbers, therefore, the boundary layer should require a smaller fraction of a disturbance cycle to separate, and a higher dimensionless pulsing frequency may be needed to control separation.

The velocity of the VGJs must also be sufficiently high to provide separation control. Since steady jets are less effective, they require a higher blowing ratio to produce the same effect as a pulsed jet. With a higher blowing ratio and 100% duty cycle, the steady jets use considerably more air than the pulsed jets, which produces higher overall losses. With pulsed jets, the necessary blowing ratio depends on the pulsing frequency. Presumably this is because at lower frequencies a strong pulse is needed to more fully reattach the boundary layer and fill out the velocity profile near the wall, thereby lengthening the time needed after the disturbance for separation. With higher frequencies the boundary layer has less time to separate, so a weaker pulse may be sufficient. If the VGJs are not strong or frequent enough to prevent separation or force the boundary layer to reattach, they may still be able to reduce the separation bubble thickness. This is particularly true at low Reynolds numbers, where the boundary layer is very prone to separation and remains thick and on the verge of separation at the downstream stations even in the best cases.

The discussion above is illustrated in terms of the integrated total pressure loss in Fig. 82. The loss is shown as a function of F and B. Data were not acquired at every possible combination of F and B, so considerable interpolation was used to fill in the contour plots. Quantitative information should therefore be taken from the figures discussed above instead of Fig. 82. Figure 82a shows that with low freestream turbulence and Re=25,000, a pulsing frequency of about F=0.5 is needed, and a blowing ratio of about B=1.0 is sufficient if the frequency is high enough. Further increasing F or B provides some additional benefit. With lower frequencies the VGJs are not helpful in terms of losses. The high blowing ratios needed to provide any separation control result in higher losses from the jets themselves than the benefit gained from reducing the separation bubble thickness.

With low freestream turbulence and Re=50,000, Fig. 82b shows that with F=0.5, low losses are possible with B as low as 0.25. With F=0.3, similar losses are possible with B of about 1.0. The separation is controlled to a sufficient extent in these cases that additional increases in F or B do not provide further benefit. At lower frequencies the separation control is not as good and losses are higher even at the highest blowing rates considered.

The addition of high freestream turbulence does not drastically change the results. When Re=100,000, high freestream turbulence causes the boundary layer to reattach without the use of flow control. At low Reynolds numbers flow control is still needed to induce reattachment. When Re=25,000, as shown in Fig. 82c, a frequency of about F=0.3 and blowing ratio of about B=1.0 are needed to significantly reduce losses, and higher B is helpful. When Re=50,000, as shown in Fig. 82d, a frequency of F=0.3 and blowing ratio of about 0.75 are sufficient, and higher frequency and blowing ratio do not appear to reduce losses further.

CFD for VGJ Cases

Previous work (Ibrahim et al., 2008, Volino et al., 2008) showed that the URANS calculations using the Transition-sst model were successful in predicting separation, transition and reattachment accurately in the baseline cases without flow control. Several other models were also tested. Many failed to predict separation. Some others did better, but not as well as the Transition-sst model. Pressure distributions and velocity profiles from the CFD and experiments were compared. The calculations matched the experiments, and correctly predicted the effects of freestream turbulence at both high and low Reynolds numbers. Also shown in Volino et al. (2009) were attempts to apply the same URANS methods with the Transition-sst model to cases with VGJ flow control. The calculations failed to predict the effect of the VGJs. Reattachment was not predicted, even in cases where the VGJs almost completely eliminated the separation in the experiments. To investigate the problem and see whether a good CFD prediction could be obtained by another method, large eddy simulations (LES) were done for some cases. The results are documented in Ibrahim et al. (2009) which is included at the end of this report. The match between the LES and experiments was not perfect, but LES was able to predict reattachment in the correct cases. It appears the much finer grid required for the LES was needed to capture the effect of the VGJs. The disadvantage of LES is the long computing time required due to the very fine grid. Further work is planned to determine how fine a grid is needed for accurate predictions with URANS.

Wakes Cases, Low Freestream Turbulence, No VGJs

Wake Characteristics. Cases without VGJ flow control were documented at Re=25,000 and 50,000 using the wake generator described above. The wakes generated by the moving rods can be characterized by comparing them to the wakes from the blades in the cascade. Figure 83 shows the mean and fluctuating velocity in the wakes of the moving rods and of the cascade blades. The cascade wakes were measured by traversing a hot-wire probe in lines $0.3C_x$ and $0.63C_x$ downstream of the trailing edges of the blades, perpendicular to the axial direction. In the $0.63C_x$ case, this is the same location used for the total pressure loss measurements. The spacing between airfoil rows in an engine is expected to be about $0.3C_x$ according to Pluim et al. (2009), so this location would be where the wake from an upstream airfoil would reach the leading edge of the next row. The moving rod wakes were measured by placing a stationary hot-wire midway between two blades in the cascade in the plane of the leading edges. The moving rods traversed $0.54C_x$ upstream of the hot-wire. The data from the probe were phase averaged on the rod passing cycle to determine the mean and fluctuating velocity as functions of time. For comparison in the figures, the rod velocity was then used to convert time to distance traversed. Curves in the figures were shifted along the horizontal axis to align the peaks for comparison. The actual positions, as shown previously, depend on the actual amount of flow turning, which varies with boundary layer separation and is a function of Reynolds number. All curves were normalized using the average local mean velocity.

The wakes from the upstream rods, when shown in dimensionless form as in Fig. 83, did not depend on Reynolds number. For all of the flow and rod velocities considered, the Reynolds number based on rod diameter is between about 400 and 2000, which should result in laminar separation for the boundary layer on the rod. With all cases in the same flow regime, the wakes should be similar. The wake for the Re=50,000 case with dimensionless wake passing frequency of F=0.28 is shown. For consistence, F is defined as above for the pulsed jet cases using the distance from the VGJ holes to the trailing edge and the average freestream velocity over this distance. In contrast to the rod wakes, the wakes of the cascade airfoils depend strongly on Reynolds number. As shown in Volino (2008) there are two flow regimes for the wakes. For Re=100,000 and below, the boundary layer separates and does not reattach. The wake is wide, the velocity deficit is large, and the peak turbulence intensity is of the order 20%. In dimensionless form, all cases in this regime are quantitatively similar. The second regime corresponds to Re=200,000 and above. The wakes in this regime are much narrower with lower velocity deficits and peak turbulence intensities of about 5%. In dimensionless form, all cases in this regime are also quantitatively similar. Figure 83 shows one case from each regime at Re=50,000 and 200,000.

The airfoil wake at Re=50,000 has a large mean velocity deficit at $0.3C_x$ which decreases in peak magnitude by 80% by $0.63C_x$. The peak turbulence intensity drops by 40% over this distance. At Re=200,000, the airfoil wake is about half as wide as at the lower Re, and the peak velocity deficit is about 25% as large. The peak turbulence intensity is 7%, which is about a third that at the lower Re. The change in the wake between $0.3C_x$ and $0.63C_x$ is much smaller than at the lower Re. The rod wake lies between the high and low Re airfoil wakes. The peak turbulence intensity is 14%. The rod wake appears to be reasonable approximation to an airfoil wake, although it does not fully match either the high or low Re case. One could conceivably use a rod of either larger or smaller diameter to match the low or high Re airfoil cases better.

Also of interest is how the rod wake compares to the airfoil wake in a low Reynolds number case with VGJs used to successfully control separation. The Re=50,000, F=0.56, B=1.0 case is used for comparison. As shown in Fig. 26, the boundary layer separates very briefly in this case at the upstream stations, but reattaches. At the most downstream station the boundary layer is attached for the full pulsing cycle, although it appears to be tending toward re-separation for part of the cycle. Figure 84 shows the wake velocity for this case and compares it to the rod wake. For the airfoil wake, the phase averaged results at 24 phases through the pulsing cycle are shown. Since the boundary layer does approach separation during part of the cycle, the wake velocity profile magnitude and position changes somewhat during the cycle. The mean velocity deficit and wake width of the upstream rod and airfoil are about the same. The peak turbulence intensity in the rod wake is about 40% higher than the highest value in the airfoil wake.

Turbulence spectra provide additional information about the wakes. The Fourier spectra of the airfoil wakes for the baseline cases are shown in Fig. 85. Dimensionless frequency on a log scale and position across the cascade at 0.63Cx downstream of the trailing edges are on the horizontal axes. The dimensionless frequency, F, is defined as above for the pulsed jet cases. The vertical axis shows the magnitude of the power spectral density premultiplied by the frequency and normalized on the nominal cascade exit velocity squared. In these coordinates the area under the surface at any position and frequency is proportional to the energy in the turbulence at that position and frequency. For the Re=50,000 case in Fig. 85a, there are peaks for each wake located at F=0.7 and smaller peaks at F=1.4. The expected vortex shedding frequency for the separation bubble on the airfoils, based on a bubble thickness of about 0.02 m, the trailing edge flow velocity, and a Strouhal number of 0.2 is about F=1.0. The observed frequencies in the wake are therefore consistent with vortex shedding. The spectra for the Re=200,000 case in Fig. 85b are much different. The peaks are two orders of magnitude lower than in the Re=50,000 case. This difference in magnitude of u'^2 is consistent with the one order of magnitude difference in u' shown in Fig. 83b. The spectral peaks are spatially narrower at Re=200,000, again consistent with the wake velocity profiles in Fig. 83. The spectral peaks are broad banded and centered at F=2.5. These peaks are likely associated with the turbulence in the airfoil boundary layers. Similar peaks at F=2.5 may also be present in the Re=50,000 case, but if they are present they are overwhelmed in the tails of the much larger low frequency peaks. Low frequency peaks are not observed at Re=200,000 because the airfoil boundary layers are attached so there is no large separation bubble to produce vortex shedding.

Fourier spectra for the cascade wakes with pulsed VGJs at Re=50,000, F=0.56, D=10%, and B=1.0 are shown in Fig. 86. The spectra have magnitude and frequency between those of the high and low Re cases of Fig. 85. Fourier spectra for this case present an incomplete picture, however, because the wake moves spatially during the jet pulsing cycle and the magnitude of the peaks also change. Fourier spectra present a time average of the quantity under consideration, so it is not possible to consider frequencies at particular times during the cycle. To overcome this, wavelet spectra can be computed. In wavelet analysis, the convolution integral between a signal of interest and a function containing oscillations at a particular frequency (the wavelet) is computed. The magnitude of the result indicates when in time the frequency of the wavelet appears in the signal. The wavelet is dilated and constricted to change its oscillation frequency and the convolution integral is computed multiple times to construct a map of the signal content as a function of time and frequency simultaneously. The particular wavelet, or function, used for the analysis determines how well time and frequency are each resolved. Two commonly used wavelets for turbulence analysis are the Mexican Hat wavelet and the Morlet wavelet. The

Mexican Hat wavelet is a real valued function with essentially a single oscillation along the time axis. It is particularly good for resolving oscillations in time, but less so for frequency. The Morlet wavelet is a complex valued with multiple oscillations at a given frequency along the time axis. Because it has a longer duration, it is less able to resolve time, but because of its multiple oscillations it can better resolve frequencies than the Mexican Hat wavelet. Figure 87 shows the wavelet spectra for the wake turbulence of the pulsed jet case at two representative times in the cycle. Figures 87a and 87b were produced with the Mexican Hat wavelet and Figs. 87c and 87d show the same data analyzed with the Morlet wavelet. Figure 87a is typical of most of the cycle and shows a peak for each wake centered at F=1.9. There is also a smaller peak, hidden in the view shown at F=0.56 at a pitchwise position about $0.4L_{\phi}$ higher than the large peak. The smaller peak is at the pulsing frequency. At the phase shown in Fig. 87b, the higher frequency peak magnitude is now about a third of its value in Fig. 87a and is split into two nearby peaks at F=1.6 and 2.2. The F=0.56 peak is still present at about the same magnitude, but now appears more prominent since the other peaks are smaller. If all phases of the wavelet spectra are time averaged, the result is close to the Fourier spectra of Fig. 86. Figure 87c shows the Morlet wavelet result at the same phase shown in Fig. 87a. The two wavelets produce similar results, but the low frequency peak at the pulsing frequency is better resolved and has a higher magnitude with the Morlet wavelet. Figure 87d shows the Morlet wavelet result at the same phase as Fig. 87b. Again the two wavelets produce similar results, with some differences in the peak magnitude and the Morlet wavelet showing a sharper peak at the pulsing frequency.

Figure 88a shows the rod wake spectrum using the Morlet wavelet. The time axis is converted to a spatial position, as explained above for Fig. 83. There is a sharp peak at F=0.28, which corresponds to the rod passing frequency. A broader peak is centered at about F=1.0. This broad peak is due to the turbulence and vortices shed by the rod. Figure 88b shows the same data analyzed with the Mexican Hat wavelet. No peak appears at the wake passing frequency because the Mexican Hat wavelet is more narrowly focused in time and does not pick up the variation in velocity across the cycle. The broad band peak is centered at F=0.8, which is slightly different than indicated by the Morlet wavelet. It is also somewhat narrower spatially due to the better time resolution of the Mexican Hat wavelet. As with the mean and rms velocity, the spectra of the rod wakes have frequency and magnitude between those of the high and low Reynolds number baseline cases. The rod wakes are more similar to those of the pulsed jet controlled case of Fig. 87. The peak magnitudes are similar, although the frequencies of the rod wakes are somewhat lower. Given that there are a variety of wakes that could be generated by an upstream airfoil depending on the flow conditions, the wakes produced by the present cylindrical rods appear to be reasonable for the present investigation. Investigating the effect of different wakes produced by rods of different diameter or shape may be an interesting topic for future work.

Pressure, loss, and velocity results. The Cp distributions for the cases with wakes are shown in Fig. 89. With the wake passing period set to F=0.28, the wakes appear to have some effect at Re=25,000, but the boundary layer does not appear to reattach. At Re=37,500 the Cp values are closer to the inviscid line near the trailing edge, suggesting possible reattachment. In the Re=50,000 case there is good agreement with the inviscid line, suggesting the boundary layer is reattached. If the wake passing frequency is doubled to F=0.56 in the Re=25,000 case, the Cp values indicate more reattachment, although the suction peak is still low compared to the higher Re cases. When the wake passing frequency is lowered to F=0.14 with Re=50,000, the wakes

have some effect in lowering Cp, but the boundary layer appears to remain separated. The boundary layer reattaches without flow control when Re=100,000 in the high freestream turbulence case and at Re slightly above 100,000 with low freestream turbulence. It is not surprising, therefore, that with Re=100,000 there is good agreement with the inviscid line even with the low wake passing frequency of F=0.14. When Re=200,000 there is no separation problem in the baseline cases, so adding wakes, regardless of the frequency does not change the Cp distribution. The wake passing frequency needed to suppress separation appears to match the pulsing frequency needed for control with VGJs at moderate blowing ratios. At Re=50,000, F=0.28 is sufficient, but at lower Reynolds numbers a higher frequency is needed.

Figure 90 shows the total pressure loss results. With F=0.28, the wakes have an effect at all Reynolds numbers, suppressing the loss peak and establishing periodicity across the cascade. At Re=25,000 the peak is wide, indicating a thick boundary layer. Results were similar with VGJs at this frequency. As Re is increased, the peak becomes narrower, indicating a thinner boundary layer and lower overall losses. When F is increased to 0.56, the peak becomes somewhat narrower at Re=25,000, but it is still wider than in the higher Re cases. Lowering F to 0.14 causes a large increase in losses and a loss of periodicity in the cascade when Re=50,000. This is consistent with the Cp results. At Re=100,000 the wakes suppress separation much like the VGJs, and the loss peaks match those obtained with VGJs. At Re=200,000 the loss peaks match those in the baseline case. Adding wakes or changing their frequency does not appear to have an effect at high Reynolds number. Any losses induced by the wakes themselves must be relatively small.

Figure 91 shows velocity profiles for the Re=25,000, F=0.28 case. Data were not acquired at Station 1. At Station 2, a disturbance in the mean profiles appears between t/T=0.375 and 0.583 due to the wake. By Station 3 the boundary layer has separated, although the separation appears to be suppressed between t/T=0.458 and 0.583. The separation bubble grows bigger at some phases at Stations 4 and 5, but it is still suppressed at some phases. At Station 5 the wake appears to be reducing the extent of the separation for about half the cycle. At Station 6 the boundary layer has an inflection point at all phases and appears on the verge of separating, but is only clearly separated for a few phases centered around t/T=0.542. The wakes significantly suppress the separation bubble compared to the baseline case, but do not eliminate it entirely. This is similar to the effect of VGJs at this Reynolds number. The result is losses much lower than the baseline case, but still significantly higher than with higher Reynolds numbers due to the thick boundary layer.

Figure 92 shows the results with Re=37,500 and F=0.28. In agreement with the Cp and loss profiles, results are similar to those at Re=25,000, but the separation bubble thickness is reduced. With Re=50,000 and F=0.28, as shown in Fig. 93, the trend continues to the point that the separation bubble is essentially eliminated. With F=0.14 at Re=50,000 in Fig. 94, the separation bubble reappears. The wake passing frequency is not high enough to keep the boundary layer attached.

Timeline and Upcoming Work

Work was delayed in the second half of 2008 so that the wind tunnel could be disassembled for fabrication and installation of the wake generator. This was completed in November 2008 and velocity data with VGJs and low freestream turbulence was acquired in late 2008 and early 2009. The turbulence grid was then installed, and pressure and velocity data were acquired for

high freestream turbulence cases with VGJs. Experiments with the wake generator began in April, and low freestream turbulence cases with wakes were documented in May and June.

Computations of cases with VGJs showed that URANS calculations with the Transition-sst model did not predict the flow control observed in the experiments. Large eddy simulations were done in the first part of 2009 to try to produce an accurate CFD prediction. The LES correctly predicted boundary layer reattachment.

Work is currently somewhat behind the original proposed schedule due to the late start at the very beginning of the project which resulted from problems with transfer of funds, and necessary pauses in the experiments for fabrication and repair of the facility, and the need to pursue different approaches with the CFD. Work is, however, proceeding as planned. Experiments with high freestream turbulence and wakes will be done next, followed by cases with wakes and VGJs combined. CFD with wakes is beginning now, and efforts to simulate cases with VGJs using URANS calculations continue.

References

Ibrahim, M., Kartuzova, O., and Volino, R.J., 2008, "Experimental and Computational Investigations of Separation and Transition on a Highly Loaded Low-Pressure Turbine Airfoil: Part 1 – Low Freestream Turbulence Intensity," ASME paper IMECE2008-68879. Presented at the ASME IMECE, Boston, MA, November 2008. In press for ASME *J. Turbomachinery*.

Ibrahim, M., Kartuzova, O., and Volino, R., 2009, "LES and URANS Computational Investigations of LPT Blade (L1A) Separation Control using Vortex Generator Jets," accepted for presentation at Turbulence, Heat and Mass Transfer 6, Rome, Italy, September 2009.

Pluim, J., Memory, C., Bons, J., and Chen, J.P., "Designing a High Fidelity Wake Simulator for Research Using Linear Cascades," ASME paper GT2009-59276. Presented at the ASME International Gas Turbine Conference, Orlando, FL, June 2009.

Volino, R.J., 2008, "Separated Flow Measurements on a Highly Loaded Low-Pressure Turbine Airfoil," ASME paper GT2008-51445. Presented at the ASME International Gas Turbine Conference, Berlin, Germany, June 2008.

Volino, R.J., Kartuzova, O., and Ibrahim, M., 2008, "Experimental and Computational Investigations of Separation and Transition on a Highly Loaded Low-Pressure Turbine Airfoil: Part 2 – High Freestream Turbulence Intensity," ASME paper IMECE2008-68776. Presented at the ASME IMECE, Boston, MA, November 2008.

Volino, R.J., Kartuzova, O., and Ibrahim, M.B., 2009, "Experimental and Computational Investigations of Low-Pressure Turbine Separation Control Using Vortex Generator Jets," ASME paper GT2009-59983. Presented at the ASME International Gas Turbine Conference, Orlando, FL, June 2009.

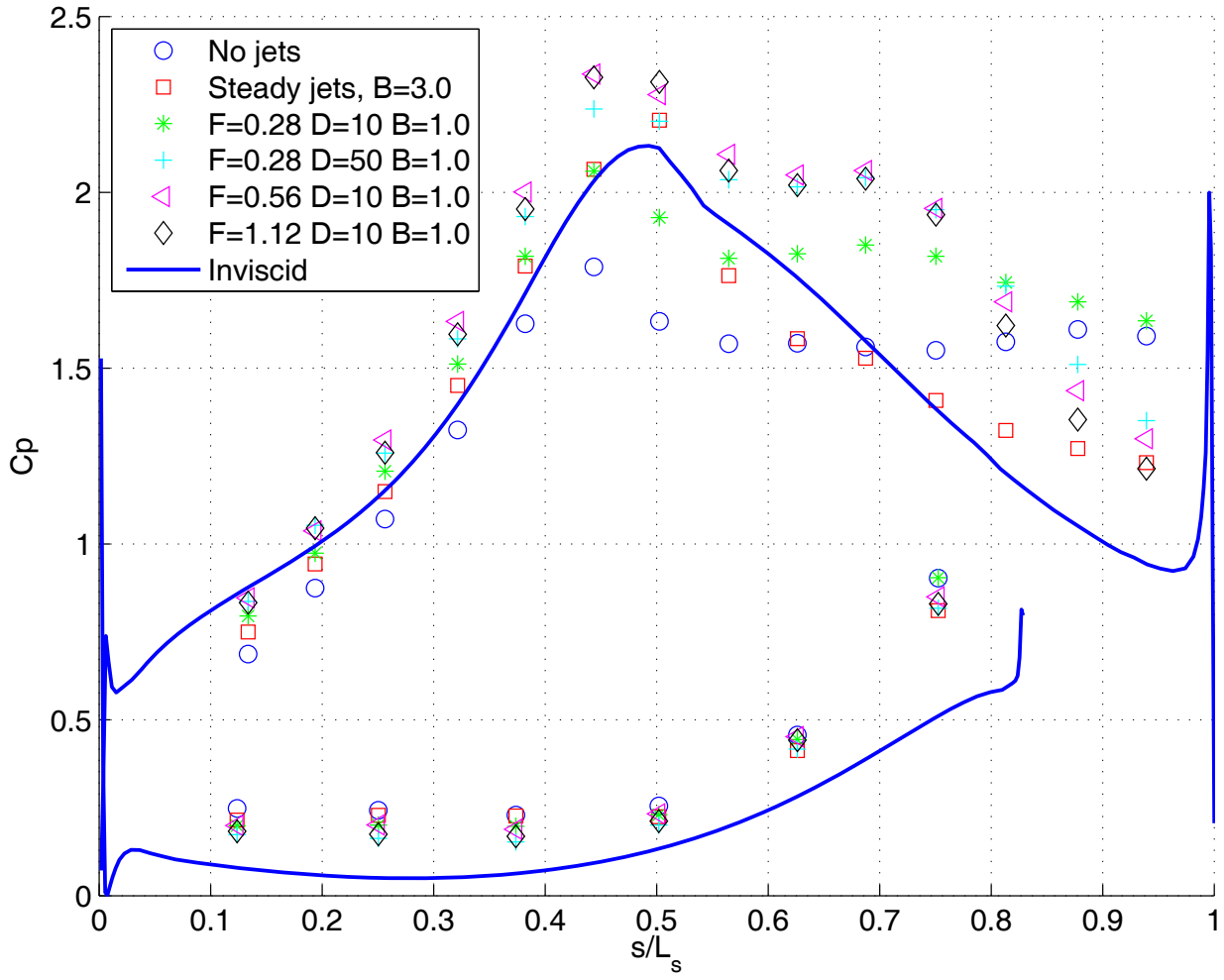
No jets
Steady jets, B=3.0
F=0.28 D=10 B=1.0
F=0.28 D=50 B=1.0
F=0.56 D=10 B=1.0
F=1.12 D=10 B=1.0
Inviscid
Cp
s/L_s
0
0.5
1
1.5
2
2.5
0.1
0.2
0.3
0.4
0.5
0.6
0.7
0.8
0.9

a)

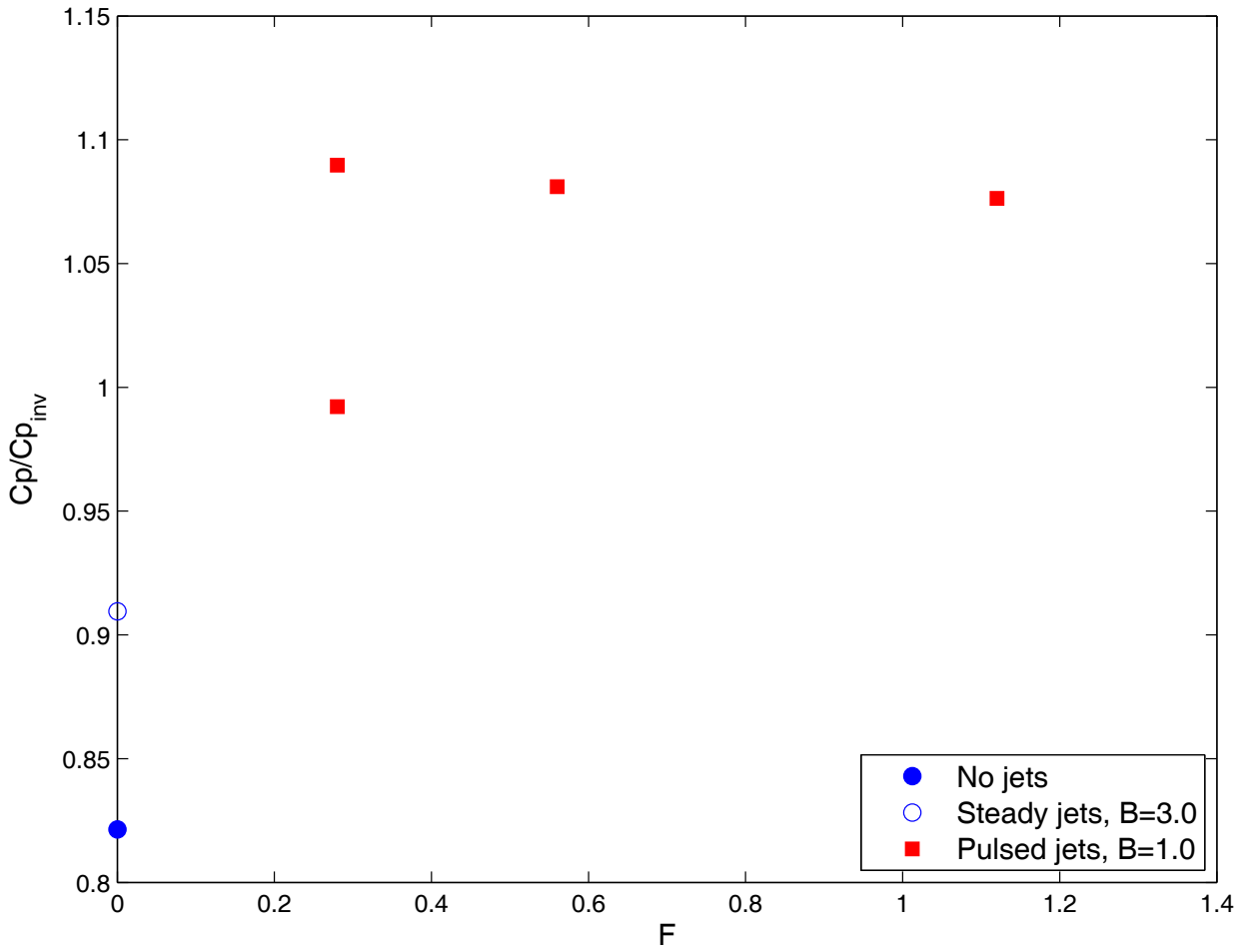

b)

Fig. 1 Cp results, low TI, Re=25,000: a) Cp profile, b) Integrated Cp.

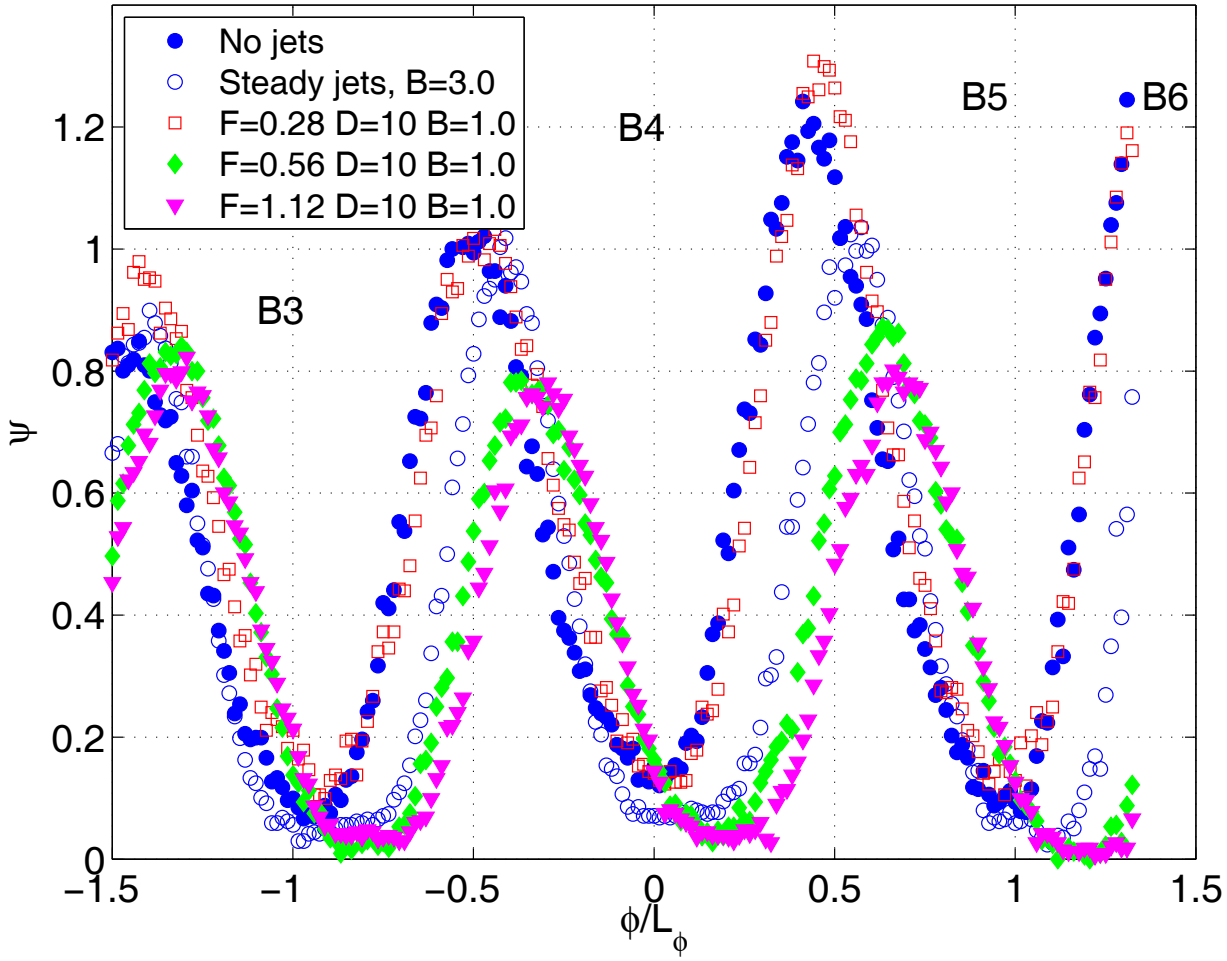
No jets
Steady jets, B=3.0
F=0.28 D=10 B=1.0
F=0.56 D=10 B=1.0
F=1.12 D=10 B=1.0
B3
B4
B5
B6
ψ
ϕ/L_ϕ
1.2
1
0.8
0.6
0.4
0.2
0
−1.5
−1
−0.5
0
0.5
1
1.5

a)

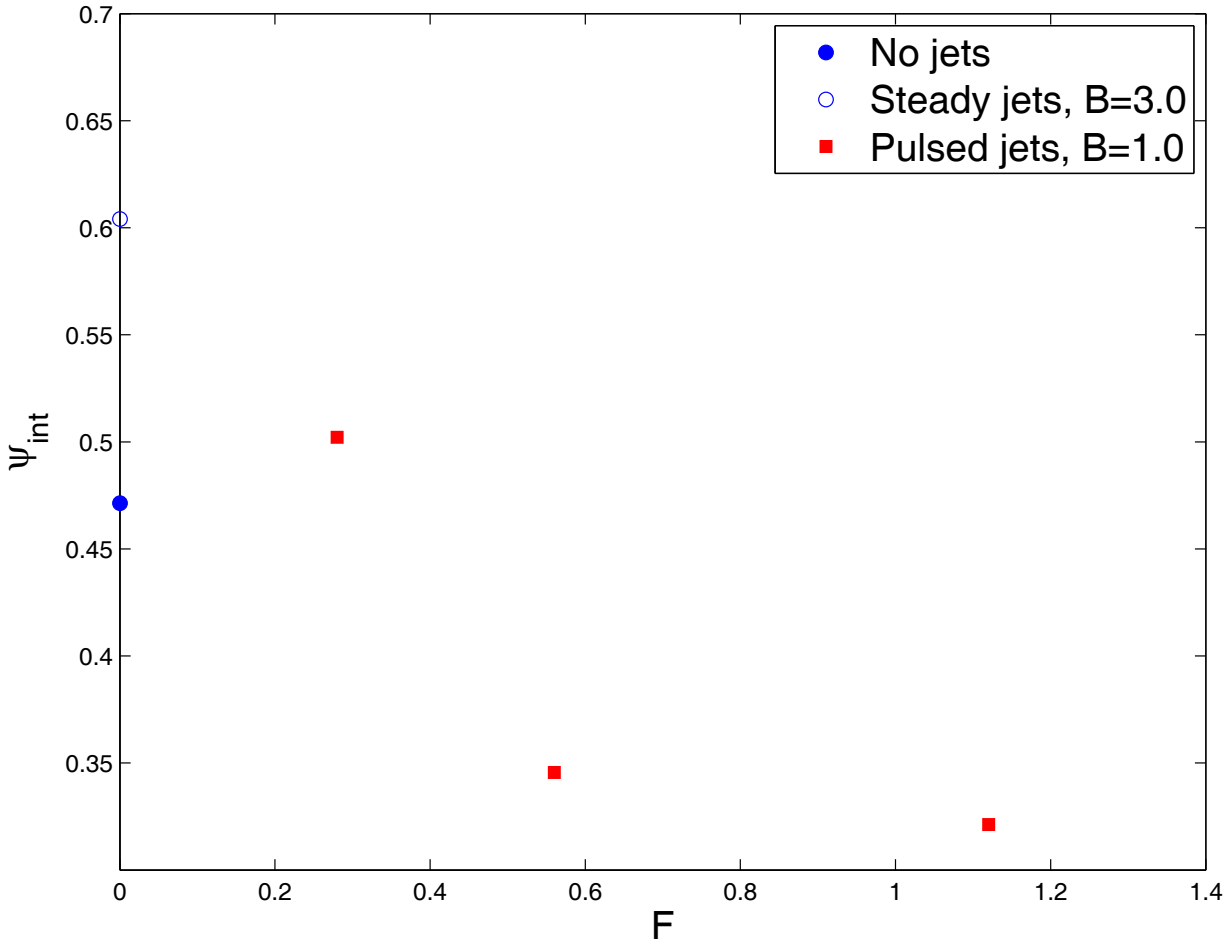

b)

Fig. 2 Ψ results, low TI, Re=25,000: a) Ψ profile, b) Integrated Ψ.

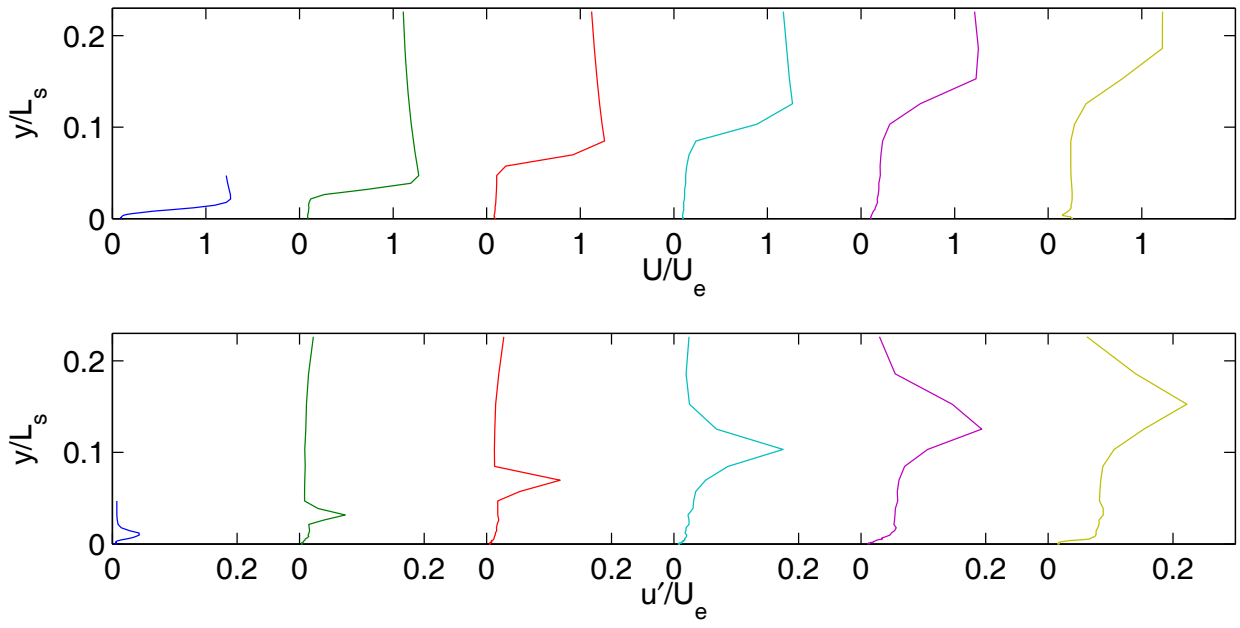

Fig. 3 Time averaged velocity profiles, low TI, Re=25,000, no VGJs: a) mean, b) rms.

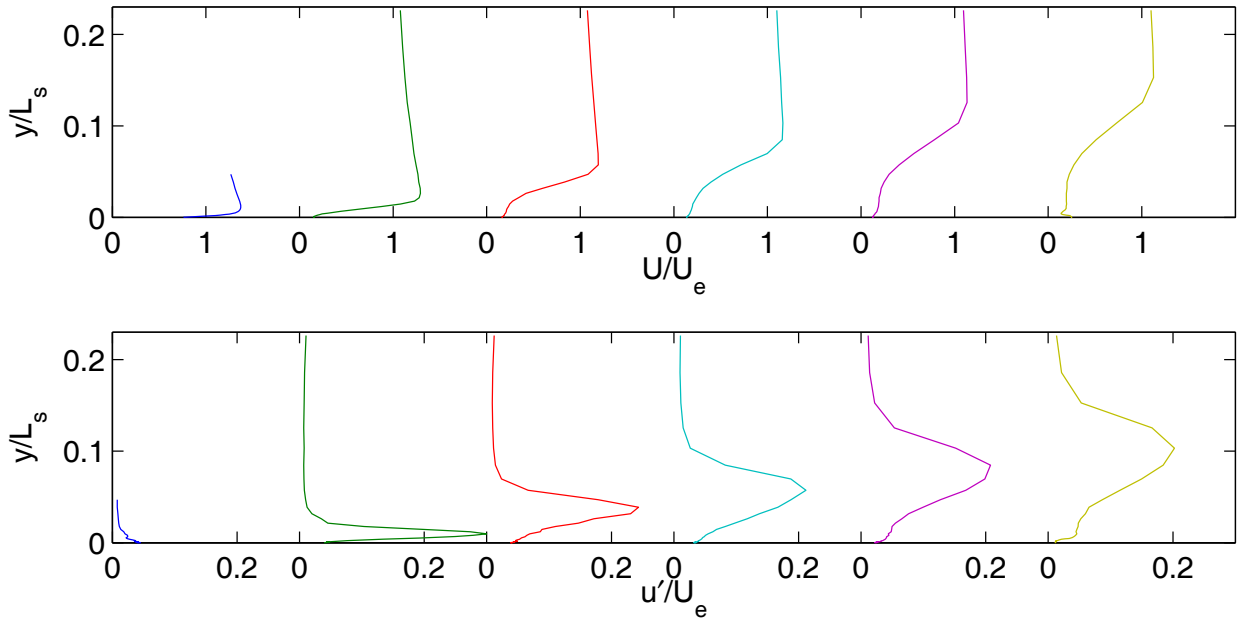

Fig. 4 Time averaged velocity profiles, low TI, Re=25,000, steady VGJs, B=3.0: a) mean, b) rms.

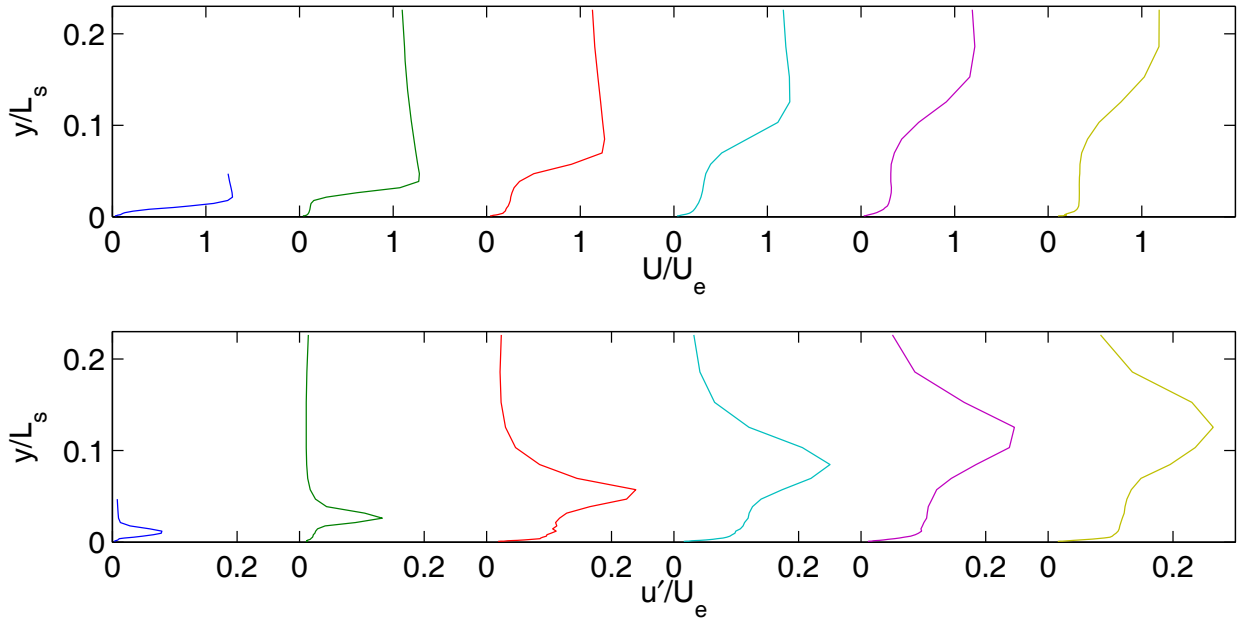

Fig. 5 Time averaged velocity profiles, low TI, Re=25,000, pulsed VGJs, F=0.28, D=10%, B=1.0: a) mean, b) rms.

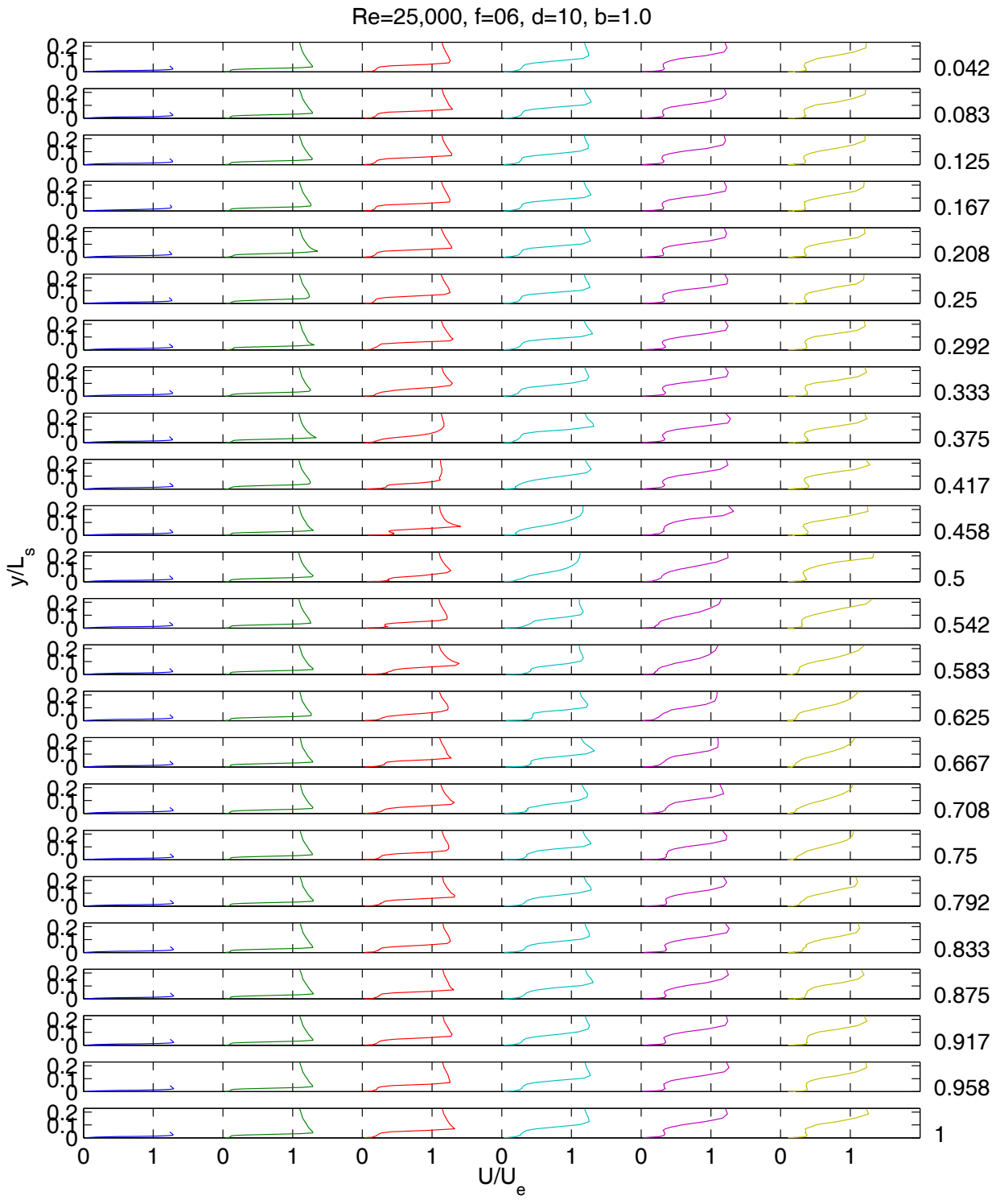
Re=25,000, f=06, d=10, b=1.0
y/L_s
U/U_e
0.042
0.083
0.125
0.167
0.208
0.25
0.292
0.333
0.375
0.417
0.458
0.5
0.542
0.583
0.625
0.667
0.708
0.75
0.792
0.833
0.875
0.917
0.958
1

a)

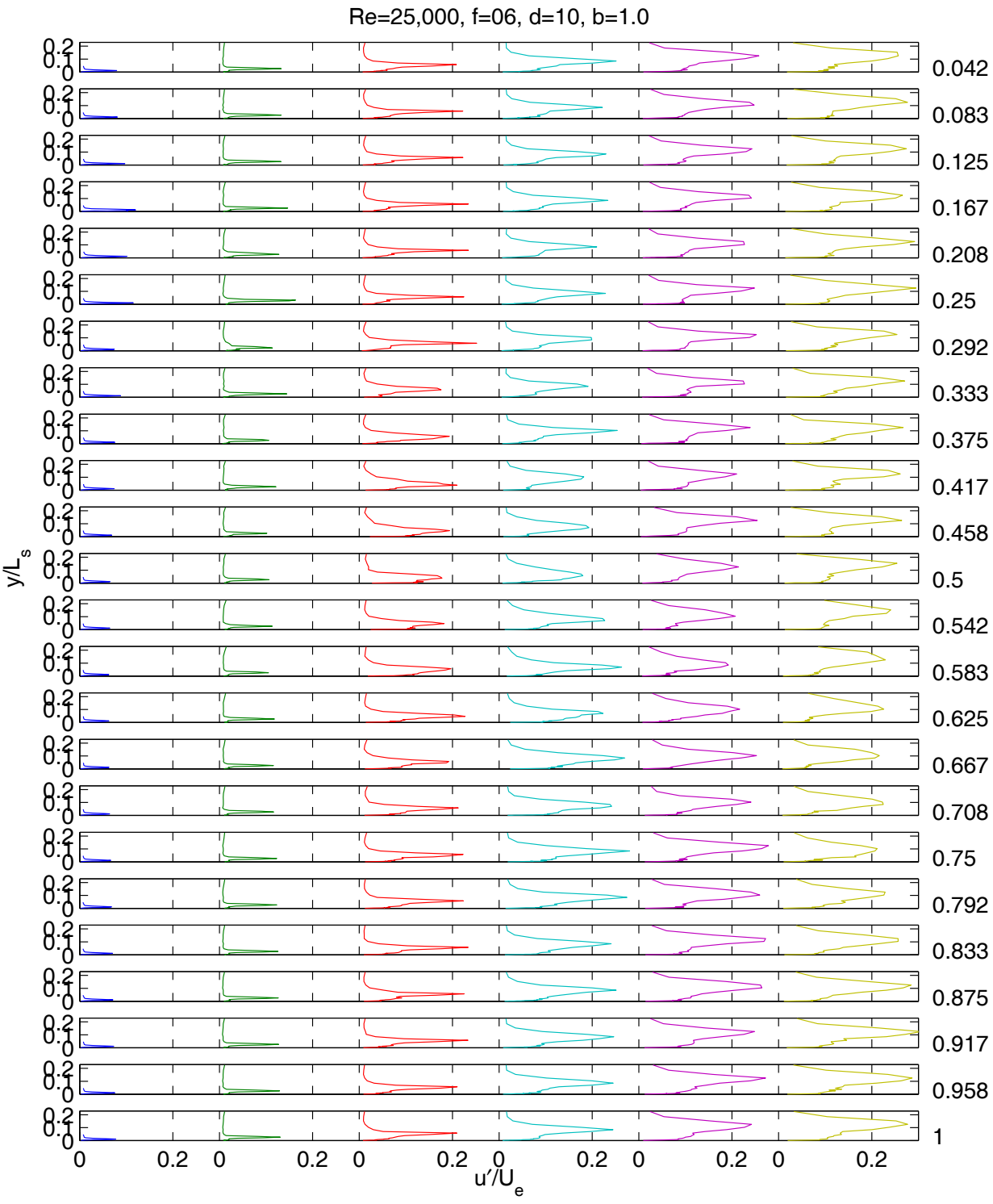

b)

Fig. 6 Phase averaged velocity profiles, low TI, Re=25,000, pulsed VGJs, F=0.28, D=10%, B=1.0: a) mean, b) rms.

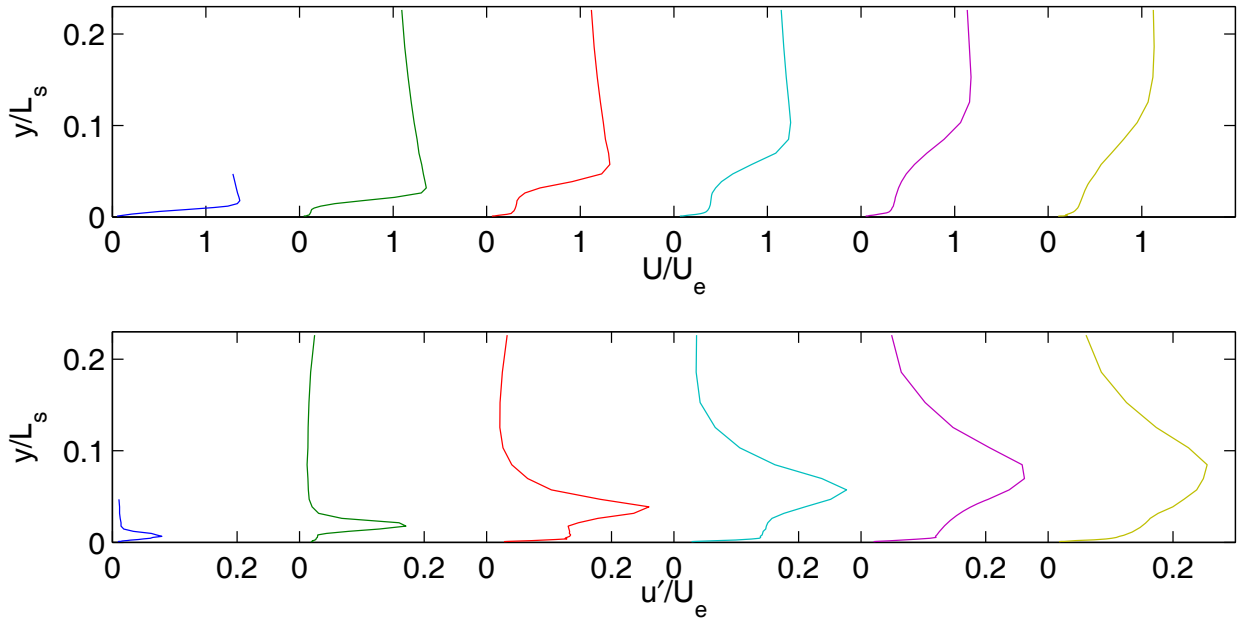

Fig. 7 Time averaged velocity profiles, low TI, Re=25,000, pulsed VGJs, F=0.28, D=50%, B=1.0: a) mean, b) rms.

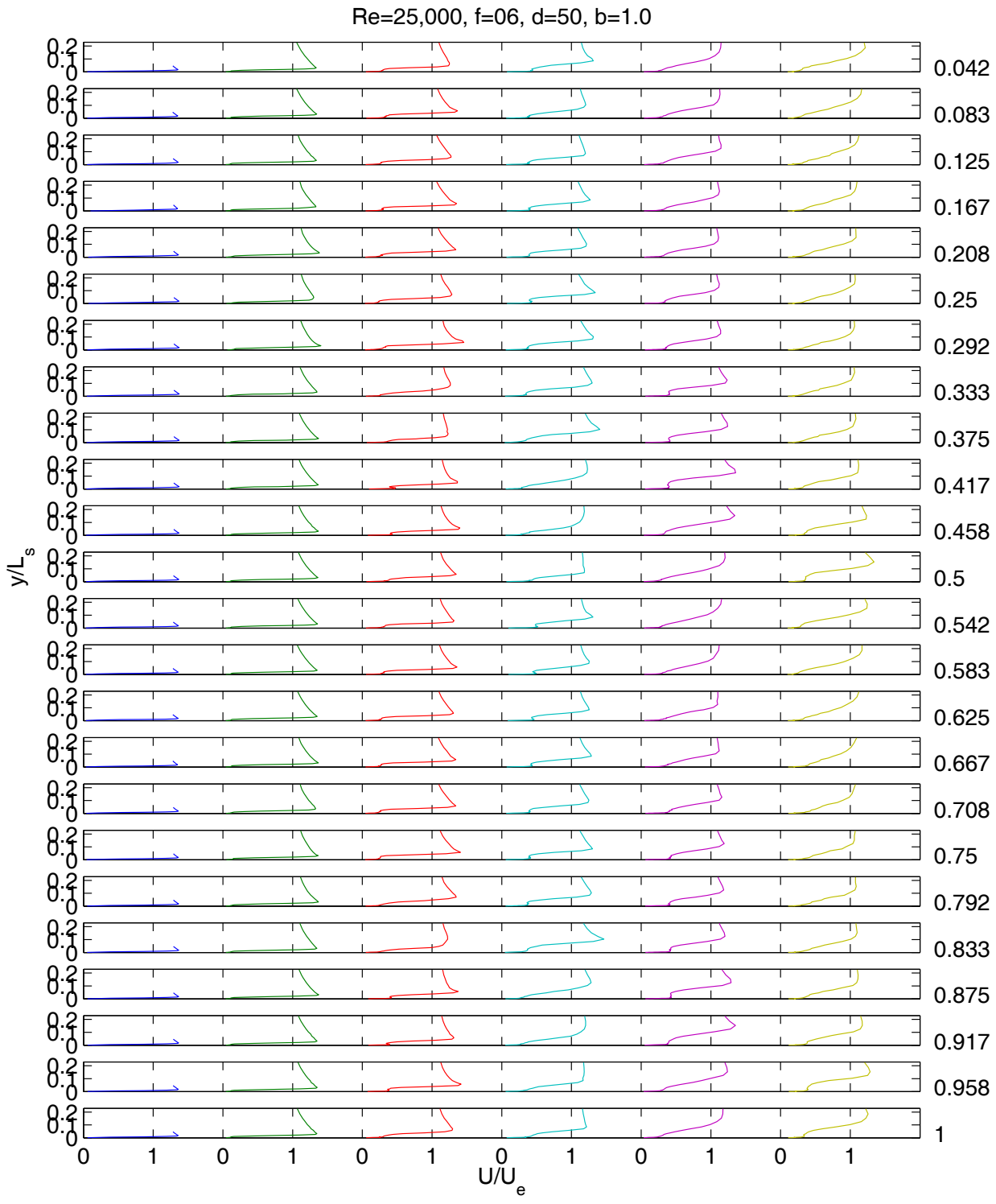
Re=25,000, f=06, d=50, b=1.0
y/L_s
U/U_e
0.042
0.083
0.125
0.167
0.208
0.25
0.292
0.333
0.375
0.417
0.458
0.5
0.542
0.583
0.625
0.667
0.708
0.75
0.792
0.833
0.875
0.917
0.958
1

a)

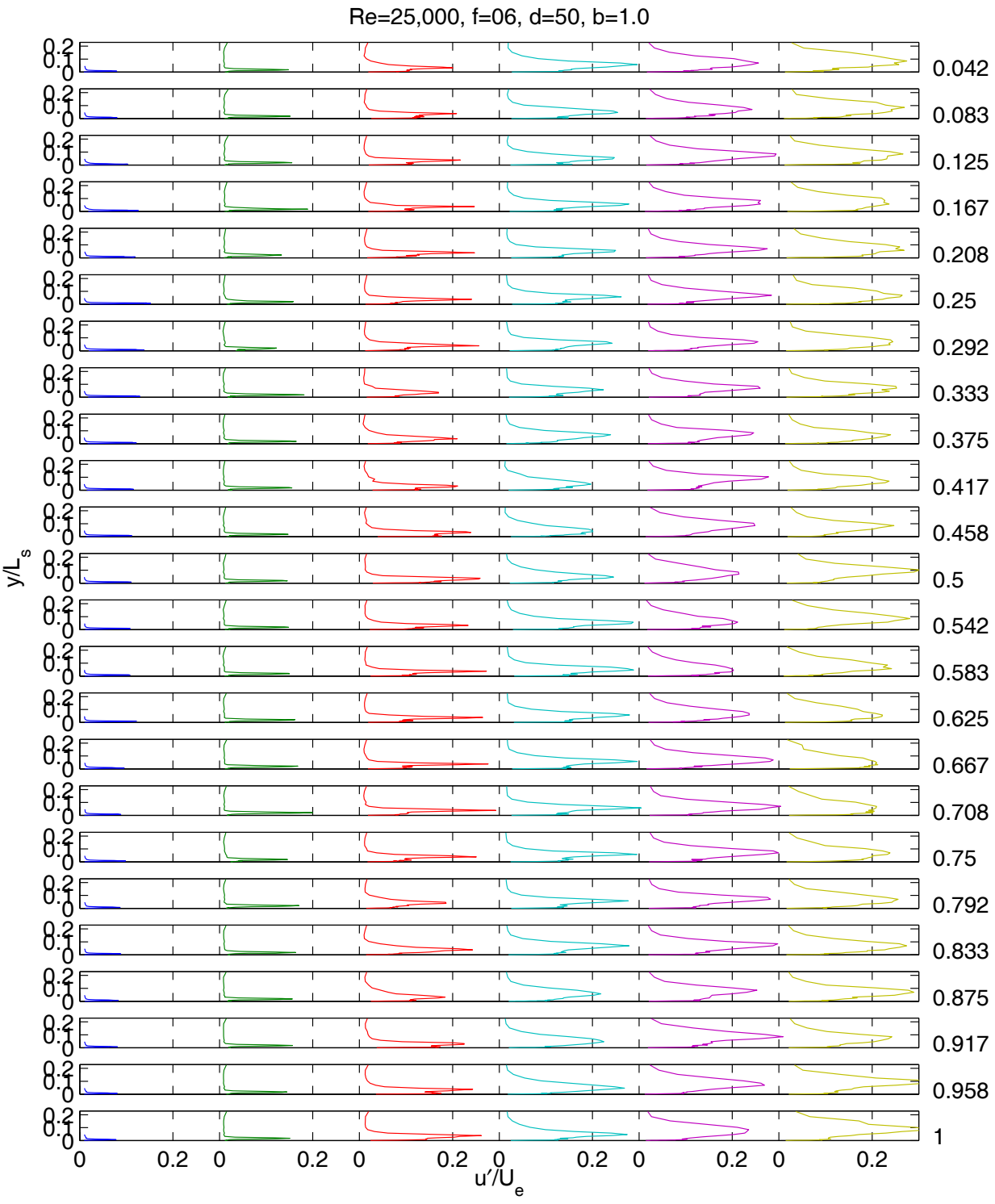

b)

Fig. 8 Phase averaged velocity profiles, low TI, Re=25,000, pulsed VGJs, F=0.28, D=50%, B=1.0: a) mean, b) rms.

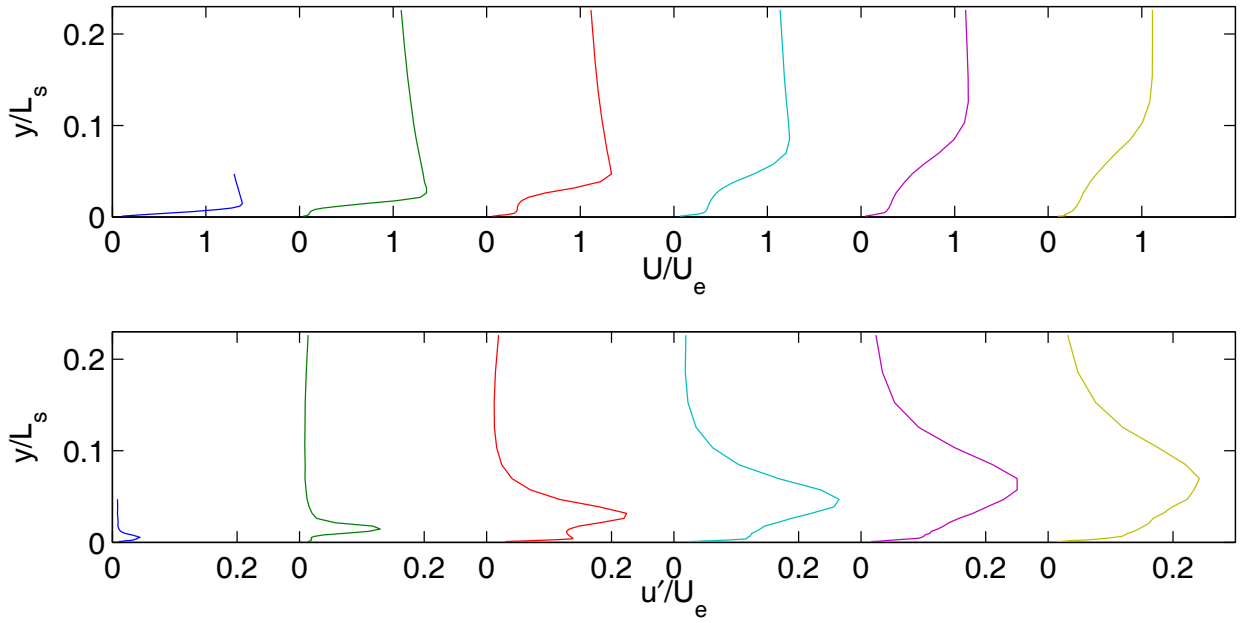

Fig. 9 Time averaged velocity profiles, low TI, Re=25,000, pulsed VGJs, F=0.56, D=10%, B=1.0: a) mean, b) rms.

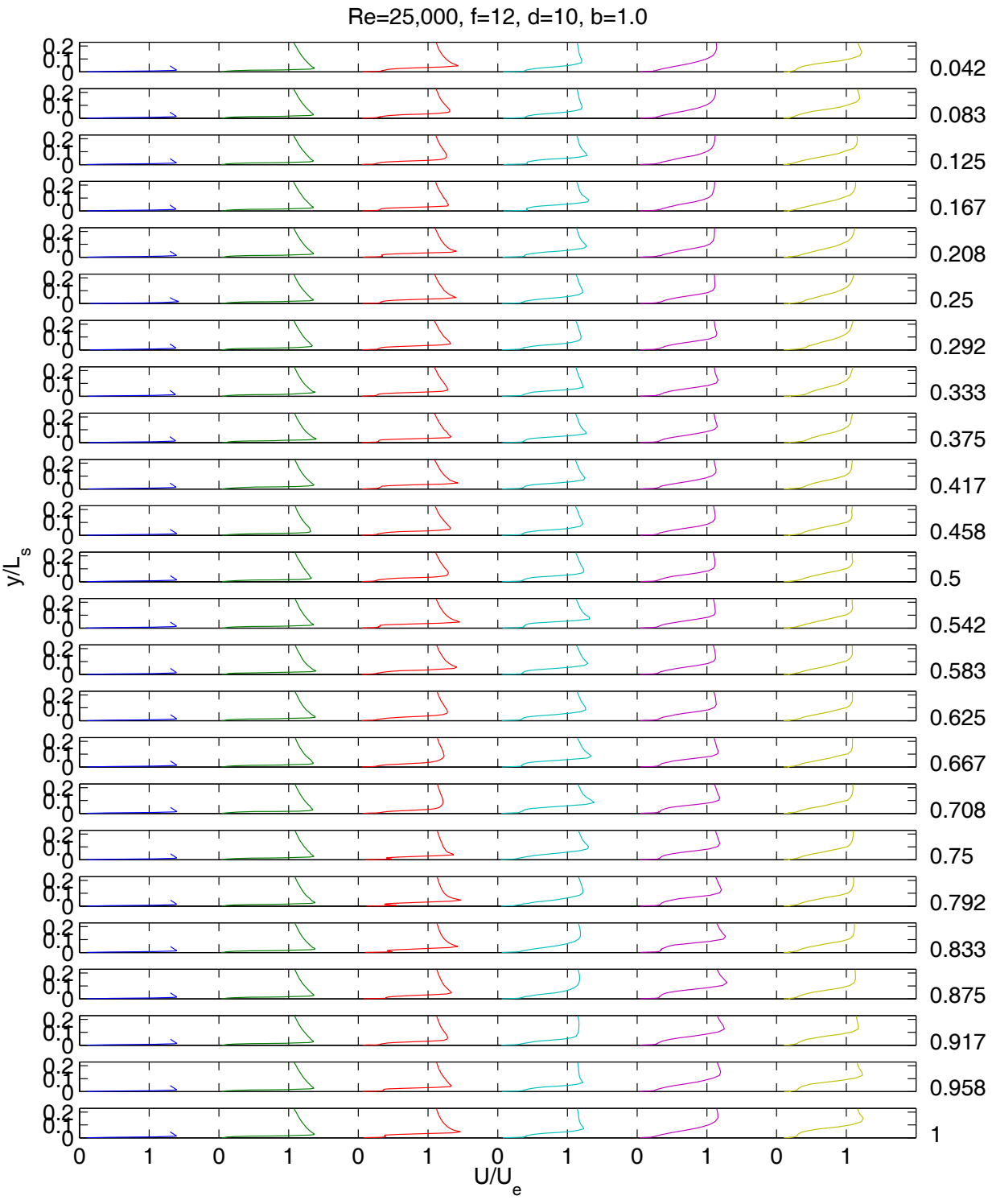
Re=25,000, f=12, d=10, b=1.0
y/L_s
U/U_e
0.042
0.083
0.125
0.167
0.208
0.25
0.292
0.333
0.375
0.417
0.458
0.5
0.542
0.583
0.625
0.667
0.708
0.75
0.792
0.833
0.875
0.917
0.958
1

a)

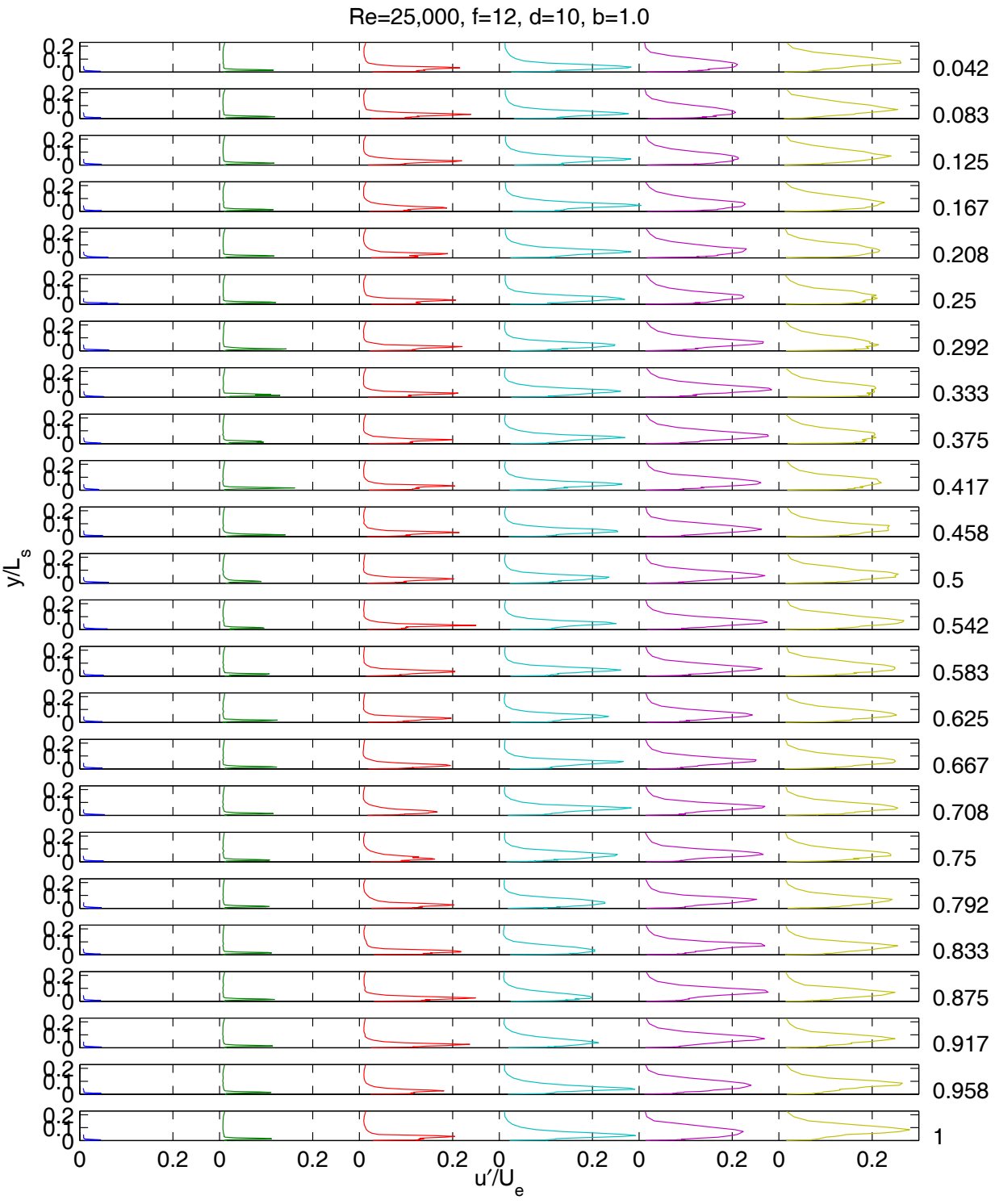

b)

Fig. 10 Phase averaged velocity profiles, low TI, Re=25,000, pulsed VGJs, F=0.56, D=10%, B=1.0: a) mean, b) rms.

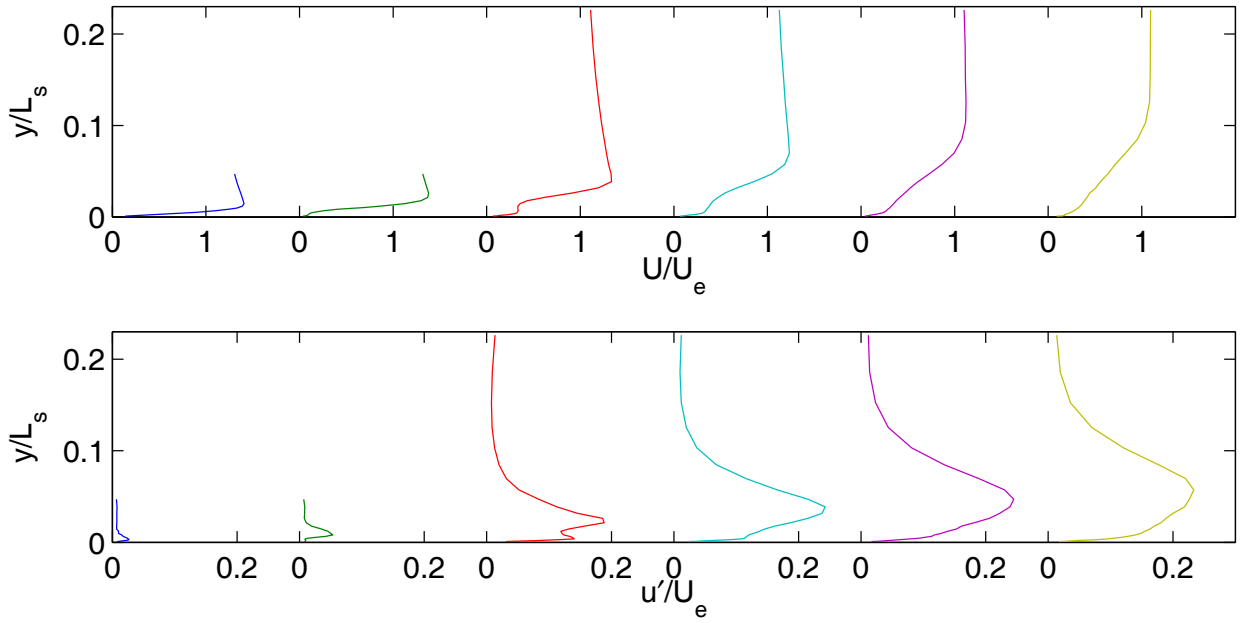

Fig. 11 Time averaged velocity profiles, low TI, Re=25,000, pulsed VGJs, F=1.12, D=10%, B=1.0: a) mean, b) rms.

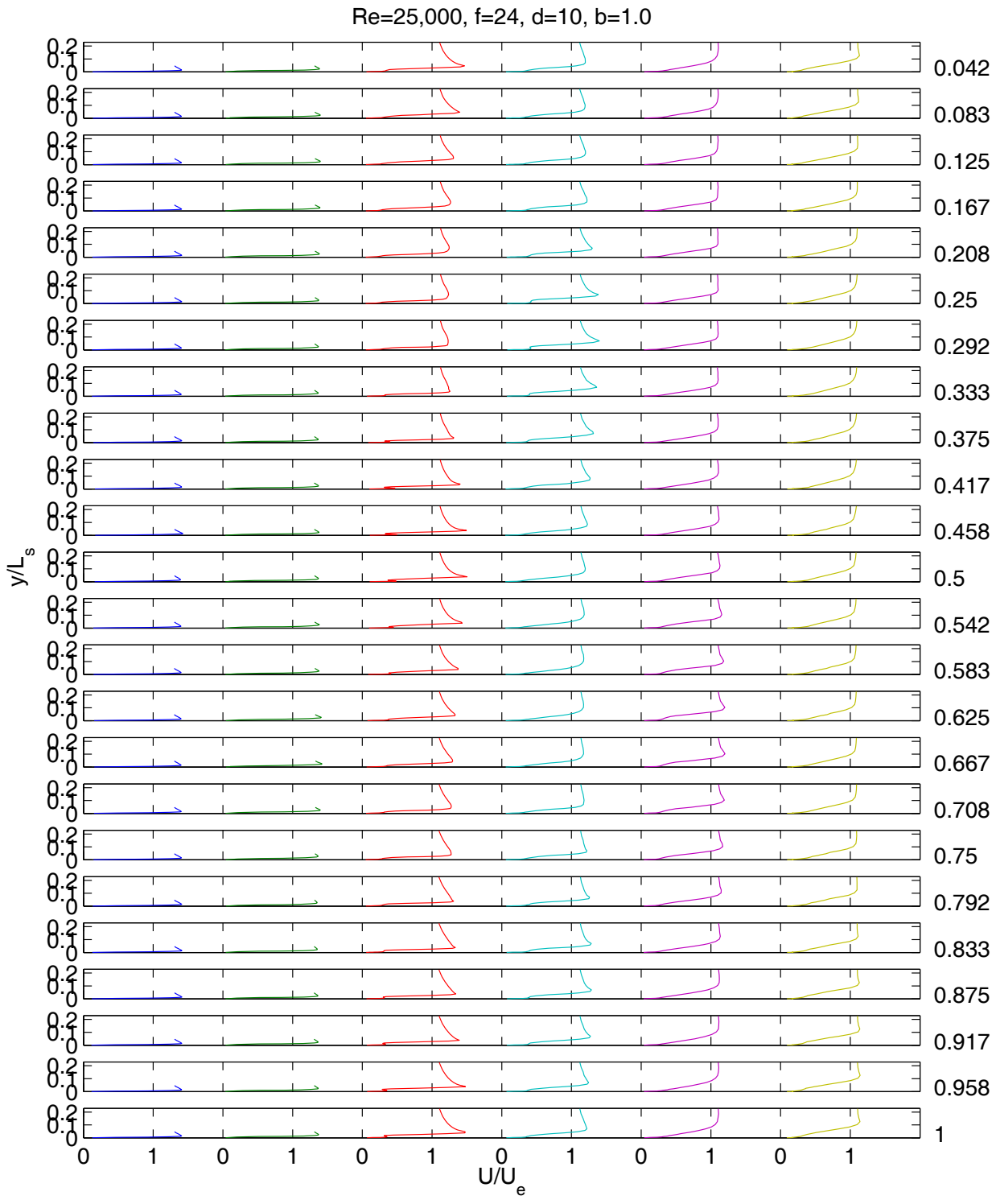
Re=25,000, f=24, d=10, b=1.0
y/L_s
U/U_e
0.042
0.083
0.125
0.167
0.208
0.25
0.292
0.333
0.375
0.417
0.458
0.5
0.542
0.583
0.625
0.667
0.708
0.75
0.792
0.833
0.875
0.917
0.958
1

a)

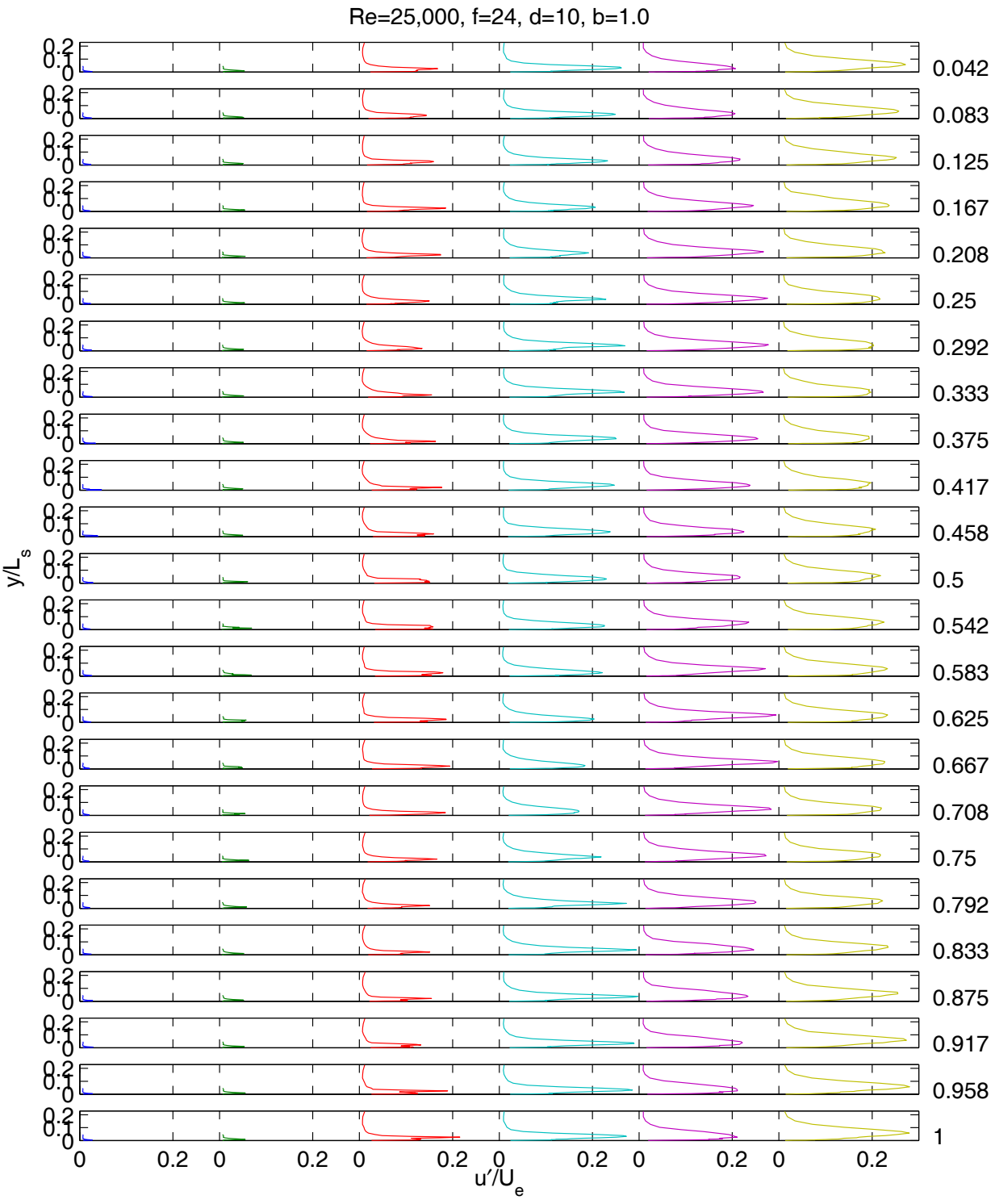

b)

Fig. 12 Phase averaged velocity profiles, low TI, Re=25,000, pulsed VGJs, F=1.12, D=10%, B=1.0: a) mean, b) rms.

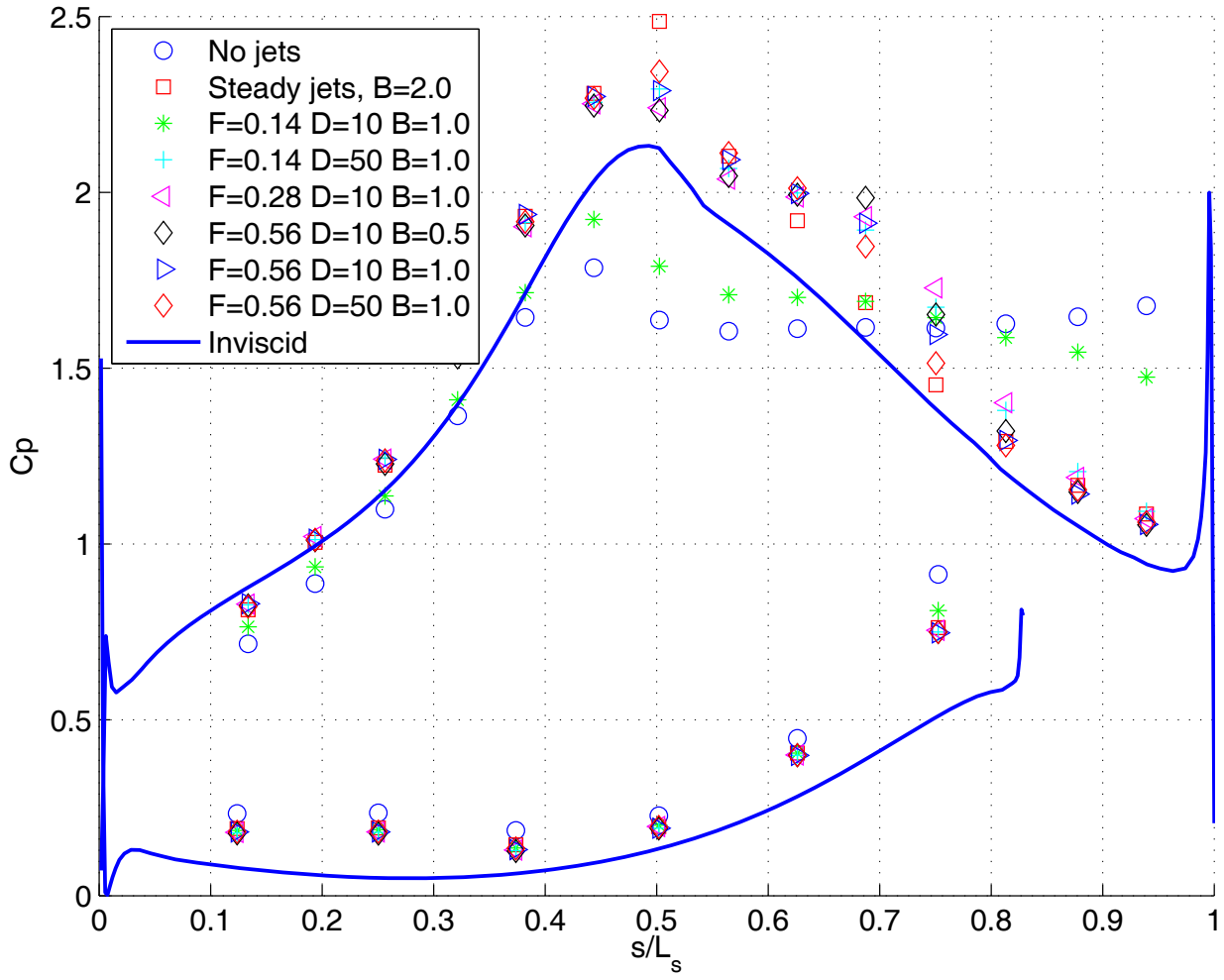
No jets
Steady jets, B=2.0
F=0.14 D=10 B=1.0
F=0.14 D=50 B=1.0
F=0.28 D=10 B=1.0
F=0.56 D=10 B=0.5
F=0.56 D=10 B=1.0
F=0.56 D=50 B=1.0
Inviscid
Cp
s/L_s
2.5
2
1.5
1
0.5
0
0
0.1
0.2
0.3
0.4
0.5
0.6
0.7
0.8
0.9
1

a)

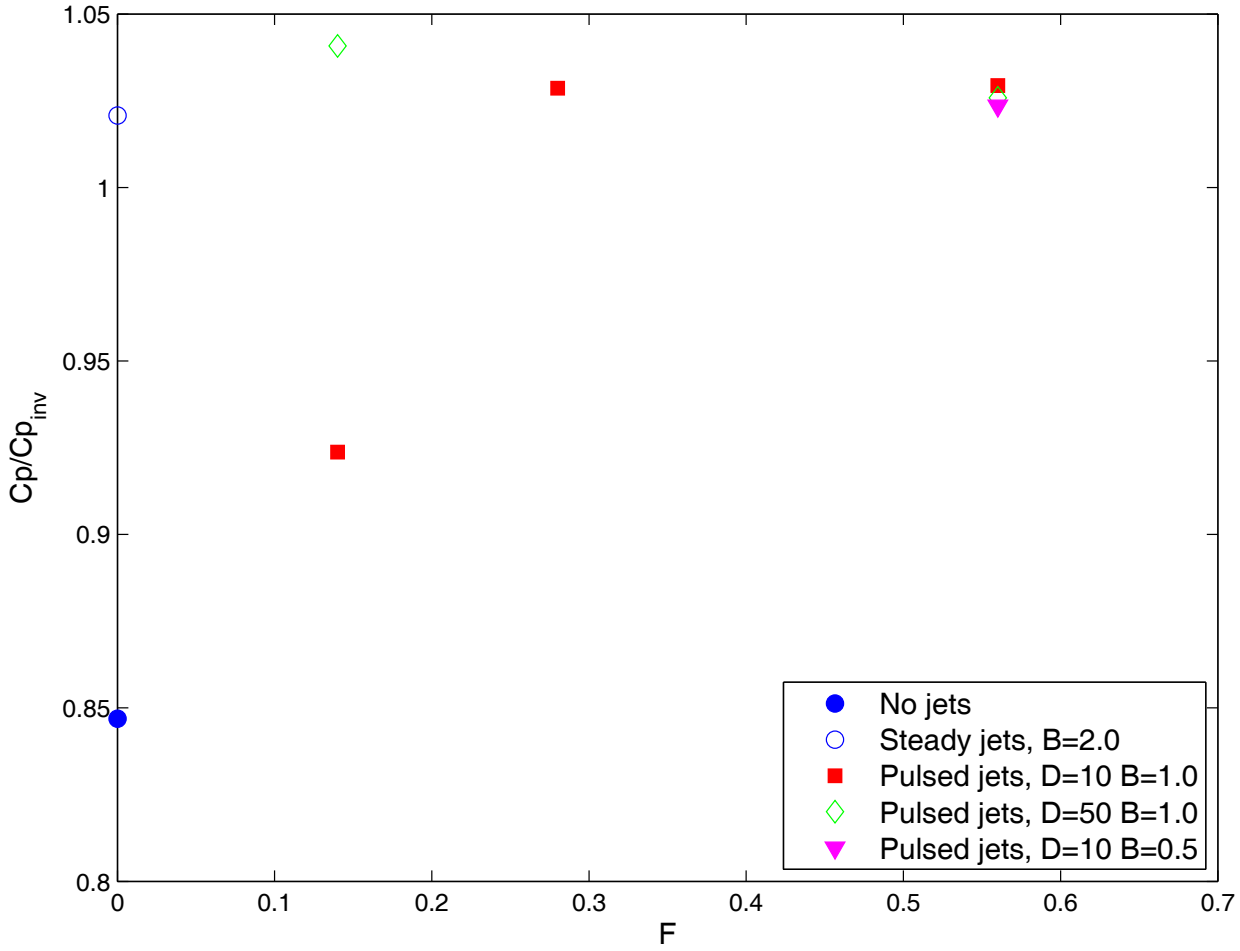

b)

Fig. 13 Cp results, low TI, Re=50,000: a) Cp profile, b) Integrated Cp.

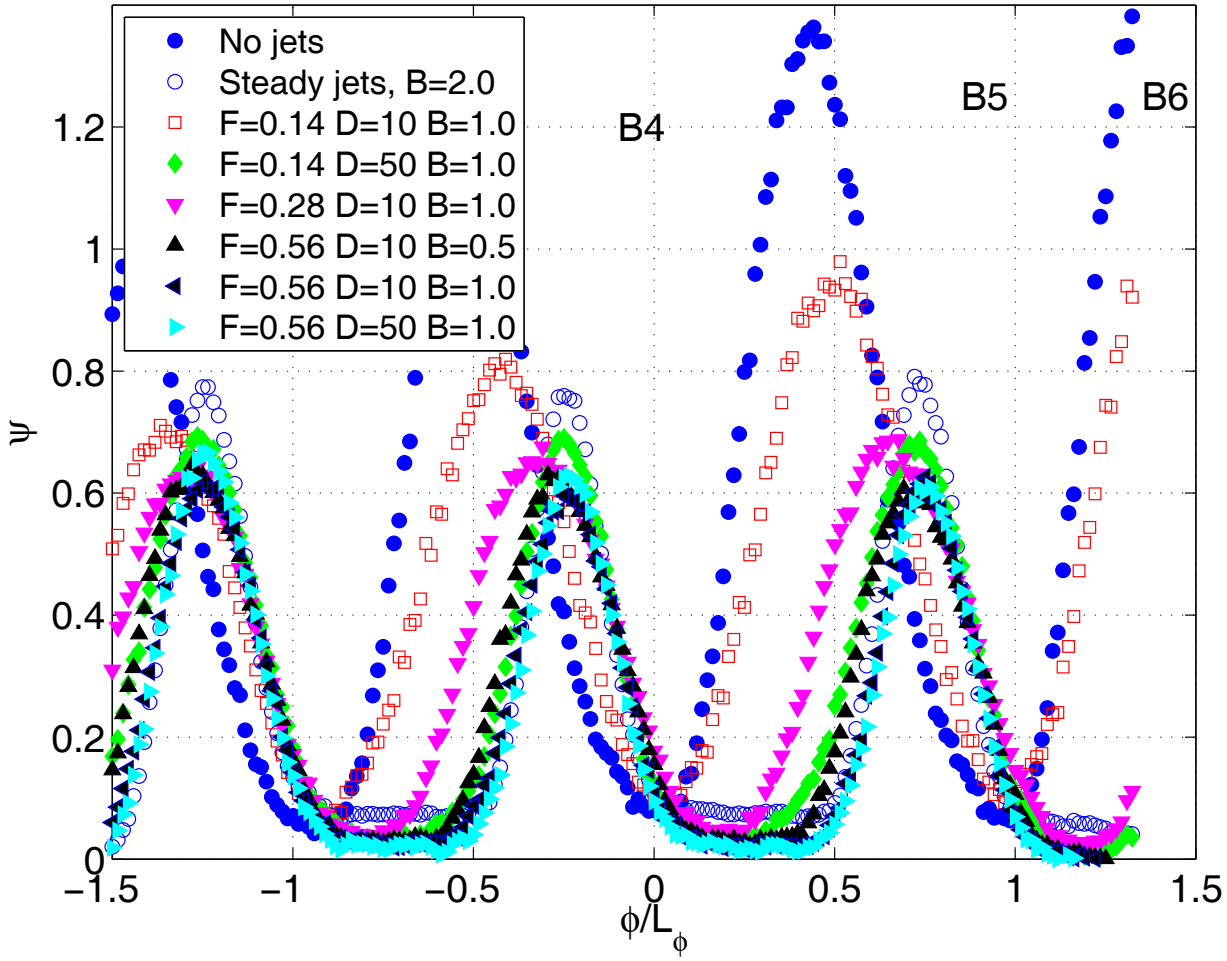
No jets
Steady jets, B=2.0
F=0.14 D=10 B=1.0
F=0.14 D=50 B=1.0
F=0.28 D=10 B=1.0
F=0.56 D=10 B=0.5
F=0.56 D=10 B=1.0
F=0.56 D=50 B=1.0
B4
B5
B6
ψ
ϕ/L_ϕ
0
0.2
0.4
0.6
0.8
1
1.2
−1.5
−1
−0.5
0
0.5
1
1.5

a)

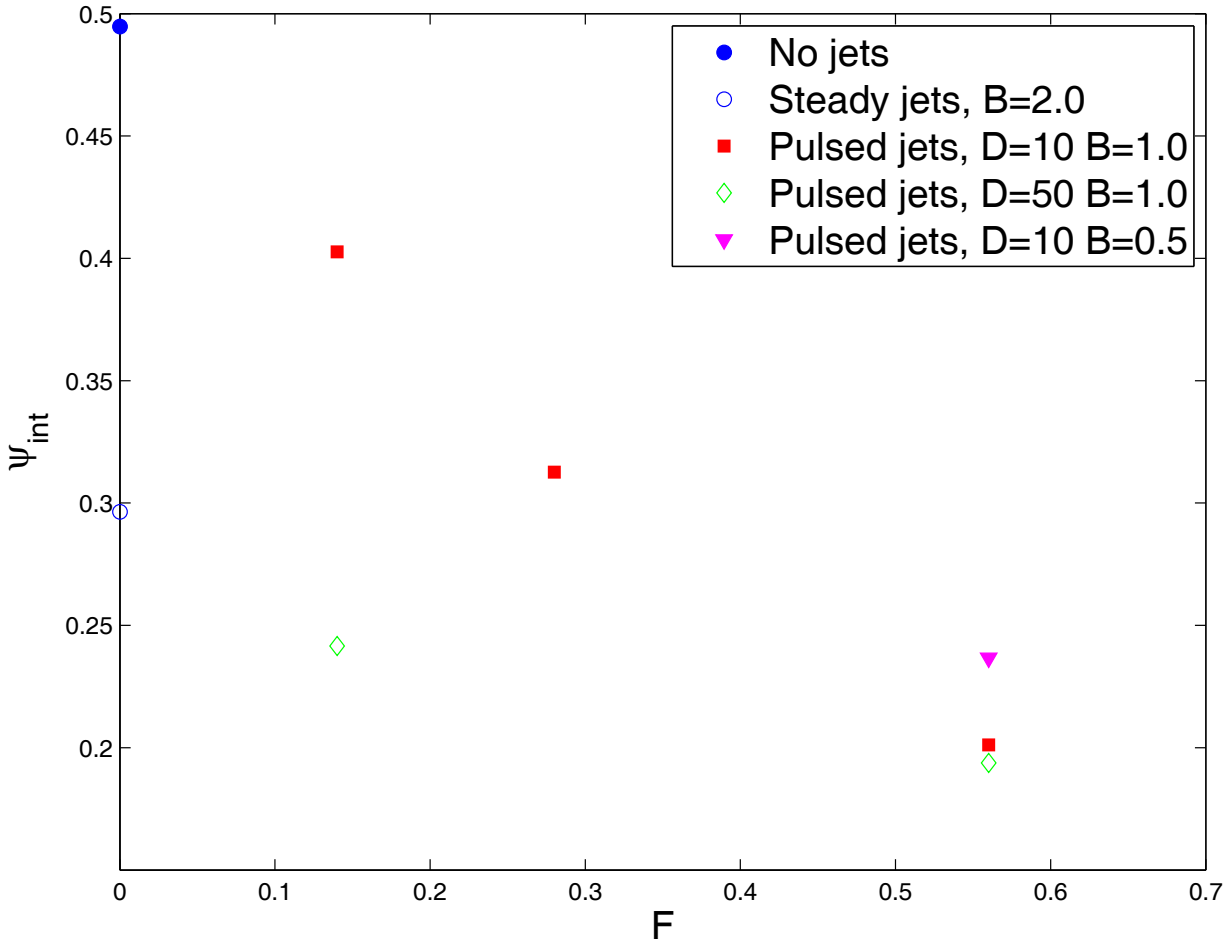

b)

Fig. 14 Ψ results, low TI, Re=50,000: a) Ψ profile, b) Integrated Ψ.

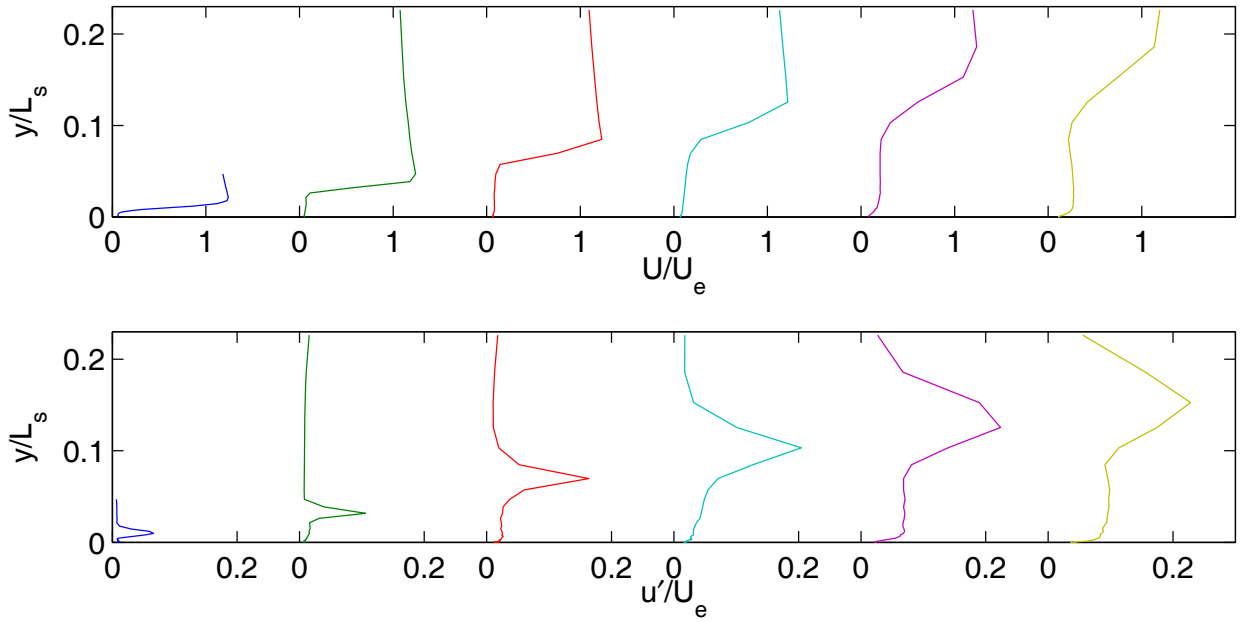

Fig. 15 Time averaged velocity profiles, low TI, Re=50,000, no VGJs: a) mean, b) rms.

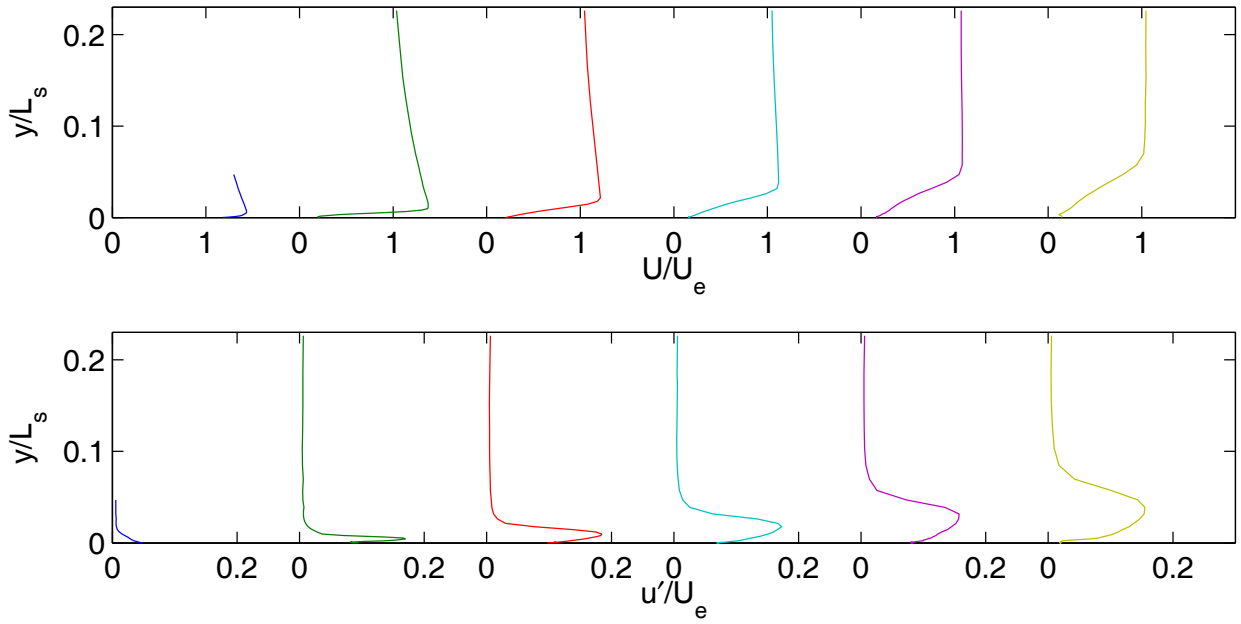

Fig. 16 Time averaged velocity profiles, low TI, Re=50,000, steady VGJs, B=2.0: a) mean, b) rms.

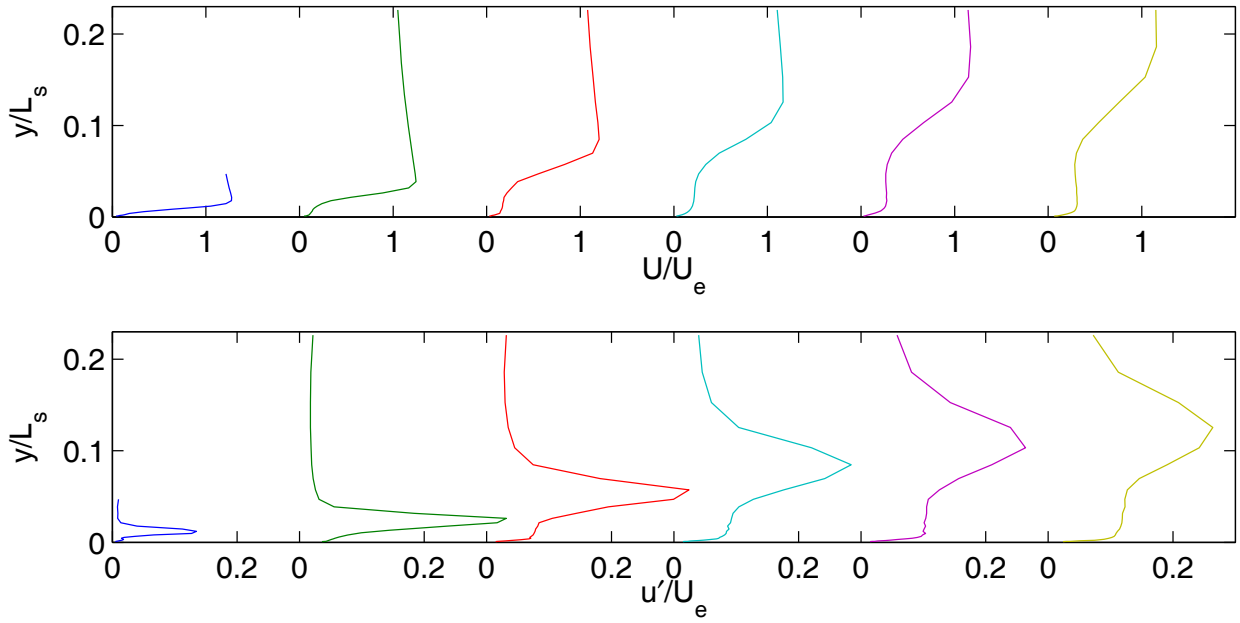

Fig. 17 Time averaged velocity profiles, low TI, Re=50,000, pulsed VGJs, F=0.07, D=50%, B=1.0: a) mean, b) rms.

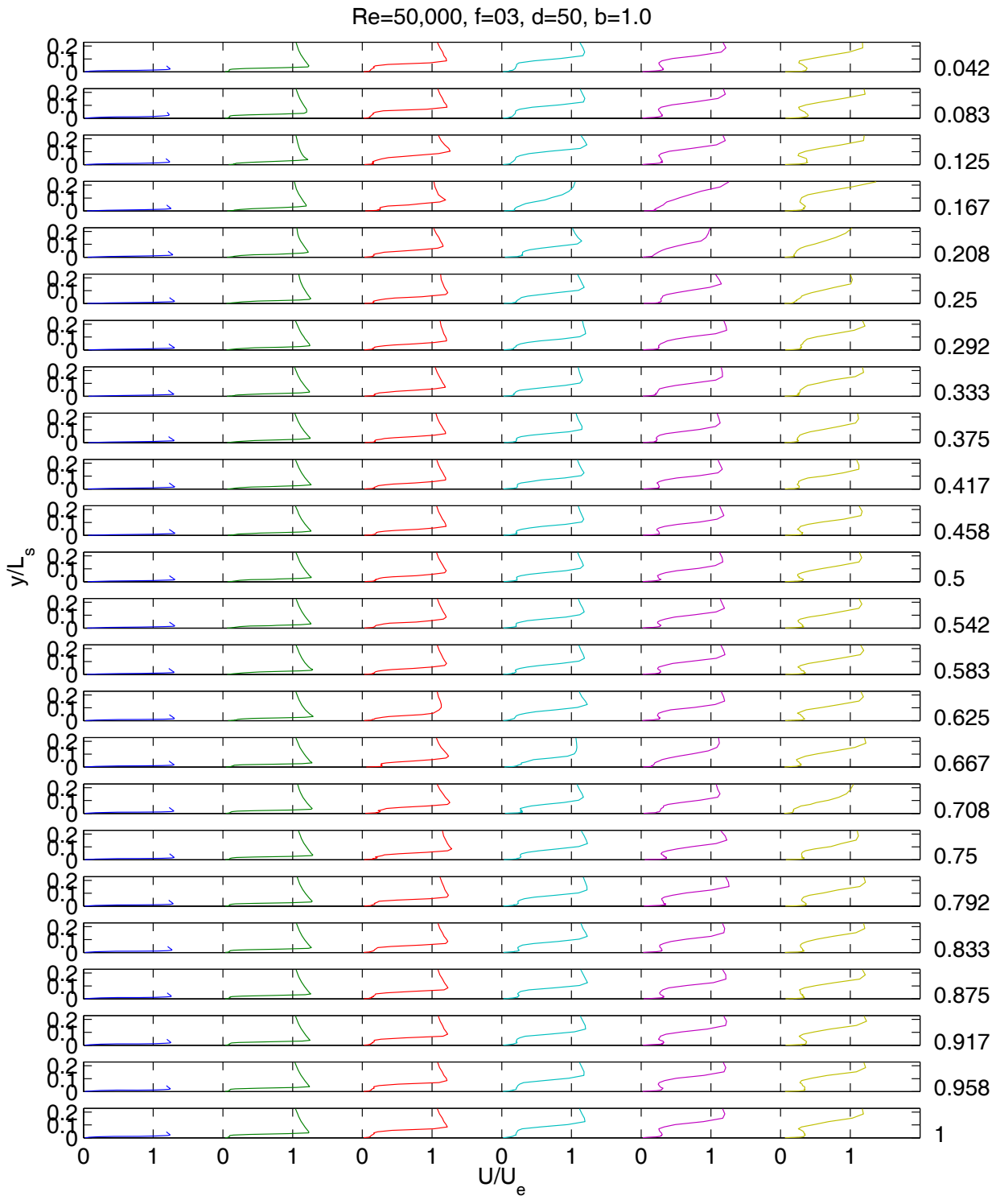
Re=50,000, f=03, d=50, b=1.0
y/L_s
U/U_e
0.042
0.083
0.125
0.167
0.208
0.25
0.292
0.333
0.375
0.417
0.458
0.5
0.542
0.583
0.625
0.667
0.708
0.75
0.792
0.833
0.875
0.917
0.958
1

a)

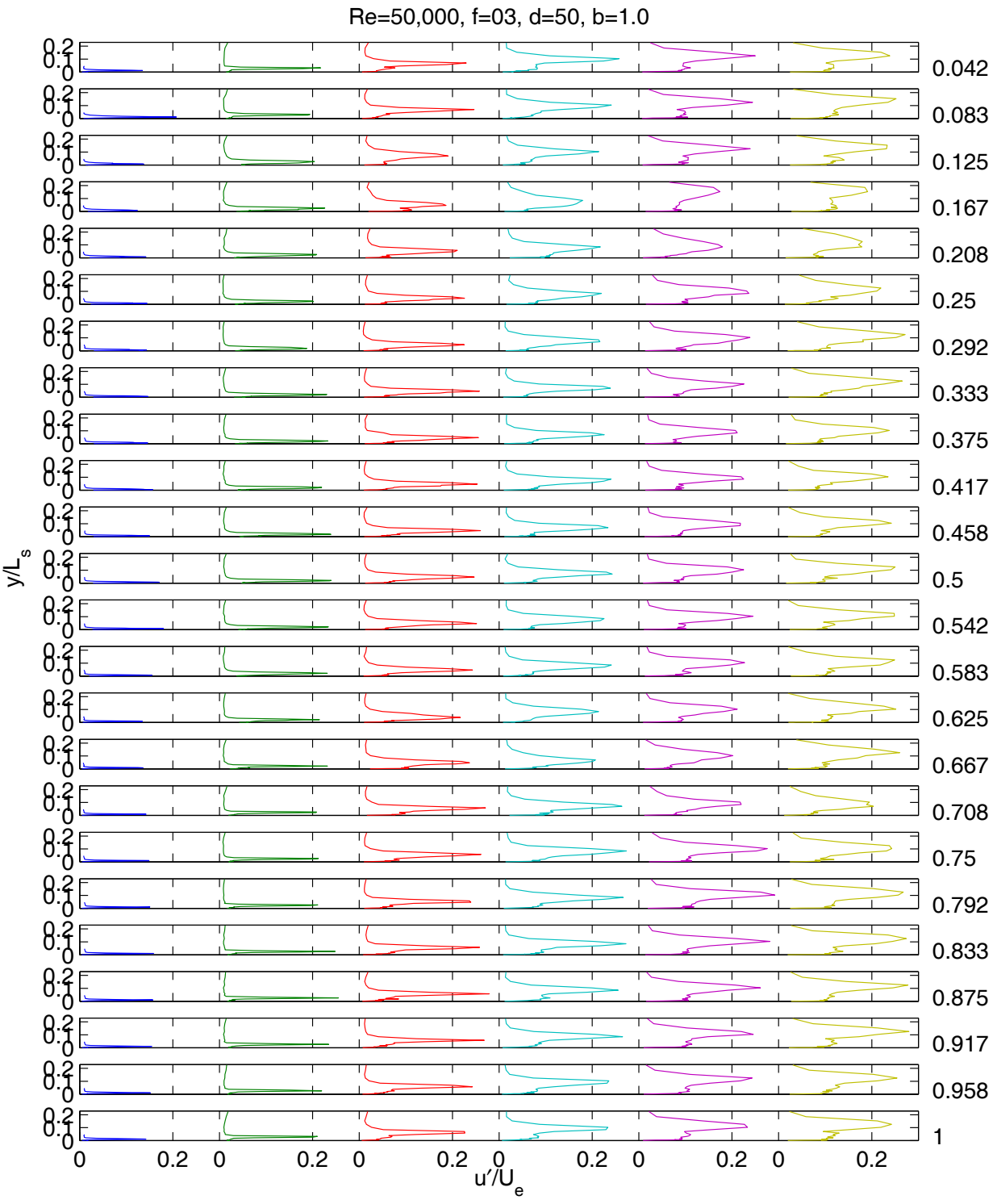

b)

Fig. 18 Phase averaged velocity profiles, low TI, Re=50,000, pulsed VGJs, F=0.07, D=50%, B=1.0: a) mean, b) rms.

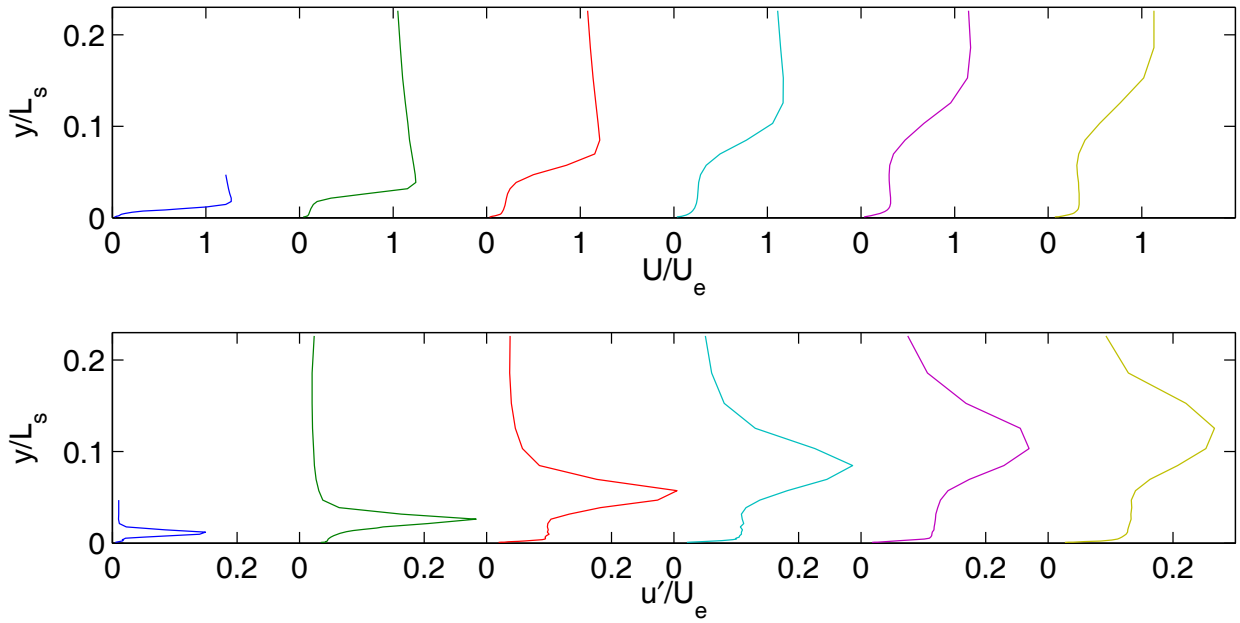

Fig. 19 Time averaged velocity profiles, low TI, Re=50,000, pulsed VGJs, F=0.14, D=10%, B=1.0: a) mean, b) rms.

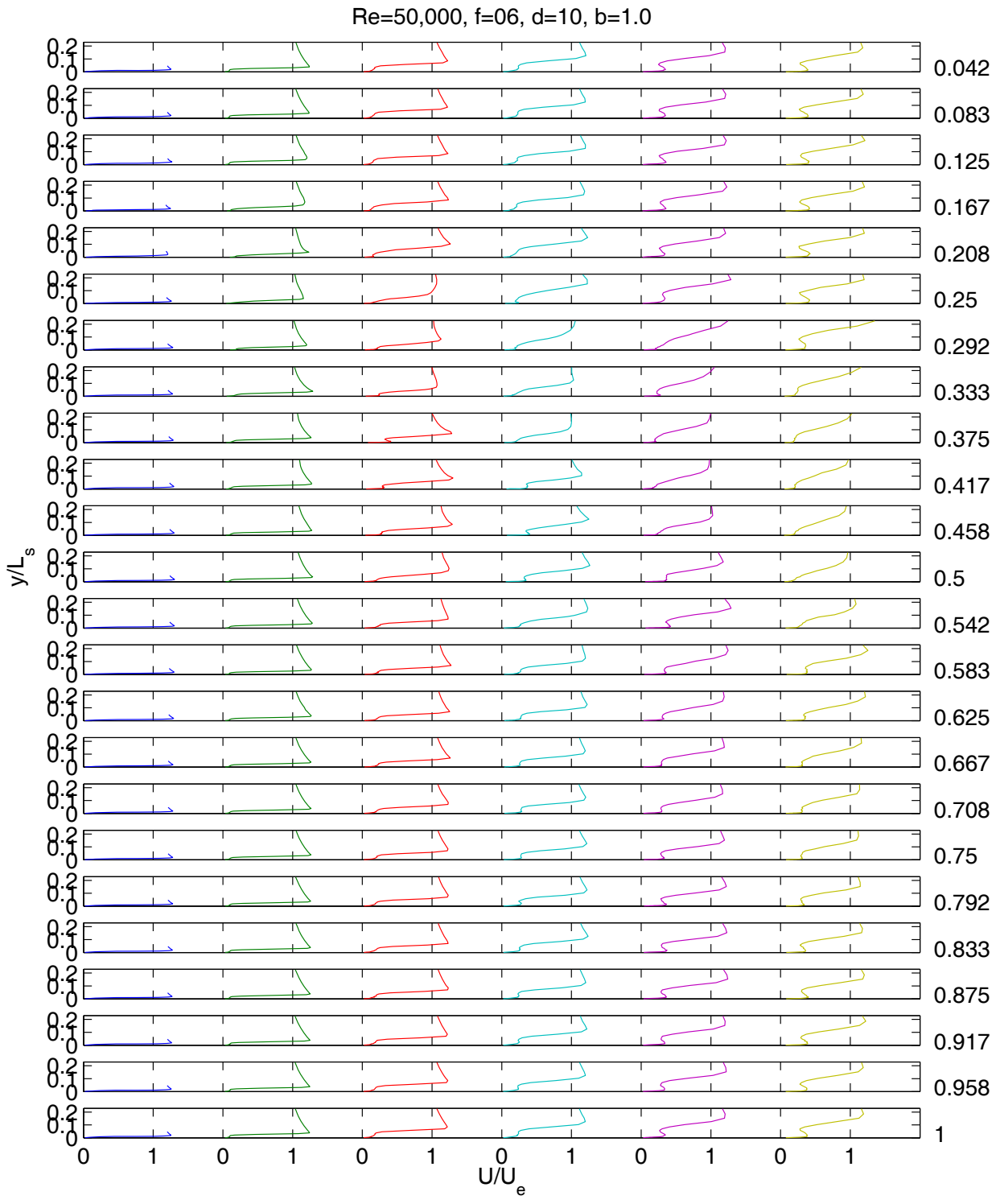
Re=50,000, f=06, d=10, b=1.0
y/L_s
U/U_e
0.042
0.083
0.125
0.167
0.208
0.25
0.292
0.333
0.375
0.417
0.458
0.5
0.542
0.583
0.625
0.667
0.708
0.75
0.792
0.833
0.875
0.917
0.958
1

a)

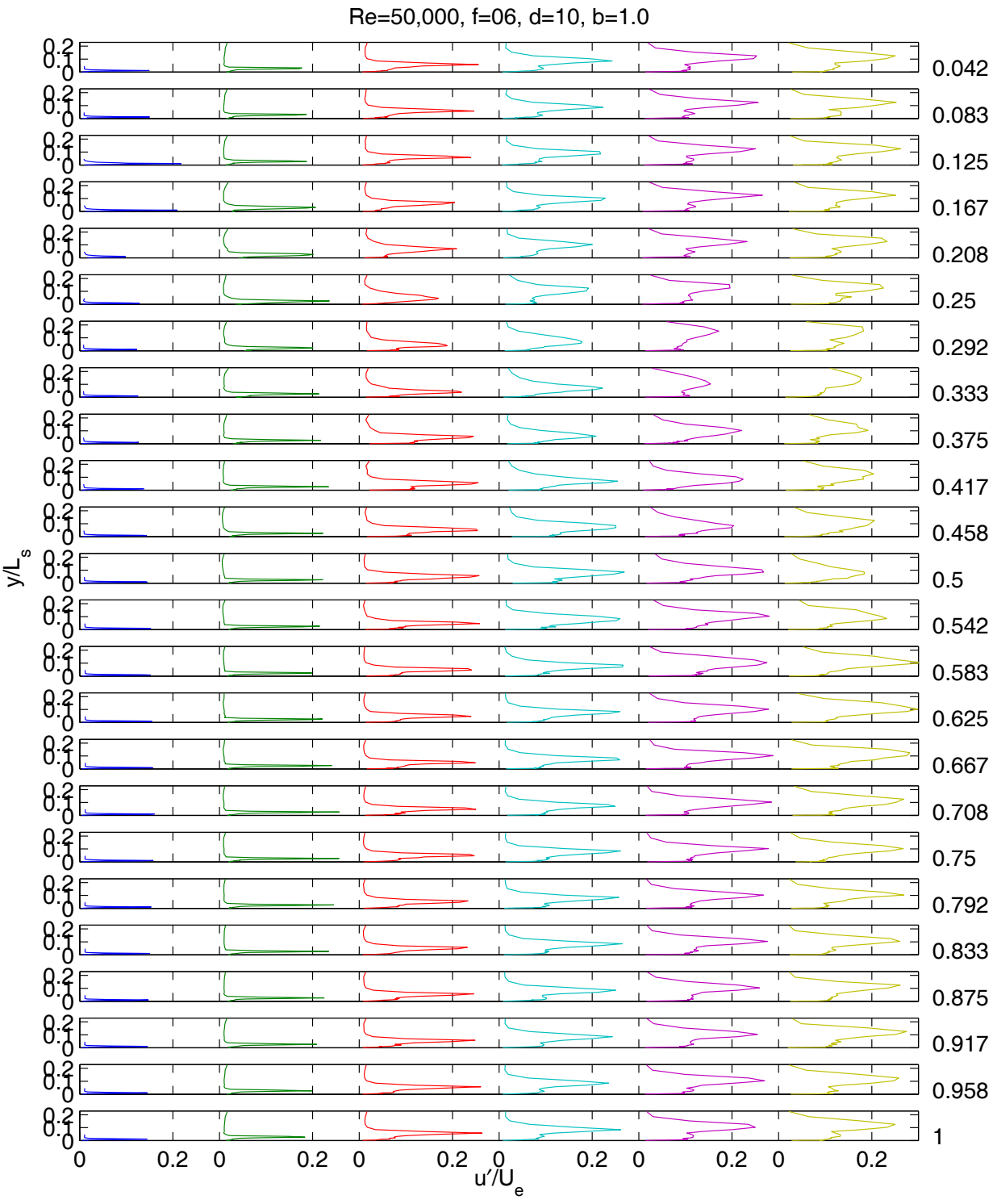

b)

Fig. 20 Phase averaged velocity profiles, low TI, Re=50,000, pulsed VGJs, F=0.14, D=10%, B=1.0: a) mean, b) rms.

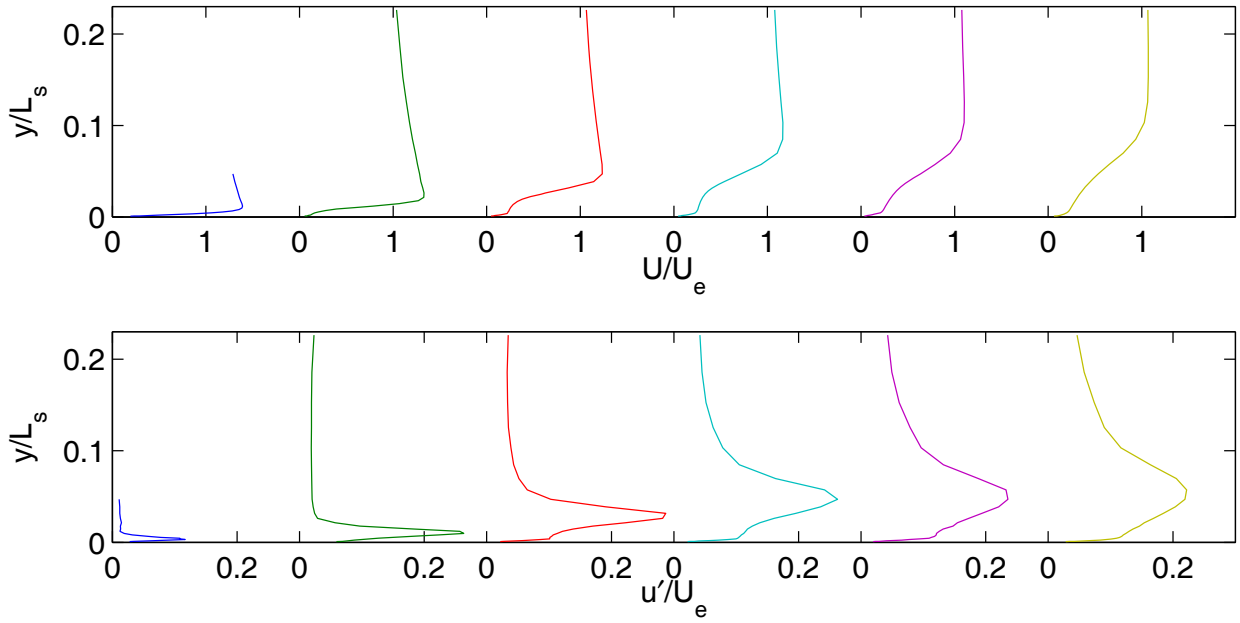

Fig. 21 Time averaged velocity profiles, low TI, Re=50,000, pulsed VGJs, F=0.14, D=50%, B=1.0: a) mean, b) rms.

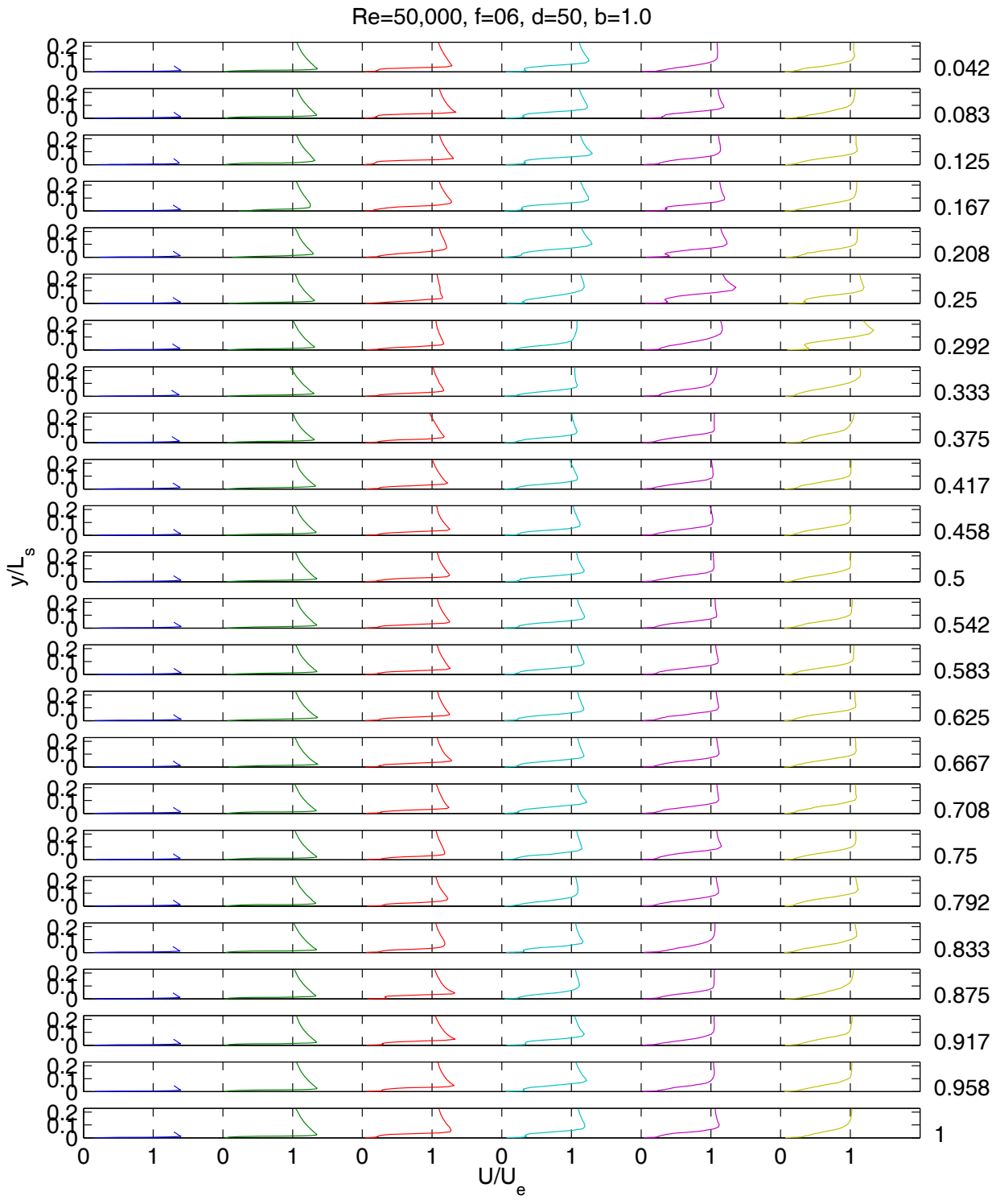
Re=50,000, f=06, d=50, b=1.0
y/L_s
U/U_e
0.042
0.083
0.125
0.167
0.208
0.25
0.292
0.333
0.375
0.417
0.458
0.5
0.542
0.583
0.625
0.667
0.708
0.75
0.792
0.833
0.875
0.917
0.958
1

a)

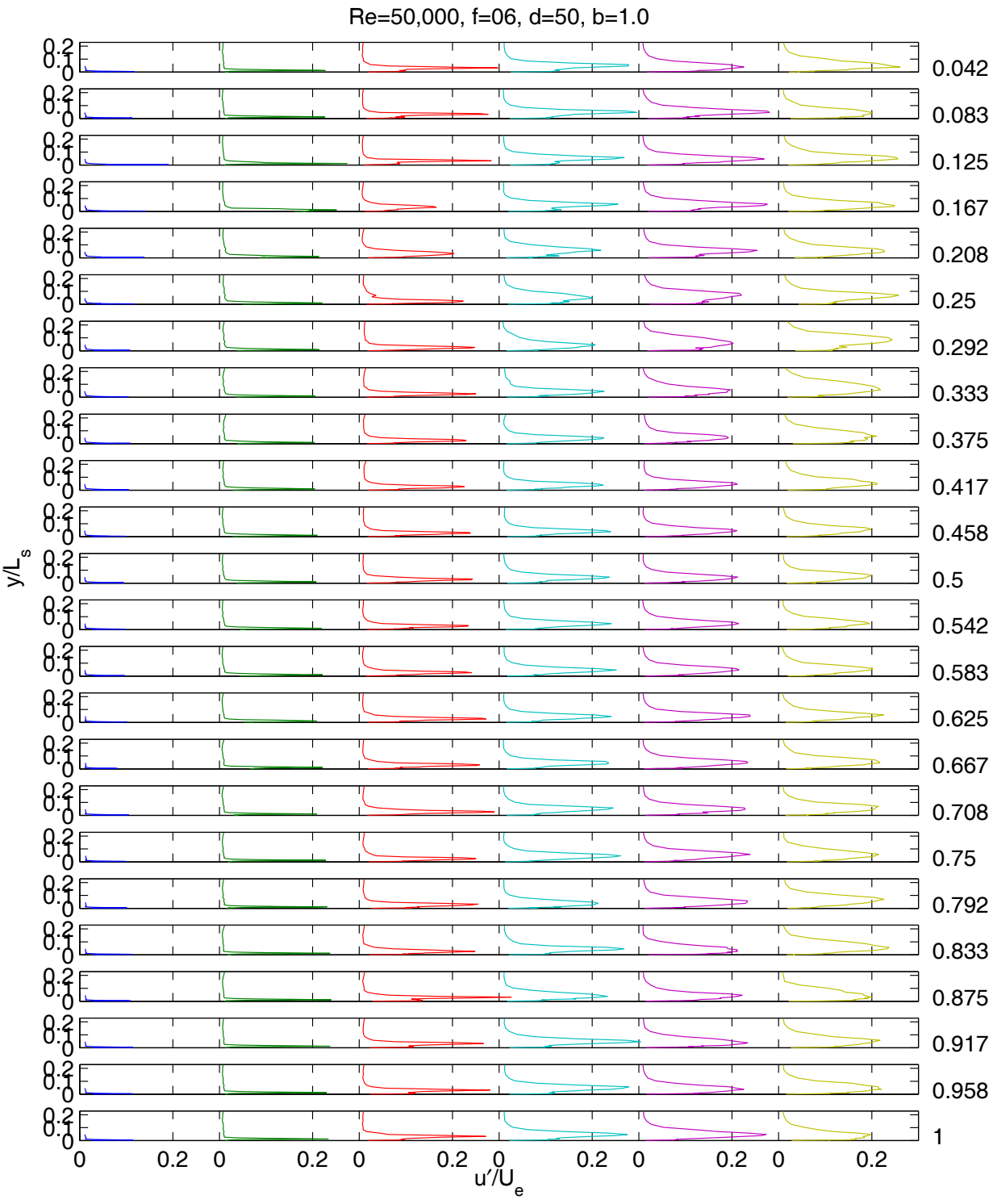

b)

Fig. 22 Phase averaged velocity profiles, low TI, Re=50,000, pulsed VGJs, F=0.14, D=50%, B=1.0: a) mean, b) rms.

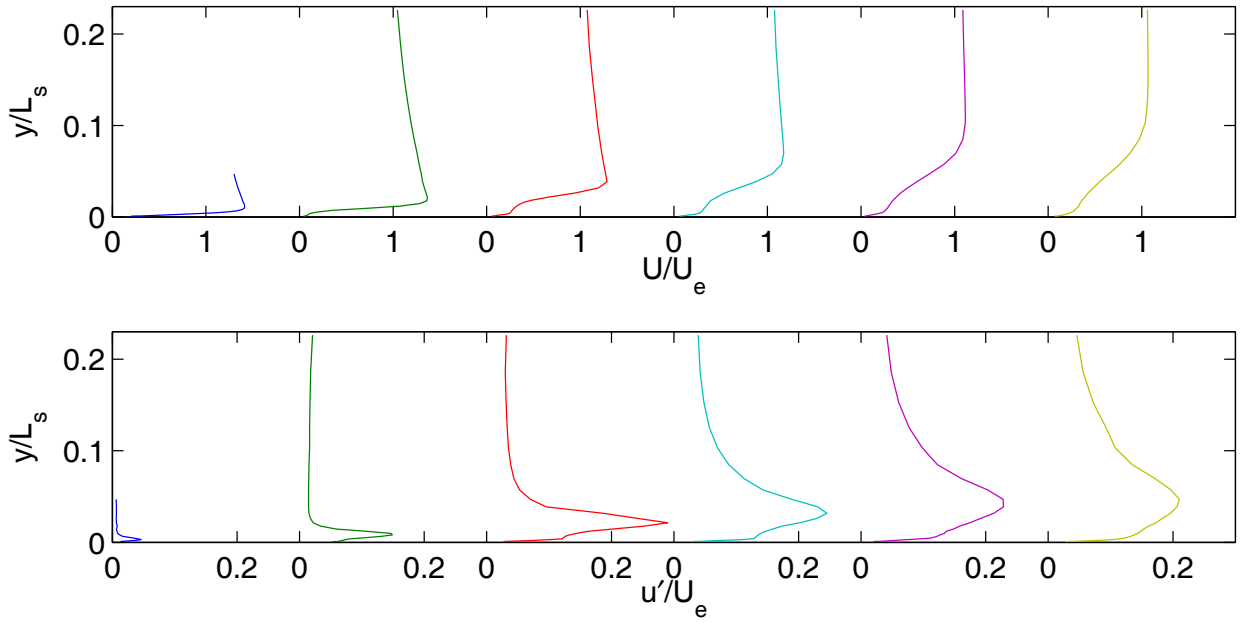

Fig. 23 Time averaged velocity profiles, low TI, Re=50,000, pulsed VGJs, F=0.28, D=10%, B=1.0: a) mean, b) rms.

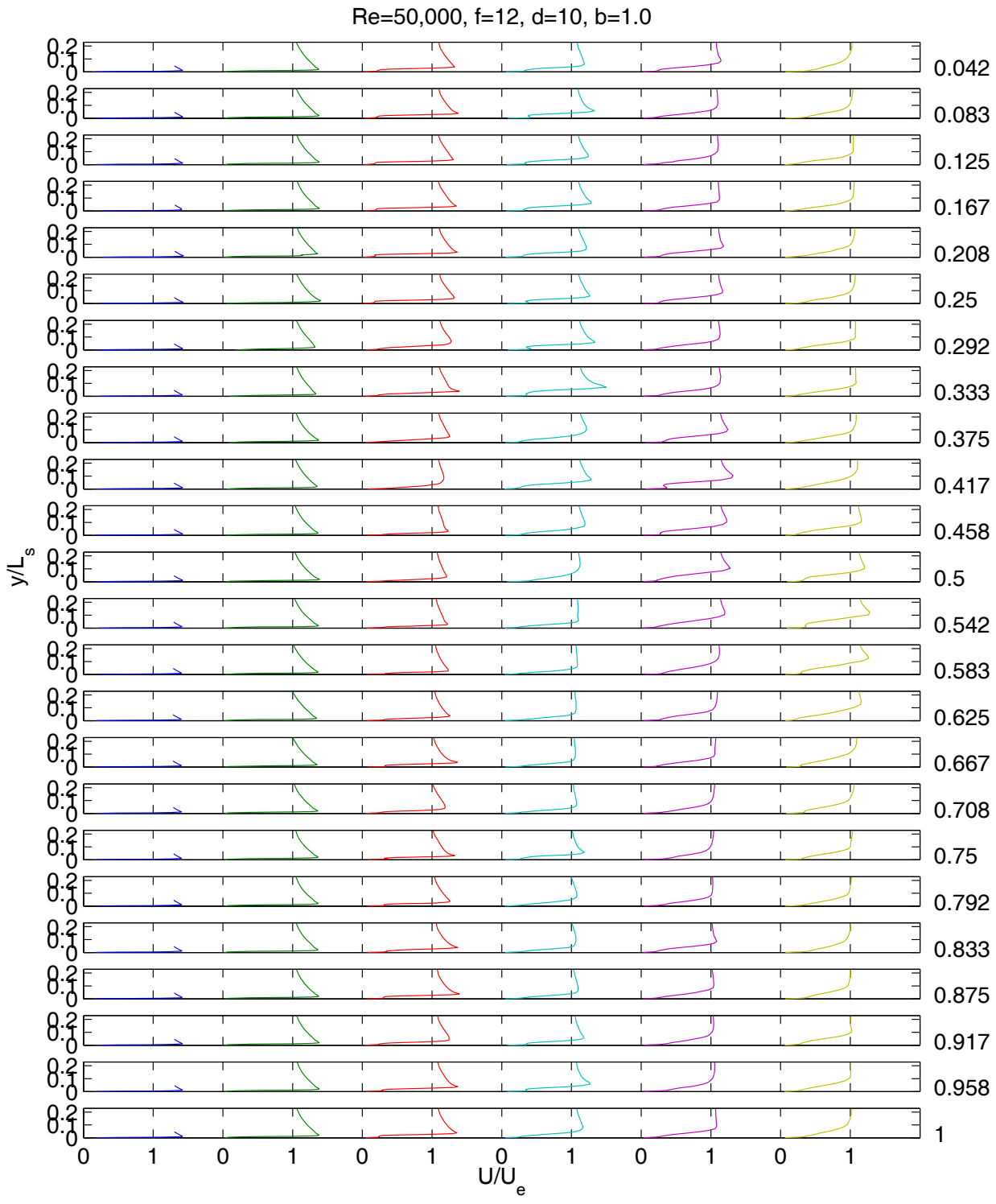
Re=50,000, f=12, d=10, b=1.0
y/L_s
U/U_e
0.042
0.083
0.125
0.167
0.208
0.25
0.292
0.333
0.375
0.417
0.458
0.5
0.542
0.583
0.625
0.667
0.708
0.75
0.792
0.833
0.875
0.917
0.958
1

a)

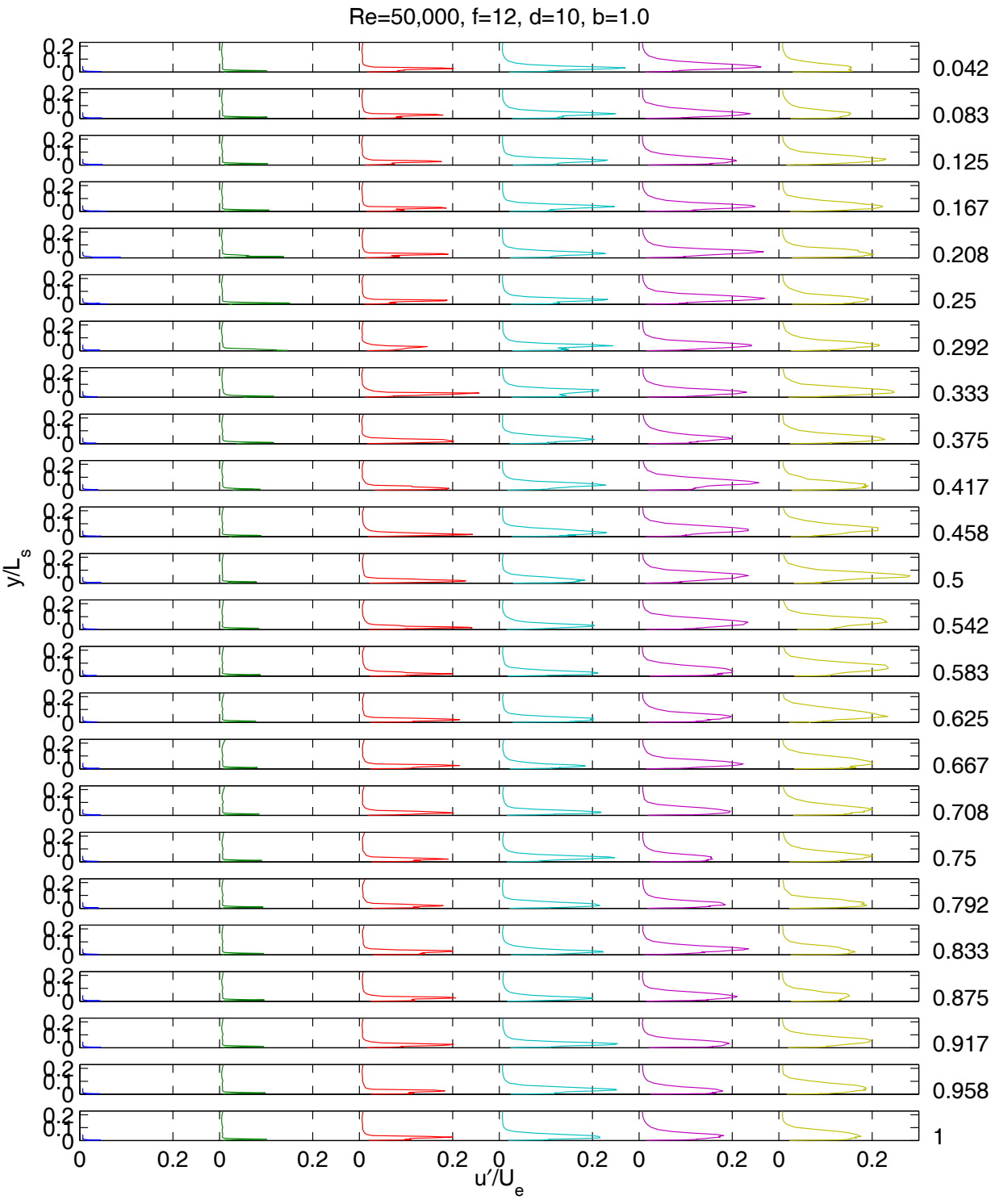

b)

Fig. 24 Phase averaged velocity profiles, low TI, Re=50,000, pulsed VGJs, F=0.28, D=10%, B=1.0: a) mean, b) rms.

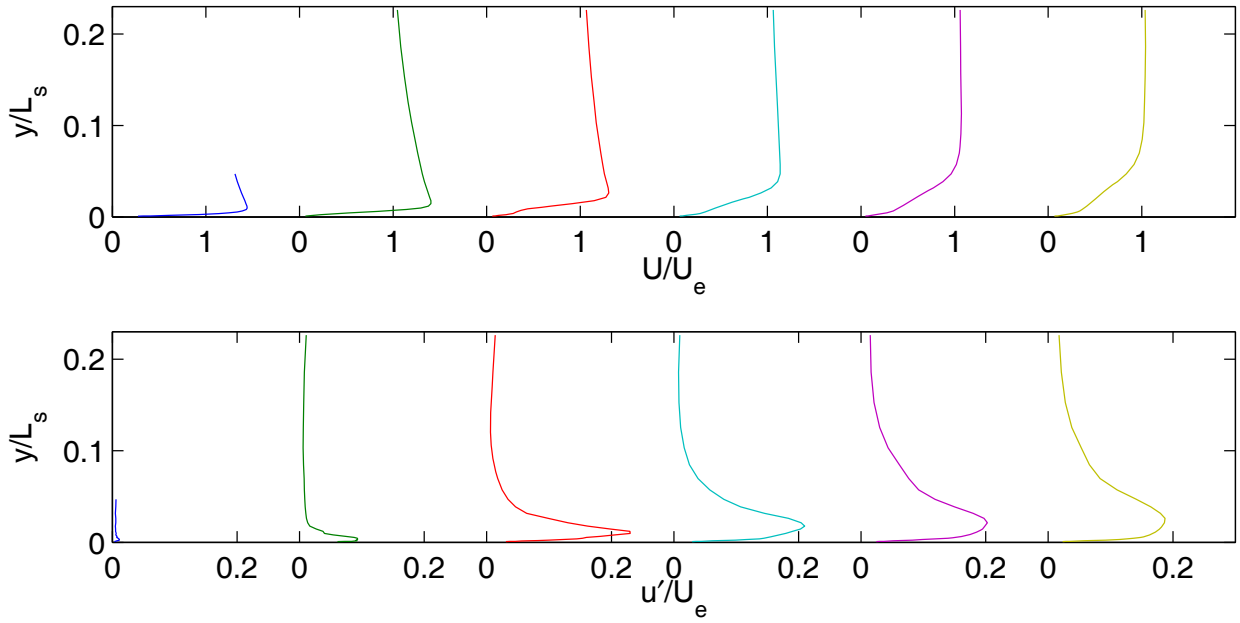

Fig. 25 Time averaged velocity profiles, low TI, Re=50,000, pulsed VGJs, F=0.56, D=10%, B=1.0: a) mean, b) rms.

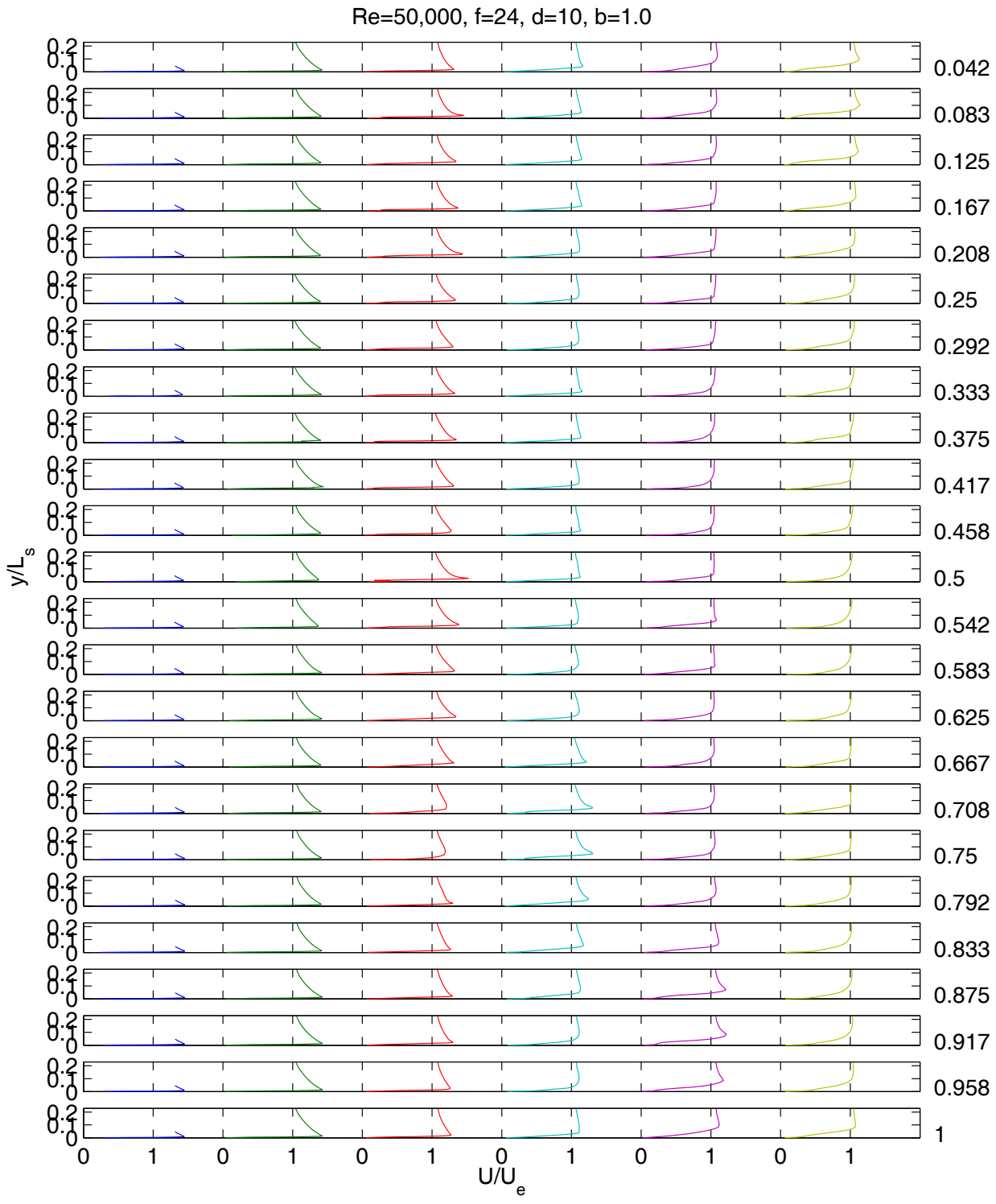
Re=50,000, f=24, d=10, b=1.0
y/L_s
U/U_e
0.042
0.083
0.125
0.167
0.208
0.25
0.292
0.333
0.375
0.417
0.458
0.5
0.542
0.583
0.625
0.667
0.708
0.75
0.792
0.833
0.875
0.917
0.958
1

a)

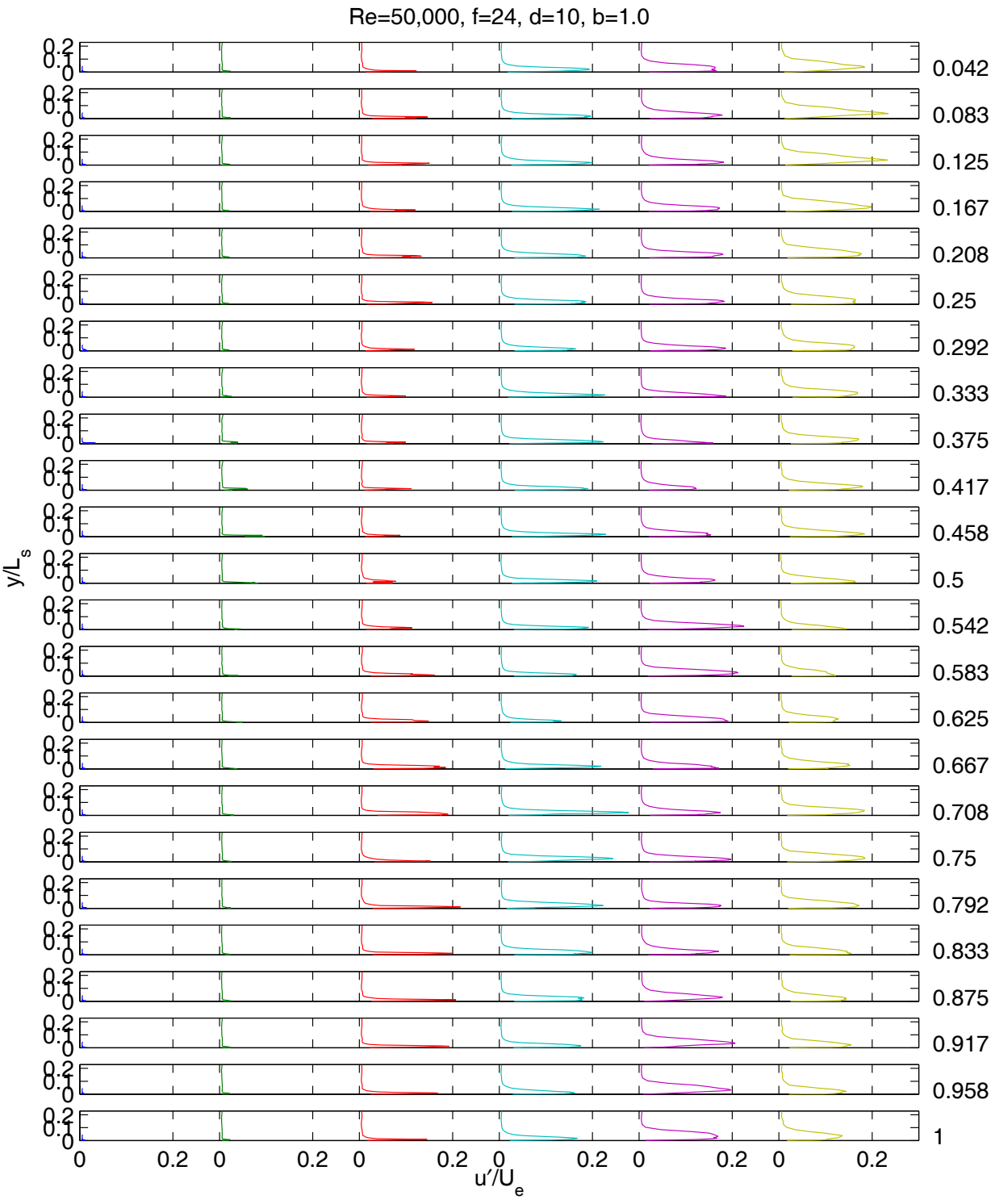

b)

Fig. 26 Phase averaged velocity profiles, low TI, Re=50,000, pulsed VGJs, F=0.56, D=10%, B=1.0: a) mean, b) rms.

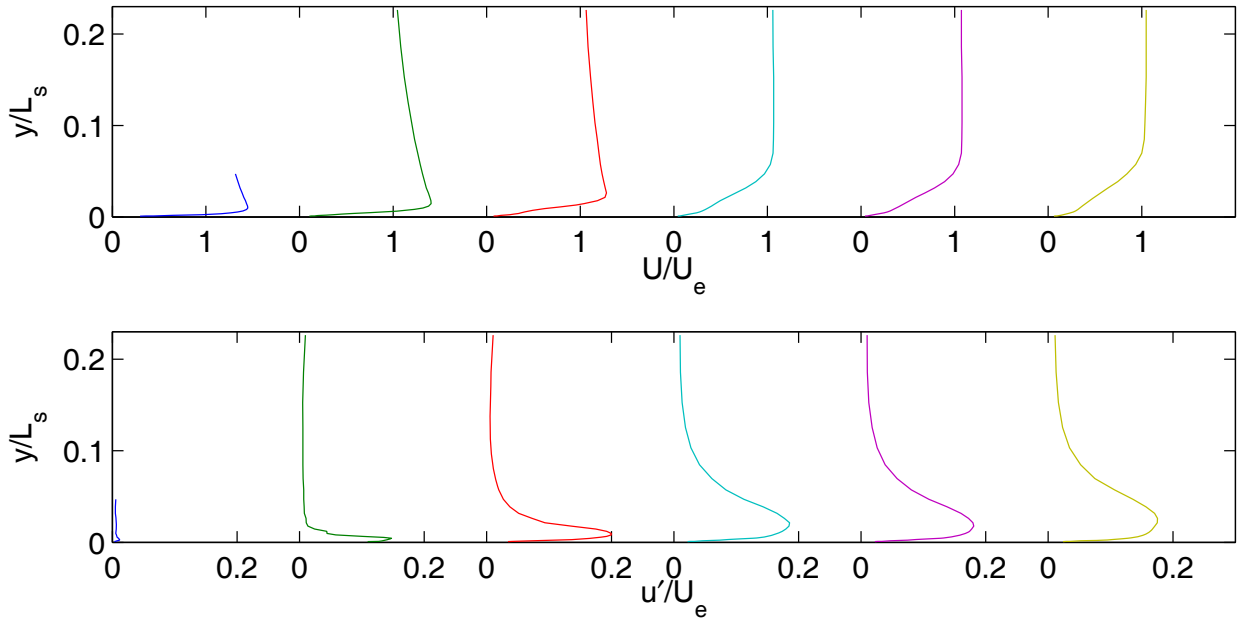

Fig. 27 Time averaged velocity profiles, low TI, Re=50,000, pulsed VGJs, F=0.56, D=50%, B=1.0: a) mean, b) rms.

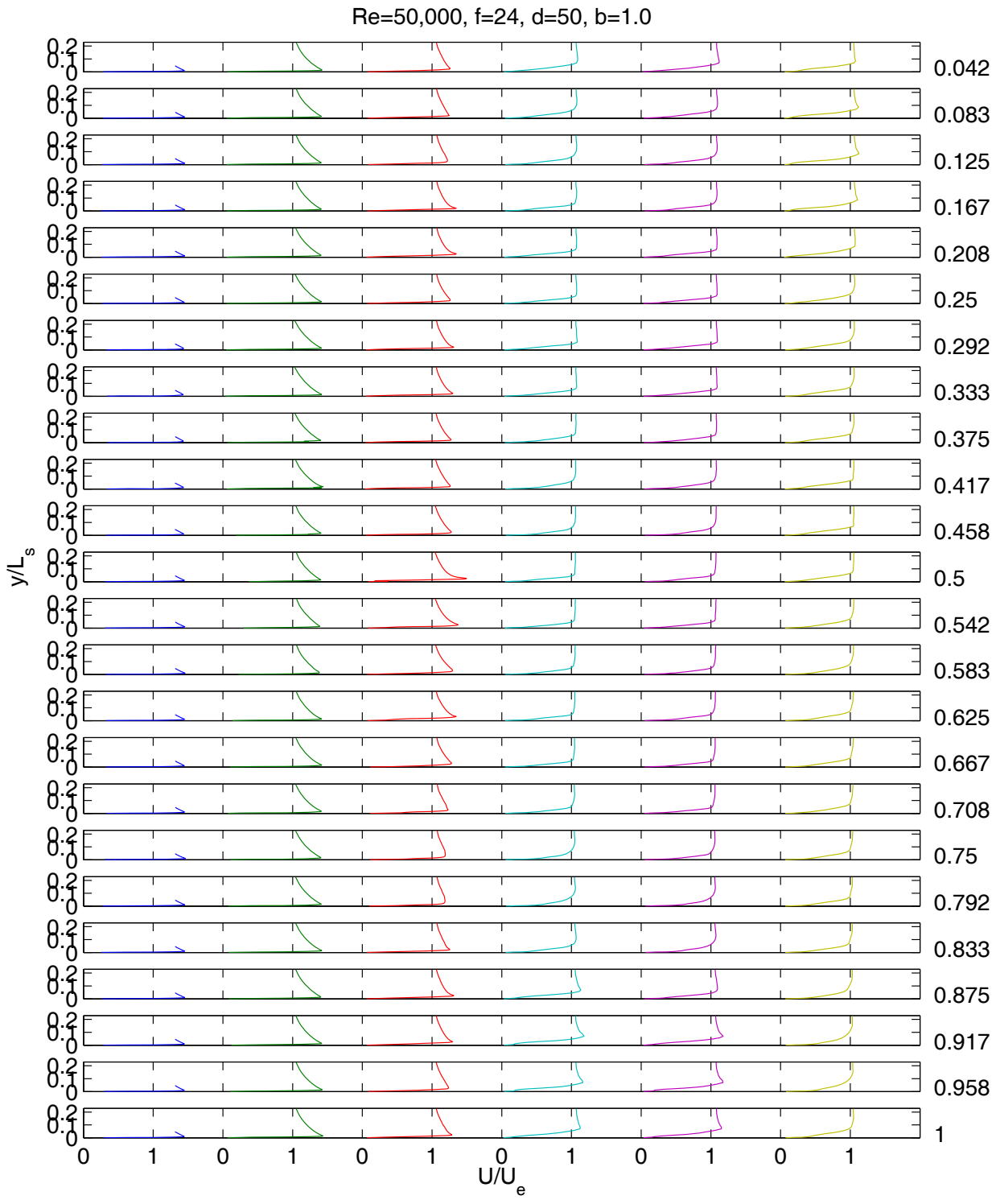
Re=50,000, f=24, d=50, b=1.0
y/L_s
U/U_e
0.042
0.083
0.125
0.167
0.208
0.25
0.292
0.333
0.375
0.417
0.458
0.5
0.542
0.583
0.625
0.667
0.708
0.75
0.792
0.833
0.875
0.917
0.958
1

a)

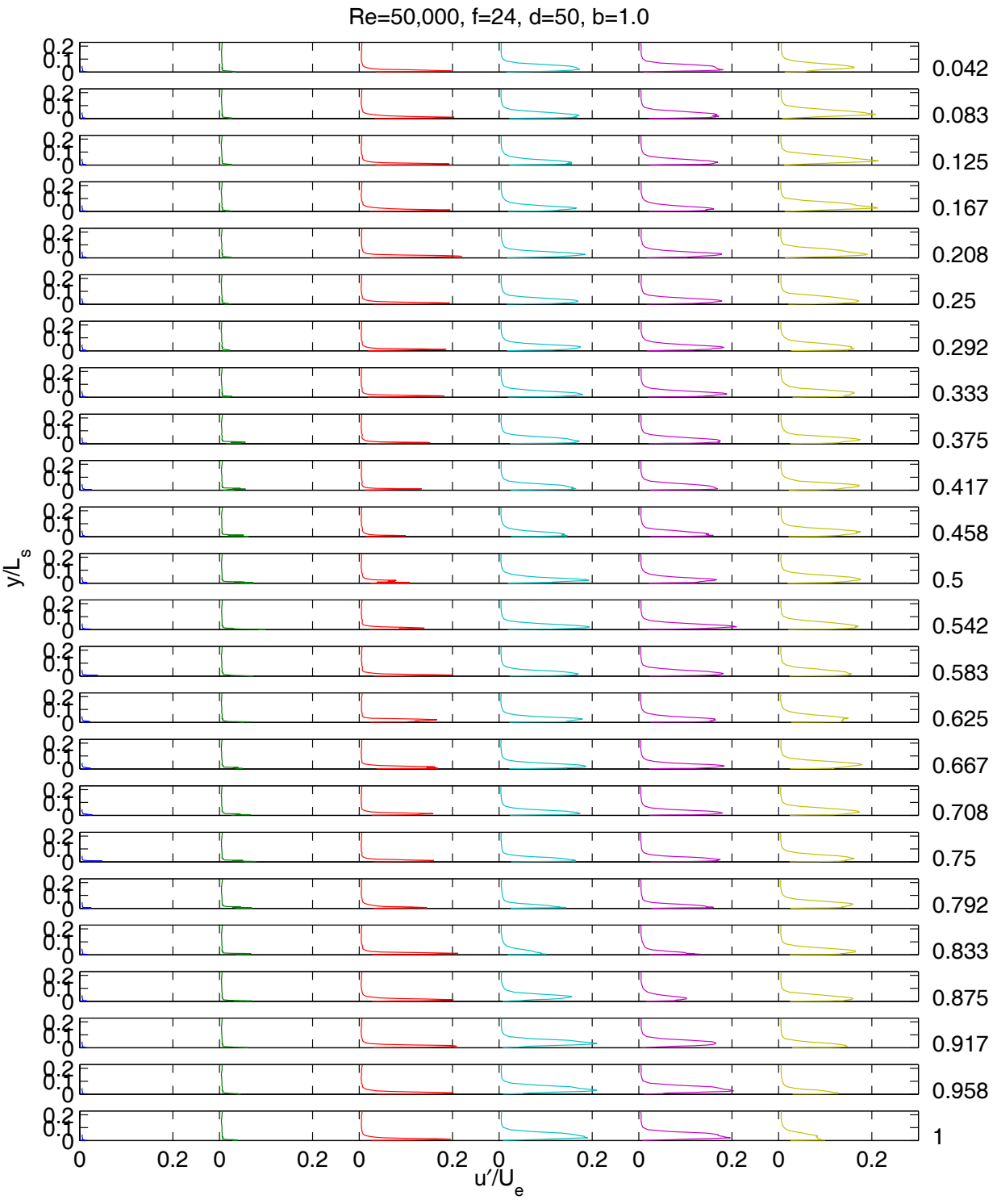

b)

Fig. 28 Phase averaged velocity profiles, low TI, Re=50,000, pulsed VGJs, F=0.56, D=50%, B=1.0: a) mean, b) rms.

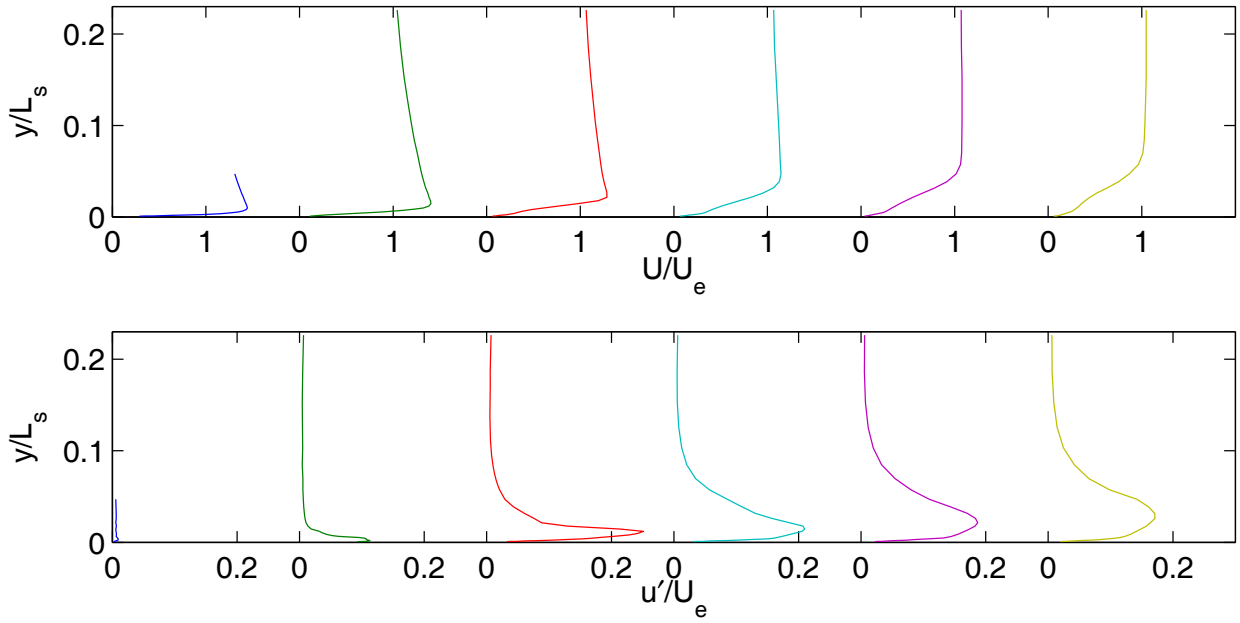

Fig. 29 Time averaged velocity profiles, low TI, Re=50,000, pulsed VGJs, F=1.12, D=10%, B=1.0: a) mean, b) rms.

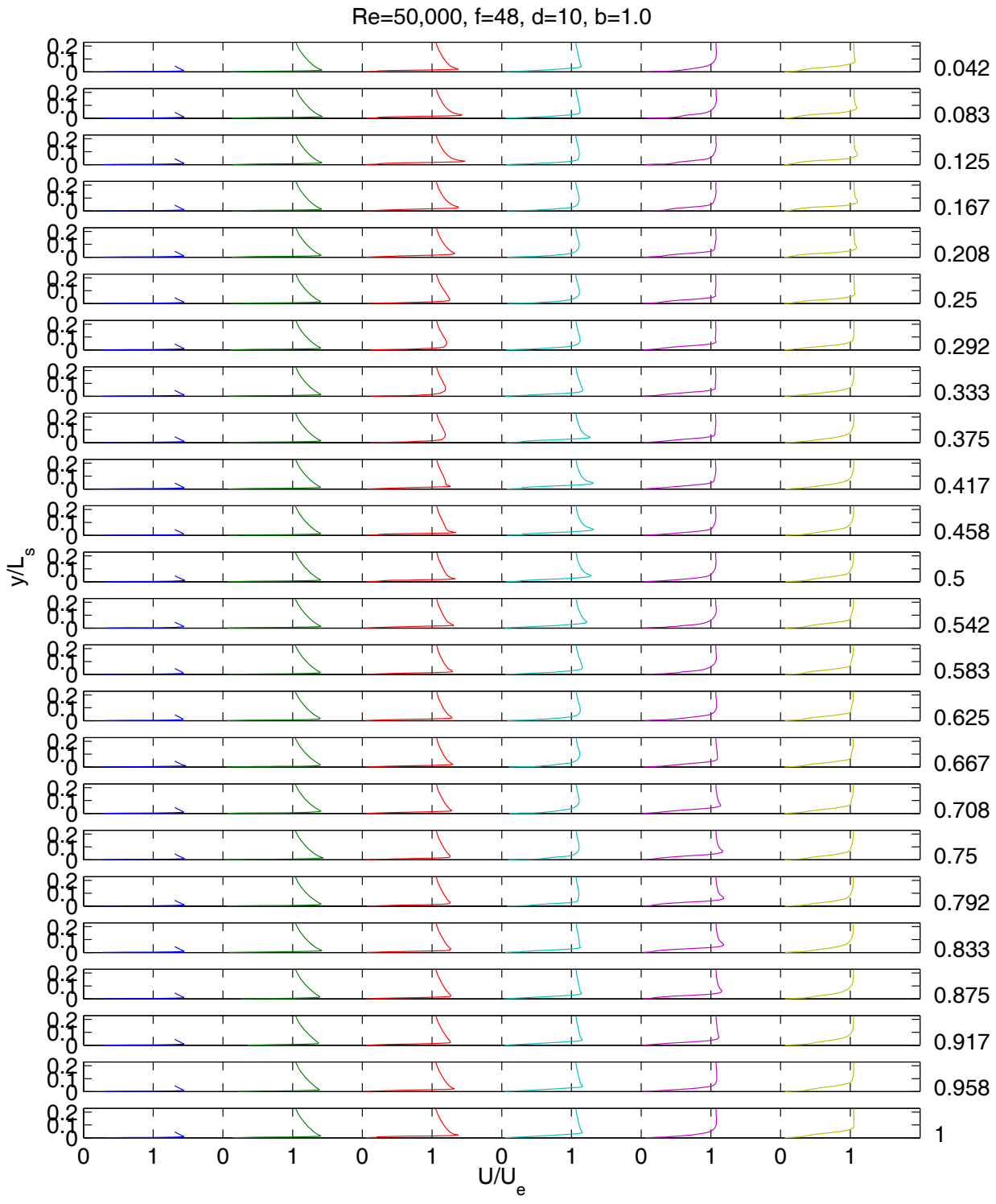
Re=50,000, f=48, d=10, b=1.0
y/L_s
U/U_e
0.042
0.083
0.125
0.167
0.208
0.25
0.292
0.333
0.375
0.417
0.458
0.5
0.542
0.583
0.625
0.667
0.708
0.75
0.792
0.833
0.875
0.917
0.958
1

a)

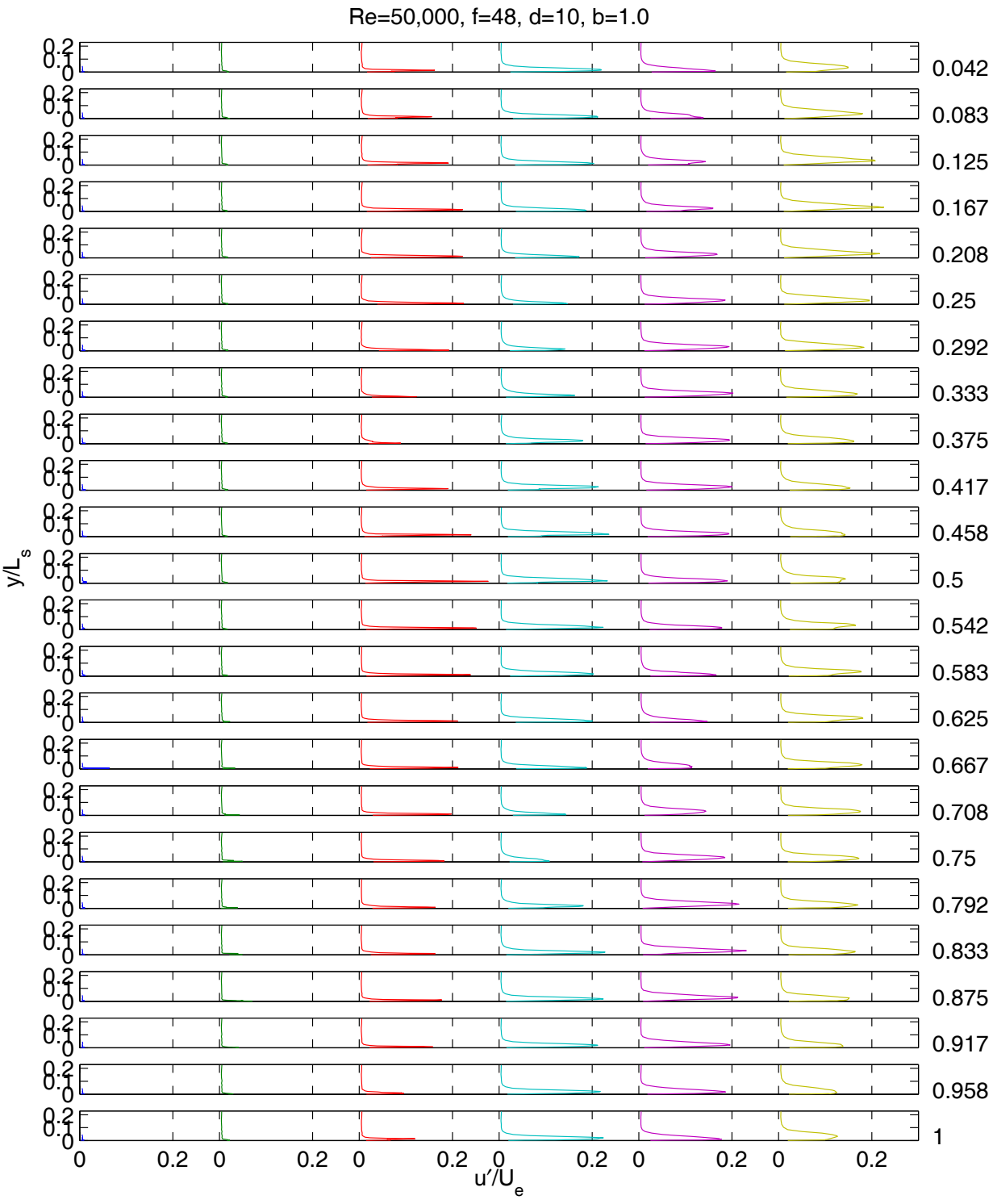

b)

Fig. 30 Phase averaged velocity profiles, low TI, Re=50,000, pulsed VGJs, F=1.12, D=10%, B=1.0: a) mean, b) rms.

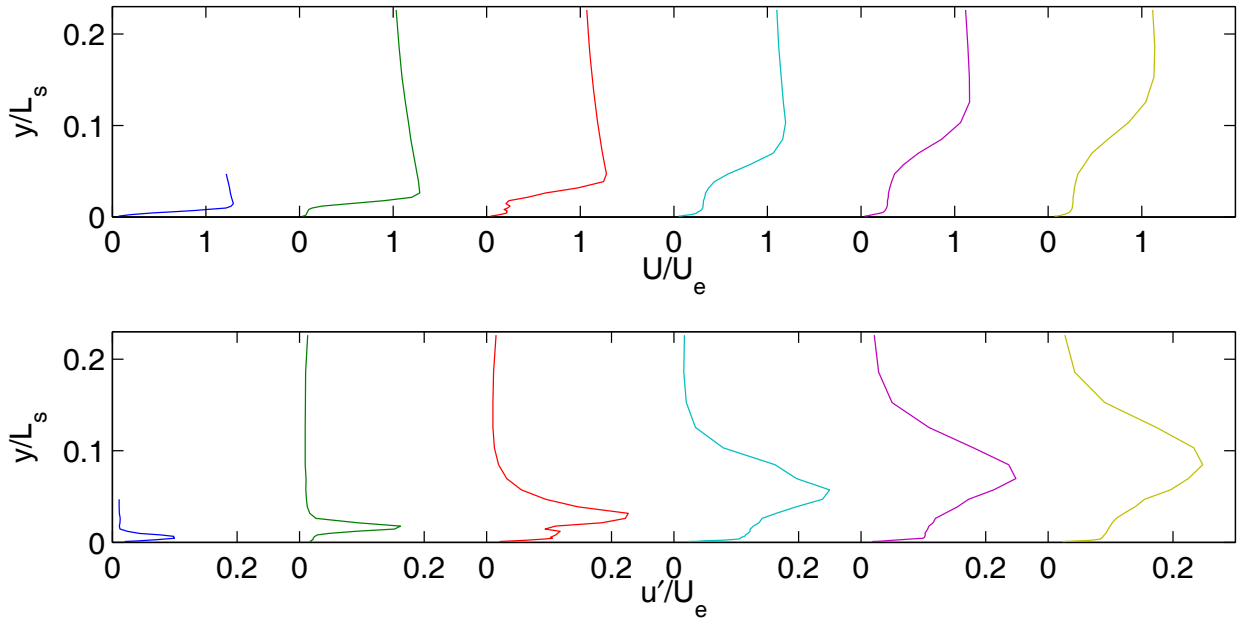

Fig. 31 Time averaged velocity profiles, low TI, Re=50,000, pulsed VGJs, F=0.56, D=10%, B=0.5: a) mean, b) rms.

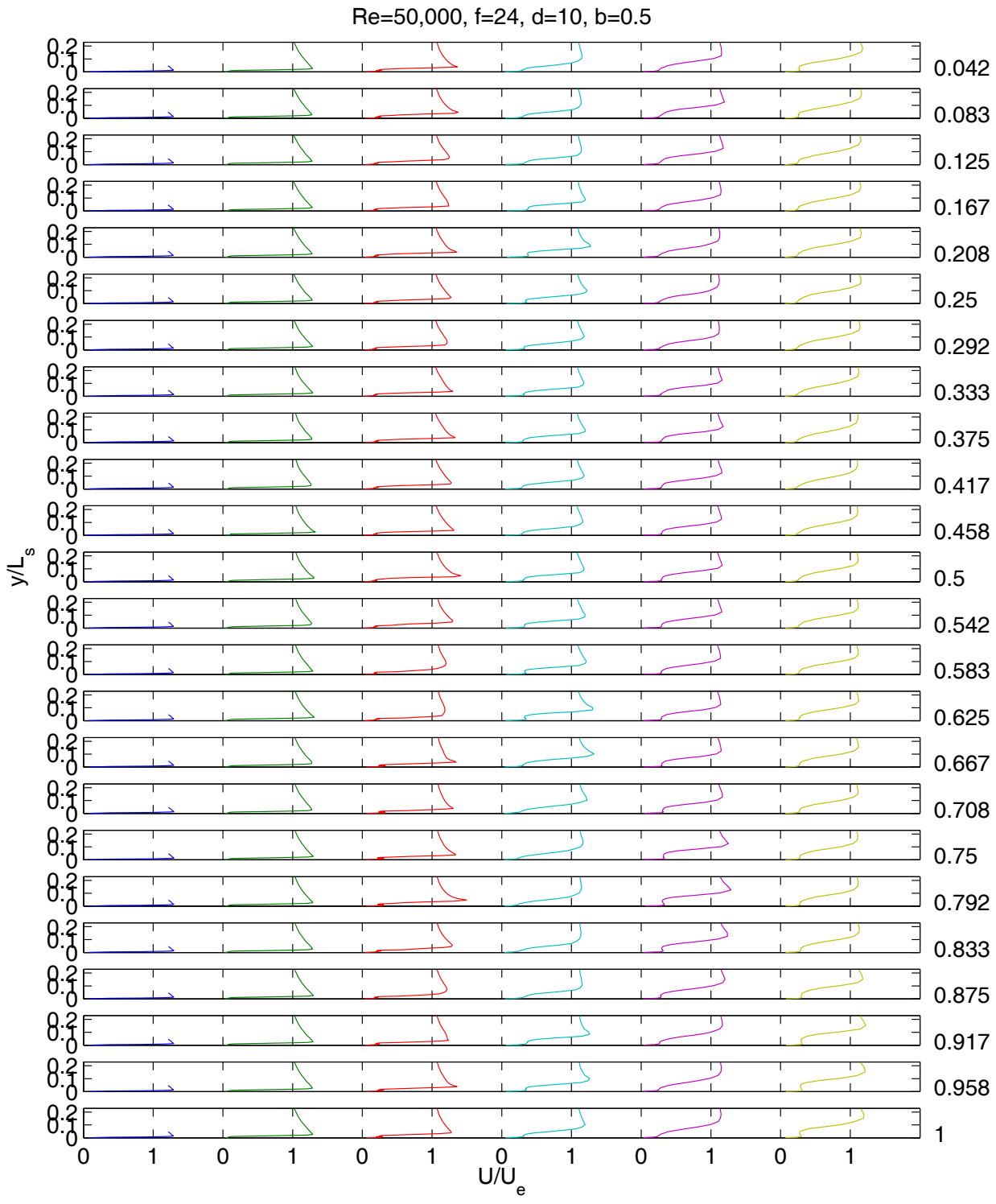
Re=50,000, f=24, d=10, b=0.5
y/L_s
U/U_e
0.042
0.083
0.125
0.167
0.208
0.25
0.292
0.333
0.375
0.417
0.458
0.5
0.542
0.583
0.625
0.667
0.708
0.75
0.792
0.833
0.875
0.917
0.958
1

a)

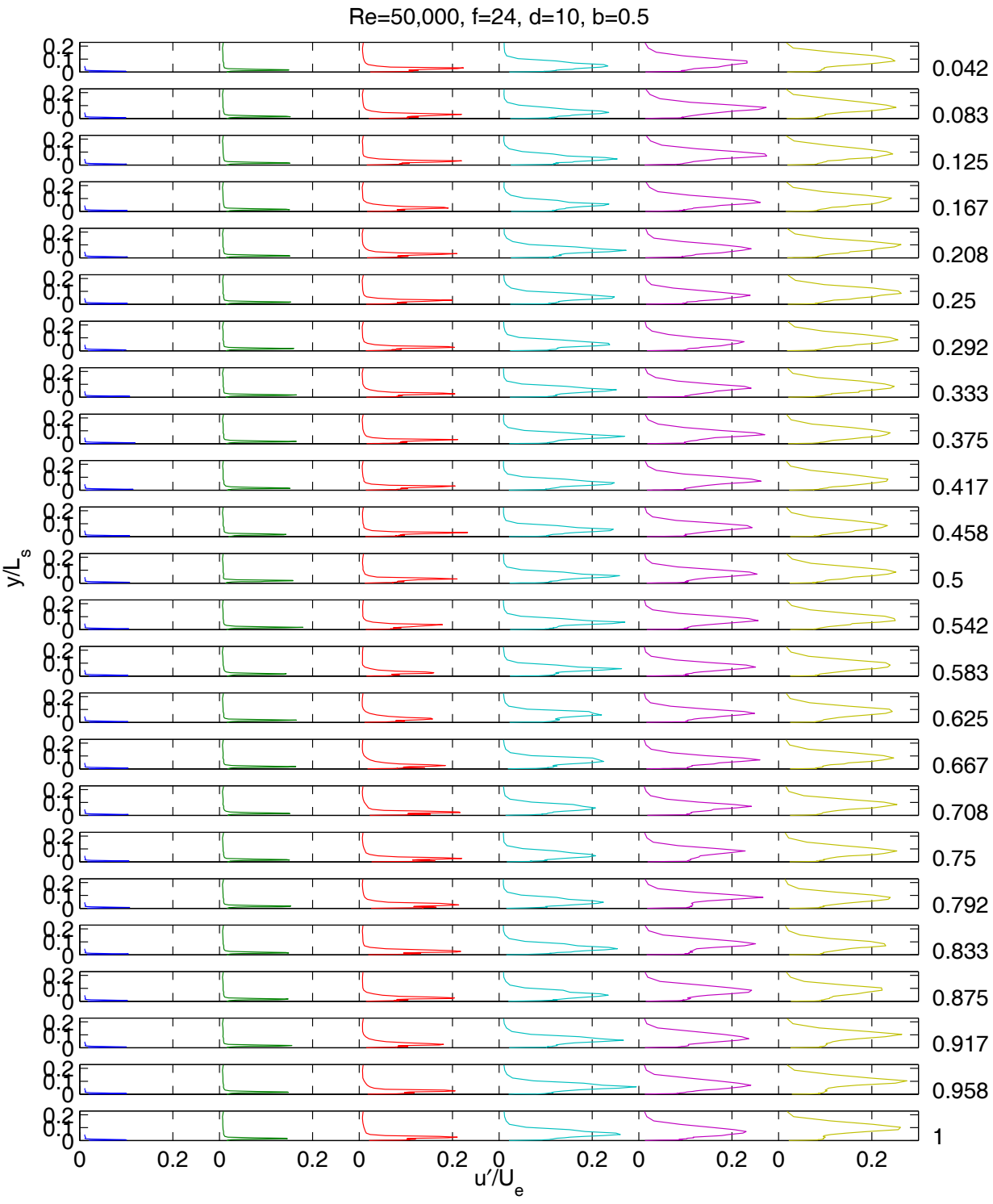

b)

Fig. 32 Phase averaged velocity profiles, low TI, Re=50,000, pulsed VGJs, F=0.56, D=10%, B=0.5: a) mean, b) rms.

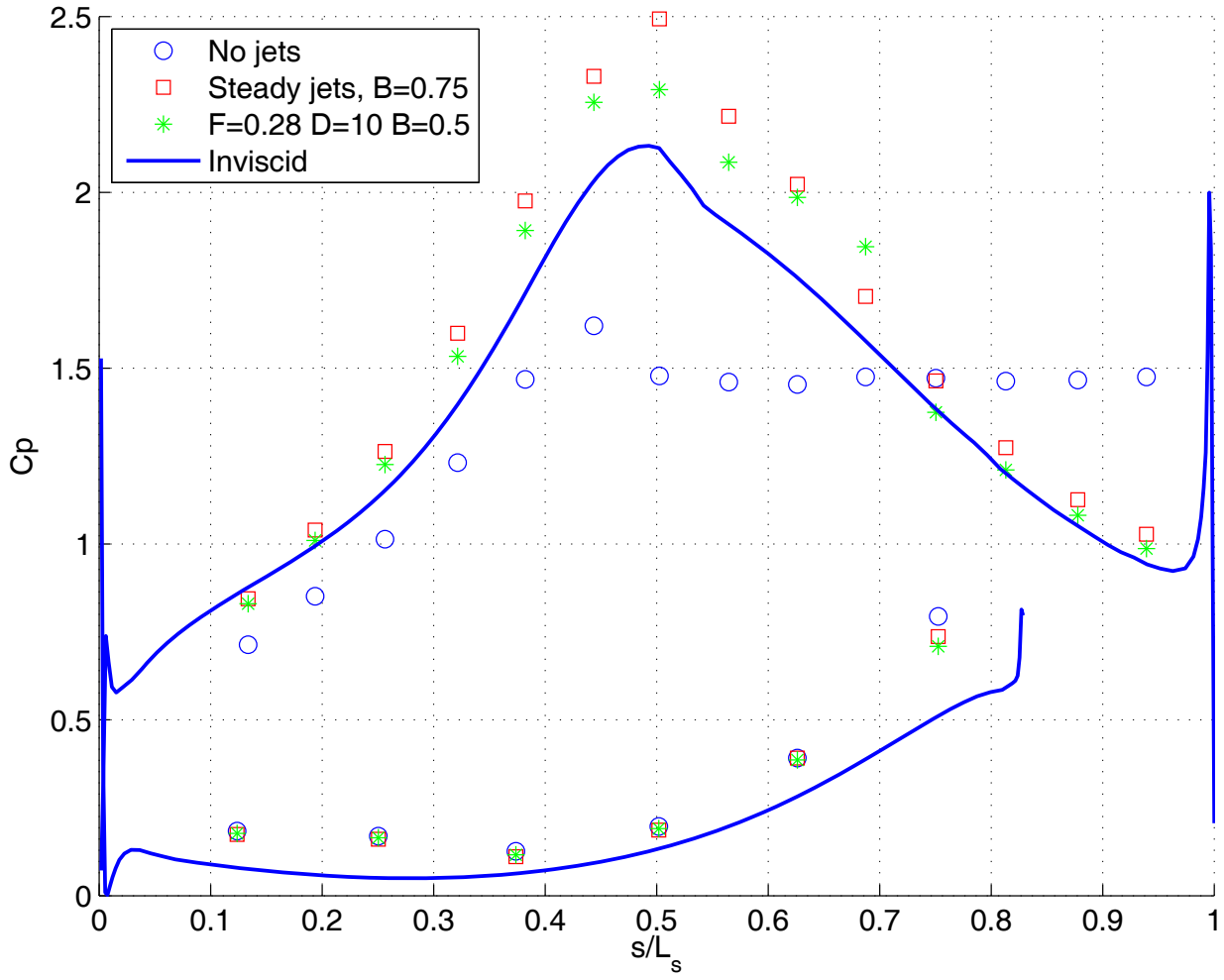
No jets
Steady jets, B=0.75
F=0.28 D=10 B=0.5
Inviscid
Cp
s/L_s
0
0.5
1
1.5
2
2.5
0.1
0.2
0.3
0.4
0.5
0.6
0.7
0.8
0.9

a)

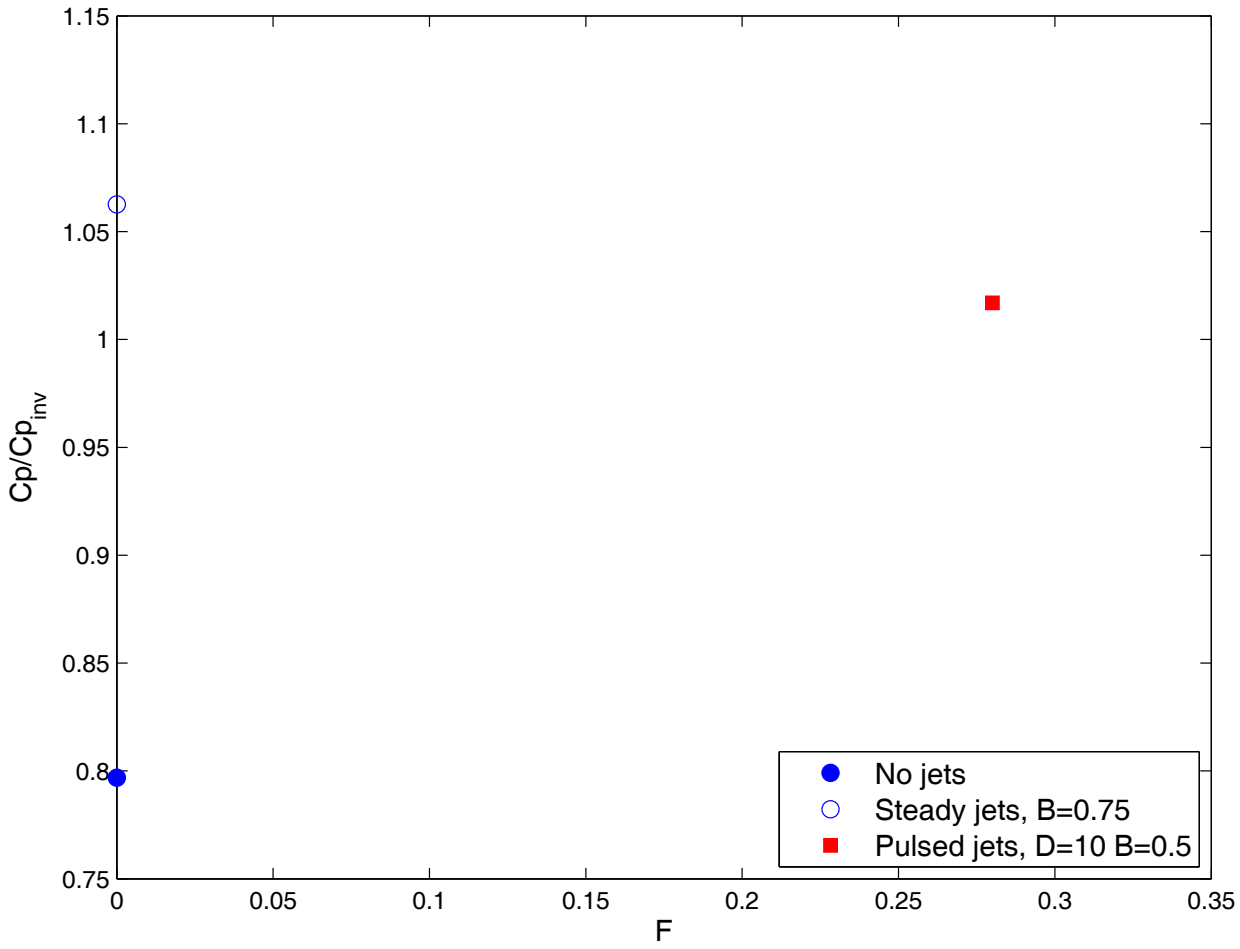

b)

Fig. 33 Cp results, low TI, Re=100,000: a) Cp profile, b) Integrated Cp.

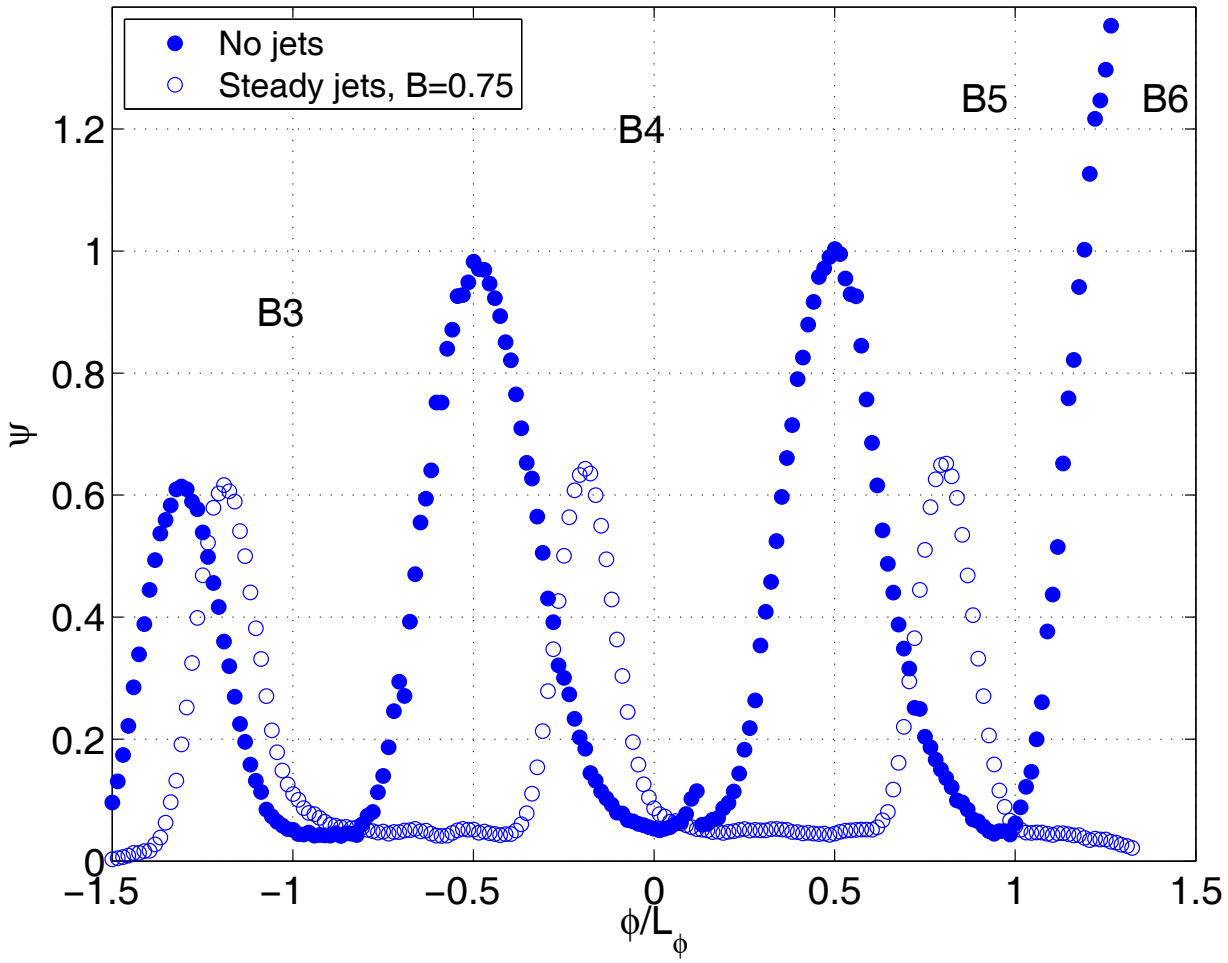
No jets
Steady jets, B=0.75
B3
B4
B5
B6
ψ
ϕ/L_ϕ
1.2
1
0.8
0.6
0.4
0.2
0
−1.5
−1
−0.5
0
0.5
1
1.5

a)

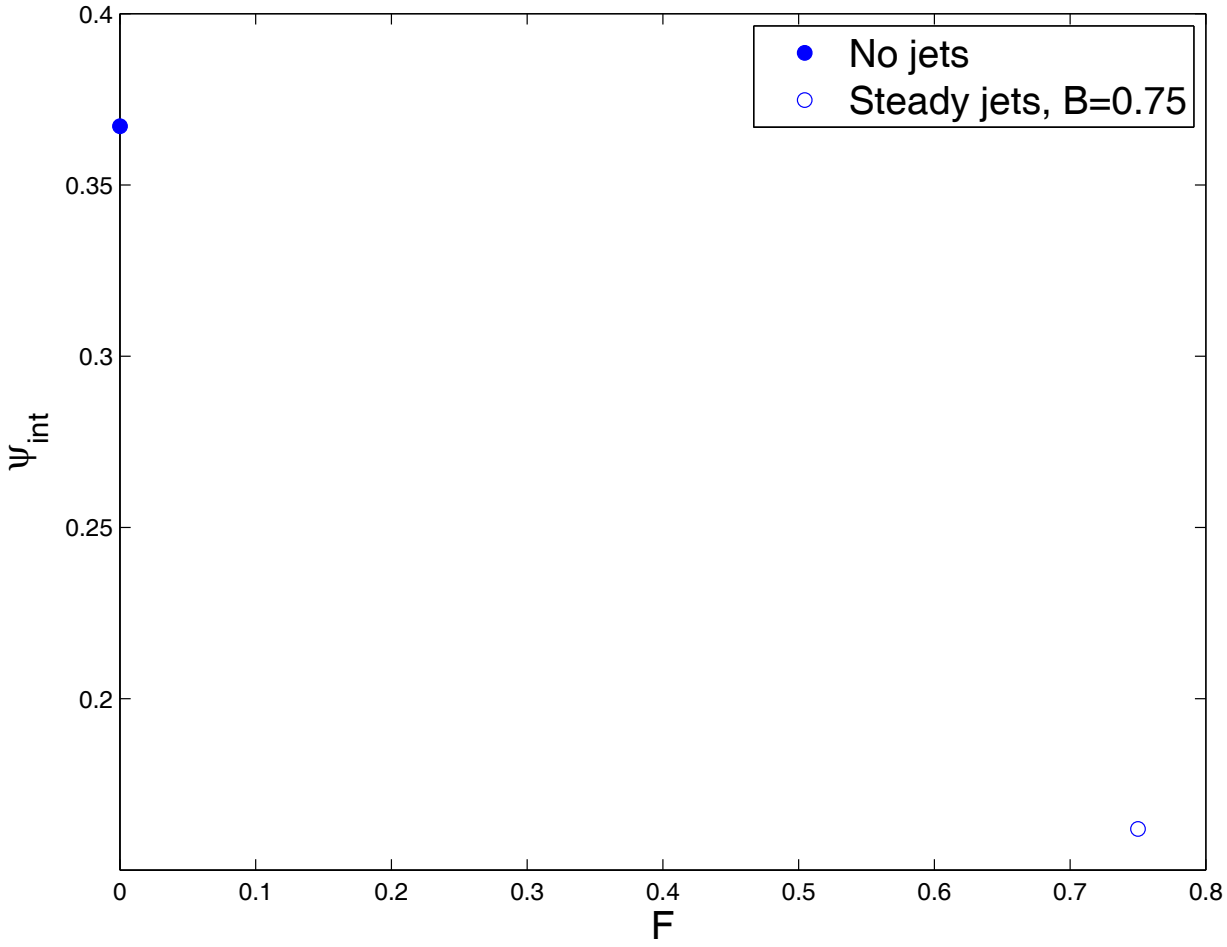

b)

Fig. 34 Ψ results, low TI, Re=100,000: a) Ψ profile, b) Integrated Ψ.

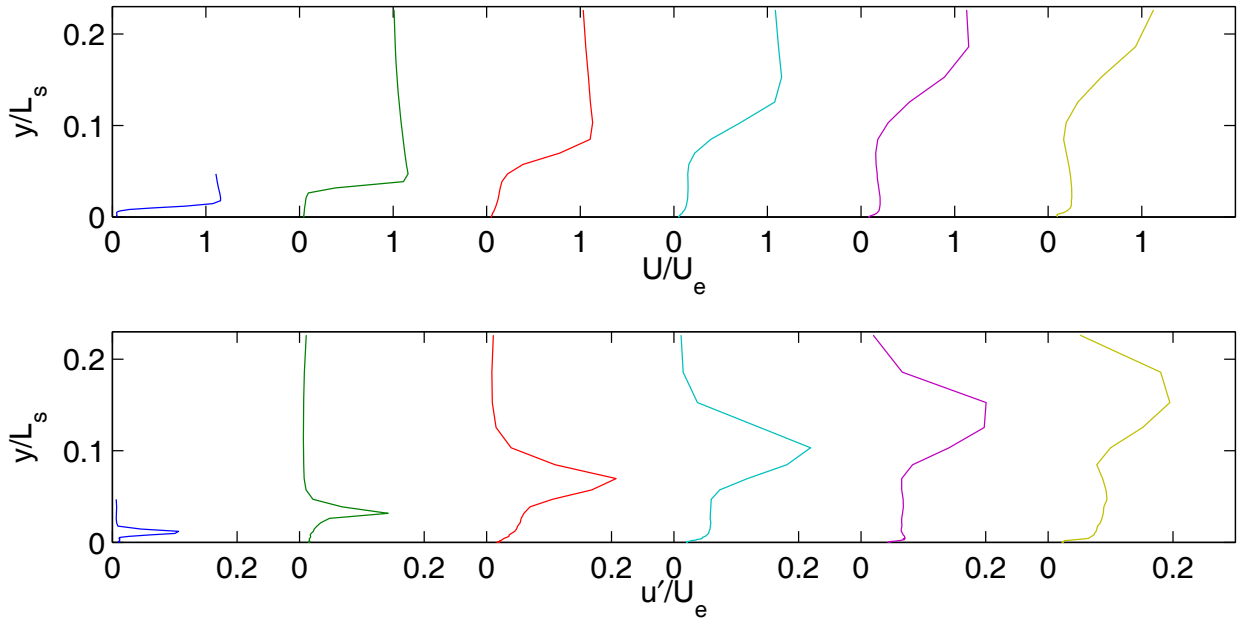

Fig. 35 Time averaged velocity profiles, low TI, Re=100,000, no VGJs: a) mean, b) rms.

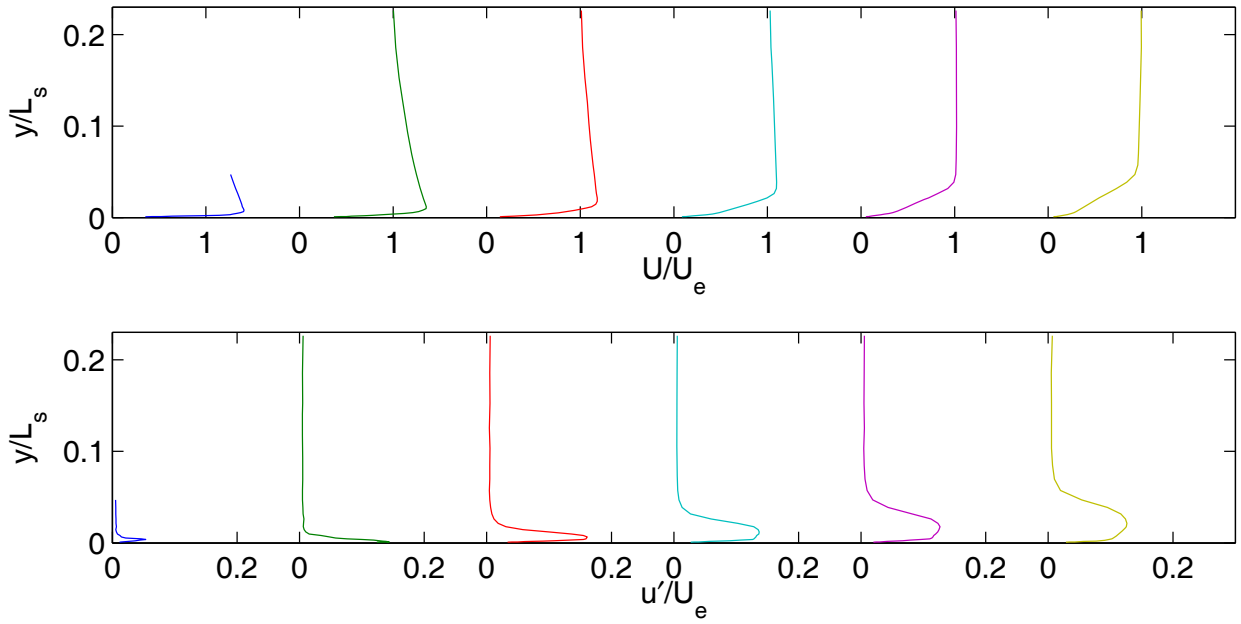

Fig. 36 Time averaged velocity profiles, low TI, Re=100,000, steady VGJs, B=0.75: a) mean, b) rms.

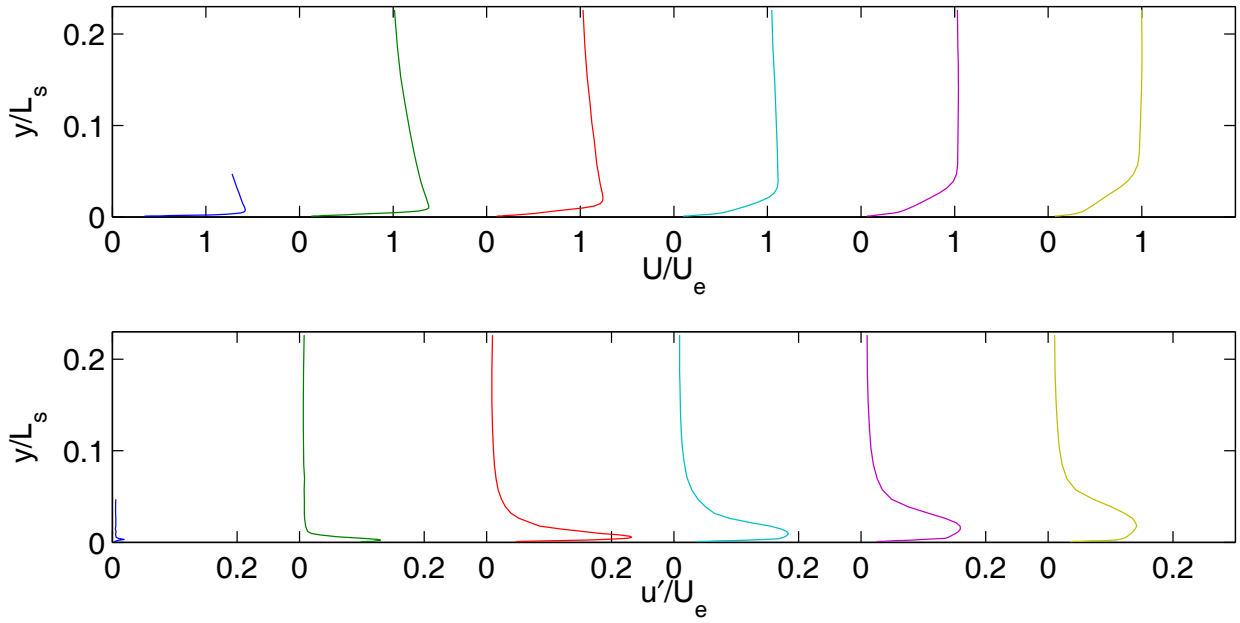

Fig. 37 Time averaged velocity profiles, low TI, Re=100,000, pulsed VGJs, F=0.28, D=10%, B=0.5: a) mean, b) rms.

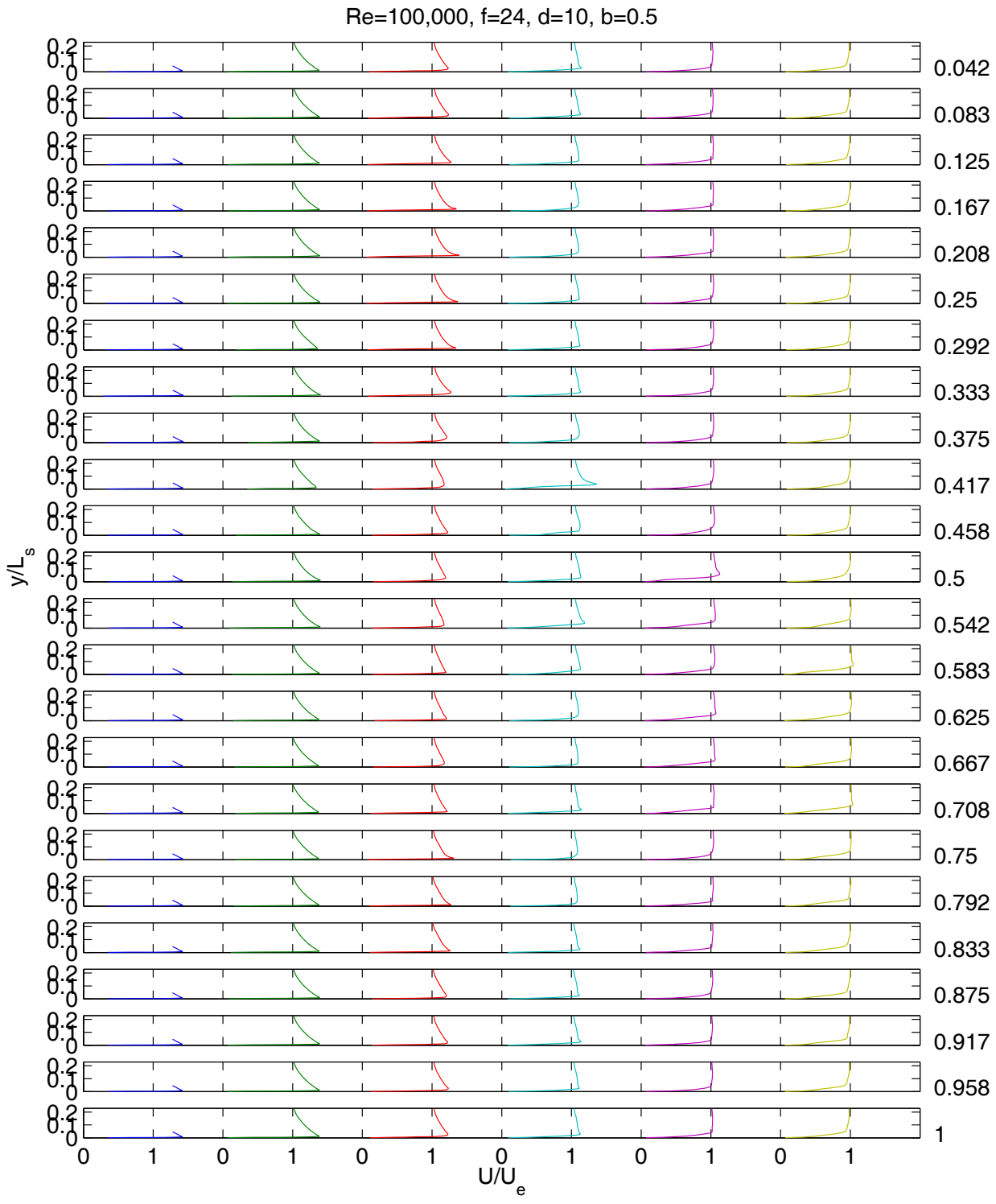
Re=100,000, f=24, d=10, b=0.5
y/L_s
U/U_e
0.042
0.083
0.125
0.167
0.208
0.25
0.292
0.333
0.375
0.417
0.458
0.5
0.542
0.583
0.625
0.667
0.708
0.75
0.792
0.833
0.875
0.917
0.958
1

a)

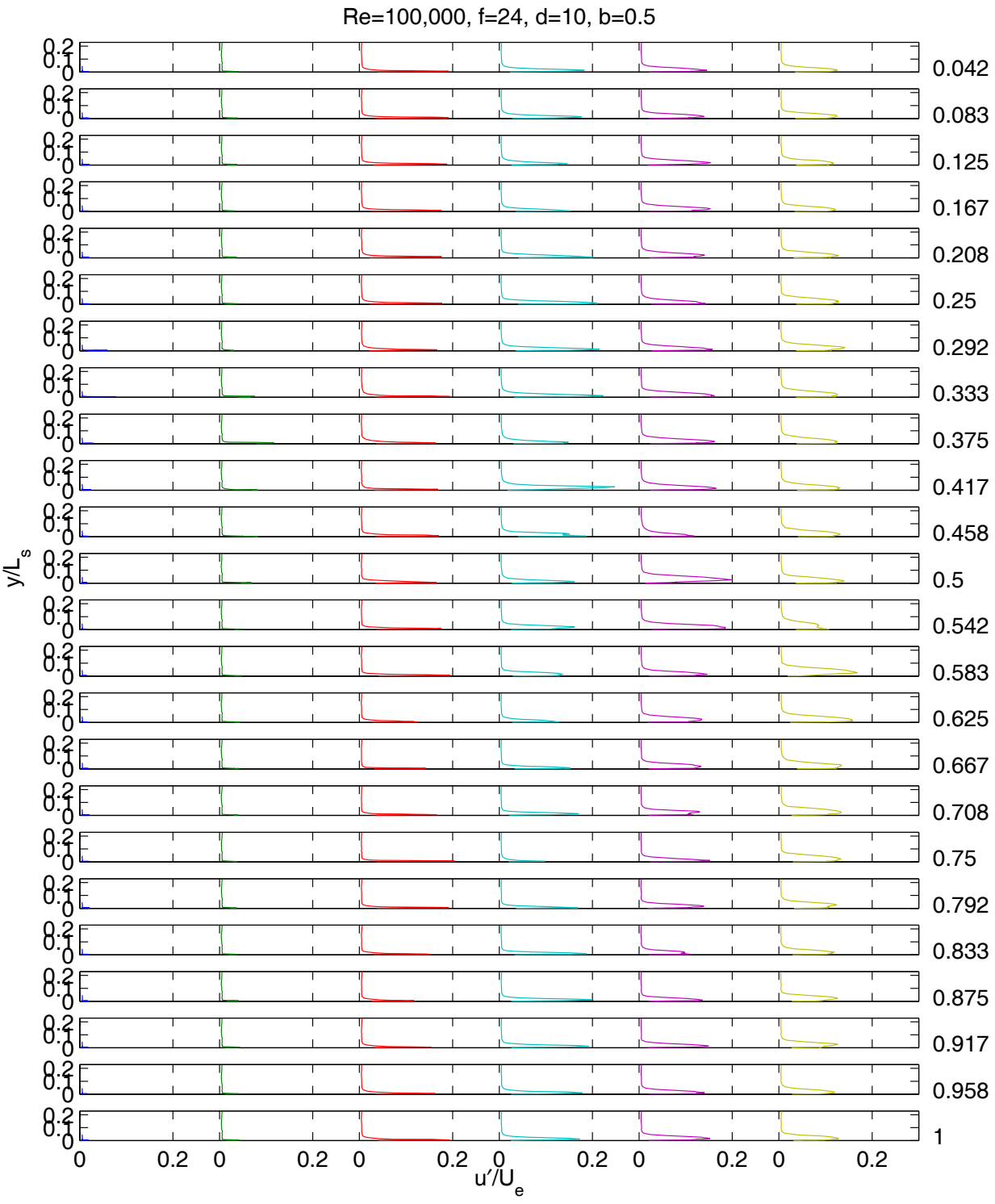

b)

Fig. 38 Phase averaged velocity profiles, low TI, Re=100,000, pulsed VGJs, F=0.28, D=10%, B=0.5: a) mean, b) rms.

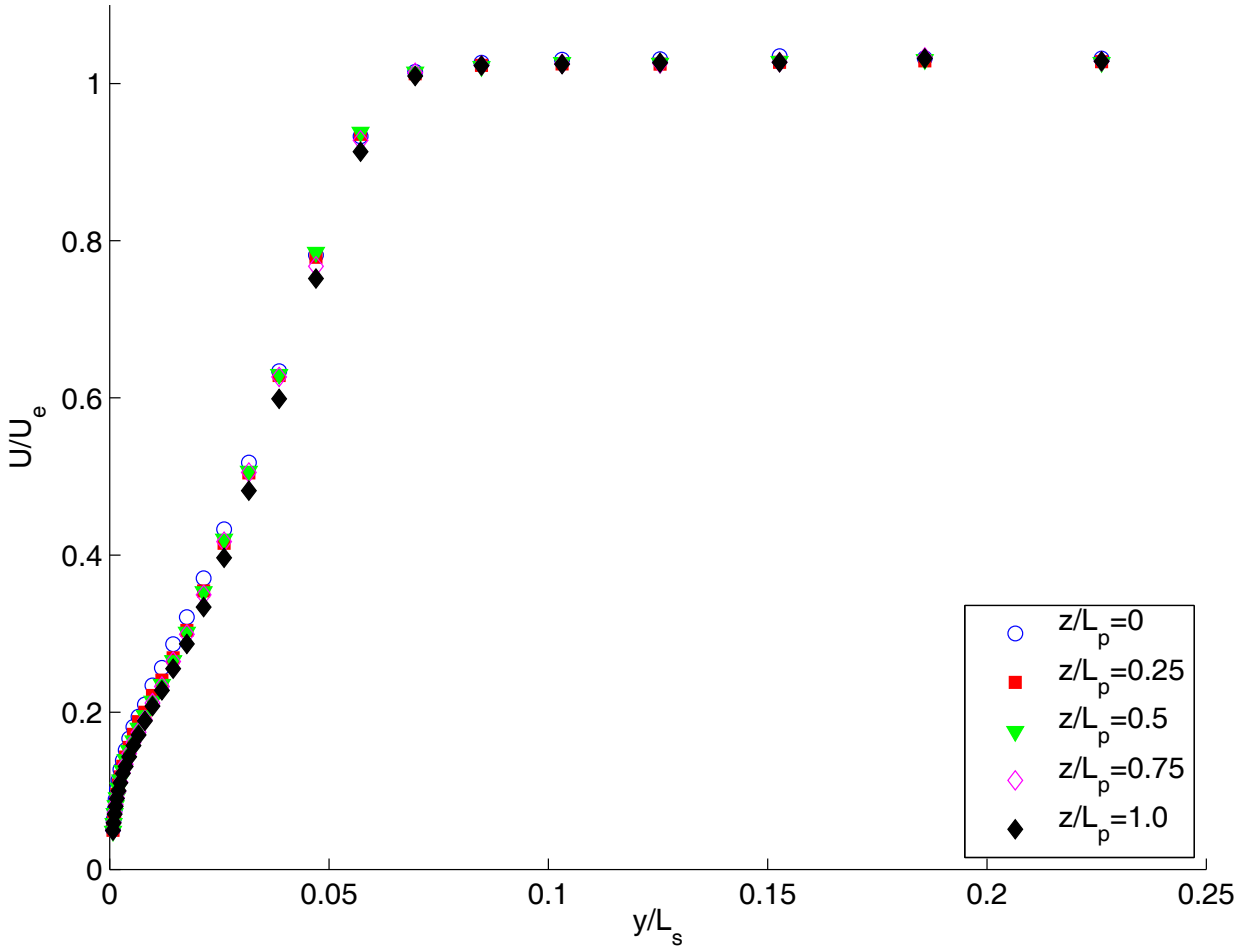
U/U_e
y/L_s
z/L_p=0
z/L_p=0.25
z/L_p=0.5
z/L_p=0.75
z/L_p=1.0
0
0.2
0.4
0.6
0.8
1
0
0.05
0.1
0.15
0.2
0.25

a)

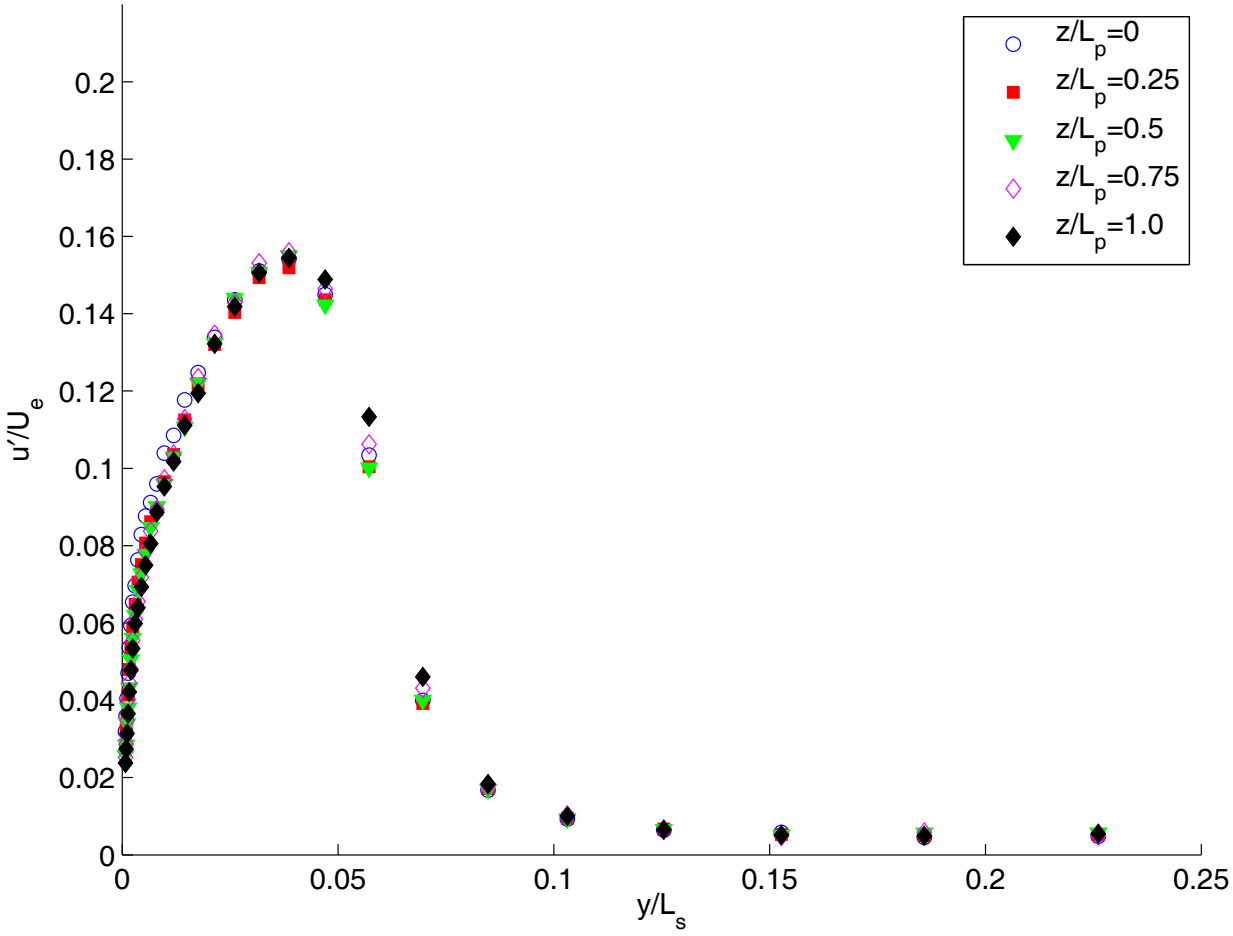

b)

Fig. 39 Time averaged velocity profiles, low TI, Re=50,000, steady VGJs, B=2.0, L_p/d=10.7: a) mean, b) rms.

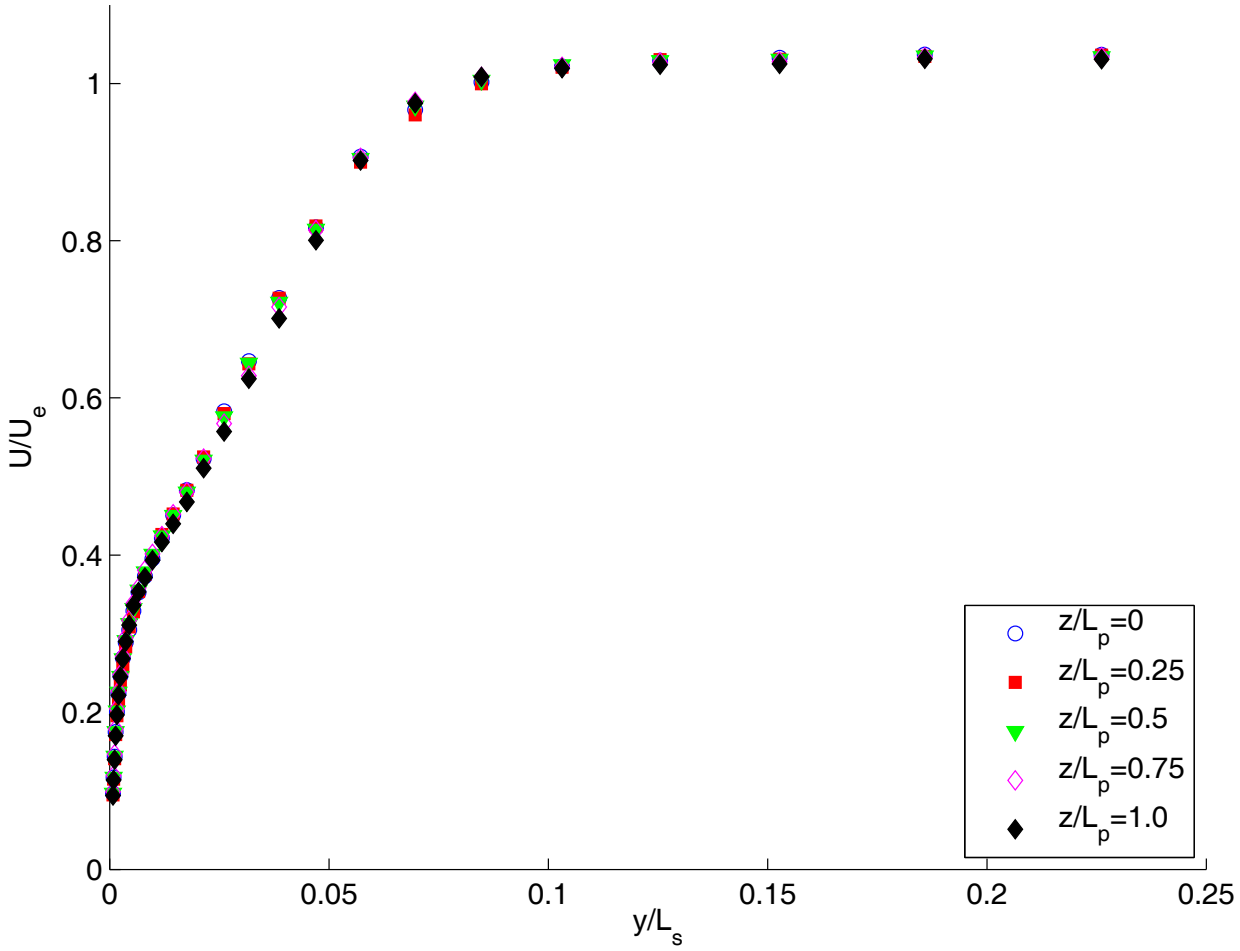
U/U_e
y/L_s
0
0.2
0.4
0.6
0.8
1
0
0.05
0.1
0.15
0.2
0.25
z/L_p=0
z/L_p=0.25
z/L_p=0.5
z/L_p=0.75
z/L_p=1.0

a)

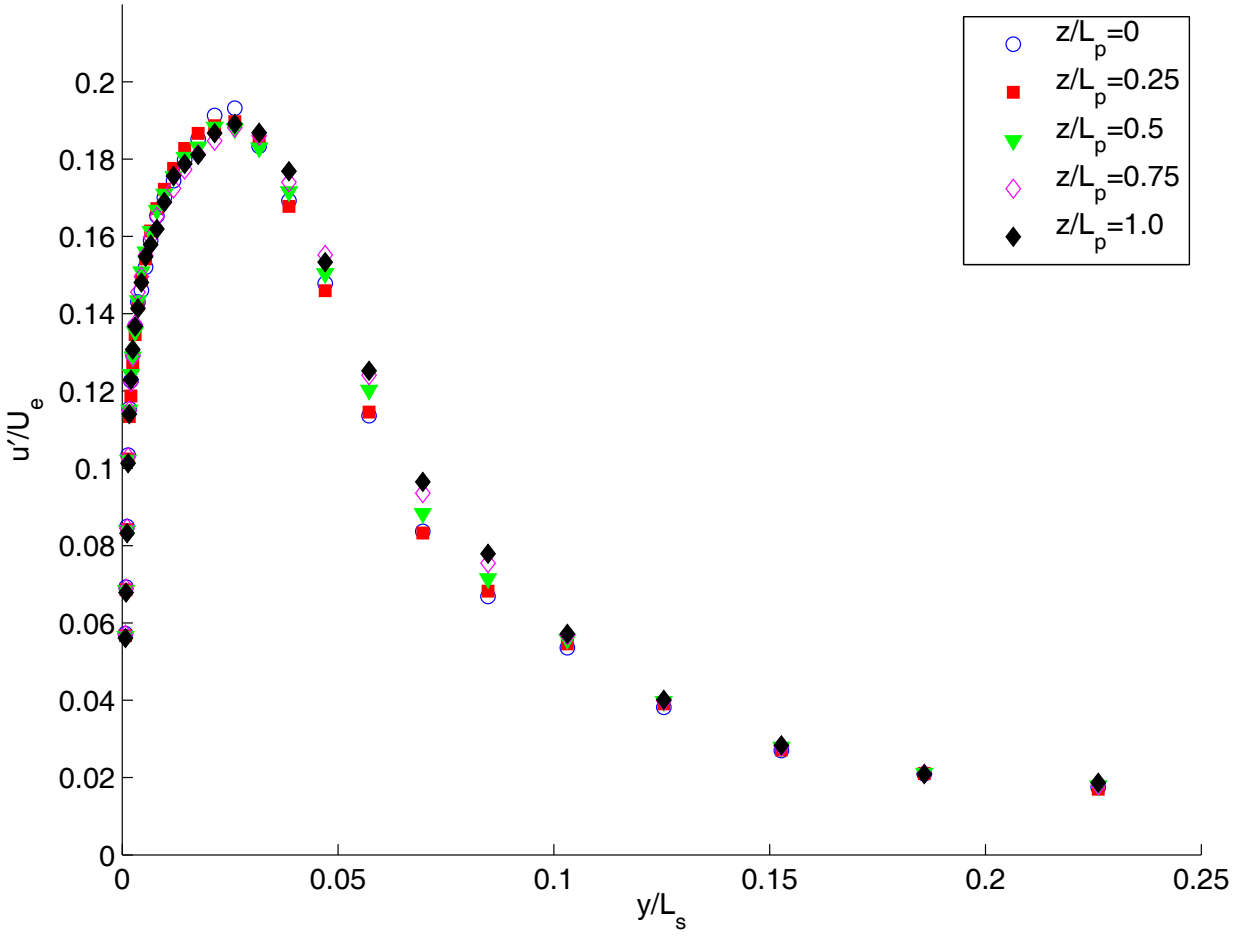

b)

Fig. 40 Time averaged velocity profiles, low TI, Re=50,000, pulsed VGJs, F=0.56, D=10%, B=1.0, L_p/d=10.7: a) mean, b) rms.

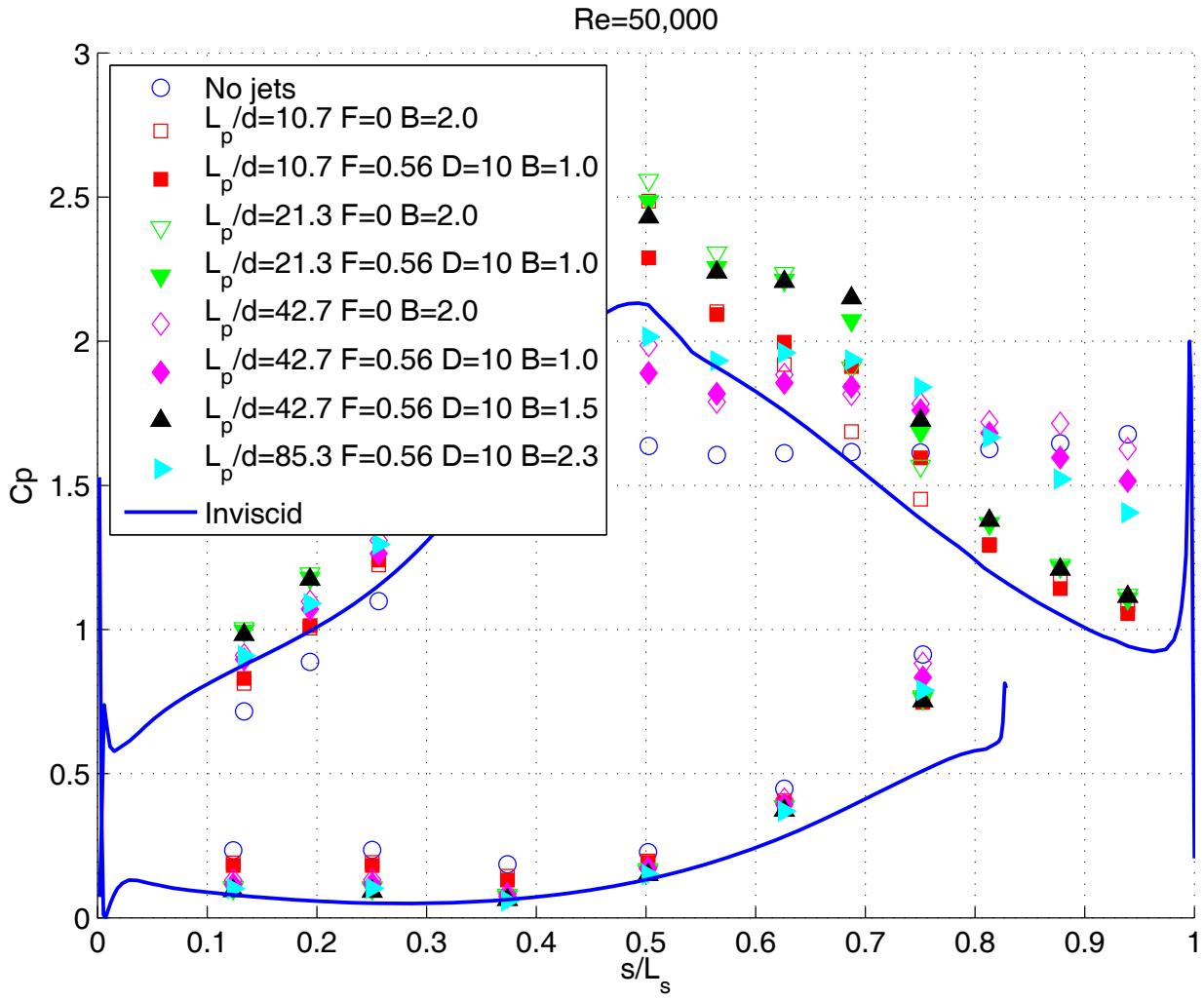
Re=50,000
No jets
Lp/d=10.7 F=0 B=2.0
Lp/d=10.7 F=0.56 D=10 B=1.0
Lp/d=21.3 F=0 B=2.0
Lp/d=21.3 F=0.56 D=10 B=1.0
Lp/d=42.7 F=0 B=2.0
Lp/d=42.7 F=0.56 D=10 B=1.0
Lp/d=42.7 F=0.56 D=10 B=1.5
Lp/d=85.3 F=0.56 D=10 B=2.3
Inviscid
Cp
s/Ls
0
0.5
1
1.5
2
2.5
3
0.1
0.2
0.3
0.4
0.5
0.6
0.7
0.8
0.9

a)

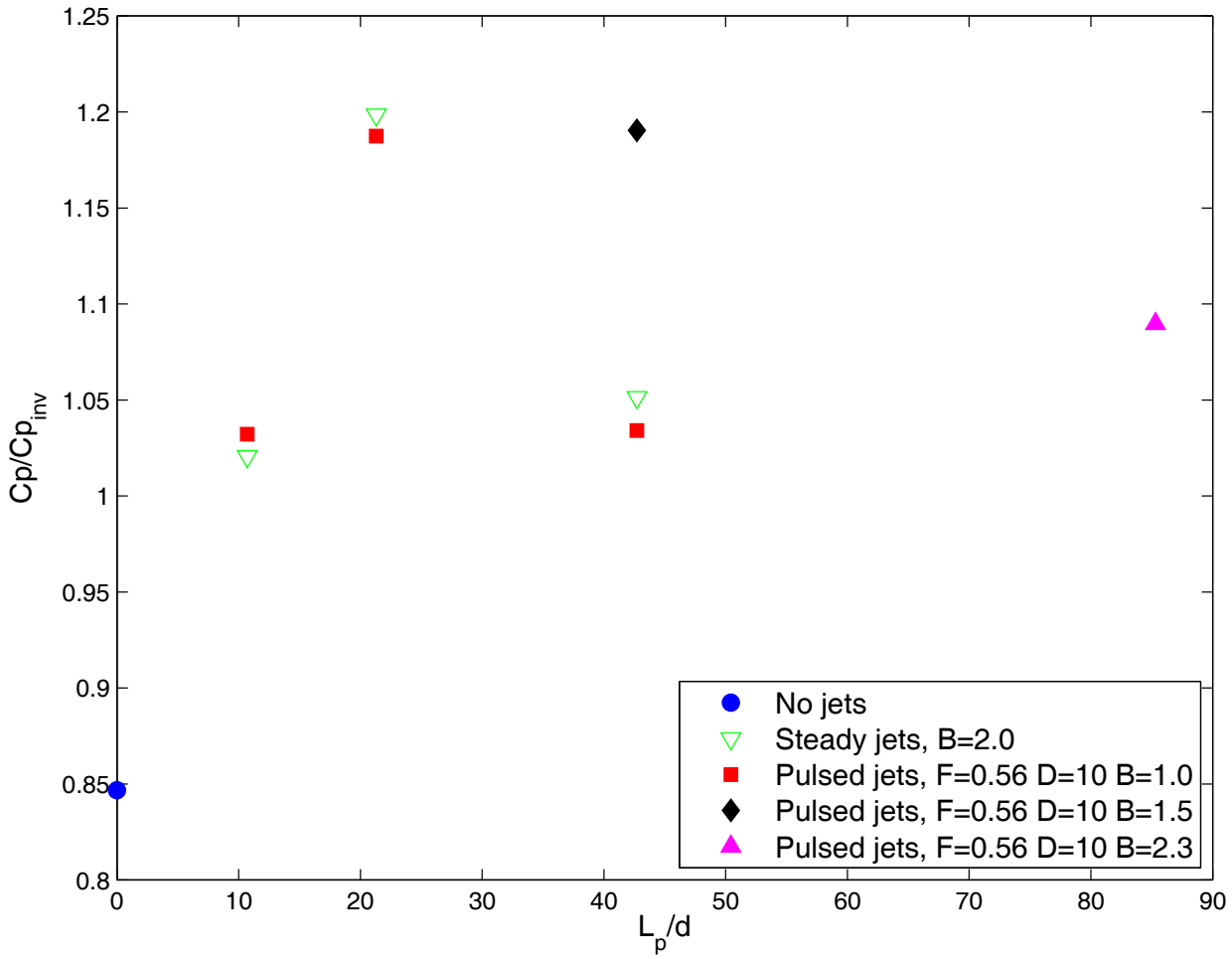

b)

Fig. 41 Cp results with various VGJ spacing, low TI, Re=50,000: a) Cp profile, b) Integrated Cp.

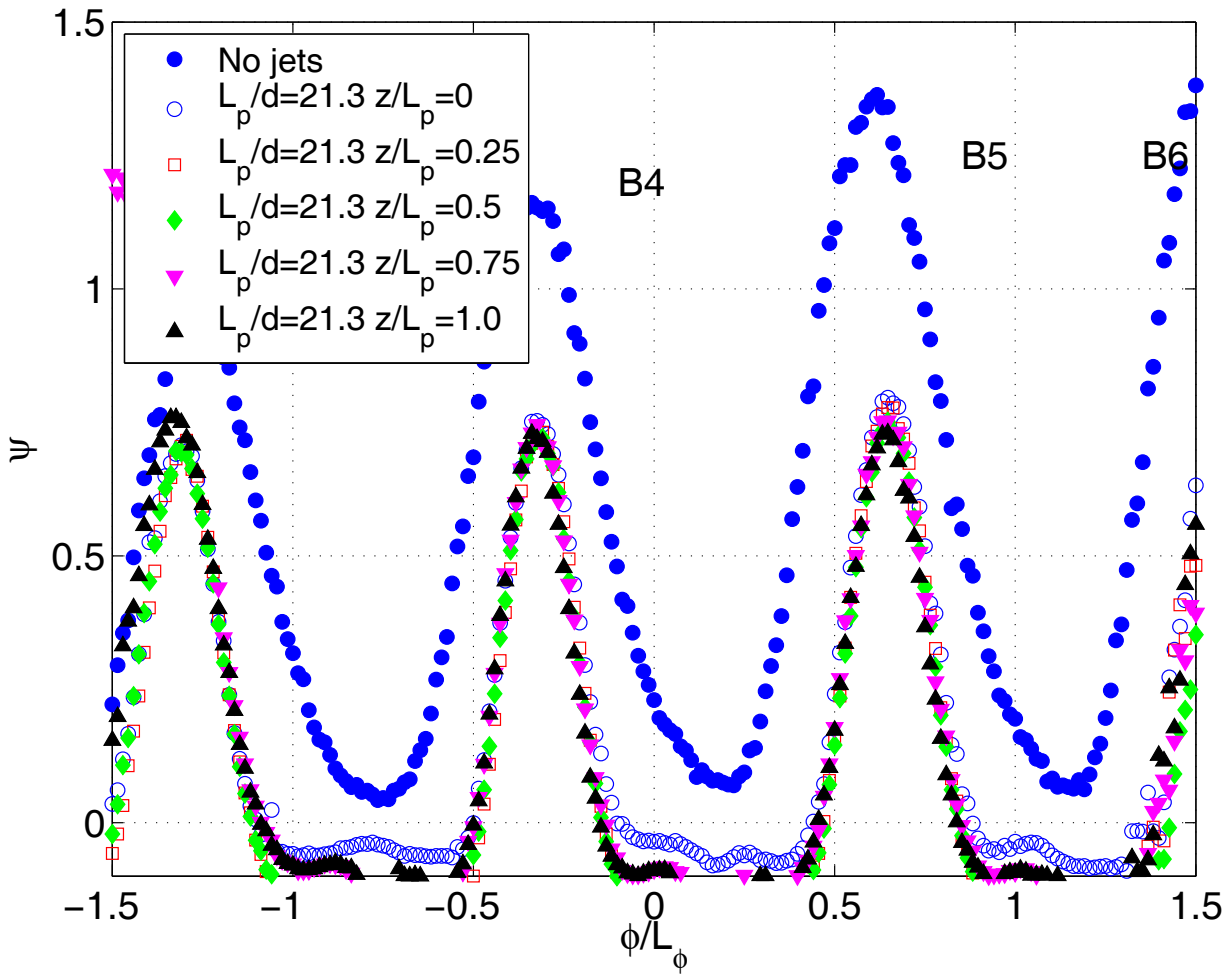

Fig. 42 Ψ profiles, low TI, Re=50,000, steady VJGs, B=2.0, L_p/d=21.3.

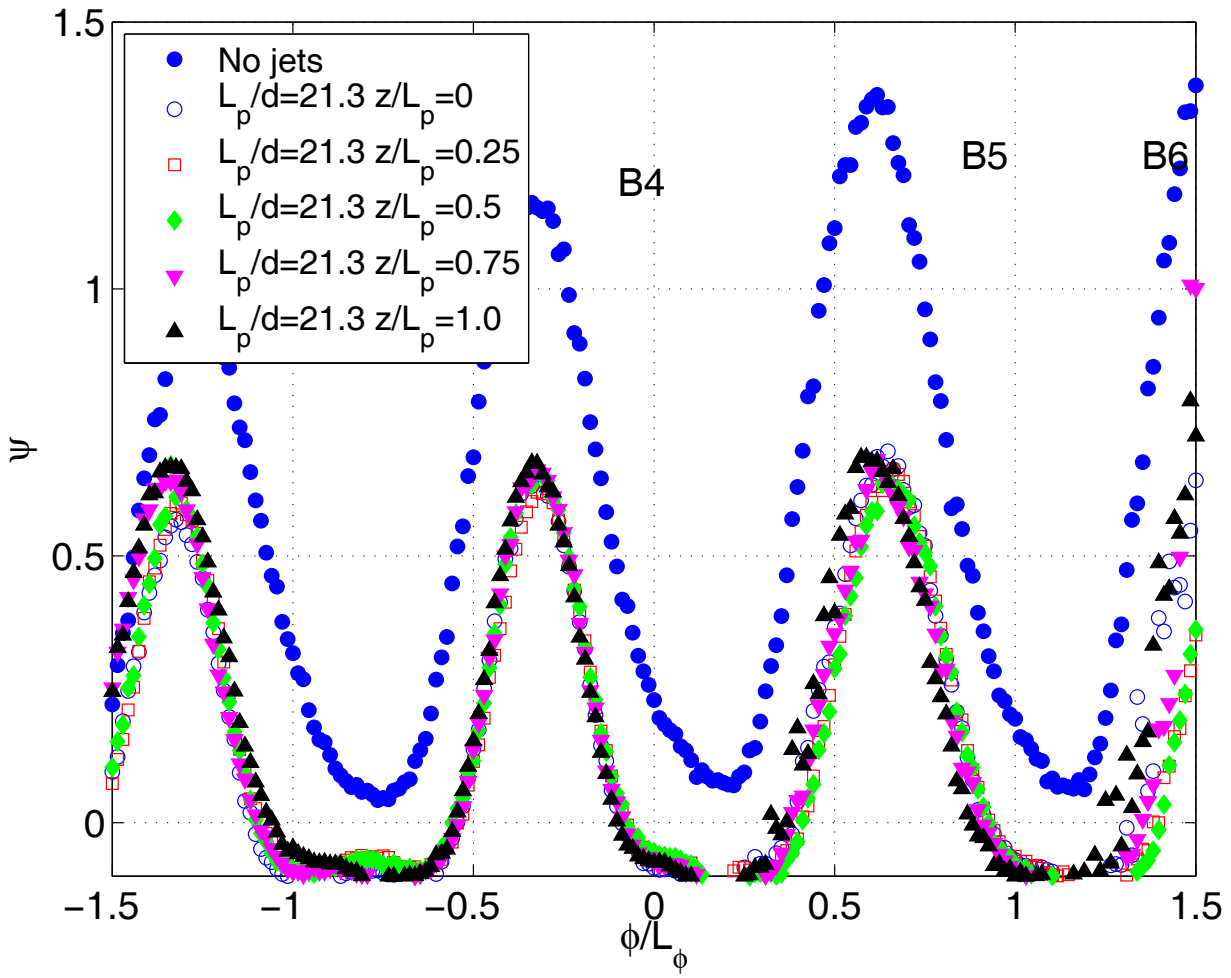

Fig. 43 Ψ profiles, low TI, Re=50,000, pulsed VJGs, F=0.56, D=10%, B=1.0, L_p/d=21.3.

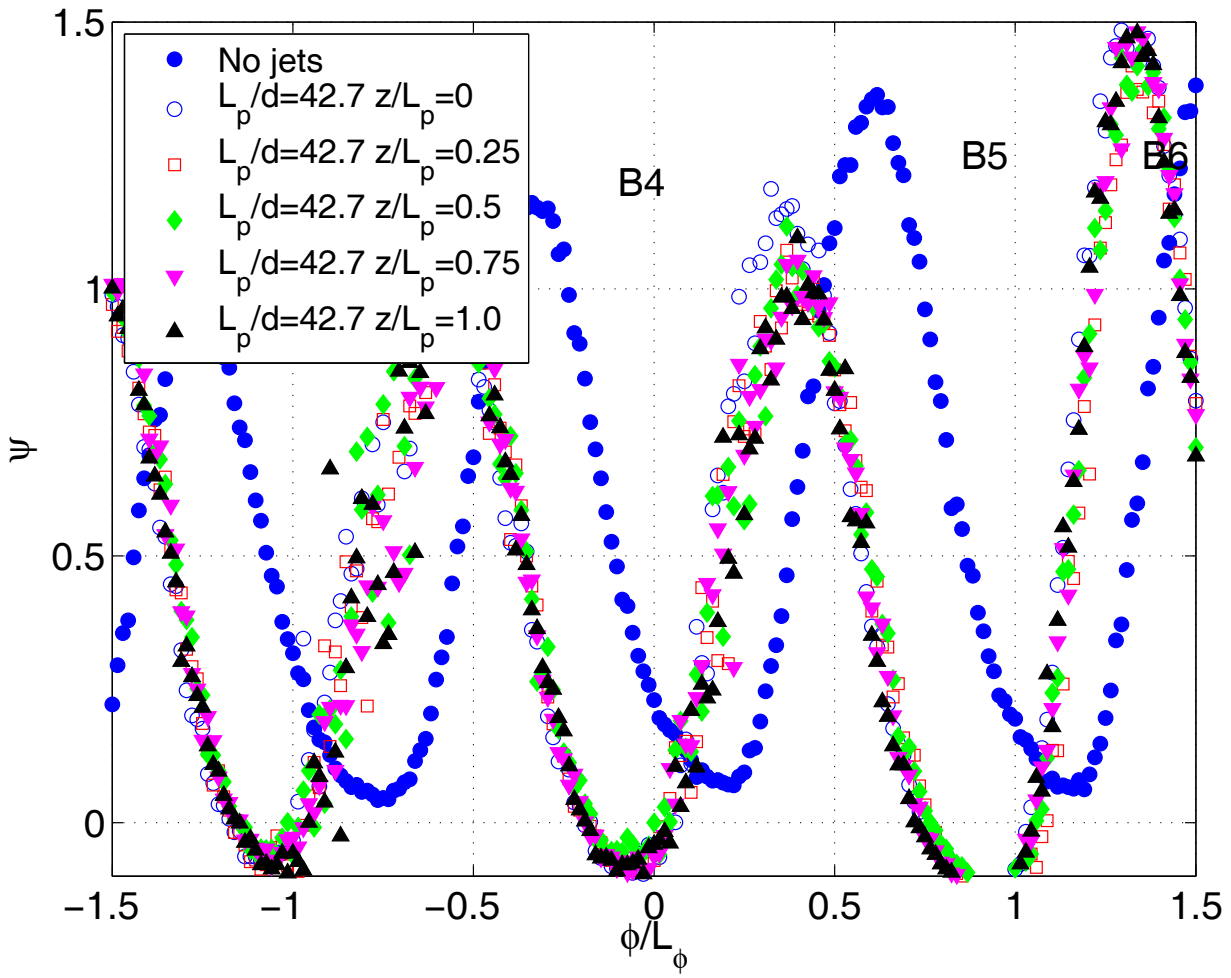

Fig. 44 Ψ profiles, low TI, Re=50,000, steady VJGs, B=2.0, L_p/d=42.7.

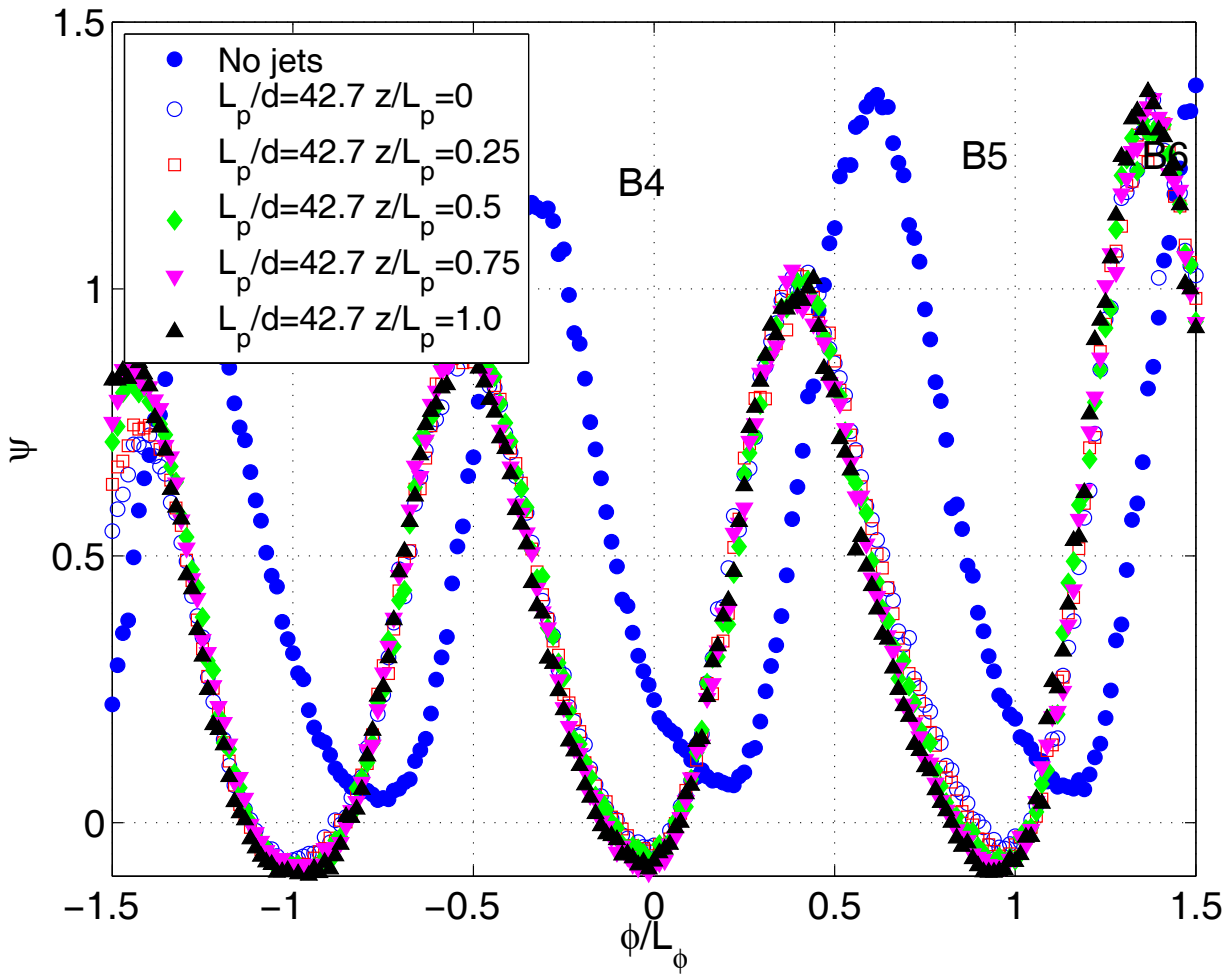

Fig. 45 Ψ profiles, low TI, Re=50,000, pulsed VJGs, F=0.56, D=10%, B=1.0, L_p/d=42.7.

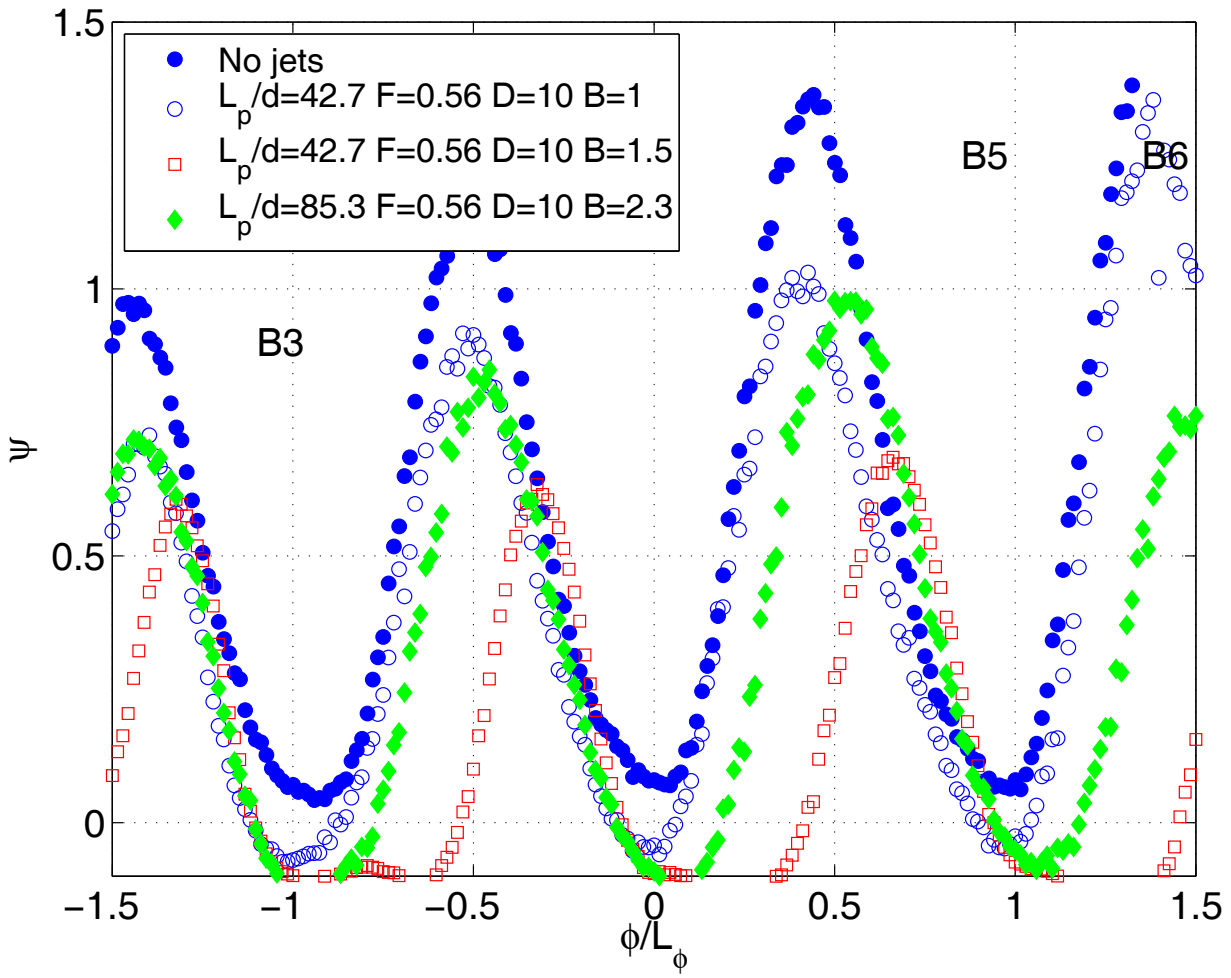

Fig. 46 Ψ profiles, low TI, Re=50,000, pulsed VJGs, F=0.56, D=10%, B=2.0, L_p/d=42.7 and 85.3, z/L_p=0, various B.

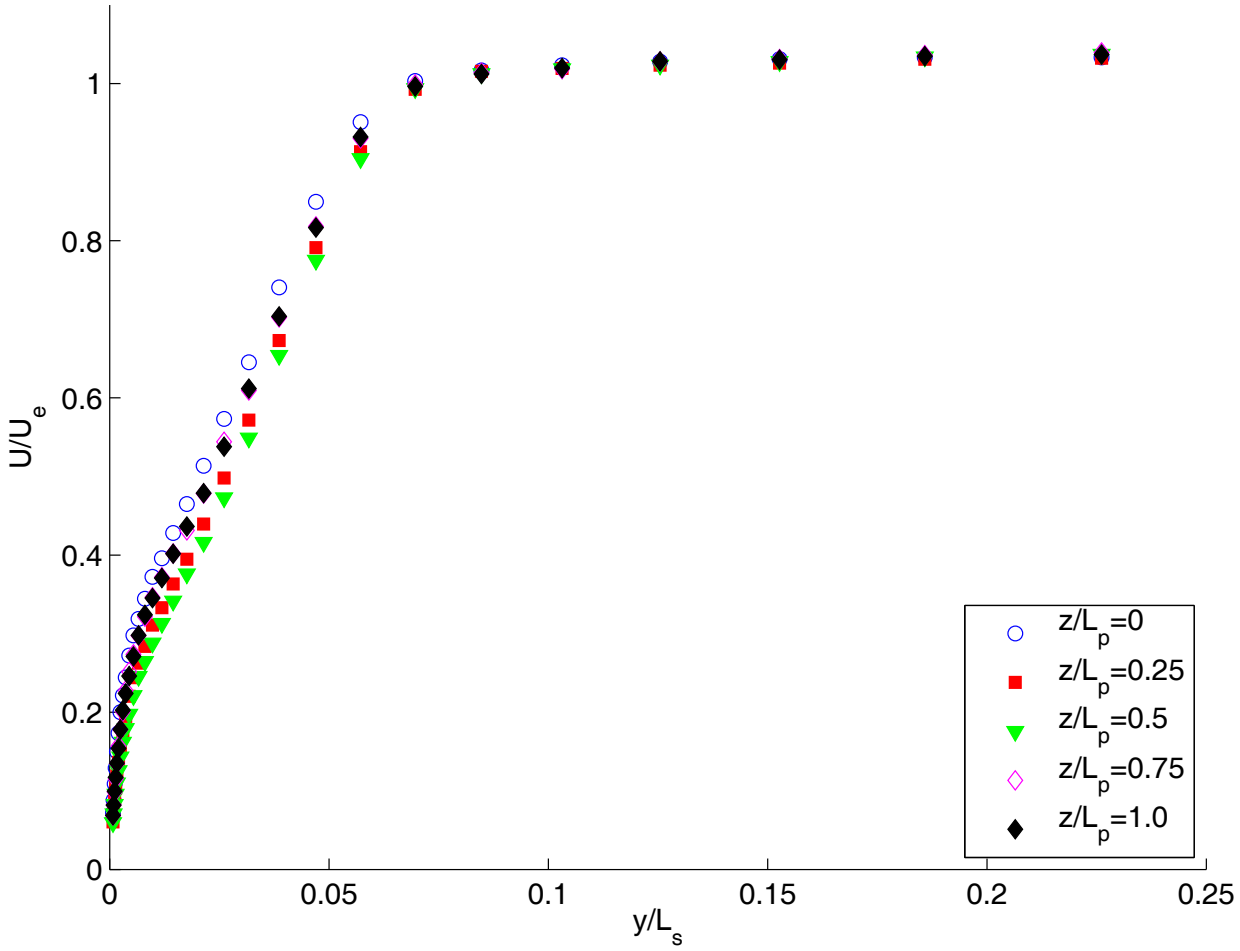
U/U_e
y/L_s
z/L_p=0
z/L_p=0.25
z/L_p=0.5
z/L_p=0.75
z/L_p=1.0
0
0.2
0.4
0.6
0.8
1
0
0.05
0.1
0.15
0.2
0.25

a)

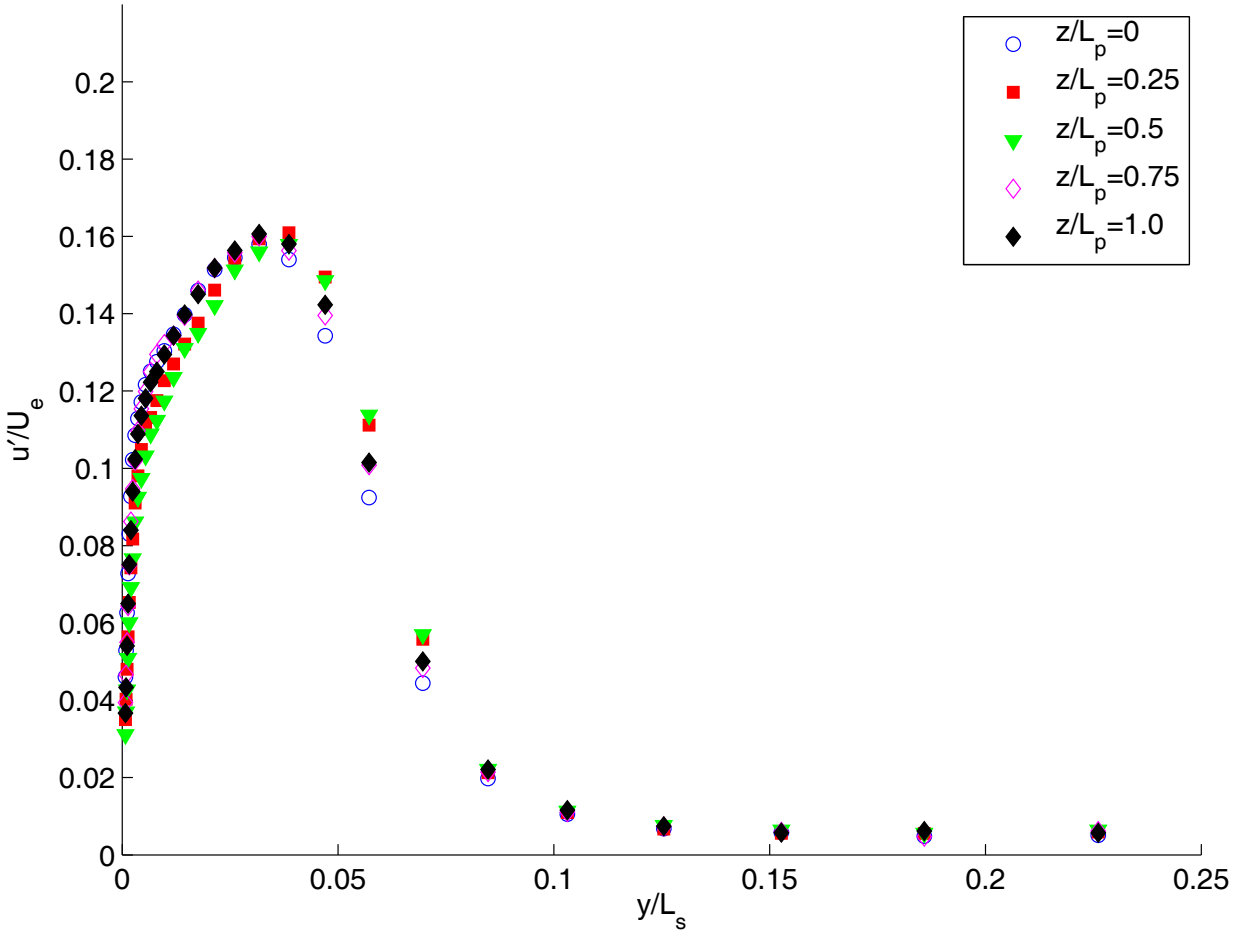

b)

Fig. 47 Time averaged velocity profiles, low TI, Re=50,000, steady VGJs, B=2.0, L_p/d=21.3: a) mean, b) rms.

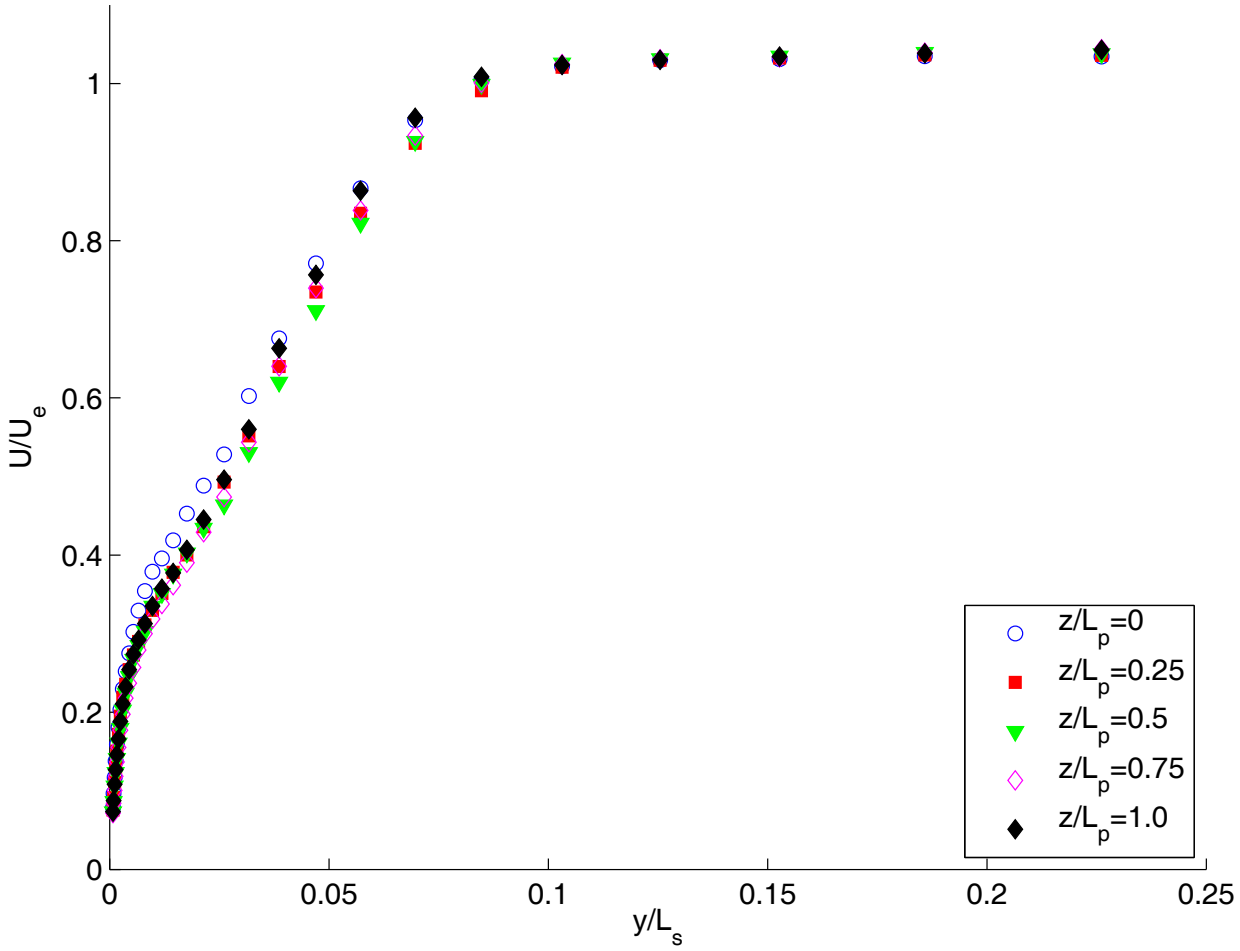
U/U_e
y/L_s
z/L_p=0
z/L_p=0.25
z/L_p=0.5
z/L_p=0.75
z/L_p=1.0
0
0.2
0.4
0.6
0.8
1
0
0.05
0.1
0.15
0.2
0.25

a)

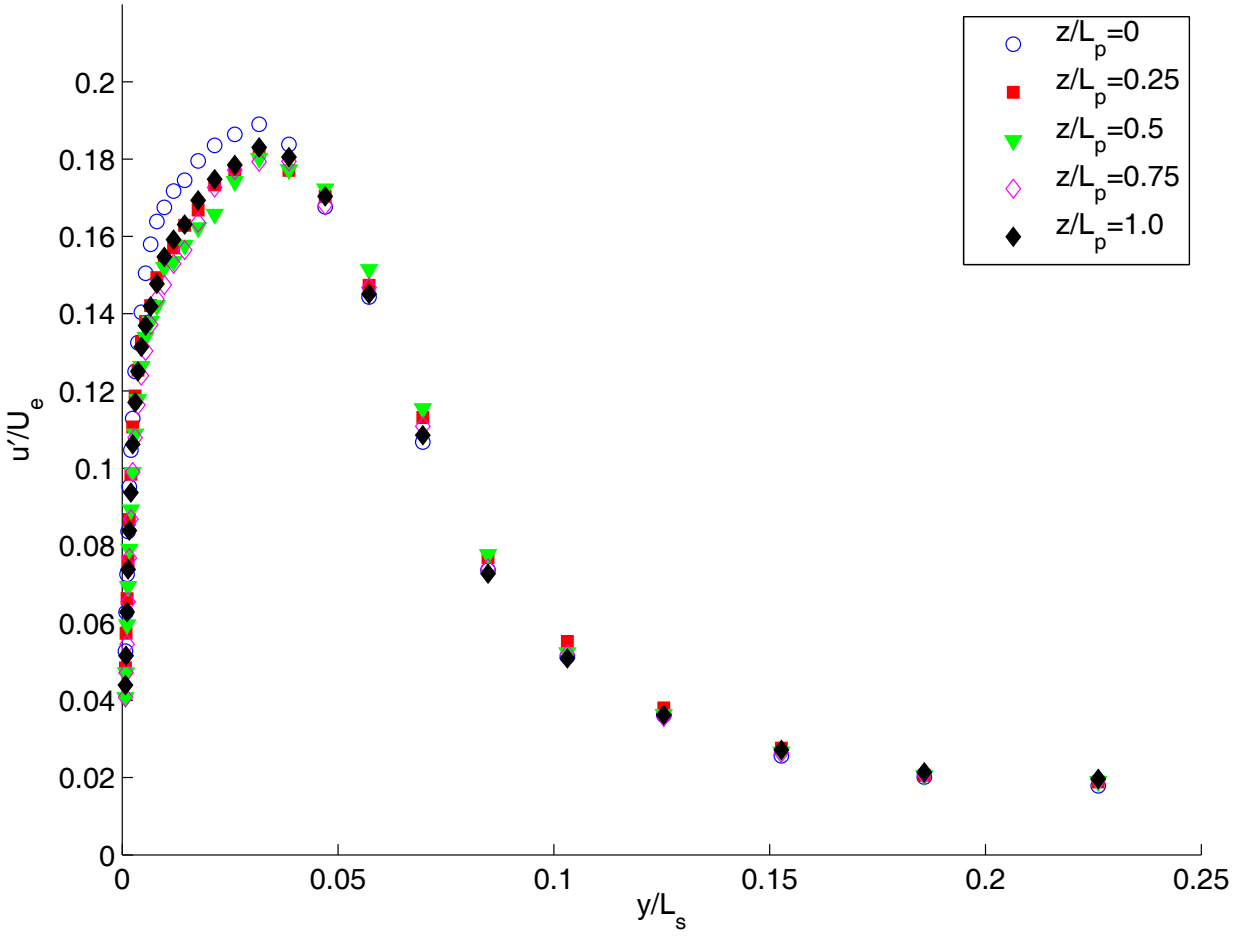

b)

Fig. 48 Time averaged velocity profiles, low TI, Re=50,000, pulsed VGJs, F=0.56, D=10%, B=1.0, L_p/d=21.3: a) mean, b) rms.

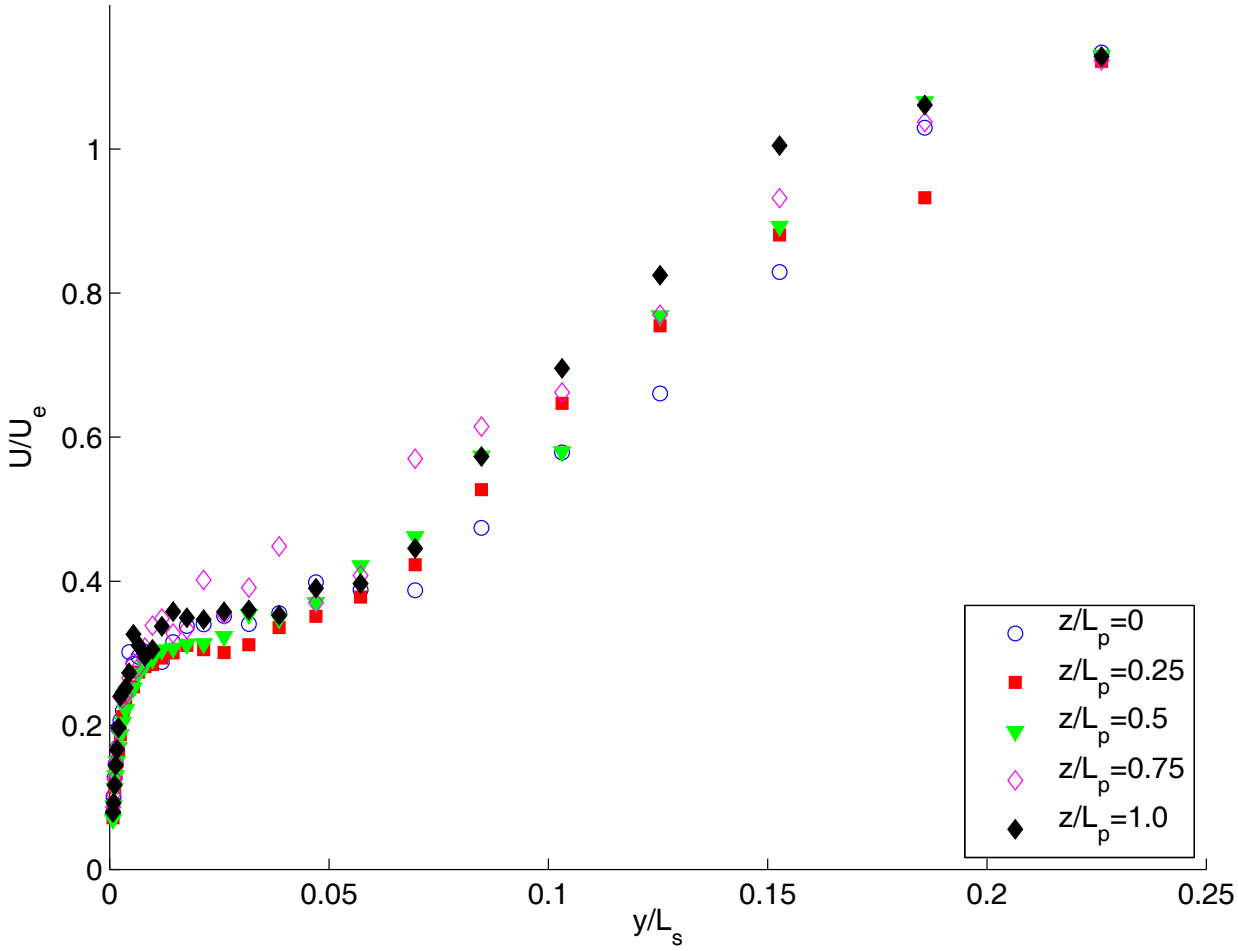
U/U_e
y/L_s
0
0.2
0.4
0.6
0.8
1
0
0.05
0.1
0.15
0.2
0.25
z/L_p=0
z/L_p=0.25
z/L_p=0.5
z/L_p=0.75
z/L_p=1.0

a)

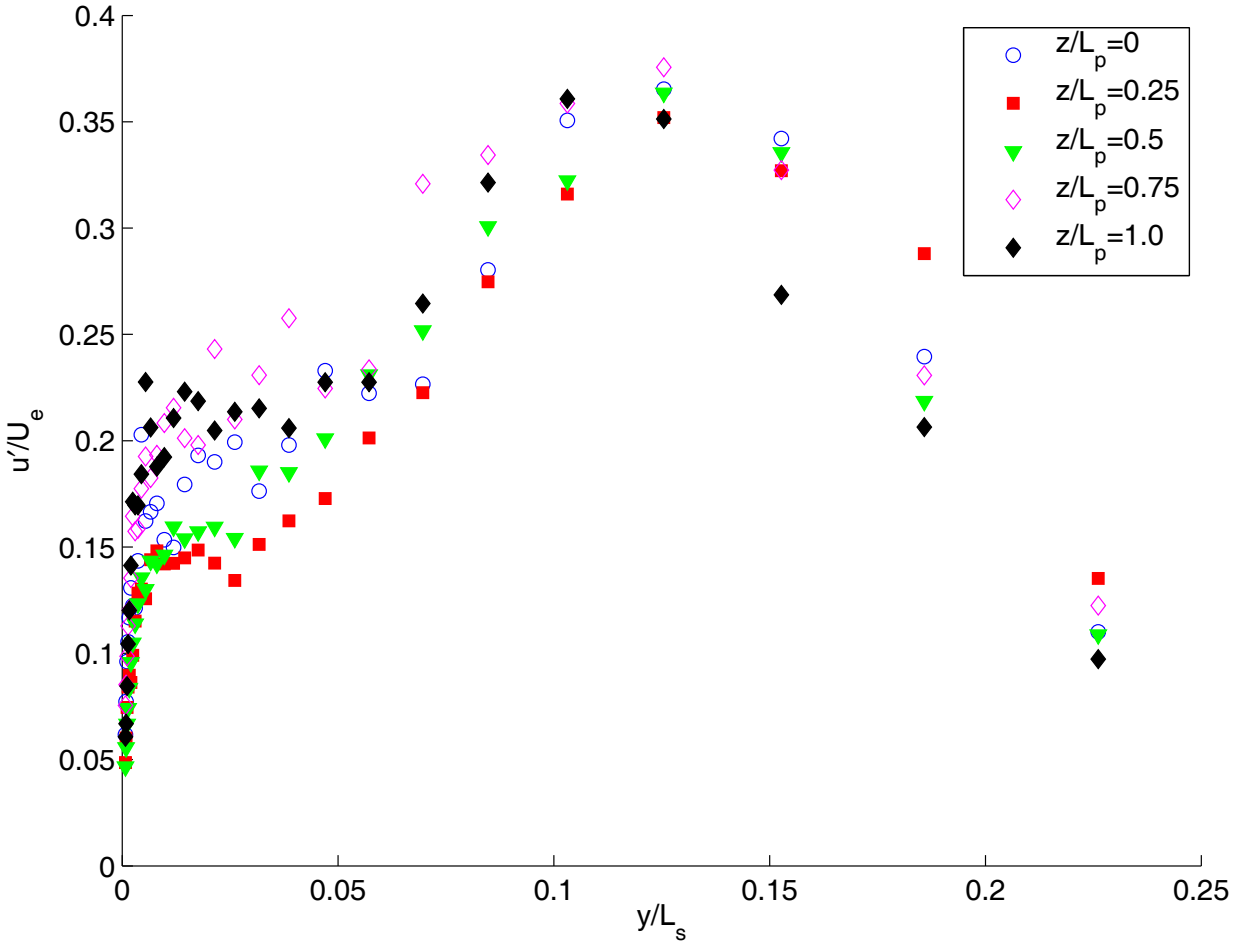

b)

Fig. 49 Time averaged velocity profiles, low TI, Re=50,000, steady VGJs, B=2.0, L_p/d=42.7: a) mean, b) rms.

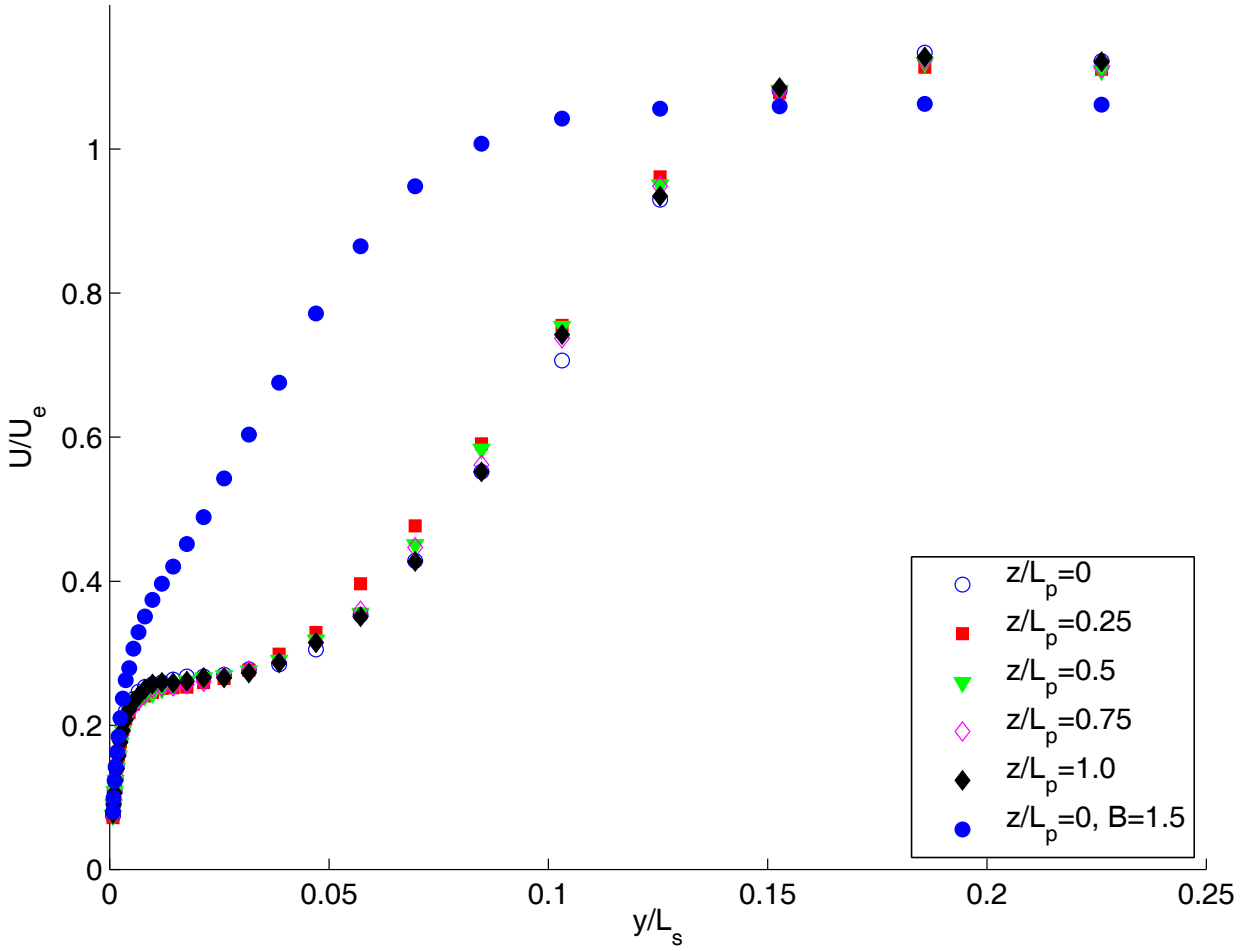
U/U_e
y/L_s
0
0.2
0.4
0.6
0.8
1
0
0.05
0.1
0.15
0.2
0.25
z/L_p=0
z/L_p=0.25
z/L_p=0.5
z/L_p=0.75
z/L_p=1.0
z/L_p=0, B=1.5

a)

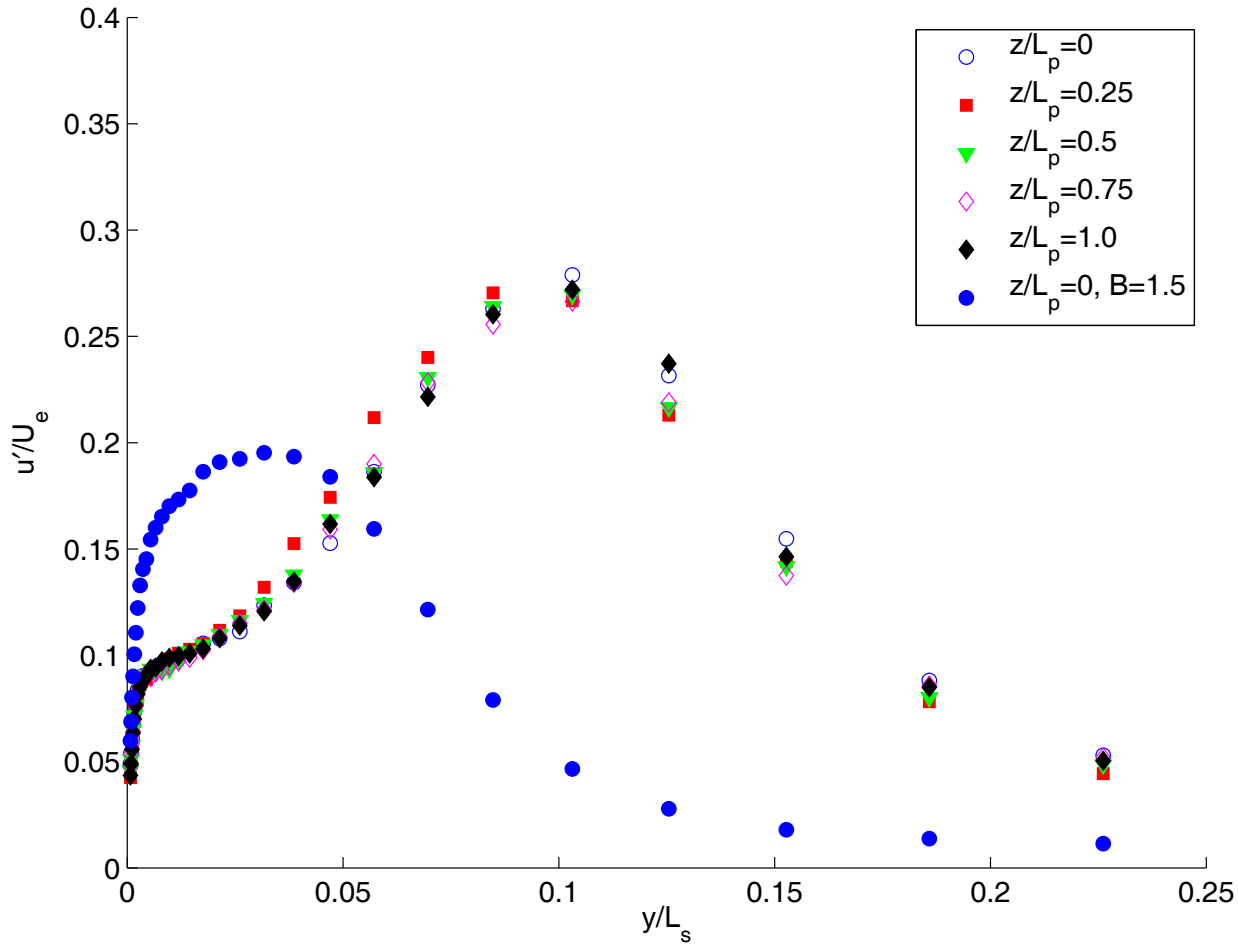

b)

Fig. 50 Time averaged velocity profiles, low TI, Re=50,000, pulsed VGJs, F=0.56, D=10%, B=1.0 and 1.5, L_p/d=42.7: a) mean, b) rms.

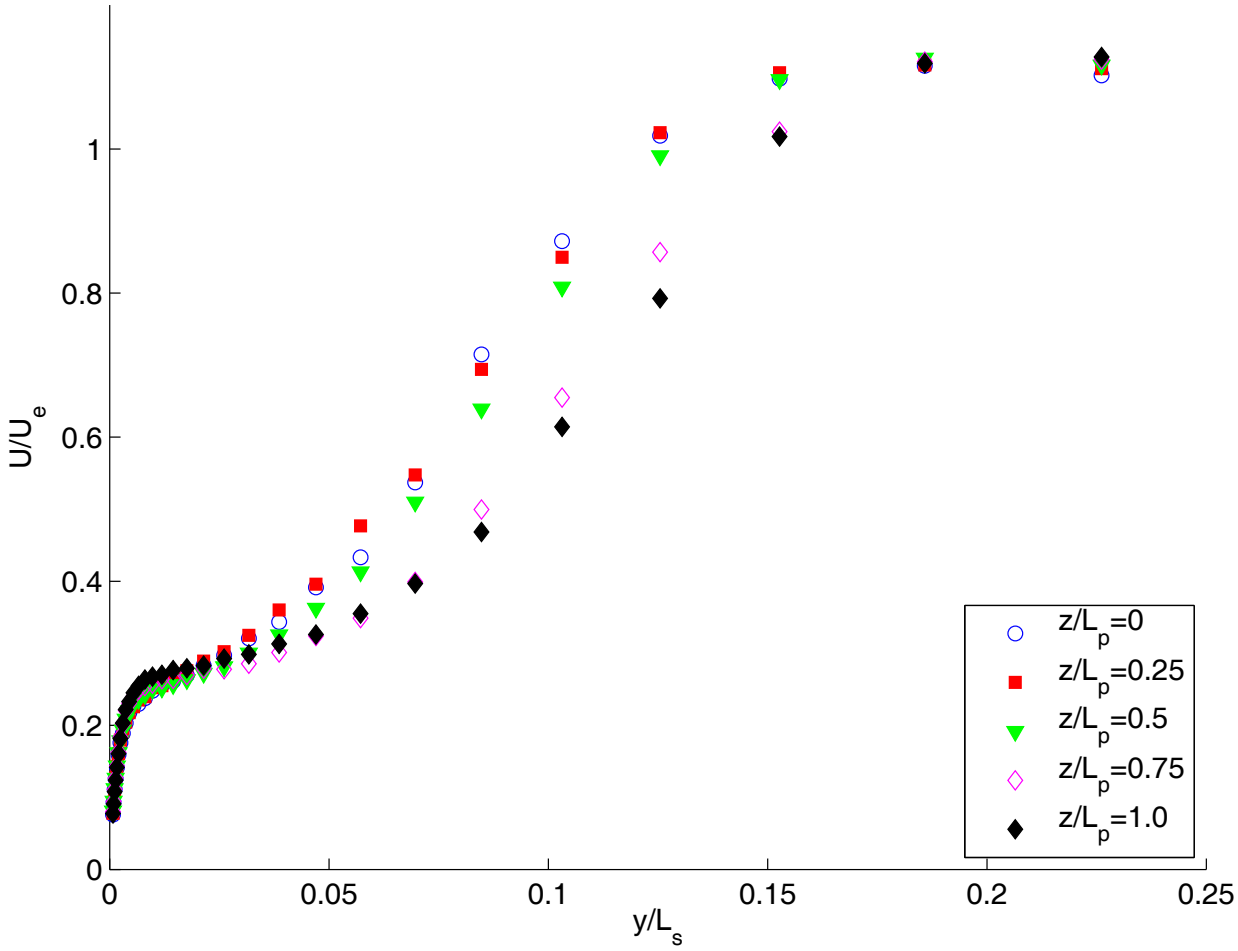
U/U_e
y/L_s
0
0.2
0.4
0.6
0.8
1
0
0.05
0.1
0.15
0.2
0.25
z/L_p=0
z/L_p=0.25
z/L_p=0.5
z/L_p=0.75
z/L_p=1.0

a)

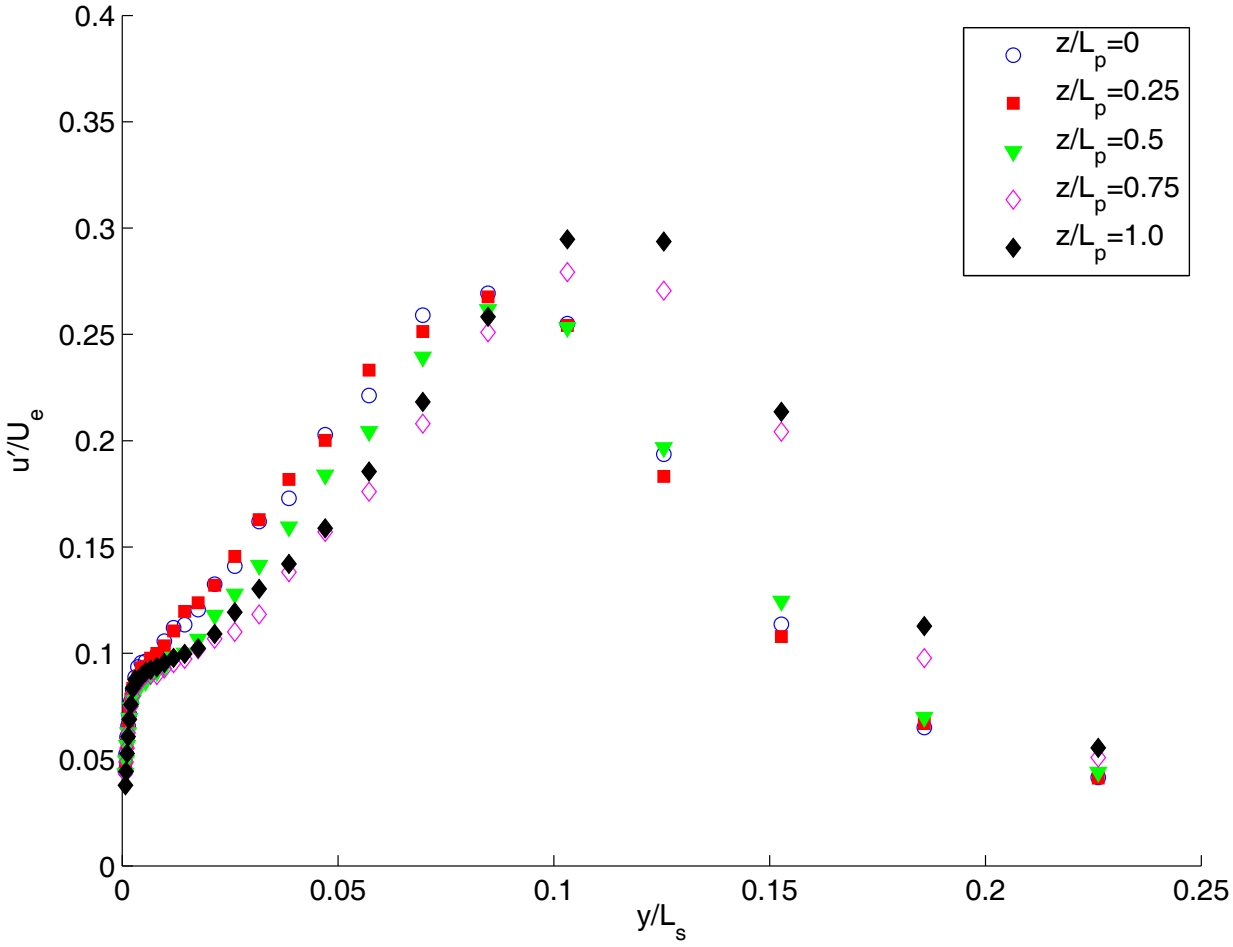

b)

Fig. 51 Time averaged velocity profiles, low TI, Re=50,000, pulsed VGJs, F=0.56, D=10%, B=2.3, L_p/d=85.3: a) mean, b) rms.

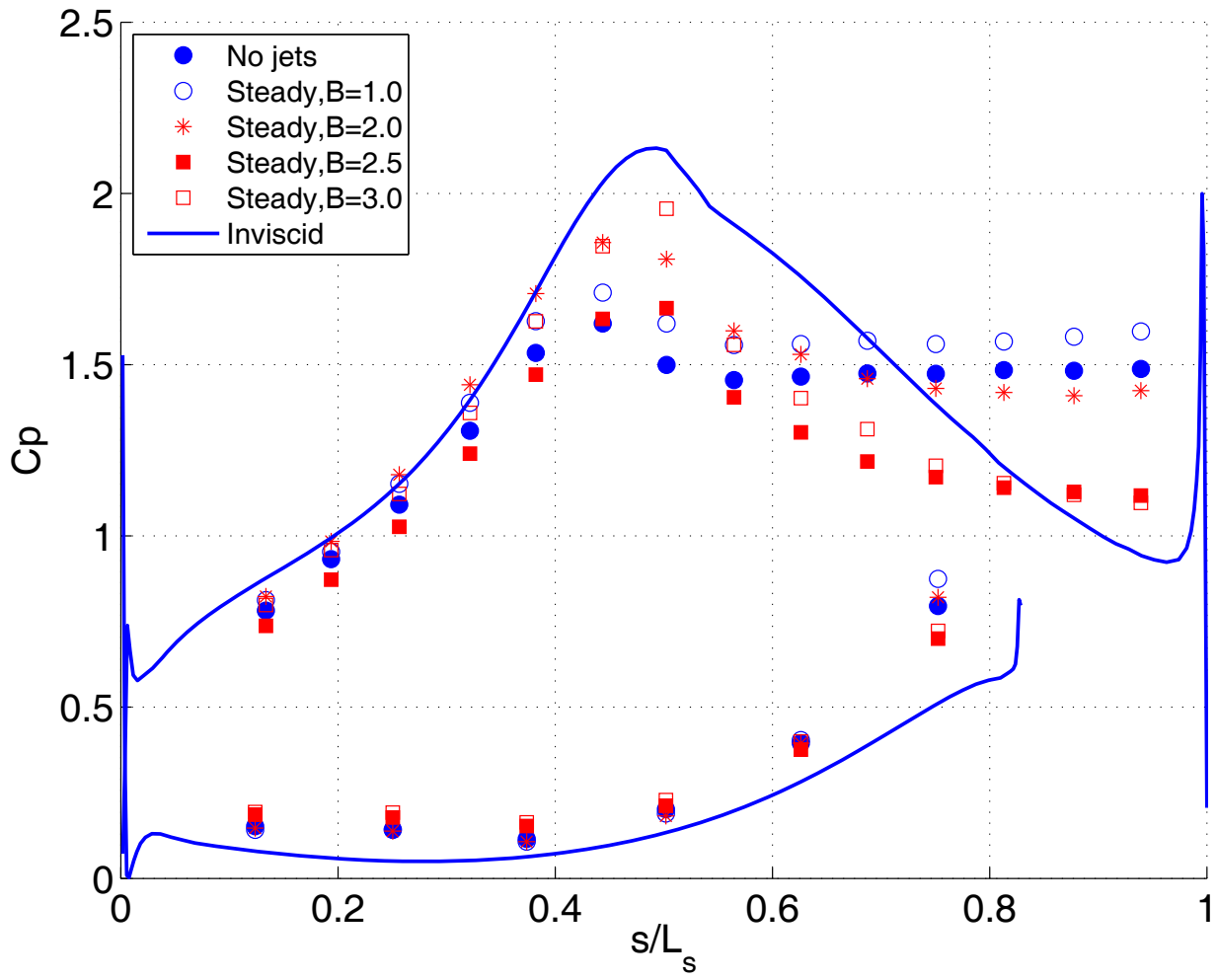
No jets
Steady,B=1.0
Steady,B=2.0
Steady,B=2.5
Steady,B=3.0
Inviscid
Cp
s/L_s
2.5
2
1.5
1
0.5
0
0
0.2
0.4
0.6
0.8
1

a)

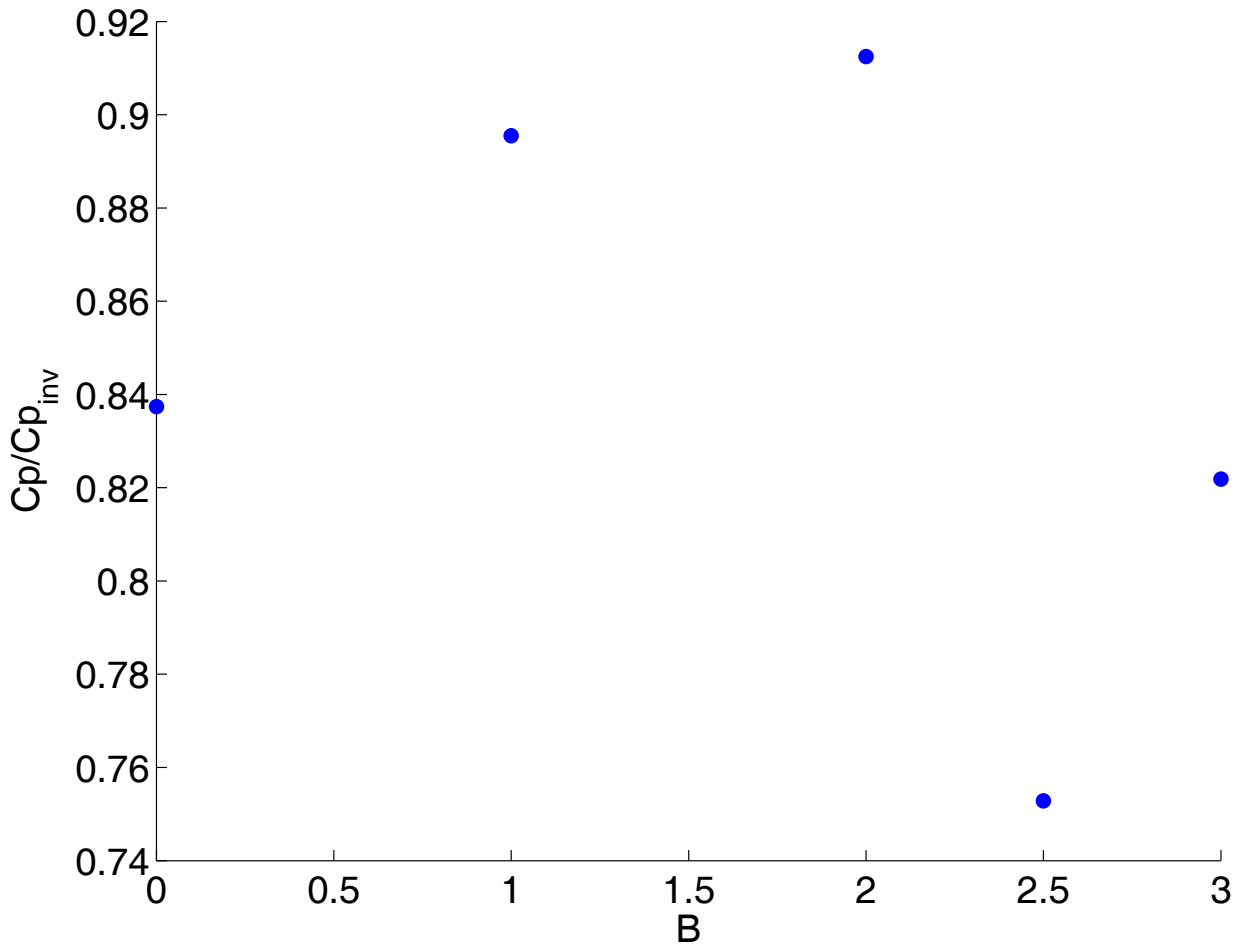

b)

Fig. 52 Cp results, high TI, Re=25,000, steady VGJs: a) Cp profile, b) Integrated Cp.

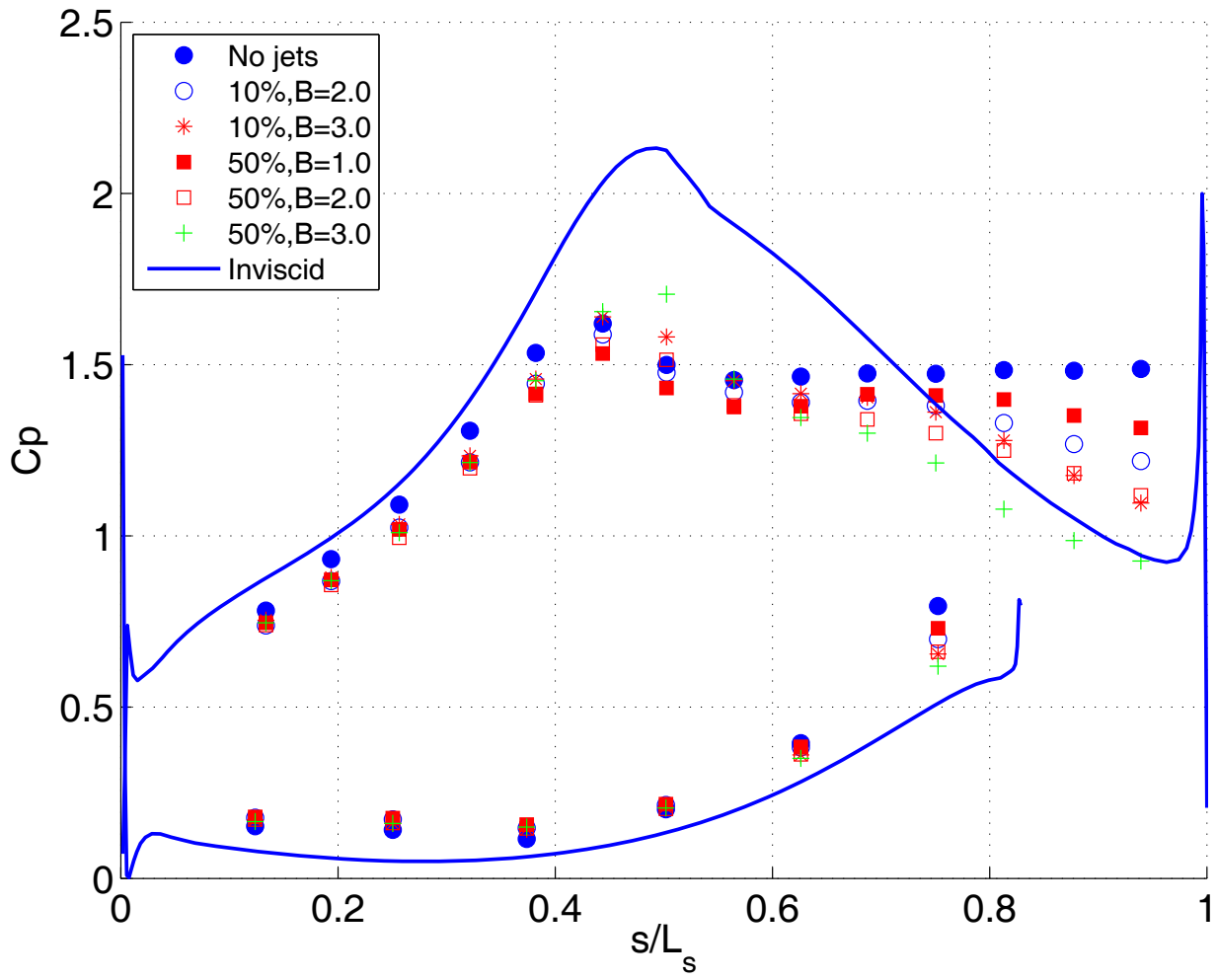
No jets
10%,B=2.0
10%,B=3.0
50%,B=1.0
50%,B=2.0
50%,B=3.0
Inviscid
Cp
s/L_s
2.5
2
1.5
1
0.5
0
0
0.2
0.4
0.6
0.8
1

a)

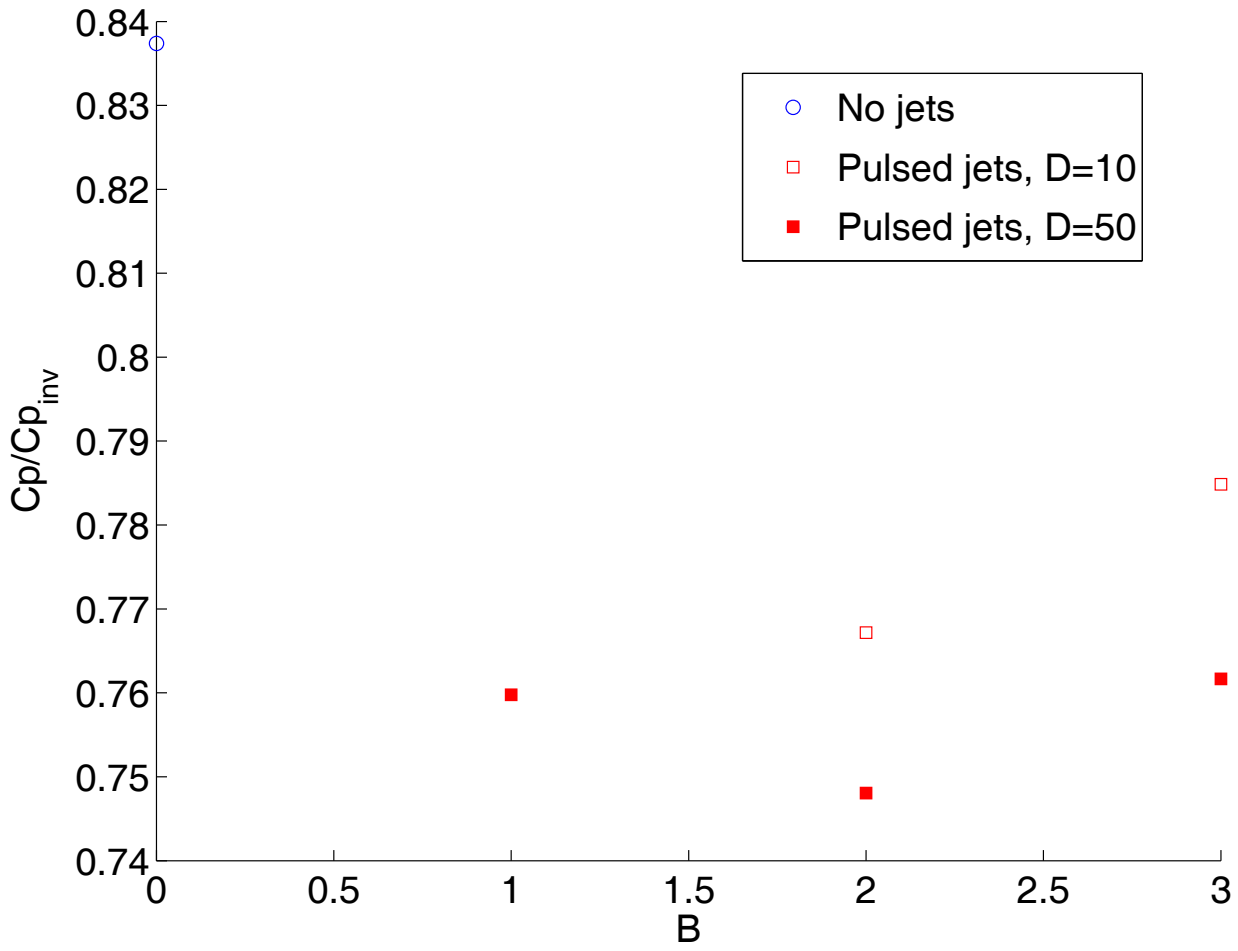

b)

Fig. 53 Cp results, high TI, Re=25,000, pulsed VGJs, F=0.14: a) Cp profile, b) Integrated Cp.

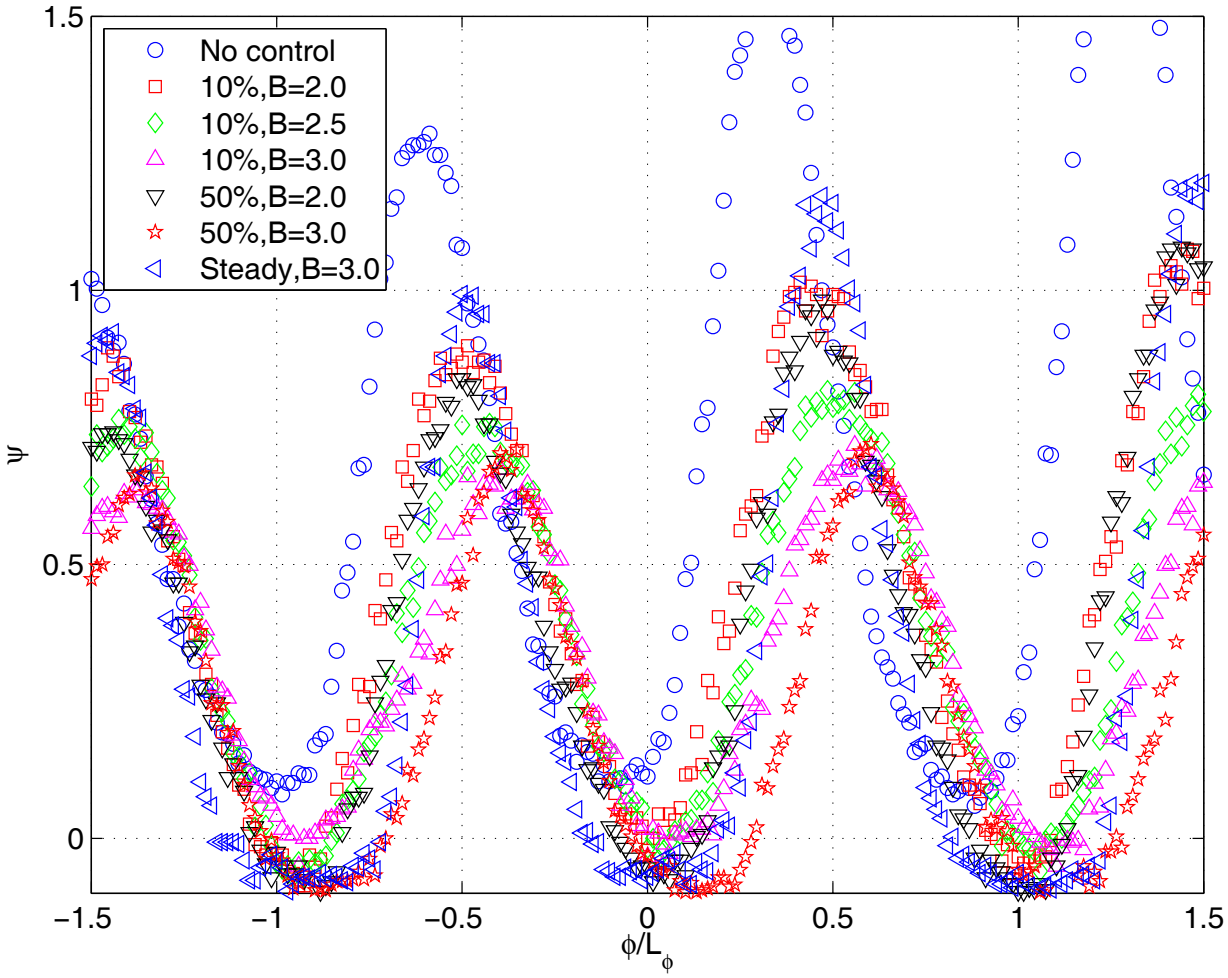
No control
10%,B=2.0
10%,B=2.5
10%,B=3.0
50%,B=2.0
50%,B=3.0
Steady,B=3.0
ψ
ϕ/L_ϕ
1.5
1
0.5
0
−1.5
−1
−0.5
0
0.5
1
1.5

a)

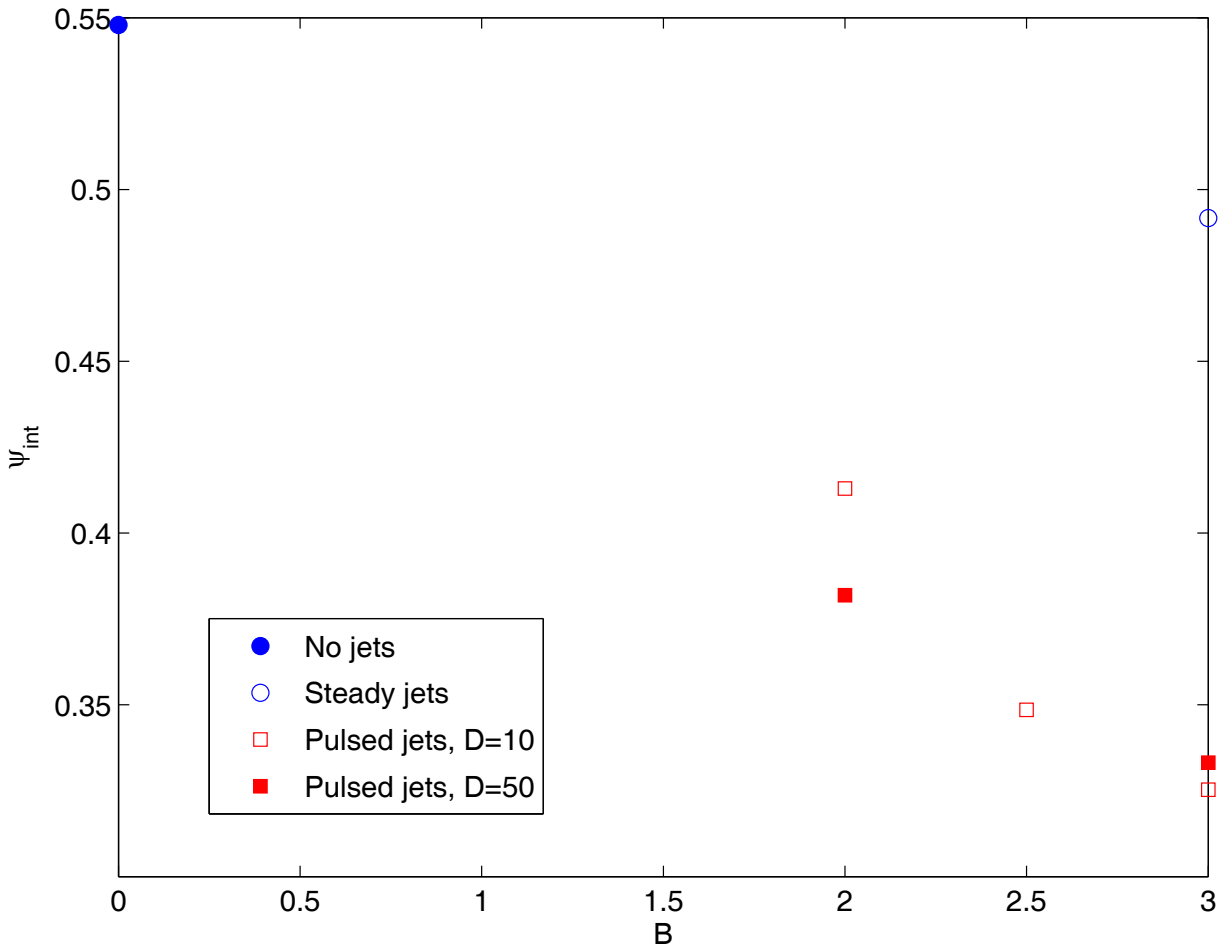

b)

Fig. 54 Ψ results, high TI, Re=25,000, pulsed VGJs, F=0.14: a) Ψ profile, b) Integrated Ψ.

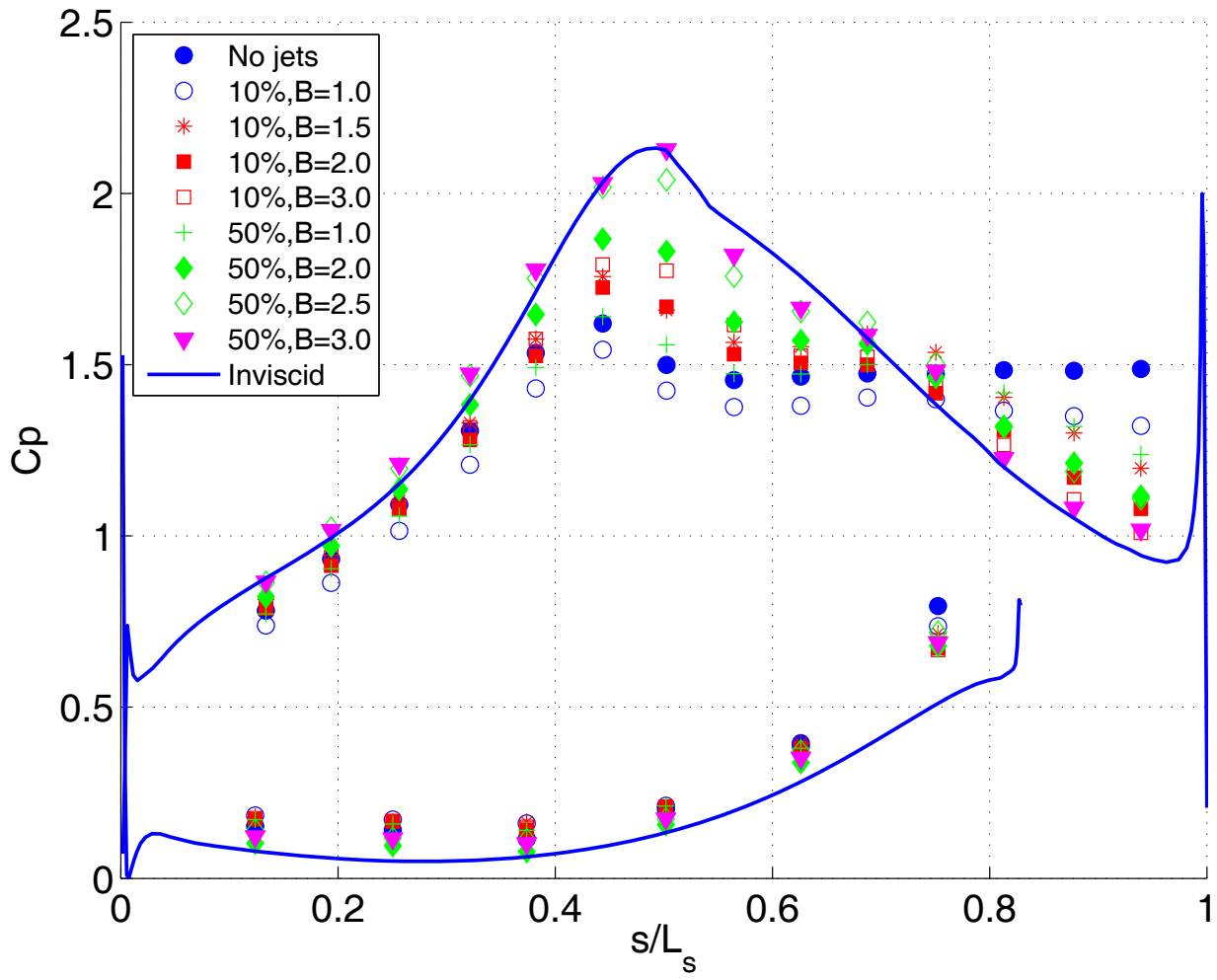
No jets
10%,B=1.0
10%,B=1.5
10%,B=2.0
10%,B=3.0
50%,B=1.0
50%,B=2.0
50%,B=2.5
50%,B=3.0
Inviscid
Cp
s/L_s
0
0.5
1
1.5
2
2.5
0.2
0.4
0.6
0.8

a)

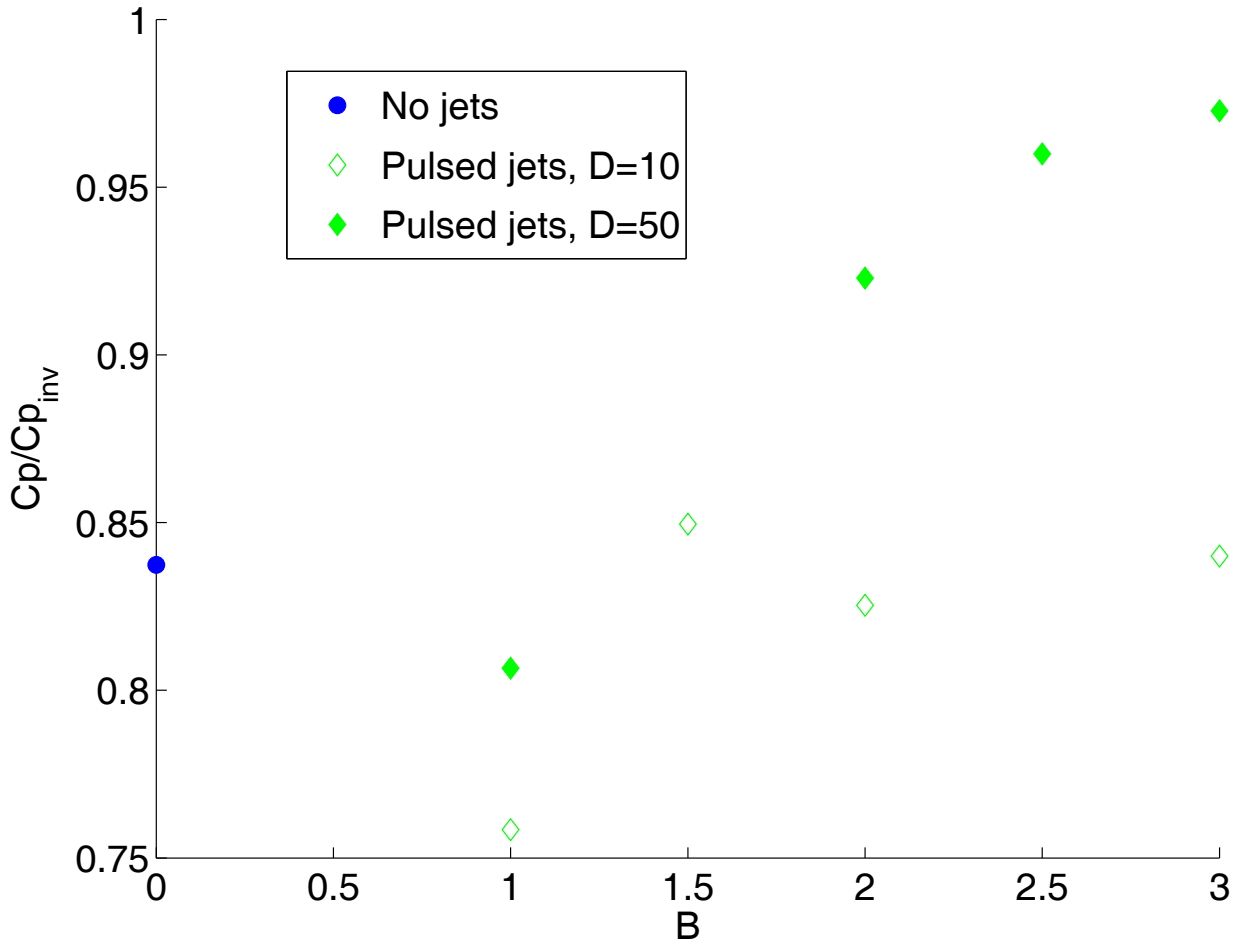

b)

Fig. 55 Cp results, high TI, Re=25,000, pulsed VGJs, F=0.28: a) Cp profile, b) Integrated Cp.

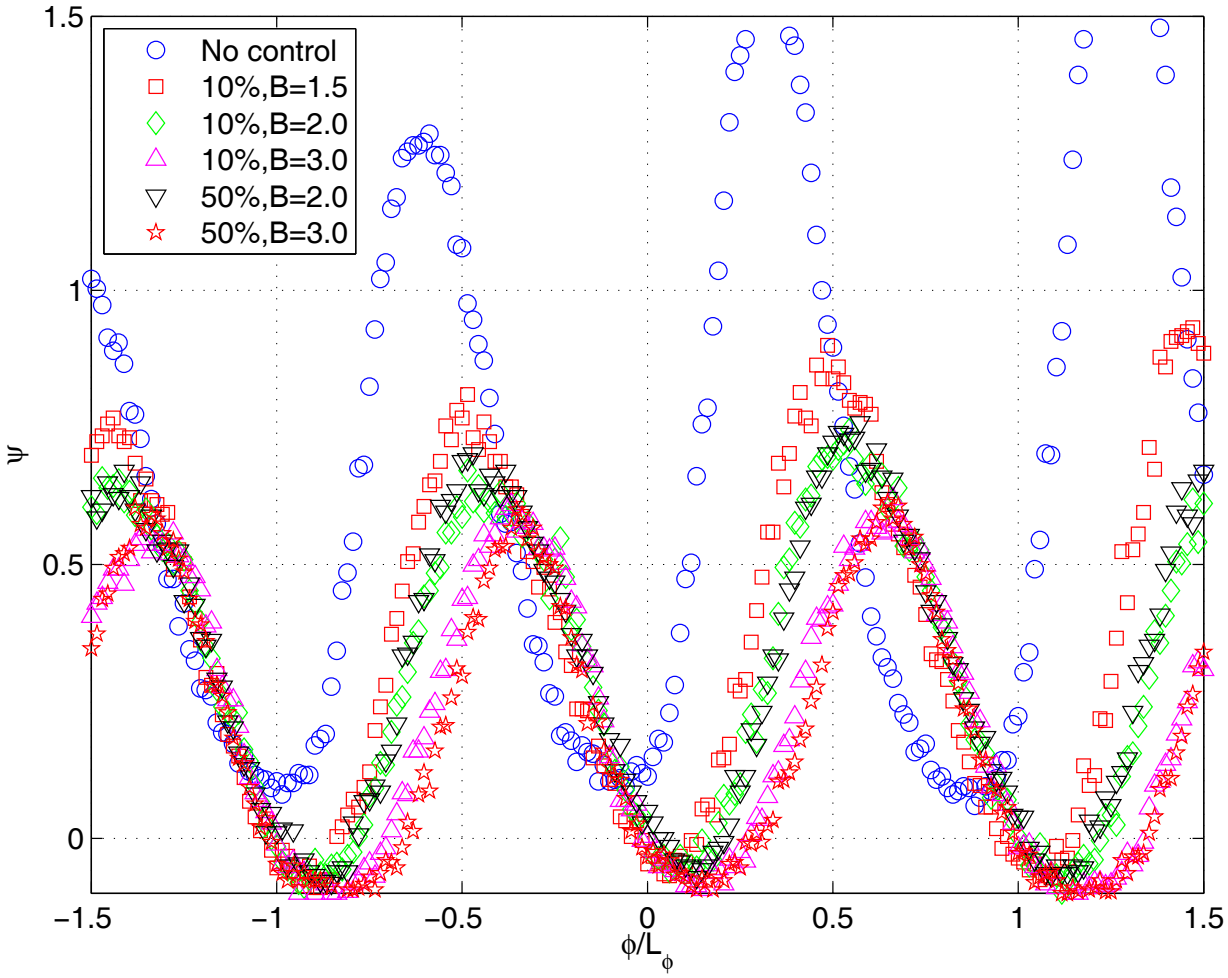
No control
10%,B=1.5
10%,B=2.0
10%,B=3.0
50%,B=2.0
50%,B=3.0
ψ
ϕ/L_ϕ
1.5
1
0.5
0
−1.5
−1
−0.5
0
0.5
1
1.5

a)

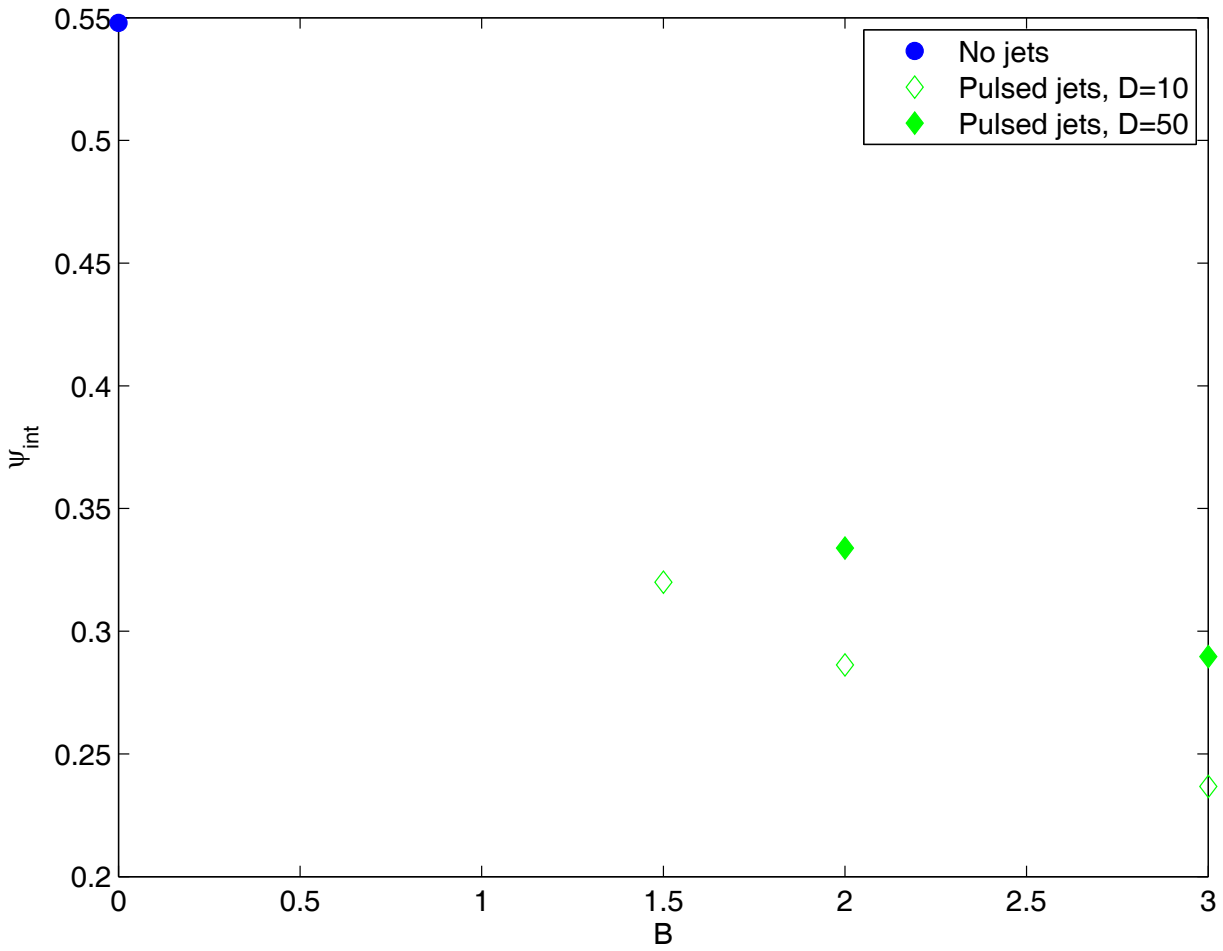

b)

Fig. 56 Ψ results, high TI, Re=25,000, pulsed VGJs, F=0.28: a) Ψ profile, b) Integrated Ψ.

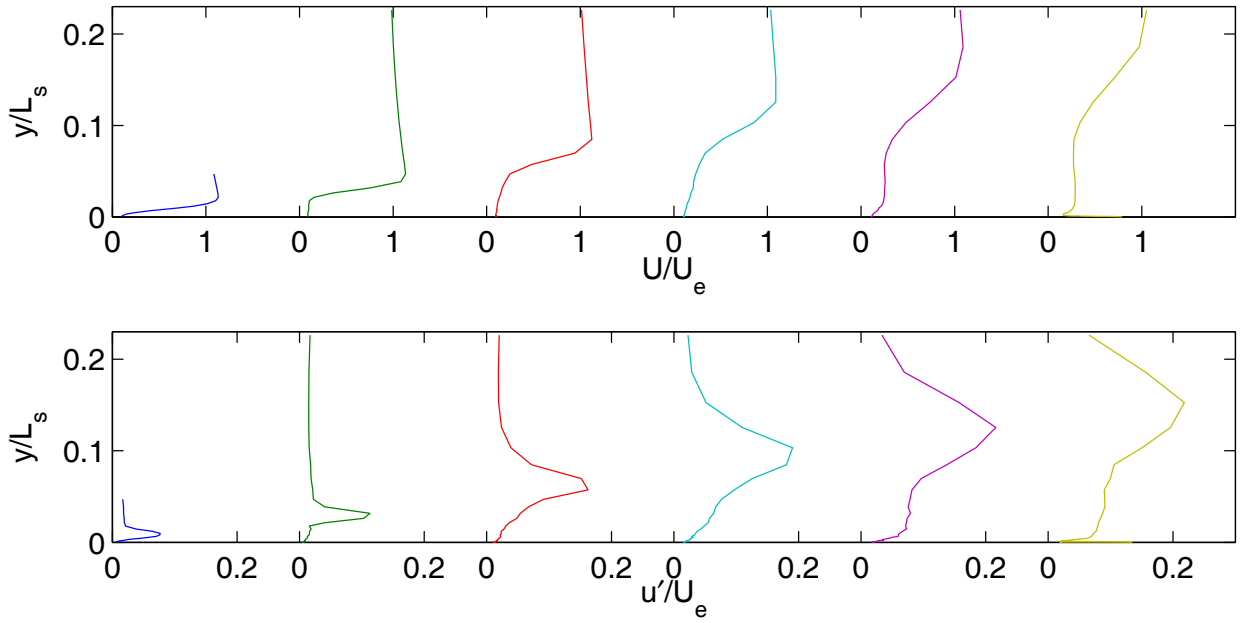

Fig. 57 Time averaged velocity profiles, high TI, Re=25,000, no VGJs: a) mean, b) rms.

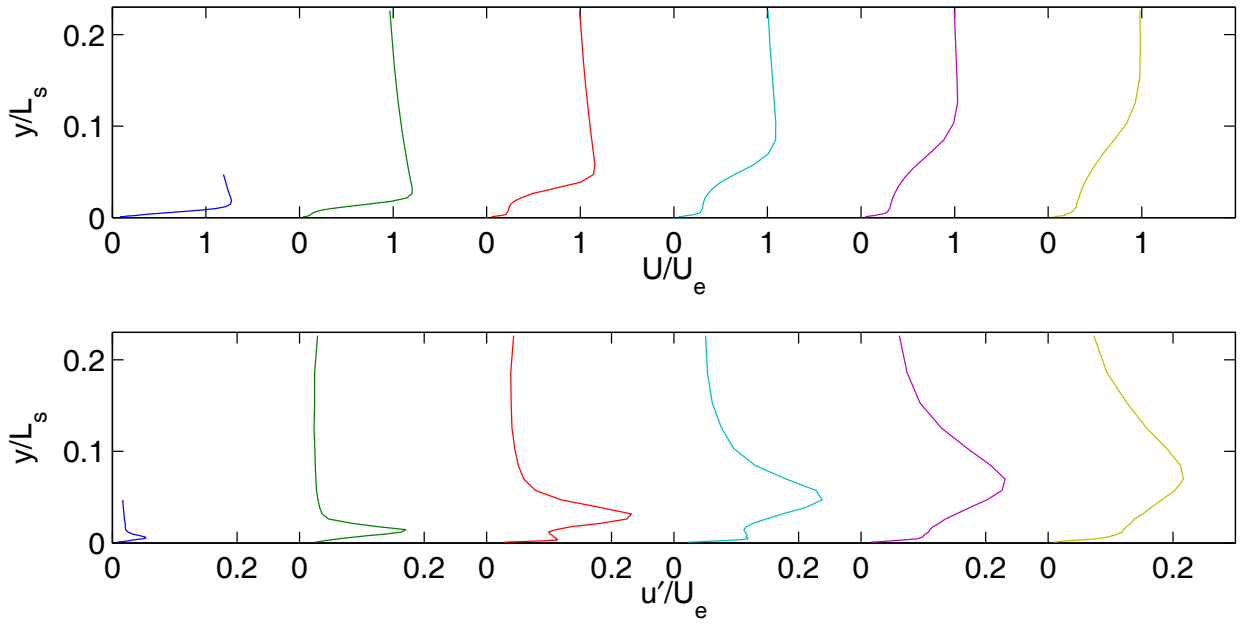

Fig. 58 Time averaged velocity profiles, high TI, Re=25,000, pulsed VGJs, F=0.28, D=10%, B=2.0: a) mean, b) rms.

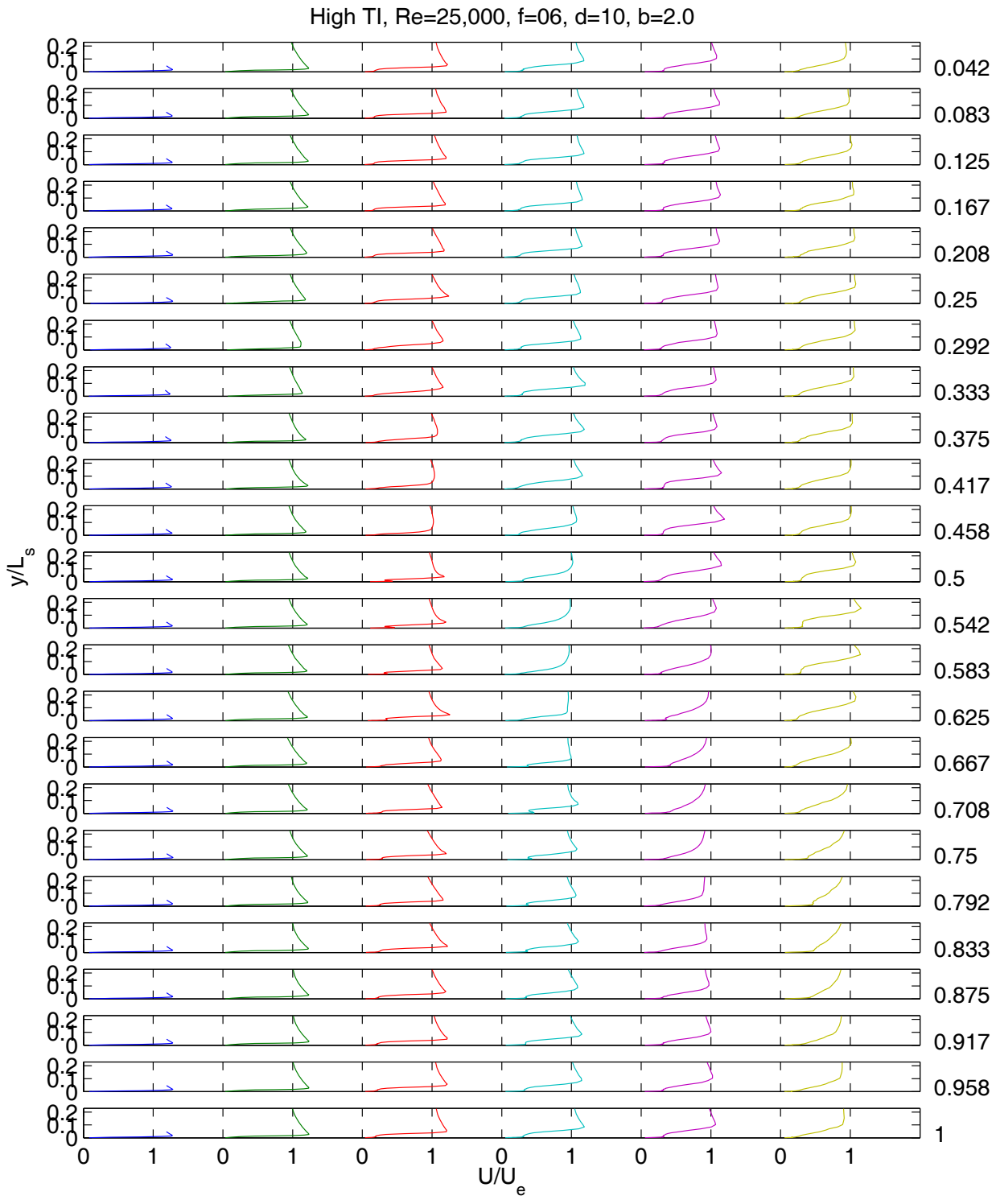
High TI, Re=25,000, f=06, d=10, b=2.0
y/L_s
U/U_e
0.042
0.083
0.125
0.167
0.208
0.25
0.292
0.333
0.375
0.417
0.458
0.5
0.542
0.583
0.625
0.667
0.708
0.75
0.792
0.833
0.875
0.917
0.958
1

a)

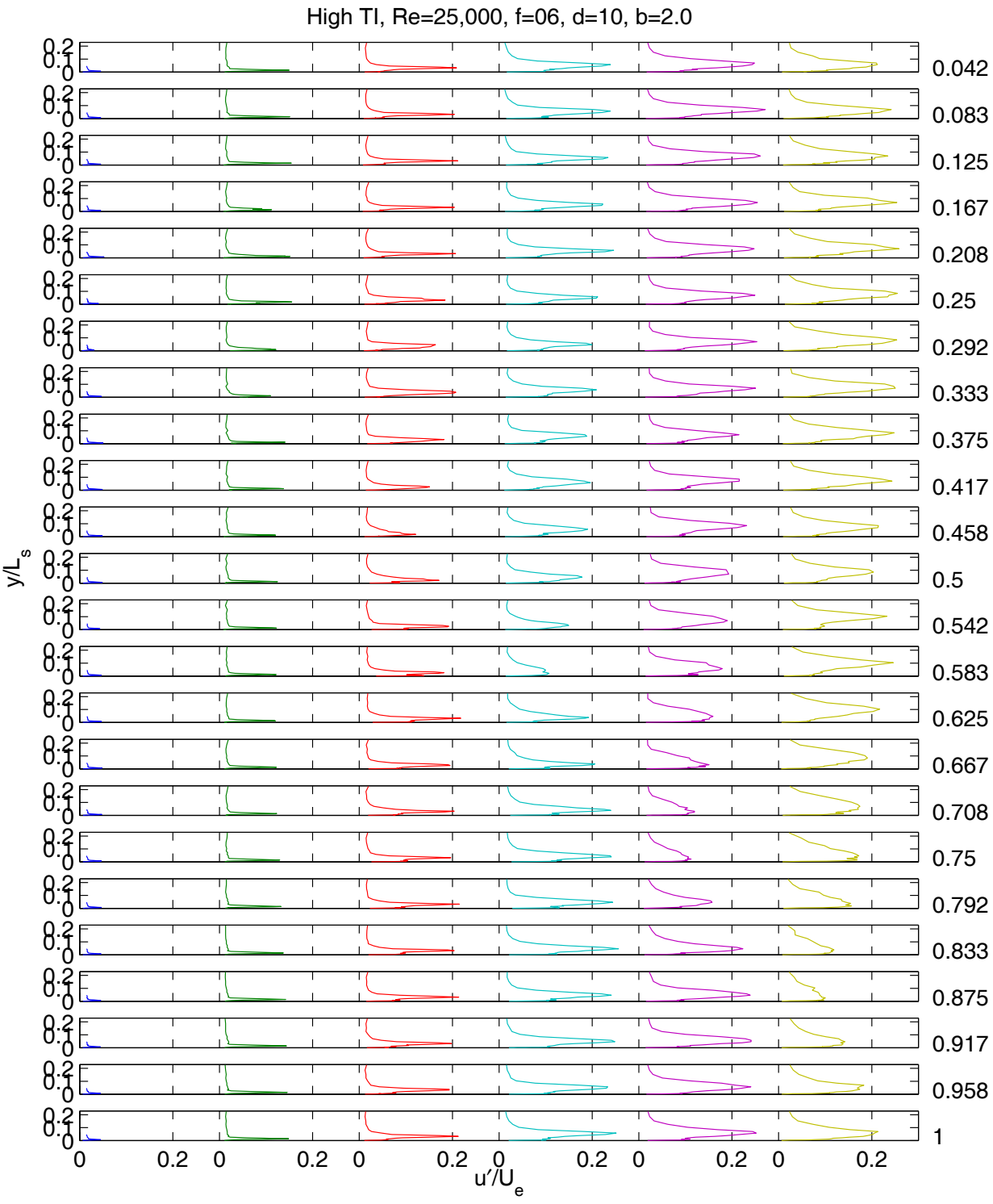

b)

Fig. 59 Phase averaged velocity profiles, high TI, Re=25,000, pulsed VGJs, F=0.28, D=10%, B=2.0: a) mean, b) rms.

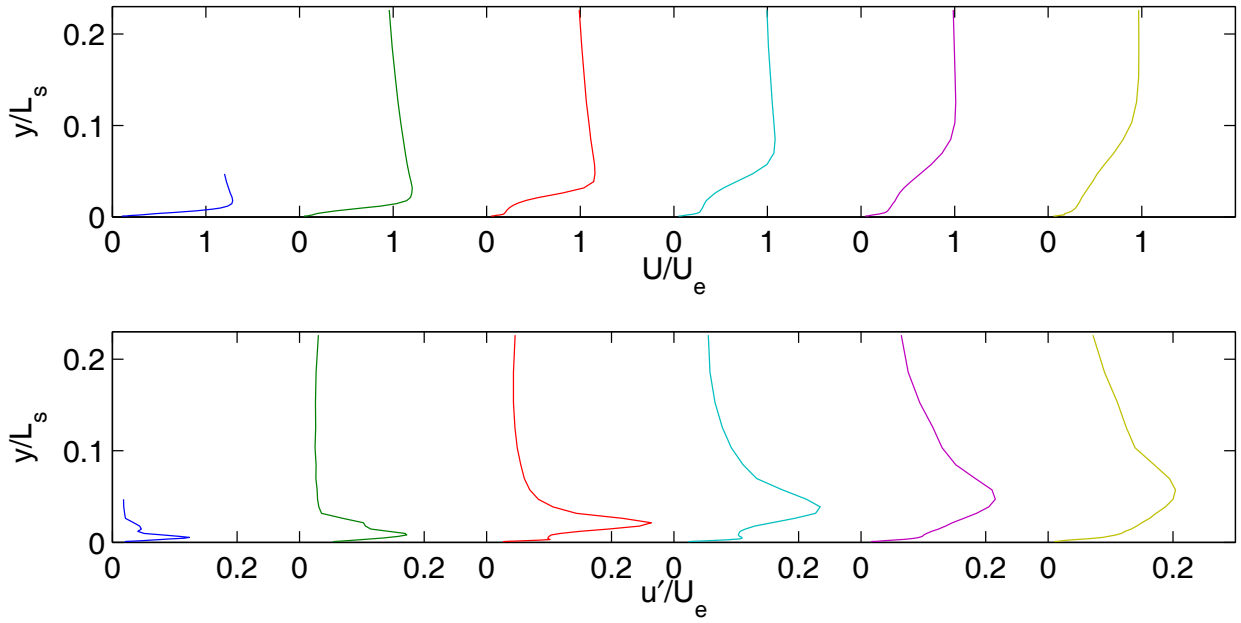

Fig. 60 Time averaged velocity profiles, high TI, Re=25,000, pulsed VGJs, F=0.28, D=10%, B=3.0: a) mean, b) rms.

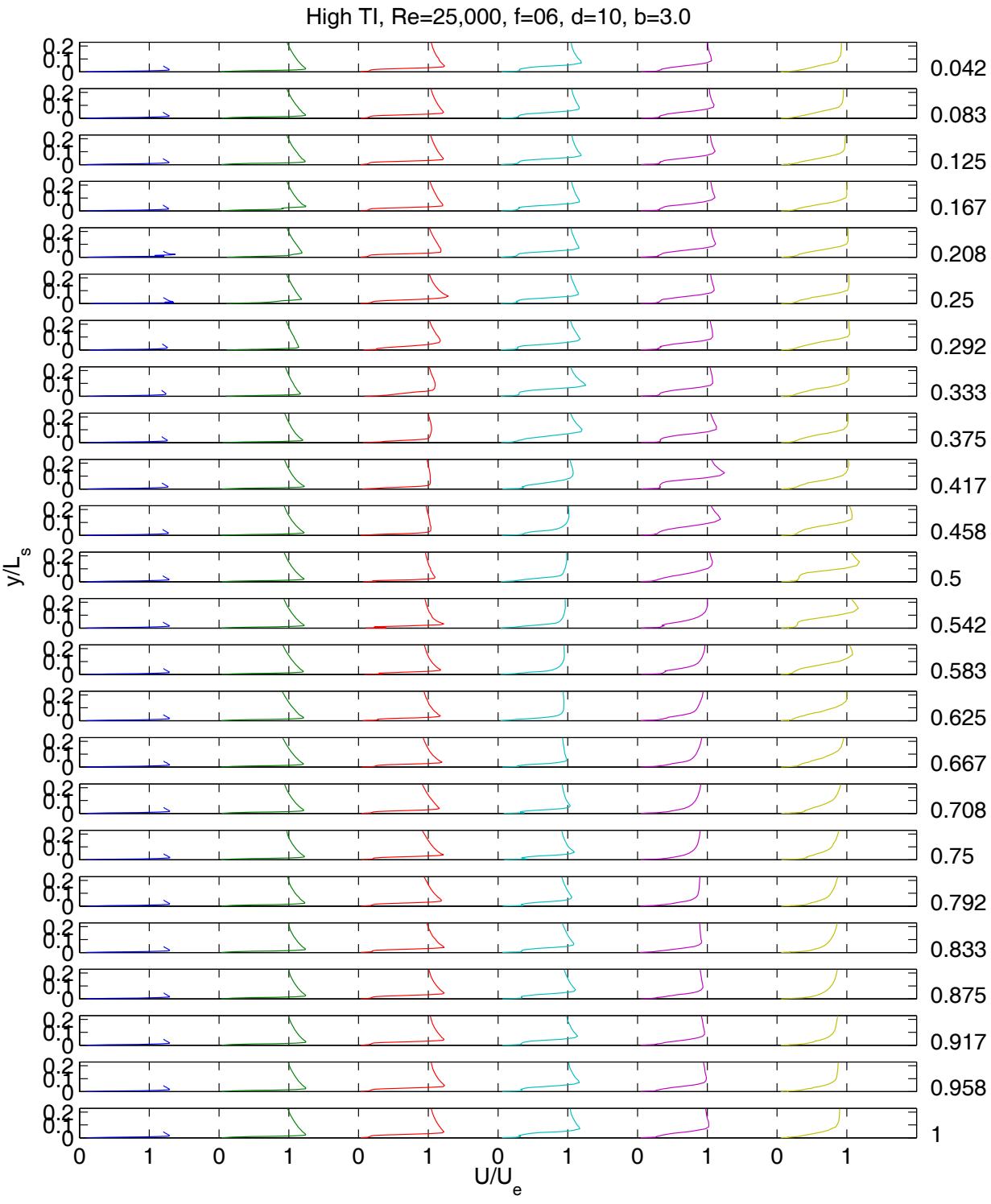
High TI, Re=25,000, f=06, d=10, b=3.0
y/L_s
U/U_e
0.042
0.083
0.125
0.167
0.208
0.25
0.292
0.333
0.375
0.417
0.458
0.5
0.542
0.583
0.625
0.667
0.708
0.75
0.792
0.833
0.875
0.917
0.958
1

a)

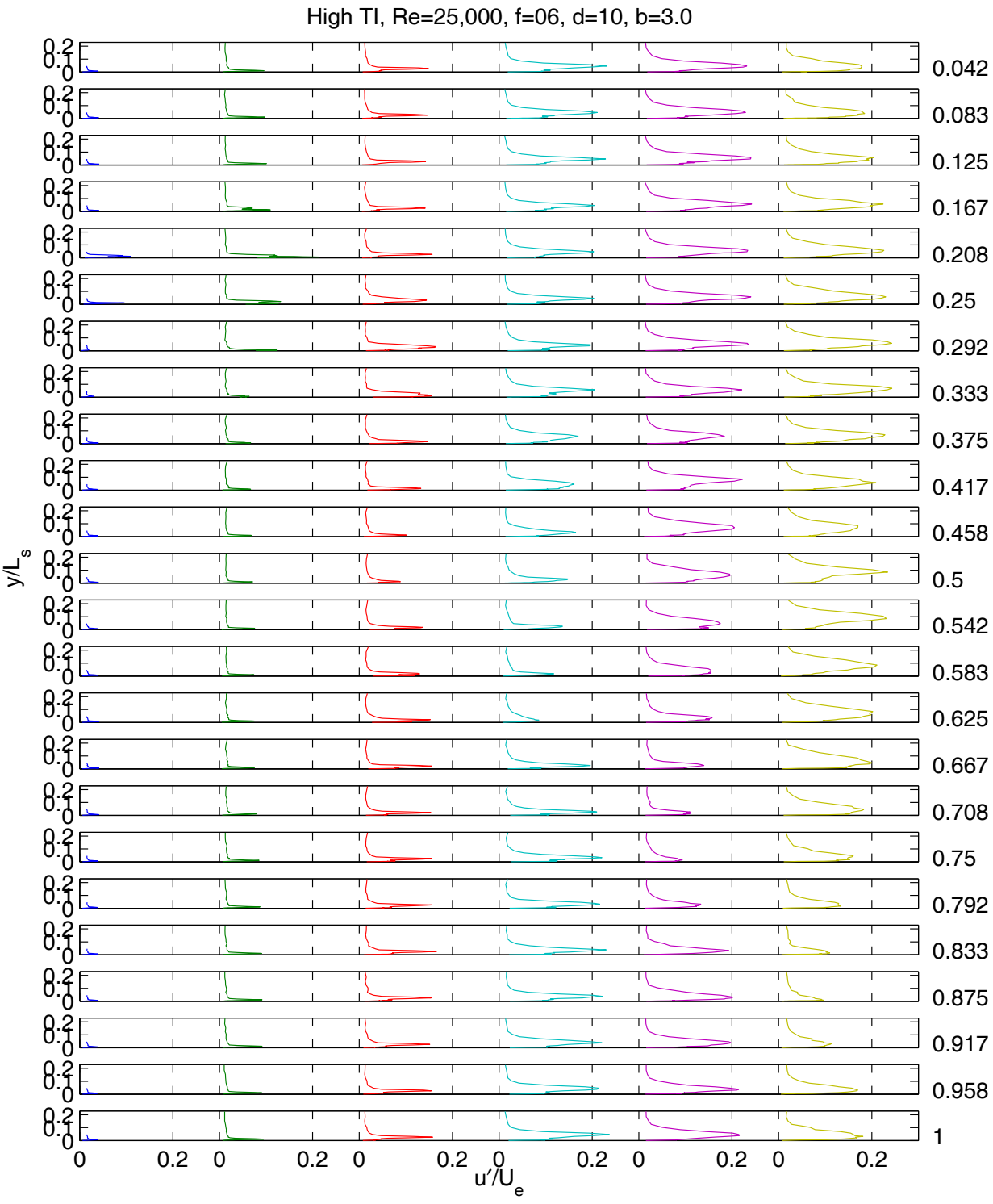

b)

Fig. 61 Phase averaged velocity profiles, high TI, Re=25,000, pulsed VGJs, F=0.28, D=10%, B=3.0: a) mean, b) rms.

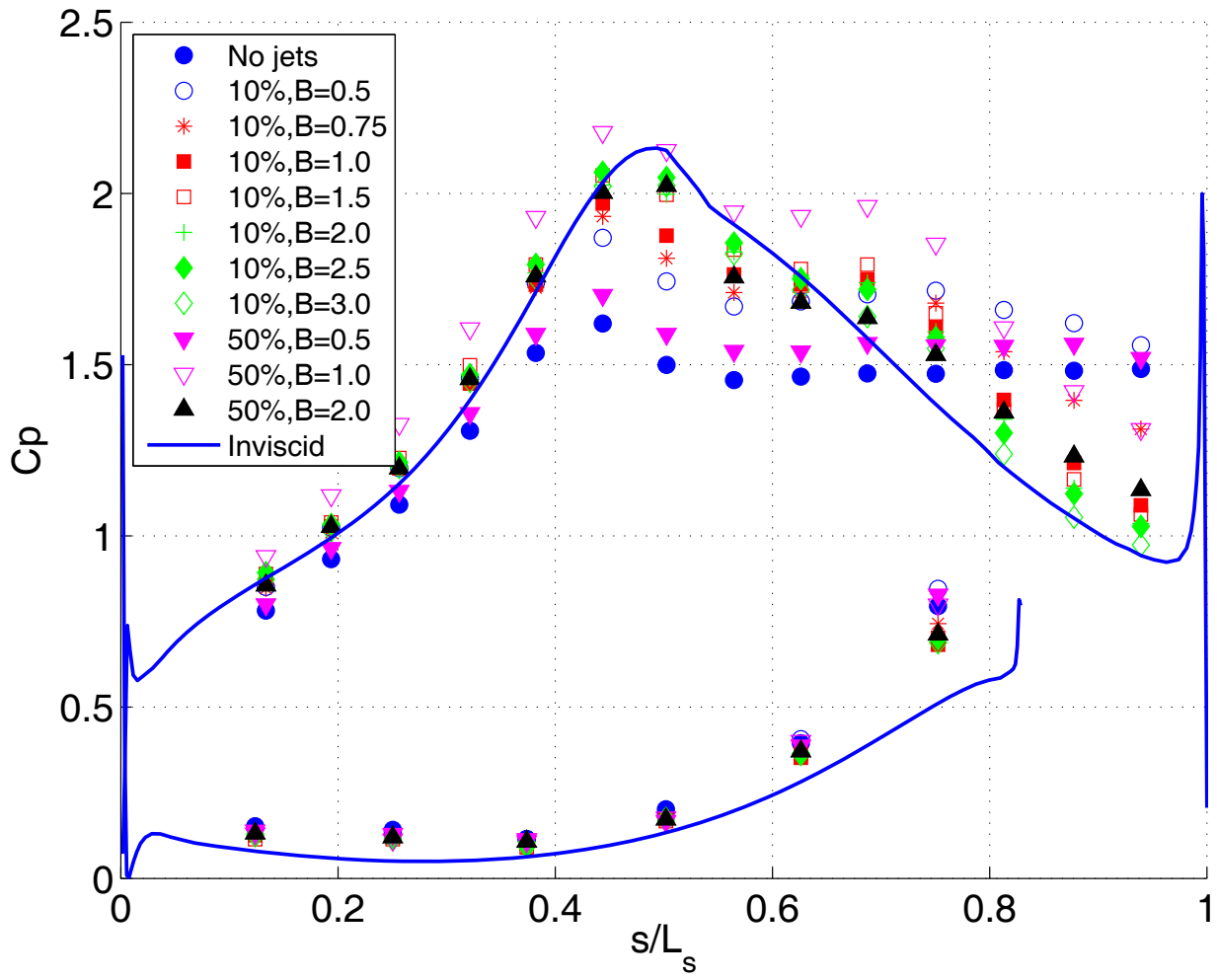
No jets
10%,B=0.5
10%,B=0.75
10%,B=1.0
10%,B=1.5
10%,B=2.0
10%,B=2.5
10%,B=3.0
50%,B=0.5
50%,B=1.0
50%,B=2.0
Inviscid
Cp
s/L_s
0
0.5
1
1.5
2
2.5
0.2
0.4
0.6
0.8

a)

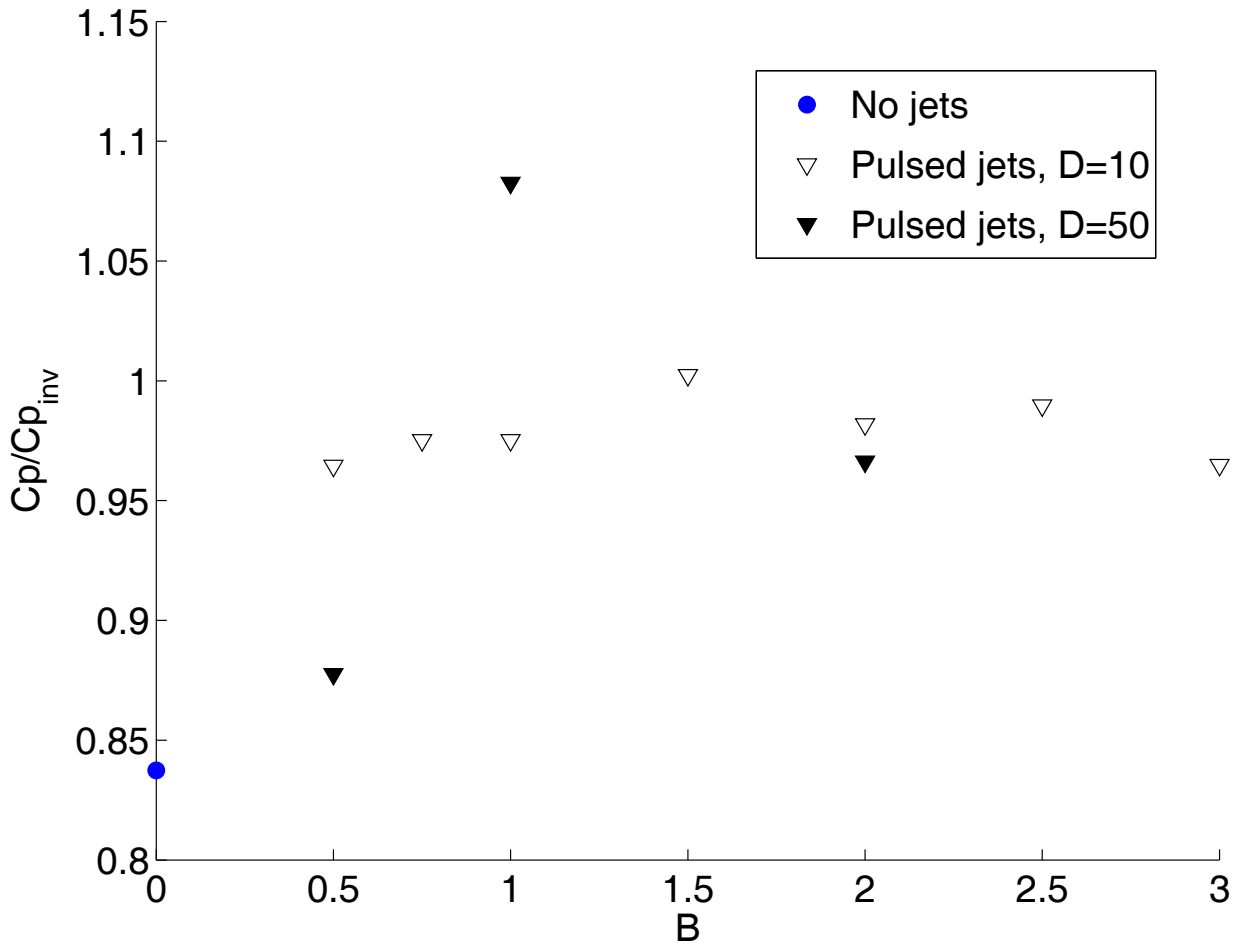

b)

Fig. 62 Cp results, high TI, Re=25,000, pulsed VGJs, F=0.56: a) Cp profile, b) Integrated Cp.

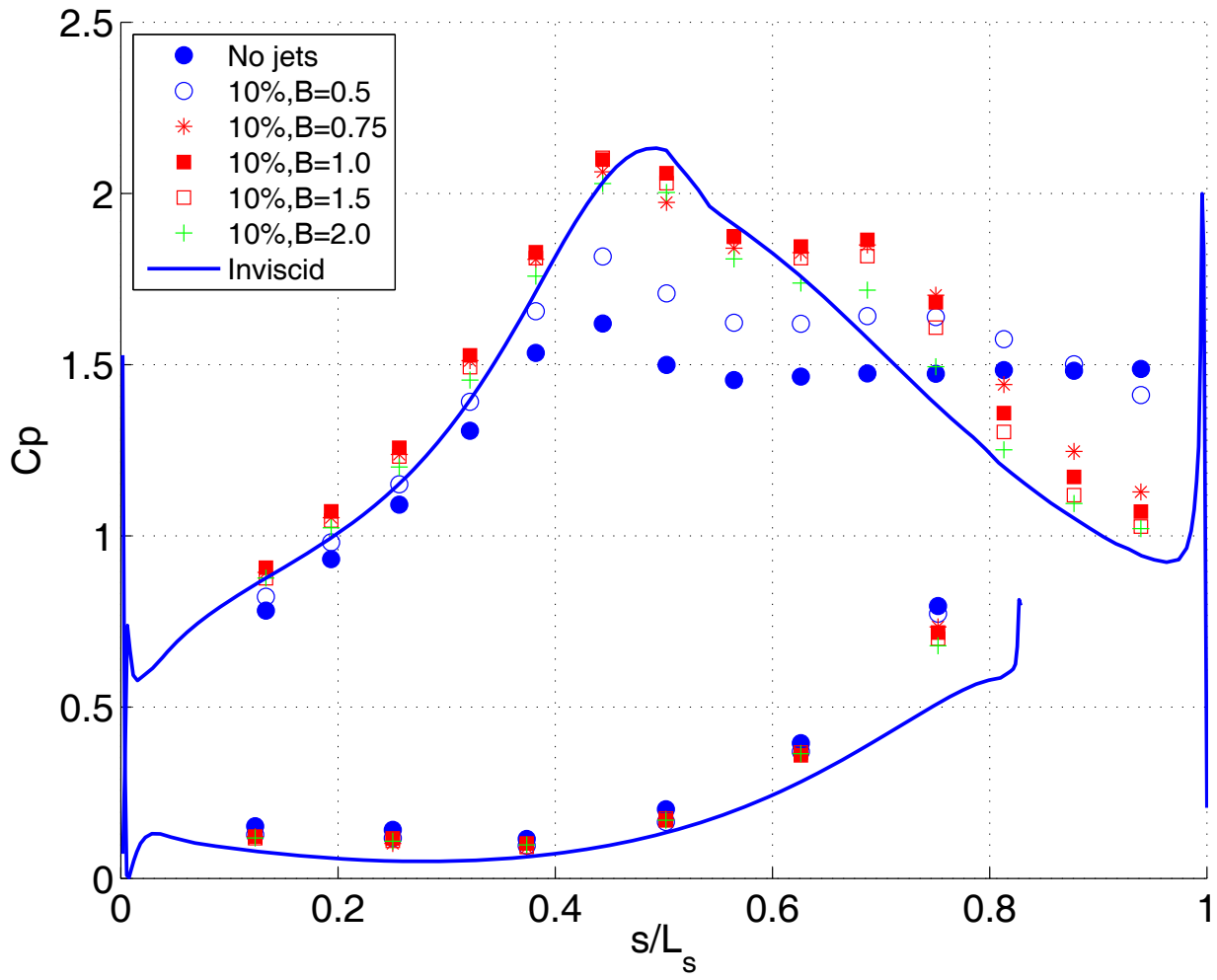
No jets
10%,B=0.5
10%,B=0.75
10%,B=1.0
10%,B=1.5
10%,B=2.0
Inviscid
Cp
s/L_s
0
0.5
1
1.5
2
2.5
0.2
0.4
0.6
0.8

a)

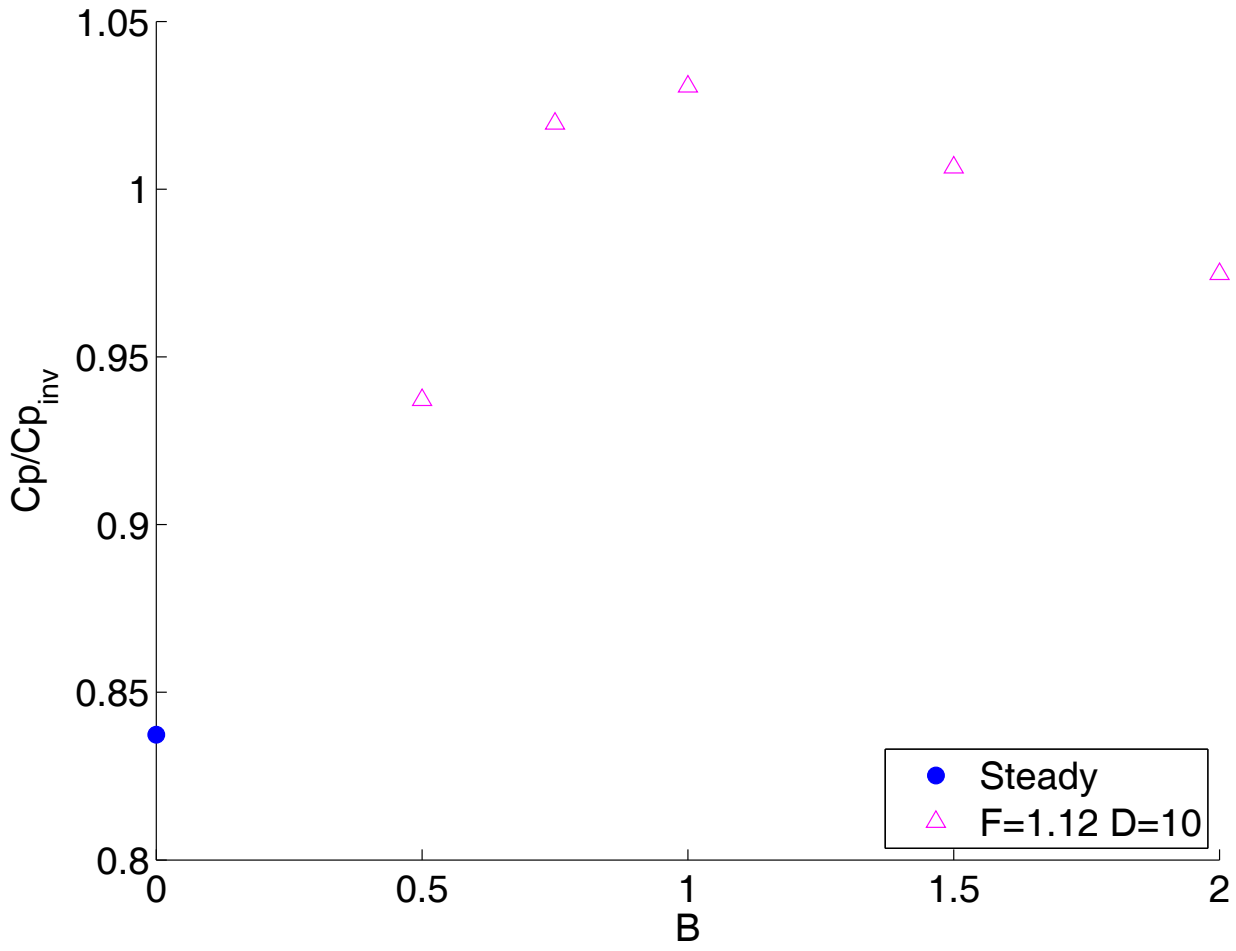

b)

Fig. 63 Cp results, high TI, Re=25,000, pulsed VGJs, F=1.12: a) Cp profile, b) Integrated Cp.

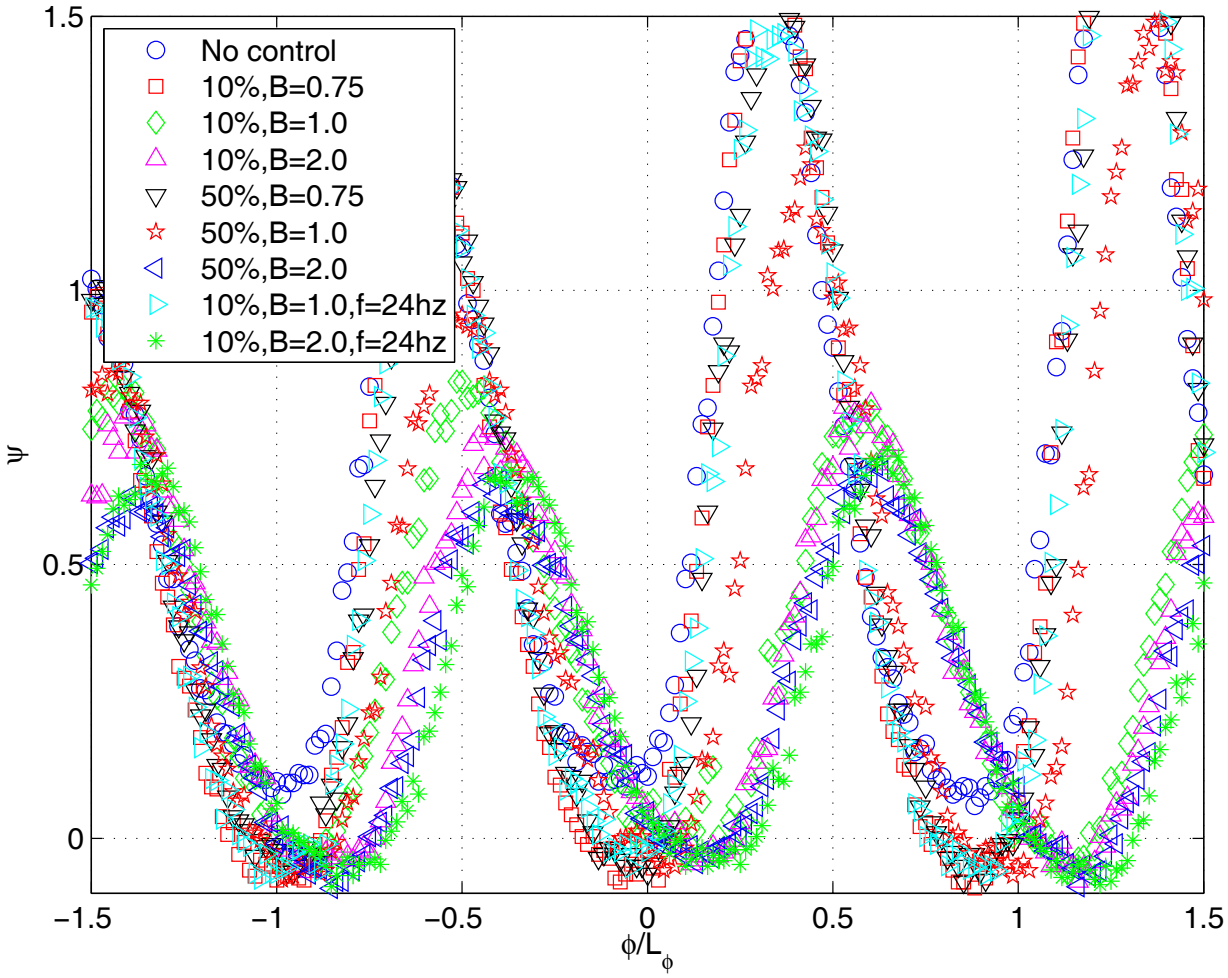
No control
10%,B=0.75
10%,B=1.0
10%,B=2.0
50%,B=0.75
50%,B=1.0
50%,B=2.0
10%,B=1.0,f=24hz
10%,B=2.0,f=24hz
ψ
ϕ/L_ϕ
1.5
1
0.5
0
−1.5
−1
−0.5
0
0.5
1
1.5

a)

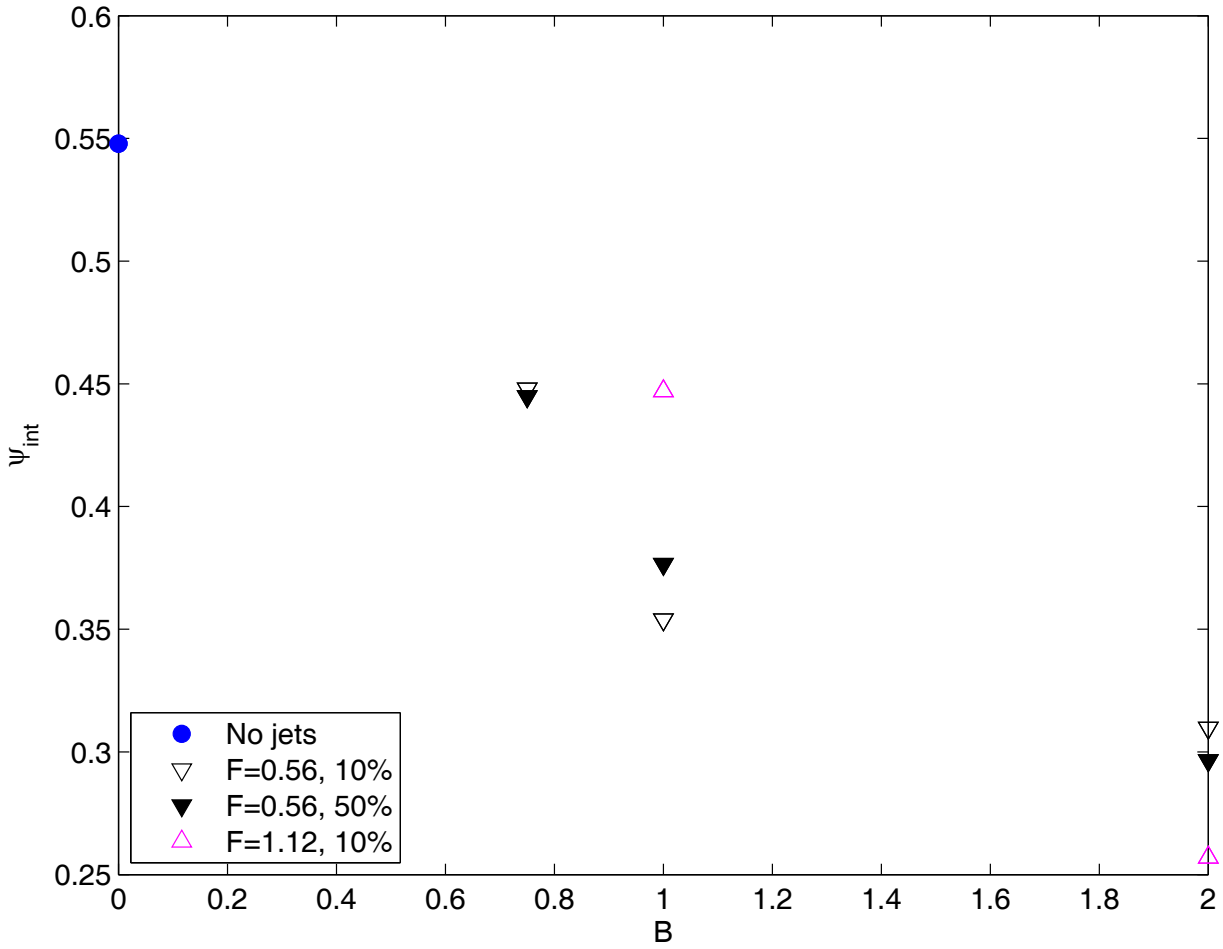

b)

Fig. 64 Ψ results, high TI, Re=25,000, pulsed VGJs, F=0.56 and 1.12: a) Ψ profile, b) Integrated Ψ.

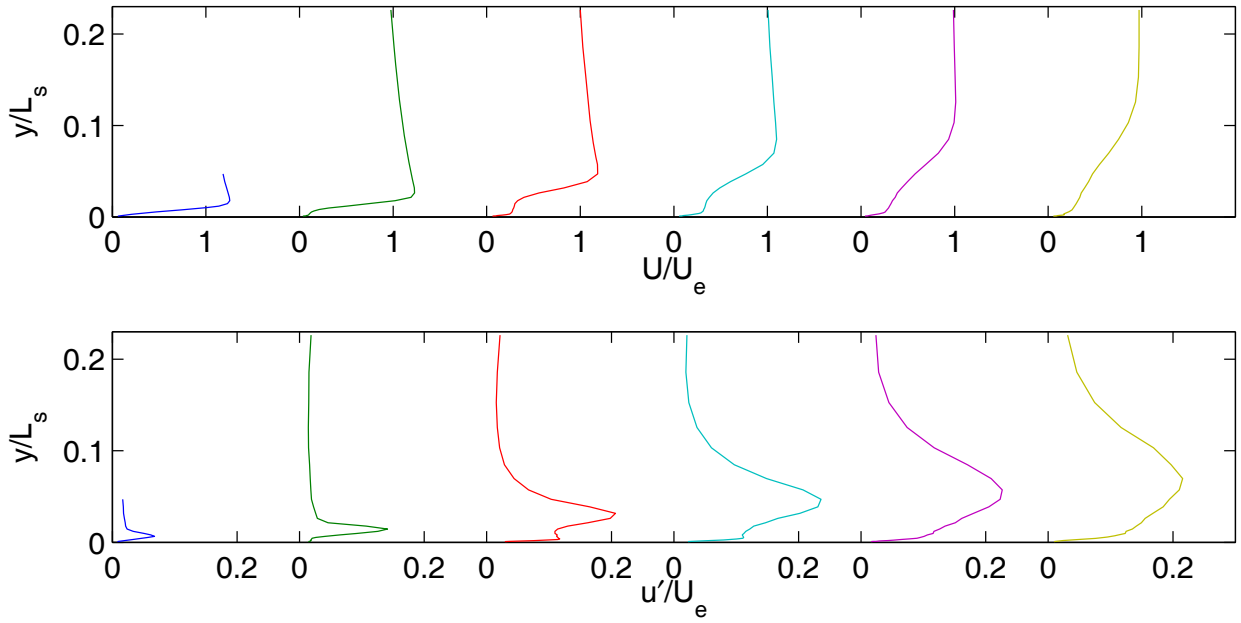

Fig. 65 Time averaged velocity profiles, high TI, Re=50,000, pulsed VGJs, F=0.56, D=10%, B=1.0: a) mean, b) rms.

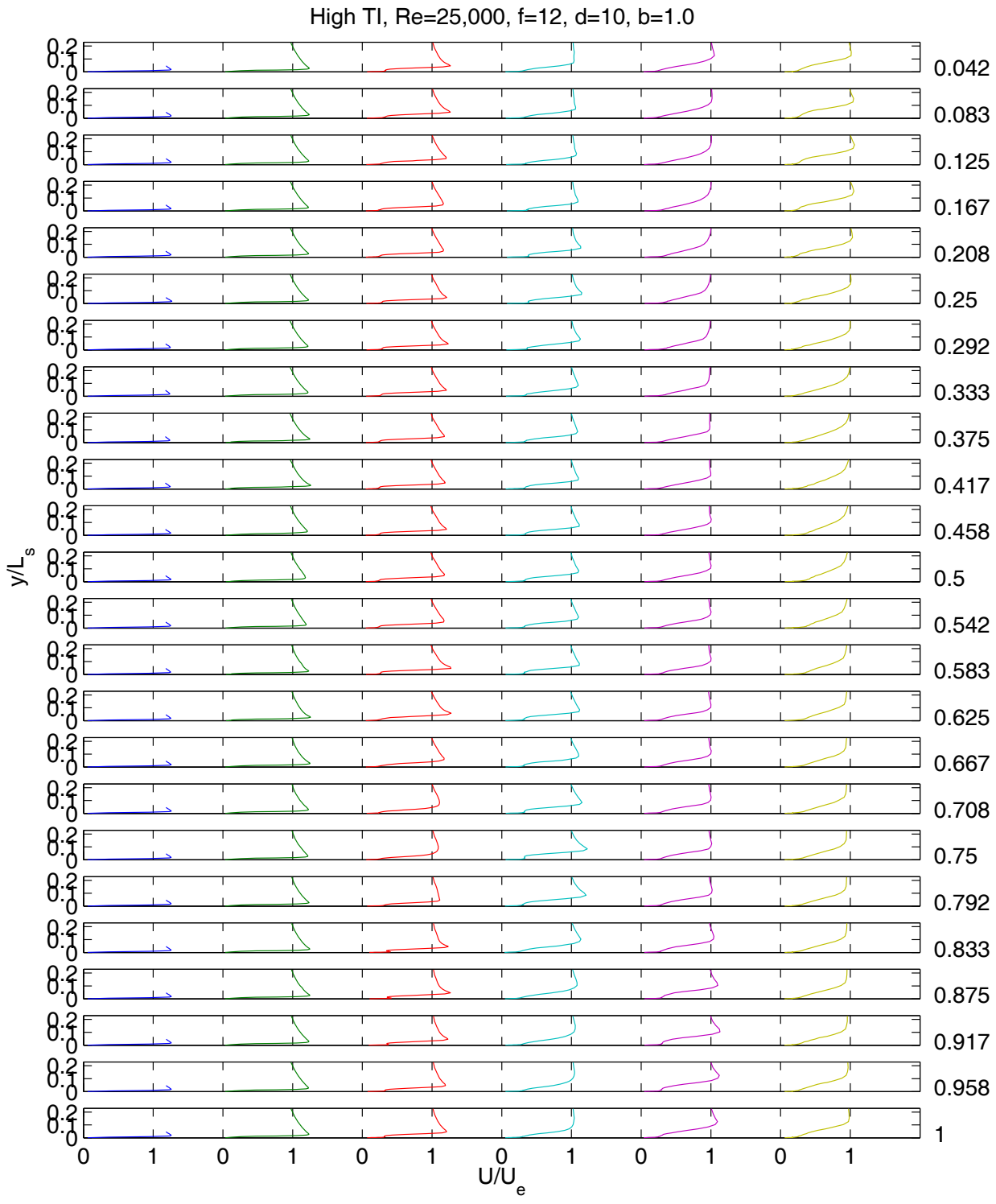
High TI, Re=25,000, f=12, d=10, b=1.0
y/L_s
U/U_e
0.042
0.083
0.125
0.167
0.208
0.25
0.292
0.333
0.375
0.417
0.458
0.5
0.542
0.583
0.625
0.667
0.708
0.75
0.792
0.833
0.875
0.917
0.958
1

a)

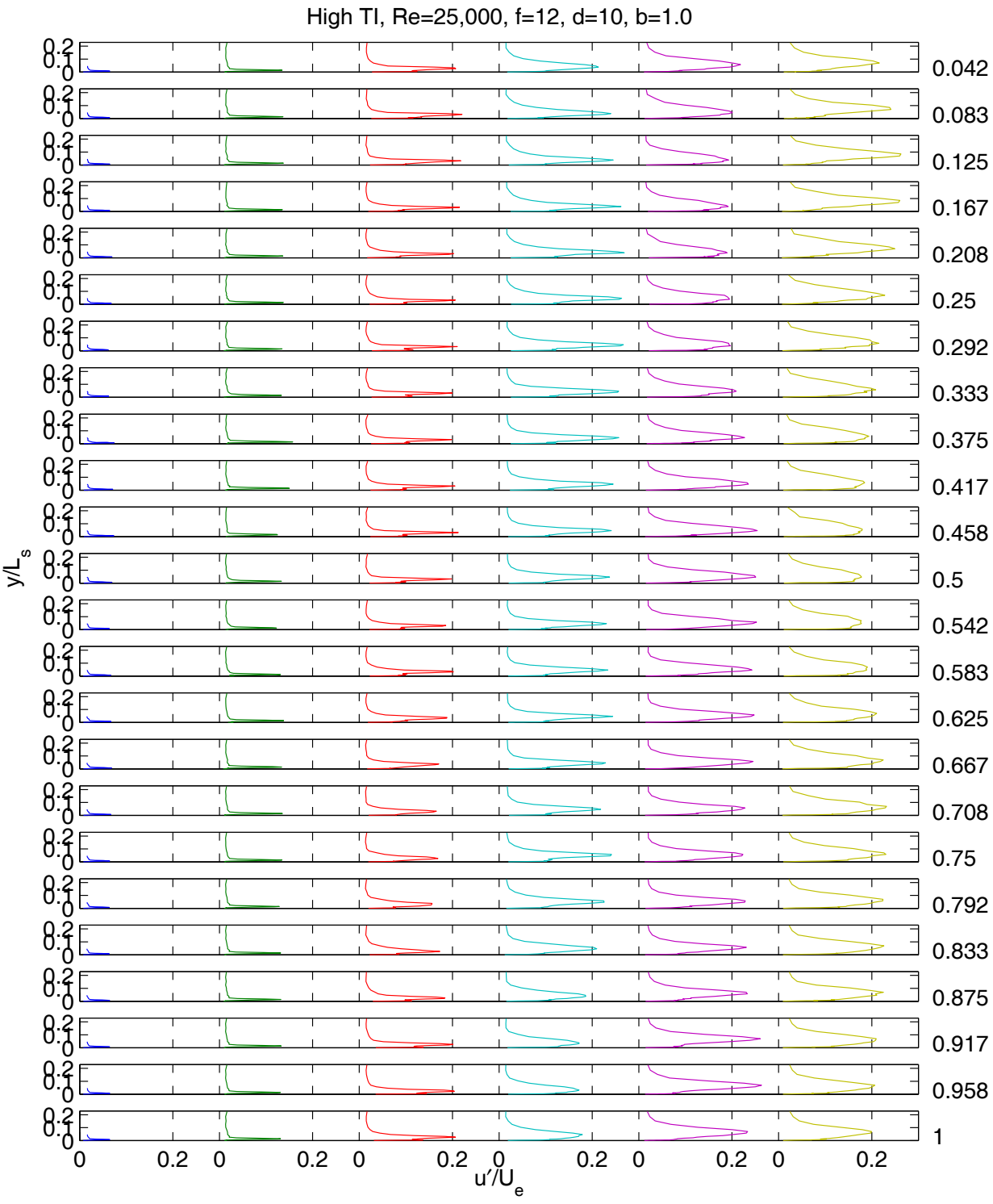

b)

Fig. 66 Phase averaged velocity profiles, high TI, Re=50,000, pulsed VGJs, F=0.56, D=10%, B=1.0: a) mean, b) rms.

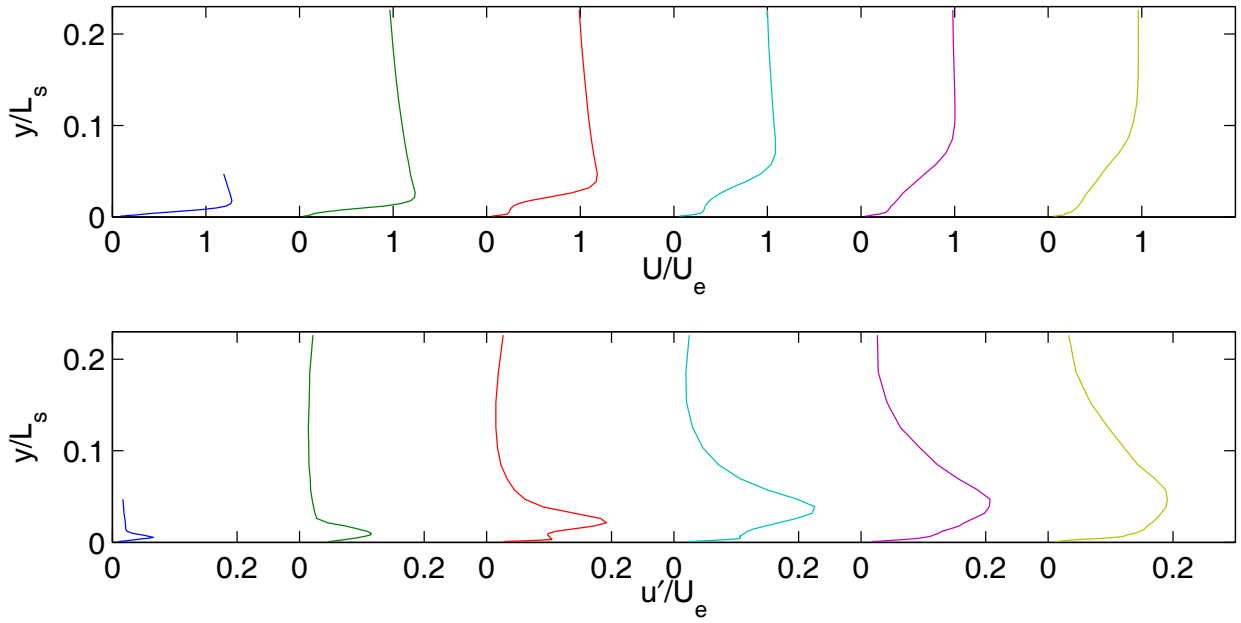

Fig. 67 Time averaged velocity profiles, high TI, Re=50,000, pulsed VGJs, F=0.56, D=10%, B=2.0: a) mean, b) rms.

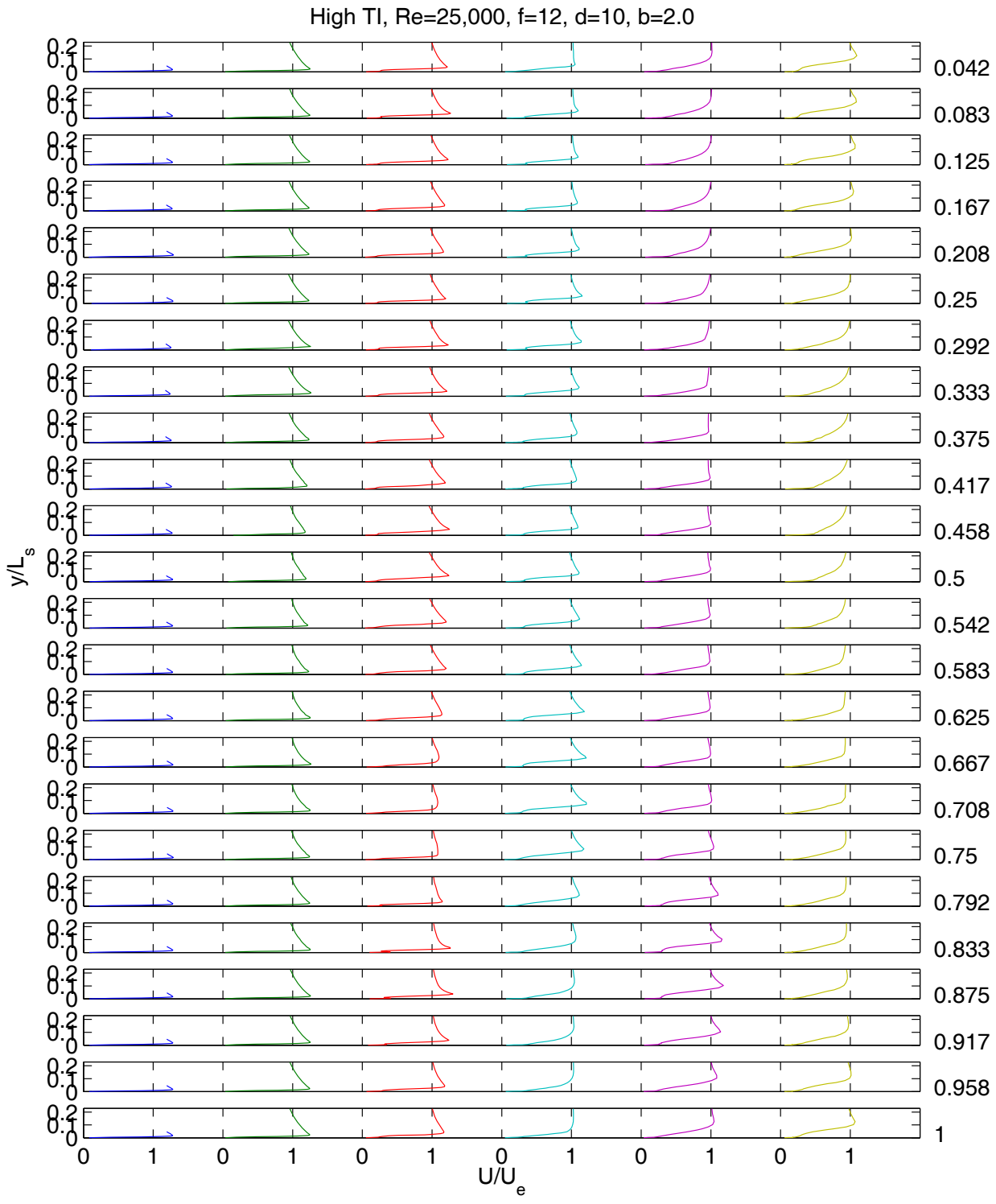
High TI, Re=25,000, f=12, d=10, b=2.0
y/L_s
U/U_e
0.042
0.083
0.125
0.167
0.208
0.25
0.292
0.333
0.375
0.417
0.458
0.5
0.542
0.583
0.625
0.667
0.708
0.75
0.792
0.833
0.875
0.917
0.958
1

a)

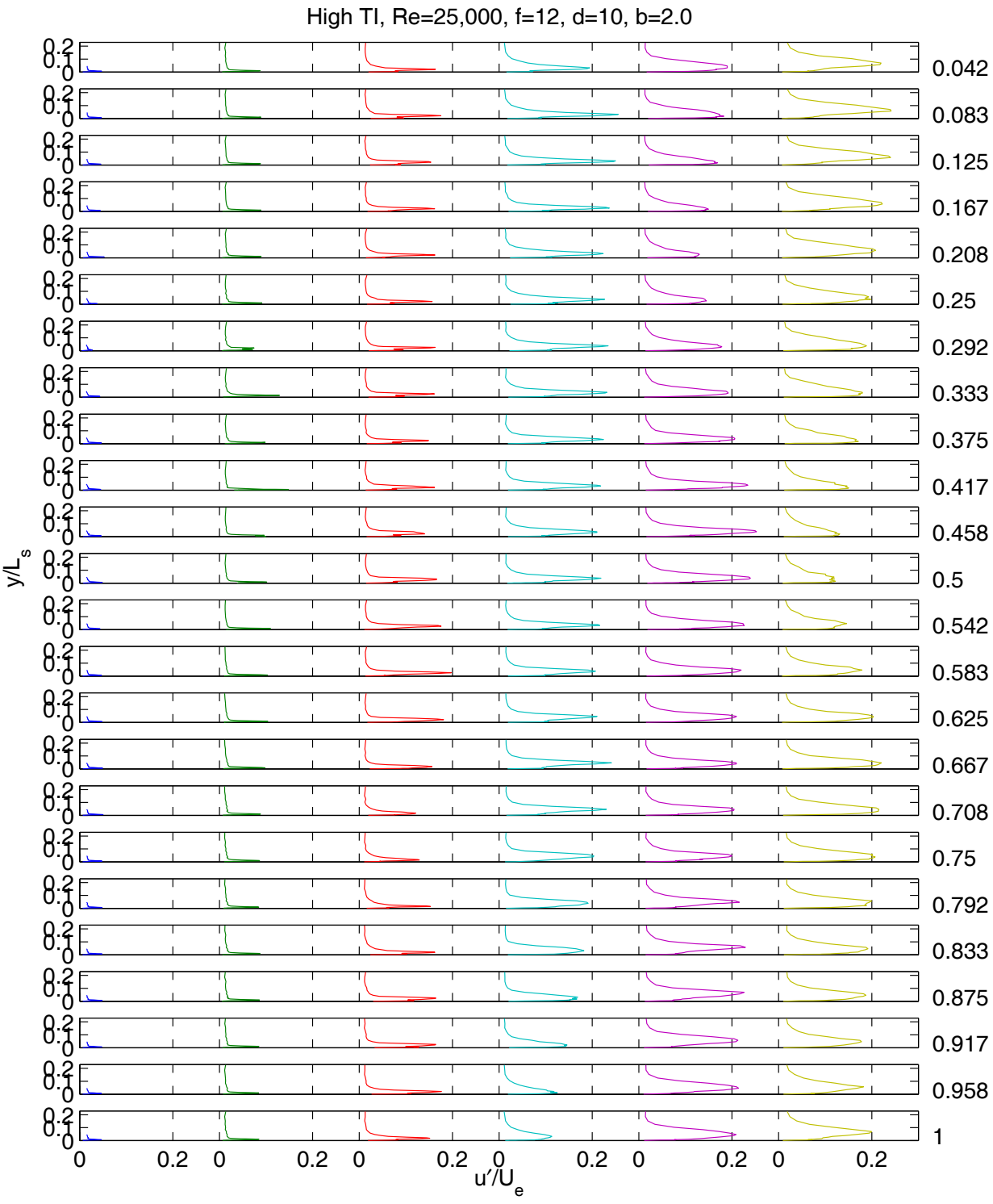

b)

Fig. 68 Phase averaged velocity profiles, high TI, Re=50,000, pulsed VGJs, F=0.56, D=10%, B=2.0: a) mean, b) rms.

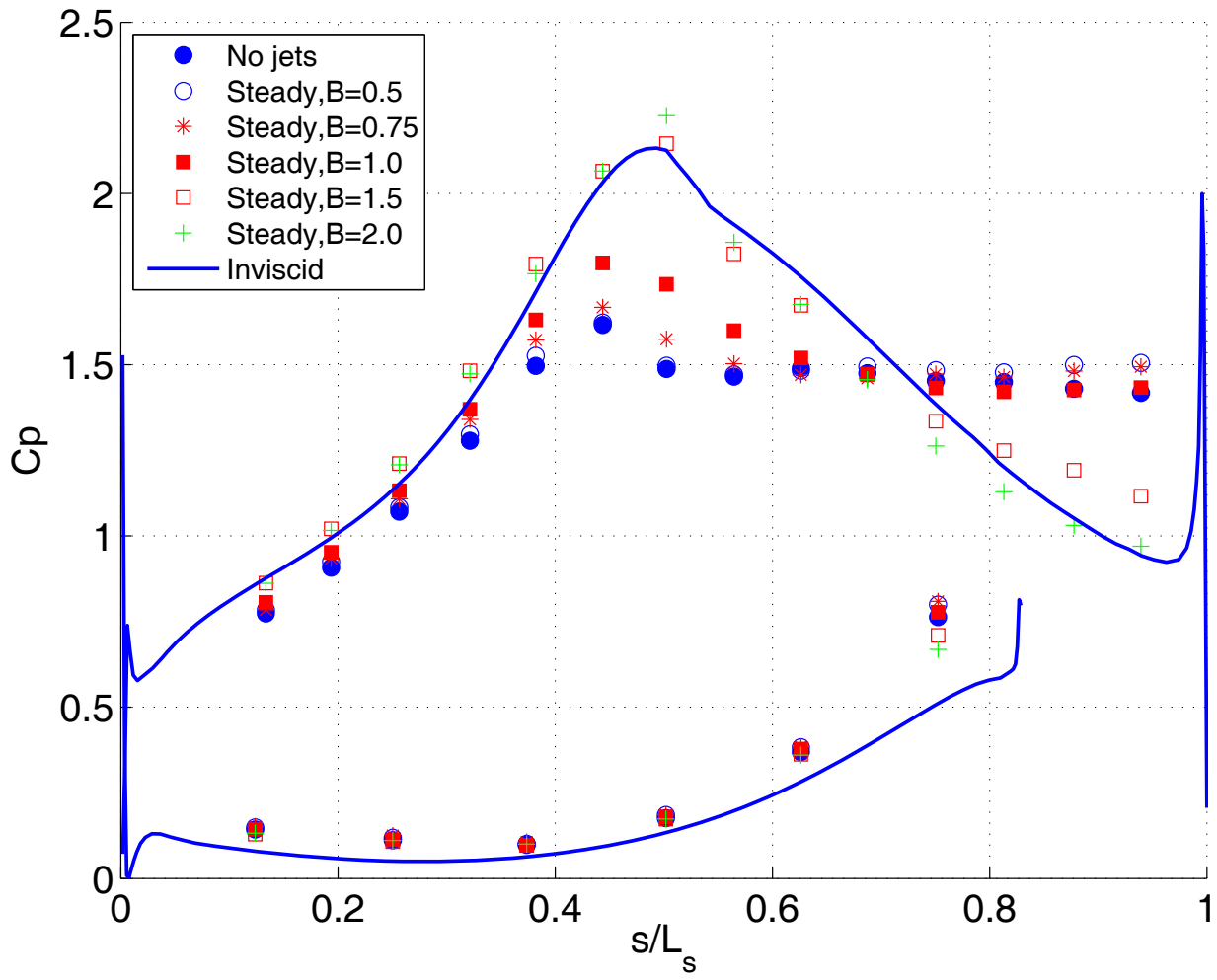
No jets
Steady,B=0.5
Steady,B=0.75
Steady,B=1.0
Steady,B=1.5
Steady,B=2.0
Inviscid
Cp
s/L_s
2.5
2
1.5
1
0.5
0
0
0.2
0.4
0.6
0.8
1

a)

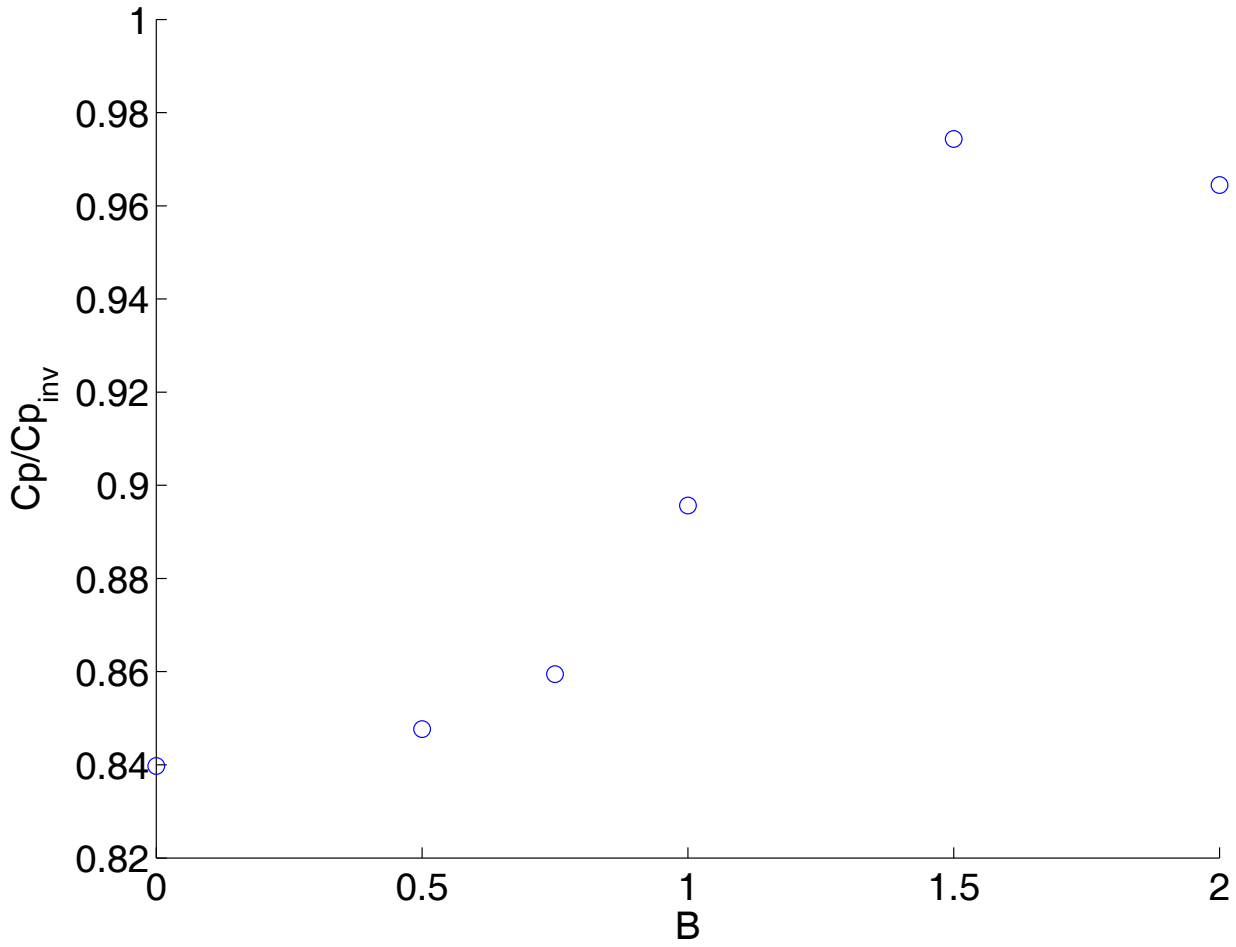

b)

Fig. 69 Cp results, high TI, Re=50,000, steady VGJs: a) Cp profile, b) Integrated Cp.

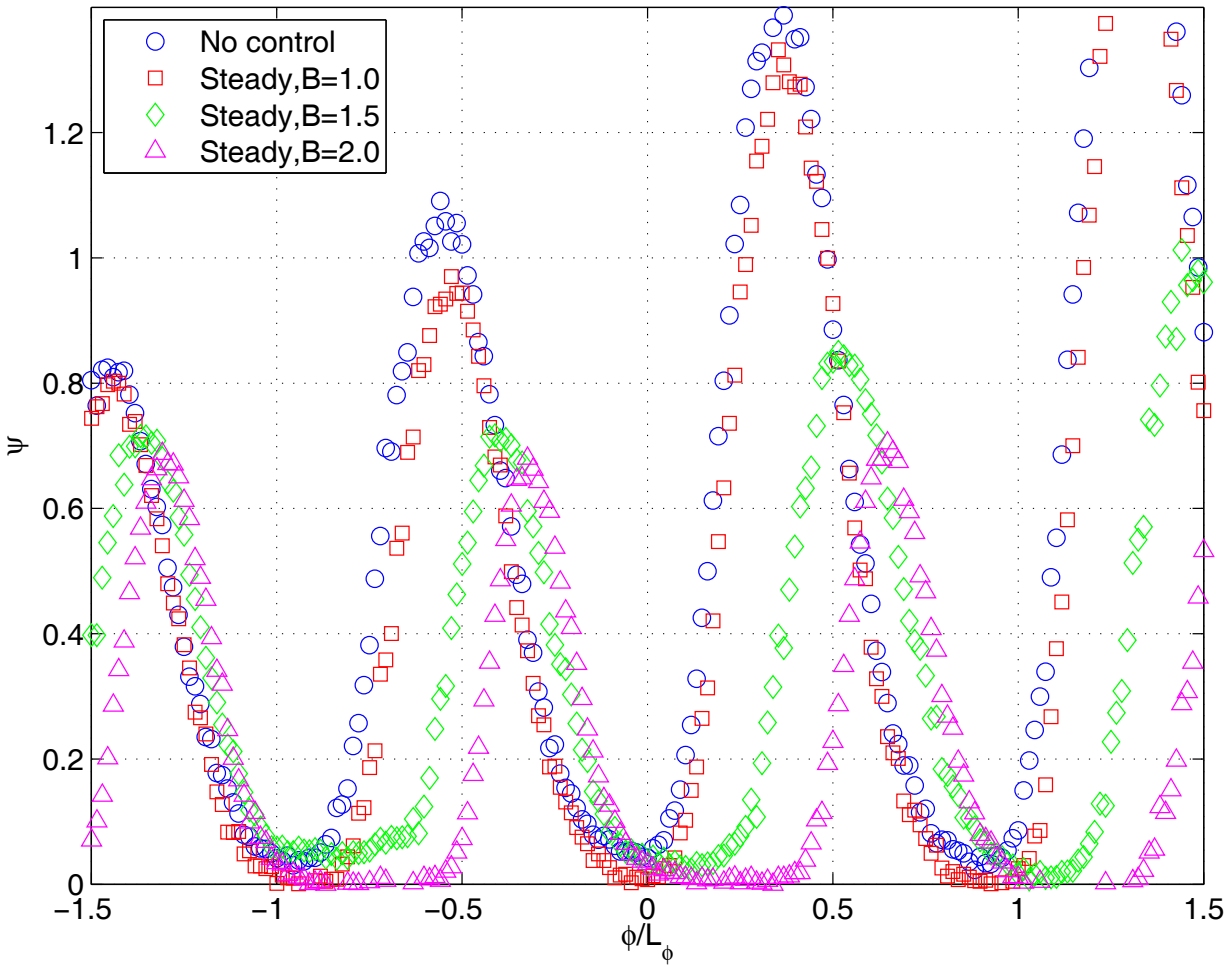
No control
Steady,B=1.0
Steady,B=1.5
Steady,B=2.0
ψ
ϕ/L_ϕ
0
0.2
0.4
0.6
0.8
1
1.2
−1.5
−1
−0.5
0
0.5
1
1.5

a)

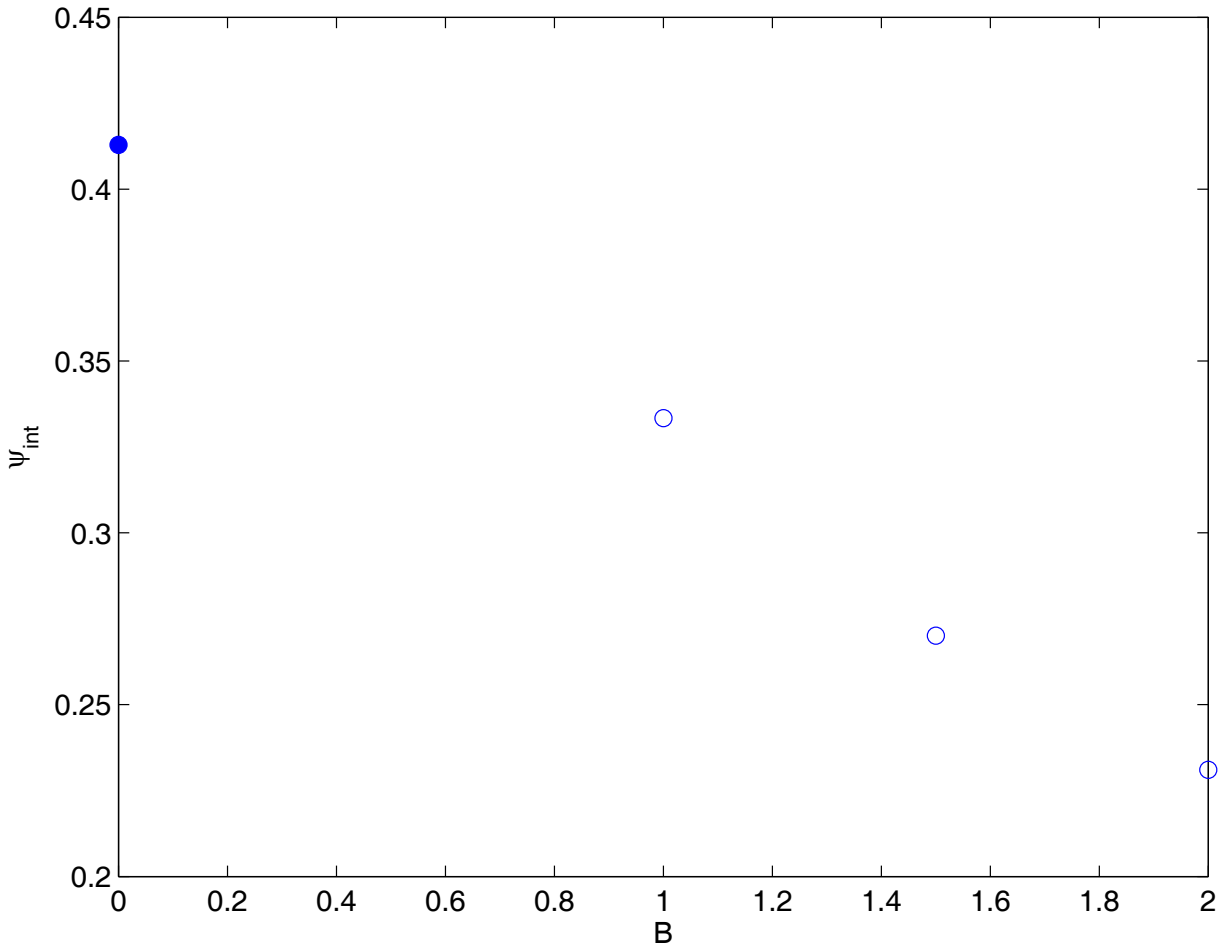

b)

Fig. 70 Ψ results, high TI, Re=50,000, steady VGJs: a) Ψ profile, b) Integrated Ψ.

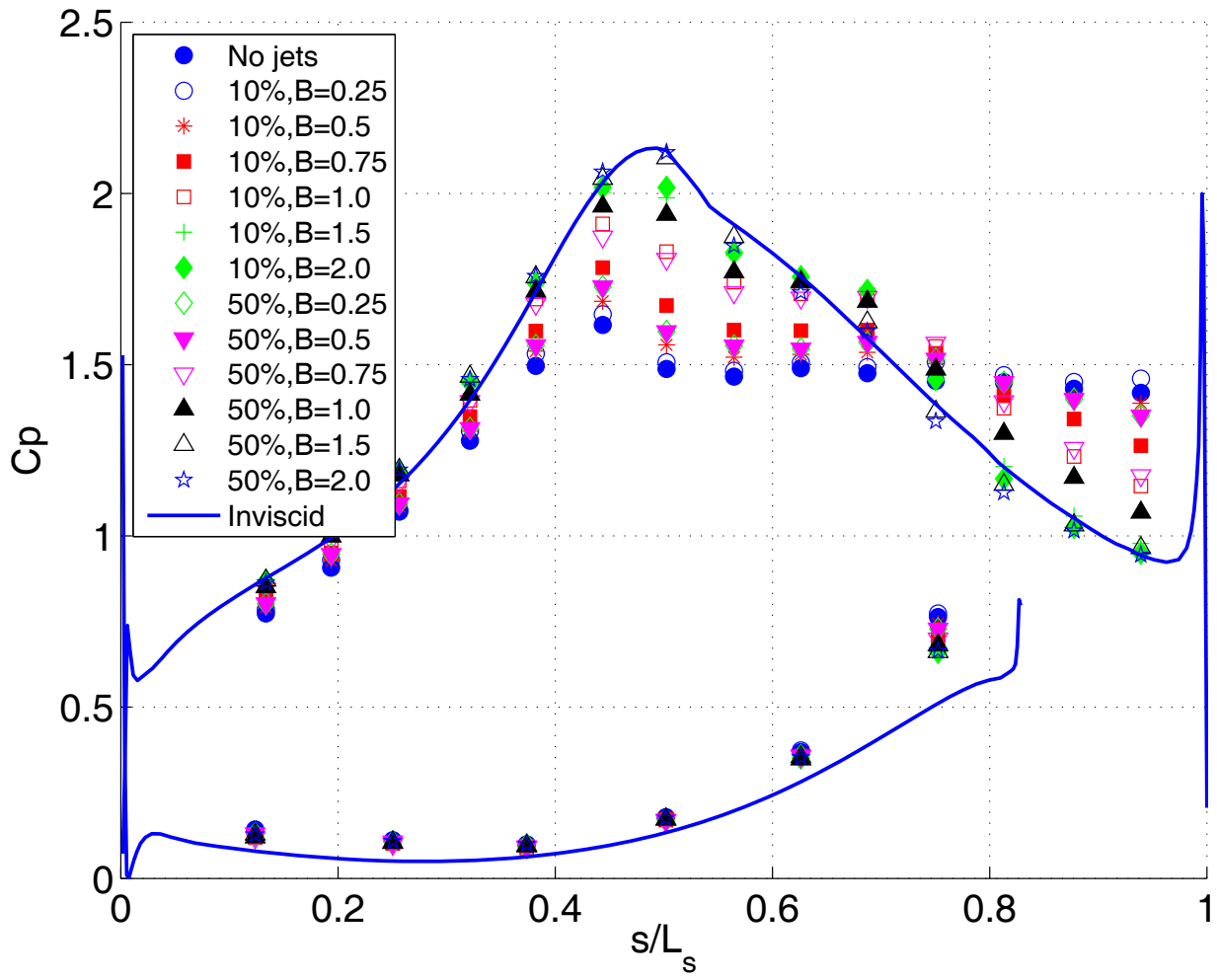
No jets
10%,B=0.25
10%,B=0.5
10%,B=0.75
10%,B=1.0
10%,B=1.5
10%,B=2.0
50%,B=0.25
50%,B=0.5
50%,B=0.75
50%,B=1.0
50%,B=1.5
50%,B=2.0
Inviscid
Cp
s/L_s
0
0.5
1
1.5
2
2.5
0.2
0.4
0.6
0.8

a)

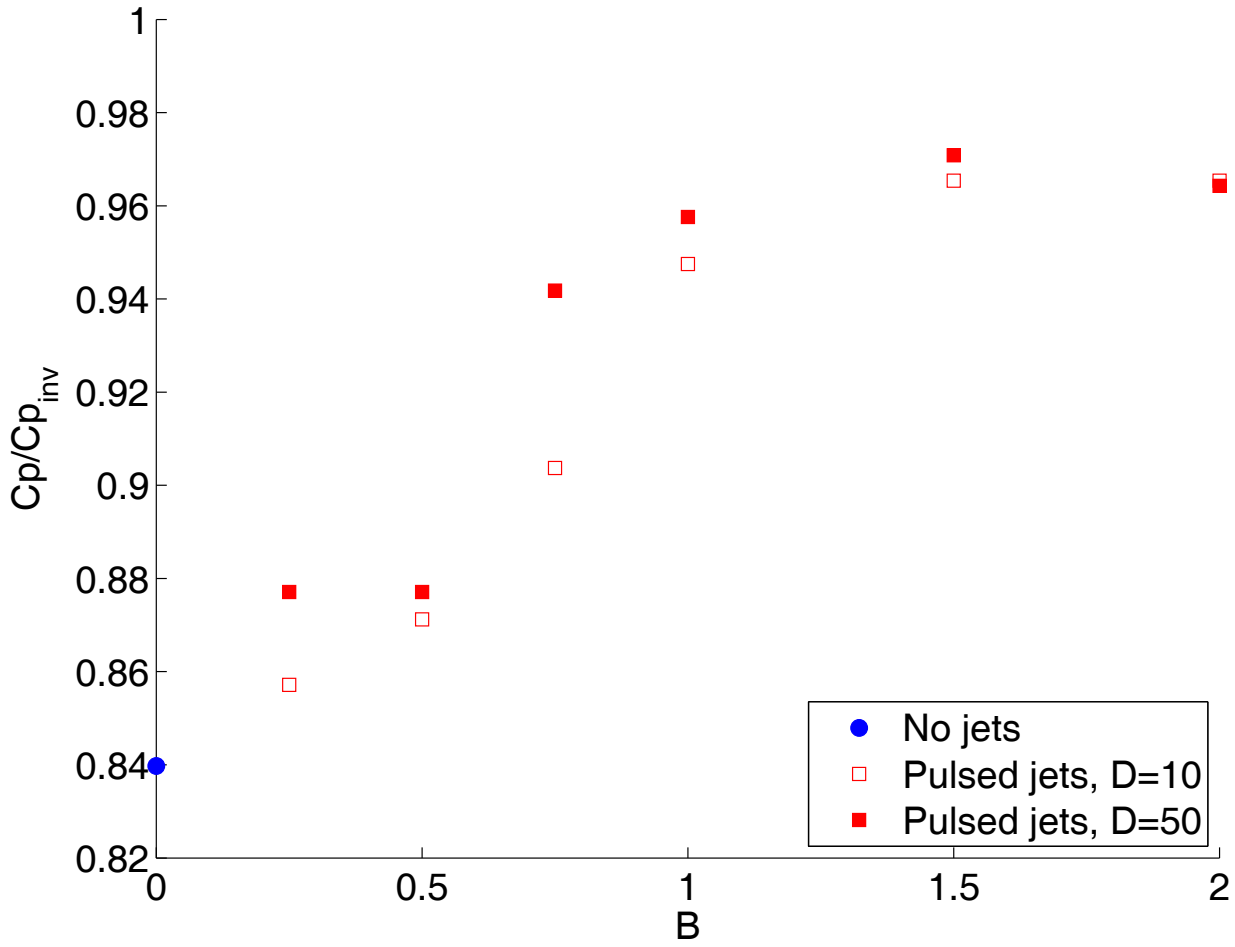

b)

Fig. 71 Cp results, high TI, Re=50,000, pulsed VGJs, F=0.14: a) Cp profile, b) Integrated Cp.

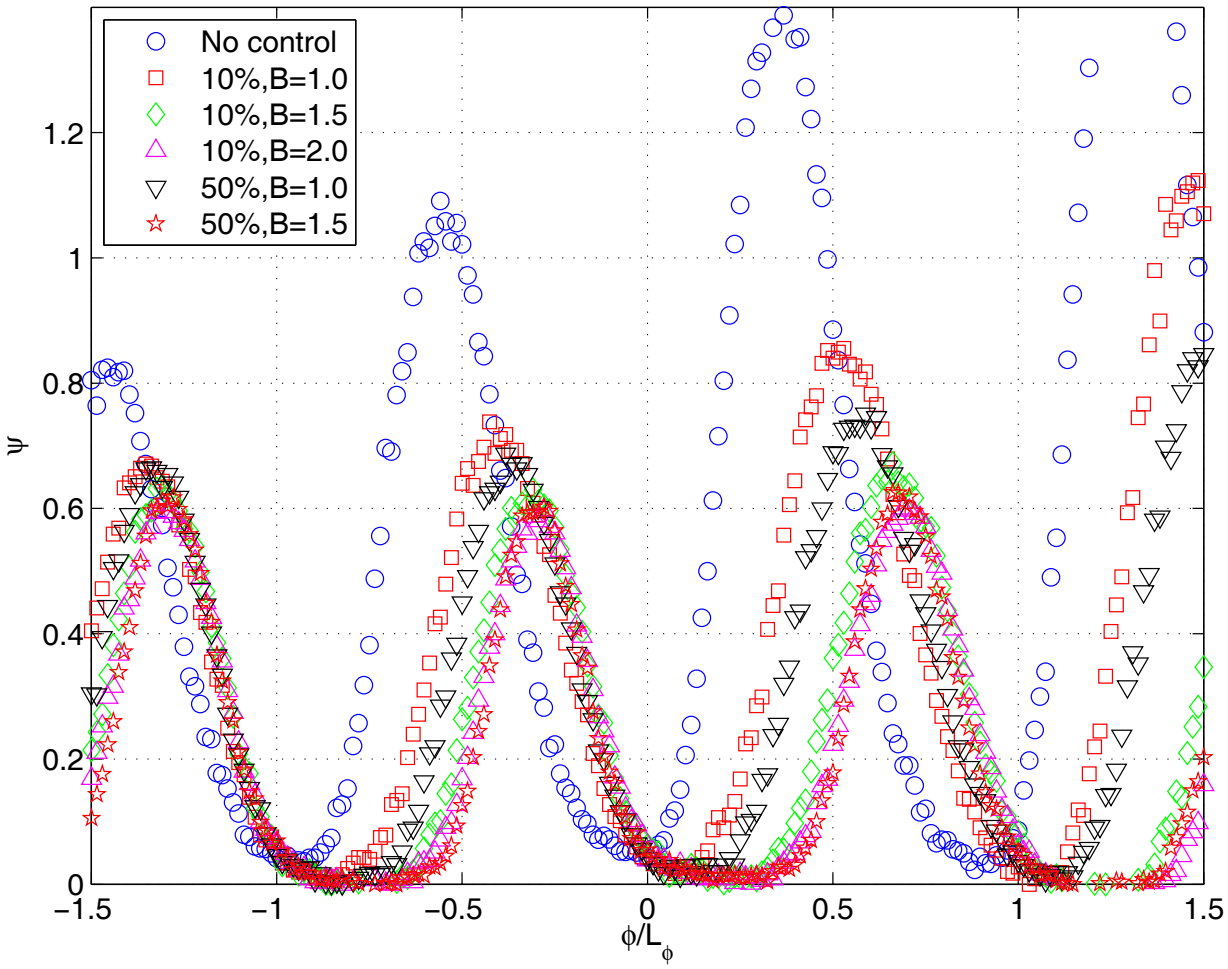
No control
10%,B=1.0
10%,B=1.5
10%,B=2.0
50%,B=1.0
50%,B=1.5
ψ
ϕ/L_ϕ
0
0.2
0.4
0.6
0.8
1
1.2
−1.5
−1
−0.5
0
0.5
1
1.5

a)

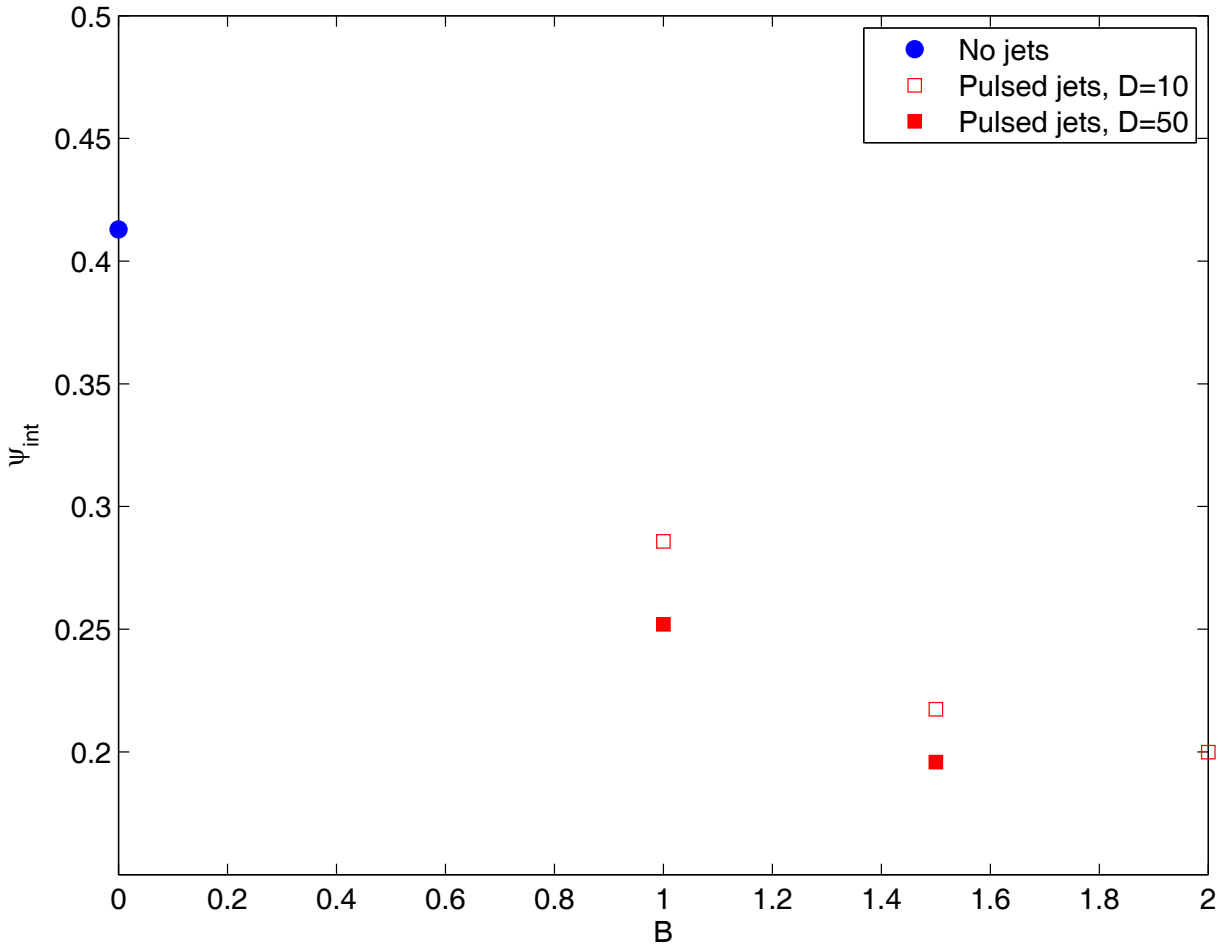

b)

Fig. 72 Ψ results, high TI, Re=50,000, pulsed VGJs, F=0.14: a) Ψ profile, b) Integrated Ψ.

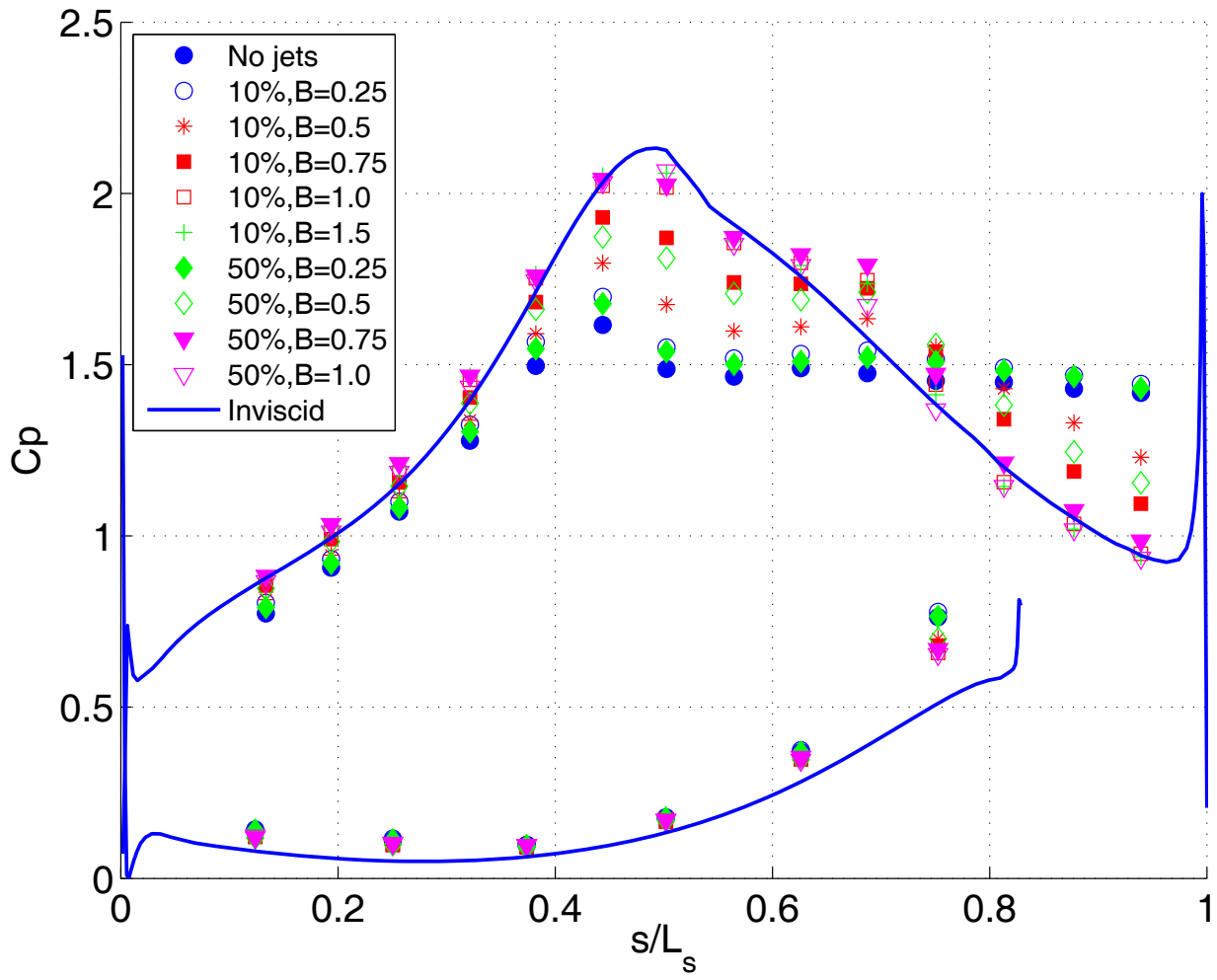
No jets
10%,B=0.25
10%,B=0.5
10%,B=0.75
10%,B=1.0
10%,B=1.5
50%,B=0.25
50%,B=0.5
50%,B=0.75
50%,B=1.0
Inviscid
Cp
s/L_s
0
0.5
1
1.5
2
2.5
0.2
0.4
0.6
0.8

a)

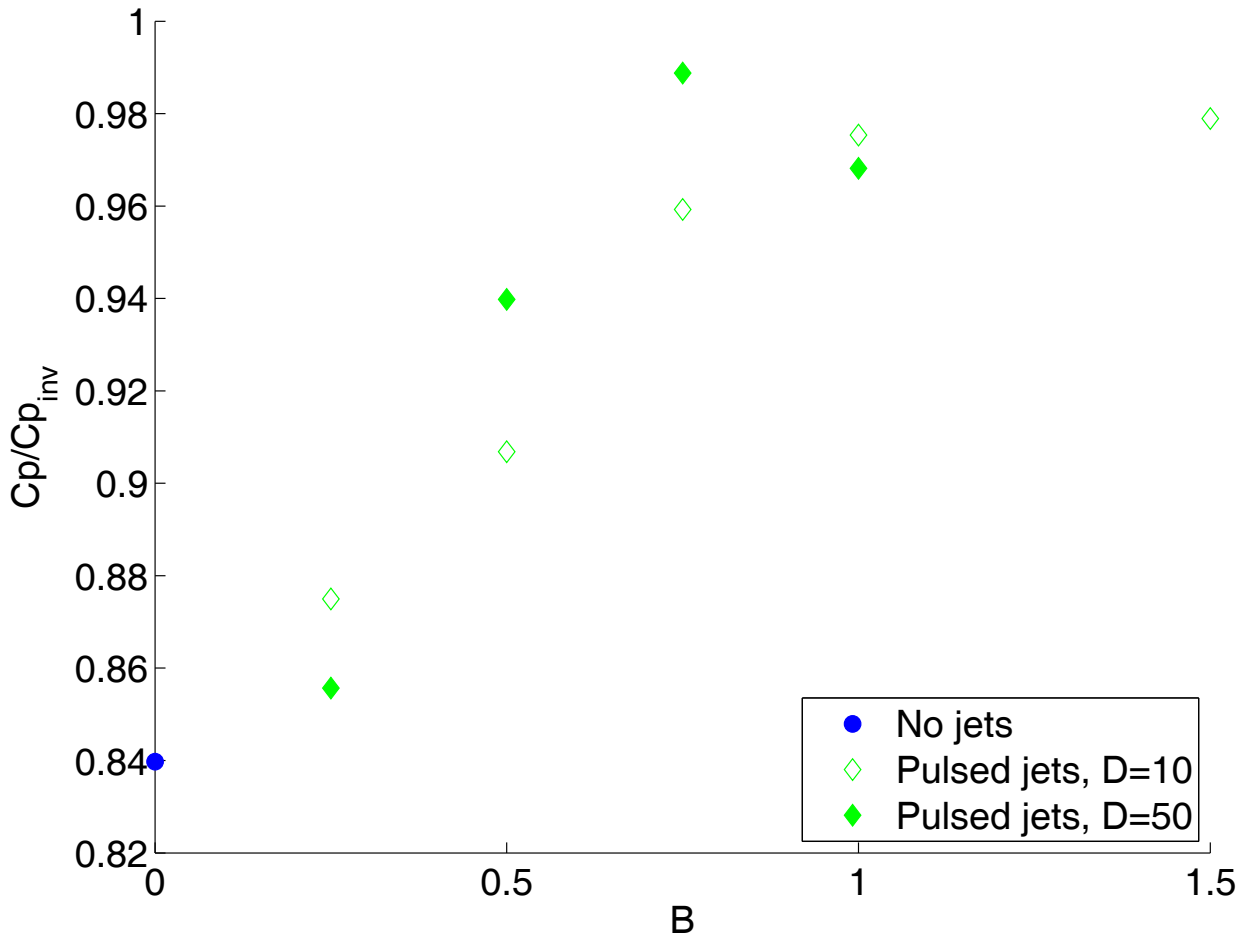

b)

Fig. 73 Cp results, high TI, Re=50,000, pulsed VGJs, F=0.28: a) Cp profile, b) Integrated Cp.

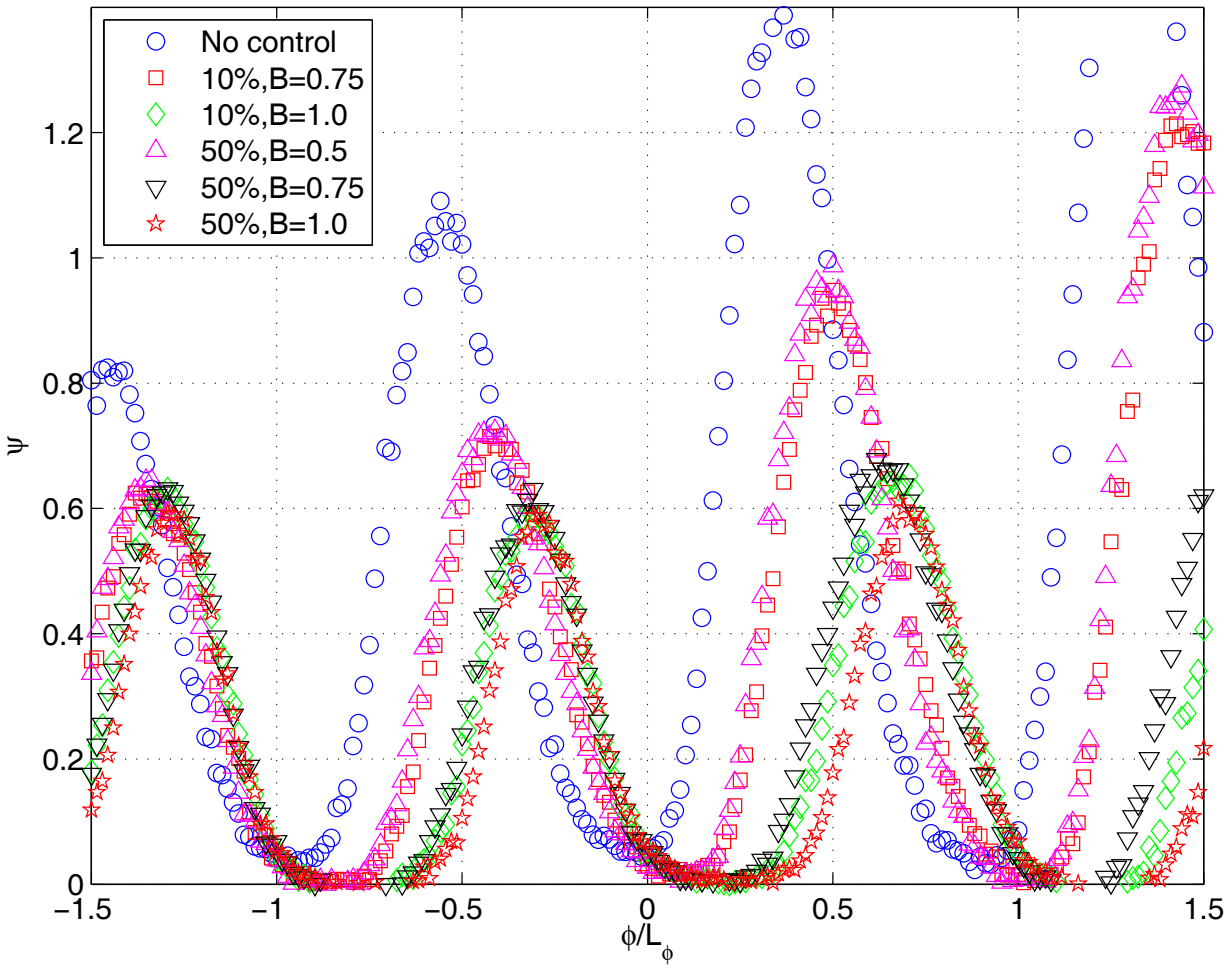
No control
10%,B=0.75
10%,B=1.0
50%,B=0.5
50%,B=0.75
50%,B=1.0
ψ
ϕ/L_ϕ
0
0.2
0.4
0.6
0.8
1
1.2
−1.5
−1
−0.5
0
0.5
1
1.5

a)

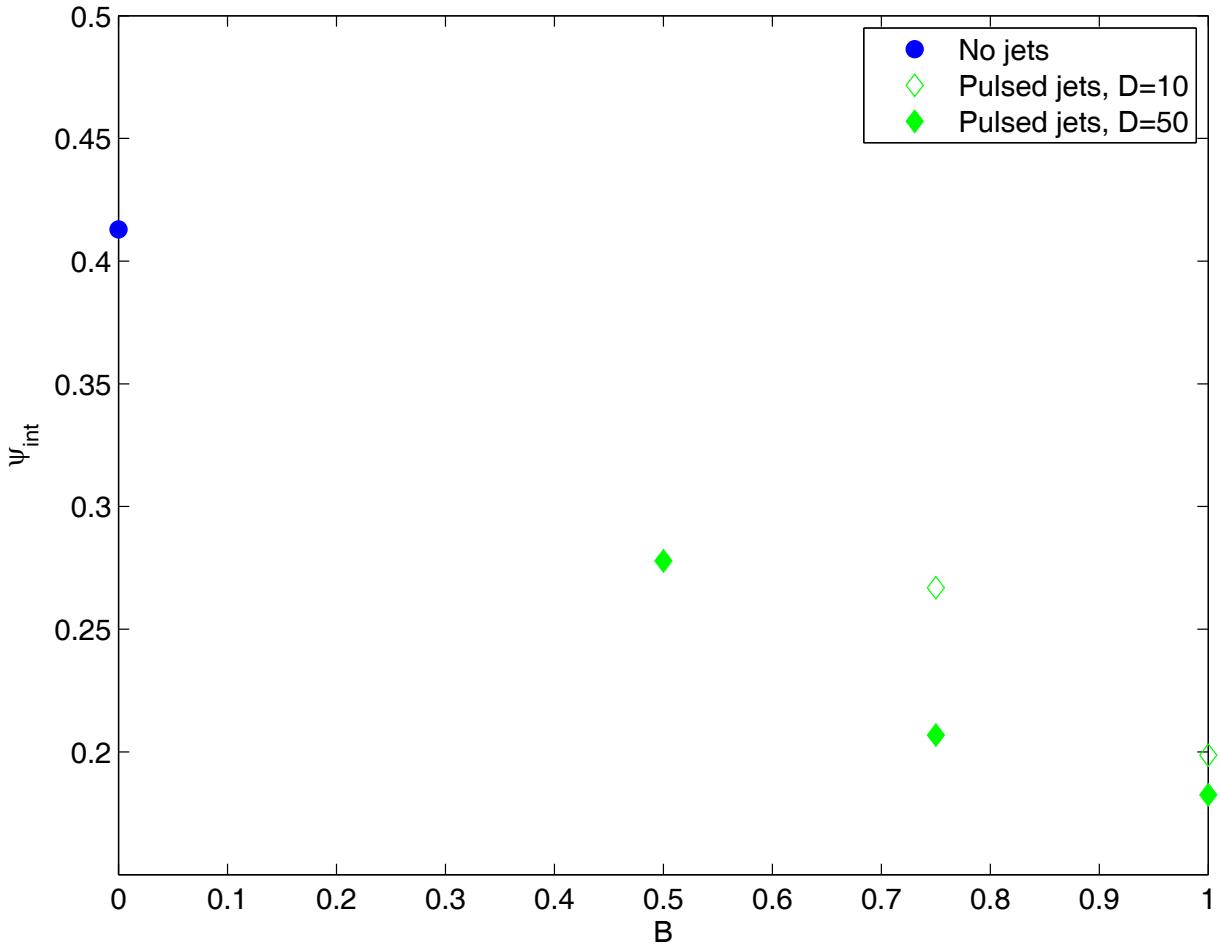

b)

Fig. 74 Ψ results, high TI, Re=50,000, pulsed VGJs, F=0.28: a) Ψ profile, b) Integrated Ψ.

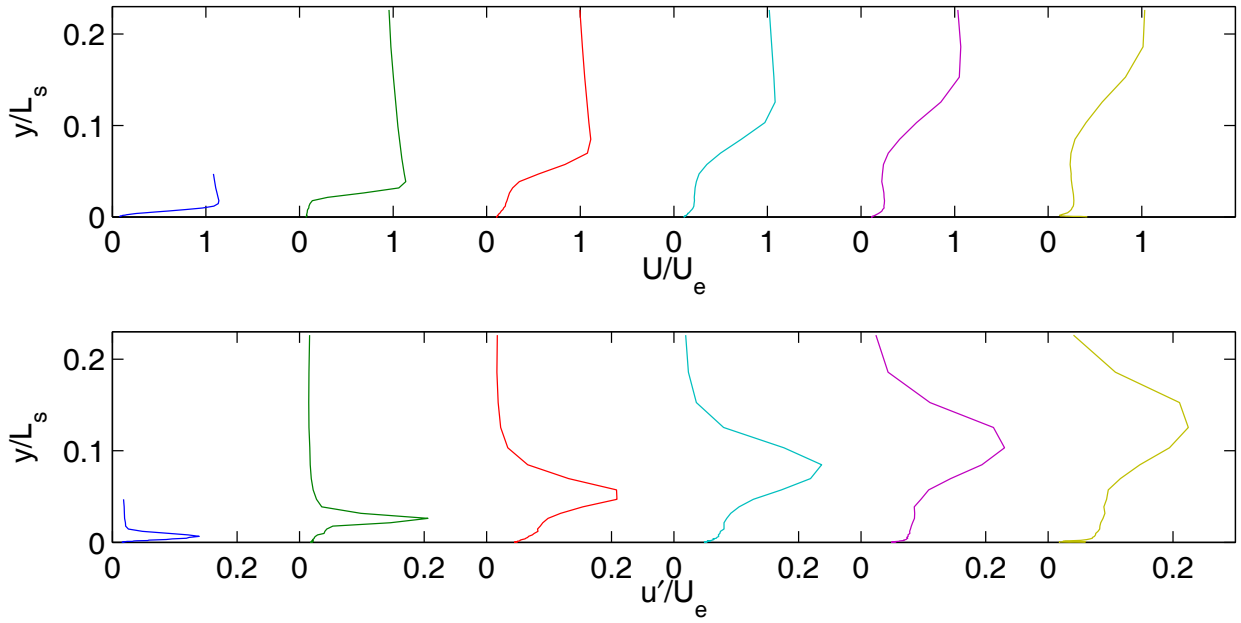

Fig. 75 Time averaged velocity profiles, high TI, Re=50,000, no VGJs: a) mean, b) rms.

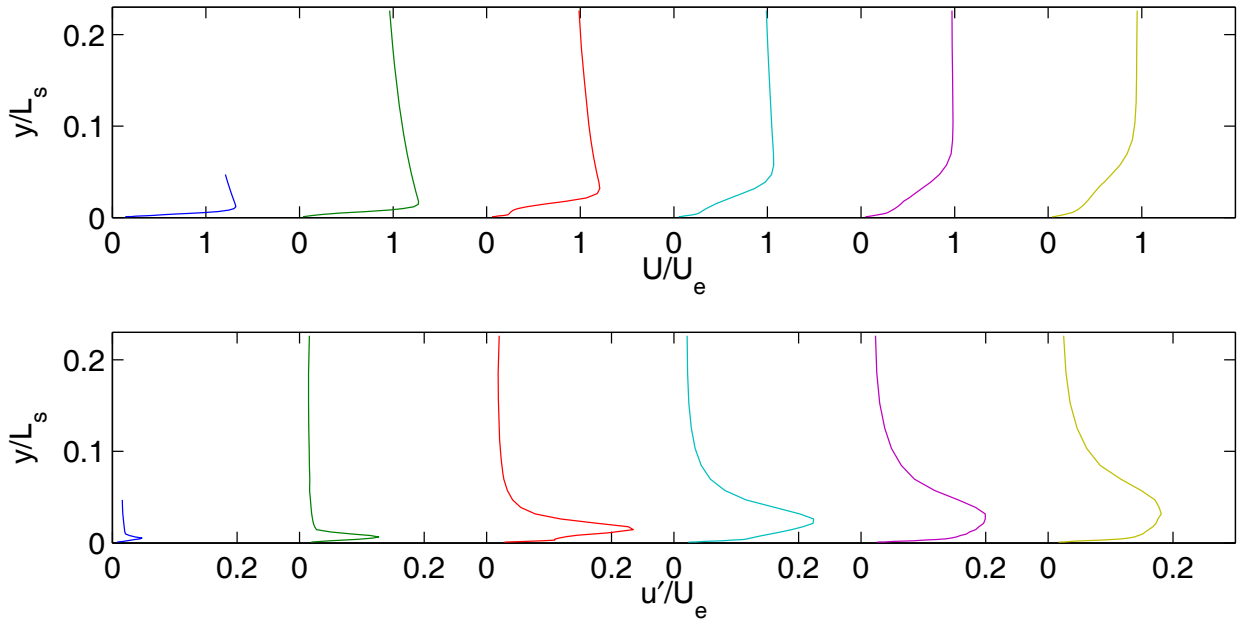

Fig. 76 Time averaged velocity profiles, high TI, Re=50,000, pulsed VGJs, F=0.28, D=10%, B=1.0: a) mean, b) rms.

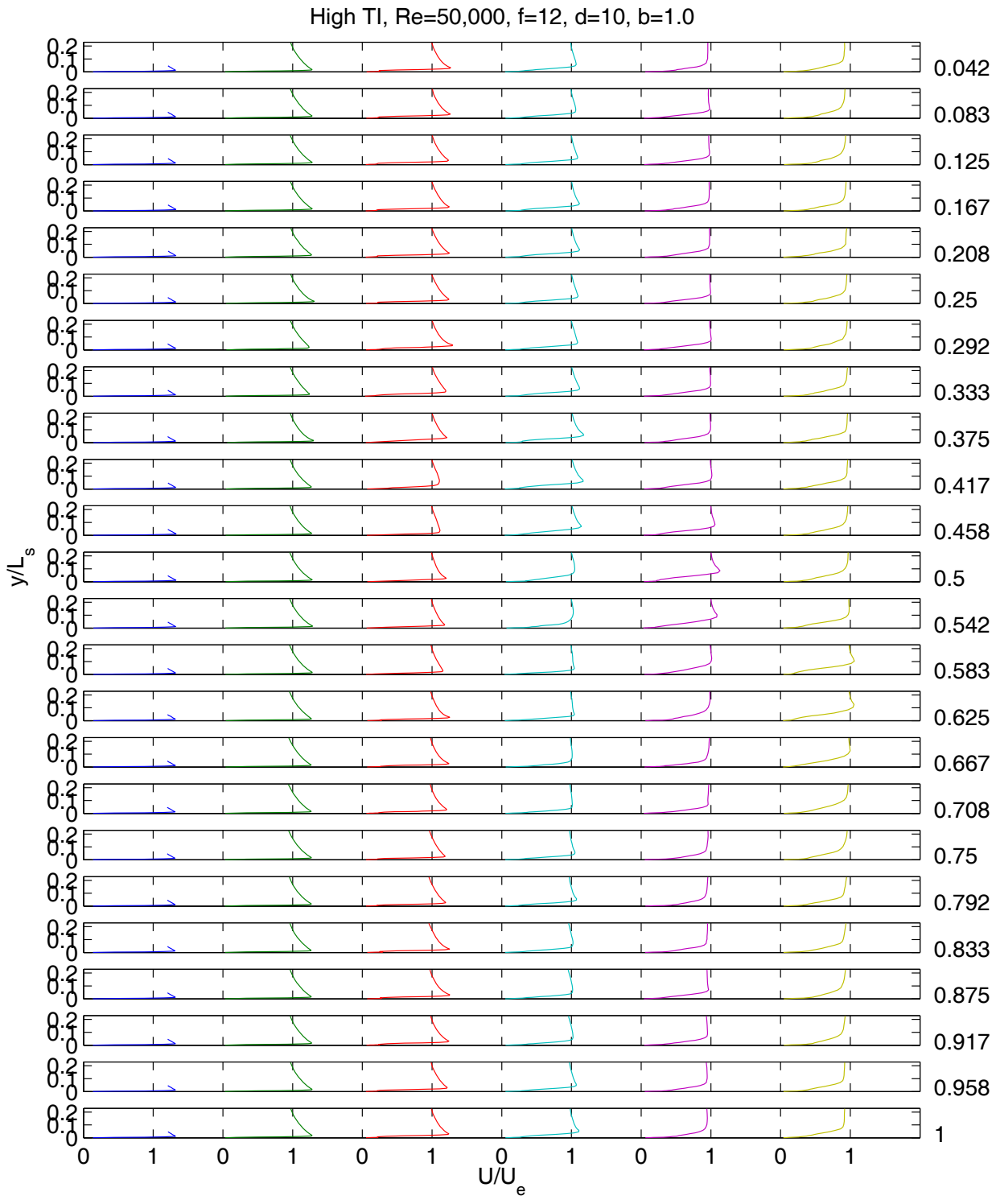
High TI, Re=50,000, f=12, d=10, b=1.0
y/L_s
U/U_e
0.042
0.083
0.125
0.167
0.208
0.25
0.292
0.333
0.375
0.417
0.458
0.5
0.542
0.583
0.625
0.667
0.708
0.75
0.792
0.833
0.875
0.917
0.958
1

a)

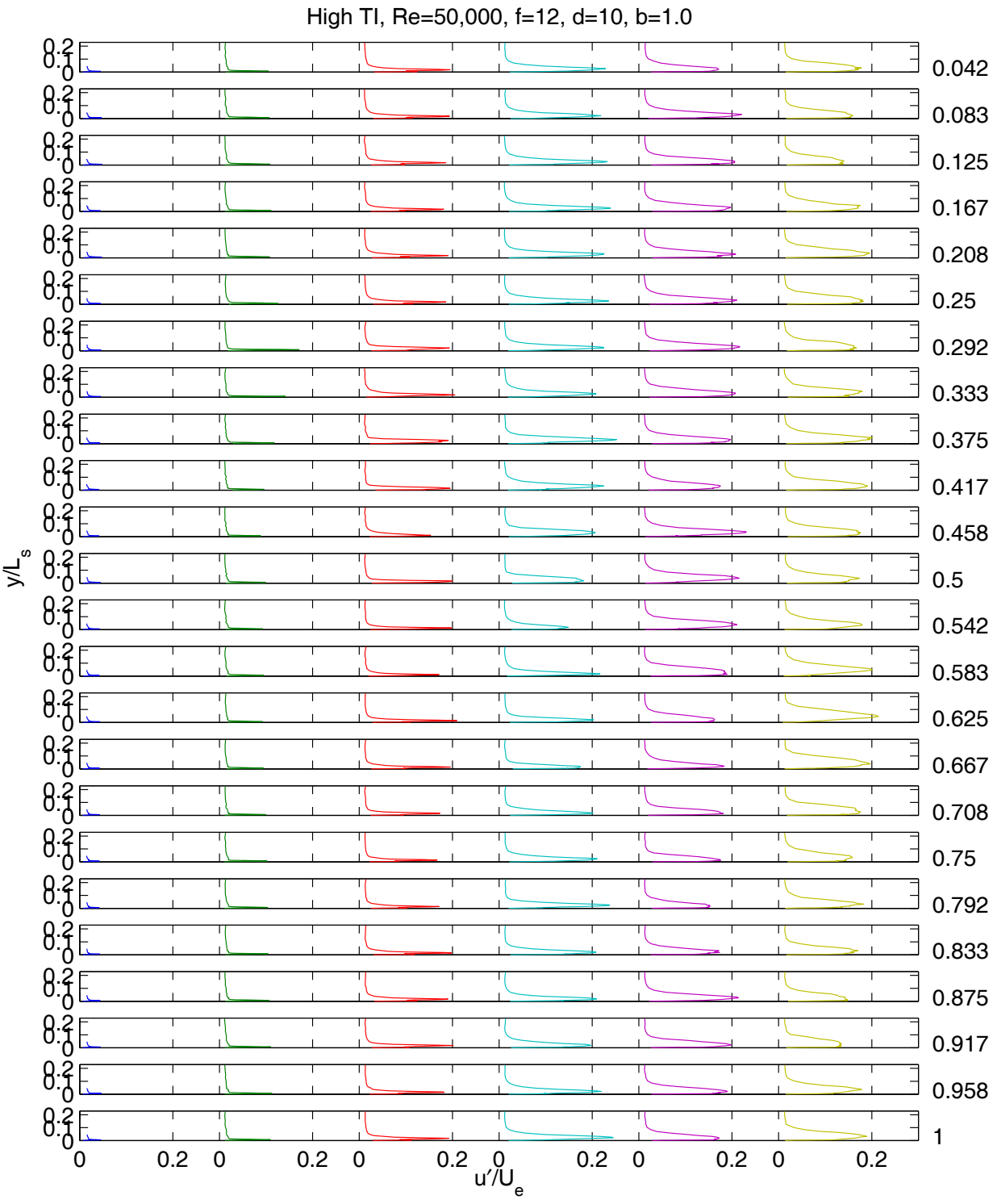

b)

Fig. 77 Phase averaged velocity profiles, high TI, Re=50,000, pulsed VGJs, F=0.28, D=10%, B=1.0: a) mean, b) rms.

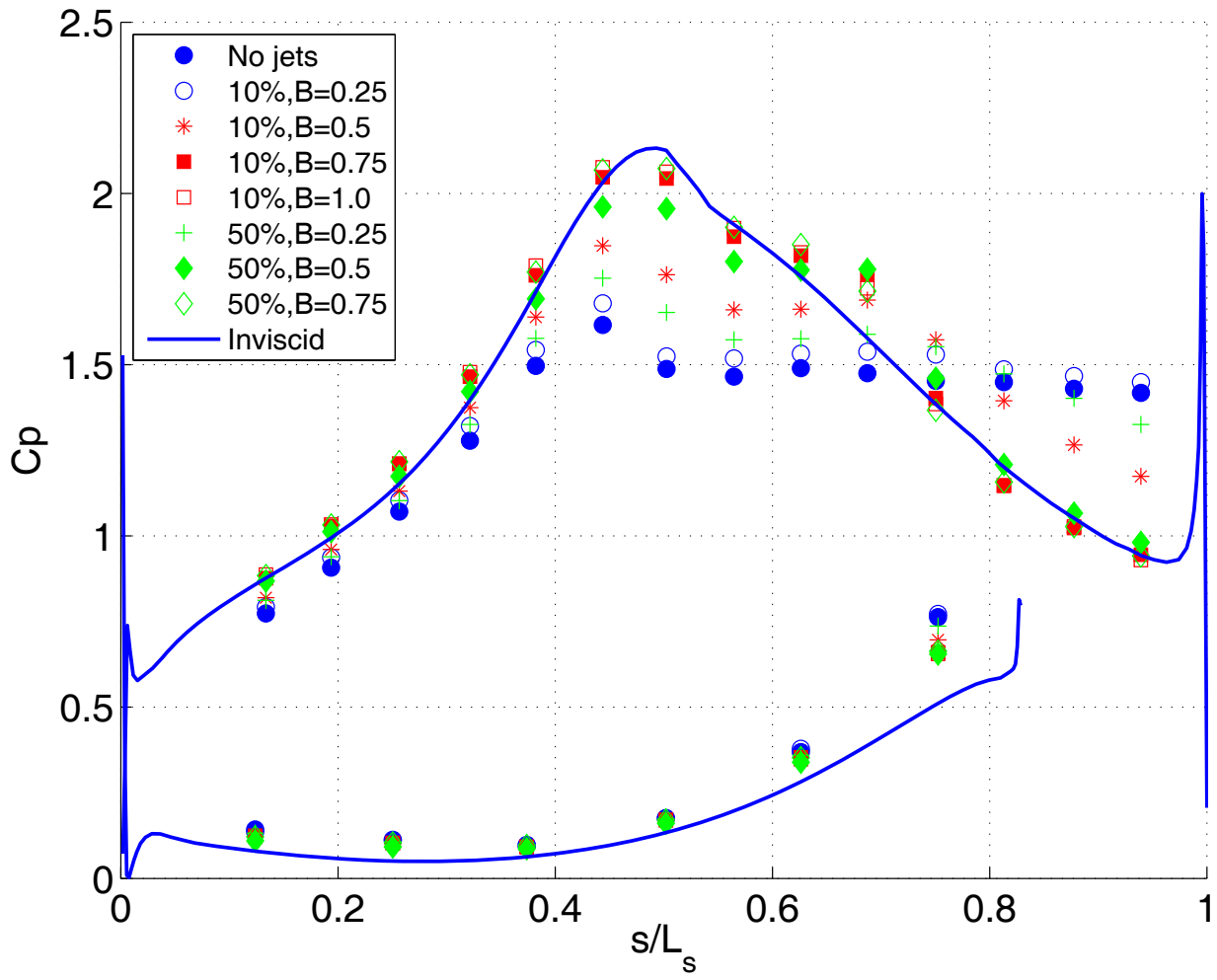
No jets
10%,B=0.25
10%,B=0.5
10%,B=0.75
10%,B=1.0
50%,B=0.25
50%,B=0.5
50%,B=0.75
Inviscid
Cp
s/L_s
2.5
2
1.5
1
0.5
0
0
0.2
0.4
0.6
0.8
1

a)

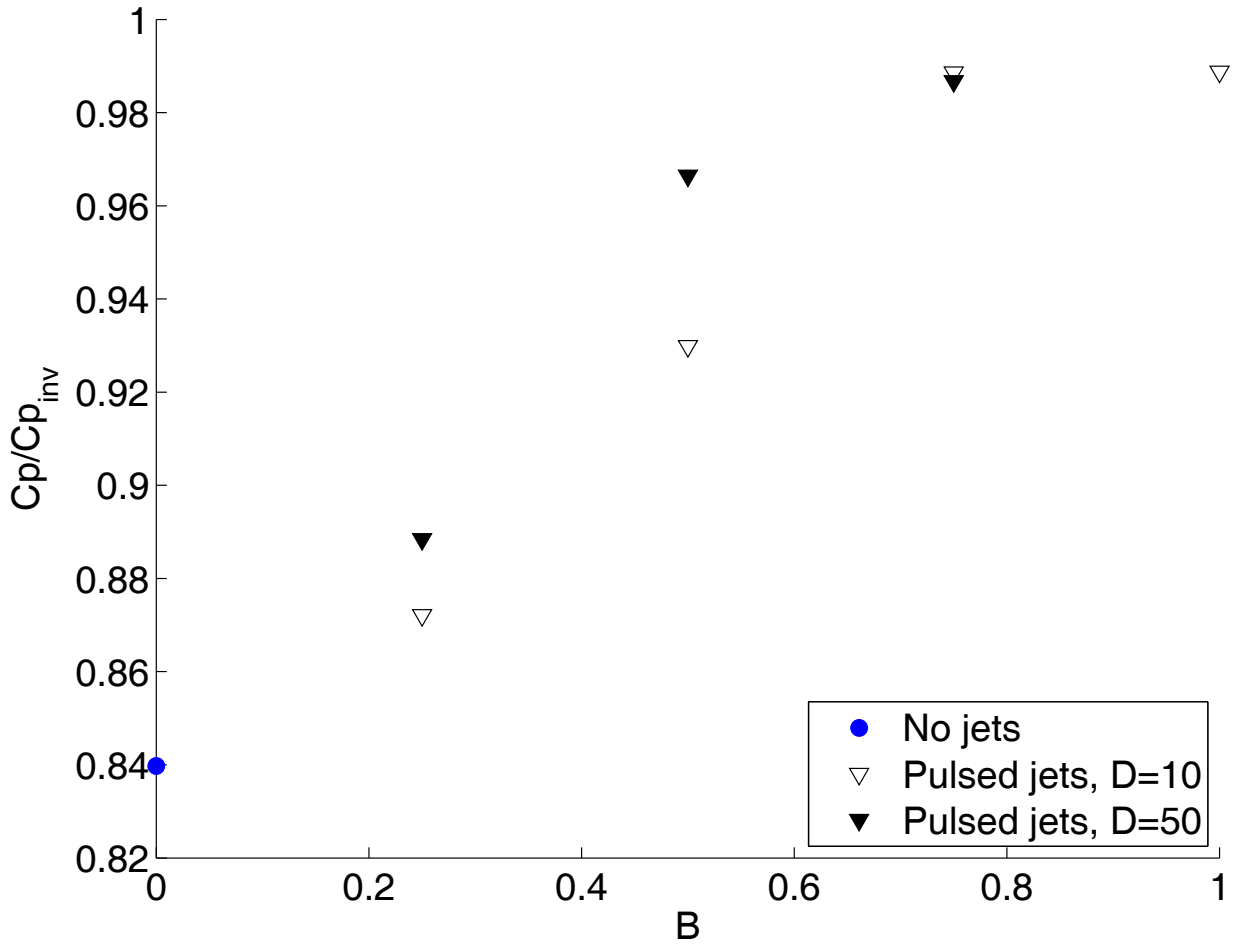

b)

Fig. 78 Cp results, high TI, Re=50,000, pulsed VGJs, F=0.56: a) Cp profile, b) Integrated Cp.

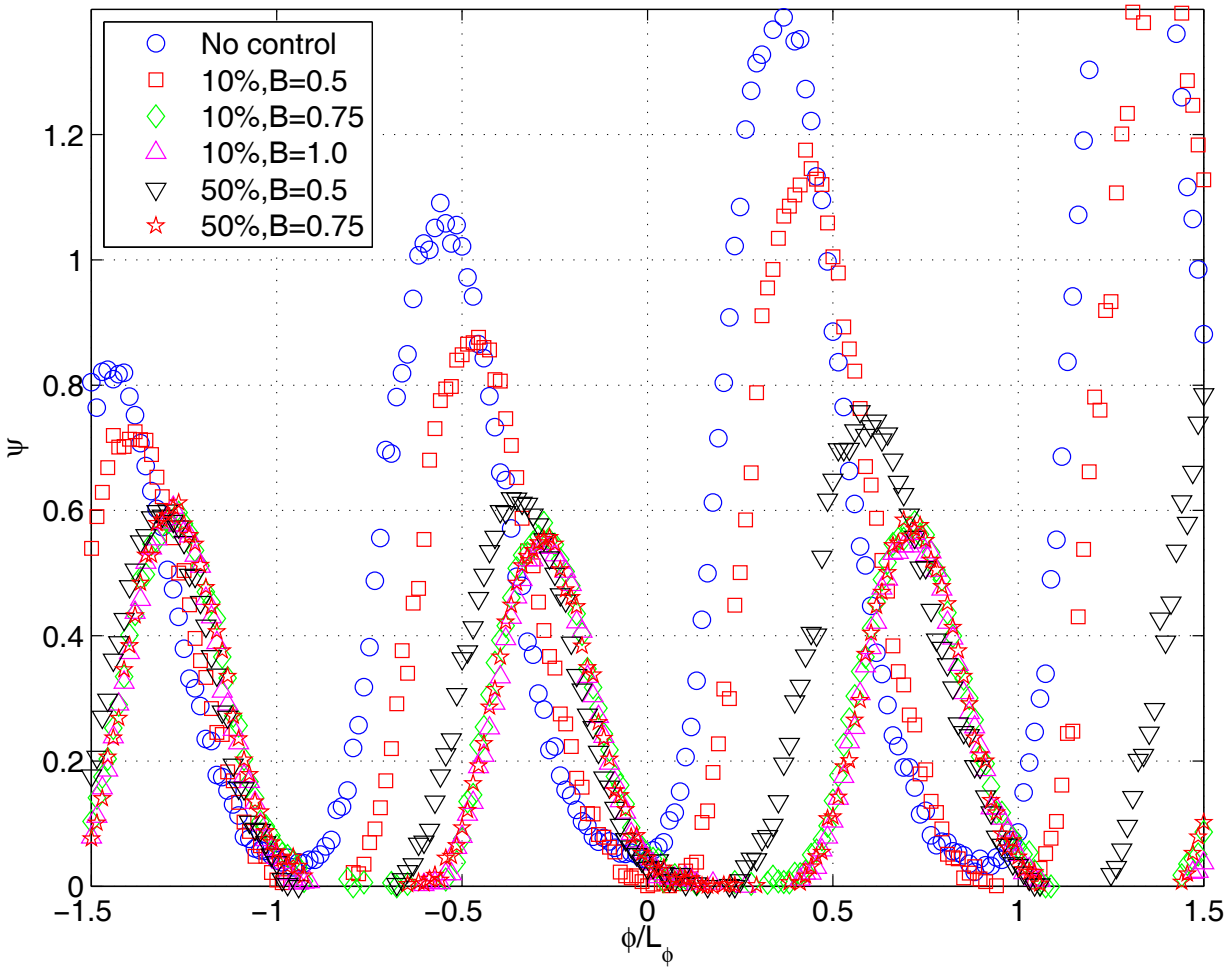
No control
10%,B=0.5
10%,B=0.75
10%,B=1.0
50%,B=0.5
50%,B=0.75
ψ
ϕ/L_ϕ
0
0.2
0.4
0.6
0.8
1
1.2
−1.5
−1
−0.5
0
0.5
1
1.5

a)

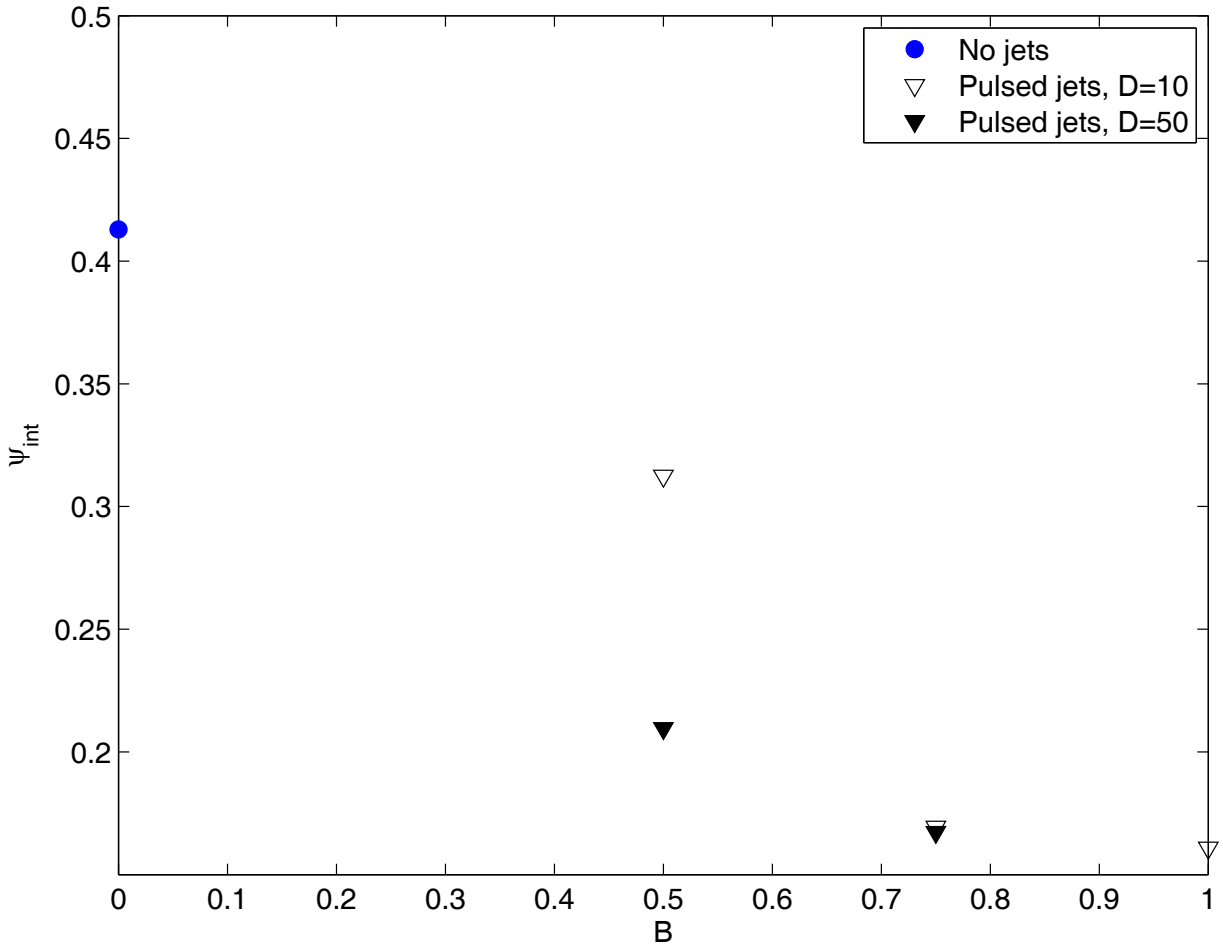

b)

Fig. 79 Ψ results, high TI, Re=50,000, pulsed VGJs, F=0.56: a) Ψ profile, b) Integrated Ψ.

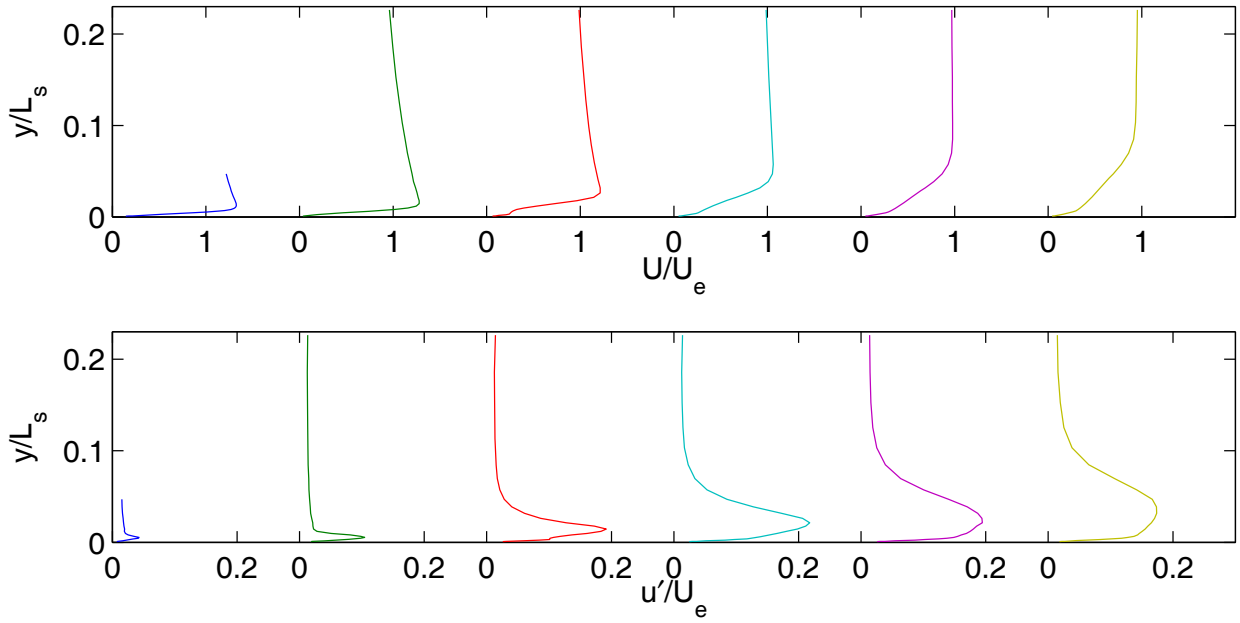

Fig. 80 Time averaged velocity profiles, high TI, Re=50,000, pulsed VGJs, F=0.56, D=10%, B=0.75: a) mean, b) rms.

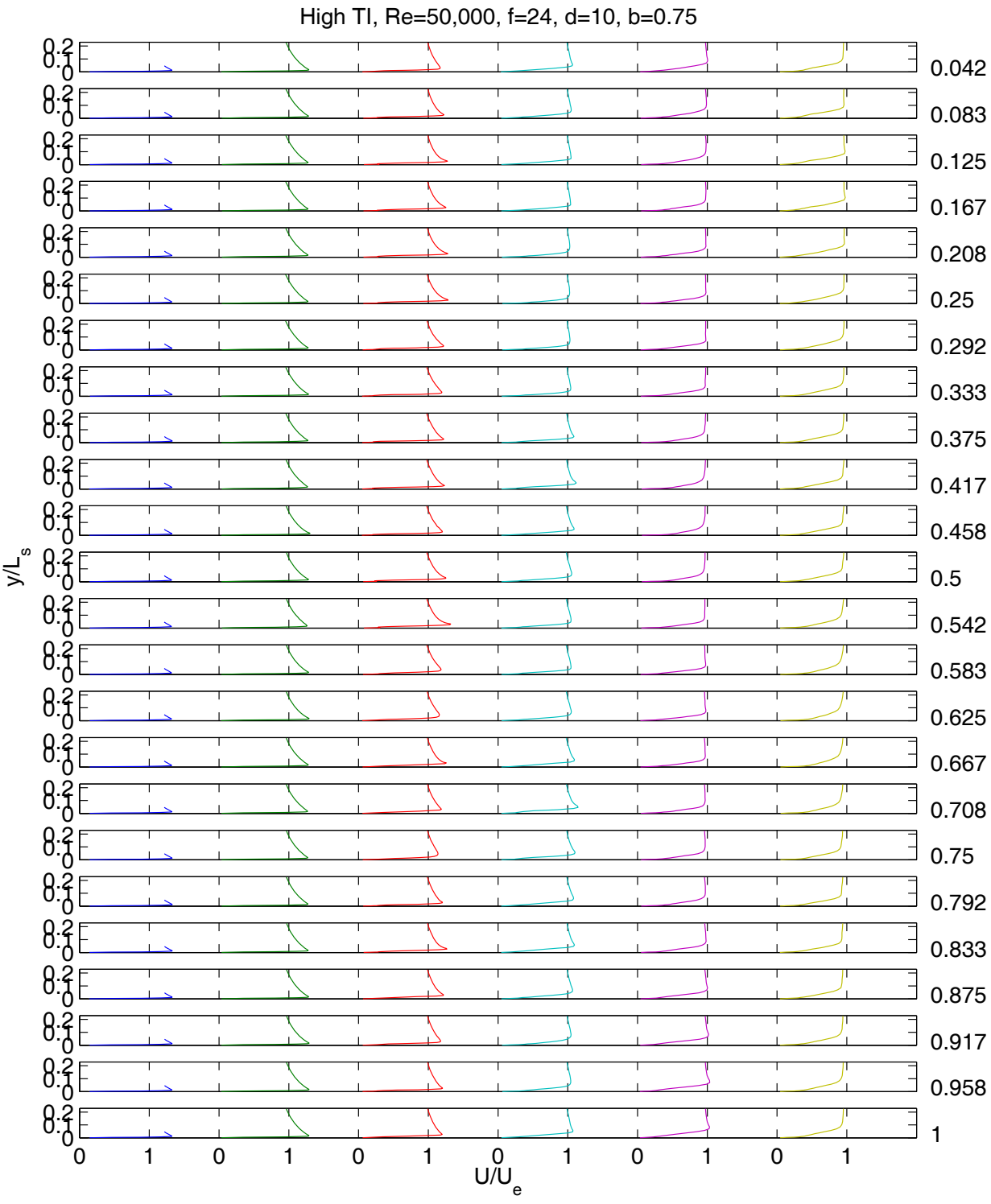
High TI, Re=50,000, f=24, d=10, b=0.75
y/L_s
U/U_e
0.042
0.083
0.125
0.167
0.208
0.25
0.292
0.333
0.375
0.417
0.458
0.5
0.542
0.583
0.625
0.667
0.708
0.75
0.792
0.833
0.875
0.917
0.958
1

a)

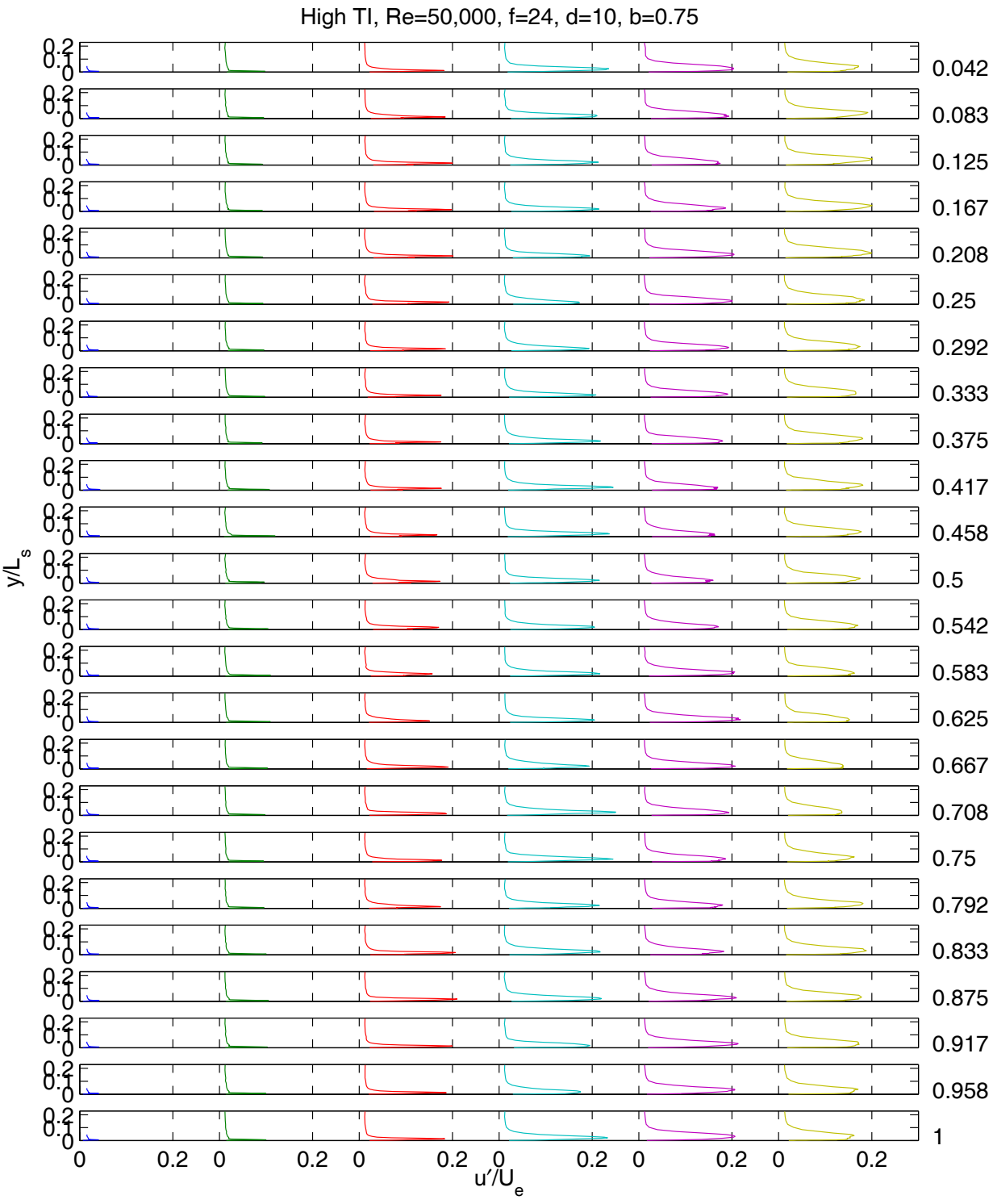

b)

Fig. 81 Phase averaged velocity profiles, high TI, Re=50,000, pulsed VGJs, F=0.56, D=10%, B=0.75: a) mean, b) rms.

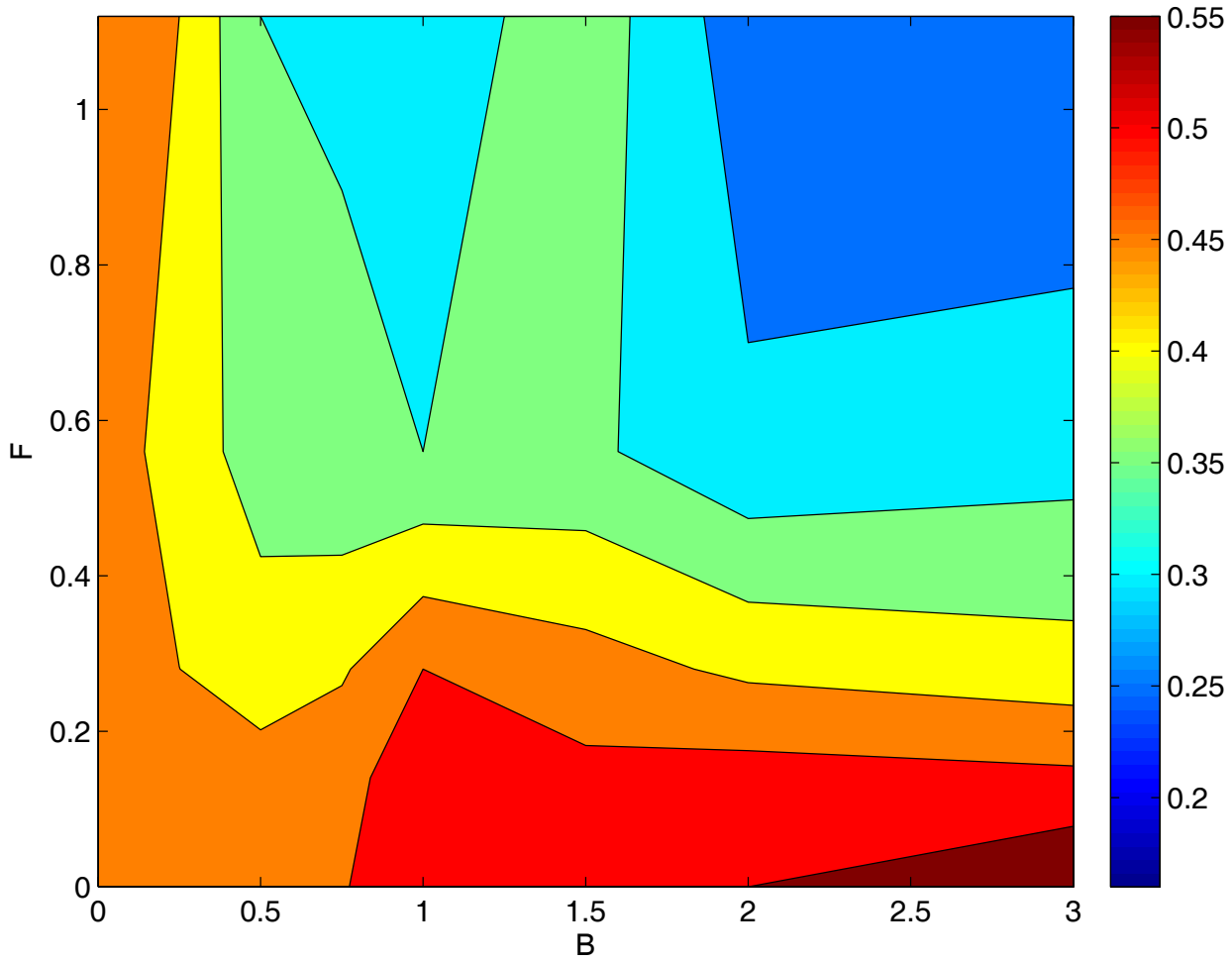

a)

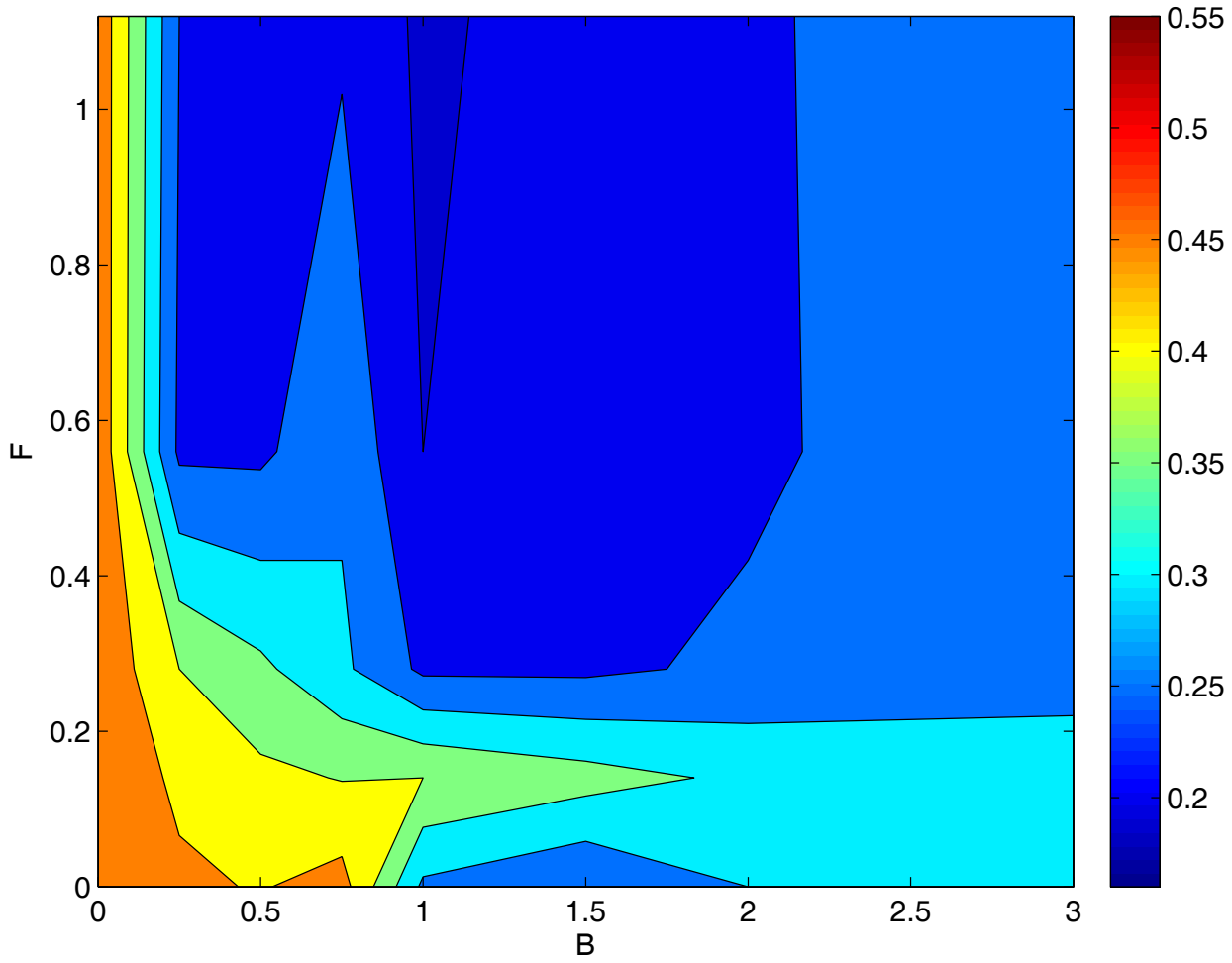

b)

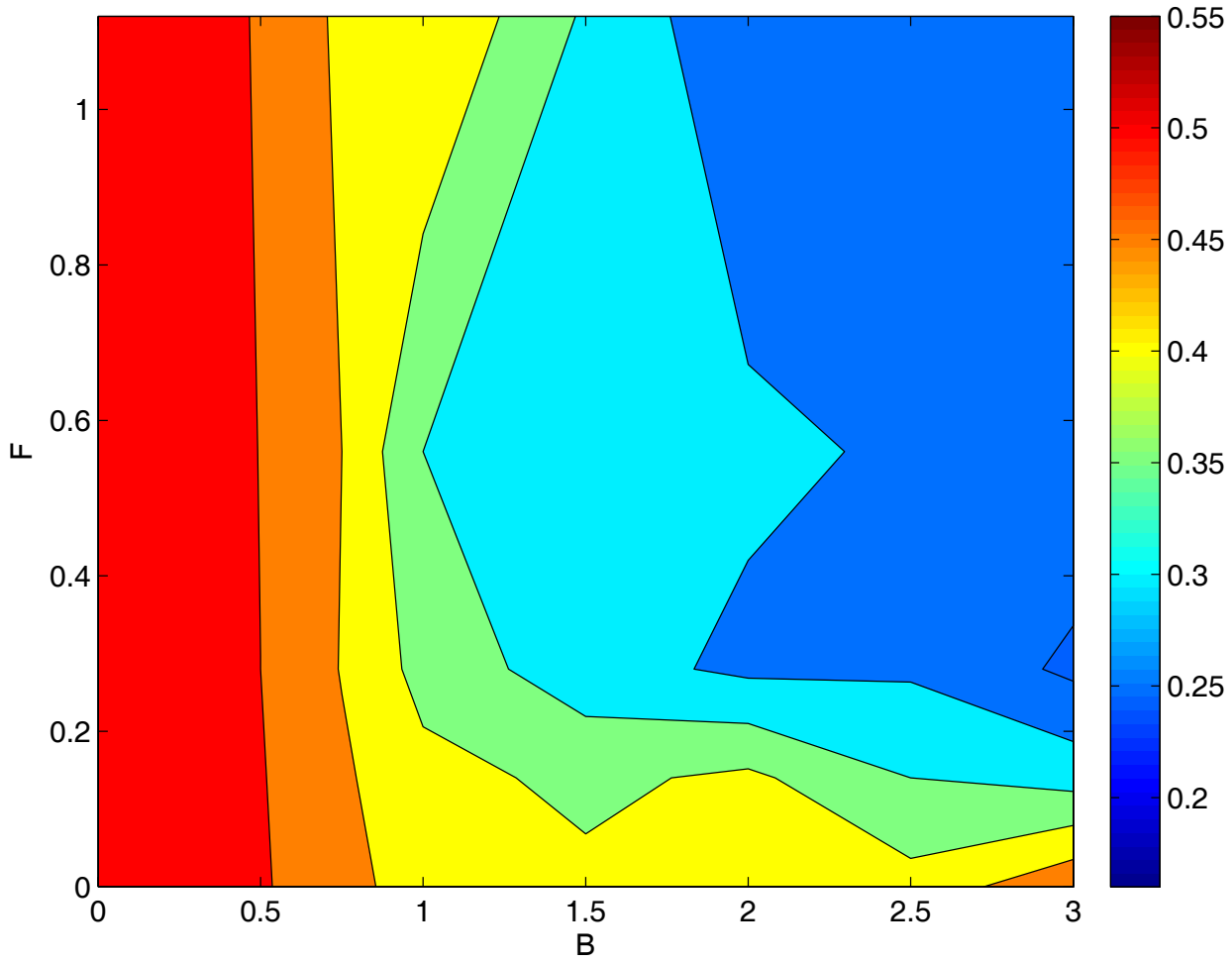

c)

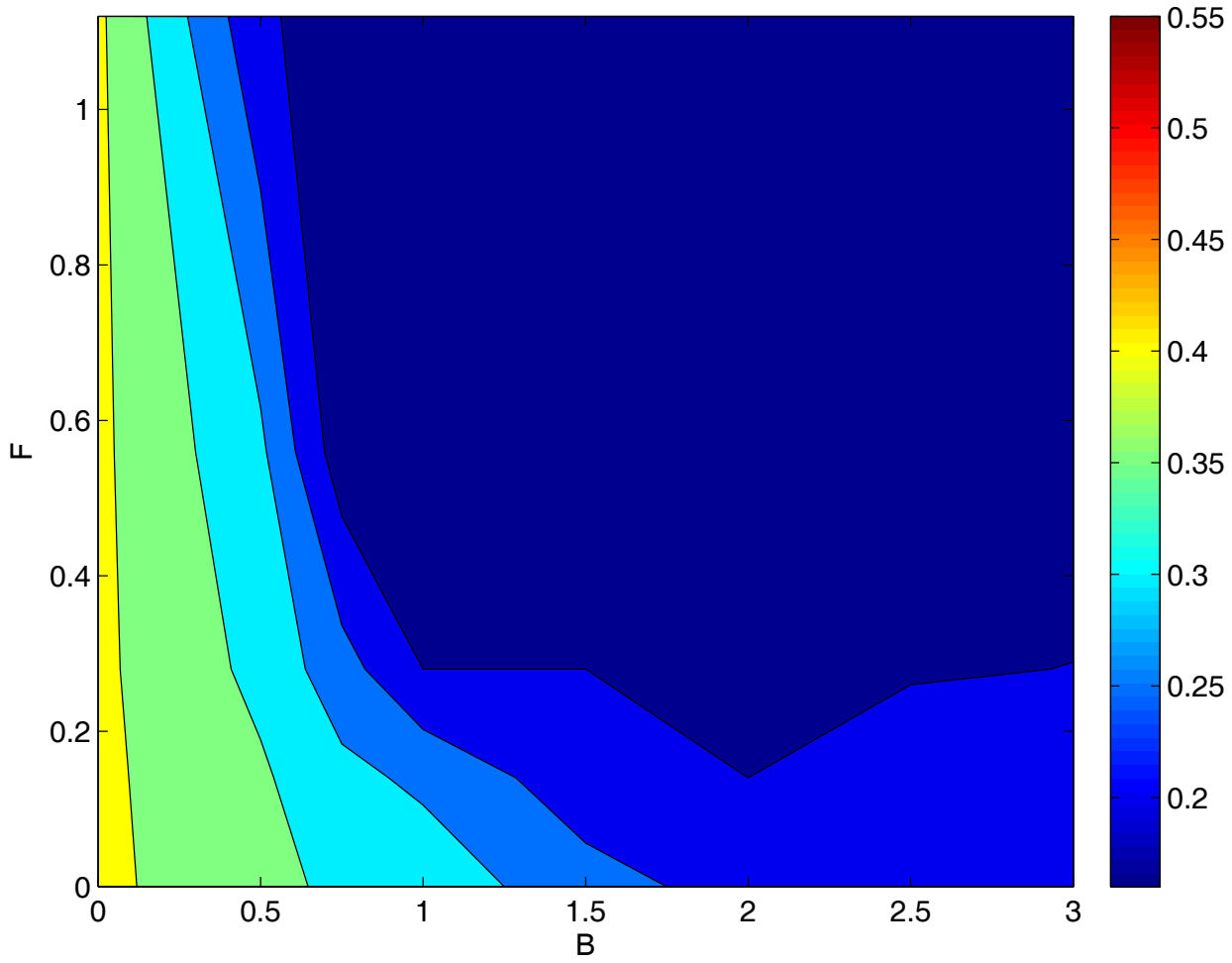

d)

Fig. 82 Integrated total pressure loss contours as function of F and B: a) low TI, Re=25,000, b) low TI, Re=50,000, c) high TI, Re=25,000, d) high TI, Re=50,000.

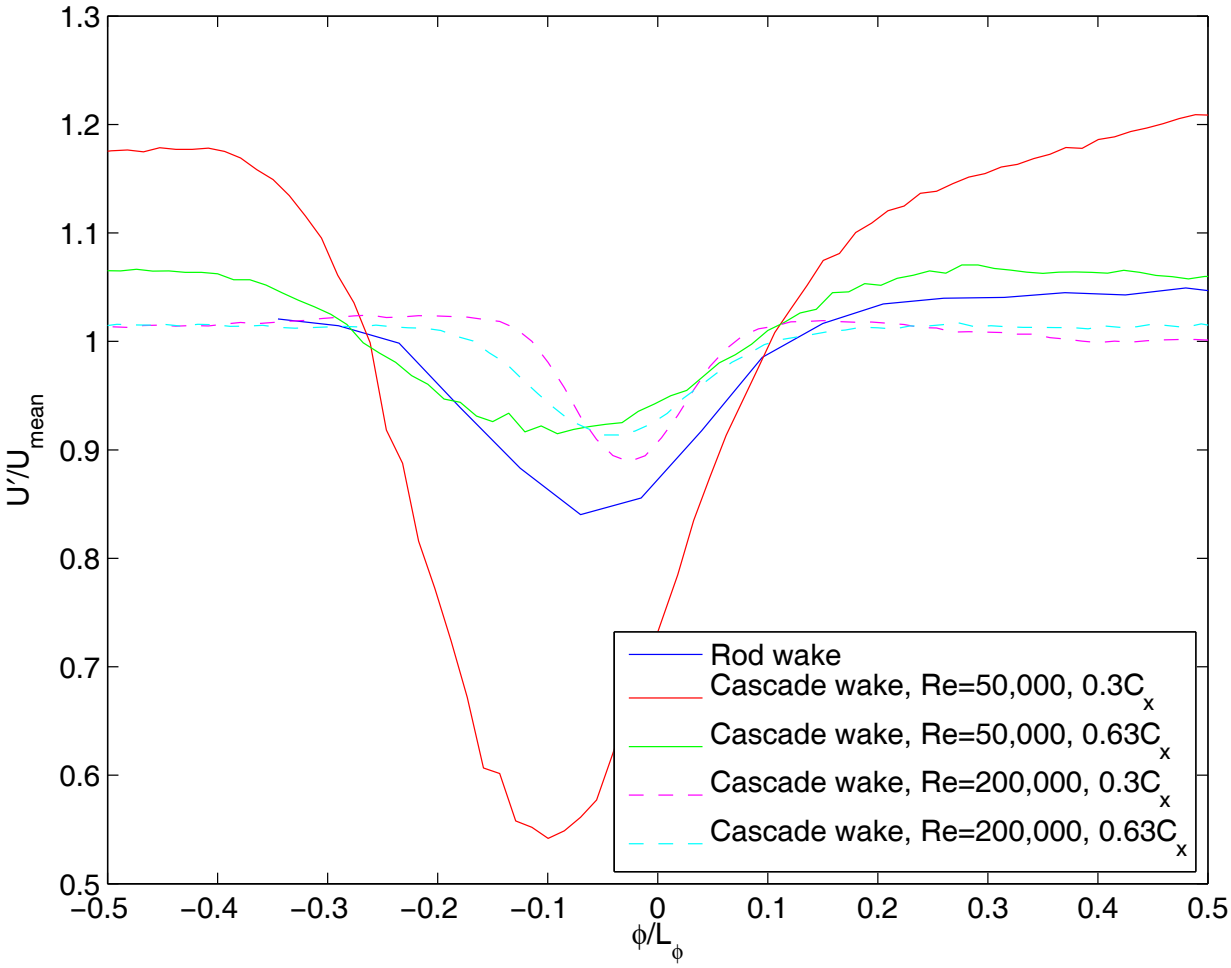
1.3
1.2
1.1
1
0.9
0.8
0.7
0.6
0.5
U'/U_mean
−0.5
−0.4
−0.3
−0.2
−0.1
0
0.1
0.2
0.3
0.4
0.5
ϕ/L_ϕ
Rod wake
Cascade wake, Re=50,000, 0.3C_x
Cascade wake, Re=50,000, 0.63C_x
Cascade wake, Re=200,000, 0.3C_x
Cascade wake, Re=200,000, 0.63C_x

a)

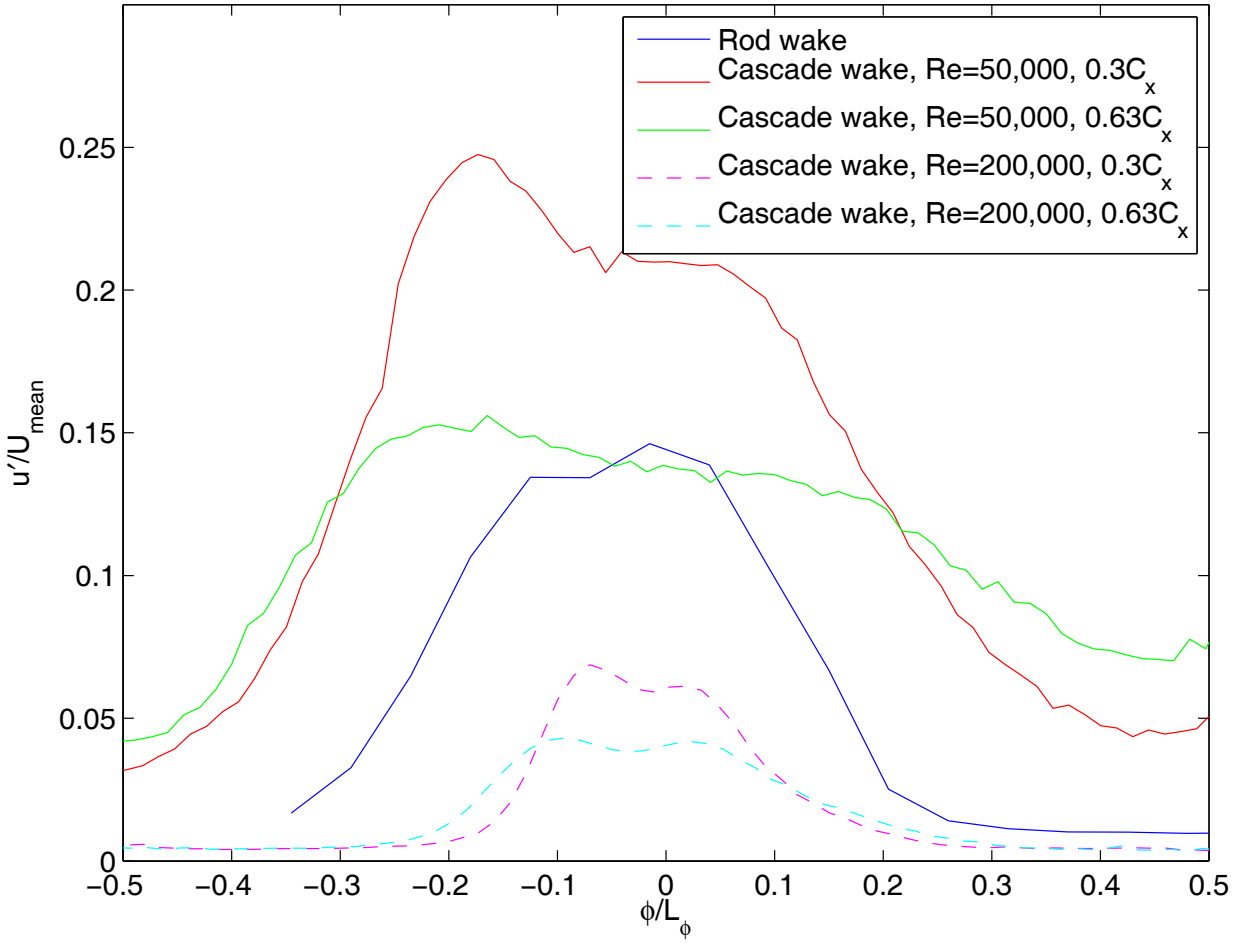

b)

Fig. 83 Velocity in wakes of cascade blades for low TI, no VGJ, no wake cases and of wake generator rods: a) mean, b) rms.

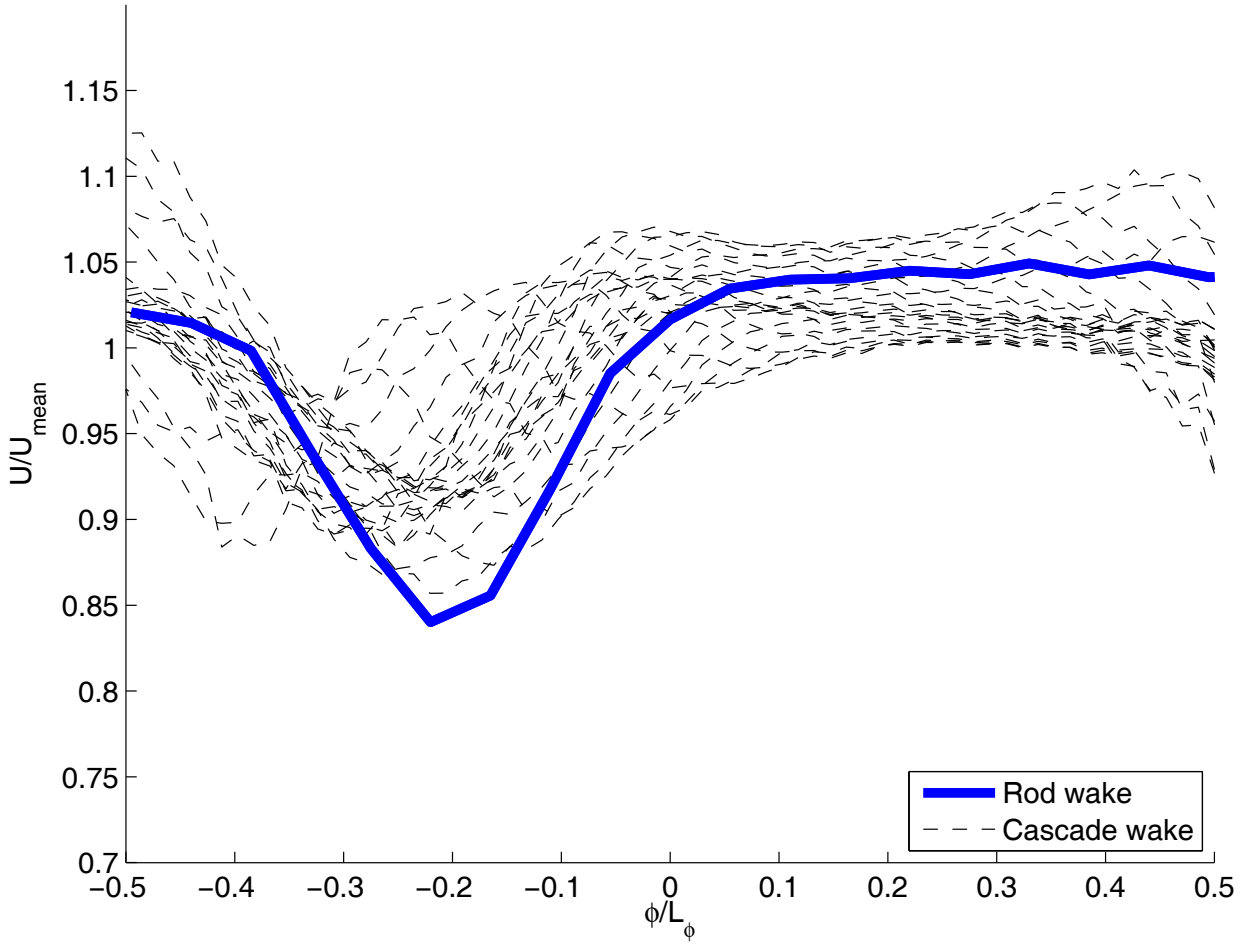
1.15
1.1
1.05
1
0.95
0.9
0.85
0.8
0.75
0.7
U/U_mean
−0.5
−0.4
−0.3
−0.2
−0.1
0
0.1
0.2
0.3
0.4
0.5
ϕ/L_ϕ
Rod wake
Cascade wake

a)

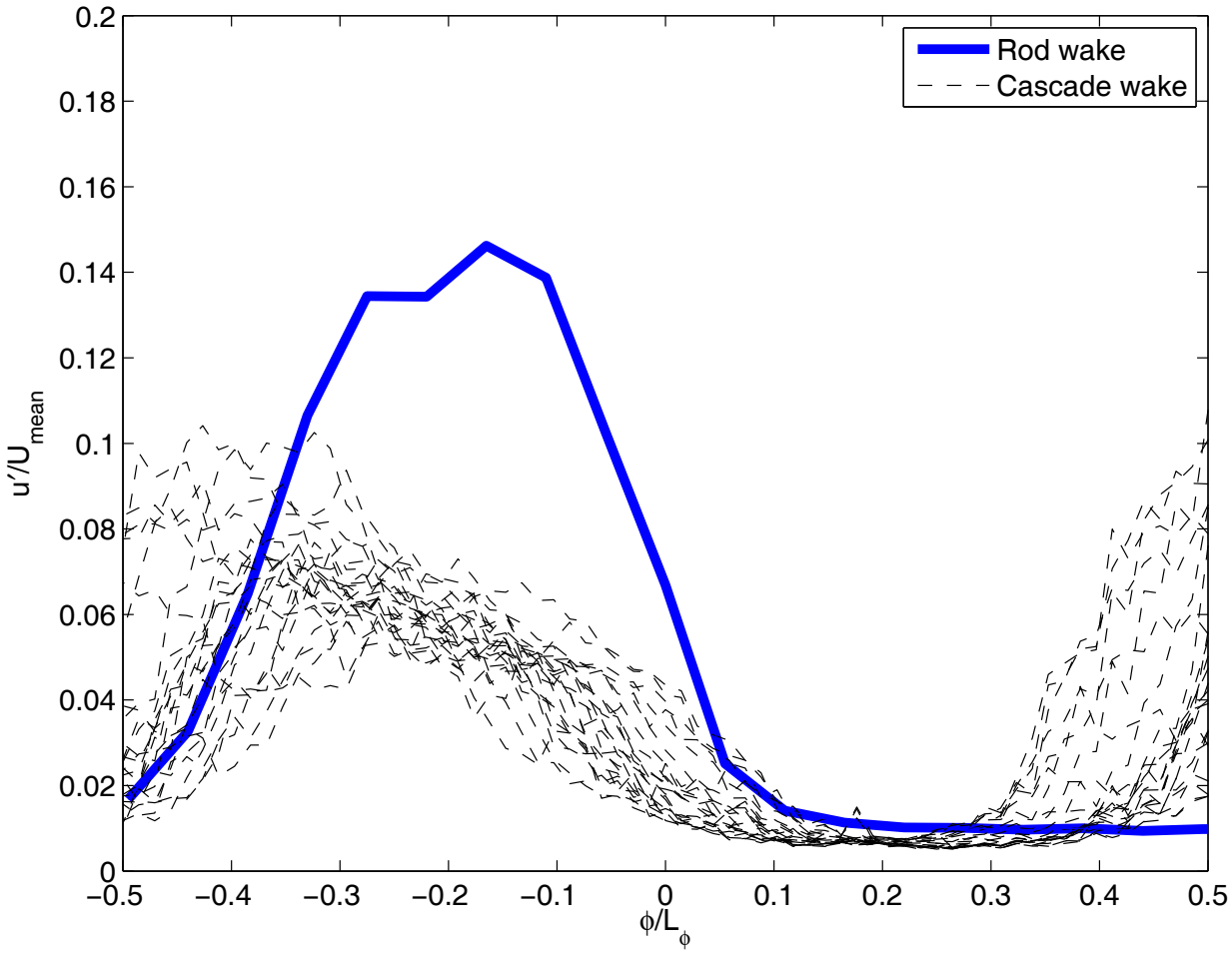

b)

Fig. 84 Phase averaged velocity in wakes of cascade blades for low TI, Re=50,000, F=0.56, D=10%, B=1.0 case and of wake generator rods: a) mean, b) rms.

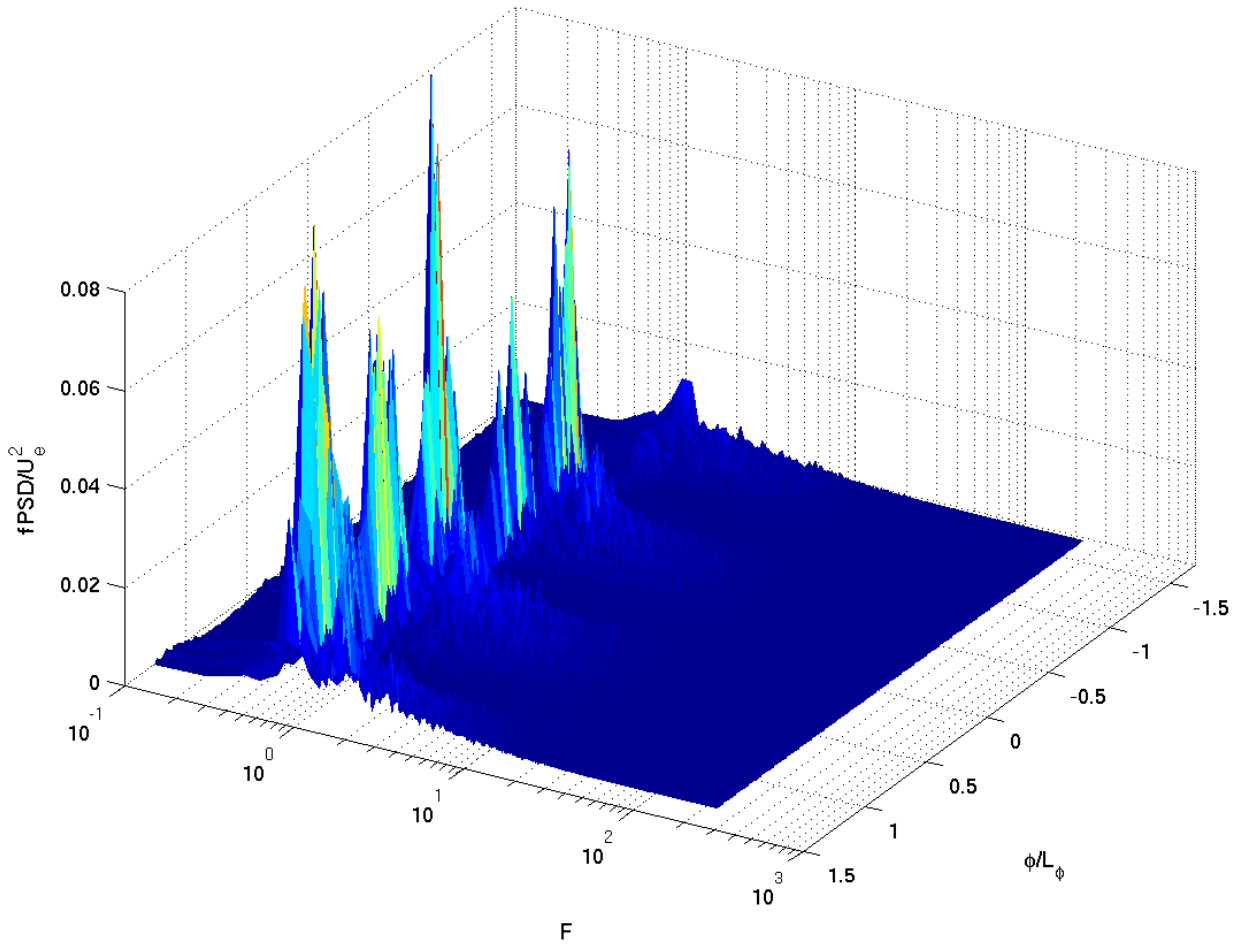
0.08
0.06
0.04
0.02
0
fPSD/U_e^2
10^-1
10^0
10^1
10^2
10^3
F
-1.5
-1
-0.5
0
0.5
1
1.5
φ/L_φ

a)

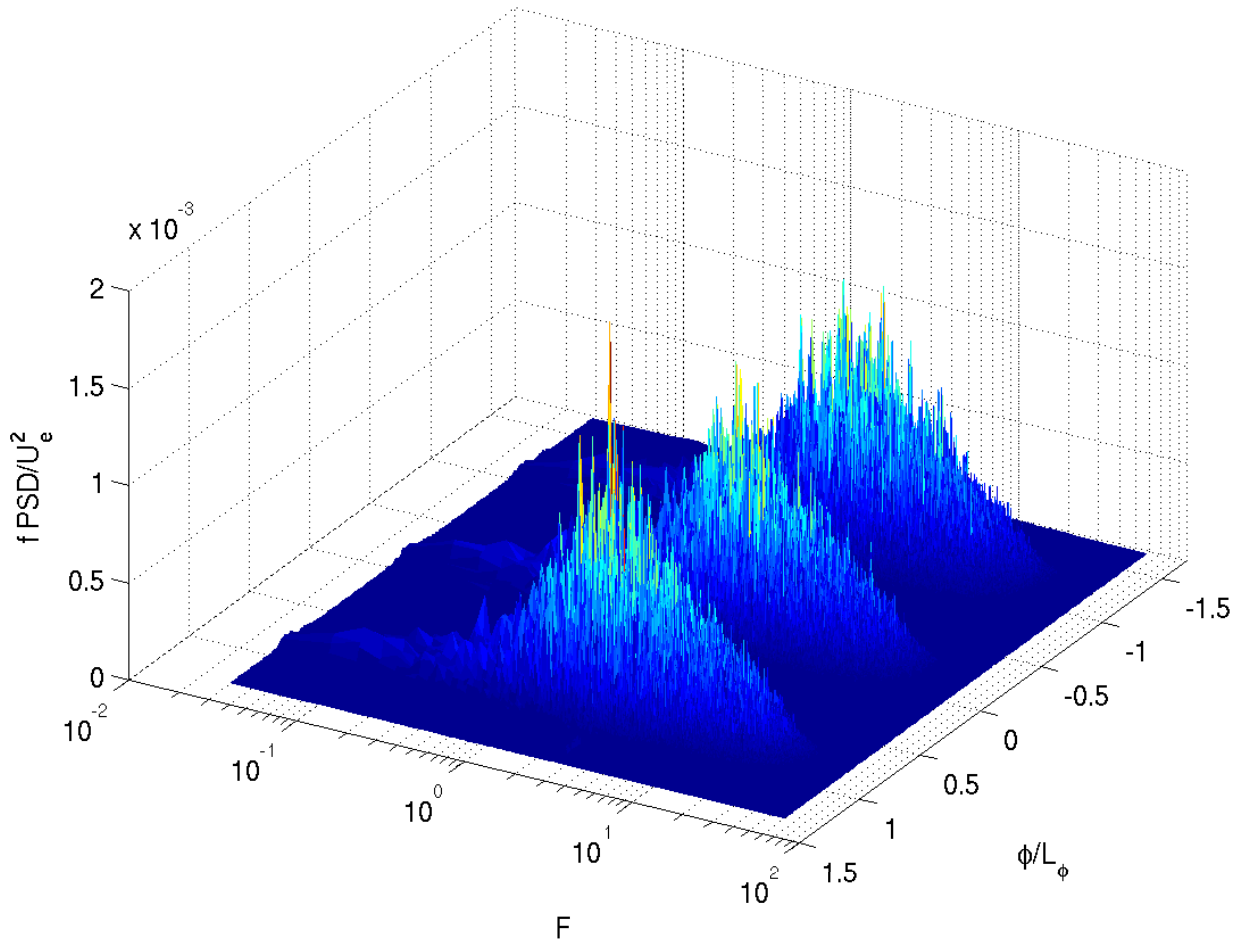

b)

Fig. 85 Fourier spectra of wake from cascade blades, no VGJs: a) Re=50,000, b) Re=200,000.

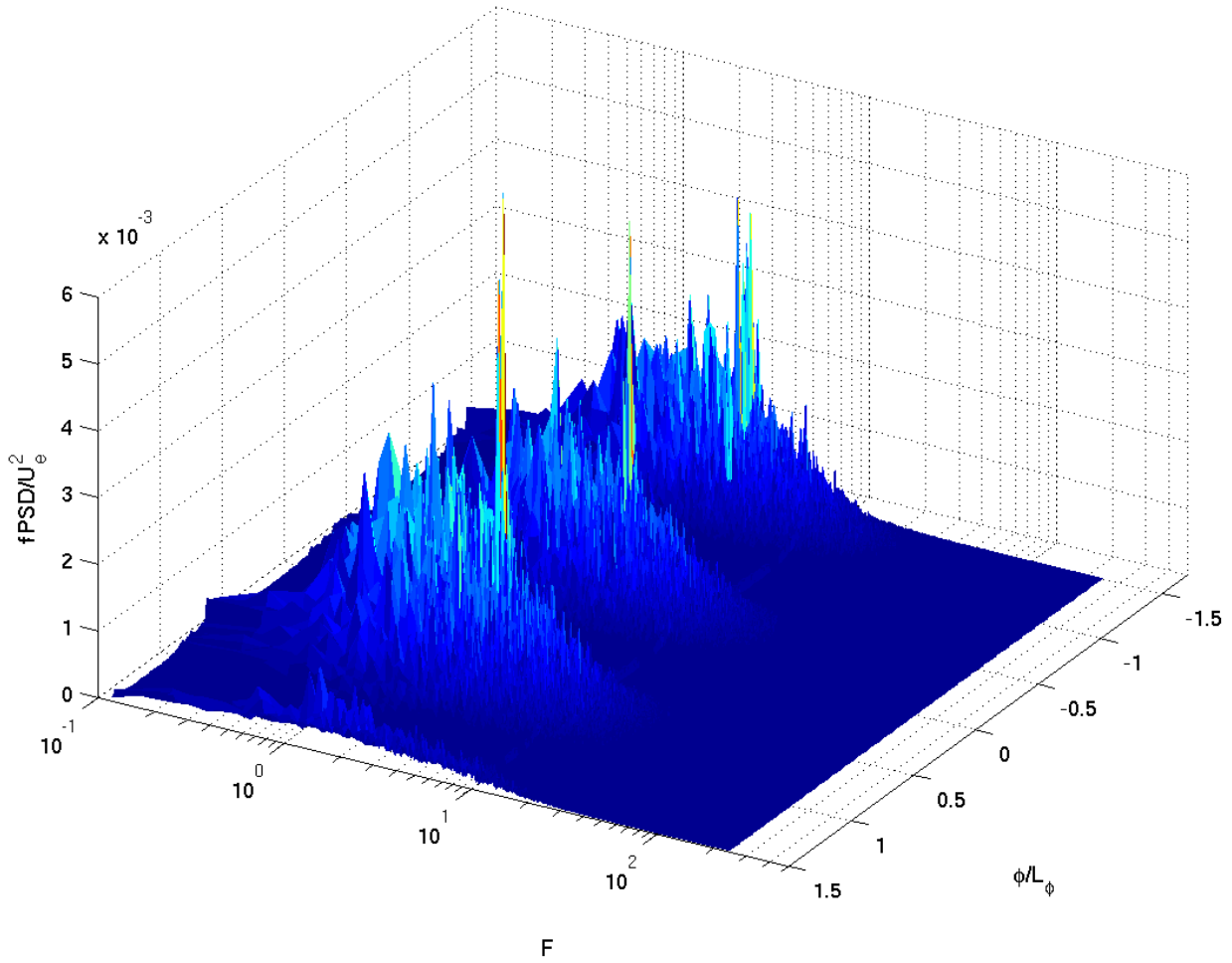

Fig. 86 Fourier spectra of wake from cascade blades, Re=50,000, pulsed VGJs, F=0.56, D=10%, B=1.0.

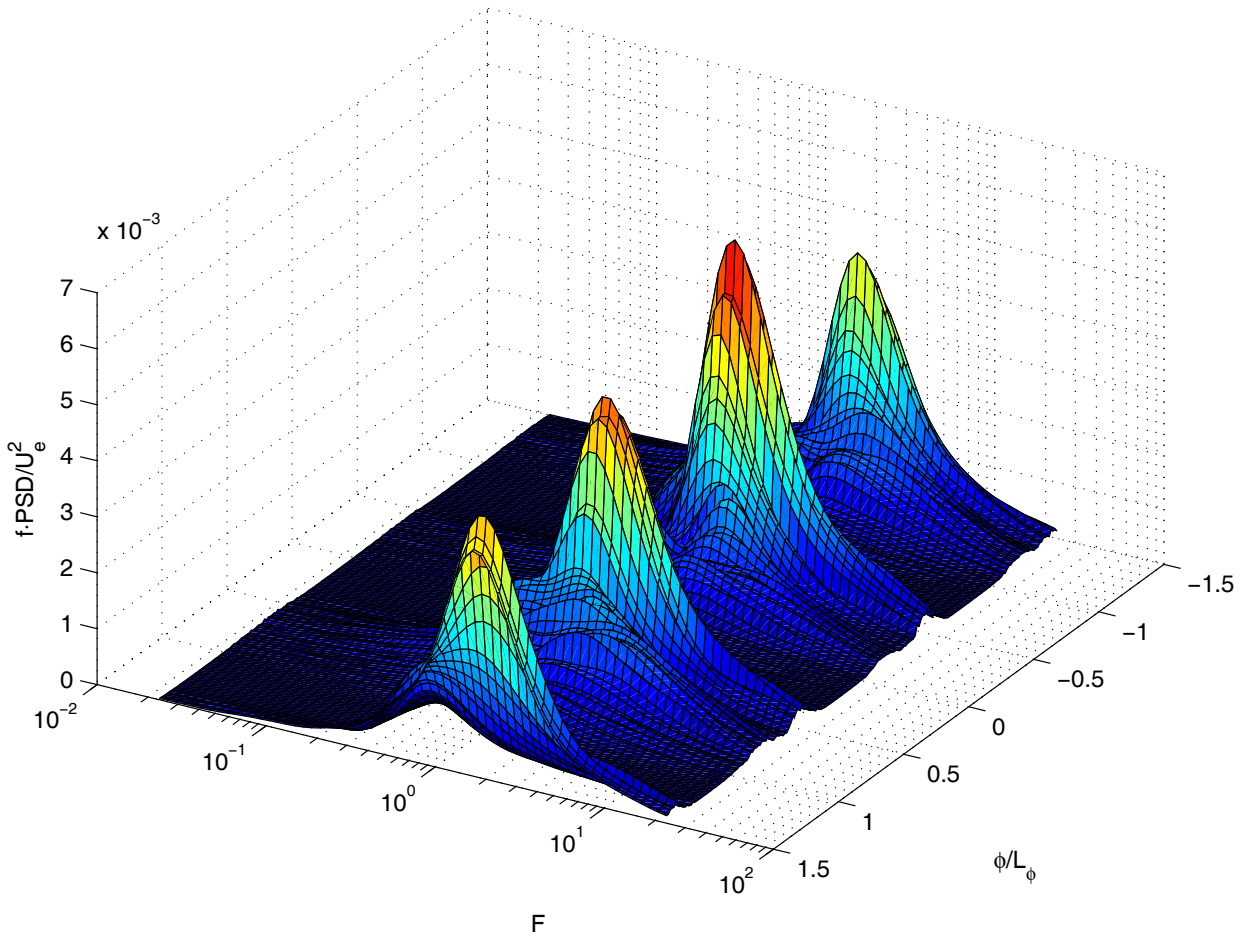

a)

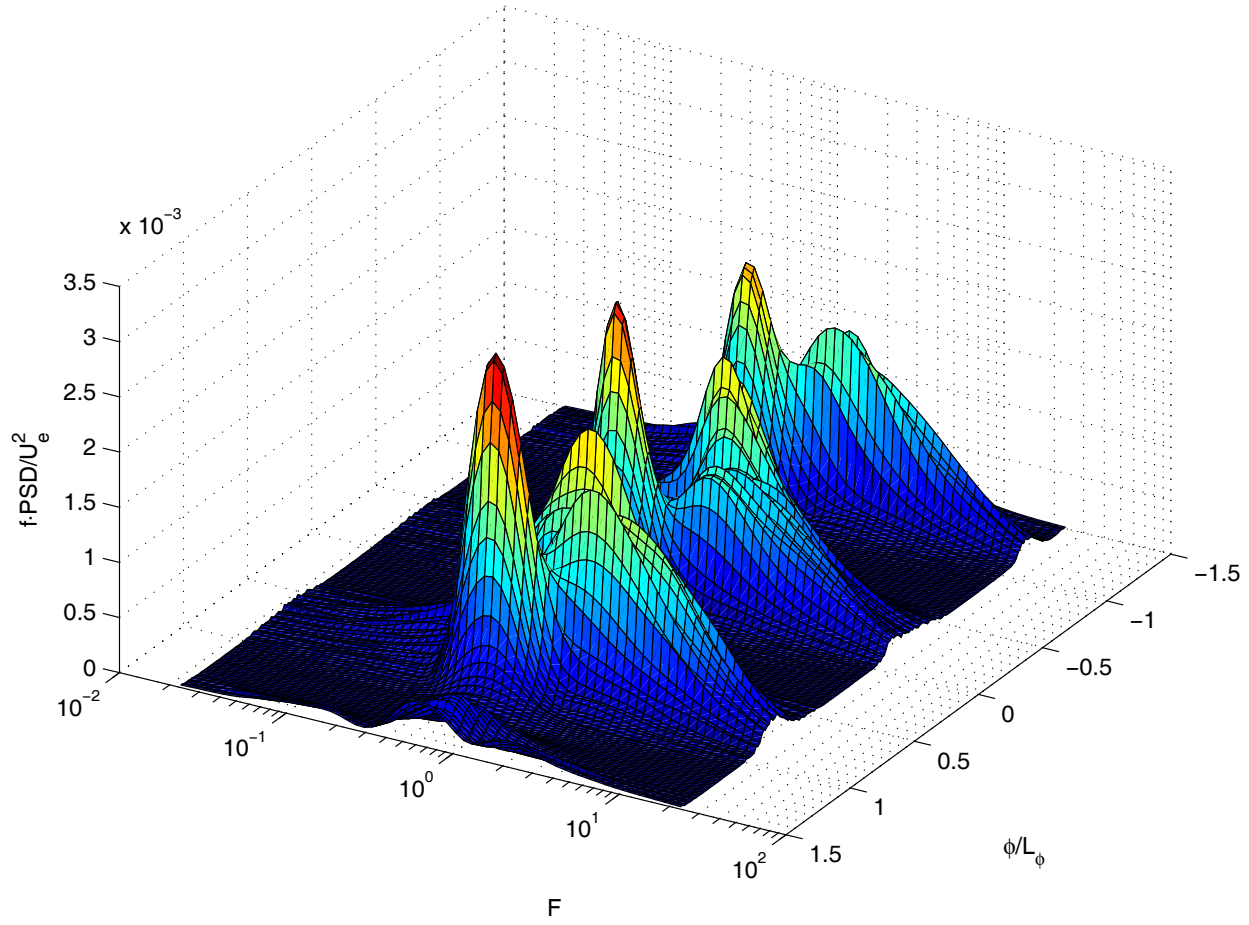
x 10^-3
3.5
3
2.5
2
1.5
1
0.5
0
f·PSD/U_e^2
10^-2
10^-1
10^0
10^1
10^2
F
1.5
1
0.5
0
−0.5
−1
−1.5
ϕ/L_ϕ

b)

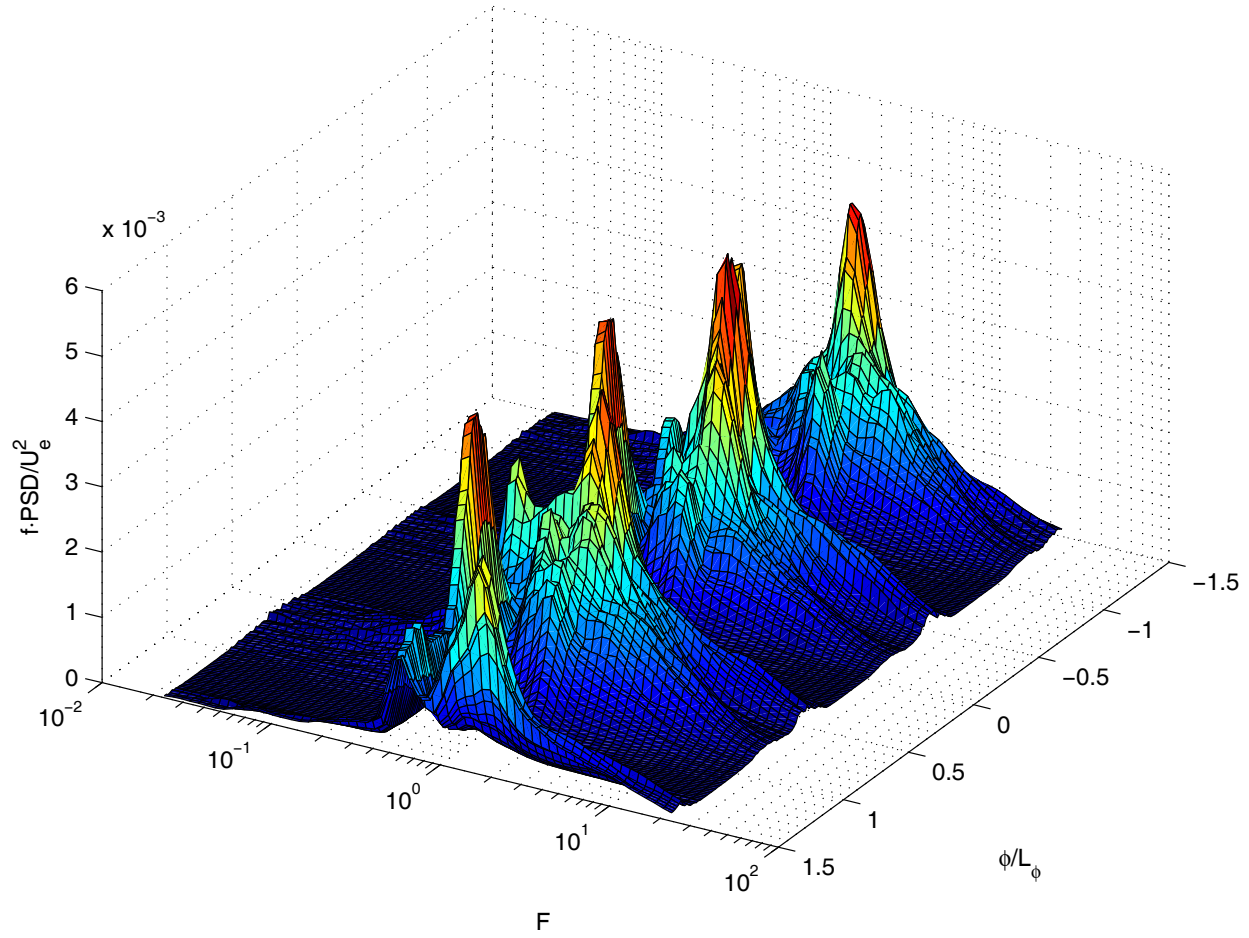

c)

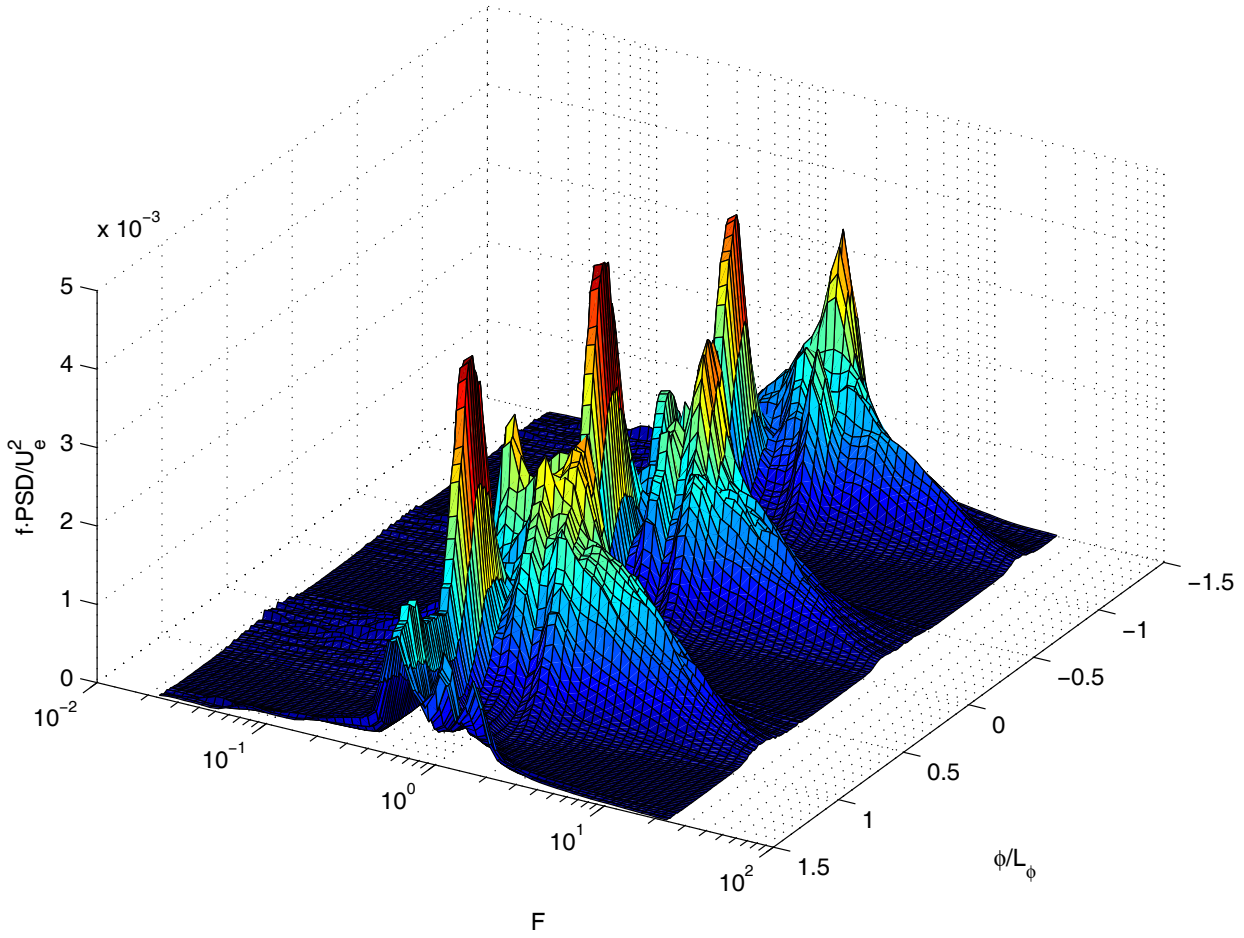

d)

Fig. 87 Wavelet spectra of wake from cascade blades, Re=50,000, pulsed VGJs, F=0.56, D=10%, B=1.0: a) Mexican Hat, t/T=0.833, b) Mexican hat, t/T=0.5, c) Morlet, t/T=0.833, d) Morlet, t/T=0.5.

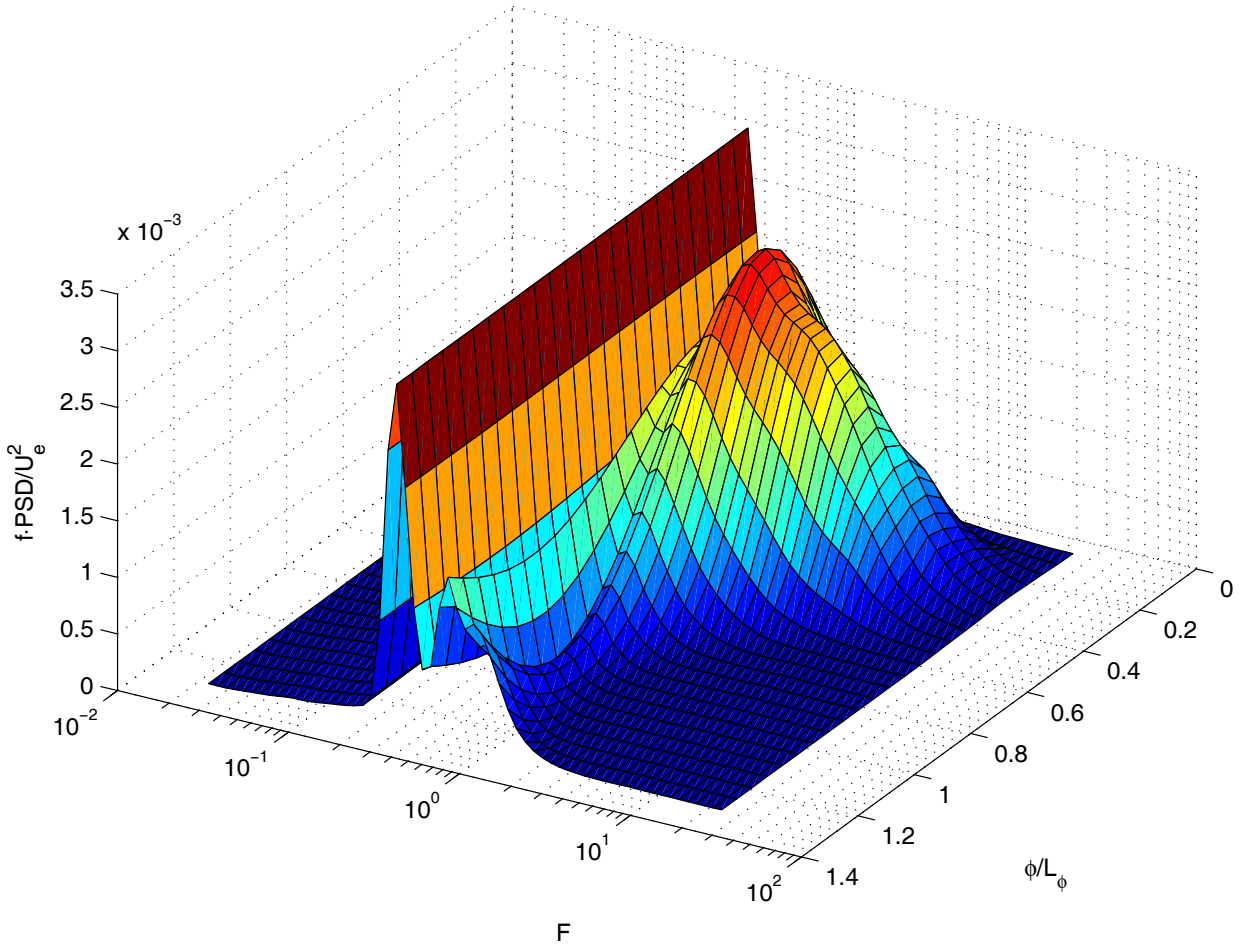
x 10^-3
3.5
3
2.5
2
1.5
1
0.5
0
f·PSD/U_e^2
10^-2
10^-1
10^0
10^1
10^2
F
0
0.2
0.4
0.6
0.8
1
1.2
1.4
ϕ/L_ϕ

a)

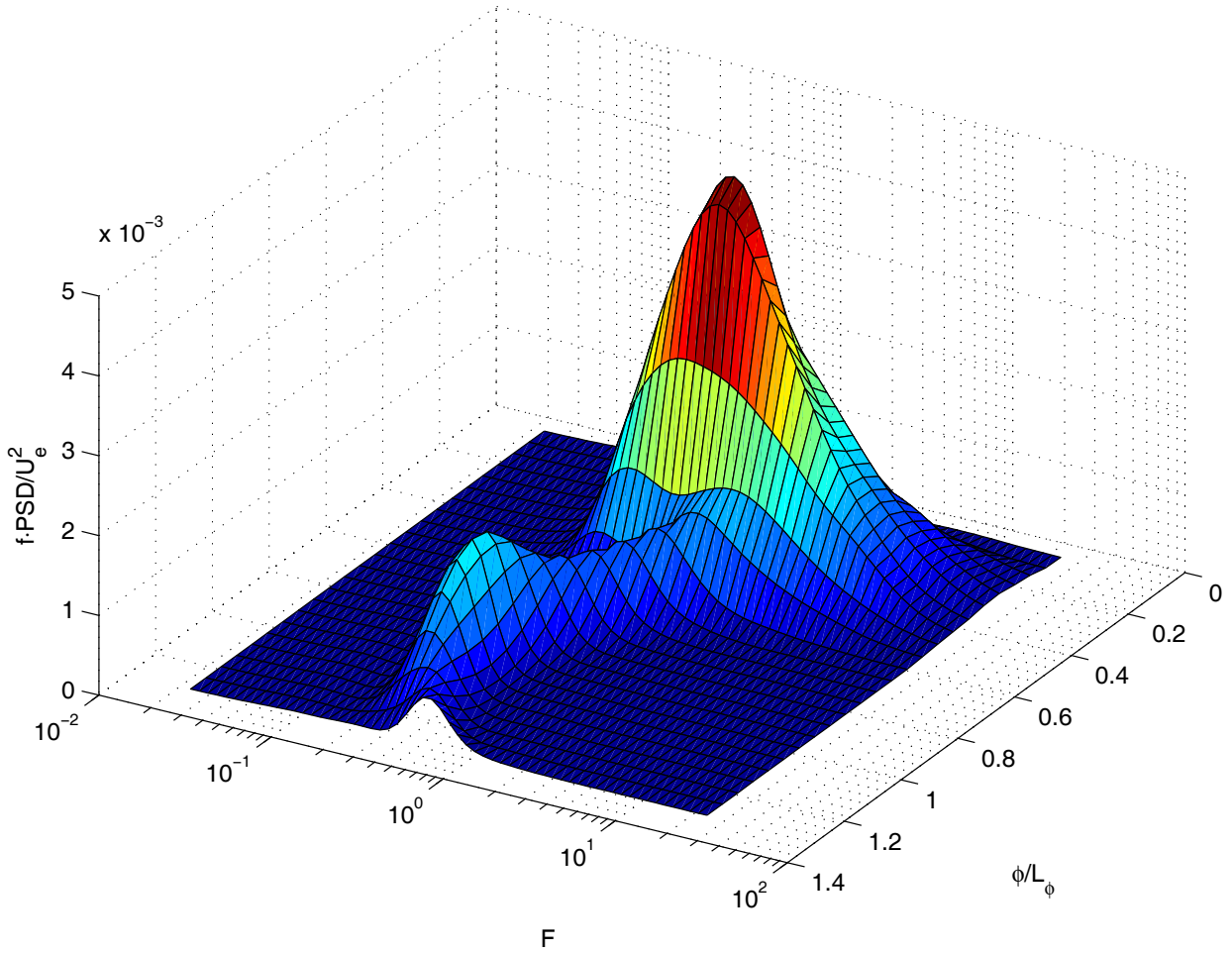

b)

Fig. 88 Wavelet spectra of wake generator rods: a) Morlet, b) Mexican Hat.

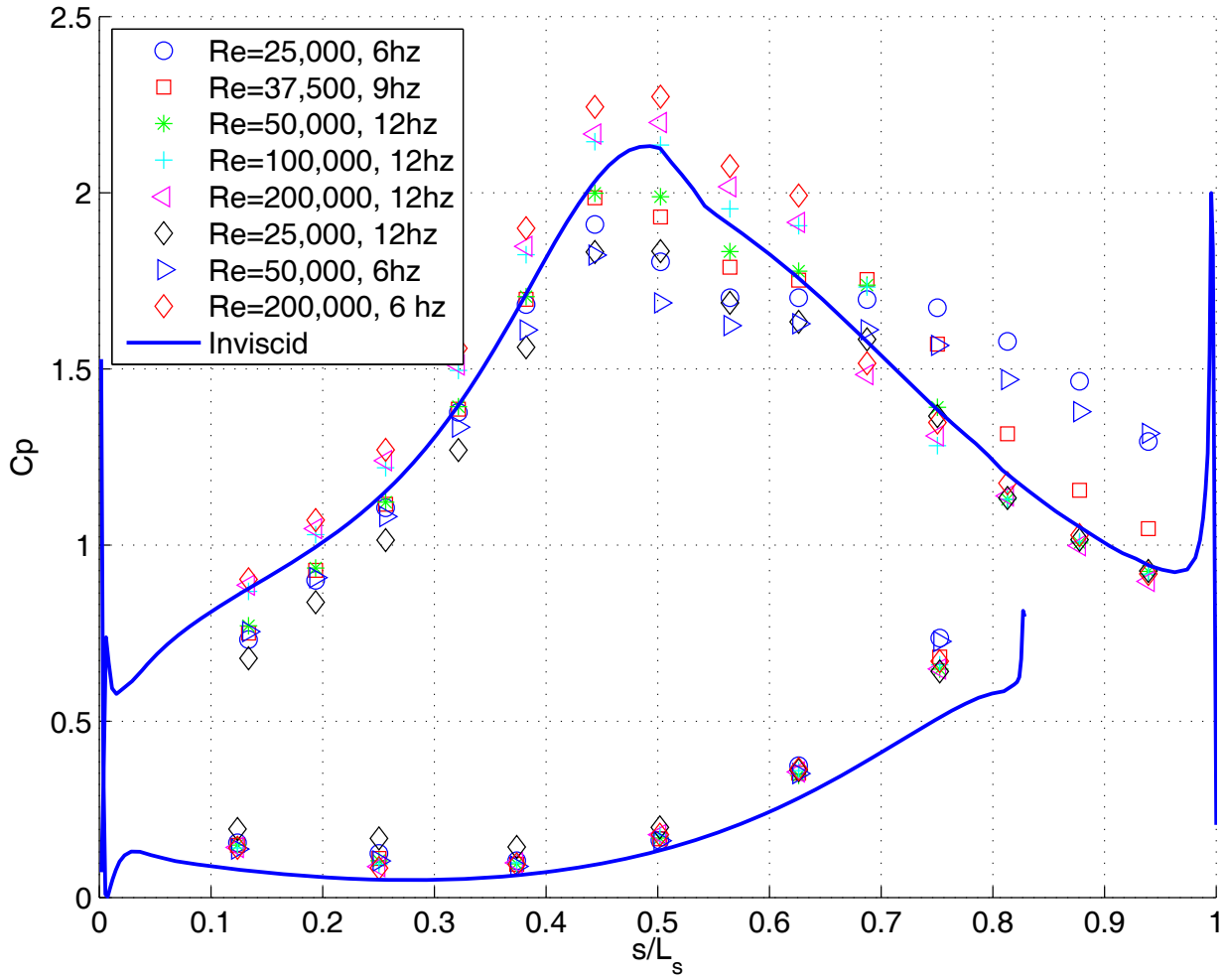

Fig. 89 Cp profiles, low TI, unsteady wakes, no VGJs.

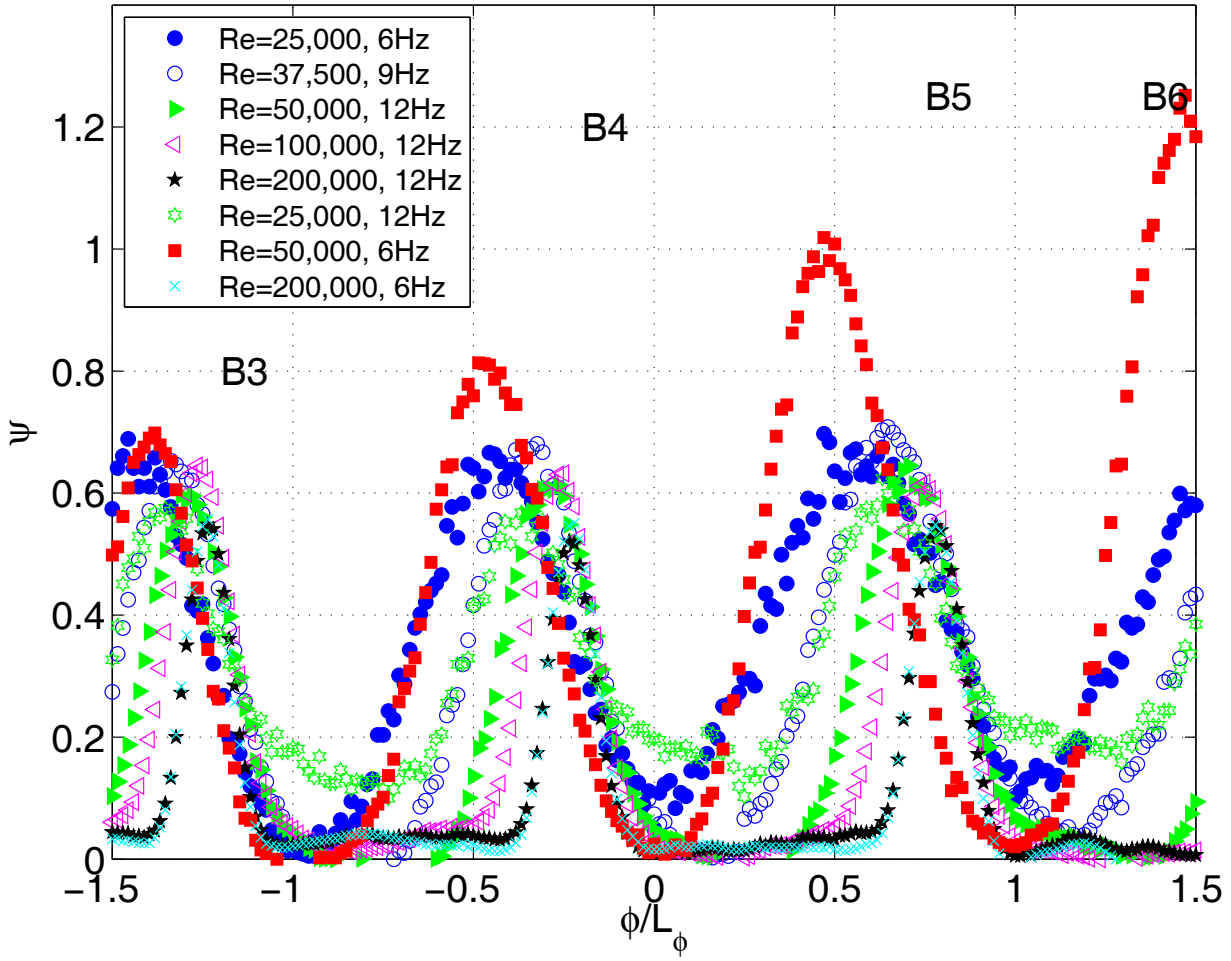

Fig. 90 Ψ profiles, low TI, unsteady wakes, no VGJs.

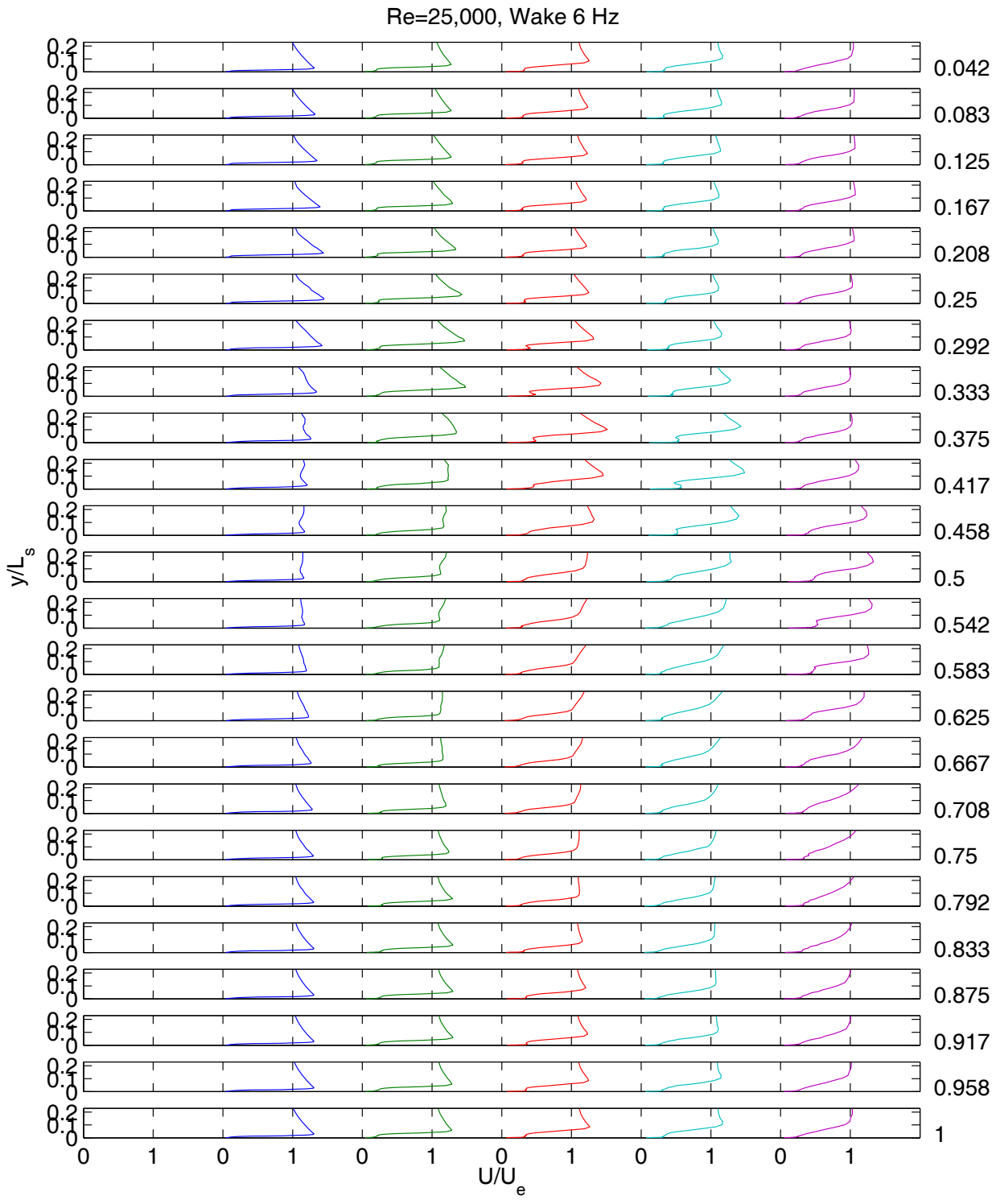
Re=25,000, Wake 6 Hz
y/L_s
U/U_e
0.042
0.083
0.125
0.167
0.208
0.25
0.292
0.333
0.375
0.417
0.458
0.5
0.542
0.583
0.625
0.667
0.708
0.75
0.792
0.833
0.875
0.917
0.958
1

a)

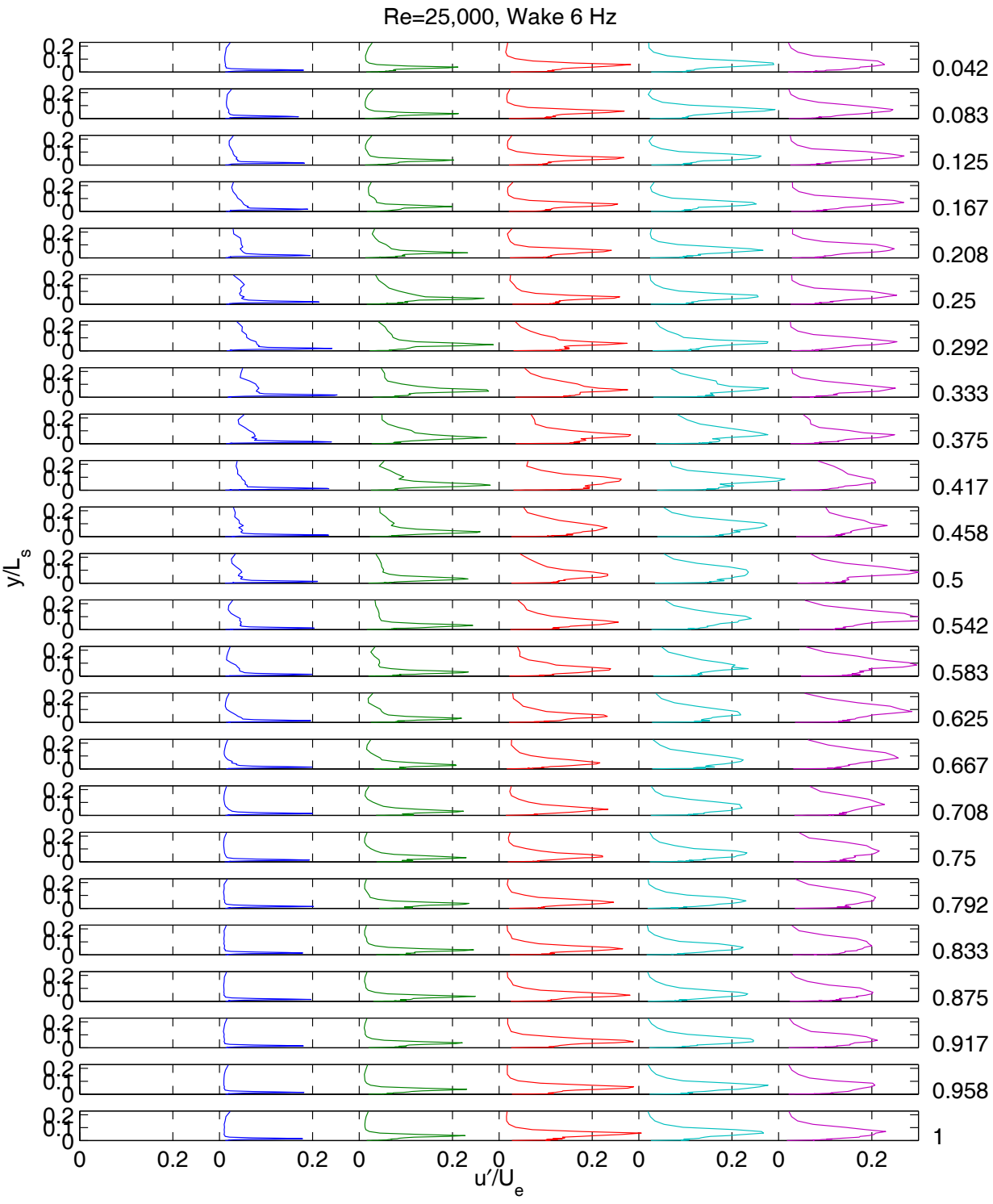

b)

Fig. 91 Phase averaged velocity profiles, low TI, Re=25,000, F=0.28 wakes: a) mean, b) rms.

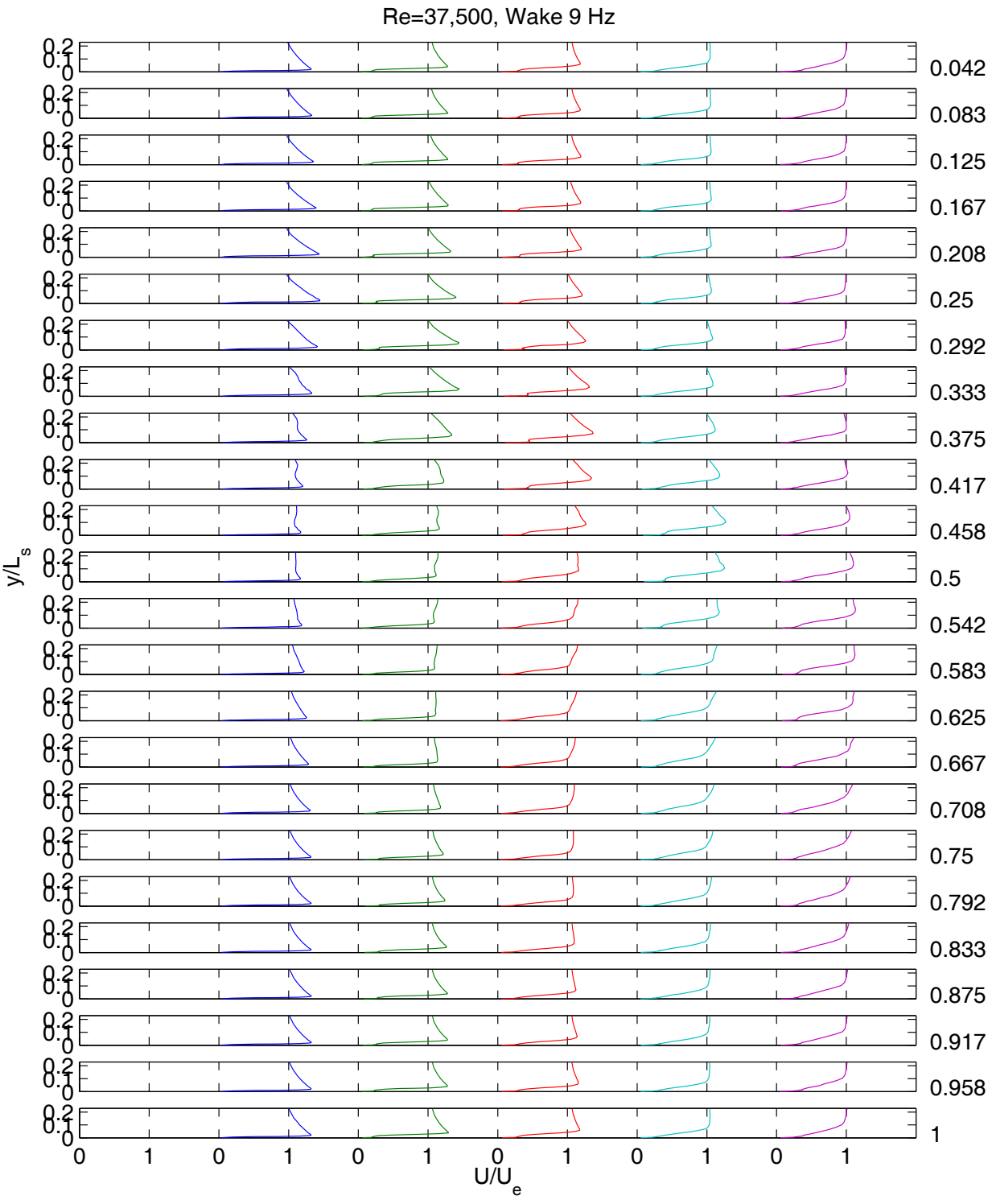
Re=37,500, Wake 9 Hz
y/L_s
U/U_e
0.042
0.083
0.125
0.167
0.208
0.25
0.292
0.333
0.375
0.417
0.458
0.5
0.542
0.583
0.625
0.667
0.708
0.75
0.792
0.833
0.875
0.917
0.958
1

a)

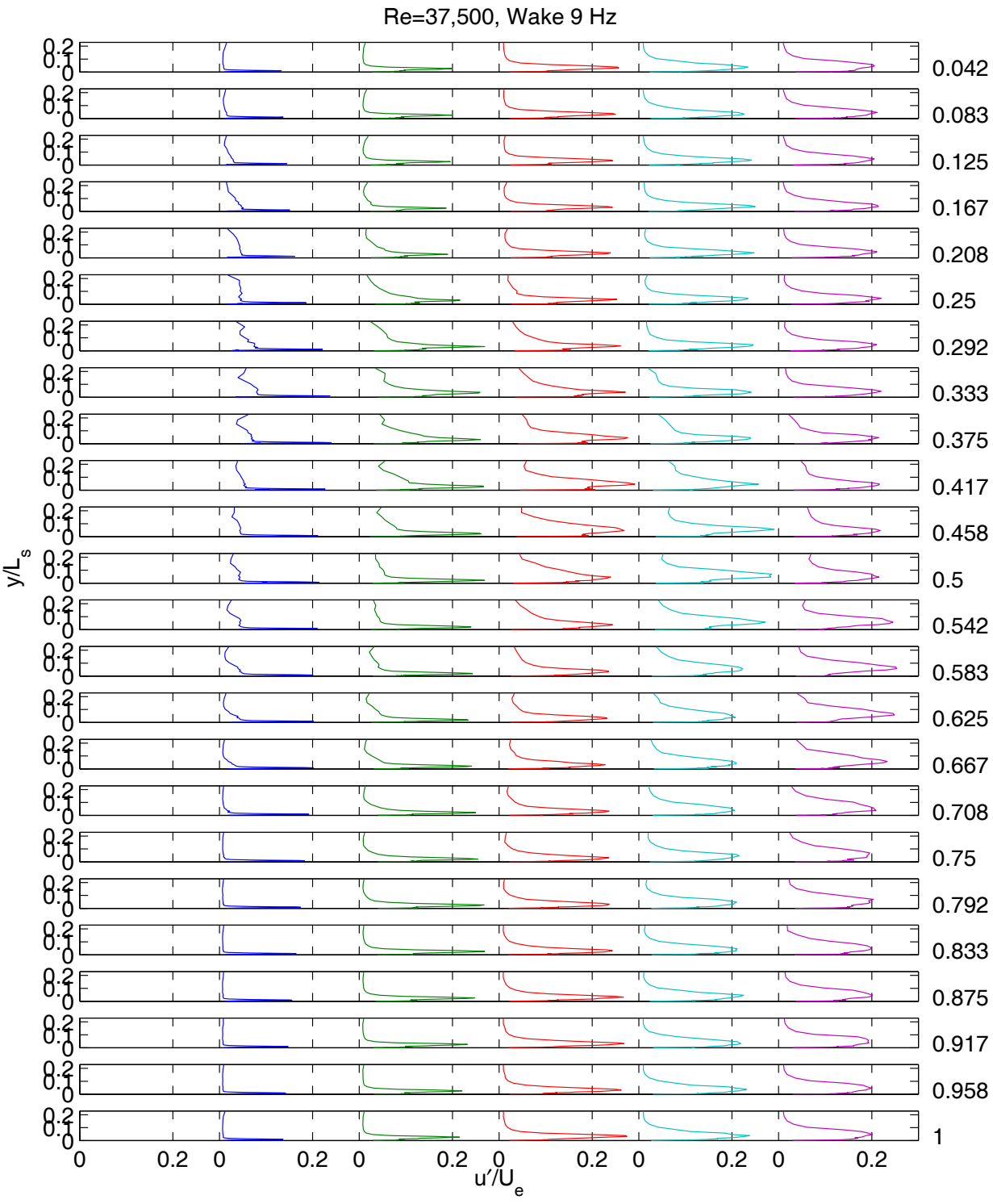

b)

Fig. 92 Phase averaged velocity profiles, low TI, Re=37,500, F=0.28 wakes: a) mean, b) rms.

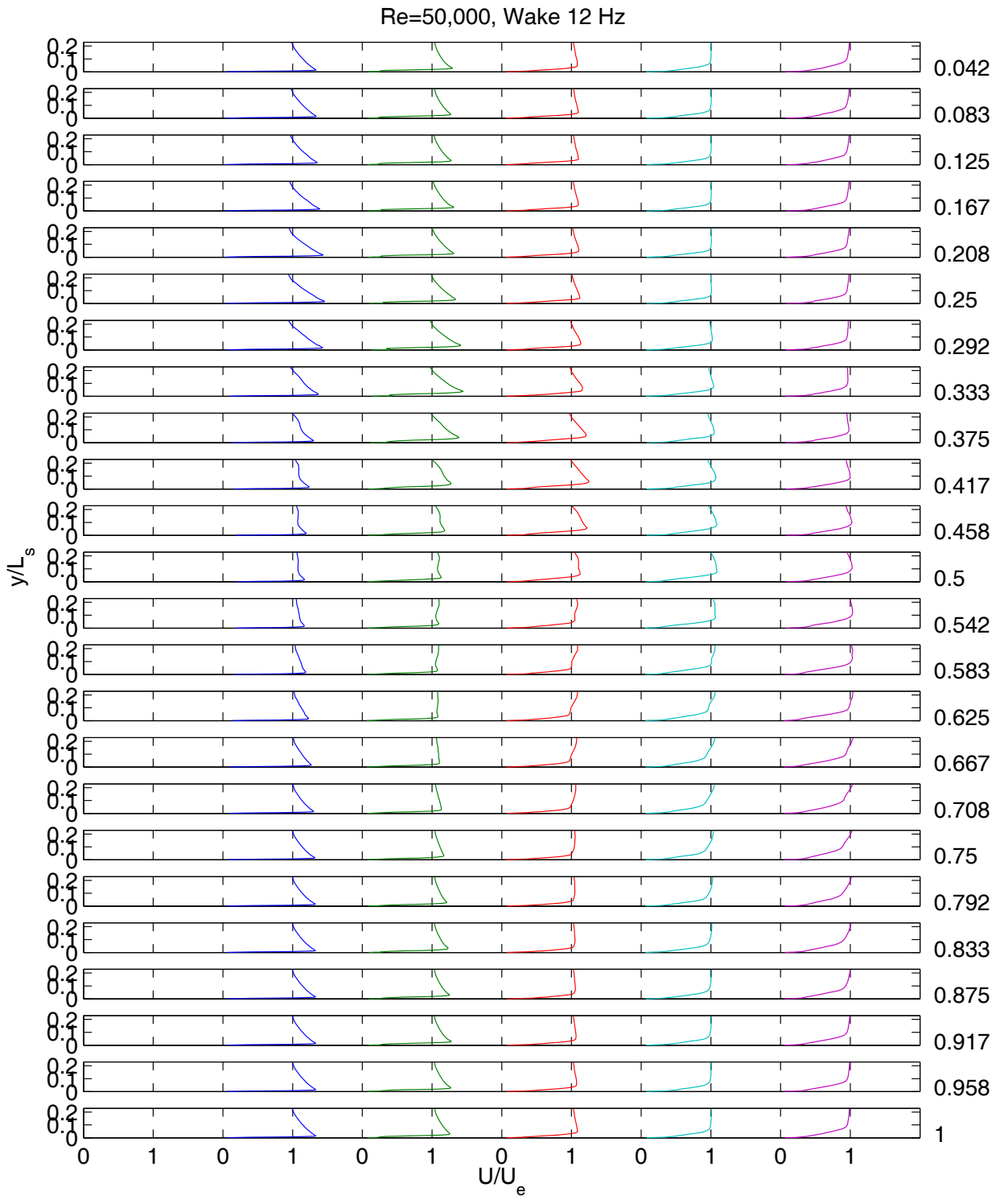
Re=50,000, Wake 12 Hz
y/L_s
U/U_e
0.042
0.083
0.125
0.167
0.208
0.25
0.292
0.333
0.375
0.417
0.458
0.5
0.542
0.583
0.625
0.667
0.708
0.75
0.792
0.833
0.875
0.917
0.958
1

a)

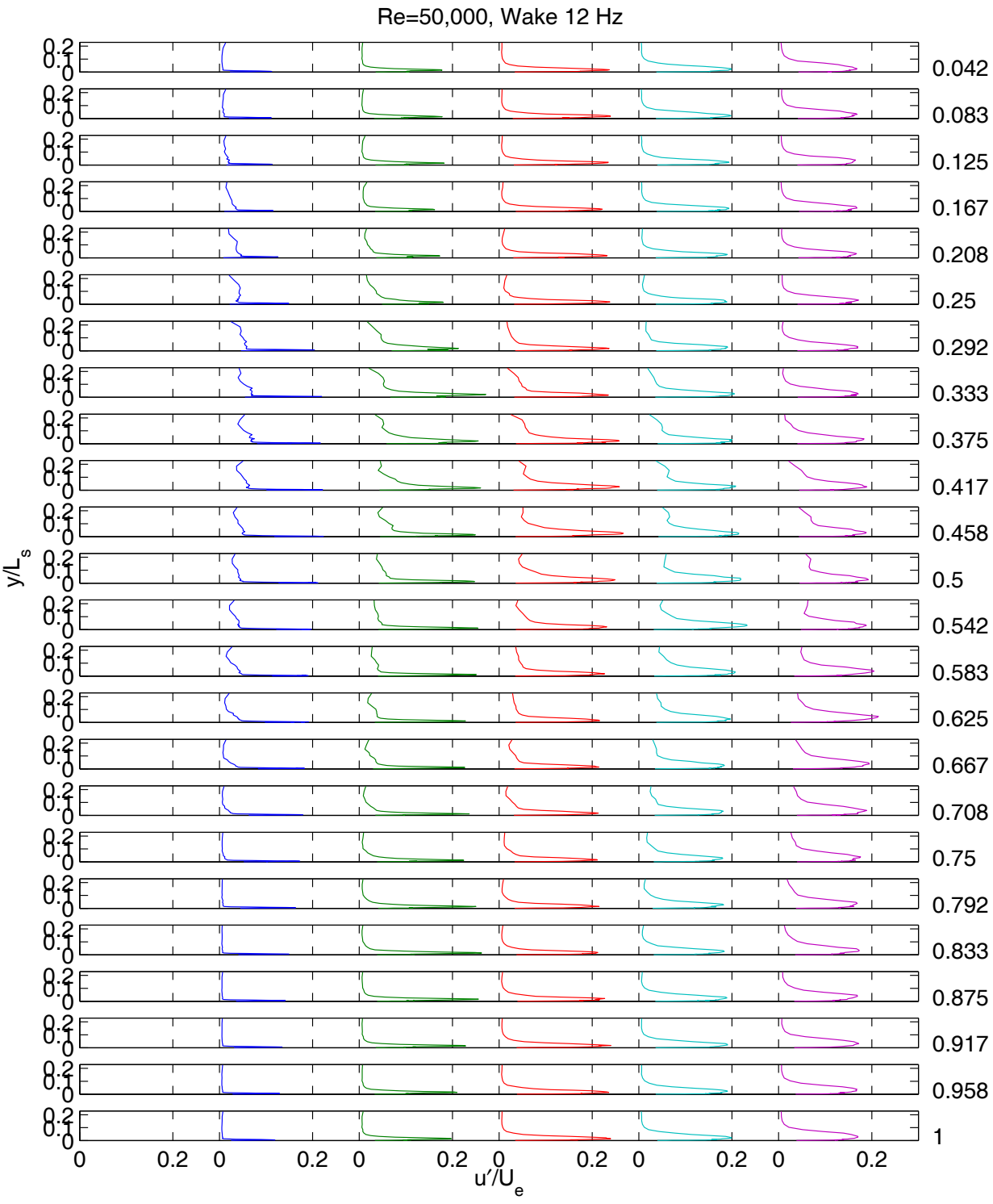

b)

Fig. 93 Phase averaged velocity profiles, low TI, Re=50,000, F=0.28 wakes: a) mean, b) rms.

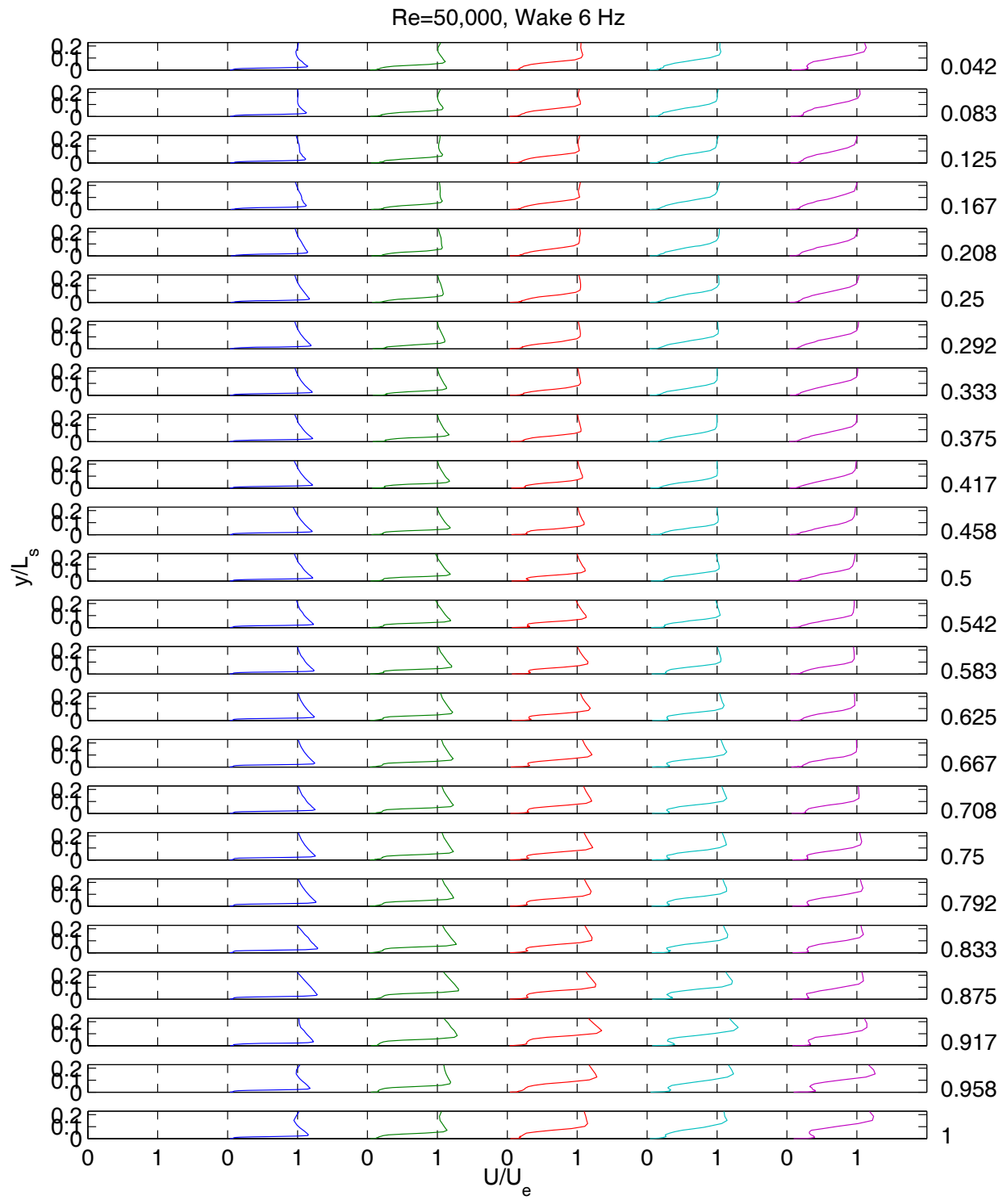
Re=50,000, Wake 6 Hz
y/L_s
U/U_e
0.042
0.083
0.125
0.167
0.208
0.25
0.292
0.333
0.375
0.417
0.458
0.5
0.542
0.583
0.625
0.667
0.708
0.75
0.792
0.833
0.875
0.917
0.958
1

a)

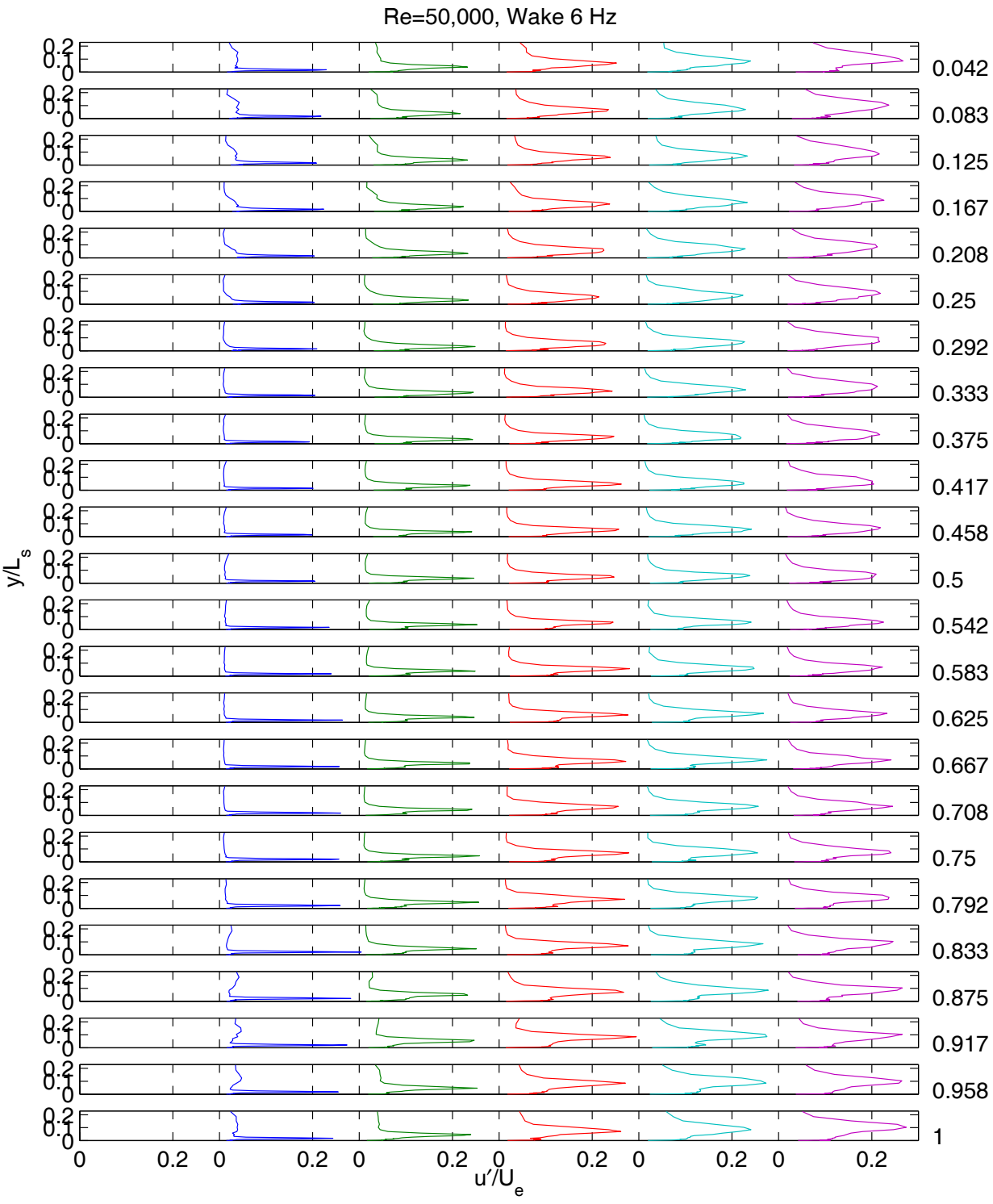

b)

Fig. 94 Phase averaged velocity profiles, low TI, Re=50,000, F=0.14 wakes: a) mean, b) rms.

The following figures show phase averaged velocity and turbulence profiles for cases with VGJs and wakes with various timings. The names for the timings correspond to the original data file names and not the new names used in conference papers.

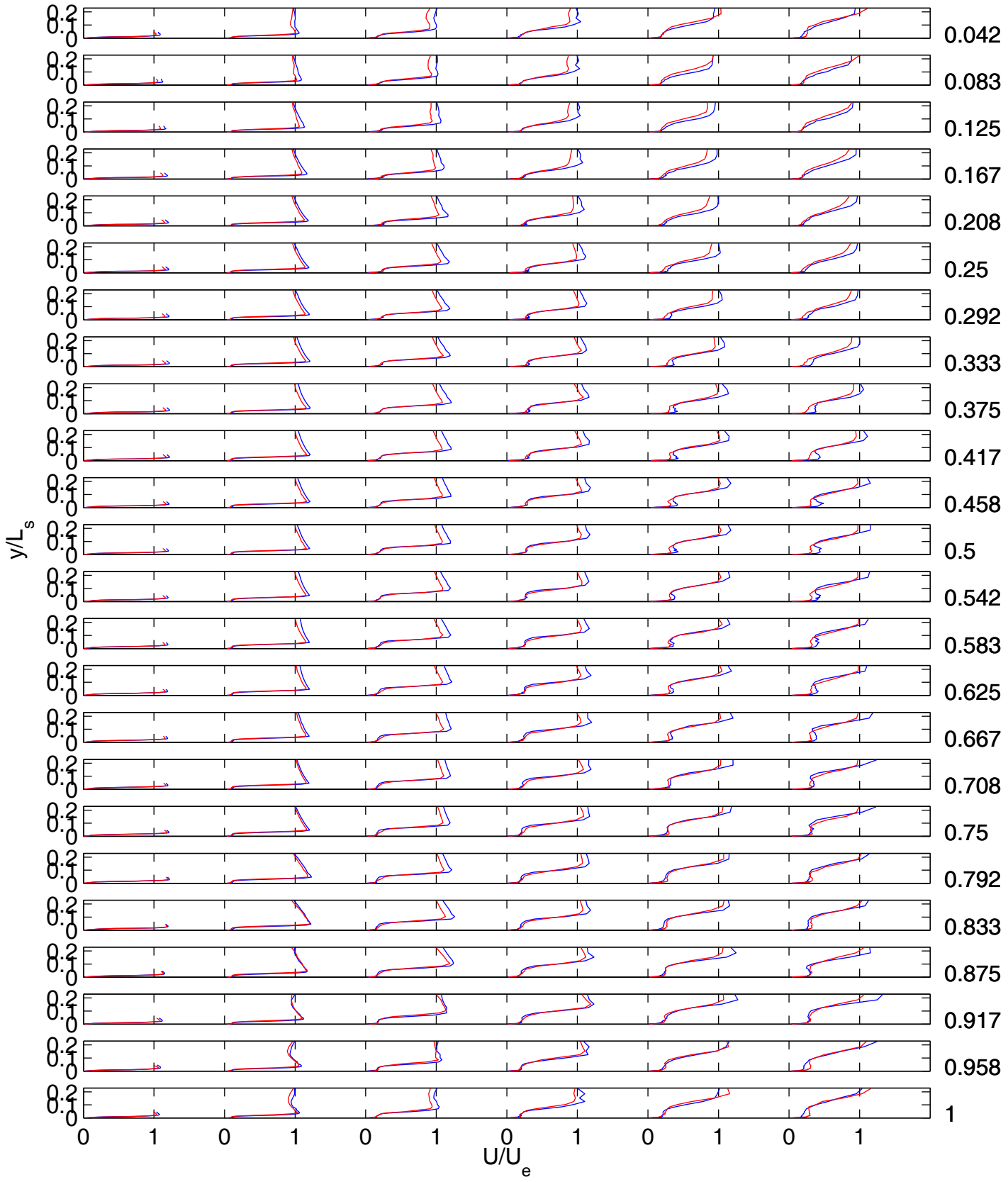

7/21/2010 Re=25,000 Blue: Low TI Red: High TI Timing a

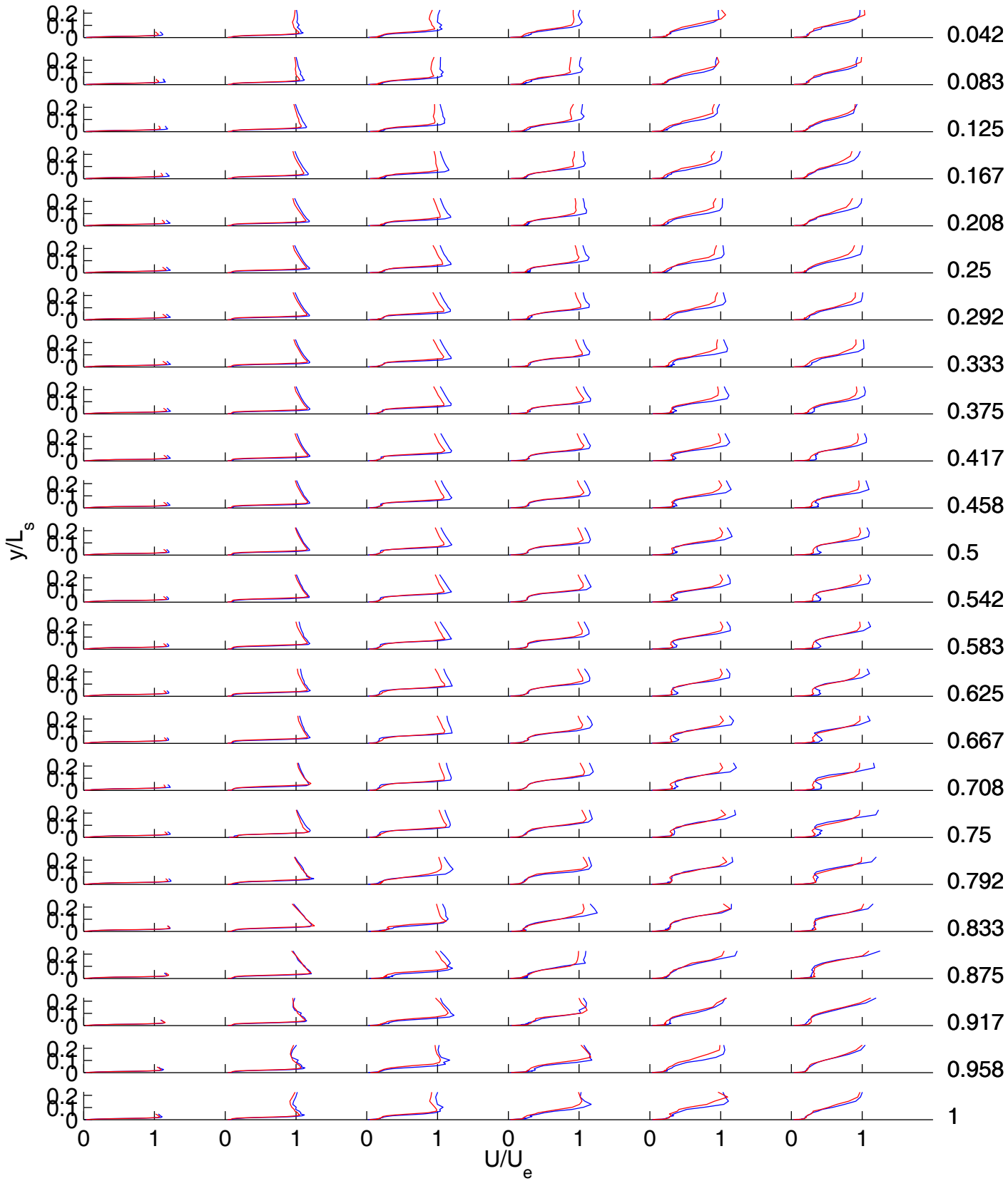

7/21/2010 Re=25,000 Blue: Low TI Red: High TI Timing b

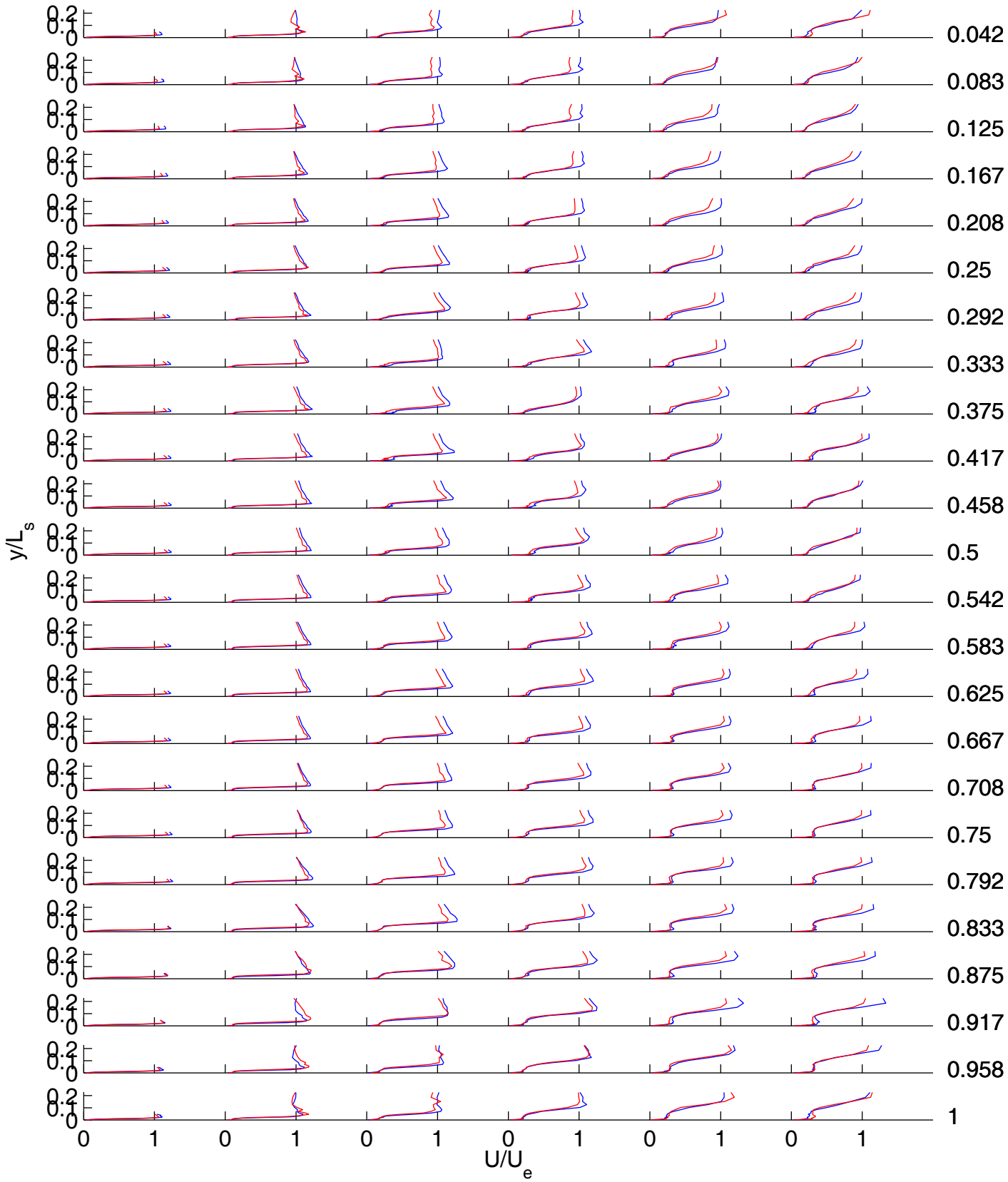

7/21/2010 Re=25,000 Blue: Low TI Red: High TI Timing c

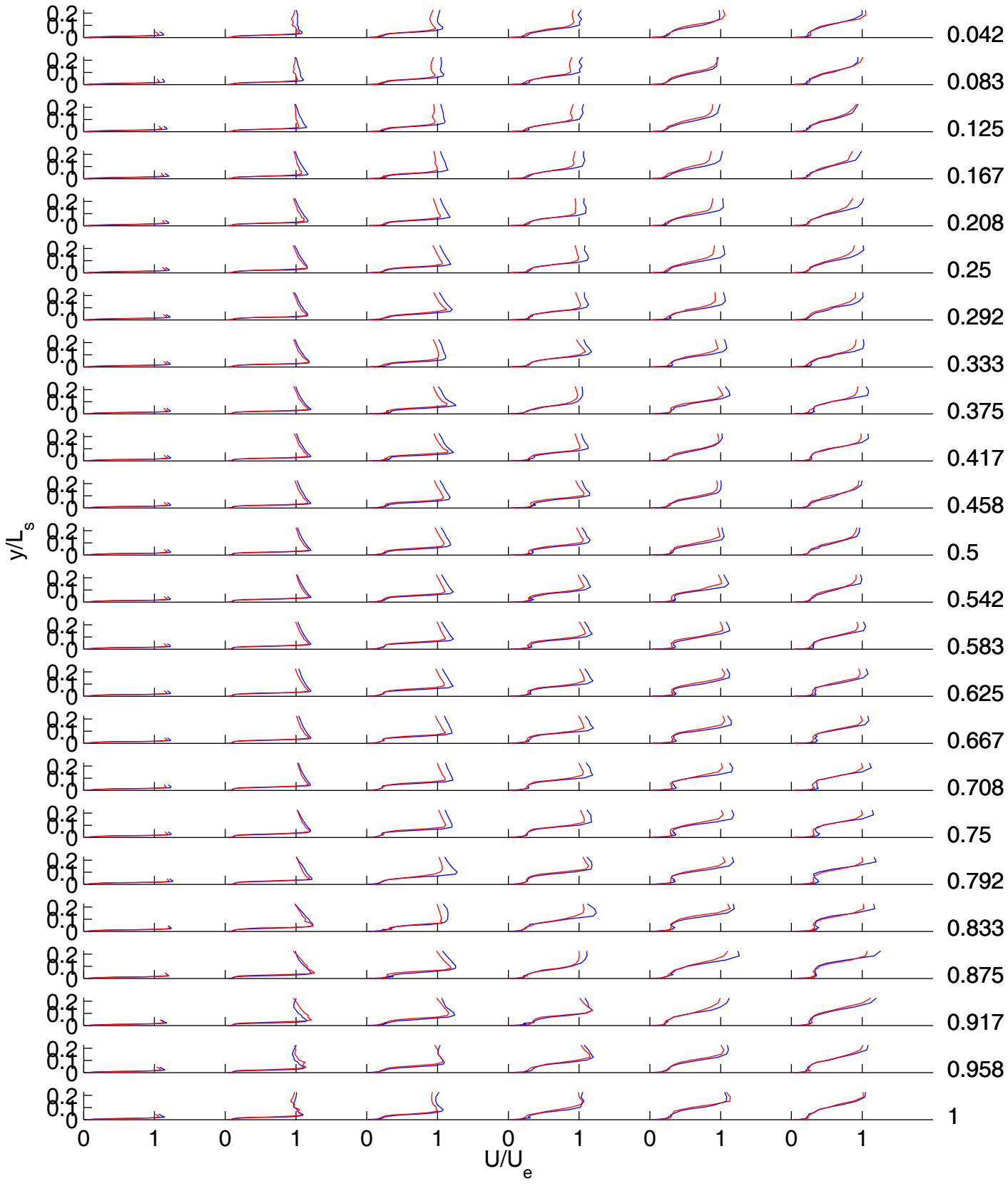

7/21/2010 Re=25,000 Blue: Low TI Red: High TI Timing d

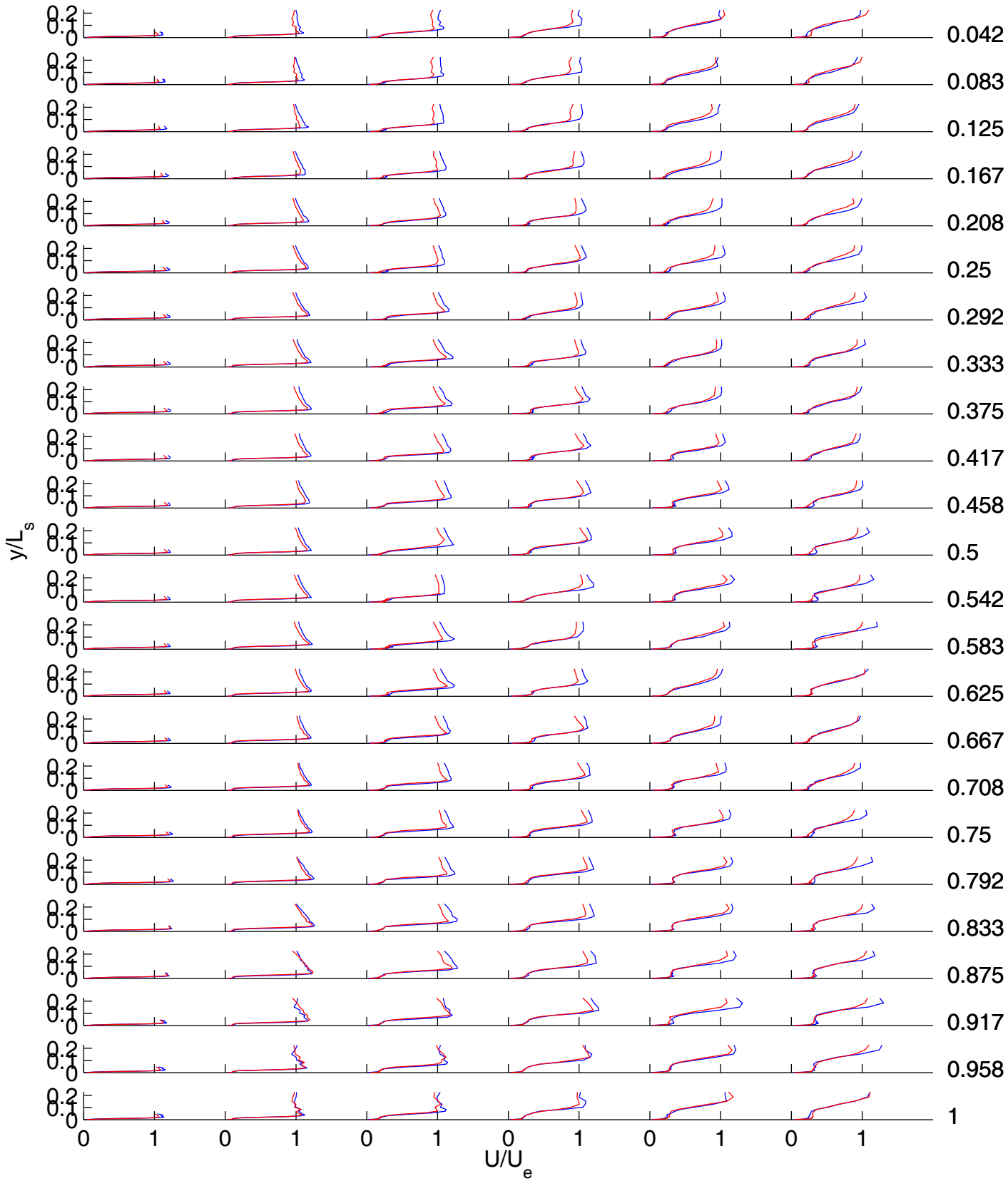

7/21/2010 Re=25,000 Blue: Low TI Red: High TI Timing e

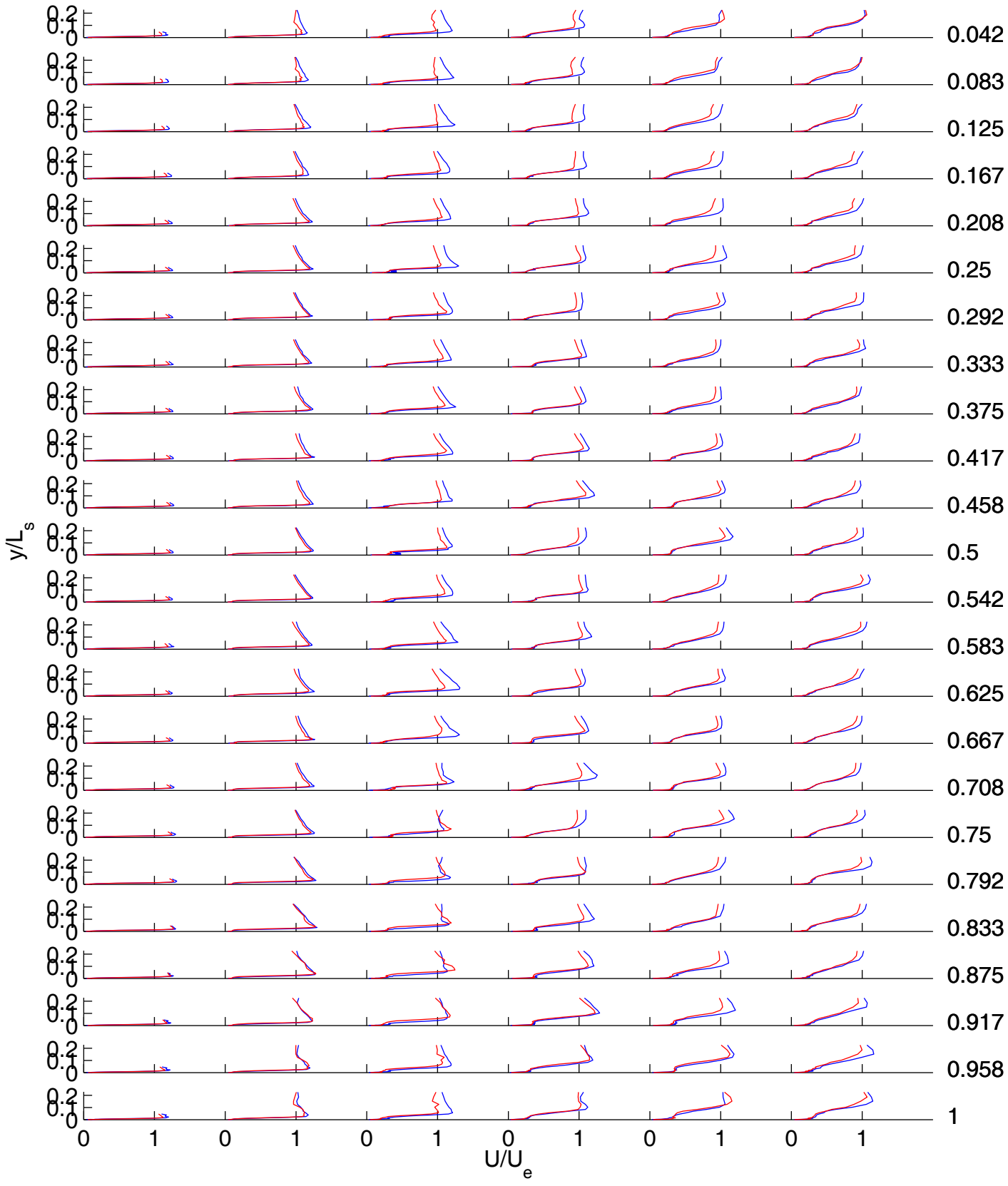

7/21/2010 Re=25,000 Blue: Low TI Red: High TI Timing f

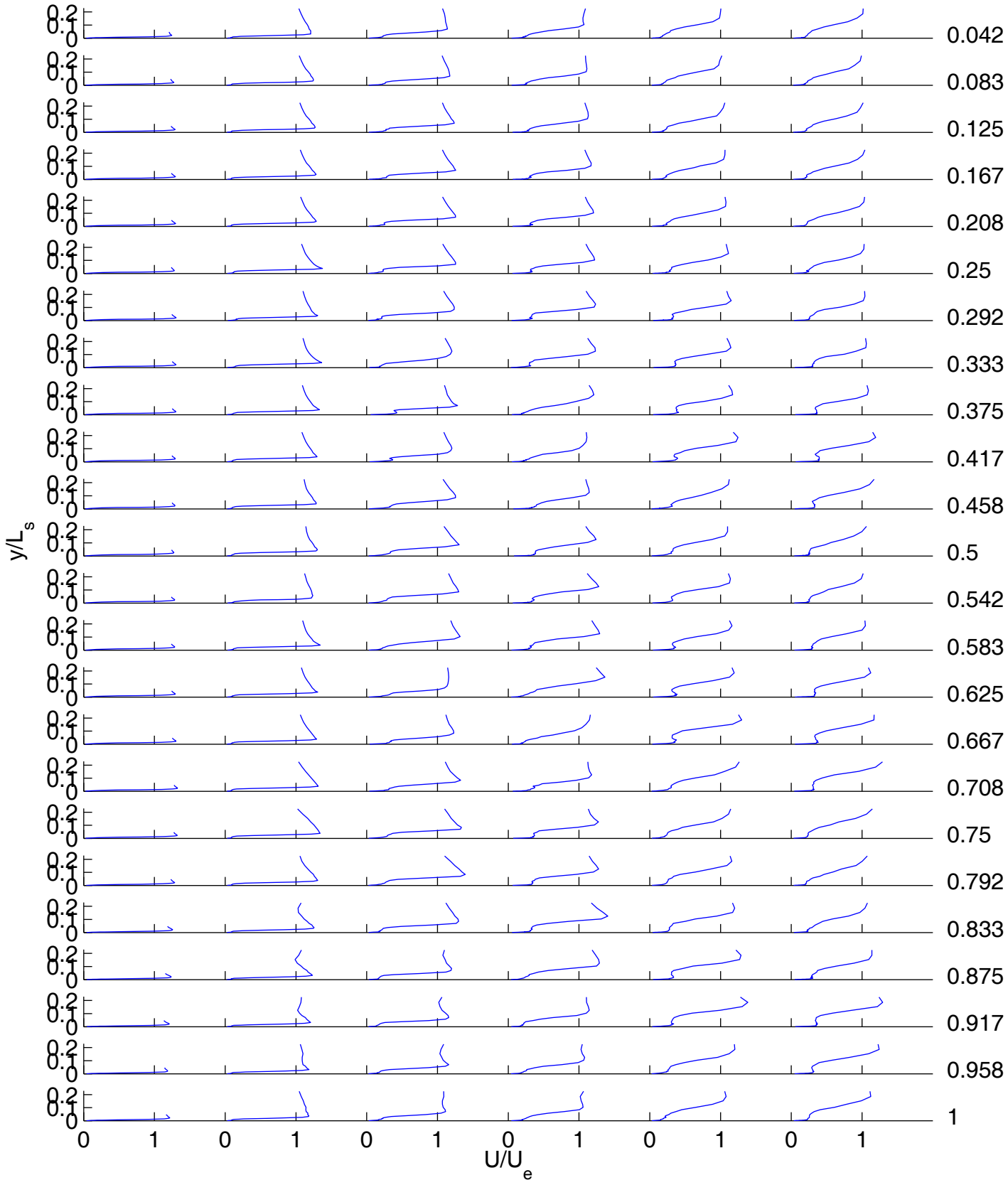

Re=25,000 Low TI Timing i

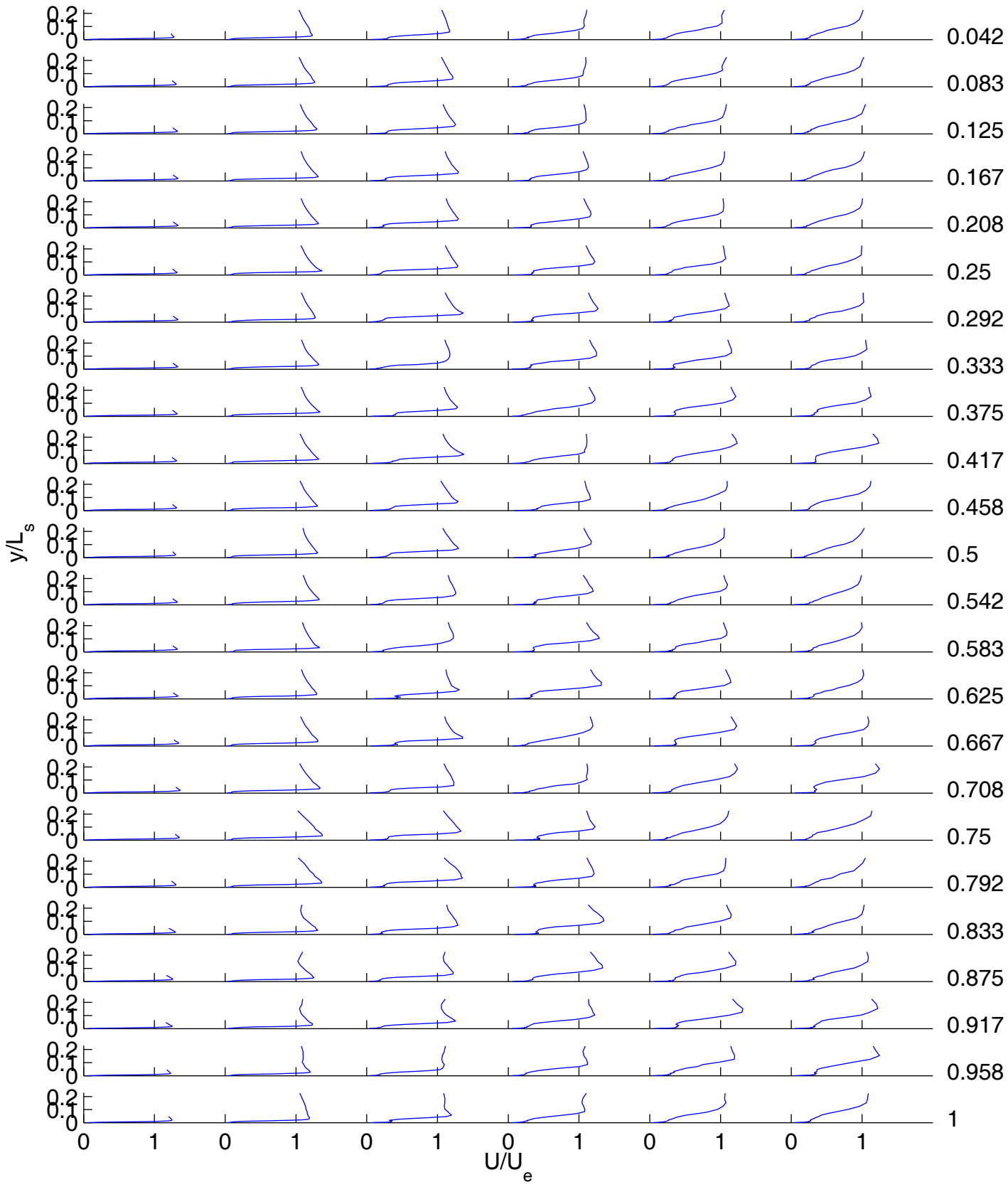

Re=25,000 Low TI Timing j

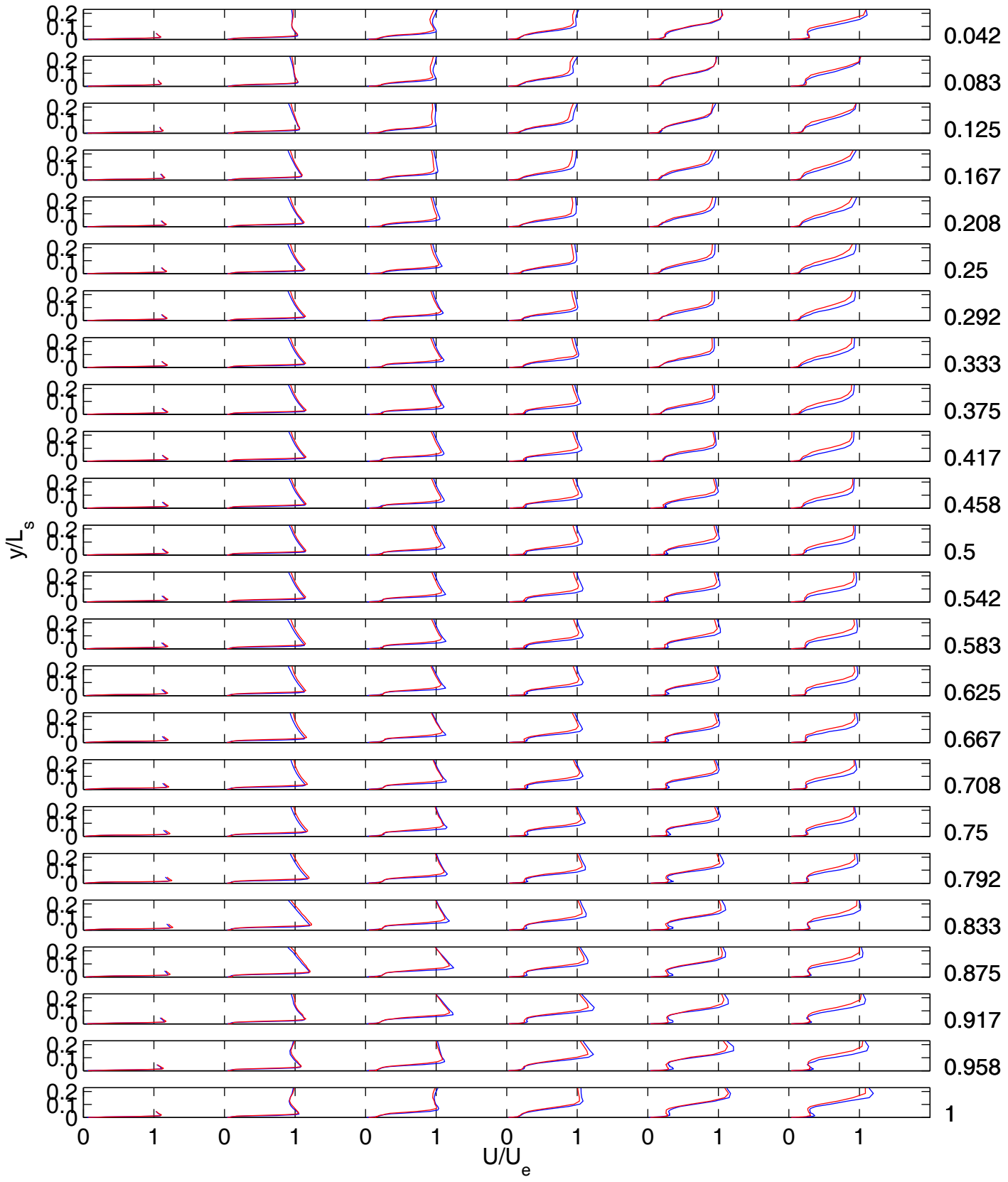

7/21/2010 Re=50,000 Blue: Low TI Red: High TI Timing a

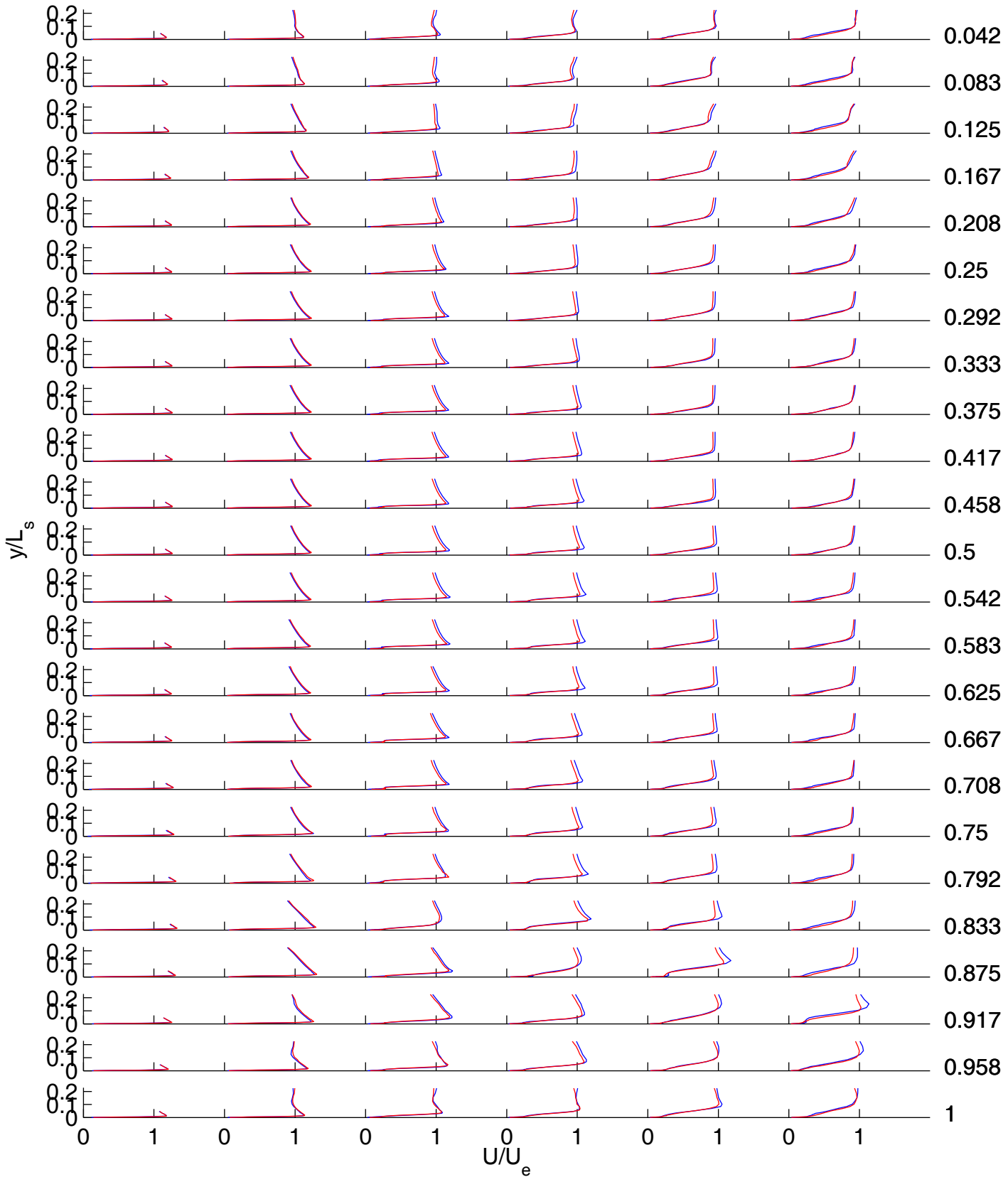

7/21/2010 Re=50,000 Blue: Low TI Red: High TI Timing b

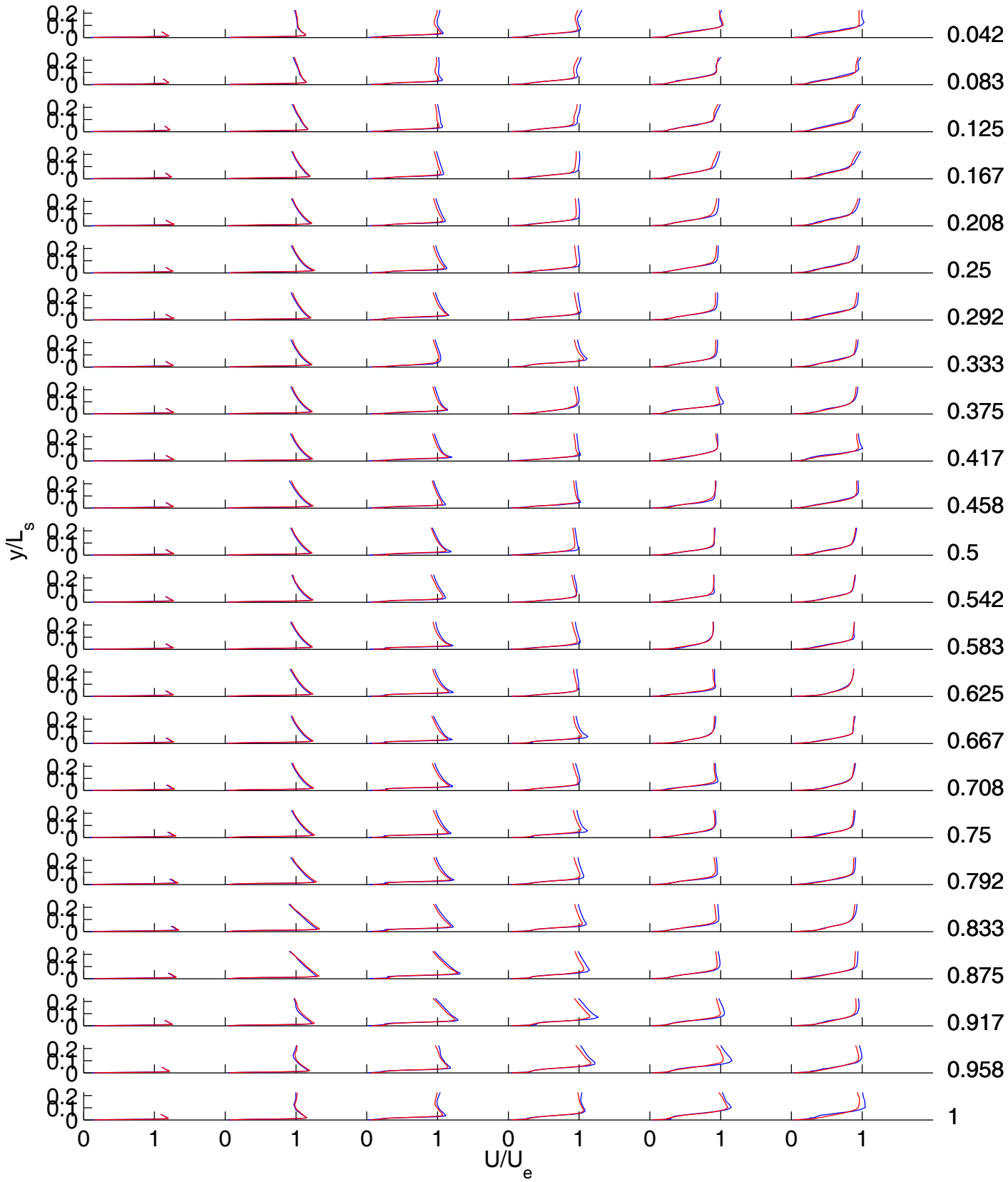

7/21/2010 Re=50,000 Blue: Low TI Red: High TI Timing c

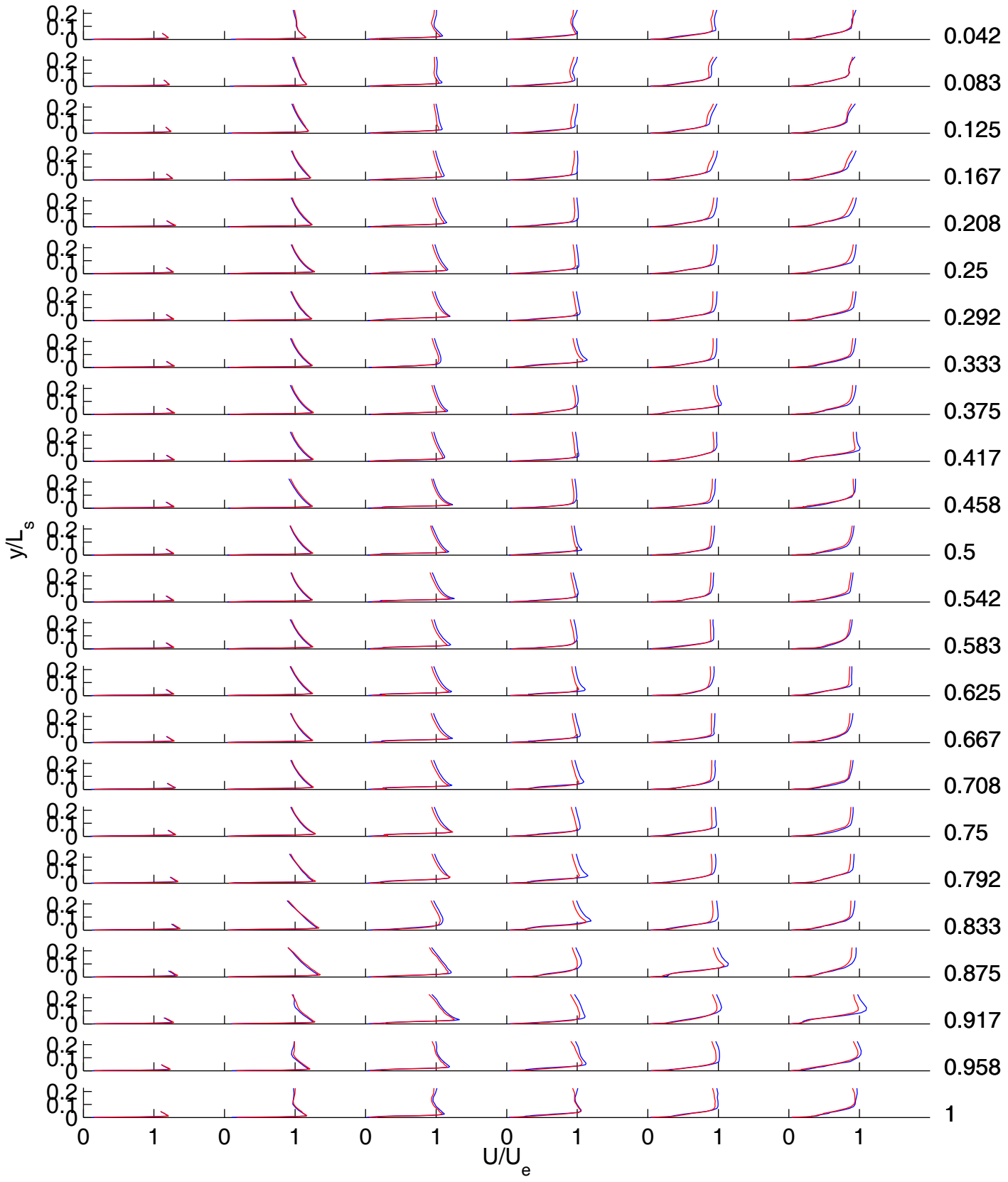

7/21/2010 Re=50,000 Blue: Low TI Red: High TI Timing d

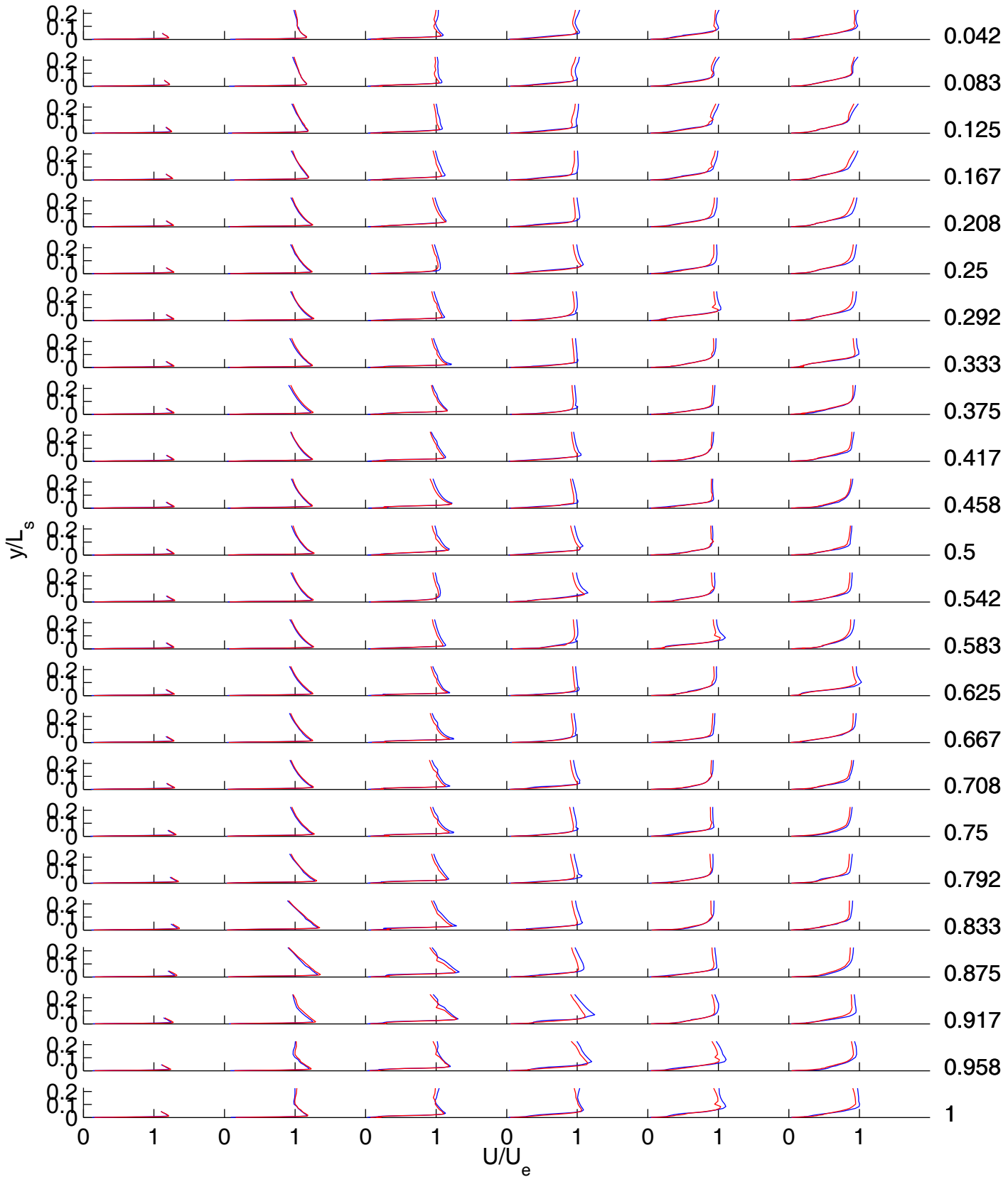

7/21/2010 Re=50,000 Blue: Low TI Red: High TI Timing e

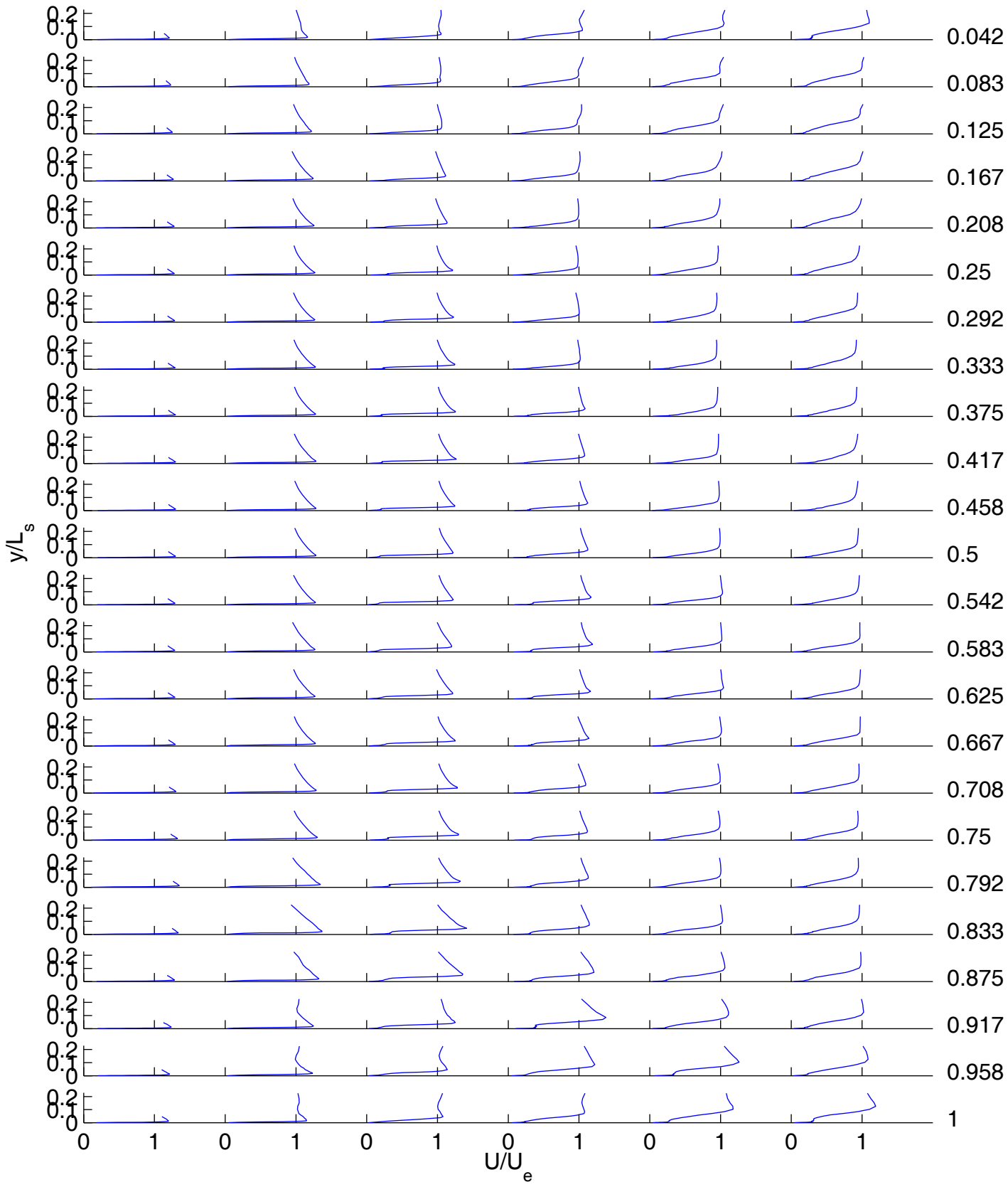

Re=50,000 Low TI Timing g

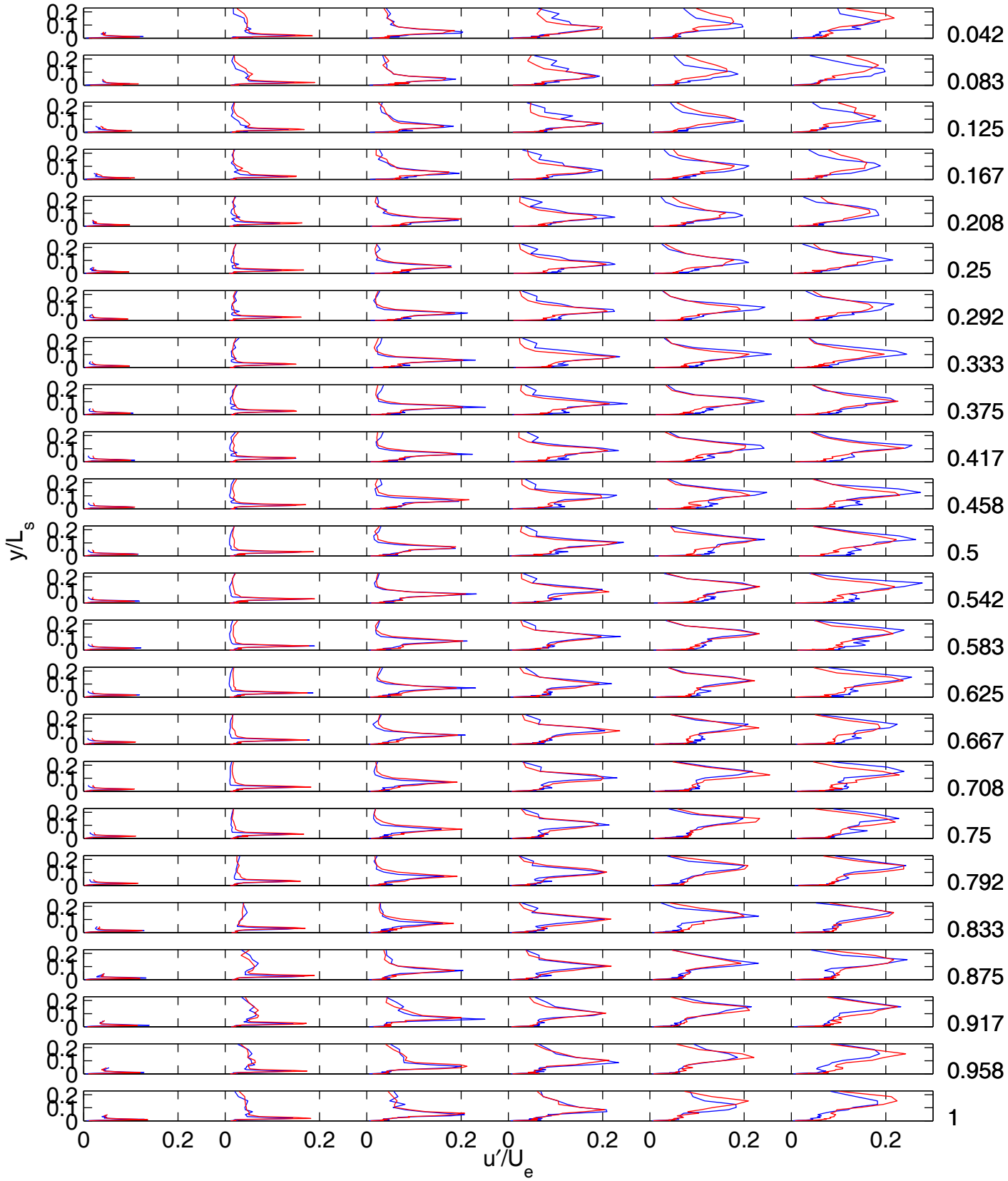

7/21/2010 Re=25,000 Blue: Low TI Red: High TI Timing a

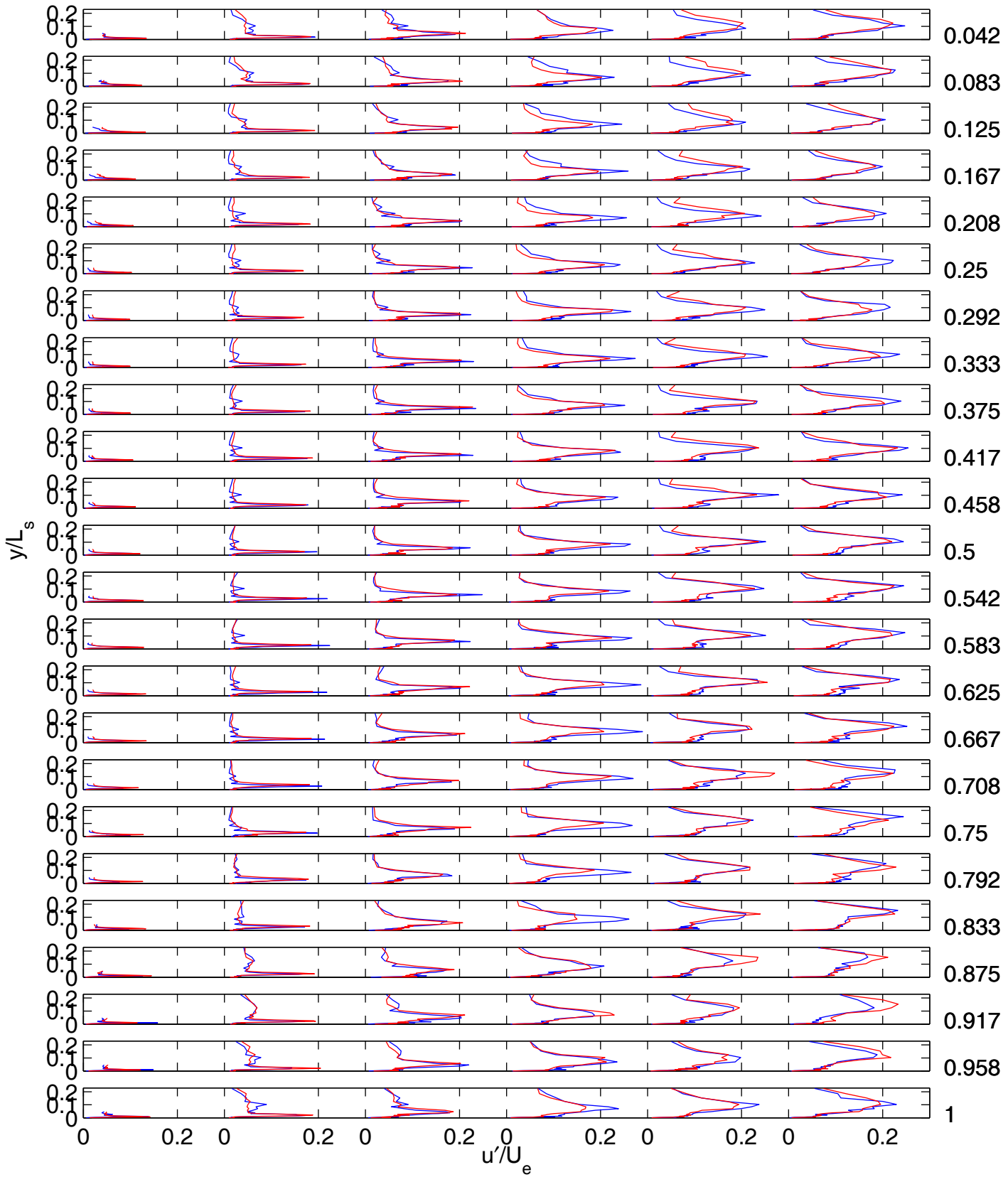

7/21/2010 Re=25,000 Blue: Low TI Red: High TI Timing b

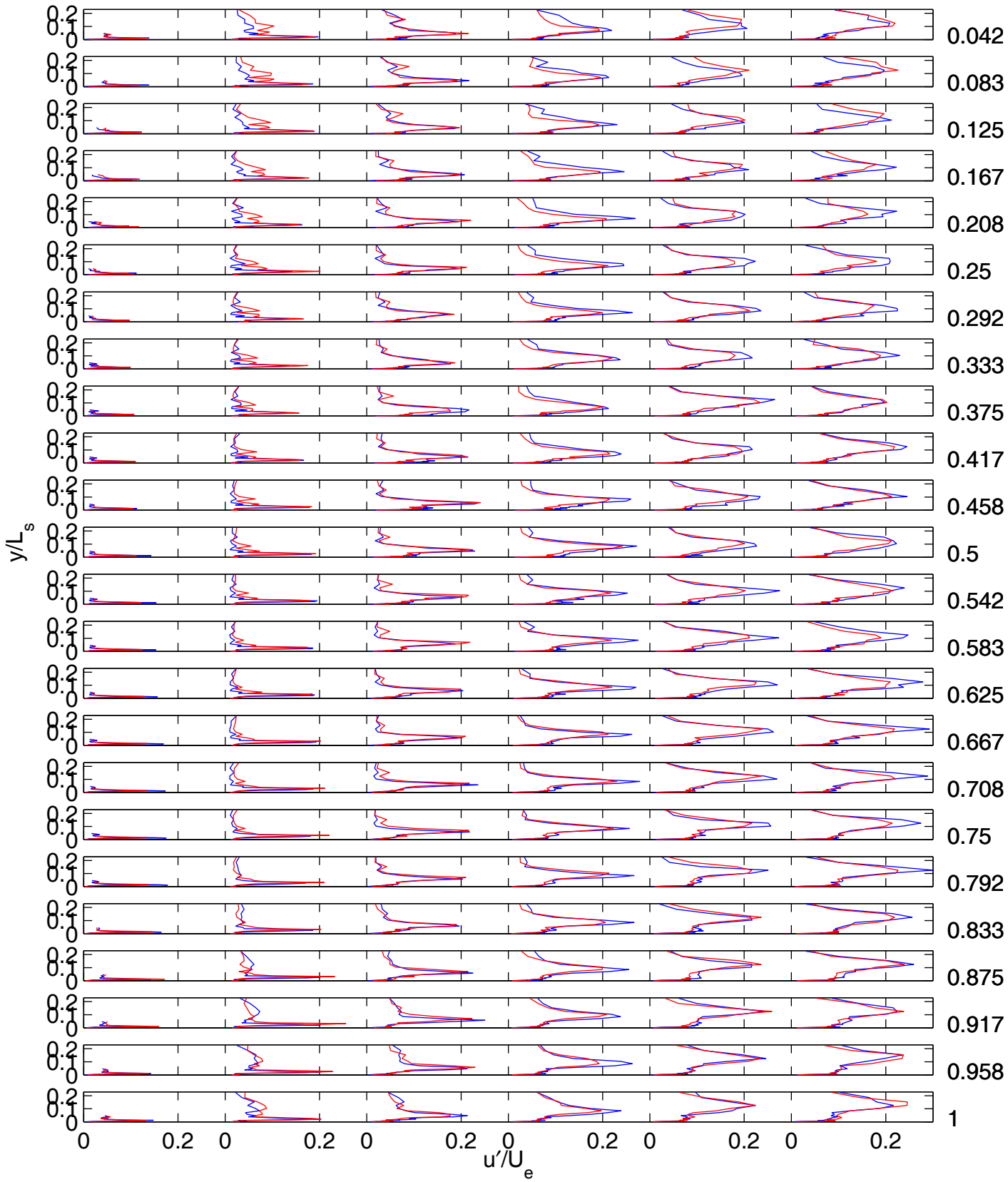

7/21/2010 Re=25,000 Blue: Low TI Red: High TI Timing c

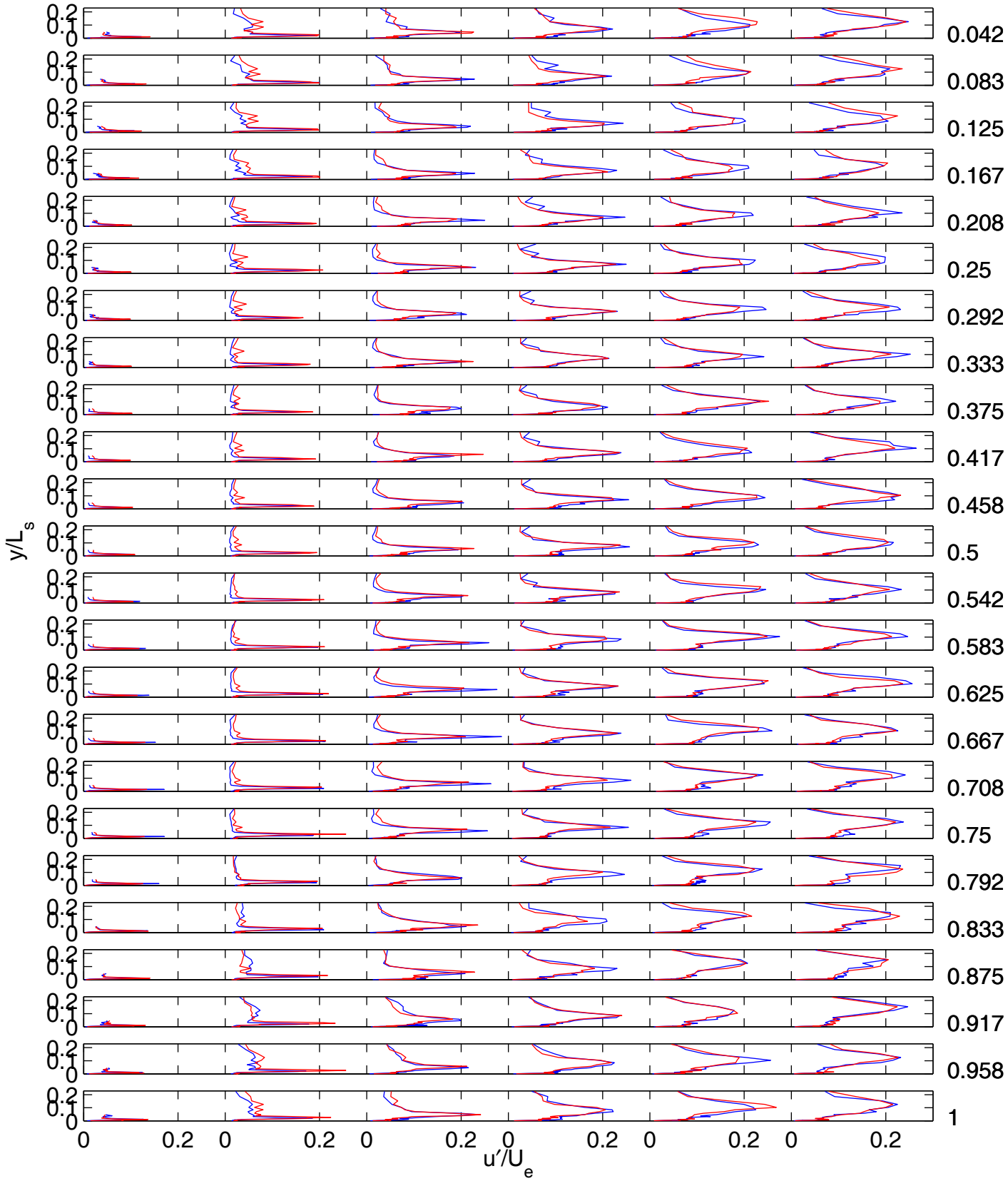

7/21/2010 Re=25,000 Blue: Low TI Red: High TI Timing d

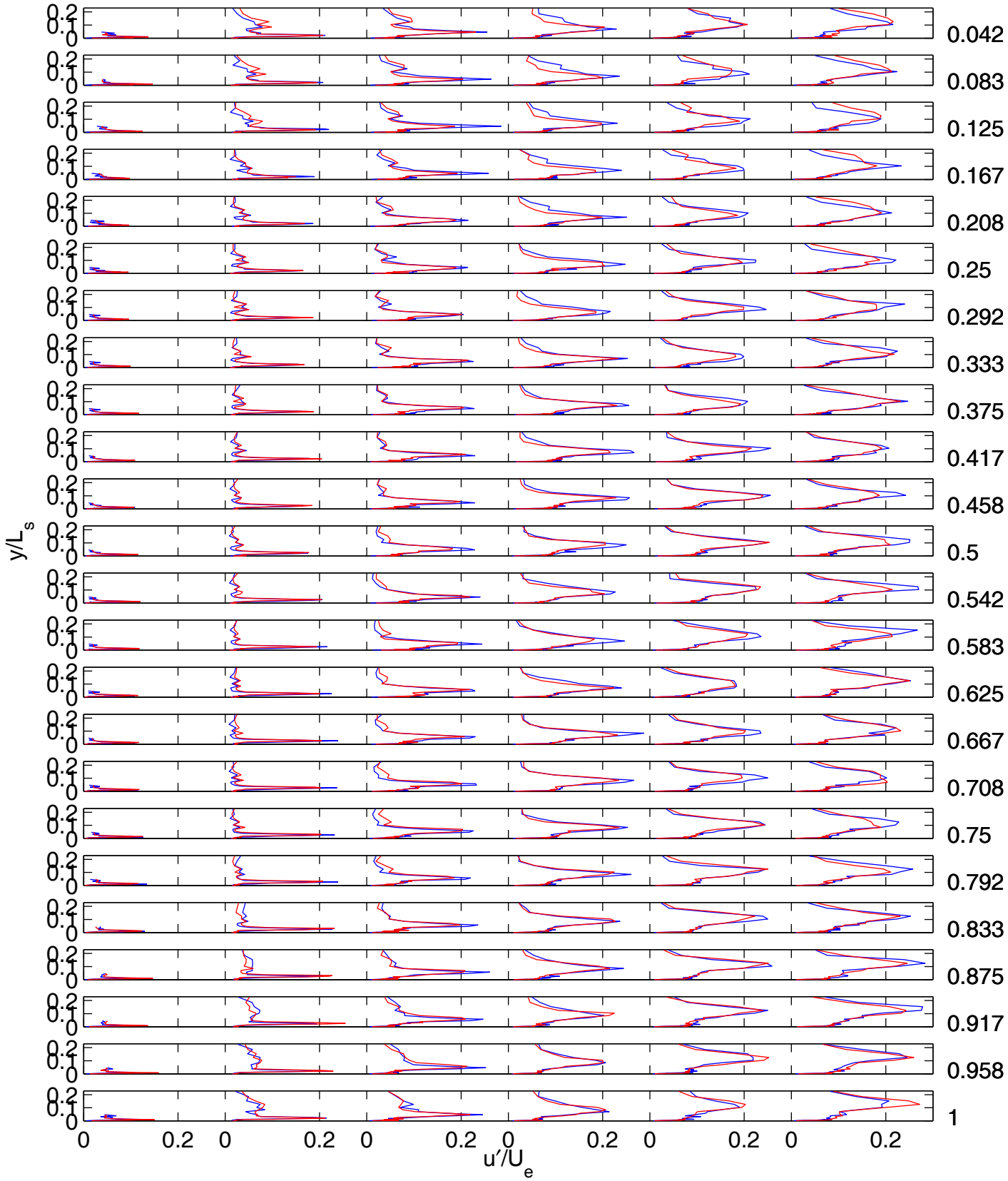

7/21/2010 Re=25,000 Blue: Low TI Red: High TI Timing e

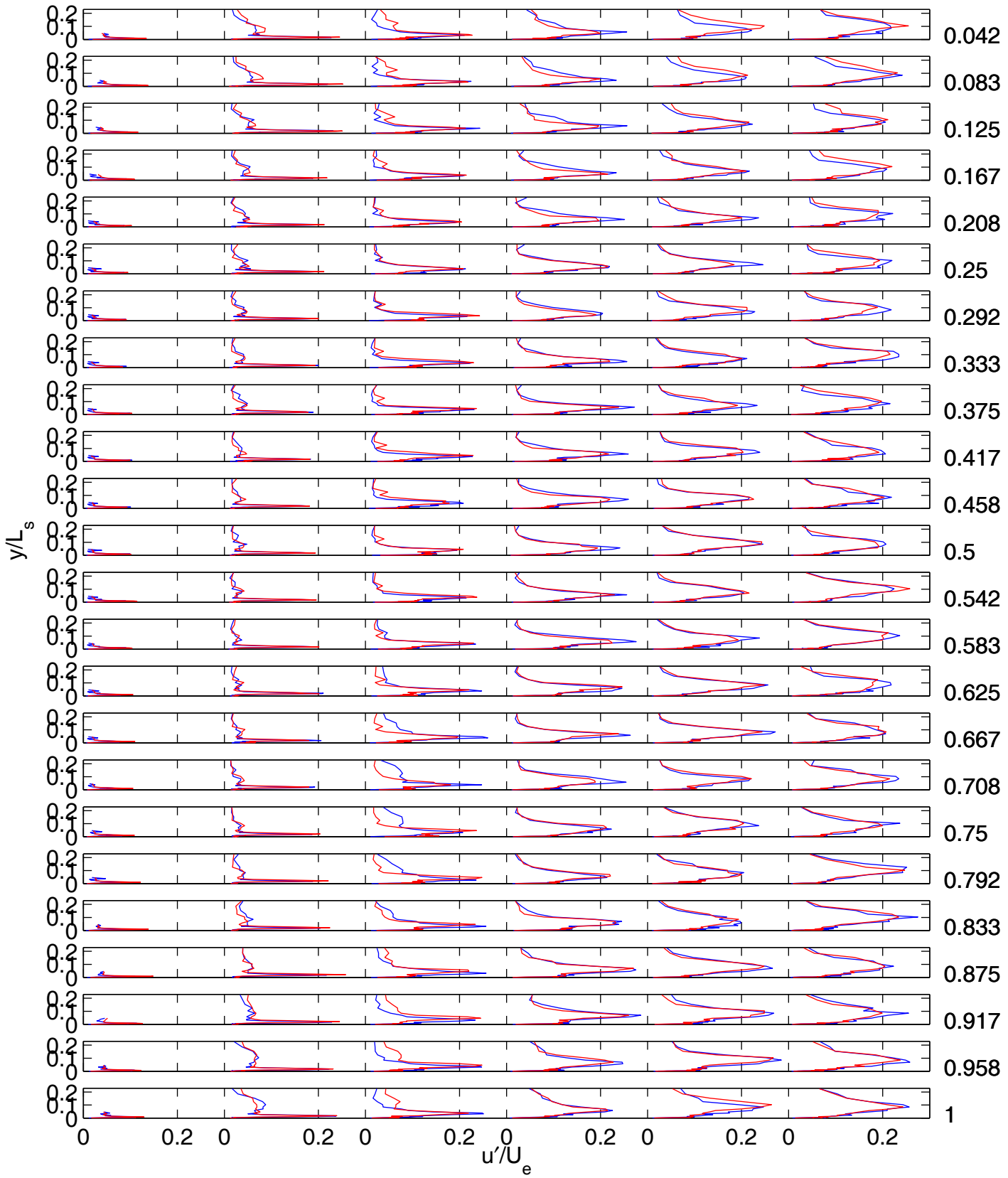

7/21/2010 Re=25,000 Blue: Low TI Red: High TI Timing f

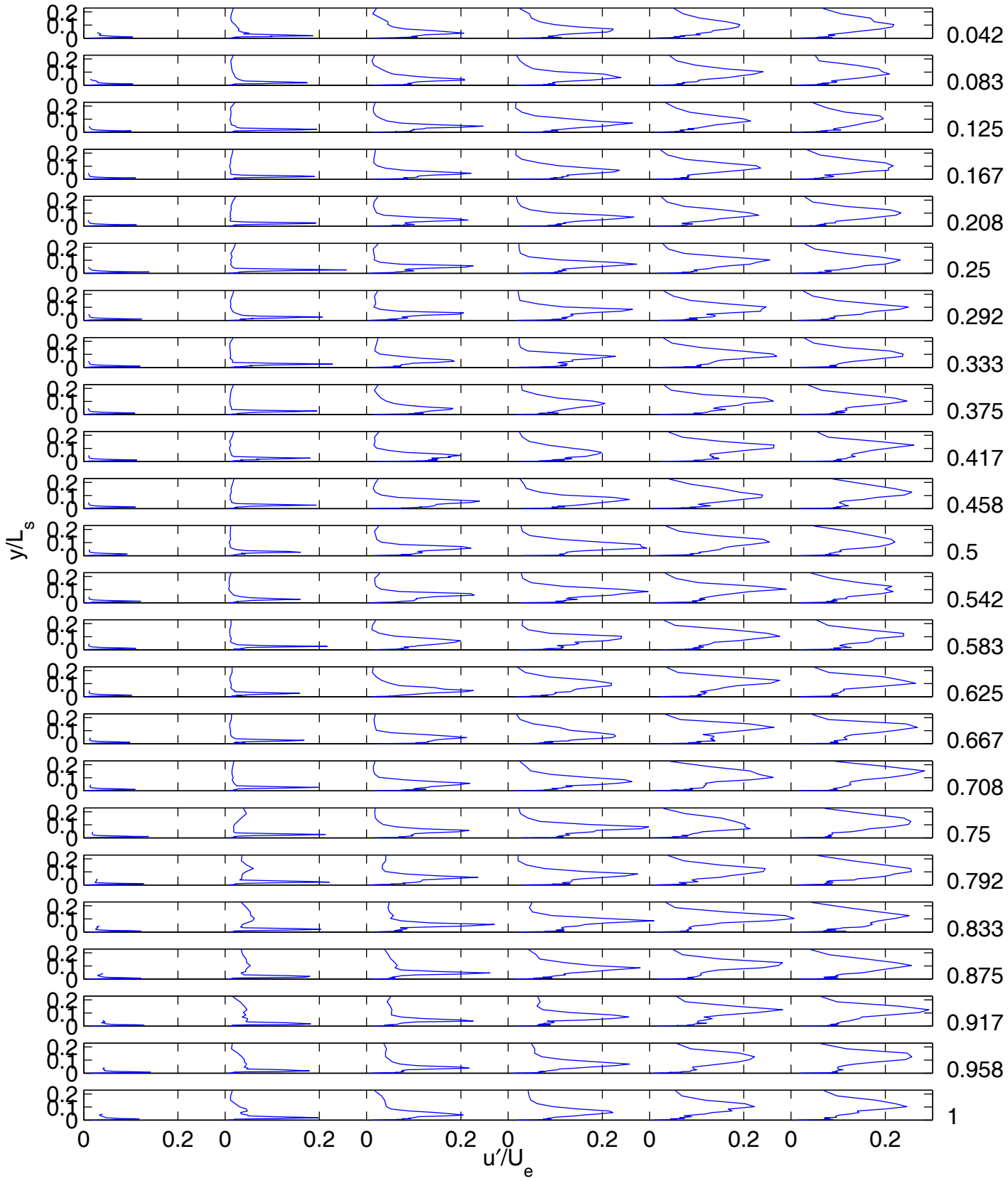

Re=25,000 Low TI Timing i

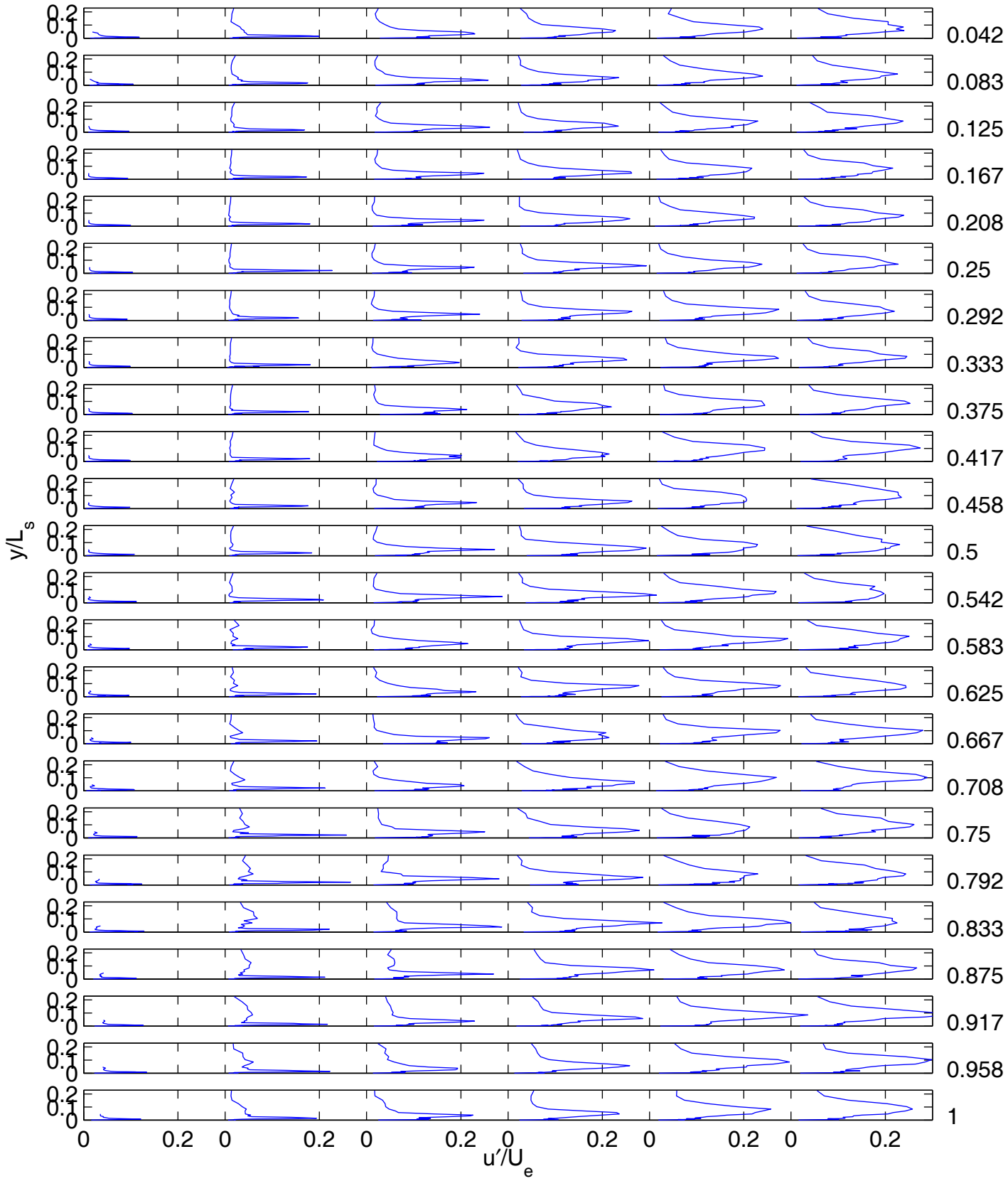

Re=25,000 Low TI Timing j

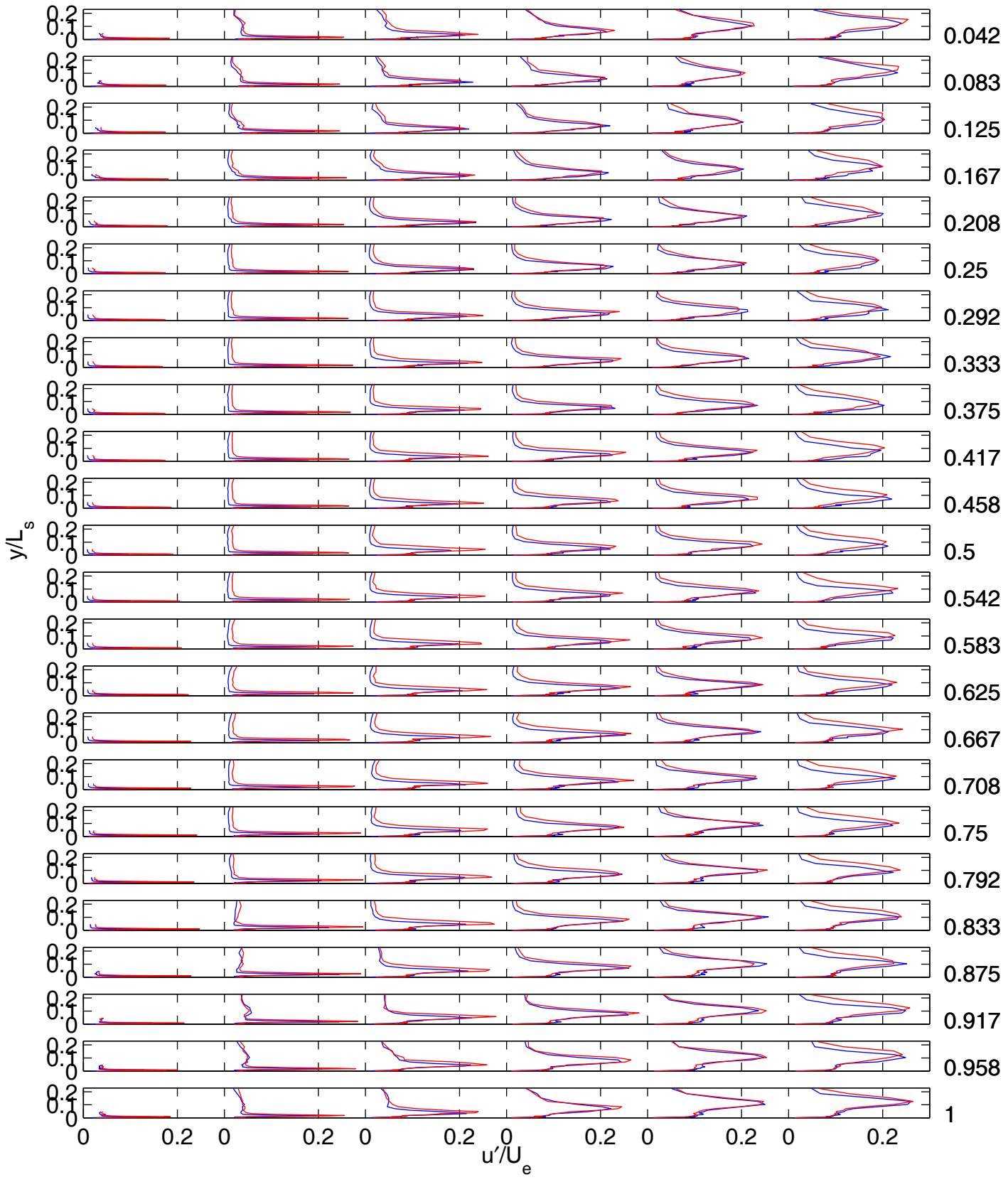

7/21/2010 Re=50,000 Blue: Low TI Red: High TI Timing a

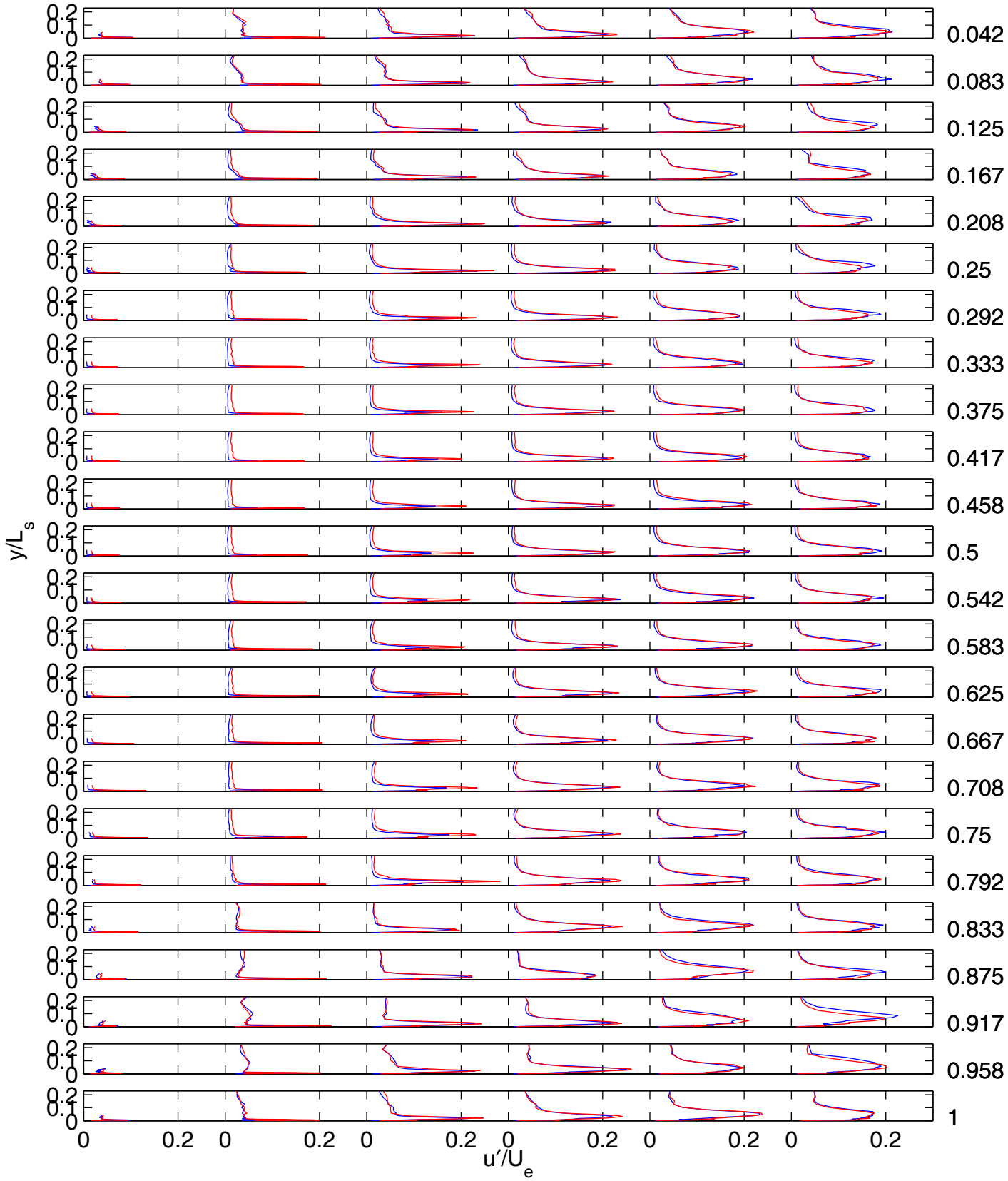

7/21/2010 Re=50,000 Blue: Low TI Red: High TI Timing b

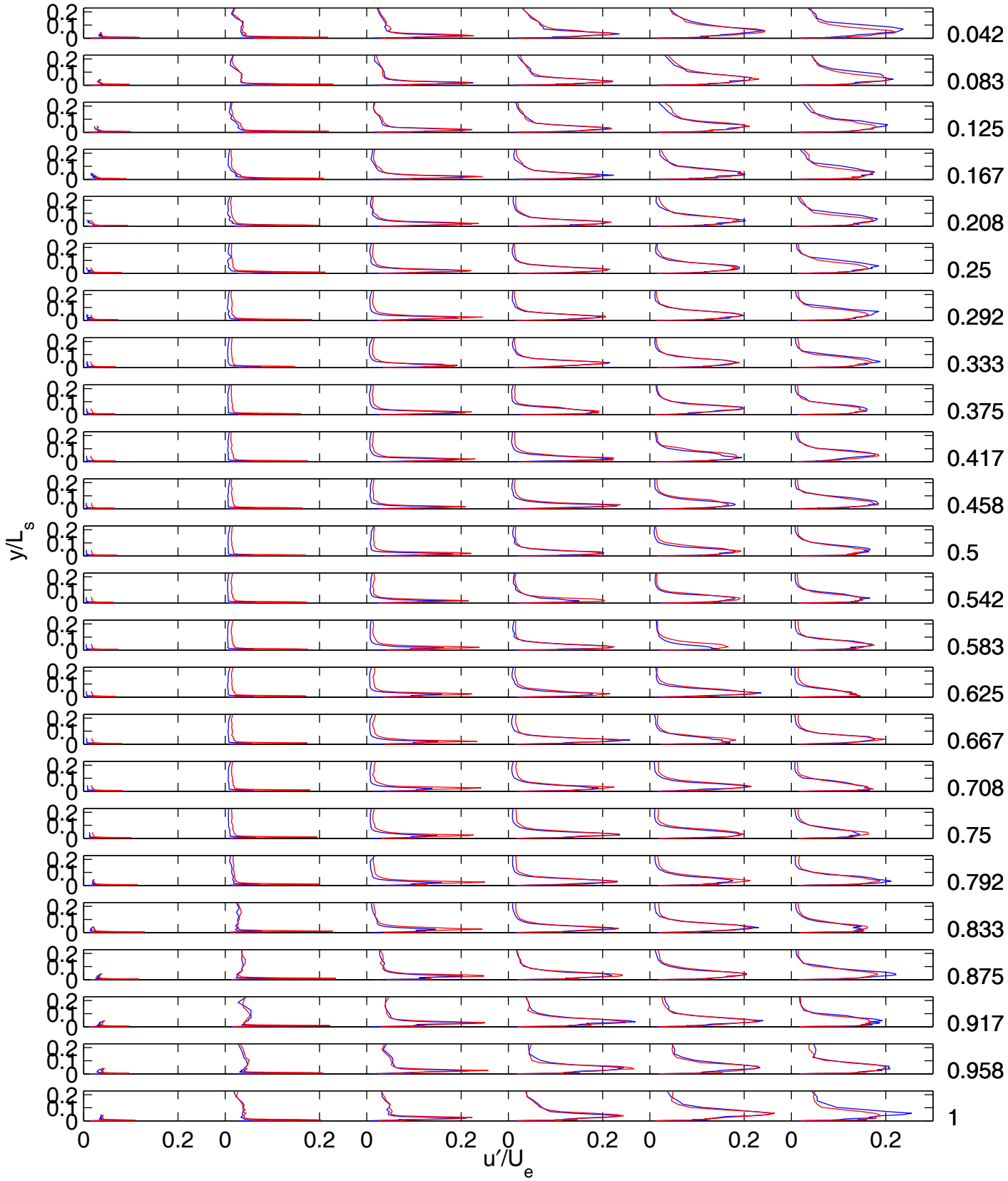

7/21/2010 Re=50,000 Blue: Low TI Red: High TI Timing c

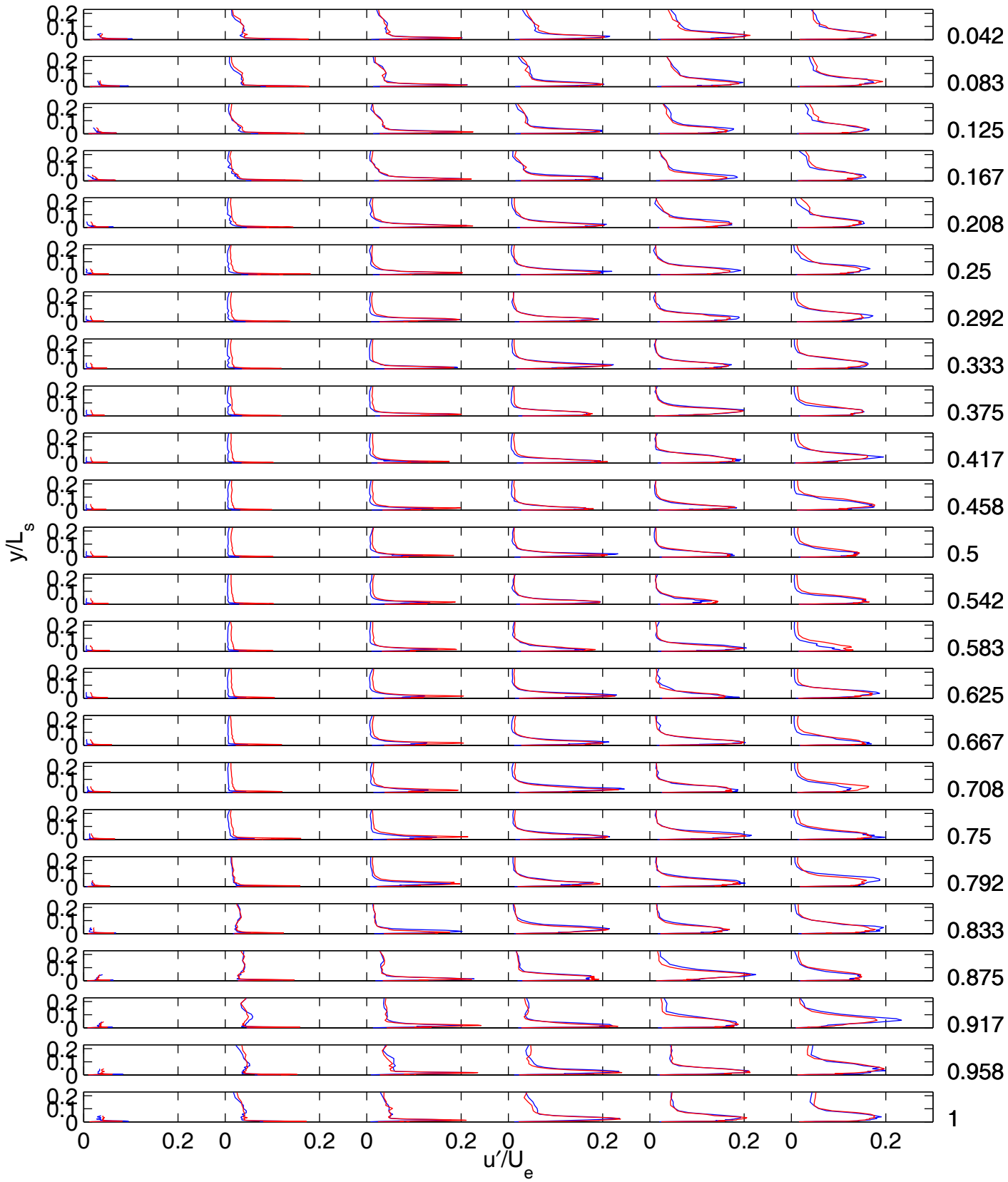

7/21/2010 Re=50,000 Blue: Low TI Red: High TI Timing d

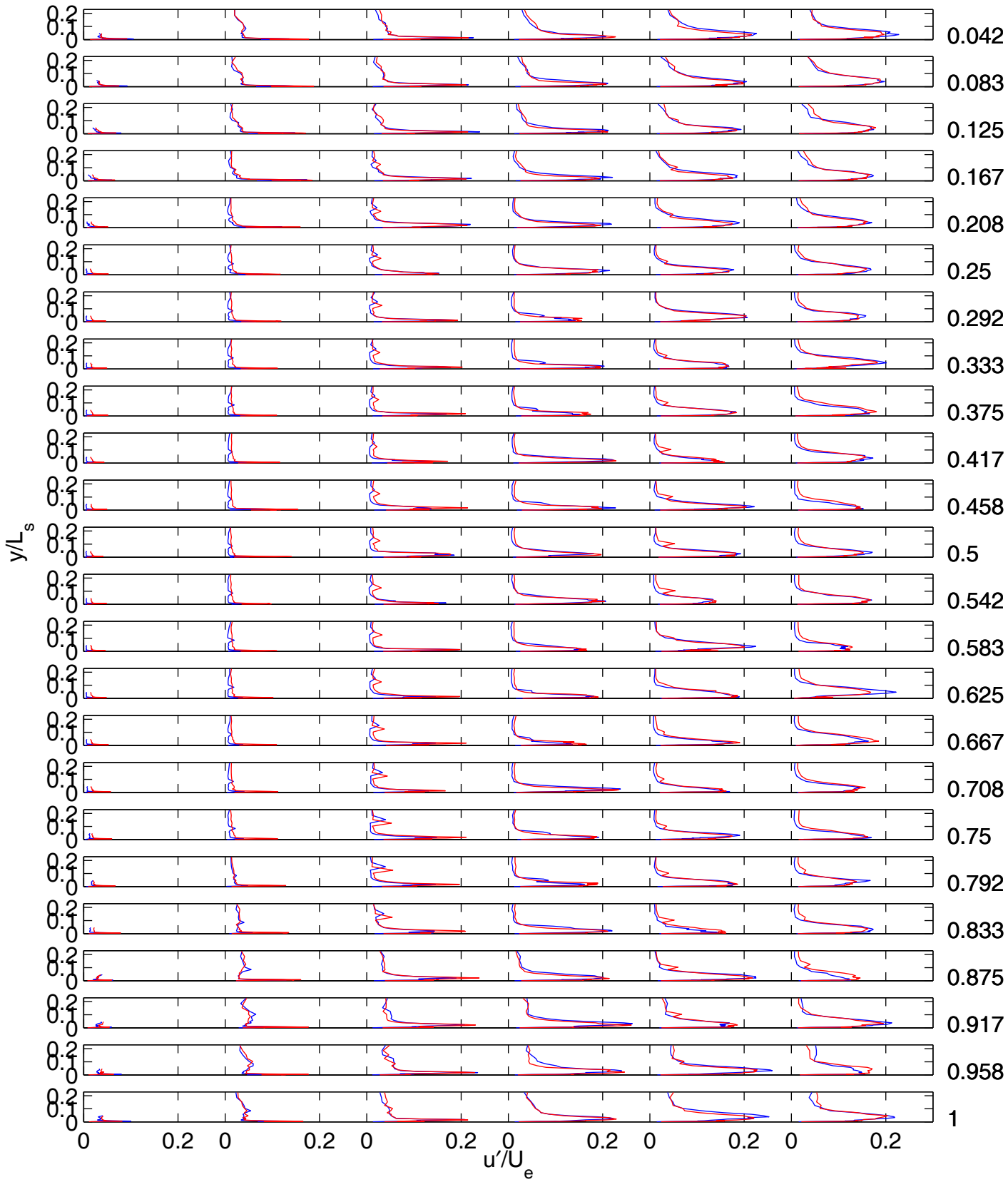

7/21/2010 Re=50,000 Blue: Low TI Red: High TI Timing e

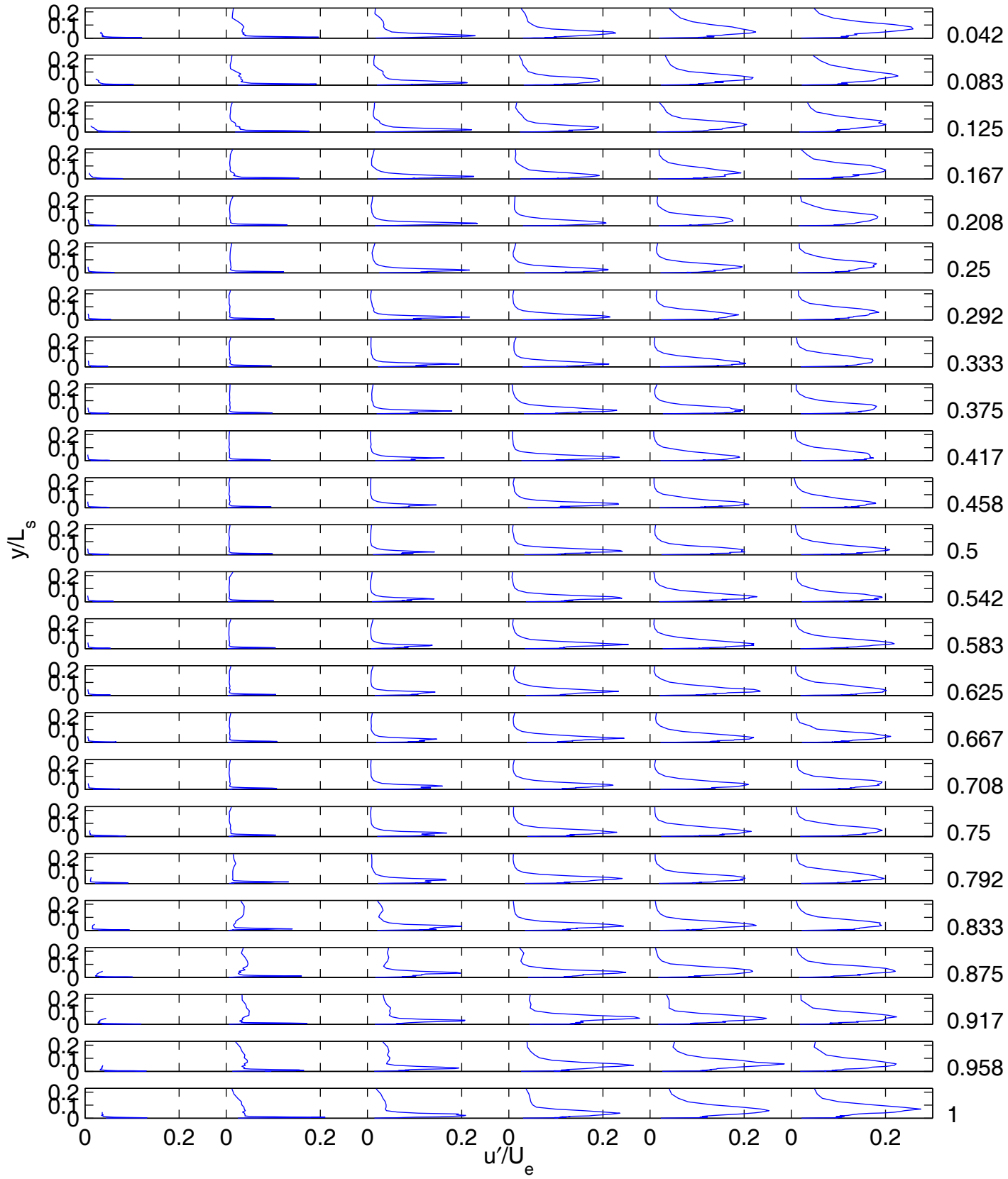

Re=50,000 Low TI Timing g

The following figures show time space plots of phase averaged velocity and turbulence in the wake 0.6 C_x downstream of the trailing edges for cases with VGJs and wakes with various timings. The names for the timings correspond to the original data file names and not the new names used in conference papers.

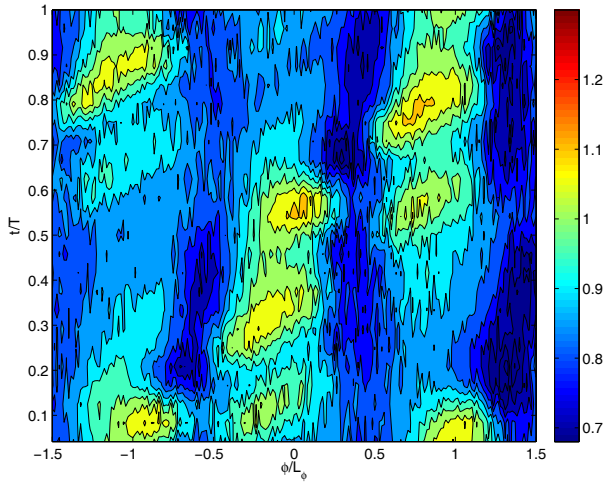

Re=25,000, Low TI, Timing a, Mean U/U_e

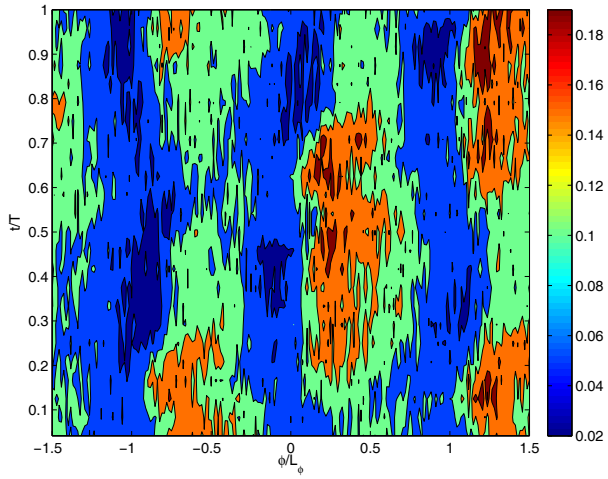

Re=25,000, Low TI, Timing a, u'/U_e

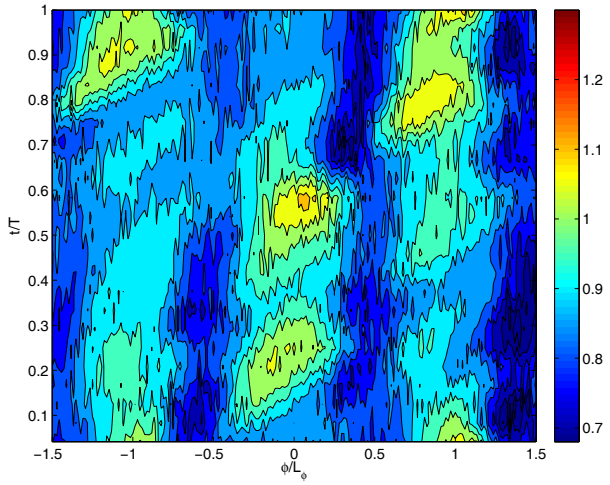

Re=25,000, Low TI, Timing b, Mean U/U_e

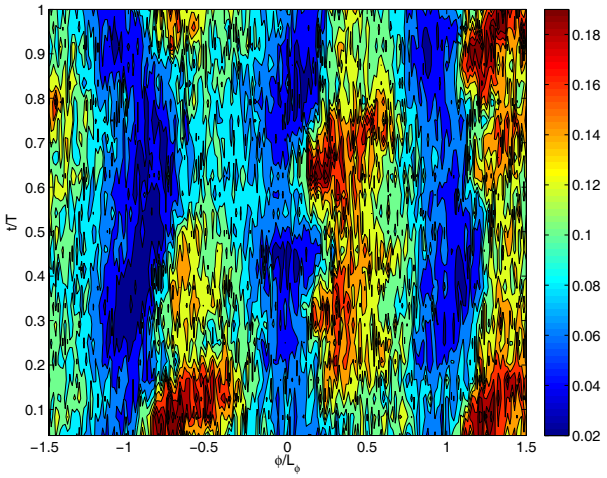

Re=25,000, Low TI, Timing b, u'/U_e

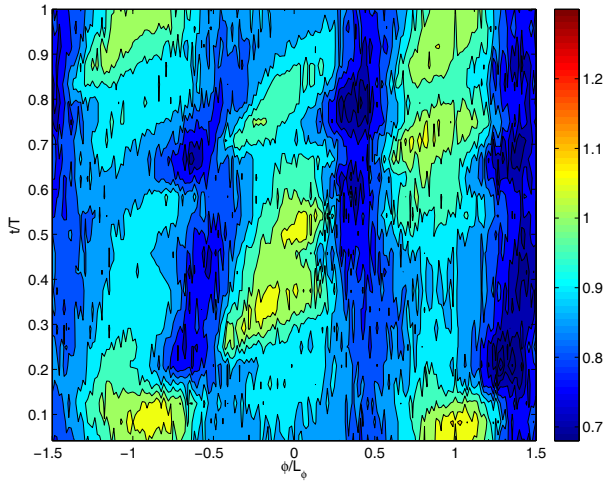

Re=25,000, Low TI, Timing c, Mean U/U_e

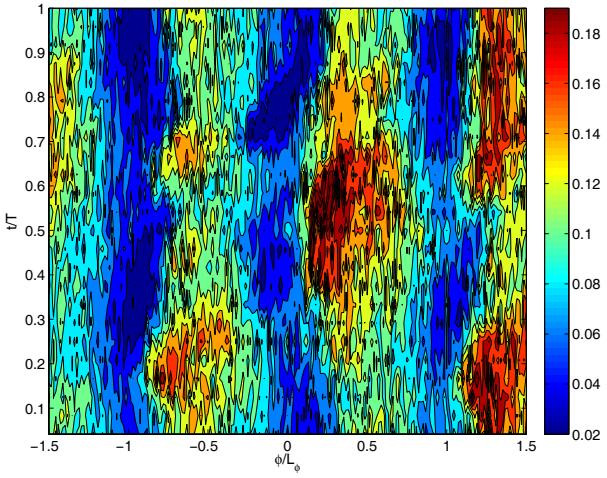

Re=25,000, Low TI, Timing c, u'/U_e

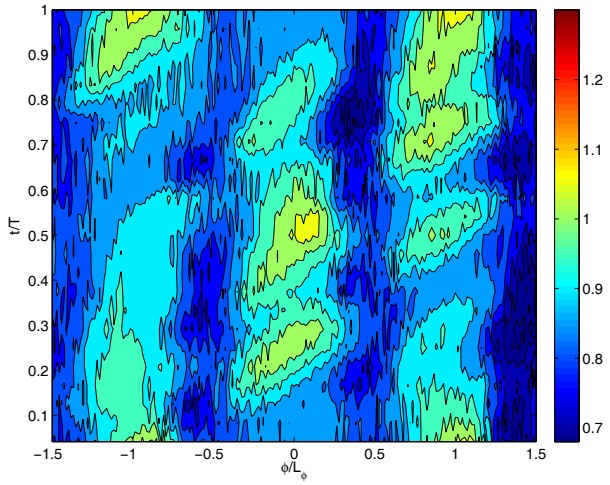

Re=25,000, Low TI, Timing d, Mean U/U_e

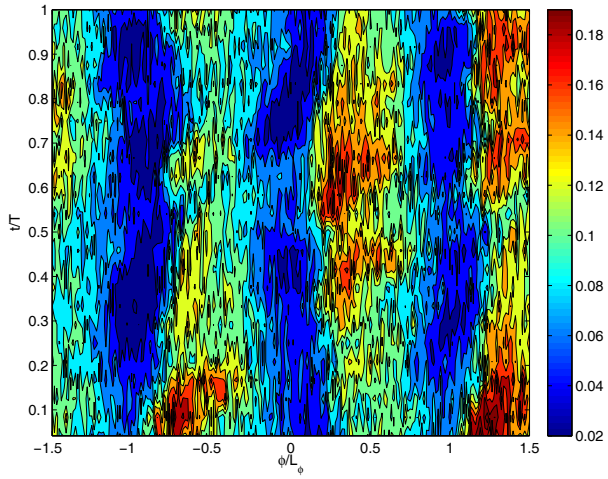

Re=25,000, Low TI, Timing d, u'/U_e

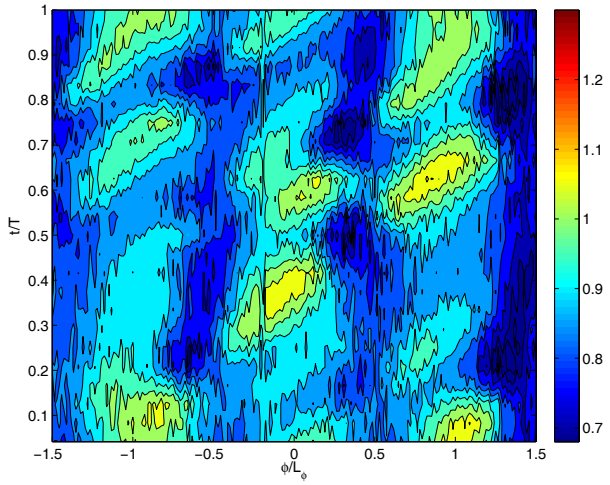

Re=25,000, Low TI, Timing e, Mean U/U_e

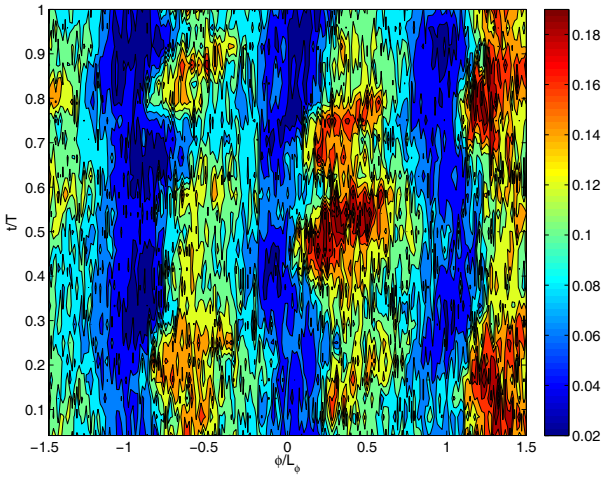

Re=25,000, Low TI, Timing e, u'/U_e

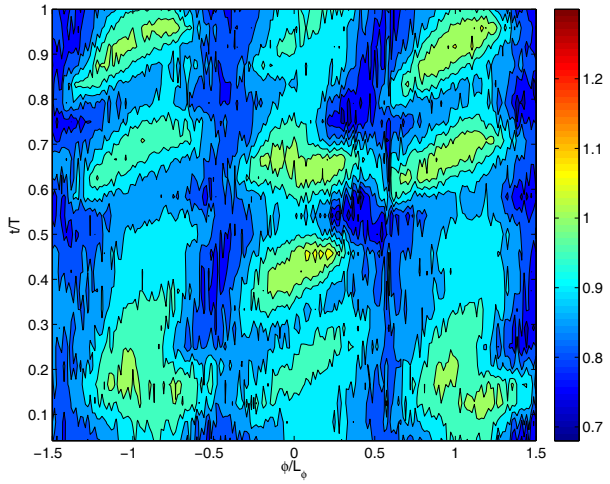

Re=25,000, Low TI, Timing f, Mean U/U_e

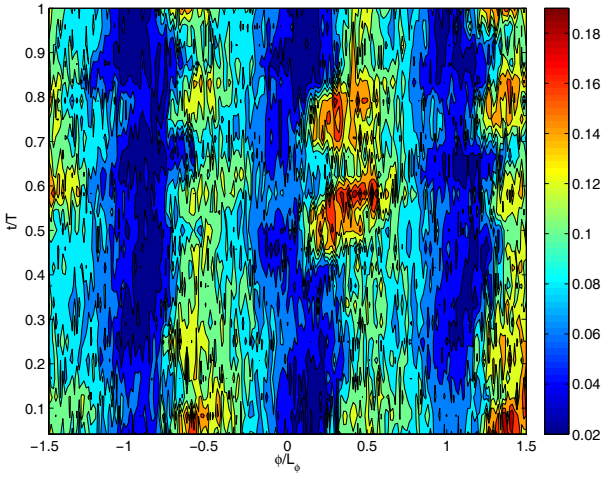

Re=25,000, Low TI, Timing f, u'/U_e

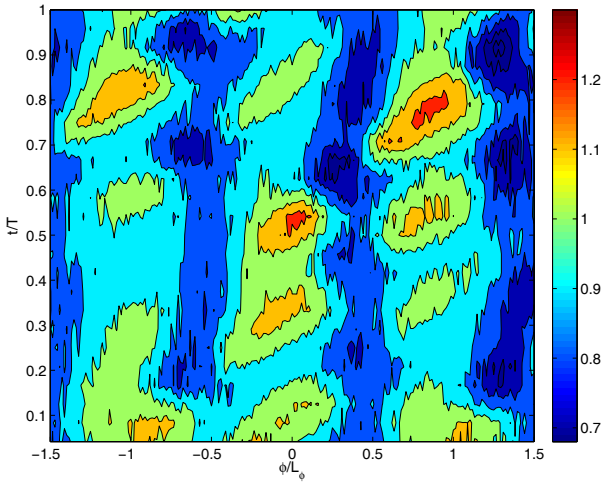

Re=25,000, Low TI, Timing i, Mean U/U_e

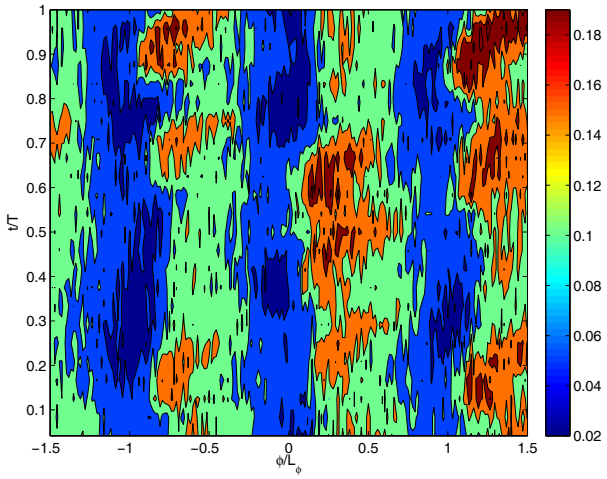

Re=25,000, Low TI, Timing i, u'/U_e

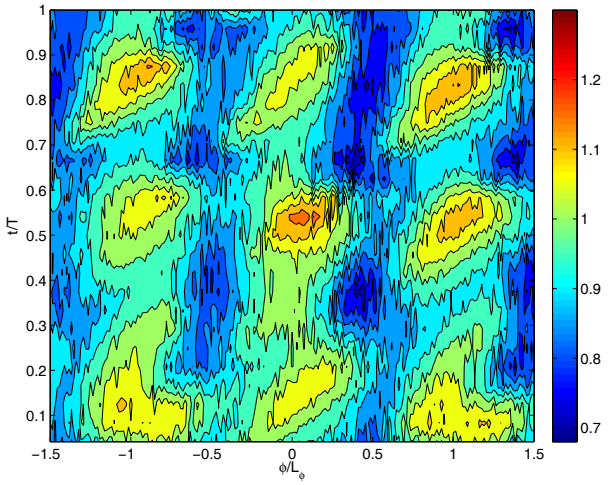

Re=25,000, Low TI, Timing j, Mean U/U_e

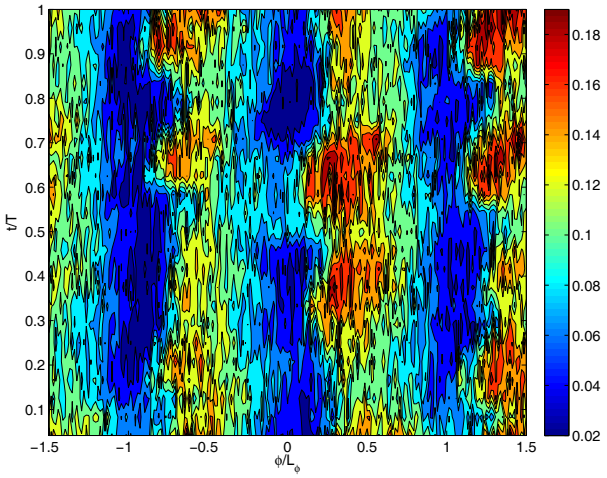

Re=25,000, Low TI, Timing j, u'/U_e

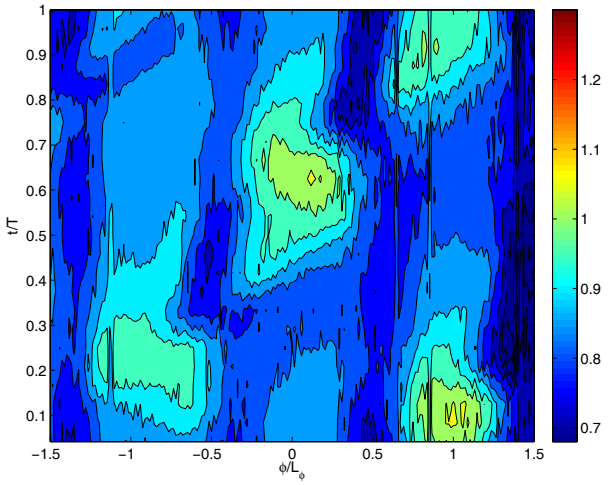

Re=50,000, Low TI, Timing a, Mean U/U_e

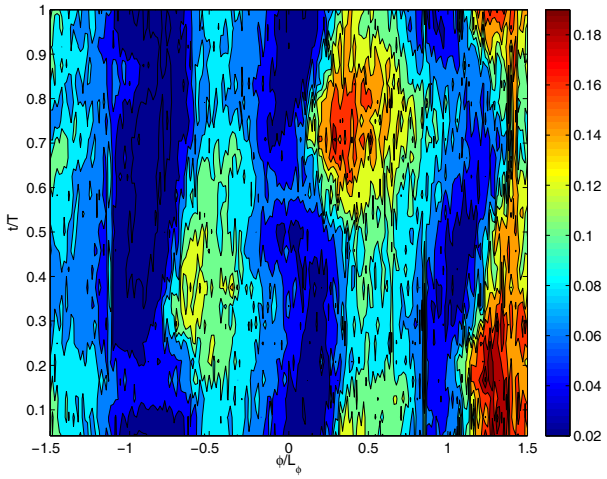

Re=50,000, Low TI, Timing a, u'/U_e

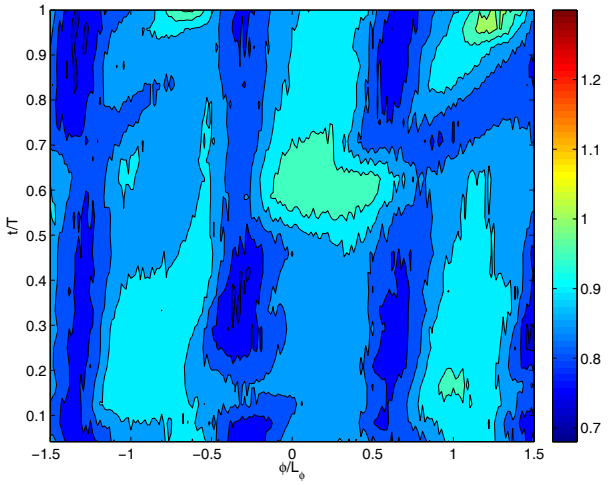

Re=50,000, Low TI, Timing b, Mean U/U_e

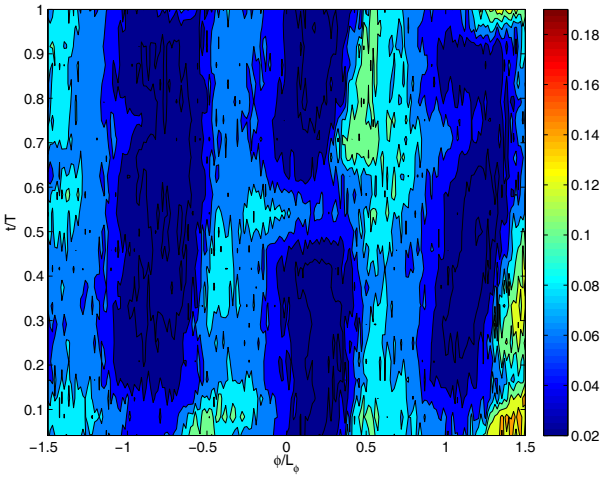

Re=50,000, Low TI, Timing b, u'/U_e

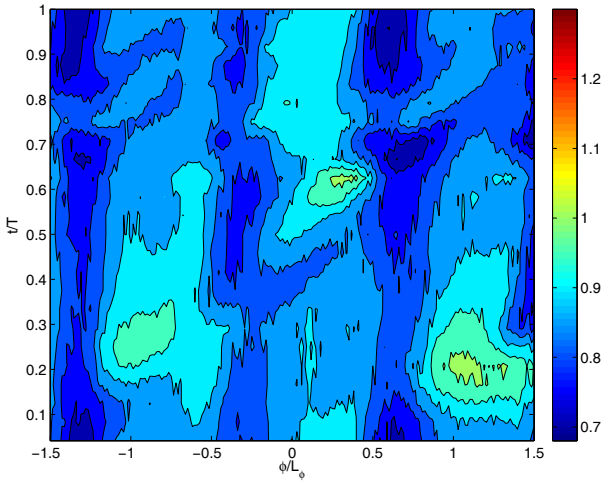

Re=50,000, Low TI, Timing c, Mean U/U_e

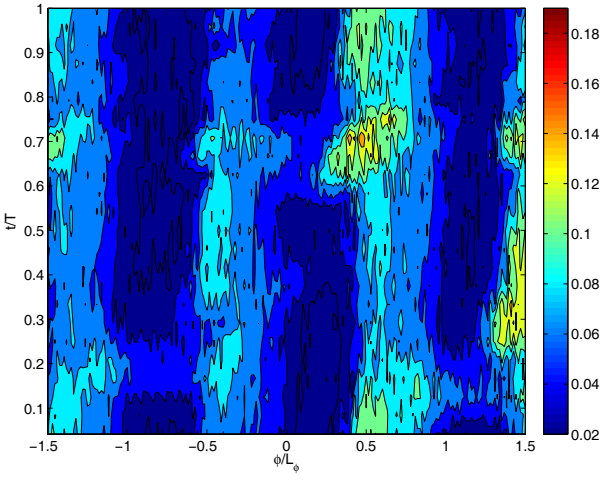

Re=50,000, Low TI, Timing c, u'/U_e

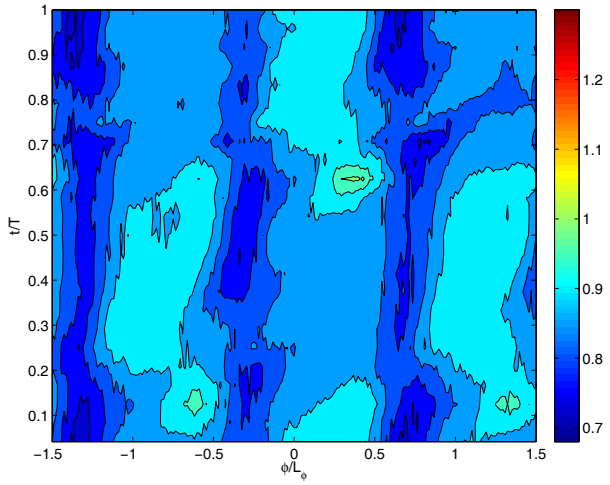

Re=50,000, Low TI, Timing d, Mean U/U_e

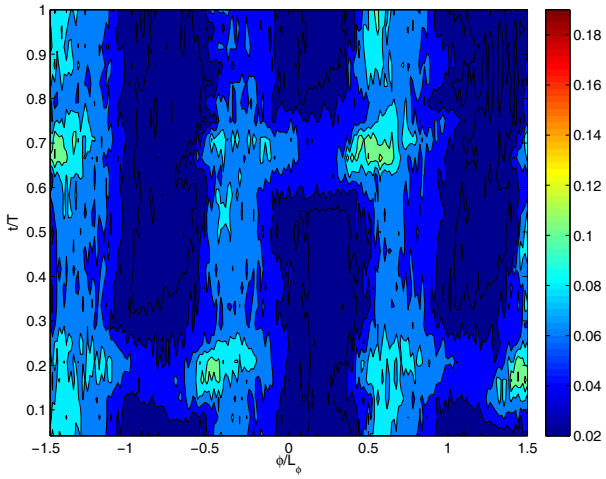

Re=50,000, Low TI, Timing d, u'/U_e

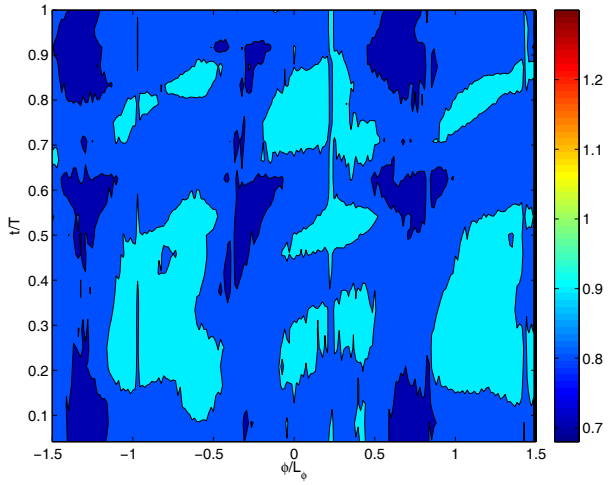

Re=50,000, Low TI, Timing e, Mean U/U_e

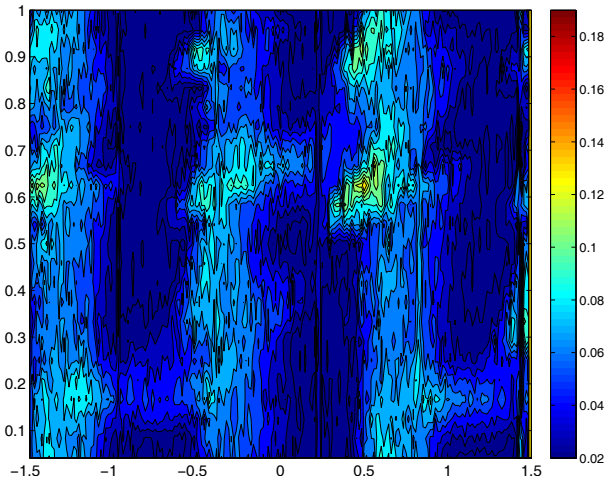

Re=50,000, Low TI, Timing e, u'/U_e

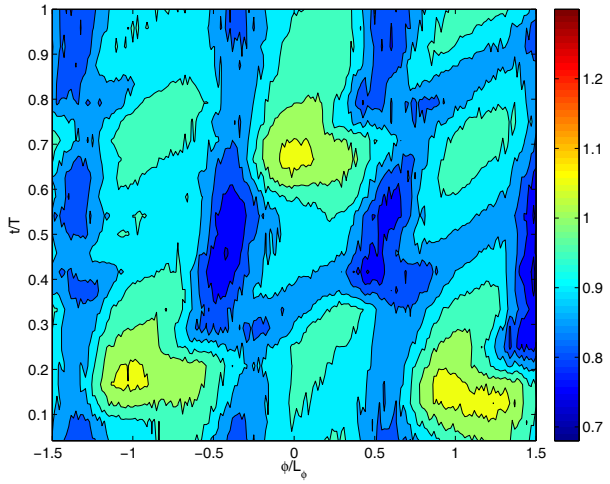

Re=50,000, Low TI, Timing g, Mean U/U_e

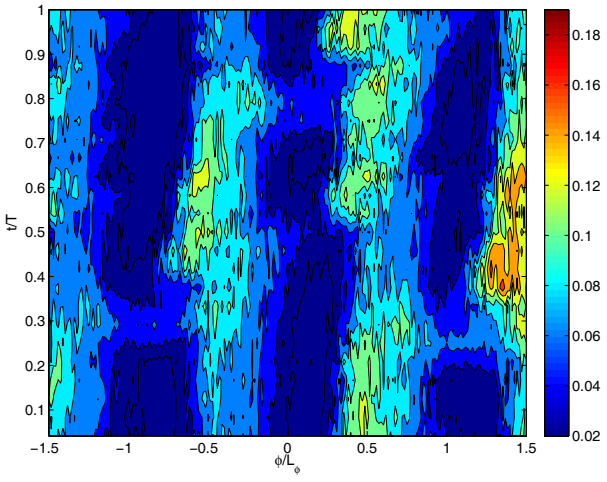

Re=50,000, Low TI, Timing g, u'/U_e

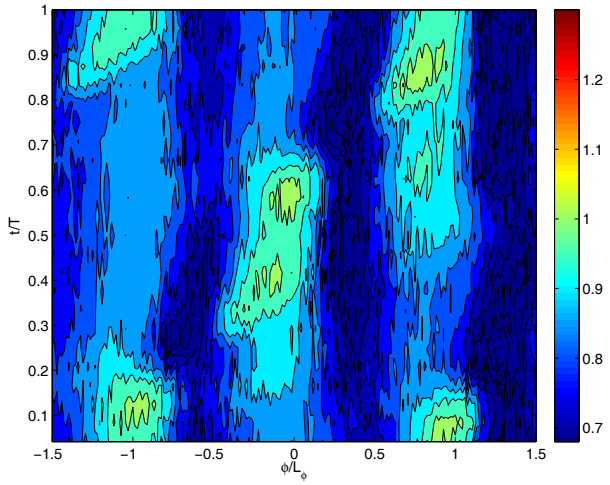

Re=25,000, High TI, Timing a, Mean U/U_e

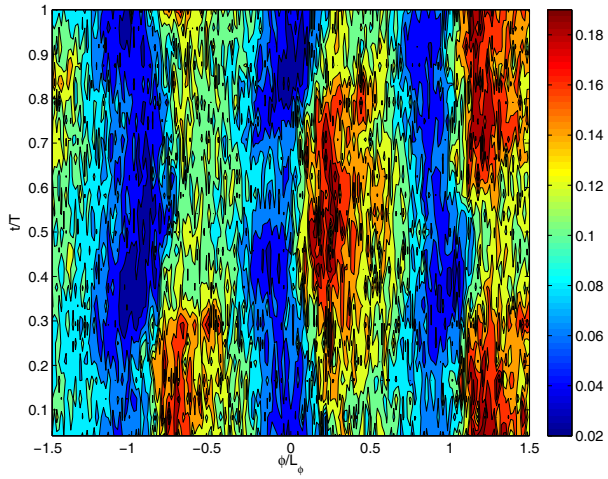

Re=25,000, High TI, Timing a, u'/U_e

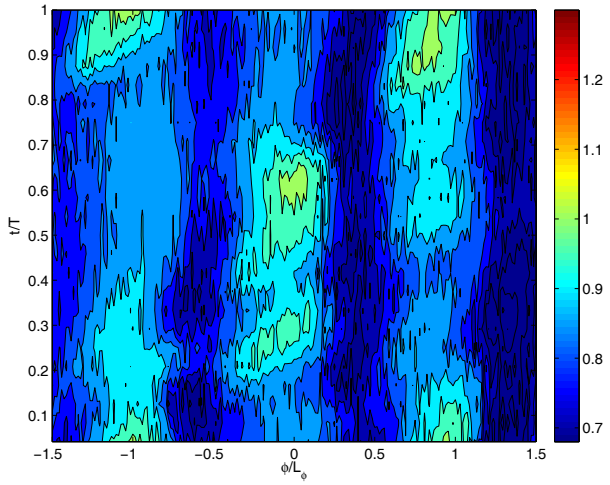

Re=25,000, High TI, Timing b, Mean U/U_e

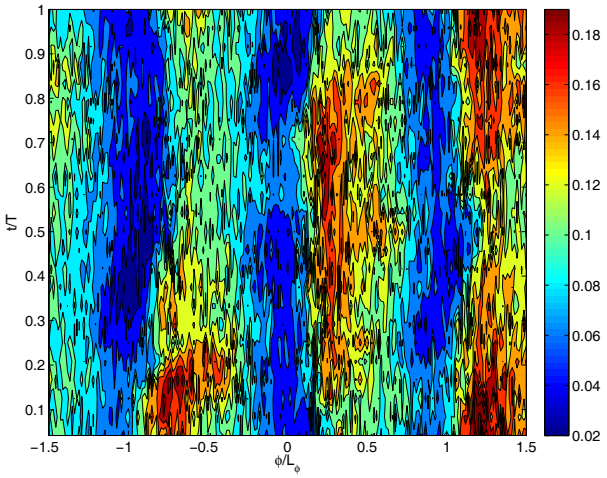

Re=25,000, High TI, Timing b, u'/U_e

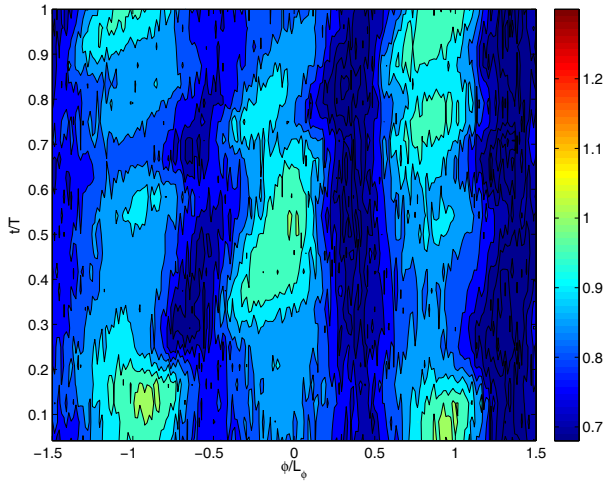

Re=25,000, High TI, Timing c, Mean U/U_e

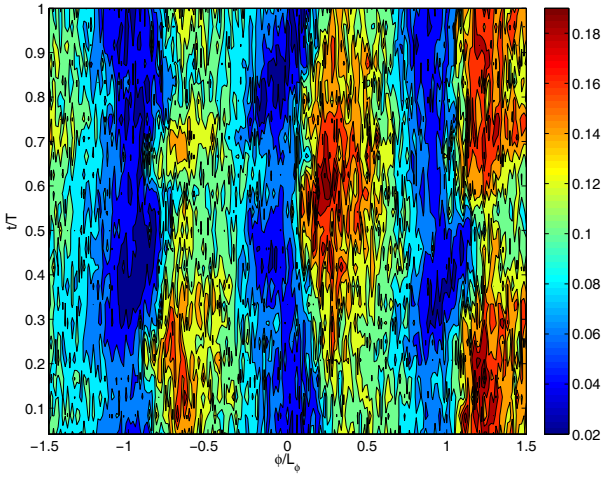

Re=25,000, High TI, Timing c, u'/U_e

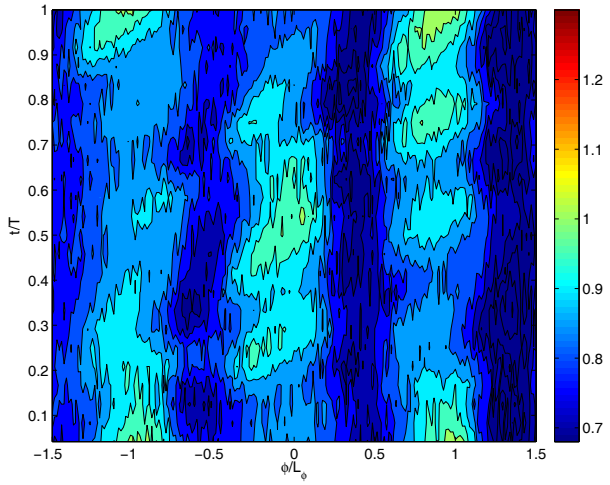

Re=25,000, High TI, Timing d, Mean U/U_e

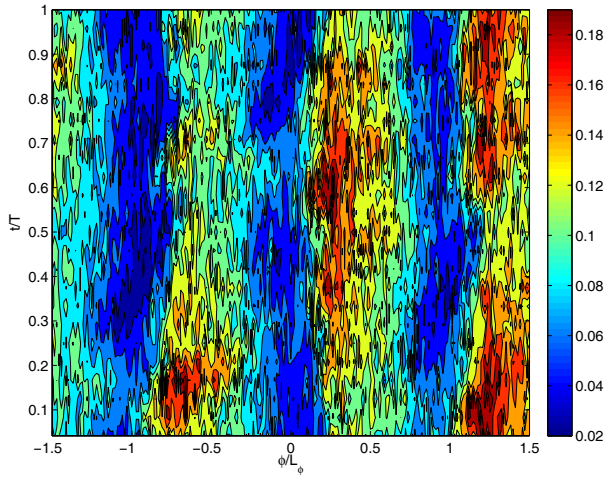

Re=25,000, High TI, Timing d, u'/U_e

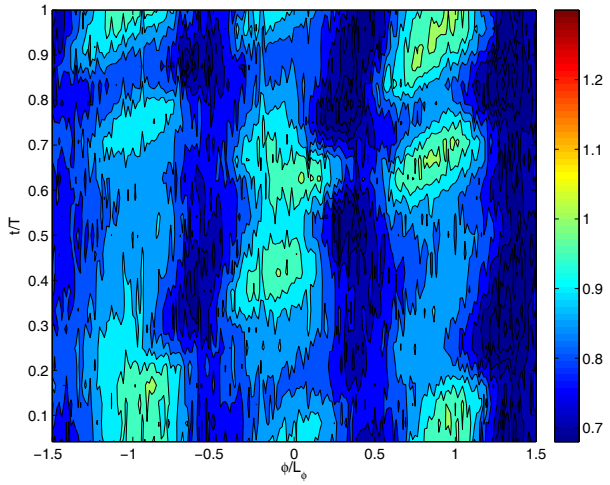

Re=25,000, High TI, Timing e, Mean U/U_e

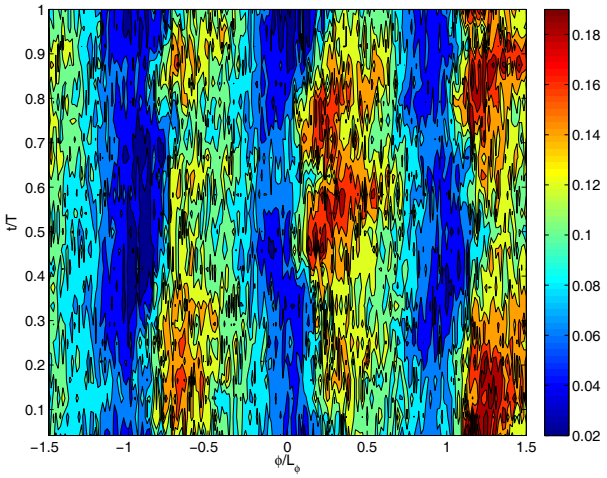

Re=25,000, High TI, Timing e, u'/U_e

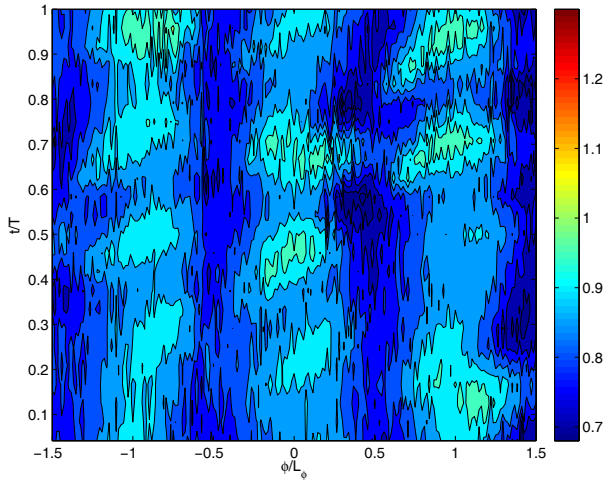

Re=25,000, High TI, Timing f, Mean U/U_e

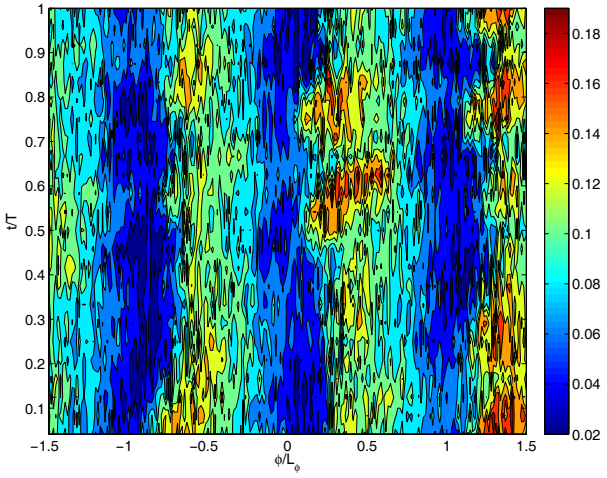

Re=25,000, High TI, Timing f, u'/U_e

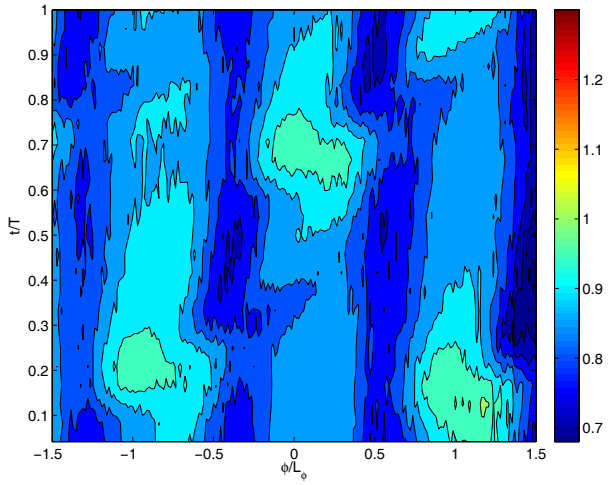

Re=50,000, High TI, Timing a, Mean U/U_e

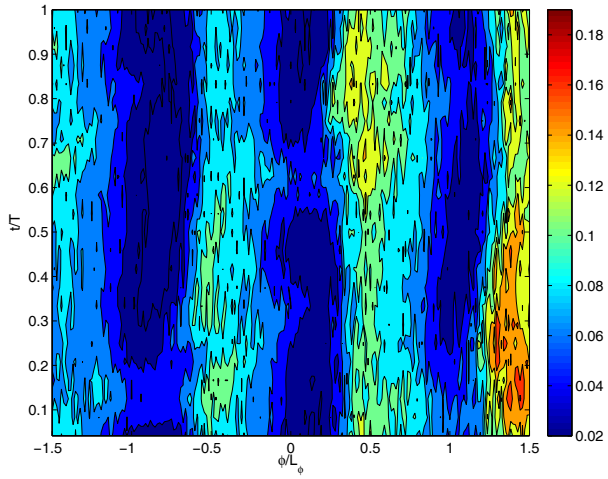

Re=50,000, High TI, Timing a, u'/U_e

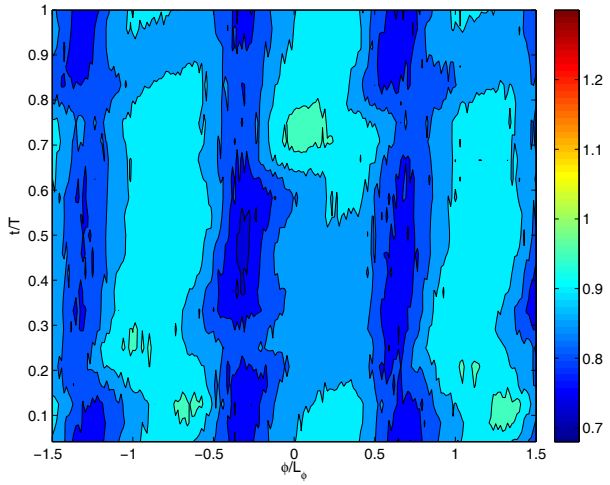

Re=50,000, High TI, Timing b, Mean U/U_e

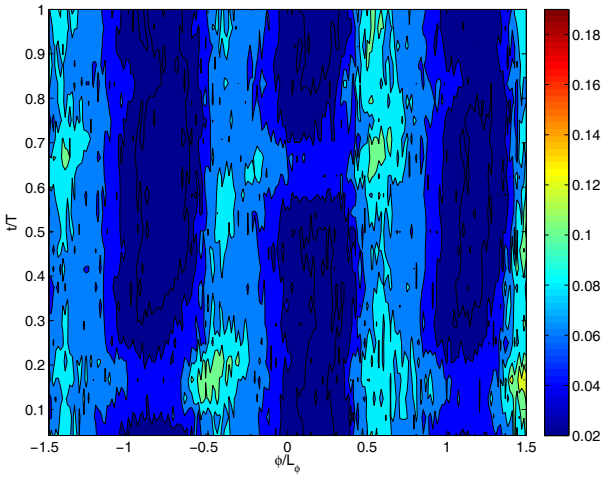

Re=50,000, High TI, Timing b, u'/U_e

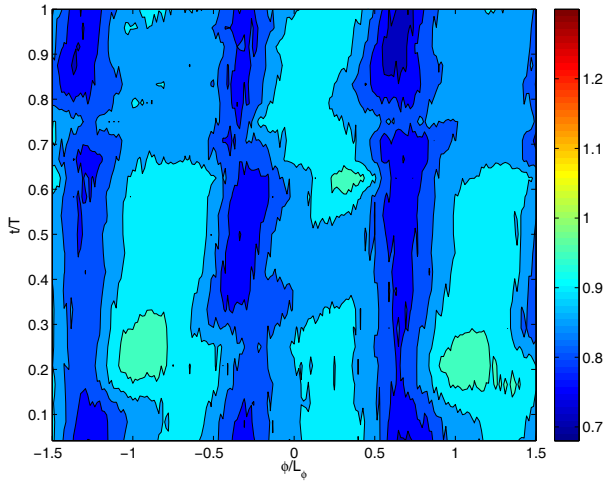

Re=50,000, High TI, Timing c, Mean U/U_e

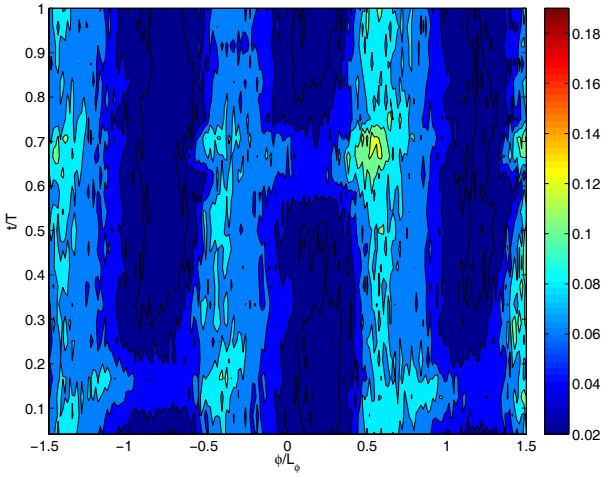

Re=50,000, High TI, Timing c, u'/U_e

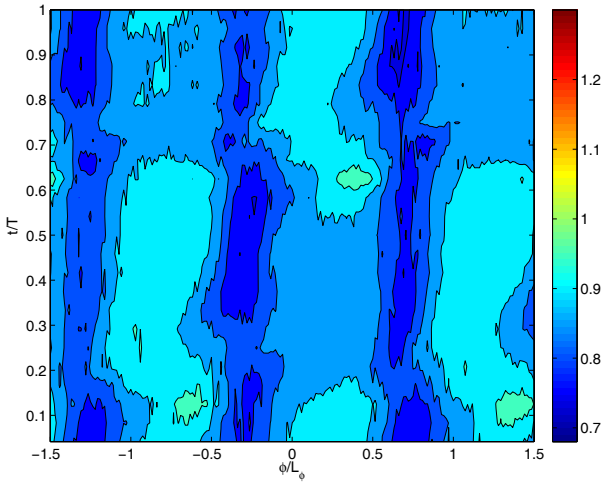

Re=50,000, High TI, Timing d, Mean U/U_e

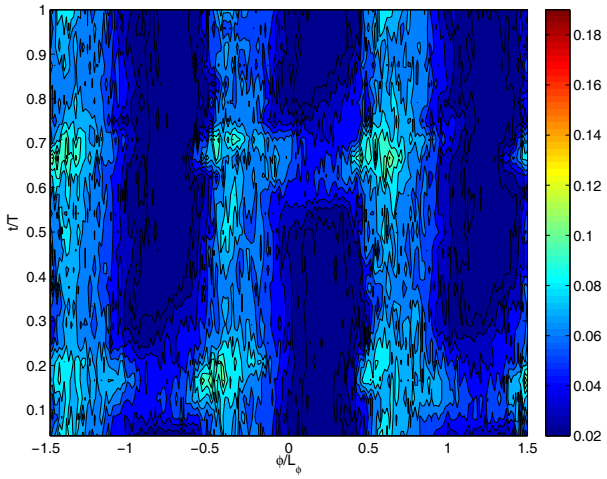

Re=50,000, High TI, Timing d, u'/U_e

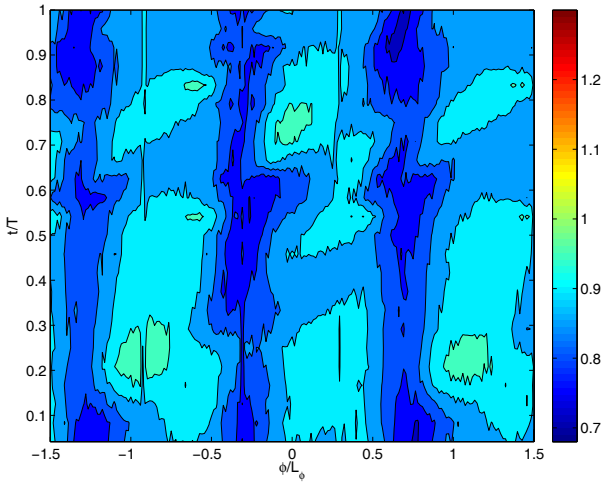

Re=50,000, High TI, Timing e, Mean U/U_e

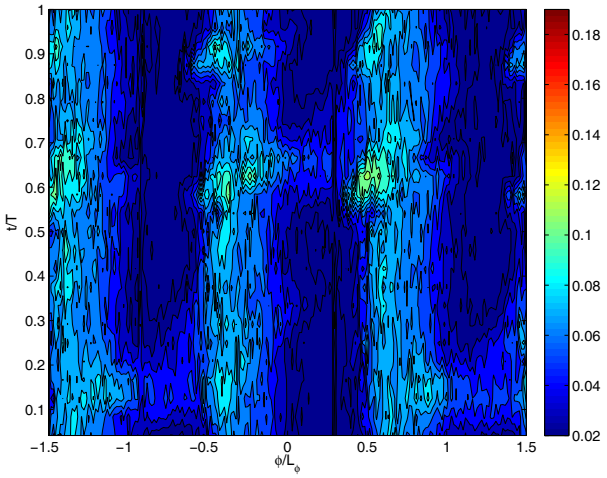

Re=50,000, High TI, Timing e, u'/U_e

Appendix C

Experimental Data Archive

A supplementary CD–ROM is available containing data files with processed experimental data from the study and text files with explanations of the file formats for the data.

The complete PDF file of Part I of this report (NASA/CR-2012-217415) along with Part II (NASA/CR-2012-217416) and Part III (NASA/CR-2012-217417), are also on the CD–ROM. The CD–ROM can be obtained from the Center for AeroSpace Information (CASI) Web site at http://www.sti.nasa.gov.

REPORT DOCUMENTATION PAGE		Form Approved OMB No. 0704-0188

1. REPORT DATE *(DD-MM-YYYY)*	2. REPORT TYPE	3. DATES COVERED *(From - To)*
01-09-2012	Final Contractor Report	January 2007 to September 2010

4. TITLE AND SUBTITLE	5a. CONTRACT NUMBER
Flow Control Under Low-Pressure Turbine Conditions Using Pulsed Jets Final Report	NNC07IA10I; N00189-07-P-A253
	5b. GRANT NUMBER
	5c. PROGRAM ELEMENT NUMBER
6. AUTHOR(S) Volino, Ralph, J.; Ibrahim, Mounir, B.	**5d. PROJECT NUMBER**
	5e. TASK NUMBER
	5f. WORK UNIT NUMBER WBS 561581.02.08.03.47.02.01
7. PERFORMING ORGANIZATION NAME(S) AND ADDRESS(ES) United States Naval Academy Annapolis, Maryland 21402	**8. PERFORMING ORGANIZATION REPORT NUMBER** E-18086
9. SPONSORING/MONITORING AGENCY NAME(S) AND ADDRESS(ES) National Aeronautics and Space Administration Washington, DC 20546-0001	**10. SPONSORING/MONITOR'S ACRONYM(S)** NASA
	11. SPONSORING/MONITORING REPORT NUMBER NASA/CR-2012-217415

12. DISTRIBUTION/AVAILABILITY STATEMENT
Unclassified-Unlimited
Subject Categories: 02, 05, 07, and 34
Available electronically at http://www.sti.nasa.gov
This publication is available from the NASA Center for AeroSpace Information, 443-757-5802

13. SUPPLEMENTARY NOTES
This report contains a supplemental CD-ROM containing detailed data along with the full text PDF files of this report and NASA/CR-2012-217416 and NASA/CR-2012-217417. The CD-ROM can be obtained from the Center for AeroSpace Information (CASI) Web site at http://www.sti.nasa.gov
Grant technical monitors, Anthony J. Strazisar, Office of the Chief Scientist, Glenn Research Center, organization code ASOO, James D. Heidmann, Aeropropulsion Division, Glenn Research Center, organization code RTTO, David E. Ashpis, Aeropropulsion Division, Glenn Research Center, organization code RTTO, ashpis@nasa.gov

14. ABSTRACT
This publication is the final report of research performed under an NRA/Cooperative Interagency Agreement, and includes a supplemental CD-ROM with detailed data. It is complemented by NASA/CR-2012-217416 and NASA/CR-2012-217417 which include a Ph.D. Dissertation and an M.S. thesis respectively, performed under this contract. In this study the effects of unsteady wakes and flow control using vortex generator jets (VGJs) were studied experimentally and computationally on the flow over the L1A low pressure turbine (LPT) airfoil. The experimental facility was a six passage linear cascade in a low speed wind tunnel at the U.S. Naval Academy. In parallel, computational work using the commercial code FLUENT (ANSYS, Inc.) was performed at Cleveland State University, using Unsteady Reynolds Averaged Navier Stokes (URANS) and Large Eddy Simulations (LES) methods. In the first phase of the work, the baseline flow was documented under steady inflow conditions without flow control. URANS calculations were done using a variety of turbulence models. In the second phase of the work, flow control was added using steady and pulsed vortex generator jets. The VGJs successfully suppressed separation and reduced aerodynamic losses. Pulsed operation was more effective and mass flow requirements are very low. Numerical simulations of the VGJs cases showed that URANS failed to capture the effect of the jets. LES results were generally better. In the third phase, effects of unsteady wakes were studied. Computations with URANS and LES captured the wake effect and generally predicted separation and reattachment to match the experiments. Quantitatively the results were mixed. In the final phase of the study, wakes and VGJs were combined and synchronized using various timing schemes. The timing of the jets with respect to the wakes had some effect, but in general once the disturbance frequency was high enough to control separation, the timing was not very important.

15. SUBJECT TERMS
Gas turbines; Tubomachinery; Turbine; Low pressure turbine; Turbulence; Flow control; Synthetic jets; CFD; LES; Turbulence models; Wakes; Separation; Vortex generated jets

16. SECURITY CLASSIFICATION OF:			17. LIMITATION OF ABSTRACT	18. NUMBER OF PAGES	19a. NAME OF RESPONSIBLE PERSON
a. REPORT	b. ABSTRACT	c. THIS PAGE			STI Help Desk (email:help@sti.nasa.gov)
U	U	U	UU	428	19b. TELEPHONE NUMBER *(include area code)* 443-757-5802

Standard Form 298 (Rev. 8-98)
Prescribed by ANSI Std. Z39-18